CHEMICAL ENGINEERING RESEARCH

Reports of the 4th year research projects in the Department of Chemical Engineering at Imperial College London

VOLUME 1

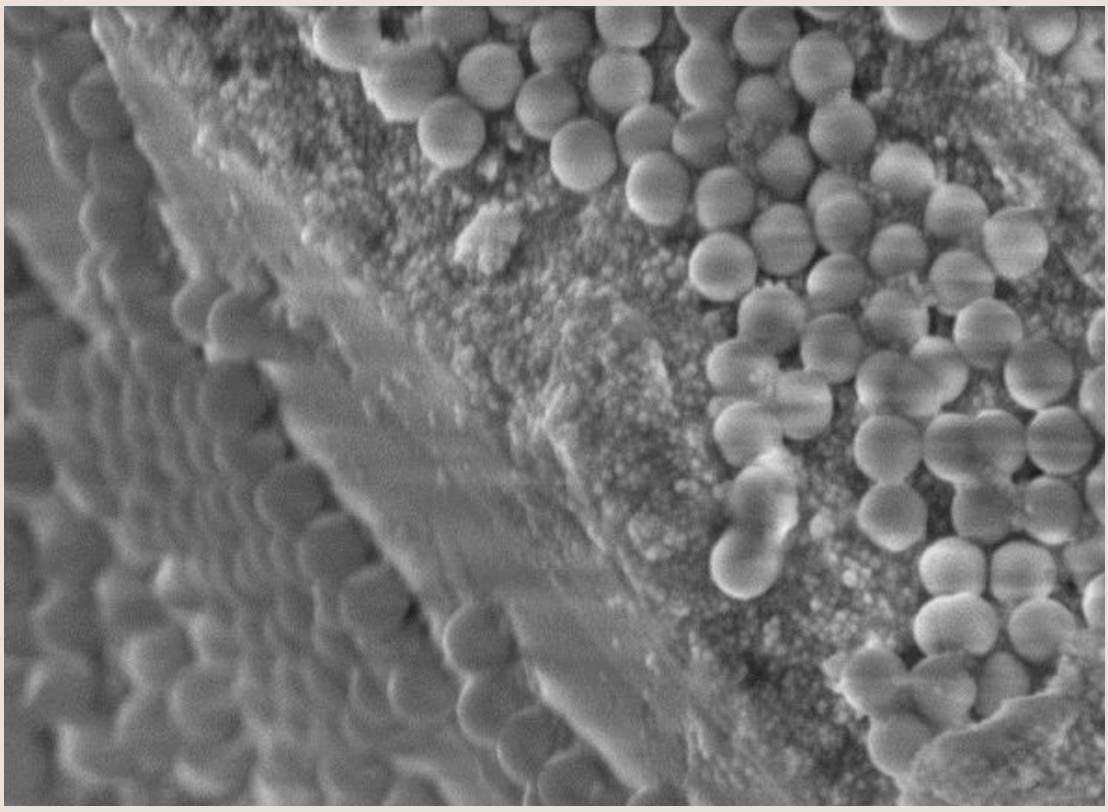

Edited by Erich A. Müller

February, 2019

CHEMICAL ENGINEERING RESEARCH

Reports of the 4th year research projects
in the Department of Chemical Engineering
at Imperial College London

Edited by Erich A. Müller

Volume 1

2019

9 781916 005006

© The Author(s) 2019.
Published by Imperial College London, London SW7 2AZ, UK
Contact details – e.muller@imperial.ac.uk

This book is a compilation of manuscripts created as part of a teaching assignment on the 4th year's Chemical Engineering CE4-01-1 course. Copyright in each paper rests with its authors. The author of each paper appearing in this book is solely responsible for the content thereof; the inclusion of a paper in the book shall not constitute or be deemed to constitute any representation by Imperial College London that the data presented therein are correct or sufficient to support the conclusions reached or that the experiment design or methodology is adequate.

The book is licensed under a Creative Commons Attribution-NonCommercial-NoDerivs 3.0 Unported (CC BY-NC-ND 3.0). Under this licence, you may copy and redistribute the material in any medium or format on the condition that: you credit the author, do not use it for commercial purposes and do not distribute modified versions of the work. When reusing or sharing this work, ensure you make the licence terms clear to others by naming the licence and linking to the licence text. Please seek permission from the copyright holder for uses of this work that are not included in this licence or permitted under UK Copyright Law. https://creativecommons.org/licenses/by-nc-nd/3.0/.

The information contained in this publication is being distributed without warranty of any kind, either expressed or implied. The responsibility for the interpretation and use of the material lies with the reader. In no event shall Imperial College London be liable for damages arising from its use.

E-ISBN 978-1-9160050-0-6

First published in 2019

Preface

This first volume of *Chemical Engineering Research* collects the unedited research project reports written by 4th year undergraduates (Class of 2019) of the M.Eng. course on Chemical Engineering in the Department of Chemical Engineering at Imperial College London. The research project spans for one term (Autumn) during the last year of the career and has an emphasis on independence, ability to plan and pursue original project work for an extended period, to produce a high quality report, and to present the work to an audience using appropriate visual aids. Students are also expected to produce a literature survey and to place their work in the context of prior art. The papers presented showcase the diversity and depth of some of the research streams in the department, but obviously only touch on a small number of research groups and interests. For a full description of the research at the department, the reader is referred to the departmental website[1].

The papers presented are in no particular order and they are identified by a manuscript number. Some papers refer to appendixes and/or supplementary information which are too lengthy to include. These files are available directly from the supervisors (see supervisor index at the end of the book). Some of the reports are missing, as they have been embargoed waiting for publication in peer-reviewed journals and or patent applications. A few reports correspond to industrial internships, called LINK projects, currently done at Shell.

Cover figure corresponds to an SEM image of a colloidal silica film (taken from the work of Carlos Sheppard and Leonardo Giustiniani, manuscript 49).

London, February 2019

[1] https://www.imperial.ac.uk/chemical-engineering

Title Index

paper	Title	page
1	Replicating Natural Antimicrobial Surfaces using Wrinkling	1
2	Continuous synthesis of glycidol from glycerol and dimethyl carbonate using A KF/sepiolite catalyst	11
3	Modelling the Carbon Sequestration Potential for Reforestation from Available Land	19
4	Contributions to the stability of particle stabilised oil foam.	29
5	Viscosity and Density of liquid Diisodecyl-phthalate with dissolved CO_2 at Temperatures between 313 and 373K and Pressures up to 800 bar	38
6	Acetylsalicylic Acid Loaded Chitosan/Tripolyphosphate Nanogels as Drug Delivery Systems	(*)
7	Effects of SBA-15 on the Kinetics of Protein Crystallisation	(*)
8	Novel Surfaces with Antimicrobial Properties	48
9	CAR-T Cell Therapy: A Unique Optimisation Problem	58
10	Mathematical Modelling to Investigate Systemic Plasma and Intracellular Area Under the Curve of Chemotherapy Drugs for Cancer Treatment	68
11	Computer-Aided Molecular and Process Design with Superstructure Optimisation of an Organic Rankine Cycle	78
12	Conceptual study to recover metals from end-of-life Li-ion batteries: Anodic electrodeposition of MnO_2 in the presence of Li^+, Co^{2+}, and Ni^{2+}	88
13	Imaging Velocity Fields and Analysing Bubble Shape in Yield-Stress Fluids	96

paper	Title	page
14	Technoeconomic Analysis: Modelling and Evaluating the Co-Electrolysis of CO_2 and H_2O for Syngas Production	105
15	Dual-polymer agglomeration of sand and ageing effects	115
16	Red Blood Cell-Derived Nanovesicles Drug Delivery System	(*)
17	Effects of polymer molecular weight and concentration, silica concentration and temperature on the relaxation of aqueous Silica-Poly(ethylene-oxide) “shake-gels”	125
18	A Comparative Analysis of the Supply Chain Models in Cold Chain Healthcare Products	134
19	Graphene exfoliation in green solvents	(*)
20	Selective Oxidation of Glucose towards Glucaric Acid using Monometallic Nanostructured Catalysts	144
21	Synthesis of a Chiral Microporous Metal Organic Framework Utilising Consumer Waste Plastics as Feedstock	154
22	A Facile Method for Fabrication of Superhydrophobic Coatings from Chicken Eggshells through Dry Blending	(*)
23	Investigation of multiphase flows in non-circular channels	162
24	Quantification of Fragrance Molecules and their Interactions on Cotton Fabrics	172
25	Thermo-economic Comparison of Subcritical and Transcritical Organic Rankine Cycles using a Medium- Temperature Geothermal Heat Source	182
26	Novel Organic Redox Flow Batteries	(*)
27	Waste-to-Resource Transformation: Gradient Boosting Models for Organic Solid Waste Prediction in the UK	(*)
28	Selective Direct Oxidation of Methane to Methanol Using Copper Containing Zeolites – Studies on the Effect of Importance of 8-Membered Ring on Activity of Reaction	192

paper	Title	page
29	Study of Metal Organic Frameworks for CO Purification.	(*)
30	Multi-Functional Metal Organic Frameworks for CO_2 Capture and Chiral Separation	202
31	Industrial Viability of Metal-Organic Frameworks in Post-Combustion Carbon Capture: The Effect of Impurities	212
32	Control of Porous Poly(2,6-diphenyl-p-phenylene oxide) Particle Size for Up-Scale Applications	222
33	Development of Sorbents from Sustainable Sources for Biobutanol Recovery	232
34	Development of a Computational Fluid Dynamics Model with Experimental Validation of an Improved Biomass Cookstove	242
35	Determination of physio-mechanical and thermo-stability of lyophilised model protein lysozyme in trehalose	252
36	α,α'-Dibromo-p-xylene Cross-Linking of Porous Membranes for Single Gas Permeation	(*)
37	The effect of porosity on the photocatalytic properties of boron nitride towards CO_2 photoreduction optimisation	261
38	Nature of lignin extracted using dissolution by p- toluenesulfonic acid hydrotrope	270
39	A Novel Techno-Economic Decision Support Framework for Biogas Exploitation in Waste Water Treatment Plants.	280
40	A Comparative Economic and Environmental Analysis of Ethylene Production via Ethane Steam Cracking and Bioethanol Dehydration	(*)
41	Simulating Fluid Adsorption on a Heterogeneous Surface	290
42	New insights into mechanically-assisted and mechano-catalysed reactions using Kraft lignin	300
43	Application of methane dry reforming, water-gas shift and carbon monoxide methanation to a chemical heat pump	311

paper	Title	page
44	Numerical Simulation and Classification of Multicomponent Polymer Precipitation	322
45	Characterisation of Distributive Three-site Phosphorylation by Parametric Scanning	332
46	Techno-Economic Analysis of the Ionic Liquid Recycle of the ionoSolv Process for Biomass Pretreatment	339
47	Modelling of Natural Gas Supply Chain Construction and Investment Pathways in Regions with Minimal Existing Infrastructure	349
48	Polymerisation of Kraft Lignin via Catalytic Oxidation with MnTACN	(*)
49	Development and Investigation of Hydrophobic Silica Nanoparticles.	359
50	Viability of Hybrid Solar PV-thermal Systems for Residential Applications in Europe: Techno-Economic Considerations	368
51	Techno-Economic Analysis of Solid Oxide Electrolysis Cells in the Production of H2, CO and Syngas	(*)
52	Assessing and Understanding Prakti Cookstove Corrosion	378
53	An Investigation into HFC Transition Strategies for a Major Food Retailer	388
54	Organic Redox-Active Materials for Flow Batteries	(*)
55	Corrosion-Resistant Sol-Gel Coatings for 304 Stainless Steel Cookstoves.	398
56	Assessing the Environmental Impact of Building the Northwest Runway at Heathrow Airport	408
57	A Nash Equilibrium Approach to Understanding the Methionine Salvage Pathway	418
58	The Influence of Soft Templates on Nucleation in Protein Crystallisation	(*)

paper	Title	page
59	Tuning and Non-Process Applications of a Novel Real-Time Optimisation Algorithm	(*)
60	Enzymatic saccharification of pretreated lignocellulosic biomass for downstream catalytic conversion of sugars to hydrocarbons	428
61	Analysis and modelling of immobilized β-1,4-galactosyltransferase for an artificial Golgi reactor	436

(*) These papers have been removed by request of the authors and/or supervisors

Author and Supervisor index at the end of the book (page 446)

Replicating Natural Antimicrobial Surfaces Using Wrinkling

Del-Wyn Ang and Shyang Shin Tan

Department of Chemical Engineering, Imperial College London, London SW7 2AZ, UK

Abstract

We investigate the possibility of replicating the pattern and size of nanostructures present on natural antimicrobial surfaces, such as cicada and dragonfly wings, by using plasma treatment and compressive stress to initiate the wrinkling process on the surface of polydimethylsiloxane. Collecting data on the dimensions of these nanostructures from literature, they are found to be 100 to 500 nm in height, 40 to 110 nm in base diameter, 40 to 120 nm in centre to centre spacing and 0.5 to 5.5 in aspect ratio. The hypothesis of using the wrinkling process to create a pattern similar to that observed on the natural surfaces is proven to be possible by superimposing the sinusoidal wrinkles in orthogonal directions. By conducting wrinkling experiments varying the plasma exposure dose (plasma power × plasma exposure time), D, it is found qualitatively through laser diffraction that the wavelength, λ, is proportional to D. Through quantified results using a reflected light microscope, λ is in the range of 2 to 7 μm and confirmed to have a logarithmic dependence on D for 0.25 to 60 kJ. Using an atomic force microscope to study the topography of the wrinkled surface, the amplitude is measured, and the aspect ratio is calculated to be approximately 0.1. We conclude by discussing the limitations of the current experimental conditions and the capabilities in producing nanostructures of similar scales through modification of the conditions, which may result in other mechanically induced instability processes.

Introduction

Deaths attributed to antimicrobial resistance (AMR), is forecasted to explode from 700,000 in 2016 to 10,000,000 in 2050. An increase of about 1330% in only 34 years; deaths from AMR will not only overtake the deaths from cancer, but also cause the global economic output to shrink by 100 trillion USD (Review on Antimicrobial Resistance, 2016).

AMR is a resistance which microbes (bacteria, viruses, fungi and parasites) develop when some of them survive exposure to antimicrobial drugs, which were supposed to kill them. These drug resistant strains will continue to grow and spread, leading to the development of 'superbugs', which are extremely difficult to treat with the current armoury of medicines. The overuse of antimicrobials has escalated the rate of AMR development, and the current way of treating disease, by developing new drugs to fight against these superbugs, is unsustainable. This leads to us fighting against a fast-growing enemy with a rapidly depleting 'weapon stockpile' (Review on Antimicrobial Resistance, 2016).

These microbes will adhere to most surfaces, from washroom floors to medical implants. The biofilms formed by the microbes are usually pathogenic in nature (Jamal, et al., 2018) and their complete removal is extremely difficult (Lewis, 2001). Therefore, it is of paramount importance to develop a new method to kill these microbes before they can form biofilms, one which they cannot form a resistance to.

In the natural world, there are some surfaces which possess antimicrobial properties. Originating some 480 million years ago (Misof, et al., 2014), insects are one of the oldest surviving classes of animals and survival of this class of animals up till today must be a result of unique features, refined through years of evolution. Cicada and dragonfly wings, for example, have been observed to be able to kill microbes by using its topography. Since this mechanism relies on physical features and does not involve external chemicals or drugs, the bacteria are not able to develop a resistance to it (Yi, et al., 2018). Replication of these surfaces, if successful and economically viable, will have the potential to save millions of lives and protect vulnerable people in places such as schools, hospitals and hospices. Thus, this paper aims to investigate the possibility of replicating these natural surfaces.

Background

Inspiration for Biomimetic Nanostructures

Inspiration for this paper came from an accidental discovery of natural antimicrobial surfaces where the wings of cicada were found to decompose much slower than their bodies (Figure 1(i)), which means that the wings must possess some form of antimicrobial property (Power, 2017). When studied under atomic force microscopy (AFM) it was found that the wings were not flat but were composed of tightly packed nanopillars (Figure 1(ii)).

Studying the effect of these nanopillars on the antimicrobial property through a confocal laser scanning microscope, live bacteria introduced onto the wing surface were killed with great efficiency. Further studies using a scanning electron microscope showed that the wings were still efficient in killing the bacteria introduced onto it even when coated with a thin gold film. Therefore, the death of the bacteria was attributed mainly to the physical topography of the wing, rather than any surface chemistry the wing might possess (Watson, et al., 2015). Shortly after this discovery, dragonflies were also found to possess wings with similar antimicrobial nanostructures (Ivanova, et al., 2013).

Theory of Antimicrobial Mechanisms

When microbes adhere to a favourable surface, they start to proliferate and form a microcolony that binds irreversibly to the surface (Høiby, et al., 2011). The microbes produce an extracellular polymeric substance (EPS), which are polymers

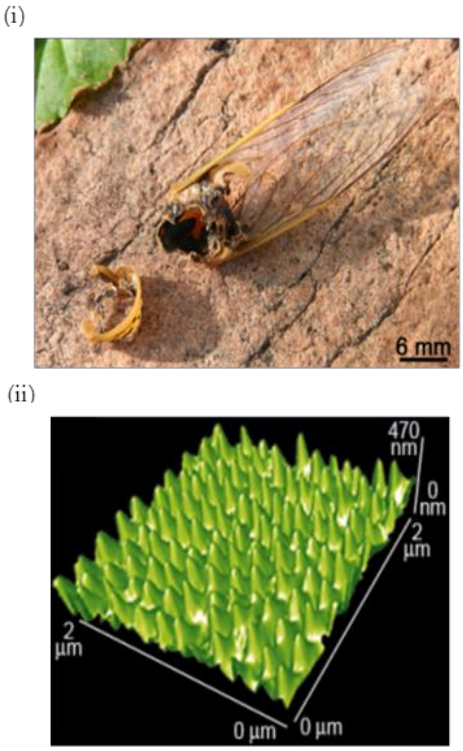

Figure 1 (i) Image of cicada remnants, showing the difference in decomposition between the cicada's wings and body. (ii) AFM image of *P. claripennis* wing. Images from (Watson, et al., 2015).

with multiple purposes, most notably for biofilm structure and growth (Staudt, et al., 2004). Thus, for a surface to be considered physically antimicrobial, it must at least be microbicidal, able to kill microbes when they attach to it, or anti-biofouling, preventing their attachment (Hasan, et al., 2013). These antimicrobial mechanisms are therefore key in preventing biofilm formation, which according to the National Institute of Health, are involved in 80% of all microbial infections (Joo & Otto, 2012).

The microbicidal mechanism, where microbes are killed by the nanopillars on the surfaces, is depicted in Figure 2(i) with bacteria as an example. Bacteria secretes EPS when it attaches to the surface and due to the large surface area between the EPS layer and the surface nanopillars, a strong adhesion force is formed. This strong adhesion creates a large shear force when it attempts to move across the surface which stretches, and ultimately tears, the bacteria's cell membrane apart (Bandara, et al., 2017).

The anti-biofouling mechanism on the other hand, prevents the attachment and colonisation of microbes. For example, lotus and taro leaves possess a hierarchical surface structure, consisting of microscale papillae on the leaves densely coated with nanoscale wax tubules (Ma, et al., 2011). This hierarchical structure traps air in between the nanostructures, preventing the penetration of water, giving rise to its superhydrophobicity, where the water contact angle is larger than 150°. Dirt and microbes prefer to attach to water droplets formed on the leaves rather than the surface itself. Consequently, when the water droplets roll off the leaf, they clean it by removing the dirt and microbes (Figure 2(ii)). This self-cleaning property is also known as the 'lotus effect' (Yamamoto, et al., 2015).

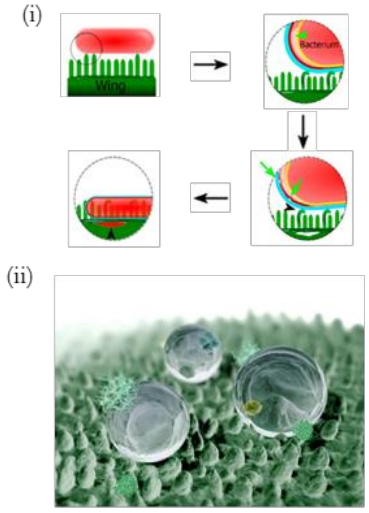

Figure 2 (i) Illustration of the microbicidal mechanism with bacteria as an example. Image adapted from (Bandara, et al., 2017). (ii) Illustration of the anti-biofouling mechanism, the lotus effect in this case. Image by (Thielicke, 2007).

Based on these two mechanisms, the common similarity and key component for a physically antimicrobial surface is the presence of nanostructures. The antimicrobial mechanism of interest for this paper is the microbicidal one, as it does not rely on water like the anti-biofouling mechanism does. Now that the focus has been chosen, to get a better understanding on the dimensions of these nanostructures, information from literature on the height, base diameter and centre to centre spacing of these nanostructures on cicada and dragonfly wings were collected in Table 1.

Current Production Methods of Artificial Surfaces

Some headway has already been made in creating biomimetic artificial surfaces through methods such as reactive ion etching and nanoimprint lithography. The nanostructures on the artificial surfaces created through these methods have also been observed to be able to kill microbes, like the natural surfaces they mimic. As such, it is important to understand the current production methods and their limitations.

Reactive ion etching involves the use of the fourth state of matter, plasma (Karouta, 2014). It exploits the synergy between high energy ion bombardment and reactive chemical species to etch the surface. The advantage of this process is its anisotropic character, since the direction of ion bombardment can be controlled, which makes structures with high aspect ratios and nearly vertical sidewalls possible (Franssila & Sainiemi, 2013).

Nanoimprint lithography is a process where a pattern is stamped onto a resist (resin). The resist is applied onto a wafer surface using inkjet technology. A mask (mold), with the negative of the pattern, is pressed like a stamp onto the resist,

Table 1 Data on the mean dimensions of nanostructures present on insect wings from literature.

Insect	*Species*	*Height (nm)*	*Diameter (nm)*	*Spacing (nm)*	*References*
Cicada	*A. bindusara*	234	84	91	(Sun, et al., 2009)
	A. spectabile	182	207	251	(Kelleher, et al., 2016)
	C. aguila	182	159	187	(Kelleher, et al., 2016)
	C. atrata	462	85	90	(Sun, et al., 2012)
	C. maculata	309	97	92	(Sun, et al., 2009)
	D. nagarasingna	316	128	47	(Sun, et al., 2009)
	D. vaginata	363	132	56	(Sun, et al., 2009)
	L. bifuscata	200	90	117	(Sun, et al., 2009)
	M. conica	159	95	115	(Sun, et al., 2009)
	M. dorsatus	250	196	227	(Oh, et al., 2017)
	M. durga	257	89	89	(Sun, et al., 2009)
	M. hebes	164	85	95	(Sun, et al., 2009)
	M. intermedia	241	156	165	(Kelleher, et al., 2016)
	M. microdon	208	82	89	(Sun, et al., 2009)
	M. mongolica	417	128	47	(Sun, et al., 2009)
	M. opalifer	418	148	48	(Sun, et al., 2009)
	M. septendecim	83.5	167	252	(Nowlin, et al., 2015)
	N. pruinosus	405	197	218	(Oh, et al., 2017)
	N. tibicen	183	104	175	(Nowlin, et al., 2015)
	P. claripennis	200	100	170	(Hasan, et al., 2013)
	P. radha	288	137	44	(Sun, et al., 2009)
	P. scitula	282	84	84	(Sun, et al., 2009)
	T. jinpingensis	391	141	46	(Sun, et al., 2009)
	T. vacua	446	141	44	(Sun, et al., 2009)
Dragonfly	*A. multipunctata*	250	80	180	(Mainwaring, et al., 2016)
	D. bipunctata	250	80	180	(Mainwaring, et al., 2016)
	H. papuensis	250	80	180	(Mainwaring, et al., 2016)
	O. villosovittatum	250	47	-	(Bandara, et al., 2017)
	P. obscurus	241	53	123	(Nowlin, et al., 2015)
	S. vulgatum	215	140	-	(Rajendran, et al., 2012)

creating the pattern's positive on it, and ultraviolet light is subsequently used to solidify the resist. The mask is then reused for the next batch (Lapedus, 2018). High resolution and reproducibility are some of the major advantages of nanoimprint lithography (Chou, et al., 1996).

Since the surfaces created through these methods were observed to be antimicrobial, data on the dimensions of their nanostructures (height, base diameter and centre to centre spacing) were collected from literature and are presented below in Table 2.

The common issue with these methods is that although they can replicate the observed pattern and size of nanostructures on the natural surfaces, they are very expensive. For example, a nanoimprint lithography machine alone can cost millions of dollars, not inclusive of the stamp, which costs tens of thousands of dollars, and other materials required (Simprint Nanotechnologies Ltd, 2016).

Theory Behind the Wrinkling Process

In nature, wrinkles can be observed on a large range of scales, such as the surface of the Earth's crust (km) (American Profile, 2001), dried fruits (cm) and aging skin (mm). Thus, the creation of nanoscale wrinkles should also be possible. Since wrinkling is a stress-driven and spontaneous process due to mechanically induced instability, it may serve as an economically viable method to produce these nanostructures.

Mechanically induced instability has been studied since a few hundred years ago. A particular example is the elastic instability introduced by Euler, explaining the theory behind the buckling of columns. When a compressive stress exceeds the critical load, bending or buckling of the structure is observed, which is related to the rigidity and length of the structure (Johnston, 1983). Wrinkling, which commonly happens on a stiff film on top of a soft substrate, is similar to buckling as it is driven by stress above a critical value.

Table 2 Data on the mean dimensions of nanostructures of biomimetic artificial surfaces from literature.

Production Method	***Surface Name***	***Height (nm)***	***Diameter (nm)***	***Spacing (nm)***	***References***
Deep Reactive Ion Etching	Nanostructured Silicon Supersurface	4000	220	-	(Hasan, et al., 2015)
Electrochemical Anodisation	Titanium Alloy Nanospike Surface	2000	10	2000	(Hizal, et al., 2015)
Nanoimprint Lithography	Nanopatterned Polymer Surface P600	300	215	595	(Dickson, et al., 2015)
	Nanopatterned Polymer Surface P300	300	190	320	(Dickson, et al., 2015)
	Nanopatterned Polymer Surface P200	210	100	170	(Dickson, et al., 2015)
Plasma Etching and Electrodeposition	Gold Nanostructured Surface	100	50	-	(Wu, et al., 2016)
Plasma Etching and Thermal Nanoimprinting	Nanostructured PMMA Film	490	160	300	(Kim, et al., 2015)
Reactive Ion Etching	Black Silicon	500	50	-	(Ivanova, et al., 2013)
	Diamond Nanocone Surface	1650	550	-	(Fisher, et al., 2016)
	Diamond Nanocone Surface	4000	650	-	(Fisher, et al., 2016)

In contrast to the buckling instability, during wrinkling the relatively stiffer and thinner film layer (thickness of film ≪ thickness of substrate) stays bonded to the soft, more elastic substrate and reorganises into highly-ordered sinusoidal wrinkles (Figure 3) instead of buckling or delaminating, to minimise the total energy in the bilayer structure (Huang, 2005). The more elastic substrate layer, on the other hand, deforms accordingly to maintain the inter-layer adhesion.

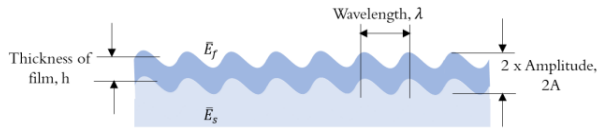

Figure 3 Schematic of a highly ordered sinusoidal wrinkled surface, showing its defined dimensions of wavelength, film thickness and amplitude.

Several methods can be used to create the film layer, namely surface fabrication and surface modification. Surface fabrication, such as dip coating (Chen & Crosby, 2014) and sputter coating (Cao, et al., 2014), may result in the delamination of the film during the stress relaxation process due to poor inter-layer adhesion. Surface modification on the other hand, uses plasma treatment or UV ozonolysis, which oxidises the substrate surface to form the film. Since the film is 'grown' from the substrate, it will have a better inter-layer adhesion, making it a better option.

In this paper, surface wrinkling will be demonstrated on polydimethylsiloxane (PDMS), the chosen soft substrate, due to the ease of handling. The surface of pre-strained PDMS is oxidised using plasma treatment, and the surface becomes glass-like (more information in Figure 4). The film has a plain-strain modulus, $\bar{E}_f$, of 1 to 3 GPa (Chung, et al., 2011), 1000 times higher than the plain-strain modulus of the initial substrate, $\bar{E}_s$, of approximately 2 MPa (Wilder, et al., 2006), causing the mismatch in elasticity. $\bar{E}$ can be related to the Young's modulus, E, by,

$$\bar{E} = \frac{E}{1 - \upsilon^2} \qquad [1]$$

where the Poisson ratio, υ, for the PDMS substrate is 0.5 (Johnston, et al., 2014).

The wavelength, λ, and amplitude, A, of the sinusoidal wrinkles, produced by the uniaxial pre-strain, ε, in the low deformation limit ($\varepsilon \leq 40\%$) (Cao, et al., 2014), can be described by using,

$$\lambda = 2\pi h \left(\frac{\bar{E}_f}{3\bar{E}_s}\right)^{\frac{1}{3}} \qquad [2]$$

$$A = h\left(\frac{\varepsilon}{\varepsilon_c} - 1\right)^{\frac{1}{2}} \qquad [3]$$

where h is the thickness of the film. The critical strain, ε_c, required to stimulate the formation of wrinkles is given by,

$$\varepsilon_c = \frac{1}{4}\left(\frac{3\bar{E}_s}{\bar{E}_f}\right)^{\frac{2}{3}} \qquad [4]$$

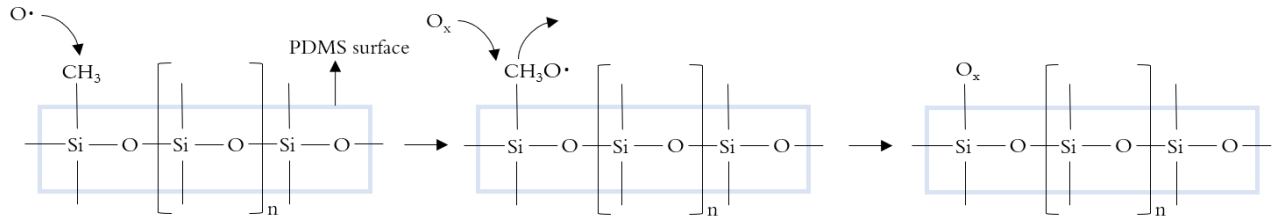

Figure 4 Chemical reaction at the PDMS surface during plasma treatment. Before the treatment, the structure has a $\bar{E}_s$ of approximately 2 MPa. The reactive oxygen radical, formed in the plasma, attacks the attached methyl group to form intermediate $CH_3O\cdot$. The unstable group then detaches and is replaced by another reactive oxygen species (Koh, et al., 2012). The SiO_x layer is glass-like and has a $\bar{E}_f$ in the range of 1 to 3 GPa.

The uniaxial strain on the bilayer structure mentioned will produce only one-directional sinusoidal wrinkles. In order to replicate the nanopillars observed on the cicada wing (Figure 1(ii)), a proposed hypothesis is to superimpose two sinusoidal wrinkles in orthogonal directions. The superimposition is simulated in MATLAB and shown in Figure 5.

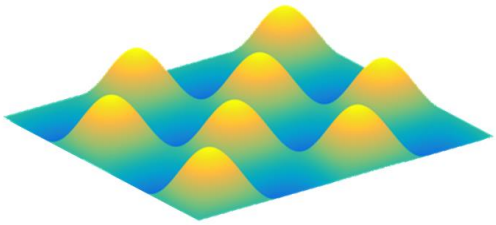

Figure 5 The surface plot of the superimposition of two sinusoidal waves in orthogonal directions, which shows great similarity with Figure 1(ii).

Leveraging on the information collected, this paper identifies the range of dimensions for antimicrobial nanostructures as a point of reference for comparison. In addition, this paper investigates the possibility of using the wrinkling process to replicate the observed pattern and size of these natural antimicrobial nanostructures, where characterisation of the dimensions will be done by using the low deformation limit equation (Equation 2) as a basis. Replication of the observed pattern will be the first objective, and replication of the observed size, will be the second.

Experimental Methods

PDMS Coupon Preparation

Slygard 184 silicone elastomer base and crosslinker from The Dow Chemical Company were used to prepare the PDMS substrate at a mass ratio of base to crosslinker of 10:1. After mixing it for five minutes, the mixture was placed in a degasifier under vacuum condition for 30 minutes to remove all the trapped air bubbles. 100 g of the mixture was cast on a 20.0 ± 0.05 cm by 20.0 ± 0.05 cm mold, making an approximately 2.60 ± 0.005 mm thick substrate, and cured in a Binder convection oven for 2 hours at 75 °C. After the PDMS was cured, it was cut into 50.00 ± 0.005 mm by 20.00 ± 0.005 mm coupons.

Creation of One-Directional (1D) Wrinkles

A PDMS coupon was clamped onto a strain stage, shown in Figure 6(i), and the sides were marked at the clamp points to monitor if the coupon slipped during the straining process. The original length, L_0, of the coupon was kept at approximately 16.00 ± 0.005 mm to ensure consistency. The PDMS coupon was given a ε to a final length, L_1, prior to oxidisation. The straining process is illustrated in Figure 6(ii). ε is given by,

$$\varepsilon = \left(\frac{L_1}{L_0} - 1\right) \times 100\% \qquad [5]$$

The plasma chamber used was a 40 kHz Diener Electronic Femto low-pressure plasma system, connected to a vacuum pump and an oxygen tank, which delivers oxygen at a pressure of 1 mbar to the chamber. The plasma power, P, was set at a constant value and the plasma exposure time, t, was varied to change the exposure dose, D, defined as,

$$D\ (J) = P\ (W) \times t\ (s) \qquad [6]$$

The strain stage was placed at the centre of the platform in the chamber and the vacuum pump was switched on to remove air from the chamber, as plasma requires vacuum condition. When the pressure had stabilised, the oxygen gas flow was turned on, and the plasma generator was switched on after three minutes, this ensures a constant pressure in the chamber. Once the desired plasma exposure time was reached, the ventilation was switched on, effectively stopping the plasma treatment process, and the gas flow and vacuum pump were then switched off. To ensure the consistent conditions in the plasma chamber, the plasma chamber was first warmed up by carrying out the plasma treatment process on an empty chamber for t of five minutes.

After the treatment, the strain stage was removed from the chamber and allowed to cool down for five minutes before releasing the strain. The strain was released by 0.1 mm over 10 seconds and then rested for 15 seconds, repeating until L_0 was achieved. Once the coupon has returned to L_0, it was unclamped from the strain stage in a cross-like manner to prevent any preferential strain field from forming.

Creation of Two-Directional (2D) Wrinkles

To create a 2D wrinkled surface, the 1D wrinkled surface needs to be pre-strained in the orthogonal direction. However, the glassy film created for the 1D wrinkled surface will be destroyed once stretched. To avoid this, the 1D wrinkled surface (master) was replicated onto another PDMS (replicated).

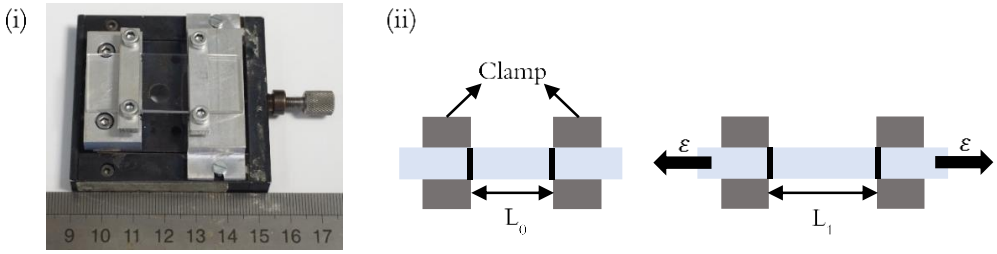

Figure 6 (i) Picture of strain stage used. (ii) Schematic illustration of the side view of the strain stage. The PDMS coupon was clamped and marked at the clamp points. PDMS coupon was then streched uniaxially by ε.

100 g of PDMS mixture was cast again on the mold and cured. Holes with the same dimensions as the master surface coupons were cut out, and the master surface coupons were placed into them with the wrinkled surface faced up. The mold was placed in a vacuum chamber for 45 minutes with liquid 95% n-octadecyltrichlorosilane (OTS) containing 5-10% branched isomers, from Alfa Aesar, in a small petri dish. The OTS vaporises under vacuum conditions and reacts with the PDMS surface forming a self-assembled monolayer (SAM). The SAM is created by the chemisorption of trichlorosilane head groups of the OTS onto the PDMS surface, forming a strong covalent bond. After sufficient time, the tail groups pack tightly, due to strong van der Waals forces, to form the monolayer (Dong, et al., 2006). This SAM ensures that the replicated PDMS can be easily peeled off. Another 100 g of PDMS mixture was cast onto the PDMS in the mold and cured. The replicated PDMS was peeled off, cut into coupons, given a ε in the orthogonal direction and went through the plasma treatment process again. The replication process is illustrated in Figure 8.

Wavelength Characterisation

The wavelength of the 1D wrinkled surface was characterized using the Olympus BX41M reflected light microscope with 50x magnification. The calibration for the image taken was 0.271 µm/pixel. Three images were taken at three different positions on the surface. The length of 20 λ was measured in pixels using ImageJ software, shown in Figure 7, and the average λ was then calculated using the equation below.

$$\lambda\ (\mu m) = \frac{Length\ of\ 20\ \lambda\ \times 0.271}{20} \qquad [7]$$

The average λ was calculated by averaging the λ obtained from each of the three different positions, while the positive and negative errors were the difference between the largest or smallest λ and the average λ.

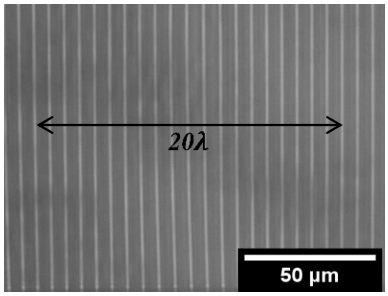

Figure 7 Reflected light microscope image of 1D wrinkled surface, showing the length of 20 λ.

Topography Characterisation

The topography of the wrinkled surface was scanned using atomic force microscopy (AFM) with the tapping mode of the Brucker Innova scanning probe. The tip used was Brucker 0.01 - 0.025 Ohm-cm Antimony (n) doped Si, with a spring constant of 40 N/m and resonant frequency of 300 kHz. The laser position was first adjusted to obtain the maximum detection before scanning, at approximately 2 V. Then, the cantilever was calibrated at auto mode, giving a suitable drive voltage. The scanning frequency and area were set at 0.8 kHz and 20 µm respectively. While scanning, drive voltage and PID parameters can be adjusted to produce better quality images. The built-in Brucker Nanodrive Analysis software was used to process the raw AFM data, allowing the extraction of data on surface features, such as λ and A, from the topography cross section.

Insect Nanostructure Observation

A LEO Gemini 1525 field emission gun scanning electron microscope (FEG SEM), was used for observation of the nanostructures on insect wings. 5.00 ± 0.005 mm by 5.00 ± 0.005 mm samples of the wings were cut, cleaned and coated with a thin gold film. The stage angle was set to 0° and the voltage was varied between 3.00 to 10.00 kV, to produce an image of higher resolution.

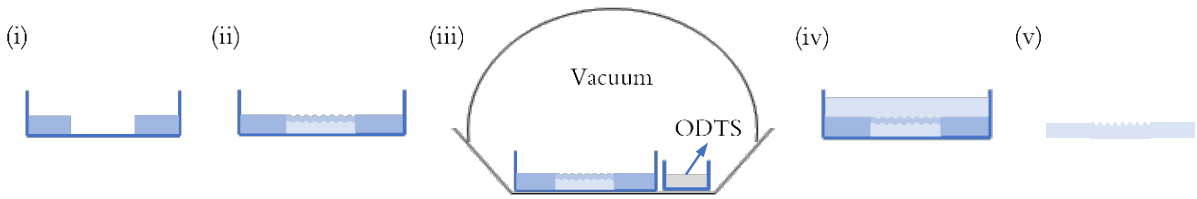

Figure 8 Schematic illustration of replicating the master wrinkled surface. (i) Hole with same dimensions as the master surface coupon was cut out. (ii) Master surface coupon put into the hole with wrinkles faced up. (iii) Vacuum condition allows OTS to vaporise and react with PDMS surface, forming a SAM. (iv) Liquid PDMS was poured onto the master surface and cured. (v) Replicated surface was peeled off.

Results and Discussions

Verification of Nanotopographies on Natural Surfaces

To verify the presence of nanostructures on these insects, a cicada, *H. incarnata*, was procured. By studying the wings of the cicada through SEM, the nanostructures and the previously defined dimensions for them can be clearly seen (Figure 9). The nanopillar pattern in Figure 9(ii) looks slightly conical with rounded tips, similar to the AFM image in Figure 1(ii) and the MATLAB surface plot in Figure 5.

Creation of 'Surface Maps' as a Point of Reference

Surface maps were created by plotting the information collected in Table 1 and Table 2 on logarithmic axes, shown in Figure 10. Also plotted on Figure 10(i) are lines of constant aspect ratio, where the aspect ratio, *AR*, is defined as,

$$Aspect\ Ratio = \frac{Height}{Diameter} \qquad [8]$$

Through these maps the nanostructures of natural surfaces were found to have an approximate height range of 100 to 500 nm, diameter range of 40 to 110 nm, spacing range of 40 to 120 nm, and *AR* range of 0.5 to 5.5. Also, since most of the artificial surfaces, that have been proven to be antimicrobial, mimic the above size ranges, it stands to reason that these size ranges give rise to antimicrobial property. Through these observations, a point of reference for comparison has been found for the wrinkled surfaces to be produced later in the experiments, important for quantifying the achievement of this paper's second objective.

Creation of Wrinkled Surfaces and Comparison with Natural Surfaces

After creating the 1D wrinkled surface using ε of 20%, t of 120 s and P of 20 W, it was noticed that the surface possessed some form of photonic property. Under the reflected light microscope, the pattern looked very similar to another natural nanostructure being investigated for photonic properties; butterfly wings (Huang, et al., 2006). In Figure 11, the SEM image of a butterfly wing and the reflected light microscope image of the 1D wrinkled surface are compared, where remarkable similarities in the pattern can be seen.

Similarly, after creating the 2D wrinkled surface using ε of 10%, t of 50s and P of 20W on the replication of the previous 1D surface, it was studied under AFM. The pattern produced on the surface, shown in Figure 12, looks like both the superimposition hypothesis put forward (Figure 5) and the cicada nanostructure (Figure 9(ii)).

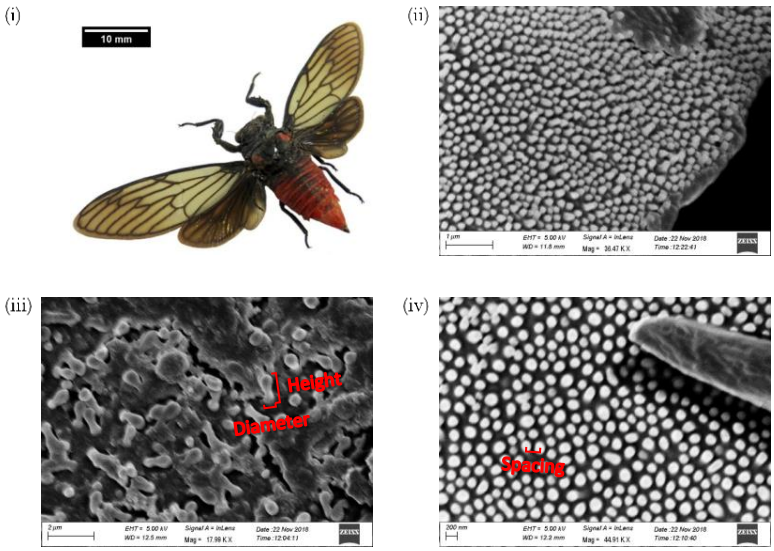

Figure 9 (i) Image of the *H. incarnata* cicada procured. (ii) SEM image of the intact hindwing at a stage angle of 2° to show the three-dimensional shape of the nanopillars. (iii) SEM image of the crushed forewing, where the height and base diameter of the nanopillars are defined. (iv) SEM image of the intact hindwing, where the centre to centre spacing between two nanopillars is defined.

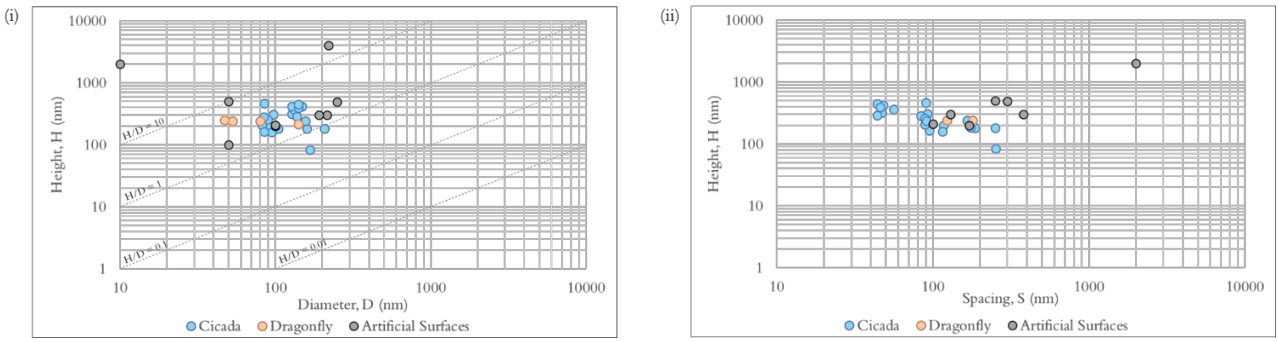

Figure 10 (i) Surface map of height against base diameter with lines of constant aspect ratio. (ii) Surface map of height against centre to centre spacing.

7

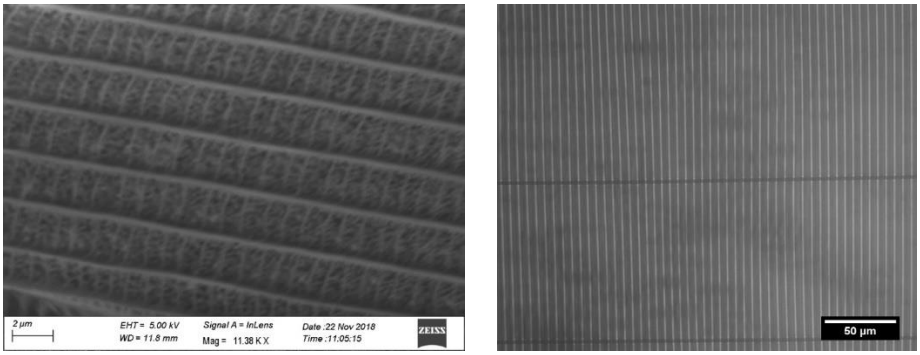

Figure 11 SEM image of a butterfly wing (left) and reflected light microscope image of the 1D wrinkled surface (right) showing similarities in pattern.

Thus, the hypothesis, where the superimposition of the sinusoidal wrinkles in orthogonal directions replicates the pattern observed on the natural surface, has been proven and the first objective of this paper has been achieved.

From Figure 12, it can be seen that like the natural surface, the wrinkled surface's structures also have the three dimensions previously defined, in this case both the base diameter and centre to centre spacing are λ, and the height is two times of A of the sinusoidal wrinkle.

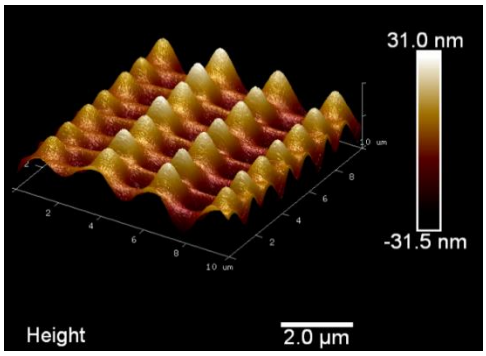

Figure 12 AFM image of the topography of the structures on the 2D wrinkled surface.

Characterisation of Wavelength of 1D Wrinkled Surfaces

Since a point of reference for comparison has been established from Figure 10, λ of the wrinkle was then characterised by using the procedure shown in the Experimental Methods section to investigate if the dimensions could be achieved. In the low deformation region, $\bar{E}_f$ and $\bar{E}_s$ are only affected by the property of the material and can be assumed to be roughly constant for the experiments (Khanafer, et al., 2009), thus reducing Equation 2 to

$$\lambda \approx 50h \qquad [9]$$

Based on this reduced equation, h, can be varied to achieve the established range of wavelengths. As h is a function of D, the dose was changed by changing t while keeping P constant at 30 W.

From Figure 11, other than being similar to butterfly wings, the wrinkled surfaces were also observed to be similar to a sinusoidal diffraction grating. Hence, to investigate the relationship between λ and D, the surfaces were first examined qualitatively using laser diffraction. From Figure 13, it was found that the number of diffraction orders, n, increases with increasing D. This can be explained by using the diffraction grating theory (Popov, 2012),

$$d \sin\theta = n\lambda_{Laser} \qquad [10]$$

where d is the spacing of the grating, in this case it is λ, θ is the diffraction angle, n is the order of diffraction and λ_{Laser} is the wavelength of the laser. Since λ_{Laser} is constant, at the maximum diffraction angle where $\theta = 90^{o}$, $\sin\theta = 1$ and thus, $\lambda \propto$ maximum n. Since Figure 13 shows that $n \propto D$, it can be said that $\lambda \propto D$. In addition, the occurrence of diffraction also shows the uniformity of the wrinkle's λ.

To further investigate the relationship between λ and D, the 1D wrinkled surfaces were examined using reflected light microscopy, and the results plotted in Figure 14. λ was confirmed to increase with increasing D, aligned with the results observed from the diffraction test. Also, λ has a logarithmic dependence on D and this can be explained by the kinetic growth of the film layer on the PDMS substrate during the plasma treatment. A frontal propagation model, with the three main steps of induction, formation and propagation, was used to describe the film growth. In this model, h was found to logarithmically depend on D and a change in the logarithm slope was observed at the change in

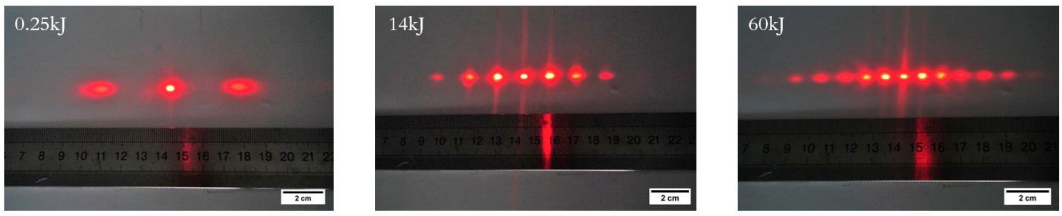

Figure 13 Diffraction patterns created when the laser was pointed normal to the wrinkled surface at a constant distance. When D increased, n increased as well.

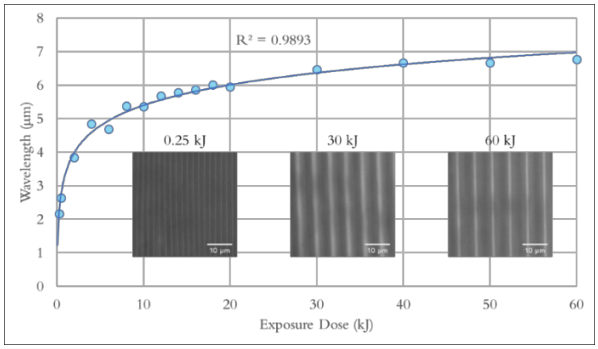

Figure 14 Graph of average λ of the wrinkled surface against D at constant P of 30 W and ε of 10%. The error bars plotted on the graph cannot be seen as the average percentage error of the wavelengths is very small, only 1.28%, and for D the error is at most 3% (based on a reaction time error of 0.25s). The three images are reflected light microscope images of the wrinkled surface at D of 0.25 kJ, 30 kJ and 60 kJ, showing the increase in λ when D increases.

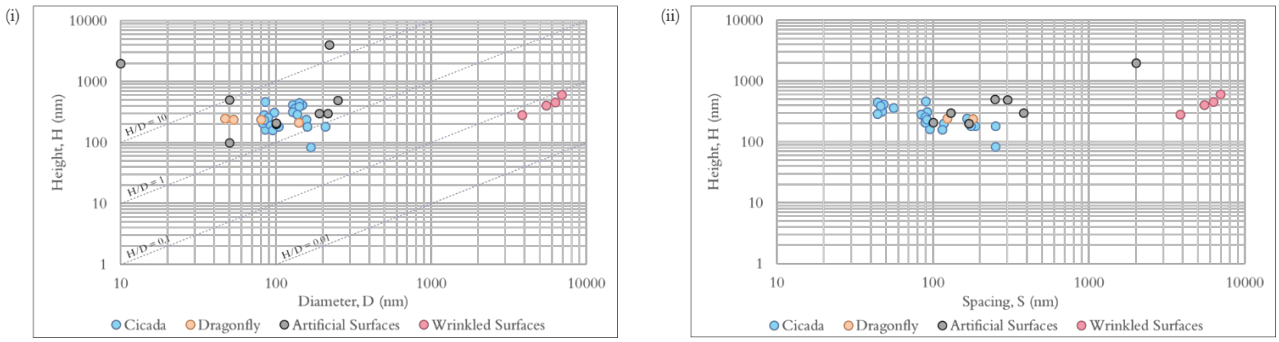

Figure 15 Dimensions of the wrinkled surfaces measured are added into the surface maps of Figure 10. (i) Surface map of height against base diameter with lines of constant aspect ratio. (ii) Surface map of height against centre to centre spacing.

regime from formation to propagation, where the surface has been fully oxidised and a further increase in D increases h (Bayley, et al., 2014).

At a low dose of 0.25 kJ, λ is 2.17 ± 0.03 μm. Although further reduction of D will reduce λ, it is not possible to reach nanoscale sizes, as D must be above the critical dose for wrinkles to form.

Investigation into the Aspect Ratio of 1D Wrinkled Surfaces

The other parameter to investigate is the AR of the wrinkle. Recalling Equations 2 and 3, and the definitions of height and base diameter for sinusoidal wrinkles, the AR is,

$$AR = \frac{Height}{Diameter} = \frac{2A}{\lambda} = \left(\frac{\varepsilon}{\varepsilon_c} - 1\right)^{\frac{1}{2}} \Big/ \pi \left(\frac{\bar{E}_f}{3\bar{E}_s}\right)^{\frac{1}{3}} \quad [11]$$

From Equation 11, AR seems to be independent of h and thus D as well. To investigate this, the heights of some wrinkled surfaces were measured by using AFM. As seen in Figure 15, λ of the wrinkles are still in the microscale and the AR falls along the line of $AR = 0.1$. This proves that reducing exposure dose alone is not sufficient to decrease λ to nanoscale and increase AR at the same time.

Moving forward, there are several areas to conduct further research. Based on Equation 2, another way of reducing wavelength is by reducing the ratio of $\bar{E}$. This can be done by changing the ratio of PDMS base to crosslinker, curing temperature or curing time. Also, by reducing this ratio, based on Equation 11, AR should be increased. Based on Equation 11, AR can be further increased by increasing ε. In addition, since wrinkling is not the only regime caused by mechanically induced instability, when ε exceeds the low deformation limit of 40%, the wrinkling process moves into other regimes such as ridging or folding. Ridging or folding is capable of creating localized nanostructures of high AR and these regimes could be potential areas for discovery.

Conclusions

Based on the experiments performed, λ is still in the microscale, 2 to 7 μm, for D of 0.25 to 60 kJ, and the AR is 0.1, not in the reference range of 0.5 to 5.5. Also, further reducing D is not sufficient to achieve the desired scales. However, the expected behavior in the low deformation limit, where λ decreases with decreasing D, was proven both qualitatively and quantitatively. In addition, the relationship between λ and D was determined to be a logarithmic dependence, described by the frontal propagation model.

The surface maps created in this paper, compiling information from various papers in literature, provides a much clearer picture of where research should be headed. Also, from the experiments performed to create the 2D wrinkled surface, it has been shown that the hypothesis, where the superimposition of two sinusoidal waves can create a pattern similar to that of the nanostructures on natural surfaces, has been proven. Although the second objective could not be met, the achievement of the first objective shows the promising potential of the processes induced by mechanical instability in being the solution to this problem.

Acknowledgements

We would like to thank Dr Ben Price, Senior Curator in the Natural History Museum (NHM), for teaching us about these insects. We also want to thank Luca Pellegrino, for teaching us about the wrinkling process in great detail, and Dr Sepideh Khodaparast for always going out of her way to provide advice and assistance to us.

References

American Profile, 2001. *https://goo.gl/pG5gNm.*

Bandara, C. D. et al., 2017. *ACS Applied Materials & Interfaces,* 9(8), pp. 6746-6760.

Bayley, F. A. et al., 2014. *Soft Matter,* 10(8), pp. 1155-1166.

Cao, C. et al., 2014. *Advanced Materials,* Volume 26, pp. 1763-1770.

Chen, Y.-C. & Crosby, A. J., 2014. *Advanced Material,* Volume 26, pp. 5626-5631.

Chou, S. Y., Krauss, P. R. & Renstrom, P. J., 1996. *Journal of Vacuum Science & Technology B,* 14(6), pp. 4129-4133.

Chung, J. Y., Nolte, A. J. & Stafford, M., 2011. *Advanced Materials,* 23(3), pp. 349-368.

Dickson, M. N. et al., 2015. *Biointerphases,* 10(2), p. 021010.

Dong, J., Wang, A., Ng, K. Y. S. & Mao, G., 2006. *Thin Solid Films,* 515(4), pp. 2116-2122.

Fisher, L. E. et al., 2016. *Biointerphases,* 11(1), p. 011014.

Franssila, S. & Sainiemi, L., 2013. *https://goo.gl/ZS1tkw.*

Hasan, J., Crawford, R. J. & Ivanova, E. P., 2013. *Trends in Biotechnology,* 31(5), pp. 295-304.

Hasan, J., Raj, S., Yadav, L. & Chatterjee, K., 2015. *RSC Advances,* 5(56), pp. 44953-44959.

Hasan, J. et al., 2013. *Applied Microbiology & Biotechnology,* 97(20), pp. 9257-9262.

Hizal, F. et al., 2015. *ACS Applied Materials & Interfaces,* 7(36), pp. 20304-20313.

Høiby, N. et al., 2011. *International Journal of Oral Science,* 3(2), pp. 55-65.

Huang, J., Wang, X. & Wang, Z. L., 2006. *Nano Letters,* 6(10), pp. 2325-2331.

Huang, R., 2005. *Journal of Mechanics and Physics of Solids,* Volume 53, pp. 63-89.

Ivanova, E. P. et al., 2013. *Nature Communications,* 4(2838), pp. 1-7.

Jamal, M. et al., 2018. *Journal of the Chinese Medical Association,* 81(1), pp. 7-11.

Johnston, B. G., 1983. *Journal of Structural Engineering,* 109(9), pp. 2086-2096.

Johnston, I. D., McCluskey, D. K., Tan, C. K. L. & Tracey, M. C., 2014. *Journal of Micromechanics and Microengineering,* 24(035017), pp. 1-7.

Joo, H.-S. & Otto, M., 2012. *Chemistry & Biology,* 19(12), pp. 1503-1513.

Karouta, F., 2014. *Journal of Physics D: Applied Physics,* 47(23), pp. 1-14.

Kelleher, S. M. et al., 2016. *ACS Applied Materials & InterfaceS,* 8(24), pp. 14966-14974.

Khanafer, K., Duprey, A., Schlicht, M. & Berguer, R., 2009. *Biomed Microdevices,* Volume 11, pp. 503-508.

Kim, S. et al., 2015. *ACS Applied Materials & Interfaces,* 7(1), pp. 326-331.

Koh, K.-S., Chin, J., Chia, J. & Chiang, C.-L., 2012. *Micromachines,* 3(2), pp. 427-441.

Lapedus, M., 2018. *https://goo.gl/RdGD8U.*

Lewis, K., 2001. *Antimicrobial Agents and Chemotherapy,* 45(4), pp. 999-1007.

Mainwaring, D. E. et al., 2016. *Nanoscale,* 8(12), pp. 6527-6534.

Ma, J. et al., 2011. *Langmuir,* 27(16), pp. 10035-10040.

Misof, B. et al., 2014. *Science,* 346(6210), pp. 763-767.

Nowlin, K., Boseman, A., Covell, A. & LaJeunesse, D., 2015. *Journal of the Royal Society Interface,* 12(102), pp. 1-12.

Oh, J. et al., 2017. *ACS Applied Materials & Interfaces,* 9(32), pp. 27173-27184.

Popov, E., 2012. *Introduction to Diffraction Gratings: Summary of Applications.* 1 ed. France: Institut Fresnel.

Power, J., 2017. *https://goo.gl/E88aF9.*

Rajendran, S., Karuppanan, K. K. & Pezhinkattil, R., 2012. *Micron,* 43(12), pp. 1299-1303.

Review on Antimicrobial Resistance, 2016. *Tackling Drug-Resistant Infections Globally: Final Report and Recommendations,* London: Review on Antimicrobial Resistance.

Simprint Nanotechnologies Ltd, 2016. *https://goo.gl/X5EceJ.*

Staudt, C., Horn, H., Hempel, D. C. & Neu, T. R., 2004. *Biotechnology and Bioengineering,* 88(5), pp. 585-592.

Sun, M. et al., 2012. *PLoS ONE,* 7(4), p. e35056.

Sun, M. et al., 2009. *Journal of Experimental Biology,* 212(19), pp. 3148-3155.

Thielicke, W., 2007. *Lotus-Effect Pic 5.* [Art].

Watson, G. S. et al., 2015. *Journal of Nanoscience with Advanced Technology,* 1(2), pp. 6-16.

Wilder, E. A. et al., 2006. *Macromolecules,* 39(12), pp. 4138-4143.

Wu, S. et al., 2016. *Nanoscale,* 8(5), pp. 2620-2625.

Yamamoto, M. et al., 2015. *Langmuir,* Volume 31, pp. 7355-7363.

Yi, G., Yuan, Y., Li, X. & Zhang, Y., 2018. *Small,* 14(14), p. 1703159.

Continuous synthesis of glycidol from glycerol and dimethyl carbonate using a KF/sepiolite catalyst

Laurence Ankers and Zu Yan Tee
Department of Chemical Engineering, Imperial College London, U.K.

Abstract Glycidol is continuously synthesised with a 2:1 dimethyl carbonate to glycerol molar ratio under mild conditions using KF/Sepiolite catalyst in a ThalesNano X-Cube™ reactor system with a 1.43mL CatCart tubular reactor. It was found that the catalyst did not perform as well as expected under flow conditions, resulting in significantly lower conversions than that observed in batch reactions. Performance of catalyst dropped after just one use under plug flow conditions and XRF results showed loss of potassium fluoride from 21.7% to 5.5% . BET results showed pore volume and internal surface area decreased after impregnation. However, internal surface area increased to near the values of unmodified sepiolite following deactivation of the catalyst.

Introduction

The rise of crude oil prices since the turn of the century has spurred the production of biodiesel. Biodiesel are long chain alkyl esters that are formed from the transesterification of cooking oil, consisting primarily of triglycerides, with methanol in the following reaction in figure 1:

Figure 1. Transesterification of Triglycerides. Figure reproduced from Energy Procedia 32 (2013) pp 64-73

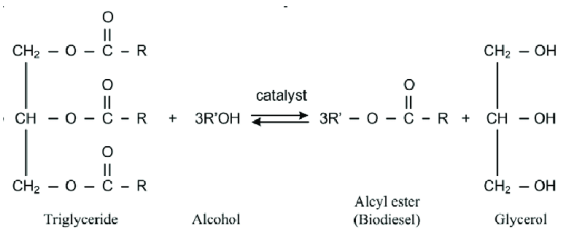

Glycerol is produced as a byproduct of this process, with approximately 1kg of glycerol formed for every 10 kg of biodiesel produced (Thompson and He, 2006). This has resulted in an oversupply of crude glycerol following the rise in biodiesel production. Excess glycerol supply has outpaced the demand for the traditional uses of glycerol; as a humectant, sweetener, thickening agent in food, personal care and pharmaceutical applications. In order to ensure the continued profitability and expansion of the biodiesel industry, new avenues of glycerol use must be developed.

Current research efforts are focused on transforming glycerol into higher value chemicals as well as developing new uses for glycerol-based derivatives. Due to its unique chemical structure with three hydroxy groups, glycerol has the potential to be transformed into a myriad of chemicals. Its potential, in combination with its relative abundance, has earned glycerol the status as a potential bio-based, renewable, platform chemical that can be used to replace petrochemical feedstock.

In addition to concerns due to the finite nature of petrochemical feedstock, glycerol possesses several other desirable properties that make it uniquely safer, such as having low toxicity, low flammability, low volatility and being readily biodegradable. Some of the possible chemicals that can be formed from glycerol are shown in figure 2.

Figure 2. Possible transformations of glycerol. Figure reproduced from Len, C. & Luque, R. Sustain Chem Process (2014) 2: 1.

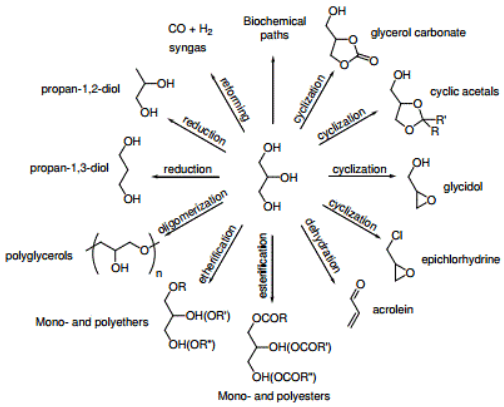

Glycidol is one such chemical. Traditionally produced from the epoxidation of allyl alcohol catalysed with hydrogen peroxide or base catalysed with epichlorohydrin, there is growing interest in finding alternatives for the allyl alcohol and epichlorohydrin to address the inherent safety and environmental concerns. Glycidol is synthesised from glycerol in a two step process by first reacting it with a carbonylating agent to form glycerol carbonate, followed by the decomposition into glycidol.

Glycerol carbonate is another valuable glycerol derivative that has garnered substantial attention from researchers. However, there is considerably less research in the subsequent reaction regarding the decomposition of glycerol carbonate into glycidol and lesser still research regarding the one pot synthesis of glycidol, which confer certain advantages in large scale industrial production of glycidol such as process simplification; requiring only a single reactor with a single set of reaction conditions to produce the desired glycidol. This paper aims to review and evaluate the feasibility of a continuous, one pot synthesis of glycidol using an appropriate single catalyst, so as to look into the early feasibility of industrialisation of the process.

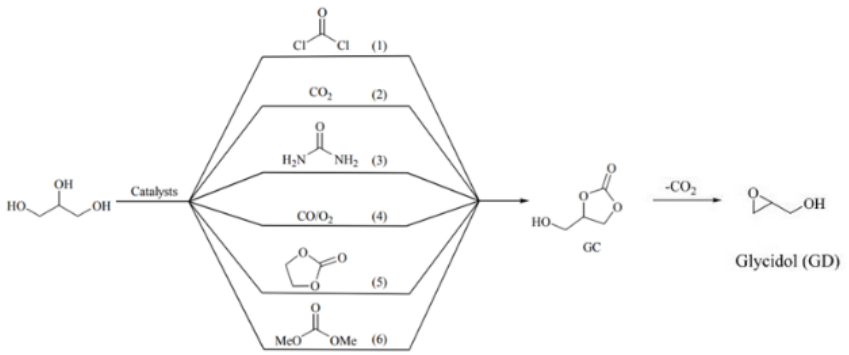

Figure 3. Reaction pathways to synthesise Glycidol from Glycerol. Figure adapted from Chin. J. Catal., 2012, 33: 1772-1777

Background

Glycerol carbonate formation

Multiple choices of reagents exist for the first reaction. Some of the possible carbonylating agents are outlined in the left half of figure 3 which has been adapted from Pan et al.

The use of phosgene is not considered due to its extreme toxicity. Direct carbonylation with carbon dioxide, whilst highly desirable, suffers from low conversion due to the highly stable nature of carbon dioxide. Oxidative carbonylation is discouraged due to the significant safety risk of the high pressure gaseous environment.

Ochoa-Gomez et al. (2012) compared the three remaining reactants, dimethyl carbonate, urea and ethylene carbonate, taking into account catalyst cost and separability, product purification, solvent usage, higher conversion and selectivity, reaction time and safety. They concluded transesterification of glycerol with dimethyl carbonate or ethylene carbonate appears to be the most suitable for the purpose of industrial glycerol carbonate production.

Decomposition of Glycerol Carbonate

Malkemus and Currier (1953) was among the first to patent the distillation of glycerol carbonate to glycidol under vacuum over small quantities of metal salts such as lithium chloride, sodium bromide and calcium carbonate in catalyst loading. Glycidol yields of 80-90% were achieved under the conditions of 175-225°C, 0.0013-0.13 bar, pH 6-7.

More recently Moulougui and Yoo (2009) have proposed using Zeolite A catalyst and glycerol as an initiator to decompose glycerol carbonate into glycerol.

One pot synthesis of Glycidol

One pot synthesis is defined here as a reaction scheme that uses one catalyst under one set of reaction conditions to catalyse both reactions. Under this definition, five distinct catalysts are identified from literature to be suitable for the one pot synthesis of glycidol with dimethyl carbonate. Algoufi et al. (2014) developed a clay supported catalyst, by impregnating potassium fluoride on Sepiolite mineral (KF/Sepiolite). Gade et al. (2012) developed tetraethylammonium hydroxide (TMA-OH). Zhou et al. (2015) developed tetraethylammonium amino acid ionic liquid (TAAILs). Kondawar et al. (2017) developed Ba—Ce mixed metal oxide heterogenous catalysts. Munshi et al. (2014) developed 1,4-diazabicyclo (2.2.2.) octane (DABCO). The performance of each catalyst is summarised in table 1. However, none of the five catalysts have been tested in a continuous mode of operation thus far, which this work aims to address.

If the definition of one pot synthesis were to be relaxed somewhat, other catalysts may join the list. Endah et al. developed $Zn(OAc)_2$ catalyst which enables synthesis of glycidol with glycerol and urea with one catalyst but two sets of reaction conditions. This is a viable option for one pot synthesis if a batch mode of production is considered. However, since

Table 1: Performance of catalysts capable of one pot synthesis of glycidol

Catalyst	Conversion of glycerol (%)	Selectivity to Glycidol (%)	Catalyst loading (% w/w)	DMC to Glycerol molar ratio	Reaction time (h)
KF/Sepiolite	99	82	4.00	2:1	1.5
TMA-OH	95	78	1.50	3:1	1.5
TAAILs	96	82	3.00	2:1	2.0
Ba-Ce	98	80	5.00	3:1	1.5
DABCO	97	83	3.35	3:1	0.5

this work mainly focus on continuous processes, this catalyst is not considered.

We decided to focus our experiments on the KF/Sepiolite catalyst studied by Algoufi et al, this decision was made following a level one Douglas economic potential calculation and basic TOPSIS analysis. KF/Sepiolite came out as the most favourable option due to its low cost compared to the ionic liquid and rare metal catalysts, as well as its relative ease of separation being a solid catalyst.

Experimental

Chemicals

Glycerol (>99%), dimethyl carbonate (>99%), potassium fluoride (>99.5%), sepiolite mineral, glycidol (>96%) and glycerol carbonate (>90%) were ordered from Sigma-Aldrich, United Kingdom.

Catalyst Preparation

The catalyst was prepared via wet impregnation. The sepiolite mineral was first washed with deionized water, the wet sepiolite paste was filtered under mild vacuum for 4 hours before being dried overnight at 100°C. The dry sepiolite was weighed and KF of an amount so as to equal 30wt. % of final catalyst mass (See Equation 1) was dissolved in deionised water to create the impregnation solution. The dry sepiolite was then mixed under agitation with the KF solution for 4 hours. The impregnated paste was again filtered for 4 hours before being dried overnight at 100°C. The catalyst was then calcined at 500°C for 4 hours. Finally, the resultant catalyst was ground and sieved to the desired particle size of 106-250 microns, to be packed into the specialist CatCart® reactor cartridge.

$$Mass\ of\ KF\ required = \frac{0.3 \times\ Dry\ sepiolite\ mass}{1 - 0.3} \quad (1)$$

Two catalyst preparations were carried out during the study. In the first preparation dry sepiolite was weighed at 4.65g and 1.99g of KF was dissolved in 10mL of water, this was added to the sepiolite and the volume was increased to a total of 100mL of impregnation solution. This was done in order to thin the paste that had formed and allow free movement of the stirrer. During the second preparation the dry sepiolite was weighed at 3.18g and 1.36g of KF was dissolved in 40ml of deionised water, in order to have the minimal amount of impregnation solution to allow the stirrer to move within the paste.

The compositions of the sepiolite mineral, the impregnated catalyst and, the spent catalyst after three experiment runs were determined via X-ray fluorescence (XRF) using a PANalytical εpsilon 3 XLE. Their BET surface area and average pore volumes were determined using nitrogen adsorption and desorption at 77K in a micromeritics 3Flex. The samples were degassed at 350°C before the adsorption analysis.

Continuous Reaction Equipment

A simplified schematic of the reaction equipment used is shown in Figure 4. All of the reaction equipment was within a fume hood. Parts labelled 2, 3, 4, as well as the pressure indicator and temperature control system are all part of a ThalesNano X-Cube™ reactor system. The 1.43mL CatCart® reactor is a stainless steel tube with filter membranes at either end to prevent loss of solid catalyst, it is covered with a purpose built insulation block. The system has a built-in touch screen control panel from which reactor temperature and built-in pump flowrates can be set. The outlet was connected to a flash separator at room temperature and pressure, with the gas outlet vented directly to the fume hood extractor. A dead volume of 12mL was determined for the reaction equipment set-up.

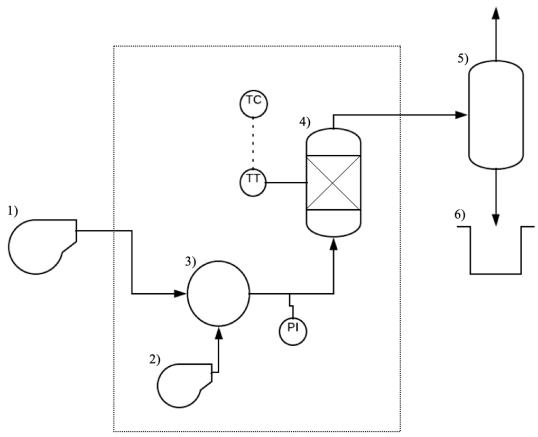

Figure 4. Simplified schematic of reactor set-up: 1) External syringe pump (KR Analytical N6000), 2) Built-in X-Cube™ pump, 3) Mixing point, 4) 1.43mL CatCart® reactor cartridge, 5) External separator, 6) Product collection point.

Reaction Procedure

Due to the relatively high minimum flowrate of the built-in pump (0.1ml/min), it was decided to pre-mix the reaction solution and inject this from the external syringe pump. Because of the immiscibility of DMC and glycerol at room temperature and pressure, N,N-Dimethylformamide was used as a solvent for the reaction mixture. The solvent was chosen based on ternary diagrams between several potential solvents, DMC and glycerol, produced using Aspen, the NRTL property package was used in creating the diagrams.

First, the reaction mixture was prepared, 13.63g of DMF was mixed with 13.36g of glycerol and 26.71g of DMC to create 50mL of solution with mole fractions of 0.3, 0.233 and 0.467 to DMF, glycerol and DMC respectively. The reaction

mixture was then loaded into the syringe pump, the desired reaction temperature of 85°C was set for the reactor, and the required flowrate set for the syringe pump as per the desired reactor residence time (see equation 2). The reactor was run until the system dead volume of 12mL had cleared before a product sample was collected from the liquid outlet of the separator unit.

$$Flowrate\ \left(\frac{mL}{min}\right) = \frac{Reactor\ Volume(mL)}{Desired\ Residence\ Time(min)} \quad (2)$$

When multiple residence time runs were performed on the same day, the flowrate was changed after sample collection and the 12mL maximum dead volume is again waited for to ensure the sample collected is accurate to the new residence time. Before shut-down of the reactor system any remaining reactant mixture was removed from the syringe pump, and the built-in pump was used to flush the system with pure DMC so as to prevent further reaction and degradation of the catalyst in the reactor.

In order to test the performance of the prepared catalyst in a more similar scenario to that of the work by Algoufi et al a solvent-free batch reaction was also carried out.

This reaction was carried out in a 50mL round bottom flask. 5.859g of glycerol and 11.462g of DMC were added to 0.722g of catalyst (so as to equal 4wt.% of the reaction mixture). The reaction mixture was heated to 50°C and stirred at 1000rpm using a hot plate with a magnetic stirrer. The reaction mixture was then cooled to room temperature. Finally the product was separated from the catalyst via filtration for analysis.

Each reaction performed is given in Table 2 the run numbers are assigned in chronological order with reactions 1 and 2 carried out sequentially within the same day and run 3 carried out on the same catalyst the next day. Reaction 4 being the solvent-free batch reaction.

Table 2: The conditions used for each reaction carried out and analysed in the project

Run	1	2	3	4
Continuous/ batch	Cont.	Cont.	Cont.	Batch
Residence Time (min)	30	40	30	90
Flowrate (mL/min)	0.047	0.036	0.047	N/A
Reaction Temperature (°C)	85	85	85	50

Product Analysis

Qualitative analysis of the product was carried out using a GC-MS (HP G1800A). A PerkinElmer Elite-5MS capillary column (30m x 0.25mm x 0.25 µm) was used, with He carrier gas, injection and detector temperatures of 280°C and an initial oven temperature of 50°C increased at a rate of 5°C/min to a final temperature of 135°C. 50µL of product sample was added to 50µL of DMF solvent, and mixed before 1µL of this sample was manually injected into the GC-MS. This method was unable to detect clear peaks for glycerol carbonate.

Analysis of the glycerol carbonate product in the product samples was performed using HPLC (Agilent 1100) with a SUPELCOGEL™ C-610H column (30cm x 7.8mm) and a refractive index detector (Agilent 1100). A 5mM H_2SO_4 solution was used as the mobile phase, with 1,6-Hexanediol used as internal standard. The column was operated at 35°C with a flowrate of 1mL/min.

Results

Catalyst Characterisation

The percentage composition of impregnated catalysts shown in table 3 demonstrate that potassium readily deposited onto the sepiolite. The characteristic X-rays of fluorine sit outside of the range measured by the XRF equipment used and therefore cannot be detected. However, the over 20% increase in potassium content observed in the second catalyst preparation is similar to that seen by Algoufi et al for 30wt.% KF loading of catalyst, suggesting overall impregnation is similar. The first preparation shows a lower increase in potassium content of below 15wt.% and so it decided to pack only the second preparation of the catalyst into the reactor cartridge.

The spent cartridge was also analysed via XRF following the three reaction runs performed and it can be seen that the weight percentage of potassium has dropped significantly after only 3 runs.

The total compositions are notably lower than 100% this discrepancy is expected to be due to mix of; elements that cannot be detected via the XRF used for example fluorine in the final catalysts and also; moisture content due to the highly water absorbent nature of the sepiolite mineral.

The adsorption isotherms for the unmodified sepiolite and the second preparation of catalyst, that used in the reactor, are shown in figure 5. Both of the isotherms shown, and those of the other samples too, are type IV isotherms and are therefore suitable for BET analysis. They also display H1 hysteresis loops indicative of mesoporous structure with a narrow distribution of uniform pores.

Table 4 shows that there was a significant change in mass (17-31%) upon the more intense degassing performed before BET analysis, suggesting that the catalyst had rapidly absorbed moisture from the air following the initial drying stages of catalyst preparation. The table also shows that there is a trend of decreasing surface area and pore volume with increasing KF content, a phenomenon seen in the Algoufi et al paper where KF loading was varied. The surface area increased again to close to that of

the unmodified sepiolite, whereas the average pore volume remained decreased.

Table 3: Composition of untreated sepiolite, preparations 1 & 2 of catalyst and that of used catalyst after 3 runs as determined by XRF

Compound	Composition (Wt. %)			
	Sepiolite	KF/Sep Prep 1	KF/Sep Prep 2	KF/Sep Spent Catalyst
MgO	13.63	12.35	12.26	14.16
Al_2O_3	1.59	-	-	1.58
SiO_2	38.49	31.80	32.19	32.83
K_2O	0.55	15.23	21.74	5.53
CaO	0.20	-	-	-
Fe_2O_3	0.53	0.62	0.57	0.65
Trace	0.12	0.14	0.17	0.14
Total	55.10	60.14	66.93	54.89

Finally, 0.5086g of catalyst were loaded into the reactor, and the spent catalyst recovered was of mass 0.4298g, a mass loss of 15.5%.

Table 4. Percentage mass change from degassing before adsorption/desorption, BET surface area and average pore volume found for untreated sepiolite, preparations 1 & 2 of catalyst and that of used catalyst after 3 runs

Sample	% Mass Change on Degassing	BET Surface Area (m^2/g)	Average Pore Volume (cm^3/g)
Unmodified Sepiolie	31.2	159.5	0.52
KF/Sepiolite Preparation 1	25.2	70.57	0.38
KF/Sepiolite Preparation 2	19.5	56.9	0.32
KF/Sep Used Catalyst	17.4	151.9	0.37

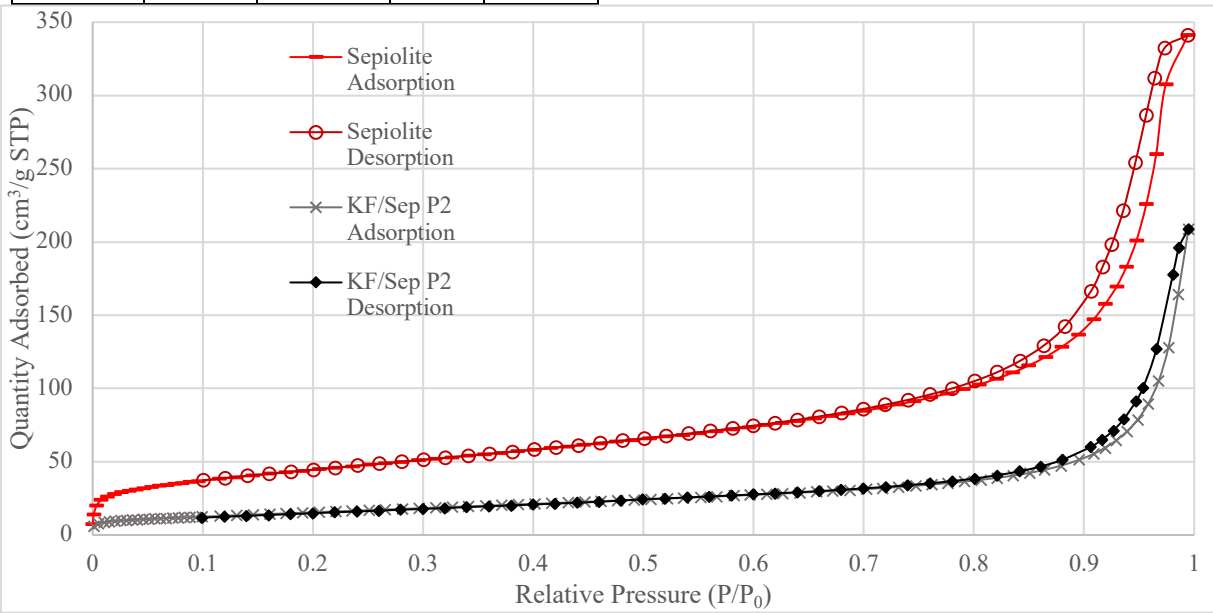

Figure 5: Adsorption and desorption isotherms for unmodified sepiolite and 2nd prepartion impregnated catalyst

Reaction Results

The glycerol and glycidol peaks on the HPLC fully overlap so it was not possible to determine their concentrations using HPLC. Those of methanol and Glycerol Carbonate also had slight overlap adding to the margin of error for these measurements which is already significant as the HPLC peaks had to be manually integrated and so were subject to a large reading error due to ambiguity in the beginning and end of a peak, the peak area calculated varying by almost 10% with only small changes to manual point selection. Given that any concentration calculations require the integration of both the desired compound peak and the internal standard peak being compared to a calibration with similar error, concentration calculations have an error of 20%.

The overlap for methanol and glycerol carbonate was sufficiently large at high concentrations such that they could no longer be distinguished, and so determination of the peak ratios could not be carried out for the batch reaction.

Table 3 shows that the continuous reactions carried out in the flow system achieved very low conversions compared to that of the original paper exploring this catalyst and compared to that of the lower temperature batch run performed. With glycidol only detected in the 1st, 30 minute residence time, run carried out on new catalyst, as shown in figure 7a A low glycerol carbonate concentration of

0.27M detected via HPLC for the same, optimal run. The initial concentration of glycerol in the reaction mixture was 2.9M. The lack of detection of CO_2 or Glycidol on the GC-MS in runs 2 or 3 shows that there was minimal 2nd reaction following the 1st reaction run. This is further supported by a significant drop in glycerol carbonate detected in the HPLC.

Table 2: Summary of key results (HPLC peak area ratios, calculated Glycerol carbonate concentration & products detected via GC-MS) for all 4 reaction runs

Reaction Number	1	2	3	4
HPLC Glyc Carb:IS ratio (±20%)	0.90	0.51	0.57	N/A
Glycerol Carbonate Conc (M) (±20%)	0.27	0.15	0.17	N/A
Products detected on GC-MS	Glycidol S-(-)-, Methanol, CO_2	Methanol	Methanol	Glycidol S-(-)-, Methanol, CO_2, Glycidol R-(+)-

The peaks seen during the HPLC in figures 6a) and 6b) correspond to: glycerol/glycidol (8.5 min); glycerol carbonate (12.4 min); DMC(17.1 min); and internal standard 1,6-butanediol (28.4 min).

Those seen during the GC-MS in figures 7a) and 7b) correspond to: CO_2/methanol (2.0 min); DMC (2.5 min); Glycidol S–(-)- (3.7 min); DMF (4.7 min); Glycerol (12.6 min) and; glycidol R-(+)- (19.8 min). It is of note that the glycerol peaks observed during GC-MS are very broad peaks.

As can be seen in figure 7b a very different story is true for the batch reaction, both isomers of glycidol are seen, and with much larger peaks than in the best continuous run. The CO_2 and methanol merged peaks are also more notable, along with the GC-MS being unable to detect any glycerol. The methanol/glycerol carbonate peak seen in the HPLC result is also significantly larger than any seen in continuous runs, with a notably lower glycerol/glycidol peak as shown in figures Due to the merging of these peaks calculation of exact concentrations was not possible, however the notably low glycerol peaks in both GC-MS and HPLC would suggest that similar conversions to those found by Algoufi et al (>90%) have been achieved.

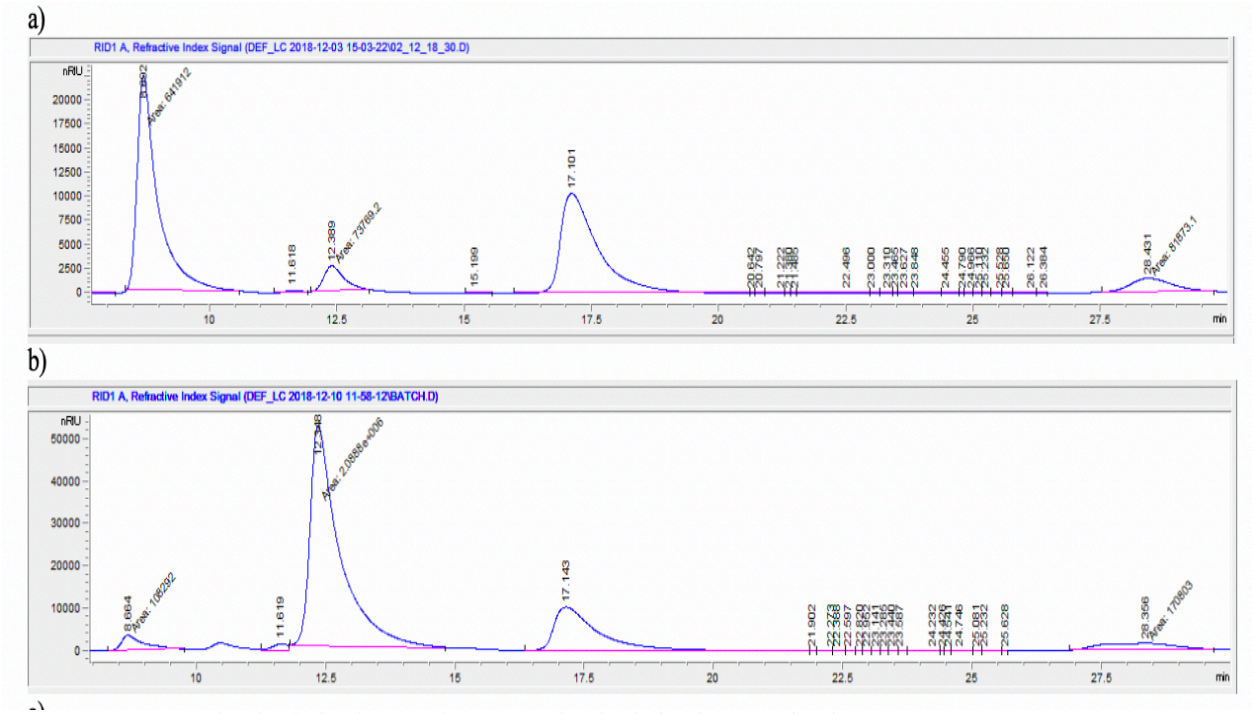

Figure 6: a) HPLC refractive index for run 1 b) HPLC refractive index for run 4 (batch).

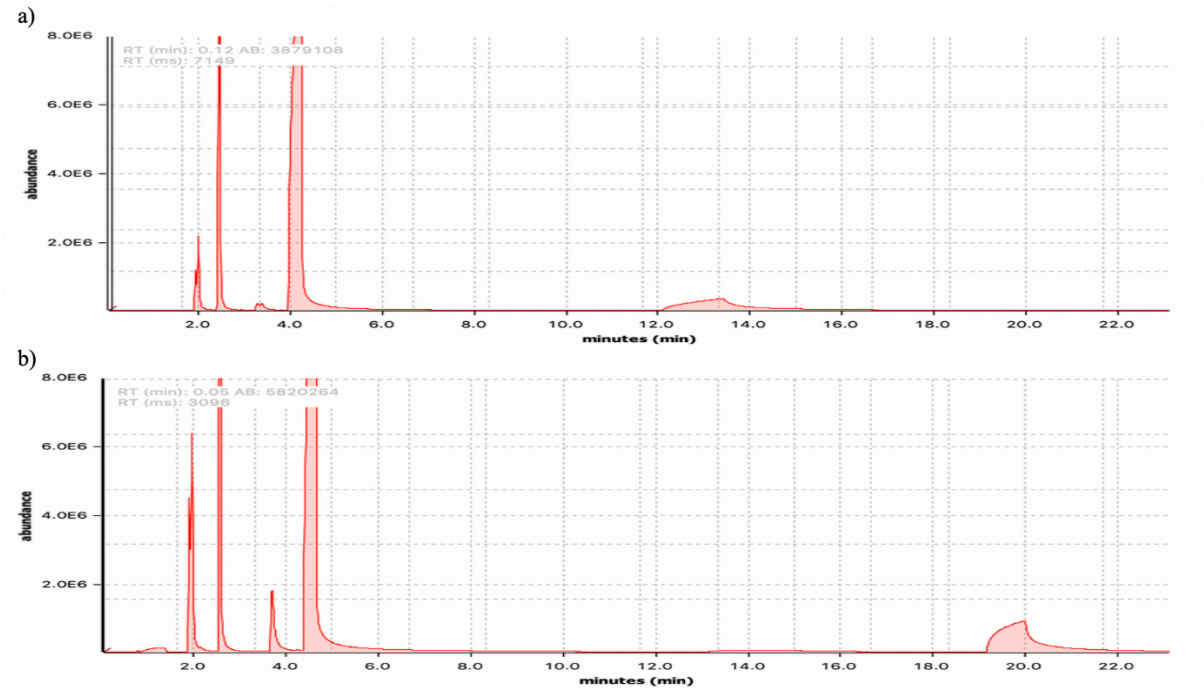

Figure 7: a) GC-MS result for run 1 b) GC-MS result for run 4 (batch)

Discussion

It is clear from the results gathered that the catalyst underperformed during continuous flow reaction conditions. It was anticipated that the superior conversion expected of a packed bed reactor would compensate the shorter contact times between the catalyst and the reactants compared to that of batch reaction. However significantly lower conversions were seen from the continuous reactions than that of batch. This is unlikely to be solely explained by the lower contact times, 30 minutes for continuous flow compared to 90 minutes for the batch reaction, this could suggest the first steps of the reaction are slow to occur and large residence times are required for high conversion to be observed. Another plausible explanation is channelling; a large amount of reactant is allowed to pass through the reactor without interacting with the catalyst surface and undergoing reaction. Currently, an insufficient number of experiments have been carried out due to time constraints and therefore more experiments into the catalyst structure and the transport kinetics between the reactants and the catalyst surface (i.e. rates of reactant adsorption and product desorption from the catalyst surface) would be required to determine the validity of this explanation. Another possible explanation is that of the DMF solvent leaching away the active groups that had been formed during impregnation and rapidly deactivating the catalyst. The evidence of catalyst deactivation is clear from the significantly lower conversions in the 2nd and 3rd experiment runs on the same catalyst. This is supported by the 16.21 wt.% drop in potassium content between the unused catalyst and the catalyst after 3 runs seen in the XRF results, as well as the surface area of the spent catalyst returning to near that of the unmodified sepiolite, suggesting the new groups formed during impregnation had been removed. . Although the percentage drop in potassium (and presumably fluorine as well) is greater than that seen in the overall catalyst mass decrease of 15.5%. This is most likely due to the deposition of other elements on the catalyst during the reaction process, Algoufi et al discovered a 12.9% increase in carbon content on their catalyst following 4 cycles of 90-minute reaction.

Going forward, it is important that the kinetics of the reaction are more thoroughly investigated if continuous flow reactions are to be considered. As for the industrial use of this catalyst for this reaction, if this were to become viable the possibility of catalyst regeneration would have to be examined as the rapid degradation of catalyst witnessed would mean regular replacement of the catalyst bed would be required, if a transport reactor were used instead this regeneration could potentially be undertaken continuously and remove the need for regular shut-down of the reactor.

Conclusions

The 30wt% KF/Sepiolite catalyst was shown to have poor performance in catalysing the synthesis of glycidol from glycerol and DMC when used in a packed bed reactor with continuous flow at low residence times. At current the rapid deactivation, and low conversions seen would prevent this catalyst being considered for use in the large scale production of glycidol. More research into the causes of the rapid catalyst deactivation, and the mechanisms by which the KF/sepiolite catalyses the

reaction would be required in order for this viability to be more thoroughly assessed.

Acknowledgements

We would like to extend our thanks to Dr Fessehaye Zemichael, Dr Patricia Carry, Dr Ben Deadman, Mr Ziyin Chen and Mr Andrew Leung for their support throughout this study.

References

José R. Ochoa-Gómez, Olga Gómez-Jiménez-Aberasturi, Camilo Ramírez-López, and Mikel Belsué A Brief Review on Industrial Alternatives for the Manufacturing of Glycerol Carbonate, a Green Chemical *Organic Process Research & Development* 2012 *16* (3), 389-399
DOI: 10.1021/op200369v

Malkemus J.D, Currier V.A, Bell John, JB (1956). US Patent No. US2856413A. Houston, United States. US Patent Office

Munshi, Mudassir K. and Gade, Swapna M. and Rane, Vilas H. and Kelkar, Ashutosh A. Role of cation–anion cooperation in the selective synthesis of glycidol from glycerol using DABCO–DMC ionic liquid as catalyst. 2014 Rsc. Adv. Volume 4 Issue 61, pp32127-32133 The Royal Society of Chemistry

Munshi, Mudassir K. and Gade, Swapna M. and Rane, Vilas H. and Kelkar, Ashutosh A. Role of cation–anion cooperation in the selective synthesis of glycidol from glycerol using DABCO–DMC ionic liquid as catalyst. 2014 Rsc. Adv. Volume 4 Issue 61, pp32127-32133 The Royal Society of Chemistry

Saiyong PAN, Liping ZHENG, Renfeng NIE, Shuixin XIA, Ping CHEN, Zhaoyin HOU, Transesterification of Glycerol with Dimethyl Carbonate to Glycerol Carbonate over Na–based Zeolites, Chinese Journal of Catalysis, Volume 33, Issues 11–12, 2012, Pages 1772-1777, ISSN 1872-2067

Sharda E. Kondawar, Chetana R. Patil, and Chandrashekhar V. Rode Tandem Synthesis of Glycidol via Transesterification of Glycerol with DMC over Ba-Mixed Metal Oxide Catalysts *ACS Sustainable Chemistry & Engineering* **2017** *5* (2), 1763-1774 DOI: 10.1021/acssuschemeng.6b02520

Swapna M. Gade, Mudassir K. Munshi, Batul M. Chherawalla, Vilas H. Rane, Ashutosh A. Kelkar, Synthesis of glycidol from glycerol and dimethyl carbonate using ionic liquid as a catalyst, Catalysis Communications, Volume 27, 2012, Pages 184-188, ISSN 1566-7367.

Thompson, J.C. & He, B.B. 2006, "Characterization of crude glycerol from biodiesel production from multiple feedstocks", Applied Engineering in Agriculture, vol. 22, no. 2, pp. 261-265.

Len, C. & Luque, R. Sustain Chem Process (2014) 2: 1. https://doi.org/10.1186/2043-7129-2-1

Widayat, Widayat & Wibowo, Agam & Hadiyanto, H. (2013). Study on Production Process of Biodiesel from Rubber Seed (Hevea Brasiliensis) by in Situ (Trans)Esterification Method with Acid Catalyst. Energy Procedia. 32. 64–73. 10.1016/j.egypro.2013.05.009.

Yan Zhou, Fan Ouyang, Zhi-Bin Song, Zhen Yang, Duan-Jian Tao, Facile one-pot synthesis of glycidol from glycerol and dimethyl carbonate catalyzed by tetraethylammonium amino acid ionic liquids, Catalysis Communications, Volume 66,2015, Pages 25-29, ISSN 1566-7367

Y.T. Algoufi, U.G. Akpan, M. Asif, B.H. Hameed, One-pot synthesis of glycidol from glycerol and dimethyl carbonate over KF/sepiolite catalyst, Applied Catalysis A: General, Volume 487, 2014, Pages 181-188, ISSN 0926-860X,

Modelling the Carbon Sequestration Potential for Reforestation from Available Land

ANSHUL BONGIRWAR[1] **AND OMAR ABDULLA**[1]

[1] *Department of Chemical Engineering, Imperial College London, London, SW7 2AZ, UK*
[*] *Corresponding authors: anshul.bongirwar15@imperial.ac.uk, omar.abdulla15@imperial.ac.uk*

Due to anthropogenic greenhouse gas emissions, the world is currently on track for a 3 degree rise in global temperature by 2050. The Paris agreement has set a goal of a 1.5 degree rise by 2050. Integrated assessment models (IAMs) are used to explore mitigation pathways for climate change. Knowledge is drawn from energy, climate and ecosystem models using mathematical algorithms. However, there is a lack of IAMs' that are linked to reforestation models. Thus, this analysis aims to build and link a reforestation model to MUSE, an IAM developed at Imperial College London. Regressions models have been built on data modelled for aboveground and belowground biomass as well as soil organic carbon. The carbon dioxide sequestered from the atmosphere was then calculated using the regression models. This was then equated to revenue generated based on the carbon abatement cost scenarios considered in this analysis and MUSE. Modelling outputs suggest the minimum NPV of reforestation in Brazil is US $ 500 bn with a minimum CO_2 sequestration potential of 7.24 Gt. The cost of carbon of reforestation in Brazil was found to be in the range of US $ 22.65 - $ 36.50/per ton of CO_2. The societal cost of carbon falls in the middle of this models' range at US $ 30.89/tn of CO_2. Using this as the initial carbon abatement cost in the technoeconomic analysis, results in a NPV of over US $ 8 bn. This report found that reforestation is a cost-effective method to meet the 1.5-degree NDC goals, however it should be complemented with CCS in the industry and power sectors.

1. INTRODUCTION & BACKGROUND

Climate change is one the most complicated yet eminent global problems. Avoiding its worst consequences would require large greenhouse gas (GHG) emission reductions across all sectors. It was at the Paris agreement in 2015 that 196 parties joined to transform their development trajectories to set the world on a course towards sustainable development, aiming at limiting global warming to an increase of 1.5-2 degrees above pre-industrial levels (UNFCCC, 2018). The agreement requests each country to outline and communicate their post- 2020 climate actions, known as their nationally determined contributions (NDCs) (UNFCCC, 2018). The NDCs of the countries are tailored towards their state, as it is understood that the peaking of emissions could take longer for developing countries. Emission reductions are undertaken on the basis of equity, and in the context of sustainable development as well as efforts to eradicate poverty, which are critical development priorities for many developing countries. The climate plan for each state member reflects the country's ambition for reducing emissions, taking into account its domestic circumstances and capabilities. In this sense NDCs represent the efforts of each country to reduce national emissions and adapt to the impacts of climate change.

Research into climate change mitigation must therefore be multisectoral. In recent years, Integrated assessment models (IAM) have been used to explore mitigation pathways. IAMs draw knowledge and strengths from various disciplines such as energy, ecosystems and climate models. Contributions from each discipline are connected using mathematical representations through unified modelling platforms. IAMs provide a holistic view of the carbon emissions in different sectors and are thus used in assessing global and regional GHG mitigation policies and climate impacts (Yang et al, 2018).

Due to climate change concerns and carbon markets, government policies for sustainability have risen. Most emission reduction efforts are focused in sectors such as power generation, transport and industry sectors. Nevertheless, the Agriculture, Land Use and Forest (AFOLU) sector hold great potential for emissions reduction. More specifically, reforestation provides a unique solution due to carbon sequestration and has broader environmental benefits. Land use models have been imbedded into land use planners to gauge whether reforestation models provide both economic development as well as biodiversity conservation (Yang et al, 2018).

Reforestation plays a very vital part in the carbon cy-

cle. Carbon enters the atmosphere as carbon dioxide from respiration and combustion. It is absorbed using photosynthesis by producers and stored as carbohydrates. When animals and plants die, the carbon in their bodies is returned to the atmosphere as carbon dioxide by decomposition. In the event that decomposition is blocked, the plant and animal material turn into fossil fuels (Visionlearning, 2018). They effectively become carbon pools. There are four different carbon pools in forests: aboveground, belowground, litter and soil organic carbon (SOC) (FAO, 2018).

Literature demonstrate the different variables that affect how carbon is stored in plants and trees. They explore the above as well below ground levels of carbon stored in reforested areas. Data demonstrated that wet life zones have the fastest rate of aboveground carbon accumulation with reforestation, followed by dry and moist forests (Lewis et al., 2018). Another study found that the transition from savanna to transitional forests can result in a fourfold increase in the total carbon sequestration in the aboveground and litter carbon pools (Carvalho et al., 2009).

Reforesting the barren lands could affect the strategy countries can take to meet the target of the 2050 Paris accord. A particular study has noted that decreasing the levels of carbon dioxide in the atmosphere led to a decrease in food crop prices. However, the model is based on Bioenergy with Carbon Capture and Storage (BECCS) which proved to present both technical as well as institutional problems (Muratori et al., 2016). Thus, building a reforestation model to provide predictions of lowering carbon dioxide levels on the economy could be extremely valuable. This could be done through an optimization model for the barren land to devote a certain percentage for biofuel growth, required for the industry as it switches to biofuel for clean energy.

Although most of IAMs combine energy and land use models, there is a lack of comprehensive reforestation models that are integrated into their land use model. This leads to not having an account for the carbon sequestration dynamics while exploring its implication on the wider energy and land use system. In addition, implementation within typical energy models such as TIMES (Iea-etsap, 2018) or GCAM (Globalchange, 2018) where different GHG reduction strategies are modelled, has not been done, particularly considering the carbon uptake dynamics with respect of the age of the new forest.

As there is a lack of such reforestation models that are linked with an energy system model, the paper focuses on the research gap involving the integration of a comprehensive reforestation model into an energy system model. The main aim is to build a reforestation model and soft-link it to MUSE (SGI, 2018), a novel IAM developed at Imperial College. Other objectives include analysing the cost of carbon in reforestation as well as determining the importance of considering different carbon pools.

2. METHODOLOGY & CASE STUDY

This research primarily involves the development of a reforestation model that aims to predict and track the levels of carbon sequestration by the age of the forest and previous land use. As MUSE only considers the availability of former pasture and agricultural land, only these two categories are considered in this model. This model also assumes a staggered acquisition of land across the simulated period. Once land has been acquired, a new forest plantation is assumed to take place instantaneously. Thus, different forests have different ages based on when the land acquisition has taken place.

The three major carbon pools considered in this model are: soil organic carbon (SOC), aboveground and belowground (Jackson et al., 2017). The above and belowground pools consider carbon stored within the tree bark, roots and tree litter, with SOC considering fine roots. The types of land with previous use considered in the land are agricultural and pastural land. Agricultural land is one where crops have been grown, where as pastural land is one where grazing has taken place. Pastural land has a higher rate of nutrient recycling and thus has a greater reserve of nutrients that aid reforestation (Ranger, 1996).

2.1. Case Study

The developed model has been applied to the Cerrado region in Brazil. This region has been subjected to high rates of deforestation due to two primary reasons: increasing agricultural land demand to grow soya bean crops and higher pastural land requirements for grazing. The Prodes Cerrado had recorded a loss of 6,777 km2 and 7,408 km2 of native area in 2016 and 2017 respectively. Compared to the estimates of 2015, this represents a reduction of 43% and 38% of forest in the Cerrado biome. Following this track of degradation could lead to the largest extinction process of plants ever recorded in history, three times as much losses of flora since 1500 (Wwf, 2018). Additionally, hundreds of bird species are critically endangered due to deforestation (Wwf, 2018).

2.2. Model Development

2.2.1. Regression models

The carbon pools considered in this model are in line with those identified in the IPCC report (IPCC, 2018).

Accumulation data for aboveground biomass in the tropical rainforest region, mapping the cumulative biomass with tree age and previous land use, was acquired from Silver et al, 2000. This data was then used to develop growth models for each previous land use, resulting in the regression curves in Table 1. The belowground carbon pool was then added onto the reforestation model by developing a relationship using data between belowground and aboveground biomass in clonal eucalyptus trees in southeast Brazil (Ribeiro et al., 2015). This relationship equation is also shown in Table 1. The average carbon concentration within aboveground and belowground

Table 1. Best fit equations for biomass (Mg/ha) with time (yrs.) based on tropical reforestation data

	Regression Model	Model R^2	Physical Significance
Pasture	aboveground biomass=22.662*ln(age)+7.765	0.711	The cumulative aboveground biomass as a function of tree age
Agriculture	aboveground biomass=17.455*ln(age)+10.064	0.592	
Biomass relationship	belowground =0.135*aboveground+3.494	0.593	Biomass dependency between above and below ground
Pasture	Soil C=18.305*ln(age)+1.7267	0.662	The cumulative SOC levels as a function of tree age.
Agriculture	Soil C=13.124*ln(age)+26.32	0.406	

Note 1: due to several anomalies found in the available data, data cleansing was done to remove outliers from the data set.
Note 2: due to a lack of available data in the first year of the pasture regression model, an average growth rate of 6.2 Mg/ha (Silver et al, 2000) was used to add a data point in this region. This avoided the nonphysical phenomenon of having a negative biomass accumulation in the first year of the regression model.
Note 3: due to the nature of the logarithmic curve, the analytical soil carbon values at age 1 is much lower than the physical case. Thus, the soil carbon for the pasture model in year 1 is equated to the year 2 value as a close approximation.

biomass was then applied to find the carbon levels in the developed regression models. Based on data acquired from Ribeiro et al., 2015, the average carbon concentration in aboveground and belowground was found to be 44.5% and 37.8% respectively. Regression models for soil organic carbon (SOC) was developed based on data that measures carbon levels in soil depth of 0-25 cm and tree age (Silver et al, 2000).

The developed regression models point to cumulative carbon uptake as a function of tree age. To find the yearly carbon uptake, the difference between the year n and n-1 is found. This value across all three carbon pools are summed resulting in a yearly carbon uptake. For the special case where n=1, the yearly carbon uptake is the carbon uptake at the end of year one as no carbon is sequestered in year zero.

As the atomic weight of carbon is 12, while carbon dioxides' is 44 (due to two oxygen atoms), the summed yearly uptake across all three carbon pools is then multiplied by 3.67 to find the weight of carbon dioxide sequestered from the atmosphere. The summation of yearly carbon uptake from the three carbon pools from the regression models resulted in the trend shown in Figure 1. As seen, the rate of carbon uptake in the first 5 years is much higher compared to the later years. This stresses the importance of acquiring land every year as it is an effective way to maximise the potential for carbon sequestration. Additionally, the forest reaches a carbon saturation point at roughly 50 years. This is in line with literature saturation periods (Silver et al, 2000).

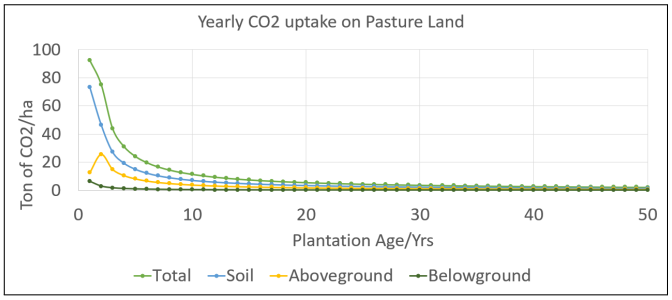

Fig. 1. Variation of yearly CO_2 uptake with plantation age

2.3. Techno-economics of reforestation

First, the land acquisition costs in Brazil (Thompson, 2018) have been found to be the largest contributor to capital expenditure (CAPEX), where other costs include equipment acquisitions required for reforestation (Guitart and Rodriguez, 2010). The summation of these costs provided an estimate of per ha capital investment cost for reforestation. The annual operational expenditure (OPEX) (per ha) was then approximated by summing management, maintenance and supplements application costs for a eucalyptus reforestation project in Brazil (Guitart and Rodriguez, 2010). All these costs have been then readjusted to 2005 USD (Statistics and Index, 2018) equivalent to account for inflation and thus have a fair comparison with the projected cost of carbon. This resulted in cost of investment of \$ 5524/ha and operational cost of \$ 51.7/ha.

Second, the CAPEX and OPEX costs have then been inflated to the appropriate simulated years using the current inflation rate of 2.4% (Bank of England, 2018). The process of inflation assumes year 2018 as the reference year (or year 0) in the analysis. A discount rate of 5% is used as it is a common base line for terrestrial carbon studies (Sullivan et al., 2005).

Third, the sequestered carbon dioxide from the atmosphere can then be equated to a monetary value (2005 USD), based on cost of carbon projections (Kriegler et al, 2014). These projections are based on limiting the atmospheric greenhouse gas concentration to 450 ppm (CO_2 equivalent) by 2100 (Kriegler et al., 2014). The explored carbon price trajectories are illustrated in the Scenario section.

Fourth, a NPV analysis using the costs and estimated sequestered carbon dioxide as potential revenue generation across all three carbon price scenarios was then

performed. The NPV was used to determine whether reforestation is an advantageous project.

$$NPV = \frac{CF_1}{1+r} + \frac{CF_2}{(1+r)^2} + \frac{CF_3}{(1+r)^3} + \cdots \quad \textbf{(1)}$$

2.4. Soft-link with MUSE

The interaction between the presented model and MUSE is shown in Figure 2. Results from MUSE such as the liberated amount of land is inputted into the reforestation model. The outputs of the model, most importantly the carbon sequestered in the simulated period is fed back into MUSE. This feedback loop provides an updated carbon price strategy for the entire modelled sectors.

2.5. Model Limitations

This model has the following main limitations.

- The albedo effect: due to reforestation, the amount of solar radiation reflected off the planet is reduced. This would lead to an elevation in global temperature due to an increase in absorption of infrared radiation from the sun. This ecological effect has been disregarded in this model as the integration with the energy model (MUSE) also does not consider it.
- Tree Litter: during the simulated period, there would be an accumulation of litter with a varying rate. However, this carbon pool is much smaller than the three considered and was thus disregarded (Smith et al., 2014).
- Species Specificity: the carbon uptake values are subject to vary with different species, this complexity has not been considered due to the lack of available data in literature.

2.6. Scenario

The cumulative land liberation data obtained from MUSE is shown in Table 2. It represents actual land area available from previous pasture or agricultural crop land. In this study, a single land scenario is explored. The presented results are based on the 'Reference' scenario, exploring the maximum amount of carbon that can be sequestered directly from the atmosphere based on the available land.

MUSE predicts (based on the Brazilian government projections), (EPE, 2018) pasture land liberation due to an increase in cow grazing efficiency, from 1 to 1.7 cattle heads per ha by 2050, while agricultural land keeps expanding at a constant rate. The results of these models are used to present a simulated scenario after reforestation has taken place with the economic and environmental benefits being assessed. The simulated period of this model is from 2025 to 2050.

As the cost of carbon could be based on emissions of greenhouse gases from the industry and the energy system, three scenarios of carbon prices are considered: no CCS, conventional technology (conv tech) and full technology implementation (full tech). The conv tech employs solar, wind and biofuels technology while full tech employs the aforementioned technology and CCS. This is the same pricing strategy as the one used in MUSE and was thus necessarily applied to this model due to link between the two models. As the carbon price data from 2005 to 2100 have been only available at 5-year intervals, linear interpolation was used to find intermediate price projections for every year during the simulated time between 2025-2054. These projections are shown in Figure 3.

3. RESULTS & DISCUSSIONS

3.1. Carbon Sequestration

The graph in Figure 4 shows the carbon sequestration potential if all the available land is either pastural or agricultural. The first insight that can be obtained from this graph is that pasture land has a higher uptake compared to agriculture land. This is possibly due to higher nutrients availability in pastural lands compared to agricultural lands. There is a peak in year 2030 as that year has the largest amount of land acquisition, thus has the largest sequestration potential. Modelling outputs suggest that the total carbon sequestration from the available land in this scenario is 7.24 Gt and 8.32 Gt of CO_2 for agriculture and pasture land respectively. For carbon sequestration to increase in the future, an increase in land acquisition is required. However, land prices may also increase beyond inflation due to increasing land demand caused by reforestation. This could result in a significant decrease in the profitability of the project and make the reforestation project no longer viable. The impact of land prices is investigated in more depth later in this report.

Once the pricing strategy introduced in the report is applied to the sequestered carbon, the revenue generated due to the cost of carbon abatement is shown in Figure 5. As there is a significant range of potential revenue based on the pricing scenario, it highlights the importance of knowing what technologies can be used at full scale to target climate change. This could have a direct impact on the profitability of the reforestation project. The introduction of carbon prices could also evolve into carbon trading schemes where countries or businesses use their ability to sequester carbon and charge other countries or businesses to capture carbon for them. Charging at a price premium, this becomes a revenue generation method for stakeholders with advanced carbon capture technology. The exact carbon price applied could be of utmost importance to these stakeholders as it could be their primary incentive to upgrade and invest into CCS and reforestation projects. Additionally, this carbon trading scheme could benefit both countries and enterprises. Carbon capture technology could add to their GDP due to resulting profits from the carbon trading scheme. On the other hand, countries and enterprises without carbon capture technology can outsource carbon sequestration, reducing

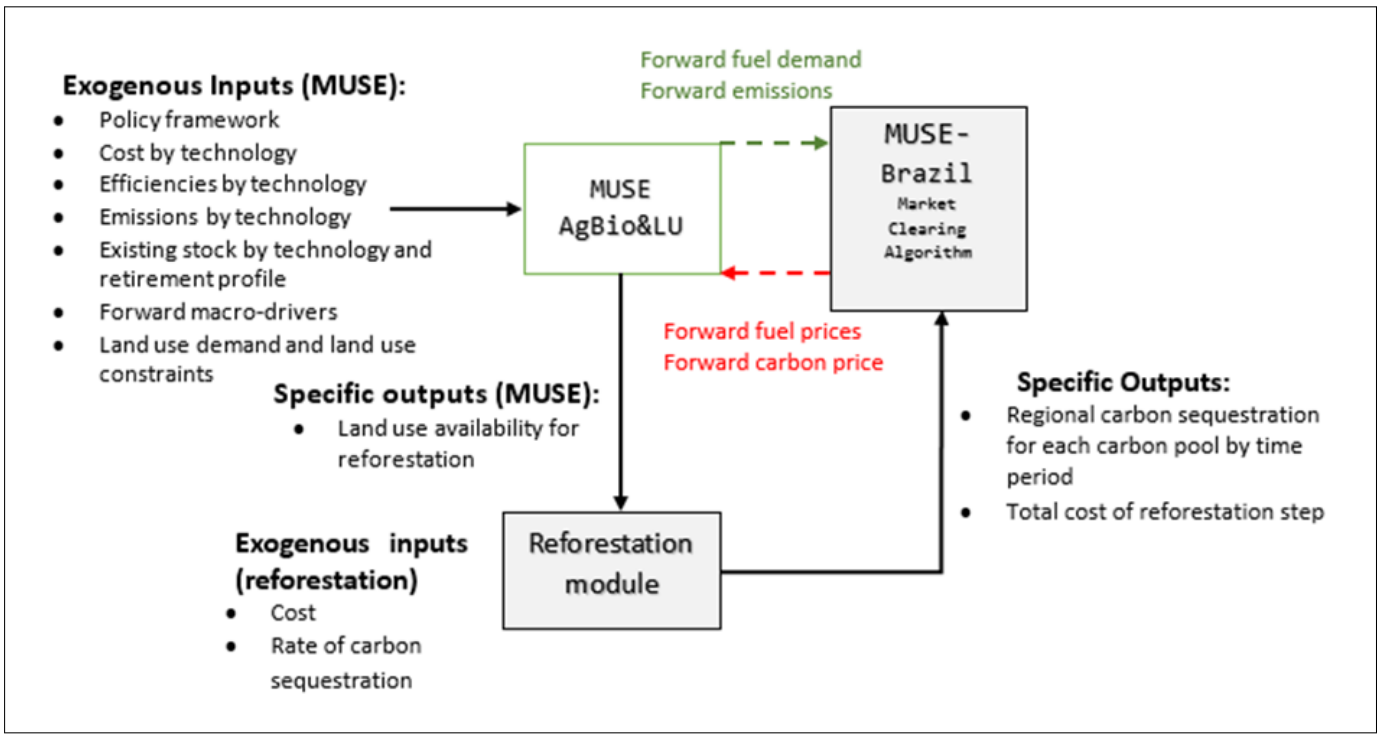

Fig. 2. MUSE Brazil - reforestation model soft-link and step by step simulation

Table 2. Modelling outputs from MUSE for three different scenarios in Cerrado showing cumulative land availability (Mha) in the simulated time

Scenarios	2015	2020	2025	2030	2035	2040	2045	2050
Reference	0.0	0.0	0.6	9.6	13.0	14.5	17.6	21.4
High Yielding agriculture	0.0	0.0	1.1	10.8	15.0	17.2	21.2	25.9
Low yielding agriculture	0.0	0.0	0.0	0.0	0.0	0.0	0.0	0.0

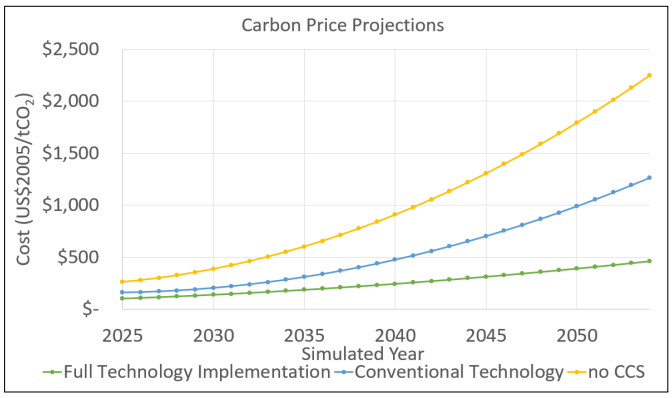

Fig. 3. Carbon cost projections across all three considered scenarios

their capital investment into this technology. The exact benefits and drawbacks for both divisions of stakeholders under the carbon trading scheme needs further research.

3.1.1. NPV Analysis

Applying the capital and operational costs based on the land available in the year considered, result in the NPV analysis shown in Table 3. Based on the carbon abatement cost applied, the project of reforestation is highly profitable, where the lowest NPV exceeds half a trillion dollars. This analysis shows that reforestation is not limited by its technoeconomic characterisation.

3.2. Sensitivity Analysis

3.2.1. Discount Rate

To analyse the risk associated with this project, a sensitivity analysis on the discount rate was conducted, varying the discount rate to 10% and 15% to explore an increase in the potential risk of the project. The results of this analysis can be found in Figure 6. It is found that even with a

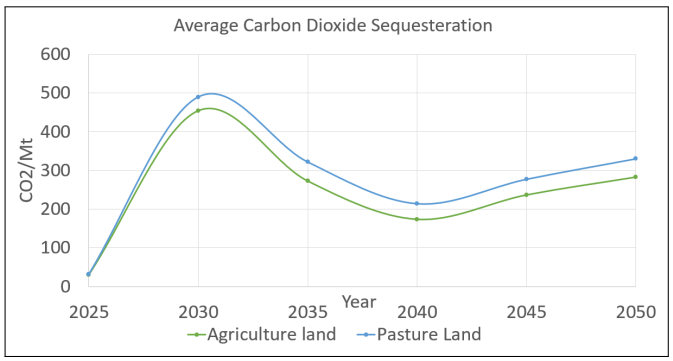

Fig. 4. Carbon dioxide sequestered from the atmosphere per year

Note: MUSE runs on a 5-year time step, thus points on the graph demonstrate average sequestration potential in the 5-year period, from the available land.

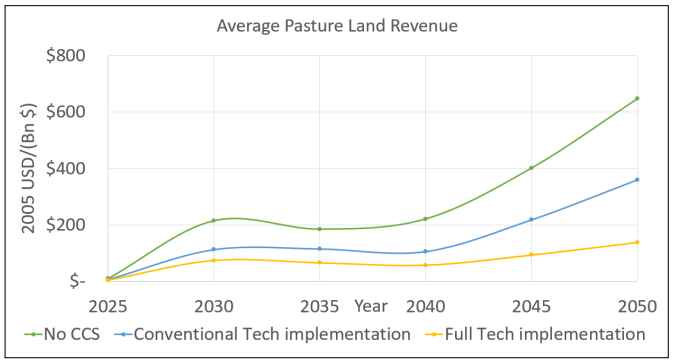

Fig. 5. Revenue generated from carbon sequestration based on the carbon abatement pricing strategy

discount rate of 15% the minimum NPV on Pastural Land is roughly $ 80 bn, reinforcing the profitability of this project. However, the carbon abatement cost proposed by Kriegler et al., 2014 is much higher compared to the societal cost of carbon (discussed further in this report). Thus, the amount of revenue generated from the process is the biggest source of risk in this project, highlighted by the astronomical and unattainable IRR of over 2500%. Thus, the uncertainty of the cashflows; the biggest risk of the project can only be managed once the carbon abatement cost is globally agreed upon.

3.2.2. Neglecting SOC

Since SOC measurements come with high uncertainty, the profitability was analysed in a scenario where this carbon pool is completely disregarded. The comparison of NPV with and without this carbon pool is shown in Figure 7. Since SOC absorbs over a third of the total carbon pools considered, this has a significant impact on the NPV, dropping over $ 400 bn. This highlights the need of an effective method to accurately measure organic carbon in soil. Additionally, a similar sensitivity analysis on the

Table 3. NPV of all 6 scenarios considered

	USD 2005 NPV/ $ Bn		
	Full Tech Implementation	*Conventional Tech*	*no CCS*
Agriculture	$ 501	$ 1,067	$ 2,068
Pasture	$ 590	$ 1,255	$ 2,420

Note: MUSE uses the Full Tech implementation pricing strategy, as such only results of this scenario are discussed further.

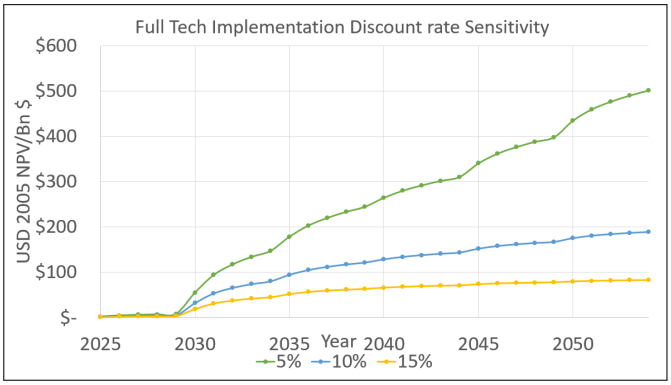

Fig. 6. Assessing the NPV of the project with increasing degree of risk

discount rate was conducted to analyse the NPV with a higher risk factor. As seen from Figure 8, even neglecting SOC and increasing the discount rate to 15%, this carbon abatement pricing strategy could still produce a NPV of around $ 20 bn. Another insight that can be drawn from Figure 8 is that every land acquisition causes a notable dip in the NPV, with a negative NPV in 2030 due to a large amount of land acquired. This stresses the biggest cost of the reforestation project; land acquisition. This is analysed further in the next section.

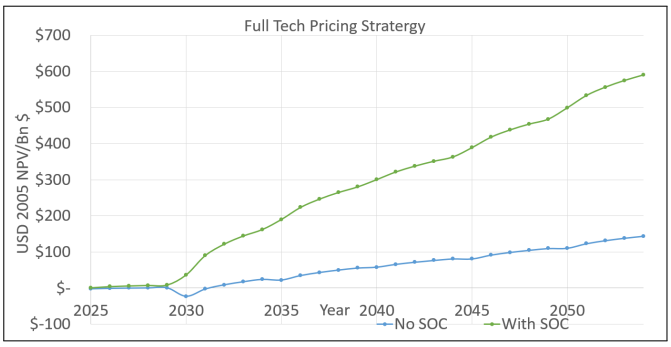

Fig. 7. Comparison of NPV with and without considering SOC

3.2.3. CAPEX & OPEX

Having established that the land acquisition cost is the biggest expenditure endured in this project, the degree of impact was then further analysed. This was done by

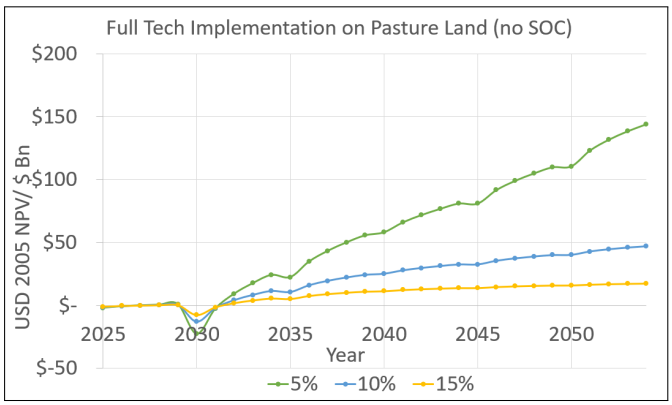

Fig. 8. Sensitivity analysis on discount rate when SOC is neglected

Table 4. Sensitivity Analysis on CAPEX and OPEX

USD 2005 Cost of CO_2 Capture/tn				
	100% Agriculture Land		*100% Pasture Land*	
Reference Cost	$ 31.27		$ 27.20	
CAPEX +20%	$ 36.50	+17%	$ 31.76	+17%
CAPEX -20%	$ 26.04	-17%	$ 22.65	-17%
OPEX +20%	$ 32.29	+3%	$ 28.09	+3%
OPEX -20%	$ 30.25	-3%	$ 26.32	-3%

considering the cost of carbon in reforestation. The cost of carbon was found by summing the total capital and operational expenditure throughout the simulated period, and then divided by total amount of carbon sequestered in the simulated period. This was found to be roughly $ 30/tn of CO_2 and is labelled as the reference value in Table 4. Varying CAPEX by 20% results in a 17% impact on the cost of carbon. Thus, CAPEX is deemed to have a moderate sensitivity on the project and more thorough, region specific data is required for more accurate analysis of the reforestation project. Similarly, OPEX has 3% sensitivity on the cost of carbon, deemed to have a low sensitivity on the project of reforestation. Although a detailed breakdown of operational cost is required, it would not have a quantitative impact on the analysis. It could however aide with the qualitative understanding of the project.

3.3. Reforestation in Brazil vs CCS

After performing the sensitivity analysis, the cost of sequestering carbon (per tonne) through reforestation has been compared to the cost of three industrial CCS technologies: Post Combustion capture using amine, Chemical Looping and Oxy-Combustion. This cost includes the cost of capture and the cost of transport - using an average value for 250 km of onshore pipeline and a transport capacity of 300 Mt of CO_2 per year. (Budinis et al., 2018). As reforestation does not require any cost for transport, this is a fair comparison between two alternate carbon capture technologies. This comparison is shown in Figure 9. It was found that reforestation in Brazil's Cerrado region is cheaper (per tn of CO_2). Additionally, even after disregarding the cost of transport in CCS (USD 2005 $ 14.42), the cost of carbon of reforestation is still cheaper than CCS. It is important to note that this comparison is only valid for the region considered in this study, it is likely that cost of carbon in reforestation may be similar or exceed the cost of CCS due to higher land prices in European and North American regions. Currently CCS technology is in early stages of development and leaves behind waste material that could be dangerous. In addition, CCS has an energy penalty, using 10-40% of the energy produced by a power station for carbon capture and storage (Greenpeace, 2018). Moreover, the total additional costs of an early stage CCS demonstration project is estimated to be 0.5-1.1 billion euros over its lifetime (Thorbjörnsson et al., 2018). Thus, reforestation could be used in the short term until CCS technology matures and becomes more cost effective.

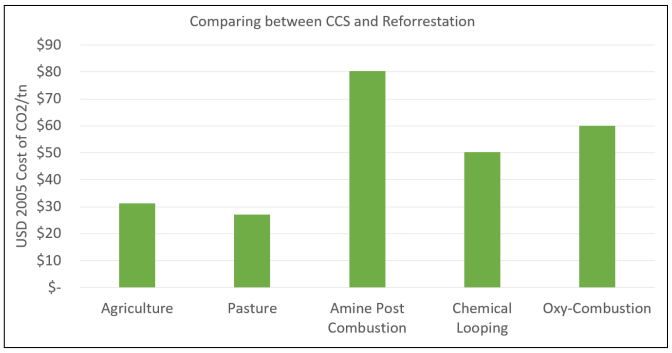

Fig. 9. A comparison of cost of capturing carbon between CCS technologies and reforestation in Brazil (Budinis et al., 2018)

3.4. Societal carbon cost Vs Carbon Abatement cost

Using the same rate of change of carbon cost as Kriegler et al., 2014, the minimum cost of carbon resulting in this project being profitable with a positive NPV has been found. This was then compared to the societal cost of carbon from literature, since the abatement costs of carbon from Kriegler et al., 2014 are very high and a scenario where someone could pay this cost is unlikely. The minimum current abatement costs that could result in a profitable NPV are demonstrated in Table 5. As every pricing strategy described by Kriegler et al., 2014 has a different growth rate, all three growth rates have been considered to find the minimum cost for both types of land considered in this model. Since sequestration potential varies by land types, the minimum cost of carbon for a positive NPV varies with land type.

The impacts of climate change costs taxpayers, businesses, families and governments billions of dollars due

Table 5. Minimum carbon cost that results in a positive NPV for reforestation in Brazil

	100% Pasture Land		100% Agriculture Land		
Scenario	*(USD 2018) Minimum initial carbon price for profitable reforestation in Brazil*	*(USD 2018) Carbon Price at the end of the simulation period using the minimum carbon price as initial price*	*(USD 2018) Minimum initial carbon price for profitable reforestation in Brazil*	*(USD 2018) Carbon Price at the end of the simulation period using the minimum carbon price as initial price*	*(USD 2018) Carbon price by Kriegler et al., 2014 at the end of the simulation period*
Full Tech	\$16.65 - \$16.66	\$75.58 - \$75.63	\$19.19 - \$19.20	\$87.09 - \$87.16	\$598.82
Conv Tech	\$13.17 - \$13.18	\$104.02 - \$104.12	\$15.33 - \$15.34	\$121.09 - \$121.20	\$1636.31
No CCS	\$11.50 - \$11.51	\$99.02 - \$99.13	\$13.39 - \$13.40	\$115.31 - \$115.41	\$2911.23

Note: The exact dollar value of carbon cost that results in a net zero NPV of the project falls in between the range provided. As such the lower carbon cost results in a negative NPV and the upper carbon cost results in a positive NPV.

to factors such as destruction of property, rising healthcare costs and increases in food prices. This is the societal cost of carbon, a monetary value that evaluates the economic damage caused by the impacts of climate change due to the emission of 1 tn of CO_2. The current social cost of carbon is valued at \$ 40/tn of CO_2 and is considered to be far lower than the true cost of carbon (Environmental Defense Fund, 2018). The already undervalued societal cost of carbon is at least double the minimum carbon cost of a profitable reforestation project in Brazil. Considering the scenario applied in MUSE, a Full Tech Pricing Strategy where the vast majority of liberated land comes from Pasture land use results in a current societal cost of carbon that is roughly 2.5 times larger than the minimum carbon abatement cost. Using the current estimated societal carbon cost (USD 2005 \$ 30.89 (Statistics and Index, 2018)) as the initial carbon cost in the technoeconomic analysis, the scenario with Full tech implementation on pasture land has a NPV of USD 2005 \$8.81 bn. Although much lower than the NPV from the carbon abatement cost used in this model, the profitability of this project with the current (undervalued) societal carbon cost strengthens the viability of reforestation in Brazil and the validity of the results produced by this model.

3.5. Brazil's efforts towards NDC targets

Brazil intends to commit to reduce greenhouse gas emissions by 37% below 2005 levels in 2025.To meet the NDC targets, Brazil plans to restore and reforest 12 million hectares by 2030, for multiple purposes. In addition, it plans to restore an additional 15 million hectares of degraded pasturelands by 2030 and enhance 5 million hectares of integrated cropland-livestock-forestry systems (ICLFS) by 2030. It also plans to prevent any illegal deforestation in the amazon rainforest by 2030. Brazil plans to decrease its GHG emissions using a combination of CCS and reforestation. Our model enables us to project the negative emissions that could result from reforestation. This is modelled assuming 90% pastural and 10% agricultural land as this is roughly the current make-up of the Cerrado region. Projecting the results until year 2050 of our reforestation model result in slightly missing the 2030 NDC target. Emissions in Figure 10 consider the negative emissions from both CCS technology implemented in power stations that could decrease the GHG emissions into the atmosphere as well as reforestation. Therefore, it is highly advantageous to implement reforestation in Brazil in tandem with CCS to meet set NDC goals. It is however important to understand that this model predicts the maximised carbon sequestration potential from the available land in the discussed scenario; in reality the sequestration may be much lower due to drop in land utilisation. This results in being much further away from the NDC target. Additionally, other sectors have proved to have a substantially slower transition to clean energy technology (Environmental Leader, 2018). Thus, to meet the Brazilian NDC target, major changes in all industries are required to lower the carbon emissions across all sectors. Since Brazil invites support from developed countries, other countries could possibly invest in Brazilian reforestation. This could be subject to negotiations: which countries NDC's could reforestation contribute to? and who gets the retained earnings from the profits of reforestation? This symbiotic relationship can result in further positive knock on effects with other countries that are currently not prioritising tackling climate change to reconsider their position.

4. CONCLUSION

The integration of a comprehensive reforestation model into an energy system model (MUSE) is the first step towards coordination between the industry and the agricultural sector.

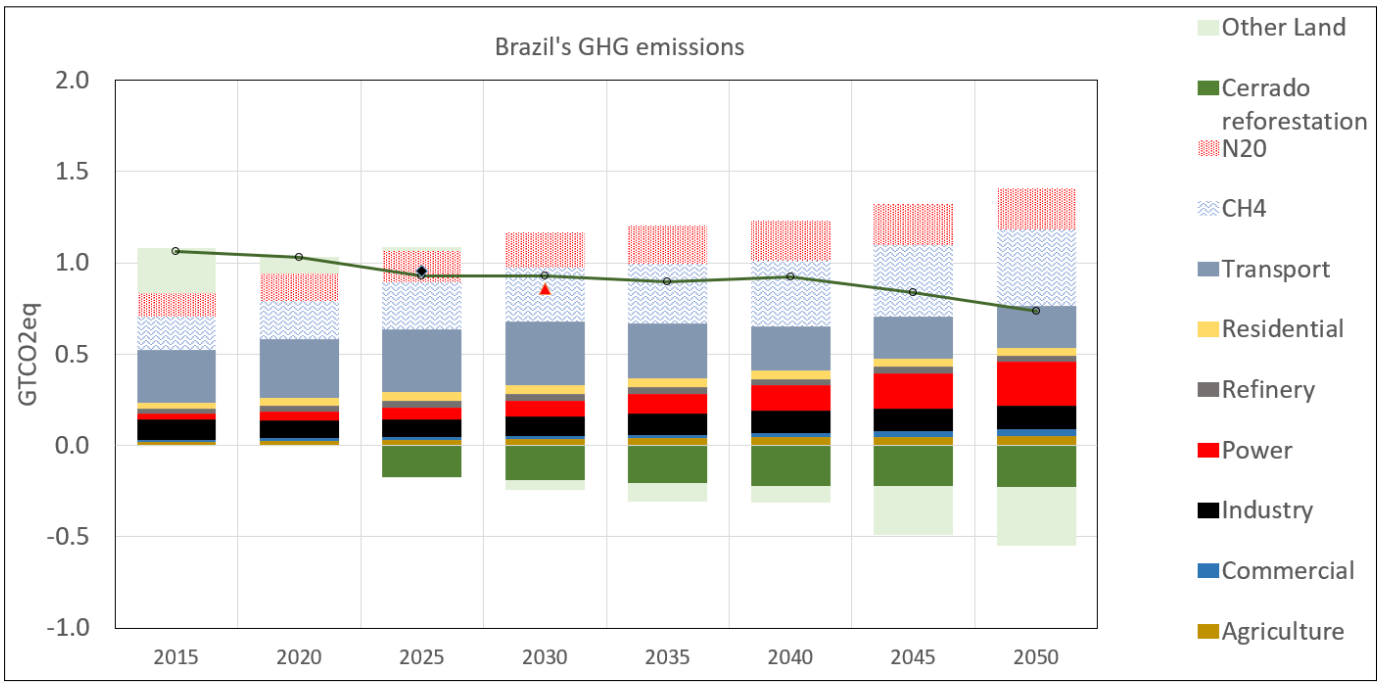

Fig. 10. Comparing negative emissions due to reforestation in the Cerrado region to the overall greenhouse gas emissions in Brazil

For the proposed framework, all carbon pools (aboveground, belowground and soil organic carbon (SOC)) have been considered in the model. As SOC is a very difficult carbon pool to measure, a scenario was considered that neglected SOC, only drawing on data from aboveground and belowground carbon pools.

Based on the scenario and the carbon abatement cost, the minimum NPV from carbon sequestration exceeds (USD 2005) $ 500 bn and still maintains a highly profitable NPV of roughly $ 80 bn at a much higher discount rate of 15%. The cost of carbon of reforestation in Brazil was found to be in the range of $ 22.65 - $ 36.50 (per ton of CO_2). The societal cost of carbon falls in the middle of this model's range at $ 30.89/ton of CO_2. Using this as the initial carbon abatement cost in the technoeconomic analysis results in a NPV of over $ 8 bn, strengthening the viability of reforestation in Brazil to combat climate change.

Due to sensitivity of CAPEX identified in this report, a more thorough breakdown of land costs that considers the region of land, previous land use, topography of land and more. This data can be applied to better understand the technoeconomic characterisation of reforestation.

Reforestation could be a bridge to transition to clean energy sources and should be used in complement with industrial CCS across other sectors. Taking an average of the CCS technologies considered, the costs of carbon dioxide absorption using CCS is $ 32.8 more per ton of carbon dioxide, an increase of 107% compared to reforestation modelled in Cerrado, Brazil. However, due to the nature of technology advancement, costs of CCS certainly could reduce over time while the cost of reforestation could increase due to increasing land prices. It is thus more advantageous to utilize reforestation more in the near-future and CCS in the longer-term future to meet NDC targets. Additionally, Brazil intends to meet their short term NDC targets by restoring and reforesting at least 12 million hectares of land, thus, this model and the modelling outputs from this analysis can be directly used to understand how these steps will impact the Brazilian GHG emissions.

5. FUTURE WORK

Further work is needed to strengthen the model link and make it a hard-link with MUSE. The feedback loop to MUSE should enable better estimations of carbon (abatement) costs, which was an area of uncertainty for this analysis. Only three factors of the operational costs have been considered in this model, other costs such as the reapplication of fertilizer, need to be accounted to build a more robust model. Finally, a model should be built to optimize the allocation of land available for reforestation and the growth of biofuel crops. This could be used to meet the increasing industry demand for biofuels and BECCS due to the expected shift in industry towards clean and sustainable energy technology.

6. ACKNOWLEDGEMENTS

The authors thank Dr. Ivan Garcia Kern for his extremely valuable insight in this analysis.

7. REFERENCES

Budinis, S., Krevor, S., Dowell, N., Brandon, N. and Hawkes, A. (2018). An assessment of CCS costs, barriers and potential. Energy Strategy Reviews, 22, pp.61-81.

Carvalho, J., Cerri, C., Feigl, B., Píccolo, M., Godinho, V. and Cerri, C. (2009). Carbon sequestration in agricultural soils in the Cerrado region of the Brazilian Amazon. Soil and Tillage Research, 103(2), pp.342-349.

Environmental Defense Fund. (2018). The true cost of carbon pollution.

Environmental Leader. (2018). Cement Industry Lags on Emissions Reductions, CDP Report Finds.

EPE. (2018). Plano Nacional de Energia - 2050.

Fao.org. (2018). Definitional issues related to reducing emissions from deforestation in developing countries.

Greenpeace. (2018). False Hope: Why carbon capture and storage won't save the climate.

Guitart, A. and Rodriguez, L. (2010). Private valuation of carbon sequestration in forest plantations. Ecological Economics, 69(3), pp.451-458.

Iea-etsap.org. (2018). IEA-ETSAP | Energy Systems Analysis.

Jackson, R., Lajtha, K., Crow, S., Hugelius, G., Kramer, M. and Piñeiro, G. (2017). The Ecology of Soil Carbon: Pools, Vulnerabilities, and Biotic and Abiotic Controls. Annual Review of Ecology, Evolution, and Systematics, 48(1), pp.419-445.

Kriegler, E., Weyant, J., Blanford, G., Krey, V., Clarke, L., Edmonds, J., Fawcett, A., Luderer, G., Riahi, K., Richels, R., Rose, S., Tavoni, M. and van Vuuren, D. (2014). The role of technology for achieving climate policy objectives: overview of the EMF 27 study on global technology and climate policy strategies. Climatic Change, 123(3-4), pp.353-367.

Lewis, T., Verstraten, L., Hogg, B., Wehr, B., Swift, S., Tindale, N., Menzies, N., Dalal, R., Bryant, P., Francis, B. and Smith, T. (2018). Reforestation of agricultural land in the tropics: The relative contribution of soil, living biomass and debris pools to carbon sequestration. Science of The Total Environment, 649, pp.1502-1513.

M. R. Allen, O. P. Dube, W. Solecki, F. Aragon–Durand, W. Cramer, S. Humphreys, M. Kainuma, J. Kala, N. Mahowald, Y. Mulugetta, R. Perez, M. Wairiu, K. Zickfeld, 2018, Framing and Context. In: Global warming of 1.5°C. An IPCC Special Report on the impacts of global warming of 1.5°C above pre-industrial levels and related global greenhouse gas emission pathways, in the context of strengthening the global response to the threat of climate change, sustainable development, and efforts to eradicate poverty [V.

Masson-Delmotte, P. Zhai, H. O. Portner, D. Roberts, J. Skea, P.R. Shukla, A. Pirani, W. Moufouma-Okia, C. Pean, R. Pidcock, S. Connors, J. B. R. Matthews, Y. Chen, X. Zhou, M. I. Gomis, E. Lonnoy, T. Maycock, M. Tignor, T. Waterfield (eds.)]. In Press.

Muratori, M., Calvin, K., Wise, M., Kyle, P. and Edmonds, J. (2016). Global economic consequences of deploying bioenergy with carbon capture and storage (BECCS). Environmental Research Letters, 11(9), p.095004.

Ranger, J. (1996). Biomass and nutrient content of extensively and intensively managed coppice stands. Forestry, 69(2), pp.91-110.

Ribeiro, S., Soares, C., Fehrmann, L., Jacovine, L. and von Gadow, K. (2015). ABOVEGROUND AND BELOWGROUND BIOMASS AND CARBON ESTIMATES FOR CLONAL EUCALYPTUS TREES IN SOUTHEAST BRAZIL. Revista Árvore, 39(2), pp.353-363.

Silver, W., Ostertag, R. and Lugo, A. (2000). The Potential for Carbon Sequestration Through Reforestation of Abandoned Tropical Agricultural and Pasture Lands. Restoration Ecology, 8(4), pp.394-407.

Smith P, Clark H, Dong H, Elsiddig EA, Haberl H, Harper R, House J, Jafari M, et al. (2014). Chapter 11 - Agriculture, forestry and other land use (AFOLU). In: Climate Change 2014: Mitigation of Climate Change. IPCC Working Group III Contribution to AR5.Cambridge University Press.

Statistics, B. and Index, C. (2018). $73 in 2015 → 2005 | Inflation Calculator. [online] In2013dollars.com.

Sullivan, J., Aggett, J., Amacher, G. and Burger, J. (2005). Financial viability of reforesting reclaimed surface mined lands, the burden of site conversion costs, and carbon payments as reforestation incentives. Resources Policy, 30(4), pp.247-258.

Sustainablegasinstitute.org. (2018). MUSE – A new Energy Systems Model - Home | Sustainable Gas Institute.

Thompson, J. (2018). Brazilian farmland is getting more expensive. .

Thorbjörnsson, A., Wachtmeister, H., Wang, J. and Höök, M. (2018). Carbon capture and coal consumption : Implications of energy penalties and large scale deployment.

Unfccc.int. (2018). Nationally Determined Contributions (NDCs) | UNFCCC.

Visionlearning. (2018). The Carbon Cycle | Earth Science | Visionlearning.

Wwf.org.br. (2018). Deforestation in the Cerrado Biome increased by 9% in 2017. Available at: https://www.wwf.org.br/?66403/Deforestation-in-the-Cerrado-Biome-increased-by-9-in-2017

Wwf.panda.org. (2018). Cerrado, the Brazilian Savanna. Available at: http://wwf.panda.org/knowledge$_hub/where_we_work/cerrado/$

Yang, Z., Wei, Y., Mi, Z., (2018). Integrated Assessment Models (IAMs) for Climate Change - Environmental Science.

Contributions to the stability of particle stabilised oil foam

Ailsa Morrison and James Buckley, supervised by Dr. Valeria Garbin, and Mr. Saikat Saha

13 December 2018

Abstract

The stabilisation of a sunflower oil-based foam using Hydropel QB wax has been studied, including the preparation and long-term stability of the foam, as well as the temperature dependence of the dissolution rate of the bubbles. In addition, an analysis of the effect of wax-crystal stabilisation at the air-oil interface was conducted using the pendent drop method. The preparation conditions of 80-110 °C and 1-3.5% (w/v) (wax in oil), resulted in the highest number of bubbles and the most stable foams. It was shown that the wax adsorbed at the interface caused a slight reduction in dissolution rate compared to clean bubbles, but that the combination of bulk and interfacial effects on stability resulted in the slowest dissolution rate at 25 °C. An increase in temperature was observed to cause the dissolution rate to increase for all sample types across the temperature range of 25 °C, 90 °C and 130 °C. The pendent drop analysis highlighted that the presence of wax crystals at the air-oil interface resulted in a reduction of the effective surface tension, (≈20-21 $mN \cdot m^{-1}$ compared to 32 $mN \cdot m^{-1}$ for pure sunflower oil) however the dilational modulus values calculated were irreproducible.

Keywords:

oil foam, dissolution rate, wax crystals, dilational modulus, Pickering stabilisation

1 Introduction

Foams are used in many industries, but whereas the behaviour of aqueous foams has been well studied and documented,[1,2] information concerning non-aqueous foams remains scarce, though interest in the topic has increased in the past few years.[3] Despite the lack of research, there are many applications of oil foams, including in personal care products, and edible foams.[4] The food industry has historically used trans-fats as the stabilising agent in many food products, but by replacing them with oil foams, the fat content of these products can be reduced.[5] In the petroleum industry, the use of non-aqueous foams as drilling fluids allows drilling to be undertaken on water-sensitive rock formations without a drop in permeability due to damage to the formation.[6-8]

Bubbles are not energetically favourable and will naturally dissolve or coalesce over time, and so in order to create stable foams, different molecules are added to the bubble surface. The stabilisation of aqueous foams has traditionally been achieved through the use of surface-active agents (surfactants),[9] which involves the adsorption of surfactants to the air-water interface, thereby leading to a reduction in the surface tension of the interface and thus a free energy gain for the system. In the case of oil foams, the surface tension of the air-oil interface is less than that of the air-water interface (≈25$mN \cdot m^{-1}$ compared to ≈72$mN \cdot m^{-1}$)[10] resulting in a smaller potential for surface tension reduction, and causing the adsorption of oil-soluble surfactants to be energetically unfavourable.[11] However, it has been found that small solid particles are effective at stabilising both aqueous and non-aqueous foams by adsorbing at the bubble interface effectively irreversibly due to the extremely high attachment energy[12] – this is called Pickering stabilisation. These particles not only reduce the effective surface tension at the interface, but also create a densely packed layer around the bubble which can prevent gas diffusion and bubble coalescence.[13] The use of these particles has a number of advantages including creating thermoresponsive systems and contributing magnetic or catalytic properties.[9]

The bubbles in foams are stabilised not only through interfacial rheology, but also the bulk rheology of the system. Kloek et al.[14] found that bulk and interfacial elasticity in combination could in fact stop bubble dissolution, and Gunes et al.[15] concluded that whereas interfacial contributions allow the formation of bubbles, the bulk rheology allows the bubbles to remain stable for a period of time. They describe structures in the bulk and bridges between neighbouring bubbles which are responsible for bulk viscous and elastic contributions to stability. Knowledge of specific parameters for different systems such as surface tension, or the dilational moduli, is also particularly useful for engineering and designing products, but these are difficult to

measure and are dependent on the composition of each individual system.[16] It is also known that the production of particle stabilised oil foams depends on the gas incorporation process, with methods such as hand shaking, depressurisation and whipping previously studied.[3,15]

Bubble dissolution at low concentrations is governed by Henry's law, and since Henry's constant is temperature dependent, temperature has a substantial effect on bubble dissolution rate.[17] It is crucial to understand the effect of temperature on dissolution so that consumer products can be formulated, stored and transported without decreasing their stability. Temperature dependence also affects the oil industry through the crystallisation of wax in oil pipelines, highlighting the wide range of applications temperature dependence research could benefit.[18] Garbin et al.[17] found that for aqueous systems, a steady reduction in temperature caused otherwise stable bubbles to coalesce and dissolve. Achakulwisut et al.[13] found the opposite behaviour for an alkane-based system, which is due to the opposite relationship between Henry's constant and temperature. However, many studies on foams do not test wide temperature ranges.[13,15]

Research on non-aqueous foams is not common and the use of wax particles to stabilise oil foams is a little studied method of stabilisation. Through our research on a sunflower oil system stabilised by Hydropel wax, we aim to address some of the current knowledge gaps relating to understanding the effect of solid particles at the bubble interface on the stability of the system, and the effect of temperature on bubble dissolution. We also use a novel method to analyse aspects of the interfacial rheology of the foam. These experiments allowed us to qualitatively and quantitively measure the effect the wax crystals have on the bubble interface and stability, and provide useful insights for food and cosmetic product companies when developing new products.

2 Background/Theory

2.1 Bubble Stability and Dissolution

2.1.1 Stability

The theory presented regarding 2.1.1.) bubble stability and 2.1.2.) bubble dissolution is primarily from Poulichet and Garbin,[17] and this paper can be referenced for more detail.

Bubbles shrink and coalesce because they are not energetically favourable. Surface tension at the curved vapour-liquid interface is responsible for creating a pressure difference known as the Laplace Pressure, given by,

$$\Delta P = \frac{2\sigma}{R} \qquad (1)$$

where σ is surface tension and R is the bubble radius. Placing a solid particle at the interface reduces the effective surface tension and the particle becomes effectively irreversibly adsorbed, with the energy of attachment being given by,

$$E = \pi r^2 \gamma_{\alpha\beta}(1 \pm cos\theta)^2 \qquad (2)$$

and the contact angle, determined by Young's Law, given by,

$$cos\theta = \frac{\gamma_{1s} - \gamma_{2s}}{\gamma_0} \qquad (3)$$

where γ_0 is the surface tension between the 2 phases, γ_{1s} between the surface and phase 1 and γ_{2s} between the surface and phase 2.[9] A contact angle as near to 90° as possible will create the greatest energy saving.

2.1.2 Bubble dissolution

Gas will diffuse in or out a bubble if the gas concentration inside the bubble is not the saturation concentration, and this depends on the concentration gradient. The saturation concentration is given by Henry's Law,

$$c_s = k_H M P_g \qquad (4)$$

where k_H is Henry's constant, M is the molar mass and P_g is the partial pressure of the gas acting on the interface. By combining this relation with the pressure inside the bubble,

$$P_g = P_0 + \Delta P \qquad (5)$$

a mass balance and Fick's Law, the rate of change of the bubble radius can be determined as,

$$\dot{R} = -Dk_H R_g T \left(1 - f + \frac{2M}{\rho_0 R_g T}\frac{2\gamma}{R}\right) \times \left(1 + \frac{2M}{3\rho_0 R_g T}\frac{2\gamma}{R}\right)^{-1} \times \left(\frac{1}{R} + \frac{1}{\sqrt{\pi D T}}\right). \qquad (6)$$

When temperature is taken to be time-dependant as in our experiments, the relation becomes,

$$\dot{R} = -Dk_H R_g T\left(1 - f + \frac{2M}{\rho_0 R_g T}\frac{2\gamma}{R}\right) \times \left(1 + \frac{2M}{3\rho_0 R_g T}\frac{2\gamma}{R}\right)^{-1} \times \left(\frac{1}{R} + \frac{1}{\sqrt{\pi DT}}\right) + \dot{T}\left(\frac{\frac{BT\rho_0}{M}R + 2\gamma + 2T\frac{d\gamma}{dT}}{3T\left(\frac{BT\rho_0}{M} + \frac{4\gamma}{3R}\right)}\right) \quad (7)$$

where $\dot{T}$ is the cooling rate. Temperature affects bubble dissolution by changing the gas density in the bubble - therefore affecting the saturation concentration and dissolution rate - and by changing the surface tension and therefore the Laplace pressure. This simplified model was developed to give a qualitative understanding of how temperature change affects bubble dissolution.

2.2 Surface tension

2.2.1 Theory and stability criterion

Surface tension is caused by cohesive forces and acts against gravity or buoyancy to hold bubbles or droplets together, so that the bubble or droplet minimises its surface energy. When a bubble shrinks, the surface compresses and the surface tension decreases. The interfacial dilational modulus is a measure of the change in surface tension with surface deformation (or A, area), given by the Gibb's elastic modulus[14],

$$E_d = \frac{d\sigma}{dA/A}. \quad (8)$$

Stabilisation occurs when $d\Delta P/dR > 0$ and so combining this with the relationship for E_d gives the following stabilisation criteria,[14]

$$E_d > \frac{\sigma}{2}. \quad (9)$$

Kloek et al.[14] were the first to model both the bulk and interfacial contributions to stability simultaneously. They conclude that solving Eq. (8) gives,

$$\sigma(R) = \sigma_0 + 2E_d ln\frac{R(t)}{R_0} \quad (10)$$

which they then include in their mass balance.

2.2.2 ImageJ pendent drop analysis

ImageJ analyses a photograph of a droplet and determines various properties including surface tension.[19] A droplet can be modelled using 3D spherical coordinates z (height), r (radius) and ψ (the angle between the tangent plane to the interface and the horizontal). By expressing the mean curvature of the droplet as a function of these parameters and including that at equilibrium the hydrostatic pressure difference is equal to the Laplace pressure, an expression for pressure equilibrium can be derived,[14]

$$-\frac{1}{l_c^2}sin\varphi = \frac{d}{ds}\left(\frac{d\varphi}{ds} + \frac{sin\varphi}{R}\right) \quad (11)$$

where l is the capillary length. The ImageJ plugin integrates this equation to obtain a drop contour and further rescales, translates and rotates the contour using five parameters to match it to the photograph. A droplet of oil coated in the wax gel is thought to be a good representation of the oil foam interface. The surface tension of sunflower oil was estimated to be around 32 $mN \cdot m^{-1}$.[20, 21]

3. Experimental procedure

3.1 Foam preparation

Hydropel wax was measured and added to Tesco sunflower oil in a vial at 2.5% (weight by volume, w/v), before being heated then mixed for 2 minutes (as established by previous research[22] as the optimum mixing time) using a Grant-bio PV-1 Vortex Mixer. The sample was spooned onto a prepared microscope slide and contained by a spacer. Diluted samples were prepared by spooning one drop of foam, then filling the spacer with pure sunflower oil. The samples were photographed using an inverted microscope and a Thorlabs DCC1645C camera.

3.2 Temperature dependence

An Olympus BXFM, BX-URA2 microscope was used in conjunction with a Thorlabs DCC1545M camera to photograph bubbles of an approximate radius of 100 μm. Slides were prepared using the same methods stated above in 3.1, and samples of pure oil, oil foam diluted with pure oil and pure oil foam were investigated. The slides were placed in a Linkam Temperature Control Stage which was connected to a T95 Temperature controller and LNP95 cooling pump with a liquid nitrogen source. This set-up allows a constant heating rate of 5 $°C \cdot min^{-1}$ to be selected during the heating phase from 17 °C and the desired temperature to be maintained during the study. Three temperatures were selected (25 °C, 90 °C and 130 °C), chosen to give a good spread over the melting temperature range of the wax (50-105 °C)[23] to test whether the melting of the wax affected the final foam quality.

Images were taken every 10 seconds and compiled into one video file. These video files were analysed in MATLAB using Otsu thresholding[24] to identify the edge of the bubble. By converting each frame into a binary

image with the bubble appearing as a dark object, the area occupied by the bubble could be obtained by counting the number of black pixels in the image and hence the radius of the bubble can be calculated. The radius data is then plotted against time to show the rate of dissolution.

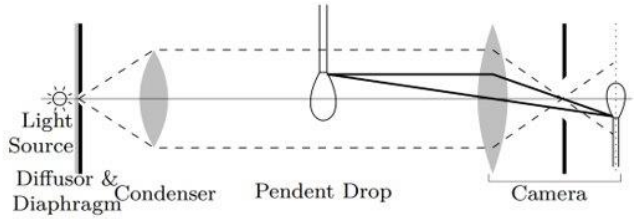

Figure 1: Pendant drop set up.[19]

3.3 Pendent drop

The set-up for the pendent drop experiment is adapted from the measurement bench described by Adrian Daerr (Fig. 1). Light originates from a source placed level with a Thorlab camera, then passes through a diffusor and a condenser, ensuring that the light rays are parallel to the optical axis. The condenser is used to prevent grazing reflections at the edge of the drop, which can cause the droplet to appear smaller than its actual size, affecting the calculated value of surface tension. The droplet is suspended between the condenser and the camera, which is focused on the drop, from a blunt needle connected to syringe pump.

The experiment begins with a droplet of pure oil, approximately one third of the maximum volume before the drop would detach from the needle. The oleogel (hot and cold were both tested) is then deposited onto the droplet using a syringe. The droplet is expanded and contracted in stages, with images taken at each stage after the droplet has come to rest. These images are analysed using the pendent drop plugin for ImageJ.[25] The data from this analysis is plotted in MATLAB on a graph of surface tension against surface area, from which E_d can be calculated using Eq. (8).

4. Results

4.1 Foam preparation

The bubbles produced were irregular in shape with textured surfaces, which is common for non-aqueous foams stabilised by solid particles.[3] As shown in Fig. 2a and 3a, it was found that the highest number of bubbles were found in the range 80-110 ˚C, which is within the melting range of the wax, suggesting that the coating of bubbles is much more successful when the wax is molten. Fig. 2a shows an approximation of the number of bubbles in the initial sample photos and 1 week later. Although the 85 ˚C sample showed a drop in bubble number, the bubbles are of a large size which is also an important factor for foam quality. Photographs that were taken one week later to check the stability of the foam, (Fig. 2b and 3b) also show that the bubbles in the range 80-110 ˚C were the most stable, and so this was chosen as the optimum range for preparation. Since earlier work[22] was completed at 90 ˚C, this was our chosen preparation temperature to allow comparison of our data.

In addition to the pure samples, diluted samples were also prepared to investigate the contribution of interfacial and bulk effects on stability. The diluted samples showed fewer bubbles, and crystals of wax were formed in the pure oil surrounding the sample, shown in Fig. 4, as found by Gunes et al.[15] In addition, no bubbles transferred into the pure oil phase. This indicates that the wax present in the bulk or 'matrix' around the bubble has a positive influence on stability, which is consistent with Kloek at al.[14] who state that both the bulk and interface play a role in stabilisation.

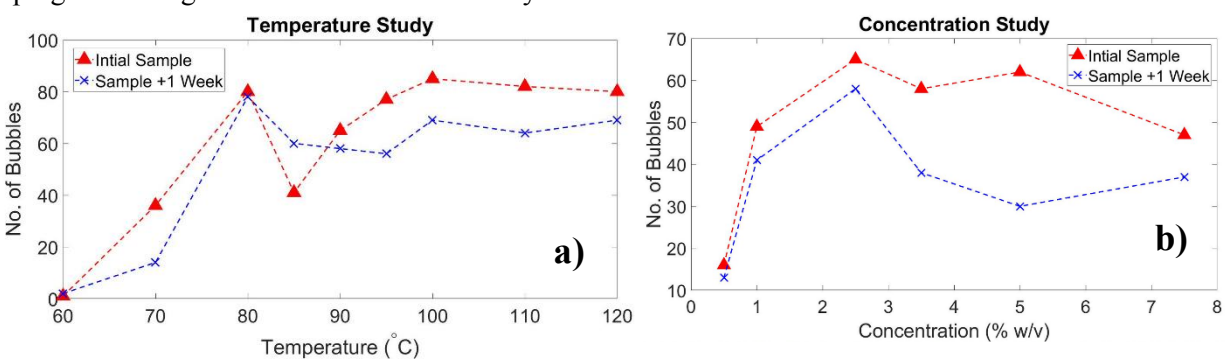

Figure 2: Number of bubbles at each temperature (a) and concentration (b) studied, immediately after sample preparation and 1 week later.

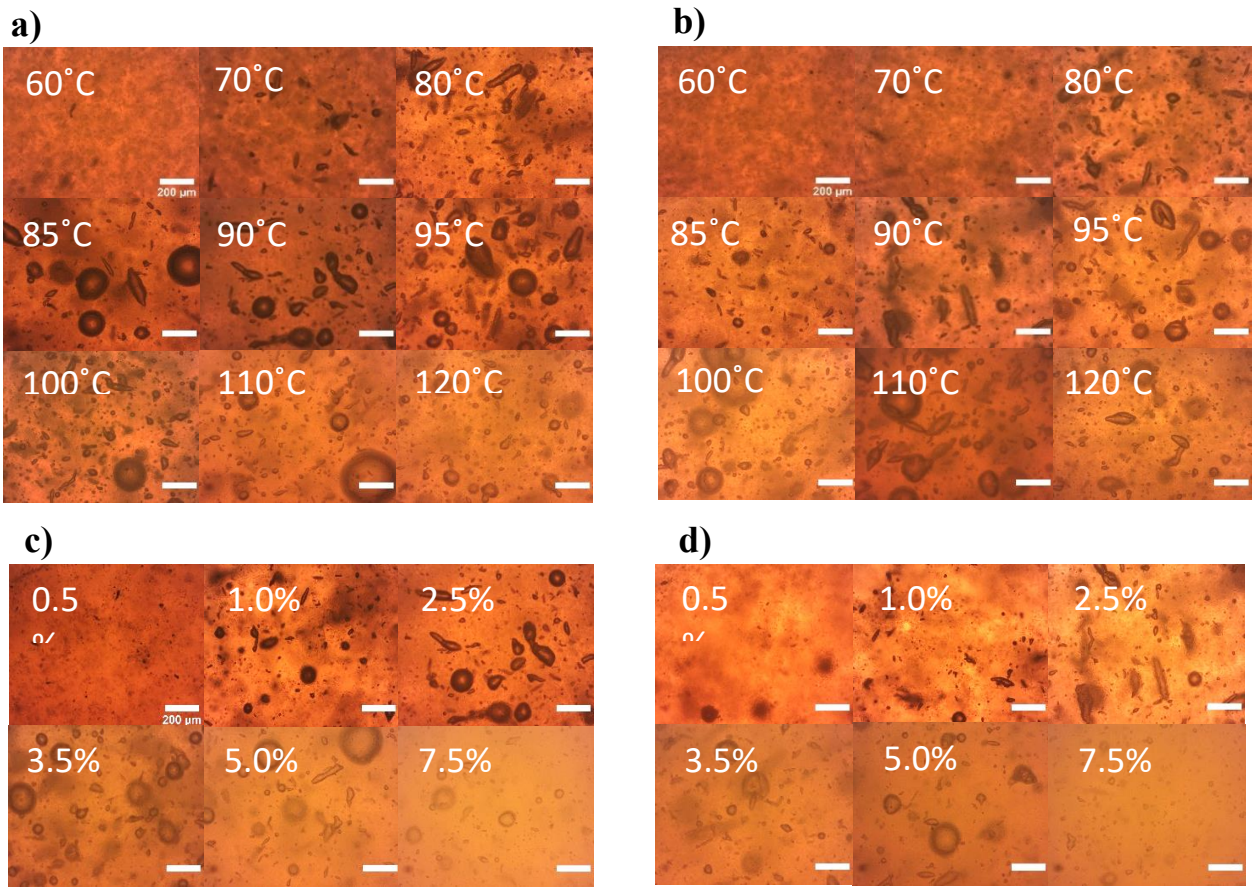

Figure 3: Bubble images at 4x magnification at different preparation temperatures (a) and after 1 week (b), and bubble images at 4x magnification at different preparation concentrations (c) and after 1 week (d).

The effect of the concentration of wax in oil was also investigated, (Fig. 3c), within the range of 0.5-7.5% (w/v), since previous work was carried out at 2.5%. Below 2.5% it was found that very few bubbles formed, and above 3.5% the mixture became extremely opaque under the microscope and difficult to observe (Fig. 3c and 3d). At low concentrations it is thought that there is not enough wax to coat the bubble surfaces and that rate of collision between the wax particles and bubbles is not high enough. At 7.5% the bubble density was observed to decrease, but this may be because the samples were very opaque and difficult to analyse. The optimum range for number of bubbles was found to be between 1-3.5% with 1% and 2.5% showing the best stability after 1 week (Fig. 2b). As none of the concentrations studied showed significant improvement on 2.5%, this was the chosen concentration for the following experiments, to again allow the comparison of our results to earlier work.[22]

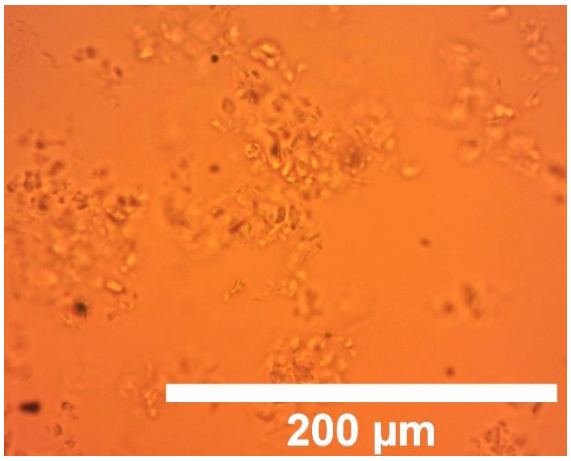

Figure 4: 16x magnification showing crystals of wax present in dilute samples.

4.2 Temperature dependence

A clear trend between temperature and bubble dissolution rate for pure sample bubbles was found (Fig. 5c). The pure sample at 130 °C dissolved the fastest, followed by the sample at 90 °C then 25 °C. Although not shown in the figure, the 25 °C sample was left for 7 hours and did not dissolve in this time. This is in agreement with Achakulwisut et al.[13] who found that dissolution rate increased with increasing temperature for a non-aqueous system. This is because Henry's constant

increases with temperature for alkanes[13] and although Henry's constant for sunflower oil was not measured, our findings suggest the same trend is true. Although the radius does not reach zero on the figure, the asymptotic ending to the curve does indicate full dissolution and is simply a feature of the image analysis.

The 25 °C samples (Fig. 5a) show clearly that the pure sample bubble experienced very little dissolution compared to the dilute sample bubble, and the clean sample bubble had the fastest dissolution rate. This shows that at this temperature, the wax coating at the interface and any wax present as a matrix in the bulk effectively contribute to bubble stability. Since the dilute sample bubble had a similar but fractionally lower dissolution rate than the clean bubble, this suggests that stabilisation at the interface is having a positive effect but that the absence of bulk contributions resulted in decreased stability. It is also known that larger bubbles dissolve slower, and the dilute sample bubble began approximately 10 µm larger than the clean bubble yet still dissolved faster. At 25 °C, none of the bubbles fully dissolved in the allocated timeframe.

The 90 °C samples (Fig. 5b) show an interesting phenomenon in which the clean bubble radius increases before the bubble shrinks, which was observed more than once. This is thought to be due to Ostwald ripening[26] but there is insufficient information regarding the surrounding bubbles to confirm this hypothesis. The bubbles in the dilute and pure samples never showed any growth so this may indicate that the wax can prevent Ostwald ripening. Another point to note is that although the clean bubble appears to have dissolved the slowest (4240 seconds), if taken from the time that the bubble returned to approximately 100 µm, the clean bubble showed the fastest dissolution rate (130 seconds, compared to 1510 seconds for the dilute sample and 2260 seconds for the pure sample). Finally, the bubble in the dilute sample again dissolved faster than the pure sample bubble, highlighting the positive contribution of bulk stabilisation.

Pure, dilute and clean sample bubbles were also tested at 130 °C however the results were not as expected. The dilute sample bubble remained stable the longest, whilst the clean and pure sample bubbles dissolved considerably faster. As this result does not agree with the previous temperatures, it is thought to be an anomaly and it is suggested that repetitions are carried out. The bubbles moved considerably due to convection, and many dissolved entirely before reaching 130 °C, which will have caused some error in the results. This experiment has not been

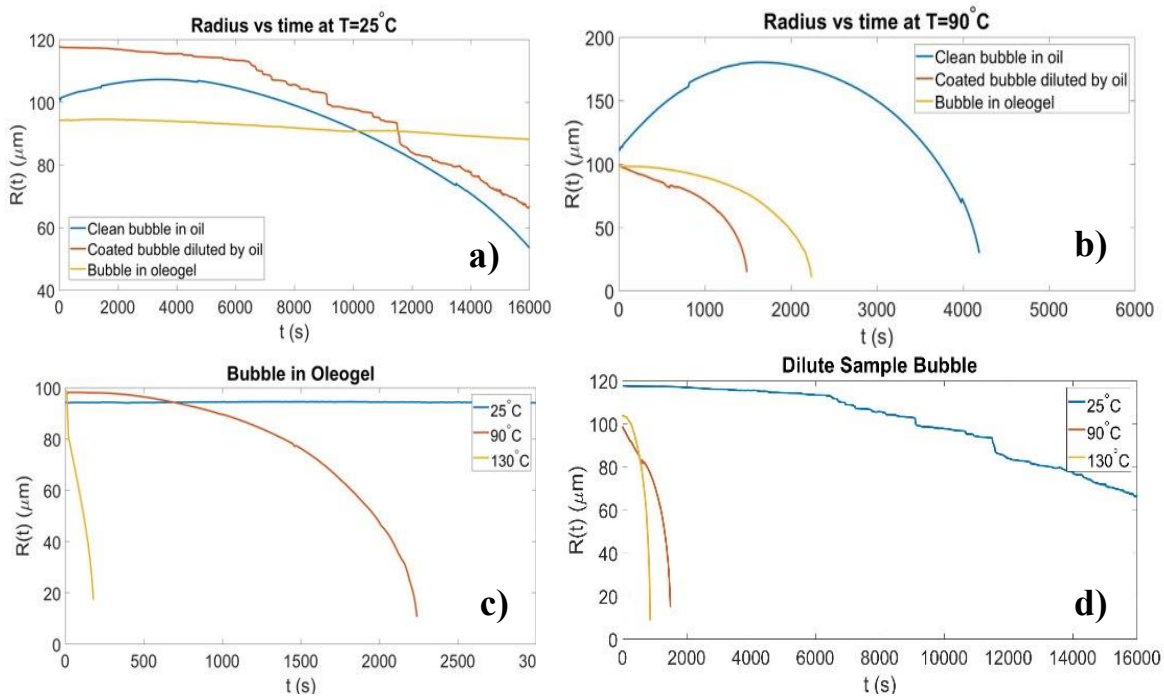

Figure 5: The clean, diluted and pure sample bubbles at 25°C (a) and 90°C (b), and the comparison of different temperatures for pure sample bubbles (c) indicating an increase in dissolution rate with temperature, and diluted sample bubbles (d), showing complete dissolution or shrinkage for each temperature.

completed at 130 °C before, and so further exploration of temperatures above the melting range of the wax is also recommended.

4.3 Pendent drop analysis

A linear relationship between surface tension and surface area was observed for the cold oleogel deposited on the pure oil droplet, as shown in Fig. 6. A significant reduction of the surface tension compared to the pure sunflower oil was recorded, ≈20-21 mN·m^{-1} down from 32 mN·m^{-1}, suggesting that there is adsorption of wax crystals at the air-oil interface. The calculated E_d values of 0.996 mN·m^{-1} and 1.34 mN·m^{-1}, for the expansion and compression phases respectively, are less than the stability criterion of ≈10.5 mN·m^{-1} (Eq. 9). These results are to be expected, as the interface does not remain stable indefinitely and in the temperature dependence study, the dilute sample bubbles either completely dissolve, as shown in Fig. 5d, or dissolve faster than the pure sample. Therefore, the E_d values should be less than the stability criterion. For the study of depositing hot oleogel onto the interface, difficulties with the set-up led to experiments with irreproducible data. Also, significant differences between the surface tensions measured suggest that further refinement is needed before reliable data can be obtained.

As this direct measurement of interfacial rheology has not been attempted in this way before, several sources of error have been identified and will require further study to be eliminated. The primary source of error in the system is due to the wetting of the needle or capillary from which the droplet is suspended, resulting in deviation from an ideal droplet shape and thus incorrect surface tension measurements. Furthermore, the coverage of the droplet by the oleogel cannot be quantified, meaning that each set of data was obtained under different conditions. In addition, data recorded for low droplet volumes resulted in artificially high surface tensions, as the Bond number is too small, so surface tension effects dominate over the gravitational effects. For the current set-up, the operating parameters were identified as a minimum droplet surface area of ≈8 mm^2 to eliminate the error from small Bond numbers.

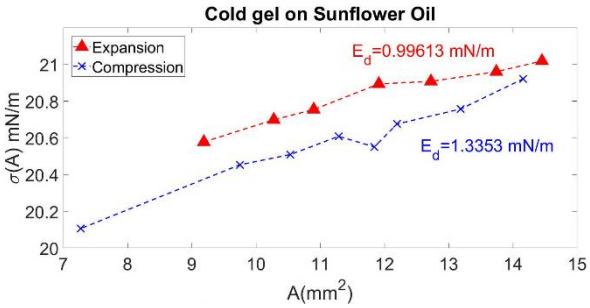

Figure 6: E_d values for air/oil interface stabilised by cold wax oleogel.

5. Conclusion

We have shown that the preparation of oil foams is dependent on temperature and concentration, whilst stability is due to contributions from the both the bulk and interfacial properties. The most stable foams were observed for preparation conditions of 80-110 °C and 1-3.5% w/v. A clear positive trend was established between temperature and dissolution rate for the three bubble types studied, knowledge of which has an important impact on the storage and transportation methods of these foams, especially in the case of aerated foods where certain products may require refrigeration. The comparison of the pure and dilute sample bubbles highlights the positive contributions of bulk elasticity to bubble stability as the coated bubble in oleogel was observed to be the most stable at 25 °C and 90 °C (once the clean bubble growth was accounted for). Interfacial contributions were also confirmed at 25 °C, as the dilute sample bubbles were stable longer than the clean bubbles. The pendent drop study confirmed that the presence of the wax crystals at the interface led to a reduction in the effective surface tension of the interface, however further refinement is needed to be able to calculate E_d reliably.

The aim of any future work should be to carry out a more thorough investigation of the interfacial rheology of the system, specifically targeting the elimination of the sources of error identified in the pendent drop set-up. If this can be achieved, then the E_d values for the interface can be compared with the stability criterion Eq. (9) allowing for a quantitative insight into the stability of these foams. Values of the bulk elasticity could also be calculated to confirm quantitively the bulk contribution to stability. In addition, the unexpected results observed for the 130 °C temperature study means that further

investigation into the behaviour of the three systems at temperatures above the melting range of the Hydropel wax is recommended.

Acknowledgements
We would like to thank Mr. Saikat Saha for assisting us in labs almost every day of our project and for contributing some invaluable insights, as well as the Garbin research group for their contribution of ideas and feedback.

References

1. Pugh, R. (2016) Bubble and Foam Chemistry.
2. Cantat, I. (2013) *Foams, structure and dynamics.* OUP Oxford.
3. Fameau, A., Lam, S., Arnould, A., Gaillard, C., Velev, O. D. & Saint-Jalmes, A. (2015) Smart Nonaqueous Foams from Lipid-Based Oleogel. *Langmuir : The ACS Journal of Surfaces and Colloids.* 31 (50), 13501-13510.
4. Patel, A. (2017) Stable 'arrested' non-aqueous edible foams based on food emulsifiers. *Royal Society of Chemistry; Food Function 8, 2115-2120.*
5. Patel, A. (2017) *Are edible oleocolloids the final frontier in food innovation?*
6. Blázquez, C., Emond, E., Schneider, S., Dalmazzone, C. & Bergeron, V. (2014) Non-Aqueous and Crude Oil Foams. *Oil & Gas Science and Technology – Revue d'IFP Energies Nouvelles.* 69 (3), 467-479.
7. DiBiasio, M., Sepulveda, J. J., Zamora, F., Shirley, G. L., Tkach, S. A., Falana, O. M., Morales, J. D., Kakadjian, S., Marshall, E. C. & Benoit, D. J. (2008) Oil-Based Foam and Proper Underbalanced-Drilling Practices Improve Drilling Efficiency in a Deep Gulf Coast Well. , SPE.
8. V . Bergeron, Jan Erik Hanssen, F.N. Shoghl. (1996) *Thin-film forces in hydrocarbon foam films and their application to gas-blocking foams in enhanced oil recovery.*
9. Garbin, V. (2013) Colloidal particles: Surfactants with a difference. *Physics Today.* 66 (10), 68-69.
10. Bernard P. Binks, Anais Roche and Mark Kirland. (2010) *Oil foams stabilised solely particles.*
11. Fameau, A., Lam, S., Arnould, A., Gaillard, C., Velev, O. D. & Saint-Jalmes, A. (2015) Smart Nonaqueous Foams from Lipid-Based Oleogel. *Langmuir : The ACS Journal of Surfaces and Colloids.* 31 (50), 13501-13510.
12. Binks, B. P. (2002) Particles as surfactants—similarities and differences. *Current Opinion in Colloid & Interface Science.* 7 (1), 21-41.
13. Achakulwisut, K., Tam, C., Huerre, A., Sammouti, R., Binks, B. P. & Garbin, V. (2017a) Stability of Clay Particle-Coated Microbubbles in Alkanes against Dissolution Induced by Heating. *Langmuir : The ACS Journal of Surfaces and Colloids.* 33 (15), 3809-3817.
14. Kloek, W., van Vliet, T. & Meinders, M. (2001) Effect of Bulk and Interfacial Rheological Properties on Bubble Dissolution. *Journal of Colloid and Interface Science.* 237 (2), 158-166.
15. Gunes, D. Z., Murith, M., Godefroid, J., Pelloux, C., Deyber, H., Schafer, O. & Breton, O. (2017) Oleofoams: Properties of Crystal-Coated Bubbles from Whipped Oleogels-Evidence for Pickering Stabilization. *Langmuir : The ACS Journal of Surfaces and Colloids.* 33 (6), 1563-1575.
16. Dyab, A. K. F. & Al-Haque, H. N. (2013) Particle-stabilised non-aqueous systems. *RSC Advances.* 3 (32), 13101.
17. Poulichet, V. & Garbin, V. (2015) Cooling Particle-Coated Bubbles: Destabilization beyond Dissolution Arrest. *Langmuir : The ACS Journal of Surfaces and Colloids.* 31 (44), 12035-12042.
18. Andrade, D., Marcelino Neto, M. & Negrão, C. (2018) Non-monotonic response of waxy oil gel strength to cooling rate. *Rheologica Acta.* 57 (10), 673-680.
19. Daerr, A. & Mogne, A. (2016) Pendent_Drop: An ImageJ Plugin to Measure the Surface Tension from an Image of a Pendent Drop. *Journal of Open Research Software.* 4
20. Esteban, B. et al. (2012) 'Characterization of the surface tension of vegetable oils to be used as fuel in diesel engines', Fuel, 102, pp. 231–238

21. Chumpitaz, L., Coutinho, L. & Meirelles, A. (1999) Surface tension of fatty acids and triglycerides. *Journal of the American Oil Chemists' Society.* 76 (3), 379-382
22. Vaughn Leynes (2018), *Thermoresponsive Wax-Stabilised Foams for Formulated Products.*
23. Shamrock. (2017) *HYDROPEL QB.* Available from: https://shamrocktechnologies.com/product/hydropel-qb/ .
24. Dongju Liu & Jian Yu. (Aug 2009) Otsu Method and K-means. *HIS.* , IEEE. pp.344-349.
25. Adrian Daerr. (2017) *Pendent Drop ImageJ plugin.* Available from: http://www.msc.univ-paris-diderot.fr/~daerr/misc/pendent_drop.html [Accessed 19 Nov 2018].
26. Xu, K., Bonnecaze, R. & Balhoff, M. (2017) Egalitarianism among Bubbles in Porous Media: An Ostwald Ripening Derived Anticoarsening Phenomenon. *Physical Review Letters.* 119 (26), 264502.

Viscosity and Density of liquid Diisodecyl-phthalate with dissolved CO_2 at Temperatures between 313 and 373K and Pressures up to 800 bar.

FESARD Axelle
Department of Chemical Engineering, Imperial College London, U.K.

Abstract The viscosity of liquid diisodecyl-phthalate (DIDP) with dissolved CO_2 was measured at temperatures between 313 and 373K and pressures up to 800 bar. Different molar fractions of dissolved CO_2 in DIDP were studied from 0.2 to 0.8. A vibrating wire viscometer was used to do the measurements of viscosity and a vibrating tube densimeter was used for the measurements of density. Some pure fluids (hexane, toluene, pure DIDP) were first used to calibrate the apparatus and verify the ability of the wire of the viscometer to furnish good results. Results with this apparatus for the pure fluids were found to be in a good agreement with the data in literature [1][2] and existing correlation (less than 2% of error for viscosity and less than 0.5% error for density for pure DIDP). The results for DIDP and dissolved CO_2 were not compared with any correlation as there is no correlation existing yet. However, the results for pure DIDP were plotted against residual entropy to validate the behaviour of the fluid even though the obtained curve was not the expected one. Nevertheless, the results for the mixture of DIDP and CO_2 were as expected: viscosity decrease with the increase of the molar fraction of CO_2. Viscosity also decrease with temperature augmentation and pressure diminution.

Introduction

Knowing the properties of fluids is very important for the good design and optimisation of a process. The knowing of properties such as viscosity and density is particularly important in oil industry were these properties affects transport phenomena and fluid mechanics for example and so the good recuperation of the oil in reservoirs. Indeed, errors in prediction could lead to 10% error on production of heavy oil and so the loss of a massive amount of money [3]. A way to facilitate the recuperation of the oils in reservoirs is to add dissolved gases to the liquids to lower their viscosities and get them more easily because of the very low viscosities of gases in general [4].

CO_2 is an environmental issue today as it is partly responsible for global warming and greenhouse gases emissions. That is why CO_2 emissions have to be decreased. Some different conventions made countries to take measures against CO_2 emissions such as the COP 21 in Paris in which countries such as France made the engagement to decrease their CO_2 emissions by 20% by 2020. However, a total decarbonation in 2100 should still lead to a 2°C global temperature rise [3].

CO_2 could be enhanced and have its emissions decreased with notions such as carbon capture and storage (CCS) or enhanced oil recovery (EoR) [5] [6] [7]. Carbon Capture and Storage consists in capturing the CO_2 and to store it in empty oil reservoirs on the ground in order to prevent it from being emitted in the atmosphere. Enhanced oil recovery consists in injecting CO_2 in an oil reservoir to lower the oil viscosity and get it more easily. The CO_2 is then recycled and reused as shown in Figure n°1.

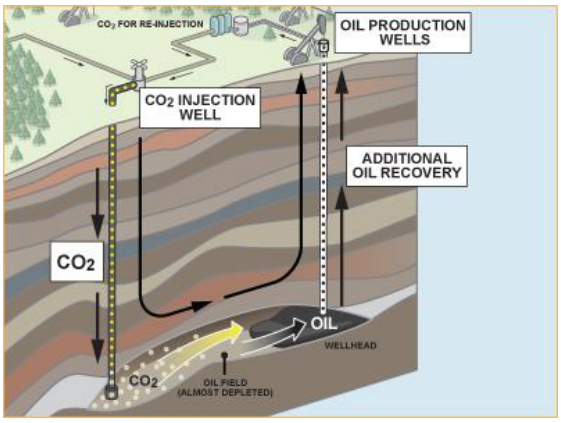

Figure 1. Principle of Enhanced Oil Recovery

But this discipline only allows to valorise a tiny amount of CO_2, that's why Carbon Capture and storage is very studied.

Diisodecyl-phthalate (DIDP) is an industrial reference liquid used for example for the calibration of viscometers at high pressures. This fluid is very viscous, 50 times more viscous than xylene for instance. His behaviour as a pure fluid is nowadays well known with a lot of different works presenting measurements of viscosity and density of DIDP among wide ranges of temperatures and pressures.

However, the behaviour of DIDP with dissolved CO_2 is not known. This work aims at starting to fill this gap. As a matter of fact, the behaviour of DIDP with dissolved CO_2 could have some similarities with hydrocarbons. With the actual issues of carbon storage and the needs for oil, being able to predict the shift of the properties by adding dissolved CO_2 in a viscous fluid could be useful. As there is not any result for DIDP with dissolved CO_2, this work will aim firstly to restart and clean the

vibrating-wire viscometer and the vibrating tube densimeter before providing some measurements and to analyse the effects of dissolved CO_2 with DIDP on both density and viscosity.

Materials

Toluene and hexane were used for the calibration and cleaning of the apparatus. Toluene and hexane were used as received.

DIDP was obtained from Merck. The Cas number of DIDP is 26761-40-0 and its purity was 99.8%. Chemical formula of DIDP is $C_{28}H_{46}O_4$ and its molar weight is 446.66g/mol. Before being used in the apparatus, DIDP was dried to eliminate traces of water. To that purpose a rotative evaporator was used during more than one hour for each sample. Moreover, pure DIDP was degassed under vacuum before being injected in the apparatus. The DIDP used was a mixture of several isomers. Figure 2 could show the general structures of the molecule. Some variations of branching $C_{10}H_{21}$ chains could occur.

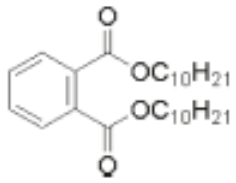

Figure 2. Representation of DIDP

Background

Three different types of work could be used to fulfil this work. First there is the use of the vibrating-wire viscometer. There is also the measurements of DIDP viscosity and density and finally there is the measurements of viscosity and density for mixture of CO_2 with another liquid.

The apparatus used for this work is a vibrating-wire viscometer associated with a vibrating tube densimeter. This apparatus could be used to get accurate measurements of viscosity and density.

A vibrating-wire viscometer is composed of a wire surrounded by a magnet. The knowing of the way it oscillates when current cross it under vacuum conditions could be compare to the way it moves when fluid surrounds it. This differences could allow to get the viscosity value. A vibrating-wire viscometer could be presented on a simple electric circuit as in Figure n°3.

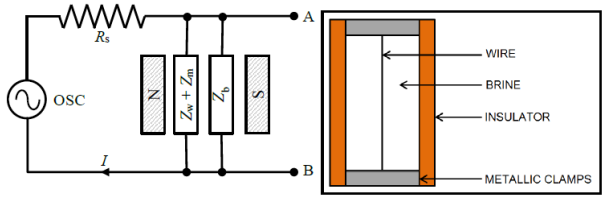

Figure 3. Electric circuit representing the vibrating-wire viscometer. N and S stands for the magnet poles. Zb is the impedance of the fluid surrounding the wire. Zw is the impedance of the wire and Zm is the impedance due to the motion of the wire in the magnetic field. OSC is the oscillator and Rs is the series resistance.

Vibrating-wire viscometers present some advantages. First, a complete theory and error analysis could be used to describe the operation of the apparatus. Vibrating-wire viscometers could also be used over a wide range of temperatures and pressures. The viscosity range could be easily changed by shifting the wire by another one more suitable. Moreover, simultaneous viscosity and density measurements could be performed. Finally, both absolute and relative viscosity measurements could be made [8]. A very tiny amount of fluid is needed to do the measurements, so this device allows measurements to high temperatures and pressures.

Vibrating-wire viscometers have been used in previous works to measure density and viscosity or only viscosity successfully. For example, in 1972 the apparatus allowed the measurement of triethylamine-water solution and methanol-cyclohexane solution in Ballaro et al work [9]. In 1991 Assael et al work [10], the n-hexane viscosity at T=298.15 K and to pressures up to 80 MPa was measured with an uncertainty of 0.5%. McBride-Wright et al [11] used also a vibrating-wire viscometer in order to measure the viscosity of aqueous solutions of carbon dioxide at pressures up to 100MPa and at temperatures from 274 to 449K with an uncertainty of 1.4%.

A vibrating tube densimeter is composed of a ‘’U’’ or ‘’V’’ tube. The difference between the resonance frequency of the empty tube under vacuum conditions and a tube fill with fluids could allow to get the density thanks to the fluid mass.

DIDP was studied during different works and its behaviour and properties as a pure fluid are nowadays well-known. As a matter of fact, a vibrating-wire viscometer was used to measure viscosity of DIDP at temperatures between 298.15 and 373.15K and pressures up to 140MPa by Peleties and Trusler [1]. Density of DIDP was studied at temperatures from 283.15 to 363.15K at pressures from 0.1 to 65 MPa by Brito e Abreu et al [2]. Thermodynamic properties of DIDP were studied by Peleties and Trusler [12].

As for studying dissolved CO_2 in mixtures, several works were provided. We can quote the work of Ciotta et al [13] who carried out viscosity and density measurements of CO_2 mixtures (CO_2 and 2,6,10,15,19,23-hexamethyltetracosane) at temperatures up to 448.15 K and pressures up to 170 MPa were accomplished with uncertainty of 2%. What's more, Calabrese [8] did viscosity measurements of dissolved CO_2 with different mixtures. We can mention sodium chloride and calcium chloride aqueous solutions with CO_2 or different crude oil mixtures with CO_2 at pressures up to 100MPa and temperatures up to 423K with an uncertainty of 1.1%.

Methods

This work can be splitted in three different axis. First, there is the start-up of the apparatus and the modification of the program used to get the results. There is also the measurements of dissolved CO_2 with DIDP. Finally a comparison work with calculus of residual entropy shall be done.

The apparatus used is a vibrating-wire viscometer connected to a vibrating-tube densimeter. To work with this apparatus fluids can be injected by a set of three pumps (QUIZIX pump) which allowed a control of the pressure in the system. In our case, there is one pump for injecting liquids, one for injecting nitrogen (gas used to clean up the system) and one for carbon dioxide. Liquid fluids could be degassed before entering the system thanks to a vacuum pump. Moreover, two chillers are available in the system: one control the temperature of the densimeter and viscometer, while the other one control the temperature in the QUIZIX pumps.

There is also different valves in the system: one fill valve and one deliver valve for each pump of the QUIZIX pump, an outlet valve to empty the system in a waste bottle and a valve linked to a vacuum pump for the cleaning of the system.

Finally, there is a circulation pump in the system, to homogenize mixtures in the system and to help for the cleaning of the apparatus. Some pressures and temperatures sensors are present in the system to help the control of the desired temperature and pressure in the whole apparatus. The scheme of the apparatus is presented on Figure n°4.
The different parts of the apparatus are detailed in Table n°1.

Number	Explanation
1	Vacuum pump
2	Injected Liquid
3	Gas bottle (CO_2)
4	Gas bottle (nitrogen)
5	QUIZIX pump
6	Circulation pump
7	Vibrating-wire viscometer
8	Vibrating-tube densimeter
9	Waste bottle

Table 1. Explanation of the different elements of the apparatus

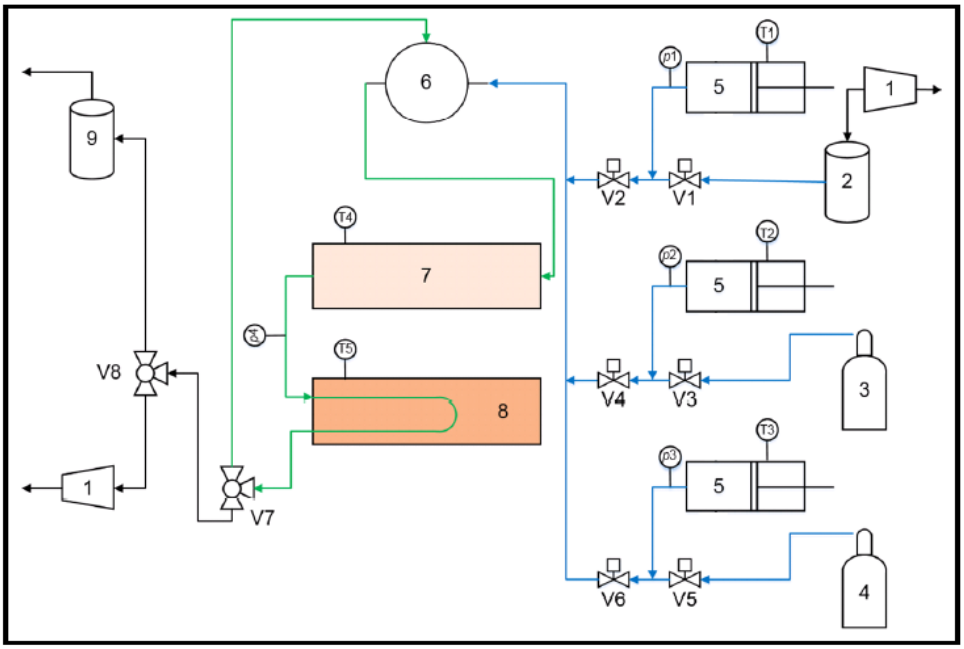

Figure 4. Representative Scheme of the apparatus used. V1, V2, V3,V4,V5 and V6 are the fill and deliver valve of each QUIZIX pump. V7 is the outlet valve and V8 allows the fluid to go to the waste bottle and the nitrogen to be evacuated thanks to the vacuum pump.

To start-up the apparatus, some pure fluids were used: hexane and toluene. Their behaviours and properties are well-known and some measurements were made in order to verify the good-working of the apparatus and its calibration. The measurements were compared with data from the REFPROP software. After doing these measurements, the apparatus had to be cleaned. To that purpose, some nitrogen is flushed in the system while opening the outlet valve and activating the circulation pump. The nitrogen allows to eject the liquid in a waste bottle. The system can be warm up to a temperature near the ebullition temperature of the fluid in order to help it going out. When there is no more fluid going out of the system, the nitrogen present in the system has to be evacuated. To that purpose the outlet valve and the valve n°8 should be opened. Moreover the vacuum pump should be switched on to flush all nitrogen out.

The program giving the values of density and viscosity is a VEE program. It asks the user to complete the resonance frequency, the est half-width, the number of half-widths to scan and the delta0 before starting a scan. The resonance frequency could be estimated by the user by using the lock-in amplifier. It could also be estimated thanks to another VEE program called ''Quick scan''. The delta0 is estimated once thanks to a calibration program and is specific of the wire. The number of half-widths to scan and the est half-width could help to get a better accuracy of the result.

A vibrating-wire viscometer could have the current crossing it represented on a very simple way by the equation n°1.

$$V = V_1 + V_2 \qquad (1)$$

With V_1 the current standing for the wire impedance and V_2 the current standing for the wire motion.

This current has an imaginary part and a reel part. To get a good resonance curve, imaginary curve should cross 0 and the real part should have a maximum. the sensitivity in term of time constant and voltage and the amplitude could also be shifted in the lock-in amplifier. Moreover, the error scale percentage should be as small as possible. An example of a good resonance curve is presented on Figure n°5.

Another VEE program used is the ''Read Temperature and Pressure'' program. It gave the temperature and pressure where there is temperature and pressure sensors in the system. One of the task of the project was to modify this program in order to get a correct value of pressure as a new pressure sensor had been added. This was done by integrating an already existing function more suitable for the pressure sensor of the apparatus to the program.

In a second time, the apparatus was filled with DIDP and some measurements were made. Using the data and correlations for density and viscosity from the literature [1] [2] the objective was to verify the suitability of the wire for DIDP. Measurements were made for various pressures (between 2 and 400 bar) at 40, 70 and 100C. The DIDP was previously dried at least one hour in a rotative evaporator in order to eliminate possible traces of water and degassed under vacuum before being injected in the system. Degassing is good enough when no more bubbles could be seen in the flask.

To compare experimental measurements to existing data, equation n°2 from Peleties and Trusler work [1] was used for viscosity.

$$\ln[\eta/(mPa.s)] = a + b(p/MPa) + \frac{c + d(p/MPa) + e(p/MPa)^2}{(T - T_0)/K} \qquad (2)$$

All the parameters are available in Table n°2

a	b	c	d	e	T_0/K
-2.5887	$-4.302.10^{-6}$	776.49	2.7918	$-2.6764.10^{-3}$	188

Table 2. Parameters of equation 2

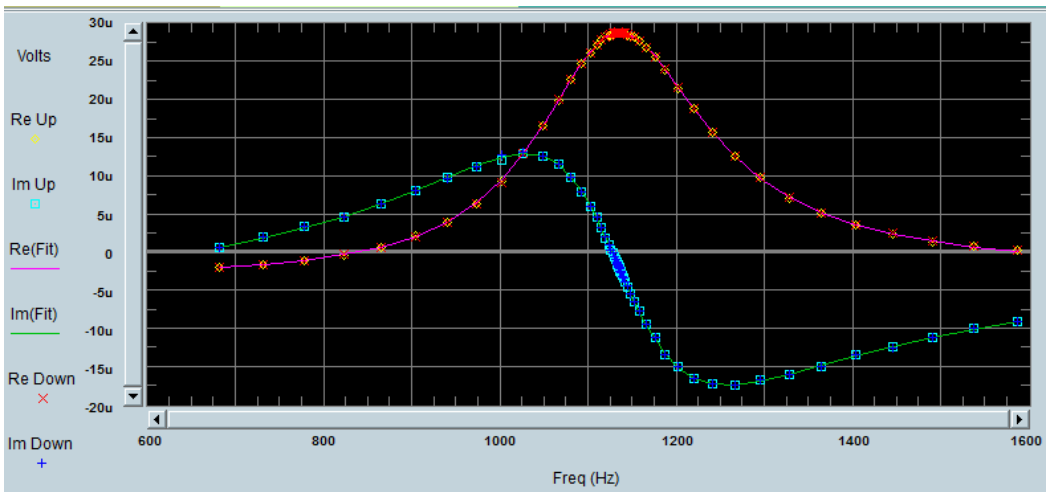

Figure 5. Representation of a good resonance curve

As for density, it's the equation of state from Peleties and Trusler work [12] which was used.

$$\delta = (a + b\varphi)^{\frac{1}{3}} + c \qquad (3)$$

With $\delta = \frac{\rho}{\rho_0}$; $\varphi = \frac{P}{P_0}$; $\tau = \frac{T}{T_0}$ and

$$a = e_1 + e_2\tau + e_3\tau^2 \qquad (4)$$
$$b = e_4 + e_5\tau + e_6\tau^2 \qquad (5)$$
$$c = e_7 + e_8\tau + e_9\tau^2 \qquad (6)$$

The parameters are available in Table n°3.

$e_1 = 1.3157.10^{-2}$	$e_2 = -8.2784.10^{-3}$	$e_3 = 1.3127.10^{-3}$
$e_4 = 3.1083.10^{-6}$	$e_5 = 1.7545.10^{-6}$	$e_6 = 1.3873.10^{-6}$
$e_7 = 9.8767.10^{-1}$	$e_8 = -1.7814.10^{-1}$	$e_9 = 6.7883.10^{-3}$
$\rho_0 = 962.92\frac{kg}{m^3}$	$T_0 = 298.15K$	$p_0 = 0.1MPa$

Table 3. Parameters for equation of state for pure DIDP

After checking the good-working of the device with pure DIDP, measurements with mixture of DIDP and CO_2 were made.

First, the apparatus was filled with a small molar fraction of CO_2 in order to be able, just by adding a little of CO_2 in the device, to increase the molar fraction of CO_2 and perform new measurements without having to flush out and clean the apparatus between two sets of measurements.

Two pump were used to fill the apparatus: one for DIDP, one for liquid CO_2. The pump for DIDP was set at 25C with the chiller. Degassed DIDP was taken from the flask into the pump. Then DIDP was pressurized at a pressure where data was known in term of density [1]. Knowing the volume taken by the DIDP in the syringe (thanks to the QUIZIX pump software) and the density, we could get the mass of DIDP to be injected in the system. This mass could be convert into moles thanks to the molar mass of DIDP. Thanks to that method, the number of moles of DIDP in the system could easily be known.

The same way of thinking for CO_2, with chiller set at 9C and pressure at 60 bar (to be sure to have liquid CO_2) was employed to know the molar fraction of CO_2 injected in the system. For carbon dioxide, data was taken from REFPROP software. Each time carbon dioxide was added in the system, circulation pump was activated several hours to homogenise the system and then stopped during one hour before any measurements to allow stabilisation of the mixture. The stabilisation could be checked thanks to the ''Read Temperature and Pressure'' VEE program. Indeed, this program presents with graphs the variations of temperature and pressure in the apparatus: if there is no more variations for temperature and pressure, the mixture is stabilised.

The first molar fraction of CO_2 studied was 0.2. One measurement was performed at one temperature and pressure. After that, some DIDP or CO_2 was added to the system to increase the pressure, recalculating each time the molar fraction of CO_2 to be the closest to 0.2. Once all the measurements to one temperature and several pressures were performed, the temperature of the system could be increased at the next level. Each time the temperature was increased, the system was let to stabilise during some hours. As a matter of fact, the temperature take more time to stabilize than pressure in the system. Here again the ''Read Temperature and Pressure'' VEE program could be used to check. Once all measurements at one molar fraction were done, CO_2 was added in the system to increase the molar fraction to the next level.

The molar fractions studied were 0.2, 0.4, 0.6 and 0.8 at 25C, 40C, 70C and 100C for pressures between 200 and 800 bar. One issue of this work was that there was no previous measurements for that mixture. Though, there is no existing phase diagram of DIDP plus CO_2. During the measurements, it was important to avoid having two phases in the apparatus. Nevertheless, with no existing data, it was hard to predict when this would happen. That's why the measurements were made in a restricted range of temperature and pressure in order to avoid a two phase mixture. However, for one measurement, the goal was to try to get two-phase mixture in order to be able to identify the phenomenon if it happen later. To that purpose, the temperature of the system was set at 40C and the pressure was significantly decreased (around 50 bar) before trying to do a measurement.

After performing all the measurements, the obtained data for pure DIDP was used to get the residual entropy of the system and to plot it with reduced viscosity. First the specific entropy of the system could be defined by equation n°7 [12].

$$S(T,p) = S_G(T) + \left(\frac{\Delta h_{vap}}{T}\right) + [s(T,p) - s(T,P_{vap})] \qquad (7)$$

Where P_{vap} is the vapour pressure at the temperature of interest

Δh_{vap} is the enthalpy of vaporisation at the same temperature

$S_G(T)$ is the specific entropy of the saturated vapour.

As the vapour pressure of DIDP is very small, we could approximate S_G by replacing it by the perfect

gas entropy $S^{PG}(T, P_{vap})$. Equation n°7 become equation n°8.

$$S(T,p) = S^{PG}(T, P_{vap}) + \left(\frac{\Delta h_{vap}}{T}\right) + [s(T,p) - s(T, P_{vap})] \quad (8)$$

Definition of residual entropy could be given by Equation n°9.

$$S^{res}(T,p) = S(T,p) - S^{PG}(T,p) \quad (9)$$

So, equation n°9 become equation n°10.

$$S^{res}(T,p) = [S^{PG}(T, P_{vap}) - S^{PG}(T,p)] + \left(\frac{\Delta h_{vap}}{T}\right) + [s(T,p) - s(T, P_{vap})] \quad (10)$$

The first term of the equation could also be written

$$[S^{PG}(T, P_{vap}) - S^{PG}(T,p)] = (R/M)\ln(p/P_{vap})$$

with M as the molar mass.
Vapour pressure was calculated with Antoine's equation n° 11.

$$log_{10}\left(\frac{P_s}{P^\circ}\right) = A - \frac{B}{T+C} \quad (11)$$

With T en K, P_s en Pa et P° = 100 000 Pa.
The parameters for Antoine's equation were obtained from DETHERM database which get them from Dormund database.

For the second term of the equation Δh_{vap}were obtained from NIST database. (The values were calculated thanks to Watson equation.)

The last term of the equation n°10 could be calculated thanks to the thermodynamic equation of state for DIDP [12]. This equation of state give access to the value of s-s0 but as the last term of equation n°10 is a difference, s0 (which is specific entropy at the reference state) would disappear.

We have:

$$s - s0 = c_3\left[c_0 \ln\tau + c_1(\tau - 1) + \frac{1}{2}c_2(\tau^2 - 1)\right] + \left\{\frac{p_0}{T_0\rho_0}\right\}[3b^{-2}b'\{F(\delta) - F(\delta_0)\} - 3b^{-1}\{F1(\delta) - F1(\delta_0)\}] \quad (11)$$

With $\tau, \delta, \varphi, a, b, c$ as previously defined, and parameters T_0, ρ_0 and p_0 available in Table n°3.

$$F(\delta) = [\frac{1}{2}\delta^2 - 2c\delta + c^2 ln\delta] \quad (12)$$

$$F1(\delta) = 2c'(cln\delta - \delta) + (\delta - 2c + c^2\delta^{-1})(\frac{\partial\delta}{\partial\tau})_\varphi \quad (13)$$

$$(\frac{\partial\delta}{\partial\tau})_\varphi = c' + \frac{1}{3}(a + b\varphi)^{-\frac{2}{3}}(a' + b''\varphi) \quad (14)$$

δ_0 is obtained from equation n°10, for $\varphi = 1$.
$a', b', c' and\ b''$ are obtained by derivating equations n°4,5 and 6.
The other parameters are available in Table n°4.

c_0	c_1	c_2
$= 1.010.10^3$	$= 3.817.10^2$	$= 3.177.10^2$

Table 4. Parameters for the calculation of s-s0

Finally $S^{res}(T,P)$ was converted into $S^{res}(T,\rho)$ thanks to

$$S^{res}(T,\rho) = S^{res}(T,P) - \left(\frac{R}{M}\right)\ln(Z)$$

With $Z = \frac{P}{\frac{R}{M}*T*\rho}$ (compressibility factor)

To have reduced viscosity, Lennard-Jonnes intramolecular potential [14] is a possible approximation. To that purpose, characteristic length and energy parameters could be estimated from critical temperature and pressure. Critical data for DIDP are available on NIST database from a weighted average from a set of experimental and predicted values.
The equations to get reduced viscosity are the following (n°15 to 19):

$$\sigma = \frac{8{,}09}{\rho c^{\frac{1}{3}}} \quad (15) \quad \text{and} \quad \varepsilon = \frac{Tc}{1{,}2593} \quad (16)$$

$$\Omega = 1{,}16145\left((\frac{T}{\varepsilon})^{-0{,}14874}\right) + 0{,}52487e^{-0{,}7732\frac{T}{\varepsilon}} + 2{,}16178e^{-2{,}43787\frac{T}{\varepsilon}} \quad (17)$$

$$\eta^0 = (26{,}692.10^{-9}\sqrt{T.1000.M})/(\sigma^2\Omega) \quad (18)$$

$$\eta^* = \frac{\eta}{\eta^0} \quad (19)$$

Results

First, the check measurements could be plotted on a graph with the deviation from the correlation from Peleties and Trusler [1] [12]. This available on Figures n°6 to 9. A calibration point (were deviation equals 0) at 40C, 1 bar was made.

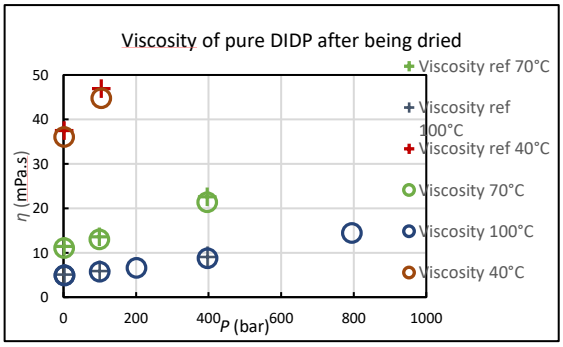

Figure 6. Viscosity against P for pure DIDP. Red stands for 40C data, green for 70C, blue for 100C. Circle stands for measurements data and cross for reference data [1].

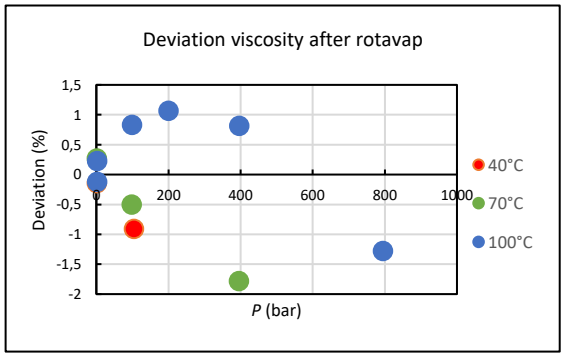

Figure 7. Deviation in % for the previous data. Red stands for 40C data, green for 70C, blue for 100C.

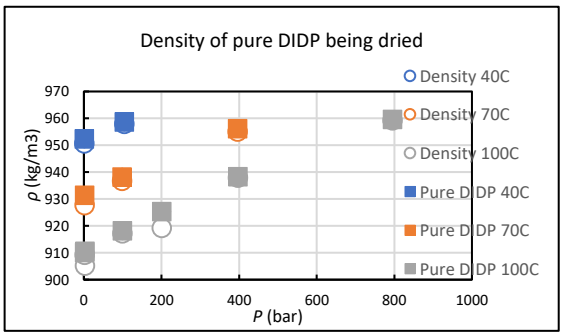

Figure 8. Density against P for pure DIDP. Blue stands for 40C data, Orange for 70C, grey for 100C. Square stands for reference data [1] and circle for measurements data.

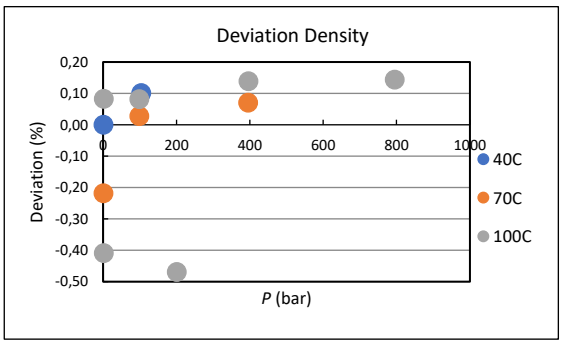

Figure 9. Deviation in % for the previous data. Blue stands for 40C data, orange for 70C, grey for 100C

The viscosity results for molar fractions of CO_2 equal to 0.2; 0.4; 0.6 and 0.8 are available on Figure n°10 to 12 .In order to present a limited number of graphs, 3 pressures have been chosen and viscosity against the molar fractions for the different temperatures is plotted.

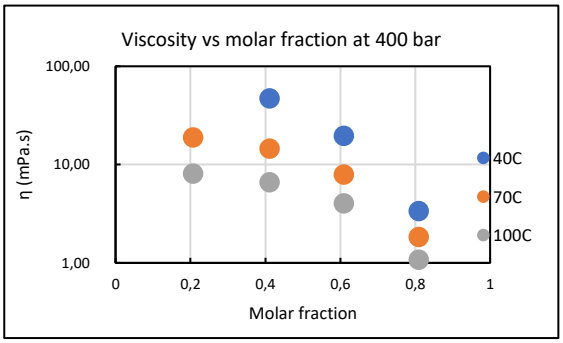

Figure 10. Viscosity against molar fraction at 400 bar. Blue stands for data at 40C, orange stands for data at 70C, grey for data at 100C.

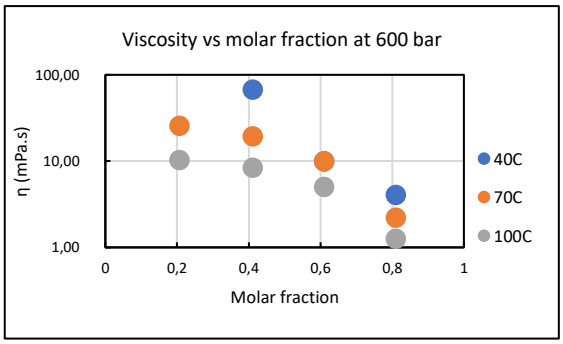

Figure 11. Viscosity against molar fraction at 600 bar. Blue stands for data at 40C, orange stands for data at 70C, grey for data at 100C.

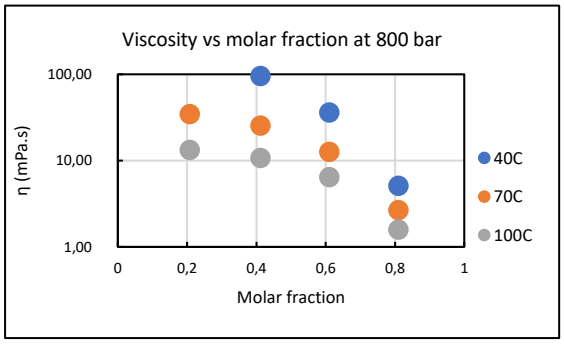

Figure 12. Viscosity against molar fraction at 800 bar. Blue stands for data at 40C, orange stands for data at 70C, grey for data at 100C.

The density results for molar fractions of CO_2 equal to 0.2; 0.4; 0.6 and 0.8 are available on Figures n°13 to 15. In order to present a limited number of graphs, 3 pressures have been chosen and density against the molar fractions for the different temperatures is plotted.

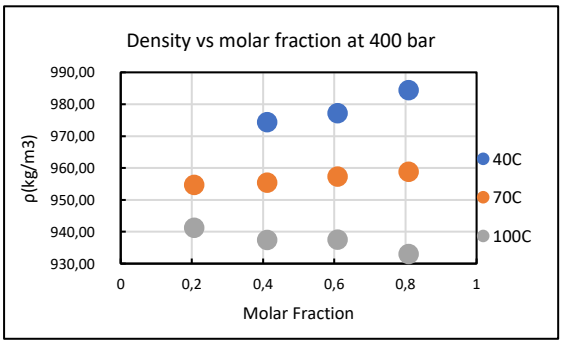

Figure 13. Density against molar fraction at 400 bar. Blue stands for data at 40C, orange stands for data at 70C, grey for data at 100C.

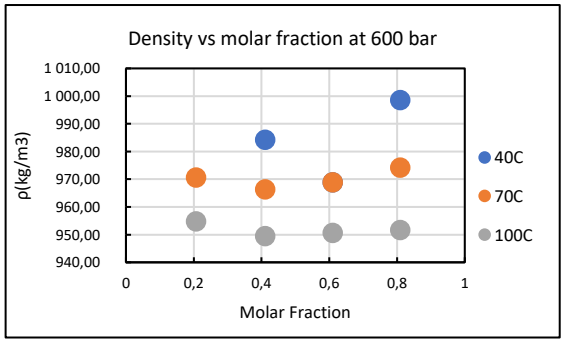

Figure 15. Density against molar fraction at 600 bar. Blue stands for data at 40C, orange stands for data at 70C, grey for data at 100C.

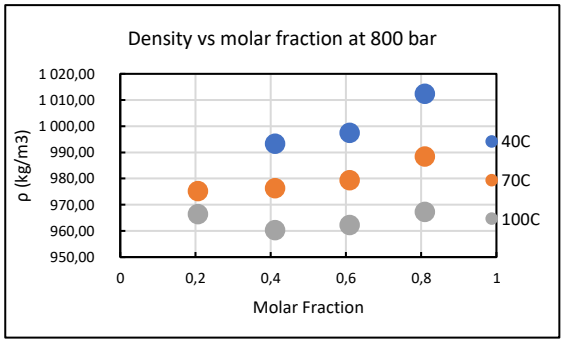

Figure 15. Density against molar fraction at 800 bar. Blue stands for data at 40C, orange stands for data at 70C, grey for data at 100C.

To see the difference between pure DIDP and mixture with CO_2, we can plot a graph showing the viscosity of pure DIDP, of pure CO_2 and of mixtures. We choose to plot that graph for different pressures and one temperature but for each temperature the mixtures would behave the same as in this graph. This graph is presented on Figure n°16.

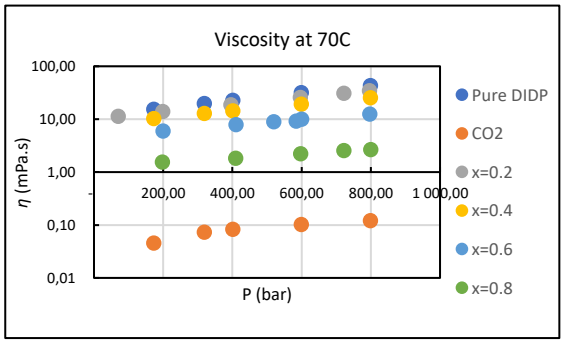

Figure 16. Viscosity against pressure at 70C. Blue stands for pure DIDP, orange for CO2, grey for a molar fraction of CO2 of 0.2, yellow for a molar fraction of 0.4, light blue for a molar fraction of 0.6 and green for a molar fraction of 0.8

The last graph to be plot was the graph presenting reduced viscosity against residual entropy. This result is available on Figure n°17.

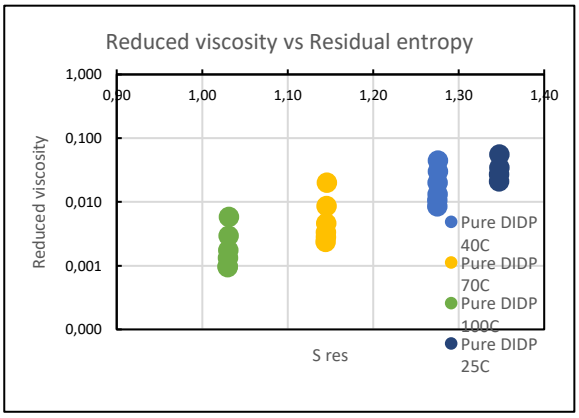

Figure 17. Reduced viscosity against residual entropy. Dark blue stands for DIDP at 25C, blue for 40C, yellow for 70C and green for 100

Discussion

For the check measurements, we can notice that for viscosity the experimental data and the correlation data show a deviation inferior to 2%. This is, according to literature, a good accuracy for the measurements. For density, we have a deviation below 0.5% which is also a good accuracy in the experimental data as for density literature recommend a more severe precision.

For the measurements of DIDP mixed with dissolved CO_2, as expected, the viscosity of DIDP was lowered when the molar fraction of CO_2 increased. When pressure increase, viscosity increase as well, which is also an expected behaviour and when temperature increased, viscosity decrease. The maximum viscosity difference between pure DIDP and mixture for each molar fraction is shown on Table n°5.

Molar fraction of CO2	Maximum viscosity difference between pure DIDP and mixture (%)	T and P where the maximum difference occur
0.2	19%	70C, 800 bar
0.4	51%	40C, 800 bar
0.6	79.9%	40C, 629 bar
0.8	97.4%	40C, 800 bar

Table 5. Presentation of the differences for viscosity between pure DIDP and mixtures

For density however, the addition of CO_2 did not seem to have a big impact. We can notice that density stay in the same range of values for each molar fraction of CO_2 even though it tend to be slightly higher when the pressure is increasing. Density is decreasing when temperature is increasing. And it also seem to decrease and then increase for one given T and different molar fractions. This behaviour was noticed for the different pressures plotted. This could eventually be due to a non-repeatability of the measurements even though check measurements were done all along the work.

For the two phase measurement that was tried, the program was not able to give any result and the lock-in amplifier was unable to stabilize. This behaviour could so help to identify a two-phase domain.

For residual entropy, the results were not what was expected. The aim of that graph was to put all the information of viscosity at different T and P in one graph and in one curve. Indeed, as explained in the work of Lötgering-Lin and Gross [14] and the work of Novak L.T [15] both based on Rosenfeld Y. work [16], for a lot of different fluids, it is possible to represent the reduced viscosity against residual entropy with one curve. This model could be used to predict viscosities with a good accuracy for linear molecules and correct accuracy for branched molecules.
In our case, the goal was to verify that trend for DIDP. But the obtained graph shows four different curves for the four temperatures used for the measurements. Here, residual entropy seems to have a strong dependence in temperature and almost no dependence in ρ.

This strange behaviour could be due:

-Antoine parameters may have not been suitable for the studied range of temperature
-The estimation of $\Delta h\ vap$ from NIST database could have been wrong (corrections have been tried with Trouton's rule and Clausius Clapeyron equation without success)
- The derivation of the equation of state in Peleties and Trusler article [12] has slight differences with a manual derivation (However, even with the manual derivation, the graph shape stay identic)
- The Lennard-Jones parameters may have not been suitable for DIDP
-Or maybe the DIDP molecular structure could create this unknown behaviour of residual entropy against reduced viscosity even though, there is no such compounds with that behaviour known till now.

Conclusions

Following these measurements, the behaviour of mixtures of DIDP and CO_2 is better known.

As for the behaviour of residual entropy of DIDP, further analysis of the chosen equations may help to find out why it did behave that way.

This work can open the path to a predictive model representing the behaviour of DIDP with dissolved CO_2.

The results support wider research on the behaviour of hydrocarbons with CO_2 for applications in Enhanced Oil Recovery and Carbon Storage technologies.

Acknowledgements

I would like to thanks Malyanah Binti Mohd Taib. Her advises and presence were a real support to me and she taught me how a lab work goes on.

Supplementary Information

All the raw data for viscosity and density measurements for each molar fraction of CO_2 are available on the supplementary information.

References

[1] Peleties, F.; Trusler, J. P. M., Viscosity of Liquid Di-isodecyl Phthalate at Temperatures Between (274 and 373) K and at Pressures up to 140 MPa. *J. Chem. Eng. Data* 2011**,** *56* (5), 2236-2241.

[2] Brito e Abreu, S. ; Avelino, H. ; Caetano, F.J.P. ; Fareleira J.M.N.A. ; Density of Diisodecyl Phthalate at Temperatures from (283.15 to 363.15) K and Pressures from (0.1 to 65) MPa, *J. Chem. Eng. Data* **2010,** *55,* 3525–3531

[3] Malta J.A.M.S.C; Measurement of viscosities and densities of synthetic crudes at high pressures, Thesis for Science Master Degree, Imperial College of London, 2017

[4] Le Neindre B., Estimation de la viscosité des gaz sous pression, *Techniques de l'ingénieur K491 V1,* 2006

[5] Bijeljic B., CO_2 storage trapping mechanism and release pathways, Lecture, Imperial College London, 2018

[6] Dumergues L., Valorisation du CO_2: Partie 1 : voies directes et voies avec transformation biologique, *Techniques de l'ingénieur G1816 V1*, 2016

[7] Fennell P., CCS and Energy Production, Lecture, Imperial College London, 2018

[8] Calabrese, C. Viscosity and Density of Reservoir Fluids with Dissolved CO_2. PhD Thesis, Imperial College of London, 2017

[9] Ballaro, S.; Maisano, G.; Migliardo, P.; Wanderlingh, F., Viscosity and light scattering in critical mixtures. Physical Review A 1972, 6, (4), 1633-1643.

[10] Assael, M. J.; Papadaki, M.; Dix, M.; Richardson, S. M.; Wakeham, W. A., An absolute vibrating-wire viscometer for liquids at high pressures. International Journal of Thermophysics 1991, 12, (2), 231-244.

[11] McBride-Wright, M.; Maitland, G. C.; Trusler, J. P. M., Viscosity and density of aqueous solutions of carbon dioxide at temperatures from (274 to 449) K and at pressures up to 100 MPa. Journal

[12] Peleties, F.; Segovia J.J.; Trusler, J. P. M.; Vega-Maza D., Thermodynamic properties and equation of state of liquid diisodecyl-phthalate at Temperatures Between (273 and 423) K and at Pressures up to 140 Mpa. *J. Chem. Thermodynamics* 42 (2010) 631–639

[13] Ciotta, F.; Maitland, G.; Smietana, M.; Trusler, J. P. M.; Vesovic, V., Viscosity and density of carbon dioxide + 2, 6, 10, 15, 19, 23-hexamethyltetracosane (squalane). Journal of Chemical and Engineering Data 2009, 54, (9), 2436-2443.

[14] Lötgering-Lin,O.; Gross J.; Group Contribution Method for Viscosities Based on Entropy Scaling Using the Perturbed-Chain Polar Statistical Associating Fluid Theory, Industrial and Engineering Chemistry Research (2015).

[15] Novak L.T. ; Predicting Natural Gas Viscosity with a Mixture Viscosity Model for the Entire Fluid Region, Industrial and Engineering Chemistry Research, 2013

[16] Rosenfeld, Y. ; Relation between the transport coefficients and the internal entropy of simple systems, Physical review A, volume 15, number 6, 1977

Novel Surfaces with Antimicrobial Properties

Alexandra Patching and Jack Thain

Department of Chemical Engineering, Imperial College London, U.K.

Abstract Antimicrobial resistance and the threat it poses to health has resulted in research into antimicrobial peptides as a way of combatting drug-resistant infections. Antimicrobial peptides have been shown to disrupt biofilm formation. The presence of biofilms hinders many industries, including the healthcare industry, chemical process industries and maritime vessels, thus these peptides could offer a potential solution for the reduction of biofilm growth. In this study, the behaviour of the α-helical antimicrobial peptides L12 $(LKKL)_3$ and W12 $(WKKW)_3$, was examined in solution through the use of Dynamic Light Scattering (DLS). Chromic acid etching of Polypropylene (PP) and Polyethylene (PE) was undertaken to modify their surfaces to allow for the immobilisation of the L12 and W12 peptides. These surfaces have been investigated through use of X-ray Photoelectron Spectroscopy (XPS), white light interferometry and contact angle measurements. An *in situ* bacterial viability assay was used to test the antimicrobial performance, based on confocal laser scanning microscopy. The results indicated that the L12 peptide was successfully immobilised onto the surface of both acid etched polymers, and the W12 peptide was successfully immobilised onto the acid etched PP surface and to a lesser extent the acid etched PE surface. These peptide coated surfaces showed enhanced antimicrobial properties when compared to an appropriate control.

Key Words: Acid Etching, Antimicrobial Peptides, Assay, Biofilm, Surface Coating

Introduction

Antibiotic resistant bacteria pose one of the greatest threats to health in modern times. With over 269 million courses of antibiotics prescribed annually in the United States alone, ensuring access to effective antibiotic agents is of great importance (Sanchez et al, 2016). This uncertainty regarding the future of a "post-antibiotic era" has spurred an increased focus into the development of new and effective alternative antimicrobials (World Health Organisation, 2014). One such effective therapeutic strategy currently under consideration is the use of antimicrobial peptides, which appear ubiquitous across almost all forms of life on earth (Zasloff, 2002). Current efforts are being made in the field to design and produce novel antimicrobial peptides for use in treatment within a hospital setting, such as the study by Khara et al (2017). This study proved the fundamental principle of *de novo* design of antimicrobial peptides, and resulted in the creation of effective broad spectrum antimicrobial peptides which acted within the bulk medium. Whilst the incentive to develop new antibacterial agents is deeply rooted for application within the healthcare and medical fields, the possible use of such agents can be extended to other applications, for example surface modified technology for consumer goods, kitchen and industrial surfaces.

One promising observation of antimicrobial peptides is that they have the ability to disrupt and destroy established biofilms (Batoni et al., 2011). More often than not, bacteria exist as a biofilm, this is the accumulation of bacterial cells on a surface (Donlan, 2002). They produce an extracellular polymeric substance that acts as a matrix providing the biofilm with a medium for nutrient transfer and mechanical support. Biofilms can possess emergent properties e.g. viscoelastic behaviour, and exhibit enhanced communal attributes such as the ability to colonise and survive in harsh conditions and withstand exposure to antimicrobials, when compared to free floating bacterial cells (Flemming et al, 2016). For example, biofilms of *k. pneumoniae* are a leading cause of nosocomial infections and are exceedingly difficult to treat with conventional antibiotics (Vuotto et al, 2017).

Due to the ubiquitous nature of biofilms they also have significant impacts in other areas of interest, such as in chemical process industries, food industries and maritime vessels. (Walsh et al, 1993) (Zottola & Sasahara,, 1994) (Mittelman, 2000). The prevention of biofilm development and growth would contribute to a reduction in the number of cases of bacterial infection, thus reducing the dependency on last line antibiotics such as colistin, that are not always successful. Additionally, a reduction in energy consumption and pollution generation from freight shipping and process industries could be achieved, as biofilms reduce the efficiency of these processes.

This study sets out to investigate the use of antimicrobial peptides, specifically those designed and specified by Khara et al. (2017), as a surface coating adhered to inorganic surfaces. These inorganic surfaces are common polymers usually found in industrial and consumer settings. The purpose of immobilising these peptides on polymeric surfaces is to examine their biocidal potential in suppressing the formation and growth of *pseudomonas aeruginosa,* a gram-negative bacterium, as a proof of concept for surface mounted antimicrobial peptides on common industrial polymer surfaces.

2. Materials and methods

2.1 Materials

Diiodomethane (DIM), potassium chloride, potassium dichromate, potassium phosphate monobasic, sodium chloride, sulfuric acid and Tryptic Soy Broth (TSB) were from Sigma-Aldrich (St Louis, MO, USA). Propidium Iodide (PI) and Syto 9 were from Invitrogen (Carlsbad, CA, USA). Peptides L12 and W12 were kindly supplied by the Langford research group at Imperial College London (Khara et al. 2017). Saline solution was from bioMerieux (Marcy-l'Étoile, Lyon, France). 1-Ethyl-3(3-dimethylaminopropyl)carbodiimide (EDAC), N-hydroxysulfosuccinimide (Sulfo-NHS) and Ethanolamine HCL were part of ProteOn™ Amine Coupling Kit from BIO-RAD (Hercules, CA, USA). High Density Polyethylene and Polypropylene surfaces were from Gilbert Curry Ltd. (Exhall, Coventry, UK)

2.2 Peptide Behaviour

Dynamic Light Scattering (DLS) was used to determine the structure of the peptides in solution, primarily to determine if secondary or tertiary structures were formed due to aggregation of the peptide. In preparation of the solution, 7.5 mg of peptide was weighed into a standard 1.5 ml aliquot. Each aliquot had been prewashed with 0.1 micron filtered deionised (DI) water. The solution was then made by addition of 1.5 ml of deionised water, filtered with a 0.22 micron filter, to the peptide containing aliquot. An additional seven aliquots were then washed three times with filtered deionised water. Solutions from 0.01 mg/ml to 1 mg/ml were made by adding deionised water passed through a 0.1 micron filter. Before transferring the contents of the aliquots to the cuvettes, the seven cuvettes were washed three times with deionised water passed through a 0.1 micron filter. The solution from each aliquot was then passed through a 0.1 micron filter into the cuvette and analysed with the Malvern Analytical Zetasizer µV light scattering detector. Each sample was run three times and 10 scans were completed during each run to obtain an average.

2.3 Acid Etching

Chromic acid etching was required to oxidise the surface in order to provide a more suitable surface chemistry for peptide coupling. PP and PE polymer surfaces were submerged in a chromic acid solution as per the instruction of Sheng et al (1995). For the preparation of 100 ml of chromic acid solution, 8.125 g of potassium dichromate (16.25 parts, by weight) was measured out and dissolved in 13 ml of deionised water (26 parts). Next, 88 ml of concentrated sulphuric acid (325 parts) was added into the mixture slowly as it was heated up to 70°C. The surfaces were left to etch in the solution for one hour. The polymers were then dipped successively in four beakers of deionsied water to remove residual reactants. The acid etched polymers were then air dried and placed in a vacuum desiccator.

2.4 Peptide Immobilisation

For the immobilisation of the L12 and W12 peptides onto the acid etched PP and PE surfaces, a Bio-Rad ProteOn™ Amine Coupling Kit was utilised and instructions were followed. First, 0.575 g of ProteOn™ EDAC powder was dissolved in 7.5 ml of deionised water to make a 10x EDAC stock solution with a concentration of 400 mM. A pipette was used to separate this solution into 75x 100 µl aliquots. Additionally, 0.163 g of ProteOn™ sulfo-NHS powder was dissolved in 7.5 ml of deionised water, resulting in a 10x sulfo-NHS stock solution of concentration 100 mM. A pipette was used to also divide the sulfo-NHS stock solution into 75x 100 µl aliquots. These aliquots were stored at -20°C until required. To prepare 2 ml of activation solution, one aliquot of the 10x EDAC stock solution and one aliquot of the 10x sulfo-NHS stock solution (both 100 µl of each respective solution), were mixed together with 1.8 ml of deionised water. This activating solution was then pipetted onto the surfaces and left for 5 minutes. 0.1 mg/ml peptide-buffer solution was then pipetted onto the surface. This peptide solution was pre-prepared using a stock solution (1 mg/ml of peptide L12 or W12 in Phosphate Buffered Saline (PBS)). Before administering onto the surface, 100 µl of the peptide-buffer stock solution was then diluted with 900 µl of PBS buffer, resulting in the working concentration of 0.1 mg/ml. Once administered onto the activated surface, the peptide-buffer solution was left for five minutes to immobilise. Finally, 1 ml of Bio-Rad ProteOn™ ethanolamine blocker solution was added to the surface. This method was carried out for each acid etched polymer, with each peptide, meaning L12 and W12 were immobilised separately on both acid etched PP and acid etched PE coupons. Additionally, acid etched PE and acid etched PP surfaces were treated only with the activating solution and blocking solution, these were for use as a negative control measurement for the microbiological assay. These surfaces that were treated with only activation solution and blocking solution, not peptide-buffer solution, will be referred to as 'control coated surfaces' henceforth.

2.5 X-Ray Photoelectron Spectrometry

To measure the elemental composition of the surface and determine whether the peptides had been immobilised, a K-Alpha X-ray photoelectron spectrometer was utilised. Before commencement, all equipment was cleaned with isopropyl alcohol. The samples were prepared and cut into 3 mm by 3 mm squares and secured on the stage ready for analysis. The stage was then mounted into the chamber and a vacuum was created. Once a pressure of 5 x 10^{-7} mbar was reached, the samples were directed to the analysis chamber where a pressure below 5 x 10^{-8} mbar was achieved, the samples were then run looking at a 400 µm spot size. The results were then analysed using Avantage software.

2.6 White Light Interferometry

Interferometry was used on all samples to determine roughness parameters of the surface after each surface treatment, these were: untreated, acid etched, acid etched with the control coating, acid etched with the L12 peptide coating and acid etched with the W12 peptide coating. Each of these samples was placed in a Wyko NT9100 Optical Profiling System. Images were taken using a lens of 5x magnification, a backscan of 120 µm, and the objective focus was set to 0.55. Images were taken and processed to find the arithmetic average roughness, R_a, of each surface.

2.7 Contact Angle Goniometry

The advancing contact angles using both deionised water and DIM were measured to determine the degree of wettability. A Ramé-Hart Contact Angle Goniometer with an automated droplet dispenser was employed for these measurements. The samples were placed onto the stage and positioned under a dispenser. The stage was then set so the dispenser was in close proximity to the sample and the sample was perfectly horizontal. For measuring the water advancing contact angle, $\theta_{w,adv,}$ 5 µl of water was initially dispensed onto the sample and the contact angle was measured using DROPimage Advanced software. Further measurements were taken in 1 µl increments until 20 µl had been added. This process was repeated three times for each sample, and the advancing angles were averaged. When measuring the contact angle with DIM, a thinner dispenser had to be employed and 25 µl of DIM was drawn into the dispenser for each sample. This method was utilised so not to contaminate the piping that is usually used for DI water. The same methodology that was used to find the advancing contact angle with water was used to find the advancing contact angle with DIM. Measuring the advancing contact angle with each respective fluid permitted the calculation of surface energy. This was achieved through the use of Fowkes theory and the work of adhesion equation as seen in Fowkes (1964).

$$W_{S-L} = 2\sqrt{\gamma_S^d \gamma_L^d} + 2\sqrt{\gamma_S^p \gamma_L^p} = \gamma_{L-V}(1 + cos\theta) \quad (1)$$

Where W_{S-L} is the work of adhesion, γ_S^d is the notation for the surface energy of the dispersive component, γ_L^d is the surface tension of the dispersive component, γ_S^p is the surface energy of the polar component, γ_L^p is the surface tension of the polar component and θ is the contact angle. Furthermore, γ_{L-V} can be expressed as

$$\gamma_{L-V} = \gamma_L^d + \gamma_L^p \quad (2)$$

Using the equations 1 and 2 and knowing for Water $\gamma_L^d = 21.8$ mJ/m^2 and $\gamma_L^p = 51.0$ mJ/m^2 and for DIM γ_L^d = 50.8 mJ/m^2 and γ_L^p= 0 mJ/m^2 (Fowkes 1964), subsequent rearrangements can be made to determine γ_S^d and γ_S^p. Finally, using the following equation, equation 3, the surface energy was calculated in mJ/m^2:

$$\gamma_S = \gamma_S^d + \gamma_S^p \quad (3)$$

2.8 Bacterial Strains and Growth Conditions

Pseudomonas aeruginosa, ATCC equivalent strain 9027 was evaluated in this study. The bacteria was inoculated in TSB media, prepared by adding 10 µl of the bacteria strain to 10 ml of media. The bacteria was incubated within an incubator at 32.5°C overnight. The TSB media was prepared by mixing 30 g of TSB powder with 1000 ml of deionised water and then autoclaving.

2.9 Biological Assay and Bioluminescence Imaging

For the preparation of the coupons, treated sample surfaces were cut into 1 cm^2 squares.
They were then covered with 200 µl of *P. aeruginosa* of optical density at wavelength 600 nm, $OD_{600,}$ equal to 0.2 A. The samples were then left for 30 minutes to allow for surface attachment before being washed in 3 beakers containing deionised water. Samples were then either left for 30 minutes under 0.85% w/w saline solution then covered with 200 µl of probe (0.15% v/v Propidium Iodide (PI), 0.15% v/v Syto 9), or covered with 200µl probe immediately after being washed with deionised water. After covering the samples with probe, they were left in the dark (under aluminium foil) for 5 minutes before being imaged.

Imaging was completed using the confocal laser scanning microscopy platform Leica TCS SP8. Images of area 465 µm by 465 µm with optical section of 15.024 µm were taken. Syto 9 was excited with a light pulse of wavelength 483 nm and the fluorescence was recorded between 3 µs and 10 µs after excitation, between wavelengths 488 nm and 529 nm. Propidium Iodide was excited by a light pulse of wavelength 534 nm and fluorescence was recorded between 3 µs and 10 µs after excitation, between wavelengths 550nm and 780nm.

For each coupon, 5 images were taken of the surface. Control images were taken before and after the samples were run to ensure no further bacterial death occurred during imaging, as this took time. Samples were tested without probe, bacteria or peptide, and every combination thereof, to ensure no auto-fluorescence occurred.

Results

3.1 Dynamic Light Scattering

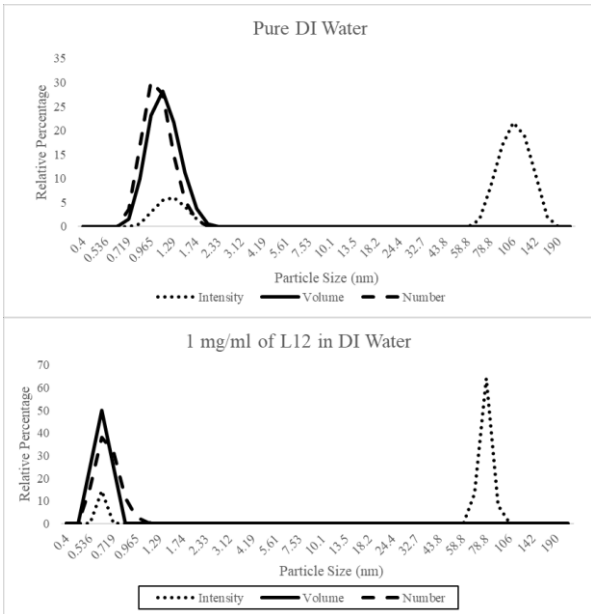

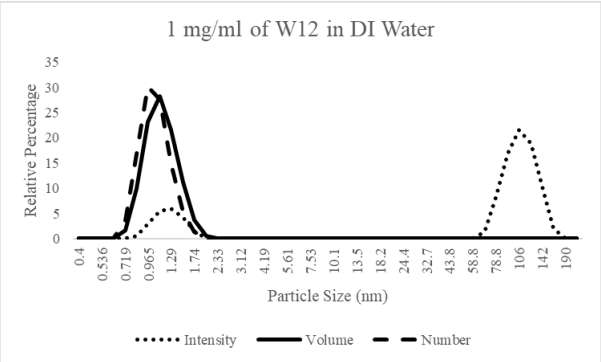

Figure 1a,1b,1c- From top to bottom, the dynamic light scattering results for pure DI water, 1 mg/ml solution of L12 in DI water and 1 mg/ml solution of W12 in DI water. The three graphs each show three lines, these correspond to three different distributions; the dotted line shows the intensity distribution of the sample, the solid line is the volume distribution of the samples and the dashed line shows the number distribution for the sample.

As seen in Figures 1a, 1b and 1c, there is a consistent peak between the lengths of 1 nm and 1.3 nm. This peak represents particulate in the solution of this length. The number distribution is the primary parameter of interest as the peptide should be the most abundant particle and therefore have the greatest relative number percentage.

3.2 X-Ray Photoelectron Spectroscopy

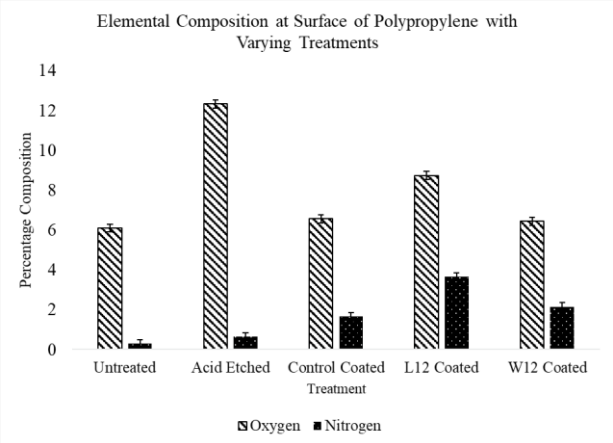

Figure 2- XPS data displaying the percentage of oxygen and nitrogen on the surface of the PP for each treatment. The lined bars show the percentage of oxygen present on the surface, and the solid bars show the percentage of nitrogen present on the surface. Error bars represent measurement error.

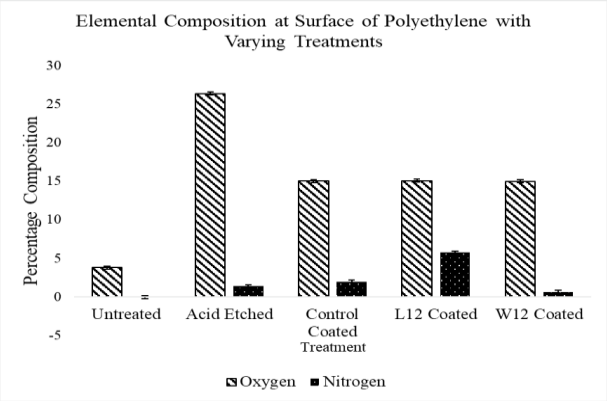

Figure 3- XPS data displaying the percentage of oxygen and nitrogen on the surface of the PE for each treatment. The lined bars show the percentage of oxygen present on the surface, and the solid bars show the percentage of nitrogen present on the surface. Error bars represent measurement error.

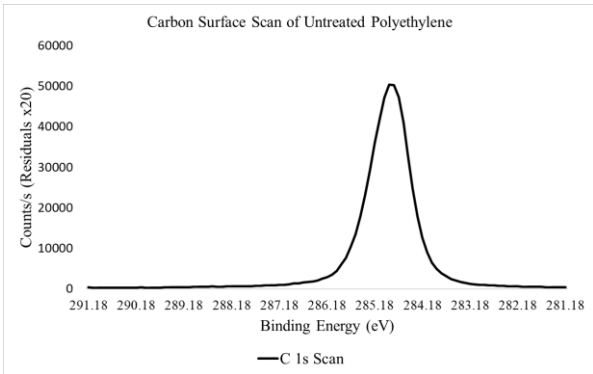

Figure 4- C 1s narrow scan XPS spectra for untreated PE.

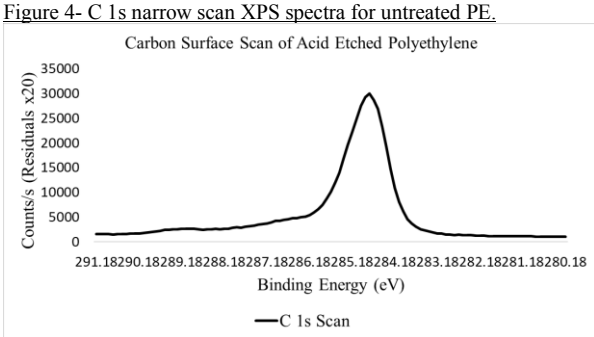

Figure 5- C 1s narrow scan XPS spectra for acid etched PE.

The results of the XPS analysis can be seen in Figures 2 and 3. One scan was taken of each sample surface (n=1) for this study, therefore reported error is due to the uncertainty in measurement, as the criteria for calculating standard deviation is not met. Due to the heterogeneous nature of the surface, it is important to note that whilst the observations stated herein provide useful information, they do not necessarily represent the entire population with accuracy. The PP and PE strips are primarily composed of carbon, but this has been omitted from the Figures as it is the change in oxygen and nitrogen composition for each surface treatment which signifies whether the peptide has been immobilised on the surface. From Figures 2 and 3, it is clear that chromic acid etching of both PP and PE surfaces significantly changes the surface composition; for PE the oxygen content increases by a factor of 6.9 upon acid etching, and for PP the oxygen content doubles. This suggests that PE is more susceptible to surface oxidation using this method, which is expected as this is observed in other studies (Blais et al, 1974). Both polymers also see a small increase in the amount of nitrogen present.

When treated with the control coating the amount of oxygen present on both polymers decreases and the amount of nitrogen increases. For PE, the W12 and L12 coatings result in no change in the amount of oxygen present compared to the control; all three show that 15% of the surface composition is comprised of oxygen. The nitrogen content however is different, the W12 coating has a surface composition with 0.68% nitrogen, approximately a third of the nitrogen present on the surface of the control coating. In contrast the L12 coating shows that almost 6% of the surface is comprised of nitrogen, thrice as much as the control and nine times as much as the W12 coating. For PP, the amount of oxygen present on the surface of the control coated sample and the W12 coated sample is

approximately 6.5%, it increases to 8.73% when coated with L12. In terms of nitrogen composition, the surfaces with the peptide coatings both have a higher amount of nitrogen present compared to that of the control; the L12 coating increased nitrogen composition by a factor of 2.2, whereas the W12 resulted in 1.3 times the amount of nitrogen present on the control coated PP.

3.3 White Light Interferometry

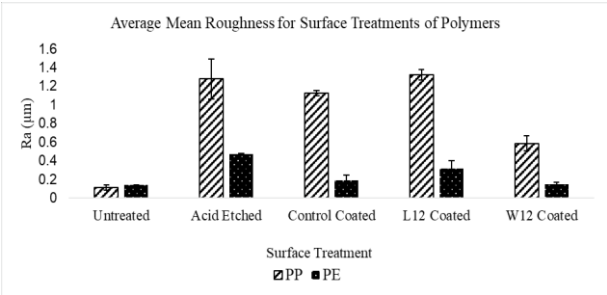

Figure 6- Bar chart to show the average mean roughness, R_a, of the polyethylene and polypropylene surfaces under the different surface treatments. The dashed bars show the R_a for each surface treatment of PP, and the solid bar shows the R_a for each surface treatment of PE. Error bars represent standard deviation.

White light interferometry was utilised to confirm the presence of peptides on the polymer surfaces. Figure 6 shows the effect the different surface treatments had on the average roughness, R_a. The first treatment the samples underwent was acid etching. This had the effect of increasing the roughness of the PP by a factor of 11.3 and PE by a factor of 3.4. When examining the effect the coatings had on the polymers, a pattern becomes apparent. For both PP and PE, the L12 coated surfaces had the highest roughness, then the control coated surfaces followed by the W12 coated surfaces. The only difference is that for PP the L12 coating resulted in a higher average roughness than the acid etched surface, and the other two coatings decreased the roughness compared to the acid etched surface. Conversely for PE, the application of any of the coatings decreased the average surface roughness when compared to the roughness of the acid etched surface. Measuring the surface roughness is important as it is a variable that effects both bacterial attachment and contact angle of liquids on a surface, therefore important to monitor and record.

3.4 Contact Angle Goniometry

Figures 7 and 8 show the results with respect to the water contact angle and the calculated surface energy for each of the surfaces and surface treatments. Upon examining the advancing contact angle of water, $\theta_{w,adv}$, it becomes very apparent that acid etching decreases the contact angle; upon acid etching, the contact angle for PP decreased by a factor of 3 compared to the untreated sample, for PE it decreased by a factor of 1.5.

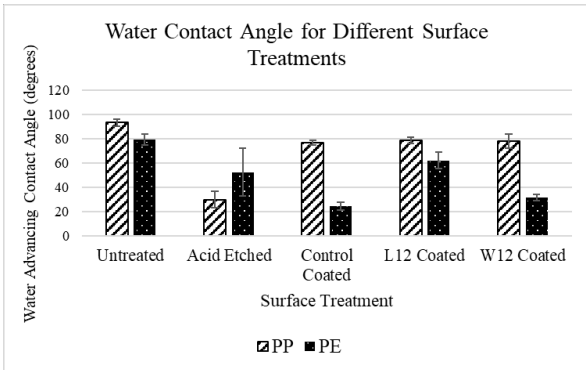

Figure 7- Bar chart to show the average advancing contact angle of water for the different treatments of the polymer surfaces. The dashed bars show the contact angle for each surface treatment of PP, and the solid bar shows the contact angle for each surface treatment of PE. Error bars represent standard deviation.

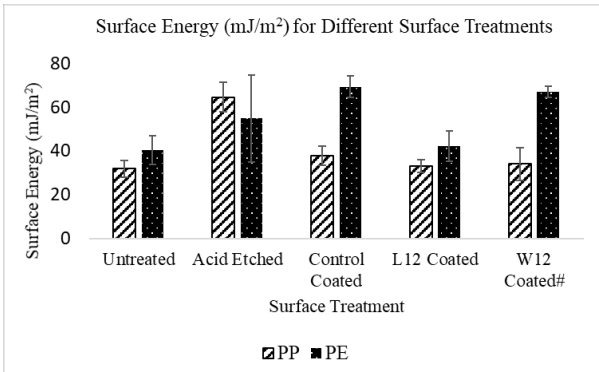

Figure 8- Bar chart to show the calculated surface energies for the different treatments of the polymer surfaces. The dashed bars show the surface energy for each treatment of PP, and the solid bar shows the surface energy for each treatment of PE. Error bars represent standard deviation.

When the coatings are applied, the PP surfaces exhibit little difference in the value for advancing contact angle; the control, L12 coating and W12 coating all have advancing contact angles of approximately 77°. Conversely, the coatings have a different effect on the PE surfaces, the control coating and W12 coating are seen to decrease the contact angle by factors of 2.2 and 1.6 respectively (compared to the acid etched value). In contrast, the L12 coating increases the contact angle, from 52° to 62°.

The surface energies, as seen in Figure 8, show how the surface energy changes with respect to the different treatment types for each surface. It is clear that the chromic acid etching increases the surface energy of the polymers, for PP the surface energy doubles after acid etching and for PE the surface energy increases by a factor of 1.5. When looking at the effects the coatings have on the polymers, the results are very similar to that of the water contact angle. For example, for PP, once coated with any coating, there is very little difference in surface energy such as in the case with contact angle: all three coatings have surface energies of approximately 35 mJ/m^2. For PE, again the control coating and W12 coating behave differently to the L12 coating. The control and W12 coatings result in higher surface energies than that of the acid etched PE, by factors of 1.3 and 1.2 respectively.

Conversely, the L12 coating results in a lower surface energy compared to the other coatings and the acid etched treatment.

3.5 Confocal Microscopy

Table 1-Table to show the ratio of dead to total bacteria on each surface as a ratio to the control. The grey highlighted results shown are proven with 95% confidence to have a greater value than the control.

Polymer	Peptide Coating	Time Bacteria Left for to Die	Experiment Repeat Number	Ratio of Dead to Total Bacteria as a Ratio to the Control (n=12)
Polypropylene	L12	0 Minutes	1	11.63±7.31
			2	0.11±0.02
			3	1.24±0.21
			Mean Average	4.33±2.44
		30 Minutes	1	53.32±9.97
			2	6.26±1.86
			3	1.58±0.31
			Mean Average	20.39±3.38
	W12	0 Minutes	1	10.63±2.34
			2	1.21±0.34
			3	6.63±1.47
			Mean Average	6.15±0.80
		30 Minutes	1	4.08±0.20
			2	2.23±0.16
			3	1.25±0.26
			Mean Average	2.52±0.12
Polyethylene	L12	0 Minutes	1	5.91±1.98
			2	1.27±0.77
			3	0.14±0.02
			Mean Average	2.44±0.66
		30 Minutes	1	2.70±0.46
			2	1.08±0.16
			3	1.01±0.09
			Mean Average	1.60±0.17
	W12	0 Minutes	1	96.02±24.51
			2	0.78±0.56
			3	0.09±0.02
			Mean Average	32.29±8.17
		30 Minutes	1	1.00±0.15
			2	0.95±0.13
			3	0.96±0.12
			Mean Average	0.99±0.08

The results from the confocal microscopy can be seen in Table 1. The immediate trend to be noted from the data is the inconsistency of the results collected, no one set of repeated experiments were consistent in being significantly different from the mean, and only one set consistently agreed with the null hypothesis; that there was no difference from the mean, this being W12 coated PE having being left for 30 minutes. Two results stand out as being the most significant, these are the results for the first repeat of L12 coated PP given 30 minutes for potential biocidal action, and the first repeat of W12 coated PE with 0 minutes given for biocidal action after the washing. These results are interesting for a number of reasons. Firstly, they are by far the highest and therefore the best antimicrobials, being 53 and 96 times more effective than the control at killing bacteria respectively, and secondly, they are in contrast to and disagree with the other repeats completed for these surfaces.

Another major result to be seen involves the L12 coated PP, the L12 coated PE and the W12 coated PP that allowed 30 minutes for possible biocidal action to occur, These peptide coatings showed with above 99.5% confidence, that the average proportion of dead bacteria was greater on these surfaces than on the control, as well as being greater than the all of samples which were not given 30 minutes possible biocidal action.

The peptide coating and polymer surface coating which displayed the greatest proportion of dead to total bacteria when compared to the control surface was L12 coated PP, with z=5.73, thereby resulting in a confidence level greater than 99.99%.

In addition to the stated experiments, the auto-fluorescence of the acid etched surfaces was also tested. For PE no auto-fluorescence was detected, however for PP it was. Due to this the apparent number of total bacteria is greater than the true value for PP surfaces. Due to random nature of the

fluorescence it has not been removed from the results stated, therefore it should be noted that the antimicrobial action of coated PP surfaces is marginally better than stated.

Discussion

4.1 Dynamic Light Scattering

From theoretical calculations, a linear α-helical peptide which is 12 residues in length, should have a length of approximately 1.4 nm (Berg et al, 2002). As can be seen in Figure 1c there are particles present in the solution which are approximately 10 percent smaller than this calculated value. However, these same particles appear in the data obtained from running pure deionised water as can be seen in Figure 1a, therefore it is likely the majority of the particles at this size are masking the presence of the peptide. The expected size of a membrane attack complex or other secondary and tertiary structures that may be forming in solution is 16 to 20 times the size of a single peptide (Serna et al, 2016). As can be seen from Figures 1b and 1c, there is no significant indication of any structure in solution of this size. The inconclusive result of the length of a single peptide in solution requires further investigation to determine this value. It is suggested to use either deionised water which has been proven to have no particulate within the size ranges 1nm to 100nm, or to repeat the experiment using size exclusion chromatography.

Due to the absence of particulate matter within the ranges expected for the formation of a membrane attack complex, it is likely that the peptides act as a single unit when killing bacteria or as a collection of two or three peptides, as this is also undetectable due to the contaminated deionised water used for measurement.

4.2 X-Ray Photoelectron Spectroscopy

The XPS data shows that PE undergoes 3 times as much oxidation upon acid etching than the PP does. This result was expected as it was confirmed by Blais et al in 1974. Figures 4 and 5 indicate the change in surface chemistry after chromic acid etching. The shift in the peak binding energy shown represents the presence of carboxyl and carbonyl bonds on the surface of the acid etched sample (Lee et al, 2001), confirming the result expected from Sheng et al. (1995), this result was also seen for PP. This oxidation is crucial as it is these functional groups which allow for the amine coupling of the peptides. The amine coupling process introduces nitrogen to the surface, the amount of which depends on the peptide coating. For the L12 and W12 coated PP surfaces, it was shown that they have a greater nitrogen surface composition than the control. This is to be expected as the blocking solution is ethanolamine, which contains one nitrogen atom per molecule, whereas L12 and W12 contain eighteen and twenty-four nitrogen atoms per molecule respectively. This increase in the percentage of nitrogen present on the surface when coated with the peptides signifies that the peptides are successfully bonding to the surface.

4.3 White Light Interferometry

From the results of Figure 6 it is clear that the acid etching has the most impact on the average of the mean surface roughness, R_a, as well as also causing a more significant increase in average mean roughness for PP than PE. This increased roughness could be attributed to the oxidation taking place. Wang et al (2009) states that for the etching time used in this study, surface oxidation takes place. The difference in roughness between the two polymers could be due to the difference in crystallinity of the polymers (E. Sheng et al 1995). This increased surface roughness has important consequences as according to Hallab et al. (2001), an increased surface roughness in polymeric surfaces results in an increase in the adhesion strength. This may explain why more peptide seems to be apparent on the PP surface than PE surface as seen in the XPS compositions in section 3.2.

Upon analysing the effect the coatings have on R_a, it is important to remember that all coatings were administered after being acid etched. Thus the subsequent significant difference between roughness of PP and PE for the coatings is most likely due to the difference in susceptibility to acid etching. However, the same pattern can be seen in both PP and PE with respect to the coatings and values for R_a: the roughness with W12 coating is less that with the control coating which in turn is less than with the L12 coating. This established pattern and the difference in values for each coating implies that the peptides are present on the surface, otherwise the R_a for the control coating would be the same as that for the two peptide coatings. To understand why this pattern exists further investigation into the surface treatments and their interactions with the polymers would have to be completed.

4.4 Contact Angle Goniometry

From the results of the advancing contact angle with water measurement it was apparent that acid etching resulted in a lower contact angle, especially with respect to PP. This lower contact angle signifies that acid etching results in an increase in hydrophilicity and wettability. This decrease in contact angle can be attributed to the oxidation of the surface during acid etching, which can be seen clearly in Section 3.2. This is also in accordance with the findings of. Sheng et al. (1995). An explanation for why the acid etching affected the PP more than PE, is outlined by Wenzel (1949), who explained that the surface

roughness of the material enhances the wettability of the material. PP was seen to be significantly rougher than PE under white light interferometry in Section 3.3, the increased roughness and thus wettability would explain the lower $\theta_{w,adv}$ seen in PP. Alternatively, another possible explanation could be that the PE surface experienced inconsistent acid etching. Sometimes during the acid etching process, the PE sheets had a tendency to coalesce with one another whilst standing in the dichromate solution. Consequently, these interactions could have prevented full surface exposure and led to the varying degrees of acid etching in the surface. This inconsistent acid etching across the surface could also explain why the standard deviation is so high, 19.5 degrees. However, the value of $\theta_{w,adv}$ for solely acid etched is not dissimilar to that stated in Blais (1974), which states measured values of 55-65°, depending on the density of the PE when etching was completed for one hour. To determine which of these is the cause, further experiments would have to be completed which address the aforementioned challenges.

The acid etching of the surfaces was also seen to increase the surface energy of the surface. This higher surface energy resulted in the acid etched PP also experiencing a higher surface tension. An explanation for this is the effect acid etching has on the surface heterogeneity, as according to Yekta-Fard and Ponter (1992), this is one of the main factors affecting surface tension. Additionally, Sheng et al (1995) attributed this change in heterogeneity to acid etching increasing the polarizability of the surface functionalities.

When examining the coating performance, similar results were seen across all the coatings on the PP surfaces signifying that for PP, the control coating is the cause for the increase in advancing water contact angle, and the decrease in surface energy. This is further exemplified in the results from the XPS data in section 3.2. The data is suggestive of the fact that the majority of the active bonding sites are most likely being occupied by ethanolamine blocker. The control coated PP is comprised of 1.65% nitrogen at its surface, for the W12 coated surface this value is 2.15% and for L12 coated surface the value is 3.65%. This implies that only 23% and 55% of the nitrogen present in the W12 and L12 coated surfaces respectively can be attributed to the peptide, the rest is to the blocker. Although only one sample was examined using XPS, the fact that the water contact angle and surface energies were similar for all coated PP surface, validates the XPS data gathered.

The $\theta_{w,adv}$ for the coated PE surfaces contrast greatly with that of the measured $\theta_{w,adv}$ for coated PP coupons. For the control coating on PE, the θ_{adv} increased again, similar to the trend for PP but at a much lesser degree. For PE, the similar behaviour of the control and the W12 coating can be explained through examining the XPS results in section 3.2 as it implies that very little W12 is present on the surface of PE; the W12 coated PE has a lower nitrogen surface composition than the non-peptide coated surface. This is indicative that the surface did either not etch sufficiently or the bonding of the peptide and blocker was not complete, which is likely a result of inadequate activation of the surface. This could be because acid etching the PE had a tendency to cause the PE to become bowed. As a result, the activation solution, peptide solution and blocking solution would congregate in the middle of the strip, thereby leading to an uneven activation and peptide immobilisation along the strip; with the outsides experience very little compared to the middle. To minimise this the plastic was straightened before applying the coatings, and the solutions were applied uniformly across the surface, but it is possible that the bowing overcame these attempts. Further investigation and repeating XPS would have to be done to confirm this. Consequently, because of the lack of peptide immobilisation, the W12 coating would be expected to behave like the control. The similar contact angle measurements and surface energy values support this observation.

However, the contact angle measurement and surface energy determination for the L12 coating does suggest that L12 is present, due to the completely different values from the other coatings. These different values are indicative that the L12 coating is affecting the surface chemistry, which is strong evidence for the presence of the peptide. Further support for this can be seen in the results from the XPS in section 3.2. For L12 coated PE, the sample tested showed 5.8% of the surface composition is comprised of nitrogen, compared to the 2% of nitrogen seen in the control. This indicates that approximately 66% of the nitrogen present on the L12 coated surface comes from L12, and thus the L12 must be present on the section tested. This would vary across the surface due to the heterogeneity of the surface and the fact only one sample was examined using XPS, but the fact that the contact angle measurement and XPS both indicate L12 presence, is promising.

4.5 Confocal Microscopy

Upon examining the results, it is evident to a high level of confidence, 95%, that the W12 coated PE surfaces provide no greater antimicrobial properties than the control. This could be explained by XPS data gathered for this surface as seen in Section 3.2, and is further corroborated by the contact angle goniometry in section 4.4. The XPS data showed no significant presence of nitrogen on the surface of the polymer, suggesting that the peptide had not bonded sufficiently and was not present after washing the surface, therefore, this surface may possess surface

chemistry similar to the control and hence exhibit the same level of antimicrobial action. Other results which were noted were the inconsistencies in the repeats of L12 coated PP left for 30 minutes and the repeats of W12 coated PE that was not left for 30 minutes. Both had one instance of significant biocide and two instances of no biocide. One likely cause of the inconsistency in significance level across the repeats for these coating was the orientation of the peptide. These specific peptides were designed by Khara et al (2017) to have one hydrophilic and one hydrophobic face and to both contain 6 leucine residues, in themselves each having one primary amine group. As the peptides were bonded to the surface via an amide bond, it is likely there is no consistent mode of orientation of the peptides when binding to the surfaces, this could then result in inconsistent antimicrobial properties. Further work should be completed to attempt to bond the peptides to the surface by means of a bond via the carboxyl group of the peptide, as this would ensure consistent orientation as there is only a single carboxylic moiety in each peptide.

The most successful experiments were those which included a 30-minute delay period after washing, allowing for the establishment of the *Pseudomonas* monolayer and any antimicrobial processes to take place. It is likely that the surfaces left for 30 minutes after the bulk was removed exhibited greater antimicrobial action than the surfaces tested instantaneously due to the nature of the formation of biofilms and the antimicrobial action of the peptide. Biofilms form as bacteria are deposited onto the surface from the bulk solution (Crouzet, et al 2014). Allocating this extra 30 minutes allowed the bacteria to settle onto the surface and experience the antimicrobial action. Applying the saline solution permitted the aforementioned processes to take place without the sample drying, and therefore allowed time for more complete lysis of the bacteria.

The final key result of this study was that L12 coated PP exhibited the greatest ratio of dead bacteria to total bacteria when compared to the control, hence the best antimicrobial properties out of all of the surfaces. This result agrees with the results from the study completed by Khara et al. (2017) as L12 was shown to be the most effective of the antimicrobial peptides tested and the only peptide which disrupted and killed a pre-established biofilm. Therefore, it follows that it possesses the greatest ability to prevent the formation of a biofilm in this study. Additionally, the L12 peptide coating provided the greatest increase in surface nitrogen composition as seen from the XPS results, indicating that it bonded to the surface more successfully resulting in the greatest surface concentration, which would explain why it exhibits the greatest performance in antimicrobial surface activity.

To validate the results of this study, a far greater number of repeat experiments needs to be completed to be able to increase both the accuracy and precision of the data. Finally, due to shortcomings with the effectiveness of Syto 9 stain on *P. aeruginosa* (Stiefel et al, 2015) it would be recommended to complete the assay again with a more suitable gram-positive bacterium such as *S. aureus* or to use an alternate probe.

Conclusion

In summary, it was confirmed that the chromic acid etching was successful in the addition of oxygen to the polymer surface, as evidenced by the XPS data. Additionally, the L12 peptide was proven to be successfully immobilised on the PP and PE surfaces, and W12 was immobilised successfully on the PP surfaces and to a lesser degree the PE surfaces. Finally, this experiment confirmed with 99.5% confidence that the peptides that were immobilised on the surface, and allocated time for bacterial death, did increase the ratio of dead to total bacteria on the surface compared to the controls, and thus exhibited improved antimicrobial performance. The best performing peptide was L12, and the best performing surface was PP, as these both exhibited better antimicrobial properties than their respective counterpart, thus the combination of these two served as the surface with the best antimicrobial properties. The experiments carried out show promising results with respect to developing surfaces with antimicrobial properties, and there are multiple avenues for developing and refining this novel concept. Most crucially the assay would need to be repeated and more experiments carried out to ensure the data is reproducible, and ideally, the study should be coupled with another micro test to validate the biocidal activity trends observed. The three main areas for future study are 1) varying the strain of bacteria used during the assay, 2) varying the surfaces for coating and 3) investigating alternate methods of coating the peptide on the surface. For example, with respect to the peptides, potential future work includes evaluating the performance of other peptides with antimicrobial properties and evaluating immobilised peptoids, as these have an increased robustness in nature and are not susceptible to enzyme degradation, although may prove more difficult to immobilise due to their stability. In examining and redesigning with surfaces in mind, the performance of other materials such as nylon could be investigated, and different oxidising techniques could be investigated, especially ones that are not antimicrobial themselves. A final key result to be explored further is the auto-fluorescence of PP surfaces after chromic acid etching, and how this noise could be mitigated or eliminated.

Acknowledgements

We would like to thank Professor Paul Langford (Imperial College London) for providing the L12 and W12 peptides, Gareth Davies and Kevin Wright at Proctor & Gamble GLIC Egham for allowing us to use their confocal microscope and finally Dr Jonathan Palmer and Fatemeh Alemi for their help and guidance throughout the project.

Supplementary documentation:

Supplementary information can be found in the file: Supplementary Material

References

[1] Batoni, G., Maisetta, G., Brancatisano, F. L., Esin, S. & Campa,. M. (2011) Use of Antimicrobial Peptides Against Microbial Biofilms: Advantages and Limits. *Current Medicinal Chemistry*. 18(2): 256-79. Available from: DOI: 10.2174/092986711794088399 [Accessed 3rd December 2018]

[2] Berg J.M., Freeman, W.H. & Stryer, L.. (2002). *Polypeptide Chains Are Flexible Yet Conformationally Restricted.* Biochemistry. 5th ed. New York, W H Freeman. Available from: https://majkf.files.wordpress.com/2010/08/lubert-stryer-biochemistry-5th-edi.pdf

[3] Blais, P., Carlsson, D.J., Csullog, G.W. & Wiles, D.M.. (1974) The Chromic Acid Etching of Polyolefin Surfaces, and Adhesive Bonding. *Journal of Colloid and Interface Science.* 47 (3): 636-649. Available from: DOI 10.1016/0021-9797(74)90241-0 [Accessed 2nd December 2018]

[4] Crouzet, M., Senechal, C.L., Brözel, V.S, Costaglioli, P., Barthe, C., Bonneu, M., Garbay, B. & Vilain, S.. (2014) Exploring early steps in biofilm formation: set-up of an experimental system for molecular studies. *BMC Microbiology.* 14:253. Available from: https://www.ncbi.nlm.nih.gov/pmc/articles/PMC4189659/ [Accessed 10th December 2018]

[5] Donlan, R.M. (2002). Biofilms: Microbial Life on Surfaces. *Emerging Infectious Diseases.* 8(9):881-890. Available from:doi:10.3201/eid0809.020063.[Accessed 3rd December 2018]

[6] Flemming, H.C., Wingender, J., Szewzyk, U., Steinberg, P., Rice, S.A. & Kjelleberg, S..(2016) Biofilms: an emergent form of bacterial life. *Nature Reviews Microbiology. 14: 563-575.* Available from: https://doi.org/10.1038/nrmicro.2016.94 [Accessed 3rd December 2018]

[7] Fowkes, F.M.. (1964) Attractive Forces at Interfaces. *Industrial and Engineering Chemistry.* 56(12): 40-52. Available from: DOI**:** 10.1021/ie50660a008 [Accessed 28th November 2018]

[8] Hallab, N.J, Bundy, K.J., O'Connor, K., Moses, R.L. & Jacobs, J.J.. (2001) Evaluation of Metallic and Polymeric Biomaterial Surface Energy and Surface Roughness Characteristics for Directed Cell Adhesion. *Tissue Engineering*. 7 (1): 55-71. Available from: DOI: 10.1089/107632700300003297. [Accessed 2nd December 2018]

[9] Khara, J.S., Obuobia, S., Wang, Y., Hamilton, M.S., Robertson, B.D., Newton, S.M., Yang, Y.Y., Langford, P.R. & . Ee, P.L.R.. (2017) Disruption of drug-resistant biofilms using de novo designed short α-helical antimicrobial peptides with idealized facial amphiphilicity. *Acta Biomaterialia.* 57: 103-114. Available from: https://doi.org/10.1016/j.actbio.2017.04.032 [Accessed 3rd December 2018]

[10]Lee, W.H, Glee, J. & Reucroft, P.J.. (2001) XPS study of carbon fiber surfaces treated by thermal oxidation in a gas mixture of O2/(O2+N2). *Applied Surface Science.* 171(1-2): 136-142. Available from: https://doi.org/10.1016/S0169-4332(00)00558-4 [Accessed 29th November 2018]

[11] Mittelman, M.W.. (2000) *Bacterial Biofilms and Biofouling: Translational Research in Marine Biotechnology*. Opportunities for Environmental Applications of Marine Biotechnology: Proceedings of the October 5-6. Washington (DC), National Academies Press (US). Available at: https://www.ncbi.nlm.nih.gov/books/NBK223017/ [Accessed 3rd December 2018]

[12] Sanchez, G.V., Fleming-Dutra, K.E, Roberts, R.M. & Hicks, L.A.. (2016) Core Elements of Outpatient Antibiotic Stewardship. *Morbidity and Mortality Weekly Report-Recommendations and Reports*. 65 (6): 1–12. Available from: DOI: http://dx.doi.org/10.15585/mmwr.rr6506a1 [Accessed 3rd December 2018]

[13] Serna, M., Giles, J.L., Morgan, B.P & Bubeck, D. (2016) Structural basis of complement membrane attack complex formation. *Nature Communications.* 7. Available from: https://doi.org/10.1038/ncomms10587 [Accessed 28th November 2018]

[14] Sheng, E. , Sutherland I., Brewis, D.M. & Heath, R.J.. (1995) Effects of the chromic acid etching on propylene polymer surfaces. *Journal of Adhesion Science and Technology.* 9(1): 47-60. Available from: DOI: 10.1163/156856195X00284 [Accessed 1st December 2018]

[15] Stiefel, P., Schmidt-Emrich, S., Maniura-Weber, K., & Ren, Q.. (2015) Critical aspects of using bacterial cell viability assays with the fluorophores SYTO9 and propidium iodide. *BMC Microbiology.* 15:36. Available from: https://www.ncbi.nlm.nih.gov/pmc/articles/PMC4337318/ [Accessed 10th December 2018]

[16] Vuotto, C., Longo, F., Pascolini, C., Donelli, G., Balice, M.P., Libori, M.F., Tiracchia, V., Salvia, A. & Varaldo, P.E.. (2017) Biofilm formation and antibiotic resistance in Klebsiella pneumoniae urinary strains. *Journal of Applied Microbology.* 123(4):1003-1018. Available from: doi: 10.1111/jam.13533 [Accessed 3rd December 2018]

[17] Walsh, D., Pope, D., Danford, M.& Huff, T.. (1993) The effect of microstructure on microbiologically influenced corrosion. *Journal of the Minerals, Metals & Materials Society.* 45(9): 22-30. Available from: https://doi.org/10.1007/BF03222429 [Accessed 3rd December 2018]

[18] Wang, H., Chen, S., & Zhang, J.. (2009) Surface treatment of LLDPE and LDPE blends by nitric acid, sulfuric acid, and chromic acid etching. *Colloid and Polymer Science*. 287 (5): 541-548. Available from: https://doi.org/10.1007/s00396-009-2000-9 [Accessed 3rd December 2018]

[19] Wenzel, R.N. (1949) Surface Roughness and Contact Angle. *The Journal of Physical and Colloid Chemistry.* 53 (9): 1466-1467. Available from: DOI: 10.1021/j150474a015 [Accessed 1st December 2018]

[20] World Health Organisation. (2014) Antimicrobial Resistance. *Global Report Surveillance.* Available from: http://apps.who.int/iris/bitstream/handle/10665/112647/WHO_HSE_PED_AIP_2014.2_eng.pdf;jsessionid=226C7D82B9BF6055E7E657F71F311D42?sequence=1[Accessed 1st December 2018]

[21] Yekta-Fard, M., & Ponter, A.B.. (1992) Factors affecting the wettability of polymer surfaces. *Journal of Adhesion Science and Technology.* 6(2): 253-277. Available from: DOI: 10.1163/156856192X00322 [Accessed 1st December 2018]

[22] Zasloff, M.. (2002) Antimicrobial peptides of multicellular organisms. *Nature.* 415: 389-395. Available from: https://doi.org/10.1038/415389a [Accessed 3rd December 2018]

[23] Zottola, E.A & Sasahara, K.C.. (1994) Microbial biofilms in the food processing industry—Should they be a concern? *International Journal of Food Microbiology.* 23(2): 125-148. Available from:https://doi.org/10.1016/0168-1605(94)90047-7 [Accessed 3rd December 2018]

CAR-T Cell Therapy: A Unique Optimisation Problem

Identification of the key bottlenecks in the current supply chain model of CAR T cell therapy

Jack Flood and Roger Percy Lister

Department of Chemical Engineering, Imperial College London, U.K.

Abstract CAR T cell therapy provides a treatment option to blood cancer patients whose outlook is terminal having exhausted all other forms of treatment. As a last chance solution, the costs associated with the therapy are high, in the hundreds of thousands of pounds. Two CAR T treatments have been approved in the UK but having received a fast approval, the product supply chain poses its own challenges. The objectives of our work were to identify the key challenges of this supply chain, produce a forecast for the demand of the treatment in the future and to propose a mathematical model for the UK. We started this with a literature review to identify the challenges, then gathered population data to forecast demand, and proposed an optimisation model that minimises the cost of the transport used as a courier for the treatment. We found that the key challenges were the requirement for needle to needle traceability, the high cost of the treatment and the mass manufacture of a product whose starting material is variable. The demand would increase due to the UK population increasing, and we proposed a scenario where 9000 people would enter remission as a result of being treated with CAR T cell therapy by 2035, with a cost of £385,000 per person entering remission. We then propose areas that could be of further research interest.

Key Words: CAR T Cell, Immunotherapy, Supply Chain, Optimisation Modelling, Demand Forecast

Introduction

The development of therapeutic medicines has evolved rapidly over the last century. In particular, the pharmaceutical industry has benefitted from advancements in our understanding of diseases. Technological advancements have also accelerated this process.

Traditional pharmaceutical medicines rely on the use of protein-based molecules to regulate medical disorders in the patient. They aim to reduce symptoms and slow down the progression of the disease thereby allowing enough time for the immune system to learn how to deal with the pathogen. These medicines are however less effective when treating patients affected by cancer as the immune system is unable to differentiate between cancerous and healthy cells. For example, chemotherapy has been traditionally used for treating the majority of cancers without the need for surgery. Chemotherapeutic agents administered to the patients interfere with cell division thereby stopping the growth of the cancer. They aim to cure the patient or prolong their life and improve quality of life, but their efficacy varies widely depending on many factors including the type and the stage of the cancer (Wei Teng, 2013).

"More than 80% of children diagnosed with ALL that arises in B cells—the predominant type of paediatric ALL—will be cured by intensive chemotherapy. But for patients whose cancers return after chemotherapy or a stem cell transplant, the treatment options are "close to none," said Stephan Grupp, M.D., Ph.D., of the Children's Hospital of Philadelphia (CHOP)'(National Cancer Institute, 2017).

As Grupp states, if chemotherapy is no longer successful in treating the cancer, there exist very few further treatment pathways for the patient. Typically, the patient will enter a palliative care regime at this point. As such, there has been an increasing need for novel therapies to treat cancer patients. One of the most promising areas of research is immunotherapy. The working principle behind these therapies is to redirect the patient's own immune system to identify the cancer or infectious disease and treat it from within. Chimeric antigen receptor (CAR) T cell therapy has emerged as one of the most promising immunotherapies to treat various types of blood cancer. Blood cancers are the third biggest cancer killers, killing more than 13,000 people a year. (Bloodwise, 2018). A treatment that can reduce the number of deaths from blood cancers clearly has a great deal of potential for a positive impact and has excited researchers and doctors alike.

The general idea of the therapy is that the patient's blood is extracted and T cells within the blood are genetically engineered to express CAR and these T cells are then administered to the same patient. As such, this is an autologous treatment. As a result of the genetic engineering, the CAR T cells are able to recognise the cancer and kill it. In clinical trials, the therapy has been very successful with children and young adults suffering from B cell malignancies such

as relapsed or refractory acute lymphoblastic Leukaemia (ALL) (Liu et al, 2018). Following the success of the therapy treating blood cancers in trials, two treatments have already been approved to treat haematological cancer patients in the UK (NHS England, 2018).

Although the therapy has been hailed as a major breakthrough in the fight against cancer, there are several challenges that need to be addressed before a major scale up can achieved. These challenges include managing the unique supply chain of an autologous cancer treatment, manufacturing limitations as well regulatory roadblocks. These limitations contribute towards the high cost of treatment, which could be prohibitive to some patients receiving treatment. Kymriah, one of the treatments approved for distribution in the US, is priced at $475,000 (Financial Times, 2018) for a single infusion.

Thus, the aim of this research was to qualitatively assess the current supply chain model used for clinical trials and identify potential risks and bottlenecks that may affect the expansion of the treatment in the UK. Research was undertaken to estimate current and future demand for the treatment in the UK. Data was collected to model the supply chain as an optimisation model with constraints, key performance indicators (KPI). The aim was to identify aspects of the supply chain where the total cost of the treatment might be reduced and to estimate the cost per patient treated. With any product, high costs associated with the supply chain will be passed onto the consumer by the manufacturing company in the form of a higher price of the product. Bottlenecks within a supply chain will inevitably cause inefficiency of the supply chain and will introduce these unnecessary, occasionally high, costs. The objective of supply chain optimisation is to identify these bottlenecks and inefficiencies within a supply chain, and to identify alternatives that will lead to an increased efficiency and responsiveness of the supply chain at a lower cost. Here, the desire is to reduce the supply chain cost of the CAR T cell therapy by identifying challenges of the supply chain, and proposing solutions to the issues raised. However, the autologous nature of the therapy and the fact it cannot be prepared and stored ahead of the time it's required as inventory make this a unique optimisation problem. We proposed an optimisation model for the unique supply chain and performed a qualitative analysis of this model. Finally, potential solutions were proposed to address the key risks that emerged throughout the research.

During the entire process, an engineering perspective was applied to the problem in the hope of address a lack of an engineering point of view in literature largely produced by medical professionals.

Background

Autologous CAR T cell therapy is an adaptive cell transfer (ACT) technique. ACT therapies work by using the patient's own cells which are genetically engineered and injected back into the same patient to improve immune system functionality. In CAR T cell therapy, T cells are used; T cells are a specific type of lymphocyte, a subset of white blood cells. T cells play a vital role in orchestrating the immune system's response to foreign bodies such as cancer, earning them the nickname the workhorse of the immune system. (National Cancer Institute, 2018)

During the manufacturing process, the T cells extracted from the patients are genetically engineered with viral or non-viral vectors to express the chimeric antigen receptor. This enables the T cells to recognise the protein or antigen on the surface of the cancer cell. Trials have also shown that the efficacy of the treatment largely depends on the degree of cell persistence in the patient. Cell persistence is affected by the quality of proliferation of the cells in the blood in the patient's body (Saad et al, 2016). This is in turn reliant on cell expansion during the manufacturing process.

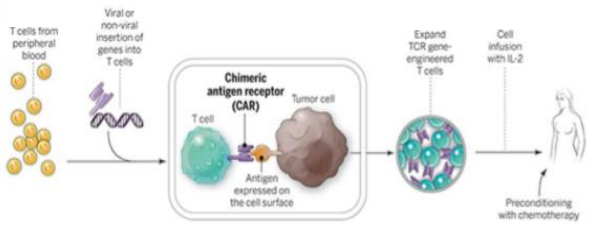

Figure1. Schematic of how T cells are engineered to produce the chimeric antigen receptor, (National Cancer Institute, 2017)

The production process for CAR T cells begins in the clinic where the patient is situated. The first step, Leukapheresis, involves blood being extracted from the patient where it is processed to separate the leukocytes. The blood is returned to the patient's circulation while the Leukapheresis product is enriched for T cells. This process, called T cell isolation, involves removing anticoagulants from the product and using counterflow centrifugal elutration to increase the concentration of the T cells.

The next critical step is the activation of the T cells, also called transduction, which involves incubating the cells for several days with viral or non-viral vectors that essentially encode the CAR genetic material into the cell. The genetic material encoded is in the form of RNA which permanently changes the genome of the cell meaning CAR expression is maintained even as the cells multiply. The resulting cell will be able to express the chimeric antigen receptor on its surface. The manufacture of the vectors does not require the patient's own cells and it is a separate process altogether.

The long-term quality of the viral vectors is maintained since they can be produced in large quantities and stored for about 9 years (Zhang et al, 2017). However, there is concern for the safety, sterility, purity and potency of the vectors due to the fact that there are different manufacturers using different practices. It is important that these long-term risks are understood and that a standardised process for producing vectors is adhered to by vector manufacturers.

The next step involves the *in-vitro* expansion of the CAR T cells. Expansion has been shown to be crucial, as the larger the degree of proliferation of CAR T cells, the greater the persistence of the cells when transferred, the greater the efficacy of the treatment. The cell culture is placed in a bioreactor and it is subjected to specific conditions that favour the multiplication of the cells. Once the required volume is produced, usually around 5 L, the cells are washed and concentrated to a volume suitable for injection into the patient. The cells are then cryopreserved in infusible mediums ready for distribution to the clinic.

The manufacturing process takes on average 10 days however some manufacturers have been able to reduce the manufacturing time down to even 7 days (National Cancer Institute, 2017). A schematic can be found in Appendix 1. Throughout the entire process several quality control checks are performed to ensure that every step and the final product meet all release criteria and Good Manufacturing Practices (GMP) guidelines.

The supply chain can be considered as a patient-to-patient model. The first step in the supply chain is done at the clinic where the patient undergoes leukapheresis and the T cells are isolated. The cells are then transported to the manufacturing site via a courier where they are processed as outlined previously to achieve the final product.

Once the final product is ready, having passed quality control checks, it is handed over to the courier for distribution to the same clinic. The clinic and medical staff are then responsible for administering the treatment to the patient and managing possible side effects. The treatment doesn't stop here as the clinic will look after the patient with monthly and yearly check-ups to make sure that the cancer is in remission or in the case of cancer recurrence, decide on a course of action regarding treatment.

What makes this treatment so unique is the fact the blood is withdrawn from the patient, engineered and then administered to the same patient. The quality of the starting material changes from patient to patient and as such the supply chain differs from patient to patient. Factors such as the health of the patient and the type of cancer all have an impact on the cells extracted and these factors will affect the cells' ability to proliferate. This essentially means that for each patient there exists a distinct supply chain with variable manufacturing times, in particular the time taken to expand the cells.

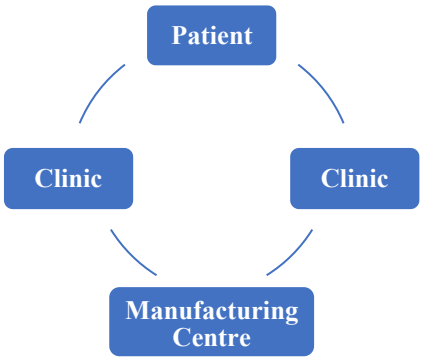

Figure 2 Schematic that shows the circular nature of the supply chain. The supply chain starts with the patient and ends with the patient.

However, the quality of the final product has to be maintained for all patients to meet regulatory standards. These challenges become ever so important when considering the tight time constraints imposed by the situation that the patients are in. Therefore, it is important that all stakeholders work efficiently to deliver the treatment to the patient in a seamless manner.

Methods

Demand forecast

To first get an understanding of the demand for a cancer treatment that is life saving for terminally ill cases, we forecast the new cases and deaths from blood cancers. The blood cancers considered were Acute Lymphoblastic Leukaemia, Chronic Myeloid Leukaemia, Chronic Lymphocytic Leukaemia, Acute Myeloid Leukaemia, Hodgkin Lymphoma, Non-Hodgkin Lymphoma and Myeloma. The number of new cases of each cancer is simply a product of the population and the individual cancer incidence rate.

$$Cases = Incidence\ rate\ \times population \quad (1)$$

Eg. Cases of ALL in 2018 = 1.23 x 664.66

Cases of ALL in 2018 = 818

Where incidence rate is per 100,000s and population is in 100,000s.

The number of deaths is similarly a product of the population and the individual cancer mortality rate. Data for the population growth was taken from Office for National Statistics (2017) while both incidence and mortality rates for each blood cancer were taken from Cancer Research UK (2015). Smittenaar et al (2016) calculated the percentage change in the incidence rates up until 2035. From this we calculated a constant yearly incidence percentage change and hence calculated the year by year incidence rate for each kind of cancer. In this model, to estimate number of deaths,

it is assumed that there are no innovations in cancer treatment, so mortality rate is kept constant. A similar method was used for the US data, assuming the same changes in incidence rates and keeping mortality data the same. US incidence and mortality data was taken from the National Cancer Institute forecasts and population data from the US Census Bureau, (2017).

To model the rollout of the treatment, various scenarios were considered. Firstly, those eligible for the treatment were those who have terminal cancer and have exhausted all other treatment options. In all scenarios there was an initial treatment of 400 in 2018. Two treatments have been accepted for use in the UK in 2018, Yescarta, which treats large cell lymphoma and is available to up to 200 patients a year, (NHS England, 2018) and Kymriah (NHS England, 2018), used to treat B cell Acute Lymphoblastic Leukaemia in children. It is assumed that Kymriah would also be available to 200 patients. Various rates of expansion were investigated, some with a constant yearly percentage increase. Another scenario where a new treatment is accepted every year, adding 200 capacity yearly and in the increasing the number of treatments accepted per year case 2 new treatments were accepted yearly for 4 years, then 3 accepted yearly for 5 years, 4 yearly for 5 years and then 5 new treatments per year for the final 3 years.

In order to assess the feasibility of the rollout scenarios, the costs of the treatment to the NHS had to be taken into consideration. The costs are built up of two parts – the costs of the drug and the cost for the 10 years of check-ups required for patients who successfully enter remission. The cost of the drug is taken to be £**282,000** (NHS England, 2018), while the cost of the check-ups is assumed to be of a similar order to the cost of the current treatment for blood cancers on the NHS, £**14,000** (Burns et al, 2016). The drug is only paid for in the case that treatment is successful, and a success rate of 80% has been assumed based on trials (Liu et al, 2018). It is assumed that a successful treatment is a patient entering full remission and that this patient will return for 10 years after treatment. The numbers eligible for check-ups are made up of those treated in a particular year, and all those who had achieved complete remission within the 10 years previous to that year.

$$Total\ annual\ cost\ (£1{,}000s) = 282N_1 + 14N_2 \quad (2)$$

Eg. Total annual cost in 2020 = (282 x 353) + (14 x 1097)

= £114.9 million

Where

N_1= number of successful treatments that year

N_2= number of patients eligible for treatment

The total yearly price was then compared to the NHS budget for haematological cancers to assess the feasibility of each scenario. The future NHS budget was projected based on recent real terms increases of £2.5 billion over 4 years, equivalent to a constant yearly increase of **0.74%** (NHS statistics), and the proportion of this spent on cancers is **6%** (Brown et al, 2014)

The proportion of the cancer budget spent on haematological cancers is **10.2**% (NHS England, 2018), and so a proportion, **0.6**%, of the NHS budget that is spent on haematological cancers was calculated. It was assumed that the proportion of the NHS budget assigned to Haematological Cancers would be constant.

Optimisation model

The optimisation model was formulated to maximize Net Present Value (NPV) from the perspective of the manufacturing company that produces the therapy. The NPV is made up of inputs and outputs; the inputs being revenue generated from sales of the drug, whilst the outputs are operating costs such as manufacturing costs and transport costs. With manufacturing costs assumed constant and revenue fixed by the yearly demand, the transport costs can be variable dependent on the mode of transportation taken. These can be optimised such that the cheapest mode of transport is selected for each treatment centre. There are 4 treatment centres (Manchester, Newcastle, Birmingham and London) and 3 modes of transport (road, rail and plane). Demand at each treatment centre is calculated as a percentage of the total demand for each year (Appendix 2).

Results

Population Data

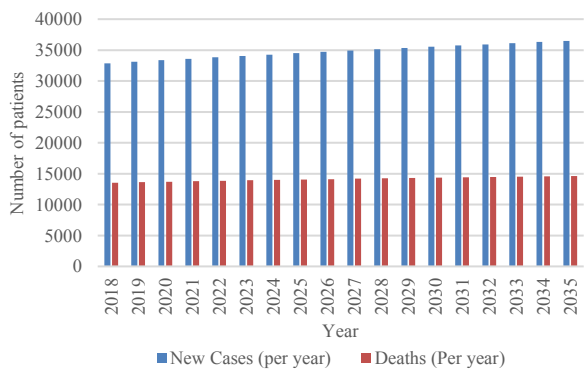

Figure 3.1 Projection of the number of cases of and deaths from blood cancers between 2018 and 2035 in the UK

Figure 3.1 projects a trend from 2018 to 2035 where the number of cases of blood cancers and the number of deaths from blood cancers is expected to increase. Indeed, from 2018 to 2035, the annual number of cases of haematological cancers is expected to increase, from **32,800** in 2018 to **36,500** in 2035. The number of yearly deaths from haematological

cancers are also expected to increase, from **13,500** in 2018 to **14,600** in 2035.

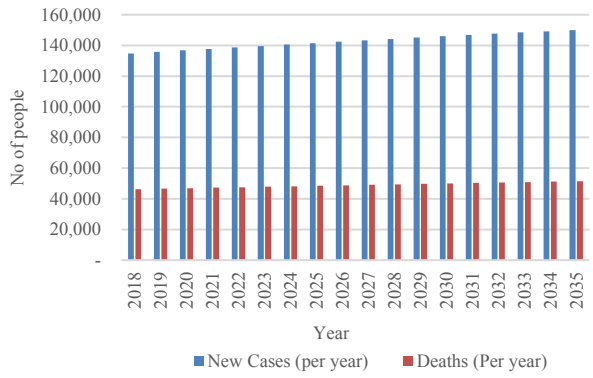

Figure 3.2 Projection of the number of cases of and deaths from blood cancers between 2018 and 2035 in the US

Figure 3.2 projects a similar trend to Figure 3.1 but for the US. From 2018 to 2035 the number of cases of blood cancers and the number of deaths increases. From 2018 to 2035, the annual number of cases of haematological cancers is expected to increase, from **134,700** in 2018 to **150,000** in 2035. The number of yearly deaths from haematological cancers are also expected to increase, from **46,200** in 2018 to **51,400** in 2035.

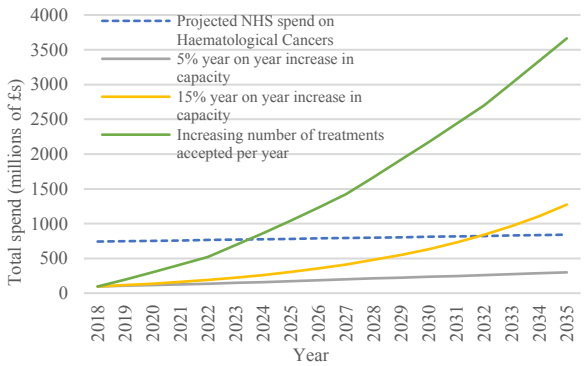

Figure 4. Plot of the total cost of various stochastic scenarios modelling the rollout of CAR T cell therapy to the Blood Cancer Population from 2018 to 2035. The dotted blue line shows the projected NHS spend on haematological cancers.

In Figure 4, the blue dotted line represents the projected NHS spend on Haematological cancers. The total cost of the increasing number of treatments accepted per year scenario exceeds the NHS budget in **2024** and represents **435%** of the NHS budget in 2035. For the 15% year on year capacity increase, its total costs exceed the total NHS haematological cancer budget in **2032** and are **151%** of the 2035 NHS budget. Within the 2018 to 2035 timeframe, the 5% year on year scenario does not exceed the projected NHS budget for haematological cancers. In 2035, the cost of this scenario will be **36%** of the allocated NHS budget.

Optimisation Model

The following optimisation model was proposed;

For treatment centres *i* and modes of transport *j*

$$Objective\ function = \sum_{i=1}^{4}\sum_{j=1}^{3} y_{ij}(U_j.D_i.T_{ij}) \quad (3)$$

Subject to

$$y_{ij} = \left\{ \begin{matrix} 1\ if\ transport\ j\ \ used\ for\ treatment\ centre\ i \\ 0\ otherwise \end{matrix} \right\} \quad (4)$$

$$\sum_{j=1}^{3} y_{ij=1} \quad \forall i=1,2,3,4 \quad (5)$$

$$TT_i = T_l + T_m + \sum_{j=1}^{3} y_{ij}.T_{ij} \quad (6)$$

$$TT_i \leq K_1 \quad (7)$$

Where

U_j = Per unit cost of using transport *j* (£/unit.hr)

D_i = Demand for units at treatment centre I (units)

T_{ij} = Time taken by transport *j* to and from the manufacturing facility from treatment centre *i*

T_l = Time taken for leukapheresis and administration of treatment

T_m = Time taken for manufacturing

TT_i = Total time taken for treatment centre *i*

K_1 = Arbitrary time constraint

The objective function, equation (3), optimises the choice of transport by selecting the cheapest mode of transport for each treatment centre. In the model, the binary variable ensures that only one mode of transportation is selected per treatment centre. As well as the binary variable, there's also 7 other variables. There's one inequality constraint in the model, equation 7; this ensures that the time taken for the overall process is below an arbitrary constant, which can be set subject to the manufacturer's requirements.

Discussion

Key Risks and Challenges

As discussed earlier there are several risks and challenges associated with CAR T cell therapy and its delivery to the patient. These include product development, logistics, delivery, supply chain requirements and side effects of the therapy.

Researchers are aware of the future risks to the commercial viability of CAR T cells. A serious risk to the commercialisation of the therapy is the severe side effects observed during clinical trials. These include: B cell aplasia, cytokine release syndrome

(CRS), macrophage activation syndrome (MAS) and neurotoxicity. CRS in particular is a particularly concerning side effect as it has caused several deaths in clinical trials. In fact, Maude et al report that Cytokine response syndrome occurred in 77% of patients in a trial using Tisagenlecleucel to treat Acute Lymphoblastic Leukaemia. The management of these side effects through supplementary drugs needs to be better understood to improve the patient experience of the treatment.

An issue with the therapy is the previously mentioned variable quality of the starting material due to treatment that the patients may have previously been through such as chemotherapy. The variable quality of the initial material can affect the expansion, and the expansion is critical in ensuring cell persistency. Cell persistency within the body plays a critical role in the efficacy of the treatment, as it has been shown that T cells must persist to provide immunosurveillance and prevent relapse (Gill et al, 2015). Studies have shown that lymphodepleting pre-treatment can reduce the number of regulatory T cells and other immune cells that are in competition with cytokines. This depletion improves greatly the T cell function, augmenting the performance of the transferred T cells. (Saad et al, 2016)

The current manufacturing process involves several steps, it is very lengthy, and it is not standardised across manufacturing sites. The time needed to manufacture the treatment for a single patient could be a serious limitation to the therapy's long-term future in treating terminally ill patients. If the therapy is not produced and delivered in time, then a scale up for a greater patient population will never be possible.

One of the reasons for the complexity in the supply chain is due to the sheer number of players involved in the treatment of just one patient. Manufacturers, medical providers, collection centres, couriers, case managers all have to work seamlessly together coordinating every step in the chain. This has to be done for each patient and hence each treatment. Needle-to-needle traceability is the main reason for this since the raw material must originate from and the product end with the exact same patient. To meet these requirements, Cell Orchestration Platforms should be used to integrate stakeholders in every step on the supply chain.

An important consideration from the supplier's point of view is the transport of the cells from the clinic and back. The trade-off between cost of transport and time is an important one here. This problem was formulated as an optimisation model for the UK.

Population Data

From 2018 to 2035, there will be an increase in the number of both the cases and deaths from blood cancers in the UK. This increase is due to the increasing population of the United Kingdom. The total population of the UK is expected to increase from 66.05 million in 2018 to 71.59 million in 2035 (Office for National Statistics, 2016), representing an **8.39%** increase in the population. There's likely to be more deaths from blood cancers also as the population is expected to age (Office for National Statistics, 2016) and the percentage chance of survival from blood cancers decreases with age. (National Cancer Institute Network, 2014). The incidence of blood cancers is unexpected to change due to changes in lifestyle, as would happen with lung and stomach cancers for example. Alastair Rankin states that "Very few cases of blood cancer can be prevented by changes in lifestyle" (Bloodwise, 2018.) In the US, the number of cases of blood cancers and the number of deaths from blood cancers is expected to increase. The same reasoning as above for the UK applies here; the US population is going to increase by **11.3%** from 2018 to 2035, and the US population is expected to age (Mather,2016) so demand for cancer blood cancer treatments will increase.

The scenario associated with the green line is not realistic as by 2035 the cost is 4.35 times the projected NHS budget. In this scenario, the treatments have been expanded to too many people, 12,000 per year in 2035, too quickly, resulting in a scenario that is unaffordable for the NHS. The grey plot, which represents a scenario where the capacity is increased by 5% every year from the baseline of 400 in 2018. In 2035, this scenario would account for **35.5%** of the projected NHS budget for Haematological Cancers. This represents a more affordable scenario for the NHS. Hence, this is our feasible scenario. In this scenario, **917** people will receive a treatment in 2035, with **733** of these entering remission assuming an 80% treatment success rate. With a lower success rate, costs are lower as the failure of the drug results in the cost being reimbursed, even though the number of people treated per year is the same (Appendix 3). Those eligible for the treatment are those who have terminal cancer and have exhausted all other treatment options. As a result of this scenario, from 2018 to 2035, **9000** people in total will enter remission, with the cost per person entering remission estimated at **£385,000**. In 2018, it was estimated there would be 32,800 cases of blood cancers. The projected NHS budget for blood cancers in 2018 is £742.3 million, resulting in a cost per case treated of approximately **£22,600**. £385,000 is a large cost compared to £22,600, **17** times larger in fact, but these people have exhausted all other treatment options and their cancers are terminal.

A possible source of error within the analysis is associated with the assumption of the price of the drug. The retail price of the drug was assumed but with the NHS committing to purchase in bulk the therapies, it is likely they will receive a reduced price. The effect of this would be that total costs will be reduced. The most feasible scenario would be cheaper. If the NHS

was committed to a higher level of spending, with the cost per treatment cheaper, it can provide more treatments. Another stochastic analysis could be carried out, where the effect of different negotiated prices for the treatments and its impact on the affordability to the NHS could be investigated.

The discussion of whether these scenarios are realistic is aided by the projected NHS spend. However, in this projection of the NHS spending for haematological cancers, it has been assumed the proportion of the budget allocated remains constant. Intuitively, introducing a more expensive treatment should require greater funds so that the extra costs are covered.

For the grey scenario in figure 4, the cost of treating blood cancers with CAR T cells is **£299 million** in 2035. This leaves **£542 million** of the budget to spend on treating people using conventional treatment methods such as radiotherapy and chemotherapy. Assuming **£22,600** per treatment, this £542 million will allow **24,200** people to be treated with conventional methods. In total this budget allows 25,117 people to be treated in 2035 in total. The number of new cases that year is projected to be 36,486 meaning that **11,369** people would go without treatment in this budget scenario. For all these people to receive a conventional treatment, an extra **£255 million** is required, which is **30.2%** of the 2035 haematological cancer budget. Clearly, this budget is insufficient to deliver the NHS's treatment for all promise. More money must be allocated to the Haematological Cancer budget each year beyond the money that it naturally receives as result of the NHS budget increasing. The NHS must annually calculate the extra cost effect of the implementation of CAR T on its budget, so that all those with blood cancers can receive treatment, whether that be with CAR T or more conventional treatments.

Optimisation Model

In the feasible scale out scenario, there are 917 treatments delivered in 2035. The capacity of a large manufacturing facility is 1200 treatments per year (Appendix 4); hence one manufacturing facility is sufficient to meet demand from 2018 to 2035. This manufacturing facility will be in Stevenage. Indeed, catapult cell and gene therapy have already invested in this site (Catapult cell and gene therapy, 2014). There are issues associated with only having one manufacturing site; if there's unexpected downtime at the manufacturing centre, perhaps due to a power cut, or an unlikely natural disaster such as a flood the supply will be disrupted. With such a crucial, life-saving treatment for patients for whom time is of the essence, any downtime could have disastrous consequence. If the manufacturer wishes to have a second medium-sized manufacturing centre, as backup for the first, it should be located in Yorkshire, in Leeds or Sheffield. This extra site would have an assumed capital cost of £50 million and extra operating costs. A cost-benefit analysis of an extra site should be performed by the manufacturing company. They can truly estimate the value of a back-up centre, as well as their capital and operating expenses.

The transportation of choice for distribution to each Advanced Therapy Treatment Centre (ATTC) is dictated by the distance from the Stevenage Manufacturing Facility to the ATTC. (FreightHub, 2018) states that for journeys of a distance below 150 miles, a road courier is typically cheaper, whilst for journeys beyond this threshold, rail will be the cheaper option. Therefore, road distribution will be used for the London and Birmingham therapy centres, and rail will be used to deliver to and from the Manchester and Newcastle therapy centres. Figure 5 indicates this in a visual format. A backup site in Yorkshire would be within driving distance of Newcastle, Manchester and Birmingham. (Appendix 5). This 150 mile criteria is an industry rule of thumb for standard freight. However, the CAR T freight is non-standard; it must be cryopreserved to maintain its quality. Further investigation could be done into whether this distance threshold is the same for the more expensive cryogenic transportation required.

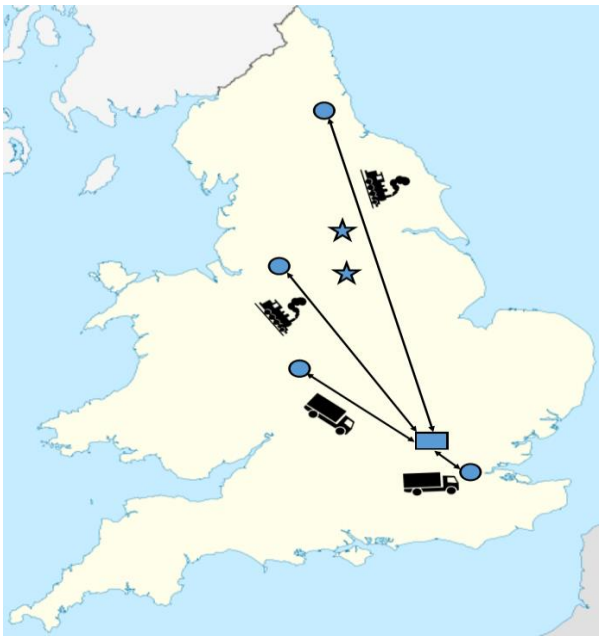

Figure 5 Visual Representation of the transport network between the ATTCs (circles) and the centralised manufacturing centre (box). The stars indicate potentials sites for new manufacturing centres.

Within the optimisation model, there is a time constraint, K_1, with the value of the constraint arbitrary, and to be selected at the discretion of the manufacturer. The value of this constant may be to set such that the company meets NHS targets, such as the target to treat patients within 31 days of diagnosis (Cancer Research Uk, 2015), or such that the company

provides a competitive service. The total time is made up of time for leukapheresis and administration (of the order hours), time for transportation (of the order of hours) and the time for manufacture (of the order of days). Therefore, the largest marginal gains on competitors with respect to time of therapy delivery can be achieved within the manufacturing time.

Currently, the black box nature of the manufacturing setup does not allow for better scheduling. Treatments are all manufactured together, and the time taken is dictated by the treatment that takes the longest to produce. One treatment could be ready whilst another is still expanding. In the future, the sample that is ready could be removed, and then the process to produce a new therapy activated, whilst the slower expanding sample is still being produced. An optimisation problem for the scheduling of manufacturing could be produced. More would have to be known about how the characteristics of the starting material such as T cell concentration and volume impact the manufacturing time.

Conclusion

Autologous CAR-T cell therapy is a promising treatment for patients affected by B cell malignancies which includes a number of blood cancers. Due to the success of several clinical trials, two treatments have been approved by the FDA in the US. There is potential for a scale up in the UK. Several challenges need to be addressed with regards to the supply chain to facilitate this scale up. A qualitative assessment of the supply chain identified possible bottlenecks and challenges. These can be summarised as: needle-to-needle traceability, high manufacturing and transport costs, variable quality of raw materials, 'black box' manufacture, future supply of optimal vectors and regulation standards.

The current and future demand for the treatment in the UK was estimated. It was found that one manufacturing centre would be enough to meet demand. A model was formulated to optimise the choice on transport mode to reduce transportation costs.

Possible solutions to optimise the supply chain were proposed. A COP would help to integrate every stakeholder in the supply chain and ensure needle-to-needle traceability. Lymphodepletion pre-treatment of the patient can be used to augment the function of the T cells once they are transferred back to the patient.

In summary, demand for the treatment will increase mainly due to a growing population. In order for the supply chain to meet this demand, the issues outlined throughout the report will have to be addressed before a scale up can be achieved in the UK.

Future Works

There are studies being conducted to improve the effectiveness of CAR T cells when faced with solid cancers. The hope is to use a combination of antigens in a pool of CAR T cells to treat the solid cancer. Preliminary results have been published but more trials with larger sample sizes need to be carried out.

Using a therapy that targets a number of antigens may also help with patients who have suffered negative relapse following CD-19 infusions. CAR T cell therapy targeting a number of antigens has been shown to prevent CD-19 relapses (National Cancer Institute, 2018). Although early reports are promising, these trials are still in the preclinical stage.

One of the most exciting developments for CAR T cell therapy is the use of universal CAR T cells, manufactured from healthy patients. The treatment has been tested in stage I trials and even two infants who suffered from ALL (Qasim et al, 2017). Universal CAR T cells have the potential of revolutionising the supply chain by solving some of the challenges with a potential scale up. It would simplify the supply chain by removing the need for a 1-to-1 model as the product could be mass manufactured and used to treat patients. Manufacturers would essentially produce off-the-shelf CAR T cells.

There are further options being researched to improve the potency of the cells and reduce their toxicity. these include improving the transduction process or using nanotechnology to produce the cells inside the patient. All of these techniques may help simplify the lengthy manufacturing process and hence streamline the supply chain. It is important that further research is carried out to achieve the above. For example, changing from the current black-box process to a more open one would help to continuously produce the final product which would speed up production time. If this was done, manufacturers could propose and solve an optimisation model into the scheduling of the manufacturing process. Manufacturers may be able to benefit from improved economies of scale and reduce the cost of the therapy.

Acknowledgments

We thank Dr Maria Papathanasiou for her generous support and guidance.

References

1. Almasbak, H. et al (2016). *CAR T Cell Therapy: A Game Changer in Cancer Treatment*. [online] NCBI. Available at: https://www.ncbi.nlm.nih.gov/pmc/articles/PMC4889848/ [Accessed 11 Dec. 2018].
2. Almasbak, H. et al (2016). *CAR T Cell Therapy: A Game Changer in Cancer Treatment*. [online] NCBI. Available at: https://www.ncbi.nlm.nih.gov/pmc/articles/PMC4889848/ [Accessed 11 Dec. 2018].
3. Bloodwise (2018). *Latest statistics released on number of blood cancer cases in England*. [online] Bloodwise. Available at: https://bloodwise.org.uk/community/blood-cancer-diagnosis-statistics-england-2016 [Accessed 16 Oct. 2018].
4. Brown, H., et al. (2014). Measuring up? The health of NHS Cancer Serrvices. Cancer research UK
5. Burns et al, (2016). Burns, R., Leal, J., Sullivan, R. and Luengo-Fernandez, R. (2016). Economic burden of malignant blood disorders across Europe: a population-based cost analysis. *The Lancet Haematology*, 3(8), pp.e362-e370.
6. Cancer Research UK. (2015).
    a. *Cancer Incidence Statistics.* [online] Available at: https://www.cancerresearchuk.org/health-professional/cancer-statistics/incidence [Accessed 10 Nov. 2018].)
    b. *Cancer Mortality Statistics* . [online] Available at: https://www.cancerresearchuk.org/health-professional/cancer-statistics/mortality [Accessed 10 Nov. 2018].)
    c. Cancer Research (2015). [online] Cancerresearchuk.org. Available at: https://www.cancerresearchuk.org/sites/default/files/cs_report_cwt.pdf [Accessed 29 Nov. 2018].
7. Catapult cell and gene therapy, 2014 Ct.catapult.org.uk. (2014). *Cell Therapy Catapult to create manufacturing centre in Stevenage*. [online] Available at: https://ct.catapult.org.uk/news-media/manufacturing-news/celltherapy-catapult-create-cell-therapy-manufacturing-site-stevenage [Accessed 22 Nov. 2018].
8. FDA Cancer Drug Announcement Creates Critical Role For Engineers. (2018). *AABME*. [online] Available at: https://aabme.asme.org/posts/fda-announcement-on-cancer-drug-creates-critical-role-for-engineers
9. Freighthub.com. (2018). [online] Available at: https://freighthub.com/en/blog/modes-transportation-explained-best/ [Accessed 1 Dec. 2018].
10. Ft.com. (2018). *Gilead dispels doubts with Car-T cancer drug trial results | Financial Times*. [online] Available at: https://www.ft.com/content/6220d244-dc6e-11e7-a039-c64b1c09b482 [Accessed 12 Dec. 2018].
11. Gill, S. (2015). Chimeric antigen receptor T cell therapy: 25 years in the making. *Blood review*. [online] Available at: http://dx.doi.org/10.1016/j.blre.2015.10.003 [Accessed 12 Dec. 2018].
12. GOV.UK. (2018). *Innovate UK*. [online] Available at: https://www.gov.uk/government/organisations/innovate-uk [Accessed 12 Dec. 2018].
13. Herbert, S. (2017). Understanding the Critical Impact of Logistics on Scale-Up & Commercialization. *Cell and Gene Therapy Insights*, 3(8), pp.655-662.
14. Kaiser, A. et al (2015). *Towards a commercial process for the manufacture of genetically modified T cells for therapy*. Cancer Gene Therapy.
15. Kenderian, S., Porter, D. and Gill, S. (2017). Chimeric Antigen Receptor T Cells and Hematopoietic Cell Transplantation: How Not to Put the CART Before the Horse. *Biology of Blood*
16. Levine, B., Miskin, J., Wonnacott, K. and Keir, C. (2017). Global Manufacturing of CAR T Cell Therapy. *Molecular Therapy - Methods & Clinical Development*, 4, pp.92-101.Liu, B., Song, Y. and Liu, D. (2017). Clinical trials of CAR-T cells in China. *Journal of Hematology & Oncology*, 10(1), p.2.
17. Mather, M. (2016). *Fact Sheet: Aging in the United States – Population Reference Bureau*. [online] Prb.org. Available at: https://www.prb.org/aging-unitedstates-fact-sheet/ [Accessed 1 Dec. 2018].
18. Maude, S., et al. (2018). Tisagenlecleucel in Children and Young Adults with B-Cell Lymphoblastic Leukemia. *New England Journal of Medicine*, 378(5), pp.439-448.
19. National Cancer Institute (2018). *CAR T Cells: Engineering Patients' Immune Cells to Treat Their Cancer*. [online] National Cancer Institute. Available at: https://www.cancer.gov/about-cancer/treatment/research/car-t-cells [Accessed 11 Dec. 2018].
20. National Cancer Institute Network, 2014 National Cancer Intelligence Network, PHE, (2014) Trends in incidence and outcome for haematological cancers in England
21. NHS England, 2018
    a. NHS statistics, f. (2018). *NHS stats, statistics, funding*. [online] Nhsconfed.org. Available at: https://www.nhsconfed.org/resources/key-statistics-on-the-nhs [Accessed 18 Nov. 2018]
    b. England, NHS. (2013). *NHS England » Programme budgeting*. [online] England.nhs.uk. Available at: https://www.england.nhs.uk/prog-budgeting/ [Accessed 11 Nov. 2018].

c. England, NHS. (2018). *NHS England » First children with cancer to begin treatment with revolutionary CAR-T therapy*. [online] England.nhs.uk. Available at: https://www.england.nhs.uk/2018/11/first-children-with-cancer-to-begin-treatment-with-revolutionary-car-t-therapy/ [Accessed 16 Nov. 2018].
d. England, NHS. (2018). *NHS England » NHS England strikes deal for ground breaking cancer treatment in a new European first*. [online] England.nhs.uk. Available at: https://www.england.nhs.uk/2018/10/nhs-england-strikes-deal-for-ground-breaking-cancer-treatment-in-a-new-european-first/ [Accessed 16 Nov. 2018].

22. Porwollik, S. (2018). *GMP-in-a-box – the future in cell therapy production? - Sampling Science®*. [online] Sampling Science®. Available at: http://www.biocision.com/blog/12819/gmp-in-a-box-cell-therapy-production [Accessed 12 Dec. 2018].
23. Qasim et al, (2018). Molecular remission of infant B-ALL after infusion of universal TALEN gene-edited CAR T cells,
24. Smittenaar, C., Petersen, K., Stewart, K. and Moitt, N. (2016). Cancer incidence and mortality projections in the UK until 2035. *British Journal of Cancer*, [online] 115(9), pp.1147-1155. Available at: https://www.ncbi.nlm.nih.gov/pmc/articles/PMC5117795/ [Accessed 11 Nov. 2018].
25. The Office for National Statistics, 2016, *UK population Estimates and projections, 1951 to 2041*
26. US Census Bureau. (2017). *Annual Estimates of the Resident Population in the United States, Regions, States and Puerto Rico.*[online]
27. Wei Teng, C., Foley, L., O'Neill, P. and Hicks, C. (2014). An analysis of supply chain strategies in the regenerative medicine industry—Implications for future development. *International Journal of Production Economics*, 149, pp.211-225.
28. Wei Teng, C., Foley, L., O'Neill, P. and Hicks, C. (2013). An analysis of supply chain strategies in the regenerative medicine industry—Implications for future development. *International Journal of Production Economics*, 149, pp.211-225.
29. Zhang, C., Liu, J., Zhong, J. and Zhang, X. (2017). Engineering CAR-T cells. *Biomarker Research*, 5(1).

Mathematical Modelling to Investigate Systemic Plasma and Intracellular Area Under the Curve of Chemotherapy Drugs for Cancer Treatment

Anisha Harris, Beth Hassan
Department of Chemical Engineering, Imperial College London, U.K.

Abstract

Delivery of chemotherapy drugs is a complex process, one that is continually trying to be understood. This study investigates conventional free drug delivery and Thermo-sensitive liposome (TSL) enhanced drug delivery. A multi-compartmental model describing drug transport through pharmacokinetics was employed to simulate intravascular release of the drug. Two indicators were used in the analysis: intracellular Area Under the Curve (AUC) and systemic plasma AUC. The former was used to infer the drug efficacy while the latter represents the level of toxicity healthy body cells are exposed to. The model allowed for comparison of the efficacy of doxorubicin (DOX), paclitaxel and fluorouracil as un-encapsulated drugs. TSL-DOX delivery was investigated with the heating regime and sensitivity analysis explored in depth. Paclitaxel was determined to be the un-encapsulated drug with the highest efficacy, this was attributed to its high Michaelis Menten transmembrane transport parameter K_i. Considering the TSL-DOX delivery, bolus injection with 3h continuous heating was deemed optimal. Sensitivity analysis of the key parameters showed those linked to TSL formulation to be highly sensitive. The analysis found an optimised drug release rate at 42°C exists, and that Thermodox® achieves this at a value of $0.30s^{-1}$. Further recommendations related to TSL formulation include minimising both release rate at 37°C and liposome plasma clearance rate.

Key Words: Doxorubicin, Fluorouracil, Paclitaxel, Area Under the Curve, Thermosensitive Liposome

Introduction

Cancer is the second most common cause of death worldwide [1]. With the number of cancer cases having been steadily growing with predications that this will continue [2,3]. While anticancer drugs are consistently being advanced and developed, their therapeutic efficacy remains underwhelming at a clinical level. Their effectiveness depends on the interplay between the tumour's biological properties, the drug's physiochemical properties and the biophysical and biochemical aspects of drug transport and cellular uptake. Understanding drug transport in solid tumours is fundamental for effective cancer treatment. Computational modelling offers a cost-effective method to improve cancer treatment; it enables the variation of many parameters which enables discovery of key factors for the optimal design of efficient drug delivery systems.

Doxorubicin (DOX) is the most widely used and tested anticancer drug available, however its cardiotoxicity limits the lifetime dose a patient may receive per unit body surface area to around 450-550 mg/m^3[4,5]. Consequently, to improve the therapeutic benefit and reduce the toxicity of DOX in normal tissue, new drug administration methods must be developed. Most other anticancer drugs (e.g. paclitaxel (PTX)) have no maximum lifetime dosage, only a maximum dosage per administration. The maximum tolerated dose of PTX given by 24h infusion every three weeks is 175-200 mg/m^2 [6]. Fluorouracil (5-FU) doses are usually around 50mg/ml, however different doses and schedules result in dramatically different patterns of qualitative toxicity. Normally dosing is based on body surface area however with 5-FU this gives considerable variability. It is therefore difficult to estimate the average dose administered [7,8].

An innovative treatment is the use of nanoparticles, such as liposomes as drug carriers. This treatment significantly reduces the limitations of conventional chemotherapy drug treatment. It offers a high drug payload, decreased drug toxicity and enhanced drug accumulation at tumour sites due to the relatively leaky tumour vasculature [9]. It also allows for an increase in the bioavailability of hydrophobic drugs such as DOX, PTX or 5-FU and can improve drug absorption [10]. DOX is the most commonly investigated liposomal-encapsulated anticancer drug and, as of 1995, the first to be FDA-approved [11]. Other drugs such as PTX being used more recently in clinical trials [12].

El-Kareh and Secomb used mathematical models to find that non-thermosensitive liposomes approach the efficacy of continuous infusion of un-encapsulated DOX only if they release drugs at optimal rates [13]. This supports the prioritisation of thermosensitive liposomes (TSL), suggested for the first time by Yatvin et al. in 1978, as a superior treatment method [14]. Encapsulating anti-cancer drugs inside temperature-sensitive nanoparticles allows accurate release of the drug, when heated, to the target area. This is because the liposomes become unstable at higher temperatures, and open up to release the drug. At body temperature, the release rate of the drug from the TSL is very low, minimising the damage to healthy cells around the body. Focused ultrasound is often used to provide localised heating within the tumour, thus resulting in a more targeted treatment compared to conventional free drug treatment. Hyperthermia (HT) is simple to implement as well as having a low cost and reduced risk of complication, making it a notable area of research for cancer treatment [15]. Additionally, heating increases the tumour vasculature permeability which enhances the transport and accumulation of drug within the interstitial space. TSLs can effectively treat cancer and diminish serious side effects resulting from the toxicity of anticancer drugs by reducing the drug concentration in the blood plasma.

Numerous review papers exist which focus on the use of TSLs for treating cancer [9,16,17] and several

studies investigate the development of TSLs to improve the efficacy of anti-cancer treatment [18-20]. While DOX is most widely research, there has been recent work into the use of TSLs with other anticancer drugs has been done [20-22]. One study, conducted by Zhang et al, investigated the efficacy of TSLs carrying PTX. They found that PTX-TSL combined with HT significantly suppressed tumour growth due to the increased targeting efficiency. The results from rodent trials showed PTX-TSL combined with HT has potential as a new therapy method for solid tumours [23].

Mathematical models have been developed to determine if liposome-encapsulated drugs improve the effectiveness of cancer treatment. Zhan and Xu developed a comprehensive mathematical model for thermosensitive liposomal delivery of doxorubicin to solid tumour, incorporating the key physical and biochemical processes involved. They compared predicted efficacies of continuous direct intravenous administration and thermosensitive liposome-mediated delivery. They determined that thermosensitive liposome-mediated delivery offers a lower drug concentration in normal tissues than direct infusion of non-encapsulated DOX, as well as finding that thermosensitive liposome delivery achieves a significantly higher peak intracellular concentration [24]. El-Kareh and Secomb predicted that continuous infusion with optimal infusion duration (typically, 1-3 hours) is superior to bolus injection and non-thermosensitive liposomal delivery for DOX. They also found that TSLs combined with hypothermia have a potential advantage over continuous infusion for some doses, but only if the blood is not heated significantly while passing through the area where hypothermia is applied. However, their model did not account for the influence of blood and lymphatic vessels and the interstitial fluid flow, nor drug binding with proteins [13]. Storm et al. concluded that both liposome encapsulation and slow drug delivery by infusion offer considerable protection against DOX's cardiotoxicity while enabling its antitumor activity to be fully expressed [25]. Sensitivity analysis carried out on TSL with DOX determines which input parameters have the greatest influence under pulse and continuous HT exposure [26].

This study seeks to advance understanding of the input parameters, which may vary depending on the heating regime implemented. This analysis relies on mathematical modelling of a compartmental system. The study compares the efficacy of three widely used anticancer drugs: DOX, PTX and 5-FU under different administration methods, something that has not previously been thoroughly undertaken. DOX as the drug with the most available parameters regarding TSL formulations, is studied further. The benefits of TSL encapsulation is investigated, after doses which are comparable to that of free drug have been determined. The heating regimes are studied as a major factor affecting TSL success. Finally, sensitivity analysis is performed to determine the most sensitive parameters and how drug delivery can be enhanced. Area Under the Curve (AUC) is used to analyse all results, which improves upon the use of peak intracellular concentration, which is most commonly used in literature; this is discussed using the results.

Method

A multi-compartmental model (*Figure 1*) is adopted to describe the transport of liposomes and un-encapsulated drug following intravenous injection. The model is divided into the systemic plasma, lumped tissue, and the tumour, with the tumour being subdivided into the tumour plasma, the tumour interstitium (Extravascular Extracellular space (EES)) and the intracellular space. The model describes a rigid, cylindrical blood vessel surrounded by the solid tumour interstitium. Tumour vasculature is heterogeneous; however, the focus of this study is the transport around individual blood vessels. Thus, an idealised tumour cord geometry is sufficient.

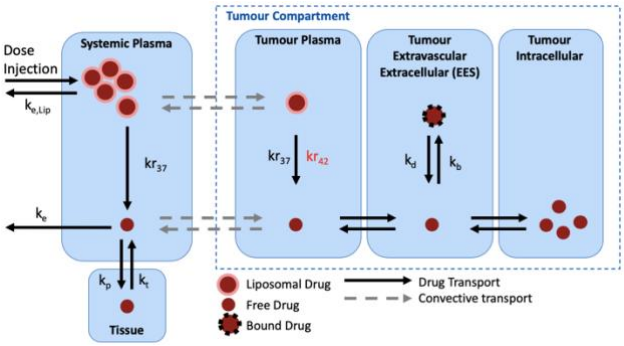

Figure 1: Schematic outlining the compartments of the mathematical model for TSL-enhanced drug delivery. Adapted from Liu and Xu [26]

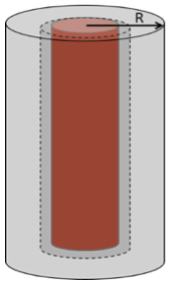

Figure 2: Schematic of tumour cord geometry

The model is reduced to a one-dimensional model, with drug transport occurring in the radial direction only (*Figure 2*), using the assumptions of axis-symmetry and homogeneous distribution in the tumour. For simplicity, blood is assumed to be an incompressible Newtonian fluid and steady. The model includes basic description of blood flow, drug transport between the compartments and cellular uptake. Transport of the drug through the interstitium is through convection and diffusion. Despite diffusion being generally less effective than convection, it is the dominant transport mode in this system. This is due to the elevated interstitial pressure within the tumour, limiting convection to regions close to the blood vessel wall. As a result, here convection is assumed to be negligible. The transvascular Peclet number is used to evaluate the importance of convection, with relevant papers confirming negligible effect on results when ignoring convection [27]. Peclet number is defined as the ratio of convective transport to diffusive transport and calculated as follows: $Pe = \frac{Lu_i}{D}$, where L is the tumour radius, D is the drug diffusivity and u_i is the interstitial fluid flow velocity.

This study compares the two drug administration techniques which can be adopted: bolus injection or continuous infusion. For delivering un-encapsulated drug, it enters the body through the blood vessel. With TSLs, the model simulates intravascular release of the drug, meaning the drug is released in the plasma. When the tumour is exposed to localised HT, this is predominantly in the tumour plasma. HT enhances the release kinetics of the drug from the TSL, accelerating the process. HT exposure

is instantaneous and assumed to occur simultaneously with dose administration. Temperature is said to be uniform and independent of radial position due to the homogeneous assumption. For this reason, the simulation of heat transfer is not reflected.

Free drug is then available to be transported into the extravascular space to be taken up by the tumour cells. Due to the low permeability of the TSLs and the nature of intravascular release, it is assumed that transvascular transport of TSLs from the tumour plasma into the EES is negligible. There will be some TSLs found in the EES, however in comparison to TSL concentration in the systemic and tumour plasma, this amount will be insignificant.

Equations in the Model

Drug transport in the model is described by pharmacokinetics. The equations outlined below describe the drug concentration in each compartment, as well as TSL concentration in the systemic and tumour plasma and the bound drug in the EES. Table 1 outlines the concentration nomenclature and the associated units, while Table 2 prescribes the volume of the key compartments.

Table 1: Concentration nomenclature for each compartment

Variable	Symbol	Unit
Concentration of TSL in systemic plasma	$c^B_{p_Lip}$	$\mu g/ml$
Concentration of free drug in systemic plasma	c^B_p	$\mu g/ml$
Concentration of free drug in the tissue	c^B_t	$\mu g/ml$
Concentration of TSL in tumour plasma	$c^T_{p_Lip}$	$\mu g/ml$
Concentration of free drug in tumour plasma	c^T_p	$\mu g/ml$
Concentration of free drug in EES	c_e	$ng/10^5\ cells$
Concentration of bound drug in EES	c^T_b	$ng/10^5\ cells$
Concentration of free drug in intracellular space	c_i	$ng/10^5\ cells$

Table 2: Volume nomenclature for each compartment

Variable	Symbol	Unit
Volume of systemic plasma	V^B_p	L
Volume of tumour plasma	V^T_p	L
Volume of body tissue	V^B_t	L
Volume of tumour	V^T	L

Pharmacokinetics within the systemic plasma and tissue compartment

Equation 1 describes the pharmacokinetics of TSL in the systemic plasma, following continuous infusion of the drug with dose D, for time T_d. To model bolus injection T_d was set to 10s. The Heaviside term $H(T_d - t)$ models a constant infusion of TSL from time $t = 0$ to T_d.

$$V^B_p \frac{dc^B_{p_Lip}}{dt} = \frac{D}{T_d} H(T_d - t) - k_{e_{Lip}} c^B_{p_Lip} V^B_p - kr_{37} c^B_{p_Lip} V^B_p + F^T_{PV} V^T_P c^T_{p_Lip} - F^T_{PV} V^T_P c^B_{p_Lip} \quad (1)$$

TSL is removed from the systemic plasma at rate $k_{e_{Lip}}$, while kr_{37} is the rate constant associated with the first order kinetics release of drug due to the instability of TSL, at body temperature. The terms consisting of F^T_{PV} reflect convective transport between the systemic plasma and tumour plasma, it is a function of the blood perfusion rate (w_{blood}) and defined as plasma flow per tumour plasma volume.

The pharmacokinetics of the free drug in the systemic plasma is described in a similar manner, as shown in Equation 2. The drug is cleared from this compartment via the body at rate k_e, while $k_p$and k_t are bidirectional linear kinetics describing the transport of free drug between the systemic plasma and body tissue.

$$V^B_p \frac{dc^B_p}{dt} = F^T_{PV} V^T_P c^T_p - F^T_{PV} V^T_P c^B_p + kr_{37} c^B_{p_{Lip}} V^B_p - k_e c^B_p V^B_p - k_p c^B_p V^B_p + k_t c^B_t V^B_t \quad (2)$$

Equation 3 describes the concentration of free drug in the tissue compartment.

$$V^B_t \frac{dc^B_t}{dt} = k_p c^B_p V^B_p - k_t c^B_t V^B_t \quad (3)$$

Pharmacokinetics within the tumour plasma

TSL in the tumour plasma is described by Equation 4. R denotes the release rate of drug from the TSL and is either kr_{37} or kr_{42}, depending on whether the tumour is subjected to HT.

$$V^T_p \frac{dc^T_{p_Lip}}{dt} = F^T_{PV} V^T_P c^B_{p_Lip} - F^T_{PV} V^T_P c^T_{p_{Lip}} - R c^T_{p_{Lip}} V^T_p \quad (4)$$

Again, free drug in the tumour plasma is modelled in a similar way, shown in Equation 5 with an additional term reflecting diffusion of the free drug through the interstitium. The term $PS(c^T_p - c^T_e)$ describes the diffusive flux across the interface of the tumour plasma and EES by the product of vascular permeability and vascular surface area (PS) and the free drug concentration difference between the tumour plasma and EES.

$$V^T_p \frac{dc^T_p}{dt} = F^T_{PV} V^T_P c^B_p - F^T_{PV} V^T_P c^T_p + R c^T_{p_{Lip}} V^T_p - V^T PS\left(c^T_p - c^T_e\right) \quad (5)$$

Pharmacokinetics within the Extravascular Extracellular Space (EES)

TSL concentration in the tumour EES is assumed to be negligible. Once in the EES, free drug can enter the intracellular space, or bind to proteins within the interstitium. Free drug in the EES is described by Equation 6.

$$\frac{dc^T_e}{dt} = D\nabla^2 c_e - \frac{V_{max} c_e}{c_e + K_e v^T_e} + \frac{V_{max} c_i}{c_i + K_i} + K_{1ci} c_e + R c_{e_{Lip}} - k_b c^T_e + k_d c^T_b \quad (6)$$

Cellular uptake of the drug is reflected in the model by two mechanics:

(i) Active transport is described by Michaelis Menten kinetics (K_i and K_e) which describe the transmembrane transport, and V_{max}, which describes the flux between the EES and the intracellular space
(ii) Passive diffusive transport (K_{1ci})

Equation 7 describes the concentration of bound and unbound drug within the EES. The binding rate is described by k_b while the disassociation rate is described by k_d. The notion of bound and unbound drug is vital and disregarding it can overestimate the efficacy of anti-cancer drugs.

$$\frac{dc_b^T}{dt} = k_b c_e^T - k_d c_b^T \quad (7)$$

Pharmacokinetics within the intracellular space

The transport of drug from the EES into the intracellular space is described above and is predominately influenced by the Michaelis Menten transport kinetics. Equation 8 shows the intracellular concentration.

$$\frac{dc_i}{dt} = \frac{v_{max} c_e}{c_e + K_e v_e^T} - \frac{v_{max} c_i}{c_i + K_i} + k_{1ci} c_e \quad (8)$$

Boundary Conditions

The differential equations outlined are solved in MATLAB using the ODE15s function (code available in Supplementary Material) by subjecting the set of equations to the boundary conditions outlined. Equation 9 describes a no-flux condition at the outer boundary of the tumour cord model. The blood vessel wall is subjected to a boundary condition describing the transmural flux normal to the vessel wall, described by Kedem-Katchalsky equation (Equation 10). It describes an inwards flux of drug into the tumour interstitium, which involves product of vascular permeability, P and free drug concentration difference between the tumour plasma and EES.

$$-D\nabla c_e + u_i c_e \underline{n_i} = 0 \quad (9)$$

$$J_S = P\left(c_p^T - c_e\right) + J_F(1 - \sigma_F)\Delta c_{lm} \ldots \Delta c_{lm} \quad (10)$$

J_F is the transmural velocity, normal to the vessel wall and can be calculated through Starling's law, in Equation 11. P_v and P_i are the blood vessel and tumour interstitium pressures, σ_d is the osmotic reflection coefficient, π_v and π_i are the osmotic pressures in the vascular and interstitial space respectively, while L_p is the vascular hydraulic conductivity. Equation 12 is a reduced version of Equation 11, valid because of the negligible effect of osmotic pressure difference in solid tumours.

$$J_F = L_p\left(P_v - P_i - \sigma_d(\pi_v - \pi_i)\right) \quad (11)$$

$$J_F = L_p(P_v - P_i) \quad (12)$$

Model Parameters

This study compares three common anti-cancer drugs: DOX, PTX and 5-FU using a 50mg dose. Values for the drug parameters are given in the supplementary information in Table A1. DOX is a widely studied drug, allowing values to be easily found based on many previous similar computational studies. When investigating the effects of introducing TSL, only DOX was considered due to the lack of available data for either PTX or 5-FU paired with TSL. $DPPG_2$-TSL was the TSL formulation investigated, with parameters outlined in Table A2 of the supplementary information. Formulation of TSLs change the release rates (kr_{42} and kr_{37}) and liposome pharmacokinetic parameters, namely the liposome plasma clearance rate ($k_{e_{Lip}}$), so not having experimental data on this for the PTX and 5-FU would make their analysis unreliable. In addition, model parameters which vary with temperature were estimated using the relationship developed by Zhan to predict diffusivity and permeability of the drugs and liposomes at 42°C [28]. The release kinetics and pharmacokinetics of TSL drug carriers vary significantly according to their composition. The baseline values for release kinetics at the temperatures investigated are given in the supplementary information. It is noted that release rates of up to $0.3s^{-1}$ have been reported in Thermodox® [29], which is approximately 30 times larger than the baseline value used.

The tumour modelled has a diameter of 120 μm and the diameter of the blood vessel is 10 μm [30]. Further, since tumour vasculature is heterogenous, there is a lack of blood perfusion to the tumour tissue, which is accounted for in this model through the term H_{ctt}.

Drug Efficacy

Area under the curve (AUC) for intracellular concentration was used to determine the efficacy of the drug at killing tumour cells. In mathematical terms, the AUC is the integral of the drug concentration over time, as such, AUC is a more accurate measure of drug efficacy than peak cellular concentration as it accounts for all the drug accumulated in the tumour cell. Additionally, the systemic plasma AUC was determined, it indicates the level of toxicity that healthy body cells are exposed to, thus a low value is desirable. For AUC to be used reliably for comparisons, the time frame in which the drug is studied must be kept constant. This study uses 10h to measure AUC. The use of AUC instead of peak intracellular concentration is tested and validated through this study.

$$Killing\ Fraction = 1 - \exp\left(\sigma c_i^{peak}(r)\right) \quad (13)$$

Killing fraction was also used to consider the efficacy of the drug as a function of the tumour radius. Equation 13 shows killing fraction to be a function of the peak intracellular concentration, which is easily determined as a function of the tumour radius, and σ is a value determined by experimental data. For DOX σ is 0.4938[31].

Local sensitivity analysis was performed on all key parameters by imposing a 10% increase, in turn, and measuring the change in intracellular AUC. This allowed for the model's robustness to be tested and can highlight how accurately the physics of the process is modelled. Also, by highlighting favourable properties, it provides motivation for future research.

Results

Un-encapsulated Drug Comparison

Firstly, Table 3 shows that 1h continuous infusion is the superior drug administration method when considering intracellular AUC, for all three drugs However, it is noteworthy that when considering peak intracellular concentration, bolus injection is preferable for DOX. This confirms the decision to adopt AUC as the measure of drug efficacy, over peak intracellular concentration. Table 3 indicates PTX to be the most effective un-encapsulated drug, with the highest intracellular AUC, while 5-FU is the least efficient due to a much higher systemic plasma AUC than the other drugs.

Table 3: *Intracellular and systemic plasma AUC and peak intracellular concentration achieved for DOX, PTX and 5-FU following both bolus injection and 1h infusion*

	DOX		PTX		5-FU	
Drug Administration	Bolus	1h Infusion	Bolus	1h Infusion	Bolus	1h Infusion
Plasma AUC (µg.h/ml)	2.63	2.59	3.46	3.45	4.27	4.26
AUC (ng.h/10^5 cells)	0.96	1.39	3.93	4.83	2.18	2.99
Peak Ci (ng/10^5 cells)	1.31	1.04	2.03	2.27	1.21	1.90

Figure 3 shows the spatial distribution of each drug through the radius of the tumour. Intuitively, as the radius increases (i.e. further away from the blood vessel), the killing fraction decreases, thus the drug is most effective close to the plasma. Interestingly, the killing fraction of 5-FU rarely alters throughout the tumour radius, unlike with DOX and PTX which both see a drop in killing fraction as distance from the plasma increases.

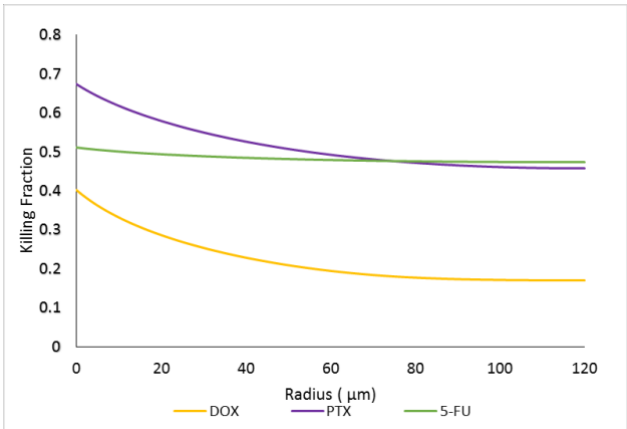

Figure 3: *Killing fraction for DOX, PTX and 5-FU as a function of the tumour radius*

TSL-DOX

With the incorporation of TSL to encompass the drug for more effective transport and delivery, this study moves forward with TSL-DOX. Due to findings in literature both bolus and continuous infusion were explored[31]. For TSLs to work, the body must be subjected to HT. There are many heating regimes possible, and considerable research has been done on which ones work best, with limited success due to a multitude of factors affecting the optimal regime. This paper compares two heating regimes: 3h continuous heating and 1h pulse heating.

There are limits to the maximum safe dose of free drug which can be bypassed by encapsulating the drug, allowing less of the toxic drug to be in the blood and areas of the body without tumour. It is difficult to determine the payload due to the TSL composition depending heavily on how it is formed. Therefore, to make free drug and TSL comparable, the dose in which the AUCs were equal was found to make further comparisons of the efficacy of TSL over free drug – these are found in Table 4.

Table 4: *Comparison of key AUC values and peak concentration for un-encapsulated drug delivery and TSL-enhanced delivery*

	Dose (mg)	c_i^{peak} (ng/10^5 cells)	$c_p^{B,peak}$ (µg/ml)	Systemic Plasma AUC (µg.h/ml)	Intracellular AUC (ng.h/10^5 cells)
Un-encapsulated DOX	50	1.31	15.88	2.63	0.96
1h Pulse TSL	124	0.96	0.27	0.33	0.96
3h Continuous TSL	87	0.67	0.19	0.41	0.96

The dose of TSL required for the AUC's to be equal is higher than that of un-encapsulated drug. This is to be expected as the dose of TSL must account for the drug and liposome carrier.

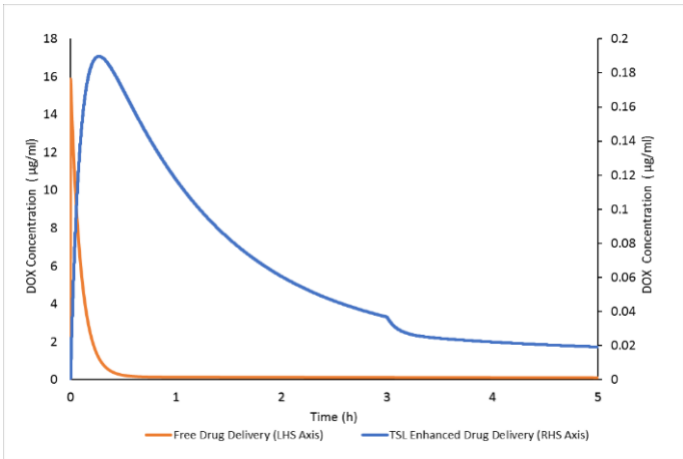

Figure 4: *Graph showing DOX concentration in the systemic plasma, following bolus injection and 3h heating of TSL-DOX (RHS) and bolus injection of un-encapsulated DOX (LHS)*

The dose value for 3h continuous heating was used going forward as it is 1.4 times lower than pulse heating, and additional study was done on continuous heating. For the peak intracellular concentration of free drug and TSL to be equal, a dose of 174mg is required. This further solidifies the decision to use AUC throughout this study as the dose required to achieve the same AUC as free drug is much lower than for peak intracellular concentrations to be equal.

With the selected doses, the results in terms of AUC and intracellular concentration are comparable, thus the area of interest is the systemic plasma concentration. One of the main reasons for using TSLs is to minimise the drug concentration in the systemic plasma, where risk of toxicity and death of healthy cells is high and should be avoided. As seen in *Figure 4* this is achieved. When

comparing TSL-DOX using bolus injection with 3h heating, with un-encapsulated DOX delivery, the systemic plasma AUC reduced by a factor of 6.5 and $c_p^{B,peak}$ concentration reduced by a factor of 83.6.

Administration Regime: Continuous Heating

The heating regime of un-encapsulated DOX and TSL-DOX was investigated to determine the optimum heating duration for patients. Bolus injection with instant HT exposure from 0-8h was tested to determine the effect on intracellular AUC, shown in *Figure 5*. Un-encapsulated DOX showed only a 0.2% change from no heating to 8h of heating. TSL-DOX begins to plateau around 3h of heating with increase in AUC from 3 to 8h heating only being 5%. Using the baseline parameter data, changing the heating time from 0.5 to 8h had no effect on c_i^{peak} - only changes seen with heating for c_i^{peak} were in the first 0.5h.

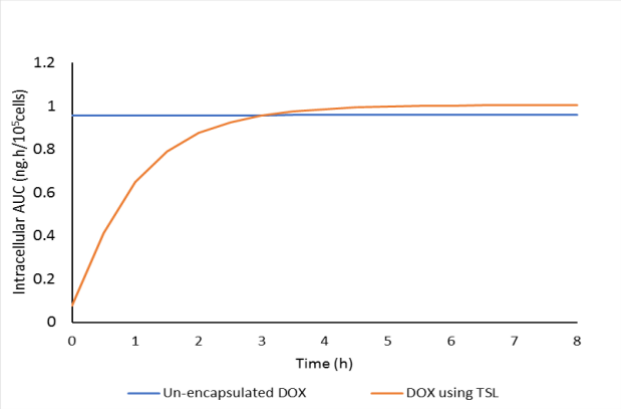

Figure 5: *Effects of different heating periods on intracellular AUC in both conventional free-drug delivery and TSL enhanced drug delivery*

Administration Regime: Pulse Heating

Pulse heating was tested to determine if multiple pulses of heat is beneficial over continuous heating. This was done for bolus injection and different continuous drug infusion times. The total heating time in each case was kept the same, with different regimes of pulse heating with rests compared to continuous heating. Continuous heating was better for bolus injection and infusion times shorter than the total heating time. However, for long infusion times, heating for a short period, with rest and then heating for a longer period was slightly beneficial to continuous heating.

Sensitivity Analysis

The output of interest for the sensitivity analysis was intracellular AUC. First, all parameters were subjected to a 10% increase to determine the most sensitive parameters – some of these were then further explored. The sensitivity of parameters was conducted for both pulse and continuous (with and without infusion time) heating, and *Figure 6* shows that except for $k_{e_{Lip}}$, the level of sensitivity of the parameters under different heating regimes is largely the same. Generally, parameters related to the TSL properties and vascular parameters (w_{blood} and PS) are highly sensitive, while the pharmacokinetic parameters of the drug are minimally impactful.

The key findings from *Figure 6* are given below:

- The most sensitive parameter for all regimes was K_i followed by K_e, the Michaelis Menten parameters
- Increasing kr_{42} significantly increases the intracellular AUC, which is most dominant under continuous heating, due to longer HT exposure time
- Increasing $k_{e_{Lip}}$ reduces the intracellular AUC, with a stronger impact felt under continuous heating. Other clearance kinetics, k_p and k_e compete with drug transport into the tumour cells, having a negative impact on intracellular AUC – the effect of these is far less influential.
- Increasing w_{blood} reduces the intracellular AUC
- Increasing PS negatively affects the intracellular AUC
- Increasing kr_{37} increases the intracellular AUC; however, this is undesirable as the systemic plasma AUC increases to enable this
- Diffusivity of DOX is shown to have no tangible impact on intracellular AUC
- Increasing the permeability and diffusivity of the liposome makes little difference, due to these values being insignificant in magnitude in the first place
- Binding and dissociation parameters (k_b and k_d) do not appear to make an impact on intracellular AUC

Figure 7 shows the intracellular AUC to vary non-linearly with kr_{42} and begin to plateau at a release rate one for $DPPG_2$-TSL, at a value of 0.29 s^{-1}. *Figure 8* shows the effects of the Michaelis Menten transport parameters, $k_{e_{Lip}}$ and PS on intracellular AUC relative to their baseline value following bolus injection and 3h continuous heating. It is shown that a change in value of both K_e and K_i drastically alters the efficacy of the drug. Decreasing the value of $k_{e_{Lip}}$ has the potential to increase the efficacy of the drug, due to the extended circulation time. Finally, the graph shows that increasing the value of PS decreases the intracellular AUC.

Discussion

Un-encapsulated Drug Comparison

The finding that 1h continuous infusion is superior to bolus injection for the drug administration of free drug agrees with the findings made by El-Kareh and Secomb [13]. However, Eikenberry found that the optimum infusion time depends on the drug dose, with bolus injection being best for low-doses but short infusion being better for high doses [31]. It was because of these conflicting findings that show the preferred method depends on many variables, both drug administration methods. were explored when introducing TSL as a drug carrier.

The high efficacy of PTX is initially surprising when considering the molecular weight and diffusivity of the drugs. PTX is the largest drug thus drug transport limitations due to poor diffusion could be anticipated. The high performance can be attributed to the transmembrane transport between the extracellular and intracellular space, modelled through Michaelis Menten kinetics. As shown in the sensitivity analysis, increasing K_i can significantly increase the intracellular AUC – for PTX Ki is 5 times DOX and 50 times 5-FU reference for K_i values [31,32], thus the strong Michaelis Menten kinetics of PTX counteract its poor diffusivity.

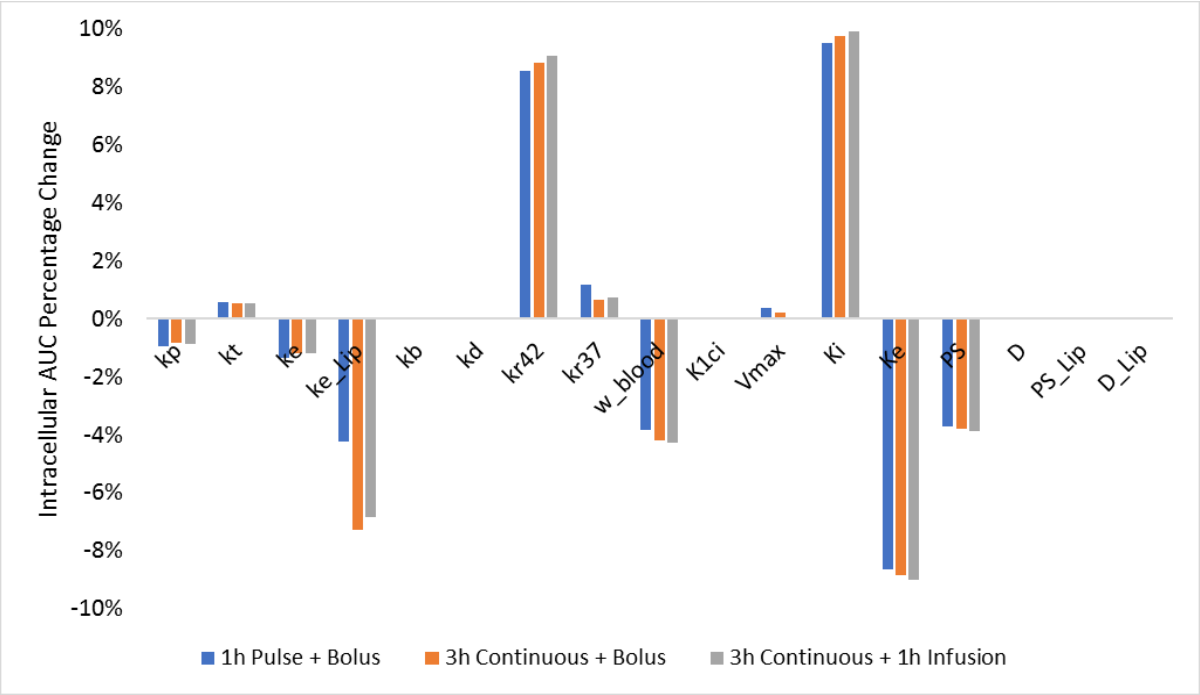

Figure 6: *Graph showing percentage change in intracellular AUC corresponding to a 10% increase in the key model parameters, for different heating and administration methods. This graph highlights to most sensitive parameters and allows for recommendations to be made on the preferred magnitude of such parameters*

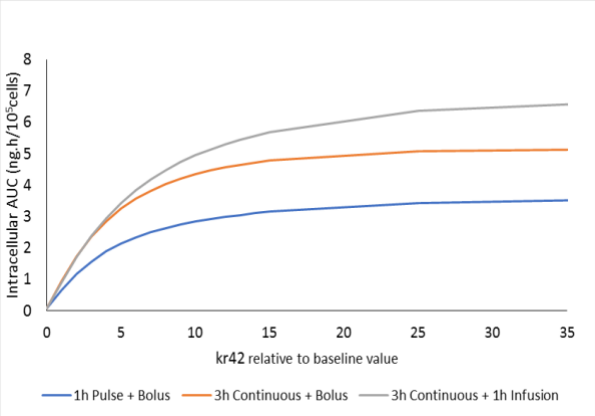

Figure 7: *Graph showing the non-linear relationship of kr42 and intracellular AUC, for different heating and administration methods relative to baseline values*

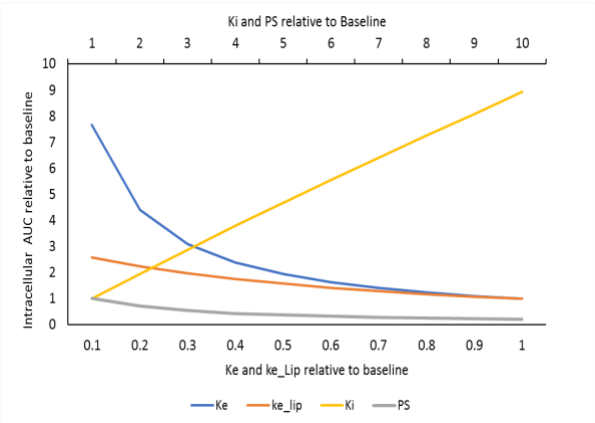

Figure 8: *Graph showing the effects changing Ki, Ke, ke_Lip and PS on intracellular AUC, following bolus injection and 3h continuous heating relative to baseline values. AUC increases with increasing Ki and increases with decreasing Ke, ke_Lip and PS*

The effect of diffusivity can be seen more clearly in *Figure 3*. As stated, the killing fraction of 5-FU remains roughly constant through-out the tumour radius. In the model, this is attributed to the diffusivity of the drugs, the value for 5-FU is an order of 10 larger than both DOX and PTX, meaning 5-FU can diffuse more effectively through the EES, with a high quantity reaching the outer boundary. This was confirmed by decreasing the diffusivity of 5-FU by a factor of 10, which saw the killing fraction reduce to 0.25 at approximately 80µm. It is expected that a decrease in killing would occur as drug transport becomes hindered further from the blood vessel, due to mechanisms such as the binding of drug with proteins, or clearance rates competing with the diffusion of the drug through the interstitium. Interestingly, diffusivity of DOX was shown to be insensitive, agreeing with the findings of Cong Liu [27]. This is because diffusivity is not only related to the physiological properties of anticancer cells but also the structure of the tumour tissues.

Considering the systemic plasma AUC, 5-FU is the least desirable anti-cancer drug, as its high AUC value reflects a higher toxicity level for the body than with either DOX or PTX. Additionally, it must be taken into consideration that 5-FU may not have been modelled well using the model due to its sensitivity to many parameters and short half-life meaning continuous high doses of 5-FU are needed to maintain concentrations high enough to be effective [33,34]. Given the findings for systemic plasma AUC for 5-FU using a relatively small dose, this is likely to severely increase toxicity to the body. Encapsulation of this drug could allow the higher doses to be safely administered for over longer time periods, however,

with limited parameters for TSL with 5-FU, this could not be further investigated reliably in this paper.

Comparison of Un-encapsulated DOX and TSL-DOX

When comparing un-encapsulated DOX with TSL-DOX using doses that result in similar intracellular AUC, it was shown that the use of TSL dramatically reduces both the $c_p^{B,peak}$ and the systemic plasma AUC. This is because the TSL releases the majority of drug in the tumour plasma under HT exposure. The only drug found in the systemic plasma is that released at 37°C through much slower release kinetics, this is unlike when the un-encapsulated drug has to itself travel through the systemic plasma to get to the tumour cells via the tumour plasma. The findings show that the use of TSL-enhanced drug delivery can significantly reduce the level of toxicity the body is exposed to. This lessens the restrictions on drug dosage, which are predominantly set in line with toxicity. In animal models, ThermoDox®, a TSL-DOX formulation, currently in clinical trials, has shown to deliver 25 times more DOX into tumours than intravenous infusion of DOX alone, and 5 times more DOX than standard liposomal formulations of the drug [12,35].

Heating Regime

With the introduction of TSLs, heating regimes need to be determined. This is challenging as changing one variable can drastically alter the efficacy of the drug under a regime that had previously been deemed effective. In general, a longer heating time is better, this is because there is a longer time-frame in which the drug can be released from the TSL in the tumour plasma.

The minor effect seen when applying heat to un-encapsulated DOX was due to not all temperature dependent parameters being expressed in the model, namely the complex vasculature changes of the tumour interstitium due to heating are not entirely accounted for thus the effects caused by heating were not fully expressed. There has been a lot of research showing the improvement offered by HT to conventional chemotherapy treatment [36-38]. Some of the reasons for the improved therapeutic efficacy when using HT is increased blood flow and vasculature permeability, which are critical factors for drug uptake [39]. This increase in tumour permeability, increases the accumulation of drug in the tumour. The improvement when using HT could be something to explore further.

Pulse heating with periods of rest is determined to be unbeneficial for treatment, and only particularly useful for long infusion times or when limits for continuous heating exist. Kong et al. found that tumours reheated after an 8h interval did not respond to HT again, and no HT-induced nanoparticle extraversion was seen [40]. It was not determined how long the rest period had to be for the reheating to render ineffective. Additionally, the model used in this study did not account for this per say but agrees with the findings that leaving time in between heating periods is generally not beneficial.

Overall, 3h continuous heating was deemed to be the optimal heating regime for TSL-DOX studied. As shown in *Figure 5,* providing extra heating past this point gave little benefit relative to the additional heating and resources required, similar results were noted by Liu and Xu [26]. Most of the drug had already been released after 3h of heating so there was a limit reached as to how much drug was left to be released, a higher dose of TSL could continue to improve heating past the point of 3h.

Sensitivity Analysis

The sensitivity analysis conducted on TSL-DOX displayed in *Figure 6* largely agrees with the findings made by Liu and Xu [26], who conducted sensitivity analysis for both a continuous and pulse heating regime, with respect to peak intracellular concentration. This suggests that the effects of the parameters on peak intracellular concentration and intracellular AUC are highly similar. This is to be expected as both assess the quantity of drug in the intracellular space, however intracellular AUC is preferable as it is considering the amount of drug in the intracellular space over a time period as opposed to at one instance.

As stated, the TSL properties and vascular parameters showed significant sensitivity. The former is promising, as the properties of the TSL depend in part on its composition and formulation, thus it is possible that the desired value of such properties can be worked towards when designing new TSL-drug formulations.

Figure 6 showed increasing $k_{e_{Lip}}$ is detrimental to the intracellular AUC, this is because it reduces the available time for the drug to be released into the tumour plasma, before the TSL gets removed from the blood. Thus, it is desirable that the TSL formulation used has a low systemic plasma clearance rate. This parameter has a far smaller impact on the intracellular AUC under pulse heating than continuous heating, this is because in this case the increased circulation time of the TSL is counterbalanced by a limited heating period. This further suggests continuous heating is the superior heating regime for effective drug delivery using TSL with DOX.

The higher intracellular AUC yielded through increasing kr_{37} is at detriment to the systemic plasma AUC, which sees a 4% increase. This is because kr_{37} reflects the release kinetics of the drug from the TSL at body temperature, thus the amount of un-encapsulated drug in the systemic plasma significantly increases. This would have a negative effect as it would increase the amount of toxic drug in the body causing harm to healthy cells, which is one of the major benefits of TSL. Thus, kr_{37} should be kept as low as possible.

In contrast, *Figure 7* shows increasing kr_{42} dramatically increase the efficacy of DOX. The plateau suggests an optimal value of kr_{42} exists. This should

be considered when exploring TSL formulation and composition when used with other drugs. The plateau is shown to occur at approximately 30 times the baseline value of kr_{42} used in this study and corresponds closely to the ultra-fast kinetics reported for Thermodox® ($0.3s^{-1}$). This shows great promise for Thermodox® once it is fully approved for clinical use. However, at $0.3s^{-1}$, continuous infusion yields higher AUC than through bolus injection – thus for TSL with a high kr_{42}, the preferred administration method may change.

Considering the vascular parameters, two are of interest: w_{blood} and PS. The negative influence on intracellular AUC through increasing the blood perfusion rate is due to a reduced time for DOX to transport from the blood into the tumour, through convection. The highest perfusion rates in the body are seen in the brain, kidney, liver, and heart, making drug transport and corresponding efficacy to tumours in these regions lower [41,42].

It is expected that an increase in permeability would increase the amount of drug capable of reaching the intracellular space as transport mechanisms become enhanced, this was shown by Liu and Xu [26]. However, increasing the permeability allows more fluid to leak into the tumour interstitium from the blood vessels, resulting in a build-up of fluid such that the interstitial pressure increases to a point where it is approximately equal, or higher than the blood vessel pressure. This can stop the drug from filtering into the interstitium and cause some of the drug particles to re-enter the vessels. Thus, at high PS levels, this model strongly shows the effects of reverse diffusion and can account for the reduced intracellular AUC.

Beyond the TSL properties, it is the Michaelis Menten kinetics which exhibit significant sensitivity. It is important to examine the effects of these parameters for two reasons:

(i) It is an assumption, and one that is difficult to prove

(ii) The parameters are not well documented

Ideally, the kinetics would be such that K_i is large and K_e is small – this is the case with PTX and was attributed to the high efficacy of the conventional free drug delivery of PTX. Therefore, it is highly likely that with the suitable TSL, PTX would perform very well, making it a potential promising future exploration. Due to the lack of documented kinetic information on TSL use for drugs other than DOX, this postulation was unable to be tested.

Finally, as mentioned, binding of the drug to proteins in the EES was modelled. Bound drug is unable to transport into the intracellular space, thus increasing the binding rate reduces the amount of available drug. As shown in

Figure 7, increasing the binding rate (k_b) by 10% made no tangible impact on the intracellular AUC. Previous papers have neglected to consider binding [13]. While this seems acceptable it is still important to consider binding in some capacity, especially due to the rate differing depending on the drug used.

Additional Limitations

As discussed previously, drug transport within the tumour interstitium was modelled through diffusion only. The assumption of negligible convection was verified through calculating the Peclet number for un-encapsulated DOX delivery to be 0.35, calculation below:

$$Pe = \frac{Lu_i}{D} = \frac{1.2 \cdot 10^{-4} m \times 1 \cdot 10^{-6} m/s}{3.4 \cdot 10^{-10} m^2/s} = 0.35$$

The model assumes negligible TSL concentration in the tumour EES due to simulating intravascular release – however there will be some found in the EES. Due to the larger size of TSL and corresponding low diffusivity, convection becomes more prevalent in TSL transport within the tumour. Through addition of an equation to describe the pharmacokinetics of TSL in the EES, the EES AUC of TSL was found to be 0.001μg/ml. This value is sufficiently low to justify the neglection of convection. However, in exploration of TSL-PTX formulations, it is likely convection would have to be considered due to the larger size of PTX and subsequent larger size of the TSL.

Finally, despite proving both intracellular and systemic plasma AUC to be a better measure of drug efficacy than peak intracellular concentration, it does have its limitation. There needs to be a certain concentration of drug in the tumour cell to kill the cell so not all area equivalates to cell killing [43].

Conclusion

This study investigated the efficacy of cancer drugs using intracellular and systemic plasma AUC, finding this to be insightful when compared to measuring peak intracellular concentration. It was found that PTX performs best in conventional free drug delivery, considering its intracellular AUC. Taking into consideration plasma AUC, 5-FU is least favourable as the body would experience high toxicity levels. PTX's strong performance was mainly due to the Michaelis Menten kinetic parameters, which give promise to the use of PTX encapsulated in TSL in the future. The use of TSL with DOX succeeded in reducing the systemic plasma concentration of DOX, thus significantly reducing the toxicity and damage to healthy cells. As a result, the use of TSL can relax the dose limits of drugs which are largely set because of the toxicity to healthy cells. Continuous heating of 3h was found to be the optimum heating time for TSL-DOX. Sensitivity analysis found the most sensitive parameters were K_i, K_e, kr_{42}, $k_{e_{Lip}}$ and PS. After further analysis, the kr_{42}, and $k_{e_{Lip}}$ were found to be significant parameters which could be optimised through composition of TSL and their formulation, by minimising $k_{e_{Lip}}$ and optimising kr_{42}. Future work would involve global sensitivity analysis, such as the Morris Method to provide a better understanding of the key parameters, as some

parameters may behave differently in different points of the parameter space. Morris Method allows for non-linear interactions between parameters and can show the change in output result of varying more than one parameter at a time. This would allow more realistic conclusions for optimisation of drug delivery to be found and allow the effect of heating to be further understood in conjunction with the parameter's sensitivity.

References

[1] World Health Organisation, Cancer, https://www.who.int/news-room/fact-sheets/detail/cancer (2018).
[2] U.K. Cancer Research, Cancer incidence for all cancers combined, https://www.cancerresearchuk.org/health-professional/cancer-statistics/incidence (2018).
[3] International Agency for Research on Cancer, Cancer Tomorrow, https://gco.iarc.fr/tomorrow/home (2018).
[4] J.D. Floyd, D.T. Nguyen, R.L. Lobins, Q. Bashir, D.C. Doll, M.C. Perry, Cardiotoxicity of Cancer Therapy, JCO. 23 (2005) 7685-7696.
[5] S.M. Swain, F.S. Whaley, M.S. Ewer, Congestive heart failure in patients treated with doxorubicin, Cancer. 97 (2003) 2869-2879.
[6] E.A. Perez, Paclitaxel in Breast Cancer, The Oncologist. 3 (1998) 373-389.
[7] J.S. Macdonald, Toxicity of 5-Fluorouracil, Oncology. 13 (1999).
[8] M.W. Saif, A. Choma, S.J. Salamone, E. Chu, Pharmacokinetically Guided Dose Adjustment of 5-Fluorouracil: A Rational Approach to Improving Therapeutic Outcomes, Journal of the National Cancer Institute. 101 (2009) 1543-1552.
[9] G. Koning, A. Eggermont, L. Lindner, T. Hagen, Hyperthermia and thermosensitive liposomes for improved delivery of chemotherapeutic drugs to solid tumors, Pharmaceutical Research. 27 (2010) 1750-1754.
[10] A.M. Rahman, S.W. Yusuf, M.S. Ewer, Anthracycline-induced cardiotoxicity and the cardiac-sparing effect of liposomal formulation, International journal of nanomedicine. 2 (2007) 567-583.
[11] Y. Barenholz, Doxil® — The first FDA-approved nano-drug: Lessons learned, Journal of Controlled Release. 160 (2012) 117-134.
[12] U. Bulbake, S. Doppalapudi, N. Kommineni, W. Khan, Liposomal Formulations in Clinical Use: An Updated Review, Pharmaceutics. 9 (2017) 12.
[13] A.W. El-Kareh, T.W. Secomb, A Mathematical Model for Comparison of Bolus Injection, Continuous Infusion, and Liposomal Delivery of Doxorubicin to Tumor Cells, Neoplasia. 2 (2000) 325-338.
[14] M.B. Yatvin, J.N. Weinstein, W.H. Dennis, R. Blumenthal, Design of liposomes for enhanced local release of drugs by hyperthermia, Science. 202 (1978) 1290-1293.
[15] D. Su, R. Ma, M. Salloum, L. Zhu, Multi-scale study of nanoparticle transport and deposition in tissues during an injection process, Med Biol Eng Comput. 48 (2010) 853-863.
[16] T. Ta, T.M. Porter, Thermosensitive liposomes for localized delivery and triggered release of chemotherapy, Journal of Controlled Release. 169 (2013) 112-125.
[17] B. Kneidl, M. Peller, G. Winter, L.H. Lindner, M. Hossann, Thermosensitive liposomal drug delivery systems: state of the art review, International journal of nanomedicine. 9 (2014) 4387-4398.
[18] M.H. Gaber, N.Z. Wu, K. Hong, S.K. Huang, M.W. Dewhirst, D. Papahadjopoulos, Thermosensitive liposomes: Extravasation and release of contents in tumor microvascular networks, International Journal of Radiation Oncology Biology Physics. 36 (1996) 1177-1187
[19] Y. Zou, M. Yamagishi, I. Horikoshi, M. Ueno, X. Gu, R. Perez-Soler, Enhanced therapeutic effect against liver W256 carcinosarcoma with temperature-sensitive liposomal adriamycin administered into the hepatic artery, Cancer Research. (1993).
[20] T.P. Chelvi, S.K. Jain, R. Ralhan, Hyperthermia-mediated targeted delivery of thermosensitive liposome-encapsulated melphalan in murine tumors, Oncology research. 7 (1995) 393.
[21] A. Sharma, R.M. Straubinger, Novel taxol formulations: preparation and characterization of taxol-containing liposomes, Pharmaceutical research. 11 (1994) 889-896.
[22] J.P. May, M.J. Ernsting, E. Undzys, S. Li, Thermosensitive liposomes for the delivery of gemcitabine and oxaliplatin to tumors, Molecular pharmaceutics. 10 (2013) 4499-4508.
[23] Z. Wang, H. Zhang, Y. Yang, X. Xie, Y. Yang, Z. Li, Y. Li, W. Gong, F. Yu, Z. Yang, M. Li, X. Mei, Preparation, characterization, and efficacy of thermosensitive liposomes containing paclitaxel, Drug delivery. 23 (2016) 1222-1231.
[24] W. Zhan, X.Y. Xu, A mathematical model for thermosensitive liposomal delivery of Doxorubicin to solid tumour, Journal of drug delivery. 2013 (2013) 172529-13.
[25] G. Storm, Q.G. van Hoesel, G. de Groot, W. Kop, P.A. Steerenberg, F.C. Hillen, A comparative study on the antitumor effect, cardiotoxicity and nephrotoxicity of doxorubicin given as a bolus, continuous infusion or entrapped in liposomes in the Lou/M Wsl rat, Cancer chemotherapy and pharmacology. 24 (1989) 341-348.
[26] C. Liu, X.Y. Xu, A systematic study of temperature sensitive liposomal delivery of doxorubicin using a mathematical model, Computers in Biology and Medicine. 60 (2015) 107-116.
[27] C. Liu, Krishnan, X.Y. Xu, Towards an integrated systems-based modelling framework for drug transport and its effect on tumour cells, Journal of biological engineering. 8 (2014) 3.
[28] W. Zhan, Mathematical Modelling of Drug; Delivery to Solid Tumour, (2014).
[29] D. Needham, J. Park, A.M. Wright, J. Tong, Materials characterization of the low temperature sensitive liposome (LTSL): effects of the lipid composition (lysolipid and DSPE-PEG2000) on the thermal transition and release of doxorubicin, Faraday discussions
[30] M.E. Hubbard, M. Jove, P.M. Loadman, R.M. Phillips, C.J. Twelves, S.W. Smye, Drug delivery in a tumour cord model: a computational simulation, Royal Society open science. 4 (2017) 170014.
[31] S. Eikenberry, A tumor cord model for doxorubicin delivery and dose optimization in solid tumors, Theoretical biology & medical modelling. 6 (2009) 16.
[32] D.Y. Arifin, K.Y.T. Lee, C. Wang, Chemotherapeutic drug transport to brain tumor, Journal of Controlled Release. 137 (2009) 203-210.
[33] J.L. Arias, Novel strategies to improve the anticancer action of 5-fluorouracil by using drug delivery systems, Molecules (Basel, Switzerland). 13 (2008) 2340-2369.
[34] O. Udofot, K. Affram, B. Israel, E. Agyare, Cytotoxicity of 5-fluorouracil-loaded pH-sensitive liposomal nanoparticles in colorectal cancer cell lines, Integrative cancer science and therapeutics. 2 (2015) 245.
[35] Celsion, Thermodox, http://celsion.com/thermodox/ (2016).
[36] M. H. Falk, R. D. Issels, Hyperthermia in oncology, International Journal of Hyperthermia. 17 (2001) 1-18.
[37] J. Zee, Heating the patient: a promising approach? Annals of Oncology. 13 (2002) 1173-1184.
[38] A. Bettaieb, P.K. Wrzal, D.A. Averill-Bates, Hyperthermia: Cancer Treatment and Beyond, Cancer Treatment. (2013).
[39] R.K. Jain, Normalization of Tumor Vasculature: An Emerging Concept in Antiangiogenic Therapy, Science. 307 (2005) 58-62.
[40] G. Kong, R.D. Braun, M.W. Dewhirst, Characterization of the Effect of Hyperthermia on Nanoparticle Extravasation from Tumor Vasculature, Cancer Research. 61 (2001) 3027.
[41] D. Bourne, A First Course in Pharmacokinetics and Biopharmaceutics, , 2017.
[42] R. Nagashima, G. Levy, Effect of Perfusion Rate and Distribution Factors on Drug Elimination Kinetics in a Perfused Organ System, Journal of Pharmaceutical Sciences. 57 (1968) 1991-1993.
[43] A. Rahman, S. Ghosh, R. Pal, Modeling of drug diffusion in a solid tumor leading to tumor cell death, (2018).

Computer-Aided Molecular and Process Design with Superstructure Optimisation of an Organic Rankine Cycle

Tse Puay Lim and Yew Shang Loh

Department of Chemical Engineering, Imperial College London, U.K.

Abstract

Simultaneous optimisation of molecular design and process conditions is highly desirable in the field of research in Organic Rankine Cycles (ORCs), and can be achieved through computer-aided molecular and process design (CAMPD). An outer-approximation algorithm presented by Bowksill et al. (2016) to solve the ORC CAMPD problem is further developed in this study. Two additional safety indices are introduced as feasibility tests to remove toxic and flammable fluids from the feasible region. Superstructure optimisation of fixed working fluids found that topology did not have significant impact on maximum net power, with an average 2% increase when introducing turbine bleeding. However, minimising cost revealed that turbine bleeding significantly increased costs. The basic ORC was found to have the lowest normalised cost in most cases, however for some fluids the addition of a regenerator further decreased cost. The new outer-approximation algorithm was applied to a heat source of 573 K at a flowrate of 66 kg/s, successfully generating a list of top working fluids and identifying novel fluids not found in previous literature in methyl acetate and allyl alcohol.
***Keywords**: computer-aided molecular and process design, feasibility tests, outer-approximation, optimisation, superstructure*

1 Introduction

The performance of a process depends on many factors, including its operating conditions and perhaps more importantly the type of fluids utilised. As these two decisions are closely interlinked, different methodologies have been developed to simultaneously optimise both the process and the molecules. One such approach is computer-aided molecular and process design (CAMPD), a reverse engineering procedure that generates molecules based on target thermodynamic properties and process design parameters (Churi and Achenie, 1996). CAMPD problems are complex to solve due to discontinuities in the feasible region and significant nonlinearities in the structural-property relations.

Two methods to improve the efficiency and robustness of the algorithm were incorporated in this study: implementing feasibility tests to eliminate infeasible molecules in advance, and initialising the search from different starting points.

The CAMPD problem discussed in this study is that of an Organic Rankine Cycle (ORC). Due to higher volatility of organic fluids compared to water, they can be vaporised with lower temperature heat sources such as geothermal heat and biomass combustion.

This study aims to maximise the net power output and minimise the specific investment cost of an ORC system by varying the operating conditions, organic fluids used, and the cycle topology.

2 Literature Review

2.1 CAMPD Problems

Developments in computational modelling have paved the way for computerised molecular design. Gani and Brignole (1983) proposed such a method later known as computer-aided molecular design (CAMD). Further developments integrated process design in tandem with molecular design, allowing for simultaneous optimising of the working fluid and ORC process, otherwise known as CAMPD (Pereira et al., 2011).

Framing CAMPD optimisation requires both continuous and discrete decision variables. Continuous variables usually describe process conditions, such as operating pressures, and flowrates, while discrete variables are used to model cycle topology and the number of functional groups in a working fluid (Gopinath et al., 2016). Because of the MINLP nature of CAMPD,

they are complex to solve, but methods exist such as outer-approximation (OA) (Schilling et al., 2016) and Generalized Benders Decomposition (Geoffrion, 1972) to help break the problem down into simpler sub problems.

Due to the discrete nature in which the working fluid is modelled, thermophysical properties are modelled using group contribution (GC) methods. The ORC process itself is modelled through material, equilibrium, summation, and heat equations with relevant assumptions and constraints (Bowskill et al., 2016).

The simultaneous optimisation of these continuous and discrete variables reduces computational effort significantly as it does not require an exhaustive list of working fluids to be optimised. However, the MINLP is usually very non-convex in nature, and thus a robust algorithm is instrumental in determining the global optimum (Bowskill et al., 2016).

2.2 Optimisation of ORC Systems

ORCs are unique because they are able to extract work from low energy heat sources effectively compared to traditional Steam Rankine Cycles. For example, ORCs can be applied to further extract mechanical and electrical work from the waste heat in existing high temperature heat sources, such as Steam Rankine Cycles in steam power plants and cars (Vanslambrouck et al., 2001). Sustainable energy sources such as geothermal, solar, and biomass generate heat sources between 75°C and 300°C, a suitable temperature range for ORCs to extract work from. However, early ORC designs only managed to achieve thermal efficiencies of approximately 10%, while recent developments have been able to raise thermal efficiency to up to 20% (Darvish et al., 2015). Thus, research in maximising power output and reducing costs of ORCs is highly relevant in the area of sustainable development as it has the potential of combating climate change, reducing carbon emissions and reliance of unsustainable fossil fuels by extracting power from sustainable energy sources.

This paper is primarily an extension to the work by Bowskill et al. (2016) which set up an outer-approximation framework, adding feasibility tests as well as permanent integer cuts to generate candidate lists of optimal working fluids for a basic 4-unit ORC. Related studies that optimise ORCs using different objective functions, molecular design space, topologies, and process conditions are summarised in Table 1. The main two objective functions optimised were maximum net power and minimum specific investment cost (SIC). SIC is the purchasing cost of the equipment required in the cycle, normalised to the net power output of that cycle. With regards to cycle topology, most papers only aimed to optimise a basic ORC, with the exception of White et al. (2018) who considered a regenerative cycle. A study by Sun et al. (2017) suggests that different ORC topologies could have an impact on ORC performance, although optimisation was not explored in these studies. In particular, ORCs that incorporated regenerative cycles and turbine bleeding were identified as possible directions of development.

The lack of research in optimising ORCs of different topologies is an interesting and important knowledge gap as it brings the potential to further improve ORC performance in terms of both net power output as well as lowering normalised cost. This study therefore aims to address this gap by incorporating superstructure optimisation into the optimisation of ORCs.

Table 1: Summary of literature review on ORC optimisation

	Study	**Objective**	**Molecular Design Space**	**Topology & Process Conditions**	**Heating Fluid T_{in}**	**Optimal Molecules**
1	Bowskill et al. (in progress)	Maximise net power	Only linear groups: alkanes, alkenes, ethers, esters, acid, alcohol (SAFT-γ Mie)	Basic ORC P_{cond}, P_{evap}, $\Delta T_{superheat}$, $\dot{m}_{WF}$	483K	n-butane, 1-butene, methyl ethyl ether
2	Schilling et al. (2016)	Maximise net power	Alkanes, alkenes, alkynes, cyclic carbons, ketones, ethers, esters etc. (PC-SAFT)	Basic ORC P_{cond}, P_{evap}, $\Delta T_{superheat}$, $\dot{m}_{WF}$	393K	Propane, propene, dimethyl ether
3	Schilling et al. (2017)	Minimise SIC	Alkanes, alkenes, aryl carbons, aldehyde (PC-SAFT)	Basic ORC $P_{r,cond}$, $P_{r,evap}$, $\Delta T_{superheat}$, $\dot{m}_{WF}$, n_{turb}	423K	Propane, propene, 1-butene
4	Kleef et al. (2018)	Minimise SIC	Alkanes, alkenes (SAFT-γ Mie)	Basic ORC T_{cond}, $P_{r,evap}$, z, $\Delta T_{min,evap}$, v_{evap}, v_{cond}	423K 523K	Propane, isobutane 2-butene, 2-pentene
5	White et al. (2018)	Minimise SIC	Linear alkanes, methyl alkanes, linear alkenes; includes binary mixtures (SAFT-γ Mie)	Basic & Regenerative ORC T_{cond}, $P_{r,evap}$, z, PP_h, y_{regen}	423K 523K 623K	Isoheptane 2-pentene 2-heptene

3 Methodology

3.1 Problem Formulation

Two problems were formulated on gPROMS ModelBuilder 5.1.1, with objective functions to maximise net power and minimise SIC respectively. Apart from the different objectives, the decision variables, model equations and constraints for both problems were exactly the same.

3.1.1 Decision Variables

Three types of decision variables were implemented in the optimisation problem: non-negative integer variables that determine molecular structure, binary variables that represent the cycle topology, and continuous variables for the process operating conditions. A total of 12 acyclic structural groups were used to build the molecule, as shown in Table 2.

Table 2: Structural groups used

Alkanes	Alkenes	Ethers	Others
CH_3 CH_2 CH C	$=CH_2$ =CH =C	CH_3-O CH_2-O	CH_2OH COOH COO

Two binary variables were formulated to represent the four topologies considered in this study: basic ORC, regenerative ORC, ORC with turbine bleeding, and regenerative ORC with turbine bleeding. The superstructure of the ORC system is illustrated in Figure 1. Variable y_1 was used to represent the presence of the regenerator, while variable y_2 was used to represent the presence of turbine bleeding.

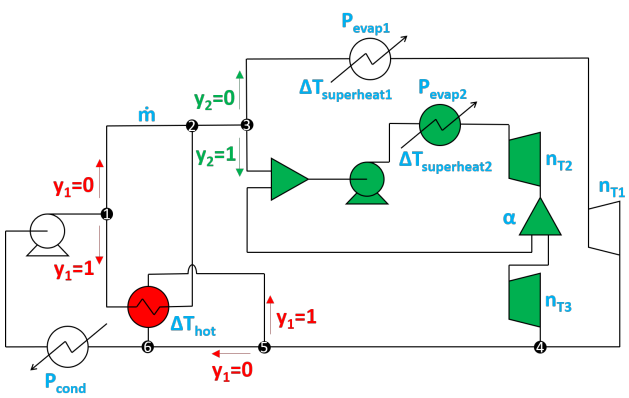

Figure 1: ORC system superstructure

The eight continuous variables included were: $\dot{m}$, P_{cond}, $P_{evap,1}$, $P_{evap,2}$, $\Delta T_{superheat,1}$, $\Delta T_{superheat,2}$, $\Delta T_{hot,regen}$, and α. Three additional integer variables, n_{T1}, n_{T2} and n_{T3}, were also added to optimise the number of stages of each turbine.

3.1.2 Model Equations

Each piece of equipment in the ORC was modelled as a single unit on gPROMS ModelBuilder. The heat exchangers – condenser, evaporators and regenerator – were assumed to have zero heat loss to surroundings, so all the energy lost by the hot streams was transferred to the cold streams. Note that the working fluid was allowed to be superheated in the evaporators, but the outlet of the condenser was fixed as a saturated liquid. The energy balances for the heat exchanges were written in the form:

$$\dot{Q} = \dot{m}c_p(T_{out} - T_{in}) \quad (1)$$

$$= \dot{m}(h_{out} - h_{in}) \quad (2)$$

The power output of each piece of rotating equipment – pumps and turbines – was calculated using:

$$\dot{W} = \dot{m}(h_{in} - h_{out}) \quad (3)$$

Although not modelled in gPROMS ModelBuilder, a generator with efficiency η_{gen} was assumed to be present. The net power output of the ORC system was thus computed by:

$$\dot{W}_{net} = \eta_{gen} \sum \dot{W} \quad (4)$$

Costing of the equipment was also performed, using correlations from Schilling et al. (2016). SIC is defined as:

$$SIC = \frac{TCI}{\dot{W}_{net}} \quad (5)$$

where TCI, the Total Capital Investment, is calculated as the sum of the capital costs of the heat exchangers and rotating equipment. The heat exchangers were modelled as shell and tube heat exchangers with streams in counter flow, and their costs were hence dependent on the heat exchange areas. The costs of the rotating equipment were determined using correlations from Astolfi et al. (2011). Pump cost is a function of pump power, generator cost is a function of net power, while turbine cost is a function of the number of turbine stages. Therefore the number of turbine stages, n_{T1}, n_{T2} and n_{T3}, had to be considered as additional degrees of freedom in the MINLP problem.

3.1.3 Molecular Property Predictions

Thermodynamic properties are most commonly predicted either using the PC-SAFT or SAFT-γ-Mie equations of state. Both equations of state rely on GC methods, where all segments of a molecule are assigned a partial contribution, and the thermodynamic property of the resulting molecule is computed by summing up all contributions.

The PC-SAFT model uses hard chains as reference fluids by including a dispersion term that accounts for dispersive interactions between chains. The model uses a square well potential to model pair potential between segments. In comparison, SAFT-γ-Mie is the more recent development, where fused spherical segments are used to represent different functional groups in a molecule. In this model, the Mie pair potential is a generalised form of the Lennard-Jones potential.

The SAFT-γ Mie equation of state was chosen in this work due to its accurate prediction of caloric properties (Dufal et al., 2015). Specific heat capacities, specific entropies, specific enthalpies and dew point temperatures of each stream were predicted using this method.

The critical point of each molecule was calculated indirectly using the SAFT-γ Mie method. Pressure was increased gradually up to the point at which vapour volume was equal to liquid volume. The temperature and pressure at this point was recorded as the critical point.

Due to limitations of the SAFT-γ Mie approach, melting points were predicted using another GC approach developed by Hukkerikar et al. (2012):

$$\exp\left(\frac{T_m}{T_{m0}}\right) = \sum_i n_i a_i \tag{6}$$

The autoignition temperature (AIT) was computed using a GC method presented by Albahri et al. (2003):

$$AIT = 729.7 + 24.9\sum_i n_i AIT_i - 1.57\sum_i (n_i AIT_i)^2 - 0.0773\sum_i (n_i AIT_i)^3 + 0.0032\sum_i (n_i AIT_i)^4 \tag{7}$$

Finally, the acute toxicity (LC_{50}) was determined using the Martin et al. (2001) GC method:

$$-\log(LC_{50}) = \sum_i n_i \alpha_i \tag{8}$$

3.1.4 Constraints

Three categories of constraints were implemented in gPROMS ModelBuilder: constraints on temperatures and pressures, constraints for molecular feasibility, as well as specific constraints for turbine design.

Pressures at every state were enforced to be between atmospheric pressure and 80% of the critical pressure.

$$10^5 \leq P \leq 0.8\ P_{crit} \tag{9}$$

Temperatures at the inlet and outlet of the heat exchangers were constrained by a minimum approach temperature, ΔT_{min} of 10K from the temperatures of the cooling and heating fluids respectively. For instance, the pinch point constraint at the inlet of the condenser was implemented as:

$$\Delta T_{cond,1} = T_{wf,in} - T_{cf,out} \geq 10 \tag{10}$$

Molecular feasibility constraints were also added to ensure that the solution molecule is feasible in terms of bonding (Odele et al., 1993 and Bowskill et al., 2016).

$$\sum_i n_i(2-\nu_i) - 2 = 0 \tag{11}$$

$$n_{=CH} + n_{=CH_2} + n_{=C} = 2Z^+ \tag{12}$$

$$n_{eO} \leq n_{CH_3} \tag{13}$$

$$n_{eO} \leq 2 \tag{14}$$

$$n_{eO} \leq 2n_{CH_2} + 3n_{CH} + 4n_C \tag{15}$$

$$n_{cO} \leq 0.96(n_{CH_2} + n_{CH} + n_C) \tag{16}$$

To prevent combinatorial explosion, an upper bound was set for the total number of groups in each molecule. The upper bound was chosen to be 10 as preliminary testing revealed that molecules containing more than 10 structural groups were too involatile to be used in the ORC system.

Lastly, two design constraints were added for each turbine to avoid high mechanical stresses, high Mach numbers and large blade heights (Astolfi et al., 2014).

$$V_{is,st}^{ratio} = (V_{is,turb}^{ratio})^{\frac{1}{n_{st}}} \leq 4 \tag{17}$$

$$\Delta h_{is,st} = \frac{\Delta h_{is,turb}}{n_{st}} \leq 65 \tag{18}$$

3.2 Proposed Algorithm

The algorithm used in this paper is a further modification to the outer-approximation framework used in Bowskill et al. (2016) and is outlined in Figure 2. The algorithm begins with a starting guess of an arbitrary molecule. The algorithm only attempts to optimise the fluid if it passes the feasibility tests implemented, thus eliminating computational effort for infeasible fluids.

3.2.1 Feasibility Tests

In total, 4 feasibility tests were implemented. Test 1 checks the melting point and saturation pressures of the fluid, while Test 2 further tightens the pressure bounds. Tests 3 and 4 are new additions to the algorithm, introducing 2 new safety indices in AIT and LC_{50} respectively. The safety thresholds were adapted from Schilling et al. (2017) and are detailed below:

$$AIT \geq T_{upper} + 30 \quad \text{(K)} \tag{19}$$

$$LC_{50} \geq 10 \quad \text{(mg/L)} \tag{20}$$

3.2.2 Primal Problem Initialisation Procedure

Once a feasible fluid has been found, the problem is initialised so that feasible starting conditions are passed to the primal problem. This allows for easier evaluation of the NLP primal problem and ensures that the the starting point of the solver is within the expected solution range.

3.2.3 Solving the Primal Problem

In a typical outer-approximation algorithm, the MINLP is broken down into an NLP problem (primal problem) and an MILP problem (master problem). The primal problem typically finds the optimum value of the objective function and the corresponding optima for the continuous variables, given a fixed working fluid. However, due to the inclusion of superstructure optimisation in this work, the primal problem is optimised over two additional binary variables, y_1 and y_2. The solution of the primal problem thus includes the objective function, the optimal continuous variables, and the optimal cycle topology (represented by y_1 and y_2).

3.2.4 Solving the Master Problem

Once the primal problem is solved, gradients of the objective function and constraints are calculated at the solution point of the primal problem and are passed to Gurobi via C++, which solves the master problem in the form of an MILP and generates a new working fluid. The MINLP is solved when the solutions to the master and primal problems converge after multiple iterations, arriving at the optimal fluid choice and corresponding process conditions as well as cycle topology.

3.2.5 Candidate List Generation

To increase the number of solutions found by the algorithm, a permanent integer cut is then applied to remove the previous optimal solution from the feasible region so that the algorithm can search for a new optimal working fluid. The list of all optimal working fluids found is reported and compiled as a candidate list. New initial guesses can then be trialled to reinitialise the problem and observe the frequency at which the optimal working fluids appear in the candidate list.

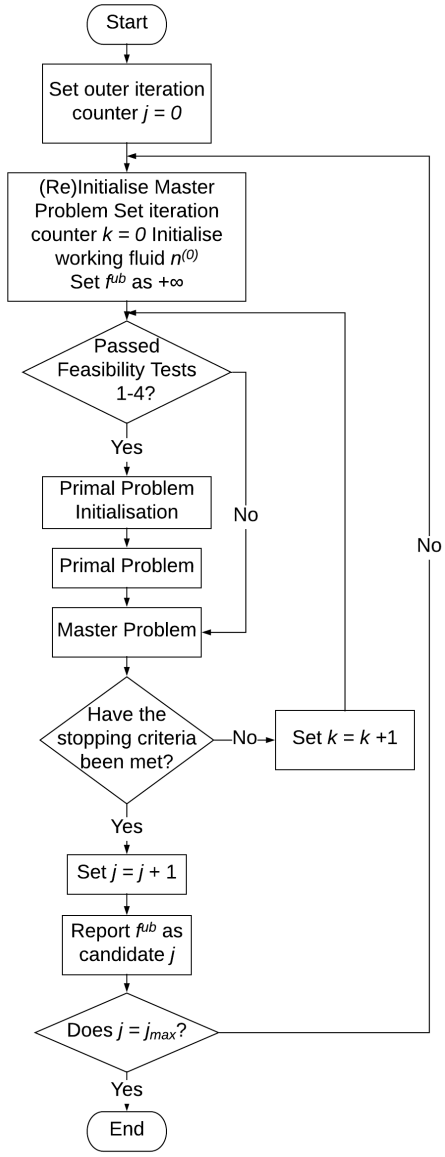

Figure 2: Overview of outer-approximation algorithm

3.3 Thermodynamic Model Validation

The thermodynamic predictions by SAFT-γ Mie were compared with experimental data extracted from Detherm, a database containing experimental thermophysical properties. Predictions using PC-SAFT were also generated for reference.

As shown in Figure 3, the saturation properties of neopentane predicted by SAFT-γ Mie were in good

agreement with the actual properties. On the other hand, PC-SAFT overpredicts the saturation pressure. SAFT-γ Mie also showed outstanding agreement with experimental data for three other organic fluids trialed – 1-butene, diethyl ether, and pentane.

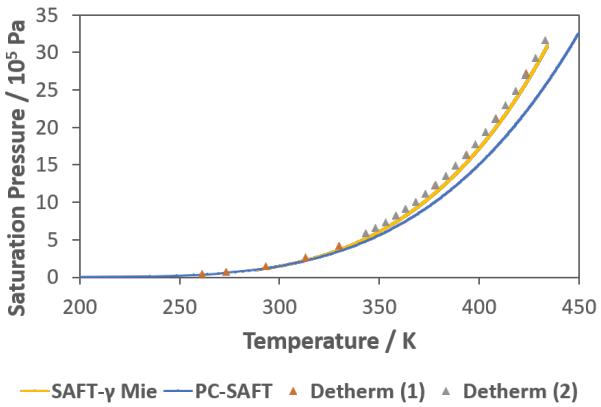

Figure 3: P-T phase diagram for neopentane

3.4 Optimisation Model Validation

3.4.1 Maximisation of Net Power Output

Results of the optimisation problems were then compared with results from literature. Net power output of the ORC system was maximised using the same process specifications as Schilling et al. (2016) for the top 10 working fluids found by Schilling.

As shown in Figure 4, results of this model showed good agreement with Schilling's model, with a maximum deviation of +6% observed for propene. However, the ranking of the top 10 working fluids is different. Differences between the results from both models may be attributed to the different equation of state used to predict molecular properties; Schilling used the PC-SAFT equation of state, while this study uses the SAFT-γ-Mie equation of state.

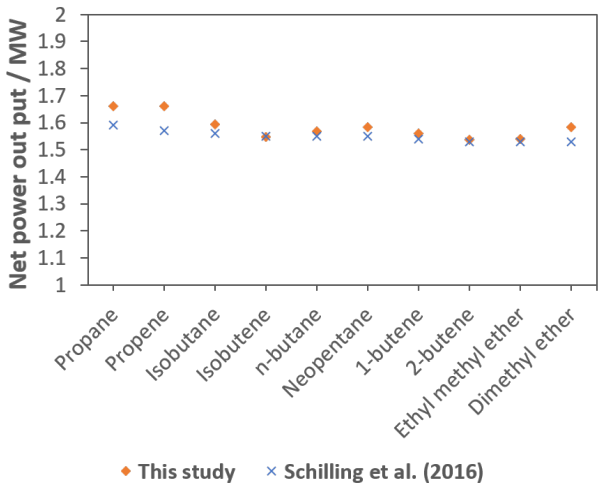

Figure 4: Comparison of net power maximisation results with literature

3.4.2 Minimisation of SIC

The costing model was also validated by comparing our results with those of Schilling et al. (2017) which used the same costing model to minimise SIC. As Schilling's ORC process model was slightly different from ours, incorporating and costing a preheater before the evaporator, some discrepancies were expected.

Table 3 compares the SIC, net power output, and TCI of the top 5 fluids found in Schilling et al. (2017). Despite under-predicting SIC for the top 5 fluids identified in the paper, the results still showed a very high degree of agreement. The discrepancies in the models can be attributed to the differences in the number of process units costed, as Schilling's results accounted for an additional preheater which is absent from our model. More importantly, the relative costs of the 5 different fluids are in very good agreement.

Table 3: Comparison of SIC minimisation results with literature

	Schilling et al. (2017)				This Study			
Working Fluid	**SIC (USD/kW)**	**Net Power (MW)**	**TCI (10^6 USD)**	**Rank**	**SIC (USD/kW)**	**Net Power (MW)**	**TCI (10^6 USD)**	**Rank**
Propene	3318	434	1.40	1	3284 (-1.0%)	424	1.39	1
Propane	3476	393	1.37	2	3379 (-2.8%)	385	1.30	2
1-butene	4646	328	1.52	3	4061 (-12.6%)	335	1.36	3
Isobutane	4722	326	1.54	4	4139 (-12.3%)	371	1.54	4
n-butane	5040	324	1.63	5	4644 (-7.9%)	328	1.52	5

3.5 Process Specifications

The specifications of the ORC process used in this study are detailed in Table 4. Cooling water temperature and flowrate were taken to be the same as Schilling et al. (2017), while heating fluid temperature was set at 573K to investigate ORC behaviour at the higher temperature range of ORC heat sources. Minimum approach temperatures of 10K in heat exchangers and isentropic efficiencies for rotating equipment were chosen to reflect more realistic systems.

Table 4: Process specifications of ORC process

Parameter	Value
Heating Fluid Temperature (K)	573
Heating Fluid Flowrate (kg/s)	66
Heating Fluid Specific Heat Capacity (kJ/kgK)	4.2
Cooling Water Temperature (K)	288
Cooling Water Flowrate (kg/s)	175
Cooling Water Specific Heat Capacity (kJ/kgK)	4.2
Minimum Approach Temperature in Heat Exchangers (K)	10
Isentropic Turbine Efficiency	0.8
Isentropic Pump Efficiency	0.9
Generator Efficiency	0.98

4 Results and Discussion

4.1 Preliminary Feasibility Tests

The LC_{50} and AIT feasibility tests were first applied to Schilling's top 10 working fluids, to get a preliminary sensing on the effect of the tests on potential working fluids. As shown in Table 5, all 10 fluids passed the LC_{50} test. More specifically, they passed with huge safety margins of 2 orders of magnitude above the safety threshold. This is because the LC_{50} partial contributions by the structural groups in these fluids are relatively small. As this study also contains similar structural groups, the likelihood of molecules generated from this study being eliminated by the LC_{50} test is low.

On the other hand, 4 of Schilling's top 10 working fluids were found to be flammable at the operating temperature used in this study. These fluids were therefore not viable at the operating conditions of this study. These preliminary results suggest that the AIT feasibility test has the potential of eliminating flammable molecules from being considered by the primal problem. By tightening the feasible region of molecules, unnecessary computational effort of the optimiser can be reduced.

Table 5: LC_{50} and AIT feasibility test results

Working Fluid	LC_{50} Test	AIT Test
Propane	Pass	Pass
Propene		
Isobutane		
Isobutene		
n-butane		
Neopentane		
1-butene		Fail
2-butene		
Ethyl methyl ether		
Dimethyl ether		

4.2 Maximisation of Net Power Output

4.2.1 Primal Problem

To obtain a preliminary sensing of the optimum topology, net power output was maximised at the above-mentioned process specifications using Schilling's top working fluids which passed the feasibility tests.

As shown in Figure 5, different topologies resulted in very similar values of maximum power for each fluid. The optimum topology for all 6 fluids trialled was the ORC with turbine bleeding, due to the presence of a second turbine. However, the addition of turbine bleeding only increased the maximum net power output by 2% on average, which is insignificant.

Of these 6 working fluids, the optimum working fluid is n-butane which generates 6.79 MW of net power with an ORC with turbine bleeding topology.

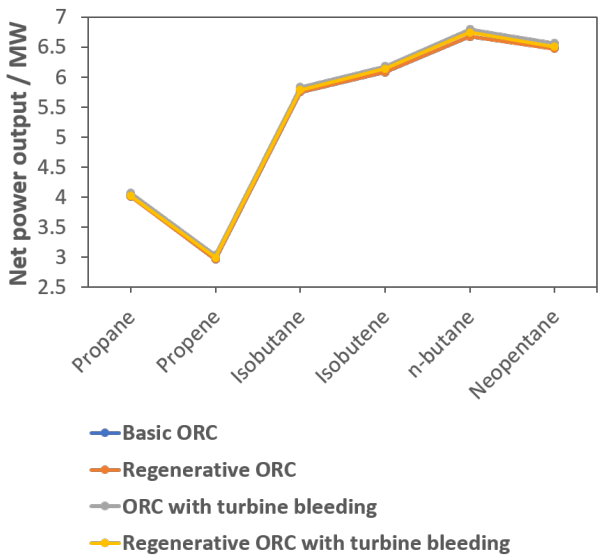

Figure 5: Maximum net power output for Schilling's top working fluids

4.2.2 Candidate List of Optimal Molecules

gPROMS ModelBuilder was incorporated into the overarching algorithm framework to solve the primal problem, while Gurobi was employed to solve the master problem. The algorithm was only able to find an average of 3 optimal working fluids for each starting point, indicating a lack of robustness. Thus, to obtain a more comprehensive list of top working fluids, a total of 20 different starting guesses using different combinations of functional groups were used. The resulting candidate lists were combined and shown in Table 6.

The algorithm determined that across all the top 10 optimal working fluids, the optimum topology was that of an ORC with turbine bleeding and no regenerator. While in line with previous findings when optimising the primal problem, it is also important to keep in mind that this usually only translates to a 2% increase in net power on average.

Novel working fluids were found in methyl acetate and allyl alcohol. Methyl acetate in particular was found to be the best working fluid out of all the solutions explored, and has an even higher net power output than any of Schilling's top working fluids at 573K. It should also be noted that despite the aforementioned lack of robustness, the algorithm was able to produce methyl acetate and ethanol, the top 2 working fluids found in this study, as optimal solutions from multiple starting points. Thus, although the current algorithm lacks breadth in terms of number of different solutions found, it finds the best solutions at a higher frequency.

Table 6: Top 10 working fluids generated by outer-approximation algorithm

Rank	**Working Fluid**	**Net Power Output / MW**	y_1	y_2
1	*Methyl acetate*	9.12	0	1
2	Ethanol	7.28	0	1
3	n-butane	6.66	0	1
4	Neopentane	6.43	0	1
5	Isobutene	6.06	0	1
6	Isobutane	5.71	0	1
7	*Allyl alcohol*	5.69	0	1
8	Ethane	4.35	0	1
9	Propane	4.00	0	1
10	Acetic acid	3.61	0	1

4.2.3 Sensitivity Analysis

Sensitivity analysis was performed on the top 5 working fluids from the candidate list, with the cycle topology fixed as an ORC with turbine bleeding. The heating fluid mass flowrate was allowed to vary within ±50%, while its inlet temperature was varied by ±50K, because 623K is the highest temperature used for power production from ORCs (EXERGY, 2018).

As illustrated in Figure 6, the optimum net power output is more sensitive to decreases in the heating fluid mass flowrate, than increases in the flowrate. Halving the mass flowrate leads to a mean 38.2% decrease in net power output, while a 50% increase in flowrate results in a mean 24.5% increase in net power output. A smaller heating fluid flowrate means that less thermal energy is transferred to the organic fluid, thus the amount of work extractable through the turbines is also less. Amongst these 5 organic fluids, ethanol is most sensitive to changes in heating fluid flowrates, with its net power output falling by 50.0% following a 50% decrease in heating fluid flowrate. At lower heating fluid flowrates, ethanol is no longer the second best organic fluid. This reveals that ethanol might only be optimum within a small range of process specifications.

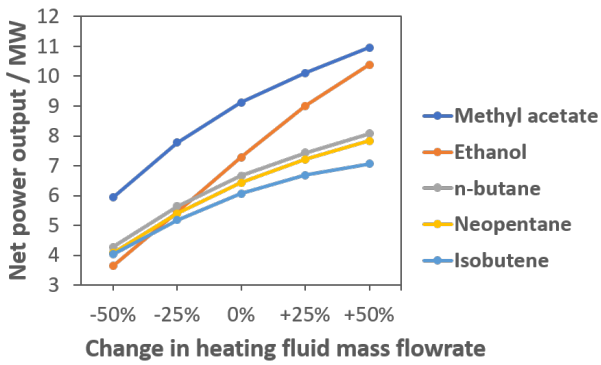

Figure 6: Sensitivity towards heating fluid mass flowrate

The effect of varying the heating fluid inlet temperature was also investigated, with results depicted in Figure 7. Decreasing the inlet temperature by 50K resulted in the optimum net power output decreasing by 27.2% on average, and increasing the inlet temperature by 50K led to a mean 26.2% increase in net power output. At higher temperatures, the heating fluid has more enthalpy thus more energy can be transferred to the organic fluid, resulting in higher net power output. Once again, ethanol was found to be most sensitive to the heating fluid inlet temperature. Its net power

output decreases by 45.3% when the inlet temperature decreases by 50K, while its net power output increases by 60.9% following a 50K increase in inlet temperature. At 623K, ethanol outperforms methyl acetate as the best working fluid. Unfortunately, the inlet temperature of the heating fluid used in ORCs should not go beyond 623K, therefore larger deviations to the inlet temperature could not be investigated.

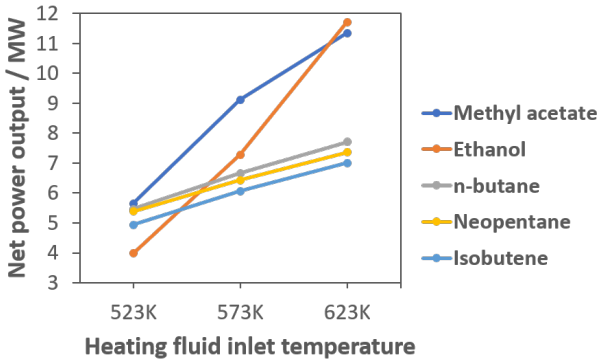

Figure 7: Sensitivity towards heating fluid inlet temperature

4.3 Minimisation of SIC

4.3.1 Primal Problem

Subsequently, the effect of topology on SIC was investigated by minimising SIC for the same 6 working fluids.

As shown in Figure 8, topologies with turbine bleeding have larger SIC values than those without turbine bleeding. This is a consequence of the larger working fluid mass flowrates passing through the first turbine, which leads to significantly higher turbine costs.

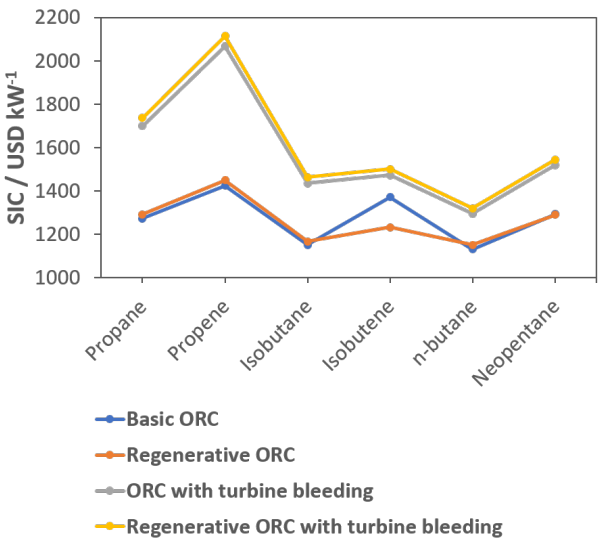

Figure 8: Minimum SIC for Schilling's top 10 working fluids

Of the 6 fluids, 4 fluids identify the basic ORC as the optimum topology, while 2 fluids – isobutene and neopentane – identify the regenerative ORC as optimum. In these 2 cases, the addition of the regenerator reduces the evaporator heat duty, resulting in lower capital costs of the evaporator.

n-butane was found to be the optimum working fluid which incurs an SIC of 1130 USD kW^{-1} with the basic ORC topology.

4.4 Algorithm Limitations

The algorithm used in this study has several limitations in different sections.

Firstly, superstructure optimisation was solved within the primal problem in gPROMS, instead of within the master problem in Gurobi. This changed the NLP problem of the original algorithm to an MINLP. While this was still within the computational ability of gPROMS, the problem was much more difficult to solve, and gPROMS faced difficulties switching between topology configurations depending on the starting guess for y_1 and y_2. Only the starting guesses of $y_1 = 0$ and $y_2 = 1$ led to optimal solutions being found, hence these guesses were used for the primal problem optimisations.

As previously discussed, the outer-approximation framework implemented to search for novel working fluids was limited in the number of optimal solutions that could be found from a single starting point. The addition of superstructure optimisation increased the number of linearised constraints passed from gPROMS to Gurobi, which may have impacted the ability of the master problem to generate new molecules.

5 Outlook

A few directions of improvement and development have been identified to take this project further.

Firstly, it was regrettable that due to time constraints, the costing model was not implemented into the master problem. Doing so would not only allow the algorithm to potentially find new working fluids that minimised SIC, but also pave the way for work on multi-objective optimisation in the future.

As previously mentioned, there is potential to improve the robustness of our algorithm. One possible way to achieve this is by incorporating the topology decision variables into the master problem instead of being solved in the primal problem. This would reduce the complexity of the primal problem, thus increasing

the performance of gPROMS. Since Gurobi is tuned to solve MILP problems, it is likely that it will be able to solve the master problem added with 2 new binary variables to a desired level of accuracy. This might lead to a heightened robustness of the overall algorithm.

Finally, the use of mixtures as working fluids can further increase design space while also bringing the potential to further increase efficiency and power output. This will be very challenging though, due to the significant increase in the design space with the addition of mixing properties as well as different compositions.

6 Conclusions

In this work, the outer-approximation algorithm used by Gopinath et al. (2016) and Bowskill et al. (2016) was modified to include new safety tests prior to optimisation, and to consider superstructure optimisation.

2 new feasibility tests were implemented to screen molecules based on their AIT and LC_{50}. Some molecules such as ethyl methyl ether were eliminated before being passed to the primal problem as they violated the AIT constraint. 3 additional structural groups for branched alkanes and alkenes were also added to Bowskill's design space which considered only linear molecules. This resulted in a wider range of top-performing molecules being found, such as isobutene.

Superstructure optimisation was incorporated into the primal problems for maximising power and minimising cost. The results for the 6 working fluids considered suggest that changing the topology does not have much impact on the maximum power, but it does result in changes in minimum SIC.

All in all, the modified outer-approximation algorithm performed to a satisfactory level by successfully generating a list of top working fluids, including novel fluids that have not been previously identified by existing studies, such as methyl acetate and allyl alcohol.

7 Acknowledgements

We would like to express our heartfelt gratitude to David Bowskill and Lauren Lee for their patience, guidance, and insight over the course of this project.

8 References

Albahri, T. and George, R. (2003). Artificial Neural Network Investigation of the Structural Group Contribution Method for Predicting Pure Components Auto Ignition Temperature. *Industrial & Engineering Chemistry Research*, 42(22), pp.5708-5714.

Astolfi, M., Romano, M., Bombarda, P. and Macchi, E. (2014). Binary ORC (Organic Rankine Cycles) power plants for the exploitation of medium–low temperature geothermal sources – Part B: Techno-economic optimization. *Energy*, 66, pp.435-446.

Bowskill, D., Tropp, U., Gopinath, S. and Adjiman, C. (2016). An Outer-Approximation Algorithm with Physical Domain Reduction using Feasibility Tests for Computer-Aided Molecular and Process Design.

Bowskill, D., Tropp, U., Gopinath, S., Jackson, G., Galindo, A. and Adjiman, C. (work in progress). Organic Rankine cycle working fluid design by application of computational methods.

Churi, N. and Achenie, L. (1996). Novel Mathematical Programming Model for Computer Aided Molecular Design. *Industrial & Engineering Chemistry Research*, 35(10), pp.3788-3794.

Darvish, K., Aliehyaei, M., Atabi, F., and Rosen, M. (2015). Selection of Optimum Working Fluid for Organic Rankine Cycles by Exergy and Exergy-Economic Analyses. *Sustainability*, 7. pp.15362-15383.

Dufal, S., Lafitte, T., Haslam, A., Galindo, A., Clark, G., Vega, C. and Jackson, G. (2015). The A in SAFT: developing the contribution of association to the Helmholtz free energy within a Wertheim TPT1 treatment of generic Mie fluids. *Molecular Physics*, 113(9-10), pp.948-984.

EXERGY - ORC Generating electricity from low-medium temperature heat sources. (2018). [online] Available at: http://www.exergy-orc.com/orc [Accessed 3 Dec. 2018].

Gani, R. and Brignole, E. (1983) Molecular design of solvents for liquid extraction based on UNIFAC. *Fluid Phase Equilibria*, 13, pp.331–340.

Geoffrion, A.M. (1972). Generalized benders decomposition. *Journal of optimization theory and applications*, 10(4), pp.237-260.

Gopinath, S., Jackson, G., Galindo, A. and Adjiman, C. (2016). Outer-approximation algorithm with physical domain reduction for computer-aided molecular and separation process design. *AIChE Journal*, 62(9), pp.3484-3504.

Hukkerikar, A.S., Sin, G., Abildskov, J., Sarup, B. and Gani, R. (2013). Development of pure component property models for chemical product-process design and analysis. *Technical University of Denmark, Department of Chemical and Biochemical Engineering, Kgs. Lyngby.*

Kleef, L., Oyewunmi, O., Harraz, A. and Markides, C. (2018). Case studies in computer-aided molecular design (CAMD) of low- and medium-grade waste-heat recovery ORC systems.

Martin, T. and Young, D. (2001). Prediction of the Acute Toxicity (96-h LC50) of Organic Compounds to the Fathead Minnow (Pimephales promelas) Using a Group Contribution Method. *Chemical Research in Toxicology*, 14(10), pp.1378-1385.

Odele, O. and Macchietto, S. (1993). Computer aided molecular design: a novel method for optimal solvent selection. *Fluid Phase Equilibria*, 82, pp.47-54.

Pereira, F., Keskes, E., Galindo, A., Jackson, G. and Adjiman, C. (2011). Integrated solvent and process design using a SAFT-VR thermodynamic description: High-pressure separation of carbon dioxide and methane. *Computers & Chemical Engineering*, 35(3), pp.474-491.

Schilling, J., Lampe, M., Gross, J. and Bardow, A. (2016). 1-stage CoMT-CAMD: An approach for integrated design of ORC process and working fluid using PC-SAFT. *Chemical Engineering Science*, 159, pp.217-230.

Schilling, J., Tillmans, D., Lampe, M., Hopp, M., Gross, J. and Bardow, A. (2017). From molecules to dollars: integrating molecular design into thermo-economic process design using consistent thermodynamic modeling. *Molecular Systems Design Engineering*, 3.

Sun, Z., Wang, F., Wang, S., Xu, F. and Lun, K. (2017). Performance analysis of different ORC configurations for thermal energy and LNG cold energy hybrid power generation system.

Vanslambrouck, B., Vankeirsbilck, I., Gusev, S. and Michel, D.P. (2011). Turn waste heat into electricity by using an Organic Rankine Cycle.

White, M.T., Oyewunmi, O.A., Chatzopoulou, M.A., Pantaleo, A.M., Haslam, A.J. and Markides, C.N., (2018), Computer-aided working-fluid design, thermodynamic optimisation and thermoeconomic assessment of ORC systems for waste-heat recovery. *Energy,* 161, pp.1181-1198.

Conceptual study to recover metals from end-of-life Li-ion batteries: Anodic electrodeposition of MnO_2 in the presence of Li^+, Co^{2+}, and Ni^{2+}

Raul Rinken
Department of Chemical Engineering, Imperial College London, U.K.

Abstract Fastly evolving market of electric vehicles along with growing portable electronics market has rapidly increased the demand for Li-ion batteries during the recent years. As the fast market growth is predicted to continue during the upcoming decades and currently less than 5% of the Li-ion batteries are recycled, novel approaches capable to economically recover metals from end-of-life batteries are needed. This study is part of the development of a new novel electrochemical reactor aiming to recover MnO_2 and metallic Li from spent Li-ion batteries. The study concentrates on MnO_2 electrochemical deposition from aqueous solutions. Cyclic voltammetry was used to assess the Mn^{2+} oxidation process. MnO_2 was deposited at constant potential 1.2V vs Ag/AgCl at pH 3 on Pt electrode from three different solutions: only Mn^{2+} present, Mn^{2+} and Li^+ present, and Mn^{2+}, Li^+, Co^{2+}, and Ni^{2+} present. Obtained deposit crystal structure was analysed with XRD, morphology with SEM and elemental composition with EDS and ICP-MS. It was found that at potentials lower than 1.5V vs Ag/AgCl, Mn^{2+} oxidation is the dominant anodic reaction while the reaction itself is relatively reversible. Obtained deposit was amorphous and contained an extensive amount of Mn(lll) species along with MnO_2 in all three deposits. Manganese metal content 99.6% with respect to other metals was detected in the deposit obtained in the presence of Li^+, Co^{2+}, and Ni^{2+}. Traces of Ni were detected forming 0.3% of the total metal content while the amount of Co and Li was negligible in the deposit. It was concluded that selective MnO_2 deposition is possible while Ni^{2+}, Co^{2+}, and Li^+ ions are present. As a next step of the reactor development, it may be desired to discover higher potentials and pHs as well as to study electrochemical leaching of MnO_2.

Introduction

Initially proposed in the 1970s, Li-ion batteries offer superior energy densities with 2-20 times more energy stored per unit weight compared to other rechargeable battery chemistries like lead-acid, nickel-cadmium and nickel- metal hydride. Li-ion battery anode is most commonly made from graphite, lithium metal oxides are used as the cathode. Copper and aluminum plates are implemented as current collectors while polyolefin separator end PF_6 as an electrolyte is most commonly used. The biggest variation between different Li-ion batteries is cathode chemistry. Modern cathode chemistries are based on lithium and transition metal oxides complexes comprising Co, Ni, and Mn while lithium iron phosphate is used mainly in electric vehicles (EVs) produced in China (Grey & Tarascon, 2016).

In 1991, Sony commercialised the first Li-ion battery. Attainment of consumer electronics since then and quickly evolving market of Electric vehicles has rapidly grown the demand for Li-ion batteries during the past decade. Since 2010, EV sales have grown over 50% on average each year reaching 1 million new vehicles in 2017 (IEA, 2018). The exponential growth is expected to continue in near future with estimated sales of 10M new EVs in 2025 and 25M in 2030 (Bloomberg New Energy Finance, 2017). It is predicted that Li-ion batteries remain dominant technology for at least upcoming two decades creating an evolving need for new batteries (Avicenne Energy, 2017). Li-ion battery production in 2017 was 135 GWh, from which 36% formed lithium iron phosphate batteries and 64% lithium and transition metal oxides. (Jaffe, 2017). It is expected that the production is exceeding 1TWh by 2028, while the market will further shift towards transition metal oxide based chemistries with an expected market share of 76% in 2026 (Benchmark mineral Intelligence, 2018) (Avicenne Energy, 2017).

Due to the vastly evolving production of Li-ion batteries, the number of end-of-life batteries will also rapidly increase during the upcoming years. Currently, only less than 5% of all Li-ion batteries are recycled (Heelan, et al., 2016). As there is no standard economically viable technology for recycling, new developments are needed to facilitate the increasing amount of Li-ion batteries. For comparison, as recycling lead-acid batteries can be profitable, currently 99% of these batteries are recycled (USEPA, 2016). The need for recycling can be divided into two large categories: resources restriction and hazardous waste. Firstly, battery production consumes more than 40% of the world's cobalt and lithium production. As the worldwide production increases at a slower pace than the demand, it is expected that Co and Li supply side face serious shortage during the upcoming years (Lv et al., 2018). Secondly, without proper disposal, Li-ion batteries can impose a serious threat to the environment. Electrolyte reacting with water creates toxic and corrosive hydrofluoric acid. Heavy metals like Mn, Co and Ni can contaminate underground water and be acute to living organisms (Lv, et al., 2018).

The aim of this project is with addressing the growing market and necessity for recycling, ultimately developing energy efficient, environmentally benign, elegant and economically viable electrochemical processes for recovering

metal-containing materials from end-of-life lithium batteries.

Background

Recycling of the Li-ion batteries starts with the collection of the batteries, followed by discharge removing any residual charge. There are two general approaches to recover the metals from the batteries: pyrometallurgical and hydrometallurgical. In the pyrometallurgical process, whole battery is smelted at high temperature, burning off anode, plastics, electrolyte, and binder. Valuable metals like Ni, Cu, and Co form an alloy, from where they can later be recovered by hydrometallurgical methods. Other metals (Li, Al, Mn) remain in slag and have to be used for low-value applications (Sun, et al., 2017). In the hydrometallurgical process, cathode material separated by mechanical and chemical pre-treatment is leached into aqueous solution. Peroxides along with strong acids are usually used, although, during the recent years, milder conditions with organic acids have also been proposed. From aqueous solution, metals could firstly selectively extracted into organic phase with solvents like D2EHPA, Cyanex272 etc. Metals are stripped back to the aqueous phase and selectively precipitated (Meshram, Pandey, & Mankhand, 2014). High purity salts and oxides could be obtained with as high recovery rates as 100% manganese, 99% cobalt, 85% nickel and 99.2% lithium (Chen & Ho, 2018). End of life Li-ion batteries recycling strategies are summarised in **Figure 1**. Commercially, hydrometallurgical methods contribute 50% of the recycling capacity, while pyrometallurgical 30% and combined methods 20% of the capacity (Lv et al., 2018).

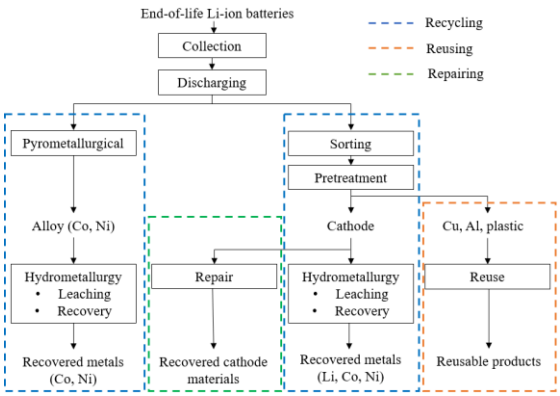

Figure 1. Recycling strategies for Li-ion batteries. Adopted from Lv et al., 2018.

Electrochemical recycling methods have received low attention, although there is a potential to be an efficient and elegant method to recover metals from spent Li-ion batteries. Efforts have been made to recover cobalt electrochemically from $LiCoO_2$ batteries with relatively high current efficiency and purity (Lupi & Pasquali, 2003) (Garcia, et al., 2012). However, when Ni is present as it is for most nowadays Li-ion batteries, Co and Ni tend to codeposit (Lupi & Pasquali, 2003).

While assuming that the cost of the electrochemical process will be dominated by the price of electricity (~0.13\$ kWh^{-1}), lithium recovery price can be estimated as 4000\$ t^{-1} compared to 13 000\$ t^{-1} market price. For MnO_2, recovery price can be estimated 600\$ t^{-1} compared to market price 1500-2500\$ t^{-1} (Benchmark mineral Intelligence, 2018). In both cases, 8V potential difference and 100% current efficiencies are assumed. Market prices for Co and Ni are 55 000\$ t^{-1} and 11000 \$ t^{-1} (Benchmark mineral Intelligence, 2018). Co and Ni could be recovered using extraction and electrochemical/ precipitation methods.

An electrochemical reactor is proposed to recover metallic lithium and MnO_2 from spent Li-ion batteries (**Figure 2**). Li^+ permeable membrane will be implemented to allow cathodic recovery of lithium. The objective of this study is to characterise Mn^{2+} oxidation process and electrodeposition of MnO_2 in an environment simulating possible conditions for the battery recovery process. It is desired to study the potentials where oxidation reaction takes place and characterise the deposit obtained with electrodeposition.

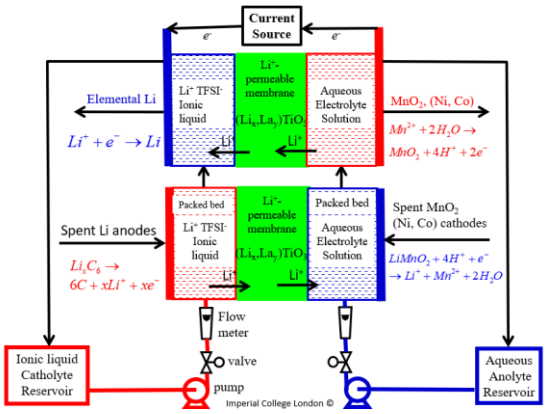

Figure 2. Li and MnO_2 recovery reactor proposed by Geoff Kelsall.

During the recent years, MnO_2 has received attention with its potential uses in supercapacitors well summarised by Weifeng, et al., 2011. Most broadly, however, MnO_2 is used in primary batteries. Efforts have been made also to deposit MnO_2 for its direct use for making cathodes for new Li-ion batteries. Behboudi- Khiavi, et al., 2018. were able to intercalate Li^+ into MnO_2 during electrodeposition and used the obtained material directly to produce high performing Li-ion batteries.

Methods and Experimental

The strategy to characterise MnO_2 anodic electrodeposition included 3 main components: firstly, thermodynamic analysis and assessment of the anodic reactions, secondly, anodic electrodeposition of MnO_2 and thirdly, characterisation of the obtained deposit. Thermodynamic stabilities of Mn, Co and Ni were

assessed with Pourbaix diagram (**Figure 3**), which is based on the thermodynamic data from (Bard, et al., 1985).

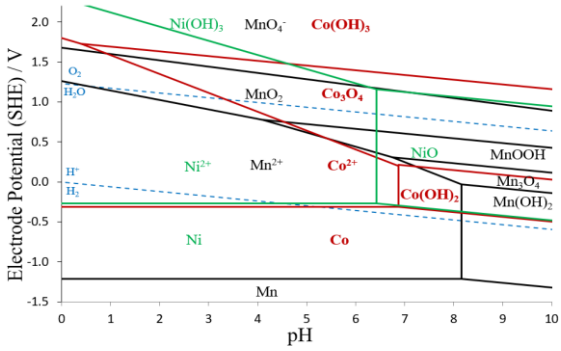

Figure 3. Pourbaix diagram of Mn, Co and Ni. a(Mn)=a(Co)=a(Ni)=0.1.

Based on the Pourbaix diagram, pH 3 was selected for the analysis allowing stability of Mn^{2+}, Co^{2+}, and Ni^{2+}. Furthermore, at pH 3, when increasing the potential, MnO_2 would be the first compound to deposit based on the thermodynamics. Based on the most common current battery chemistries and future predictions for cathode chemistries, experiments were carried out with 3 different solutions summarised in **Table 1**.

Table 1. Solutions used during the experiments.

Solution	Concentration/ M	pH
Mn	$c(Mn(NO_3)_2)$= 0.1	3
Mn/Li	$c(Mn(NO_3)_2)$= 0.1 $c(LiNO_3)$= 0.1	3
Mn/Li/Co/Ni	$c(Mn(NO_3)_2)$= 0.1 $c(LiNO_3)$= 0.1 $c(Co(NO_3)_2)$= 0 .1 $c(Ni(NO_3)_2)$= 0.1	3
Blank	$c(Na2SO_4)$=0.1	3

All chemicals were supplied by Alfa Aesar with purity >98%. pH was adjusted using HNO_3. Electrochemical reactor with two 12ml compartments separated by Nafion membrane was used for the experiments (**Figure 4**). Ti and Pt working electrodes were used for cyclic voltammetry (CV) scans and only Pt electrode for electrodeposition. Pt coated Ti mesh was used as the

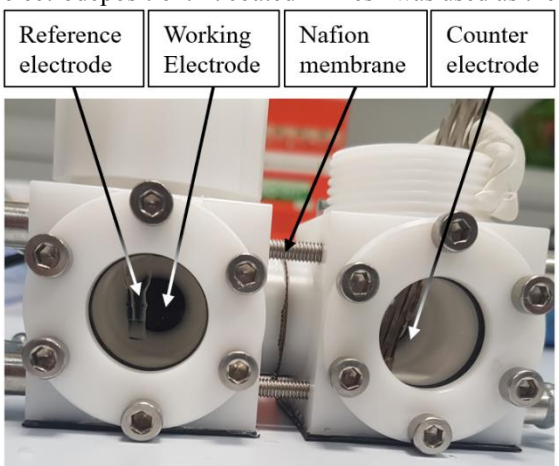

Figure 4. Electrochemical reactor used for the experiments.

counter electrode throughout all experiments. Ag/AgCl/ sat. KCl (0.197 V vs SHE) was implemented as the reference electrode.

Experiments involve two main electrochemical reactions:

$$Anode: Mn^{2+} + 2H_2O \rightarrow MnO_2 + 4H^+ + 2e^- \quad 1$$

$$Cathode: 2H^+ + 2e^- \rightarrow H_2 \quad 2$$

To investigate the deposition process, cyclic voltammetry scans were performed. Titanium and platinum electrodes were used to assess the suitability of Ti electrode for electrodeposition. 0.5M Oxalic acid solution was used to remove TiO_2 layer. The potential was scanned from -0.2V to 1.2 and 1.5V with respect to Ag/AgCl reference. Scan rate 50 mV s^{-1} was used. Pt electrode was picked as the suitable one for electrodeposition and constant potential 1.2V was applied for 10 hours. Obtained deposit was washed with DI water and dried in a vacuum oven for 24h at 40°C.

The deposit crystal structure was analysed with X-ray diffraction (XRD) employing Cu Kα radiation source and operated at 40kV and 20mA. The surface morphology and deposit thickness were analysed using scanning electron microscope (SEM). Elemental analysis of the deposit was carried out with energy-dispersive x-ray spectroscopy (EDS) recorded along with the SEM image. Due to Li low energy characteristic radiation and for more precise measurements, induced coupled plasma coupled with a mass spectrometer (ICP-MS) was used to detect the amount of elements in the deposit as well as in anolyte and catholyte after deposition. The standard for Li, Mn, Co, and Ni was supplied by Sigma Aldrich.

Results

Different potentials were scanned on Ti electrode in order to assess its suitability as an electrode for anodic electrodeposition (**Figure 5**). The same voltages were scanned for the Pt electrode (**Figure 6**). As the current densities were two orders of magnitude larger for Pt than they were for titanium electrode, it was decided to proceed with Pt electrode for electrodeposition in order to obtain enough deposit for further analysis.

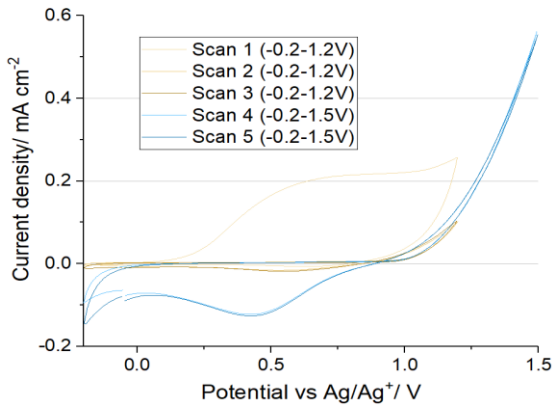

Figure 5. CV voltammogram for 0.1M $Mn(NO_3)_2$ solution at pH3 with Ti working electrode. Scan rate 50 mV s^{-1}.

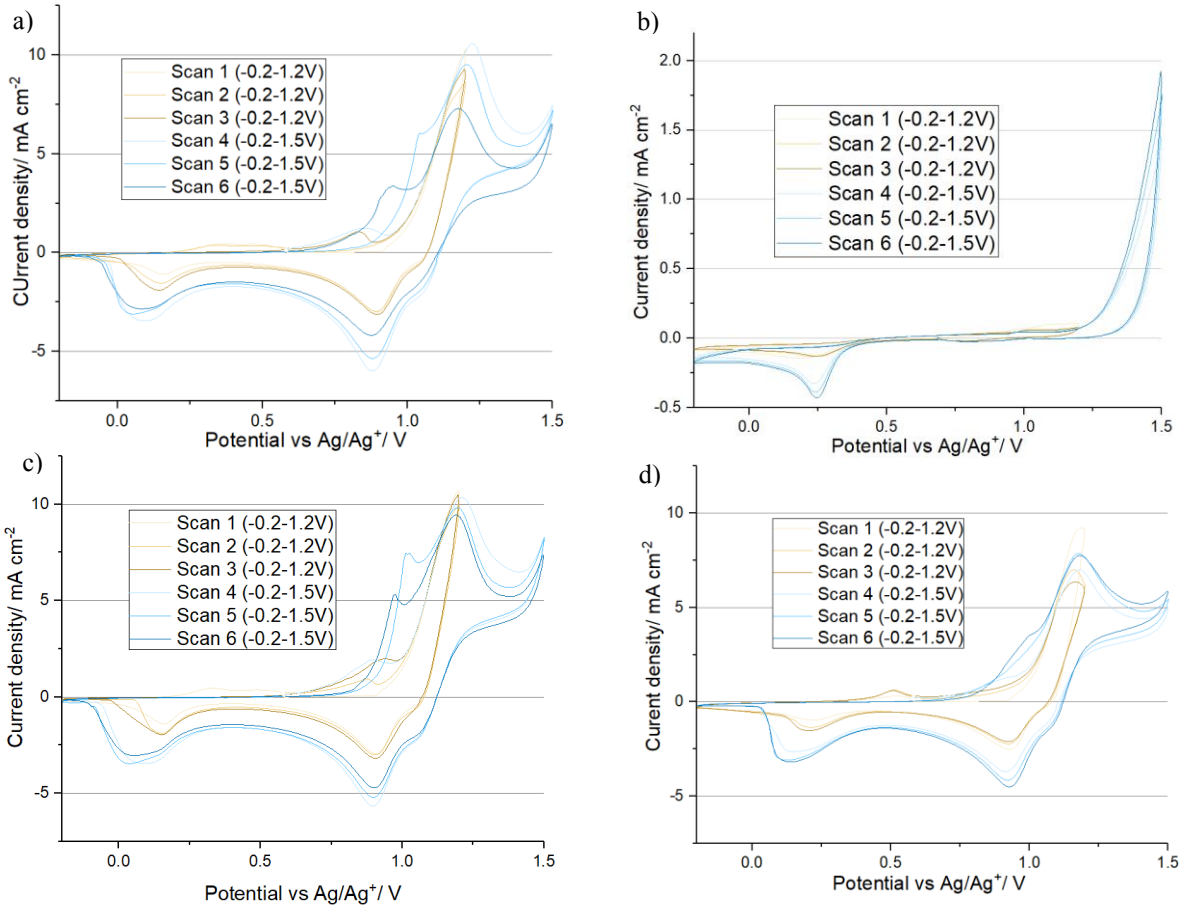

Figure 6 CV voltammograms at pH 3 with Pt working electrode, **a)** 0.1M $Mn(NO_3)_2$ b) 0.1M Na_2SO_4 (blank) **c)** 0.1M $Mn(NO_3)_2$ 0.1M $LiNO_3$ **d)** 0.1M $Mn(NO_3)_2$, 0.3M $LiNO_3$, 0.1M $Co(NO_3)_2$, 0.1M $Ni(NO_3)_2$. Scan rate 50 mV s^{-1}.

Based on the voltammograms, constant potential 1.2 V vs Ag/AgCl was picked as the operating voltage for electrodeposition. Electrodeposition was carried out for 10 hours to obtain enough material for further analysis (**Figure 7**).

Total charge through the anode was 51.2C for Mn/Li/Co/Ni, 53.8C for Mn/Li and 55.1C for Mn experiment. When assuming 100% current efficiency towards the formation of MnO_2, around 25mg deposit was obtained during each deposition. The deposit was ground and analysed with XRD (**Figure 8**).

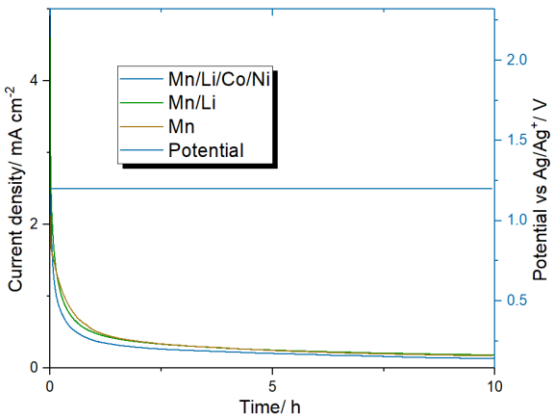

Figure 8. Current and potential during the electrodeposition of MnO_2.

Expected pattern for α- MnO_2 has plotted along with the crystallograms to see if characteristic peaks are present. The strongest characteristic peak at 2θ~37° corresponding to (211) plane can be observed. In general, it can be said that obtained deposit is amorphous. SEM images of the ground deposit were obtained (**Figure 9**). Deposit thicknesses of 34µm for Mn, 36µm for Mn/Li and 38µm for Mn/Li/Co/Ni were measured.

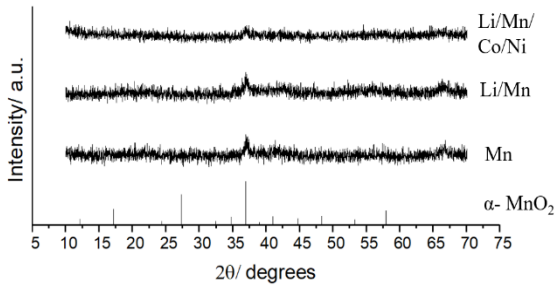

Figure 7. X-ray diffraction pattern for obtained deposits in the presence of different metal ions.

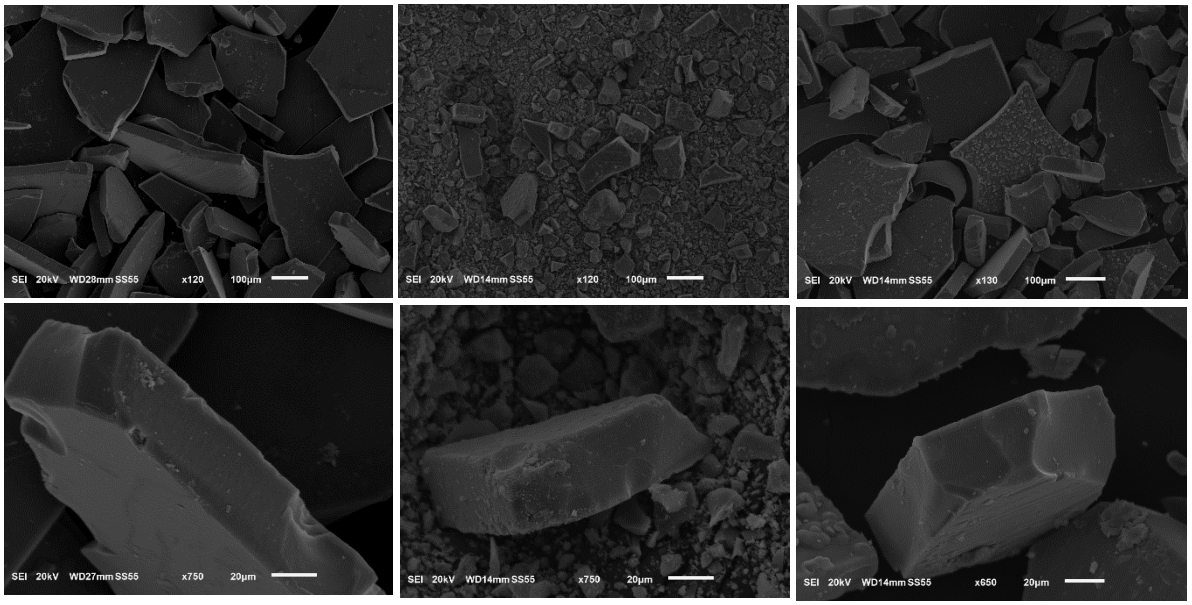

Figure 9. SEM images of deposits. a-b) Mn c-d) Mn/Li e-f) Mn/Li/Co/Ni

Along with SEM images, energy-dispersive x-ray spectrums were obtained. No traces of other than oxygen and manganese were found in any of the samples. Four different points for each sample were analysed and the results are summarised in **Table 2**.

Table 2 Molar ratio of oxygen and manganese detected with EDS. SD- Standard deviation for molar %.

Sample	element	Average	SD	Mn: O
Mn	Mn	36.2	5.0	1:1.76
	O	63.8		
Mn/Li	Mn	50.8	10.2	1:0.97
	O	49.2		
Mn/Li/ Co/Ni	Mn	35.8	6.8	1:1.79
	O	64.2		

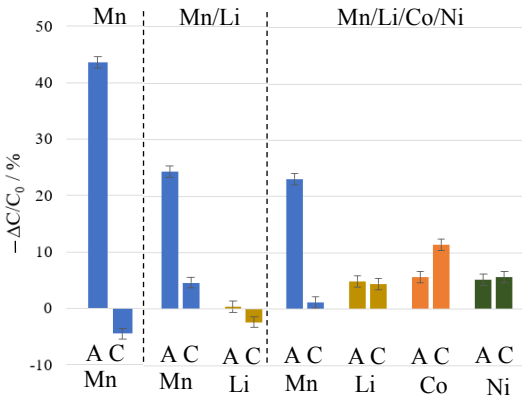

Figure 10. Concentration change in anolyte (A) and catholyte (C) during the electrodeposition.

After electrodeposition, a sample was taken from both, anolyte and catholyte, and analysed with ICP-MS (**Figure 10**). A green deposit was observed on cathode after electrodeposition with Ni^{2+} and Co^{2+} present indicating reduction of these metal ions. Based on concentration change and total current during the electrodeposition, current efficiency towards the formation of MnO_2 was calculated and is summarised in **Table 3**.

Table 3. Current efficiency towards the formation of MnO_2 during the electrodeposition.

Deposition	Current efficiency
Mn	158%± 5.4%
Mn/Li	117%± 5.4%
Mn/Li/Co/Ni	109%± 5.4%

Deposit obtained during the Mn/Li/Co/Ni electrodeposition was dissolved in 2M HNO_3 and 5% H_2O_2 solution and analysed with ICP-MS. The deposit contained 99.6% Mn and 0.3% Ni with respect to total metal content in the sample.

Discussion

Due to the high price of platinum for commercial applications, an initial attempt was made to implement titanium as the working electrode. Ti electrode was held in the oxalic acid solution to remove TiO_2 by its reduction to soluble Ti^{3+}. During the CV scans, high anodic current was observed during the first scan (**Figure 5**). Experiment was repeated with Ti electrode from where TiO_2 layer was removed mechanically. Similar anodic current was observed indicating fast formation of TiO_2 layer when increasing the potential. Due to formed TiO_2 layer created resistance, the current densities observed were relatively low: 0.1 mA cm^{-2} at 1.2V (**Figure 5**). Relatively slow nucleation process for MnO_2 on Ti electrode was also observed as when lowering the potential, the anodic current dropped slower then it increased with increasing potential. When lower scan rates than 50 mV s^{-1} would have been used, the crossing of increasing and decreasing current would not have been observed. In order to use Ti as the working electrode in the future, treatment of the

electrode is required to retain the electrode surface conductivity.

In order to assess the current densities and reaction mechanism without resistive passivating layer present, Pt was used as the working electrode. Blank scan without any of the transitional metal present indicated offset current for oxygen evolution to be 1.25V and O_2 reduced around 0.2V (**Figure 6b**). When scanning the solution with Mn^{2+} present, relatively chaotic behavior between 0.75-1V when increasing the potential was observed (**Figure 6a, 6c, 6d).** The main reason for this is the MnO_2 formation mechanism from Mn^{2+}, which includes adsorption process and formation of Mn(lll) species forming various complexes with water (Fleischmann, et al., 1962). Simplified reaction mechanism could be described by following consecutive reactions:

$$Mn^{2+} \rightarrow Mn^{3+} + e^- \quad 3$$

$$Mn^{3+} + 2H_2O \rightarrow MnOOH + 3H^+ \quad 4$$

$$MnOOH \rightarrow MnO_2 + H^+ + e^- \quad 5$$

When the scan rate would be lowered, a smoother curve would be expected in this region allowing the total $2e^-$ transfer process to proceed smoother. A mass transfer limit for Mn^{2+} oxidation was reached at 1.3V and at a current density of 5 mA cm^{-2}. At 1.4V, O_2 evolution started to become a significant anodic reaction. When scanning down from 1.5V, two peaks between 1.5V and 0.5V appeared, corresponding to the reduction of MnOOH (1.1V) and MnO_2 (0.9V). It must be noticed, that although MnOOH is not thermodynamically favored compound at this pH and potential, it forms as an intermediate for MnO_2 formation. As the formation mechanism for MnOOH is less complex than for MnO_2 and involves only $1e^-$ transfer, the peak separation is also smaller as is the overpotential needed. When comparing total oxidation current for the scan from -0.2V to 1.2V where O_2 evolution and reduction contribution is small, total charge transferred by oxidative current is 35% larger than by reductive current. This means that Mn^{2+} oxidation and MnO_2 reduction are relatively reversible and reduction of MnO_2 in the proposed reactor can be possible.

During the electrodeposition, current density decreased in time while the voltage was kept constant. This is due to the low conductivity of forming MnO_2, creating resistance. Based on the deposit thickness and the resistance growth in the system while assuming the conductivity of electrolyte and membrane remained the same during experiments, the resistance of amorphous mixture of MnOOH and MnO_2 is $2 * 10^6$ Ω cm (slightly higher as literature values $10^5 * 10^6$ Ω cm obtained for γ-MnO_2 (Owen, et al., 2007). The lower conductivity is observed due to the amorphous nature of the deposit. High resistance means that if in future it is desired to commercialise the process, deposit conductivity has to be increased or higher potentials have to be applied meaning less selectivity towards Mn^{2+} oxidation process. Another approach could be continuously removing the deposit from the electrode.

XRD revealed the amorphous structure of the deposit, having a slight presence of (211) plane characteristic to α-MnO_2. Similar amorphous MnO_2 was obtained also by Ragupathy, et al., 2008. When they obtained MnO_2 at 50 °C, the structure was amorphous having same XRD pattern measured in this study. When they heated the sample in air, a well-defined α-MnO_2 structure was obtained when heating the solid at 600°C for 3 hours. Oxidation of MnOOH to MnO_2 in the air can be the main contributor to well-defined crystal structure formation as it makes the solid more uniform and high temperature allows rearrangement of atoms in the crystal structure. Therefore, with the correct heat treatment of the obtained amorphous MnO_2, it would be possible to obtain material directly for the usage in new batteries.

SEM images were obtained simultaneously with EDS spectrums. The deposit was crushed after deposition and small plates were obtained (**Figure 9**). Depending on the future prospective usage of the MnO_2, different size particles could be obtained with well-defined thickness depending on electrodeposition time. EDS spectrums did not indicate any traces of any metal other than Mn for all three deposits. However, there was a relatively large variation in terms of the molar fraction of oxygen and manganese varying from 1-1.8 with a relatively high deviation between measurements. This is due to non-isotropic nature of the sample and in order to account it matrix corrections should be implemented. However, EDS is a quick method for the qualitative detection of metals present in a sample.

ICP-MS analysis of the catholyte and anolyte revealed the change of metal content in both side of the membrane during the electrodeposition compared to the initial solution. Based on Mn^{2+} concentration change and total charge transferred during electrodeposition, current efficiencies were calculated with respect to MnO_2 formation. In all three cases, the efficiency exceeded 100% indicating relatively large amount of Mn(lll) species like MnOOH present while O_2 evolution is negligible at 1.2V. Dissolved deposit from Mn/Li/Co/Ni experiment had Mn content larger than 99.5% in terms of metals while also traces of Ni were present. No traces of Co or Li were detected. This indicates that Co and Ni coprecipitation is negligible at 1.2V. No lithium intercalation was detected. In principle, Li^+ could go through ion exchange process with proton obtained by formation of MnO_2 precursor MnOOH. Generally, Li^+ intercalation into the MnO_2 crystal structure has been identified as an ion exchange process in which protons in the surface, vacancy, and groutite sites are successively replaced

by lithium ions (Behboudi-Khiavi, et al., 2017). Behboudi et al. 2018 used facile pulse electrodeposition at 10 mA cm^{-2} which is order of magnitude larger than in this study. In order to achieve that high current density, potential had to be at least 3V vs Ag/AgCl., probably even higher. Facile pulsation may have enhanced Li^+ diffusion to the surface and therefore intercalation was achieved. In current study, $[Li^+]/[Mn^{2+}]$= 3 for Mn/Li/Co/Ni experiment, in their case $Li_{0.07}MnO_2$ was obtained with $[Li^+]/[Mn^{2+}]$=2 and $Li_{0.17}MnO_2$ was obtained with $[Li^+]/[Mn^{2+}]$=7. Catholyte and anolyte ICP-MS results indicate depletion of Ni and Co. Visually, a deposition on cathode side was observed indicating reduction of Ni and Co in catholyte. This also explains the decline in Co and Ni concentration. As there was a very small amount of Ni and no traces of Co present in final deposit, but large concentration change is present in both anolyte and catholyte, Nafion membrane is Co and Ni ion permeable. This agrees with the literature (Martí-Calatayud, et al., 2011). It must be noted that there is a competition between different ions moving diffusing through the membrane rising an uneven concentration of metal ions in anolyte and catholyte. Change in lithium ion concentration remains unclear at this point as no traces of Li in anode deposit was detected. One could argue that interaction with cathodically deposited Co and Ni on the cathode may have lowered the concentration. However, in order to evaluate the hypothesis, analysis of the cathodic deposit is required. For the proposed reactor, Li^+ permeable membrane is proposed meaning that cathodic reactions with Co and Ni become impossible.

Conclusions

Series of experiments were carried out to detect Mn^{2+} oxidation properties. Due to fast formation of TiO_2 passivating layer on working electrode causing low current flow at desired potentials, Pt electrode was implemented. Mass transport limiting current of 5 mA cm^{-2} was detected in 0.1M Mn^{2+} solution. It was found that the Mn^{2+} oxidation is a relatively reversible process which proceeds via Mn(lll) intermediate. This indicates that electrochemical leaching of MnO_2 based cathode material can be possible in principle. As a result of electrodeposition, amorphous material was obtained, what according to literature could be converted into MnO_2 at high temperatures with well defined crystal structure. Manganese content larger than 99.5% with respect to other metals was detected for electrodeposition with Co^{2+}, Ni^{2+}, and Li^+ present. This indicates that when applying constant potential 1.2V vs Ag/AgCl, MnO_2 can be selectively deposited without co-deposition of Co or Ni and without intercalation of Li into the deposit.

To broaden knowledge about the anodic recovery process, it may be desired to investigate also higher potentials, allowing larger current densities with smaller capital costs. Higher pH-s might also offer interest as the lithium ion permeable membrane may be unstable at low pH-s. To obtain fully functioning reactor for electrochemical recovery of metals from Li-ion batteries, it would be desired to investigate MnO_2 reduction process to leach battery cathode material into aqueous solution. When whole reactor could be run, information about operating potential and energy efficiency could be obtained allowing economical comparison with current technologies and potential for scale-up.

Acknowledgements

Many thanks to Xiaochu Wei for being helpful with the analysis of the samples, Dr. Franky Bedoya Lora, Dr. Sze Yin Tan and Dr. Nicholas Farandos for their help with potentiostat as well as all research group for useful and productive discussions.

References

Avicenne Energy, **2017**. *The Rechargeable Battery Market and Main Trends 2016-2025 ,* Fort Lauderdale: Avicenne Energy.

Bard, A., Parsons, R. & Jordan, J., **1985**. *Standard Potentials in Aqueous Solution.* New York: Marcel Dekker.

Behboudi-Khiavi, A., Javanbakht, M., Mozaffari, S. & Ghaemi, M., **2017**. Synthesis of mesoporous Li_xMnO_2 as a cathode material of Lithium ion battery via one-pot galvanostatic electrodeposition method. *Journal of Elelctroanalytical Chemistry,* 801(July), pp. 224-234.

Behboudi-Khiavi, S., Javanbakht, M., Mozaffari, S. & Ghaemi, M., **2018**. Facile pulse electrodeposition of Li_xMnO_2 nano-structures as high performance cathode materials for lithium ion battrey. *Electrochimica Acta,* Volume 261, pp. 491-502.

Benchmark mineral Intelligence, **2018**. *Benchmark's Lithium ion Battery Megafactory Assessment,* London: Benchmark mineral Intelligence.

Bloomberg New Energy Finance, **2017**. *Electric Vehicle Outlook 2017,* New York: Bloomberg.

Chen, W. & Ho, H., 2018. Recovery of Valuable Metals from Lithium-Ion Batteries NMC Cathode Wase Materials by Hydrometallurgical Methods. *Metals,* 8(5), pp. 321-337.

Fleischmann, M., Thirsk, H. & Tordesillas, I., **1962**. Kinetics of electrodeposition of gamma-manganese dioxide. *Transactions of the Faraday Society,* Volume 58, pp. 1865-1877.

Garcia, E. et al., **2012.** Electrochemical recycling of cobalt from spent cathodes of lithium-ion batteries: its application as supercapacitor.. *J.Appl. Electrochemistry,* pp. 361-366.

Grey, C. & Tarascon, J., **2016**. Sustainability and in situ monitoring in battery development. *Nature Materials,* 16(1), pp. 45-56.

Heelan, J. et al., **2016**. Current and Prospective Li-ion Recycling and Recovery Processes. *JOM,* 68(10), pp. 2632-2638.

IEA, **2018**. *Global EV Outlook 2018,* France: OECD/IEA.

Jaffe, S., 2017. Vulnerable Links in the Lithium-Ion Battery Supply Chain. *Joule,* pp. 220-228.

Lupi, C. & Pasquali, M., **2003**. Electrolytic nickel recovery from lithium-ion batteries. *Minerals Engineering,* pp. 537-542.

Lv, W. et al., **2018**. A Critical Review and Analysis on the Recycling of Spent Lithium-Ion Batteries. *ACS Sustainable Chemistry & Engineering,* Volume 6, pp. 1504-1521.

Martí-Calatayud, M., García-Gabaldón, M. & Pérez-Herranz, V., **2011**. Determination of transport properties of Ni(II) through a Nafion cation-exchange membrane in chromic acid solutions. *Journal of Membrane Science,* pp. 449-458.

Owen, M., Lawrence, G. & Donne, S., **2007**. An electrochemical quartz crystal microbalance study into the deposition of manganese dioxide. *Electrochemica Acta,* 52(14), pp. 4630-4639.

Ragupathy, P., Vasan, H. & Munichandraiah, N., **2008**. Synthesis of Nano-MnO_2 for Electrochemical Supercapacitor Studies. *Journal of Electrochemical Society,* 1(155), pp. 34-40.

Sun, Z. et al., **2017**. Toward Sustainability for Recovery of Critical Metals from Electronic Waste: The Hydrochemistry Process. *ACS Sustainable Chemistry & Engineering,* Volume 5, pp. 21-40.

USEPA, **2016**. *Advancing Sustainable Material Management: 2014 Fact Sheet,* Washington: United States Environmental Protection Agency.

Weifeng, W. et al., **2011**. Morphology evolution in anodically electrodeposited manganese oxide nanostructures for electrochemical supercapacitor applications- Effect of supersaturation ratio. *Electrochemica Acta,* pp. 1619-1628.

Imaging Velocity Fields and Analysing Bubble Shape in Yield-Stress Fluids

Emily Daborn and Prashant Shivdas

Department of Chemical Engineering, Imperial College London, U.K.

Abstract

This research article aims to better understand the characteristics of bubbles rising in yield-stress fluids and to relate this to the fluid behaviour induced by these bubbles. This was done by analysing bubbles rising in Carbopol gels in a transparent column. Carbopol gels were used as they behave as a typical yield stress fluid and they are easy to observe due to their transparent nature. Data was processed in MATLAB and subsequently the Reynolds, Bingham and Bond numbers were calculated. No simple two dimensional relationship between any two of these numbers was found. The fluid behaviour was studied using particle image velocimetry (PIV), a technique which allows the velocity field of the fluid around the rising bubble to be visualised. These velocity fields were also generated on MATLAB using the PIVlab application and estimates of the yielded region of the fluid caused by the motion of a rising bubble were obtained by analysing displacement vector fields and strain rate fields. By averaging over an entire bubble rise video, detailed and accurate velocity and strain rate fields were obtained.

1 Introduction

Many industrial sectors use yield-stress fluids in their manufacturing process. From pharmaceuticals to food to oil and gas, yield-stress fluids are ubiquitous in the production of goods. During the manufacturing process, bubbles can become embedded into these fluids. Bubbles are undesirable in many commercial products as they can encourage microbial growth, reduce the structural stability of the products and can even cause cause spontaneous ignition of energetic materials [1] [2]. However, bubbles can also be desirable if a certain texture or appearance is preferred [3].

It is important, especially for industry, to understand the motion of bubbles in yield-stress materials and how they affect the macroscopic properties of the surrounding fluid so that the formation, retention, and removal of bubbles can be controlled. This is particularly true in yield-stress fluids where bubbles can be easily retained. Yield-stress fluids are a special class of non-Newtonian fluids that exhibit distinct characteristics that are useful in a wide range of applications.

The control of bubbles is particularly important to the cosmetics industry. For example, in lipsticks, bubbles present in the mixture can cause a poor texture making them unpleasant to use, as well as being more likely to break [3]. The inclusion of bubbles in cosmetic products serves mainly to change the texture by making the materials softer [4]. Additionally, bubbles might also make cosmetic products less aesthetically appealing whilst also inducing instability in the final product [1]. The factors that affect the stability of these bubbles are not widely understood.

As shown in Figure 1, bubbles present may be advantageous in some situations. As such, the behaviour of bubbles in these fluids needs to be investigated further to better understand their how they behave in specific applications. The velocity field and yielded region of the fluid around the bubble are both important in understanding how the bubbles affect fluid behaviour and vice versa.

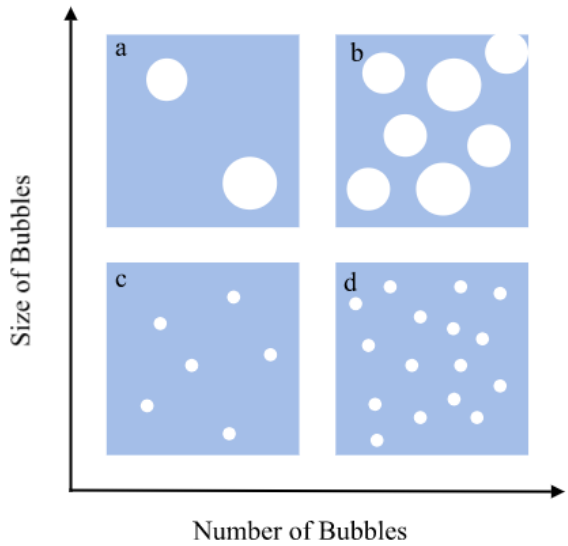

Figure 1: Different quantities and sizes of bubbles can be desired for various reasons. Possible applications are as follows. a) transparent gel like cosmetics for aesthetic reasons. b) aerated foods such as chocolate. c) generally undesirable due to coarse texture. d) ice cream and mousse products.

These velocity fields were studied by Mougin et al. who investigated the fluid dynamics in Carbopol gels resulting from bubble motion through the fluid using par-

ticle image velocimetry (PIV). Through PIV, they found that three zones exist as a consequence of bubble motion through the fluid; one where the particles are displaced, one where the particle distribution remains constant and one where the fluid remains stationary [5]. Ortiz et al. also imaged the velocity field when they looked at air, water, and oil droplets rising through a viscoelastic medium [6]. Similar studies were performed by Holenberg et al. and Firouznia et al. who extensively studied the velocity fields resulting from spherical particles moving under the influence of gravity in yield-stress fluids [7] [8].

Some researchers investigated the bubble characteristics rather than the fluid behaviour. Sirkoski et al. researched the velocity and shape of rising air bubbles through Carbopol ETD 2050. They examined how the shape of the bubble is affected by the magnitude of the yield stress and also attempted to understand the role elasticity plays. Their studies showed that in fluids with larger yield stresses bubbles have a larger length-to-radius aspect ratio making them less round and closer to an inverted teardrop shape. In addition, they found that the rise velocity and the bubble radius share a linear relationship [9].

More recently, Lopez et al. conducted a similar study, but instead examined the competing effects of inertia and elasticity on bubble shape by looking at the ratio of Reynolds and Deborah numbers. Stronger inertial forces were found to cause rounder bubble shapes [10].

Research has also been done on computationally simulating the yielded regions and velocity fields around rising bubbles and falling spheres in these yield-stress fluids. Tsamopoulos et al., and Singh and Denn, have both looked at modelling rising bubbles through yield-stress fluids, with both predicting an unyielded region near the equator of the bubble [11] [12]. The inverted teardrop shape seen in the experimental results was predicted in the simulations of Lind and Phillips, however the negative wake from experiments was not predicted [13] [5] [14].

These discrepancies between the experiments and model predictions are due to many conventional approximations made in fluid mechanics being no longer applicable in a yield-stress fluid which makes numerical simulations more challenging. In addition, since the yield surface is not known a priori simulating these phenomena is substantially more difficult [15].

Taking the experimental results of Holenberg et al. [7], Fraggedakis et al., created a computational model that matched the experimental results of the velocity field magnitude for a falling sphere [16]. However, the model still differed on the prediction of the yield surface from the experimental results.

In this study, we aim to relate the velocity field and shape of a bubble rising through a yield stress fluid. This will help in gaining a better understanding of the fluid dynamics and the major effects at play in the manufacturing processes. Ultimately this will aid in our ability to manipulate these bubbles in practical applications and therefore improve product quality and performance.

2 Theory

Flow curves and oscillatory tests were used to assess the rheological properties of the fluids. These are usually measured by either manipulating the shear stress applied and measuring the strain rate response or vice versa. Various models have been used in literature to fit experimental flow curve data. Amongst these is the Herschel-Bulkley model which is used to describe the flow curves of certain yield-stress fluids. This model has been shown to accurately fit the flow curves of Carbopol gels [17]. The Herschel-Bulkley model is given below:

$$\tau = \tau_0 + k\dot{\gamma}^n \tag{1}$$

In the above equation, τ is the shear stress,τ_0 is the yield stress, $\dot{\gamma}$ is the strain rate, k is the consistency index and n is the flow index. Due to the behaviour of yield-stress fluids, bubbles may remain stationary when the yield stress of the fluid is not matched (or exceeded) by the forces exerted by the bubble as it rises [2].

Oscillatory shear tests on the other hand are used to determine if a fluid exhibits elastic behaviour. The relative values of the storage and loss moduli indicate whether the fluid is capable of storing energy when strain is induced which would give an indication of the fluid's elastic characteristics. When the storage modulus (G') is larger than the loss modulus (G'') the fluid retains its microstructure and does not flow. When G'' is larger than G', the fluid flows. The shear rate at which these two values intersect is known as the flow point.

The shapes of bubbles in fluids can depend on a number of fluid properties. Dimensionless numbers have been used to describe the properties of these bubbles and can therefore give a reasonable description of the bubble shapes [5] [10].

In our analysis, these dimensionless numbers include the Reynolds number, Re, the Bond number, Bo, and the Bingham number, Bn. The following definitions were used to calculate these quantities:

$$Re = \frac{\rho v_0 R_{eff}}{\eta_c} \tag{2}$$

$$Bo = \frac{\rho g {R_{eff}}^2}{\sigma} \tag{3}$$

$$Bn = \frac{\tau_y}{\rho g L} \tag{4}$$

Where v_0 is the terminal rise velocity of the bubble, ρ is the fluid density, g is the gravitational constant, η_c

is the effective fluid viscosity, σ is the surface tension, R_{eff} is the effective radius, L is the bubble length and τ_y is the yield stress. The surface tension is taken to be $\sigma = 63mNm^{-1}$ as this was found in literature to be an average value for Carbopol gels [18]. R_{eff} is defined as follows:

$$R_{eff} = \sqrt[3]{W^2 L} \tag{5}$$

With W being the maximum width of the bubble. The definition of these numbers are similar to that of Lopez et al., however for the Bingham number we use the length instead of R_{eff} [10]. This is because the Bingham number is the ratio yield stress (proportional to the volume) and the buoyancy (proportional to the surface area). As the surface area in question is the cross sectional area, we use the length of the bubble in our computation of the Bingham number.

Each of the above numbers gives different insights into the characteristics of bubbles in these fluids. The Bond number compares the effects of buoyancy and surface tension on the bubble. At small Bond numbers, the bubble cannot deform from the spherical shape while at large Bond numbers, the bubble more easily squeezes through the fluid while adopting a more streamlined shape [11]. The Reynolds number compares the effects of inertia and viscosity of the bubble moving through the fluid. At low Reynolds number, the bubbles are nearly complete oblate spheroids while at higher values (and lower viscosity), the bubbles become a smaller segment of an oblate spheroid [19]. The Bingham number compares the effects of yield stress to viscous stress. As the Bingham number increases, the shape of the bubble becomes more elongated and the yield surface around the bubble shifts closer to the bubble, indicating that less fluid is deformed as the Bingham number increases [11].

3 Method

Carbopol 980 NF gels (manufactured by Lubrizol) of various concentrations (0.1 wt%, 0.0875 wt% and 0.075 wt%) were the fluids used in this research due to them exhibiting properties typical of yield-stress fluids [20]. Additionally, these fluids are transparent, easy to observe and their properties are well known. These Carbopol gels were prepared by mixing the appropriate measured weight of Carbopol 980 NF powder with 550 ml of water. The mixture was stirred using a high shear mixer for 30 minutes after which the solutions were neutralised using 50 ml of 37% sodium hydroxide solution in order to obtain a mixture with as close to a neutral pH as possible. After the neutralisation, the solution was left to mix using a high shear impeller at a rotation velocity of approximately 850 – 2000 rpm for about 24 hours. A vacuum pump was subsequently used to remove bubbles present in the fluid before the experiments were performed.

The rheological properties of the fluid were measured using an Anton Paar MCR 302 rheometer. A cone and plane geometry plate was used in the rheometer with a cone angle of 1°. Sandpaper was used to prevent wall slip by fixing it to the plates of the rheometer. Flow curves and oscillatory tests were then performed.

A container of dimensions 41.76mm x 49.67mm x 300mm was constructed from four PMMA plates. These plates were mounted on a 3D printed base (designed on AutoCAD) to ensure the it was structurally sound. A needle was inserted into the centre of the base for the injection of bubbles. Superglue and silicone glue were used to prevent leaks from the sides and base of the apparatus and a syringe was connected to the needle via a T-junction. A schematic of the experimental setup is shown in Figure 2.

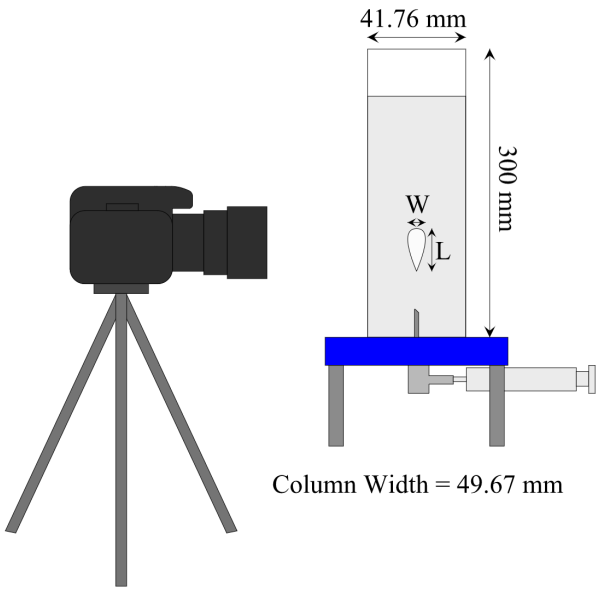

Figure 2: Schematic of the experimental setup which consisted of the camera, a transparent container, a needle and a syringe. The light source (not shown) varied between the two types of experiments; a white monitor screen was used for bubble behaviour experiments while a fibre optic light was used for PIV experiments.

For bubble behaviour experiments, a white screen was used behind the set up to provide homogeneous light while a Nikon D5300 camera and a Tamron 90mm macro f/2.8 lens were used to capture videos of the experiments. In the experiments, bubbles were injected manually and were filmed while rising. The fluid was stirred between each experiment then allowed to rest for 3 minutes to mitigate the effect of residual stresses [10].

The videos taken of the bubble rising were first converted into images and then analysed on MATLAB. De-

tection of the bubble boundary and the speed at which it moves through the fluid allowed numerous parameters, including the aforementioned dimensionless numbers listed, to be calculated.

The boundary of the bubble was detected and fitted to the following ellipse equation:

$$w(y) = W y^{\alpha}(h-y)^{\beta} \tag{6}$$

Where w is the width of the bubble, y is the position along the major axis in its local reference frame, W is the maximum width of the bubble, h is the length of the bubble, α the exponent governing the shape of the head, and β the exponent governing the shape of the tail. This equation is similar to that used by Sirkoski et al [9].

Visualisation of the velocity field and yielded region was done using PIV. This technique involves homogeneously mixing tracer particles in the fluid then subsequently using a light source and camera to illuminate these particles and simultaneously capture their movement and position [21].

In our PIV experiments, 6.0 milligrams of Sphericel® 110P8 hollow glass microspheres were mixed into the Carbopol gels using a high shear mixer then a vacuum pump was used to remove residual bubbles. A fibre optic light source was used to illuminate the PIV particles and the same camera was used to capture the motion of the bubbles injected as well as motion of the PIV particles.

The videos of PIV experiments were also converted to images. These images were then processed on MATLAB using an improved technique that changes the reference frame of the video to one on the bubble which enabled the tracking of particles. The PIVlab [22] application on MATLAB was then used to split each image into a grid-like array in which groups of particles were tracked. Velocity fields were then generated between each pair of images analysed which were then averaged throughout the entire video to produce a mean velocity field.

More specific information on the data processing in MATLAB can be found in the supplementary information.

4 Results and Discussion

4.1 Rheology of Fluids Used

Shear response and oscillatory tests were conducted on each fluid used. The shear stress response of the fluid was measured and the flow curves in Figure 3 were obtained. This figure also shows the results of the frequency sweep tests that collected data on the storage and loss moduli.

The averaged results from the rheological tests and the parameters used to model the flow curves in the Herschel-Bulkley model are summarised in Table 1.

Oscillatory tests were used to characterise the elastic behaviour of the fluid. Figure 3 shows the resulting stress response from an ascending imposed shear rate and a descending imposed shear rate for each of the three Carbopol gel solutions used. The ascending and descending tests all show slight discrepancies from each other which indicate that the stress response is dependent on previously imposed shear rates. This dependency on the previous state of the fluid indicates that the fluid exhibits mild thixotropic behaviour. The presence of thixotropy meant that the stresses in the fluid needed to be fully relaxed in between experiments. A rest period of three minutes was used between bubble injections to mitigate this effect.

Table 1: Summarised results of rheological tests. Average values were calculated for the Herschel-Bulkley parameters and the storage and loss moduli for each of the Carbopol solutions prepared.

Concentration	τ_y (Pa)	n (-)	k (Pa)	G' (Pa)	G'' (Pa)
0.1%	6.40	0.44	3.06	43.8	8.07
0.0875%	2.65	0.47	1.37	59.4	20.5
0.075%	1.02	0.47	1.09	9.63	2.71

The plot of the storage and loss moduli against frequency (Figure 3) show that the storage moduli lie above the loss moduli in the linear regime of the frequency sweep (which is the region where the fluid is not yet flowing). This result is similar to that obtained by Lopez et al. [10].

The results in Table 1 show that for an increase in Carbopol concentration, the yield stress increases. This is expected as the microstructure formed by the polymer molecules becomes more tightly packed together as the concentration increases since the Carbopol particles are more compactly arranged upon interaction with water.

4.2 Bubble Behaviour Experiments

The dimensionless numbers in Figure 4 correspond to the results published by Lopez et al. [10], where a similar trend is observed for individual fluids but no master curve exists to relate the numbers studied as functions of each other. As there is no key link between the Reynolds, Bond and Bingham numbers, it is clear that there are other factors affecting how the bubble moves through the fluid other than just the buoyancy, inertia, viscosity, and yield stress.

All the experiments were conducted at low Reynolds numbers; the largest of which was 1.29. The small values of Reynolds number indicate that the inertial forces are almost negligible compared to the viscous forces. From this we can conclude that inertia does not significantly affect the behaviour and shape of the bubbles in comparison to the viscosity for the set of experiments conducted

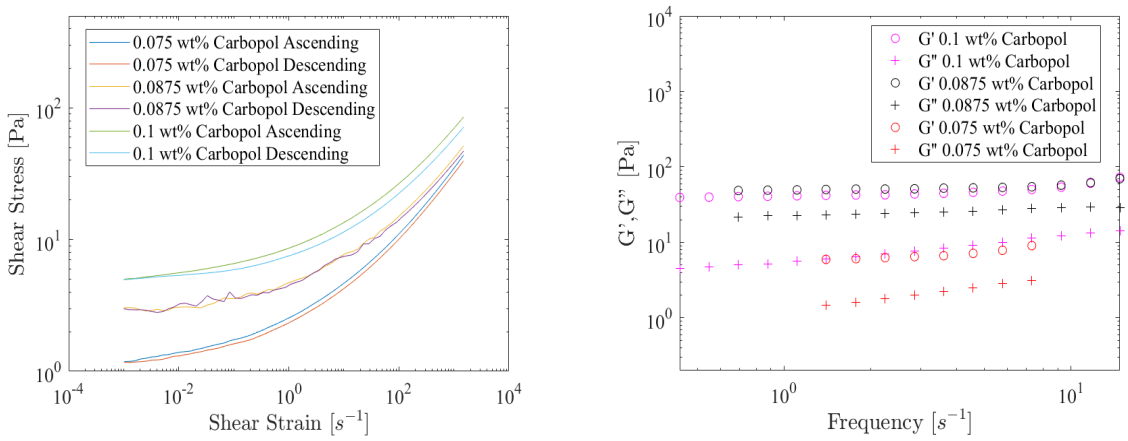

(a) **(b)**

Figure 3: (a) The flow curves measured for each fluid experimented on, (b) the average storage and loss moduli estimated for each fluid used using the range of characteristic strain rates of each fluid used.

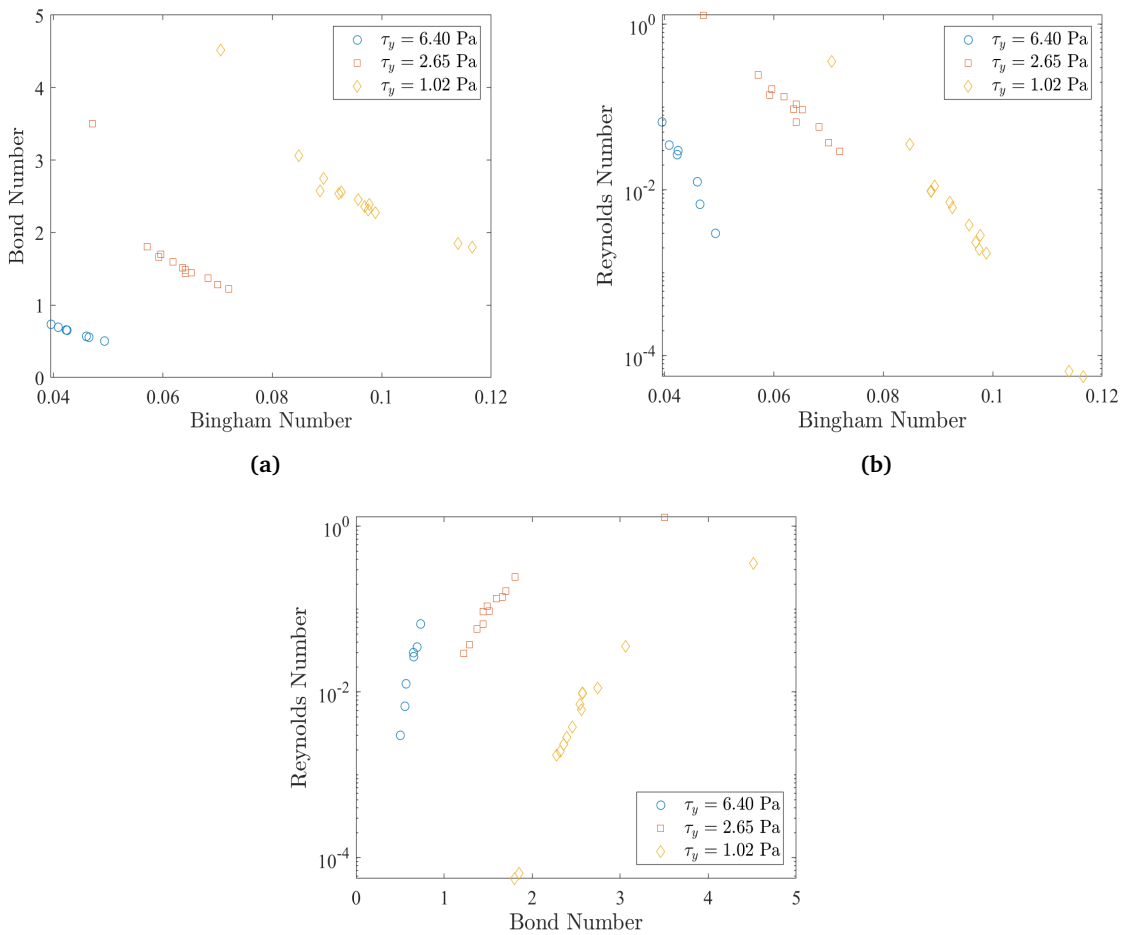

(a) **(b)**

(c)

Figure 4: Plots of the three key dimensionless numbers studied for the three Carbopol concentrations examined: (a) the Bond number against the Bingham number, (b) the Reynolds number against the Bingham number, (c) the Reynolds number against the Bond number.

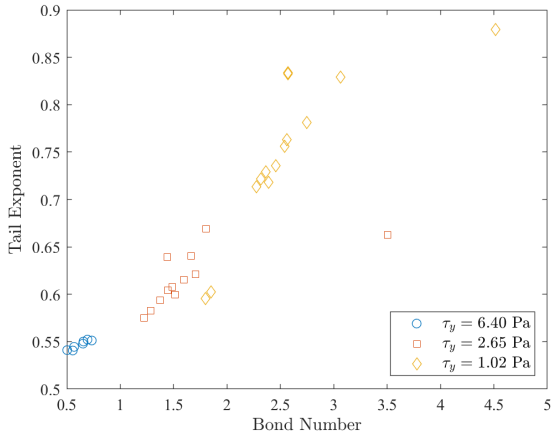

Figure 5: Tail exponent from the ellipse equation against the Bond number for all the concentrations of Carbopol used.

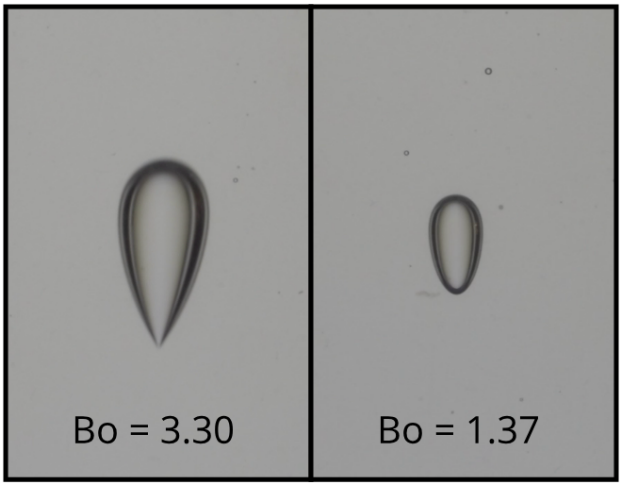

Figure 6: Photos of two bubbles within the same fluid with τ_y = 6.40 Pa. The two bubbles have different volumes and Bond numbers with the one on the right having a rounder shape.

in this research.

The relationship between the Bond number and the shape of the bubble tail (through the tail exponent) is shown in Figure 5. From the graph, we see that the tail exponent can be expressed as a monotonic function of the Bond number and that a master curve exists across all the fluids used. The gradient appears to increase initially and subsequently decreases again, although more experimental data would be needed to draw conclusions about this.

Since the surface tension is constant in all three fluids, the buoyancy is the key variable that changes in the Bond number. Bubbles with larger volumes have larger buoyancy forces and pointier bubble shapes are observed. This is further illustrated in Figure 6 where we can see that within the same fluid, bubbles with different volumes have different Bond numbers and different shapes. We can directly see the results of Figure 5; lower Bond numbers mean a rounder shape.

4.3 Particle Image Velocimetry

After processing the results for the PIV experiments on MATLAB, three main plots were obtained. These are the mean velocity field plots, the before and after displacement vector plots and the strain rate field plots, shown in Figures 7, 8 and 9 respectively.

4.3.1 Velocity Fields

Through data processing of PIV videos we calculated mean velocity field plots for each bubble rise experiment, an example of which is seen in Figure 7. These plots had several key features. This included phenomena like the negative wake and stagnation zone behind the bubbles; both features of which have been observed in yield stress fluids. Herrera-Velarde et al. observed negative wakes while studying bubbles rising through a yield stress fluid when the volume of the bubble was above some critical volume, and Holenberg et al. observed stagnation zones behind falling spheres in Carbopol gels [14] [7]. At the sides of the bubbles, the fluid exhibited regions of recirculation where the fluid moved from the top to the bottom of the column. Similar zones of recirculation were observed by Mougin et al. [5] and in the computational model of Lind and Phillips [13]. On these velocity field plots, there were also regions far away from the bubble with no apparent velocity. These regions were especially important as the negligible velocity implied that this particular region of the fluid had not been affected by the motion of the bubble or had not yielded. Characterising the size of the region that yielded due to the motion of the bubble combined with inertial forces is particularly important. To further investigate the extent of this region, displacement vector fields and strain rate fields were studied.

4.3.2 Displacement Fields

Figure 8 is an example of a typical before and after displacement vector field which shows an estimate of the extent of the yielded region of the fluid. The image is rotated, with the top of the column being on the right hand side of the image. Particles far away from the bubble path have not moved significantly and are considered unyielded. The resulting displacement fields are similar to those published by Mougin et al. [5].

The transition region between the yielded and unyielded regions is difficult to estimate using this analysis. This is because the particles in the transition region could have moved and returned to their original position

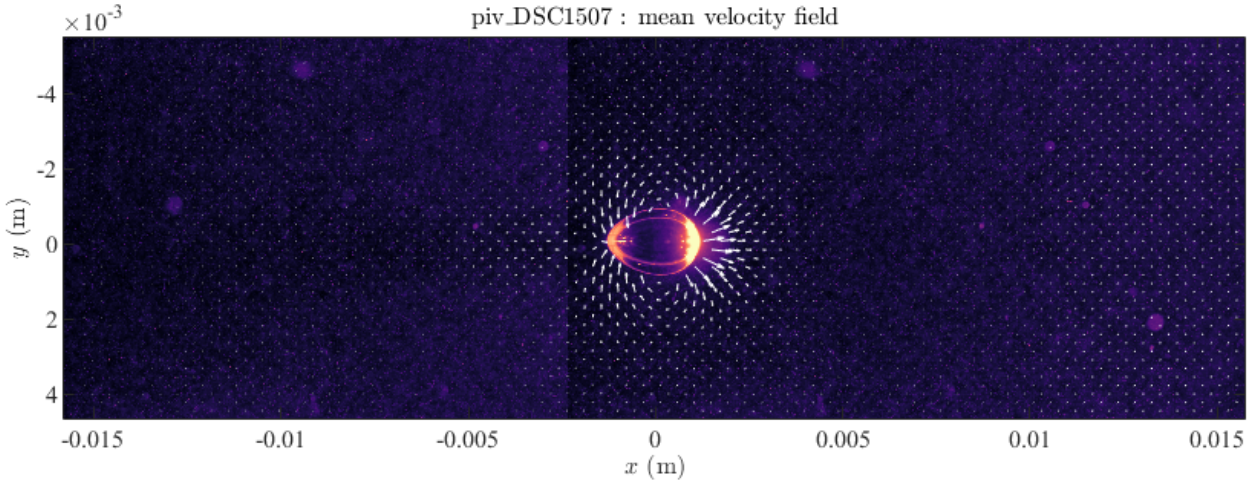

Figure 7: Resultant mean velocity field caused by the motion of the bubble. The image is rotated, with the top of the column being on the right hand side of the image. This was generated from PIV experiments by averaging through every frame of the video of the bubble rising.

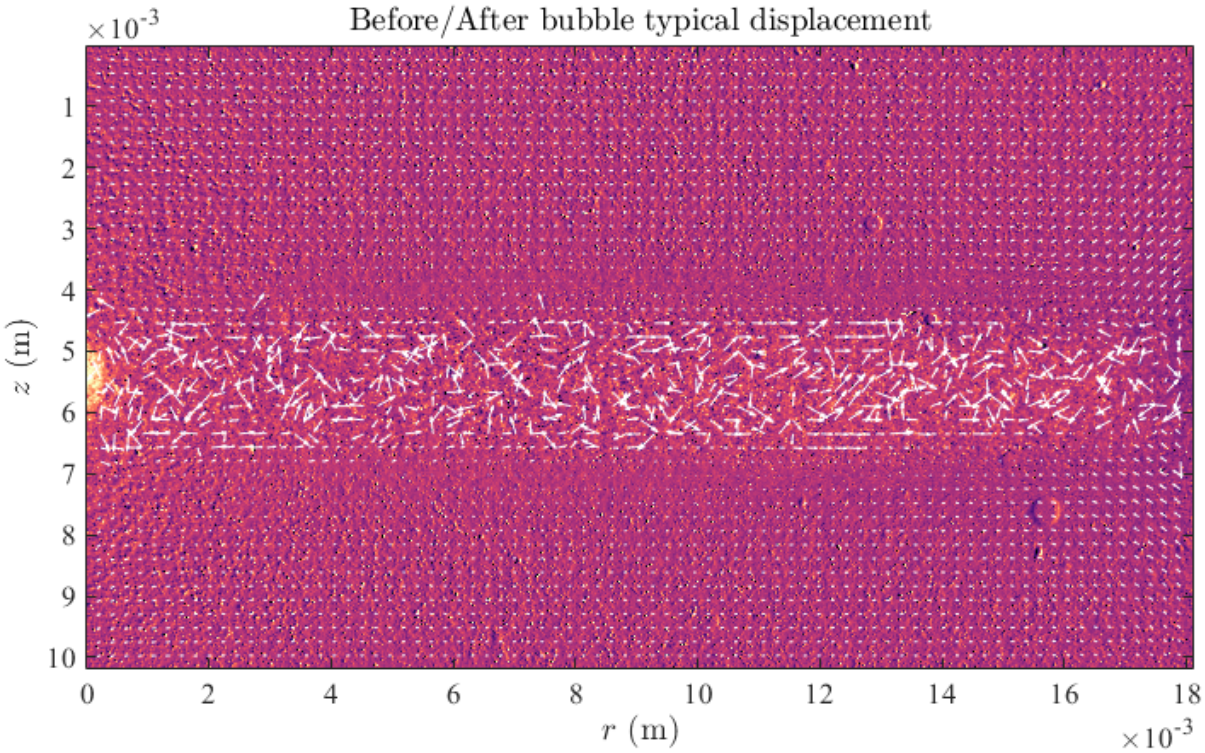

Figure 8: Resultant before and after displacement vector field caused by the motion of the bubble. The image is rotated, with the top of the column being on the right hand side of the image. This vector field shows the motion of particles between two images; one taken before the bubble moves through the fluid and one taken after it has moved through the fluid.

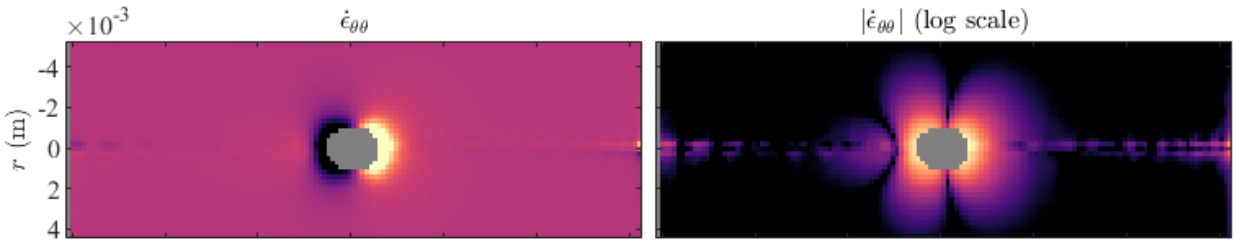

Figure 9: Resultant strain rate field caused by the motion of the bubble. Similar to the previous two figures, the image is rotated, with the top of the column being on the right hand side of the image. The plot shows the radius plotted against the $\dot{\gamma}_{\theta\theta}$ component of the strain rate tensor.

in before and after plots like this one. On these plots, the particles would be characterised as unyielded even though they have moved due to the fluid yielding. For this region, Mougin et al. describe a yielded region where the particle distribution remains the same which captures the particles that have returned to their original positions [5]. A more precise definition of the yielded region can be obtained through comparison with the strain rate field.

4.3.3 Strain Rate Fields

The plots of the strain rate fields generated on MATLAB and shown in Figure 9 indicate the regions of the fluid that experience a tension or compression. Similar to the before and after displacement vector field plots, this plot gives an estimate of the extent of the yielded region of the fluid caused by the inertia of the bubble. By examining the $\dot{\gamma}_{\theta\theta}$ the size of the yielded region can be estimated. This estimate can then be compared to the before and after displacement field to more precisely define the yielded region using more statistics.

5 Conclusion

We have experimentally studied the behaviour and shapes of bubbles rising in Carbopol gel. Through analysis of the bubble rise experiments we have found no clear trend between the Reynolds, Bingham and Bond numbers. This indicates that there are other significant parameters at play other than the viscous stresses, buoyancy, yield stresses and inertia, which influence the behaviour of the fluid. Additionally, the tail exponent defined in the shape fitting of the bubble was found to be a monotonic function of the Bond number, and consequently the shape of the bubble only depended on the Bond number.

Through particle image velocimetry combined with analysis on MATLAB, velocity fields were measured around bubbles rising through the Carbopol gels. These velocity fields were found to contain classic characteristics of yield stress fluids such as the stagnation region, negative wake and regions of recirculation. An estimate of the size of the yielded region around bubbles of various sizes was determined using before and after displacement fields and strain rate fields which were also developed through analysis on MATLAB. The displacement fields were found to match results obtained by other researchers.

In order to better characterise the behaviour of these bubbles and fluids, more dimensionless parameters should be studied in order to better understand the major effects at play. These possibly could include the effect of elasticity and drag. A more rigorous definition of the yielded region can be obtained in future works through comparison of the strain rate fields and the before and after displacement vector fields which will in turn help to determine the yield surface.

6 Acknowledgements

This research would not have been possible without the help of Brice Saint-Michel, who we are incredibly grateful to.

References

[1] Tong Joe Lin. Mechanisms and control of gas bubble formation in cosmetics. *Journal of the Society of Cosmetic Chemistry*, 22:323–337, 1971.

[2] N. Dubash and I.A. Frigaard. Propagation and stopping of air bubbles in carbopol solutions. *Journal of Non-Newtonian Fluid Mechanics*, 142(1):123 – 134, 2007. Viscoplastic fluids: From theory to application.

[3] D. Williams and W. Schmitt. *Chemistry and Technology of the Cosmetics and Toiletries Industry*. Springer Netherlands, 2 edition, 1996.

[4] Sato Tomoko, Matsuzaki Fumiaki, and Yanaki Toshio. Whipped o/w emulsion cosmetic and processes for producing the same, 2003.

[5] Nicolas Mougin, Albert Magnin, and Jean-Michel Piau. The significant influence of internal stresses

on the dynamics of bubbles in a yield stress fluid. *Journal of Non-Newtonian Fluid Mechanics*, 171-172:42 – 55, 2012.

[6] Julia S. Ortiz, Susana L.and Lee, Bernardo Figueroa-Espinoza, and Baltasar Mena. An experimental note on the deformation and breakup of viscoelastic droplets rising in non-newtonian fluids. *Rheologica Acta*, 55(11):879–887, Dec 2016.

[7] Yulia Holenberg, Olga M. Lavrenteva, Uri Shavit, and Avinoam Nir. Particle tracking velocimetry and particle image velocimetry study of the slow motion of rough and smooth solid spheres in a yield-stress fluid. *Physical Review E*, 86(6), 2012.

[8] Mohammadhossein Firouznia, Bloen Metzger, Guillaume Ovarlez, and Sarah Hormozi. The interaction of two spherical particles in simple-shear flows of yield stress fluids. *Journal of Non-Newtonian Fluid Mechanics*, 255:19 – 38, 2018.

[9] Darek Sikorski, Hervé Tabuteau, and John R. de Bruyn. Motion and shape of bubbles rising through a yield-stress fluid. *Journal of Non-Newtonian Fluid Mechanics*, 159(1):10 – 16, 2009.

[10] William F. Lopez, Mônica F. Naccache, and Paulo R. de Souza Mendes. Rising bubbles in yield stress materials. *Journal of Rheology*, 62(1):209–219, 2018.

[11] J. Tsamopoulos, Y. Dimakopoulos, N. Chatzidai, G. Karapetsas, and M. Pavlidis. Steady bubble rise and deformation in newtonian and viscoplastic fluids and conditions for bubble entrapment. *Journal of Fluid Mechanics*, 601:123–164, 2008.

[12] John P. Singh and Morton M. Denn. Interacting two-dimensional bubbles and droplets in a yield-stress fluid. *Physics of Fluids*, 20(4):040901, 2008.

[13] S.J. Lind and T.N. Phillips. The effect of viscoelasticity on a rising gas bubble. *Journal of Non-Newtonian Fluid Mechanics*, 165(15):852 – 865, 2010.

[14] J.R Herrera-Velarde, R Zenit, D Chehata, and B Mena. The flow of non-newtonian fluids around bubbles and its connection to the jump discontinuity. *Journal of Non-Newtonian Fluid Mechanics*, 111(2):199 – 209, 2003.

[15] Daniel Bonn and Morton M. Denn. Yield stress fluids slowly yield to analysis. *Science*, 324(5933):1401–1402, 2009.

[16] D. Fraggedakis, Y. Dimakopoulos, and J. Tsamopoulos. Yielding the yield-stress analysis: a study focused on the effects of elasticity on the settling of a single spherical particle in simple yield-stress fluids. *Soft Matter*, 12:5378–5401, 2016.

[17] P. Coussot. Yield stress fluid flows: A review of experimental data. *Journal of Non-Newtonian Fluid Mechanics*, 211:31 – 49, 2014.

[18] Loren Jørgensen, Marie Le Merrer, Hélène Delanoë-Ayari, and Catherine Barentin. Yield stress and elasticity influence on surface tension measurements. *Soft Matter*, 11:5111–5121, 2015.

[19] D. Bhaga and M. E. Weber. Bubbles in viscous liquids: shapes, wakes and velocities. *Journal of Fluid Mechanics*, 105:61–85, 1981.

[20] S.J. Curran, R.E. Hayes, A. Afacan, M.C. Williams, and P.A. Tanguy. Properties of carbopol solutions as models for yield-stress fluids. *Journal of Food Science*, 67(1):176–180, 2006.

[21] Ajay K Prasad. Particle image velocimetry. *Current Science-Bangalore-*, 79(1):51–60, 2000.

[22] William Thielicke and Eize J. Stamhuis. PIVlab – towards user-friendly, affordable and accurate digital particle image velocimetry in MATLAB. *Journal of Open Research Software*, 2, oct 2014.

Technoeconomic Analysis: Modelling and Evaluating the Co-Electrolysis of CO_2 and H_2O for Syngas Production

Dugald Fraser, George Savage
Department of Chemical Engineering, Imperial College London, U.K.

Abstract
An alternative route to syngas production for use in the methanol industry has been analysed. The primary production method is currently steam reforming and this has been compared to the emerging technology of H_2O/CO_2 co-electrolysis. A quasi 2d model of a solid oxide electrolyser cell (SOEC) for the electrochemical conversion of H_2O and CO_2 was created using gPROMS software. The model used a potential balance, incorporating Nernst potentials, activation overpotentials and the Ohmic overpotential to describe the electrochemistry. Mass transfer was modelled by the Dusty Gas model and convection. The results of the model were extracted for economic analysis. Based purely on economic viability, under current environmental legislation in most countries, steam reforming is significantly more attractive, with a levelized lifetime cost totalling 38% of that for co-electrolysis. When introducing other financial metrics, the co-electrolysis process performs relatively better. Evaluating the social cost of carbon (SCC), considering the costs to the economy of CO_2 release, revealed replacement of steam reforming with co-electrolysis could positively impact a country's economy in the long term. The savings from the mitigated CO_2 release are 45% higher than the lifetime costs for co-electrolysis for the median country-level SCC. It has also been shown that the introduction of a realistic level of carbon tax, £78/tCO_2, would make the co-electrolysis process financially favourable in the best-case performance scenario.

Introduction
With increasing levels of atmospheric CO_2 causing adverse environmental effects, society has demanded a reduction in the release of CO_2 in industry. The main method of achieving this is reducing the amount of fossil fuel usage. However, due to economic reasons, fossil fuel usage shows no sign of decreasing in the near future [1]. The introduction of new extraction technologies, such as hydraulic fracturing ('fracking'), to extract unconventional resources such as shale gas further reinforces this claim [2]. Carbon capture and storage was proposed as a method to reduce CO_2 emissions from fossil fuel combustion in power plants. However, this process does not provide a complete solution due to its high investment costs, uncertainty about its storage capacity and the potential for leakage [3]. This led to the industry turning to carbon capture and utilisation (CCU) to provide a solution by using CO_2 for industrial processes, as it can offset the costs for carbon capture and add value to the waste CO_2 produced from coal power plants [2].

Renewable energy sources provide an alternative to fossil fuel usage. However, the two most promising sources of renewable energy, wind and solar, pose a problem of intermittency due to weather variations. This can lead to sudden increases in energy production, but can be such a large increase that it exceeds the demand and causes negative energy prices [4]. Fossil fuel and nuclear power stations avoid this by varying the energy production of the plant to meet the varying demand of electricity at different times of day. For renewable sources, storage of electrical energy is required to solve this intermittency problem, however, large scale storage of electrical energy has been proven to be difficult. A solution to this is converting the electrical energy into chemical energy within liquids, which can be stored and transported more easily than in vapour form [2].

A potential liquid for this purpose is methanol, the simplest C_1 liquid product, which can easily be produced from synthesis gas (syngas) [5], a mixture of CO and H_2. Fig. 1 shows a schematic of the possible uses of syngas, which mainly come from producing methanol [6]. Methanol is a liquid that is widely used in industry, mainly as a feedstock for formaldehyde, MTBE, acetic acid and olefins which can be further processed to make hydrocarbons. It also has potential uses in transport, due to its high octane number compared to petrol in internal combustion engines [7]. Market research has shown that the global demand for methanol is rapidly increasing. This is largely due to China's huge increase in demand for methanol derivatives, mainly olefins. Demand is expected to increase from 49 million metric tonnes (MMT) in 2010 to 95 MMT in 2021 [8]. These factors make the process of conversion to methanol more economically viable.

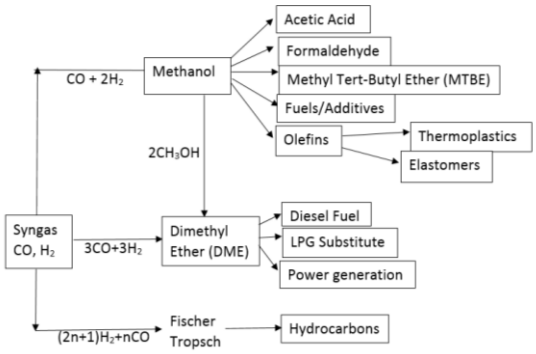

Fig. 1 [16] *Schematic of possible uses for syngas.*

Unfortunately, the dominant process for syngas production today is steam reforming of natural gas [5]. This process uses fossil fuels and leads to a net

production of CO_2 caused by heating duties and by the water gas shift reaction (WGSR), needed for producing syngas with a higher H_2:CO ratio [5]. The focus of this study is to provide an economic analysis on a CCU alternative to steam reforming of natural gas for syngas production. The alternative investigated is electrochemical reduction of CO_2, with the electrical supply coming from renewable energy sources. The type of cell used extensively in research for this type of electrolysis, is the solid oxide electrolyser cell (SOEC).

Background

Modelling of Co-Electrolysis

The use of co-electrolysis of CO_2 and H_2O was first investigated in the 1960s as a method for O_2 production [9], as the produced oxide ions from the electrolysis of CO_2 and H_2O can combine to produce an oxygen molecule. This would have been a useful application in conditions of low oxygen availability, such as spacecrafts and submarines. However, it was not until recently that this process was investigated for applications in CCU.

Hankin et al [10] investigated methanol and dimethyl ether (DME) production from carbon dioxide and water. Their studies involved analysing four different processes for methanol/DME production, that were: methanol synthesis, direct DME synthesis from syngas, and two step DME synthesis with methanol as an intermediate, with and without recycle of unconverted syngas. The processes were analysed in terms of energy efficiency and CO_2 emissions. The direct DME synthesis process was found to have the highest energy efficiency with the lowest carbon emissions. However, it was stated that DME synthesis in industry still mainly takes place in a two-step process with methanol as an intermediate. Our study therefore was chosen to be based on methanol production. Their investigation also came to the conclusion that CO_2 can be utilised directly to produce DME, however conversion of CO_2 to CO is necessary for methanol production. In terms of the correct H_2:CO ratio of syngas for methanol production, a ratio of 2, in line with the stoichiometric ratio, was found to be the most effective. Finally, high temperature co-electrolysis of H_2O and CO_2 was identified as the best technology for CO based syngas production in terms of energy efficiency and CO_2 conversion, hence this study is based on this technology.

Among the first investigators of co-electrolysis were Fu et al. [11], who carried out a techno-economic analysis on high temperature CO_2/H_2O co-electrolysis using a SOEC. Their approach to modelling of the process was estimating the outlet flows of CO and H_2 from the stoichiometric coefficients of each reactant and product. Their study showed the benefit of conducting the electrolysis process at high temperature, as higher temperatures reduce the electricity demand due to increased electrolyser conductivity and heating duties being much cheaper than electrical energy [10]. It also showed the benefits of conducting co-electrolysis as opposed to electrolysis of H_2O and CO_2 separately, stating that co-electrolysis of H_2O and CO_2 together provide benefits of increased CO_2 reduction due to the WGSR. CO_2 reduction on its own also adds a risk of carbon deposition on the cathode, reducing its efficiency. Another reason for using co-electrolysis is that the widely utilised Ni catalyst, used for the cathode, performs worse with CO_2 than with H_2O, so electrolysing a mixture of H_2O and CO_2 would increase the performance of the process [11]. For their economic analysis, they based their parameters on current data of solid oxide fuel cell (SOFC) technology. This study, however, only modelled the conversions of H_2O and CO_2, it did not investigate how different phenomena, such as the rate of WGSR, would affect the outlet syngas production.

Menon et al [12] modelled the CO_2/H_2O co-electrolysis process with more consideration of the physical phenomena occurring inside the SOEC. The model included mass transfer of the components through the cathode and electrochemistry to describe the charge transfer occurring between the components. For the electrochemistry, a potential balance was formulated considering the cell overpotentials that occur during operation. Charge transfer was only modelled at the triple-phase boundary of the electro-catalyst, electrolyte and gas phase, not throughout the entire electrode utilisation region. The potential balance involves the Nernst potentials for the reversible cell voltage and the Butler-Volmer equations for the activation overpotentials. Mass transport in the electro-catalyst was modelled using multi-component diffusion in one dimension along the electro-catalyst depth with WGSR. The dusty gas model (DGM) was used for this, as this model describes the required mass transport well [13].

Menon et al. [14] later investigated the use of SOECs again for H_2O and CO_2 electrolysis. The same concepts for electrochemistry were used and the variation of component molar fluxes inside the cathode pores were again modelled by the DGM. However, this time, a quasi 2d model was implemented to include a gas flow channel above the cathode. The channel was only modelled in 1 dimension along its length, thus neglecting changes in concentration along the height and width dimensions. The channel height was also modelled to be small enough that plug flow occurs in the channel. The investigation showed the importance of selection of the inlet gas velocity, stating that a velocity too low would decrease the amount of reactant available at the electrolyte interface, however a velocity too high would lead to

accumulation of unreacted gas, as the gas consumption is limited by the cell voltage.

Ni et al. [15] also modelled a SOEC using a potential balance for the electrochemistry and the DGM for diffusion. Common occurrences in previous models are potential balances with the Nernst, activation and Ohmic overpotentials to model the cell irreversibilities, required cell voltage and current density values. Using the DGM for mass transfer also occurred frequently. The model produced by Ni et al. includes all of these components, therefore it was used as a basis for the model in this study. Previous work of modelling a SOEC had a purpose of investigating different operating conditions on the output of the cell. However, little investigation has been carried out on extending a detailed model including different physical phenomena to an economic analysis on the cell to investigate the cell feasibility. This is therefore the focus of this paper.

Economic Analysis

SOEC co-electrolysis technology has not yet been fully commercialised so there is little data on the costs involved with its implementation. However, a number of smaller and pilot scale CO_2 to methanol facilities exist using H_2 obtained through water electrolysis [16]. One of the largest in operation is the George Olah CO_2 to renewable methanol plant in Iceland. With a capacity of 50,000 litres a year, it cost £6.2M. This production rate is 3 orders of magnitude smaller than standard commercial scale renewable methanol facilities planned across Europe, so economic data may not completely align [17]. Fortunately, a large amount of costing data is available for solid oxide fuel cells (SOFCs). These operate in the reverse manner to a SOEC, producing electricity through the oxidation of fuels [18]. They share largely the same structure and catalyst materials so can be produced at a similar cost.

The cost of raw materials must also be considered under the economics of the plant. Water can be sourced readily and at negligible cost, however CO_2 must be obtained from dilute sources, generally flue gas. Carbon capture technology is relatively further developed than that of the SOEC. The world's largest carbon capture facility came online at the 240MW, W.A. Parish Generating Station in 2018 [19]. This technology clearly has the scope for expansion and has been examined in the context of co-electrolysis previously [20].

The main motivation for switching to co-electrolysis technology, aside from potential economic benefits, is CO_2 emission reduction. The CO_2 captured for processing would otherwise be emitted into the atmosphere. The global methanol demand can be used to quantify the potential for CO_2 reduction through the implementation of this technology. Reduction in emissions could result in financial gain. Many countries are introducing carbon taxation and carbon trading schemes [21]. It is also possible to quantify a social cost of carbon (SCC) which is evaluated as the economic damages from CO_2 emissions [22].

Methods

Process Overview

Fig. 2 shows a schematic of the process. At the cathode end, H_2O and CO_2 flow in through the gas flow channel located above the cathode catalyst bed. Some of the H_2O and CO_2 then flow through the catalyst pores from the cathode surface (y=0) to the electrolyte ($y=d_c$), where they are both reduced to H_2 and CO, shown by equations (1) and (2). The WGSR also occurs inside the cathode catalyst pores, with the equilibrium reaction shown by equation (3).

$$H_2O + 2e^- \rightarrow H_2 + O^{2-} \quad (1)$$

$$CO_2 + 2e^- \rightarrow CO + O^{2-} \quad (2)$$

$$H_2O + CO \rightleftharpoons H_2 + CO_2 \quad (3)$$

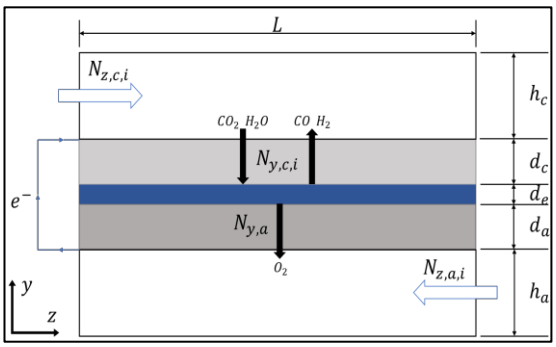

Fig. 2 Schematic of the overall process. Where $N_{Z,C,i}$ is the molar flux of component i in the z direction inside the flow channel of the cathode, c. $N_{Y,C,i}$ is the molar flux of component i in the y direction inside the electrode of the cathode. a is the anode. e is the electrolyte. d is the thickness of the electrode/electrolyte. h is the height of the gas flow channel.

These newly formed molecules then flow up the pores back to the gas flow channel. The O^{2-} ions produced in the process then move through the electrolyte to the anode, where they are oxidised to form an oxygen molecule, shown by equation (4). This oxygen molecule flows through the anode catalyst pores to the anode gas flow channel.

$$2O^{2-} \rightarrow O_2 + 4e^- \quad (4)$$

This study involved modelling the SOEC to determine the cell dimensions and current density values required for a certain syngas production rate. Also, to determine a specific feed composition for the desired H_2:CO ratio of 2 for methanol production. Due to its suitability for process simulation and for dynamic models with numerous variables and interlinked equations, gPROMS was chosen to model the process.

Electrochemistry

To model the electrochemistry of the process, a potential balance was used, shown by equation (5) [15].

$$V = E_i + \eta_{act,c,i} + \eta_{act,a} + \eta_{ohmic} \quad (5)$$

Where V is the applied cell potential. There are two electrolysis reactions occurring, one for CO_2 and one for H_2O, therefore there is a potential balance for both reactions. This is represented by the i term indicating the H_2 or CO reaction. The applied potential difference must be satisfied for both reactions as it is an inherent property of the electrons within the cell (i.e. $V_{H2}=V_{CO}$).

The E term in equation (5) represents the Nernst potential of each reaction, occurring due to concentration differences between the bulk gas and at the cathode-electrolyte interface, shown by equations (6) and (7) [15].

$$E_{H_2} = E^0_{H_2} + \frac{RT}{2F}\ln\left[\frac{P^I_{H_2}\left(P^I_{O_2}\right)^{\frac{1}{2}}}{P^I_{H_2O}}\right] \quad (6)$$

$$E_{CO} = E^0_{CO} + \frac{RT}{2F}\ln\left[\frac{P^I_{CO}\left(P^I_{O_2}\right)^{\frac{1}{2}}}{P^I_{CO_2}}\right] \quad (7)$$

The E^0 term, which represents the Nernst potential under standard conditions, can be calculated from thermodynamics. However, in this model it is approximated by a linear relationship with temperature, used from experimental data at 600K and 1200K, shown by equations (8) and (9) [15].

$$E^0_{H_2} = 1.253 - 0.00024516T \quad (8)$$

$$E^0_{CO} = 1.46713 - 0.0004527T \quad (9)$$

P^I_i represents the partial pressure of component i at the interface, I. It is important to note that the oxygen partial pressure at the interface remains constant due to air being in excess in the anode flow channel.

Next, there are the activation overpotentials, η_{act}, required for electron transfer between the electrode and analyte, shown by equations (10) and (11) [15]. This was modelled by the linearised Butler-Volmer equations, linearised due to previous experimentation showing that activation overpotential varies linearly with current density [15].

$$\eta_{act,i,c} = \frac{RTJ_i}{2FJ^0_i} \quad (10)$$

$$\eta_{act,O_2,a} = \frac{RTJ_{O_2}}{4FJ^0_{O_2}} \quad (11)$$

$$J_{O_2} = J_{H_2} + J_{CO} \quad (12)$$

Where i, again, represents H_2 or CO. c is the cathode and a is the anode. J_i represents the current density of H_2 or CO production. J^0 is the exchange current density and F is Faraday's constant. The current in the anode side, J_{O_2}, which is the oxygen current density, is equal to the sum of the current densities of the two reactions, due to oxygen being formed by the electrochemical reactions of both H_2O and CO_2, this is shown by equation (12).

Finally, there is the Ohmic overpotential, η_{ohmic}, due to the electric resistance of the electrolyte. Equation (13) represents this term [15].

$$\eta_{ohmic} = 2.99 \times 10^{-5} J_{O_2} L\, exp\left(\frac{10300}{T}\right) \quad (13)$$

Where L is the electrolyte thickness.

Mass Transfer

H_2O and CO2 enter the cathode and are consumed at the electrolyte interface. The movement of these components to the interface was modelled by multi-component, 1 dimensional diffusion through a porous material with reaction. The DGM was therefore used, shown by equations 14 and 15 [15].

$$\frac{\varepsilon}{RT}\frac{\partial(y_iP)}{\partial t} = -\frac{dN_i}{dy} + R_i \quad (14)$$

$$\frac{N_i}{D^{eff}_{i,k}} + \sum_{j=1,j\neq i}^{n}\frac{y_jN_i - y_iN_j}{D^{eff}_{ij}} = -\frac{P}{Rt}\frac{dy_i}{dy} \quad (15)$$

The reaction diffusion equation shown by (14) for each component along the cathode depth is used to model diffusion and WGSR occurring simultaneously. Where N_i is the molar flux of component i, R_i is the rate of production of component i in the WGSR, ε is the cathode porosity, R is the molar gas constant, T is the temperature, y_i is the mole fraction of component i, y is the distribution domain along the cathode thickness and P is the pressure. Equation (15) represents the multi-component part of the diffusion model. $D^{eff}_{i,k}$ is the effective Knudsen diffusion coefficient for component i and D^{eff}_{ij} is the effective binary diffusion coefficient of components i and j.

The rate of WGSR, R_i, is given by the kinetic equation (16).

$$R_{WGSR} = k_{sf}\left(P_{H_2O}P_{CO} - \frac{P_{H_2}P_{CO_2}}{K_{ps}}\right) \quad (16)$$

The boundary conditions for the flux at the cathode-electrolyte interface, dc, are shown by equations (17) and (18), relating the flux of each component to the current densities, therefore relating the mass transfer component of the model to the electrochemistry component [15].

$$N_{H_2}|_{y=dc} = -\frac{J_{H_2}}{2F}, N_{H_2O}|_{y=dc} = \frac{J_{H_2}}{2F} \quad (17)$$

$$N_{CO}|_{y=dc} = -\frac{J_{CO}}{2F}, N_{CO_2}|_{y=dc} = \frac{J_{CO}}{2F} \quad (18)$$

Where y is the distribution domain along the cathode thickness.

As the oxygen mole fraction at the anode was modelled to be constant, no mass transfer model was implemented for the anode.

All parameters and variables used in the model and the equations needed to calculate the diffusion coefficients and WGSR rate constants can be found in Ni's paper [15].

Quasi 2D Model

To minimise the gas separator cost, most of the CO_2 needs to be converted within the electrolyser. It is unreasonable to assume this can be achieved with 1d flow, as this would mean the cell must work in batch operation. The 1d model must be converted to a quasi 2d model by incorporating the gas flow channel above the electrodes. This conversion is to find the required length of the SOEC for a set syngas production rate at a certain composition. The complete schematic including the gas flow channels is shown in fig. 2. The movement of gas between the porous electrode and the flow channel is modelled by convection. This can be justified by the Péclet number calculated to have a value of 2020, meaning that mass transport by convection dominates over diffusion.

As there is no catalyst in the channel, the rate of WGSR is assumed to be zero. The narrow channel height and relatively fast flow speeds lead to poor longitudinal mixing so plug flow is assumed to occur, with no mixing in the z direction and full mixing in the y direction as a first approximation.

$$\frac{\partial C_{f,i}(t,z)}{\partial t} + h\frac{\partial N_{z,c,i}(t,z)}{\partial z} = -N_{y,c,i}(t,z,y=0) \quad (19)$$

The differential equation (19) was derived to describe the movement of gas from the porous bed to the flow channel. It was derived from a mass balance on an infinitesimal control volume inside the gas channel. Where $C_{f,i}$ represents the concentration of component i in the gas flow channel. All other variables are explained in the caption for fig. 2. It has also been assumed that the anode does not provide limitation to cathode reactions. This is because air can be provided in excess to remove the oxygen so there will be little increase in oxygen concentration along the length of the anode channel. This assumption is backed up by previous studies [23].

Operating Conditions

A degree of freedom analysis on the 1d system required the specification of 3 operating conditions. The pressures in the diffusion equations are modelled as constant due to the WGSR resulting in no net change in number of moles. Ambient pressure is used, as the effect of pressure on performance is not enough to justify the additional costs incurred by changing it.

Due to heat energy being cheap and electrolyte performance increasing at high temperature [11], isothermal high temperature operation was implemented. 1073K was chosen to be consistent with Ni's model [15].

Every investigation reviewed for the process used a constant voltage close to 1V, so the cell voltage was set to 1.3V, again making it consistent to Ni's model [15].

Two further degrees of freedom occur in the channel, leading to the decision to set the gas velocity and the channel height. The gas velocity was set to 1 ms^{-1} to make it consistent to the order of magnitude found in previous work [14].

The channel height was set to 0.01 m, again making it consistent to the order of magnitude of previous work. It was also chosen as a compromise between increasing the electrode area exposed to the gas by decreasing the height, and lowering the gas flow rate by increasing the height. Both factors increase the gas conversion.

Economic methods

A base case scenario must be created to compare co-electrolysis to traditional syngas production methods. The co-electrolysis process plant must be located close to a plentiful source of carbon dioxide. Currently, captured CO_2 from other facilities provides the most viable source for this, with the burning of fossil fuels for energy production contributing over half of global CO2 emissions [24].

A 500MW power station is intermediate in size and facilities of this capacity can be found all over the world, therefore this size has been chosen as the CO_2 source under analysis. [25] This has been compared to a similarly sized existing steam reforming facility [26]. The associated costs have been explained below.

Operating costs

Electricity: The electrical energy driving the reaction provides the greatest contribution towards the operating costs. The model outputs of current density and SOEC area allow an estimate for the electrical energy consumption via **(20)**.

$$E_{Electrical} = \frac{VA(J_{CO} + J_{H_2})}{\varepsilon_f} \quad (20)$$

Where V is the applied voltage, A is the surface area, J is the current density and ε_f is the faradaic efficiency. The faradaic efficiency is assumed to be 100% as any other electrochemical reactions occur at a negligible rate [20].

The cost for this electrical energy was estimated using the price of renewable electricity. Currently, onshore wind is the cheapest form of renewable energy with a levelized cost of £22.7/MWh [27]. If the process is to be considered worthwhile, the plant must be built in conjunction with a renewable energy facility and either directly utilise the energy produced or drawing it from the national grid. If this were not the case, fuel would be burned to produce electricity and carbon dioxide, then the electrolysis would just be directly reversing this process.

Separation: Separation costs are assumed to be negligible in comparison to electrical costs. Carbon dioxide can be reduced to minimal quantities in the SOEC output stream which means only separation of water is required. This can inexpensively be done through flash separation [20].

Maintenance: A maintenance cost of 3.2% SOEC and carbon capture capital cost has been applied based on previous studies of electrolysis [27].

Capital Costs

Carbon Capture: Literature values for the cost of converting a coal fired power station to incorporate carbon capture were used. They were specific to a 500MW power station [20].

SOEC Cell: The quasi 2d model in gPROMS was used to calculate the required SOEC area and the value for cost per unit area of £1350/m^2 was estimated from previous studies who based their costing on SOFC technology [11]. The value of the membrane was then scaled up using a cost factor of 0.4 for the equipment cost relative to full plant capital cost [28].

Key Performance Metrics

Lifetime cost of the plant was chosen as the key performance metric. This is the net present cost of the plant over its assumed lifetime of 20 years, divided by the amount of syngas produced during this period. The gPROMS model was used to find the production rate of syngas.

Environmental performance can be incorporated into the costs by considering the SCC. A median country-level SCC of £325/tCO_2 was chosen. [29] This was multiplied by the CO_2 consumption rate of co-electrolysis. The CO_2 formed through heating requirements in both processes was considered negligible since it is small relative to electrolytic consumption and similar for both processes. The calculated SCC was then added to the steam reforming costs to allow comparison to co-electrolysis.

Results

1D Model

The molar flux results of the 1d model along the cathode depth are shown in fig. 3. These results are for an inlet composition of H_2:CO_2:H_2O:CO as 0.067:0.25:0.65:0.033. The mole fraction values were chosen based on Fu et. Al [11] using an inlet gas composition of 90% H_2O and CO_2 and 10% H_2 and CO. The ratio of H_2 to CO is chosen to be 2:1 because it is modelled to come from a recycle stream, while the ratio of H_2O to CO_2 was chosen as an initial estimate, considering the required outlet H_2:CO ratio.

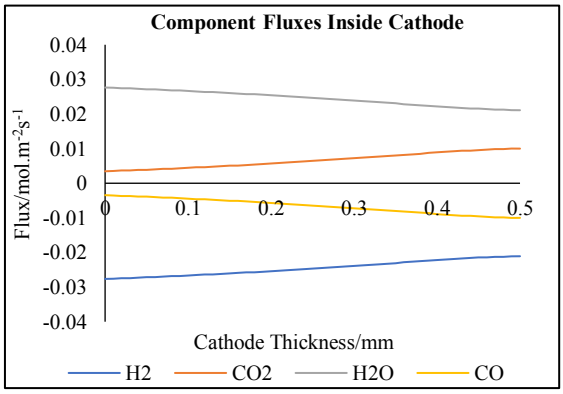

fig. 3 *Molar flux of each component inside the cathode catalyst pores.*

One can observe that the molar flux of H_2O is decreasing along the cathode thickness, however, the H_2 flux is increasing in magnitude from the electrolyte interface (cathode thickness = 0.5mm) to the cathode surface (cathode thickness = 0mm). The opposite is true for the CO_2 and CO flux.

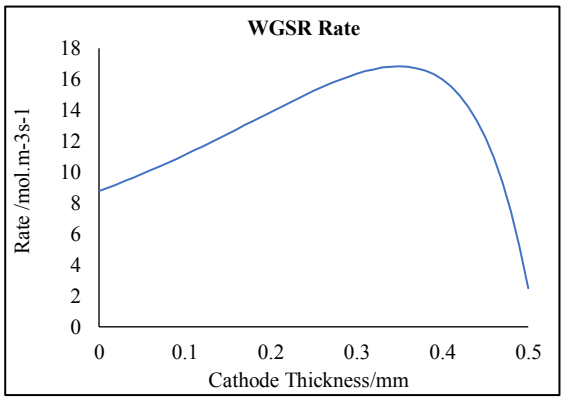

fig. 4 *WGSR inside the cathode catalyst pores.*

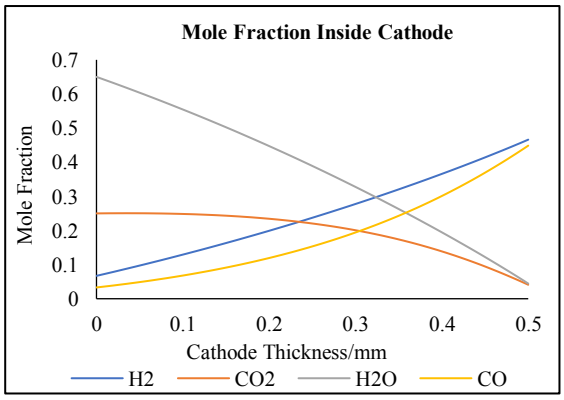

fig. 5 *Mole fraction of each component inside the cathode catalyst pores.*

Fig. 4 shows the variation of the rate of the water gas reaction with cathode thickness.

The rate is positive throughout the cathode thickness due to the high H_2O mole fraction.

The variation of mole fraction with cathode thickness due to multi-component diffusion can be seen in fig. 5.

The graph shows that the H_2O mole fraction has a larger variation with cathode thickness than that for CO_2.

Quasi 2D Model

Fig. 6 shows the results of extending the 1d model to the gas flow channel to find the SOEC length and the required inlet composition (at SOEC length = 0). It gives the mole fraction in the gas flow channel of each component. The trend would be identical for the fluxes in the channel due to the perfect mixing assumption.

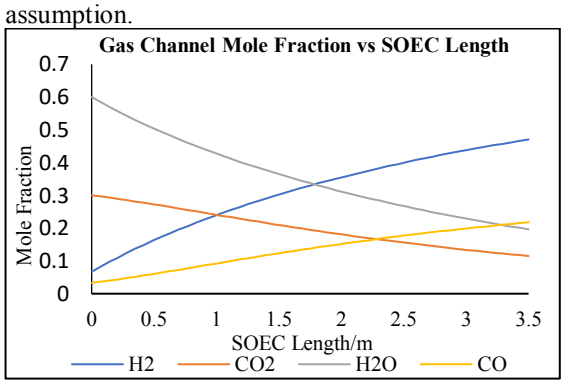

fig. 6 *Mole fraction of components in the cathode gas flow channel as a function of the channel length.*

After multiple trials with different inlet compositions and lengths, the required SOEC length was 3.5m and an inlet composition of a H_2O:CO_2 of 2:1 was found to give a desirable outlet composition of H_2:CO of 2.16. The outlet mole fraction of CO_2 is 0.115. However, this is consistent with industry standards of syngas having a CO_2 mole fraction between 5% and 15% [30].

The H_2O can be removed cheaply via flash separation [20]. Once removed, the CO_2 mole fraction increases to 15%, therefore still within range.

Economic and Environmental Performance

(Fig. 7) displays the results obtained from the economic analysis. It compares the constituent price components for various co-electrolysis and steam reforming situations. A best and worst case scenario has been devised for the purpose of sensitivity analysis, taking into account the economic factors that will influence the capital and operating costs of the process the most.

Base Case: Parameters and variables used were those described in the methods section.

Best Case: Operating cost has been reduced by assuming a continued year on year decrease of renewable energy prices of 12.2%, in line with the reduction of 69% over the past 9 years [27]. The capital expenditure is lower since a best case SOEC cell cost of £450/m^2 has been used. [11]

Worst Case: The worst case scenario takes into account the possible over-prediction of efficiency of the cell by adding an additional 20% to the applied voltage. This will increase the energy requirement, and consequentially the operating cost. It also uses the upper limit for cell cost per unit area of £4500/m^2, increasing capital cost. [11]

The results also display the effects of carbon taxation and the SCC on the relative performance of steam reforming. With carbon taxing, the economic performance of co-electrolysis becomes significantly more attractive, with the best case scenario becoming cheaper than steam reforming. Furthermore, when the SCC is considered, co-electrolysis is around half the cost of steam reforming. This shows that beyond purely financial metrics, there is scope for consideration of the new technology.

Discussion

SOEC Model

Fig. 3 can be explained by fig. 4 showing a constant positive WGSR rate. If this is the case, H_2O is being consumed to produce H_2 and CO is being consumed to produce CO_2. These results are consistent with Ni's study [11].

In fig. 4, the WGSR rate is initially increasing from 8.79 mol.m^{-3}.s^{-1} to 16.84 mol.m^{-3}.s^{-1} at 0.35 mm. After this point, the rate decreases to 2.49 mol.m^{-3}.s^{-1} at 5 mm. This is due to the variations in mole fraction shown by fig. 5. This graph shows the mole fractions of H_2O and CO_2 decreasing from the cathode surface to the electrolyte interface. This is because H_2O and CO_2 enter at the cathode surface and diffuse across to the electrolyte interface. The reverse is true for H_2 and CO, which are formed at the electrolyte interface and diffuse to the cathode surface.

The difference between the product of the H_2O and CO mole fractions and that of the CO_2 and H_2 mole fractions is increasing, until at 0.35 mm where it starts to decrease. This is caused by the initial mole fraction of H_2O being much larger than the other components, making the product with CO consistently higher, the effect of this on the kinetic WGSR rate can be seen by (16), where a higher amount of reactants favours the forward reaction. Fig. 5 also shows that the variation of the H_2O mole fraction is larger than CO_2 along the cathode thickness, this is due to H_2O being a lighter component, therefore diffusing faster. This is again consistent with Ni's study [15].

Positive WGSR rates lead to the inlet to the SOEC being favoured to have a high H_2O mole fraction. For the desired 2:1 ratio of the outlet syngas, the magnitude of the flux of H_2 entering the gas flow channel from the cathode surface needs to be larger than that for CO. A positive WGSR would lead to H_2 formation and therefore a higher H_2 flux.

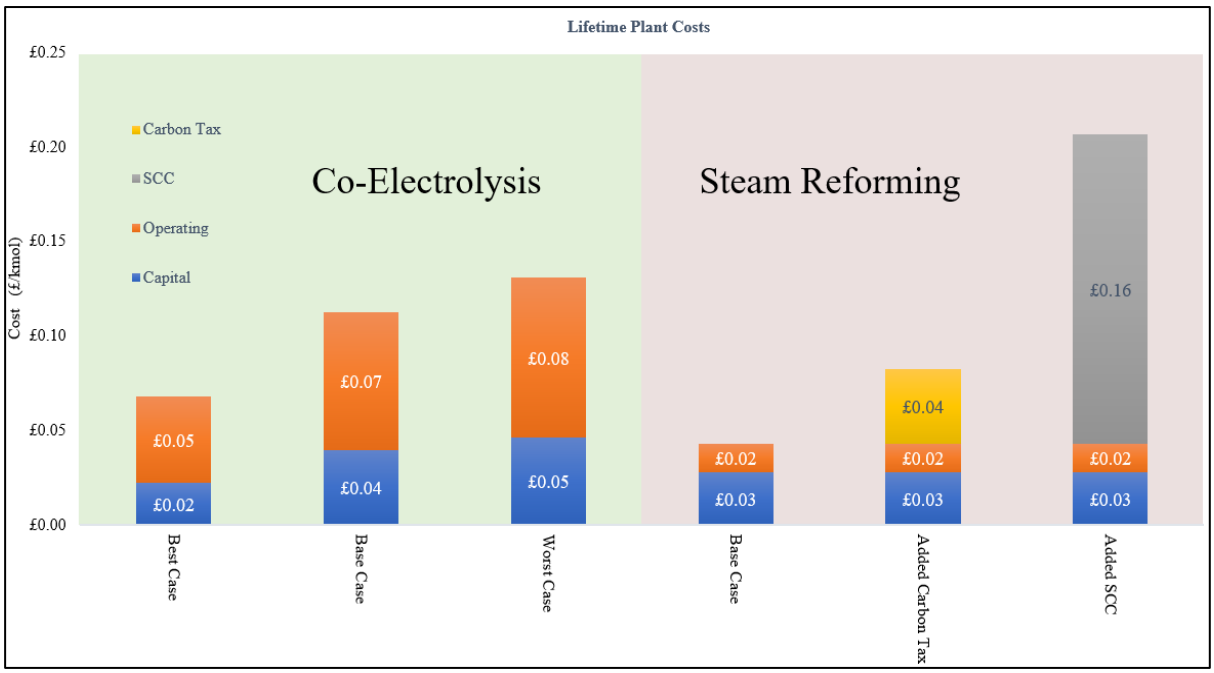

Fig 7. Comparison of lifetime plant costs for different scenarios of operation for co-electrolysis and steam reforming plants.

Fig. 6 represents this, as the increase in the mole fraction of H_2 is larger than that for CO. Notice how the gradient of each curve decreases in magnitude along the SOEC length. This is because as the mole fraction of CO_2 and H_2O at the cathode surface decreases with SOEC length, the Nernst potential, (6) and (7), increases, due to the mole fractions of H_2 and CO being larger at the electrolyte interface and the CO_2 and H_2O concentrations varying more between the bulk gas and the electrolyte surface. From the potential balance (5), this would decrease the activation overpotential, and therefore current density for both reactions. From the boundary conditions (17) and (18), this lowers the molar flux of each component throughout the cathode thickness, reducing the gradient of the channel molar fluxes, shown by equation (19).

Economic Analysis

The economic analysis falls strongly in favour of steam reforming as the preferred technology for syngas production. Therefore, from a purely business perspective it makes the most sense to invest in this technology to meet the growing market demand for methanol. The capital costs for the co-electrolysis process are comparable to that of steam reforming, however, 64% of the technology's lifetime cost is contributed by the operating cost. Under this investigation's assumptions, this is mainly from the cost of electricity. The base case scenario uses the most optimistic renewable electricity prices, coming from onshore wind farms. Renewable energy output varies significantly with time and location, so the electrical energy costs incurred are likely to be even higher. That being said, the levelised cost of renewable energy is falling sharply, which would significantly improve the economic performance of the technology, proven by the decrease in operating costs shown in the best case scenario analysis.

The SOEC model itself also uses optimistic design assumptions. Although the electrochemistry, mass transfer and reaction models within the cathode catalyst bed have been shown previously to correlate well with previous experimental work [15], there is significantly less data available for the quasi 2d flow model. The assumption of perfect mixing in the y direction is too simplistic since the calculated Reynolds number of 69.3 reveals that the air will be flowing in a laminar regime. With less than ideal mixing, there will be a higher concentration of reaction products and a lower concentration of reactants in the cathode bed and electrolyte surface. This will lead to a reduction in conversion, increasing the length of reactor required and the potential difference needed to drive the reaction. Hence, there will be negative implications on both the capital and operating costs.

Environmental consideration

Fortunately, global awareness of the issues caused by CO_2 emissions is improving. The implications of climate change on the environment and also the economy is becoming increasingly well understood. Studies on its precise effects on the economy have allowed for the SCC to be quantified. This means this study has been able to compare steam reforming to co-electrolysis using its effects on a country's economy as a whole. The economic analysis results have shown that there are significant benefits in using co-electrolysis. Interestingly, the countries which have the highest SCC correlate well to those who's methanol demand is highest. Central and northeast Asia have amongst the highest SCC values

and account for around 2/3 of the global methanol demand, driven by their methanol to olefins state mandate and increasing petrol blending [31] [22]. These countries also have the greatest increase in coal fired power capacity [25]. With a significant number of new stations planned and under construction, it would be advisable for them to invest in the integration of co-electrolysis to methanol technology.

Many governments are now more accepting of the idea of putting a cost on carbon and are introducing carbon taxes. These come in many forms including subsidy schemes and carbon trading [21]. The exact cost of CO_2 emissions can be highly variable, but an optimistic value of £78/tCO_2 has been used for the case of adding carbon tax. This has had drastic implications on the financial viability of the process. It is clear that taking the economic climate change implications into consideration, co-electrolysis is significantly more appealing and even more so when ethical, environmental reasons are added too.

Recommendations for Future Work

To resolve the modelling issues associated the low Reynolds number compromising the perfect mixing assumption, an improved model would incorporate fluid dynamics. Previous studies have used computational fluid dynamics (CFD) [32] to model concentration variation in 2 dimensions, which can be applied to this model.

Another potential area of research can be investigating different CO_2 to syngas methods to find an optimum process in terms of economics. For example, a process that does not electrolyse CO_2 but converts it via the WGSR, while producing hydrogen by electrolysis could decrease the operating cost of the process, which is the major component of the overall cost, shown by fig. 7.

In this report, the economic analysis has been based on global averages. Further research could be conducted to identify target locations to implement the technology. Using location specific costing, energy prices, renewable energy capability and emissions legislation would give a better idea of the viability of co-electrolysis.

Future studies could also extend the downstream extent of the research, incorporating the costs for methanol production and determining profitability by including methanol demand and sale price. The extent of the higher cost of syngas production may not affect the cost of methanol as much when the entire production sequence is considered.

Conclusion

The analysis on a CCU alternative to syngas production for use in the methanol industry has been carried out. The CCU alternative investigated is electrochemical conversion of CO_2 and H_2O using a SOEC. Co-electrolysis of CO_2 and H_2O together has previously been shown to improve the efficiency of the process, therefore modelling of the SOEC has used this. For the 1d electrochemical and mass transfer model inside the catalyst pores, Ni's investigation [32] was used as a basis, which was then extended to a quasi 2d PFR model to include the gas flow channel above the catalyst pores. gPROMS software was used to implement the quasi 2d model of the SOEC, with the results of cell dimensions, electrical energy requirements and syngas production rate being used for economic analysis.

The economic analysis involved comparing the lifetime costs of a syngas production plant using the modelled SOEC technology to one using steam reforming, the dominant production method today. The environmental impacts of both processes were also taken into account. The economic analysis with no consideration of environmental effects showed that steam reforming is much more economically viable, with a levelized lifetime cost 38% of that for the SOEC technology. However, the SOEC technology has the potential to remove CO_2 emissions from other industrial processes, which has an overall positive environmental effect. The SOEC technology also uses renewable energy for its electricity source, increasing the feasibility of this source. This investigation also considered the economic costs of the potential environmental effects of climate change caused by CO_2 emissions, quantified as the SCC. Taking this into account, the SOEC technology performs much better economically and environmentally than steam reforming. It is therefore in the interest of governments to mitigate CO_2 emissions from syngas production processes. Introduction of carbon taxation can be done to reduce these emissions, with this study showing that a realistic value of £78/tCO_2 would make the SOEC technology more economically viable in comparison to steam reforming, should it be performing under the stated best case scenario.

Acknowledgements

Special thanks to Dr. Andrea Bernardi for his invaluable supervision when conducting this study.

References

[1] "Why can't we quit fossil fuels?," *The Guardian,* 13 April 2013.

[2] A. Goeppert, "Recycling of Carbon Dioxide to Methanol and Derived Products – Closing the Loop," *Chem.Soc.Rev,* vol. 43, p. 7995, 2014.

[3] P. S. D. Jansen, "Carbon Capture and Utilisation in the Green Economy," The Centre for Low Carbon Futures 2011 and CO2Chem Publishing 2012, 2011.

[4] D. Bolton, “People in germany now being paid to consume electricity,” *The Independent,* 8 May 2016.

[5] K.Peterson, “Large Scale Methanol Production From Natural Gas,” Haldor Topsoe.

[6] S. K. Abbas, “https://www.slideshare.net/sajjad_al-amery/episode-3-production-of-synthesis-gas-by-steam-methane-reforming,” 8 December 2018.

[7] Bp, “Fuel, Octane and Power,” *Fuel News,* 15 January 2010.

[8] “IHS Markit: Methanol demand growth driven by methanol-to-olefins, China demand,” *Hydrocarbon Processing,* 13 June 2017.

[9] C.Graves, “Co-electrolysis of CO2 and H2O in solid oxide cells: Performance and durability,” *Solid State Ionics,* vol. 192, no. 1, pp. 398-403, 2011.

[10] A.Hankin, “Process Exploration and Assessment for the Production of Methanol and Dimethyl Ether From Carbon Dioxide and Water,” *Sustainable Energy Fuels,* vol. 1, p. 1541, 2017.

[11] Q.Fu, “Syngas Production via High-Temperature Steam/CO2 Co-Electrolysis: An Economic Assessment,” *Energy&Environmental Science,* no. 3, p. 1382, 2010.

[12] V.Menon, “Modeling of Solid-Oxide Electrolyser Cells: From H2, CO Electrolysis to Co-Electrolysis,” *The Electrochemical Society,* vol. 57, no. 1, p. 3207, 2010.

[13] J.Veldsink, “The use of the dusty-gas model for the description of mass transport with chemical reaction in porous media,” *The Chemical Engineering Journal,* vol. 57, p. 115, 1995.

[14] V.Menon, “A model-based understanding of solid-oxide electrolysis cells (SOECs) for syngas production by H2O/CO2 co-electrolysis,” *Journal of Power Sources,* vol. 274, p. 768, 2015.

[15] M.Ni, “An electrochemical model for syngas production by co-electrolysis of H2O and CO2,” *Journal of Power Sources,* vol. 202, pp. 209-216, 2011.

[16] R.Andika, “Co-Electrolysis for Power-to-Methanol Applications,” *Renewable and Sustainable Energy Reviews,* vol. 95, pp. 227-241, 2018.

[17] G.Olah, “CO2 to Renewable Methanol Plant, Reykjanes”.*Chemicals Technology.*

[18] S.Badwal, “Review of Progress in High Temperature Solid Oxide Fuel Cells,” *Journal of the Australian Ceramics Society ,* vol. 50, no. 1, pp. 23-27, 2014.

[19] “World’s Largest Carbon-Capture Plant to Open Soon!,” *Grand View Research,* p. 2018, 5 9 2018.

[20] B. J.Spurgeon, “A comparative technoeconomic analysis of pathways for commercial electrochemical CO2 Reduction to Liquid Products,” *Energy.environ.sci,* vol. 11, p. 1536, 2018.

[21] https://priceoncarbon.org/pricing-mechanisms/pricing-pricing/, “Carbon Pricing,” *Price on Carbon,* 2014.

[22] K.Ricke, “Country-Level Social Cost of Carbon,” *Nature Climate Change,* pp. 895-900, 24 September 2018.

[23] H.Xu, “Modeling of CH4-assisted SOEC for H2O/CO2 Co-Electrolysis,” *International Journal of Hydrogen Energy,* vol. 41, no. 47, pp. 21839-21849, 2016.

[24] EPA, “Global Greenhouse Gas Emissions Data,” *Greenhouse Gas Emissions,* 2014.

[25] CarbonBrief, “https://www.carbonbrief.org/mapped-worlds-coal-power-plants,” 6 May 2018.

[26] P.Pei, “Cost comparison of syngas production from natural gas conversion and underground coal gasification,” *ResearchGate,* 2014.

[27] Lazard, “Levelized Cost of Energy and Levelized Cost of Storage 2018,” 8 November 2018.

[28] R.Sari, “GENERAL PROCESS PLANT COST ESTIMATING,” *KLM Technology Group,* 1 June 2014.

[29] K.Ricke, “Country-level social cost of carbon,” *Nature Climate Change,* vol. 8, pp. 895-900, 2018.

[30] N. E. T. Library, “Syngas Composition,” *U.S. Department of Energy,* 2015.

[31] M. Institute, “https://www.methanol.org/energy/,” Accessed 5 December 2018.

[32] M.Ni, “2D Thermal Modeling of a Solid Oxide Electrolyzer Cell (SOEC) for Syngas Production by H2O/CO2 Co-Electrolysis,” *Int. Journal. Hydrogen. ENergy,* vol. 37, pp. 6389-6399, 2011.

`

Dual-polymer agglomeration of sand and ageing effects

Sang Ju, Lee; Marvin, Lee;

Department of Chemical Engineering, Imperial College London, United Kingdom

Abstract: Sand production in oil reservoirs remain a persistent problem in the oil and gas industry due to the safety risk it poses in addition to affecting productivity of the well. This leads to extra expenses for producers and could even stop production permanently. A measure to combat this is via the use of sand screens. Chemical consolidation is increasingly being used as it is relatively more cost effective and does not reduce permeability as much.

This research aims to investigate the dual-polymer technique to aggregate sand fines and thus allow the sand screen to function effectively. Dual-polymer aggregation involves coagulation followed by flocculation through the addition of a cationic polymer layer first, followed by an anionic polymer layer. This technique has shown better agglomeration results than using just a single agglomerant. In this paper, the type of cationic polymers will be varied, while keeping the anionic agglomerant, an organic polymer, constant. This paper explored cationic bioflocculants (chitosan), organic polymers (polyacrylamide, polyDADMAC) and inorganic polymers (Poly Aluminium Chloride (PAC), Poly Ferric Sulfate (PFS)). It investigated each of their interaction with a single type of anionic organic polymer (AN934VHM) to deduce the best performing combination based on how well the agglomerants aged and their agglomeration ability.

Experiments were conducted using light scattering to measure the mean square weighted particle size of sand before and after addition of the agglomerants. A rotational rheometer was also used to measure viscosity of the agglomerant dispersion. Experiments were repeated over a span of 3 weeks for each cationic polymer and it was found that polyacrylamide, specifically FO4650VHM, had the best agglomeration ability but this decreased significantly with age while PAC, PFS and polyDADMAC displayed decent agglomeration ability and did not appear to perform any poorer over time.

Keywords: Dual-polymer, ageing, agglomeration, sand, sand screens, organic polymers, inorganic polymers, bioflocculants, dual-agglomerant

Introduction

A global decline in discovery rates and a lack of spare capacity in crude oil production has led to further need for technological developments to maximise the productivity of each oil source (Bentley, 2002). While maximising the recovery factor is important, it is equally important to maintain and prevent productivity loss through effective control measures.

Approximately 90% of hydrocarbon wells are in sandstone reservoirs, and around 30% of these sandstones may be weak enough to produce sand (Bellarby, 2009). Sand production can cause severe operational problems: damaging equipment such as valves, pipelines, pumps, and must be separated at the surface which incurs extra costs. In the worst cases, oil production can be partially or fully inhibited, requiring expensive work-overs or shutting down of the well completely (Dehghani, 2010). Some problems associated with sand production is tabled below in Table 1 (Ikporo, 2015).

Table 1: Effect of sand production at different stages of oil production

Area	Problem	Effect
Reservoir	Wellbore fill	• Access restricted to production interval
Surface Equipment	Sand fouling	• Damage to safety valve
	Erosion	• Equipment wear and failure
Surface Installation	Sand accumulation	• Malfunction of control equipment • Capacity reduction • Unscheduled shut-downs • Separation and disposal costs

There are multiple control measures producers can use to control sand production, and can largely be

`

classified into two categories: passive and active sand control (DrillingFormulas, 2016). Passive sand control relies on non-intrusive methods of control, and involve:

- Oriented perforation
- Selective perforation
- Sand management

Active sand control measures, on the other hand, use filters to control sand production:

- Stand-alone screens
- Expandable sand screens
- Gravel packs & frac-packs
- Chemical consolidation

There has been recent development in using the chemical consolidation method in sand control using a sand agglomeration system (SAS) that alters the zeta potential of any solid surface when in contact. This technique is beneficial as it can be used on existing wells already employing mechanical sand control, and can be used in both low and high permeability formations. It also does not cause formation damage (Mishra et. al., 2015). In comparison with gravel packs and frac-packs, this method is also relatively cheaper.

Research has only just begun emerging for a dual-polymer technique for agglomeration of sand fines. While used in the wastewater-treatment industry (Tzoupanos et. al., 2008) , its applications in the oil and gas production sector has been limited.

This research aims to further the study of dual-polymer agglomeration of sand fines in oil reservoirs using a variety of cationic polymers, pairing each with a single type of anionic organic polymer, AN934VHM. The cationic polymers used are categorised in Table 2 below.

Table 2: Cationic agglomerants explored

Category	Type	Mol. Wt.	Charge Density
Organic Polymer	FO4650	6-10 mil.	40-80%
	FO4650VHM	>15 mil.	
	DB45SH	10-15 mil.	80-100%
	DB45VHM	>15 mil.	
Bio-flocculant	High MW Chitosan	3-4 mil.	40-80%
	Low MW Chitosan	50k-190k	
Inorganic Polymer	Poly Aluminium Chloride (PAC)	30% Al_2O_3	
	Poly Ferric Sulfate (PFS)	19% Fe	

FO4650 and FO4650VHM from Table 2 above represent polyacrylamide samples, while DB45SH and DB45VHM represent poly diallyldimethylammonium chloride (polyDADMAC).

While it is important to address each agglomerant's ability to agglomerate sand fines, it is also important to consider the effects of ageing on the agglomerant's ability to agglomerate.

The effects of ageing were investigated because polymers undergo changes in molecular weight and structure which affects its ability to agglomerate sand fines. In order to measure this, the viscosity of the agglomerant was measured at regular intervals as the changes in molecular weight (MW) would directly affect this. Additionally, the preparation of polymers was carried out in an environment with minimal exposure to oxygen to minimise oxidative degradation due to radical attacks.

Therefore, the objective of the study is to delve deeper into how the different agglomerants stack up to one another and how ageing affects them when added with AN934VHM based on two criteria: the agglomeration ability and the effects of ageing on this. The preparation of polymers will be conducted in an oxygen-free environment, and viscosity measurements at regular intervals will be taken.

Concept

Suspension of Sand in Seawater

Reservoir sand fines come in various sizes. In seawater, the sand fines form a suspension in which they fall very slowly to the bottom due to gravity. However, to maintain dispersion of sand fines within the medium, a stirrer can be used to keep sand fines from settling. The sand used here is sand directly obtained from a *Petronas* oil well.

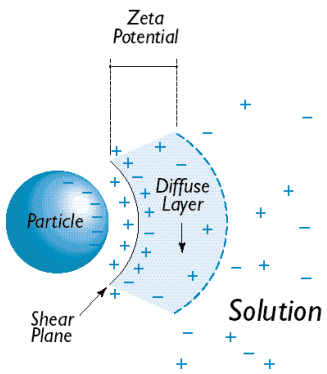

Figure 1: Suspension of negatively-charged sand particles

`

Sand particles are negatively-charged. Figure 1 above shows how an electric double layer is formed around the negatively-charged particle when in an aqueous medium.

The balance between the attractive Van der Waals' forces and the repulsive electrostatic forces form the basis for the stability of the suspension in the medium. Sand fines form a relatively stable suspension due to their negative charge and high Zeta potential.

The Zeta potential is the potential difference between the shear plane and the solution. For sand in seawater, the Zeta potential is between 40 to 130mV (Pravdic, 1970). In order for sand particles to agglomerate, the Zeta potential must be close to zero (isoelectric point) in which the colloidal suspension is no longer stable. This process is known as charge-neutralisation. This reduces the diffuse layer potential surrounding the particle, allowing moving particles to collide with each other more due to Brownian motion, convection, and gravitational forces. A reduced Zeta potential thus promotes the formation of flocs.

Dual-Polymer Flocculation Mechanism

The agglomerants in Table 2 are all water-soluble. The principle behind the mechanism is to use cationic agglomerants to reduce the Zeta potential of the system, thus promoting the formation of small flocs. Following that, high molecular weight (MW) anionic agglomerants form polymer bridges to form even larger flocs.

The mechanism can be described through a 4-step process (SNF, 2017) as per Figure 2:

a) Addition to cationic polymer to a suspension of sand in seawater, neutralisation and formation of charge patches

b) Formation of small flocs due to positive charge patches on a particle becoming attracted to negatively-charged regions of other sand particles

c) Addition of high MW anionic organic polymer (AN934VHM)

d) Formation of large flocs due to polymer bridging as positive charge patches get attracted to negatively-charged sites on long chain polymer

The effect of the dual-polymer mechanism is that larger flocs can be formed than if only a cationic agglomerant were used to agglomerate the sand fines. This technique is used in the wastewater treatment industry (Tzoupanos et. al., 2008), but has seen little use in the oil and gas industry.

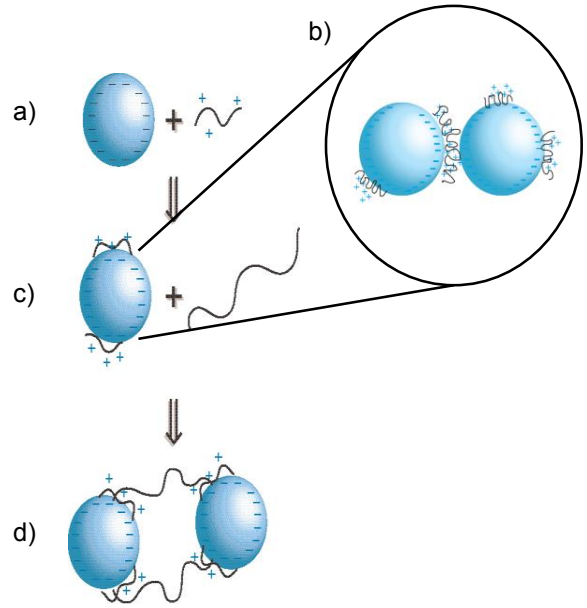

Figure 2: Dual-agglomeration flocculation mechanism

Effects of Ageing

A combination of things (Polymer Database, 2015) lead to the degradation of polymers:

- Heat (thermal degradation)
- Oxygen (oxidative/thermal-oxidative degradation)
- Light (photodegradation)
- Weathering (UV/ozone degradation)

These factors accelerate the mechanical degradation that polymers undergo, which are caused by changes to the molecular weight, weight distribution and composition of the polymer. Mechanical degradation results from chain scission and conformation of the polymers, which affects their agglomeration ability. By eliminating as many of these external factors as possible, an isolated study can be made on the mechanical degradation effects of the polymers to serve as the criteria for their stability.

`

Methodology

Equipment

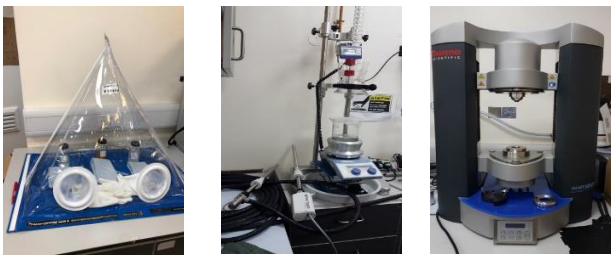

Figure 3: Left to Right: Glove Box, Shear Test Rig, and Rotational Rheometer

For the conduct of experiments, three main pieces of equipment were used as seen in Figure 3.

The glove box was used to prepare the agglomerant solutions in an oxygen-free environment. A nitrogen tank would be connected to the rig to evacuate any air in the glove box. Only then were the bottles uncapped and samples extracted.

The shear test rig has a vessel which contained the sand particles suspended in seawater. A Fisherbrand™ Double-Ended PTFE Stir Bar, was used to keep the sand particles in suspension. Two probes, the Mettler Toledo™ Focused Beam Reflectance Measurement (FBRM) and the Particle Vision and Measurement (PVM) were inserted into the vessel.

The FBRM probe takes measurements via a laser beam that passes through an optical lens and focus on a fixed beam spot on the sapphire window of the probe. The optical lens is rotated via a compressed air at a speed of 2m/s. Rapidly scanned particles will reflect or 'backscatter' the laser beam into the detector and this backscattered light is registered as distinct pulses. The distance across each particle (chord length) was then calculated by multiplying the duration of each pulse with the scan speed of 2 m/s (Mettler Toledo, 2015). These procedural steps are shown in Figure 4. From the FBRM software, key particle parameters such as the mean chord length (square weighted) and particle size distribution can be measured.

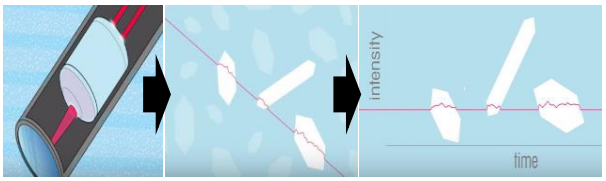

Figure 4: FBRM Method of Measurement

The PVM uses a video microscope attached to the probe tip to capture high-resolution images of particles as they exist in process (Mettler Toledo, 2014). Images were captured at intervals of 2 seconds with the optical zoom set at 790x which allowed for the capture of clearer images.

The Thermo™ scientific viscometer experiments were performed using the concentric cylinder configuration to minimise error. One cylinder is rotated at a constant speed, and a shear rate is determined. The liquid then drags the other cylinder around, exerting a shear stress, from which the viscosity can be measured.

Outline

To effectively test the effects of ageing on the agglomeration ability of each of the agglomerants, solutions of agglomerants would be left to sit and age. Each day, a small amount of solution was measured out into sealed containers inside the glove box and a shear test experiment was run and the agglomeration ability measured using the FBRM. At the same time, the sample would also be loaded into the viscometer for viscosity measurements to be taken. Two cationic polymers were tested in the morning and two other in the afternoon. Experiments were conducted across a span of 3 weeks.

Preparation of Seawater and Brine Solutions

Seawater was chosen as the medium for the polymers as it is the easiest solvent to source to prepare the polymers on offshore rigs prior to deployment. The ions in seawater were found to enhance the net negative charge on sand particles (Anderson, 1986). Brine was chosen to simulate the actual solution used in industry to dissolve and store polymers. The following tables show the compounds and their concentration used to make up the artificial seawater (Table 3) and brine (Table 4) respectively.

Table 3: Composition of compounds used in the preparation of artificial seawater

Ingredients	Composition (g/L)
NaCl	24.6
KCl	0.67
$CaCl.2H_2O$	1.36
$MgSO_4.7H_2O$	6.29
$MgCl_2.6H_2O$	4.66
$NaHCO_3$	0.18

`

Table 4: Composition of compounds used in the preparation of brine

Ingredients	Composition (mg/L)
$CaCl_2.2H_2O$	954.55
$MgCl_2.6H_2O$	1412.95
KCl	142.62
$BaCl_2.2H_2O$	2.77
$SrCl_2.6H_2O$	26.89
$NaHCO_3$	1514.56
Na_2SO_4	102.02
NaCl	26825.11

Preparation of Agglomerant Solutions

A measured mass of polymer beads/powder was added to a stirring glass bottle containing 100ml brine. These were labelled with the date it was prepared, left to stand for 1 minute under high-speed stirring, and then left overnight on low-speed stirring (to minimise ageing due to mechanical stress). This was to ensure even dispersion of the polymer within the solution to ensure better dissolution.

The exception to this was chitosan, which were dissolved in 6ml 2% HCl and 33.3ml DI water prior to being added to the brine solution.

The polymers were dissolved to a concentration of 2000ppm. This concentration was chosen because a high viscosity is required to obtain good readings on the viscometer.

The temperature of the solution was set to room temperature at 25°C to eliminate the effects of thermal degradation, as the focus was on the ageing effects due to polymer dissolution. The temperature remained a fixed variable throughout the experiment.

Determination of Polymer Concentration

Before the conduct of the experiment, the polymer concentration had to be determined. To accomplish this, a shake test was conducted. In centrifuge tubes containing 5g sand and 25ml seawater, varying volumes of 200ppm samples were added and then shaken. It was found that 2ml of 200ppm of each polymer gave the fastest settling time for the sand particles and thus it was determined that for 2000ppm samples, 0.2ml of polymer will be added.

Glove Box Preparation

In the preparation phase, the samples were placed in the glove box. The nitrogen tank was then connected to the glove box to evacuate the air. 1ml of each sample was extracted into cuvettes and sealed. Another 3ml of each was also extracted into the droppers. The 1ml samples were used for the shear test rig, and the 3ml samples for the viscometer. The viscosity of AN934VHM were tested twice since they were paired with each cationic polymer.

Shear Test Experiment

In the shear test experiment, a vessel was filled with 500ml seawater and set to rest on a stirring plate. The stirring speed was set to 400rpm to create a vortex. 2.5g of sand was then poured slowly into the centre of the vortex. The vessel was then sealed, and FBRM and PVM probes inserted. On the computer, the particle count below 250µm was observed for the FBRM. Once the sand fines became fully suspended within the medium (consistent turbidity throughout), the stirrer speed was reduced to 200rpm to reduce shear effects.

Once steady state count was reached, 0.2ml of cationic polymer was added. Only after steady state was reached, then 0.2ml of the anionic polymer AN934VHM was added. This was repeated for 2 more dual-polymer additions to see if further agglomeration was possible.

Viscometer Experiment

For the viscometer, a 30 second ageing test was set-up at a constant temperature of 25°C. After calibration, a 3ml sample was loaded into the cup. The experiment was started with the rotating rotor left to run at a constant shear rate of $10s^{-1}$ for 30 seconds. The viscosity measurement based on shear stress was then recorded and plotted. This was repeated for each cationic and anionic sample.

Results & Discussion

Particle size measurement data was collected on the FBRM software. One key indicator was the mean square weighted size (MSWS) of particles.

Figure 5 shows how upon addition of a cationic polymer, FO4650VHM, the MSWS increases. This is due to the formation of flocs which are larger in size, and so would contribute more to the MSWS, bringing the overall value up. Upon addition of AN934VHM, this value increases even further, and peaked at about 285µm. Further addition of FO4650VHM or AN934VHM did not induce more agglomeration. The slight decline in mean square weighted size after addition is attributed to the shear caused by the stirrer.

`

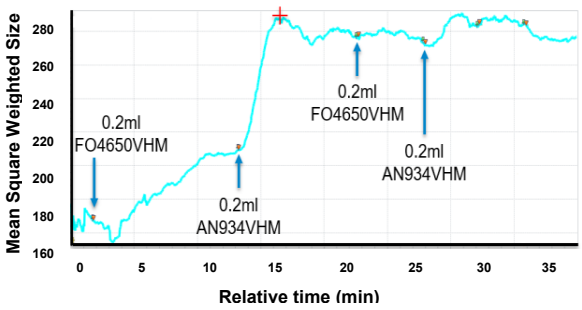

Figure 5: Mean square weighted size of sand particles across time

The PVM captured images of flocculation taking place. The following images show the dual-polymer agglomeration mechanism taking place. Sand fines flocculate into small flocs from the cationic polymer, then larger flocs on addition of the anionic polymer.

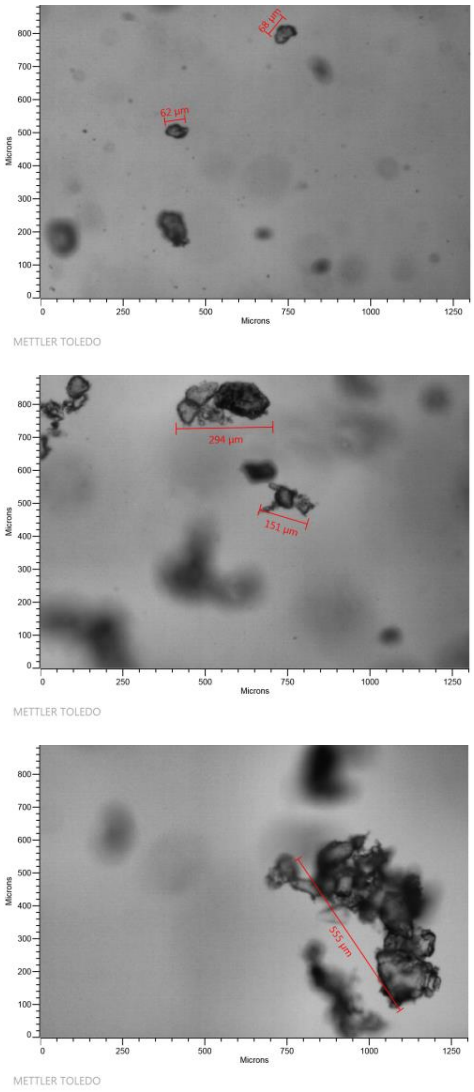

Figure 6: Flocculation of sand fines

On the viscometer, the average viscosity was taken for each experiment. Points were plotted for each day and the readings were taken to deduce how viscosity changed over the 3 weeks. The trends observed in the agglomeration ability due to ageing were analysed for 4 different cationic polymers and were compared with their respective polymer's viscosity.

Effects on Agglomeration Ability with Ageing

Both polyacrylamide and polyDADMAC (FO and DB samples) showed a similar trend in their agglomeration ability as seen in Figure 7 and Figure 8. This is because they both are organic polymers and thus have similar dissolution mechanisms, leading to similar coiling and uncoiling effects. There was an increase in the MSWS of sand particles for the first few days which peaked at about an average of 470µm for polyacrylamide and 447µm for polyDADMAC. For an ageing time of 3 weeks, both showed a clear ability to agglomerate sand above the nominal sand screen rating of 250µm.

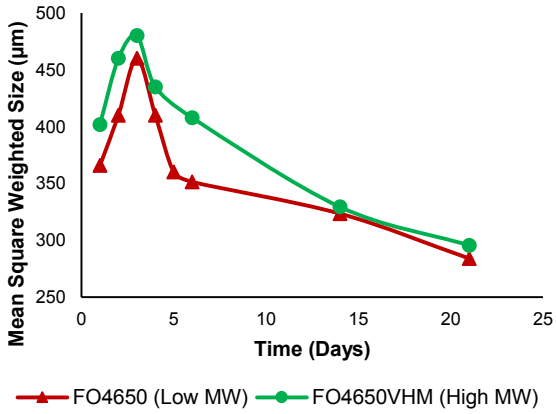

Figure 7: Polyacrylamide agglomeration ability with age

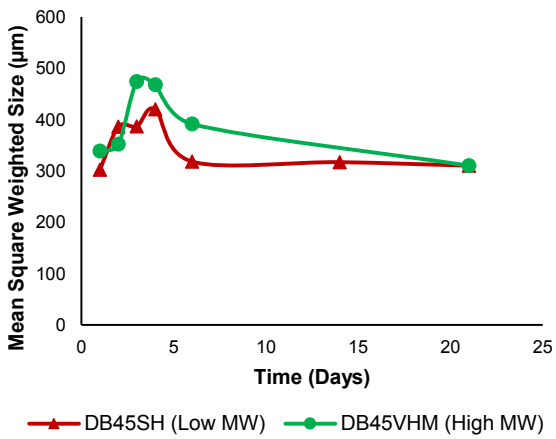

Figure 8: PolyDADMAC agglomeration ability with age

`

The agglomeration ability profile obtained for both polyacrylamides and polyDADMACs peaked between Days 3 and 4. This is possibly explained by the dissolution mechanism of polyacrylamide proposed by Owen (Owen et. al., 2002). On the first day, a few solid powder polymers exist in the solution that forms large gel-lumps with no agglomeration ability. These gel-lumps are few compared to the dispersed chains in solution, but they make up the majority of the polymer's mass. Thus, polymers are dissolved and dispersed to a very small extent. The peak is then observed due to optimal dispersion and dissolution of the polymer that allows for maximum flocculation. The reduction in the agglomeration ability after Day 4 could be due to an extended ageing effect on the polymer that led to conformation changes (Narkis et. al, 1966) and polymer degradation (Shyluk et. al., 1969).

However, polyacrylamide showed a steep decreasing trend in their agglomeration ability across time compared to polyDADMAC which showed a gentler decreasing trend. The faster rate of degradation of polyacrylamide means that after a few weeks, polyacrylamide can no longer agglomerate to form clusters of sand bigger than 250µm whereas polyDADMAC can still agglomerate to the size of 300µm. Therefore, polyDADMAC showed better performance in maintaining a good agglomeration ability over 3 weeks while polyacrylamide had better peak agglomeration ability as seen by the MSWS on Day 3.

For the bioflocculants (Figure 9), the high MW chitosan had higher agglomeration ability for first 3 days, but both higher and lower MW chitosans began to show similar agglomeration ability after Day 3. Both showed the ability to agglomerate sand above the nominal sand screen rating of 250µm for the first 10 days. However, their flocculation ability continued to drop to below 250µm in 2 weeks. This means that the biofocculants can only flocculate sands effectively for the first 10 days.

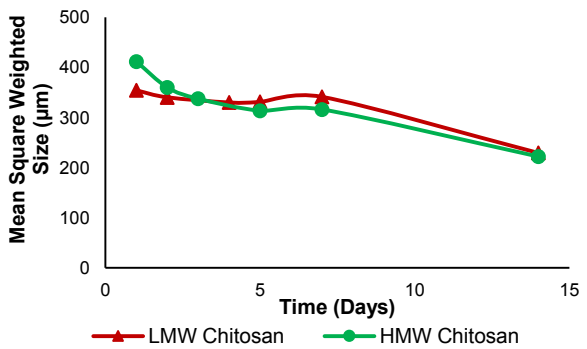

Figure 9: Bioflocculants agglomeration ability with age

The inorganic polymers PAC and PFS showed a linear decrease in their agglomeration ability with time as seen in Figure 10. PAC has a general formula of $(Al_nOH_mCl_{3n-m})_x$ and due to hydrolysis, many different aluminium species are formed such as $Al_{13}O_4(OH)_{24}{}^{7+}$, which is the most effective for coagulation that will help to neutralise the negatively charged sand fines (Parthasarathy, 1985). However, PAC loses its coagulation efficiency over time in the presence of $SO_4{}^{2-}$ ions as it reacts with $Al_{13}O_4(OH)_{24}{}^{7+}$ to form a $Al(OH)_3$ gel or precipitates (Wu et. al., 2012). A high concentration of $SO_4{}^{2-}$ ions is present in brine solution, which could give rise to this decrease.

Similarly, PFS undergoes 2 step hydrolysis-polymerisation process to produce an Fe(III) solution $\left(Fe_2OH_n(SO_4)_{3-\left(\frac{n}{2}\right)}\right)_m$. In an alkaline medium, the Fe(III) solution interacts with the OH^- ions via an uncontrolled hydration process to produce negative charged species such as $Fe(OH)_4{}^-$ (Wei et. al., 2015). These negatively charged ions are unable to participate in the charge neutralisation process and thus reduces the ability of the PAC polymer to bridge effectively. The kinetics of formation of these species would most likely follow the zero-order reaction as the solutions are stirred constantly at low RPM and have low concentration of polymers. Therefore, these effects encountered in PAC and PFS account for the linear decrease in the MSWS over time.

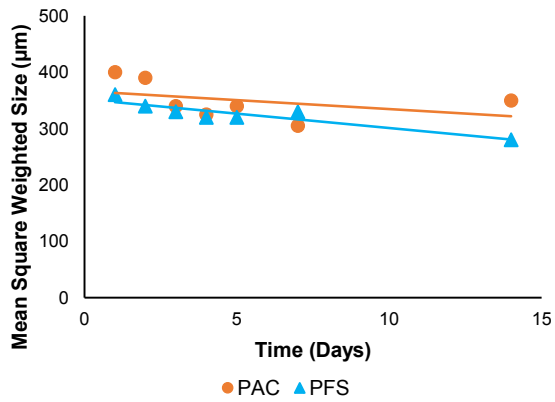

Figure 10: PAC and PFS agglomeration ability with age

`

Effects of Viscosity with Ageing

An interesting characteristic of the viscosity profile for FO4650 and FO4650VHM was observed in Figure 11. Initially, for both samples, there was a sharp drop from Day 1 to 2, but viscosity remained constant for the next 5 days.

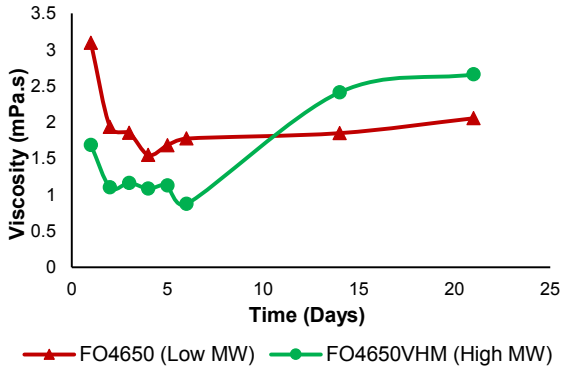

Figure 11: Viscosity of polyacrylamide across time

Unexpectedly, the FO4650VHM (high MW) had lower viscosity for first 10 days. This is most likely due to the polymer interaction with the brine solution which contains a high concentration of negatively-charged divalent ions such as SO_4^{2-}. The anion interacted with the positively charged polymer chain that caused it to form a coil onto itself via the ion bridging effect (Saeed et. al., 2017). The effect of ion bridging is more prominent for high MWs as it has a longer chain for coiling and thus FO4650VHM showed lower viscosity. However, a coiled polymer should have resulted in higher viscosity, but the lower measured viscosity could have been due to errors associated with polymer sampling. The viscosity of FO4650VHM began to rise after week 1 possibly due to a stronger gel effect where the higher MW polymer took a longer time to achieve higher dispersion. This led eventually to a fully dispersed FO4650VHM that allowed it to retain relatively higher agglomeration ability than FO4650 between Day 4 to 14.

Both polyDADMAC samples in Figure 12 showed an increase in the viscosity in the first few days, peaking on Day 3 and then decreasing sharply in the next few days. Following that, the viscosity for both samples increased gradually. The viscosity profile observed for polyDADMAC was similar to its agglomeration ability profile across time as in Figure 8. As explained earlier, the large gel-lumps dissolved in the early stage led to better dispersion of polymers and hence a rise in viscosity for first few days. The polymer chains were then fully extended and dispersed in the solution, thus giving rise to the peak viscosity on Day 3. The sudden drop in viscosity could be due to the ion bridging effect as the fully extended polymer chains were more exposed. Over time, the degradation of the organic polymer chains coupled with the diminishing ion bridging effect led to uncoiled and fragmented polymer chains that resulted in a slow increase in viscosity.

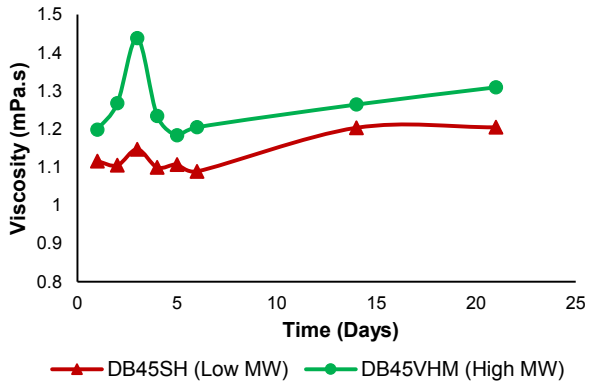

Figure 12: Viscosity of polyDADMAC across time

For bioflocculants, Figure 13 shows that the viscosity of higher MW (HMW) chitosan decreased rapidly while that of lower MW (LMW) chitosan decreased slowly. The higher viscosity of high MW chitosan on the first few days contributed to its higher agglomeration ability profile while the rapid fall in its viscosity led to approach of similar agglomeration ability with lower MW chitosan seen in Figure 9.

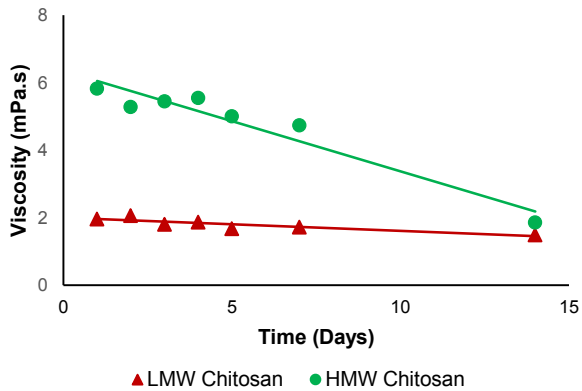

Figure 13: Viscosity of bioflocculants across time

Inorganic polymers PFS and PAC both show a generally constant viscosity across time in Figure 14. A wide fluctuating range of viscosity was measured for the inorganic polymers. They have viscosity that are very low that led to higher errors associated with the data and thus gave a misrepresentation of the rheology data. Instead, alkali titration and Ferron species analysis could be performed for future work to better understand the hydrolysis performance and species distribution of the inorganic polymers (Wei et. al., 2015).

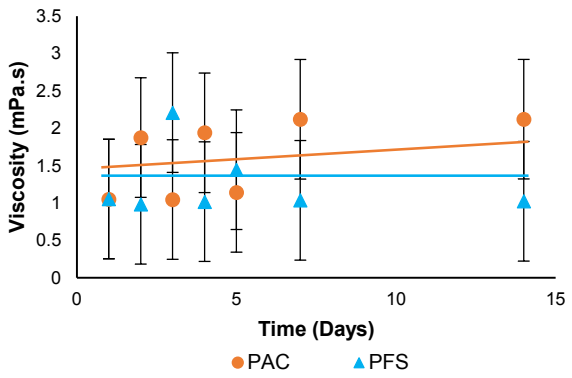

Figure 14: Viscosity of inorganic polymers across time

Charge Density Effect on Agglomeration Ability

The difference in the MSWS between polyacrylamides and polyDADMACs was explored further. The agglomeration mechanism associated with lower cationic charge density like FO4650VHM is more dependent on either a combination of charge neutralisation and bridging or bridging only, depending on shear effects and polymer concentration. A high charge density polymer like DB45VHM would have an agglomeration mechanism that depends more on electrostatic patch flocculation (Ying et. al., 2006). This would hold the bridged flocs together stronger, but not bigger. The flocculation mechanism for FO4650VHM depends on the combination of charge neutralisation and bridging as the MSWS of the sand particles increased from 160µm to 210µm upon the addition of first 0.2ml of 2000ppm FO4650VHM (Figure 5). The addition of the negatively charged polymer, AN934VHM further bridges the flocs and thus creating bigger sized flocs.

Agglomeration Ability Against Viscosity for All Polymers

Finally, the relationship between each polymer's agglomeration and viscosity profiles was compared. In Figure 15, bioflocculant shows a positive linear relationship between their MSWS and viscosity. This is an expected result where a longer chain polymer with higher viscosity is able to produce agglomerants that are bigger and vice versa. PolyDADMAC shows variation in MSWS while its viscosity remained relatively constant. However, an interesting relationship was observed for the organic polyacrylamide polymer where there was a strong negative linear relationship. From the macro perspective, the organic polyacrylamide was added to the shear test rig vessel that contained 500ml of seawater. Due to its higher viscosity, the dispersion of the polymer would have been slower in the aqueous medium and thus could have led to lower agglomeration ability of the polymer.

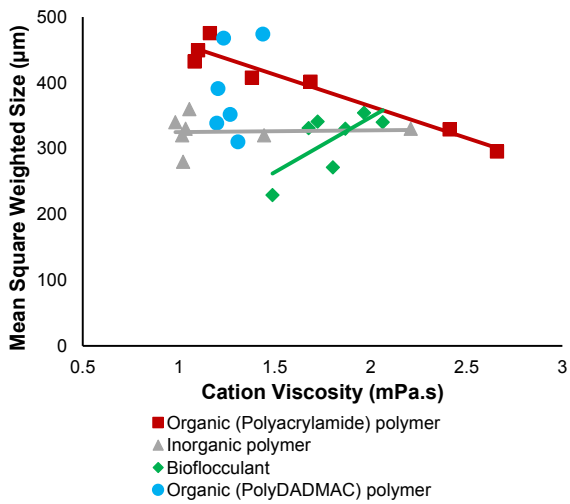

Figure 15: Mean square weighted size against viscosity for all polymers

Conclusion

With the aim of finding the best performing agglomerant, each sample was assessed based on two main criteria: agglomeration ability and ageing stability. The agglomeration ability was the highest for higher molecular weight and medium charge density polyacrylamide (FO4650VHM) but this was limited to a time span of 3 weeks. Beyond that, the agglomeration ability would have continued to fall and thus reaching below the threshold of 250µm. On the other hand, both inorganic polymer, PAC and PFS, as well as the polyDADMAC showed stable flocculation across time. These polymers may be preferred in oil extraction as there would be fewer frequency needed to inject polymers and offering higher reliability of filtering out the sand effectively.

Further work could be done on repeating the first week's viscosity measurement of polyacrylamides to obtain better and more reliable rheology data that relates to the agglomeration profile. New techniques such as alkali titration and Ferron species analysis can be explored for inorganic polymers to better understand their agglomeration profile.

Acknowledgements

We would like to thank our PhD supervisor, Ryan Lee and undergraduate student, Huang Guan for their contribution and guidance towards this research.

`

References

Barlas, U., 2018. *Investigating Dual-Polymer Flocculation for Agglomeration of Sand Particles in Oil Reservoirs,* London: Imperial College.

Bellarby, J., 2009. Sand Control. In: J. Bellarby, ed. *Well Completion Design.* Aberdeen, UK: Elsevier, pp. 1-711.

Bentley, R., 2002. Global oil & gass depletion: an overview. *Elsevier,* pp. 189-205.

Dehghani, M., 2010. *Oil Well Sand Production Control.* Mashhad, Iran, Islamic Azad University.

DrillingFormulas, 2016. *Basic Sand Control Methods in Oil and Gas Industry.* [Online]
Available at: http://www.drillingformulas.com/basic-sand-control-methods-in-oil-and-gas-industry/
[Accessed 9 December 2018].

Ikporo, B., 2015. Effect of Sand Invasion on Oil Well Production: A Case Study of Garon Field in the Niger Delta. *The International Journal Of Engineering and Sciences (IJES),* 4(5), pp. 64-72.

Mettler Toledo, 2014. *ParticleView V19.* [Online]
Available at:
https://www.mt.com/gb/en/home/products/L1_AutochemProducts/FBRM-PVM-Particle-System-Characterization/PVM/ParticleView-V19-PVM-Technology.html
[Accessed 11 December 2018].

Mettler Toledo, 2015. *FBRM Method of Measurement.* [Online]
Available at:
https://www.youtube.com/watch?v=Wr35BHuDgqc&feature=youtu.be
[Accessed 11 December 2018].

Mishra et. al., S., 2015. Chemical Sand Consolidation: An Overview. *Journal of Petroleum Engineering & Technology,* 5(2), pp. 21-34.

Narkis et. al, N., 1966. Ageing effects in measurement of polyacrylamide solution viscosities. *Elsevier,* 7(10), pp. 507-512.

Owen et. al., A., 2002. The impact of polyacrylamide flocculant solution age on flocculation performance. *International Journal of Mineral Processing,* 67(1-4), pp. 123-144.

Parthasarathy, N., 1985. Study of polymeric aluminium (III) hydroxide solutions for application in waste water treatment. *Water Research,* 19(1), pp. 25-36.

Polymer Database, 2015. *Thermal-Oxidative Degradation of Polymers.* [Online]
Available at:
https://polymerdatabase.com/polymer%20chemistry/Thermal%20Degradation.html
[Accessed 12 December 2018].

Pravdic, V., 1970. *Surface Charge Characterization of Sea Sediments,* Zagreb: Department of Physical Chemistry, Institute "Ruder Boskovic".

Saeed et. al., A. S. M. M. I. M. T. H. G. O. L. L., 2017. Assessment of Polyacrylamide Based Co-Polymers Enhanced by Functional Group Modifications with Regards to Salinity and Hardness. *Polymers,* 9(12), p. 647.

Shyluk et. al., W., 1969. Aging and loss of flocculation activity of aqueous polyacrylamide solutions. *Journal of Applied Polymer Science,* 13(5), pp. 1023-1036.

SNF, 2017. *Water Soluble Polymers.* [Online]
Available at: https://www.snf-group.com/library/?search=water+soluble+polymers
[Accessed 12 December 2018].

Tzoupanos et. al., N., 2008. *Coagulation-Flocculation Processes in Water/Wastewater Treatment: The Application of New Generation of Chemical Reagents.* Rhodes, Division of Chemical Technology, Department of Chemistry, Aristotle University of Thessaloniki.

Wei et. al., C. H. Z. H. T. Y. W. Y. Z. C. Z. Y. L., 2015. Enhanced Coagulation-Flocculation Performance of Iron-Based Coagulants. *PLoS ONE,* 10(9), pp. 1-20.

Wu et. al., Z. Z. P. Z. G. Z. M. a. J. J., 2012. Humic Acid Removal from Water with Polyaluminium Coagulants: Effect of Sulfate on Aluminium Polymerization. *Journal of Environmental Engineering,* 138(3), pp. 293-298.

Ying et. al., Z. G. V. F., 2006. Flocculation Mechanism Induced by Cationic Polymers Investigated by Light Scattering. *American Chemical Society,* 22(16), pp. 6775-6786.

Effects of polymer molecular weight and concentration, silica concentration and temperature on the relaxation of aqueous Silica-Poly(ethylene-oxide) "shake-gels"

Conor Thomas, Eleni Papaeracleous
Department of Chemical Engineering, Imperial College London, Prince Consort Road, London SW7 2BB, UK.

Graphical Abstract

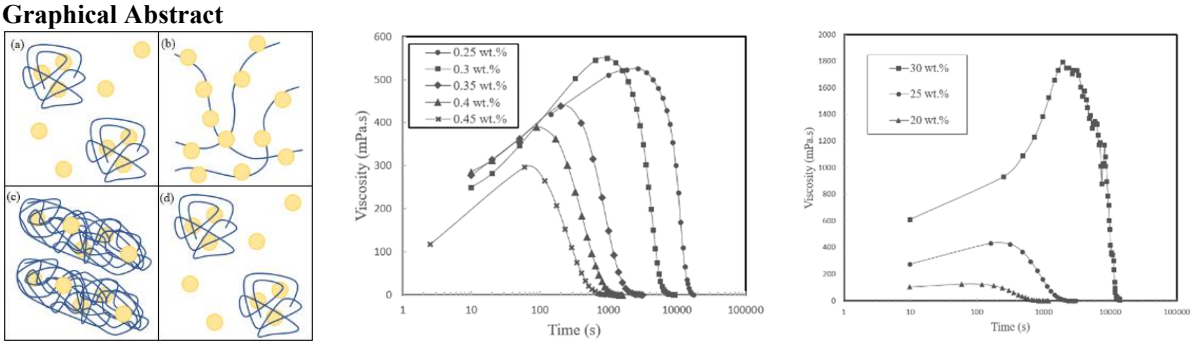

Abstract
The rheology of the relaxation process of "shake-gels" is the focus of this investigation, involving aqueous mixtures of Poly(ethylene-oxide) (PEO) and silica nanoparticles that form reversible solid structures upon exposure to an increased shear. The relaxation process in this study is defined as the period in which the shake-gel relaxes back to its original liquid state from the point the shear rate is reduced from a high shear rate of $1750s^{-1}$ to a low shear rate of $0.1s^{-1}$. Changing the concentration of the polymer and silica in the system, polymer molecular weight and temperature is shown to affect the time taken for the solid shake-gel structure to return to its initial state by varying orders of magnitude. The relaxation profile showed a region of increasing viscosity of the gel attributed to the process of forming the large 3-D gelled network, followed by its relaxation. The relaxation time decreases exponentially with increasing polymer to particle ratio due to saturation of silica surfaces resulting in inefficient polymer bridging. The relaxation time increases exponentially with increasing polymer molecular weight as longer chains provide more adsorption sites per chain promoting increased polymer cross-linkage. Increasing temperature is also found to exponentially decrease relaxation time as kinetic effects dominate the thermodynamic and structural forces that keep the solid gelled structure intact.

Keywords: shake-gel, poly(ethylene-oxide), silica, rheology, relaxation

Introduction

Suspensions of colloids and polymers are non-Newtonian fluids which have reversible, shear-thickening properties. They are usually comprised of high molecular weight polymer, such as polyethylene oxide (PEO) and colloidal particles such as silica or laponite. When subjected to shaking, the low viscosity fluid transforms into a high viscosity gel known as "shake-gel", which relaxes back to its liquid form after some time with no force applied. These mixtures have a wide range of applications, mainly industrial and biomedical, and recent advancements in these sectors have caused an interest in their physical properties [4,12,29-30]. The rheological properties as well as the relaxation time vary for different concentrations of the components and different temperatures [12].

Colloidal silica used in this study is a dispersion of amorphous nano-silica [32]. It has various uses in industry, for example acting as a surfactant for polymers. PEO in solution exists in the form of aggregates, otherwise known as clusters, which interact with water in hydrophilic and hydrophobic interactions due to the oxygen molecule and organic chains respectively. Water molecules form a hydration layer around the PEO monomers by hydrogen bonds between the oxygen ends and water. This way the hydrophobic chains do not meet the water molecules and thus do not cause repulsion, allowing the polymer to dissolve in water [12]. This is

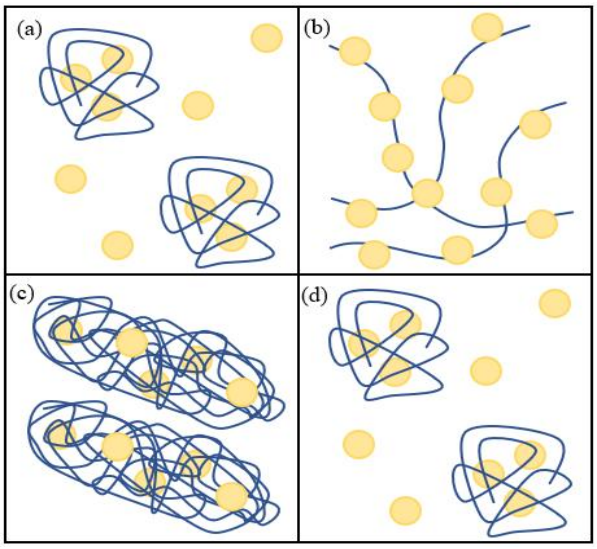

Fig. 1. (a) Initial liquid state of the gel, (b) Applied shear of $1750s^{-1}$ elongates polymer chains, (c) Solid gelled state in a tight coiled structure, (d) Relaxed back to initial liquid form

only possible because of the similarity in oxygen-oxygen interdistance in water and polymer molecules [7]. This clusterisation however can easily become disturbed under a change in conditions, such as applied shear or even a change in concentration, and the solution may transition from clear to opaque.

The formation of shake-gels has been studied thoroughly in research before alongside the underlying mechanism that governs the process [2-3,6,10-17,20-23,27]. A schematic has been drawn to show the process, seen in Fig. 1, which will be used to describe in our own terms the process from liquid gel at rest, through the process of applied shear, then relaxation back to its initial state. Under no applied shear (a), silica particles usually interact and adsorb to various active sites along the polymer chains, breaking off PEO aggregates and forming new SiO2-PEO complexes by hydrogen bonding [11]. This equilibrium state and the number of silica particles adsorbed to each polymer chain is dependent on factors such as the concentration of both polymer and silica in the system which affects the silica to polymer ratio, their electrostatic interactions, and the radius of gyration of the polymer.

When shear is applied, the polymer chains extend and in doing so, break some of the already formed PEO-silica bonds. This extension of the polymer chain provides more sites for the silica particles to adsorb to which in turn provides the potential for other polymer chains to bond and cross-link to form bridges between different aggregates. This results in the growth of a 3-D silica-PEO complex [10]. Upon increased shear, polymer chains adsorb to different silica disks forming bridges between the two substances. These bridges extend throughout the solution eventually resulting in the formation of a macroscopic gel complex (c). The solution remains in its solid gelled state for a certain period that is dependent on various compositions and conditions, and when there is no shear applied to this structure, it will eventually return to a fluid as the polymer chains desorb [1-2,7,15,26]. While reports in the past have focused on the different aspects of the formation of the shake-gel, this report will aim to investigate how different gel compositions and the conditions they are subject to influence the relaxation process. In the schematic (Fig.1), this is the process from state (c) to state (d). Yuji Hirose previously performed work on this relaxation process investigating the rheological properties of shake-gels with small amounts sodium chloride (NaCl). It was found that if more sodium chloride was added to the system, the time taken for the gel to return to its original state increased due to the NaCl weakening the repulsive interactions between silica particles. This lead to the particles binding closer together forming a tighter gel complex that took longer to relax [8]. This study will thus look at different effects, involving changing the PEO concentration and molecular weight, the silica concentration and lastly the temperature.

Materials

The "shake-gels" used in this work were formulated from a mixture of poly(ethyleneoxide) (PEO), silica (LUDOX) and deionised water. This involved preparing a 2 wt.% PEO solution by dissolving solid PEO particles in deionised water, and to be able to study the effects of PEO molecular weight on relaxation rate, four batches were made at the following molecular weights: 400,000gmol^{-1} (Sigma Aldrich, Batch # 09218EE), 600,000gmol^{-1} (Sigma Aldrich, Lot # MKCF3158), 900,000gmol^{-1} (Sigma Aldrich, Lot # MKBS9423V), 2,000,000gmol^{-1} (Sigma Aldrich, Lot # MKBZ2508V) and 4,000,000gmol^{-1} (Sigma Aldrich, Batch # MKAA0451). These were then used to create 30ml "shake-gels" samples varying in PEO concentration from 0.1 to 1 wt.% and LUDOX® TM-50 colloidal silica (Sigma Aldrich, 50 wt.% suspension in H_2O, Lot # MKCD9192) concentration from 15 to 35 wt.%. The concentration range chosen was determined from literature on work previously carried out with "shake-gels" [10].For example, to prepare a mixture containing 25 wt.% silica and 0.3 wt.% PEO, 4.5 ml of the 2 wt.% PEO stock solution was added to 15 ml of silica and 10.5 ml of deionised water in a centrifuge tube to make the 30 ml shake-gel mixture. The samples were manually agitated several times and left to rest for a period of 24 hours to allow sufficient mixing between the components as it was noticed initially that the more times the gel was shook, the stronger it became.

Methodology

There has been ample literature previously conducted on the formulation of shake-gels and the PEO and silica compositions at which they exist. However, results will differ slightly depending on the type of polymer and silica used and hence for this investigation a phase diagram was constructed. The method for doing so involved observing a manual agitation of the gel samples categorising them into one of the following categories: no gel, weak gel, strong gel or permanent gel. No gel was observed when the sample exhibited no solid-like characteristics, weak gel when the sample relaxed quickly, in the range of minutes, strong gel when the sample remained a solid-like material for an extended period and lastly a permanent gel when there was no relaxation process back to a liquid state. It is worth noting that the distinction between a weak and strong gel is somewhat subjective and may differ from the criteria used in previous literature. The purpose of this phase diagram would be to provide identification of the gels that were to be used for this study. It is important to use the shake-gels that are classified as strong gels in this investigation as these take a longer time to relax which allows us sufficient time to investigate different effects on this process.

To be able to study the different effects on the relaxation process, a Thermo Scientific HAAKE MARS 60 rheometer with a serrated double gap cup (Type CCB27 DG/SS) and serrated cylinder rotor (Type CC20/Ti/SE) was used. A program was designed using the HAAKE RheoWin Job Manager which involved loading

17.2ml liquid gel samples, a specification of the equipment, into the rheometer and allowing it to settle to the desired experiment temperature. The load was then sheared at a low shear rate of $0.1s^{-1}$ for sixty seconds, which was done to determine the base viscosity of the liquid state without forming the solid shake-gel. The shear rate was then immediately increased to a value of $1750s^{-1}$ and kept constant for five minutes to elongate the PEO chains inducing formation of the solid gel state by allowing binding with the silica particles and promoting cross-linking and bridging. This process is plotted in Fig.2. The line reaches a plateau value during the first sixty seconds which is determined to be this base viscosity and the sharp peak slightly after sixty seconds indicates the forming of the shake-gel at the high shear rate. This graph demonstrates the transition from shear-thickening behaviour of the solution when shear is first applied to shear thinning after polymer saturates the silica surfaces [13].

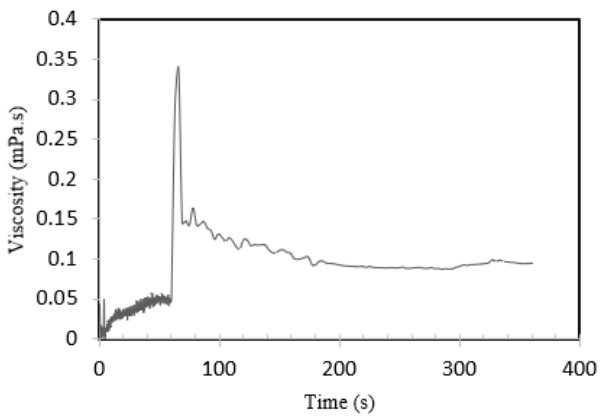

Fig. 2. A graph showing the results of the program used to determine base viscosity at shear of $0.1s^{-1}$ (first 60 seconds), and formation of solid shake-gel at shear of $1750s^{-1}$ (following 300 seconds)

The shear rate was then immediately reduced back down to $0.1s^{-1}$ to allow the gel to relax (not shown in Fig.2), with the focus of the study being on this relaxation profile. It was assumed that at zero-shear viscosity, there exists a static equilibrium structure of the gel in its liquid form which behaves as an equilibrium which is not affected by the applied shear. The gel therefore will always return to the same exact state even after multiple shears to the same sample.

Results

Phase Diagram

In this study, varying concentrations of PEO and silica produced a spectrum of different solutions with different phase properties upon shaking, which were classified into four categories to construct a phase diagram. At rest, all the solutions exhibited low viscosity behaviour and the gels were clear. However, after shearing the gels demonstrated high-viscosity non-Newtonian behaviour where the gels became increasingly opaque in colour and stuck to the walls of the centrifuge tubes. Some solutions formed a permanent gel upon shaking, whilst others formed no gel at all and the rest were classified into strong and weak gels. When left to relax, the fluids slowly reversed back to their low viscosity forms, each one in a different time scale

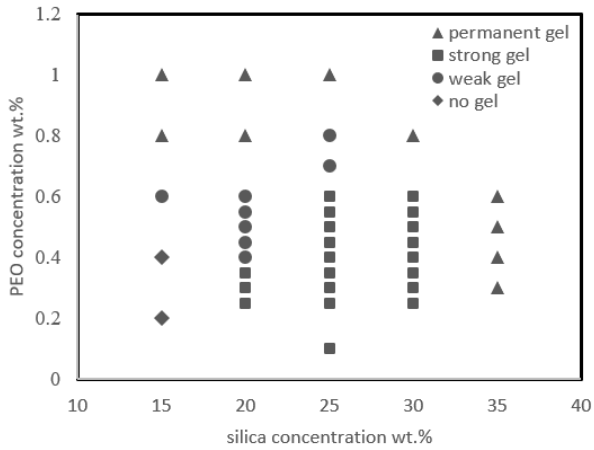

Fig. 3. A phase diagram of shake-gel samples ranging in PEO ($900{,}000gmol^{-1}$) and silica concentration characterised based on their physical properties.

The constructed phase diagram (Fig.3) shows that no gels were formed at low PEO and silica concentrations and permanent gels were formed at high PEO and silica concentrations. At these high concentrations, the polymer chains exist in dynamic adsorption-desorption equilibrium with silica particles resulting in the formation of this permanent network [5]. Between these regions around roughly 20-30 wt.% silica concentration and 0.2-0.6 wt.% PEO concentration, weak and strong shake-gels were observed with the stronger gels forming at slightly lower PEO and higher silica concentrations. These results are in accordance with the literature previously performing this work, differing slightly possibly due to different gel characterisations and materials used.

These results can be explained by looking at the bonding between silica and PEO molecules. When the PEO concentration is too high, the silica surfaces become saturated with polymer chains. This completely stabilizes the aggregates and prevents any reversing back to the liquid form from taking place leading to the formation of a permanent gel. When the concentration of silica is too low, specifically 15% and concentration of polymer is also low (0.2-0.4%), there are insufficient numbers of molecules to create the bridged complexes ultimately leading to no gel formation. Keeping the silica concentration low and increasing the polymer leads to the transition from no gel to weak gel to permanent gel, which can be explained from the fact that the solution becomes increasingly saturated. The ratio of silica particles per polymer chain was calculated knowing their physical properties and Fig.4 plots this ratio against PEO concentration at different silica concentrations, also showing the regions at which the four different shake-gel characterisations are observed.

From this work, it was decided that for the investigation, gels with PEO concentration ranging from 0.25-0.45 wt.% and silica concentrations ranging from 20-30 wt.% would be used. The particle to polymer ratios at these concentrations lie roughly between 10 and 30.

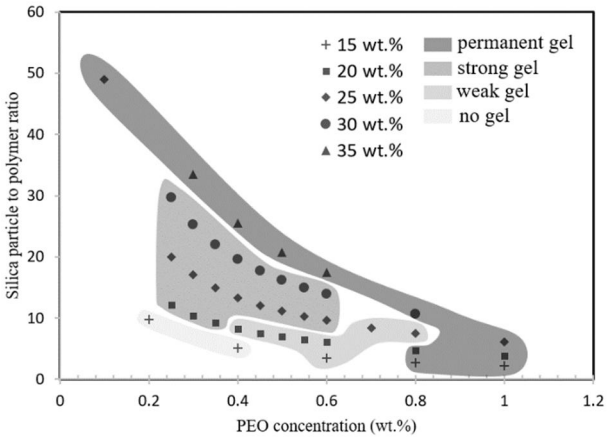

Fig. 4. Plot of the particle to polymer ratio against PEO concentration at different silica concentrations ranging from 15 to 35 wt.%. Greyed regions indicate observed characteristic of the shake-gel

PEO concentration effects

The effects of poly(ethyleneoxide) concentration on the relaxation of the gels were studied. From the data obtained in creating the phase diagram, it was observed that strong gels formed around silica concentrations of 25 wt.% so this was kept constant, as well as keeping temperature constant at 25 degrees C. Five PEO concentrations at molecular weight of 900,000gmol^{-1} were chosen to be investigated ranging from 0.25 to 0.45 wt.% and the results can be seen in Fig. 5. Further similar tests involving altering the PEO concentration at molecular weights of 400,000gmol^{-1} were conducted with similar results being observed.

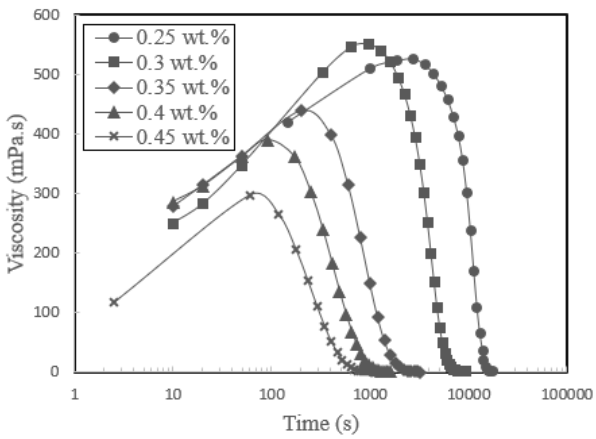

Fig. 5. A viscosity (mPa.s) against time (s) semi-log plot of the relaxation profile of shake-gels with PEO (900,000gmol^{-1}) concentrations 0.25-0.45 wt.% keeping silica concentration constant at 25 wt.% and temperature at 25°C

The relaxation time is determined by the time taken for the gel to relax back to its original viscosity once the shear rate had been reduced to 0.1s^{-1} which has been plotted as a function of PEO concentration in Fig.7. J. Zebrowski (2003) previously discussed that the time for gel relaxation is primarily dependent on the bonds formed under the applied shear and carried out a similar experiment using laponite instead of silica changing PEO concentration in a similar fashion to that done here [10]. The trend observed is identical of decreasing relaxation time with increasing PEO concentration. At low polymer concentration, there is a high particle to polymer ratio leading to good efficiency of bridging between polymer chains. As the polymer concentration is increased, the ratio of particle to polymer decreases, reducing the efficiency at which bridging occurs in the system. A schematic of this process is shown in Fig.6.

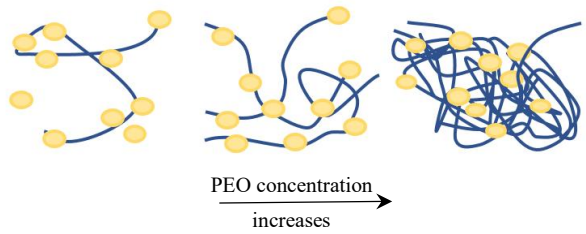

Fig. 6. A schematic illustrating the saturation of silica particles by increased PEO concentration

Table 1 shows the values of the particle to polymer ratio investigated here at constant silica concentration of 25 wt.%. As suggested by Walker (2004), the excess polymer prevents bridging by saturating the silica surface. The higher the efficiency of the bridging between the interacting polymer and particle, the longer it will take for the resulting gelled state to return to its original state [2].

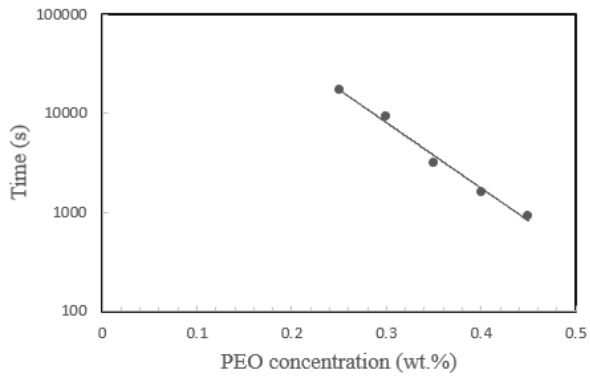

Fig. 7. A semi-log plot of relaxation time against PEO (900,000gmol^{-1}) concentration showing an exponential decrease with increasing concentration.

A feature of the relaxation profile (Fig 5) that was not expected prior to this investigation was the initial increase in zero-shear viscosity, reaching a maximum value, then decreasing. From Fig.1, which is a schematic of the gelation and de-gelation process, this initial increase in zero-shear viscosity is hypothesized to occur between states (b) and (c) during which the supra-molecular polymer assembly seems to be strengthening immediately after the shear is reduced. This period lasted roughly 65 seconds at a PEO concentration of 0.45 wt.% and increasing to 41 minutes for a PEO concentration of 0.25 wt.%. This seemed to be a significant time for the gelled state to be increasing in zero-shear viscosity and

thus an observation test was carried out which involved manually shaking the gel samples and seeing if there was any noticeable change in gel characteristics after the shaking had stopped, however this test was unsuccessful as no clear further thickening of the gel was visually observed.

Table 1. Particle to polymer ratio for the PEO concentrations investigated at constant silica concentration of 25 wt.%

PEO concentration (wt.%)	Silica (25 wt.%) to polymer ratio
0.25	20.0
0.3	17.0
0.35	14.9
0.4	13.3
0.45	12.1

This observation led to looking at whether there was any relationship between the maximum apparent viscosity reached and the PEO concentration. It was necessary to do further tests to obtain more data at low PEO concentration, so another experiment was run at PEO concentration of 0.2 wt.%. The maximum viscosity reached at each PEO concentration is plotted in Fig.8. What can be seen from this is that it is not a linear or exponential relationship like with the relaxation times, but there exists some maximum at which this maximum viscosity is observed.

For the relaxation times, it was reasoned that the low PEO concentrations take longer to relax as the silica to polymer ratio is high and so there is efficient bridging between the polymer chains. However in the case of the maximum apparent viscosity of the relaxing gel, low PEO concentrations seemed to produce a weaker gel, despite taking longer to relax. It is possible that at low PEO concentrations, there is good bridging between polymer chains, and so increased interaction between particles and polymer leads to a more complex 3-D structure and so takes longer for particles to desorb, however the concentration of polymer chains is low and the concentration of water in the system is high so the apparent strength of the resulting solid gel is low. As the PEO concentration is increased, the efficiency of interaction between polymer and particle is reduced but the increased concentration increases the viscosity and strength of the gel formed. This only occurs up to a point at which further increase of PEO concentration decreases the strength of the gel as the efficiency of the silica-polymer binding takes over and the saturation of silica particles means weaker gels are observed at high PEO concentrations. The two competing effects seen here show that there is a PEO concentration between 0.25 and 0.3 wt.% that yields the strongest solid gel at this particular silica concentration.

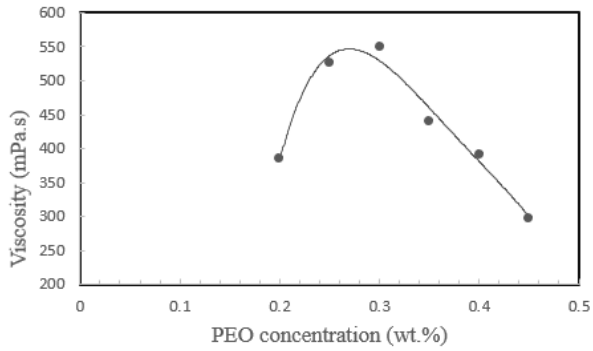

Fig. 8. A plot of the maximum viscosity (mPa.s) reached at each PEO concentration (wt.%)

These results have shown that there is a time region where the PEO-silica 3-D assembly is increasing in strength and reaches a maximum. It was not initially hypothesized that this region in which the gel strengthens would be as prominent as it turned out to be so the definition of the "relaxation" process changed to incorporate this initial rise in viscosity.

Kinetics

The results obtained from studying the effects of PEO concentration on the relaxation profile indicate that the shake-gels relax as a first-order process. This can be studied by removing the area of the graph where the gels increase in viscosity and focus only on the actual relaxation of the gel back to its initial state. This is shown in Fig.9, which shows the profile of the relaxing gel, removing the initial viscosity increase, at a PEO and silica concentration of 0.45 and 25 wt.% respectively.

From first order kinetics, the decrease in viscosity over time can be written as follows:

$$-\frac{d[\eta]}{dt} = k[\eta] \qquad (1)$$

From this, the integrated form for first-order kinetics can be determined as follows where η is the viscosity (mPa.s), k is the rate constant (s^{-1}) and t is time (s):

$$\ln[\eta] = -kt + ln[\eta]_o \qquad (2)$$

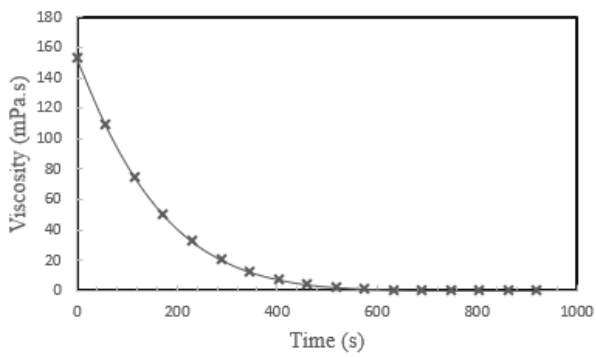

Fig. 9. A plot of viscosity (mPa.s) against time (s) showing a first order decay process of the relaxing gel at PEO and silica concentrations of 0.45 and 25 wt.% respectively.

Thus, the rate constant can be calculated as the negative slope of the line of a graph of $\ln[\eta]$ against t. The results are shown in Table 2, confirming the trend of decreasing relaxation time with increasing PEO concentration for the actual relaxation process with the rate constant values seeming to increase almost linearly.

Table 2. Rate constant values (s^{-1}) at different PEO concentrations (wt.%).

PEO concentration (wt.%)	Rate constant (s^{-1})
0.25	0.0008
0.3	0.001
0.35	0.003
0.4	0.006
0.45	0.009

PEO molecular weight effects

Investigating the effects of changing the molecular weight of the polymer proved to be the most challenging. Initially, three 2 wt.% PEO in water solutions were made using PEO at molecular weights of 400,000gmol^{-1}, 900,000gmol^{-1} and 4,000,000gmol^{-1}. As expected, the solutions were visibly more viscous at the higher molecular weights and thus harder to work with, particularly at 4,000,000gmol^{-1}, as accurate measurements were required to formulate the 30ml gel samples. Once the samples were manually shaken and left for some time, the gel sample with polymer weight of 4,000,000gmol^{-1} was still visibly a non-homogenous mixture so it was required to be shaken several times further. Plastic syringes were used to deliver 17.2ml gel solution samples into the rheometer, which for the 400,000gmol^{-1} and 900,000gmol^{-1} polymer weight liquid samples was easy to do, however proved hard to achieve with the 4,000,000gmol^{-1} liquid gel as it was transitioning into its solid gelled state upon ejection from the syringe. This was an effect observed in previous studies indicating that the shear applied to the solution whilst it was ejected from the syringe was enough to cause it to form its solid gelled state. The experiment however was conducted despite this, producing results for the 4,000,000gmol^{-1} sample that were not fitting trends or reproducible. This is hypothesized to be due to several factors. Firstly, the challenging preparation of the gel sample meant that the concentrations desired could differ from those used as it was difficult to be accurate in measuring small amounts of viscous polymer solution. Secondly, the problems with the mixing of solutions lead to potentially non-homogenous samples and thus the small sample loaded into the rheometer could have a different concentration composition to the whole sample. This led to abandoning experiments with the 4,000,000gmol^{-1} polymer and further investigation with other molecular weight PEO at 600,000gmol^{-1} and 2,000,00gmol^{-1}.

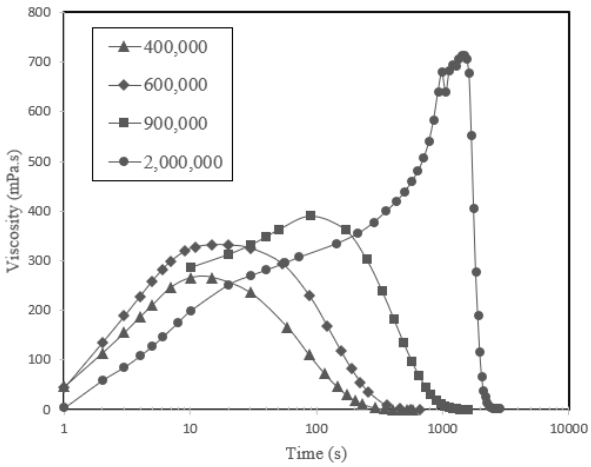

Fig. 10. A semi-log plot of viscosity (mPa.s) against time (s) for four different PEO molecular weights (gmol^{-1}) at 25°C. PEO and silica concentrations constant at 0.4 wt.% and 25 wt.% respectively.

Fig. 10 plots the relaxation profile, viscosity against time, at four different PEO molecular weights, keeping PEO concentration constant at 0.4 wt.%, silica concentration at 25 wt.% and temperature at 25°C. The trend shows that shake-gels containing higher PEO molecular weights have longer relaxation times. This is expected to be the case as the longer polymer chains will interact with more silica particles and when applied with a high shear rate will form larger complexes with stronger intermolecular forces as there is potential for increased bridging per polymer chain. These large coiled gels will take longer to unwind and return to its original state. Once again, the characteristic 'hump' in the relaxation profile is observed to suggest an initial thickening of the gel at zero-shear. Fig.11 plots the time taken for the gel to relax to its equilibrium liquid state as a function of the molecular weight of the polymer used and there exists an exponential trend of increasing relaxation time with increasing polymer weight.

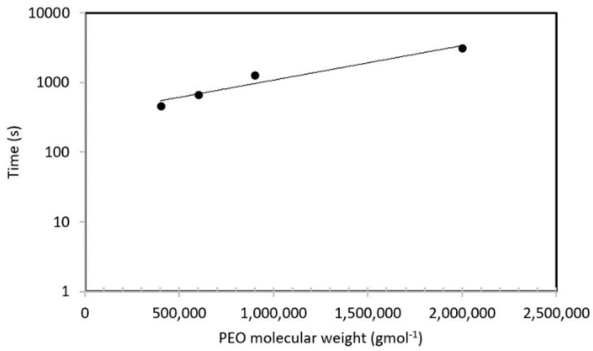

Fig. 11. A semi-log plot of relaxation time against PEO molecular weight showing an exponential increase with increasing polymer weight.

Silica concentration effects

The effects of altering the silica concentration were investigated, keeping PEO (900,000gmol^{-1}) constant at 0.35 wt.% and temperature constant at 25°C. The results are shown in Fig.12 showing a trend of increasing relaxation time with increasing silica concentration. This agrees with the previous section results when the PEO

concentration was altered whereby increasing the silica to PEO ratio will exponentially increase the relaxation time. Furthermore, as silica concentration increases, the distance between adjacent particles decreases leading to shorter length PEO bridges with a higher stability. The maximum in zero-shear viscosity discussed in the previous section is observable again here, increasing roughly 3 times between 20 and 25 wt.% and roughly 4 times between 25 and 30 wt.%.

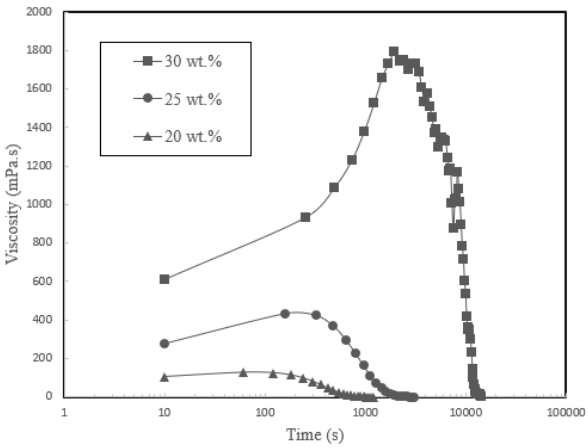

Fig. 12. A semi-log plot of viscosity (mPa.s) against time (s) varying silica concentration from 20-30 wt.% at constant PEO (900,000gmol^{-1}) concentration of 0.35 wt.% and temperature of 25°C.

Table 3 shows the values of the particle to polymer ratio keeping the polymer concentration constant at 0.35 wt.% and changing the silica concentration between 20 and 30 wt.%. Fig.13 plots the relaxation time against silica concentration and shows a strong trend of an exponential increase in relaxation time with increasing concentration.

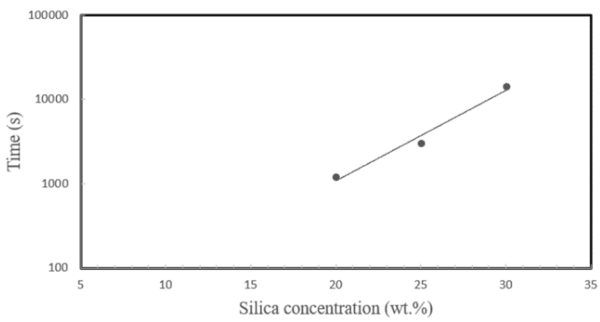

Fig. 13. A semi-log plot of relaxation time (s) against silica concentration (wt.%) showing an exponential increase with increasing concentration

Table 3. Particle to polymer ratio for the silica concentrations investigated at constant PEO concentration of 0.35 wt.%

Silica concentration (wt.%)	Silica to polymer (0.35 wt.%) ratio
20	9.2
25	14.9
30	22.0

Temperature effects

The conditions chosen to investigate the effects of temperature were at 0.45 wt.% PEO and 25 wt.% silica concentrations because the previous results have shown a relatively fast relaxation period at these conditions. Seven different temperatures were chosen to investigate, ensuring they were below the cloud point temperature of PEO. The cloud point temperature (CPT) corresponds to the temperature at which a PEO solution turns cloudy due to a macroscopic phase separation of the PEO-H_2O system. Two phases are produces; a polymer-rich phase and a polymer-lean phase [19] (Peter Pang, 2001). It is found that the apparent viscosity increases with increasing temperature above this cloud point temperature and obeys the Arrhenius equation below it. It has been reported from literature that the cloud point temperature exists at 90-95°C, and thus for this study, shake-gels were not studied near this temperature to avoid any influence of the effects of the CPT on results [9,24-25,31].

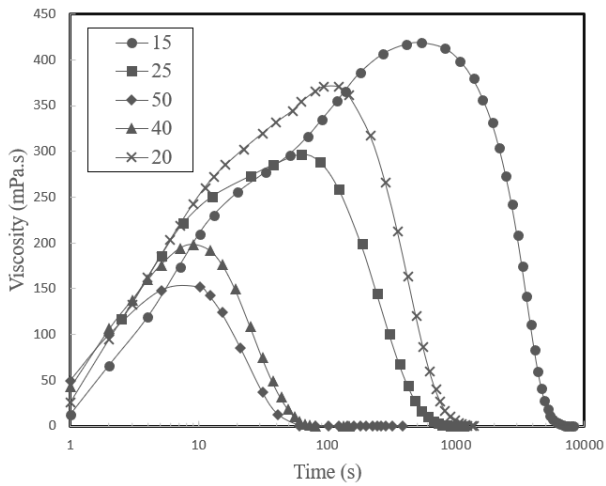

Fig. 14. A semi-log plot of viscosity (mPa.s) against time (s) varying temperature (°C) at constant PEO (900,000gmol^{-1}) concentration of 0.45 wt.% and silica concentration of 25 wt.%

There exists a good trend of increasing relaxation time with decreasing temperature between temperatures of 15°C and 50°C as can be seen in Fig.14. The results at 40 and 50°C are very similar and the time region in which samples at both these temperatures relaxed back to its initial state is between one and two minutes which is very fast, indicating a quick breakup of the polymer particle complex at higher temperatures. Temperatures below 15°C, specifically 5°C and 10°C, produced results that did not fit this trend with the relaxation being significantly slowed and incomplete after several hours. At 5°C the plot oscillated between increasing and decreasing viscosity before reaching a plateau value of around 148 mPa.s where it remained for roughly half an hour. Similarly, for 10°C, the results did not fit any obvious trend and both these cooler temperature tests were abandoned before there was any indication of the gel returning to its liquid state due to a time constraint. Fig.15 plots the relaxation times as a function of temperature, and an exponential relationship is observed.

Walker (2004) suggested that for the slightly higher temperatures (15°C to 50°C), the observed trend in relaxation period is consistent with the thermal motion of particle and polymer, and at the lower temperatures (5°C and 10°C) where relaxation appears to be incomplete, the

aggregate breakup of the polymer particle complex depends on an activated process. This suggests that there is some existence of an energetic barrier for the desorption of the unstable anchoring polymer segments [2]. Interestingly, at these low temperatures, when the hood to the rheometer was removed, a significant amount of the gel had come up out of the serrated double gap cup which was not observed at the higher temperatures.

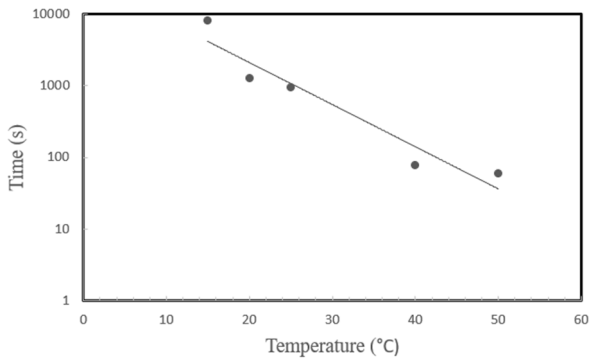

Fig. 15. A semi-log plot of relaxation time (s) against temperature (°C) showing an exponential increase with decreasing temperature

Conclusion

This research builds upon previous studies that have performed work on the relaxation process of these shake-gels [8,10], looking further into depth on the relaxation process post the increased shear rate and showing that the gel composition and temperature influence the relaxation of mixtures of poly(ethylene-oxide) and silica nanoparticles by orders of magnitude. The relaxation time is found to depend exponentially on the particle to polymer ratio with the saturation of silica particles by long polymer chains forming an inefficiently networked structure. The relaxation time also exponentially increases with increasing polymer molecular weight, due to longer chains providing more adsorption sites per chain, and decreasing temperature, as particles with lower kinetic energy desorb slower. There also existed a maximum viscosity reached by the gel during the process by which the polymer chains start to coil from their elongated state at high shear. There appeared to be two competing effects that determined the strength of the gel, and the time taken to reach this maximum viscosity also varied at different silica and PEO concentrations. This prompted discussion that further work should be conducted to learn more about the underlying mechanisms behind time taken for the gel to reach its peak viscosity.

References

[1] B. Cabane, K. W. (1997). Shear induced gelation of colloidal dispersions . *J. Rheol.*, 531.

[2] D.C. Pozzo, L. W. (2004). Reversible shear gelation of polymer-clay dispersions. *Colloids Surfaces A: Physiochem Eng. Aspect. 240*, 187-198.

[3] F. Lafuma, K. W. (1991). Bridging of colloidal particles through adsorbed polymers . *J. Colloid Interface Sci. 143*, 9-21.

[4] Goodwin, D. D. (2013). Characterization of Polymer Adsorption onto Drug Nanoparticles Using Depletion Measurements and Small-Angle Neutron Scattering. *Molecular Pharmaceuticals, 10*, 4146-4158.

[5] Gundrun Schmidt, M. M. (2003). Properties of polymer-nanoparticle composites. *Current Opinion in Colloid and Interface Science 8*, 103-108.

[6] H.J. Ploehn, W. R. (1990). Interactions betwenn Colloidal Particles and Soluble Polymers. *Advances in Chemical Engineering*, 137-228.

[7] Hammouda B., H. a. (2004). Insight into Clusteriing in Poly(ethylene oxide) Solutions. *Macromolecules*, 6932-6937.

[8] Hirose, Y. (2017). Rheological Behavior of Nanosilica Suspensions in Poly(Ethylene Oxide) Solutions with Sodium Chloride. *Materials Sciences and Applications, 8*, 333-341.

[9] Ilies Bahlouli, A. B. (2013). The effect of temperature on the rheological behavior of polyethylene oxide (PEO) solutions. *Applied Rheology* .

[10] J. Zebrowski, V. P. (2003). Shake-gels: shear-induced gelation of lapoonite-PEO mixtures. *Colloids and Surfaces A: Physiochem. Eng. Aspects 213*, 189-197.

[11] Jun Yang, C.-R. H.-F.-C. (2013). Interaction of Silica Nanoparticle/ Polymer Nanocomposite Cluster Network Structure: Revisiting the Reinforcement Mechanism. *J.Phys. Chem. C*, 8223-8230.

[12] Kamihayashi M., O. H. (2006). Rheological Behavior of Suspensions of Silica Nanoparticles in Associating Polymer Solutions . *Industrial and Engineering Chemistry Research*, 6899-6905.

[13] Lei Ye, Y. X. (2014). Particle shape dependence of rheological behavior for colloid-polymer mixtures. *Chinese Journal of Polymer Science*, 1515-1523.

[14] M. Takeda, T. M. (2010). Rheo-SANS studies on shear thickening in clay-poly(ethylene oxide) mixed solutions. *Macromolecules 43*, 7793-7799.

[15] M.M. Ramos-Tejada, P. L. (015). Shaken but not stirred: The formation of reversible particle-polymer gels under shear. *Colloids Surfaces A: Physiochem Eng. Aspect. 471*, 164-169.

[16] N. Patel, S. E. (2004). Interactions between colloidal particles in polymer solutions: A density functional theory study. *Journal of Chemical Physics*.

[17] Otsubo, Y. (1999). A nonlinear elastic model for shear thickening of suspensions flocculated by reversible bridging. *Langmuir 15*, 1960-1965.

[18] P.A. Pincus, C. S. (1984). Polymer adsorption on colloidal particles. *J. Phys. 45*, 725-729.

[19] Peter Pang, P. E. (2001). Kinetics of the aggregation of polyethylene oxide at temperatures above the polyethylene oxide–water cloud point temperature. *Colloids and Surfaces A: Physiochemical and Engineering Aspects, Volume 204, Issues 1-3*, 23-30.

[20] Q. Zhang, L. A. (2002). Poly(ethylene oxide)/silica nanocomposites:structure and rheology. *Langmuir 18*, 10435-10442.

[21] S.F. Liu, F. L. (1994). Rheological behavior of moderately concentrated silica suspensions in the presence of adsorbed poly(ethylene oxide). *Colloid Polym Sci 272*, 196-203.

[22] S.I Jeon, J. L. (1991). Protein-surface interactions in the presence of polyehylene oxide: I. Simplified Theory. *Journal of Colloid and Interface Science*, 149-158.

[23] S.Wang. (1992). Transient network theory for shear-thickening fluids and physically crosslinked networks . *Macromolecules 25*, 7003-7010.

[24] Stefan Bekiranov, R. B. (1997). Solution behavior of polyethylene oxide in water as a function of temperature and pressure. *Physical Review E, Volume 55, Number 1*, 577-585.

[25] Th. F. Tadros, B. V. (1980). Influence of Temperature and Electrolyres on the Adsorption of Poly(propylene oxide) Block Copolymer on Polystyrene Latex and on the Stability of the Polymer-Coated Particles. *J. Phys. Chem* , 1575-1580.

[26] V.Can, O. O. (2005). Shake gels Based on Laponite-PEO mixtures: effect of polymer molecular weight. *Des. Monomers Polym. 8*, 452-462.

[27] Y. Otsubo, K. W. (1990). Rheological studies on bridging flocculation. *Colloids and surfaces 50*, 341-352.

[28] Yan, F. Y. (2016). Effect of Particle/Polymer Number Ratio on the Structure and Dynamics of Complex between Large Polymer and Nanoparticle. *Colloids and Surfaces A: Physiochemical and Engineering Aspects, 507*, 67-75.

[29] Yang, W. Q. (2004). A Novel Flocculent of Al(OH)3-Polyacrylamide Ionic Hybrid. *Journal of Colloid and Interface Science, 273*, 400-405.

[30] Ye, L. T. (2014). Enhance the Mechanical Performance of Polyacrylamide Hydrogel Byaluminium-Modified Colloidal Silica. *Colloids and Surfaces A: Physiochemical and Engineering Aspects, 447*, 103-110.

[31] Yoshimasa Murakami, R. E. (1998). Studies on Interaction between Silica Gel and Polymer Blend by Inverse Gas Chromatography. *Polymer Journal, Vol.30, No.6* , 520-525.

[32] Z.C. Pandolfelli, R. d. (2008). Workability and setting parameters evaluation of colloidal silica bonded refractory suspensions. *Ceramics International*, 165-171.

A Comparative Analysis of the Supply Chain Models in Cold Chain Healthcare Products

Bowen Zheng and Xiyue Xu
Department of Chemical Engineering, Imperial College London, U.K.

Abstract CAR T-cell therapy is one of the largest breakthroughs in blood cancer treatment recently. Two therapies have been approved by the FDA in 2017 and the NHS in 2018 to treat certain blood cancers. Numerous researches have been done on developing the manufacturing process while little has been done on optimising the supply chain of the therapy. This paper, therefore, aimed to identify possible improvements on autologous CAR T-cell supply chain in England. Current autologous supply chain and proposed allogeneic supply chain were analysed. A comparative analysis was performed on red blood cell, cord blood and the autologous CAR T-cell supply chains to highlight the similarities and differences. Results suggest that autologous CAR T-cell supply chain can employ existing distribution concepts, transportation facilities, collection facilities and cell banks from the blood product supply chains. Four conceptual models and their optimisation formulations were proposed to improve the current supply chain model, where in the future models can be applied to a larger scale and to reduce cost while maintaining the same patient responsiveness.

1. Introduction

Chimeric antigen receptor T cell (CAR T-cell) therapy is a type of adoptive cell immunotherapy (Gill, et al., 2016). A T-cell is a subtype of white blood cell that functions in cell-mediated immunity. The T-cells are genetically modified with receptors, which allow the T-cells to recognize the target cancerous cells. The T-cells are then infused into the patient's bloodstream and the infused cells will aid the patient's immune system in attacking specific blood cancer cells (Crow, 2017; Gill, et al., 2016). In 2017, the U.S. Food and Drug Administration (FDA) approved two CAR T-cell therapies, Tisagenlecleuce (marketed as Kymriah®) and Axicabtagene ciloleuce (marketed as Yescarta®). Kymriah® is designed for treatments of children and young adults with recurrent acute lymphoblastic leukaemia (ALL). Results from a clinical trial with children and young adults who had no responses to standard treatments indicate that the therapy has successfully sent the cancer into 82.5% remission while 75% of the patients had no sign of recurrence after 6 months (Guthrie, 2018). Yescarta® is used for patients with advanced diffuse large B-Cell lymphoma (DLBCL) and primary mediastinal B-cell lymphoma (PMBCL), who had no effective responses to two or more previous treatments. Studies show that the therapy had 54% of the patients' cancer completely disappeared and 82% of the patients' cancer growth slowed or inhibited. Moreover, about 40% of the patients had no signs of cancer after nearly 9 months (Guthrie, 2018). Although most of the CAR T-cell therapies are offered through clinical trials, the therapy is expected to be largely commercialised soon due to its promising outcomes.

A recent market survey suggests that CAR T-cell financing rounds exceed $950 million U.S. dollars and the market has seen nearly $20 million U.S. dollars of capitalization from CAR-T companies (Bioinformant, 2018). Even though the CAR T-cell therapies have demonstrated strong market potential through growing investment, the high cost of $1 million US dollars per therapy remains the major barrier for patients to receive such treatment (Szabo, 2017).

This work studied the similarities and differences between the CAR T-cell supply chain and existing blood product supply chains under public setting in England. Possible improvements of the current CAR T-cell supply were identified following the comparative analysis. The investigation on the current supply chain models including autologous and allogeneic CAR T-cell was carried out first.

2. Background

Although the autologous CAR T-cell therapy has been proven effective in treating patients with ALL, DLBCL and PMBCL, both the high cost and readiness of the therapy have encouraged companies to develop allogeneic CAR T-cell therapies. Allogeneic CAR T-cell therapy refers to the treatment that uses the T-cells obtained from a healthy donor. Currently, the key challenges lie in minimizing rejection risks related to donor compatibility which improves the effectiveness of the therapy (Yang, et al., 2015). Researchers from different institutions have done numerous studies and some methods have been discovered including gene editing to eliminate expression of the endogenous T cell receptor (TCR) (MacLeod, et al., 2017). Allogeneic CAR T-cells were only tested in lab scale until the first allogeneic CAR T-cell therapy clinical trial, UCART123 by Cellectis, was approved by the FDA in July 2017 (Fernández, 2017). However, only 2 months after the approval, the FDA halted the clinical trial due to a patient's death 9 days after being admitted to the clinical trial. The patient experienced severe cytokine release syndrome (CRS), which is a common post CAR T-cell therapy complication (Fernández, 2017). After the FDA lifted the clinical hold, Cellectis has reported an 83% cancer remission rate and raised around $164 million US dollars for this ongoing clinical development (Burik, 2018). Even though a few clinical trials have shown positive outcomes, the chance of developing complication after the therapy remains high and all the clinical trials are still at a very early stage.

To date, all the CAR T-cell therapies approved by the FDA are autologous, which means that the T-cells are obtained from the patient itself. The production process of CAR T-cells involves several steps and quality control

testing is carried out throughout the process. Apheresis is used as the collection process to obtain a lymphocyte enriched product and then counterflow centrifugal elutriation is performed to separate suitable T-cell subsets. The collected T-cells are transported to a laboratory and genetically modified under the Good Manufacturing Practices (GMP). During the modification process, the T-cells are incubated with a viral vector. The viral vector brings genetic material of CAR in the form of RNA, which is then reverse-transcribed into DNA. While the modified T-cells multiply in the laboratory and subsequently in the patient's body, the CAR is kept on the T-cells since the DNA is permanently integrated into the genome of the patient T-cells. As a result, the engineered T-cells will all have the CARs expressed on their cell surface (Levine, et al., 2017). Following the manufacturing process, the CAR T-cells are returned to the hospital and infused into the patient. The CAR T-cells will continue to replicate within the patient's body, recognise and eliminate cancerous cells that have the targeted antigen attached to their surface (Pfizer, 2017).

Despite the promising results of autologous CAR T-cell therapies, the first CAR T-cell therapy approved by the FDA, Kymriah®, has generated only $12 million US dollars in the first quarter of 2018, nearly 4 times below the expected sales revenue. CAR T-cells are currently offered as the final line of therapy to patients who have failed (or were not eligible) for all other standard treatments. The high cost is mainly due to the small target population, there are only several hundred patients every year who failed the standard treatments and are eligible to receive CAR T-cells. Nevertheless, Kymriah® is only available at 32 sites in the US, which further limited the number of patients receiving this therapy (Labiotech, 2018). Both challenges have resulted in a relatively high price of $475,000 US dollars per patient. This price is also due to the boutique-type of manufacturing and the patient-centric nature of the therapy. All costs (manufacturing, transport, storage) are reflected on a single patient, which is different from batch-manufactured drugs (e.g. tablets or antibodies), where one production batch serves thousands of patients. In May 2018, the FDA has approved the use of Kymriah® to be extended to adults with DLBCL and are now competing with Gilead's Yescarta®, which is priced at $373,000 per patient (Fernández, 2018). All the above emphasize the importance of reducing the cost of the therapy in order to reduce the price and allow a wider population to have access to this therapy.

In October 2018, NHS has reached agreements with both Novartis and Gilead. Kymriah® would be available at treatment sites in London, Manchester and Newcastle for patients with ALL while Yescarta® would be provided in London, Manchester, Bristol, Birmingham and Newcastle for patients with DLCBL and PMBCL. Every year, around 30 patients would receive Kymriah® and up to 200 patients would receive Yescarta® (NHS England, 2018).

Following the approvals, this research was conducted to fill the knowledge gaps in autologous CAR T-cell supply chains. Since allogeneic CAR T-cell therapy is still in early stage of clinical trials, this work will mainly focus on investing possible improvements of the supply chains for autologous CAR T-cell therapies in England.

3. Research Methodology

This report studied and compared the manufacturing and distribution supply chains of 4 cold chain healthcare products, namely: (1) autologous CAR T-cell, (2) allogeneic CAR T-cell, (3) red blood cell (RBC), and (4) cord blood (CB).

3.1 Comparative Analysis

The supply chain model and product nature were studied for autologous CAR T-cells to identify the current standard practice. Following that, an analysis on the allogeneic CAR T-cell therapy was performed to explore how using T-cells from healthy donors and the formation of a cell bank may affect the manufacturing and distribution supply chain model. Moreover, the supply chains of RBC and CB were studied with the aim to carry out a comparative analysis on different phases of the two blood products and autologous CAR T-cells in their supply chains. CB was chosen as it involves a cell bank in its supply chain. RBC was selected as it is produced solely in England and has a well-developed and adaptable infrastructure. However, as allogeneic CAR T-cells are facing considerable hurdles in clinical trials due to immunocompatibility issues, it was excluded from the comparative analysis. The phases we compared were: (a) Collection, (b) Quality control, (c) Manufacturing techniques, (d) Storage conditions, (e) Transport conditions, (f) Distribution of products, and (g) Patient matching. For each phase, similarities, differences and the potential of applying successful practices from red blood cell and cord blood supply chain models to the autologous CAR T-cell case were discussed. Following the analysis, conceptual supply chain models were developed for autologous and allergenic CAR T-cell therapies. These models aimed to adopt all possible improvements identified in the comparative analysis.

3.2 Production and Distribution Optimisation Model

Given the nature of the conceptual supply chain models developed, a general supply chain optimisation model was designed to help determine the optimal production and distribution network. The design was formulated as a mixed integer linear programming (MILP) optimisation model, aiming to optimise the economic performance of the CAR T-cells supply chain network (Guillén-Gosálbez, et al., 2010). Inspired by the snapshot model, our optimisation model was formulated over a fixed time horizon with a time-invariant number of patients (Almansoori & Shah, 2006).

3.3 Model Feasibility Analysis and Case Studies

Subsequently, the key challenges and bottlenecks of autologous CAR T-cell supply chains were discussed

along with the feasibility analysis of the four conceptual models. Lastly, a case study was performed to determine the optimal production and distribution network of autologous CAR T-cells in England. The case study was done in the light of NHS approval, therefore, all facilities employed are current NHS facilities except for the manufacturing sites.

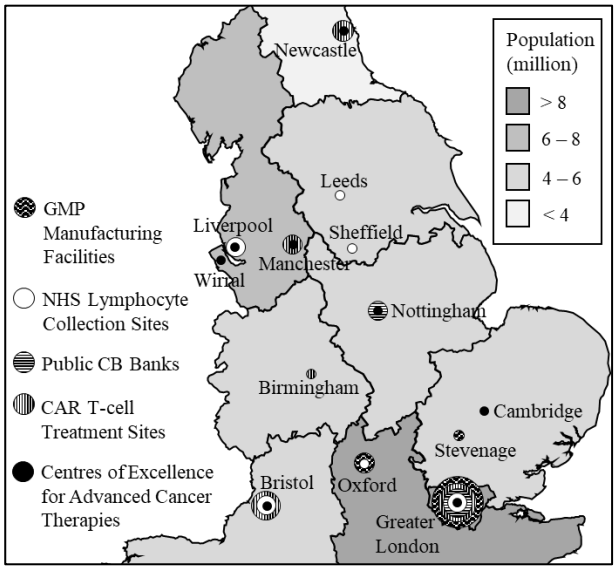

Figure 1, Distribution of different facilities related to a CAR T-cell supply chain in England.

Locations of facilities involved in blood product supply chains that can be adapted to CAR T-cell supply chain as identified in the comparative analysis were compiled in Figure 1. The map helps formulate the case study in England and analyse the feasibility of the conceptual models. Data has been collected from multiple sources as detailed in the supplementary information. Six NHS lymphocytes collection sites are NHS blood centres with T-cell apheresis equipment. Both the hospitals and NHS blood centres can act as collection sites. GMP manufacturing facilities refer to existing Medicines and Healthcare products Regulation Agency (MHRA)-licenced multifunctional cell and gene therapy manufacturing facilities, which can produce CAR T-cells. The treatment sites are hospitals that would provide CAR T-cell therapies as proposed by NHS. Two NHS cord blood cell banks in London and Nottingham are marked as storage facilities in CAR T-cell supply chains. Centres of Excellence for Advanced Cancer Therapies are where the patients receive standard treatments, which gives a reasonable indication of patient distribution.

4. Results

4.1 Supply Chain Model Identification

4.1.1 CAR T-cell

A CAR T-cell therapy by nature is infusing a large number of modified T-cells that can enable and facilitate an immune response in fighting cancerous cells into the bloodstream. A common CAR T-cell supply chain can be divided into the following parts. Firstly, T-cells need to be obtained from the patient itself (autologous) or a healthy donor (allogeneic) by apheresis. These T-cells need to be cryopreserved and transported to a Good Manufacturing Practice (GMP) cell processing facility to be genetically modified via viral vectors. The modified

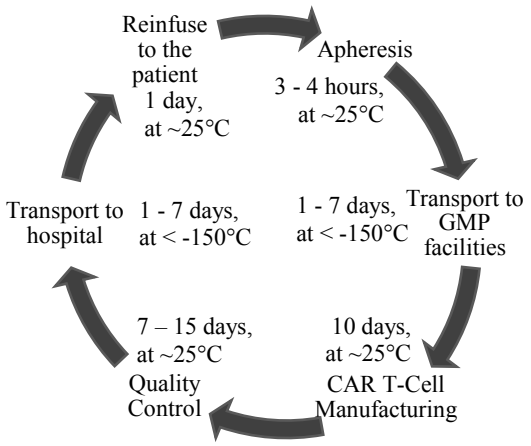

cells are then expanded in population after which a quality control will be performed to ensure that no contaminant returns to the patient's bloodstream. Figure 2 illustrates the autologous CAR T-cell supply chain.

Figure 2, Process flowsheet of autologous CAR-T cell therapy. Adapted from (Sangamo Therapeutics, 2018)

As shown in figure 3, the therapy becomes allogeneic when the modified T-cells to be infused to a patient originally came from a healthy donor (Kochenderfer, et al., 2013). This enables a mass production of off-the-shelf clinical-grade T-cells, which can benefit multiple patients. These T-cells can be modified according to the type of cancer that is being targeted. A mass of modified T-cells is reproduced and stored at cell banks or sent to different clinics for infusion. Even though the allogeneic nature speeds up the readiness and reduce the manufacturing cost of the therapy, the maximum storage time is unknown as there were barely long-term storage requirements in pre-clinical and early-stage clinical trials for allogeneic CAR T-cell therapies.

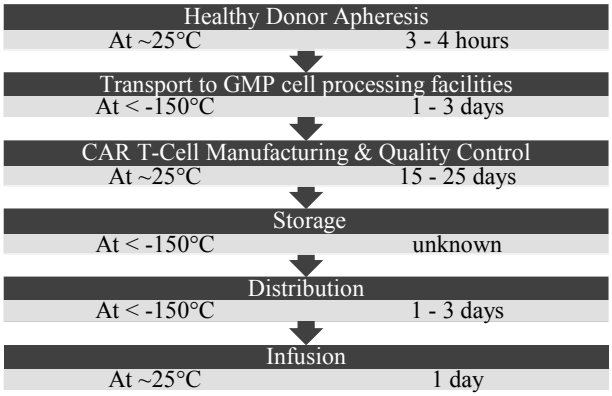

Figure 3, Process flowsheet of allogeneic CAR-T cell therapy. Adapted from (Sangamo Therapeutics, 2018)

4.1.2 Umbilical Cord Blood (CB)

CB is a source of stem cells. In 1988, the first cord blood transplantation (CBT) was successfully conducted by Dr Gluckman. The CB of a new-born cured her brother's Fanconi anaemia (Gluckman, et al., 1989). Following this initial success, the first unrelated donor CB cell bank was established by Dr Rubinstein in 1992 (Kurtzberg, et al., 1996). Nowadays, there are more than 760,000 cord

blood units (CBU) available in public CB banks worldwide (World Marrow Donor Association, 2018). Figure 4 shows a typical CB supply chain.

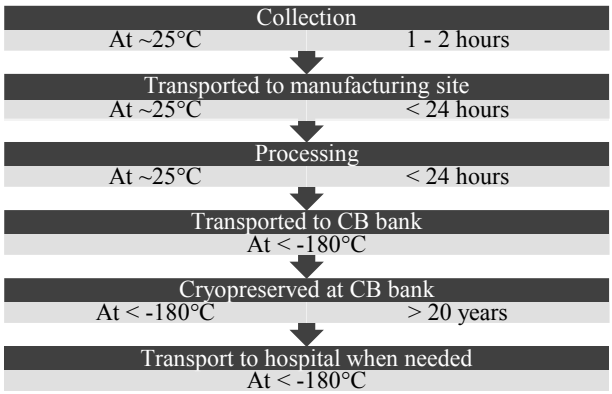

Figure 4, Process flowsheet of cord blood supply chain.

4.1.3 Red Blood Cell (RBC)

RBC is a common blood component used in blood transfusion and surgeries. It is solely produced in the UK, unlike other blood components which are partially imported. Figure 5 shows a typical RBC supply chain.

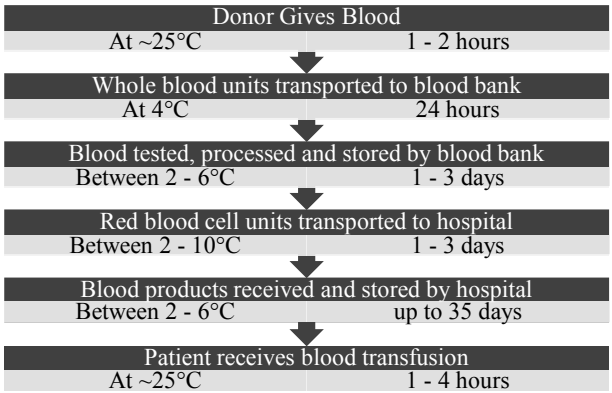

Figure 5, A typical blood product supply chain. Adapted from: (MaxQ Ltd., 2018)

4.2 Comparative Analysis

4.2.1 Good Manufacturing Practice

Since product consistency, purity and quality are essential in medical manufacturing, the implementation of GMP is required for all three healthcare products. The World Health Organisation (WHO) sets out a quality assurance system in obedience to GMP principles for collection, processing and quality control of blood products (WHO, 2011). Similar guidelines for the EU have come into operation on 30 November 2011 (European Commission, 2011). The European Commission also established GMP guidelines specific to Advanced Therapy Medicinal Products which is applicable to CAR T-cell therapies. These guidelines for ATMP manufacturers have come into operation since 22 May 2018 (European Commission, 2017).

In the UK, GMP medical manufacturer licences are issued by the MHRA. Regular inspections are conducted under different categories (MHRA, 2018). Currently, there are five MHRA-licenced multifunctional cell and gene therapy manufacturing sites in England. The average spare capacity of these facilities showed a decreasing trend while the total number of clean rooms has gone up from 21 in 2016 to 27 in 2018 (Cell and Gene Therapy Catapult, 2018).

4.2.2 Collection

RBC: RBCs mainly come from whole blood donations. There are in total 23 blood centres across the UK (NHSBT, 2018). Donors must satisfy certain health-related criteria before they can register as blood donors via phone, online or through a designated app – NHSGiveBlood. The whole donation process normally takes less than an hour. 470 ml of whole blood will be obtained and packed into a blood bag with a unique donor identification number. (NHSBT, 2018)

CB: NHS Cord Blood Bank (NHS CBB) offers public CB donation service at five hospitals in London and its surrounding vicinity. The locations are purposely selected so that CB units collected are from the widest ethnic mix and the greatest variety of tissue types (NHSBT, 2018). The NHS CBB adopts an ex utero collection technique, where the placenta is taken to a dedicated room within the delivery suite for CB collection. The amount of CB collected is usually between 60 ml and 150 ml.

CAR T-cell: The T-cells are collected by apheresis where a specialised equipment takes whole blood from a patient, isolates the T-cells and returns the rest of whole blood to the patient. The whole process will normally take 3 to 4 hours (Kite Pharma, 2018), which is slightly longer than that of a RBC collection process. The therapeutic apheresis treatments that the NHS offers include lymphocyte collection. There are 6 out of 23 blood centres which provide this service in England and can act as collection sites in a CAR T-cell supply chain. The existing registration process for RBC donation can be adopted by T-cell donation from a healthy donor for allogeneic CAR T-cell therapies.

4.2.3 Quality Control

RBC: The donations are tested for infectious agents and blood group before delivering to storage. Viruses tests for Hepatitis B, human immunodeficiency virus (HIV), Hepatitis C, Syphilis and human T-cell lymphotropic virus (HTLV) are mandatory. The donors' blood groups are checked against previous records (NHSBT, 2018).

CB: The CB collected and the mother's blood sample are firstly tested for the same group of viruses as the RBCs. Afterwards, the sample will be tissue typed, performed with a blood count and tested for bacterial and fungal contamination (NHSBT, 2018).

CAR T-cell: The quality control process includes preclinical experiments, in-progress testing and final product testing. Tests are done to ensure the safety, sterility, purity, potency and identity of the product. Common in-progress tests performed are cell phenotype, mycoplasma assay on preharvest cells, and assays analysing whether contaminated tumour cells have disappeared. Final product testing is carried out to certify the transduction efficiency, the residual amount from vector production and the absence of replicate competent

virus. CAR T-cells produced are cryopreserved as the release testing is time-consuming (Levine, 2015).

The quality control for CAR T-cells involves testing throughout the whole manufacturing process, while most of the tests carried out for blood products are preclinical. All the testing for blood products can take place in parallel with the manufacturing process since there is no in-progress and final product testing required. The testing undertaken by the CAR T-cells is labour intensive and requires a higher level of skills as the tests are more complex in nature. Consequently, the quality control significantly slows done the CAR T-cells manufacturing process while it has little impact on the manufacturing turnaround time for blood products. The average turnaround time is 15 - 28 days for CAR T-cells and more than half of it is spent on the quality control process.

4.2.4 Manufacturing Techniques

RBC: The whole blood donations transported to the blood manufacturing centres are firstly sorted and registered (NHSBT, 2018). Due to the overlap of the specific gravity of RBCs and the white blood cells, the white blood cells are filtered out of the whole blood donations before centrifugation (NATA, 2011). Operating around 3800 revolutions per minute (rpm), the centrifugation process would separate RBCs, plasma and platelets (Evans, 2018). The RBCs are then extracted and packed into separate units for storage. The whole process takes less than an hour (Legacy Health, 2018). The packed products are then held at a specific area and waiting for test results. Those which passed the test will be labelled and delivered to storage (NHSBT, 2018).

CB: The collected CB units are processed through sedimentation or centrifugation (Lam, et al., 2014) to remove RBCs and plasma. The removal of RBCs is necessary as they could result in harmful or fatal side effects during transplants. The plasma is removed to reduce the storage volume (HTA, 2018). While only the vital blood stem cells are left in the stored CB, the volume will be reduced to around 20 ml. The whole process takes less than an hour and should take place within 24 hours of collection or within 48 hours of birth (Page, et al., 2019). A cryopreservative (DMSO) is mixed with the CB products to protect the stem cells when they are frozen (NHSBT, 2018).

CAR T-cell: Both the manufacturing processes of CB and RBCs involve only separation processes and take less than an hour. Presently, the average turnaround time for Kymriah® is 25-28 days (Novartis, 2018) and for Yescarta® is 17 days (Gilead, 2017). The manufacturing time of CAR T-cells is significantly longer than that of the blood products. The main reason is that the manufacturing process of CAR T-cells is more complicated. The manufacturing process of CAR T-cells consists of multiple steps which involve high levels of skills, complex biological materials and gene modification (Sagentia Ltd, 2018). Moreover, CB and RBCs are produced in large scales as a single batch can handle a greater number of products and benefit multiple patients. For autologous CAR T-cells, the patient-specific process has ruled out the possibility of scaling up a single batch to benefit more than one patient.

4.2.5 Storage Conditions

RBC: The RBCs need to be stored between 2 and 6°C in approved blood bank refrigerators located in hospitals. Under this condition, RBCs have a shelf life of 35 days from donation (Homerton NHS Trust, 2015).

CB: DMSO (10% concentration) along with 5% dextran or hydroxyethyl starch is added into processed CB before storage. The cryopreservation will take place through controlled rate freezing. Afterwards, the frozen CB is stored in the liquid or gas phase liquid nitrogen below – 180°C (Page, et al., 2019).

CAR T-cell: CAR T-cells are packed and stored in infusion bags that are individually packed in metal cassettes. Each bag contains around 68ml of frozen suspension of modified autologous T-cells in 5% DMSO and 2.5% albumin. The packed T-cells are then stored in the vapour phase of liquid nitrogen below – 150°C (JPAC, 2018). As CAR T-cells are stored in very similar conditions with CB, CB cell banks could be employed as the storage facilities in CAR T-cell supply chains.

4.2.6 Transport Conditions

RBC: Ideally the same as the storage condition, but it can be transported between 2°C and 10°C (JPAC, 2018).

CB: The collected CB is transported between 15°C and 25°C (PGCB Foundation, 2018). The processed CB is transported in liquid nitrogen dry shippers (JPAC, 2018).

CAR T-cell: The collected T-cells are cryopreserved within 24 hours and transported to the manufacturing site. The manufactured T-cells are transported in liquid nitrogen dry shippers, which is the same as CB. Thus, NHS's current contract for cord blood dry shipper services could be extended to CAR T-cell transportation.

4.2.7 Distribution of Products

RBC: Following the manufacturing process, the packed RBCs are delivered to hospitals for storage. The RBCs would be ready for transfusion after some checks (NHSBT, 2018). The RBCs can only be removed from the controlled storage one unit at a time and within 30 minutes before the transfusion. If the unit of RBCs has been out of controlled storage for more than 30 minutes, it would be handed over to the hospital's blood bank right away for safe disposal (Homerton NHS Trust, 2015).

CB: The CB units are transported to and stored in public cell banks until required by a matching patient domestically or internationally. These units are registered on national and international databases such as the British Bone Marrow Registry, Bone Marrow Donors Worldwide and the European Marrow Donor Information System (HTA, 2018). Once there is a match found, the CB unit will be delivered to the patient site for transplant.

CAR T-cell: The modified autologous CAR T-cells are delivered to patient sites and thawed before infusion. Unlike the RBCs, CAR T-cells are delivered to specific hospitals where the treatment is taking place.

4.2.8 Patient Matching

RBC: It takes less than 15 minutes to complete a blood type test. Patients are then matched according to the RBC compatibility. The hospitals normally stock Rh-positive RBC units. The supply of Rh-negative RBCs is unstable due to its relatively small population and patients may need to receive transfusion upon prior requests.

CB: The time required for the process is uncertain as it depends on whether there is a suitable cord blood unit. Organisations can search for a suitable match in the databases listed above on behalf of any patient in need.

CAR T-cell: The autologous CAR T-cell therapy requires no patient matching process. We would expect in the future allogeneic CAR T-cell therapy can adapt the patient matching model used for CB.

4.3 Conceptual Supply Chain Models

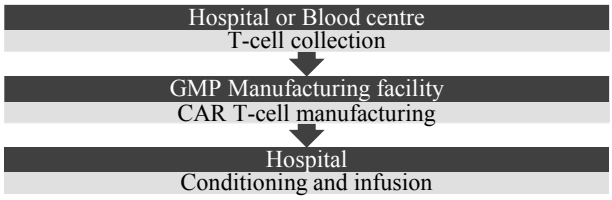

Figure 6, Schematic for model 1 and model 2.

Model 1: Autologous – Collection at Treatment Sites

Figure 6 shows the supply chain model employed currently in most of the clinical trials in England. Patients' T-cells are collected at treatment sites and then sent for manufacturing. The processed CAR T-cells are returned to the same treatment site for infusion.

Model 2: Autologous – Collection at Blood Centres

The difference between model 1 and 2 is that RBC blood centres are used for T-cell collection, as shown in figure 6. By incorporating blood centres into the supply chain, patients can get their T-cells collected sooner instead of travelling to certain hospitals in the first place.

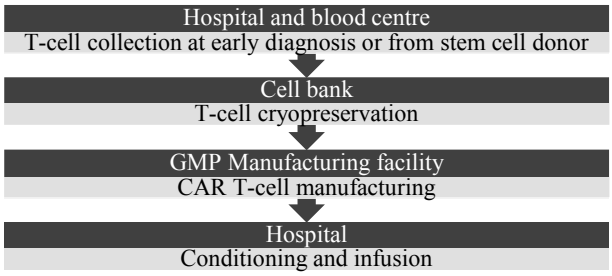

Figure 7, Schematic for model 3 and model 4.

Model 3: Autologous – Collection at Early Diagnosis

In this model, T-cells are collected when a patient is diagnosed with relevant cancers. As patients are only eligible for CAR T-cell therapies after they failed at least two standard treatments, T-cells collected at early diagnosis will have better quality than those in previous models. To store the T-cells for future uses, the distribution and cell bank storage systems for CB are incorporated into this model as shown in figure 7. Since the manufacturing cost of CAR T-cells is significantly higher than that of CB, the collected T-cells are stored before being processed. The cryopreserved T-cells will stay in satisfactory cell counts. Once the patient becomes eligible and decides to start the therapy, the T-cells will be sent for manufacturing. Since better starting material quality shortens the processing time and improves product quality, this model helps reduce the turnaround time and ensure patient responsiveness to the therapy.

Model 4: Allogeneic – Stem Cell Donor

Following the research done by Graham et al., model 4 as shown in figure 7 was designed. The facilities used are the same as model 3. The main difference is that T-cells are collected from the previous allogeneic haematopoietic stem cell transplant (HCST) donor instead of from the patient itself as healthy donors can donate T-cells with better quality (Graham, et al., 2018).

4.4 Optimisation Model Formulation

The model is formulated as a MILP to help assess the optimum distribution network. The conceptual supply chain models were developed for NHS England CAR T-cell therapies, therefore, the number of facilities is as specified in figure 1. The fixed costs and capital investment were not considered since all facilities are existed and in operation. Since the therapy will be provided to 230 patients per year by NHS England, we simplified the model by reducing the scope to a fixed time horizon of 1 month and using a time-invariant patient number of 20.

4.4.1 Notation

Table 1, Notations for the optimisation model.

Indices	
c	Collection site
h	Treatment site
i	Method of transportation
m	Manufacture site
p	Patient
s	Storage site
Parameters	
$C_M(m)$	Manufacturing cost at site m
$d(a,b)$	Distance required to travel between sites a and b
$t_T(a,b,i)$	Transport time between site a and site b by method i
t_S	Storage time
$U_S(s)$	Storage cost at site s per unit of 1 time
$U_T(i)$	Transport cost of method i per unit of time
$v(i)$	Speed of transport method i
Continuous variables	
C	Total cost
C_M	Total manufacture cost
C_T	Total transport cost
C_S	Total storage cost
Integer variables	
$y(p,c)$	1 if patient p's T-cells are collected at site c, 0 otherwise.
$y(p,h)$	1 if patient p is treated at site h, 0 otherwise.
$y(p,m)$	1 if patient p's T-cells are manufactured at site m, 0 otherwise.
$y(p,s)$	1 if patient p's T-cells are stored at site s, 0 otherwise
$y(p,c,s,i)$	1 if patient p's T-cells are collected at site c, stored at site s, and transport in between by method i, 0 otherwise
$y(p,m,c,i)$	1 if patient p's T-cells are collected at site c, manufactured at site m, and transported in between by method i, 0 otherwise
$y(p,m,h,i)$	1 if patient p's T-cells are manufactured at site m, the patient is treated at site h, and transported in between by method i, 0 otherwise

$y(p,s,m,i)$ 1 if patient p's T-cells are stored at site s, manufactured at site m, and transported in between by method i, 0 otherwise

4.4.2 Capacity Constraints

Experts suggest that the maximum capacity for a single commercial manufacture site is around 10. The average turnaround time for CAR T-cells are 20-30 days, therefore, we assume that all manufacture sites have a capacity of manufacturing 10 CAR T-cells per month:

$$\sum_{p=1}^{20} y(p,m) \leq 10 \quad \forall m \tag{1}$$

Since NHS has appointed 5 treatment sites across England, we assume that each treatment site has an equal capacity of treating 4 patients per month:

$$\sum_{p=1}^{20} y(p,h) \leq 4 \quad \forall h \tag{2}$$

For conceptual model 3 and 4 which have storage sites involved, we assume each storage site can equally accept a maximum of 10 new CAR T-cells per month:

$$\sum_{p=1}^{20} y(p,s) \leq 10 \quad \forall s \tag{3}$$

As one patient's T-cell can only be collected at one site, manufactured at one site and the patient must be treated at one site:

$$\sum_{m=1}^{5} y(p,m) = 1 \quad \forall p \tag{4}$$

$$\sum_{c=1}^{11} y(p,c) = 1 \quad \forall p \tag{5}$$

$$\sum_{h=1}^{5} y(p,h) = 1 \quad \forall p \tag{6}$$

For model 3 and 4 where the patient's T-cell will also need to be stored at one site:

$$\sum_{s=1}^{2} y(p,s) = 1 \quad \forall p \tag{7}$$

4.4.3 Objective Function

The model aims to minimise the total operating cost of the CAR T-cell supply chain over one month for 20 patients. The total manufacturing cost for 20 patients is:

$$C_M = \sum_{p=1}^{20} \sum_{m=1}^{5} [y(p,m) C_M(m)] \tag{8}$$

The transport cost is the product of the unit cost of a transport method i and the time taken to transport in between facilities. The transport time is either obtained from reliable sources or calculated from dividing the distance in between sites by the speed of the transport method i:

$$t_T(m,h,i) = d(m,h)/v(i) \tag{9}$$

$$t_T(c,s,i) = d(c,s)/v(i) \tag{10}$$

The total transport cost for conceptual model 1 and 2 is:

$$C_T = \sum_{p=1}^{20} \sum_{m=1}^{5} \sum_{h=1}^{5} \sum_{c=1}^{11} \sum_{i=1}^{3} [y(p,m,c,i) U_T(i) t_T(m,c,i) + y(p,m,h,i) U_T(i) t_T(m,h,i)] \tag{11}$$

For conceptual model 3 and 4 with storage sites, the transport time and the total transport cost is:

$$t_T(m,h,i) = d(m,h)/v(i) \tag{9}$$

$$t_T(c,s,i) = d(c,s)/v(i) \tag{12}$$

$$t_T(s,m,i) = d(s,m)/v(i) \tag{13}$$

$$C_T = \sum_{p=1}^{20} \sum_{s=1}^{2} \sum_{m=1}^{5} \sum_{h=1}^{5} \sum_{c=1}^{11} \sum_{i=1}^{3} [y(p,c,s,i) U_T(i) t_T(c,s,i) + y(p,s,m,i) U_T(i) t_T(s,m,i) + y(p,m,h,i) U_T(i) t_T(m,h,i)] \tag{14}$$

Only conceptual model 3 and 4 will need to consider the storage cost. The total storage cost is calculated by the cost of storing at site s per unit time times the time required to store the product:

$$C_S = \sum_{p=1}^{20} \sum_{s=1}^{2} [y(p,s) U(s) t_S] \tag{15}$$

4.4.4 Model Summary

The total monthly cost of the network for conceptual model 1 and 2 is minimised by the optimisation:

$$\min \; C = C_M + C_T \tag{16}$$

For conceptual model C and D, the total monthly cost of the network is minimised by the optimisation:

$$\min \; C = C_M + C_T + C_S \tag{17}$$

5. Discussion

5.1 Key Challenges in Autologous CAR T-cell Supply Chain

5.1.1 Scaling up

Following the NHS approvals, the demand for the therapy will be much higher than that during clinical trials, which makes scaling up the key challenge right now. The main problem associated with scaling up the autologous CAR T-cell supply chain is standardisation. Currently, the therapy is labour intensive and mostly carried out at a single academic institution. A Key step to scale up is establishing a controlled and standard process that can be implemented across many collection, manufacturing and treatment sites (Levine, et al., 2017). The development of a cost-effective manufacturing process of CAR T-cells would require effective coordination among the facilities.

Unlike the traditional therapies, the autologous CAR T-cell therapy is highly patient-centric and has relatively small patient population. The treatment decision solely depends on the patient's health condition and willingness to receive the therapy (Lamb, et al., 2017), therefore, the demand of the therapy is highly unpredictable. The unpredictable demand imposes difficulties on allocating the workforce and the facility capability. Quality of the collected T-cells vary as both the patients' health conditions and apheresis centres are different (Lamb, et al., 2017). Viral vector, as another key raw material of the manufacturing process, is also subject to multiple suppliers and has inconsistent quality (Levine, et al., 2017). Consequently, the final product effectiveness would be inconsistent. All above will largely hinder the standardisation and scalability of the manufacturing process.

Due to the patient-specific nature of the therapy, the traceability of the product is extremely important when

transitioning from production in a single academic institution to standardised processes in various commercial sites. If the supply chain were to scale up, the chances of mislabelling are higher, which may cost patients' lives. The design of suitable commercial systems in tracing and managing the products is also a key challenge in scaling up (Lamb, et al., 2017).

In order to avoid cross-contamination, the manufacturing process for each patient's T-cell is required to be in a closed system. Thus, the challenge also lies in developing production technologies which could accommodate multiple independent productions in parallel since manufacturing multiple patient products in a larger batch is not an option (Kaiser, et al., 2015). As each production will only benefit a single patient, scaling up will remain challenging even with a standardised and reproducible manufacturing process.

5.1.2 Cost Reduction

Autologous CAR T-cell therapies are extremely expensive. As the therapy is patient-centric, its manufacturing process is highly customised and can only take place after a patient' T-cell has been collected. The unpredictable demand prevents a company from planning and optimising its supply chain effectively. Companies are currently working on developing new technology to disrupt manufacturing processes (Staines, 2018). Advanced technology can improve resource productivity and delivery efficiency, which will eventually lead to cost reduction. An automated production line is one of the solutions. However, this would require extremely high upfront capital investment cost and skilled labour are still needed to enable the handling steps throughout the process (Kaiser, et al., 2015). In the meantime, manufacturers are developing allogeneic CAR T-cell therapies, which has significantly lower cost as it is not patient-centric, and companies can plan and scale up the production more easily.

5.1.3 Maintain the Same Patient Responsiveness:

The WHO defines patient responsiveness as the outcome can be achieved when institutions respond to a patient's expectations appropriately (Darby, et al., 2003). As discussed in section 5.1.1, the therapy is patient-centric, and the manufacturing process is boutique-type. The success of the whole therapy solely depends on the outcome of a single patient. Thus, maintaining the same level of patient responsiveness while reducing the cost and scaling up the manufacturing the production process is crucial.

5.1.4 Point of Care versus Centralised Manufacturing

Scientists suggest that GMP-in-a-box might be a solution to cost reduction and patient responsiveness improvement. To date, most of the manufacturers have a centralised manufacturing site and some of them are looking to relocate the facilities closer to the treatment sites (Staines, 2018). GMP-in-a-box refers to manufacturing the collected T-cells in an automated cell culture system at the site where both treatment and collection take place (Porwollik, 2016). This will result in a high level of standardisation, as the whole process will be in a single closed system. The transport cost will be virtually zero and the turnaround time will be lower. The concept is debatable as the cost of constructing GMP facilities and training skilled labour will be extremely high and may not be offset by the reduced transport cost.

5.2 Feasibility of the Conceptual Models

Model 1: Model 1 follows the same supply chain rational employed in the clinical trials. The only difference is that more treatment and manufacturing sites as shown in figure 1 are involved, which helps scale up the supply chain. The scaling up potential is also applicable to all following models, as more facilities are employed. All facilities involved have no upfront capital investment required as they are existing facilities. The model is feasible since it is abided by current practices.

Model 2: Model 2 uses NHS blood centres as T-cell collection sites. As shown in figure 1, there are six of NHS blood centres which have the equipment for T-cell apheresis. Employing these facilities requires no capital investment and patients can benefit from having their T-cells collected more conveniently. This would also free up hospital capacity which is used for T-cell apheresis. However, coordination and approval from the NHS Blood and Transplant (NHSBT) is key to realise this model.

Model 3: Model 3 requires T-cell storage facilities. Currently, NHS has two public cell banks in London and Nottingham which satisfy the T-cell storage conditions. Though adopting these facilities require no capital investment, coordination and approval from NHSBT are still required to implement this model. Ultimately, patients' willingness to have their T-cells collected at early diagnosis will determine the feasibility of the model.

Model 4: Model 4 differs from Model 3 in that T-cells collected are from a stem cell donor. The previous stem cell donor is Human Leukocyte Antigen (HLA) matched to the patient, so CAR-T cells collected from them are less likely to cause immunocompatibility issues. HCST is a treatment for ALL only, therefore, this model is only applicable to patients with ALL (Graham, et al., 2018). As the patient population of ALL is one degree of magnitude smaller than that of other CAR T-cell therapy targeted cancers, this model may not be scaled up as quickly as others. Similar to model 3, donor's willingness availability will determine the feasibility of the mode. It is suggested that the donor donates T-cells for storage before the stem cell donation to help implement the model.

5.4 Reduced Case Study

A reduced case study for conceptual model 1 was carried out using the optimisation model formulated. It assessed the feasibility of the model with existing facilities and NHS's therapy quota of 230 patients per year. The capacity of each manufacturing site was assigned according to the nature of the institution. The therapy has not yet been fully commercialised in England, therefore, there is no accurate data for the cost of manufacturing and

the hospital fees. Hence, we assume that all manufacturing sites and hospitals have the same cost. The main consideration of this case study is, therefore, the transport cost between the hospitals and manufacturing sites. The optimum distribution network for model 1 is shown in Figure 8.

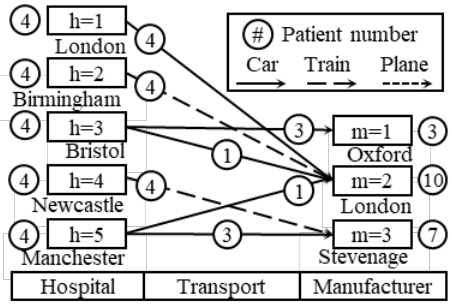

Figure 8, Supply chain network from the reduced case study.

Two of the manufacturing sites in London and one in Oxford are academic institutions, which means the capacity of these sites will remain low. As the Stevenage and the other London manufacturing sites are commercial institutions, a higher capacity could be allocated to them if NHS were to increase its quota. Therefore, we would expect with this model, T-cells collected from the South, the Southwest and the Midlands will be processed in London while those collected from the North and the Northwest will be processed in Stevenage if the manufacturing process were to scale up.

6. Conclusions and Outlook

The CAR T-cell supply chain has similarities with blood product supply chains in terms of raw material collections, storage conditions and transport conditions. Proposed conceptual models adopted relevant practices and existing facilities from the blood product supply chains to reduce capital investment, scale up the supply chain and improve patient responsiveness. The key challenges identified for the autologous CAR T-cell supply chain are the standardisation of the manufacturing process and the traceability of the product in the distribution process due to the patient-centric nature of the therapy.

Future work can be done to (1) Investigate suitable locations of new manufacturing sites and whether GMP-in-a-box can be employed in CAR T-cell supply chains. (2) Develop new technology to disrupt the production process, with the aim of reducing the manufacturing cost and scaling up the manufacturing capacity. (3) Explore the extent of cost reduction when allogenic CAR T-cell therapies are available on a larger scale.

7. References

Almansoori, A. & Shah, N., 2006. Design and Operation of a Future Hydrogen Supply Chain: Snapshot Model. *Chemical Engineering Research and Design,* 84(6), pp. 423-438.

Bioinformant, 2018. *Global Database of CAR-T Cell Therapy Companies (2018),* Washington: Bioinformant.

Burik, A., 2018. *French Biotech Develops a New Generation of Safer CAR-T Cells.* [Online]
Available at: https://labiotech.eu/medical/cellectis-car-t-safety/

Cell and Gene Therapy Catapult, 2018. *Cell and gene therapy GMP manufacturing in the UK Capability and Capacity Analysis,* London: Cell Therapy Catapult Limited.

Darby, C., Valentine, N., Murray, C. & Silva, A., 2003. *World Health Organization (WHO): strategy on measuring responsiveness,* Geneva: World Health Organization.

European Commission, 2011. *Annex 14 Manufacture of Medicinal Products Derived from Human Blood or Plasma.* [Online]
Available at:
https://ec.europa.eu/health/sites/health/files/files/eudralex/vol-4/annex14_rev30-03_2011_en.pdf

European Commission, 2017. *Guidelines on Good Manufacturing Practice specific to Advanced Therapy Medicinal Products.* [Online]
Available at:
https://ec.europa.eu/health/sites/health/files/files/eudralex/vol-4/2017_11_22_guidelines_gmp_for_atmps.pdf

Evans, R., 2018. *Journey of a Blood Bag- Blood Centre. Processing and Testing.* [Online]
Available at: http://hospital.blood.co.uk/media/28964/10-journey-of-a-blood-bag-blood-centre-processing-and-testing.pdf

Fernández, C. R., 2017. *Off-the-Shelf CAR-T Cells Struggle to Improve Cancer Treatment.* [Online]
Available at: https://labiotech.eu/medical/allogeneic-car-t-cells-cellectis/

Fernández, C. R., 2018. *Novartis and Gilead's CAR-T Therapies Now Compete for the Same Cancer Patients.* [Online]
Available at: https://labiotech.eu/medical/car-t-therapy-novartis-gilead/

Gilead, 2017. *Kite's Yescarta™ (Axicabtagene Ciloleucel) Becomes First CAR T Therapy Approved by the FDA for the Treatment of Adult Patients With Relapsed or Refractory Large B-Cell Lymphoma After Two or More Lines of Systemic Therapy.* [Online]
Available at: https://www.gilead.com/news/press-releases/

Gill, S., Maus, M. V. & Porter, D. L., 2016. Chimeric antigen receptor T cell therapy: 25years in the making. *Blood Reviews,* 30(3), pp. 157-167.

Gluckman, E. et al., 1989. Hematopoietic Reconstitution in a Patient with Fanconi's Anemia by Means of Umbilical-Cord Blood from an HLA-Identical Sibling. *N Engl J Med,* 321(17), pp. 1174-1178.

Graham, C., Jozwik, A., Pepper, A. & Benjamin, R., 2018. Allogeneic CAR-T Cells: More than Ease of Access?. *Cells,* 7(10), p. 155.

Guillén-Gosálbez, G., Mele, F. D. & Grossmann, I. E., 2010. A bi-criterion optimization approach for the design and planning of hydrogen supply chains for vehicle use. *AIChE Journal,* 56(3), pp. 650-667.

Guthrie, G., 2018. *CAR T-Cell Immunotherapy: The 2018 Advance of the Year.* [Online]
Available at: https://www.cancer.net/blog/2018-01/car-t-cell-immunotherapy-2018-advance-year

Homerton NHS Trust, 2015. *Storage of blood and blood products.* [Online]
Available at: http://www.homerton.nhs.uk/our-services/services-a-z/p/pathology/blood-transfusion/storage-of-blood-and-blood-products/

HTA, 2018. *After collection - Cord blood banking.* [Online]
Available at: https://www.hta.gov.uk/guidance-public/cord-blood-banking-guide-parents/cord-blood-banking-faqs/after-collection

HTA, 2018. *Storage and uses of stored cord blood.* [Online]
Available at: https://www.hta.gov.uk/guidance-public/cord-blood-banking-guide-parents/cord-blood-banking-faqs/storage-and-uses-stored
JPAC, 2018. *Chapter 22.14: Transportation.* [Online]
Available at: https://www.transfusionguidelines.org/red-book
JPAC, 2018. *Chapter 6.11: Transportation of blood components.* [Online]
Available at: https://www.transfusionguidelines.org/red-book
Kaiser, A. D. et al., 2015. Towards a commercial process for the manufacture of genetically modified T cells for therapy. *Cancer Gene Therapy,* Volume 22, p. 72–78.
Kite Pharma, 2018. *How Will I Receive Treatment.* [Online]
Available at: https://www.yescarta.com/car-t-treatment-process
Kochenderfer, J. N. et al., 2013. Donor-derived CD19-targeted T cells cause regression of malignancy persisting after allogeneic hematopoietic stem cell transplantation. *Blood,* 122(25), pp. 4129-4139.
Kurtzberg, J. et al., 1996. Placental Blood as a Source of Hematopoietic Stem Cells for Transplantation into Unrelated Recipients. *N Engl J Med,* 335(3), pp. 157-166.
Labiotech, 2018. *The First CAR-T Therapy Is Not Living Up to Commercial Expectations.* [Online]
Available at: https://labiotech.eu/medical/kymriah-car-t-therapy-novartis-sales/
Lamb, M., Margolin, R. E. & Vitale, J., 2017. Personalized supply chains for cell therapies. *Cell Gene Therapy Insights,* 3(10), pp. 815-833.
Lam, B. S. et al., 2014. Depletion of Red Blood Cells from Cord Blood Using a Simple and Rapid Immunomagnetic Separation Method. *Blood,* 124(21), p. 3853.
Legacy Health, 2018. *Centrifuging Blood.* [Online]
Available at: https://www.legacyhealth.org/for-health-professionals/refer-a-patient/laboratory-services/collection-guidelines/centrifuging-blood.aspx
Levine, B. L., 2015. Performance-enhancing drugs: design and production of redirected chimeric antigen receptor (CAR) T cells. *Cancer gene therapy,* Volume 22, pp. 79-84.
Levine, B. L., Miskin, J., Wonnacott, K. & Keir, C., 2017. Global Manufacturing of CAR T Cell Therapy,. *Molecular Therapy - Methods & Clinical Development,,* Volume 4, pp. 92-101.
MacLeod, D. T. et al., 2017. Integration of a CD19 CAR into the TCR Alpha Chain Locus Streamlines Production of Allogeneic Gene-Edited CAR T Cells. *Molecular Therapy,* 25(4), pp. 949-961.
MaxQ Ltd., 2018. *Innovative, Validated, No-Bench-Time blood packaging, shipping and storage solutions.* [Online]
Available at: https://www.packmaxq.com/blood-packaging
MHRA, 2018. *Good manufacturing practice and good distribution practice.* [Online]
Available at: https://www.gov.uk/guidance/good-manufacturing-practice-and-good-distribution-practice
NATA, 2011. *RBC Filtration and Allogeneic Blood Transfusion.* [Online]
Available at: https://nataonline.com/np/147/rbc-filtration-and-allogeneic-blood-transfusion
NHS England, 2018. *NHS England strikes deal for ground breaking cancer treatment in a new European first.* [Online]
Available at: https://www.england.nhs.uk/2018/10/nhs-england-strikes-deal-for-ground-breaking-cancer-treatment-in-a-new-european-first/
NHSBT, 2018. *About our donation venues.* [Online]
Available at: https://www.blood.co.uk/the-donation-process/about-our-donation-venues/
NHSBT, 2018. *How is it used - Cord Blood Bank.* [Online]
Available at: https://www.nhsbt.nhs.uk/cord-blood-bank/how-is-it-used/
NHSBT, 2018. *The journey of a blood donation.* [Online]
Available at: https://www.blood.co.uk/the-donation-process/after-your-donation/the-journey-of-a-blood-donation/
NHSBT, 2018. *What happens on the day.* [Online]
Available at: https://www.blood.co.uk/the-donation-process/what-happens-on-the-day/
NHSBT, 2018. *Where can I donate.* [Online]
Available at: https://www.nhsbt.nhs.uk/cord-blood-bank/donate/where-can-i-donate/
Novartis, 2018. *Kymriah® (tisagenlecleucel), first-in-class CAR-T therapy from Novartis, receives second FDA approval to treat appropriate r/r patients with large B-cell lymphoma.* [Online]
Available at: https://www.novartis.com/news/media-releases/
Page, K. M., Sun, J. M. & Kurtzberg, J., 2019. Chapter 10 - Cord Blood Stem Cells. In: A. Atala, R. Lanza, A. G. Mikos & R. Nerem, eds. *Principles of Regenerative Medicine (Third Edition).* Cambridge, Massachusetts: Academic Press, pp. 149-167.
Pfizer, 2017. *CAR-T Cell Therapy.* [Online]
Available at: https://www.pfizer.com/files/news/asco/Pfizer_IO_CART_FactSheet.pdf
PGCB Foundation, 2018. *Why is it important to ship cord blood in a special transportation container.* [Online]
Available at: https://parentsguidecordblood.org/en/faqs/why-is-it-important-to-ship-cord-blood-with-a-special-courier
Porwollik, S., 2016. *GMP-in-a-box – the future in cell therapy production.* [Online]
Available at: http://www.biocision.com/blog/12819/gmp-in-a-box-cell-therapy-production
Sagentia Ltd, 2018. *Quality control testing in CAR-T cell manufacture.* [Online]
Available at: https://www.sagentia.com/insight/quality-control-testing-in-car-t-cell-manufacture/
Sangamo Therapeutics, 2018. *Cell Therapy.* [Online]
Available at: https://www.sangamo.com/technology/cell-therapy
Staines, R., 2018. *Novartis focusing on cutting CAR-T costs ahead of EU launches.* [Online]
Available at: https://pharmaphorum.com/news/novartis-focusing-on-cutting-car-t-costs-ahead-of-eu-launches/
Szabo, L., 2017. *Cascade of Costs Could Push New Gene Therapy Above $1 Million Per Patient.* [Online]
Available at: https://khn.org/news/-cascade-of-costs-could-push-new-gene-therapy-above-1-million-per-patient/
WHO, 2011. *WHO guidelines on good manufacturing practices for blood establishments.* [Online]
Available at: http://www.who.int/bloodproducts/publications/GMP_Bloodestablishments.pdf
World Marrow Donor Association, 2018. *Total Number of Donors and Cord blood units.* [Online]
Available at: https://statistics.wmda.info
Yang, Y., Jacoby, E. & Fry, T., 2015. Challenges and opportunities of allogeneic donor-derived CAR T cells. *Current Opinion in Hematology,* 22(6), pp. 509-515.

8. Supplementary Information

See the attached zip file for data for figure 1 and 8.

Selective Oxidation of Glucose towards Glucaric Acid using Monometallic Nanostructured Catalysts

Wang, Xiyu and Shi, Wenbo
Department of Chemical Engineering, Imperial College London, U.K.

Abstract Glucaric acid (GA) is a naturally existing chemical which can be used in the production of adipic acid (AA). In this study, two different monometallic nanostructured catalysts (Au-TiNT^{sol} and Pt-TiNT^{SEA}) were synthesised with nominal 2 wt% metal loading and tested for selective oxidation of glucose towards GA. High selectivity towards GA with 69% molar yield was obtained using Au-TiNT^{sol} under 60 ˚C, 1 bar oxygen pressure (P_{Ox}) and 1 wt% initial glucose concentration ($C_{glu,0}$). The selectivity towards GA was enhanced with higher temperature and lower $C_{glu,0}$, while P_{Ox} had little effect in the range studied in this report. Pt-TiNT^{SEA} had inferior selectivity comparing with Au-TiNT^{sol}. Metal leaching was proved to be minor for Au-TiNT^{sol} but more significant for Pt-TiNT^{SEA} under the conditions in this study, which agrees with the activity observed. The kinetics of gluconic acid (GO) to GA is not solely dependent on the reactants and further investigation including kinetic parameter estimation is suggested to better understand the reaction.

Introduction and background

Conversion of biomass to fuels and other high-value chemicals has become increasingly important as a carbon-neutral or at least more environmentally friendly alternative to the current main energy and chemical production processes based on fossil resources. [1] To make the processes economically viable, the produced bio-based chemicals should be demanded in large quantities and have competitive prices as well as properties. Therefore, sugar is considered as an important platform to produce such chemicals. [2] There are many potential pathways via the sugar platform with notable potential market size, such as the production of isobutene, acrylic acid and adipic acid. [3]

Adipic acid (AA) is a very versatile platform molecule with a projected market size of USD 6.68 billion in 2020 [4]. It is extensively used in large scale chemical processes such as the synthesis of the polyamide Nylon-6,6 as well as the production of polyester and polyurethane resins. It is also recognised as an approved additive in lubricants, cosmetic, paper and wax. [5] It is currently produced by the oxidation of cyclohexanol and cyclohexanone mixture catalysed by nitric acid industrially. [6] Since the Rennovia patent of AA production from glucose via glucaric acid (GA) and its derivative was released in 2010 [7], a large focus has been put on this synthesis route as glucose can be obtained from biomass relatively easily. In this patent, the reaction is carried out in acidic condition with Pt and Pd being the recommended catalytic metals. [7] However, as GA and its derivatives are sticky liquids which are hard to handle, the production plant must be built close to the biomass processing plant. This would require transportation of either the biomass or the produced GA, which is inconvenient. A paper in 2017 claimed the crystallisation of GA in basic condition [8], which makes it easier to transport. Hence, the production of GA with high purity from glucose has become more desirable. Also, GA itself is a natural, non-toxic compound found in many fruits and vegetables, and is produced in small amount by the human body [9] with many implications in the food and pharmaceutical industry [10] [7] [11]. However, for the studies conducted on glucose oxidation, most of them focused on the conversion to GO only [12] [13]. Very few studies investigated further oxidation towards GA [14], which is the area this project focused on.

In previous studies, various catalysts were investigated on the selective oxidation of glucose. *Jin et al.* presented that a 46% selectivity towards GA can be achieved in basic condition (1M NaOH) with TiO_2 supported bimetallic Pt-Cu nanocatalyst at 45 °C and 0.1 MPa O_2. [15] *Solmi et al.* stated that the use of carbon-supported Au nanoparticles in direct oxidation from glucose to GA was extremely active in the presence of NaOH comparing with previously reported Pt/C catalysts and could give a maximum GA yield of 31%. [1] *Derrien et al.* reported that a 50% yield of GA can be obtained at complete conversion of glucose and GO at 100 °C, under 40 bar air, using Au-Pt/ZrO2 catalyst under base-free condition. [16] As some of the reactions were carried out in basic condition instead of acidic condition suggested in the Rennovia patent, Au was considered as a valid option, because it

demonstrated good activity and little leaching in basic condition [17] [12].

The catalytic activity of Au has been found to be strongly affected by the surface area of the support, the higher the surface area, the better the metal dispersion [18], therefore, better catalytic activity. Titanate (TiO_2) exhibits good stability and strong metal support interaction with high surface area and mesoporous structure which helps stabilising the catalyst. [19] Titanate nanotubes (TiNTs) has an even higher surface area and surface hydroxyl group density compared with TiO_2 and is therefore considered to be a better support for Au catalyst. There are many methods for synthesising nanostructured catalysts, such as deposition-precipitation, solid grinding and adsorption. Sol-immobilisation was chosen as it allows the control of metal particle size independent of the support material. [20] A stable and highly active Au catalyst for selective oxidation has been produced previously using this method on essentially sodium-free TiNTs in this research group. Higher turnover frequencies (TOFs) were achieved using the catalyst synthesised by sol-immobilisation comparing with similar Au-Pd/TiO_2 catalysts reported in literature and a catalyst prepared by impregnation. [21]

Pt, one of the suggested catalytic metal in the Rennovia patent [7], has also been confirmed to be active in this reactions by many other studies [22] [14] [15]. However, Pt on TiNTs produced by strong electrostatic adsorption (SEA) has not been investigated before. This is an attractive option as SEA is a relatively simple yet effective method which gives high metal dispersion comparing with other methods including dry/wet impregnation. [23]

Kinetics of glucose oxidation to GA via GO was explored briefly in this report. A number of kinetic studies were conducted on glucose oxidation towards GO and reported that the reaction is likely to follow the Langmuir-Hinshelwood model, where both reactants adsorb on the catalyst surface. [13] [1] However, there are not many studies conducted on the kinetics of glucose oxidation towards GA. The reaction conditions for this study were selected based on previous kinetic studies of glucose to GO, so literature kinetic data of this reaction can be compared with in order to access the validity of this analysis.

A range of temperatures (T), initial glucose concentrations ($C_{glu.0.}$) and oxygen pressures (P_{Ox}) were investigated and their effect on activity as well as selectivity were analysed. Metal leaching of catalysts were also analysed by Inductively Coupled Plasma (ICP).

Experimental

Materials

Most of the materials used in this study were purchased from Sigma–Aldrich: Titanium (IV) oxide (anatase, <25 nm particle size, 99.7% trace metals basis), D-(+)-Glucose (≥99.5%), Formic acid (ACS reagent, ≥98%), HCl (ACS reagent, 37%), Tetraammineplatinum(II) nitrate (99.995% trace metals basis), H_3PO_4 (85 wt.% in H2O, 99.99% trace metals basis). The others were from VWR Chemicals: NaOH (98.5-100.5%), NaOH (1M, NF volumetric solution), H_2SO_4 (95.0-97.0%), HNO_3 (68-70%). O_2 (99.9999% purity) and synthetic air was supplied by BOC.

Synthesis of titanate nanotubes (TiNTs)

The method reported by Kasuga and his group was employed for the synthesis of TiNTs. [24] 11 g of TiO_2 and 185 mL of 10M NaOH were mixed in a PTFE-liner, stirred at 800 rpm for 25 min, and sonicated for 30 min. The liner was then placed in a steel autoclave and was heated at 140 °C for 24 hr. The resulting slurry was washed with DI water till pH 7 and filtered. After drying the filter cake overnight, sodium form titanate nanotubes (Na-TiNTs) were obtained. Na-TiNTs were then washed and filtered with 0.1M H_2SO_4 three times and then with DI water back to pH 7. The dried filter cake was the essentially sodium-free form titanate nanotubes (H-TiNTs) desired for catalyst synthesis.

Synthesis of Au-TiNT^{sol}

Au-TiNT^{sol} was produced by Mr. Motaz Khawaji, using previously reported sol-immobilisation method [25] with nominal 2 wt% metal loading from the H-TiNTs synthesised in this project as outlined above.

Synthesis of Pt-TiNT^{SEA}

The method for Pt-TiNT^{SEA} synthesis referred to the SEA method presented by Miller and his colleagues. [23] To determine the best pH for Pt adsorption, pH isotherm was determined for the desired Pt precursor and support. 500 mg of H-TiNTs were mixed with 39.7 mg Pt precursor, tetraammineplatinum(II) nitrate, in 0.1 M H_2SO_4, stirred and gradually added 2 M NaOH to adjust pH value. Samples were taken at pH 2, 4, 8, 11 and 13 and were analysed with ICP (Agilent Technologies – 7900 ICP-MS). 2 wt% metal loading was aimed for Pt catalyst

synthesis. 100 mg Pt precursor in 125 mL DI water was mixed with 2.5 g TiNTs in 22 mL DI water. The mixture was adjusted to pH 10.5 and stirred overnight. The catalyst was then washed and filtered till pH 7 with DI water and the resulting filter cake was dried at 100 °C. The dried catalyst was calcinated at 675 °C with a ramp rate of 20 °C/min from room temperature (RT) and was hold for 1 hr under air in 1200 °C Tube Furnaces – LTF made by Lenton. Finally, the catalyst was reduced in small batches (300 mg each) at 250 °C (20 °C/min from RT) with flowing H_2 (15 cm^3/min) and was hold for 2 hr in Tube Furnace made by Lenton. Different batches were mixed together after all batches were finished.

Catalyst characterisation

200 mg samples from Na-TiNTs and H-TiNTs were degassed at 140 °C in Micromeritics FlowPrep 069 and analysed in Micromeritics Tristar separately to test for surface area and porosity.

Two samples of final catalysts, Pt-TiNT^{SEA} and Au-TiNT^{Sol}, were sent to MEDAC Ltd for ICP tests for metal loading analysis.

X-Ray Diffraction (XRD) and Transmission Electron Microscopy (TEM) analysis was performed by Mr. Motaz Khawaji to determine the structure of the H-TiNTs due to technical limitations.

Reaction procedure

Reactions took place in 200 mL miniclaves by Büchi AG with reaction volume of 20 mL and 80 mg catalyst. It was found that basic condition is preferred to perform the reaction. [12] Due to small reaction volume, injecting NaOH solution to control the pH would have a large impact on reactant/product concentrations. Therefore, a highly basic solution (1M NaOH) was used at the start of each run to maintain basic condition throughout the reaction instead of monitoring the pH at a fixed value.

Glucose was chosen to be the starting reactant but not GO because GO cannot compete with O_2 for active site adsorption. The rate of conversion with GO as starting material is slower than that with glucose according to previous study. [14] In addition, the industrial process of bio-based GA production would need to start from glucose, which can be obtained from the hydrolysis of biomass derivatives [2]. Therefore, glucose was used in this research although the main objective is to explore the oxidation from GO to GA.

Three parameters, temperature (T), oxygen pressure (P_{Ox}) and initial glucose concentration ($C_{glu,0}$) were manipulated to investigate their effect on catalyst activity and selectivity. The temperature range for optimum reaction rate of glucose oxidation to GO under basic condition has been reported to be 40 to 60 °C. [12] However, there were studies suggesting that higher temperatures (80 °C and 100 °C) would provide better selectivity towards GA under high P_{Ox} but slightly less basic conditions [22] [16]. Therefore, the temperature range investigated was first decided to be 40 – 90 °C. The upper P_{Ox} limit was set to be 4 bar because it was suggested that a slight excess in oxygen is preferred[26] and the lower limit was 1 bar as commonly employed for this reaction[7]. The optimum $C_{glu,0}$ was found to be around 20 wt% at 40 °C with P_{Ox} ranging from 1.5 bar to 9 bar.[13] However, when applying these conditions on our catalyst in highly basic condition, sticky brown product was observed suggesting undesirable deep oxidation producing various lactones at high $C_{glu,0}$. Therefore, milder ranges of 1 – 10 wt% $C_{glu,0}$ and 40 – 60 °C were used. A stirring rate of 1000 rpm was chosen to eliminate mass transfer effect [21] [13].

Most of existing studies run batch reactions with different time lengths and only take sample at the end of each run. However, this would introduce variation in conditions between batches. For instance, temperature as a vital parameter, is hard to be controlled precisely to the same value between batches. To eliminate this inconsistency, long reaction with continuous sampling procedure was employed. The change in condition during sampling could be neglected since the sampling time was short comparing to the reaction time and the reactants/products inside the reactor were well mixed.

The reactor loaded with 1M NaOH and the catalyst was first filled with N_2 for leak test, purged with O_2 4 times then set to the desired P_{Ox}. Glucose was injected at time zero after the reactor was heated to the targeted T in oil bath. The reactor was vented every time for sampling using a needle and then re-pressurised.

Samples were analysed in High Pressure Liquid Chromatography (HPLC) Shimadzu with SUPELCOGEL C-610H column using 0.1 vol% phosphoric acid as mobile phase and 1 wt% formic acid as standard. Other than the main products, GO and GA, many possible by-products, e.g. glycolic acid (GY), tartronic acid (TA), glucaric acid lactone (GAAL) were tested

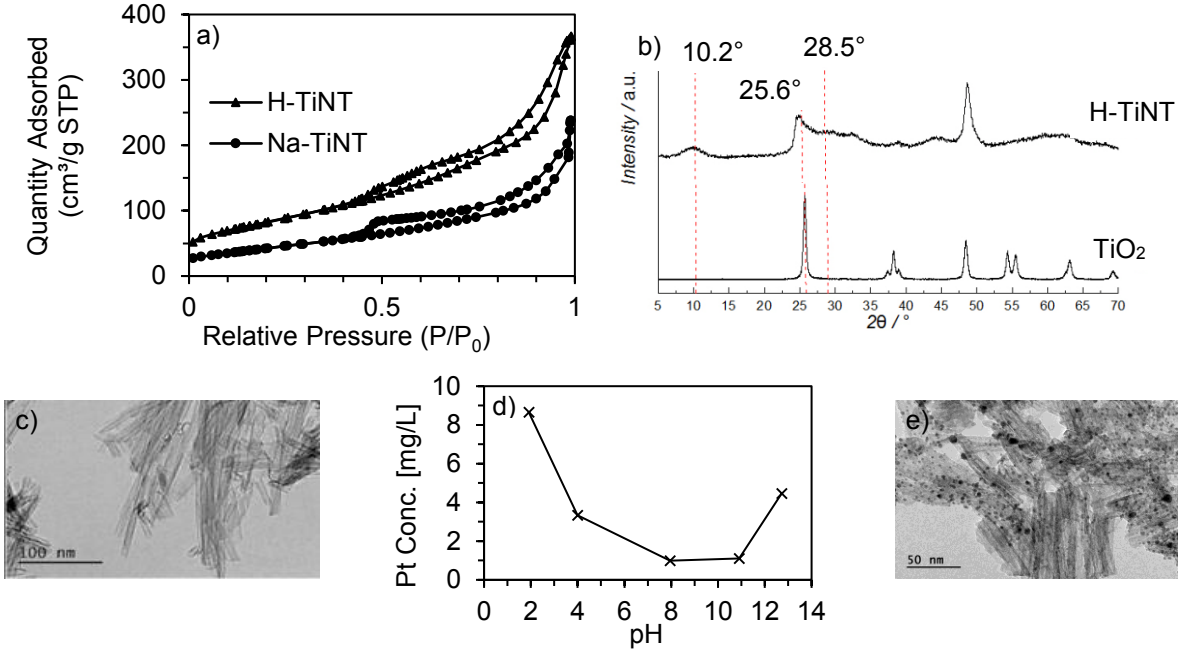

Figure 1 a) BET analysis; b) XRD analys [21] is; c) TEM image for TiNT [21]; d) Pt pH isotherm; e) TEM image for Au-TiNT

and those appeared in the samples were calibrated to ensure more accurate results. The test, calibration and sample calculation are provided in Sections S1, S2 of the Supplementary Materials.

Results and discussion

Catalyst characterisation

The BET analysis of the TiNTs (Figure 1-a) gave surface areas of 293 m^2/g and 152 m^2/g, pore volumes of 0.587 cm^3/g and 0.378 cm^3/g for the H-TiNTs and Na-TiNTs respectively. These values are comparable with previously reported values for the same material. [27] The average pore diameter shown in Table 1 suggested that the majority of the pores are mesopores, which is also supported by the shape of the N_2 isotherm.

Table 1 BET results

	Surface Area (m^2/g)	Pore Volume (cm^3/g)	Average Pore Diameter (nm)
H-TiNT	293	0.587	7.23
Na-TiNT	152	0.378	8.02

The XRD analysis (Figure 1-b) proved that the structure of the material synthesised is indeed nanotube rather than TiO_2 powder. The broadening of the peak at 10.2° is characteristic for TiNTs. The formation of the nanotubes is also evidenced by TEM images as the structure can be clearly seen in Figure 1-c.

The pH isotherm performed for the Pt complex on H-TiNT support (Figure 1-d) illustrated that the maximum adsorption can be obtained in the pH range of 8-11. Therefore, the final adsorption for the synthesis of Pt-TiNT^{SEA} was performed at pH 10.5.

The catalysts prepared in this study both have nominal loading of 2 wt% and the ICP analysis showed metal loadings of 1.8 wt% and 1.5 wt % for Au-TiNT^{sol} and Pt-TiNT^{SEA} respectively, which are close to the expected metal loadings. The structure and morphology of Au-TiNT^{sol} ought to be analysed using TEM. But due to technical limitations, it could not be performed. However, analysis for the catalyst prepared previously using the same method is presented in Figure 1-e demonstrating that Au is dispersed well on the support.

Blank Reactions

Blank reactions were performed with and without the catalyst supports (H-TiNTs) under 90 °C, 4 bar P_{Ox} and 1 wt% $C_{glu,0}$ in 1M NaOH to measure the performance of reaction in highly basic condition and the effect of the support under these conditions. These conditions were chosen to allow the reaction to occur and reach its uttermost in the range of condition examined in this study without the presence of catalyst.

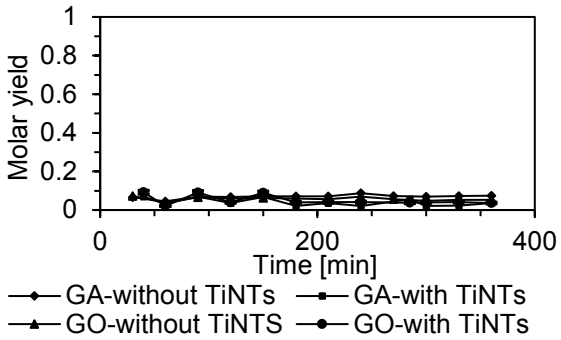

Figure 2 GO/GA molar yield for blank reaction

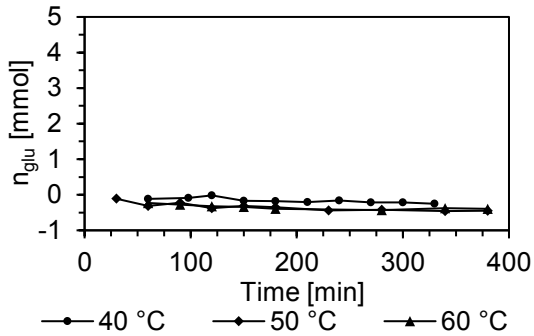

Figure 3 Conversion of glucose @ 1 bar, 1 wt% $C_{glu,0}$

Reaction took place to some extent in the condition provided with and without H-TiNTs as expected [1]. The major product obtained was GY in both cases with other products including GO, GA, oxalic acid (OX) and 5-ketogluconic acid (KT). The molar yield of the target products, i.e. GO and GA, were lower than 10% in both cases, representing no selectivity towards either of them. (Figure 2) The addition of H-TiNTs promoted the molar yield of GO by about 5 wt% but not any of the other products. However, the carbon balance for the reactions with H-TiNTs is about 70% with high glucose conversion (>90%) since the start of reaction. This suggests the possibility of organic compounds adsorbing on the support surface and probably even inside the nanotubes, which agrees with literature published before. [22]

Reaction with Au-TiNT^{sol}

Glucose conversion

As illustrated in Figure 3, the amount of glucose retaining in the reactor reached zero after about 30 minutes and fluctuated around zero thereafter. This is probably due to the almost instant conversion of glucose to GO under the conditions studied here. Organic compound adsorption on the catalyst could be another reason behind this, as evidenced by the blank reaction with H-TiNTs.

Selectivity

For the reactions performed with Au-TiNT^{sol} under various conditions, the molar yield of GA was plotted against time for the first 6 hours as shown in Figure 4. The molar yield varied from 15% to 55% depending on the reaction conditions, which are considerably higher than in the blank reactions. This indicates that the catalyst provided selectivity towards GA as desired.

The molar yields of GA under different reaction conditions were compared as in Figure 4. It can be concluded that glucose oxidation becomes more selective towards GA under higher temperature and lower $C_{glu.0}$. P_{Ox} has little effect in the range of 1 to 4 bar under the

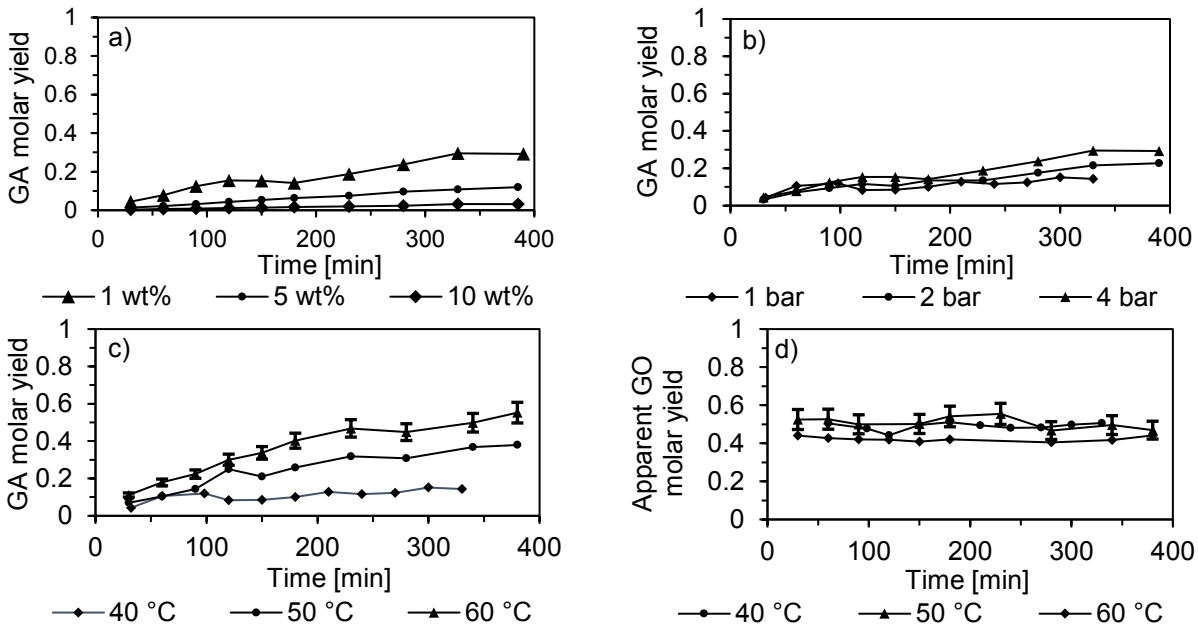

Figure 2 GA molar yield at (a) 40 °C, 4 bar; (b) 40 °C, 1 wt% $C_{glu,0}$; (c) 1 bar, 1 wt% $C_{glu,0}$ and (d) apparent GO molar yield at 1 bar, 1 wt% $C_{glu,0}$

conditions employed in this study. The highest GA molar yield of 55% after 6 hr and 69% after 22 hr was observed under 60 °C, 1 bar P_{Ox} and 1 wt% $C_{glu.0}$.

There were also other products produced, with GO and GY (5% -20% molar yield depending on reaction conditions) being the main ones.

GY, formed through retro-aldol reaction from glucose and intermediate GO [22], is the main side product affecting the selectivity towards GA in this study. For higher temperature, there are more molecules with energy higher than the activation energy. Furthermore, as the energy requirement for GO oxidation to GA is lower than that for the retro-aldol reaction to form GY, the increase in GA formation rate is greater than that in GY formation rate. Therefore, the reaction becomes more selective towards GA at higher temperature. In addition, high $C_{glu.0}$ leads to fewer available catalytic sites for the oxidation towards GA, since a great number of active sites are occupied by glucose through adsorption.[1] Hence, the amount of GA produced is reduced. In contrast, GY can be produced without the aid of catalyst as observed in the blank reactions. Therefore, the amount of GY produced remained almost constant regardless of the amount of glucose added at the beginning. Therefore, the reaction favours GA less under high $C_{glu.0}$.

In all reactions performed with Au-TiNT^{sol}, the amount of GO in the system fluctuated in a small range with time (Figure 4-d)). However, it should follow a downward trend as more GA is produced under the assumption of instant conversion from glucose to GO. There are 2 possible reasons for this observation.

Firstly, after glucose adsorbed to the active site on the catalyst surface and converted to GO, there can be 2 routes for the reaction onward to GA (shown in Schematic 1). In the first route, GO desorbs from the surface back to the solution and then re-adsorbs in order to convert to GA. In the other route, after being converted to GO from glucose, it stays on the surface and converts to GA directly without desorption[27]. Theoretically, the second route is faster and is the main route taken by this

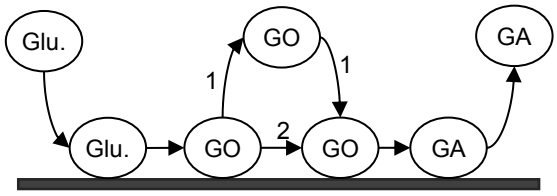

Schematic 1 Two-route mechanism

reaction. Because of the alternative routes, not all GO existing in the reactor could be observed, since HPLC can only detect GO in solution but not those on the catalyst surface.

Moreover, there are likely to be other side products produced from GO with similar molar mass as GO gets converted. They can interfere with the HPLC sample analysis by overlapping with the GO peaks.

Combing both factors, no clear trend could be observed for GO molar yield and the apparent GO molar yield fluctuated in a small range as shown above.

Reaction with Pt-TiNT^{SEA}

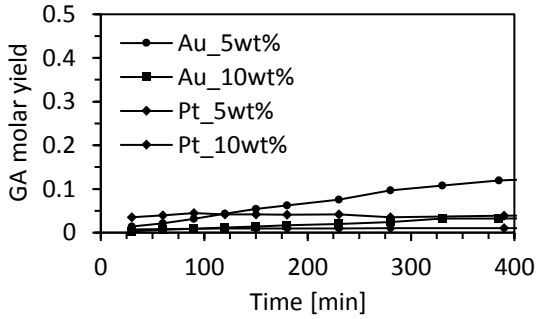

Figure 5 comparison between Au and Pt catalyst @ 40 °C, 4 bar

2 reactions were performed using Pt-TiNT^{SEA} to compare with Au-TiNT^{sol} in terms of selectivity and activity. The reactions were performed under 40 °C, 4 bar P_{Ox}, 5 wt% and 10 wt% $C_{glu.0}$ respectively. The amount of catalyst and reaction volume were the same as those used for Au-TiNT^{sol}. As demonstrated in Figure 5, the molar yield of GA obtained using Pt-TiNT^{SEA} is lower than that obtained using Au-TiNT^{sol} under the same conditions. The reaction using Pt-TiNT^{SEA} also gave slightly higher GY molar yield of 10% and much greater yield of 15% for fructose compared with Au-TiNT^{sol} (7% and 3% respectively). This illustrates that Pt-TiNT^{SEA} is less selective towards GA compared with Au-TiNT^{sol} under these conditions There might be a considerable amount of GAAL produced (molar yield of 30%) with the presence of Pt-TiNT^{SEA}. However, this would need to be confirmed with further experiments.

Metal Leaching

Metal leaching was tested for all reactions on the final 22 hr samples using ICP. The result shows 0.16 ± 0.10% leaching for Au-TiNT^{sol} and 10.36 ± 4.41% leaching for Pt-TiNT^{SEA}. This proves that the highly basic condition successfully prevented leaching of the Au catalyst which helped maintaining its activity

throughout the reaction. Pt-TiNT^{SEA} had a greater extent of metal leaching under these conditions, which can possibly explain its relatively poor performance comparing to literature studies [27].

Activation energy

Activation energy was calculated before deriving kinetic equations. The initial reaction rate for this study was estimated by taking derivatives of the equations fitted as in Figure 6 between 0 and 1 minute. The activation energy of the production of GA was found to be 41.3 kJ/mol as shown in Figure 7 based on the calculation of Arrhenius' Equation. (Calculation detailed in Section S3 of the Supplementary Materials) The result is close to that for the oxidation from glucose to GO reported previously as 54 kJ/mol[13]. However, the result showed slight inconformity with the expectation of being higher, since the reaction to produce GA is slower than that of GO. Besides the maximum ±4% error introduced by calibration, other errors from, for example, misidentifying HPLC peaks and inaccurate estimation of the peak area could have large impact on results. However, these errors could not be quantified properly. Despite being slightly lower than expected due to errors, the result is still reasonable as it has the right magnitude.

The experiments were carried out in a moderate temperature range (40 – 60 °C), which helps to maintain consistent mechanism and catalyst properties throughout the analysis while providing a sensible range to provide statistical significance.

Kinetics

Langmuir-Hinshelwood (LH) mechanism and Eley–Rideal (ER) mechanism were usually proposed for bimolecular reactions on the surface. Several previous reports claimed that the oxidation of glucose to GO on catalysts can be explained by LH mechanism. [13] [12] To

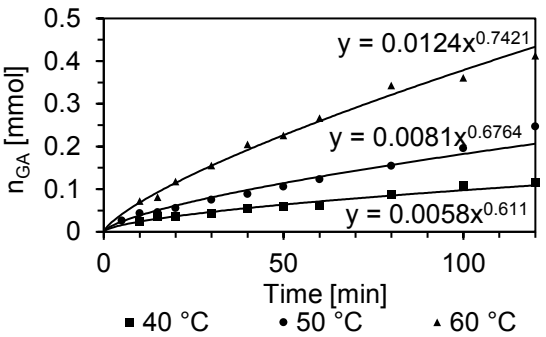

Figure 6 Formation of GA @ 1 bar and 1 wt% $C_{glu,0}$

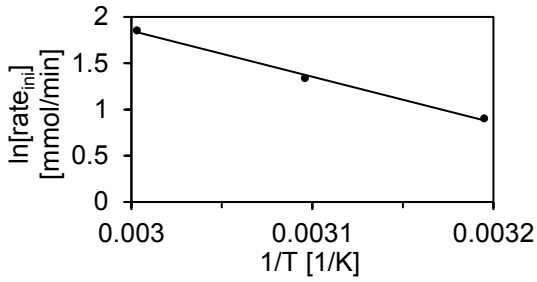

Figure 7 Effect of temperature @ 1 bar and 1 wt% $C_{glu,0}$

investigate the reaction kinetics and mechanism of GA production, several 2-hour reactions were carried out under various conditions. Assuming glucose converted to GO instantly, the appearance of GA as a function of time was fitted with power law as presented in Figure 6. It was found that only fractional powers can be fitted and vary with temperature. It shows that more than one species is affecting the rate and have dependence on temperature. Furthermore, a general rate equation in the form of Equation 1 is manipulated into logarithm form as Equation 2.

$$\mathrm{rate} = \mathrm{k}\mathrm{C}_{\mathrm{glu},0}^{\mathrm{m}}\mathrm{C}_{\mathrm{Ox}}^{\mathrm{n}}C_{GO}^{p}\cdots \text{ and } \mathrm{k} = \mathrm{k}_0\mathrm{e}^{-\mathrm{E_a}/\mathrm{RT}} \quad [1]$$

$$\ln[\mathrm{rate}] = \ln\mathrm{k} + \mathrm{m}\ln\mathrm{C}_{\mathrm{glu}} + \mathrm{n}\ln\mathrm{C}_{\mathrm{Ox}} + \mathrm{p}\ln C_{GO}\cdots \quad [2]$$

By varying $C_{glu,0}$ and P_{Ox} independently at constant temperature, the impact of glucose concentration and oxygen concentration in solution on the rate was tested, where oxygen concentrations were calculated from Henry's law based on information provided on NIST[28]. The results are presented in Table 2. It would be beneficial to examine the power respect to GO concentration as well to better understand the kinetics and mechanism of this reaction. However, due to timescale and technical limitations, this cannot be achieved in this study.

The results below proved that the reaction from GO to GA matches the LH competitive bimolecular adsorption mechanism. O_2 and GO should be the main species considered in LH model as they are the reactants for GA formation. However, more compounds other than O_2 and GO should be considered in the kinetic equation. The negative power on glucose concentration indicates that high concentration of glucose would hinder the reaction. This is also in agreement with the discussion of selectivity dependence on $C_{glu,0}$ in a previous section and reported study.[1] Other species such as fructose, KT, formed as by-products, can possibly have impacts on the rate due to various adsorption and desorption

effects affected by temperature and concentration.

Table 2 Effect of P_{Ox} and C_{glu} @ 40 °C

	1 bar	2 bar	4 bar
m	-0.995	-1.214	-0.609
	1 wt%	5 wt%	10 wt%
n	0.118	0.209	1.0509

Outlook

The activation energy reported here is only valid in the temperature range of 40 – 60 °C under the conditions used in this study. Further investigations can be done on different or wider temperature ranges to determine an activation energy with wider range of validity. Also, as the reaction mechanism is likely to change with the temperature range, it can be suggested to investigate the activation energy in a range of relatively small temperature intervals to derive a series of more accurate activation energies and their dependence on temperature. In addition, Au-TiNT^{sol} can be tested in a wider range of conditions and varying catalyst amount, so that a more confirming optimum operating condition can be determined.

To better determine the complex kinetic equation, the side products that can possibly affect the reactions can be added to the system individually at start of the reaction to determine their own effect by enhancing their concentration.

More chemicals can be calibrated for HPLC analysis, so that more possible products can be identified and the measurement for main reactants/products can be more accurate. Different column and/or methods can be tested to provide better separation between similar chemicals. Ion Chromatography can be used to analyse the acids produced, while Nuclear Magnetic Resonance (NMR) can be employed to identify the products with similar molar mass but different structures.

Pt catalyst was usually claimed to be active and selective in previous reports and is widely used in industry. [22] Therefore, more reaction under wider range of condition is suggested for Pt-TiNT^{SEA} to test for its optimum operating condition. Also, the spent catalysts can be reused to test for their recyclability.

Conclusion

Two monometallic nanostructured catalysts (Au-TiNT^{sol} and Pt-TiNT^{SEA}) were synthesised successfully by loading Au and Pt on H-TiNT support respectively. Desired morphology and metal loading of 1.8 wt% and 1.5 wt% were achieved.

Blank reactions with only catalyst support showed low activity and little selectivity towards GA and GO with significant chemical adsorption suggested by the low carbon balance (70%).

Au-TiNT^{sol} provided better selectivity towards GA than Pt-TiNT^{SEA} in the reactions carried out in 1M NaOH at 40 °C, 4 bar P_{Ox} , 5 wt% and 10 wt% $C_{glu.0}$. Further investigation on Pt-TiNT^{SEA} is suggested to find its optimum operating condition.

Oxidation of GO to GA favours high temperature and low $C_{glu,0}$ with the aid of Au catalyst under the range of conditions studied here due to the higher energy requirement for the side reaction and chemical adsorption on catalyst surface. A maximum molar yield of GA at 22 hr under 60 °C, 1 bar P_{Ox} and 1 wt% $C_{glu,0}$ in 1M NaOH was achieved.

The activation energy for this step is calculated to be 41.3 kJ/mol, which is slightly lower than expected. The complex kinetics matches the bimolecular competitive adsorption mechanism proposed in Langmuir-Hinshelwood model. However, more species should be considered in the kinetic model to provide more comprehensive and in depth understanding of the reaction.

Acknowledgements

Xiyu Wang and Wenbo Shi gratefully acknowledge the guidance from Prof. David Chadwick and his group along the project. We gratefully acknowledge Mr. Motaz Khawaji for his support with catalyst synthesis, XRD and TEM, Miss. Yiming Zhang for her support with HPLC data analysis and Melody Loh Tze Yin for the HPLC calibration.

References

[1] S. Solmi, C. Morreale, F. Ospitali, S. Agnoli and F. Cavani, "Oxidation of d-Glucose to Glucaric Acid Using Au/C Catalysts," ChemCatChem, vol. 9, no. 14, pp. 2797-2806, 2017.

[2] R. A. Sheldon, "The Road to Biorenewables: Carbohydrates to Commodity Chemicals," ACS Sustainable Chemistry & Engineering, vol. 6, no. 4, pp. 4464-4480, 2018.

[3] R. Taylor, L. Nattrass, G. Alberts, P. Robson, C. Chudziak, A. Bauen, I. Libelli, G. Lotti, M. Prussi, R. Nistri, D. Chiaramonti, A. López-Contreras, H. Bos, G. Eggink, J. Springer, B. Robert and v. R. Rene, "From the Sugar Platform to biofuels and biochemicals," E4Tech, UK, 2015.

[4] Grand View Research, "Adipic Acid Market Size, Share & Trends Analysis Report By Application (Nylon 66 Fiber, Nylon 66 Resin, Polyurethane, Adipate Ester), By Region (APAC, North America, Europe, MEA, CSA), And Segment Forecasts, 2018 - 2024," Grand View Research, San Francisco, 2018.

[5] V. d. V. Stijn and R.-L. Yuriy, "Emerging catalytic processes for the production of adipic acid," Catal. Sci. Technol, vol. 3, no. 6, pp. 1465-1479, 2013.

[6] I. Hermans, P. A. Jacobs and J. Peeters, "To the Core of Autocatalysis in Cyclohexane Autoxidation," Chemistry - A European Journal, vol. 12, no. 16, pp. 4229 - 4240, 2006.

[7] T. R. Boussie, E. L. Dias, Z. M. Fresco, V. J. Murphy, J. Sheomaker, R. Archer and H. Jiang, "Production of Adipic Acid and Derivatives from Carbohydrate-containing Materials". United States Patent US 2010/0317823 A1, 2010.

[8] R. D. Armstrong, B. M. Kariuki, D. W. Knight and G. J. Hutching, "How to Synthesise High Purity, Crystalline D-Glucaric Acid Selectively," European Journal of Organic Chemistry, vol. 2017, no. 45, pp. 6811-6814, 2017.

[9] Z. Walaszek, J. Szemraj, M. Hanausek, A. K. Adams and U. Sherman, "D-Glucaric acid content of various fruits and vegetables and cholesterol-lowering effects of dietary d-glucarate in the rat," Nutrition Research, vol. 16, no. 4, pp. 673-681, 1996.

[10] Z. Walaszek, J. Szemraj, M. Narog, A. Adams, J. Kilgore, U. Sherman and M. Hanausek, "Metabolism, uptake, and excretion of a D-glucaric acid salt and its potential use in cancer prevention," Cancer Detection and Prevention, vol. 21, no. 2, pp. 178-190, 1997.

[11] Z. Walaszek, J. Szemraj, M. Hanausek, A. K. Adams and U. Sherman, "d-Glucaric acid content of various fruits and vegetables and cholesterol-lowering effects of dietary d-glucarate in the rat," Nutrition Research, vol. 16, no. 4, pp. 673-681, 1996.

[12] Y. Önal, S. Schimpf and P. Claus, "Structure sensitivity and kinetics of D-glucose oxidation to D-gluconic acid over carbon-supported gold catalysts," Journal of Catalysis, vol. 223, no. 1, p. 122–133, 2004.

[13] U. Prüße, M. Herrmann, C. Baatz and N. Decker, "Gold-catalyzed selective glucose oxidation at high glucose concentrations and oxygen partial pressures," Applied Catalysis A: General, vol. 406, no. 1, pp. 89-93, 2011.

[14] J. Dirkx and H. S. V. D. Baan, "The Oxidation of Gluconic Acid with Platinum on Carbon as Catalyst," Journal of Catalysis, vol. 67, no. 1, pp. 14-20, 1981.

[15] X. Jin, M. Zhao, J. Shen, W. Yan, L. He, P. S. Thapa, S. Ren, B. Subramaniam and R. V. Chaudhari, "Exceptional performance of bimetallic Pt1Cu3/TiO2 nanocatalysts for oxidation of gluconic acid and glucose with O2 to glucaric acid," Journal of Catalysis, vol. 330, pp. 323-329, 2015.

[16] E. Darrien, M. Mounguengui-Diallo, N. Perret, P. Marion, C. Pinel and M. Besson, "Aerobic Oxidation of Glucose to Glucaric Acid under Alkaline-Free Conditions: Au-Based Bimetallic Catalysts and the Effect of Residues in a Hemicellulose Hydrolysate," Industrial & Engineering Chemistry Research, vol. 56, pp. 13175-13189, 2017.

[17] S. Biella, L. Prati and M. Rossi, "Selective Oxidation of D-Glucose on Gold Catalyst," Journal of Catalysis, vol. 206, no. 2, pp. 242-247, 2002.

[18] A. Villa, D. Wang, G. M. Veith, F. Vindigni and L. Prati, "Sol immobilization technique: a delicate balance between activity, selectivity and stability of gold catalysts," RSC Catalysis Science & Technology, vol. 3, no. 11, pp. 3036-3041, 2013.

[19] S. Bagheri, N. M. Julkapli and S. B. A. Hamid, "Titanium Dioxide as a Catalyst Support in Heterogeneous Catalysts," The Scientific Journal, vol. 2014, pp. 1-21, 2014.

[20] F. Porta, L. Prati, M. Rossi, S. Coluccia and G. Martra, "Metal sols as a useful tool for heterogeneous gold catalyst preparation: reinvestigation of a liquid phase oxidation," Catalysis Today, vol. 61, no. 1-4, pp. 165-172, 2000.

[21] M. Khawaji and D. Chadwick, "Au-Pd Bimetallic Nanoparticles Immobilised on Titanate Nanotubes: A Highly Active Catalyst for Selective Oxidation," ChemCatChem, vol. 9, no. 3, pp. 4353-5363, 2017.

[22] J. Lee, B. Saha and D. G. Vlachos, "Pt catalysts for efficient aerobic oxidation of glucose to glucaric acid in water," Green Chemistry, vol. 18, no. 13, pp. 3815-3822, 2016.

[23] J. T. Miller, M. Schreier, A. J. Kropf and J. R. Regalbuto, "A fundamental study of platinum tetraammine impregnation of silica2. The effect of method of preparation, loading, and calcination temperature on (reduced) particle size," Journal of Catalysis, vol. 225, no. 1, pp. 203-212, 2004.

[24] K. Tomoko, H. Masayoshi, H. Akihiko, S. Toru and N. Koichi, "Titania Nanotubes Prepared by Chemical Processing," Advanced Material, vol. 11, no. 15, pp. 1307-1311, 1999.

[25] N. Dimitratos, J. A. Lopez-Sanchez, D. David Morgan, A. F. Carley, R. Tiruvalam, C. J. Kiely, D. Bethell and G. J. Hutchings, "Solvent-free oxidation of benzyl alcohol using Au–Pd catalysts prepared by sol immobilisation," Phys. Chem. Chem. Phys., vol. 11, no. 25, pp. 5142-5153, 2009.

[26] H. Klaus Deller, R. Helmfried Krause, H. Erik Peldszus and H. Bertrand Despeyruux, "Method for preparation of gluconic acid by catalytic oxidation of glucose". U,S, Patent 5,132,452, 21 July 1992.

[27] M. Watanabe, Y. Aizawa, T. Iida, T. M. Aida, C. Levy, K. Sue and H. Inomata, "Glucose reactions with acid and base catalysts in hot compressed water at 473 K," Carbohydrate Research, vol. 340, no. 12, pp. 1925-1930, 2005.

[28] "NIST," U.S. Department of Conmmerce, 2018. [Online]. Available: https://webbook.nist.gov/cgi/cbook.cgi?ID=C7782447&Mask=10. [Accessed 2018].

[29] Melody Loh Tze Yin, 2017, 'Catalytic selective oxidation of glucose on bimetallic gold-based catalysts for bio-polymers', MSc Thesis, Imperial College London, London UK.

Synthesis of a Chiral Microporous Metal Organic Framework Utilising Consumer Waste Plastics as Feedstock

Andrew S. Duckworth, So-On Wong

Department of Chemical Engineering, Imperial College London, UK

Abstract

Metal organic frameworks (MOFs) are relatively new class of material, with potential applications spanning a variety of industries. There are currently significant challenges facing their usage: MOFs are too expensive and sometimes harmful to the environment to be synthesized on a commercial scale. In this study, we attempted synthesis of the MOF ZnBLD, formulated as [Zn_2(bdc)(L-lac)(dmf)], using waste materials as a means of mitigating the above issues, whilst still retaining the unique properties of the material – chiefly its ability to separate racemic mixtures. Consumer waste PLA (Polylactic acid) and PET (Polyethylene terephthalate) were introduced as potential reagents, sourced from PLA plastic cups and PET plastic bottles. We successfully synthesized a clear crystalline solid using waste PLA as a reagent and showed that it produces the same structure as ZnBLD and maintains chiral separative properties. We also investigated potential methods of utilising PET as a reagent and attempted two different methods of digesting the material in-situ for use as a reactant, but the work did not display successful results.

1. Introduction

Metal organic frameworks (MOFs) are a revolutionary class of crystalline materials, formed of metal ions coordinated to organic linkers in a repeating structure. In the past few years they have been receiving an increasing amount of attention due to their remarkable properties, which include high surface area, light responsiveness and tuneable pore size (1) (2). Some MOFs are even "flexible", meaning that they can change their structure in response to external stimuli. Their applications are diverse, and range from chiral separations and gas storage to biomedicine and chemical catalysis (3) (4).

The chiral separation properties of MOFs are especially relevant in the pharmaceuticals industry. Here, two opposing enantiomers of the same active pharmaceutical ingredient (API) can have drastically different effects on the human body, which has resulted in some tragic events in the past (5).

As such, the focus of this study was the MOF ZnBLD, one which has displayed great potential in the areas of chemoselective catalysis and enantioselective sorption – most notably in the separation of racemic mixtures of sulfoxides and the chemoselective oxidation of thioethers (6). ZnBLD is formulated as [Zn(bdc)(l-lac)(dmf)]·(DMF), it is made up of Zn^{2+} ions coordinated to organic linkers provided by terephthalic acid (H_2bdc) and L-(+)-lactic acid (L-H_2lac). Dimethylformamide (DMF) is coordinated but it is not actually a linker as it only coordinates once. Figure 1 shows the crystalline structure of the ligand. The porous framework of the MOF is clear to see, along with the chiral C atoms of the lactate ligand (which are marked in white). It is this

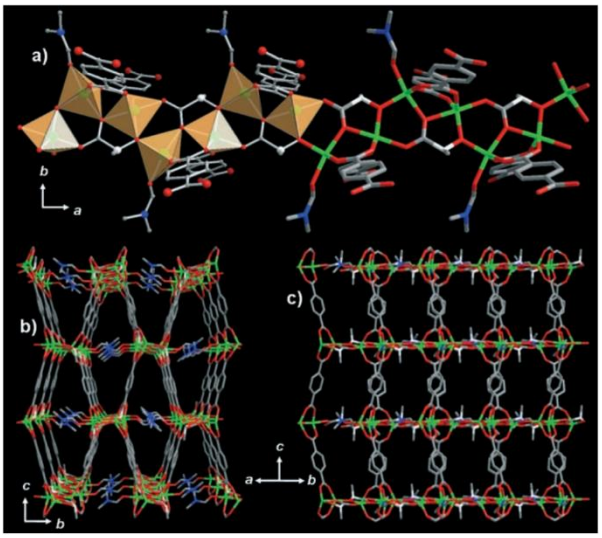

Figure 1 - The structure of ZnBLD from several viewpoints. Hydrogen atoms and guest molecules are emitted. Zn green, N blue, O red, C grey, Chiral C atoms of lactic acid white. (6)

combination of porosity and chirality that makes ZnBLD unique, and thus suited to purpose.

2. Metal Organic Frameworks: Background and Literature

The term "metal organic framework" was first coined in 1995 by Omar M. Yaghi in his paper "Hydrothermal Synthesis of a Metal-Organic Framework Containing Large Rectangular Channels" (7). The idea behind the study was to synthesize a microporous zeolite-like material, and to design and build the structure on the molecular level. Such materials have been always been important due to their ability to retain molecules within their porous structure, allowing them to be used in an array of applications, including separations and shape selective catalysis (8), to name but a few. The great advantage of MOFs is that their pore size and properties can be fine-tuned, allowing for purpose-built structures (2). Another advantage of MOFs over zeolites is their organic/inorganic hybrid makeup, as opposed to zeolites, which are purely inorganic (9). This means that there is a far greater array of options when it comes to choosing a MOF.

Hailin Li et al later synthesized and published MOF-5 (10), a zinc and terephthalic acid based MOF, in the paper "Design and synthesis of an exceptionally stable and highly porous metal-organic framework". It is formulated as $Zn_4O(BDC)_3 \cdot (DMF)_8(C_6H_5Cl)$, its structure can be seen in Figure 2. What made it so special was the fact that it displayed such high pore volume and surface area. Analysis showed that it displayed pores that were 0.54-0.61 cm^3cm^{-3}. Zeolites, on the other hand, have pore volumes in the range 0.18-0.47 cm^3cm^{-3}.

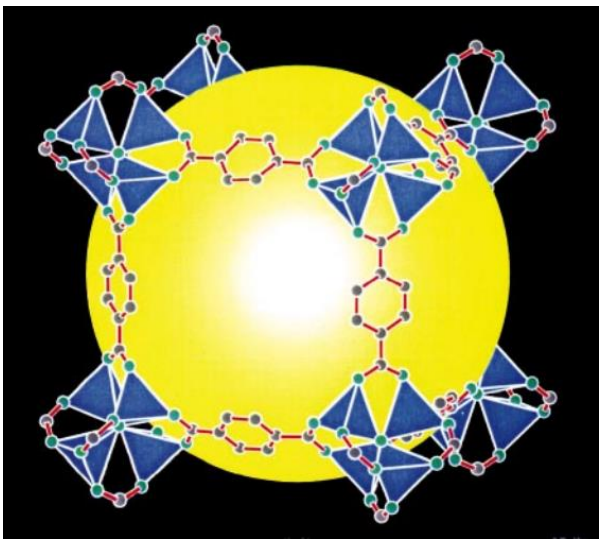

Figure 2 - The framework of MOF-5, with eight clusters forming a unit cell. O is green and C grey; the Zn_4O tetrehedra are shown in blue. The pore cavity is indicated by the yellow sphere. (10)

One of the first proposed uses for MOFs was chemical catalysis, as they are similar in structure to zeolites, which are one of the most industrially relevant catalysts. They catalyse reactions by reversibly binding molecules within their porous structure, providing a site for reaction to take place. Catalysis is chemoselective, meaning that reactant molecules will only be catalysed for reaction if they can fit within the microporous structure. Generally, catalysis using MOFs favours those reagent molecules that have the relatively smaller substituent groups. The paper "Metal–organic framework materials as catalysts" by JeongYong Lee et al. (3) goes into further detail on this, and also catalogues known catalytic MOFs and the reactions they catalyse.

The large pores and high surface area displayed by MOFs makes them a strong candidate for usage in gas storage and separation (1). A good example of this is carbon capture and storage (CCS) technology. Kenji Sumida et al., in their paper "Carbon Dioxide Capture in Metal-Organic Frameworks" (11) compare MOFs to current CCS techniques and examine their CO_2 adsorption capabilities, alongside their robustness and ability to withstand a given flue gas stream.

The near-endless combination of metal ions and linkers for the synthesis of MOFs has made them a popular object of study in biomedicine, as it has proved difficult in the past to find microporous materials that were not overly toxic to humans. The paper by Patricia Horcajada et al., "Metal-Organic Frameworks in Biomedicine " (4) examine the usage of MOFs in targeted drug delivery, whereby the MOF is loaded with an active agent molecule to be released when required.

3. Sulfoxides in the Pharmaceuticals Industry

Enantiopure sulfoxides are a key starting reagent in the pharmaceuticals industry. Some examples of such drugs include Armodafinil (12), the R-enantiomer of the wake-promoting agent Modafinil and Esomeprazole (13), the S-enantiomer of Omeprazole. Esomeprazole is a drug used in the

treatment of gastric ulcers and is one of the most sold drugs in the world (14). It is a huge global market in which ZnBLD could play a very significant role.

4. An Original Approach

In the previous work done by Dybtsev et al (6), the reactant feedstock for H_2bdc and L-H_2lac in ZnBLD synthesis was provided by the chemicals in their pure form. Pure L-H_2lac is expensive, due to the requirement for asymmetric synthesis, costing upwards of £10 per gram (15). H_2bdc, on the other hand, is a monomer derived from the oxidation of the petroleum derivative p-xylene (16), which is not sustainable. The polymerised forms of these chemicals are polylactic acid (PLA), for L-H_2lac, and polyethylene terephthalate (PET), for H_2bdc. These, unlike the pure chemicals, are commonly available in the form of consumer plastic products such as cups and bottles. The use of waste PET as a starting feedstock for chemicals synthesis has been demonstrated with MOFs in the past, as evidenced by the papers by Manju et al (17) and Sheng-Han Lo et al (18). One fact to note about PET is that, when it breaks down, it forms both terephthalic acid and ethylene glycol – this was taken into account by contaminating the pure terephthalic acid during synthesis. The use of waste PLA as a feedstock, however, has not yet been attempted, and here we have developed, for the first time, methods to synthesize MOFs using consumer waste PLA as the source of L-H_2lac. The use of plastics PET and PLA in the synthesis of ZnBLD provides a method of synthesis that is both more economical and more environmentally friendly. It is also important to note that a cheaper way to produce the chemical will allow it to become more viable and widespread throughout the pharmaceuticals industry.

5. The Issue of Consumer Waste Plastic Pollution

Waste plastic pollution is a serious and growing concern on a global scale. In 2010, it was estimated that 275 million metric tons (MT) of plastic waste was generated in 192 coastal countries in 2010, with 4.8 to 12.7 million MT entering the ocean. This was predicted to rise to ~250 million MT by 2025 (19). Plastics in the ocean are a concern because of their effects on the ocean and wildlife, as well as the fact that they are extremely persistent. Waste plastics on land are also an issue, and have a detrimental effect on organisms in soil based ecosystems. This is explored further by Yooeun Chae and Youn-Joo An in their paper, "Current research trends on plastic pollution and ecological impacts on the soil ecosystem: A review" (20).Without waste management, this problem will become exponentially worse as more of the world industrialises and starts to manufacture these products. ZnBLD has potential usage in the synthesis of one of the biggest drugs in the world (Esomeprazole). MOF synthesis from plastics can therefore provide greener routes in pharmaceuticals production.

6. Methodology

6.1 Chemicals & Reagents

The PLA and PET used throughout this study were procured from waste and thoroughly washed before usage, once with distilled water and then again with acetone. Dimethylformamide (DMF), L-lactic acid, terephthalic acid and zinc nitrate hexahydrate were purchased from Sigma Aldrich at analytical grade and used without further purification.

6.2 Synthesis: Pure and Ethylene Glycol Contaminated

ZnBLD was synthesised from DMF, L-lactic acid, terephthalic acid and zinc nitrate hexahydrate. The procedure followed is based off the one outlined in Dybtsev's paper (6). For the initial synthesis of pure ZnBLD, 664 mg of terephthalic acid, 392 mg of L-lactic acid and 2400 mg of zinc nitrate hexahydrate were added to 80 ml of DMF in a 200 ml Teflon lined container. The quantities here represent a molar ratio of 1:1:2 for terephthalic acid to L-lactic acid to zinc nitrate hexahydrate. This was then placed in a Teflon lined steel bomb and heated in a sealed autoclave at 110°C for two days. The solid product was collected and washed with DMF, and then vacuum filtered until dry. The above procedure was then repeated with the addition of 0.223 ml of ethylene glycol.

6.3 Synthesis: Waste

For the synthesis using PLA to replace L-lactic acid, 320 mg of PLA was used to maintain the molar ratios, and the rest of the procedure was kept the same.

When using waste PET: 840 mg of PET was added to 80 ml of DMF and this was placed in the autoclave and heated to 180°C for two days to

attempt digestion. The same amounts of PLA and zinc nitrate hexahydrate added previously were then introduced into the PET-DMF mixture, and the initial procedure repeated. PET was also digested in DMF using a MARS 6 microwave oven (21) which heated the reaction mixture to 180°C for 5 minutes. The waste PLA and zinc salt were added after the mixture was allowed to cool, and the rest of the procedure repeated.

6.4 Chiral Separation

Racemic mixtures of several different chemicals were used to test the separative procedures of the synthesised MOFs. 100 mg of MOF was separately added to 1 ml of 1-phenylethanol, 2-methyl-2,4pentanediol or 2-butanol. After 24h desorption time, all samples were washed with DCM and vacuum filtered. The dried solid was then immersed in 8 ml of DCM and left for another 24h. 0.2-0.6 ml of the resulting supernatant was then collected and later analysed.

6.5 Characterisation

6.5.1 Characterisation: Powder XRD

To analyse the crystallinity and structure of each material, samples were ground into a fine powder and then analysed in a PANalytical X'Pert Pro X-ray diffractometer (22). Each sample was analysed between the incident angles of 5° and 50°, whilst the XRD was set to the reflection-transmission mode. The sample stage was set to spin at 2 revolutions a minute, and the anode voltage was set to 40 kV and the current set to 20 mA. The X-ray detector used was the provided X'Celerator strip, and monochromatic Cu-Kα radiation.

To accommodate for the possibility of anomalous results, each sample was run in triplicate and subsequently averaged.

6.6 Gas Chromatography

Analysis of the supernatant retrieved from the separations experiment was carried out using a Shimadzu GC-2010 Plus (23) fitted with an autosampler and a flame ionization detector. Every sample was analysed in triplicate, and the average result was taken from each.

7. Results & Discussion

7.1 Synthesis

The products collected from our synthesis samples were all inspected after filtering as a simple means of visual verification. Figure 3 shows each of the samples collected from the vacuum filtration. As reported in Dybtsev's paper, ZnBLD manifests as clear needle-like crystals. These crystals are present in the Pure, Ethylene Glycol Contaminated and Waste PLA variants, indicating that the correct crystal phase of ZnBLD had been formed in each case. The expected crystals were not observed in the All Waste variants, instead a powder was retrieved, white in the case of the oven digested PET, and grey in the case of the microwave digested PET. We have considered several reasons

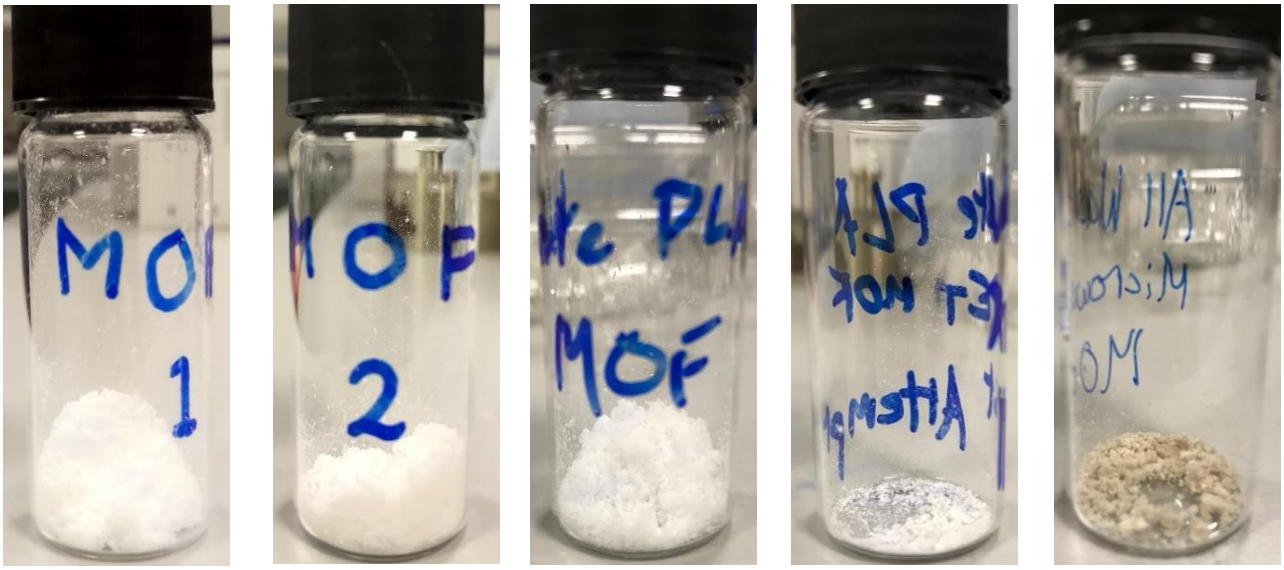

Figure 3 - Pictures depicting the collected samples following synthesis. From left to right: Pure; Ethylene Glycol Contaminated; Waste PLA; All Waste (Oven PET) and All Waste (Microwave PET)

as to why the crystals failed to form. Firstly, there may have been incomplete digestion of the PET. The PET may have failed to digest because the temperature was not high enough. It may have also failed to digest in the microwave because this was done in DMF as opposed to NaOH, which is used in Manju's study (17), due to the possibility of NaOH reacting with the DMF at a later date. This would lead to an absence of terephthalic acid in the reaction mixture and prevent the formation of ZnBLD. Another possibility for the failure may be due to a breakdown of the DMF, resulting in the formation of dimethyl amine. This was supported by the presence of a strong ammonia smell upon the opening of the reaction vessel, which is indicative of the presence of dimethyl amine. There is also the possibility that in the all waste synthesis, a different MOF altogether was formed. One possibility is MOF-5 (10), a framework formed from zinc nitrate hexahydrate and terephthalic acid. In regard to the final synthesis product, we attribute the change in colour to aging of the zinc salt. As the salt ages and absorbs water, its colour darkens, and as such effects the colour of the product.

7.2 Powder XRD

Following the isolation of the synthesised materials, the structure and crystallinity were analysed via powder XRD. Figure 4 displays the averaged XRD scans of all the synthesised materials. The collected scans were compared against the simulated scan produced using the crystal structure program Mercury (24) to determine whether or not the correct material had been synthesised. The XRD scans of the Pure, Ethylene Glycol and Waste PLA show a similar peak distribution to that of the simulation, indicating a likely production of ZnBLD. However, the intensity of the peaks are lower than those of the simulation. This is likely due to incomplete grinding of the scanned samples, which would leave large crystals in a preferred orientation, reducing the intensity of the scan. The All Waste XRD scan also maintains a similar peak distribution to that of the simulation, bar a select

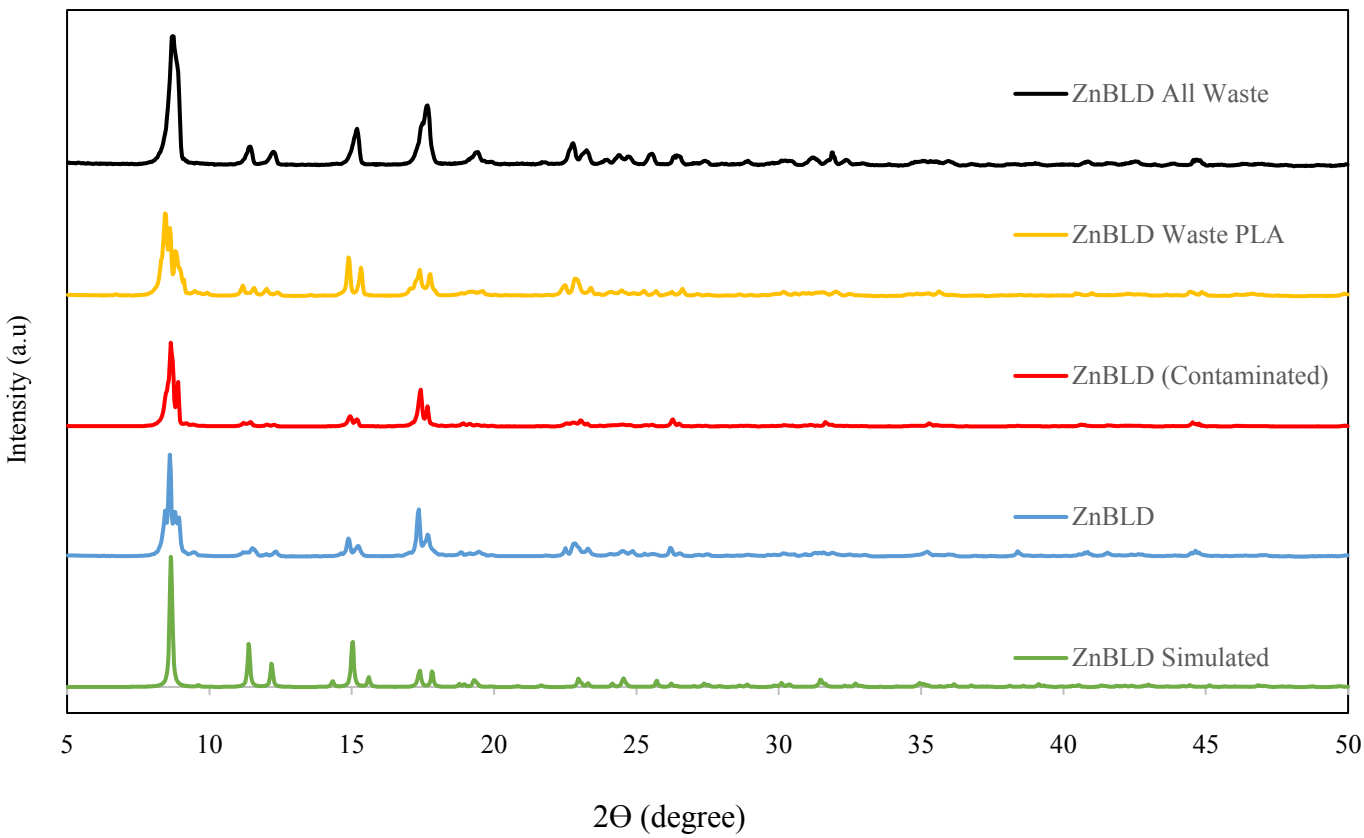

Figure 4 - Powder XRD scans of the as-synthesised MOFs used in this study

Table 1 - Enantiomeric excesses of each MOF and racemic mixture combination

	MOF	Pure	Ethylene Glycol Contaminated	Waste PLA	All Waste
Enantiomeric excess of chemical	1-Phenylethanol	27.3%	20.0%	10.5%	0.2%
	2-Methyl-2,4-Pentanediol	2.6%	2.9%	23.3%	0.1%
	2-Butanol	13.5%	10.8%	4.3%	0.4%

few small peaks at 15° and 18°. This suggests that the All Waste material demonstrates remarkable crystallinity, and whilst it may not be ZnBLD, it is a crystalline structure of some description.

7.3 Gas Chromatography

The supernatants collected from the separations experiments were investigated to determine the enantiomeric excess of each enantiomer. Table 1 shows the enantiomeric excess measured in each sample of MOF and racemic mixture. The microwaved PET variant was not tested due to time restrictions, so the All Waste variant shown is the one that was only heated. As expected , the pure sample demonstrates separative properties, and both the ethylene glycol contaminated and Waste PLA variants also demonstrate separative properties. Both the Pure and Contaminated variants follow a similar trend in terms of their separative performance over a small range of chemicals, however the contaminated variant exhibits slightly weaker abilities in the majority of cases. This may be due to the occupation of the pores by ethylene glycol, which reduces the pore volume available for separations When compared to the pure and contaminated variants, the Waste PLA sample demonstrates a profoundly different trend in its separative capabilities. It is significantly worse at separating 1-Phenylethanol and 2-Butanol, but displays a marked incresase in its performance with 2-Methyl-2,4-pentanediol. A potential explanation for this difference may be the breakdown chemistry of PLA, as when it is broken down into lactic acid, it takes in water. The only readily available water source is the zinc salt, and as such the PLA breakdown may take or preferentially bond to the water on the salt and alter the MOF structure slightly, affecting its perfomance. Despite its lack of apparent capability when it come the chiral separations, the intensity of the GC scans for the All Waste variants imply that a great deal of each chemical had been absorbed into the pores of the material. This indcates a porous structure of some sort and hints at the possibility that another MOF had been formed by accident. MOF 5 is once again a potential candidate, especially when one considers its high degree of porousity and the fact that it lacks any chiral centres.

8. Conclusion

To conclude, we have demonstrated the possibility of greatly reducing the economic and environmental impact of synthesising ZnBLD by successfully reproducing a sample of the MOF using waste PLA as a precursor. Gas chromatography data suggests that the synthesised MOF demonstrates remarkable chiral separative

properties and may be applicable to different separations than that of pure ZnBLD (perhaps broadening its potential pool of uses). We have also investigated the usage of consumer waste PET as a possible reagent for ZnBLD synthesis, however this was unsuccessful and further study may be required in this area.

9. Outlook

Methods to digest PET merit further investigation, given its potential usage in a variety of MOFs. Other future enquiries could also be made into MOFs that require L-lactic acid as a reagent, such as MOF 1201 and 1203 (25), both of which are calcium based MOFs currently used as naturally degradable carriers of pesticides, and using waste PLA as a substitute reagent.

10. Acknowledgements

We would like to acknowledge Ben Slater for his expertise and support regarding MOF synthesis and Gas Chromatography. Patricia Carry and Kaho Cheung are acknowledged for their assistance and advice regarding the MARS 6 microwave oven and the XRD process and equipment.

11. References

1. *Structural diversity and chemical trends in hybrid inorganic-organic framework materials.* **Anthony Cheetham, Rao, Russell Feller.** 2006, ChemComm, pp. 4780-4795.

2. *Metal-organic frameworks: a new class of porous materials.* **Jesse Rowsell, Omar Yaghi.** 2004, Elsevier, Vol. 73, pp. 3-14.

3. *Metal-organic framework materials as catalysts.* **JeongYong Lee, Omar Farha, John Roberts, Karl Scheidt, SonBinh Nguyen, Joseph Hupp.** 2009, Chemical Society Reviews, Vol. 38, pp. 1450-1459.

4. *Metal-Organic Frameworks in Biomedicine.* **Patricia Horcajada, Ruxandra Gref, Tarek Baati, Phoebe Allan, Guillaume Maurin, Patrick Couvreur, Gerard Ferey, Russel Morris, Christian Serre.** 2012, Chemical Reviews, Vol. 112, pp. 1232-1268.

5. *Thaliomide.* **Eric E. Prommer, Robert Twycross, Mary Mihalyo, Andrew Wilcock.** 2011, Journal of Pain and Symptom Management, Vol. 41, pp. 140-145.

6. *A Homochiral Metal–Organic Material with Permanent Porosity, Enantioselective Sorption Properties and Catalytic Activity.* **Danil N. Dybtsev, Alexey L. Nuzhin, Hyungphil Chun, Konstantin P. Bryliakov, Evgeniy P. Talsi, Vladimir P. Fedin, Kimoon Kim.** 2006, Angewandte Chemie International Edition , Vol. 45, pp. 916-920.

7. *Hydrothermal Synthesis of a Metal-Organic Framework Containing Large Rectangular Channels.* **Omar Yaghi, Hailin Li.** 1995, American Chemical Society, Vol. 117, pp. 10401-10402.

8. *New Vistas in Zeolite and Molecular Sieve Catalysis.* **Davis, Mark E.** 1993, American Chemical Society, Vol. 26, pp. 111-115.

9. *Emerging Multifunctional Metal-Organic Framework Materials.* **Bin Li, Hui-Min Wen, Yuanjing Cui, Wei Zhou, Guodong Qian, Banglin Chen.** 2016, Advanced Materials, Vol. 28, pp. 8819-8860.

10. *Design and synthesis of an exceptionally stable and highly porous metal-organic framework.* **Hailian Li, Mohamed Eddaoudi, O'Keefe, Omar Yaghi.** 1999, Nature, Vol. 402, pp. 276-279.

11. *Carbon Dioxide Capture in Metal-Organic Frameworks.* **Kenji Sumida, David Rogow, Jarad Mason, Thomas McDonald, Eric Bloch, Zoey Herm, Tae-Hyun Bae, Jeffrey Long.** 2012, Chemical Reviews, Vol. 112, pp. 724-781.

12. *Armodafinil.* **Karly P. Garnock-Jones, Sohita Dhillon, Lesley Scott.** 2009, CNS Drugs, Vol. 23, pp. 793-803.

13. *Esomeprazole, A Review of its Use in the Management of Gastric Acid-Related Diseases in Adults.* **Kate McKeage, Stephanie Blick, Jamie Croxtall, Katherine Lyseng-Williamson, Gillian Keating.** 2008, Drugs, Vol. 68, pp. 1571-1607.

14. *Transient Sulfenic Acids in the Sythesis of Biologically Relevant Products.* **Anna Barattucci, Maria Chiara Aversa, Aurora Mancuso, Tania Maria Grazia Salerno, Paola Bonaccorsi.** 2018, Molecules, Vol. 23.

15. **Sigma Alrich.** L-(+)-Lactic Acid. [Online] [Cited: 12 9, 2018.] https://www.sigmaaldrich.com/catalog/product/sigma/l1750?lang=en&region=GB.

16. *Synthesis of terephthalic acid via Diels-Alder reactions with ethylene and oxidized variants of 5-hydroxymethylfurfural.* **Joshua J. Pacheco, Mark E. David.** 23, 2015, PNAS, Vol. 111, pp. 8363-8367.

17. *Post conumer PET waste as a potential feedstock for metal organic frameworks.* **Manju, Prasun Kumar Roy, Arunachalam Ramanan, Chitra Rajagopal.** 2013, Materials Letters, Vol. 106, pp. 390-392.

18. *Waste polyethylene terephthalate (PET) materials as sustainable precursors for the synthesis of nanoporous MOFs, MIL-47, MIL-53(Cr, Al, Ga) and MIL-101(Cr).* **Sheng-Han Lo, Duraisamy Senthil Raja, Chia-Wei Chen, Yu-Hao Kang, Jiun-Jen Chen, Chia-Her Lin.** 2016, Dalton Transactions , Vol. 45, pp. 9565-9573.

19. *Marine Pollution: Plastic waste inputs from land into the ocean.* **Jenna Jambeck, Roland Geyer, Chris Wilcox, Theodore Siegler.** 6223, 2015, Science, Vol. 347, pp. 768-771.

20. *Current research trends on plastic pollution and ecological impacts on the soil ecosystem: A review.* **Yooeun Chae, Youn-Joo An.** 2018, Elsevier, Vol. 240, pp. 387-395.

21. **CEM.** MARS 6 Microwave Digestion System. *CEM.* [Online] [Cited: 12 10, 2018.] http://cem.com/mars-6/.

22. **Malvern Panalytical.** Xpert3-Powder. [Online] [Cited: 12 11, 2018.] https://www.malvernpanalytical.com/en/products/product-range/xpert3-range/xpert3-powder/index.html.

23. **Shimadzu.** GC. [Online] [Cited: 12 11, 2018.] https://www.shimadzu.com/an/gc/2010plus.html.

24. **CCDC.** Mercury - Crystal Structure Visualisation, Exploration and Analysis Made Easy. [Online] [Cited: 12 10, 2018.] https://www.ccdc.cam.ac.uk/solutions/csd-system/components/mercury/.

25. *Calcium L-Lactate Frameworks as Naturally Degradable Carriers for Pesticides.* **Jingjing Yang, Christopher Trickett, Salman Alahmadi, Ahmad Alshammari, Omar Yaghi.** s.l. : Journal of the American Chemical Society, 2017, Vol. 139, pp. 8118-8121.

Investigation of multiphase flows in non-circular channels

Karlson Dickman, Zhi Yuan Chua, Omar Matar*, Mirco Magnini
Department of Chemical Engineering, Imperial College London, U.K.

Abstract

The steady propagation of an air bubble through non-circular microchannels of aspect ratio (AR) 2 and 4 are investigated. This paper is primarily focused on identifying relationships between the flow parameters - Capillary number (Ca) and Reynolds number (Re) and the hydrodynamic bubble properties such as wet fraction, terminal bubble velocity, bubble shape and the minimum film thickness. Simulations were performed with an open-source CFD package OpenFOAM (release 2.3.1) and the built in Volume of Fluid (VOF) method, for Ca = 10^{-2} -10^{-1} and Re 10 - 1500. Results showed that with these rectangular geometries, bubbles are never axisymmetric for Ca > 10^{-2}. Overall, bubbles flowing in rectangular channels exhibit a smaller minimum film thickness compared to flows in square channels. Simulations also reveal that for channels of AR = 2, the bubble has a saddle-like shape at low Re and Ca which develops to an elliptical shape with increasing Re and Ca. A saddle shape is observed for all cases in channels of AR = 4. Increasing Ca results in an increase in film thickness for both ARs and hence, increasing minimum film thickness. A critical Re, (Re_c) exists where flow properties with Re beyond this critical value exhibits a new trend. At sufficiently high inertia effects, increasing Re results in a greater rate of decrease in film thickness. A strong correlation between the bubble shape and bubble terminal velocity is also observed.

Keywords: Microfluidics, Bubble, Multiphase, Non-circular, Hydrodynamics

1. Introduction

Multi-phase flow within a non-circular channel is applicable in various industries that include enhanced oil recovery, lab-on-chip devices and biological systems (Fan, 2016). In recent years, focus on multiphase flow in microchannels has grown as there has been emphasis on improving the performance of compact heat exchangers. This is the case as compact heat exchangers exhibit enhanced heat performance and a higher heat transfer coefficient resulting from the large heat exchange surface to volume ratio (Traian Popescu, 2012). These heat exchangers have non-circular channels of varying dimensions, but their hydraulic diameters (d_h) are typically smaller than 1mm (Navid Borhani, 2010).

The liquid film formed around the confined vapour bubble is known to be essential in understanding the flow regime of two-phase flows in microchannels. (Naoki Shikazono, 2009). The extensive understanding of the hydrodynamics in macro-scale does not directly apply to microchannels as significant deviations were noticed from the experimental data (Traian Popescu, 2012). Hence, prior to rapid implementation of these microfluidic microchannel devices, precise predictions of the heat transfer performance which is determined by the film thickness that varies with flow properties is necessary. This is essential as formation of gas bubbles can present significant problems in microfluidic systems by disturbing and blocking the channel of flow. When a gas bubble advances through a tube which is initially filled with viscous fluid, there will be a thin layer of liquid film trapped between the bubble and the channel walls. As the minimum film thickness in rectangular channels are smaller than that of square channels, they are more at risk of liquid film rupture and consequent dryout. This is the case as this thin film coupled with perturbations originating from the tail of the bubble or axial perturbations cause film rupture. Consequently, affecting the heat transfer performance within the heat exchanger tube. (Navid Borhani, 2010)

Henceforth, multiphase flow has been studied, focusing on average flow properties such a film thickness, bubble shape, wet fraction and fluid flow. These properties are studied as a function of Capillary number, Ca and Reynolds number, Re. Asymptotic theory was employed to study the cases for Ca approaching 0 at negligible Re (Wong, 1995a).

As Ca increases, the fluid films thicken and in near-square tubes the ultimate finger shape becomes axisymmetric at sufficiently high Ca (Chang, 1989). However, at low Ca the gas phase is confined by tube walls in square/ rectangular channels which leads to the formation of asymmetrical (non-axisymmetric) bubbles (Jingzhi Zhang, 2016). Simulations were conducted to investigate cases of $Ca = 10^{-3} - 10$, at negligible Re values for rectangular channels of aspect ratio 1-15 (Alberto de L´ozar, 2008). Laser displacement meter was then used to observe the effect of Ca and Re in circular and square channels only (Naoki Shikazono, 2009).

Thus, it is evident that cases at noticeable inertia have not been studied extensively; while it is known that inertial forces do affect the fluid characteristics, it is not known the extent of it.

Hence, this report concentrates on the effect of flow parameters Ca and Re on the two-phase flow of a bubble in liquid filled channel; thus, affecting the minimum film thickness along the plane of the walls. Gravitational effects were neglected as these cases had a Bond number in the order of 10^{-3}. The investigated geometry are rectangular channels of aspect ratio 2 and 4.

*Corresponding authors
Email: o.matar@imperial.ac.uk

2. Methods

Figure 1 shows the schematic of the bubble flow

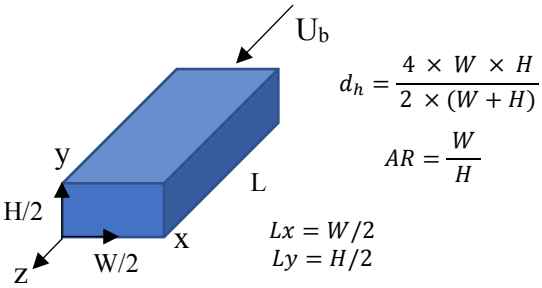

Figure 1 Schematic of quarter channel, with U_b referring to the velocity of bubble in the channel, d_h corresponding to the hydraulic diameter. AR represents the aspect ratio of the channel and is defined as the ratio of the width to the height. W and H are the width and height of the whole channel respectively. Lx and Ly are defined as the width and height of the quarter channel respectively.

through a quarter channel with velocity U_b. The d_h of the channel is used as the characteristic length in the calculation of the dimensionless numbers. Channels of length 75 d_h or 37.5 d_h were used in the simulations depending on the required length for the bubble to fully develop.

2.1. Numerical model

To study 2-phase flows in a micro-fluidic channel, fluid flow equations were implemented and solved in the opensource software OpenFOAM. To track the gas-liquid interface, the volume of fluid (VOF) algorithm was used, where the phases were assumed to be incompressible and do not penetrate each other. A marker, $I(x)$ was used to identify the two phases across the domain, where $I(x) = 1$ located the gas phase while $I(x) = 0$ located the liquid phase. The VOF method captured the interface between these 2 phases by identifying the marker function as the volume fraction, α. The volume fraction is the fraction of a computational grid cell that is occupied by liquid, and is given by:

$$\alpha = \frac{1}{V}\int I(x)\, dV \qquad (1)$$

where V is the computational cell volume. α takes any value between 0 and 1. Intermediate values between represent a gas and liquid interface of the bubble. Based on α, the properties, φ, of the mixture fluids 1 and 2 are computed as a weighted average on the specific weight properties:

$$\varphi = \varphi_1\alpha + \varphi_2(1 - \alpha) \qquad (2)$$

In this case, the properties concerned were the dynamic viscosity, μ and density, ρ.

The mass equation was obtained from the Reynolds Transport Theorem equation.

As an incompressible flow at steady state was considered, this equation simplifies to:

$$\nabla \cdot \boldsymbol{u} = 0 \qquad (3)$$

Accounting for incompressible flow and Newtonian fluid assumption, the conservation of momentum equation simplifies to the Navier-stokes equation.

In 2-phase flows, a surface tension term, F_σ was introduced as a source of interfacial forces between the 2 phases which was proposed by Brackbill et al (1992). As mentioned earlier, gravity is neglected in this analysis. The momentum equation can thus be represented by:

$$\frac{\partial \rho \mathbf{u}}{\partial t} + \nabla \cdot (\rho \boldsymbol{uu}) = \nabla \cdot (\mu \nabla \boldsymbol{u}) - \nabla P + F_\sigma \qquad (4)$$

The terms in equation (4) are defined as follows:

$$F_\sigma = (\sigma \kappa \boldsymbol{n})|\nabla \alpha| \qquad (5)$$

$$\kappa = -\nabla \cdot \left(\frac{\nabla \alpha}{|\nabla \alpha|}\right) \qquad (6)$$

$$\boldsymbol{n} = \frac{\nabla \alpha}{|\nabla \alpha|} \qquad (7)$$

with σ as the constant surface tension coefficient between the liquid and the gas, κ as the gradient of volume fraction scalar used to calculate the interface curvature, and the interface unit vector, **n.**

The simulation was then executed by solving with an InterFOAM solver on OpenFOAM via High Performance Clusters (HPCs).

2.2. Simulation methods

Flow domains with AR 2 and 4 were considered. Due to flow symmetry, only a quarter of the channel cross-section was simulated. A structured mesh, that was finer closer to the edges of the channels, was constructed to ensure accuracy in solving the flow in the thin liquid film. The mesh was divided into 2 parts on each axis. The first part of the mesh was constructed by dividing 90% of the channel length and height into 38 equal slices. The remaining 10% which was closer to the edge of the channel had a finer mesh. The length of the adjacent mesh reduces in length to 4.29% of the previous mesh; hence, progressively get narrower until the edge of the channel was reached. This was essential to ensure the interactions along the interface of the 2 phases were accurately captured.

At time t=0, the prescribed gas bubble was initialised at the entrance of the channel. The bubble had a length of 9 d_h, with a bubble width and height that was 90% of Lx and Ly respectively. At the channel inlet, a fully developed liquid flow was imposed with an average liquid velocity U_L=1 m/s. No-slip boundary conditions were imposed on the walls. The liquid to gas density ratio was fixed at 1000 while the liquid to gas dynamic viscosity ratio was fixed at 100 to mimic air-water flow liquid.

Time dependent plots, shape profiles of the different parameters were analysed using MATLAB R2018b.

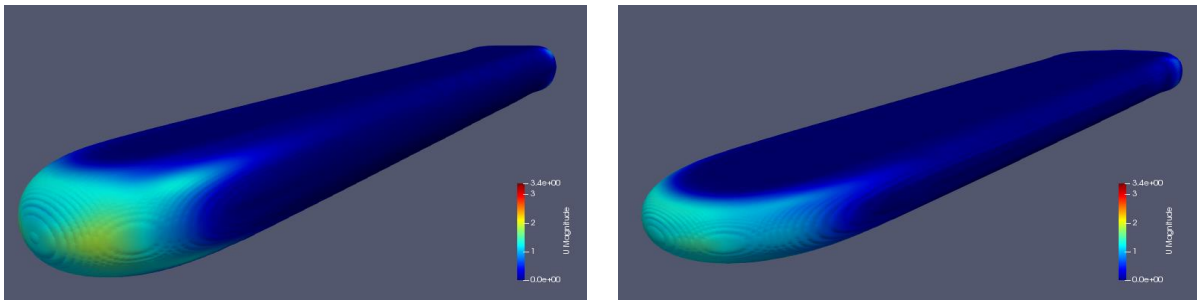

(a) (b)

Figure 2 Steady state bubble profile for a specific case of Ca = 0.01, Re = 100 (a) AR = 2 (b) AR = 4 as viewed on ParaView 5.5.2 (Sandia National Laboratory, Kitware Inc, Los Alams National Laboratory).

2.3. Dimensionless numbers

To analyse the physical effects of capillary, viscous and inertia effects on the bubble shape, the dimensionless numbers were determined. The ratio of viscous to surface tension forces is defined by the dimensionless the capillary number:

$$Ca = \frac{\mu_l u_b}{\sigma} \tag{8}$$

where μ_l is the dynamic viscosity of the liquid phase. The Reynolds number, Re, was also included in the analysis to quantify the relationship between inertial and viscous forces. It is defined as follows:

$$Re = \frac{\rho_l u_b d_h}{\mu_l} \tag{9}$$

where d_h was defined as the characteristic length of the channel. Another important dimensionless number, the Weber number was crucial in understanding the relative importance of the effect of inertia to surface tension. It is the product of the Capillary and Reynolds Number:

$$We = \frac{\rho_l u_l^2 d_h}{\sigma} \tag{10}$$

2.4. Steady state conditions

Quantitative and qualitative findings of the simulation results for confined air-water flows in rectangular channels of AR 2 and 4 are presented here. Ca was varied at 0.01, 0.05 and 0.1. For the cases of Ca = 0.01, the Re was varied from 1 to 1500, while for the cases of Ca = 0.05 and 0.1, the Re was varied from 10 to 500. Results were validated against literature obtained from (Heil, 2002) and (Viboonyotin, 2018). The bubble velocities, cross sectional shape profiles, radii and film thickness were plotted against time to identify corresponding steady state values. Ultimately, these flow properties were observed as a function of Re and Ca to draw reasonable trends and correlations. The bubble hydrodynamics were then quantified and analysed separately for each case by understanding how they were affected by Re, Ca and AR of the channels respectively.

The overall steady state bubble is shown in Figure 2 for a selected case. In both profiles for AR = 2 (a) and AR = 4 (b), the interfacial velocity at the edges of the bubble are close to zero, but they are the highest near the nose and at the tail. The bubble in channel of AR = 4 has a longer stretched profile relative to the bubble in channels of lower AR. The velocity field at the middle of the channel is more distributed across the surface of the bubble.

In all the simulations, it was essential to determine the points where the bubble had achieved steady state before comparing results obtained from other methods. At steady state, the dimensionless bubble radius in x-direction along the symmetry plane (R_x) in y-direction (R_y) and diagonal (R_d) remains constant. They were measured as:

$$R_x = \frac{x_b}{Lx}, R_y = \frac{y_b}{Ly}, R_d = \frac{d_b}{d_h} \tag{11}$$

where d_h is the d_h of the channel.

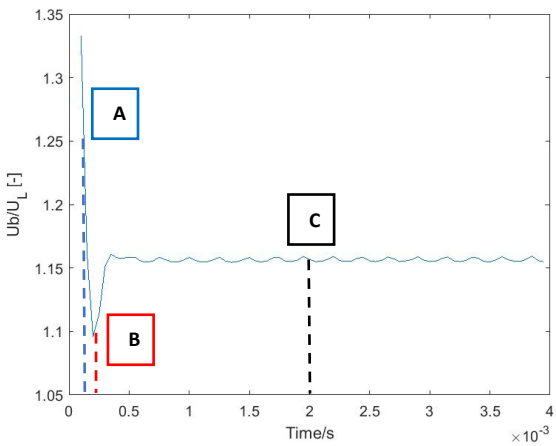

Figure 3 Evolution of bubble velocity with time for a flow in a channel AR = 2, with Re = 100, Ca = 0.01.

The bubble's velocity evolution can be observed in Figure 3. 3 main stages of bubble velocity development have been identified – A is the point of initialisation, B is the point of minimum velocity and C is the steady state stage.

The evolution of the bubble shape can be observed in Figure 4, where the dimensionless bubble radius measured at 11 halves of hydraulic diameters ($11d_h/2$) for each of the stages A-C (as defined in the Figure 3) were plotted. Initially (A), the bubble's cross-sectional profile is shortest in bubble height. At B, the bubble length increases in y-direction, but its width reduces slightly in the x-direction. Once the bubble is fully developed, it adopts a bubble cross-sectional shape as seen in C. Unlike flow in square

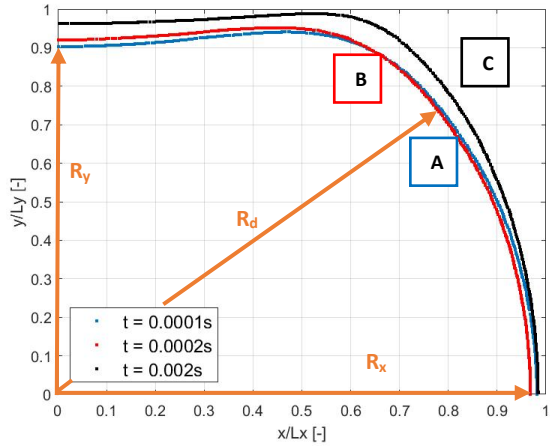

Figure 4 Development of cross-section profiles measured at A (initial), B (minimum velocity), C (terminal) stages at 11-half diameter from bubble nose for Ca=0.01, Re = 100.

channels, bubbles in rectangular channels never exhibit the axisymmetric shape. This result agrees with (Heil, 2002). At stage C, the film thickness is the thinnest across three stages. This justifies the need to analyse the results when the bubble has fully developed at steady state.

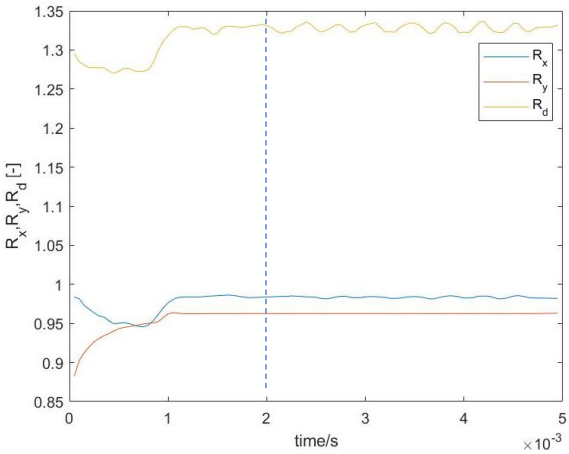

Figure 5 Time development of R_d, R_x and R_y for Ca = 0.01, Re = 100 AR = 2.

The development of the dimensionless bubbles radius (R_x, R_y and R_d that were defined in Figure 4) with time can be seen in Figure 5. Unlike a square channel where the angle of 45º from the centre of the channel is used to calculate R_d, an angle of 26.56° and 14.04° were used for AR = 2 and AR = 4 respectively. At 2×10^{-3}s, R_x and R_y cease to fluctuate while R_d exhibits a steady sinusoidal oscillation at about 1.32 m/s; therefore, only data beyond this point was considered for evaluation. During the initial stages, the bubble is more compacted toward the centre of the channel. As the bubble develops with time, the bubble progressively adopts a saddle like shape.

2.5. Validation of results

Few available work on rectangular channels of AR 2 and 4 have been published. Numerical results of wet fraction (Wf) published by A. de Lo'zar (2007) for Re << 1 served as one source of validation for the numerical model. It is also important to note that Hazel et al's simulations were performed on an air finger (half of a full bubble) whilst the current simulations were performed on a full bubble. The second validation was comparing bubble terminal velocity against literature. Results from AR = 2 cases were validated against Hazel et al's (2008) simulations and AR = 4 results were compared with Viboonyotin (2018).

3. Results and discussion

3.1. Wet fraction

In Hazel et al's simulations, inertia effects were neglected. Therefore, wet fraction results obtained at low Re (Re = 1 for Ca = 0.01, and Re = 10 for Ca = 0.05 and 0.1) were used in the validation. There were 3 points of validation per AR to compare with the literature results.

The Wf is the ratio of the cross-sectional area of the quarter channel which is filled with liquid to the cross-sectional area of the quarter channel. The averaged steady state profile of bubbles was obtained and its profile at $11d_h/2$ bubble length from the nose bubble was plotted. Wf was then determined by calculating the percentage of the cross-section occupied by liquid:

$$Wf = {A_l}/{A_c} \tag{12}$$

where A_l is the area of the channel occupied by the film and A_c is the cross-sectional area of the channel.

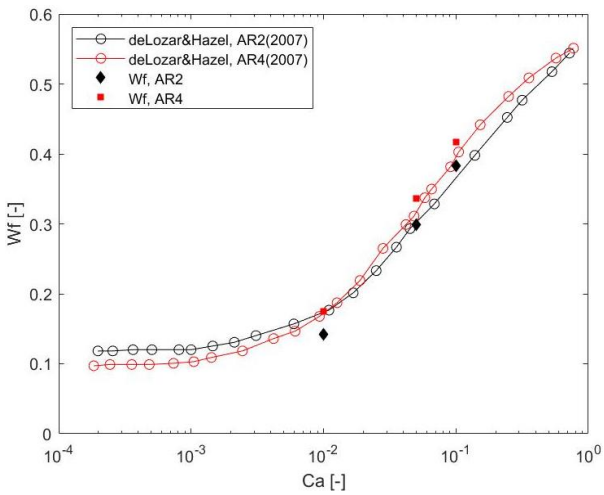

Figure 6 Plot of wet fraction as a function of capillary number for AR = 2 (black line) and AR = 4 (red line) from Hazel and de Lozar (2007) and simulation results values AR = 2 (black diamonds) and AR = 4 (red squares).

Figure 6 depicts the relationship between Wf and Ca where Wf increases with increasing Ca. The 3 points of validation are represented by the scatter plots. According to results from A. de Lo'zar (2008), at high Ca values beyond 0.01, the Wf of a channel of AR = 2 is lower than that of AR = 4. At low Ca, the opposite is true, with Wf of AR = 2 cases greater than that of AR = 4 cases.

The average absolute deviation obtained from the results obtained from the simulations and interpolated results from A. de Lo'zar (2007) for the AR = 2 case is 9.67%. However, this large value is due to a single point of deviation at Ca = 0.01 where the deviation is at ±24.4%. For the AR = 4 cases, the deviation is significantly smaller at ±3.84%. these deviations could have been due to the simulations being performed at a higher Re where inertia was not completely negligible. Nevertheless, a deviation of about ±6.8% for all the obtained results is reasonable and thus, validates the implemented model.

3.2. Bubble terminal velocity

The effects on terminal velocity are discussed in this section. A fully developed bubble velocity profile with no slip boundary conditions at the wall was considered. The velocity increases from zero at the walls to the middle of the channel where the velocity is at its maximum. This bubble velocity is scaled with the mean liquid velocity, U_L. The ratio of these 2 velocities were examined to understand how bubble terminal velocity varies with respect to Ca, Re and AR of the channel. These simulated results were compared against literature as shown in Figure 7 where data from Viboonyotin (2018) and Heil (2002) were used to validate results for AR = 2 and AR = 4 respectively.

The bubble velocity will always be greater than the mean liquid velocity hence, the ratio of the two velocities is always greater than 1 (Abadie, 2013).

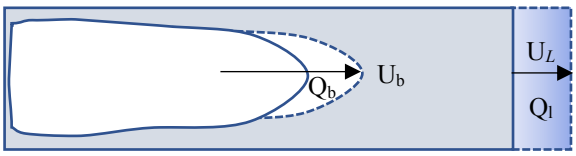

Figure 7 Schematic of bubble displacing liquid at a volumetric flowrate (Q_b) equivalent to the volumetric flowrate of the liquid (Q_l).

Based on Figure 7, as $Q_b = Q_l$ the conservation of mass equation simplifies as follows (14):

$$\frac{Ub}{U} = \frac{1}{1 - Wf} \tag{14}$$

where Wf is defined as in equation (12). As Wf is a non-integer bounded between 0 and 1, which results in the ratios of the two velocities to be always greater than 1.

3.2.1. *Effect of Ca*

As exhibited in Figure 8, the bubble terminal velocity increases with Ca at any given Re. This can be expected as Ca is proportional to U_b. As determined in the earlier section, higher values of Ca resulted in thicker liquid film between the bubble and the channel. Accounting for this increase in film thickness, coupled with the no slip boundary conditions at the wall experienced by the parabolic velocity profile results in higher velocity for thicker films.

At Ca = 0.01, the liquid film is very thin and despite the large increases in Re, the inertia effects are not strong in the liquid film as shown by the relatively linear line. This validates that the flow properties are governed by Ca and not inertia effects at low values of Ca.

3.2.2. *Effect of Re*

Figure 8 validates that the inertia forces are negligible at low Ca numbers. This is observed as the variations in U_b with Re remain moderate at lower Re. For the case of Ca = 0.01, a sharp increase in terminal velocity of bubbles at very high Re is observed. At moderate values of Ca (0.05), a different profile is adopted. For both ARs, at a low range of Re numbers, increases in Re will lead to a reduction in bubble velocity. However, the bubble reaches a minimum terminal velocity close to a Re of about 100 – 200. At higher Ca and film thickness, there is an increasing influence of inertia on the bubble terminal velocity.

The U_b curves are more pronounced, with a sharper drop and increase in U_b (after about Re = 100)

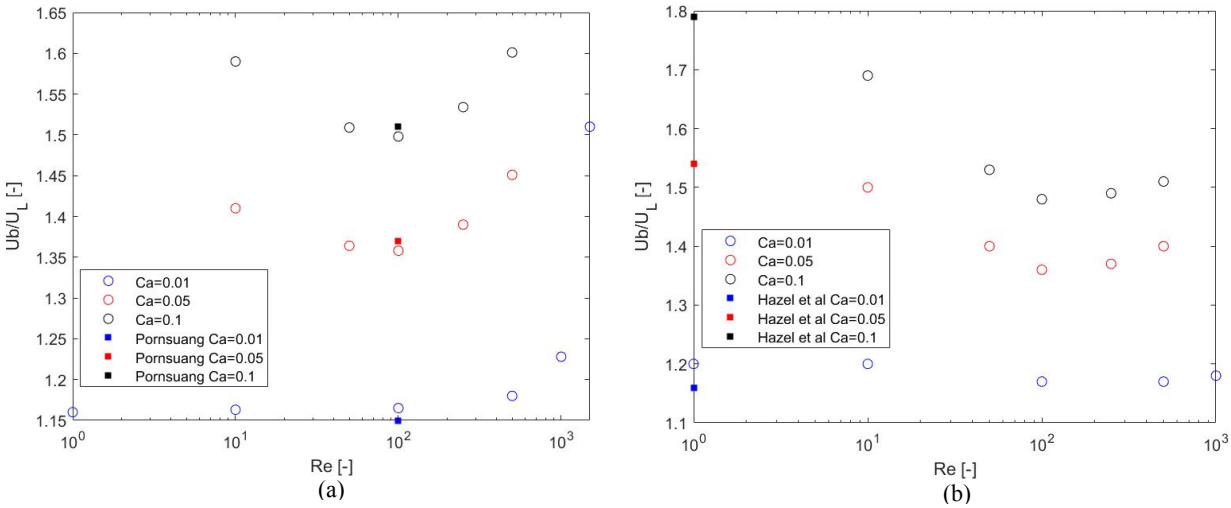

Figure 8 Ratio of bubble terminal velocity to mean liquid velocity for an AR = 2, with validation results obtained from Hazel et al. (2008) (a) and for an AR = 4, with validation results obtained from Pornsuang (2018) (b). Ca = 0.01 (blue), Ca = 0.05 (red), Ca = 0.1 (black).

across the Re. This observation is coherent with Abadie's discovery. A general conclusion that can be drawn is that inertia of the liquid plays little to no role in the determination of the bubble terminal velocity at low Ca.

3.3. Shape of bubble

The hydrodynamic effects of Ca, Re and varying AR are explored in this section. The bubble shapes that will be examined are the bubble profiles taken from an axial slice, bubble cross sectional shapes at 11 $d_h/2$ length from the bubble nose and bubble radii.

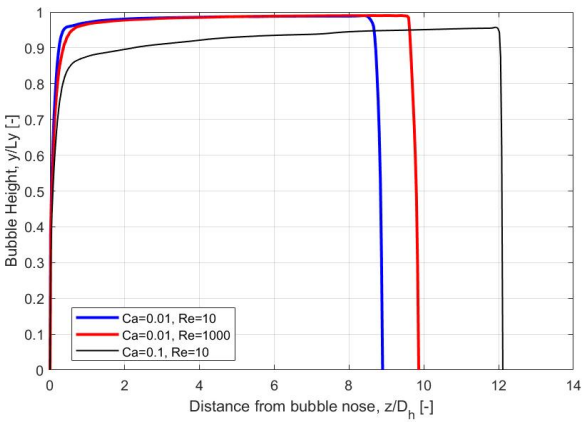

Figure 9 Bubble side profiles of Ca = 0.01, Re =10 (blue); Ca = 0.01, Re = 1000 (red) and Ca = 0.1, Re = 10 (black).

Figure 9 shows how the fully developed bubble profile along the length (z-axis) for AR = 2. The resulting axial profile of Re and Ca were plotted to draw trends on the bubble length and bubble nose shape.

3.3.1. Effect of Ca

In Figure 9, the bubble is flowing in the channel from the right to the left. For elongated bubbles at low Ca where there is a dominating effect of surface tension, the bubble nose is flat. The bubble approaches the shape of the channel as the bubble height (R_y) approaches 1 at low Ca. These observations are coherent with studies by Alberto de L'ozar (2008) and Abadie (2013). With increasing Ca, the bubble nose becomes sharper and the bubble tail becomes flatter. An elongated bullet like shape is observed for Ca ≥ 0.05.

According to Abiev (2010), the product of the bubble length and mean bubble cross-sectional area will be constant due to conservation of mass with the assumption of constant bubble density. Therefore, increasing Ca will lead to a thickening of the liquid film, resulting in an increase in Wf. This results in bubble at low Ca being shorter compared to bubbles at higher Ca. These observations agree with Jingzhi Zhang (2016). The average length of 9.55 $d_h/2$ is observed for Ca = 0.01 and 10.61 $d_h/2$ for Ca = 0.05. At higher AR of 4, the bubble lengths are longer due to a larger wet fraction compared to the AR = 2 case at the same Ca. It was also observed that the bubble nose for AR = 4 is sharper compared to the bubbles observed for AR = 2 cases at a specific Ca and Re.

Bubbles in rectangular channels will never adopt an axisymmetric cross-sectional profile (Alberto de L´ozar, 2008). At a fixed Re value, for the case of AR = 2, the bubble adopts a saddle shape for cases of low Ca (0.01) as seen in Figure 10. With increasing Ca, viscous forces start to dominate the surface tension forces, and the bubble shape transits to a more elliptical shape. The fluid film will be thicker along the longer of 2 axes (x/Lx). This thicker film offers less resistance to the fluid; hence the fluid is driven from the shorter semi-axis (y/Ly) toward the longer axis. The pressure gradient also drives liquid towards the corner of the channel. With increasing Ca, stronger viscous forces push the bubble inwards, forming a more compact shape where both the R_x and R_y decrease.

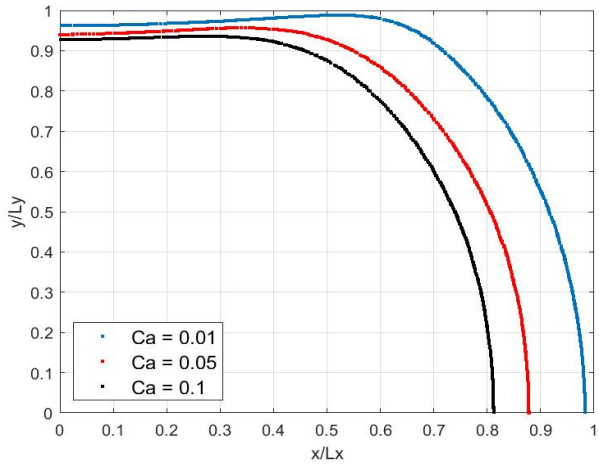

Figure 10 Bubble cross-section measured at 11 $d_h/2$ bubble lengths from bubble nose for AR = 2 of Ca = 0.01 (blue), 0.05 (red) and 0.1 (black) at Re = 100.

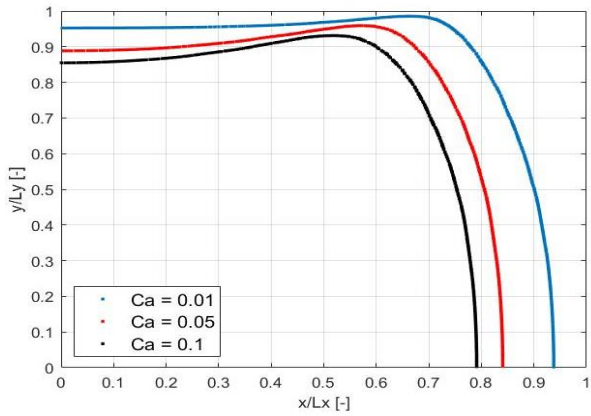

Figure 11 Bubble cross section measured at 11 $d_h/2$ from the bubble nose for Ca = 0.01 (blue), 0.05 (red) and 0.1 (black) at Re = 100 for an AR = 4.

For the AR = 4 cases, there is no transition toward an elliptical shape from a saddle shape at higher Ca. The saddle shape is maintained for all values of Ca as seen in Figure 11. With increasing Ca, there is an increasingly pronounced saddle shape and the location of the minimum film thickness shifts closer toward the centre plane of the bubble.

These observations are coherent with findings from Heil (2002). It was identified that with AR ≥ 2.04, the bubble will never have an axisymmetric or elliptical configuration.

3.3.2. *Effect of Re*

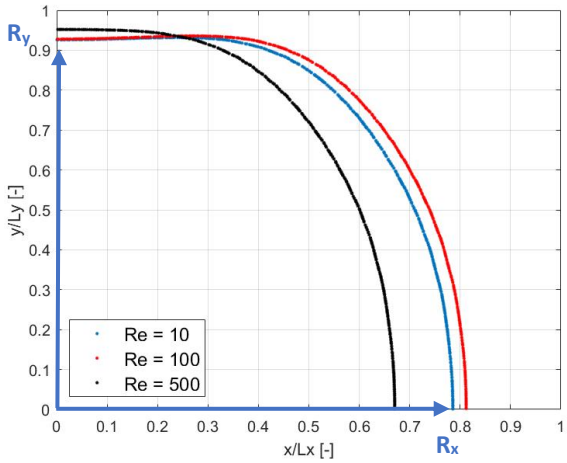

Figure 12 The cross-sectional profiles of a bubble measured $11d_h/2$ from the bubble nose of Ca = 0.1 for Re =10, 100 and 500 for an AR = 2.

The effects of inertia on the hydrodynamics of Taylor flow bubbles are often neglected in microchannels (Heil, 2002). Abadie had observed that although the flow is laminar, the bubble will be subjected to inertial effects of We numbers greater than 0.7 (Abadie, 2013). It is thus essential to understand the impact of inertia on the development of the bubble shapes.

As observed in Figure 12, for the cases of AR = 2, at low values of Re, there is a saddle like shape. With increasing Re, the bubble increases in R_x and the bubble develops an elliptical shape. However, when inertia forces are significant enough, the bubble exhibits a different hydrodynamic behaviour. Beyond a critical value of Re, Re_c, the bubble is pushed in to the central of the channel along the width as it offers the lowest resistance to flow. The result is that R_y increases significantly to accommodate the compression of the bubble width.

This phenomenon is also observed in the AR = 4 cases, where beyond Re_c, a change in bubble shape behaviour is observed. However, the saddle like shape is maintained through all the ranges of Re tested.

Inertia effects experienced by the liquid film is more significant along the x-direction for channels AR greater than 1. This is due to the film thickness measured in the x-direction being thicker than the thickness measured along the y-direction. Therefore, when there are sufficient inertia effects, the film pushes against the bubble along its width, causing a reduction in R_x.

When inertia effects are non-negligible, the bubble nose develops a bullet-like shape and the tail of the bubble is flatter compared to bubbles observed at flows with low Re. This phenomenon is observed in Figure 7.

With increasing Re, the time taken for the bubble to achieve an equilibrium steady state shape in the axial direction. According to Abadie, the effects of inertia become particularly significant at Re = 1000 (Abadie, 2013). Beyond this Re, the time taken to achieve steady state is significantly greater compared to lower values of Re.

3.3.3. *Bubble radii*

The bubble radius plots provide a summary of the trends in the shapes of the bubbles at varying conditions. The bubble radii, R_x and R_y, are defined in Figure 8.

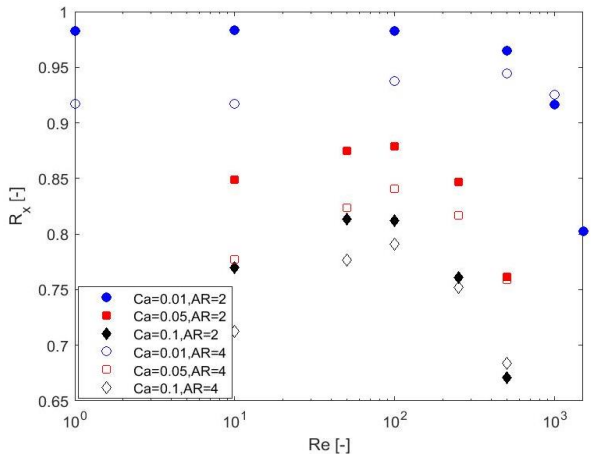

Figure 13 R_x variation with Re for all Ca = 0.01, 0.05 and 0.1 for Re = 1 to 1500, with R_x defined in Figure 12.

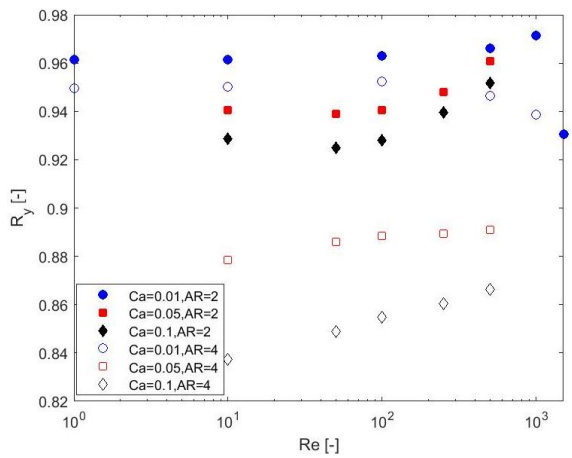

Figure 14 R_y variation with Re for all Ca = 0.01, 0.05 and 0.1 for Re = 1 to 1500, with Ry defined in Figure 11.

The first trend that is exhibited by the curves are that both bubble radii decreases with increasing Ca. As acknowledged earlier, with decreasing effects of surface tension, the bubble occupies a smaller cross-sectional area in the channel resulting in a smaller cross-sectional shape. Another trend that can be drawn is the negligible influence of inertia at low Ca. The Ca = 0.01 curves (blue) in Figure 13 do not vary much with changing Re. For the Ca = 0.01 cases of AR = 2 and 4, only when Re is sufficiently high at about 1000 there exists a sharp drop in both bubble radius.

An important observation is the influence of inertia at higher Ca. As seen in these cases, at low Re, when there is an increase in Re, both R_x and R_y increases.

However, beyond a critical Re, Re_c, the R_x attains a maximum value and starts to reduce while R_y increases at a much faster rate. This trend is strongly corelated to the bubble terminal velocity as plotted in Figure 7, where beyond the Re_c, bubble terminal velocity rises with falling R_x.

For the cases of AR = 2, at Re = 1500, Ca = 0.01, a very sharp decrease in both bubble radius was observed. A postulation is that due to the significant impact of inertia, the bubble film thickness has not fully developed at $11d_h/2$ bubble lengths from the bubble nose. Therefore, the value obtained there may not be representative of the steady state film.

3.3.4. Overall effect of We

The range of We numbers worked with were from 0.1 to 25.

At high We > 5 for Ca ≥ 0.05, there is an increasing prevalence of bubble breakup. At this point there are 3 competing forces – the capillary forces that prevent the breaking of the bubbles; and the opposing forces - the viscous stress and pressure forces along the channel that act against the bubble to deform the interface. With increasing Ca, capillary forces are negligible in comparison to the other 2 forces. Inertia effects are also observed to promote the deformation of bubbles at the rear cap of the bubble (Abadie, 2013). With an increasing inertial effect (increasing Re) and reducing capillary force (increasing Ca) resulting in an overall increase in We, there is an increased frequency and extent of deformation of bubbles.

When examining the bubble radii plots for R_x in Figure 13, a distinct observation is that the value of Re_c where a maximum value of R_x decreases with increasing Ca. This may point to the existence of a global critical Weber number, We_c, where multiphase flows with We numbers greater than this value will experience significant inertial effects for any combination of Ca and Re.

3.4. Liquid film thickness

The liquid film thickness is particularly important with regards to heat transfer. This is the case as heat exchanger and chemical reactors experience enhanced heat transfer at regions of thin liquid film (Taha roshdy Taha, 2006).

Figure 15 encapsulates how the film thickness varies across a 2-D space. At a given distance from the bubble nose (z/d_h), the respective film thickness across the width of the quadrant (x/Lx) is indicated by the intensity of the heatmap. The contours enable the identification of the region of minimum film thickness at a point in time as the film thickness begins to vary depending on the location at a distance from the channel midplane (x/Lx). Similar to a square channel just beyond the bubble nose, the bubble shape is non-axisymmetric.

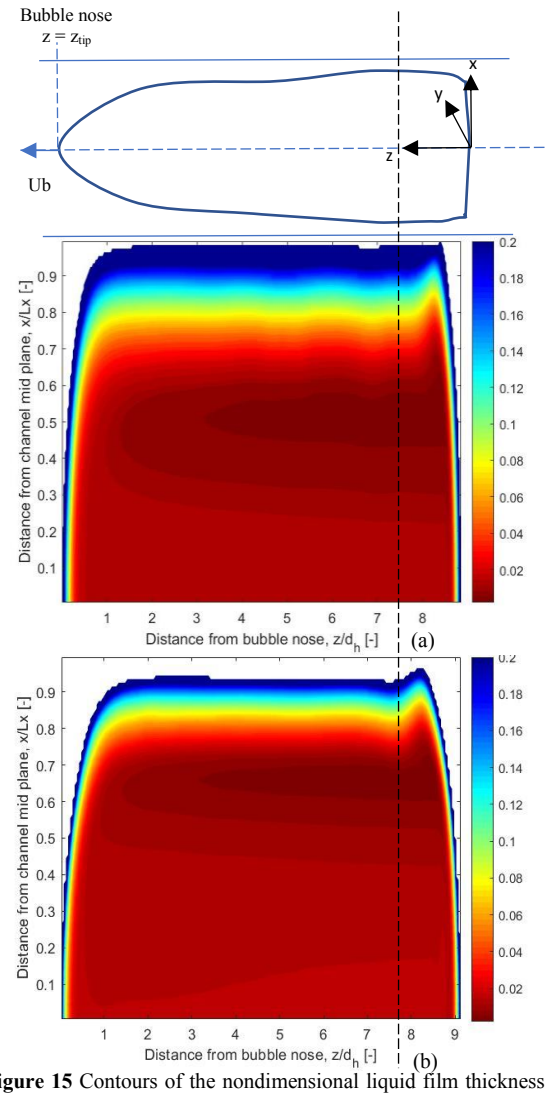

Figure 15 Contours of the nondimensional liquid film thickness $\delta(x,z)/L_y$ measured between the channel wall(y=L) and the liquid-gas interface for (a)Ca=0.01, Re=100, AR=2 (b)Ca=0.01, Re=100, AR=4.

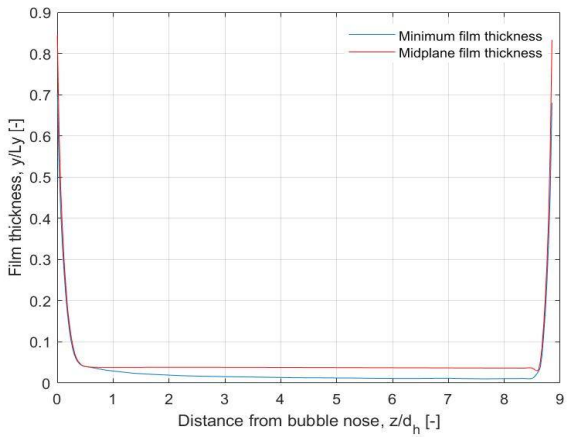

Figure 16 Film thickness measured at midplane (blue) at minimum film thickness (red) for Ca = 0.01, Re = 100 and AR = 2.

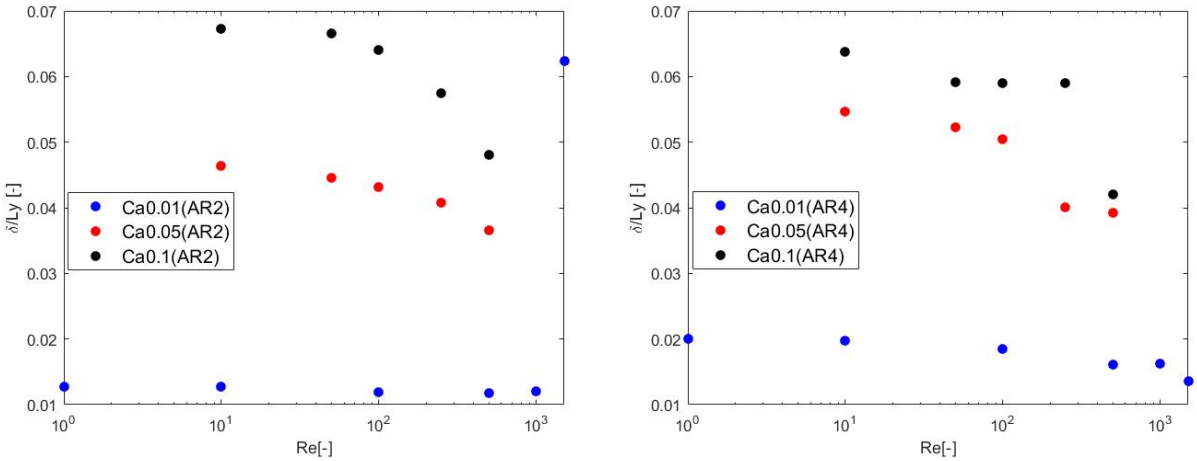

(a) (b)

Figure 17 Minimum film thickness scaled over L_y against Re for AR = 2 (a) and AR = 4 (b) with cases Ca=0.01(blue), Ca=0.05(red), Ca=0.1(black).

The film thickness has a more prominent deviation in the case of AR = 4 as it exceeds the AR of 2.04 where no elliptical shape was observed (Alberto de L´ozar, 2008).

Based on Figure 16, it was determined that the measured film thickness at the top of the channel is always lower than the film thickness measured at the mid-plane along the height of the channel in all cases. This occurs because there exists a difference in the film thickness between the film along the width and the height. Thus, this difference causes the fluid to flow from the thinner film towards the thicker film as it offers a lower resistance. However, this direction of flow is opposed by surface tension that works towards forming an axisymmetric film. (Alberto de L´ozar, 2008) Thus, the film thickness at the top of the channel was measured at $11d_h/2$ behind the bubble nose. The results are as shown in Figure 17.

3.4.1. Effect of Ca

As Ca increases, an increase in the film thickness is observed irrespective of geometry. (Abadie, 2013) This is expected, as at higher Ca the flow is viscous dominating thus surface tension becomes negligible. A large increase in the film thickness between Ca = 0.01 and Ca = 0.05 is observed in Figure 17. However, from Ca = 0.05 to Ca = 0.1, the increase in film thickness is less significant. This is prominent as inertial effects become significant at Ca > 0.01 (S. Khodaparest, 2015). At low Ca, the film thickness is determined by the Ca only; however, inertial forces cannot be neglected at higher values of Ca for it was found to vary with Re. (Naoki Shikazono, 2009) Using the theoretical analysis conducted by Bretherton (1961), a relation was obtained:

$$\frac{\delta}{\frac{d_h}{2}} = \frac{Ca^{\frac{2}{3}}}{1 + Ca^{\frac{2}{3}}} \tag{13}$$

Thus, it can be concluded that the film thickness asymptotes to a finite value as Ca is increased. This is clearly observed as an increase in Ca results in a smaller increase in film thickness as higher values of Ca. This trend is observed in the both AR cases.

3.4.2. Effect of Re

The effects of inertia at low Ca values are negligible as shown in Figure 17. This is apparent with a relatively linear trend of film thickness at Ca = 0.01 across all values of Re. However, with AR = 2 at Re = 1500 for Ca = 0.01 there is a spike in film thickness. This is speculated to occur as the bubble has yet to fully develop thus achieve a steady film thickness.

Apart from that, it can be observed that the minimum film thickness decreases with increasing Re. There exists a point in Re at which the negative gradient of film thickness begins to increase. This can be expected as it was noticed in Figure 14 that the bubble radii, R_y continues to increase with increasing Re, thus resulting in thinner film.

4. Conclusions

The effect of key bubble parameters on bubble shape, minimum film thickness and bubble terminal velocity for 2 phase flows in channels AR = 2 and AR = 4 have been investigated. During these studies, a range of Ca (0.01 to 0.1) and Re (1 to 1500) were covered. These studies have revealed some interesting findings that exhibit 2 different profiles beyond critical Ca and Re.

The bubbles in channels AR = 2 have a saddle like shape at low values of Ca and Re; however, it transitions to an elliptical shape at higher values. For AR = 4 the bubble maintains a saddle like shape within the investigated range of Re and Ca. Secondly, upon investigation of the three flow properties it can be concluded that the inertia forces are negligible at low Ca values. This was evident as an increase in Re had insignificant effects on the bubble shape, film thickness and terminal velocity. Subsequently, it was observed that a correlation exists between the bubble velocity and bubble radii which enables prediction of the film thickness. This was particularly apparent with the R_x bubble radii. Lastly, a Re_c was noticed when

increasing the Re value where flow properties began to deviate and exhibit a new relationship. This was evident as the terminal velocity began to increase and the bubble shape changed where the R_x started to decrease beyond the Re_c. A possible We_c may also exist that is unique to a specific AR.

This experiment can be further improved by conducting more simulations within the current range of Re and Ca. These additional data points would generate a more robust relationship between flow parameters and bubble hydraulics thus enabling the identification of the exact Re_c where the trends start to change. Subsequently, correlations relating the film thickness to the fluid velocity can be determined. This will be particularly useful in industrial applications as fluid velocity is a parameter that can be readily varied thus enabling better control over the film thickness.

Lastly, these studies need to be conducted beyond AR = 4 as the current results only provide two data points of AR = 2 and AR = 4 which is insufficient to draw reasonable trends. Expanding the studies will provide a more reliable understanding of how AR affects these flow properties. Ultimately, the hydrodynamics of two-phase flow in microchannels require further studies to be extensively understood; however, these findings have aided in the comprehension of the flow properties.

5. Acknowledgements

We would like to thank Dr Mirco Magnini for his patience and guidance when teaching how to navigate around OpenFOAM and explaining complex concepts. We appreciate the help received by the Matar Fluids Group for providing valuable feedback on the presentation and technical assistance when using the HPCs.

Lastly, we will like to express our gratitude to Professor Omar Matar for providing us with an opportunity to work on a highly interesting and technical project in the field of CFD.

6. Supplementary information

Supplementary information that contains key graphics and videos, Matlab codes, mesh constructions and a presentation can be found here.

7. References

A. de Lo´zar, A. L. H. A. J., 2007. *Scaling Properties of Coating Flows in Rectangular Channels,* s.l.: s.n.

Abadie, M. T., 2013. *Hydrodynamics of gas-liquid taylor flow in microchannels,* Toulouse: Universite de Toulouse.

Abiev, R. S., 2010. Method for Calculating the Void Fraction and Relative Length of Bubbles under Slug Flow Conditions in Capillaries. *Theoretical Foundations of Chemical Engineering,* 44(1), pp. 86-101.

Alberto de L´ozar, A. J. A. L. H., 2008. *The steady propagation of an air finger into a rectangular tube,* s.l.: Cambridge University Press.

Bretherton, F. P., 1961. The motion of long bubbles in tubes. *Journal of Fluid Mechanics,* 10(2).

Chang, J. R. a. H. C., 1989. *Transport of gas bubbles in capillaries,,* s.l.: Phys. Fluids A 1, 1642.

Fan, K. C. Z. H., 2016. Chapter 2: Introduction to Microfluidics. In: Z. H. Fan, ed. *Circulating Tumor Cells: Isolation and Analysis.* s.l.:s.n.

Heil, A. L. H. M., 2002. *The steady propagation of a semi-infinite bubble into a tube of elliptical or rectangular cross section,* s.l.: Cambridge University Press.

Jingzhi Zhang, D. F. F. W. L., 2016. Heat transfer and pressure drop characteristics of gas–liquid Taylor flow in mini ducts of square and rectangular cross-sections. *International Journal of Heat and Mass Transfer 103 (2016),* pp. 45-56.

Naoki Shikazono, Y. H., 2009. *Liquid Film Thickness in Micro Channel Slug Flow,* s.l.: Proceedings of the Seventh International ASME Conference on Nanochannels, Microchannels and Minichannel.

Navid Borhani, B. A. J. R. T., 2010. A novel time strip flow visualisation technique for investigation of intermittent. *International Journal of Heat and Mass Transfer.*

S. Khodaparest, M. M. N. B. J. T., 2015. Dynamics of isolated confined air bubbles in liquid flows through circular microchannels: an experimental and numerical study. *Microfluid Nanofluid (2015) 19,* pp. 209-234.

Taha roshdy Taha, Z. F. C., 2006. CFD modelling of slug flow inside square capillaries. *Chemical Engineering Science.*

Traian Popescu, M. M. H. P. G. P. M. F., 2012. *Microchannel Heat Exchangers - Present and Perspective,* s.l.: s.n.

Viboonyotin, P., 2018. *Numerical analysis of micro-fluidic two-phase flows in non-circular channels,* London: Imperial College London.

Wong, H. R. C. J. &. M. S., 1995a. *The motion of long bubbles in polygonal capillaries.,* s.l.: s.n.

Quantification of Fragrance Molecules and their Interactions on Cotton Fabrics

Darunrat Pooranawattankul and Saranchana Ramyananda
Department of Chemical Engineering, Imperial College London, U.K.

ABSTRACT: The work focused on using Inverse Gas Chromatography (IGC) and Dynamic Vapour Sorption (DVS) to quantify fragrance molecules on cotton fabrics. IGC is a fast and versatile technique that can detect low volatility Perfume Raw Material (PRM) in an aqueous surfactant solution when preloaded onto cotton samples. The IGC shows that some PRM release profiles are dependent on Relative Humidity (RH). DVS allows real-time mass loss to be measured which can be used to obtain release times of different PRMs on cotton. Straight line evaporation was shown for all PRM. The physical properties (molecular weight, boiling point, vapour pressure and Log (P)) of the PRM were compared to the release time of the fragrance from the cotton. Generally, PRMs with low molecular weight, boiling point and log(P) have slower release time while high vapour pressure PRMs have a faster release time. However, this was not the case for all PRM investigated in this study. This work provides evidence supporting the potential of IGC and DVS studying non-equilibrium impact on release for industrial application such as fabric care.

1. INTRODUCTION

The study of fragrance molecules interaction on cotton fabrics allows the analytical tools capabilities to be studied in its ability to quantifying the amount of fragrance retained for fragrances with various physiochemical properties and functional groups. Cotton fibres are nature's most abundant polymer and are widely used in textile industry. Therefore, cotton is a big focus for testing fabric care product. In the laundry process, consumers desire freshness experience through odour as well as a long retention time for fragrance molecules. Therefore, quantifying fragrance molecules on cotton using analytical methods could provide an important insight into a development of fabric care formulation.

In this study, two different analytical methods have been used to study the quantification of fragrance molecules on cotton fabrics; Inverse Gas Chromatography (IGC) and Dynamic Vapour Sorption (DVS).

IGC is an extension of gas chromatography where non-volatile phase is investigated in a column as a stationary phase. IGC is a versatile and sensitive technique for characterising the physicochemical properties of materials. It became an increasingly popular technique for studying the surface and bulk characteristics of polymers in the 1970s. [1]

DVS is a technique that has been used more recently to investigate sorption properties of different cellulosic materials. [2] DVS is highly reproducible and provide real-time mass uptake and mass loss profile at a pre-set temperature as well as allowing humidity effects to be studied.

IGC was used to measure the FID signal of a solution mimicking fabric care formulation (perfume raw material in aqueous surfactant solution) and DVS was used to measure the kinetics of fragrance release from cotton. The results obtained were then compared to fragrance's physical properties such as its boiling point and vapour pressure.

2. BACKGROUND

The adsorption of fragrance from aqueous surfactant solution on cotton is an important study for the fabric care industry. Understanding the deposition of fragrances and its retention has remained a challenge due to many variables involved such as cotton structure and type of surfactant used. A study by Liu H. et al. [3] involved changing the type and concentration of surfactant, water solubility and fibre morphology. By analysing the results from GC-MS, they found that fragrance adsorption increased with increasing surfactant concentration and then decreased after the surfactant concentration reached the critical micelle concentration. It is believed that a monolayer of surfactant is adsorbed onto the fibre structure and fragrance may then adsorbed onto the surfactant layer through the hydrophobic interaction. Another important conclusion from the study is that adsorption of fragrance increases with water solubility.

Different functional groups on fragrance molecules also influenced how they adsorb onto cotton. Esters generally had low adsorption on cotton fabric compared to alcohols, aldehydes and ketones. However, study suggested that molecular shape within a

chemical class of compounds also influences adsorption.[4]

IGC is a suitable method to characterise surface properties, such as free energy of adsorption, of cellulosic substrates including cotton. However, polar probes are not retained on fibrous cotton at any temperature.[5] Different IGC results are obtained in different scientific literature due to the complexity of cellulosic materials and other factors.[6]

Reutenauer and Thielman[7] used fragrances as a probe molecule to study the surface energy of cotton. Their findings suggested that at higher relative humidity, some of the active sites on cotton fabrics are covered by water molecules and less active sites will be involved in the interactions with probe molecules. This is shown by decrease in heat of sorption as relative humidity increases. Cantergiani and Benczedi[8] also studied the impact of relative humidity on fragrance molecules adsorption and found that the dispersive component of surface energy decreases slightly as a function of relative humidity. Furthermore, they found that hydroxyl groups could orient in a way that induced stronger interactions with the hydrophilic cotton surface through hydrogen bonding.

A limited amount of research was done for the systems that better resembled uses within commercial products and no research has explored the use of IGC as a tool to measure fragrance release profiles from cotton which has been preloaded with fragrance molecules. As IGC is limited to volatile probes with generally, more than 250 g/mol in molecular weight and more than 0.02 kPa in vapour pressure, preloading compounds could allow release profile of a more volatile probes to be studied and analysed.

3. EXPERIMENTAL PROCEDURES

3.1 Inverse Gas Chromatography

Glass column (SMS standard column with 4 mm ID and 300 mm length) was packed with cotton samples as shown in Table 1. The CW120 cotton fabrics, provided by Procter and Gamble (P&G) were cut into strips of 85 mg before being rolled and pushed through the column with a thin wooden rod.

From Table 1, other than experiments 1-3, 85 µL of solution, vigorously shaken, is pipetted to the cotton fabric and air-dried for 16 hours. The base-line solution is prepared by adding 22 µL of Tide Free & Gentle, provided by P&G, in 50 mL of deionised water. For experiments 10-21, 1.5% of the PRM are added, by volume, to the base-line solution, which from now on would be referred to as PRM solution. The PRM used in IGC are listed in the first 4 rows in Table 2 and were used as received.

All the experiments were done on Inverse Gas Chromatography-Surface Energy Analyser (iGC-SEA), at a fixed temperature of 30ºC and carrier gas (Helium) flow rate of 10 sccm. All the columns were placed in the first position in the iGC-SEA, as only 1 column was run at a time and FID signals were recorded right away. Each experiment was a total of 4 h, with 1 h conditioning at 0% RH followed by 3 h of running at either 30%, 60% or 90% RH, as shown in Table 1.

3.2 Dynamic Vapour Sorption

After setting the DVS Endeavour at 0% RH and a fixed temperature of 60°C, the balances of the sample pans were tared and 2 cotton squares of 7.5 mg each were placed into each sample pan. The samples were left to stabilised for at least 7 h, before 6 µL of PRM are pipetted directly on to the sample pan. The experiment was stopped once all the 5 sample pans have reached a stable final mass or if the experiments exceeds 4 days. A plot of mass was obtained as a function of time. The PRM used for DVS are as listed in Table 2 and were used as received.

TABLE 1
iGC-SEA Sample and Experimental Description

Experiment		Relative Humidity (RH)	Cotton Sample Descriptions
Run	1	0%, 30%	Cotton (as received)

	2	0%, 60%	
	3	0%. 90%	
	4	0%, 30%	
Run	5	0%, 60%	Cotton + Deionised Water
	6	0%. 90%	
	7	0%, 30%	
Run	8	0%, 60%	Cotton + Base-Line Solution
	9	0%. 90%	
	10	0%, 30%	
Run	11	0%, 60%	Cotton + Base-Line Solution + Limonene
	12	0%. 90%	
	13	0%, 30%	
Run	14	0%, 60%	Cotton + Base-Line Solution + Iso E Super
	15	0%. 90%	
	16	0%, 30%	
Run	17	0%, 60%	Cotton + Base-Line Solution + Isopropyl Myristate
	18	0%. 90%	
	19	0%, 30%	
Run	20	0%, 60%	Cotton + Base-Line Solution + Phenylethyl Alcohol
	21	0%. 90%	

TABLE 2
Parameters and providers of PRM

Perfume Raw Material	Structure	MW (g/mol)	Boiling Point (°C)	Vapour Pressure (mmHg)	Log P	Provider
Limonene	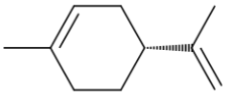	136.23[9]	175.5[10]	1.98[10]	4.57[11]	Alfa Aesar
Iso E Super	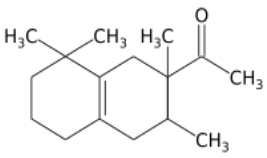	234.38[12]	312.2[13]	0.001[13]	5.65[13]	Toronto Research Chemicals Inc
Isopropyl Myristate	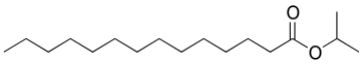	270.45[14]	319.9[15]	9.35×10^{-5}[16]	7.25[17]	Sigma-Aldrich Corporation

Phenylethyl Alcohol	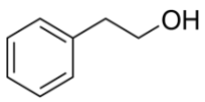	122.16[18]	218.2[18]	0.07[18]	1.36[18]	Vigon International, Inc
Dipropylene Glycol	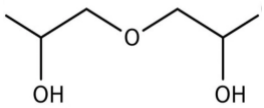	134.18[19]	231.9[19]	0.0319[20]	-0.59[20]	Carolina International Sales Co., Inc
Florocyclene	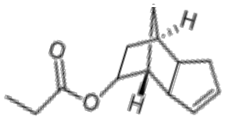	204.27[21]	276.2[22]	0.005[22]	3.63[22]	Vigon International, Inc
Cyclogalbanate	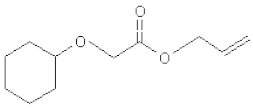	198.26[23]	282.0[23]	0.003[23]	2.64[24]	Vigon International, Inc
Amber Xtreme	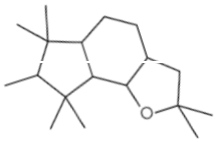	264.45[25]	292.3[26]	1.23x10^{-3}[27]	5.88[27]	Internaional Flavors & Fragrances Inc
Habanolide	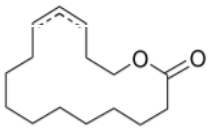	238.37[28]	383.5[28]	4x10^{-6}[29]	5.02[29]	Vigon International Inc

4. RESULTS AND DISCUSSIONS

4.1 Inverse Gas Chromatography

As the experiments were done at different %RH, three sets of data were obtained for each solution. The data were then combined into one single plot, as shown in Figure 1.

The FID signals were then averaged and the difference between the signals of PRMs solutions and the base-line solution (deionised water with Tide) were calculated and plotted as shown in Figure 2. As the number of ions detected by the FID is expected to be proportional to the FID signal, the area under the FID curves were integrated and calculated with reference to the base-line solution. Table 3 shows the % change in number of ions at different %RH for each PRM.

When Limonene and Isopropyl Myristate was added, negative values were observed for both the ΔFID signal and the % change. This

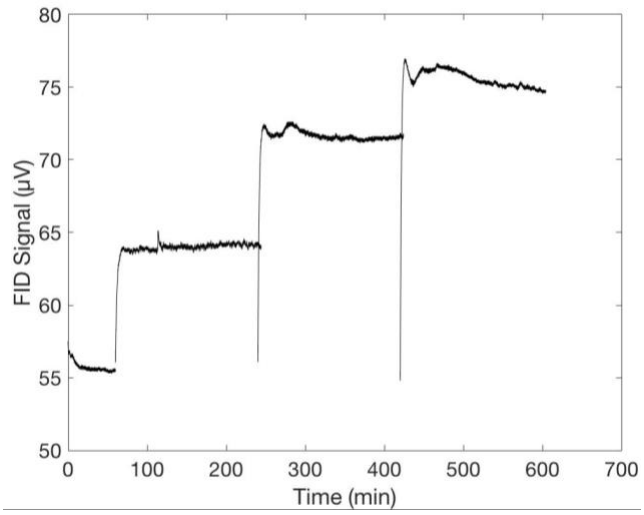

FIG 1. *Sample FID Signal plot for base-line solution where the initial 60 mins was at 0% RH, followed by 180 mins of 30% RH, then 180 mins of 60% RH and finally, 180 mins of 90% RH*

suggests that the PRMs are suppressing the FID signal. According to Obendorf S. et al.,[4] the hydrophobicity, or log P, of molecules played a major role in the adsorption of PRM

in a system where surfactant is present. This could explain the small and negative ΔFID signal observed, as Isopropyl Myristate has the highest hydrophobicity, with a log P value of 7.25. As for Limonene, due to its high vapour pressure, the PRM would likely to have evaporated prior to the packing process causing its FID signal difference to be negligible.

For Iso E Super and Phenylethyl Alcohol, although both PRMs have positive ΔFID signal and % change in number of ions, values obtained for Iso E Super seems relatively constant across all % RH in comparison to Phenylethyl Alcohol. Approximately 9 times as much ions were detected at 90% RH compared to 60% RH, which suggests that the release of Phenylethyl Alcohol is highly dependent on humidity. Due to its hydrophilic nature, at higher humidity, there's an increase in competition with water for the hydrophilic sites on the cotton. The presence of water can cause a large impact on the strength of interactions in a system,[8] as more water molecules are available to displace the PRM from their sites on the cotton at higher RH. As discussed in literature, a more polar and hydrophilic Amyl Acetate has a larger difference in heat of sorption at higher humidities compared to Limonene.[7]

Adsorption of PRM are dependent upon the interactions between PRM and surfactant molecules as well.[3] The higher the hydrophobicity of PRM, the more significant the micellar growth, as the PRM would be located in the hydrophobic region, expanding the micelle.[30] As for a more hydrophilic PRM, it would be located at the hydrophobic-hydrophilic interface, replacing some surfactant and acting as a cosurfactant. This could help explain the behaviours of Isopropyl Myristate and Phenylethyl Alcohol, as the Isopropyl Myristate would be bonded hydrophobically with the surfactant while Phenylethyl Alcohol would act as a cosurfactant, forming Hydrogen bond with surface of cotton.

Even though IGC is highly sensitive[7] and can detect PRM with volatilities less than 0.02 kPa, it cannot classify what molecules the FID has detected. So the peaks obtained could be due to other impurities that have entered the system either during drying or packing process. This leaves potential for a method development where a mass spectrometer could

be used to determine the release of PRM. Additionally, as only 85 µL of the prepared solution was pipetted onto the cotton fabric, the actual amount of PRM on the fabric prior to air drying is unknown. To improve this method, pipetting the entire prepared solution would ensure that all of the PRM has been added to the cotton fabric prior to drying.

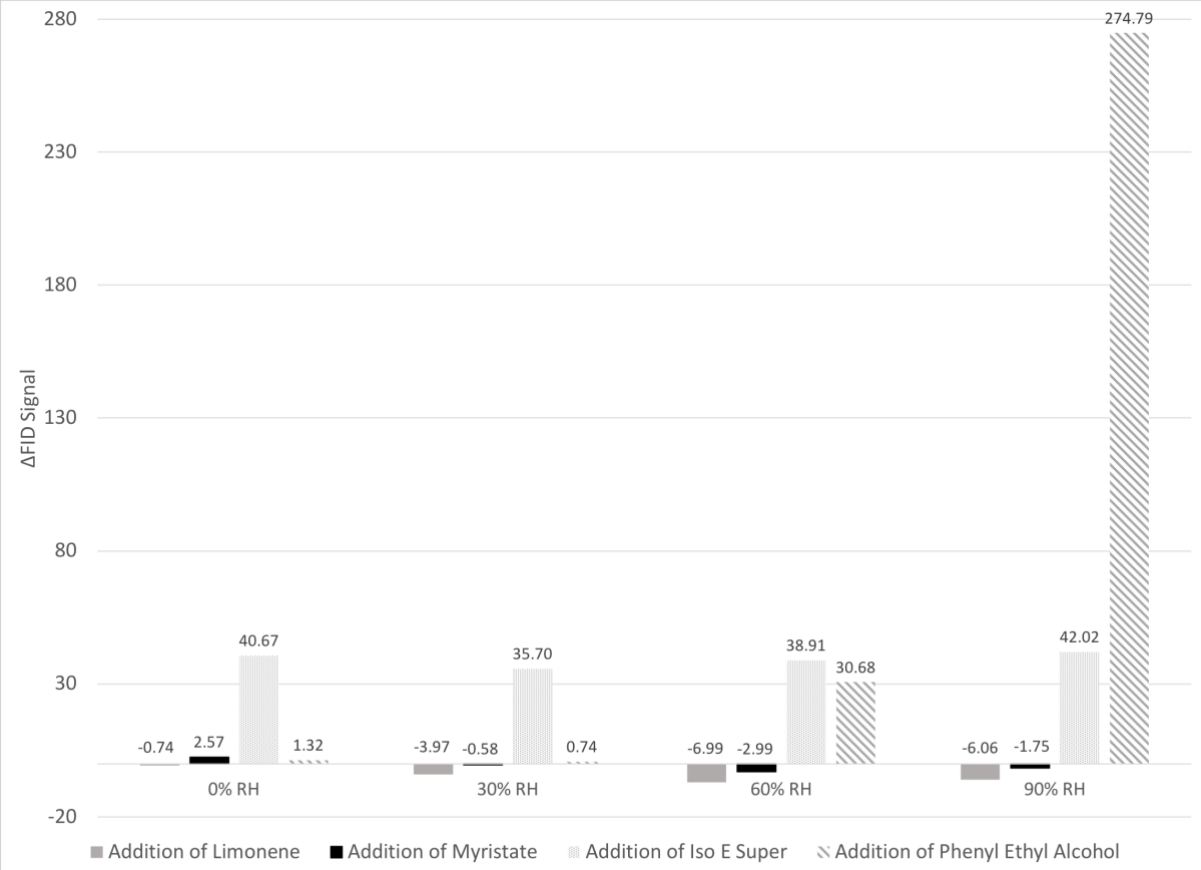

FIG 2. *Bar graphs indicate changes in FID signal when PRM solutions were used instead of base-line solution at four different Relative Humidity*

TABLE 3
Effects of Humidity on Number of Ions

Addition of PRM	% RH	% Change	Average % Change
Limonene	30	-4.7	-3.7
	60	-2.9	
	90	-3.5	
Isopropyl Myristate	30	-0.2	-1.8
	60	-3.2	
	90	-1.8	
Iso E Super	30	58.8	57.7
	60	56.1	
	90	58.3	
Phenylethyl Alcohol	30	0.8	94.9
	60	32.2	
	90	251.6	

4.2 Dynamic Vapour Sorption

Time taken for the PRMs to be fully released from the cotton were taken from the release profiles as represented by Figure 3, which shows both a fully released profile of Iso E Super and an incomplete release profile of Isopropyl Myristate.

The following equation was used to calculate the PRM release time:

$$t = T_2 - T_1 \qquad (1)$$

Where t is the PRM release time, T_1 is the time when PRM is added and T_2 is the time when final mass is initially reached, as shown in Figure 3.

The release times were then compared, as shown in Figure 4. However, the release times of Isopropyl Myristate and Cyclogalbanate were extrapolated, using a linear relationship fitted from the last 10 hours of the experiment, giving a R^2 value of 0.968 and and 0.997, respectively.

The effect of absence of cotton on the mass loss rate was briefly touched upon. Table 4 compares the release time required for each PRM with and without cotton. Generally, the presence of cotton only shortens the PRM release time. Additionally, all the release profiles are linear and downward sloping, which suggests that the mass loss of PRM are only due to evaporation of fragrance from the surface of the cotton. If diffusion is present, the rate of mass loss would decrease over time. This suggests that PRMs are only adsorbed on the cotton surface and that the presence of cotton only increases the surface area for evaporation.

Pybus and Sell[31] stated that molecular weight and boiling point could provide guidelines to their release profile behaviour. As molecular weight, boiling point and log P of PRM increases, the release time increases accordingly while increase in vapour pressure would have the opposite effect. Physical properties of PRMs listed in Table 2 were plotted against release time, which shows the same trend as mentioned by Pybus and Sell[31], as shown in Figure 5. A weak linear positive correlation is observed for molecular weight, with a R^2 value of 0.4207 in Figure 5a, which is relatively low compared to a positive exponential correlation for boiling point, in Figure 5b with a R^2 value of 0.7425.

Vapour pressure is a more direct way of assessing evaporation of PRM as it is directly related to the mass present in the gas phase. Therefore, it was expected that the relationship between vapour pressure and release time is relatively strong, with a R^2 value of 0.7499 as shown in Figure 5c.

The correlation between log P and release time is the weakest, as shown in Figure 5d, which might be due to the different hydrophobicity nature of cotton surface and PRMs. In general, the delivery of PRM, such as ones in laundry detergent requires the transfer of PRM from the aqueous surfactant solution to the surface. [4] In the presence of surfactant, the effect of log P on adsorption was proven to be significant,[4] as the partitioning of PRM onto surfactant phases become dominant.[31] However, this experiment was done in absence of surfactant, which would result in less PRM adsorption[3] and therefore less influence of log P on release time.

Another factor influencing the release time is the molecular interactions occuring between the cotton and the PRM.[3] Looking at the structures of PRMs shown in the Table 2, Limonene, for example, is the only aliphatic compound so only Dispersion forces would be present. As for Isopropyl Myristate and Cyclogalbanate, both can form Hydrogen bonds with the hydrophilic sites of cotton. Although Cyclogalbanate can form up to 3 Hydrogen bonds which is more than Isopropyl Myristate, less release time is required. This suggests that there's a complex relationship between physical properties and the molecular interactions of PRM. A larger set of PRM should be investigated, however, independent variable should be investigated individually. For example, having several PRM with similar molecular weight, but different functional groups, to investigate the effect of functional groups on release time.

TABLE 4
Effect of Cotton on the PRM Release Time

PRM	Release Time (with cotton)	Release Time (without cotton)
Limonene	0.2	0.2
Dipropylene Glycol	9	19
Florocyclene	10	17

Phenylethyl Alcohol	3	6
Amber Xtreme	29	38

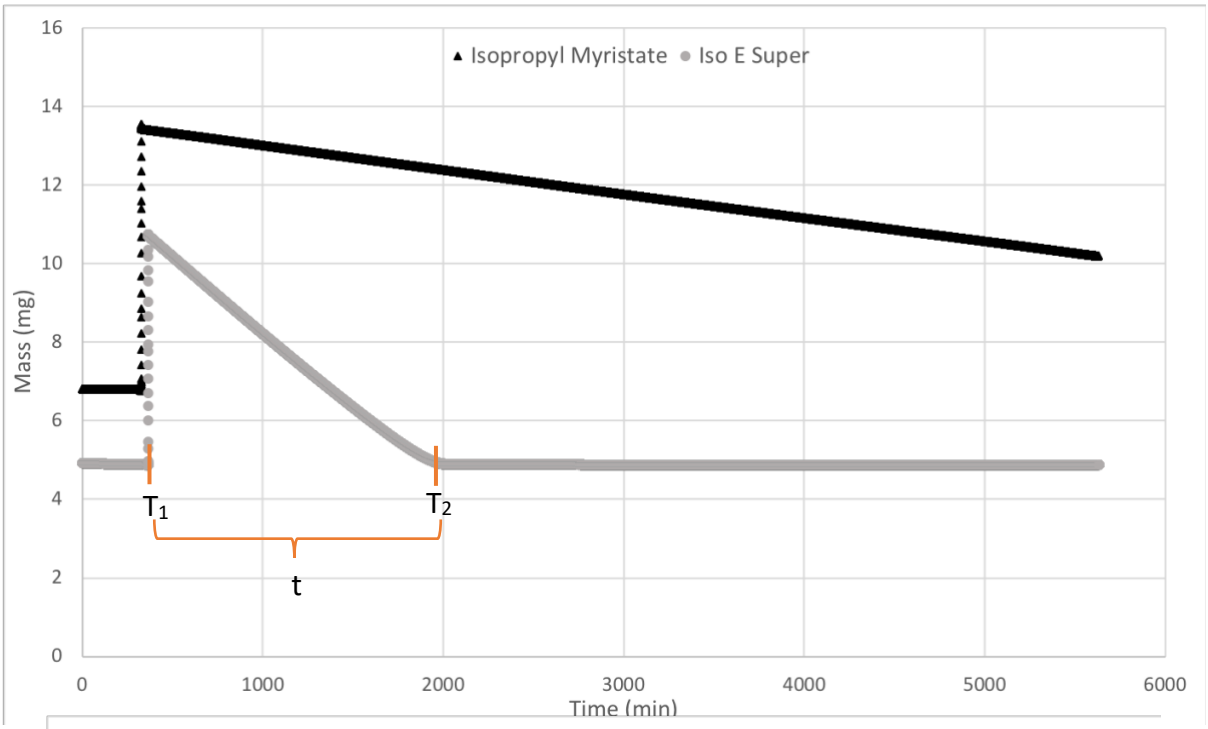

FIG 3

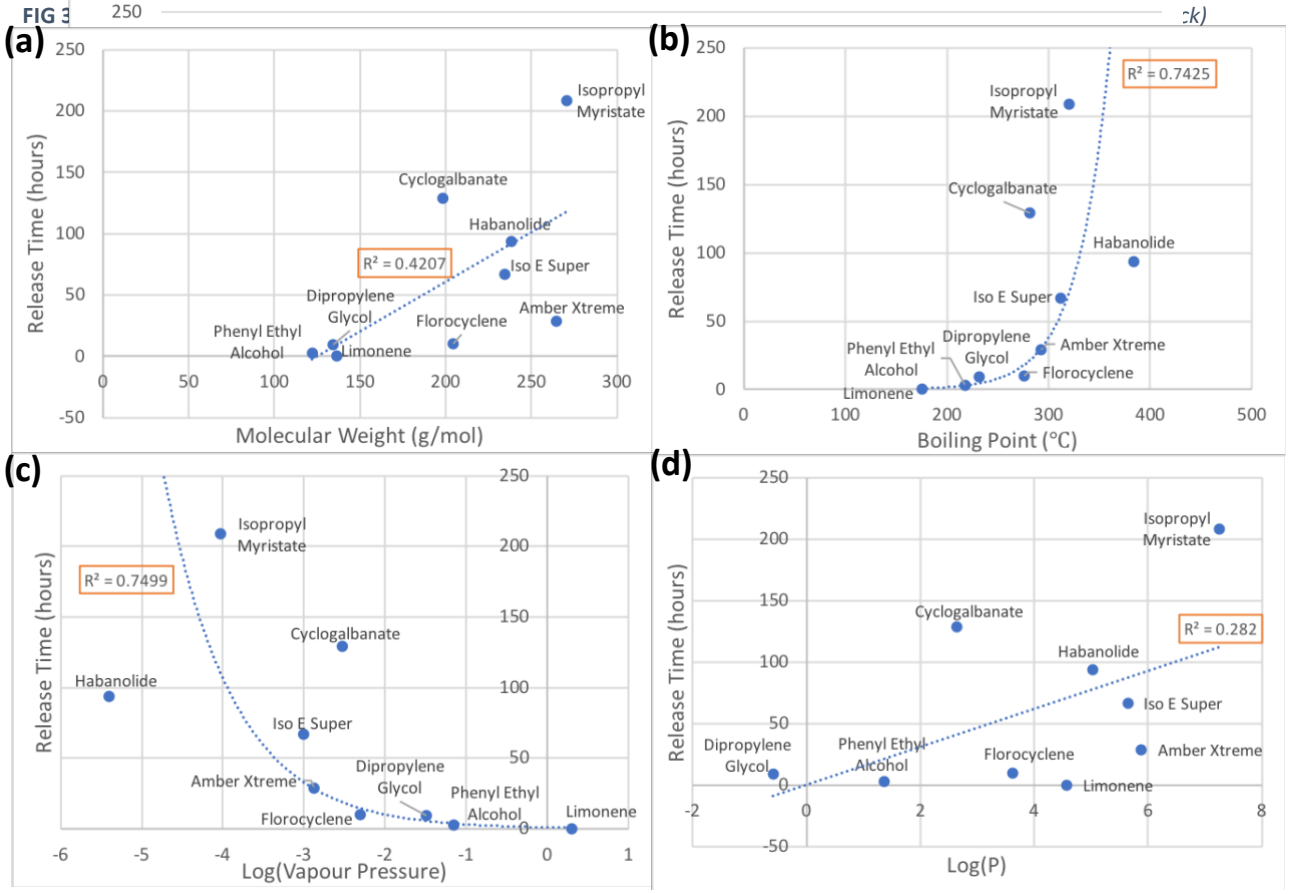

FIG 5. *Shows the relationship between the PRM release time and its physical properties (a) Molecular Weight, (b) Boiling Point, (c) Vapour Pressure and (d) Hydrophobicity*

6. CONCLUSIONS

This study used IGC to investigate FID signal difference when PRM was added to the system of aqueous surfactant solution. The release profiles of these PRMs can be detected using this method but some shows significantly less FID signal difference than others. FID signal difference for Limonene and Isopropyl Myristate are negative due to PRMs suppressing signal from FID. Hydrophobicity increases adsorption in the system with surfactant as shown from Isopropyl Myristate result. Phenylethyl alcohol release profile is highly dependent on humidity due to its hydrophilic nature and its increase in competition with water for hydrophilic sites at higher humidity. Iso E super is hydrophobic, and its release did not depend on relative humidity. Results shows that IGC is a sensitive technique that can be used to quantify low concentration of PRMs releases and has potential to be studied for non-equilibrium impact on release, such as changing humidity, for real world application.

Modifications, such as incorporating a mass spectrometer with the iGC-SEA and using a known amount of PRM on cotton could improve results. From this knowledge, future experiments can be done to observe fragrance deposition based on real washing cycle, in order to improve detergents formulation. If there are no changes in FID signal compared to baseline, it is evident that fragrance molecules used got washed away with water during the laundry process.

DVS is a good gravimetric tool in measuring PRM mass loss profile in real time. Mass loss profiles obtained from this set of experiments is linear due to evaporation. PRM release time depends on its physical properties. Generally, increase in molecular weight, boiling point and log P of PRMs increases release time and increase in vapour pressure has the opposite effect. The release profiles behaviour of PRMs are broadly comprehensible in terms of its physical properties. However, the complexity of the interactions when other components involved leave rooms for further studies.

Future experiments could explore moisture diffusion and permeability of vapours on fragrance adsorption and desorption which could determine final product performance. The outcomes of the experiment have direct implications in fabric care industry and could be expanded into other industries that require perfume and odour delivery, such as in the cosmetic industry.

7. ACKNOWLEDGEMENTS

The authors would like to acknowledge Jona Ramadani and Susannah Molisso from Imperial College London for sharing their expertise in the area and Dr. Steve Page from P&G for supplying fragrances and cotton fabrics used in this study.

8. REFERENCES

[1] Conder, J.R. and Young, C.L., 1979. *Physicochemical measurement by gas chromatography*. John Wiley & Sons.

[2] Hill, C.A., Norton, A. and Newman, G., 2009. The water vapor sorption behavior of natural fibers. *Journal of Applied Polymer Science*, *112*(3), pp.1524-1537.

[3] Liu, H., Obendorf, S.K., Leonard, M.J., Young, T.J. and Incorvia, M.J., 2005. Adsorption of aroma chemicals on cotton fabric from aqueous systems. *Journal of surfactants and detergents*, *8*(4), pp.311-317.

[4] Obendorf, S.K., Liu, H., Tan, K., Leonard, M.J., Young, T.J. and Incorvia, M.J., 2009. Adsorption of aroma chemicals on cotton fabric in different aqueous environments. *Journal of surfactants and detergents*, *12*(1), pp.43-58.

[5] Fekete, E. and Csiszár, E., 2017. Characterization of the surface properties of cellulosic fibers in fibrous and ground forms by IGC and contact angle measurements. *Fibers and Polymers*, *18*(7), pp.1255-1262.

[6] Papirer, E., Brendle, E., Balard, H. and Vergelati, C., 2000. Inverse gas chromatography investigation of the surface properties of cellulose. *Journal of adhesion science and technology*, *14*(3), pp.321-337.

[7] Reutenauer, S. and Thielmann, F., 2003. The characterisation of cotton fabrics and the interaction with perfume molecules by inverse gas chromatography (IGC). *Journal of materials science*, *38*(10), pp.2205-2208.

[8] Cantergiani, E. and Benczédi, D., 2002. Use of inverse gas chromatography to characterize cotton fabrics and their interactions with fragrance molecules at controlled relative humidity. *Journal of Chromatography A*, *969*(1-2), pp.103-110.

[9] Alfa Aesar, n.d. *Alfa Aesar by Thermo Fisher Scientific.* [Online] Available at: https://www.alfa.com/en/catalog/L04733/

[10] Johnson, M. A., 2013. *Physical Properties of chemicals in PAC Revision 27 Listing,* pp.28

[11] Anon., n.d. *The Good Scents Company Information System.* [Online] Available at: http://www.thegoodscentscompany.com/data/rw1013772.html

[12] Toronto Research Chemicals Inc., 2015. *Toronto Research Chemicals.* [Online] Available at: https://www.trc-canada.com/prod-img/MSDS/I815500MSDS.pdf

[13] Anon., n.d. *The Good Scents Company Information System.* [Online]
Available at:
http://www.thegoodscentscompany.com/data/rw1020612.html

[14] Sigma-Aldrich, n.d. *Sigma-Aldrich.* [Online]
Available at:
https://www.sigmaaldrich.com/MSDS/MSDS/DisplayMSDSPage.do?country=GB&language=en&productNumber=172472&brand=ALDRICH&PageToGoToURL=https%3A%2F%2Fwww.sigmaaldrich.com%2Fcatalog%2Fproduct%2Faldrich%2F172472%3Flang%3Den

[15] Anon., n.d. *ChemSpider.* [Online]
Available at: http://www.chemspider.com/Chemical-Structure.7751.html?rid=deb4bee6-027a-4e22-9cef-a41007d4a7e2

[16] Johnson, M. A., 2013. *Physical Properties of chemicals in PAC Revision 27 Listing,* pp.33

[17] Anon., n.d. *The Good Scents Company Information System.* [Online]
Available at:
http://www.thegoodscentscompany.com/data/rw1019332.html

[18] Vigon International Inc, 2018. *Vigon.* [Online]
Available at: https://www.vigon.com/product/phenyl-ethyl-alcohol-natural/

[19] Carolina International Sales Co., Inc, 2015. *CISCO.* [Online]
Available at:
https://www.ciscochem.com/assets/dipropylene-glycol-sds.pdf

[20] non., n.d. *The Good Scents Company Information System.* [Online]
Available at:
http://www.thegoodscentscompany.com/data/rw1018712.html

[21] Vigon International Inc, 2018. *Vigon.* [Online]
Available at:
https://www.vigon.com/product/florocyclene-tricyclododecenyl-propionate-cyclaprop/

[22] Anon., n.d. *The Good Scents Company Information System.* [Online]
Available at:
http://www.thegoodscentscompany.com/data/rw1011151.html

[23] Vigon International Inc, 2018. *Vigon.* [Online]
Available at:
https://www.vigon.com/product/cyclogalbanate-allyl-cyclohexyl-glycolate/

[24] Anon., n.d. *The Good Scents Company Information System.* [Online]
Available at:
http://www.thegoodscentscompany.com/data/rw1038701.html

[25] International Flavors & Fragrances Inc, n.d. *IFF.* [Online]
Available at: https://www.iff.com/en/smell/fragrance-ingredients/online-compendium#amber-xtreme

[26] Anon., n.d. *Chemspider.* [Online]
Available at: http://www.chemspider.com/Chemical-Structure.57523118.html?rid=4901492f-2f0a-4602-8d83-88b01c9c11f0

[27] Anon., n.d. *Environmental Protection Agency.* [Online]
Available at:
https://comptox.epa.gov/dashboard/dsstoxdb/results?utf8=✓&search=476332-65-7#properties

[28] Vigon International Inc, 2018. *Vigon.* [Online]
Available at: https://www.vigon.com/product/habanolide/

[29] Anon., n.d. *The Good Scents Company Information System.* [Online]
Available at:
http://www.thegoodscentscompany.com/data/rw1103401.html

[30] Penfold, J., Tucker, I., Green, A., Grainger, D., Jones, C., Ford, G., Roberts, C., Hubbard, J., Petkov, J., Thomas, R.K. and Grillo, I., 2008. Impact of model perfumes on surfactant and mixed surfactant self-assembly. *Langmuir*, *24*(21), pp.12209-12220.

[31] Pybus, D. and Sell, C. eds., 2007. *The chemistry of fragrances*. Royal Society of Chemistry.

Thermo-economic Comparison of Subcritical and Transcritical Organic Rankine Cycles using a Medium-Temperature Geothermal Heat Source

Ping Loo, Jaime Teo
Department of Chemical Engineering, Imperial College London, U.K.

Abstract

Due to its suitability and reliability to extract low and medium grade heat, Organic Rankine cycle (ORC) technology on geothermal applications is becoming increasingly promising. This study seeks to investigate the relative thermo-economic performance of subcritical and transcritical ORCs using a medium-temperature geothermal heat source (180.7℃) covering 7 working fluids and the possible addition of a recuperator. Multi-objective parametric optimisation was simulated on MATLAB to optimise the selected parameters based on the thermo-economic optimisation framework (payback period and exergy efficiency) or pure economic optimisation framework (payback period and annual profits). For each working fluid, it has been found that TCORC provides better thermo-economic performance under most operating conditions due to its superior thermal match. Through optimising the selection of working fluid, the relative performance of SCORC and TCORC, with and without recuperation, is highly dependent on the prioritisation of different objective functions. At low generation capacities, the cycle architecture has a very minimal effect on the performance and the selection of working fluid becomes a more important factor relatively. As power generation capacity increases, non-recuperative SCORC reveals the best thermo-economic performance whilst recuperative TCORC can achieve the highest possible annual profits, albeit higher payback periods.

1. Introduction

Increasing environmental concerns and accelerated consumption of fossil fuels in recent years have led to the increasing importance of renewable energies, such as solar, wind, biomass and geothermal energy. One of the main advantages of geothermal energy in comparison to other renewables is its reliability for base-load energy production with an installed capacity of 14,060MW worldwide [1]. Currently, most commercial geothermal electricity production is using high-temperature (>220°C) geothermal energy generated via dry steam and flash steam systems. However, the largest availability of geothermal resources is between 100°C to 220°C, known as medium-temperature geothermal resources. They are typically used for energy generation through binary plants such as Organic Rankine Cycles (ORC) and Kalina cycles [2].

ORCs take advantage of the considerable amount of low and medium grade heat energy available in the heat source which would otherwise be vented or wasted. It is becoming increasingly promising to extract useful energy in a range of applications, including natural sources and industrial waste heat recovery. The traditional ORC configuration includes a pump, evaporator, expander and condenser. Large amounts of research have been conducted on a variety of applications to further understand ORC and optimise the system based on different working fluids and cycle design to achieve the objective function. Sun [3] optimised the system using a genetic algorithm and found that organic working fluids are more efficient than traditional steam Rankine cycles in converting waste heat to useful work.

Power output can be increased using a recuperator in the cycle architecture which reduces the amount of heat required in the evaporator through recovering it from after the expansion process. Cáceres [4] studied the impact of 39 different working fluids on a low-temperature geothermal heat source and found that the use of a recuperator increases second law efficiency in all cases except for the wet working fluids. Moreover, it showed that the efficiency was highest when working fluids with a critical temperature close to the maximum cycle temperature. However, Oyewunmi (2017) [5] found that systems without the recuperator could result in 3 times more generated power under relaxed operating constraints.

In addition, transcritical operations can enhance plant performance as it allows for both supercritical heat addition and subcritical heat rejection by pumping the working fluid to above its critical pressure. For supercritical cycles, it is important to consider fluids with critical temperatures slightly below the heat source temperature. [6] Studies have shown transcritical ORCs (TCORC) with an internal heat exchanger results in improved thermodynamic performance but worsened economics using an exhaust flue-gas stream [7]. This is strengthened through Lecompte's [8] findings that TCORC resulted in 31.5% increase in net power output but 72.8% increase in specific investment costs for waste heat recovery applications.

Despite numerous studies on ORC, there is a lack of understanding on subcritical and transcritical operations on geothermal applications from a thermo-economic perspective. For geothermal applications, numerous studies have been done on low-temperature resources through first and second law thermodynamic analysis. For example, Sun [3] studied double-pressure SCORC systems whilst Kai [9] found that pinch

Nomenclature

η_{ex}	Exergy efficiency	μ	Viscosity, m²/s
F	F-factor	ρ	Density, kg/m³
h	Film heat transfer coefficient, W/m²K	*Subscripts*	
g	Gravitational acceleration, m/s2	0	reference state
Q	Heat duty, J/s	b	supercritical state
η_{is}^{p}	Isentropic efficiency of pump	boiling	boiling
η_{is}^{t}	Isentropic efficiency of turbine	C	cooling water
j	j-factor	cr	critical
ΔT_{lm}	Log mean temperature difference, K	evap	evaporation
$\dot{m}$	Mass flowrate, kg/s	FC	forced convection
G''	Mass flowrate per unit film, kg/(m.s)	H	heat source
G_m	Mass flux, kg/m².s	in	at the inlet
gpm	Volumetric flowrate, gallons/min	L	liquid phase
U	Overall heat transfer coefficient, W/m²K	NB	nucleate boiling
HP	Power produced in turbine, horsepower	out	at the outlet
Pr	Prandtl number	pp	pinch point
P	Pressure, bar	sh	superheat
Re	Reynolds number	shellside	shell side of heat exchanger
C_p	Specific heat capacity, J/kg.K	single	single-phase
w_n	Specific net power output, J/kg	TP	two-phase
T	Temperature, K	w	wall
k	Thermal conductivity, W/m.K	sat	Saturation

temperature has a bigger effect on net power output per unit mass than superheating through parametric optimisation. Due to its low temperature application, it prevents the study of TCORC on these applications.

The aim of this study is to explore the optimisation of subcritical and transcritical systems based on both its thermodynamic and economic performance, represented by minimising payback period and either maximising annual profit or exergy efficiency. It will consider two cycles architectures (with and without recuperator) using a variety of different pure working fluids applied on a medium-temperature geothermal heat source at 180.7°C.

2. Methodology

2.1 Cycle description

The four ORC systems studied in this paper were SCORC and TCORC systems, with and without recuperation. The difference between SCORC and TCORC is that in TCORC, the working fluid is evaporated at a temperature and pressure above its critical point, i.e in supercritical state. A basic ORC system consists of a pump, turbine, evaporator and condenser while a recuperative ORC system includes an additional component, a recuperator. The component diagram of a basic and recuperative ORC system is shown in Fig. 1 and 2 respectively whilst the T-s diagram of a recuperative SCORC and TCORC is shown in Fig. 3 and 4 respectively (in a non-recuperative cycle, state point 2a and 6a are excluded). The recuperator is designed to exchange heat between the high temperature vapour at the turbine outlet and the low temperature fluid at the pump outlet. This will reduce the cooling duty of the condenser and thus, reducing the amount of cooling water needed.

Transcritical systems were achieved by pressurizing the working fluid to a pressure above its critical pressure and superheating it by a certain degree above its critical temperature.

2.2 Heat Source Conditions and Working Fluid Selection

The heat source being considered in this study is a medium-temperature geothermal source at Wayang Windu Geothermal Field, that discharges geothermal brine at 180.7°C and 1.02MPa with a mass flowrate of 40kg/s [10,11]. Working fluids for ORCs can be classified into three types; dry, wet and isentropic. Dry and isentropic fluids are preferred over wet working fluids as they do not undergo condensation during expansion in the turbine [12].

This paper focuses on two main classes of dry working fluids (fluids with positively-sloped saturated vapour curve), which are alkanes and refrigerants as these are most commonly used in ORC power generation. The chosen fluids are shown in Table 1 and only three fluids (R134a, R1234yf, isobutane) can be used for TCORC. This is because, to be able to operate in transcritical cycles, working fluids must have critical temperatures below the heat source temperature.

Table 1. Selected working fluids and their critical temperature

Working Fluid	T_{cr} (°C)
Heptane	267.0
Hexane	234.6
Isopentane	188.0
R245fa	174.4
Isobutane	134.7
R134a	101.1
R1234yf	94.9

2.3 Thermodynamic Modelling

The modelling of both SCORC and TCORC were based on the first and second laws of thermodynamics. Thermodynamic properties of the fluids were calculated using REFPROP and energy balances were carried out across all components. Thermodynamic performance of the system was measured by the overall exergy efficiency of the system, which is the ratio of net power output to total exergy input into the system, as defined by Eq. (1). Exergy input is defined relative to a reference state which is taken as temperature of the environment at standard state. Pinch point analysis was included in the energy balances across all heat exchangers. It considers pinch point temperature difference, which is the minimum temperature difference between the two streams in a heat exchanger, representing the minimum driving force required for heat transfer. A smaller pinch point temperature difference allows better heat transfer, but it also leads to higher heat exchanger costs.

$$\eta_{ex} = \frac{\dot{m_{wf}} \times w_n}{\dot{m}_h c_{p,h}\left(\left(T_{h,in} - T_0\right) - T_0 \ln\left(\frac{T_{h,in}}{T_0}\right)\right)} \quad (1)$$

Table 2. Constant design parameters for ORC system modelling

Parameters	Values
Isentropic efficiency of pump, η_{is}^{p}	0.8
Isentropic efficiency of turbine, η_{is}^{t}	0.8
Heat source inlet temperature, $T_{h,in}$ (K)	453.7
Heat source inlet pressure, $P_{h,in}$ (bar)	10.2
Heat source discharge rate m_h (kg)	40
Heat source and sink media	Water
Heat sink inlet temperature, $T_{c,in}$ (K)	293
Reference temperature, T_0 (K)	298

Shell-and-tube heat exchangers were chosen as these are the most commonly used type of heat exchangers in large-scale power generation (installed power generating capacity of greater than hundreds of kilowatts) [13,14]. The following assumptions were made to the modelling of the ORC cycles:

- All processes are assumed to be under steady-state.
- There are no pressure drops and heat losses to the environment in the heat exchangers.
- Both pumps and turbines have an isentropic efficiency of 0.8.
- Working fluid enters the pump as a saturated liquid.
- Geothermal fluid is assumed to be pure water and saturated liquid. [15]
- Heat addition and rejection processes are isobaric.

2.4 Economic Modelling

Two economic indicators, payback period and annual profit, were defined to evaluate the performance of the ORC systems. Payback period and annual profit are calculated using Eq. (2) and (3) respectively. All cost and profit are quoted in $USD.

$$Annual\ Profit = Cash\ Inflow - Cash\ Outflow \quad (2)$$

$$Payback\ Period = \frac{Total\ Capital\ Investment}{Annual\ Net\ Profit} \quad (3)$$

Cash inflow is the revenue obtained by selling the power generated at a price of $0.0836/kWh [16] (industrial tariff) and projected to increase at a rate of 1.2% per year [17]. For cash outflow, variable costs considered included the operation and maintenance costs, and cooling water costs, priced at $0.02/kWh [18] and $0.08/1000kg [19] respectively. The capital investment of the system is calculated by summing the purchased cost of all components (pump, turbine and heat exchangers). The plant is modelled to operate for 8000 hours per year.

2.5 Component sizing and costing

2.5.1 Heat Exchanger Sizing

The total heat exchange surface area needed for a heat exchanger of specified design specifications are as shown in Table 3, was calculated with Eq. (4).

$$Q = UA\Delta T_{lm}F \quad (4)$$

It is common practice to have the more fouling fluid to be on the tube side as it is easier to clean the interior than the exterior of tubes. [20]. In our analysis, working fluids have higher fouling factors than water. Therefore, in the evaporator and condenser, the working fluid flows on the tube side while the geothermal fluid and cooling water flows on the shell side. Tube dimensions were chosen based on the Birmingham Wire Gauge (BWG) standards. The choice of which correlations to use to calculate film heat transfer coefficients (HTC) of a fluid depend on the side (shell or tube) in which it flows in the heat exchanger and the type of heat transfer (single or two-phase, boiling or condensation). Therefore, the correlations used to calculate the film HTC of fluids in each heat exchangers varies, depending on the type of heat transfer, as summarized in Table 3.

2.5.2 Component Costing

A power block cost was obtained by summing the costs of all main components and was subsequently converted into a total capital investment. In an ORC system, the power block cost makes up 77% of the total capital investment of an ORC system. The remainder of the total capital investment accounts for in site preparation, service facilities, contingencies, start-up costs, and contractors' fees [22]. The cost correlations used to cost the components are shown in Table 5 where f_d, f_p, f_m , C_b are factors considers of the type,

operating pressure, material and total area of the heat exchanger.

Table 3. Correlations for film heat transfer coefficients where E, C, R stands for evaporator, condenser and recuperator respectively where $\xi_h, X\ \varphi$ are the bypass, number-of-tube-rows and window correction factors respectively.

Side	Component	Type of heat transfer	Equation
Shell	E, C, R	Single-phase	$h_{shellside} = jc_p G_m \Pr^{-\frac{2}{3}} \left(\frac{\mu}{\mu_w}\right)^{0.14} \varphi \xi_h X$ (Bell – Delaware Method) (5)
Tube	E, C, R	Single-phase	$h_{single} = 0.023 Re^{0.8} Pr^{0.33} \left(\frac{\mu}{\mu_w}\right)^{0.14}$ (6)
	E	Two-phase (Boiling)	$h_{boiling} = h_{NB} + h_{FC}$ (Chen correlation) (7) $h_{NB} = 0.0012 \left(\frac{k_L^{0.79} c_p^{0.45} \rho_L^{0.49}}{\sigma^{0.5}\ \mu_L^{0.29} \lambda^{0.24} \rho_V^{0.24}}\right) \Delta T_{sat}^{0.24} \Delta P_{sat}^{0.75} S$ (8) $h_{FC} = 0.023 Re_L^{0.8} \Pr_L^{0.4} \left(\frac{k_L}{D_i}\right) \left(\frac{Re_{TP}}{Re_L}\right)^{0.8}$ (Dittus – Boelter type) (9)
		Supercritical fluid [21]	$h_b = \frac{f_r Re_b \overline{Pr_b}}{1.07 + 12.7 \sqrt{\frac{f_r}{8}} \left(\overline{Pr_b}^{\frac{2}{3}} - 1\right)} \overline{(c_p/c_{p.b})}^{0.65}$ (10) $f_r = (1.82 \log_{10}(Re_b) - 1.64)^{-2} \left(\frac{\rho_w}{\rho_b}\right)^{0.18} \left(\frac{\mu_w}{\mu_b}\right)^{0.18}$ (11)
	C	Two-phase (Condensation)	$h_{condensation} = 1.51 \left(\frac{4G''\mu}{k^3 \rho^2 g}\right)^{-\frac{1}{3}}$ (12)

Table 4. Cost correlations of components [23]

Component	Cost Correlation
Heat Exchangers	$C_{HEX}(\$) = 1.218 f_d f_m f_p C_b$ (13)
Pump	$C_{pump}(K\$) = 0.044(gpm)^{0.82}$ (14)
Turbine	$C_{turbine}(K\$) = 0.378(HP)^{0.81}$ (15)

2.6 Parametric Analysis and Optimization

Two types of simulations of the ORC models were carried out; parametric analysis and multi-variable multi-objective optimization, both of which were modelled using MATLAB. This paper considers three objective functions: overall exergy efficiency, annual profit and payback period, and five (for non-recuperative ORCs) or six (for recuperative cycles) parameters. The parameters considered were evaporating pressure, condensation temperature, degree of superheat and pinch point temperature differences in heat exchangers.

In parametric analysis, the objective functions were calculated by varying a chosen variable while keeping the remaining variables constant. This was aimed at studying the relationship between each variable and each objective function.

On the other hand, due to the conflict between objective functions, a single optimal solution does not exist. Instead, there exists a set of non-dominated solutions that makes up a Pareto Optimal front. Non-Dominated Sorting Genetic Algorithm II (NSGA-II), which is a type of MOEA (multi-objective evolutionary algorithm), was implemented to determine the Pareto Optimal front. NSGA II was chosen as it performs better in finding a diverse set of solutions and in converging near the true Pareto-optimal set, as compared to two other contemporary MOEAs; Pareto-archived evolution strategy (PAES) and strength-Pareto EA(SPEA) [24]. NSGA-II works by initializing random individuals subjected to a set of constraints. The fitness functions of each individual were then calculated, evaluated and ranked, and only the non-dominated individuals survive to the next generation. A non-dominated solution is a solution where there exists no other solution that outperforms it in both objective functions. Two types of optimisations were evaluated; thermo-economic and economic, as shown in Table 5.

Table 5. Optimisation problems and constraints, where subscript E,C,R stand for evaporator, condenser and recuperator, respectively

Thermo-economic Optimisation
$minimise\ f_1(x) = -\eta_{ex}$ $f_2(x) = (Payback\ Period)$ $T_1 \geq 300$ $\Delta T_{sh} \geq 0$ $P_{evap} \leq 0.95 \quad or \quad P_{evap} \leq 1.05$ $\Delta T_{pp,i} \geq 0 \ \ i = E, C, R$
Economic Optimisation
$minimise\ f_1(x) = -(Annualised\ Net\ Profit)$ $f_2(x) = (Payback\ Period)$ $T_1 \geq 300$ $\Delta T_{sh} \geq 0$ $P_{evap} \leq 0.95 \quad or \quad P_{evap} \leq 1.05$ $\Delta T_{pp,i} \geq 0 \ \ i = E, C, R$

Objective functions that needed to be maximized were multiplied by a factor of -1 as the optimization code was set up to minimise all objective functions that were defined. The evaporation pressure in a subcritical and transcritical cycle was limited to lower than $0.95P_{crit}$ and higher than $1.05P_{crit}$ respectively to exclude the critical region and to prevent numerical instabilities with the equation of state and optimizer [5]. In SCORCs, degree of superheat is defined as the temperature difference between evaporation temperature and point 5 in the T-s profile of the fluid while in TCORCs, it is defined as the temperature difference between the critical temperature of the fluid and point 5.

3. Results and Discussion

3.1 Parametric Analysis

The trends obtained from parametric analysis are summarized in Table 6. From Eq. (1), it can be said that for a geothermal source of constant temperature and mass flowrate, the overall exergy efficiency is directly proportional to the net power output of the system, which is related to the amount of heat extracted from the heat source. Net power output depends on the mass flowrate of working fluid and specific net power output, which decreases and increases respectively as evaporation pressure increases. Therefore, this leads to the existence of an optimum point in the system where net power output is a maximum, corresponding to a maximum overall exergy efficiency and minimum payback period.

Table 6. Relationship between the objective functions and increasing value of each parameter

Parameter/ Objective function	η_{ex}	Payback period
T_{sh}	Decreases	Decreases
T_1	Decreases	Initially decreases to a minimum value and subsequently increases
P_{evap}	Initially increases up to a maximum value and subsequently decreases	Initially decreases to a minimum value and subsequently increases
$T_{pp,E}$	Decreases	Initially decreases and subsequently increases
$T_{pp,C}$	Does not vary	Initially decreases and subsequently increases
$T_{pp,R}$		

An increase in the condensation temperature results in a decrease in net power output while mass flowrate of working fluid remains constant and hence, lower exergy efficiency. This leads to lower revenue generated but also lower capital cost. A minimum payback period exists because beyond this point, savings from capital costs cannot compensate enough for decrease in revenue. The above argument can also be applied to the relationship between pinch point temperature difference in the heat exchangers and payback period, and the relationship between pinch point temperature difference in the evaporator and overall exergy efficiency. In this case, smaller pinch point temperature difference will increase revenue but also the capital cost of the system.

3.2 SCORC Thermo-economic Multi-objective Optimisation

Fig. 5 and 6 shows the Pareto front from the thermo-economic optimisation for non-recuperative and recuperative SCORC. In ORCs, thermal match, which considers the temperature difference between the working fluid and the heat source, plays a vital role in the performance of a fluid. Fluid performances are compared in terms of their individual payback period needed to achieve the same exergy efficiency.

Poor thermal match causes large irreversibility in the cycle, allowing less heat to be extracted from the heat source, which leads to low exergy efficiency. To achieve a good thermal match, the temperature difference between the working fluid and the heat source must be small, corresponding to a small pinch point temperature difference in the evaporator.

The evaporating temperature in SCORC is limited to less than the critical temperature of the fluid being considered. Therefore, the evaporating temperature of R1234yf, R134a and isobutane is limited to a temperature that is much lower than that of the heat source, resulting in considerably worse performances than the other fluids due to worse thermal match, as shown in Fig. 5.

At low exergy efficiency of $\eta_{ex} < 0.3$, fluids with $T_{cr} > T_{h,in}$ reveal the best performance as these fluids can achieve a significantly smaller temperature difference with the heat source while remaining below their saturation curve. However, as efficiency increases, these fluids were outperformed by R245fa, which has a lower critical temperature. One of the main barriers in SCORC is the isothermal boiling section in the evaporator which has poor thermal match. As explained in Section 3.1, a higher exergy efficiency corresponds to more heat being extracted from the heat source, causing the exit temperature of the heat source to be lower. As the inlet temperature of the heat source is constant, this causes the temperature profile of the heat source to end at a lower point in the T-s diagram, thus moving closer towards the cycle profile of R245fa, as compared to during low efficiency. This allows R245fa to be the fluid

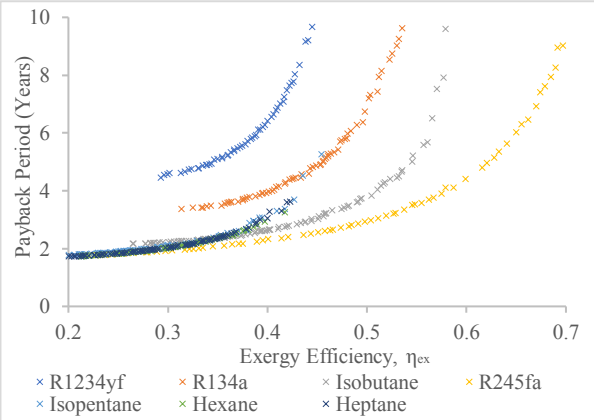

Figure 5. SCORC without Recuperator

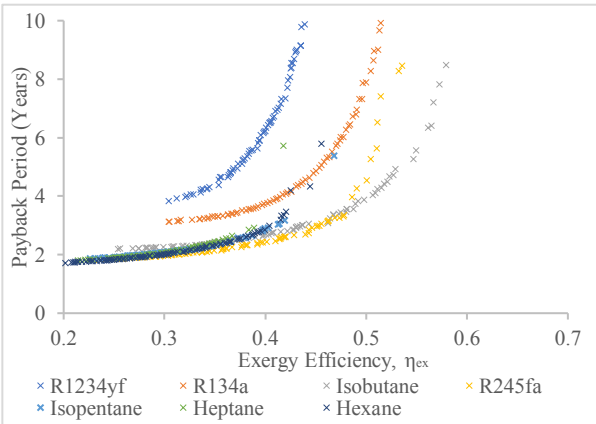

Figure 1. SCORC with Recuperator

with the least proportion of its cycle profile in the isothermal boiling region.

As the temperature profile of the heat source lies below the critical point of isopentane, hexane and heptane, causing the isothermal boiling region in their respective cycle profile to be much 'wider' than that of R245fa. Hence, R245fa can achieve the best thermal match amongst all the fluids at high exergy efficiency.

As shown in Fig. 6, recuperative SCORC shows similar trends as non-recuperative SCORC, where fluids with $T_{cr} > T_{h,in}$ perform better at $\eta_{ex} < 0.3$, but these fluids were subsequently outperformed by R245fa. However, in recuperative SCORC, R245fa does not remain to be the best performing fluid as exergy efficiency increases. It was instead outperformed by isobutane at $\eta_{ex} > 0.48$. This is because the percentage of total cooling duty of the system that was satisfied by the recuperator increases for isobutane but decreases for R245fa, as compared to when $\eta_{ex} < 0.48$, causing R245fa to have a higher cooling water requirement than isobutane to compensate for the increase in condenser duty. Therefore, even though R245fa has a better thermal match than isobutane, the effect of higher cooling water requirements dominates at $\eta_{ex} > 0.48$, allowing isobutane to outperform R245fa.

3.3 TCORC Thermo-economic Mutli-objective Optimisation

Fig. 7 and 8 shows the Pareto front from the thermo-economic optimisation for non-recuperative and recuperative TCORC, respectively. In both non-recuperative and recuperative TCORC, R1234yf is the worst-performing fluid as it has the worst thermal match. In general, in TCORC, R134a has a higher cooling water requirement than isobutane, causing isobutane to have a higher total cooling water cost. However, due to isobutane's density being much lower than that of R134a, isobutane has a higher volumetric flowrate of working fluid, resulting in larger components and higher capital costs. In the case of non-recuperative TCORC, at $\eta_{ex} < 0.49$, the effect of higher capital costs dominates, causing R134a to perform slightly better than isobutane. However, at $\eta_{ex} > 0.49$, the effect of R134a having higher total cooling water costs dominates, causing isobutane to outperform R134a. On the other hand, in the case of recuperative TCORC, R134a remains as the best performing fluid throughout as efficiency increases. This is because, with the addition of a recuperator, isobutane still has a higher capital cost due to it having higher volumetric flowrate of working fluid. However, some of R134a total cooling duty was satisfied by the recuperator and thus reducing

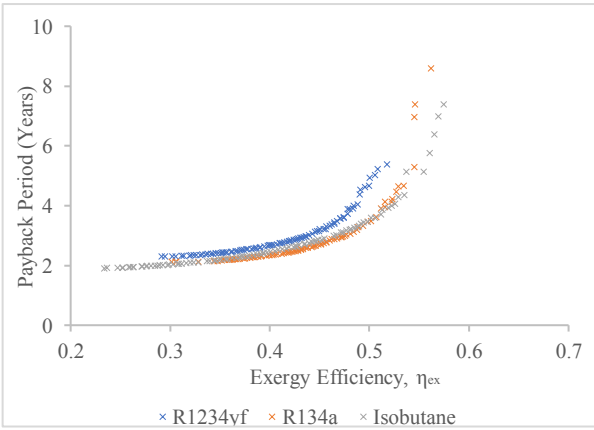

Figure 7. TCORC without Recuperator

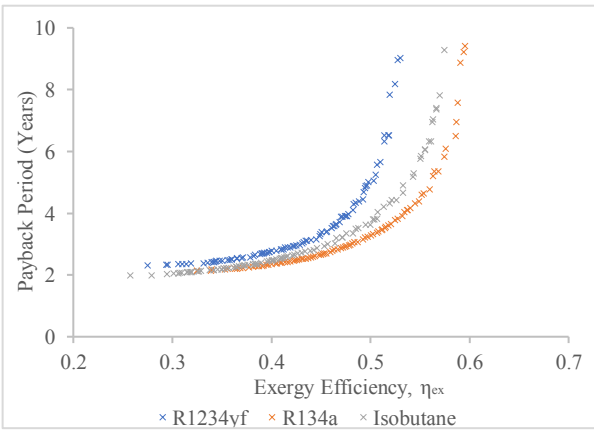

Figure 8. TCORC with Recuperator

its total cooling water cost, allowing it to remain outperforming isobutane as efficiency increases.

3.4 Comparison between Non-recuperative and Recuperative ORC

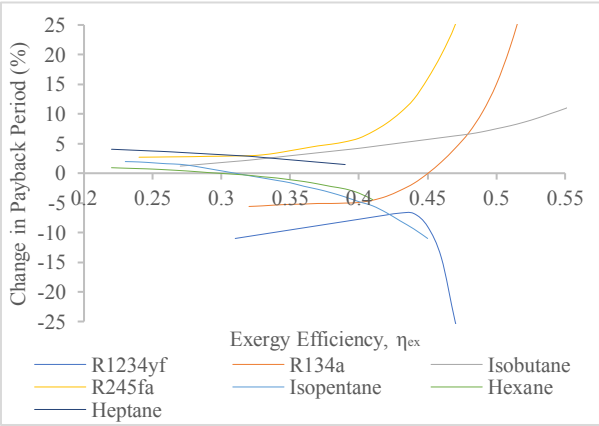

Fig 9. Change in Payback Period of Recuperative relative to Non-recuperative SCORC systems

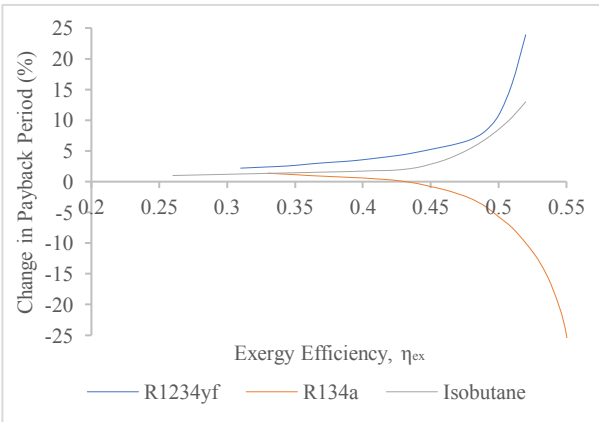

Fig 10. Change in Payback Period of Recuperative relative to Non-recuperative TCORC systems

Fig. 9 and 10 demonstrates the percentage change in payback period of a recuperative system relative to a non-recuperative system for SCORC and TCORC systems, respectively. Since one of the objectives of the optimisation is to minimise payback period, it would only be beneficial to implement a recuperator if the percentage change in payback period is negative, proving that the payback period for the same efficiency would be reduced through the addition of a recuperator.

As shown in Fig. 9, for fluids with $T_{cr} < T_{h,in}$, it is evident that percentage change in payback period increases with increasing exergy efficiency. As shown in Fig. 3, the heating segment in a SCORC consists of three distinct sections; subcooled heating (2→3), boiling (3→4) and superheating (4→5), where the boiling section has the worst thermal match due to its isothermal nature. Recuperative SCORC has a reduced subcooled heating requirement in the evaporator (inlet of evaporator starts at point 2a instead of point 2), so for the same amount of heat duty needed for boiling, a recuperative SCORC has a larger proportion of its T-s profile being in the boiling section. In addition, as explained earlier, higher exergy efficiency corresponds to steeper temperature profile of the heat source. Hence, the importance of thermal match becomes increasingly important, causing the magnitude of the rate of change in payback period to increase.

R1234yf and R134a are the only working fluids that favours recuperative systems initially. As the critical temperature of these fluids is much lower than other fluids, a much lower condensation temperature is needed, which requires much higher cooling water requirements. Therefore, even though the addition of a recuperator increases the capital cost of the system, this increase in capital cost is compensated for, by the substantial cost savings from lower cooling water requirements. This leads to an overall cost savings and lower payback period for R1234yf and R134a in recuperative SCORC.

Percentage change in payback period of R1234yf peaks at η_{ex}~0.43, followed by sharp decline. Since R1234yf has the lowest critical temperature of 94.9℃, for it to operate in subcritical conditions, the condensation temperature would have to be very low. Additionally, the condensation temperature would have to be even lower at high generation capacities, therefore, requiring very large quantities of cooling water. As a result, recuperation brings a much larger benefit towards the poor-performing system.

On the other hand, Fig. 9 demonstrates that working fluids with $T_{cr} > T_{h,in}$ in TCORC initially performs worse with recuperation but as exergy efficiency increases, the percentage change in payback period gradually decreases due to decreasing cooling water requirement. As the critical temperature of the fluid increases, the rate of change in payback period decreases because the proportion of the fluid's T-s diagram that lies in the subcooled heating region decreases, resulting in less heat that can be exchanged within the recuperator.

At low exergy efficiencies ($\eta_{ex} < 0.31$), the impact that recuperation has on SCORC systems of all fluids is very low (a positive change in payback period ranging from 0.9% to 3.3%). This is because at low efficiencies (smaller power generation capacity), the savings from reduced cooling water requirement is less than the increase in capital cost from adding a recuperator.

As shown in Fig. 10, for TCORC systems with $\eta_{ex} < 0.43$, the payback period of all working fluids increases with the addition of a recuperator. Like SCORC systems, savings from cooling water cannot compensate enough for the cost of a recuperator. The behaviour of the fluids as exergy efficiency increases, follows the same explanation as in Section 3.3. At $\eta_{ex} > 0.43$, percentage change in payback period for R134a decreases exponentially due to substantial savings from reduced cooling water requirements.

3.5 Comparison between TCORC and SCORC

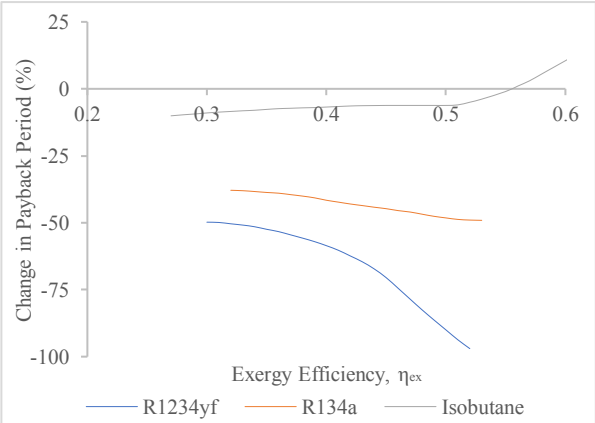

Fig 11. Change in Payback Period of TCORC relative to SCORC for Non-recuperative systems

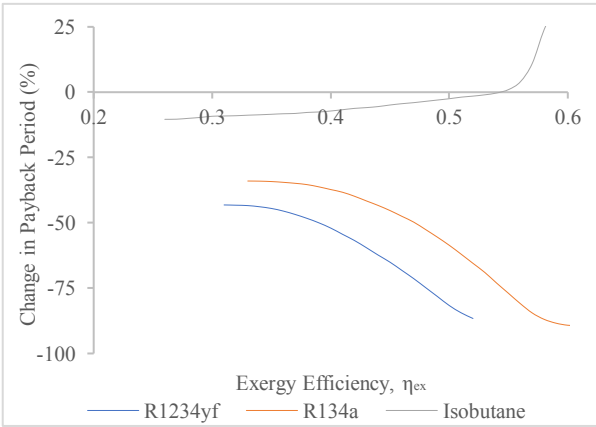

Fig 12. Change in Payback Period of TCORC relative to SCORC for Recuperative Systems

Fig. 11 and 12 works similarly to the graphs discussed in Section 2.4 but here, the graphs show the percentage change in payback period of a TCORC relative to the SCORC system for the same exergy efficiency, for non-recuperative and recuperative systems respectively.

Both Fig. 11 and 12 shows that for all fluids, TCORC, with or without recuperator, outperforms SCORC under most exergy efficiencies. This is because in transcritical cycles, the heating of fluids will be carried out under supercritical condition, thereby bypassing the two-phase isothermal boiling region, resulting in an improved thermal match relative to SCORC.

As exergy efficiency increases, the heat source temperature profile becomes steeper, further enhancing the thermal match. This results in better heat integration, allowing for more heat to be transferred from the heat source to the working fluid which explains the downward sloping trend observed for both R1234yf and R134a. Also, TCORC requires less superheat, leading to reduced cooling duty requirements in the condenser, and thus a decrease in heat exchanger size and cost, and cooling water flowrate.

In both recuperative and non-recuperative systems, R1234yf shows larger improvements in performance than R134a because it has the lowest critical temperature. As for isobutane, it initially performs better in TCORC but as exergy efficiency increases, SCORC becomes the better performing system. The thermal match effect is less important here due to its higher critical temperature, instead, cooling water requirements will drastically increase with increasing power generation capacity since condensation temperature will approach the heat sink temperature.

For isobutane and R1234yf, their respective non-recuperative and recuperative systems show relatively similar rate of change in their performance. On the other hand, R134a experiences higher rate of improvement in recuperative than in non-recuperative system, for the same reason as in Section 3.3, where recuperation significantly reduces cooling water costs for R134a causing the curve to have a steeper gradient.

3.6 Thermo-economic Global Optimisation

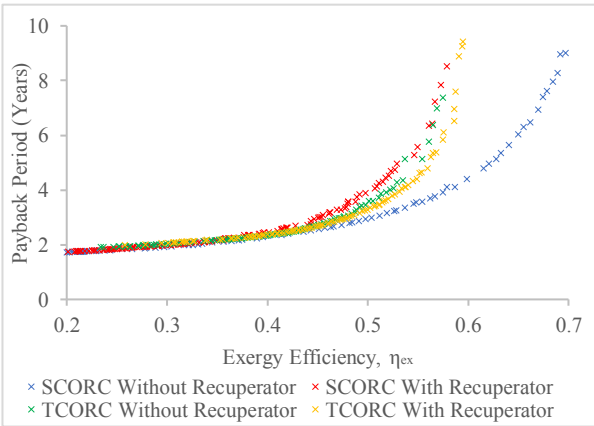

Fig 13. Thermo-economic Global Optimisation

Fig. 13 shows the Pareto fronts for the global thermo-economic optimisation between payback period and exergy efficiency, using the different cycle designs outlined in Section 2.1. It takes into consideration of the working fluid which would give the best performance at each set of operating condition.

It can be observed that at low efficiency, cycle architecture has little impact on the performance, where payback period tends towards approximately 1.7 years as exergy efficiency approaches zero. As exergy efficiency is directly proportional to the power generation capacity, this suggests that the choice of cycle architectures has minimal impact for systems with small power generation capacity and this could be because the magnitude of benefits and drawbacks for different cycle architectures is negligible. Different cycle architectures mainly affect the total cost of heat exchangers and total cooling water cost. For this case, this conclusion is drawn for exergy efficiencies less than 0.4 which is equivalent to power generation capacities of less than 2.2MW.

As exergy efficiency increases, the performances of the different cycle architectures start to diverge from each other at η_{ex}~0.40. At $\eta_{ex} > 0.40$, it is most preferable to employ a non-recuperative SCORC,

followed by recuperative TCORC, non-recuperative TCORC and recuperative SCORC. This is mainly due to geothermal sources having a generally lower temperature than other potential heat sources for ORC applications.

Whilst TCORC tends to outperform SCORC, when considering a single fluid, the use of TCORC is highly limited by the range of working fluids that can be used due to the requirement on working fluid to have critical temperature below heat source temperature. The improvement in performance from SCORC to TCORC on a standalone basis is insufficient to conclude if TCORC is always the best choice of system because SCORC can use a much larger range of working fluids. Based on this insight, it can be concluded that the selection of working fluid is extremely crucial when designing an ORC, more so than the choice of cycle design.

3.7 Economic Global Optimisation

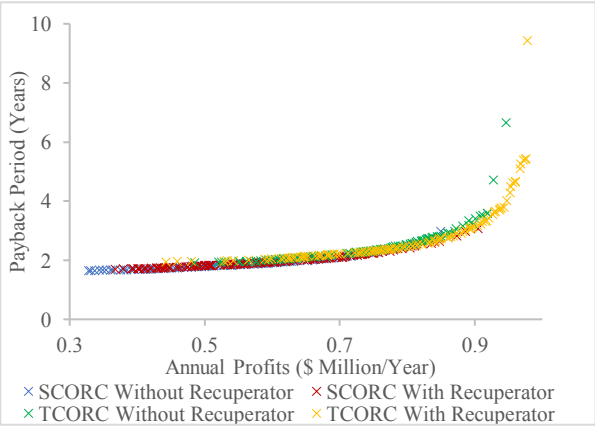

Fig 14. Economic Global Optimisation

Fig. 14 displays the pareto fronts from the economic global optimisation between payback period and annual profit. This optimisation serves the purpose of understanding how magnitude of earnings are able to influence investors' decisions on the most appropriate cycle design. Since annual profit takes into consideration of revenue from electricity sales and all variable costs, it serves as a representation of the economic value of the ORC in the long term.

Fig. 14 demonstrates a clear trend where all cycle architectures displays very similar economic performances. This shows that the cycle design has a small influence on the economic performance. The reason for this is similar to that for the performance of thermo-economic global optimisation at small exergy efficiencies as observed in Fig. 13.

The difference between Fig. 13 and 14 is that in Fig. 14, the curves do not diverge as payback period increases. As the power generation capacity increases, the payback period will increase since larger components are required to accommodate for the additional power capacity, resulting in higher capital costs. However, at higher power generation capacity, more units of electricity can be sold, thereby increasing the revenue, which is increasing at a greater rate than total capital cost. Hence, explains the shape of the curve in Fig. 14. However, this is only applicable for a certain range. As energy generation strives to further increase, it becomes increasingly difficult to extract the remaining energy from the heat source since the heat source temperature and condensation temperature would need to drop further resulting in poorer heat transfer in the condenser. This would require significantly larger evaporators and condensers, as well as high cooling water flowrates. The large increase in capital costs cannot be compensated by the increase in revenue. Hence, annual profits would start to decline. Therefore, there is a turning point for each cycle architecture which corresponds to the maximum annual profit that the cycle design can achieve, as shown in Table 7.

As shown in Table 7, recuperative TCORC has the highest maximum potential annual profit, which comes at a cost of higher payback period. Recuperative TCORCs can achieve higher annual profits because it has the benefit of being able to extract more energy from the heat source. As a result, an investor who aims to prioritise annual profits only, would choose to use recuperative TCORCs. Otherwise, cycle design does not play a major role in terms of its economic performance.

Table 7. Maximum potential annual profit achievable by each cycle architecture

Cycle Architecture	Maximum Potential Annual Profit ($M/Year)	Payback Period (Years)
Non-recuperative SCORC	0.85	3.0
Recuperative SCORC	0.91	3.2
Non-recuperative TCORC	0.95	6.7
Recuperative TCORC	0.98	9.4

4. Conclusion

In this study, a multi-objective optimisation framework was proposed to investigate the thermodynamic and economic performance of SCORC and TCORC systems, with the option of adding a recuperator. Through different combinations of objective functions, parametric optimisation was performed to allow better understanding on how thermo-economic and economic perspectives could affected cycle design selection.

Through the presented results, it was found that the most suitable cycle architecture which can yield the best performance is highly dependent on the prioritisation of different perspectives and objectives. On a standalone basis, most working fluids yield better thermo-economic performance in TCORC, regardless of whether it is recuperative or not. The magnitude of this improvement is highly dependent on the critical temperature of the

working fluid, which affects the thermal match of the temperature profile between the working fluid and heat source, and the cooling duty, which affects cooling water costs. These two factors play an offsetting effect and the strength of each effect is highly dependent on the power generation capacity of the system.

The global optimisation of the ORC systems, which includes selecting the most optimum working fluid, yields different results. For thermo-economic considerations, at low power generation capacities of less than 2.2MW, all cycle architectures yield very similar performances with a minimum payback time of 1.7 years. As power generation capacity increases, non-recuperative SCORC yields the lowest payback period instead. On the other hand, from an investor's perspective, the economic global optimisation revealed that cycle architecture has little impact on economic performance, evaluated based on both payback period and annual profit. It has an influence on the maximum attainable annual profit, which comes at a cost of higher payback period, where recuperative TCORC yields the highest maximum attainable annual profit of $0.98 million per year where the capital investment can be recovered 9.4 years.

The presented results and findings are only valid for the specified heat source conditions and assumptions within the scope of this study. To provide a generalised recommendation, the scope of study needs to be expanded to include the considerations of more heat source conditions, wider range of working fluids (pure and mixture), different types of thermodynamic and economic indicators and sensitivity analysis on the assumptions made.

5. References

[1] Exergy-orccom. EXERGY - Efficient and tailor-made Organic Rankine Cycle geothermal binary power plants. 2018. Available from: http://www.exergy-orc.com/geothermal [Accessed 10th December 2018]

[2] Hettiarachchi M and Golubovic M. Optimum design criteria for an Organic Rankine cycle using low-temperature geothermal heat sources. *Energy*. 2007;32(9): 1689-1706.

[3] Sun Q, Wang Y and Cheng Z. Thermodynamic Optimization of a Double-pressure Organic Rankine Cycle Driven by Geothermal Heat Source. *Energy Procedia*. 2017;129: 591–598.

[4] Cáceres I, Agromayor R and Nord L. Thermodynamic Optimization of an Organic Rankine Cycle for Power Generation from a Low Temperature Geothermal Heat Source. Proceedings of the 58th Conference on Simulation and Modelling, Iceland, September 25 – 27, 2017;138.

[5] Oyewunmi O. Thermoeconomic analysis of recuperative sub- and transcritical organic Rankine cycle systems. *Energy Procedia.* 2017;129: 58-65.

[6] Astolfi M. Binary ORC (organic Rankine cycles) power plants for the exploitation of medium–low temperature geothermal sources – Part A: Thermodynamic optimization. *Energy.* 2014;66: 423-434.

[7] Oyewunmi O and Ferré-Serresa S. An assessment of subcritical and trans-critical organic Rankine cycles for waste-heat recovery. *Energy Procedia*. 2017;105: 1870-1876.

[8] Lecompte S. Multi-Objective Thermo-Economic Optimization Strategy for ORCs Applied to Subcritical and Transcritical Cycles for Waste Heat Recovery. *Energies*. 2015;8: 2714-2741.

[9] Kai Z. Parametric Optimization of Low Temperature ORC System. Energy Procedia. 2015;75: 1596-1602.

[10] Suyanto. Design of a Geothermal Energy Dryer for Tea Withering and Drying in Wayang Windu Geothermal Field. Proceedings World Geothermal Congress 2010. Bali, Indonesia, April 25 – 29th. 2010

[11] Prananto L. Use of the Kalina cycle as a bottoming cycle in a geothermal power plant: Case study of the Wayang Windu geothermal power plant. *Applied Thermal Engineering.* 2018;132: 686-696.

[12] Li G. Organic Rankine cycle performance evaluation and thermoeconomic assessment with various applications part II: Economic assessment aspect. *Renewable and Sustainable Energy Reviews.* 2017;64: 490–505.

[13] Quoilin S. Techno-economic survey of Organic Rankine Cycle (ORC) systems. *Renewable and Sustainable Energy Reviews.* 2013;22: 168–186.

[14] Li T. Thermodynamic optimization of organic Rankine cycle using two-stage evaporation. *Renewable Energy.* 2015;75: 654-664.

[15] Moloney F. Working fluid parametric analysis for regenerative supercritical organic Rankine cycles for medium geothermal reservoir temperatures. *Energy Procedia.* 2017;129: 599-606.

[16] Infrastructure Asia Online. Indonesia Electricity Tariff Still Competitive in ASEAN Region. 2018. Available from: https://www.infrastructureasiaonline.com/government/indonesia-electricity-tariff-still-competitive-asean-region [Accessed 10th December 2018]

[17] Secretariate General of National Energy Council. Indonesia Energy Outlook 2016. 2016.

[18] U.S. Department of Energy FEMP. Geothermal Electric Energy. 2016.

[19] Hewitt G.F. Multiphase Science and Technology. 1986. Volume 2.

[20] Cao E. Heat Transfer in Process Engineering. 2010.

[21] Chen W. An assessment of correlations of forced convection heat transfer to water at supercritical pressure. Annals of Nuclear Energy. 2015;76: 451–460.

Selective Direct Oxidation of Methane to Methanol Using Copper Containing Zeolites – Studies on the Effect of Importance of 8-Membered Ring on Activity of Reaction

Seong Ho Baek and Zhiyan Qiu
Department of Chemical Engineering, Imperial College London, SW7 2AZ, U.K.

Abstract The direct conversion of methane to methanol has been a "holy grail" in catalysis for decades. The higher activity reported for zeolites containing mono(μ-oxo) dicopper active sites within 8-membered rings (8MR) inspires the investigation of the 8MR in more detail. In this study, four different copper containing zeolite frameworks, namely EDI, MER, PHI and GIS, which only contain 4 and 8MRs within their structures, have been synthesized and tested for direct methane to methanol reaction (DMTM) using a stepwise process. The potential importance of geometrical differences of 8 MRs forming the copper active site is discussed. Copper exchanged EDI produced 4.55μmol CH_3OH/g catalyst, while no methanol was produced using the other three topologies. The characterisation of zeolites revealed the acidity of ion exchange solution has caused the dealumination of the framework and destabilisation of the structure. The importance of the Si/Al ratio of zeolite frameworks is also discussed and how the shape of 8MR in 3D space may also play a crucial role in the activity of DMTM reaction.

Introduction

Methane, a major component of natural gas, plays an important role in current energy sector with increasing availability of cheap natural gas.[1,2] However, methane is not being utilised effectively in the remote gas drill sites as the transportation of gaseous methane is difficult and no direct industrial process is available to convert methane directly into more easily transportable liquid derivatives such as methanol. Currently, methane is converted to methanol via a two-step process through the formation of syn-gas by a methane reforming process, which is energy intensive and is only economically feasible at a large scale.[2] As a result, methane is flared and wasted at remote locations. Therefore, a direct transformation of methane to methanol is highly desirable. However, due to the high stability of the C-H bond of methane and the tendency of overoxidation to carbon dioxide,[3,4] direct and selective oxidation of methane to methanol has been a major challenge in catalysis. Various homogeneous and heterogeneous catalysts have been tested for the direct synthesis of methane to methanol,[2,5-7] but none has been able to meet industrial requirements due to low selectivity and conversion.

In nature, a biological enzyme, methane monooxygenase (MMO) is able to activate the C-H bond of methane and selectively oxidise methane to methanol at ambient conditions.[4,8,9] There are two forms of MMOs, which are the soluble form (sMMO) and the particulate form (pMMO). Methane hydroxylation is believed to occur at the diiron and dicopper active sites in sMMO and pMMO in a peptide ligand environment.[8,9] Inspired by enzyme systems, various copper and iron exchanged zeolites have been studied as inorganic analogues to the MMOs to mimic the chemical environment of MMOs.[8-13] Zeolites are aluminosilicate microporous crystalline materials consisting of rings of different numbers of T (Si or Al) atoms. Their aluminosilicate frameworks consist of different pore/ring channels. A schematic of ring systems is shown in Figure 1. Zeolites can accommodate metal cations in extra-framework positions. Exchanging the cations in zeolites is known to lead to the formation of metal-oxo species and these can form metal active sites, similar to MMOs, hosted on the ring systems.[8,9]

A continuous process with a heterogeneous catalyst at low temperature conditions would be ideal to produce methanol at an industrial scale as high turnover can be achieved without a need of complex separation system. A stepwise process is implemented for the selective oxidation of methane using metal exchanged zeolites. It consists of three steps. The metal active sites are activated through flowing He over the catalyst at an elevated temperature and heated at a constant ramp rate. Methane molecules are then adsorbed onto the active sites and produce chemisorbed methoxy species. However, as the chemisorbed methoxy species do not readily desorb from the catalyst surface, water vapour is required to hydrate the methoxy species and extract methanol molecules from the catalyst surface.

With the pioneering work by Grooteart et al,[10] commercially available zeolites, ZSM-5 and mordenite have been shown to produce methanol when exchanged with copper ions. Moreover, other copper exchanged zeolite frameworks are also known to be active for partial oxidation of methane including well-known structures of ferrierite (FER), beta (BEA), zeolite Y (FAU).[11] More recently, small pore frameworks like

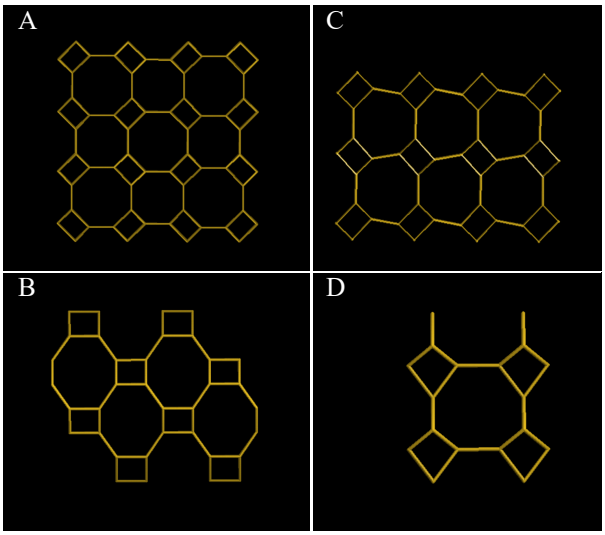

Figure 1. (A) MER framework at (001) position. **(B)** GIS framework at (100) position. **(C)** PHI framework at (100) position. **(D)** EDI framework at (100) position. Figures obtained from IZA website.

SSZ-13 (CHA), SSZ-16 (AFX), SSZ-39 (AEI) and SAPO-34 (CHA) with 8-membered ring (8MR) systems have been shown to yield more methanol per copper atom.[12] Furthermore, large pore frameworks like ECR-1 (EON), Omega (MAZ), PST-11 (MEI), UZM-22 (MEI), UZM-4 (BPH) are also active for methanol synthesis.[13] The key feature of copper exchanged zeolites with good activity is the presence of 8MR within the framework which are believed to form the copper active site required for the reaction.[12,13]

With advancement in spectroscopic techniques, numerous studies have attempted to elucidate the active site motif of copper in the zeolite framework. However, the nature of the active site on zeolites remains a controversial topic. The copper active site was initially suggested as a bis(μ-oxo) dicopper site for ZSM-5,[10] but the active site was reassigned as mono(μ-oxo) dicopper site at 10MR through further analysis.[14] The active species of Cu-MOR is believed to be the same mono(μ-oxo) dicopper site located at two 8MR side pockets of framework[15] although recent studies suggest the possibility of formation of tricopper sites[16] and copper oligomers cluster[17] acting as active sites during the reaction. Kulkarni et al.[18] also suggest monocopper active species for small pore zeolite frameworks. Furthermore, recent studies also discuss the possibility of formation of a mixture of active site motifs within a single framework.[19,20] Thus, active site motif of copper containing zeolite is still a matter of debate and a definitive conclusion is still to be made.

Although no consensus has been reached for the copper active site motif, the position of the active sites is generally accepted to be located at the 8MR, 10MR and 12MR of zeolite frameworks.[21] Recent studies conducted using both small and large pore 8MR zeolites showed superior activity compared to other ring systems[12,13] suggesting that 8MRs are highly favoured for the formation of the active sites.

Four different zeolite topologies of EDI, MER, GIS and PHI have been tested in this study for the selective oxidation of methane through a stepwise process. EDI, MER, GIS and PHI zeolite frameworks only have 4 and 8MRs in their framework;[22] thus this excludes the possibility of 10 and 12MR system participating by hosting active sites and an effective comparison of the structural and geometrical differences of 8MR within the zeolite framework on the activity of the reaction can be achieved.

Methodology

Material Potassium hydroxide (pellets, ≥85%) and sodium hydroxide (pellets, ≥98%) from VWR, aluminium sulfate hydrate (≥97%) and sodium aluminate (technical) from Alfa Aesar, LUDOX AS-40 colloidal silica (40%) from Sigma Aldrich were used in MER, GIS and PHI synthesis. Potassium hydroxide (pellets, ≥85%) from VWR, amorphous fumed Silica (Cab-O-Sil® M5) from INOXIA, and aluminium wire (99.999%) from Sigma Aldrich were used in EDI synthesis. Copper (II) nitrate trihydrate (≥99%) from Sigma Aldrich was used in copper ion exchange for all zeolite frameworks. Deionised (DI) water was used in all processes.

Catalyst Synthesis The synthetic pathways of zeolites framework types of EDI, MER, GIS and PHI were adopted from previous works found in literature.[24,25] All zeolites were hydrothermally synthesized with a Si/Al ratio ranging from 3 to 5, with OSDA (organic structure directing agent) -free routes. Table 1 shows the molar composition of each growth solution.

Ion Exchange Copper ions were introduced into the studied zeolite structures, using an aqueous solution of copper (II) nitrate trihydrate, ($Cu(NO_3)_2 \cdot 3H_2O$). Synthesis procedure involved adding 1.5g of as-synthesized zeolite powder to 75mL of copper (II) solution. These solutions were stirred and heated under reflux at 323K overnight. The suspension was then filtered at room temperature and washed with DI water until the pH was neutral. The wet crystals were dried overnight at 373K in a drying oven, and subsequently calcined at 723K for 4 h at a constant ramp rate of 3K min^{-1} in static air prior to use. The copper content in the zeolite structures was also investigated by using different concentrations of copper (II) precursors (0.001M – 0.05M) and a different number of ion exchange cycles (1 – 3 cycles).

Physicochemical Characterisation X-Ray Powder Diffraction (XRD) (X-ray Diffractometer PANalytical X'Pert Pro powder, Cu Kα radiation, 40 kV, 20 mA, 1.54 Å) was used for phase identification of the crystalline material. The diffraction patterns of the synthesized zeolites were recorded in the 5 – 50° 2θ range with a step scan of 0.106° min^{-1}.

The elemental composition of the materials was determined using X-Ray Fluorescence (XRF) (PANalytical Epsilon 3 XLE X-ray Fluorescence Spectroscopy), to confirm the SiO_2/Al_2O_3 molar ratio of the synthesized zeolites. Approximately 1g of zeolite powder was loaded into the sample spinner cup.

Scanning Electron Microscopy analysis (SEM) (JSM-6010LA InTouchScope™ Multiple touch panel scanning electron microscope) was performed to capture the close-up images of the synthesized crystals.

Table 1. Summary of the molar composition of the different framework type zeolites in synthesis method.

Zeolite framework type	SiO_2	Al_2O_3	MOH*	H_2O	K_2O	SiO_2/Al_2O_3	Time (days)
EDI	3.00	1.00	-	94.5	5.26	3.00	4
MER	2.45	0.50	10	505	-	4.90	4
GIS	8.20	2.05	10	173	-	4.00	7
PHI	12.20	2.90	10	201	-	4.21	7

* MOH = KOH for MER; MOH = NaOH for GIS; MOH = 75% NaOH + 25% KOH for PHI.

Methane to Methanol Reaction A custom-made reactor set-up was used for the methane oxidation reaction, which is shown in Figure 2. 0.4g of catalyst were loaded into a tubular reactor (stainless steel, D = ¼ in, L = 30 cm), and kept in place by quartz wool to form a fixed bed. Following a stepwise process, the catalyst was first heated from 298K to 673K at a constant ramp rate of 10K min^{-1} in a 25mL min^{-1} gas flow of dry helium (He). The temperature was then gradually cooled to reaction temperature (473K) at a constant ramp rate of 12K min^{-1} in He flow. The gas flow was then switched to methane (CH_4) at 25mL min^{-1} and allowed the reaction of CH_4 with copper active sites at catalyst surface to take place for 1 hr. The reactor was flushed with dry He for 30 mins when the reaction completed to remove any remaining or physisorbed CH_4. Thereafter, a wet helium stream (2.3% v/v H_2O) at 25mL min^{-1} was formed by passing the dry He through a water bubbler, containing deionized water, at ambient temperature. It was then introduced to the reactor which led to desorption of the products and monitored by mass spectrometer (ThermoStar™ GSD 320 T Pfeiffer Vacuum).

The temperature was controlled by NEWTRONIC Micro 96 Temperature Programmer Controller and the gas flowrates were controlled by AALBORG mass flow controller GFC 17 and Brooks Instrument Smart series Mass Flow meters 5850S together with Brooks Instrument Read Out and Control Electronics 0152.

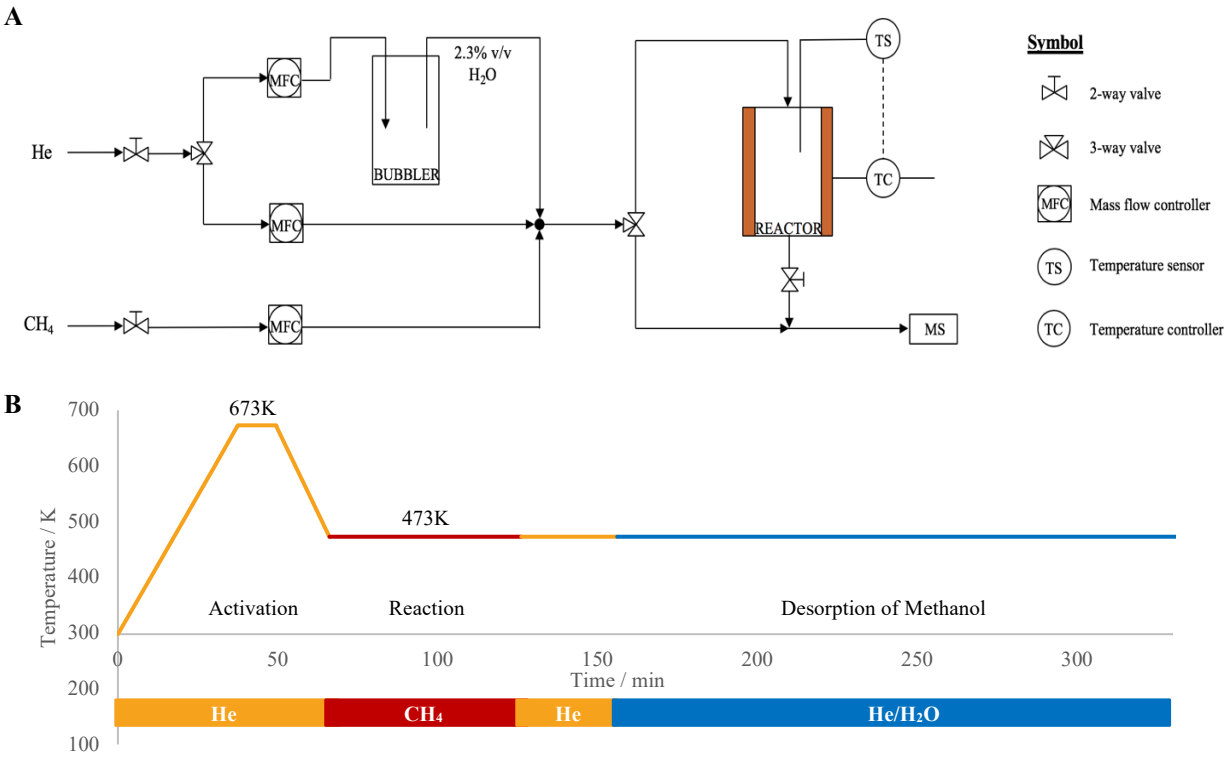

Figure 2. (A) Experimental set-up used for the selective oxidation of methane to methanol. **(B)** Stepwise process for the selective oxidation of methane to methanol.

Results

Zeolite Characterisation Figures 3A-D show the XRD patterns of all zeolites frameworks before and after calcination compared with the theoretical XRD patterns obtained from IZA database.[22]

The X-Ray patterns of as-synthesized zeolites matched very well with the theoretical XRD patterns before calcination at 450°C, which suggests that all four frameworks of EDI, MER, GIS and PHI have been synthesized successfully. No changes were observed for the XRD patterns of EDI, MER and PHI frameworks after calcination, however major changes in the peaks of GIS framework can be observed at peak positions 13°, 17°, 21°, 28° and 33°, suggesting significant changes were made to the GIS zeolite structure.

Figures 3E-H show the XRD patterns of as-synthesized zeolites before and after copper ion exchange and subsequent calcination of copper exchanged zeolites.

XRD patterns of Cu-EDI and Cu-MER after three rounds of copper ion exchange with a 0.05M copper (II) nitrate solution shows significant changes to the structures after calcination. Calcination and copper ion exchange of EDI and MER framework resulted in the collapse of zeolite framework as the characteristic peaks of EDI and MER framework were absent and a curved baseline with sharp peaks at 35 and 40 degrees was observed for Cu-EDI, characteristic of copper oxide (CuO) nanoparticles.[26]

XRD patterns of Cu-MER and Cu-EDI after one round of ion exchange at high concentration copper (II) nitrate solution show a complete loss of crystallinity. Decrease in peak intensities for Cu-EDI and Cu-MER as

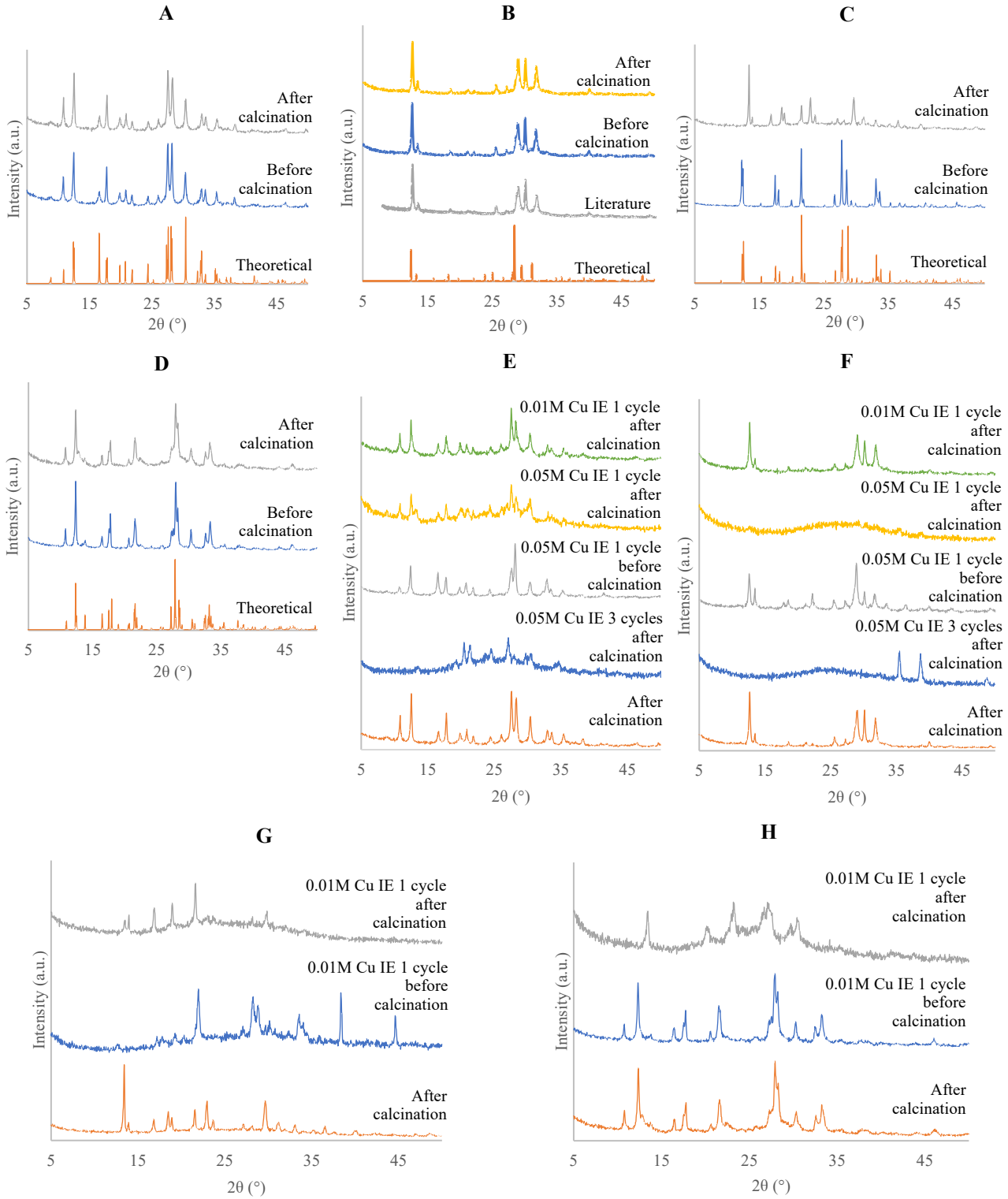

Figure 3. Measured and theoretical XRD patterns before and after calcination. **(A)** MER **(B)** EDI **(C)** GIS **(D)** PHI. Measured XRD patterns before and after Copper ion exchange. **(E)** MER **(F)** EDI **(G)** GIS **(H)** PHI.

well as the transformation of the flat baseline to a curved baseline both suggest a decrease in crystallinity of the zeolite framework after the ion exchange process. Subsequent calcination of Cu-EDI and Cu-MER again resulted in significant changes of zeolite frameworks.

When a lower concentration solution was used, Cu-MER and Cu-EDI structures remained stable. However, significant changes were observed for Cu-PHI after calcination even when treated with a 0.01M solution.

The chemical compositions of as-synthesized zeolites before and after copper ion exchange were analysed using XRF, and are summarised in Table 2.

Results have shown that the actual Si/Al ratios of zeolites matched very well with the Si/Al ratios in the synthesis methods. As the concentration of copper (II) nitrate solution increased, the degree of ion exchange increased. Multiple cycles of ion exchange also resulted in higher concentration of copper ions present in the zeolite samples.

Table 2. Summary of the chemical compositions of as-synthesized zeolites and the copper content after ion exchange with varying solution concentration and number of ion exchange cycles.

Zeolite	SiO_2/Al_2O_3 Actual	SiO_2/Al_2O_3 in Synthesis Method	Cu^{2+} Conc. (M)	IE Cycle	Cu (wt%)	Cu/Al
			0.05	3	14.26	0.55
EDI	2.69	3	0.05	1	10.96	0.46
			0.01	1	3.07	0.13
			0.05	3	6.74	0.40
MER	4.94	4.87	0.05	1	3.88	0.28
			0.01	1	2.23	0.21
GIS	3.81	4	-	-	-	-
PHI	4.12	4.2	0.01	1	2.88	0.17

To further investigate the effect of copper (II) nitrate solution concentration and ion exchange conditions on the copper content present in the zeolite structure, a much lower solution concentration and varying ion exchange times taken as well as ion exchange temperature were examined using the EDI zeolite.

Varying ion exchange conditions suggested that lowering the solution concentration has the greatest effect on copper content in the EDI structure, while the exchange time and the temperature of ion exchange are not as significant. Results are summarised in Table 3.

Table 3. Copper content of Cu-exchanged EDI with varying ion exchange conditions.

Zeolite	Cu^{2+} conc. (M)	IE Time last	Temperature (K)	Cu (wt%)
	0.01	3 hours	323	2.70
EDI	0.01	overnight	293	2.64
	0.001	overnight	323	0.28

The images of crystalline structures of zeolite framework types of MER and EDI were taken by SEM and are shown in Figure 4. A significant change in the structure of MER framework is also shown by the change in the SEM images before and after calcination of copper ion exchanged MER at 0.05M copper (II) nitrate solution.

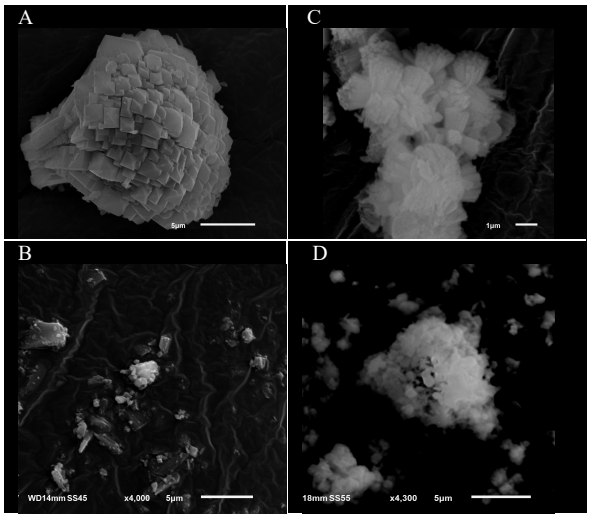

Figure 4. SEM images A) MER framework type before copper ion exchange. **B)** MER framework type after copper ion exchange and subsequent calcination. **C)** EDI framework type before copper ion exchange. **D)** EDI framework type after copper ion exchange and subsequent calcination.

Reaction Results The reaction results of all copper exchanged zeolites are summarised in the Table 4.

Copper exchanged MER, PHI and GIS did not form any methanol as the copper ion exchange and subsequent calcination resulted in a structural change of the framework. However, copper exchanged EDI using 0.01M copper (II) nitrate solution with 1 cycle of ion exchange and heated at 323K overnight yielded 4.55µmol methanol/g catalyst and it is compared to the commercial copper exchanged Na-MOR and NH_4-MOR zeolites using 0.05M copper (II) nitrate solution under same ion exchange conditions.

Table 4. Reaction results of copper exchanged zeolites.

Cu-Zeolite	Cu/Al	Cu (wt%)	mol CH_3OH/mol Cu	µmol CH_3OH/g catalyst
NH_4MOR	0.42	1.75	0.204	22.45
NaMOR	0.58	3.41	0.053	11.33
EDI	0.13	3.07	0.024	4.55

Discussion

Zeolite Degradation Oleksiak et al.[25] reported to synthesize thermally stable P2 polymorph which can withstand calcination above 400°C, and the P2 polymorph was synthesized following the exact same procedure. However, as-synthesized P2 (GIS) framework was thermally unstable above 450°C as the XRD pattern of P2 zeolite before and after calcination shows the significant changes in GIS framework (Fig x). GIS framework is well-known to be thermally unstable at temperature above 200°C, which is reported by Derkowski et al.[27] Hence, GIS framework is not suitable for the direct methane to methanol reaction due to its thermal instability.

The results of XRD analysis and SEM images both agree that copper ion exchange using a highly concentrated (0.05M) copper (II) nitrate solution and a subsequent calcination resulted in the collapse of the zeolite frameworks. The varying concentration of copper (II) nitrate solution showed mildly acidic pH values between 4.8 and 5.7. Dealumination, as a result of the acidity copper (II) nitrate solution, is the cause of the destabilisation of zeolite framework. Consequently, the zeolite framework collapsed with subsequent calcination.

Past studies have shown that some common zeolites, zeolite A and X, are more sensitive to acidity of aqueous media and removal of aluminium atoms from the framework occurs readily even at mild pH conditions.[28-30] This chemical modification of the zeolite framework by the removal of Al atoms is known as dealumination.[31]

Acid leaching is a common technique implemented for dealumination in which zeolites are treated with a strong concentrated acid. Dealumination occurs by the removal of Al atoms from the framework by breaking of Al-O bond and this leaves atomic gaps and silanol nest.[31] As a result, dealumination produces lattice defects, such as vacancies and mesopores in the framework.[31] Therefore, removal of excessive number of Al atoms from the zeolite framework can form a high concentration of lattice defects, and it may lead to the collapse of entire zeolite structure.[29,31,32] This is particularly more damaging for low Si/Al ratio zeolites.[31] Hence, we suspect that synthesized EDI, MER and PHI zeolites are all very sensitive to acidity and their structural stabilities were heavily affected by the pH of the copper (II) nitrate solution. This argument is also supported by XRD results of Cu-EDI and Cu-MER ion exchanged using 0.01M copper (II) nitrate solution, overnight at 323K where the structures of two zeolites were maintained, as 0.01M copper (II) nitrate solution was less acidic than 0.05M copper (II) nitrate solution.

Silica to Alumina Ratio Si/Al ratio is a key zeolite parameter and it influences various important physical and chemical characteristics of zeolites such as, the number of cations in the zeolite structure and number of Al atoms in a unit cell of zeolite. In general, copper exchanged zeolites with low Si/Al ratios produce more methanol than those with higher Si/Al ratios even when zeolites have the same topologies.[33] Therefore, a direct comparison of methanol production between commercial zeolites with EDI and MER zeolite is difficult due to the large difference in Si/Al ratio.

Aluminium and silicon have different valencies and this leads to a negatively charged framework, which has to be balanced by the extra-framework cations. Therefore, more copper ions can be accommodated into the zeolite structure as the Al concentration increases. Therefore, high Si/Al ratio favours the formation of monomeric copper active site, whereas low Si/Al ratio favours the formation of copper clusters.[33] Thus, it is possible that the EDI framework with a very low Si/Al ratio favoured the formation of copper clusters and only a limited amount of $[Cu_2(\mu\text{-}O)]^{2+}$ has formed. As we hypothesise that the 8MR is most adequate environment for the formation of mono(μ-oxo) dicopper active site, the formation of copper clusters is not desired for the (8,4) MR framework.

Moreover, the Al concentration in the zeolite structure may also play a crucial role in the formation of mono(μ-oxo) dicopper active site as it can affect the distribution of number of Al atoms present in a 8-membered ring. Mahyuddin et al.[15] suggests that the formation of $[Cu_2(\mu\text{-}O)]^{2+}$ site requires two Al atoms separated by two Si atoms in a 8-membered ring. Therefore, it is possible that an optimal value of Si/Al atomic ratio of 6/2 favours the formation of the $[Cu_2(\mu\text{-}O)]^{2+}$ active site. Consequently, any Si/Al atomic ratio significantly lower or higher than 3 may reduce the activity of zeolite. Hence, the lower activity of copper exchanged EDI compared to copper exchanged mordenite may be attributed to the difference in the Si/Al ratio.

Structural Differences of 8MRs Both MER and EDI topologies have a small pore size around 3 Å whereas mordenite has a big pore size of 6.45Å.[22] Lobo et al. recently tested small pore zeolites for DMTM reaction and yielded better activity compared to previous studies.[12] The possible causes of good activity of small pore zeolites is further elucidated by Mahyuddin et al. by DFT studies.[34] They calculated the bond angles of the Cu-O-Cu bridge of mono(μ-oxo) dicopper active site of 8MR small pore zeolites and they found that lowering the bond angle of the Cu-O-Cu bridge stabilises the transition state for C-H bond cleavage. Thus, difference in pore size of zeolites cannot explain the lower activity of Cu-EDI compared to Cu-MOR.

As Cu-O-Cu bond angle is an important factor for the activation of the C-H bond of methane, the geometrical features of 8MR may play an important role in the activity of DMTM reaction. Hence, the 8MR structure of EDI and MER framework were compared to identify the difference in activity of MER and EDI frameworks for the DMTM reaction.

The schematic of the curvature of 8MR is shown in Figure 5. We will refer to θ shown in Figure 5 as bending angle of 8MR. Figure 6 shows the images of 8MRs present in EDI and MER framework viewed along (100) and (001) positions.

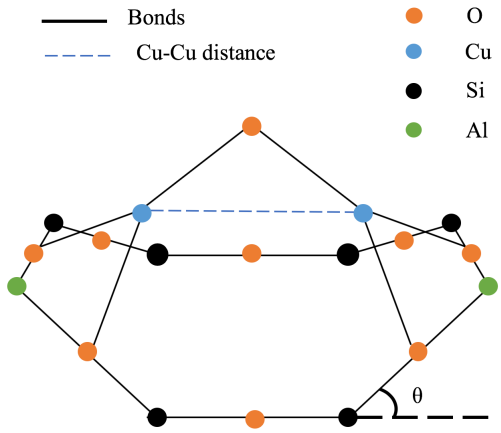

Figure 5. Schematic of a Cu-O-Cu active site formed in a bent 8MR.

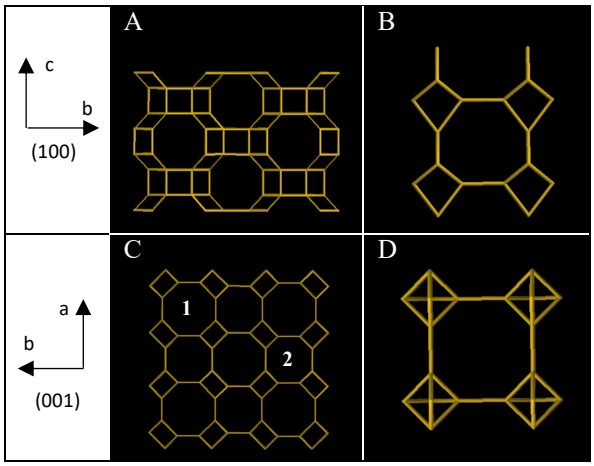

Figure 6. (A) MER and **(B)** EDI framework at (100) position. **(C)** MER and **(D)** EDI framework at (001) position.

As shown in Figure 6, EDI framework contains both regular (D) and irregular (B) 8MRs. Both 8MRs are not flat and form skewed structures in a 3D space similar to the 8MR structure shown in Figure 5. Irregular 8MR of EDI is less likely to act as a host for active sites for DMTM reaction as 8MRs of other topologies studied in past literatures mostly have regular shapes. For example, it has been verified that two 8MRs at the side pockets of mordenite have a regular octagon shape and can effectively form mono(μ-oxo) dicopper sites.[15] Therefore, we hypothesise that regular shaped 8MR is acting as the host of active sites in the case of EDI.

In contrast, MER framework only contains regular shaped 8 membered rings and the 8 MRs shown in A, C1 and C2 (Figure 6). The shape of 8MR in C1 is flat and all T atoms in the 8MR are located at the same plane, which has a bending angle of 0°. The shapes of 8 MRs shown in A and C2 are very similar and they are both skewed with high bending angles of around 45°.

The major difference of geometry of regular 8MRs of MER and EDI is the bending angle. Regular 8MR of EDI has a much lower bending angle compared to skewed 8MRs of MER. MER also contains 8MR with bending angle of 0. As mentioned earlier, two Al atoms need to be separated by two Si atoms to effectively form mono(μ-oxo) dicopper active sites. Therefore, we can consider the position of Al atoms within the 8MR structure as shown in Figure 5. The bending angle, θ, influences the distance between two Al atoms and this also affects the distance between two Cu^{2+} ions forming the active site. Increasing the bending angle of 8MR decreases the distance between two Al atoms and consequently, the distance between two copper ions also shortens. The distance between two copper ions directly affects the Cu-O-Cu angle;[34] hence, difference in bending angle can lead to a difference in activity of DMTM reaction. It is possible that the bending angle of flat 8MR was too low and skewed 8MR of MER was too high to form the optimal distance between copper ions. We believe that there may be an optimal value of bending angle which results in most effective C-H bond activation of methane. Thus, the difference in bending angle could be the cause of difference in activity between MER and EDI framework for the DMTM reaction.

Conclusion

Four different copper containing zeolite topologies of EDI, MER, PHI and GIS were tested for their suitability for direct methane to methanol (DMTM) reaction. As GIS framework is thermally unstable, it is not suitable for the DMTM reaction as it cannot withstand the high temperature activation step. The pH of copper (II) nitrate solution needs a careful monitoring as acidity causes dealumination of zeolites, which leads to the removal of Al atoms from the zeolite framework. Consequently, lattice defects formed by dealumination damage the zeolite framework and destabilise the structure. PHI structure, in particular, was more sensitive to this effect of acidity than the other structures studied. Cu-MER was not able to produce any methanol whereas Cu-EDI produced 4.55μmol CH_3OH/g catalyst. We also suggest there may be an optimal value of Si/Al ratio which favours the formation of $[Cu_2(\mu\text{-}O)]^{2+}$ active sites at 8MR as the Si/Al ratio affects important physical and chemical properties of the zeolite structure. We also hypothesise that the geometrical difference of 8MR of EDI and MER affects the distance between Cu^{2+} ions which may also affect the Cu-O-Cu bond angle. Therefore, the bending angle of 8MR may need to be in a certain range to achieve an optimal distance between two copper ions to stabilise the transition state for C-H bond cleavage and to effectively activate the C-H bond of methane.

Moreover, all as-synthesized zeolites should be tested for the reaction after ion exchange with a more dilute copper (II) nitrate solution, to ensure the structures are maintained. Hence, a more detailed analysis of structural difference of 8 MR can be achieved.

The effect of the Si/Al ratio on the DMTM reaction activity can also be further investigated by synthesizing studied zeolites with higher Si/Al ratios.

DFT modelling can effectively analyse the structural differences of 8MRs of different topologies and detailed data of distance between Cu^{2+} ions and Cu-O-Cu bond angle can be calculated. Thus, DFT modelling should be adopted to validate our hypothesis.

Acknowledgement

The authors greatly acknowledge the support of Ioannis Tzouganatos for the supervision of the project. We also acknowledge Patricia Carry and Kaho Cheung for the use of XRD and XRF equipment and providing relevant trainings. We thank Dr. Ines Biscaya Sememdo Pereira da Graca for providing thoughtful advices on zeolite synthesis and ion exchange. We acknowledge Professor David Chadwick for the use of heating plate and oven. The authors also acknowledge Dr. Mahmoud Ardakani for the use of SEM equipment and helping with the operation. We also thank Chin Lang for providing help on electrical equipment.

References

1. Lunsford, J. H. (2000) *Catalytic conversion of methane to more useful chemicals and fuels: a challenge for the 21st century.* Available from: http://www.sciencedirect.com/science/article/pii/S0920586100004569.

2. da Silva, M. J. (2016) *Synthesis of methanol from methane: Challenges and advances on the multi-step (syngas) and one-step routes (DMTM).* Available from: http://www.sciencedirect.com/science/article/pii/S0378382016300224.

3. Ravi, M., Ranocchiari, M. & van Bokhoven, J. A. (2017) The Direct Catalytic Oxidation of Methane

to Methanol—A Critical Assessment. *Angewandte Chemie International Edition.* 56 (52), 16464-16483. Available from: https://onlinelibrary.wiley.com/doi/abs/10.1002/anie.201702550. Available from: doi: 10.1002/anie.201702550.

4. Dinh, K. T., Sullivan, M. M., Serna, P., Meyer, R. J., Dincă, M. & Román-Leshkov, Y. (2018) Viewpoint on the Partial Oxidation of Methane to Methanol Using Cu- and Fe-Exchanged Zeolites. *ACS Catalysis.* 8 (9), 8306-8313. Available from: doi: 10.1021/acscatal.8b01180.

5. Periana, R. A., Taube, D. J., Evitt, E. R., Loffler, D. G., Wentrcek, P. R., Voss, G. & Masuda, T. (1993) A Mercury-Catalyzed, High-Yield System for the Oxidation of Methane to Methanol. *Science.* 259 (5093), 340-343. Available from: http://www.sciencemag.org/cgi/content/abstract/259/5093/340. Available from: doi: 10.1126/science.259.5093.340.

6. Periana, R. A., Taube, D. J., Gamble, S., Taube, H., Satoh, T. & Fujii, H. (1998) Platinum Catalysts for the High-Yield Oxidation of Methane to a Methanol Derivative. *Science.* 280 (5363), 560-564. Available from: http://www.sciencemag.org/cgi/content/abstract/280/5363/560. Available from: doi: 10.1126/science.280.5363.560.

7. Palkovits, R., Antonietti, M., Kuhn, P., Thomas, A. & Schüth, F. (2009) Solid catalysts for the selective low-temperature oxidation of methane to methanol. *Angewandte Chemie (International Ed. in English).* 48 (37), 6909-6912. Available from: https://www.ncbi.nlm.nih.gov/pubmed/19655358. Available from: doi: 10.1002/anie.200902009.

8. Mahyuddin, M. H., Shiota, Y., Staykov, A. & Yoshizawa, K. (2018a) Theoretical Overview of Methane Hydroxylation by Copper-Oxygen Species in Enzymatic and Zeolitic Catalysts. *Accounts of Chemical Research.* 51 (10), 2382-2390. Available from: https://www.ncbi.nlm.nih.gov/pubmed/30207444. Available from: doi: 10.1021/acs.accounts.8b00236.

9. Snyder, B. E. R., Bols, M. L., Schoonheydt, R. A., Sels, B. F. & Solomon, E. I. (2018) Iron and Copper Active Sites in Zeolites and Their Correlation to Metalloenzymes. *Chemical Reviews.* 118 (5), 2718-2768. Available from: https://www.ncbi.nlm.nih.gov/pubmed/29256242. Available from: doi: 10.1021/acs.chemrev.7b00344.

10. Groothaert, M. H., Smeets, P. J., Sels, B. F., Jacobs, P. A. & Schoonheydt, R. A. (2005) Selective Oxidation of Methane by the Bis(μ-oxo)dicopper Core Stabilized on ZSM-5 and Mordenite Zeolites. *Journal of the American Chemical Society.* 127 (5), 1394-1395. Available from: https://doi.org/10.1021/ja047158u. Available from: doi: 10.1021/ja047158u.

11. Smeets, P. J., Groothaert, M. H. & Schoonheydt, R. A. (2005) Cu based zeolites: A UV–vis study of the active site in the selective methane oxidation at low temperatures. *Catalysis Today.* 110 (3), 303-309. Available from: https://www.sciencedirect.com/science/article/pii/S0920586105006474. Available from: doi: 10.1016/j.cattod.2005.09.028.

12. Wulfers, M. J., Teketel, S., Ipek, B. & Lobo, R. F. (2015) Conversion of methane to methanol on copper-containing small-pore zeolites and zeotypes. *Chemical Communications (Cambridge, England).* 51 (21), 4447-4450. Available from: https://www.ncbi.nlm.nih.gov/pubmed/25679753. Available from: doi: 10.1039/C4CC09645B.

13. Park, M. B., Ahn, S. H., Mansouri, A., Ranocchiari, M. & van Bokhoven, J. A. (2017) Comparative Study of Diverse Copper Zeolites for the Conversion of Methane into Methanol. *ChemCatChem.* 9 (19), 3705-3713. Available from: https://onlinelibrary.wiley.com/doi/abs/10.1002/cctc.201700768. Available from: doi: 10.1002/cctc.201700768.

14. Woertink, J. S., Smeets, P. J., Groothaert, M. H., Vance, M. A., Sels, B. F., Schoonheydt, R. A. & Solomon, E. I. (2009) A $Cu_2O]^{2+}$ core in Cu-ZSM-5, the active site in the oxidation of methane to methanol. *Proc Natl Acad Sci USA.* 106 (45), 18908. Available from: http://www.pnas.org/content/106/45/18908.abstract. Available from: doi: 10.1073/pnas.0910461106.

15. Mahyuddin, M. H., Tanaka, T., Shiota, Y., Staykov, A. & Yoshizawa, K. (2018b) Methane Partial Oxidation over [Cu2(μ-O)]2+ and [Cu3(μ-O)3]2+ Active Species in Large-Pore Zeolites. *ACS Catalysis.* 8 (2), 1500-1509. Available from: doi: 10.1021/acscatal.7b03389.

16. Grundner, S., Markovits, M. A. C., Li, G., Tromp, M., Pidko, E. A., Hensen, E. J. M., Jentys, A., Sanchez-Sanchez, M. & Lercher, J. A. (2015) Single-site trinuclear copper oxygen clusters in mordenite for selective conversion of methane to methanol. *Nature Communications.* 6 7546. Available from: https://doi.org/10.1038/ncomms8546.

17. Palagin, D., Knorpp, A. J., Pinar, A. B., Ranocchiari, M. & van Bokhoven, J. A. (2017) Assessing the relative stability of copper oxide clusters as active sites of a CuMOR zeolite for methane to methanol conversion: size matters? *Nanoscale.* 9 (3), 1144-1153. Available from: http://dx.doi.org/10.1039/C6NR07723D. Available from: doi: 10.1039/C6NR07723D.

18. Kulkarni, A. R., Zhao, Z., Siahrostami, S., Nørskov, J. K. & Studt, F. (2016) Monocopper Active Site for

Partial Methane Oxidation in Cu-Exchanged 8MR Zeolites. *ACS Catalysis.* 6 (10), 6531-6536. Available from: doi: 10.1021/acscatal.6b01895.

19. Tomkins, P., Mansouri, A., Bozbag, S. E., Krumeich, F., Park, M. B., Alayon, E. M. C., Ranocchiari, M. & van Bokhoven, J. A. (2016) Isothermal Cyclic Conversion of Methane into Methanol over Copper-Exchanged Zeolite at Low Temperature. *Angewandte Chemie (International Ed. in English).* 55 (18), 5467-5471. Available from: https://www.ncbi.nlm.nih.gov/pubmed/27010863. Available from: doi: 10.1002/anie.201511065.

20. Tomkins, P., Ranocchiari, M. & van Bokhoven, J. A. (2017) Direct Conversion of Methane to Methanol under Mild Conditions over Cu-Zeolites and beyond. *Accounts of Chemical Research.* 50 (2), 418-425. Available from: https://www.ncbi.nlm.nih.gov/pubmed/28151649. Available from: doi: 10.1021/acs.accounts.6b00534.

21. Kulkarni, A. R., Zhao, Z., Siahrostami, S., Nørskov, J. K. & Studt, F. (2018) Cation-exchanged zeolites for the selective oxidation of methane to methanol. *Catalysis Science & Technology.* 8 (1), 114-123. Available from: doi: 10.1039/C7CY01229B.

22. Baerlocher, C. & McCusker, L. B. Database of Zeolite Structures: http://www.iza-structure.org/databases/

23. Sushkevich, V. L., Palagin, D., Ranocchiari, M. & van Bokhoven, J. A. (2017) Selective anaerobic oxidation of methane enables direct synthesis of methanol. *Science.* 356 (6337), 523. Available from: http://science.sciencemag.org/content/356/6337/523.abstract. Available from: doi: 10.1126/science.aam9035.

24. Chapter 41 - EDI Linde Type F Si(50), Al(50). In: (2001) Robson, H. & Lillerud, K. P. (eds.). *Verified Syntheses of Zeolitic Materials.* [e-book] Amsterdam, Elsevier Science. pp. 142-144. Available from: http://www.sciencedirect.com/science/article/pii/B9780444507037501393.

25. Oleksiak, M. D., Ghorbanpour, A., Conato, M. T., McGrail, B. P., Grabow, L. C., Motkuri, R. K. & Rimer, J. D. (2016) Synthesis Strategies for Ultrastable Zeolite GIS Polymorphs as Sorbents for Selective Separations. *Chemistry (Weinheim an Der Bergstrasse, Germany).* 22 (45), 16078. Available from: https://www.ncbi.nlm.nih.gov/pubmed/27588557.

26. Suresh, S., Karthikeyan, S. & Jayamoorthy, K. (2016) FTIR and multivariate analysis to study the effect of bulk and nano copper oxide on peanut plant leaves. *Journal of Science: Advanced Materials and Devices.* 1 (3), 343-350. Available from: https://www.sciencedirect.com/science/article/pii/S2468217916301125. Available from: doi: 10.1016/j.jsamd.2016.08.004.

27. Derkowski, A., Franus, W., Beran, E. & Czímerová, A. (2006) Properties and potential applications of zeolitic materials produced from fly ash using simple method of synthesis. *Powder Technology.* 166 (1), 47-54. Available from: http://www.sciencedirect.com/science/article/pii/S0032591006001628. Available from: doi: //doi.org/10.1016/j.powtec.2006.05.004.

28. Fletcher, P. & Townsend, R. P. (1985) Ion exchange in zeolites. The exchange of cadmium and calcium in sodium X using different anionic backgrounds. *Journal of the Chemical Society, Faraday Transactions 1: Physical Chemistry in Condensed Phases.* 81 (7), 1731-1744. Available from: doi: 10.1039/F19858101731.

29. Townsend, R. P. & Coker, E. N. (2001) Chapter 11 Ion exchange in zeolites. In: van Bekkum, H., Flanigen, E. M., Jacobs, P. A. & Jansen, J. C. (eds.). *Studies in Surface Science and Catalysis.* [e-book] , Elsevier. pp. 467-524. Available from: http://www.sciencedirect.com/science/article/pii/S0167299101802536.

30. Cook, T. E., Cilley, W. A., Savitsky, A. C. & Wiers, B. H. (1982) Zeolite A hydrolysis and degradation. *Environmental Science & Technology.* 16 (6), 344-350. Available from: https://doi.org/10.1021/es00100a008. Available from: doi: 10.1021/es00100a008.

31. Silaghi, M., Chizallet, C. & Raybaud, P. (2014) Challenges on molecular aspects of dealumination and desilication of zeolites. *Microporous and Mesoporous Materials.* 191 (June), 82-96. Available from: https://www.sciencedirect.com/science/article/pii/S1387181114001115. Available from: doi: 10.1016/j.micromeso.2014.02.040.

32. Sato, K., Nishimura, Y., Matsubayashi, N., Imamura, M. & Shimada, H. (2003) Structural changes of Y zeolites during ion exchange treatment: effects of Si/Al ratio of the starting NaY. *Microporous and Mesoporous Materials.* 59 (2), 133-146. Available from: https://www.sciencedirect.com/science/article/pii/S1387181103003056. Available from: doi: 10.1016/S1387-1811(03)00305-6.

33. Sushkevich, V. L., Palagin, D. & van Bokhoven, J. A. (2018) The Effect of the Active-Site Structure on the Activity of Copper Mordenite in the Aerobic and Anaerobic Conversion of Methane into Methanol. *Angewandte Chemie International Edition.* 57 (29), 8906-8910. Available from: https://onlinelibrary.wiley.com/doi/abs/10.1002/anie.201802922. Available from: doi: 10.1002/anie.201802922.

34. Mahyuddin, M. H., Staykov, A., Shiota, Y., Miyanishi, M. & Yoshizawa, K. (2017) Roles of Zeolite Confinement and Cu–O–Cu Angle on the

Direct Conversion of Methane to Methanol by [Cu2(μ-O)]2+-Exchanged AEI, CHA, AFX, and MFI Zeolites. *ACS Catalysis.* 7 (6), 3741-3751. Available from: doi: 10.1021/acscatal.7b00588.

Multi-Functional Metal Organic Frameworks for CO_2 Capture and Chiral Separation

Jessica Quigley and Narumi Wong
Department of Chemical Engineering, Imperial College London, U.K.

Abstract Metal organic frameworks (MOFs) have shown potential in both carbon capture and chiral separation and designing multi-functional MOFs for these two applications would enable easier entry into the market. In this work, we present an investigation into two isoreticular MOFs [Co-*L*-GG(bipy)$_{0.5}$]·(H_2O) (**1**) and [Co-*L*-GG(azpy)$_{0.5}$]·(H_2O) (**2**) (*L*-GG = glycyl-*L*(S)-glutamate, bipy = 4,4'-bipyridine, azpy = 4,4'-azobipyridine), synthesised from the chiral dipeptide *L*-GG and in the case of **2**, the photo-responsive azpy linker ligand. To assess their suitability as multi-functional MOFs, CO_2 adsorption tests and chiral separation studies were conducted, followed by a study into combined photo-responsive chiral separation. **1** showed comparable performance of CO_2 adsorption with other commonly reported MOFs designed for carbon capture, whilst changing the linker ligand between **1** and **2** led to adsorption of opposite enantiomers of 1-phenylethanol. UV illumination was observed to have the potential to increase enantiomeric excess of both MOFs, but the results were not entirely conclusive and merit further investigation.

Introduction

Metal organic frameworks (MOFs) have gained increased attention as an emerging class of materials due to their high porosity, large surface areas and structural tunability[1]. Fundamentally consisting of inorganic metals combined with organic linkers[2], MOFs exhibit a high degree of structural tunability; desirable properties such as chirality and stimuli-responsivity can be engineered into the structure through addition of carefully-selected ligands[3] .

With such attractive properties, MOFs have the potential for ubiquitous use, including clean energy applications such as gas storage, separation adsorbents, and catalysis[1]. Development of multi-functional MOFs that have more than one industrial application is desirable, as these will allow for potentially easier market penetration[4], along with the ability to handle more complex systems such as mixed pollutants[5] .

Combining the functionalities of CO_2 capture and chiral separation are investigated herein as these are two major applications in which MOFs are highly valuable. With rising atmospheric CO_2 levels[6], there is an increasing need for materials that are capable of capturing CO_2, especially from the outlet streams of process plants[7]. Liquid amines are commonly used industrial carbon capture agents; however, their regeneration process is energy-intensive[8], and there are economic and environmental concerns related to the degradation of amines[9]. Hence, there is a need for solid gas sorbents with high surface areas, high selectivity towards CO_2 but with sufficiently low interactions to minimise energy requirements of regeneration[7].

Previous research conducted on zeolites and activated carbon as potential sorbents did not yield satisfactory results with regards to the aforementioned criteria[7]. MOFs provide an alternative opportunity as a class of materials which may be suitable for CO_2 capture in industry as they can be structurally tuned to satisfy the requirements.

Another important application of MOFs is in chiral separation. Particularly in the pharmaceutical and fine chemicals industries, the separation of racemic molecules is a vital step[10] as our bodies are sensitive to differences in stereochemistry[11]. Difficulties in developing achiral synthesis methods of drug molecules[12] and the comparative ease of enantiomeric separation and its repeatability has led to extensive research being conducted on separation techniques of racemic mixtures[13].

Applicability of techniques such as chromatography and crystallisation resolution have been widely studied. High Performance Liquid Chromatography (HPLC) and Gas Chromatography (GC) use for separation are popular[13], but are costly. Additionally, crystallisation for enantiomeric separation, although lower in cost, does not recurrently meet the enantiomeric excess (**ee**) required by regulatory boards[14]. Synthesis of chiral zeolites was found to be challenging, and the low stability of developed prototypes upon removal of the guest solvent has rendered them unusable[15]. In contrast, synthesising MOFs with chiral functionalities is easier, making them excellent contenders as an alternative that is both low cost and highly effective at separation[1]. Furthermore, with their versatile structures, it is

possible to implement additional properties into these MOFs beyond chirality and high affinity for CO_2, such as photo-responsivity[3]. This gives rise to potential further applications in catalysis and separations for which the MOF can undergo cyclical regeneration by change of the stimulus, removing the need for high temperatures or pressures[3]. As an example, UV light could be used to induce desorption to regenerate the MOF.

A notable downside of MOFs is their need to undergo activation after synthesis, a process in which guest molecules trapped inside the pores of the MOF structure must be removed for the MOF to attain permanent porosity. This is necessary to access the very large internal surface areas of MOFs required to enable their high adsorption capacities. Current research into activation methods of MOFs is largely empirical[16] and has thus limited industrial implementation.

Previously, a family of isoreticular MOFs were synthesised using cobalt and a chiral dipeptide glycyl-*L*(S)-glutamate (*L*-GG) as part of a rigid 1D ladder backbone, separated by different sized linkers to change the pore size[17]. Although the MOFs were tested for CO_2 adsorption, and the effect of pore size on the chiral separation of glycidol and hydrobenzoin investigated, the possibility of applying the MOFs for CO_2 capture and chiral separation of other racemic mixtures was not investigated. In addition, of the linkers investigated, the 4,4'-azobipyridine (azpy) responds to UV light due to the presence of the azo bond, which causes the azpy ligand to undergo photochemical and thermal interconversion between the *trans* and *cis* forms[18] as shown in Figure 1. This implicates [Co-*L*-GG(azpy)$_{0.5}$] for increased multi-functionality and further applications.

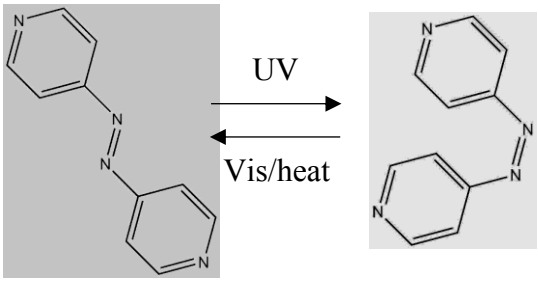

Figure 1. Reversible photochemical and thermal structural change of the azpy ligand from *trans* to *cis* when illuminated with UV, and from *cis* to *trans* when heated or illuminated with visible light.

In this work, we have synthesised the previously reported [Co-*L*-GG(bipy)$_{0.5}$]·(H_2O) (**1**) and [Co-*L*-GG(azpy)$_{0.5}$]·(H_2O) (**2**) MOFs shown in Figure 2, and investigated their applicability as multi-functional MOFs for CO_2 capture and chiral separation of other racemic mixtures. Furthermore, a novel setup was constructed to determine how UV light may affect the chiral separation ability of our MOFs. Combinations of chiral and light-responsive MOFs have been reported for catalysis[19,20], but to our knowledge, no research has been conducted on MOFs for light-responsive chiral separation.

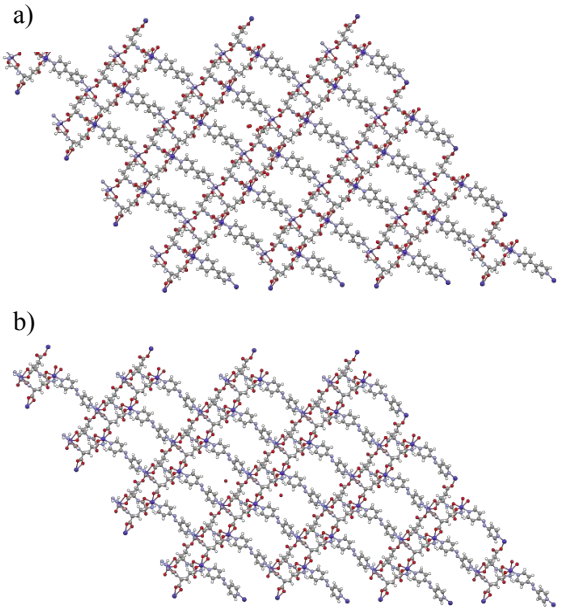

Figure 2. Ball-and-stick schematics of the framework structures of a) **1** and b) **2**[17].

Methods

Reagents and solvents. All reagents and solvents were used as received without further purification.

Synthesis of [Co-*L*-GG(bipy)$_{0.5}$]·(H_2O) (1) and [Co-*L*-GG(azpy)$_{0.5}$]·(H_2O) (2). This was synthesised following the previously reported procedure[17] with adaptations detailed in Section S1. Briefly, a mixture of $Co(OAc)_2 \cdot 4H_2O$ (0.3 mmol), Gly-Glu (*L*(S)-GG, 0.3 mmol), H_2O (6 mL), methanol (6 mL) and 4,4'-bipyridine (bipy, 0.3 mmol, structure shown in Figure S2) for **1** and 4,4'-azobipyridine (azpy, 0.3 mmol) for **2** were sealed in a scintillation vial and sonicated for 15 minutes to ensure the contents were fully dissolved, before heating in the oven at 80 °C for 2 hours. After cooling down to room temperature, the crystals were filtered and washed with methanol.

Powder X-ray diffraction (PXRD). PXRD spectra were obtained using a PANalytical X-Ray Diffractometer Instrument. The power

was set to 40 kV and 20 mA, and the X-ray source used was Copper K_α at 293 K.

Conventional activation. Non-activated forms of **1** and **2** were heated at 40 °C under vacuum for 4 hours to obtain [Co-*L*-GG(bipy)$_{0.5}$] (**1'**) and [Co-*L*-GG(azpy)$_{0.5}$] (**2'**), respectively.

Solvent exchange activation. **2** was immersed in solvents (ethanol, n-heptane, diethyl ether, n-pentane) for 5 days, filtered and washed with the same solvent as used in the immersion step. The samples were then treated at 25 °C under vacuum for 4 hours.

Collapsed MOF regeneration. After vacuum treatment, **2'** was immersed in tested solvents (ethanol, n-heptane, diethyl ether, n-pentane) for 24 hours at room temperature. In preparation for PXRD analysis, the samples were filtered and washed with the same solvent as used in the immersion step.

CO_2 sorption measurements. CO_2 adsorption isotherms were measured using the 3 Flex Micromeritic Instrument. The samples were activated under vacuum at 40 ºC overnight prior to measurement. Temperature was controlled by the Micromeritic ISO Controller. CO_2 adsorption was measured at low pressures from 0 to 750 mmHg.

Procedure for chiral adsorption. The samples (0.010 g) were placed in a glass vial and immersed in 0.1 mL of racemic mixture of 1-phenylethanol, 2-butanol or limonene. Samples were left for 24 hours at room temperature.

Procedure for chiral desorption. After adsorption, the samples were filtered and washed with diethyl ether to remove surface residue. The crystals were collected and transferred into a glass vial and immersed in 0.8 mL of methanol. After 24 hours at room temperature, 0.4 mL of the supernatant was extracted for analysis by gas chromatography.

Chiral gas chromatography. The GC chromatographs were obtained using a Shimadzu 2010 Plus gas chromatograph with an autosampler and a flame ionisation detector (FID). The analytes were separated using a Supelco Beta Dex 120 capillary column. For 1-phenylethanol, the conditions were: inject 1 µL with split ratio of 100:1, injection port temperature at 200 ºC, column temperature at 120 ºC for 19 min then ramped at 10 ºC/min to 170 ºC and holding for 6 min (post-elution of both enantiomers), FID at 210 ºC, helium carrier gas at 30 cm/s. For 2-butanol, the conditions were: inject 1 µL with split ratio of 40:1, injection port temperature at 200 ºC, column temperature at 30 ºC for 40 min then ramped at 10 ºC/min to 170 ºC and holding for 6 min, FID at 210 ºC, helium carrier gas at 15 cm/s. For limonene, the conditions were: inject 1 µL with split ratio of 50:1, injection port temperature at 250 ºC, column temperature at 80 ºC for 26 min then ramped at 10 ºC/min to 170 ºC and holding for 6 min, FID at 250 ºC, helium carrier gas at 25 cm/s.

Combined UV and Chiral Separation. Similar to the procedure for chiral adsorption and desorption aforementioned, the samples were immersed in 1-phenylethanol for 24 hours then desorbed in methanol whilst submerged in a water bath at pre-set temperatures to reduce impact of heating from the UV light. For the UV-illuminated samples, these were placed in an aluminium light-box as designed previously[21] to maximise UV exposure of the samples and block UV exposure for the non-UV-illuminated samples. Omnicure S1500 equipped with a 365 nm filter was used as the UV light source, and the intensity was set at half of the maximum (around 1.9 W/cm^2, measured with a R2000 radiometer). A photograph of the setup can be found in Figure S3.

Enantiomeric Excess (ee, %). Each sample was tested in triplicate, and the standard deviation was used to calculate the errors. To obtain the **ee** (%) values, the respective areas of each enantiomeric peak were obtained from the chromatograph and substituted into Equation (1):

$$\mathbf{ee}\ [\%] = \left(\frac{R-S}{R+S}\right) \times 100\% \qquad (1)$$

Results & Discussion

Synthesis and characterisation of new MOFs

PXRD calculated peaks[17] were used as comparisons for characterising both MOFs. Figure 3a) shows **1** was successfully synthesised and activated with a crystalline structure in accordance with that of the calculated peaks. The two peaks at 5.5° and 6.0° in Figure 3a) were previously seen when **1** was exposed to air, supporting the hypothesis that the leftmost peak arises from the increased torsion between the two pyridine rings across some of the bipy ligands, decreasing symmetry[17]. This is caused by the presence of solvent molecules left in the structure after the synthesis process. PXRD of **1'** shows these guest molecules were removed during the activation process, leaving a single peak at 6.0°. Guest molecule removal during activation therefore decreases the maximum pore size present in the framework[22].

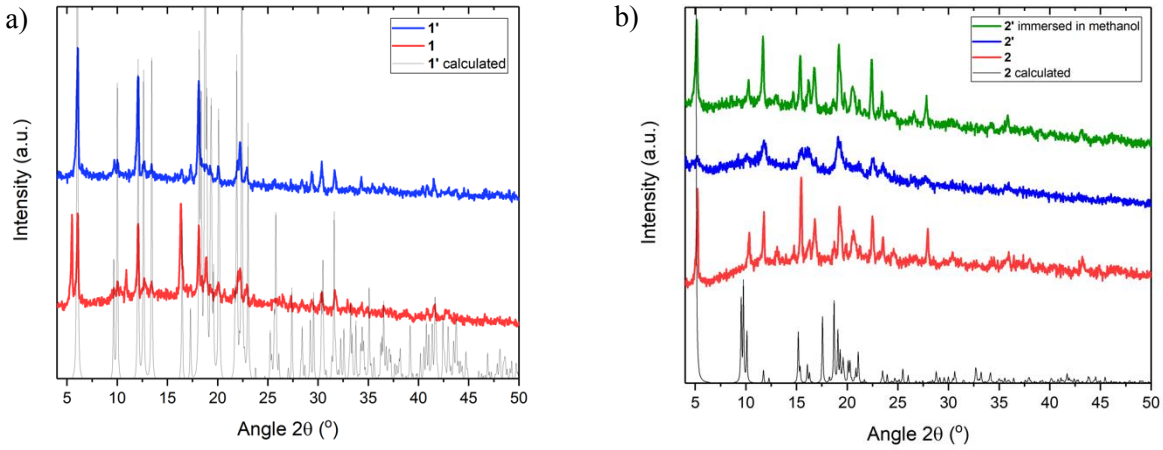

Figure 3. PXRD patterns showing a) the calculated peaks[17] of **1'**, experimentally obtained **1** and **1'**, and b) the calculated peaks[17] of **2**, experimentally obtained **2** and **2'**, and **2'** after immersion in methanol overnight.

Figure 3b) shows that whilst **2** was successfully synthesised in crystalline form, the conventional activation procedure used for **1** caused structural collapse and loss of crystallinity for **2'**. This loss of structural integrity can be attributed to the capillary forces caused by the surface tension of the guest solvent molecules, occurring during their phase change from liquid to gas as **2** is heated under vacuum[23-25]. Although it was reported that the MOFs maintained high structural integrity after undergoing the conventional activation procedure[17], this was not observed for **2**, so a series of alternative methods were considered. The first of these was liquid solvent exchange followed by heating under vacuum. By replacing the guest solvents in the MOF structure after synthesis with a lower surface tension solvent, a gentler heating under vacuum process can be applied, as lower surface tension solvents have lower cohesive forces and reduced boiling points, minimising the capillary forces causing structural collapse[16,26]. Ethanol, n-heptane, diethyl ether and n-pentane were selected as they have a lower surface tension than methanol. The solvent exchange procedure followed by vacuum treatment was applied but Figure S4 shows the evacuation process continued to cause structural collapse of **2** for every solvent.

Current activation methods are largely empirical[16], so a series of other changes to the activation procedure were attempted as outlined below, and the results are shown in Figure S5. These were considered as they have been reported as ensuring successful activation of other MOFs in literature. Increasing the rate of cooling upon removal from the vacuum oven, changing the rate of evacuation, and heating the MOFs without vacuum were attempted without success[27].

The experimentally obtained internal surface area can be estimated via the Brunauer-Emmett-Teller (BET) method using CO_2 adsorption isotherms[28], and compared to the predicted surface areas calculated using grand-canonical Monte Carlo simulations[29], enabling broad assessment of the effectiveness of different activation procedures. It is therefore possible that the activation of **1** could be improved, but this was not explored further in this report. Similarly, activation of **2** could be optimised using a different method that avoids the liquid-gas phase change – both use of supercritical CO_2 or freeze-drying using benzene or cyclohexane have been shown as effective activation methods of MOFs that undergo structural collapse during conventional activation[30].

Another noteworthy observation was the possible regeneration of the structurally collapsed **2'** to the previously observed post-synthesis structure of **2**. Figure 3b) shows that immersion in methanol resulted in restoration of porosity and structural integrity, whilst Figure S6 shows immersion in solvents with a surface tension lower than methanol (ethanol, n-heptane, diethyl ether, n-pentane) had no effect on restoring porosity. This indicates that **2** does not experience permanent structural collapse since the presence of methanol as a guest molecule can restore its original porosity and structure.

There is limited literature documenting the phenomenon of structural regeneration of collapsed MOFs when immersed in a solvent, most of which explicitly identifies the restoring solvents as solvents participating in the synthesis process[31,32], which applies in the case of **2**. This structural restoration is more widely reported for coordination polymers, where the change between crystalline and amorphous structures has indicated a "recoverable collapsing" through

use of a restoring solvent agent, thereby decreasing the need for robust coordination polymers[33].

CO_2 adsorption measurements

To investigate the suitability of these MOFs for CO_2 capture, CO_2 sorption measurements were conducted at two different temperatures: 273 K and 298 K. The resulting isotherms are presented in Figure 4.

As it was observed that **2** collapsed when the guest solvent was removed by vacuum, sorption measurements were conducted on **1**, **1'**, **2**, and **2'** to also assess the effect of the conventional activation procedure.

Figure 4a) and Figure 4b) show that, at 750 mmHg, **1'** adsorbed 56.75 cm^3/g at 273 K and 40.67 cm^3/g of CO_2 at 298 K, consistently achieving a higher quantity of CO_2 adsorbed compared to **1**. This is as expected, since the PXRD measurements of **1'** indicated successful removal of the guest solvent molecules, rendering a larger accessible pore area for CO_2 molecules.

As the CO_2 adsorption tests were conducted under vacuum, necessitated by the testing equipment, it is likely that **2** underwent a reduction in porosity, forming a structure similar to that of **2'**. Thus, as exhibited in Figure 4c) and Figure 4d), both **2** and **2'** had comparatively lower values for CO_2 adsorption quantity, with **2'** adsorbing, at 750 mmHg, 7.04 cm^3/g at 273 K and 5.86 cm^3/g at 298 K. **2** had a higher adsorption at 298 K compared to **2'**, as it did not undergo the overnight vacuum treatment and so retained greater structural integrity. However, at 273 K, we do not see a significant difference between **2** and **2'**, likely because the 273 K isotherms were obtained after the 298 K isotherms were measured, during which the structure of **2** was affected. Comparing the quantity of CO_2 adsorbed at 1 bar (750 mmHg) 298 K with other reported MOFs in literature for carbon capture, the performance of **1'** is approximately similar to that of UiO-66[34], whereas **2'** is an order of magnitude lower, suggesting that it is unsuitable as a carbon capture material.

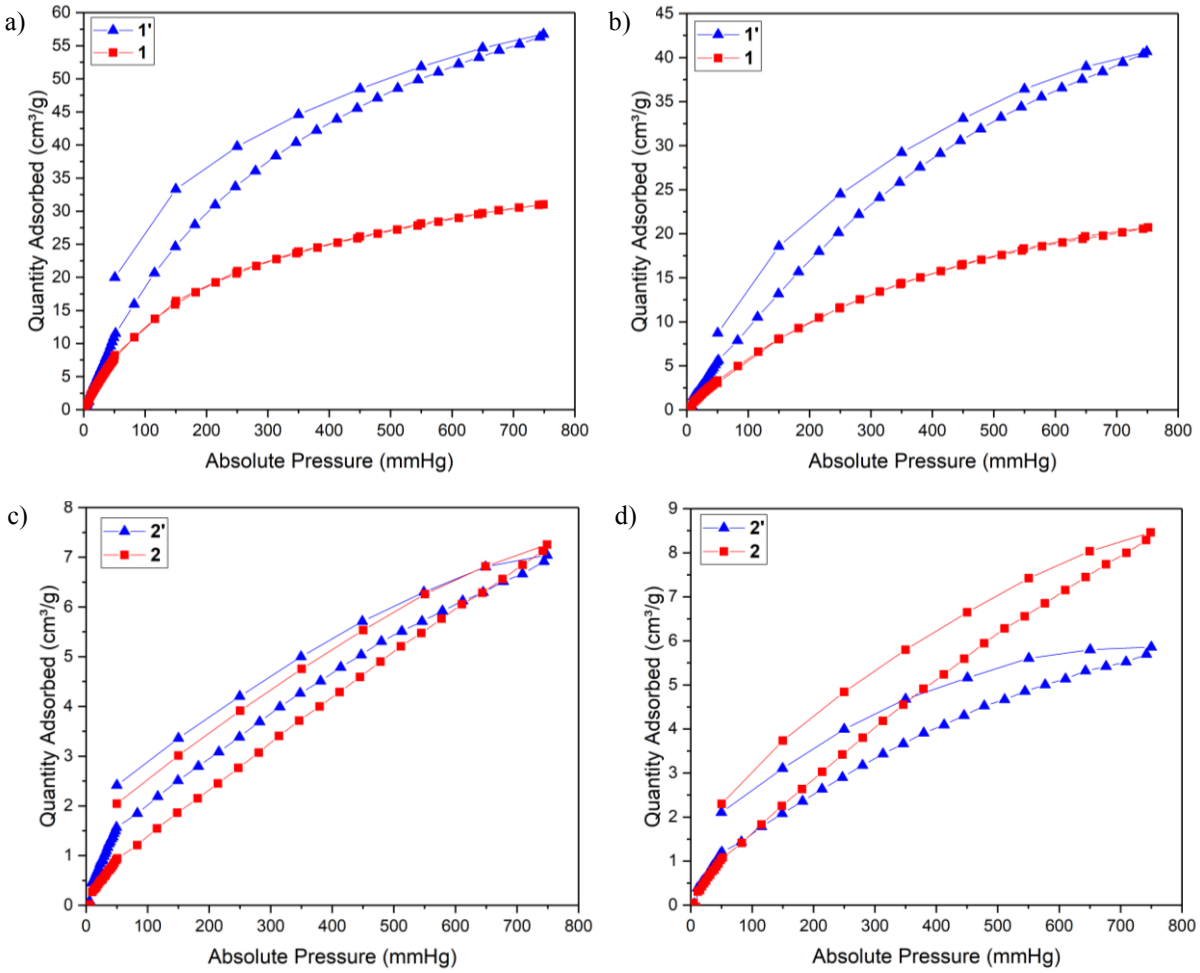

Figure 4. CO_2 adsorption isotherms of **1** and **1'** measured at a) 273 K, b) 298 K, and **2** and **2'** at c) 273 K, and d) 298 K.

From these isotherms at 273 K and 298 K, Clausius-Clapeyron fitting[35] was performed to obtain the respective heats of adsorption of CO_2 for both vacuum treated samples (see Figure S7). **1'** had an isosteric heat of adsorption of -21.81 ± 1.65 kJ/mol and **2'** of -7.74 ± 1.25 kJ/mol in the calculated loading ranges. The negative values indicate the exothermic nature of the adsorption process and explain the higher amount of CO_2 adsorbed at lower temperatures[36]. The isosteric heat values decreased by a small amount when the surface loading increased but given the values did not differ significantly over the range, both surfaces are energetically homogeneous[37]. Interestingly, **1'** had an isosteric heat of adsorption in a range similar to that of the commonly explored UiO-66[34], and outperforms several cases of industrially used activated carbon[38,39], which has been studied for CO_2 capture due to its large surface area and moderate adsorption strength compared to zeolites, leading to easier desorption[40]. The higher magnitude of the heat of adsorption of **1'** indicates a greater selectivity towards CO_2, thereby demonstrating its potential in industry.

There is potential for **2** to be used as a light-responsive MOF for CO_2 capture, and this could be confirmed by carrying out CO_2 sorption measurements under UV light[21]. This, along with BET surface area calculations which would require an elevated operating pressure, were not pursued due to equipment setup limitations.

Chiral separation studies

The synthesised MOFs were expected to display chiral recognition behaviour due to the presence of the chiral *L*-GG ligand. They were tested with three different racemic mixtures (1-phenylethanol, 2-butanol and limonene) to assess their suitability for chiral separation. 1-phenylethanol would show the MOFs' affinity for aromatic secondary alcohols, 2-butanol for aliphatic secondary alcohols and limonene for bulkier terpenes.

The resulting **ee** values can be found in Table 1. Interestingly, **1** and **2** (and by extension **1'** and **2'**) preferentially adsorbed opposite enantiomers of 1-phenylethanol. This is postulated to be due to hydrogen bonding interactions between the -OH group of the 1-phenylethanol and the O and N of the chiral pillars in the MOF structures. The difference in **1** and **2** arises from the respective linker ligands used. These additional N atoms within the azo bond in the azpy linker compared to the bipy linker provide more possibilities for hydrogen bonding and affect the position of the chiral pillars in the structure. These structural changes could cause this preferential adsorption of the S enantiomer by **2** and the R enantiomer by **1**, as hydrogen bonding has been reported to play a key role in enantiomer selection[41]. To elucidate the interactions from the hydrogen bonds between the chiral MOF scaffolds and the 1-phenylethanol, X-ray single-crystal diffraction could be used, but this would require synthesis of larger MOF crystals[41]. Regardless, this implies substituting a linker ligand, as opposed to developing a synthesis procedure for a new MOF, can be used to facilitate adsorption of opposite enantiomers.

Table 1. Averaged **ee** values of **1**, **1'**, **2**, and **2'** for chiral separation of 1-phenylethanol, 2-butanol and limonene. Positive values indicate the R enantiomer in excess; negative values indicate the S enantiomer in excess.

Racemic Mixture	MOF	ee [%]
1-phenylethanol	**1**	13.4 ± 0.6
	1'	9.6 ± 0.9
	2	- 20.5 ± 0.5
	2'	- 9.8 ± 3.3
2-butanol	**1**	-
	1'	-
	2	-
	2'	-
Limonene	**1**	0.3 ± 0.1
	1'	4.6 ± 1.4
	2	-
	2'	-

Another interesting result was that neither **1**, **1'**, **2** nor **2'** adsorbed 2-butanol. The size of 2-butanol is smaller than 1-phenylethanol, eliminating the possibility of the pores being too small to adsorb 2-butanol. The MOFs' adsorption preferences for 1-phenylethanol over 2-butanol may be due to interactions between the benzene ring in the 1-phenylethanol and the MOFs.

As for the limonene, **2** and **2'** did not adsorb any, whereas **1** and **1'** showed adsorption, but weak chiral separation with preference for the R enantiomer. The low stereoselectivity of **1** and **1'** could be due to the small pore size relative to the limonene molecules such that they are spatially constrained and significantly limiting the effect of the chiral recognition functionality[42]. Increased flexibility of the azpy ligand relative to the bipy ligand could have led to a less rigid framework; as a result, the pore size of **2** may not be fixed during liquid adsorption processes, resulting in no limonene adsorption.

Regarding the difference between the vacuum treated and non-vacuum treated samples, both **1** and **2** exhibited a higher **ee** than **1'** and **2'**. For **2**

and **2'**, this is consistent with the loss of porosity after vacuum treatment. As for **1** and **1'**, the reduced performance following vacuum treatment is likely to result from the decrease in pore length from **1** to **1'** seen from the PXRD measurements, in accordance with literature[43].

Combined UV light and chiral separation studies

As the azo bond in the azpy linker of the structure of **2** is photo-responsive, as reported in literature[18,21], combined UV light and chiral separation tests were carried out to explore further possible applications. To evaluate the effect of UV light on the chiral separation of 1-phenylethanol, the samples were exposed to UV light during both the adsorption and desorption steps.

Table 2. Averaged **ee** values of **1** and **2** for chiral separation of 1-phenylethanol at 30 ºC and 50 ºC with UV and without UV treatment. Positive values indicate the R enantiomer in excess; negative values indicate the S enantiomer in excess.

Temperature [ºC]	MOF	UV (Y/N)	ee [%]
30	**1**	Y	16.5 ± 0.1
		N	13.6 ± 0.1
	2	Y	- 22.5 ± 0.5
		N	- 18.0 ± 0.1
50	**1**	Y	20.6 ± 0.2
		N	12.6 ± 0.1
	2	Y	- 21.6 ± 0.1
		N	- 21.8 ± 0.1

Table 2 gives the resulting **ee** values. As observed in the previous chiral separation studies, **1** and **2** continue to show a preference for opposite enantiomers. For the tests conducted at 30 ºC, the effect of the UV light on the chiral separation was inconclusive, as the **ee** for both **1** and **2** increased by an **ee**-magnitude of only 2.9 % and 4.5 %, respectively, when exposed to UV light. Although the experiments were conducted in a water bath to maintain temperature uniformity across all samples, it is possible that the UV-exposed samples underwent additional heating from the UV source, affecting their **ee** values.

Measurements were also conducted at 50 ºC to reduce this heating effect. Interestingly, **1** showed an 8 % increase in **ee**, even though the bipy ligand has not been reported in literature to respond to UV light[44]. In comparison, the effect of the UV light on **2** was negligible. Regarding the lack of noticeable effect of the UV light on **2** at 50 ºC, this could be due to competing thermal and UV effects. Azobenzene, which features the photo-responsive azo bond, is reported to undergo conformation changes from *trans* to *cis* when illuminated with UV light of 320 - 350 nm, which can be reversed by heating above 40 ºC[18]. It is therefore likely that **2** also exhibits structural sensitivity to both temperature and UV light. Further investigation into the transformation temperature is necessary to discern their competing effects. Hence, it is postulated that the results taken at 50 ºC are similar because the temperature is above the transformation temperature, effectively undoing the structural change caused by the UV light. The role of UV light in the increase in **ee** of **1** is not clear and merits further investigation using X-ray single-crystal diffraction. Recently, the use of UV light to activate MOFs, including HKUST-1, via a localised photothermal effect was reported[45]. Though these tests were conducted on samples that were dried and not immersed in solvent, it was shown that when UV light was placed too near to HKUST-1, it resulted in reduced crystallinity and porosity due to thermal degradation. The original synthesis paper also suggests that there is an inverse relationship between the amount adsorbed and the **ee**[17]. Hence, it is possible that the UV treatment of **1** is too intense, causing a decrease in crystallinity and subsequently reducing the amount adsorbed, leading to a higher **ee**. These results warrant further exploration using this novel technique, and the effect of UV on other chiral MOFs should be investigated to see if the increase in **ee** is a recurring trend. If so, UV light could be introduced as a means of enhancing enantiomeric selectivity for chiral separation.

Conclusions

Upon successful synthesis of **1** and **2**, the conventional activation method of heating under vacuum increased the crystallinity across **1** to **1'** but was unsuitable for activation of **2** as it resulted in structural collapse. This reduction in porosity was found to be a reversible change; immersion of **2'** in methanol restored its initial structure of **2**. This ability to recover MOFs after structural collapse has applications in both MOF activation research, where structural collapse is a common result of unsuccessful activation procedures, and industry, as it presents a more sustainable alternative to repeated MOF synthesis.

With regards to carbon capture functionality, **1'** has a similar isosteric heat of adsorption of CO_2 to that of activated charcoal and other MOFs designed for carbon capture as well as a

comparable CO_2 adsorption capacity, indicating its potential applications in this field.

The presence of either the azpy or bipy linker has a significant effect on the MOF properties; **1** and **2** adsorb opposite enantiomers when exposed to the same racemic mixture and their chiral recognition responds differently to temperature changes and UV illumination. The effect of activation of MOFs on the adsorption and **ee** has not been quantitatively assessed but vacuum treatment has been shown to decrease the **ee** for both **1** and **2**. Although the UV chirality studies are inconclusive due to potential temperature differences across samples, the results suggest that exposure to UV light influences the chiral recognition of both MOFs. Thus, combined UV and chiral separation opens up new research directions of accessing enhanced enantiomeric separation efficiency.

Acknowledgements
J. Q. and N. W. would like to thank everyone in the Ladewig Group for the support and help received, particularly Nicholaus Prasetya and Ben Slater for their insight on photo-responsive and chiral MOFs.

Supporting Information
Supporting information is accessible in the file attached.

References
1. Zhou, H.; Long, J. R.; Yaghi, O. M. Introduction to metal-organic frameworks. *Chem. Rev.* **2012**, *112*, 673-674.
2. Furukawa, H.; Cordova, K. E.; O'Keeffe, M.; Yaghi, O. M. The Chemistry and Applications of Metal-Organic Frameworks. *Science* **2013**, *341*, 1230444.
3. Coudert, F. Responsive Metal-Organic Frameworks and Framework Materials: Under Pressure, Taking the Heat, in the Spotlight, with Friends. *Chem. Mater.* **2015**, *27*, 1905-1916.
4. Silva, P.; Vilela, S. M. F.; Tomé, J. P. C.; Almeida Paz, F. A. Multifunctional Metal-Organic Frameworks: from Academia to Industrial Applications. *Chem. Soc. Rev.* **2015**, *44*, 6774-6803.
5. Chen, Y.; Chen, F.; Zhang, S.; Cai, Y.; Cao, S.; Li, S.; Zhao, W.; Yuan, S.; Feng, X.; Cao, A.; Ma, X.; Wang, B. Facile Fabrication of Multifunctional Metal-Organic Framework Hollow Tubes To Trap Pollutants. *J. Am. Chem. Soc.* **2017**, *139*, 16482-16485.
6. ProOxygen CO2.earth. *https://www.co2.earth/* (accessed 1st December, 2018).
7. Sumida, K.; Rogow, D. L.; Mason, J. A.; McDonald, T. M.; Bloch, E. D.; Herm, Z. R.; Bae, T.; Long, J. R. Carbon Dioxide Capture in Metal-Organic Frameworks. *Chem. Rev.* **2012**, *112*, 724-781.
8. Haszeldine, R. S. Carbon Capture and Storage: How Green Can Black Be? *Science* **2009**, *325*, 1647-1652.
9. Yu, C.; Huang, C.; Tan, C. A Review of CO2 Capture by Absorption and Adsorption. *Aerosol and Air Quality Research* **2012**, *12*, 745-769.
10. Peng, Y.; Gong, T.; Zhang, K.; Lin, X.; Liu, Y.; Jiang, J.; Cui, Y. Engineering chiral porous metal-organic frameworks for enantioselective adsorption and separation. *Nature Communications* **2014**, *5*, 4406.
11. Maier, N. M.; Franco, P.; Lindner, W. Separation of enantiomers: needs, challenges, perspectives. *J. Chromatogr. A* **2001**, *906*, 3-33.
12. Toda, F. *Enantiomer Separation: Fundamentals and Practical Methods;* Springer Netherlands: 2004; .
13. Ward, T. J.; Ward, K. D. Chiral Separations: A Review of Current Topics and Trends. *Anal. Chem.* **2012**, *84*, 626-635.
14. Wang, Y.; Chen, A. M. Enantioenrichment by Crystallization. *Organic Process Research & Development* **2008**, *12*, 282-290.
15. Yu, J.; Xu, R. Chiral zeolitic materials: structural insights and synthetic challenges. *J. Mater. Chem.* **2008**, *18*, 4021-4030.
16. Ma, J.; Kalenak, A. P.; Wong-Foy, A. G.; Matzger, A. J. Rapid Guest Exchange and Ultra-Low Surface Tension Solvents Optimize Metal–Organic Framework Activation. *Angew. Chem. Int. Ed.* **2017**, *56*, 14618-14621.
17. Stylianou, K. C.; Gómez, L.; Imaz, I.; Verdugo-Escamilla, C.; Ribas, X.; Maspoch, D. Engineering Homochiral Metal-Organic Frameworks by Spatially Separating 1D Chiral Metal-Peptide Ladders: Tuning the Pore Size for Enantioselective Adsorption. *Chem. Eur. J.* **2015**, *21*, 9964-9969.
18. Merino, E.; Ribagorda, M. Control over molecular motion using the cis-trans photoisomerization of the azo group. *Beilstein J. Org. Chem.* **2012**, *8*, 1071-1090.
19. Wu, P.; He, C.; Wang, J.; Peng, X.; Li, X.; An, Y.; Duan, C. Photoactive Chiral Metal–

Organic Frameworks for Light-Driven Asymmetric α-Alkylation of Aldehydes. *J. Am. Chem. Soc.* **2012**, *134*, 14991-14999.
20. Zhang, Y.; Guo, J.; Shi, L.; Zhu, Y.; Hou, K.; Zheng, Y.; Tang, Z. Tunable chiral metal organic frameworks toward visible light–driven asymmetric catalysis. *Sci. Adv.* **2017**, *3*, e1701162.
21. Prasetya, N.; Ladewig, B. P. Dynamic photo-switching in light-responsive JUC-62 for CO 2 capture. *Scientific Reports* **2017**, *7*, 13355.
22. Bragg, W. L. The diffraction of short electromagnetic waves by a crystal. *Proc. Camb. Phil. Soc.* **1912**, *XVII*, 43-57.
23. Mondloch, J. E.; Karagiaridi, O.; Farha, O. K.; Hupp, J. T. Activation of metal-organic framework materials. *CrystEngComm* **2013**, *15*, 9258-9264.
24. Howarth, A. J.; Peters, A. W.; Vermeulen, N. A.; Wang, T. C.; Hupp, J. T.; Farha, O. K. Best Practices for the Synthesis, Activation, and Characterization of Metal–Organic Frameworks. *Chem. Mater.* **2017**, *29*, 26-39.
25. Mondloch, J. E.; Katz, M. J.; Planas, N.; Semrouni, D.; Gagliardi, L.; Hupp, J. T.; Farha, O. K. Are Zr6-based MOFs water stable? Linker hydrolysis vs. capillary-force-driven channel collapse. *Chem. Commun.* **2014**, *50*, 8944-8946.
26. Engel, E. R.; Jouaiti, A.; Bezuidenhout, C. X.; Hosseini, M. W.; Barbour, L. J. Activation-Dependent Breathing in a Flexible Metal–Organic Framework and the Effects of Repeated Sorption/Desorption Cycling. *Angew. Chem. Int. Ed.* **2017**, *56*, 8874-8878.
27. Barrio, J. P.; Rebilly, J.; Carter, B.; Bradshaw, D.; Bacsa, J.; Ganin, A. Y.; Park, H.; Trewin, A.; Vaidhyanathan, R.; Cooper, A. I.; Warren, J. E.; Rosseinsky, M. J. Control of Porosity Geometry in Amino Acid Derived Nanoporous Materials. *Chem. Eur. J.* **2008**, *14*, 4521-4532.
28. Kim, K. C.; Yoon, T. U.; Bae, T. S. Applicability of using CO_2 adsorption isotherms to determine BET surface areas of microporous materials. *Microporous and Mesoporous Materials* **2016**, *224*, 294-301.
29. Walton, K. S.; Snurr, R. Q. Applicability of the BET Method for Determining Surface Areas of Microporous Metal-Organic Frameworks. *J. Am. Chem. Soc.* **2007**, *129*, 8552-8556.
30. Farha, O. K.; Hupp, J. T. Rational Design, Synthesis, Purification, and Activation of Metal-Organic Framework Materials. *Accounts of Chemical Research* **2010**, *43*, 1166-1175.
31. Xue, M.; Li, B.; Qiu, S.; Chen, B. Emerging functional chiral microporous materials: synthetic strategies and enantioselective separations. *Materials Today* **2016**, *19*, 503-515.
32. Seo, J. S.; Whang, D.; Lee, H.; Jun, S. I.; Oh, J.; Jeon, Y. J.; Kim, K. A homochiral metal-organic porous material for enantioselective separation and catalysis. *Nature* **2000**, *404*, 982-986.
33. Uemura, K.; Kitagawa, S.; Kondo, M.; Fukui, K.; Kitaura, R.; Chang, H.; Mizutani, T. Novel Flexible Frameworks of Porous Cobalt(II) Coordination Polymers That Show Selective Guest Adsorption Based on the Switching of Hydrogen-Bond Pairs of Amide Groups. *Chem. Eur. J.* **2002**, *8*, 3587-3600.
34. Cmarik, G. E.; Kim, M.; Cohen, S. M.; Walton, K. S. Tuning the Adsorption Properties of UiO-66 via Ligand Functionalization. *Langmuir* **2012**, *28*, 15606-15613.
35. Hill, T. L. Statistical Mechanics of Adsorption. V. Thermodynamics and Heat of Adsorption. *J. Chem. Phys.* **1949**, *17*, 520-535.
36. Shafeeyan, M. S.; Daud, W. M. A. W.; Shamiri, A.; Aghamohammadi, N. Adsorption equilibrium of carbon dioxide on ammonia-modified activated carbon. *Chemical Engineering Research and Design* **2015**, *104*, 42-52.
37. He, Y.; Yun, J.; Seaton, N. A. Adsorption Equilibrium of Binary Methane/Ethane Mixtures in BPL Activated Carbon: Isotherms and Calorimetric Heats of Adsorption. *Langmuir* **2004**, *20*, 6668-6678.
38. Guo, B.; Chang, L.; Xie, K. Adsorption of Carbon Dioxide on Activated Carbon. *Journal of Natural Gas Chemistry* **2006**, *15*, 223-229.
39. Garcés, S. I.; Villarroel-Rocha, J.; Sapag, K.; Korili, S. A.; Gil, A. Comparative Study of the Adsorption Equilibrium of CO2 on Microporous Commercial Materials at Low Pressures. *Ind. Eng. Chem. Res.* **2013**, *52*, 6785-6793.
40. Sircar, S.; Golden, T. C.; Rao, M. B. Activated Carbon for Gas Separation and Storage. *Carbon* **1996**, *34*, 1-12.

41. Li, P.; He, Y.; Guang, J.; Weng, L.; Zhao, J. C.; Xiang, S.; Chen, B. A Homochiral Microporous Hydrogen-Bonded Organic Framework for Highly Enantioselective Separation of Secondary Alcohols. *J. Am. Chem. Soc.* **2014***, 136*, 547-549.
42. Gu, Z.; Grosjean, S.; Bräse, S.; Wöll, C.; Heinke, L. Enantioselective adsorption in homochiral metal-organic frameworks: the pore size influence. *Chem. Commun.* **2015***, 51*, 8998-9001.
43. Navarro-Sánchez, J.; Argente-García, A. I.; Moliner-Martínez, Y.; Roca-Sanjuán, D.; Antypov, D.; Campíns-Falcó, P.; Rosseinsky, M. J.; Martí-Gastaldo, C. Peptide Metal-Organic Frameworks for Enantioselective Separation of Chiral Drugs. *J. Am. Chem. Soc.* **2017***, 139*, 4294-4297.
44. Coleman, B. D.; Fuoss, R. M. Quaternization kinetics. I. Some pyridine derivatives in tetramethylene sulfone. *J. Am. Chem. Soc.* **1955***, 77*, 5472-5476.
45. Espín, J.; Garzón-Tovar, L.; Carné-Sánchez, A.; Imaz, I.; Maspoch, D. Photothermal Activation of Metal−Organic Frameworks Using a UV−Vis Light Source. *ACS Appl. Mater. Interfaces* **2018***, 10*, 9555-9562.

Industrial Viability of Metal-Organic Frameworks in Post-Combustion Carbon Capture: The Effect of Impurities

Caitlin Doherty and George Wright
Department of Chemical Engineering, Imperial College London, U.K.

Abstract: Metal-Organic Frameworks (MOFs) are a promising class of adsorbent materials for post combustion carbon capture. However, the effect of flue gas impurities on CO_2 uptake in MOFs is not well studied. This study investigates the effect of pre-exposure to water and aqueous SO_2 on the CO_2 capacity in two MOFs: HKUST-1 and UiO-66-NH_2. Single component CO_2 uptake was measured using thermogravimetric analysis (TGA) at 1.0 bara and 30°C. HKUST-1 demonstrated the highest CO_2 uptake of 2.23 mmol g^{-1} without pre-exposure to aqueous environments. Water and aqueous SO_2 solution were observed to degrade the crystalline form of HKUST-1, decreasing the porosity and reducing CO_2 uptake. Interestingly, UiO-66-NH_2 displayed opposite trends, showing the highest uptake of 1.86 mmol g^{-1} after exposure to water, and an uptake of 1.66 mmol g^{-1} after exposure to aqueous SO_2. This was attributed to an increased porosity and the possible formation of missing-linker defects. Similar effects were observed in a binary CO_2:N_2 system using a dynamic breakthrough analyser at 1.1 barg and 25°C. The heat capacity of both MOFs was measured to gain insight into the industrial viability of MOFs for temperature swing adsorption (TSA). HKUST-1 showed a heat capacity ranging from 1.56-2.46 J g^{-1} °C^{-1}, with UiO-66-NH_2 ranging from 1.13-1.94 J g^{-1} °C^{-1} in the temperature range 40-200°C. These low values imply potential regeneration energy savings compared to existing alkanolamine absorbent processes. Overall, pre-treating UiO-66-NH_2 with water could be a promising technique to enhance CO_2 uptake in post-combustion carbon capture, and the low heat capacity range of MOFs further validates their potential.

Keywords: Metal-Organic Frameworks, UiO-66-NH_2, HKUST-1, water, SO_2, CO_2 uptake, heat capacity, missing-linker defects, porosity, adsorption

1. Introduction

It is well known that rising atmospheric carbon dioxide (CO_2) levels are one of the greatest threats to the environment this generation faces. The International Panel on Climate Change (IPCC) recently reported that CO_2 levels need to reduce by 45% by 2030 in order to limit global warming to 1.5°C and alleviate the greenhouse effect.[1] This requires rapid and substantial action. Post-combustion capture of CO_2 from flue gas will play a vital role in helping to solve this problem. This can be carried out at point source locations such as power stations which are large CO_2 emitters.[2]

A new class of porous solids known as metal-organic frameworks (MOFs) have emerged as a promising carbon capture technology in this field.[3, 4] Metal-organic frameworks are highly crystalline materials comprised of inorganic metal nodes and interconnecting organic linkers.[5] The characteristic and unique features of these materials include a high surface area, high pore volume and high tunability, making them an ideal material for gas adsorption processes.[6] The primary methods for gas separation using MOFs are temperature swing adsorption (TSA) and pressure swing adsorption (PSA) processes.[7]

CO_2 adsorption in MOFs has been extensively studied for single and binary component systems of CO_2/N_2, with promising CO_2 adsorption capabilities demonstrated.[4] However, flue gas is a complex mixture of CO_2, N_2, NO_x, SO_2 and water vapour that cannot be effectively modelled using a binary system. To validate the potential of MOFs on industrial scale it is important to understand how they work in more realistic conditions. Also, energy efficiency is an important factor in designing a TSA process, which is closely related to the specific heat capacity of the adsorbent. There is insufficient heat capacity data published on MOFs thus far.

This paper aims to provide a thorough investigation into the CO_2 adsorption performance of two MOFs, UiO-66-NH_2 and HKUST-1, after a variety of exposures to replicate the impurities in flue gas. UiO-66-NH_2 contains aromatic amine moieties, while HKUST-1 contains coordinatively unsaturated open metal sites. This report provides insight into the effect of water and aqueous SO_2 exposures on these two structurally diverse frameworks. An additional study into the heat capacity range of each MOF will be carried out to provide a well-rounded overview into their industrial potential.

2. Background

Post-combustion carbon capture involves preferential adsorption of CO_2 over N_2. MOFs containing open metal sites have shown promise for this separation.[4] These sites are coordinatively unsaturated, resulting in locally high charge density.[8] Due to its higher quadrupole moment and polarisability, CO_2 physisorbs more strongly than N_2 at these sites.[9] Notable examples include Mg_2(DOBDC), Ni_2(DOBDC) and HKUST-1. These have demonstrated high CO_2 uptake and CO_2:N_2

selectivity at ambient temperature and 0.15 bara (the partial pressure of CO_2 in flue gas [10]).[7, 11-13]

MOFs containing linkers with polarising moieties, such as aromatic amine groups, have also demonstrated promising carbon capture performance.[4] Examples include UiO-66-NH_2, USO-2-Ni-A and bio-MOF-11.[14-16] Note that aromatic amines are weak Lewis bases and are likely to uptake CO_2 via a physisorptive mechanism, unlike alkylamines which do so via chemisorption in a Lewis acid-base reaction.[4]

The flue gas composition of a typical coal-fired power station is shown in **Table 1.** Water vapour is present in significant volumes. As a polar molecule in such high concentration, H_2O can compete with CO_2 for adsorption sites, and can also cause structural degradation in MOFs with low water stability.[4] As such, the effect of H_2O on post-combustion carbon capture in MOFs has been a strong focus for many studies.[17-25]

Table 1. Approximate flue gas composition from a low sulfur eastern bituminous coal burning power station. Table adapted from Granite et al. [10]

Species	Concentration (by volume)
H_2O	5-7%
O_2	3-4%
CO_2	15-16%
SO_2	800 ppm
NO_x	500 ppm
N_2	balance

The most extensive investigation to date is that of Chanut *et al.* ,[17] in which 45 frameworks were exposed to water vapour, followed by CO_2 adsorption/desorption cycling in a thermogravimetric analyser (TGA). The desorption steps were carried out at incrementally higher temperatures to remove more pre-adsorbed water and thus, determine CO_2 uptake for a range of moisture contents. Among the highest performing MOFs investigated were MIL-96(Al), UiO-66-2Me and UiO-66-NH_2. HKUST-1 also showed promising uptakes, though other studies have reported low water stability of this MOF with repeated cycling.[18]

In efforts to model post-combustion carbon capture more accurately, dynamic breakthrough investigations have also been conducted.[19-23] In these experiments, gas mixtures typically emulate a simplified post-combustion carbon capture process, consisting only of CO_2, N_2, and H_2O. Using such a setup, Kizzie *et al.* [19] demonstrated vast differences in carbon capture performance of MOFs at different humidities. For example, while in dry conditions, the Mg variant of M_2(DOBDC) showed higher CO_2 uptake to the Co variant. However, the Co variant showed superior uptake at 70% relative humidity (RH). Fracaroli *et al.* [20] carried out breakthrough experiments for CO_2/N_2 separations in dry and humid conditions for variants of IRMOF-74-III. For IRMOF-74-III-CH_3, in which CO_2 sorption occurs at open metal sites, the breakthrough time was found to decrease significantly in humid conditions. This was attributed to H_2O competing strongly with CO_2 for these sites. However, for IRMOF-74-III-CH_2NH_2, in which CO_2 sorption occurs at the alkyl-amine sites, breakthrough time was not significantly affected, because H_2O competes far less for these sites.

A limited number of multicomponent equilibrium investigations have also been reported,[18, 24, 25] though it is notoriously difficult to interpret such experiments due to ambiguity in the composition of the adsorbed phase.[26] The most extensive is that of Mason *et al.* [25] , in which equilibrium adsorption was determined for 15 metal-organic frameworks in the presence of N_2, CO_2 and H_2O in a ratio similar to that of a typical flue gas. Most notably, the alkylamine-functionalised mmen-Mg_2(DOBPDC) was found to adsorb more CO_2 in the multicomponent experiments than for pure CO_2 with the same partial pressure.

As is shown in **Table 1.** , SO_2 and NO_x are both present in non-negligible quantities in flue gas, with typical concentrations of 800 and 500 ppm respectively. Multi-component investigations which include these trace gases are scarce. Liu *et al.* [22] demonstrated that in dynamic breakthrough experiments, MIL-101(Cr) is relatively resistant to SO_2 and NO over a range of concentrations typical of flue gas streams. However, with the lack of research in this area, one can only speculate as to the effects of these impurities on other MOFs. SO_2 is a polar molecule, with a dipole moment of 1.6 D.[9] As such, it is expected to compete with CO_2 for open metal sites of high charge density. In a pair of studies by Rezaei *et al.* ,[27, 28] the effects of impurities in the absence of CO_2 was tested for aminosilica adsorbents using thermogravimetric analysis. The amine groups adsorbed significant amounts of SO_2 (particularly the secondary amine groups) and also adsorbed small amounts of NO_2 irreversibly. However, in dynamic CO_2 breakthrough experiments, the adsorbents maintained their CO_2 capacities when exposed to all impurities in realistic concentrations.

Aside from impurity effects, heat capacity is another important property of MOFs in post-combustion carbon capture using TSA. This property helps to determine if MOFs are a potential alternative to conventional aqueous alkanolamine absorbents. Despite this, little work has been done in determining the heat capacities of MOFs. A study by Mu *et al.* [29] tested the heat capacity of several MOFs and compared these with other solid adsorbents. Measurements for HKUST-1 were included in this investigation, but no known measurements exist for UiO-66-NH_2.

Overall there has been significant progress in studying the effects of water on carbon capture performance in MOFs. However, there are large knowledge gaps in understanding the effects of SO_2. Further to this, more work is needed in documenting heat capacity data for a wider variety of MOFs.

3. Methods

3.1. Materials

1,2-aminoterephthalic acid (99%), copper oxide (CuO, 99.99%), sulfurous acid (SO_2, 5-6%), zirconium (IV) chloride ($ZrCl_4$, 99.5%) and zirconium oxide (ZrO_2, 99%) were all purchased from Sigma-Aldrich. Ethanol (99.8%), hydrochloric acid (HCl, 37%), methanol (100%), N,N-Dimethylformamide (DMF, 99.9%) were all purchased from VWR chemicals. HKUST-1 (MOF-111) was purchased from Promethean Particles.

3.2. UiO-66-NH_2 Synthesis

An open vessel synthesis of UiO-66-NH_2 was carried out using methods previously reported in literature.[30, 31]

3.3. Aqueous SO_2 Exposure

An aqueous SO_2 exposure was carried out for both UiO-66-NH_2 and HKUST-1. The method was based on published literature [32] but SO_2 concentration was amended to replicate realistic concentrations present in flue gas and exposure time was shortened. A stock solution of aqueous SO_2 (6%, Sigma-Aldrich) was diluted to a concentration of 6.55 x 10^{-3} M (420 ppm). For 500 mL of solution, 3.5 mL of stock SO_2 was added to a 500 mL volumetric flask and topped up with DI water. 60 mL of aqueous SO_2 solution and 200 mg of MOF were added to a 60 mL glass vial and sealed. Vials were placed in a sonication bath for 1 hour at room temperature. The obtained suspension was centrifuged at 4500 rpm for 5 minutes, washing repeatedly with methanol and DI water. Samples were dried overnight at 60°C. Aqueous SO_2 exposures were chosen over gaseous exposures with consideration for safety.

3.4. Liquid Water Exposure

A water exposure was carried out for both UiO-66-NH_2 and HKUST-1. 60 mL of DI water and 200 mg of MOF were added to a 60 mL glass vial and sealed. Vials were placed in a sonication bath for 1 hour at room temperature. The obtained suspension was centrifuged at 4500 rpm for 5 minutes washing repeatedly with methanol and DI water. Samples were dried overnight at 60°C to ensure the effects of pre-adsorbed water on CO_2 uptake were observed.

3.5. Single Component CO_2 Sorption

Thermogravimetric analysis (TGA) was carried out to determine CO_2 uptake for each MOF using a Netzsch TG 209 F1 Libra instrument. To measure the effect of pre-adsorbed water on CO_2 adsorption, desorption temperature was increased stepwise (30, 60, 100, 140°C) after each TSA cycle. This was based on a similar method outlined by Chanut *et al.* [17], but amended with consideration for the thermal stability of the chosen MOFs as detailed in **Supplementary Material: S1**. The system pressure was constant at 1.0 bara. Initial sample masses of around 50 mg were used. CO_2 flowrate was set at 100 mL min^{-1}. A purge stream of N_2 was introduced after each cycle, at a flowrate at 100 mL min^{-1}. After each adsorption cycle, a new mass basis was used to reflect the mass at the start of the cycle. Uptake, u (mmol g^{-1}), was calculated for each cycle using **Equation 1** where m_1 (g) is the sample mass at the end of each cycle, m_0 (g) is the sample mass at the start of each cycle, and M_{CO_2} (g mol^{-1}) is the molar mass of CO_2.

$$u = \left(\frac{m_1 - m_0}{m_0}\right) \times \frac{1}{M_{CO_2}} \times 10^3 \qquad \textbf{[Equation 1]}$$

3.6. Binary CO_2 Sorption (Dynamic)

To validate uptake results in a binary mixture, a dynamic breakthrough sorption analyser connected to a European Spectroscopy Services Quadrupole Mass Spectrometer (MS) 200 controlled by Quadstar 32-bit software was used. Samples were packed in a column and activated at 60°C overnight for the exposed samples. Note that dry samples were activated at 120°C overnight to remove all traces of moisture. Then, a gas mixture of 15 mol% CO_2 and 85 mol% N_2 was passed through the column at room temperature at 1.1 barg. MS was used to measure outlet ion concentration, thus, observe when breakthrough occurred. CO_2 uptake was calculated by integrating the difference between CO_2 inlet and outlet flow over the total time taken to reach saturation, accounting for the dead volume of the column. Detailed equations are outlined in the **Supplementary Material: S2**.

3.7. Materials Characterisation

3.7.1. BET

A Micrometric 3Flex Sorption analyser was used to characterise the surface area and pore volume of each MOF before exposure, after exposure and after CO_2 sorption. Nitrogen adsorption and desorption isotherms were measured at 77 K. Dry samples were degassed at 180°C and wet samples were degassed at 60°C for 24 hours prior to measurements. The surface area was determined using the Brunauer-Emmett-Teller (BET) method specified in the 3Flex software. Single point adsorption total pore volume was measured at a value between 0.85<P/Po<0.98 for all experiments, depending on the sample.

3.7.2. XRD

X-ray diffraction measurements were conducted using a PANalytical X'Pert PRO instrument (Cu$K\alpha$ radiation, 40 kV, 20 mA, α1 = 1.540598 Å, α2 = 1.544426 Å, weighted average = 1.542512 Å). A step scan method was used in the range of 5°<2θ<55°. Powdered samples were prepared and tested at room temperature.

3.7.3. FTIR

Spectra were collected using the attenuated total reflectance Fourier transform-infrared (ATR-FTIR) method on a Perkin-Elmer Spectrum 100 Spectrometer.

Prior to measurements, background noise was corrected for. Per sample, 8 measurements were taken. Powdered samples were prepared and tested at room temperature.

3.7.4. DSC

To measure heat capacity, a TA dynamic scanning calorimeter (DSC) Q2000 was used, operating with a helium atmosphere at a flowrate of 50 mL min^{-1}. Heat flow measurements were taken over a temperature range 20-200°C with a heating rate of 10°C min^{-1}. An average sample mass of 6.5 mg was measured for each MOF. The powdered sample was packed into an aluminium pan with a sample press, to ensure a uniform packing. The heat capacity (c_p (J mol^{-1} °C^{-1})) was then calculated using **Equation 2** , where m (g) is the mass of sample, ΔP (W) is the absolute heat flow to the sample, and β (°C s^{-1}) is the heating rate.

$$c_p = \frac{1}{m}\frac{\Delta P}{\beta} \qquad \textbf{[Equation 2]}$$

4. Results and Discussion

4.1. Characterisation of dry materials

ATR-FTIR spectroscopy was utilised to gain insight into the bonds present in the dry materials. **Figure 1.** shows HKUST-1 spectra with bands at 1372 cm^{-1}, 1451 cm^{-1}, 1592 cm^{-1} and 1645 cm^{-1}. The spectra are in close agreement with those reported in literature.[33, 34] Synthesised UiO-66-NH_2 spectra displayed in **Figure 1.** exhibits bands at 1255 cm^{-1}, 1340 cm^{-1}, 1561 cm^{-1} and 3473 cm^{-1}. Similar results for UiO-66-NH_2 have been published in literature.[30, 35]

X-ray diffraction (XRD) patterns were first compared with simulated data to ensure the dry samples had the correct crystalline structure. **Figure 2.** shows simulated HKUST-1 XRD patterns [36] with characteristic peaks at 2θ= 6.7°, 9.5°, 11.6° and 13.5°. The dry HKUST-1 sample has coinciding characteristic peaks, demonstrating it is in the HKUST-1 crystalline form. **Figure 2.** displays the simulated UiO-66 diffraction pattern,[37] in absence of the amine group. There are characteristic peaks present at 2θ= 7.4° and 8.54°. The synthesised sample of dry UiO-66-NH_2 has peaks in agreement with the simulation, confirming that the synthesis formed the correct crystalline phase.

The BET surface area and pore volume of dry samples are reported in **Table 2.** . Surface area of HKUST-1 was determined as 1238 m^2 g^{-1}. Literature reports a similar surface area of 1387 m^2 g^{-1}. [38] The pore volume of HKUST-1 was measured as 0.497 cm^3 g^{-1} with literature quoting a value of 0.56 cm^3 g^{-1}.[38] Slight differences can be attributed to unknown synthesis conditions of the purchased HKUST-1. The synthesised UiO-66-NH_2 had a surface area of 963 m^2 g^{-1}. This compares well with the published literature value of 871 m^2 g^{-1}.[30] The pore volume of UiO-66-NH_2 was measured as 0.398 cm^3 g^{-1}, which is in close agreement with literature values of 0.41 cm^3 g^{-1}.[30]

4.2. Single Component CO_2 Sorption

Figure 3. demonstrates the single component CO_2 uptake at a pressure of 1.0 bara for each MOF after the various pre-exposures. The most significant observation for HKUST-1 (**Figure 3.a.**), is that the dry sample has the highest CO_2 uptake, followed by the aqueous exposed sample, followed by the aqueous SO_2 exposed sample. For comparison, at a desorption temperature of 30°C, the dry sample has an uptake of 2.23 mmol g^{-1}. The aqueous exposed sample has an uptake of 1.77 mmol g^{-1} (21% decrease). The aqueous SO_2 exposed sample has an uptake of 0.78 mmol g^{-1}. It is clear the exposure to aqueous SO_2 has an extreme negative effect on uptake, equating to a 65% loss in capacity. In the case of the dry sample, uptake remains constant at all desorption temperatures. There is as general increase in uptake for both the aqueous and aqueous SO_2 exposed samples, at progressively increasing desorption temperatures, with the aqueous exposed sample converging to that of the dry sample at 140°C.

A key finding from **Figure 3.b.** , is that for UiO-66-NH_2, uptake is highest after an aqueous exposure, followed by an aqueous SO_2 exposure. Contrary to the hypothesis, the dry sample shows the lowest uptake. For comparison, at a desorption temperature of 30°C, the dry sample has an uptake of 1.35 mmol g^{-1}. The aqueous exposed sample has a corresponding uptake of 1.86 mmol g^{-1} (38% increase), while the aqueous SO_2 exposed sample has an uptake of 1.66 mmol g^{-1} (23% increase). Interestingly, no increase in uptake is observed with increasing temperature for the aqueous and aqueous SO_2 exposed samples. In fact, a slight decrease is observed.

Overall, HKUST-1 performs much better than UiO-66-NH_2 in dry conditions. However, after an aqueous exposure to SO_2, the uptakes of UiO-66-NH_2 exceed those of HKUST-1 for all desorption temperatures. Measurements were repeated 3 times for both dry MOFs. Error bars on **Figure 3.** represent +/- 1 standard deviation from the mean of the 3 runs. Error is deemed sufficiently small for the trends observed in both MOFs to be convincing. Notably, error is somewhat larger in the case of UiO-66-NH_2. This could be a result of the less homogeneous properties of the synthesised UiO-66-NH_2 powder relative to purchased HKUST-1.

4.3. Dynamic CO_2/N_2 system

To further substantiate the CO_2 uptake results in gas concentrations closer to that of flue gas, dynamic breakthrough experiments were conducted. A gas mix of 15 mol% CO_2 and 85 mol% N_2 was used. **Figure 4.a.** confirms that for HKUST-1, the dry sample, indeed, has the highest CO_2 uptake at 2.12 mmol g^{-1}. Both the aqueous and aqueous SO_2 exposed samples have a considerably lower CO_2

Table 2. BET Surface area and pore volume of UiO-66-NH_2 and HKUST-1 compared with literature values

	UiO-66-NH_2		HKUST-1	
	Dry	Literature[30]	Dry	Literature[38]
BET Surface Area / m^2 g^{-1}	963	871	1238	1387
Pore Volume / cm^3 g^{-1}	0.398	0.41	0.497	0.56

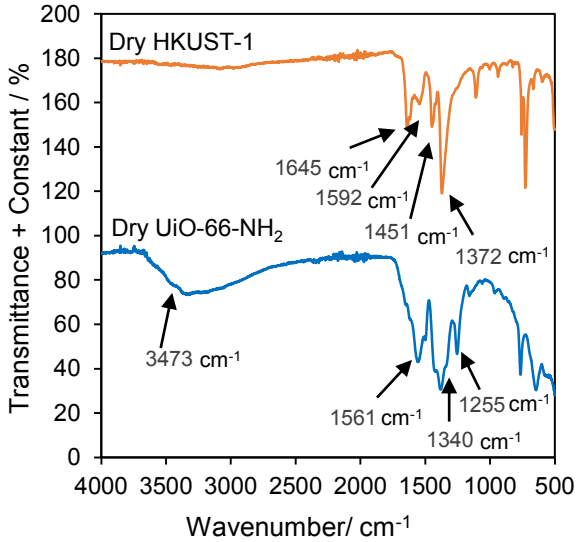

Figure 1. ATR-FTIR of dry HKUST-1 and dry synthesised UiO-66-NH_2

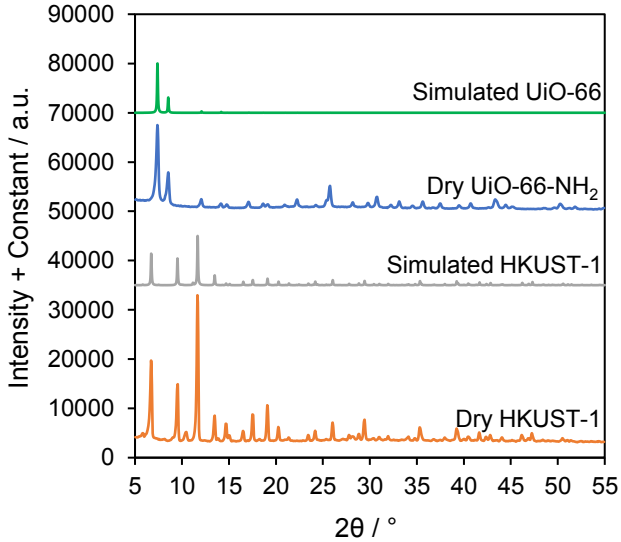

Figure 2. XRD patterns of simulated UiO-66, dry synthesised UiO-66-NH_2[37] , simulated HKUST-1[36], and dry HKUST-1

uptake than the dry MOF, which directly confirms the pure CO_2 sorption results. The aqueous sample has an uptake of 1.05 mmol g^{-1} (50% decrease) and the aqueous SO_2 exposed sample has an uptake of 1.07 mmol g^{-1} (50% decrease).

Figure 4.b. validates the trend observed in pure CO_2 sorption, that UiO-66-NH_2 has increased uptake after exposure to aqueous environments. The dry sample has the lowest uptake at 1.72 mmol g^{-1}, with aqueous exposed and the aqueous SO_2 exposed samples having uptakes of 1.89 mmol g^{-1} (10% increase) and 3.25 mmol g^{-1} (88% increase), respectively. Contrary to the single component results, the SO_2 exposed sample has higher CO_2 uptake relative to the aqueous exposed sample in both MOFs. Although CO_2 uptake is the primary criteria investigated in this paper, selectivity and separation factor are also important factors when considering MOF performance. For details see **Supplementary Material: S3.**

Error is deemed far greater for the dynamic breakthrough system, relative to the single component system. Variation in the packing of the prepared columns leads to a large source of human error. Since the MOFs are cohesive powders, channelling of the bed can occur in the more densely packed columns, leading to significant gas bypass. Inefficient control of the column pressure drop was also a suspected source of error. Repeat measurements were not conducted, leading to high uncertainty of the results.

4.4. CO_2 Uptake Performance

Dry HKUST-1 had high uptakes because the open metal sites interact strongly with CO_2. However, the loss in uptake observed after exposure to aqueous environments can be attributed to the fact that H_2O binds more strongly to the open metal sites than CO_2.[3] Previous investigations have identified a slight increase in CO_2 uptake with increased water content for HKUST-1, due to the interaction between the quadrupole moment of CO_2 and the H_2O molecules adsorbed at the open metal sites for very low humidity exposures.[4, 24, 39] This trend is not observed here, as the aqueous exposure is too extreme compared with conventional vapour exposures. The decrease in uptake after exposure to aqueous solution is consistent with previous studies for high humidity vapour exposures.[3, 17, 39] At higher desorption temperatures, when the MOF is dried, there is less competition for adsorption sites. Thus, at higher temperatures, the uptake for the aqueous exposed sample converges to those of the dry sample.

The aqueous SO_2 exposure results in a much larger decrease in uptake for HKUST-1. The uptake increases with increased desorption temperature, as moisture is removed from the framework. However, the fact that this trend does not converge to that of the dry MOF suggests that polar SO_2 molecules reside in the framework, even at high temperatures, and compete with CO_2 for adsorption sites.

The single component CO_2 sorption results obtained for UiO-66-NH_2 contradict the study by Chanut *et al.* [17], upon which this TGA method was based. They found that exposure to 100% RH results in a 25%

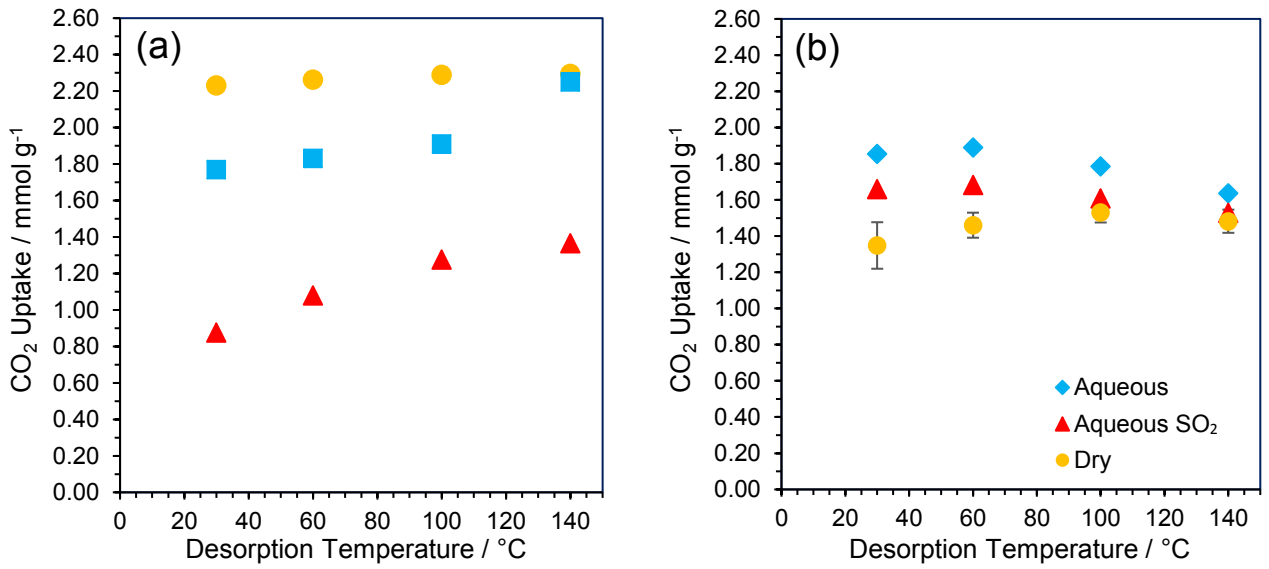

Figure 3. Single component CO_2 uptakes for dry, aqueous exposed and aqueous SO_2 exposed MOFs and increasing desorption temperatures. (a) shows HKUST-1 and (b) shows UiO-66-NH_2. In both cases, the dry data represents the average of 3 runs, with error bars representing +/- 1 standard deviation from the mean (too small to observe for HKUST-1)

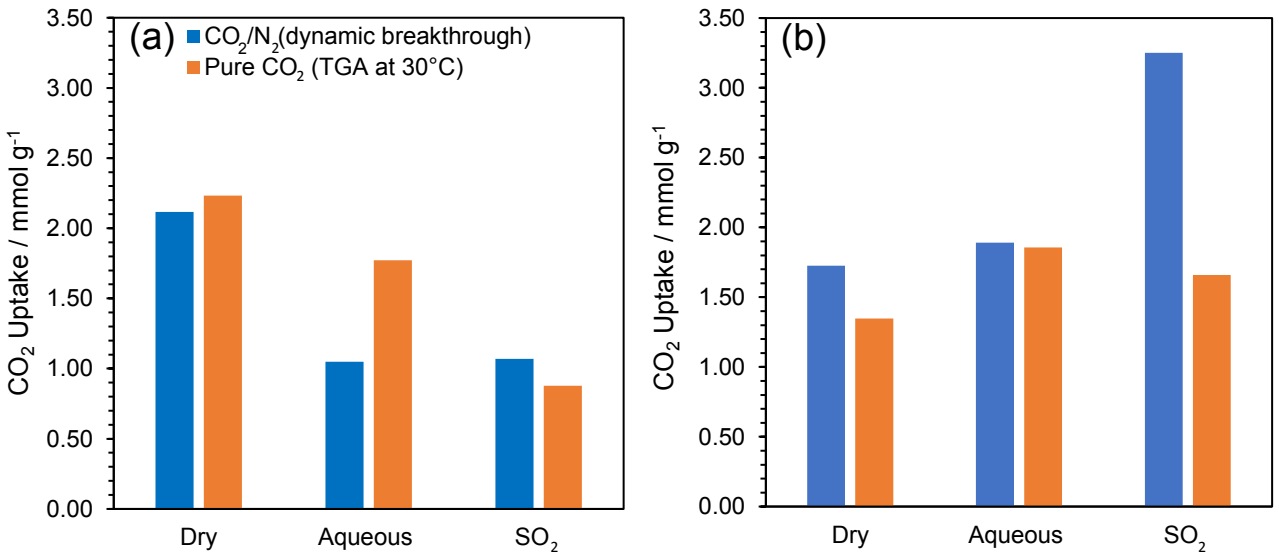

Figure 4. Binary component CO_2 uptakes for dynamic breakthrough experiments at 25°C and 1.1 barg, compared with single component CO_2 uptakes at 1 atm and 30°C for dry, aqueous exposed and aqueous SO_2 exposed MOFs. (a) shows HKUST-1 and (b) shows UiO-66-NH_2

decrease in uptake relative to the dry framework. However, in the aforementioned investigation, the pre-exposure was carried out using water vapour; a more realistic representation of the conditions in a flue gas stream. The aqueous exposure must therefore impact the framework differently to the vapour exposure.

A possible explanation for the increased uptake after aqueous exposure is the introduction of missing-linker defects in the framework, by which amino benzene dicarboxylate (NH_2-BDC^{2-}) linkers scattered throughout the framework detach from the zirconium metal nodes. Missing-linker defects have been reported in UiO-66 and its derivatives by various methods, both during and post synthesis.[40-44] The primary method by which defects were introduced involved soaking in an aqueous acid solution.[40] Loss of the NH_2-BDC^{2-} linkers from the structure would require some compensating species to 'plug' the defects and retain charge neutrality.[41] Trickett *et al.* [44] showed that in UiO-66 synthesised with missing-linker defects, water binds at the vacant zirconium metal sites, and hydroxide anions compensate for the loss of charge from the missing linkers. The same could apply to the proposed defects in this investigation.

Nonetheless, this theory is treated with scepticism, since post-synthetic missing-linker defects have not been reported for such short exposure times and low temperatures. Although the high water stability of UiO-66 and its derivatives is widely reported in literature,[45-47] there are few reports of liquid water alone causing post-synthetic missing-linker defects. However, there is significant evidence for liquid water facilitating post synthetic ligand exchange in UiO-66-NH_2.[47] This

provides substantial evidence that water exposure enables liberation of ligands. Further investigations are required to validate this hypothesis. The aqueous SO_2 exposed sample displays uptakes between those of the dry and aqueous exposed. This suggests that H_2O and SO_2 have a competing effect on uptake, with enhancement from H_2O (due to missing-linker defects), but a reduction caused by SO_2.

The missing-linker theory does not account for the slight decrease in uptake for UiO-66-NH_2 with increasing desorption temperature. While the aqueous exposure may cause these missing-linker defects, any residual H_2O in the framework would still be expected to compete with CO_2 for adsorption sites. Hence, CO_2 uptake should increase with increasing desorption temperature. A possible explanation for the opposite trend is that the thermal stability of the framework with the missing-linker defects may be lower than that of the dry framework. In this case, higher temperatures would cause greater structural degradation to the pre-exposed MOF. This hypothesis could be tested by carrying out TGA stability tests for exposed UiO-66-NH_2, combined with mass spectrometry (MS). MS is necessary to identify the cause of mass decrease: residual moisture in the structure or organic matter. The latter would indicate structural degradation.

4.5. Characterisation of exposed materials

4.5.1. XRD

To explain the uptake results, XRD measurements were conducted to characterise the crystallinity of the samples before and after exposure. **Figure 5.** shows there is a significant change in crystalline structure observed for both aqueous exposed and aqueous SO_2 exposed samples of HKUST-1. This suggests significant degradation of the material structure after aqueous exposure. It is widely reported in literature that HKUST-1 loses its crystallinity after exposure to moisture.[17, 48] Both aqueous and aqueous SO_2 exposed samples have characteristic peaks observed at 2θ= 38.4° and 44.6°. Both copper(II) oxide (CuO) and the precursor chemical, copper nitrate (Cu(NO3)2), have corresponding characteristic peaks. Despite a large degree of similarity, the diffraction patterns are not identical to CuO. It is likely that the material formed is some crystal structure containing Cu(II), but further tests are needed to determine the precise crystalline structure of the degraded HKUST-1.

Figure 6. shows aqueous exposed UiO-66-NH_2 has characteristic peaks at the same location as the dry sample. However, the relative intensity is much lower. This suggests that the structure may have some loss in crystallinity. Yet, numerous studies have used XRD measurements to confirm the high water stability of UiO-66-NH_2 after liquid water exposures.[45-47] In all cases, XRD measurements of the exposed samples yield characteristic peaks at the same intensity and location relative to the dry samples, confirming stability. The

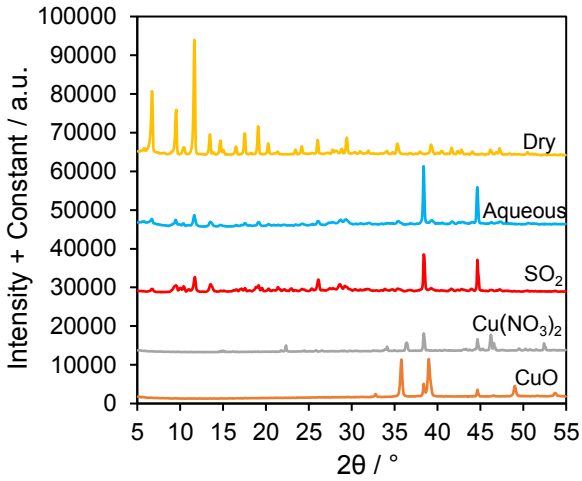

Figure 5. XRD plots showing dry, aqueous exposed, aqueous SO_2 exposed HKUST-1, $Cu(NO_3)_2$ precursor and CuO

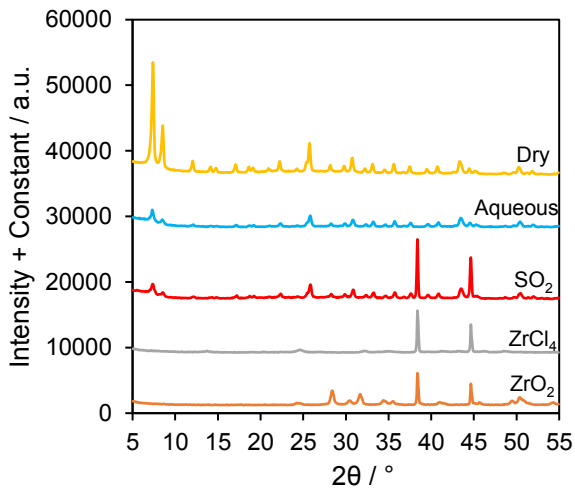

Figure 6. XRD plots showing dry, aqueous exposed, and aqueous SO_2 exposed UiO-66-NH_2, $ZrCl_4$ precursor and ZrO_2

lower intensity XRD peaks observed in this study are likely attributed to the remaining pre-adsorbed water in the sample, that was a result of the low temperature drying step. Guest water molecules trapped in pores have been known to reduce peak intensity.[49, 50] In contrast, XRD measurements of exposed samples in previous investigations have been conducted after thorough drying of the samples.[45-47]

UiO-66-NH_2 exposed to aqueous SO_2 experienced a dramatic change in crystal pattern, with characteristic peaks observed at 2θ = 38.2° and 44.6°. Both the precursor species, $ZrCl_4$, and zirconium (IV) oxide (ZrO_2) were characterised using XRD measurements. ZrO_2 diffraction patterns had coinciding characteristic peaks with the SO_2 exposed sample. This suggests an SO_2 exposure breaks down the crystal structure of UiO-66-NH_2, forming ZrO_2. XRD simulations of the metal sulfates and sulfites were also compared to the aqueous SO_2 exposed samples. These simulations do not indicate formation of sulfate or sulfite species after exposure. These comparisons are detailed in the **Supplementary Material: S4**.

Table 3. BET surface area and pore volume for dry, aqueous exposed and aqueous SO_2 exposed samples of HKUST-1 and UiO-66-NH_2

	HKUST-1			UiO-66-NH_2		
	Dry	Aqueous	SO_2	Dry	Aqueous	SO_2
BET Surface Area/ $m^2 g^{-1}$	1238	860	874	963	1190	1437
Pore Volume/ $cm^3 g^{-1}$	0.497	0.367	0.338	0.398	0.493	0.536

4.5.2. Porosity

Increased surface area and pore volume are associated with higher CO_2 capacity in porous materials. BET measurements were taken to determine the surface area and pore volume of samples before and after exposure. **Table 3.** confirms that dry UiO-66-NH_2 has a significantly lower surface area and pore volume than both samples exposed to an aqueous environment. This directly corresponds to the uptake trends observed, with dry UiO-66-NH_2 demonstrating the lowest uptake in both experiments. The increased pore volume in aqueous exposed samples is likely attributed to the missing-linker defects described above. The absence of NH_2-BDC^{2-} linkers throughout the framework results in larger voids, increasing the porosity in the crystal structure. This provides more space for guest molecules to adsorb.

As expected, dry HKUST-1 shows the greatest surface area and pore volume compared with aqueous and aqueous SO_2 exposed samples. Again, this validates CO_2 uptake results in both pure and binary systems, as the dry sample had the highest uptake. This can be attributed to the dramatic loss in crystallinity after an aqueous exposure, as observed in the diffraction patterns.

Experiments were conducted up to 1.1 barg. At such low pressures, surface area and pore volume are not likely to be the limiting factor in CO_2 uptake. Physical interactions between CO_2 and the framework are what dominate adsorption.[51] At higher pressures, large porosity will have a more significant effect on uptake.

A higher surface area is expected for aqueous exposed samples compared with the aqueous SO_2 exposed samples, as this would reflect the uptake trends observed in the single component system. Interestingly, an aqueous SO_2 exposure resulted in a higher surface area for both MOFs relative to the aqueous exposure, but a lower uptake. One possible explanation for the lower CO_2 uptake is that SO_2 molecules are competing with CO_2 for adsorption sites.

4.6. Heat Capacity Analysis

Figure 7. displays the heat capacity results for each MOF in the range of 40 to 200°C; a range representative of industrial TSA processes.[7] Both HKUST-1 and UiO-66-NH_2 display a monotonic increase in heat capacity with temperature. HKUST-1 ranges from 1.56 to 2.46 J g^{-1} °C^{-1}. UiO-66-NH_2 ranges from 1.13 to 1.94 J g^{-1} °C^{-1}. At any given temperature, UiO-66-NH_2 displays a lower heat capacity than HKUST-1, though both are significantly lower than a 20 mol% MEA solution [52] (note that heat capacity values for MEA solutions at temperatures higher than 120°C are scarce, due to the low thermal stability of MEA above these temperatures[53]). The measured values for HKUST-1 were much larger than those reported by Mu *et al* [29]. Consequently, reference heat capacity measurements were conducted for CuO using the same DSC programme employed for the MOF measurements. These were compared with well documented CuO literature values [54] to check the validity of the measurements made for the MOFs. Indeed, a close fit is observed for the experimental and literature CuO heat capacities shown in **Figure 7.** . Thus, the heat capacities measured for the MOFs are deemed reliable.

Both HKUST-1 and UiO-66-NH_2 exhibit heat capacities less than half the values of a 20 mol% MEA solution. This solution is representative of the type employed in industrial post-combustion carbon capture processes. Hence, the heat capacity analysis implies that considerable energy savings could be made if these MOFs were used in place of liquid alkanolamine absorbents. Of course, the inferior heat transfer in solid beds compared to liquids may limit the benefits of the lower heat capacities of these MOFs. A more detailed study of this factor, and others such as capital and operating costs and uptake comparisons, would be required to determine industrial viability of MOFs.

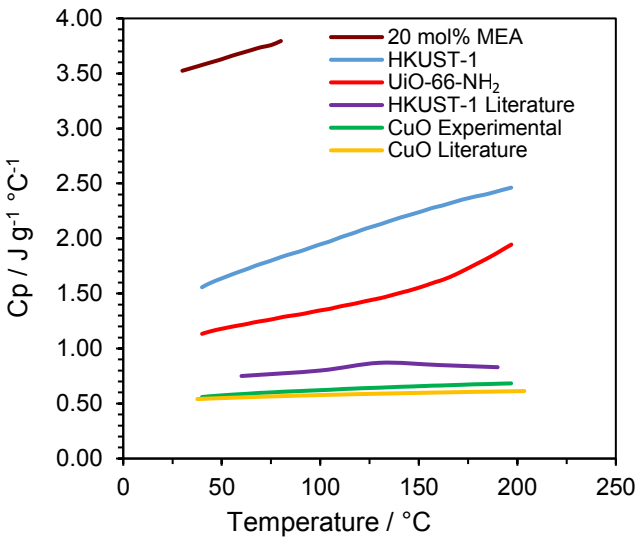

Figure 7. Heat capacity comparisons between 40 and 200°C for HKUST-1 and UiO-66-NH_2. Also shown is a 20 mol% MEA solution for comparison.[52] CuO values were also measured for comparison with literature values,[54] to check validity.

5. Conclusion

CO_2 sorption was studied after exposing two MOFs, HKUST-1 and UiO-66-NH_2, to water and aqueous SO_2 solution. A dynamic breakthrough analyser was used to validate the results of these experiments in a binary CO_2/N_2 system. It was shown that the impurities had differing effects on each MOF. HKUST-1 demonstrated decreased CO_2 uptake after aqueous exposure to water and SO_2 in both pure and binary systems. This was attributed to a decrease in surface area and pore volume of the framework. UiO-66-NH_2 showed opposite trends, with an increase in CO_2 uptake after aqueous exposure to water and SO_2 in both pure and binary systems. This was a result of a porosity increase of the framework. Missing-linker defects in UiO-66-NH_2 were explored to reason the unexpected trend. DSC measurements were conducted to determine the heat capacity of both MOFs. Both demonstrated significantly lower heat capacities than traditional carbon capture technology. Overall, it was shown that water and SO_2 impurities had significant effects on the material properties of both MOFs and hence, their carbon capture potential.

6. Outlook

The study has potentially positive implications for industry. Pre-treating UiO-66-NH_2 in water could enhance CO_2 uptake in post-combustion carbon capture. This unique pre-treatment method is highly scalable and would have low costs, indicating it could be viable for industrial use. Although HKUST-1 has demonstrated high uptake in dry conditions, it would be less suitable for carbon capture in flue gas, as the water and SO_2 present are likely to decrease its stability. Low heat capacities demonstrated by MOFs suggest they could be an industrially viable material for TSA, having lower energy penalties relative to existing carbon capture methods.

An area for further study would be pre-treating UiO-66-NH_2 with water, then conducting multicomponent breakthrough experiments with a gas stream resembling flue gas, containing both SO_2 and NO_x. This would provide further evidence for the industrial potential of this pre-treatment method. Although this pre-treatment method has shown promise with TSA, further experiments should be conducted using PSA, a method commonly used in industry. In the future, CO_2 adsorption isotherms can be measured and the Clausius-Clapeyron equation can be used to identify the bond enthalpy[4] . This is necessary to determine the regeneration energy requirements for the pre-treated UiO-66-NH_2.

Additional stability tests should be carried out using TGA combined with Mass Spectrometry to identify whether there is indeed a drop in thermal stability of UiO-66-NH_2 following aqueous exposure. Confirming the missing-linker theory with further tests, such as Neutron Diffraction is also an interesting area for subsequent studies. If confirmed, factors such as exposure time and pH could be investigated to manipulate the extent of defects, and thus optimise CO_2 uptakes.

7. Acknowledgements

Thank you to Arwyn Evans and Ravi Shankar for their continual help and encouragement throughout this research.

8. References

1. IPCC. Global Warming of 1.5 °C an IPCC special report on the impacts of global warming of 1.5 °C above pre-industrial levels and related global greenhouse gas emission pathways, in the context of strengthening the global response to the threat of climate change, sustainable development, and efforts to eradicate poverty. *International Panel on Climate Change* (2018).
2. IPCC. Climate change 2014 : synthesis report : approved summary for policymakers. (2014).
3. Li, H. *et al*. Recent advances in gas storage and separation using metal–organic frameworks. *Materials Today* **21**, 108-121 (2018).
4. Kenji Sumida *et al*. Carbon Dioxide Capture in Metal-Organic Frameworks. *Chemical Reviews* **112**, 724-781 (2012).
5. Jian-Rong Li, Julian Sculley & Hong-Cai Zhou. Metal-Organic Frameworks for Separations. *Chemical Reviews* **112**, 869-932 (2012).
6. Hiroyasu Furukawa *et al*. Ultrahigh Porosity in Metal-Organic Frameworks. *Science* **329**, 424-428 (2010).
7. Mason, J. A., Sumida, K., Herm, Z. R., Krishna, R. & Long, J. R. Evaluating metal–organic frameworks for post-combustion carbon dioxide capture via temperature swing adsorption. *Energy Environ. Sci.* **4**, 3030-3040 (2011).
8. Burtch, N., Jasuja, H. & Walton, K. Water Stability and Adsorption in Metal-Organic Frameworks. *Chem. Rev.* **114**, 10575-10612 (2014).
9. Bae, Y. -. & Lee, C. -. Sorption kinetics of eight gases on a carbon molecular sieve at elevated pressure. *Carbon* **43**, 95-107 (2005).
10. Granite, E. J. & Pennline, H. W. Photochemical Removal of Mercury from Flue Gas. *Industrial & Engineering Chemistry Research* **41**, 5470-5476 (2002).
11. Aprea, P., Caputo, D., Gargiulo, N., Iucolano, F. & Pepe, F. Modeling Carbon Dioxide Adsorption on Microporous Substrates: Comparison between Cu-BTC Metal−Organic Framework and 13X Zeolitic Molecular Sieve. *Journal of Chemical & Engineering Data* **55**, 3655-3661 (2010).
12. Dietzel, P. D. C., Besikiotis, V. & Blom, R. Application of metal–organic frameworks with coordinatively unsaturated metal sites in storage and separation of methane and carbon dioxide. *Journal of Materials Chemistry* **19**, 7362 (2009).
13. Yazaydin, A. O. *et al*. Screening of Metal-Organic Frameworks for Carbon Dioxide Capture from Flue Gas Using a Combined Experimental and Modeling Approach. *JACS*, 18198-18199 (2009).
14. Cmarik, G. E., Kim, M., Cohen, S. M. & Walton, K. S. Tuning the Adsorption Properties of UiO-66 via Ligand Functionalization. *Langmuir* **28**, 15606-15613 (2012).
15. Arstad, B., Fjellvåg, H., Kongshaug, K., Swang, O. & Blom, R. Amine functionalised metal organic frameworks (MOFs) as adsorbents for carbon dioxide. *Adsorption* **14**, 755-762 (2008).
16. An, J., Geib, S. J. & Rosi, N. L. High and Selective CO2 Uptake in a Cobalt Adeninate Metal−Organic Framework Exhibiting Pyrimidine- and Amino-Decorated Pores. *J. Am. Chem. Soc.* **132**, 38-39 (2010).
17. Chanut, N. *et al*. Screening the Effect of Water Vapour on Gas Adsorption Performance: Application to CO2 Capture from Flue Gas in Metal–Organic Frameworks. *ChemSusChem* **10**, 1543-1553 (2017).

18. Soubeyrand-Lenoir, E. *et al*. How Water Fosters a Remarkable 5-Fold Increase in Low-Pressure CO2 Uptake within Mesoporous MIL-100(Fe). *JOURNAL OF THE AMERICAN CHEMICAL SOCIETY* (2012).

19. Kizzie, A. C., Wong-Foy, A. G. & Matzger, A. J. Effect of humidity on the performance of microporous coordination polymers as adsorbents for CO2 capture. *Langmuir : the ACS journal of surfaces and colloids* **27**, 6368 (2011).

20. Fracaroli, A. M. *et al*. Metal–Organic Frameworks with Precisely Designed Interior for Carbon Dioxide Capture in the Presence of Water. *JACS* (2014).

21. Pirngruber, G. D. *et al*. A method for screening the potential of MOFs as CO2 adsorbents in pressure swing adsorption processes. *ChemSusChem* **5**, 762-776 (2012).

22. Liu, Q. *et al*. Adsorption of carbon dioxide by MIL-101(Cr): regeneration conditions and influence of flue gas contaminants. *Scientific reports* **3**, 2916 (2013).

23. Dan Li *et al*. Designed amyloid fibers as materials for selective carbon dioxide capture. *Proceedings of the National Academy of Sciences* **111**, 191-196 (2014).

24. Liu, J. *et al*. CO2/H2O adsorption equilibrium and rates on metal-organic frameworks: HKUST-1 and Ni/DOBDC. *Langmuir : the ACS journal of surfaces and colloids* **26**, 14301-14307 (2010).

25. Mason, J. A. *et al*. Application of a High-Throughput Analyzer in Evaluating Solid Adsorbents for Post-Combustion Carbon Capture via Multicomponent Adsorption of CO2, N-2, and H2O. *Journal of the American Chemical Society* (2015).

26. Darren P Broom & K Mark Thomas. Gas adsorption by nanoporous materials: Future applications and experimental challenges. *MRS Bulletin* **38**, 412-421 (2013).

27. Rezaei, F. & Jones, C. W. Stability of Supported Amine Adsorbents to SO2 and NOx in Postcombustion CO2 Capture. 1. Single-Component Adsorption. *Ind Eng Chem Res* **52**, 12192-12201 (2013).

28. Rezaei, F. & Jones, C. W. Stability of Supported Amine Adsorbents to SO2 and NOx in Postcombustion CO2 Capture. 2. Multicomponent Adsorption. *Ind Eng Chem Res* **53**, 12103-12110 (2014).

29. Mu, B. & Walton, K. S. Thermal Analysis and Heat Capacity Study of Metal–Organic Frameworks. *J. Phys. Chem. C* **115**, 22748-22754 (2011).

30. Crake, A., Christoforidis, K. C., Kafizas, A., Zafeiratos, S. & Petit, C. CO2 capture and photocatalytic reduction using bifunctional TiO2/MOF nanocomposites under UV–vis irradiation. *Applied Catalysis B: Environmental* **210**, 131-140 (2017).

31. Katz, M. J. *et al*. A facile synthesis of UiO-66, UiO-67 and their derivatives. *Chemical Communications* **49**, 9449-9451 (2013).

32. Bhattacharyya, S. *et al*. Interactions of SO2-Containing Acid Gases with ZIF-8: Structural Changes and Mechanistic Investigations. *J. Phys. Chem. C* **120**, 27221-27229 (2016).

33. Petit, C., Burress, J. & Bandosz, T. J. The synthesis and characterization of copper-based metal–organic framework/graphite oxide composites. *Carbon* **49**, 563-572 (2011).

34. Raganati, F., Gargiulo, V., Ammendola, P., Alfe, M. & Chirone, R. CO2 capture performance of HKUST-1 in a sound assisted fluidized bed. *Chemical Engineering Journal* **239**, 75-86 (2014).

35. Cam Loc Luu and Thi Thuy Van Nguyen and Tri Nguyen and Tien, Cuong Hoang. Synthesis, characterization and adsorption ability of UiO-66-NH 2. *Advances in Natural Sciences: Nanoscience and Nanotechnology* **6**, 025004 (2015).

36. Ahmed, A. *et al*. Macroporous metal–organic framework microparticles with improved liquid phase separation. *J. Mater. Chem. A* **2**, 9085-9090 (2014).

37. Ghorbanpour, A., Huelsenbeck, L. D., Smilgies, D. & Giri, G. Oriented UiO-66 thin films through solution shearing. *CrystEngComm* **20**, 294-300 (2018).

38. Khoshhal, S., Ghoreyshi, A. A., Jahanshahi, M. & Mohammadi, M. Study of the temperature and solvent content effects on the structure of Cu-BTC metal organic framework for hydrogen storage. *RSC Advances* **5**, 24758-24768 (2015).

39. Yazaydın, A. Ö *et al*. Enhanced CO2 Adsorption in Metal-Organic Frameworks via Occupation of Open-Metal Sites by Coordinated Water Molecules. *Chem. Mater.* **21**, 1425-1430 (2009).

40. Wu, H. *et al*. Unusual and Highly Tunable Missing-Linker Defects in Zirconium Metal–Organic Framework UiO-66 and Their Important Effects on Gas Adsorption. *J. Am. Chem. Soc.* **135**, 10525-10532 (2013).

41. Taddei, M., Wakeham, R. J., Koutsianos, A., Andreoli, E. & Barron, A. R. Post- Synthetic Ligand Exchange in Zirconium-Based Metal–Organic Frameworks: Beware of The Defects. *Angewandte Chemie International Edition* **57**, 11706-11710 (2018).

42. Shearer, G. C. *et al*. Defect Engineering: Tuning the Porosity and Composition of the Metal–Organic Framework UiO-66 via Modulated Synthesis. *Chem. Mater.* **28**, 3749-3761 (2016).

43. Hong, D. H. & Suh, M. P. Enhancing CO2 Separation Ability of a Metal–Organic Framework by Post-Synthetic Ligand Exchange with Flexible Aliphatic Carboxylates. *Chem. Eur. J.* **20**, 426-434 (2014).

44. Trickett, C. A. *et al*. Definitive Molecular Level Characterization of Defects in UiO-66 Crystals. *Angew. Chem. Int. Ed.* **54**, 11162-11167 (2015).

45. Liu, X., Demir, N. K., Wu, Z. & Li, K. Highly Water-Stable Zirconium Metal–Organic Framework UiO-66 Membranes Supported on Alumina Hollow Fibers for Desalination. *J. Am. Chem. Soc.* **137**, 6999-7002 (2015).

46. Lin, K. A., Liu, Y. & Chen, S. Adsorption of fluoride to UiO-66-NH2 in water: Stability, kinetic, isotherm and thermodynamic studies. *Journal of Colloid and Interface Science* **461**, 79-87 (2016).

47. Kim, M., Cahill, J. F., Su, Y., Prather, K. A. & Cohen, S. M. Postsynthetic ligand exchange as a route to functionalization of 'inert' metal–organic frameworks. *Chem. Sci.* **3**, 126-130 (2012).

48. Al-Janabi, N. *et al*. Mapping the Cu-BTC metal–organic framework (HKUST-1) stability envelope in the presence of water vapour for CO2 adsorption from flue gases. *Chem. Eng. J.* **281**, 669-677 (2015).

49. Schlichte, K., Kratzke, T. & Kaskel, S. Improved synthesis, thermal stability and catalytic properties of the metal-organic framework compound Cu3(BTC)2. *Microporous and Mesoporous Materials; Metal-Organic Open Frameworks* **73**, 81-88 (2004).

50. Agarwal, U. P., Ralph, S. A., Baez, C., Reiner, R. S. & Verrill, S. P. Effect of sample moisture content on XRD-estimated cellulose crystallinity index and crystallite size. *Cellulose* **24**, 1971-1984 (2017).

51. Wróbel, R. & Arabczyk, W. Solid−Gas Reaction with Adsorption as the Rate Limiting Step. *J Phys Chem A* **110**, 9219-9224 (2006).

52. Chiu, L. & Li, M. Heat Capacity of Alkanolamine Aqueous Solutions. *J. Chem. Eng. Data* **44**, 1396-1401 (1999).

53. Davis, J. & Rochelle, G. Thermal degradation of monoethanolamine at stripper conditions. *Energy Procedia* **1**, 327-333 (2009).

54. M. W. Chase. NIST-JANAF thermochemical tables. (1998).

Control of Porous Poly(2,6-diphenyl-p-phenylene oxide) Particle Size for Up-Scale Applications

Thomas McAuliffe and Sophia Moore
Department of Chemical Engineering, Imperial College London, U.K.

Abstract: Particle size control of porous poly(2,6-diphenyl-p-phenylene oxide) (PPPO), exploiting the process of non-solvent induced phase separation (NIPS), has been investigated. Two technologies have been compared; microfluidics and flash nanoprecipitation (FNP), both of which pertain the potential of industrial scale-up. Firstly, microfluidics is utilised using the NIPS process to produce droplets which are extracted to form microparticles. Secondly, two jetting streams are impinged using FNP to produce nanoparticles. A polydimethylsiloxane (PDMS) microfluidic device is used generate droplets containing PPPO, before solidification, to measure the effect of both flow rate ratios and non-solvent concentration on templated particle size. A confined impingement jet mixer with dilution (CIJ-D) is used to investigate the effect of initial polymer concentration and dilution volume, or quench volume, on particle size using the process of FNP. FNP nanoparticle samples were further characterized by dynamic light scattering (DLS) and scanning electron microscopy (SEM) to determine the size of particles. Micro-sized particles from 200 µm to 1100 µm and nano-sized particles from 114 nm to 360 nm were produced using microfluidics and FNP respectively. It has been observed that both the concentration of non-solvent in microfluidics and polymer concentration in FNP, have a positive correlation with associated particle size. A clear relationship between flow rate ratios in microfluidics, and quench volume in FNP have been observed. This research highlights the clear ability to independently control particle size via two scalable approaches; microfluidics and FNP. We demonstrate the possibility of upscaling these techniques to fabricate particles, from a previously unexplored porous organic polymer, across multiple length scales.

Keywords: PPPO; ternary phase diagram; non-solvent induced phase separation; microfluidics; nanoparticles; flash nanoprecipitation; CIJ-D.

1. Introduction

Porous polymeric structures are of great interest due to their wide range of important applications, from carbon capture and gas sensing, to drug delivery as nanocarriers in medicine. [1] A key industrial application is its use in gas sensing equipment as an adsorbent of volatile organic compounds (VOCs). [2] The response of a gas detector is very dependent on the size of particles used, with small sizes leading to high sensitivity, allowing for the accurate detection of trace amount of gases. [3]

PPPO is an organic porous polymer which is trademarked with the name Tenax. [4] Tenax-TA is the improved version of the original commercial resin Tenax-GC. [5] Harmful VOCS are often collected from gaseous samples by adsorption to polymers such as Tenax-TA. The adsorbed compounds are released from these materials by thermal desorption and separated by gas chromatography. [6] Many polymer adsorbents are limited by their temperature stability, restricting their application for thermal desorption. [7] In this regard, Tenax stands out among porous polymers due to its high thermal stability, allowing for separation of components up to 400-450^{0}C. [8]

PPPO was first used as an adsorbent for trapping VOCs by the National Aeronautics and Space Administration (NASA) for monitoring the cabin atmosphere in Skylab-4. [9] It is currently used as a stationary phase in packed column gas chromatography, membrane separation technology and in devices as an adsorbent material for monitoring personal exposure, air quality, emissions from industry [5] and commercial products. [4]

Recent studies have indicated that Tenax has potential for use in micro preconcentrators (PCs), which are concentration amplifiers used to improve chemical detection systems. [5] This is achieved by increasing the concentration of an analyte before detection, using high surface-area adsorbents and rapid thermal desorption of the trapped analytes. [10] Miniaturization of PCs increases process efficiency, arising from ratio of sample capacity to device size and the ratio of energy needed to desorb trapped compounds. [5] However, there are issues surrounding the implementation of packing the absorbent particles into the micro-devices, due to a wide particle size distribution and a subsequent high cost to separate this distribution. [5] One solution would be to produce particles of specific size relevant to the scope of each piece of equipment, for ease of application. It is therefore important to understand their design, synthesis and functionality.

There are a number of synthetic processing routes that can produce organic porous polymers, such as the presence of porogens which are subsequently removed to leave a porous structure. However, these processing agents often require removal under harsh conditions which may compromise particle structure. [11] Another method exploits the process of phase separation from a homogenous polymer solution. It occurs when there is an

increase in Gibbs free energy of a system induced by either the addition of a non-solvent (non-solvent induced phase separation, NIPS) or a change in temperature (thermally induced phase separation, TIPS), which causes the polymer solution to de-mix, inducing a porous internal microstructure. The process of NIPS will be the motivation of this study. [12]

Despite the technology advancements, there are still a number of difficulties with some techniques for production of polymer particles on an industrial scale [1]. These include being able to achieve a stable and uniform environment throughout chemical baths, and particle agglomeration resulting from the use of high polymer concentration to meet increase in production rates. [13] Droplet microfluidic approaches to particle formation address some of these issues by monodispersing droplets, of controllable size (1-1000 μm), before simple scalable solidification methods are applied. Recent studies have established NIPS, via this microfluidic approach, for polymer particle formation with well-defined shapes, morphologies and control over porosity. [11] [14] This method also has long-term cost advantages, resulting from the lower material and energy consumption. [15] FNP is another technique that has recently gained interest due to its combination of simplicity, rapidity, repeatability, stability, and control of particle size distribution. [1]

The aim of this research is twofold; firstly, to investigate these complementary techniques, both using the process of NIPS, in order to develop an understanding of how to control PPPO particle size and size distributions through processing parameters to the control of polymer particle size. By controlling the size and hence the demixing and coarsening process, the porosity can also be manipulated. Additionally, this research aims to evaluate these two techniques and their potential for industrial scale production, with a goal to reduce costs and advance the use of PPPO applications.

2. Background

2.1. *Non-solvent induced phase separation (NIPS)*

Phase inversion is a process of controlled polymer transformation whereby, upon demixing, the majority phase within the two-phase system transitions from a liquid to a solid. Initial homogeneous polymer solutions can tolerate small additions of a thermodynamically poor solvent. Upon reaching of a critical non-solvent fraction in these three constituent systems, the solution phase separates to minimise its free energy. Droplets comprising of these mixtures are relevant for particle formation by this approach, utilising microfluidics. Non-solvent can be added to the initial droplet solvent or introduced by interfacial solvent exchange. Upon removal of the good solvent within the droplet, the internal composition approaches this phase boundary, crosses and demixes into two discrete phases, a polymer-rich phase and a polymer-lean phase. The polymer-lean phase, which demixes into droplets by nucleation and growth, coarsens as it attempts to minimise their contact area with the surrounding polymer-rich matrix. The polymer rich phase continues to increase in non-solvent concentration moving along the phase boundary before it eventually solidifies, known as kinetic arrest. This process is illustrated by Fig. 1. This current method is largely used in the production of membranes. [16]

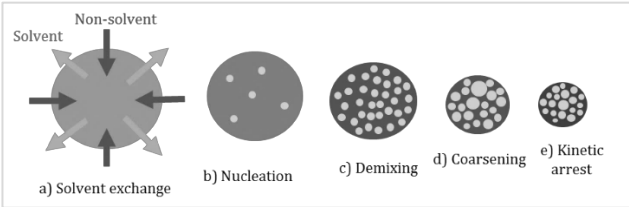

Fig. 1. Schematic to dictate the process of non-solvent induced phase separation (NIPS). a) Solvent exchange. b) Nucleation c) Demixing. d) Coarsening. e) Kinetic arrest. Modified from [14].

2.2. *Microfluidics*

Microfluidic devices are engineered systems containing micro-sized channels, where flows are described by low Reynolds numbers, are highly ordered [15] and can be used to template monodisperse droplets into particles ranging from the micron to nano-size. Initial developments of microfluidics began in the 1990's [17] and has since been widely researched. Many studies investigate the factors influencing droplet size control including type of solvents, [14] flow geometries [18], concentrations [19] and flow rates [20].

The microfluidic devices used for this technique are most commonly made of PDMS due to its low expense and rapid prototyping procedure. [17] There are three common types of channel geometry found in microfluidics; flow-focusing (Fig. 2), co-flow, and T-junction. Flow-focusing the focus of this experiment due to its ability to produce monodisperse droplets with sizes smaller than that of the orifice. [21]

In microfluidics using a flow-focusing geometry, three fluid streams which are pressurized with constant flow rates, converge into a main channel via a narrow orifice (Fig. 2), generally by the aid of syringe pumps. [17] [21] The central stream contains a discrete phase and the outer two streams contain a continuous phase, which are immiscible with each other. It is the immiscibility, hence the interfacial tension, that allow a discrete phase droplet to form at the orifice. [21] Eventually the droplet reaches a critical size and the pressure of the outer liquid overcomes the interfacial tension, and the droplet pinches off from the orifice and travels along the channels in the continuous phase. [21] The pinch-off is largely dictated by the opposition of viscous shear stresses and capillary pressure acting to resist the deformation, which is expressed by the capillary number, Ca (Eq. 1). [17]

$$Ca = \frac{\mu V}{\sigma} \qquad (1)$$

Where μ is the dynamic viscosity of the fluid, V is the fluid velocity and σ is the interfacial surface tension.

Microfluidic technology is an adaptable platform for creating polymeric particles and also offers several unique advantages. These include their precise control of

handling liquids [22] and its significantly reduced volume of reagents and energy input, hence reduction in costs. [17]

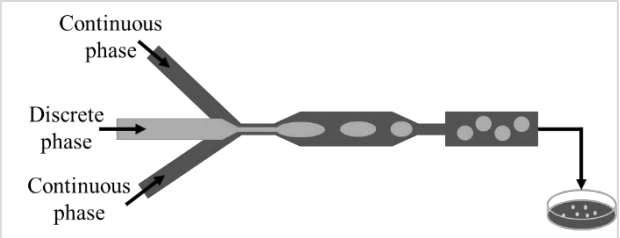

Fig. 2. Schematic of droplet formation using flow-focusing microfluidic geometry, with two converging continuous phase streams to a single discrete phase stream. Modified from [21].

2.3. Flash Nanoprecipitation (FNP)

Polymeric nanoparticles (NPs) have been a subject of growing interest over the past decade, due to their capabilities as a drug delivery tool. [23] They have proved their effectiveness in stabilising and protecting drug molecules such as proteins, peptides, or DNA molecules from degradation in their surrounding environmental [24], as well as controlling their release properties. [25]

Despite the progress made, the effect of NP size on transport properties remains poorly understood, which is largely due to the limited number of methods utilised to generate NPs with a well-controlled particle size and a high degree of uniformity. [12]

FNP is a simple, fast and reproducible technique to produce NPs. [12] This technique was first described by Johnson and Prud'homme at Princeton University, [26] to produce NPs to encapsulate hydrophobic drugs. The method is easily scalable, and the post processing of formulations produced by FNP ensures particle stability. [27] It is therefore easily translatable to larger-scale manufacturing.

Particles are formed by rapid mixing of two streams in a confined volume which creates turbulent mixing and high supersaturation conditions. [23] One stream contains the dissolved polymer in organic good solvent, and the other contains an aqueous stream of a water-miscible non-solvent, which allows instant precipitation of the polymer. [1] This mixture is then quenched into a volume of the non-solvent, defined as the quench volume.

A key requirement for designing nano-particulate delivery systems is understanding of how to effectively control the particle size. [24] In rapid precipitation, mixing conditions control the final particle size distribution. [27] Current research has investigated the influence of different operating conditions on the particle size, such as; polymer or drug amount, polymer molecular weight, immiscible phase ratios and inlet phase addition rates. [28] The impact of certain parameters on particle size, such as polymer concentration have been corroborated by different authors. However, there are contradicting conclusions about other parameters, for example increasing the immiscible phase ratio. [28]

Clearly there is still need for further research into the production of NPs and how particle size can be controlled through FNP process conditions. After extensive literature review, very little previous research was found to have been conducted to specifically investigate implementation of FNP using PPPO.

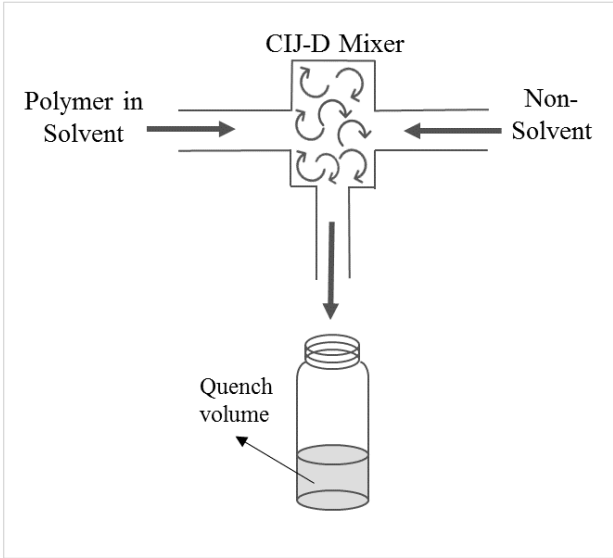

Fig. 3. Schematic to represent process of flash nanoprecipitation (FNP) to produce nanoparticles in a suspension. Modified from [29].

3. Materials and methods

3.1. Materials

Tenax-TA (100/200 mesh) (Buchem BV, The Netherlands), poly(vinyl alcohol) (Sigma Aldrich, Mw = 13-23k, 363170, 87-89% hydrolysed), dichloromethane (VWR, Analar Normapur Grade), tetrahydrofuran (VWR, Analar Normapur Grade), hexane (Sigma Aldrich, ACS Reagent 99%) were used without further purification. Deionized (DI) water was obtained from ELGA CENTRA filtration system.

3.2. Creation of Ternary Phase Diagrams

Two ternary-phase diagrams were produced. One system comprised of PPPO, DCM as the chosen good solvent, and hexane as the chosen non-solvent (this will now be referred to as system 1). The second system comprised of PPPO, THF as the chosen good solvent, and DI water as the chosen non-solvent (this shall now be referred to as system 2). Solutions of PPPO in good solvent were produced with varying concentrations of PPPO from 1 to 25 wt%. These solutions were gravimetrically prepared by adding PPPO to DCM to reach a set concentration, then thoroughly mixed. A micropipette was then used to add the non-solvent drop wise to the solution until it turned turbid. At this point the solution has hit the two-phase boundary of the system. Using the total number of drops, the volume of the pipette, and the density of non-solvent, the composition of the system at the two-phase boundary is calculated and plotted.

3.3. Templated droplets using microfluidics

A PDMS microfluidic device was produced via the common soft lithography technique, which was bonded to a glass cover slide by surface plasma treatment in air. [30] A flow-focussing geometry, with a serpentine channel layout, was used. The channel dimensions were: 500 µm width, 126 µm height, and a constriction width of 150 µm. The two continuous phase streams meet the discrete phase stream at angles of ± 45^0. Channel inlets and outlets of the PDMS are connected to PTFE Microbore Tubing (Sigma Aldrich) with ID 0.031" inner diameter. These are inserted and sealed using epoxy (Araldite, rapid 5 minute).

The continuous phase in all experiments consisted of 10 wt% solution of aqueous PVA. For experiments to investigate the impact of flow ratio from 0.5 to 0.95 on particle size, 1.0 wt% PPPO in DCM solutions were used as the discrete phase. A system of PPPO/DCM/Hexane (1.0 wt% PPPO) was used as the discrete phase for investigating the effects of varying solvent/non-solvent concentration on particle size, at an inlet flow rate of 7 µL min^{-} . For these experiments the PVA flow rate was set to 12 µL min^{-} . Fluids were injected via syringe pumps (Braintree Scientific BS-8000).

Outlet tubing released templated droplets into a petri dish containing an excess solution of PVA. Droplet behaviour was observed using an inverted microscope (Olympus IX71) and images were acquired with a CCD camera (Manta G235, Allied Vision). Images were analysed using open-source image analysis software (ImageJ).

3.4. Nanoparticle preparation using FNP

NPs were prepared using a CIJ-D mixer made of high-density polyethylene, with dimensions described by Han et al. (2012) (0.5 mm inlet tube diameter, 2.5 mm chamber diameter, 5 mm chamber height). [23] A stream of 0.5 mL PPPO in good solvent THF was rapidly mixed with an equal volume of aqueous non-solvent DI water, via manual injection at high flow rates (1 mL s^{-} each stream). The two solutions were injected into the CIJ-D geometry using 1 mL syringes. The collision of the two jets induces supersaturation conditions and hence polymer precipitation in the form of NPs. [1]

The effluent stream was immediately dispensed into a magnetically stirred reservoir containing a quench volume of DI water, using a PTFE coated magnetic stirrer bar. The quenched samples were kept stirring for 1 minute, then left overnight for partial evaporation of THF solvent before DLS characterisation.

Firstly, the quench volume was varied from 0.5 mL to 8 mL, whilst the PPPO/THF concentration was fixed to 0.1 wt% PPPO. Secondly, the concentration was investigated, whilst fixing the quench volume of DI water to 2 mL.

3.5. Nanoparticle size characterisation

Particle size from FNP was measured using a DLS Zetasizer Nanoseries ZS90, Malvern Instruments (Malvern, UK). The light intensity correlation function was collected at a scattering angle $\theta = 173^0$ at $T = 25^0C$. The correlation data reported is a mean average of three separate measurements. The obtained NP suspension was prepared by dilution of 100 µL, extracted using micropipette, into 900 µL of DI water.

In this study, cumulant analysis was employed to obtain particle size. The correlation data is related to the field-field time autocorrelation function $g^{(1)}(\tau)$ (Eq. 2) as:

$$g^{(1)}(\tau) = \frac{\langle E(t)E\times(t+\tau)\rangle}{\langle E(t)E\times(t)\rangle} \quad (2)$$

Where E(t) and E(t + τ) are the scattered electric fields at times t and t + τ. For monodisperse particle in solution the field correlation function decays exponentially (Eq. 3) [31]:

$$g^{(1)}(\tau) = \exp(-\Gamma\tau) \quad (3)$$

Where the decay rate $\Gamma = Dq^2$, D is the translational diffusion coefficient and q is the magnitude of the scattering vector, given by (Eq. 4). [31]

$$q = \frac{4\pi.n\,sin\left(\frac{\theta}{2}\right)}{\lambda} \quad (4)$$

Where refractive index n = 1.333 and wavelength λ = 630nm.

Each sample is a function of the translational diffusion coefficient D, which can be rearranged for particle diameter d_i using the Stokes-Einstein equation for particles in Brownian motion (Eq. 5). [32]

$$d_i = \frac{k_B T}{3\pi\eta D} \quad (5)$$

Where k_B is the Boltzmann constant and dynamic viscosity η = 0.88mPa.s.

3.6. Scanning Electron Microscopy (SEM)

Samples were prepared by drop casting NP suspensions onto clean silicon wafers and subsequently dried in air under reduced pressure. Samples were then coated with a 10 nm layer of Cr before imaging. Measurements were performed on a JEOL JSM6010LA @ using the accelerating voltages from the images (18 kV – 20 kV).

4. Results and discussion

4.1. Ternary phase diagrams

Fig. 4 shows a composite ternary phase diagram that describes the phase boundaries for system 1 and 2, through the method discussed in section 3.2. The boundary for system 1 is indicated by the black line while system 2 is shown using the grey line. The phase behaviour is key to characterising the process of particle formation in microfluidics. The process is illustrated for an initially homogenous droplet, containing 1 wt% PPPO, 20 wt% hexane, and 79 wt% DCM. Fig. 5 shows imaging taken from the microscope used with a 10x objective to characterise this process in real time. Each image is labelled with its associated composition on the phase boundary.

It can be seen that the one-phase region for system 2 is much smaller than that of system 1. This disparity indicates that a lower non-solvent concentration is required for phase separation to occur. This occurred at values of 23-29 wt% concentration of non-solvent for system 1 and 6-13 wt% for system 2. The judicial choice of non-solvent on the size, morphology and porosity of resulting particles, produced by NIPS from microfluidic droplets, is discussed by Udoh, et al. [14] We note similar differences in the position of the phase boundaries with the systems investigated here but have not further characterised the link with morphology within this paper. System 2 was not used in microfluidics as THF is both miscible with the aqueous carrier phase and incompatible with PDMS, which would likely result in severe swelling of the channels. Miscibility with the organic solvent is a requirement for success of FNP, hence the implementation of system 2.

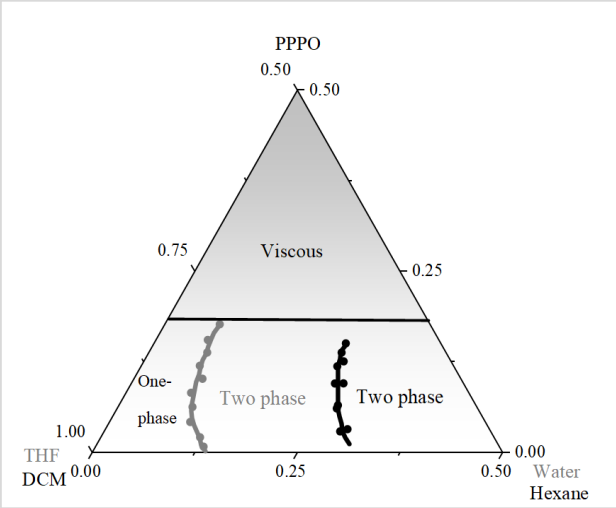

Fig. 4. Ternary Phase Diagram of two systems. System 1 consists of polymer; PPPO, solvent; DCM, and non-solvent; hexane. System 2 consists of polymer; PPPO, solvent; THF, and non-solvent; water.

4.2. Microfluidics

4.2.1. Effect of flow rate ratio

Fig. 6 shows the changing of the diameter of droplets at varying flow rate ratios, which is defined as the flow rate of the continuous phase divided by the total flow rate. For this measurement the discrete phase used contained DCM and PPPO only, while the continuous phase used was PVA. Acquiring microscopic images at modest frame rates (45 fps), coupled with ImageJ analysis, allowed for the accurate measurement of droplets within the channel. Each point is the average diameter of three different droplets examined at different times for the same flow rate ratio. The error bars are taken as one standard deviation from the size of the three droplets. Flow rate ratio measurements begin at 0.53 as flow rate ratios below this value did not produce droplets that could be analysed.

Results indicate that droplet diameter highly depends on the chosen flow rate ratio. Templating droplets in microfluidics is restricted by the necessity for low flow rates, for this experiment various overall flowrates were tested with a final chosen flowrate of 19 µL min^{-1}, this is the flowrate found to produce the most consistent droplet formation for our chosen system and channel geometry in the range of flowrates tested. As the purpose of the investigation was to determine the effects of flow rate ratios, no further flowrates were tested once stable droplet formation had been achieved. However, there is the potential for stable droplet formation at other flow rates.

It was seen through the course of the experiment that flow rate ratios below 0.53 failed to produce consistent and stable monodispersed droplets. For low flow rate ratios and hence low discrete phase flow rates, the droplet formed at the tip of the orifice has increased proportions of the discrete phase added and thus does not allow the continuous phase to narrow the thread, and pinch off from the orifice, resulting in failure to form droplets. [21]

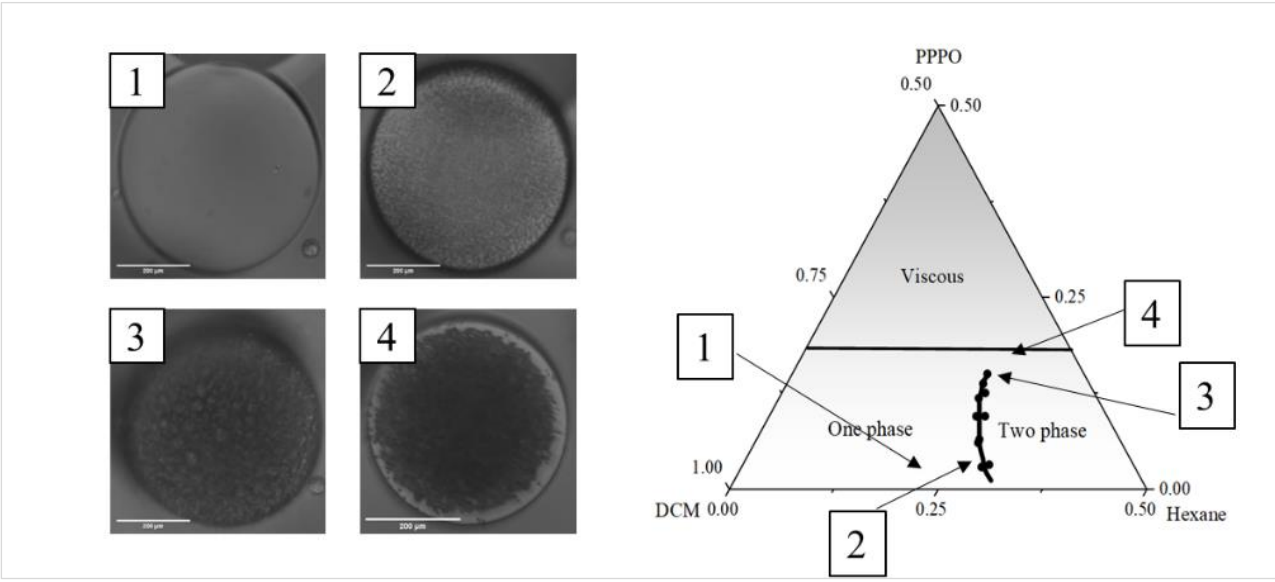

Fig. 5. Images captured using an inverted microscope with 10x objective, for a system of 20 wt% hexane, 1.0 wt% PPPO and 79 wt% DCM. Droplets were formed via NIPS process and their corresponding positions on its ternary phase diagram are displayed.

The flow rate ratio effect on droplet diameter is relatively linear with a regression value of 0.9817. The magnitude of change brought about by changing flow rate ratios is considerable, up to almost a factor of 10. The results show that variation of droplet, and therefore particle sizes, can be achieved across an order of magnitude by simply altering flow rate ratios at a given flowrate for a chosen system.

The Reynolds number can be calculated for the case of microfluidic droplet formation using (Eq. 6) for Reynolds number:

$$Re = \frac{\rho U R_H}{\mu} \quad (6)$$

For multiple streams mixing together, this equation is shown by (Eq. 7): [23]

$$Re = \sum_{i=1}^{n} Re_i = \sum_{i=1}^{n} \frac{\rho_i U_i R_H}{\mu_i} = \sum_{i=1}^{n} \frac{\rho_i Q_i R_H}{\mu_i A} \quad (7)$$

Where ρ_i is the density of component i, Q_i is the flow rate of component i, μ_i is the viscosity of component i, A is the area of the channel, and R_H is the hydraulic radius, given by (Eq. 8):

$$R_H = \frac{4A}{P} \quad (8)$$

Where P is the perimeter of the channel.

For flow through the microfluidic channel this Reynolds number is calculated at 1.03, suggesting a highly laminar flow.

Capillary number can also be used to characterise flow (Eq. 1). For this system the fluid of interest is the continuous phase, PVA. The interfacial surface tension coefficient is that of DCM and PVA which is 1.8 dyn/cm. [33] Using these values the capillary number can be calculated to be 0.05, which suggests that in this system interfacial surface tension dominates and hence this flow is within the dripping regime as discussed by Utada et al. [34] These match observations made within the channel.

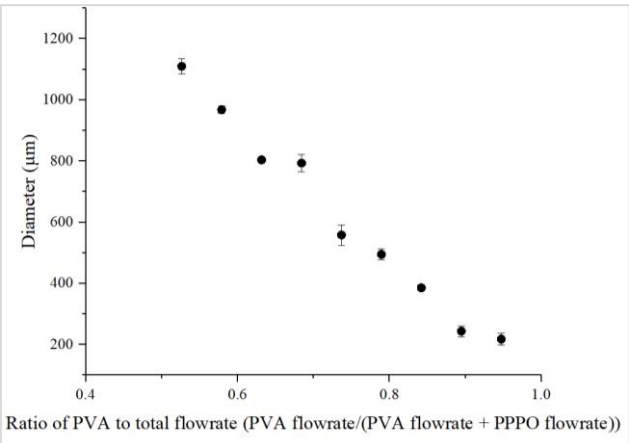

Fig. 6. Droplet diameter with varying flow rate ratios from 0.5 to 0.95 for a 1.0 wt% PPPO/DCM discrete phase and PVA continuous phase.

4.2.2. Effect of polymer concentration

Fig. 7 illustrates the effect of non-solvent concentration in the discrete phase, on droplet diameter with time. The two chosen concentrations investigated were 10 wt% and 20 wt% hexane, due to their varying relative proximity to the phase boundary for system 1. A single droplet for each system was chosen and tracked throughout the process. For comparison, the size reduction of a droplet containing no hexane is given. The images were taken using a microscope at 10x objective and analysed using ImageJ for a single droplet. The error was given by a single pixel on the image, which corresponds to 1 µm. This error is within 1% of the size and hence negligible for this case. The key steps of the process are labelled with images taken to demonstrate the effect of concentration on the NIPS process, in Fig. 5.

Fig. 7 shows the extraction profile for the chosen concentrations. For a solution containing no non-solvent, the droplet diameter reduction can be simply modelled by the following descriptive model (Eq. 9), which is discussed in depth by Watanabe, T. et al. [11]

$$R(t) = (R_0 - R_\infty)\left(1 - \frac{t}{\tau}\right)^{\alpha} + R_\infty \quad (9)$$

Where R_0 is the initial droplet radius, R_∞ is the final particle radius, τ is the time required to reach a constant particle size, t is the time in minutes and α is a parameter to characterize diffusive behaviour. $\alpha = 0.5$ is indicative of Fickian diffusion. Using the radii extraction from the analysis of droplets containing no non-solvent, the following values for the discussed parameters can be found. At time t = 1 mins R(t) is approximately 405 µm, R_0 = 425 µm, R_∞ = 125 µm τ = 6.4 mins, rearranging for α gives us a value of 0.4 suggesting that diffusion is almost Fickian.

It is seen that concentration does have an observable effect on the final size of a particle. At higher concentrations the ratio of final particle to initial droplet size is 12% compared to that of a lower concentration of 33%. This is consistent with findings from Watanabe et al. [11], Udoh et al. [14] and Sharratt et al. [19].

An attempt to model the particle size, using Eq. 9, was attempted. The model can closely describe the size reduction profile for either 10 wt% concentration or 20 wt% before kinetic arrest (with regression values of 0.96 and 0.94 respectively). Interestingly both have alpha values of above 1 (approximately 1.1 and 2 respectively), which suggests a hyperdiffusive process most likely caused by phase inversion. [11]

The results are in line with proposed mechanisms related to the formation of particles by NIPS/solvent extraction. A visual indication of the particle formation is given by a schematic in Fig. 5, along with their position within its respective ternary phase diagram. From the phase behaviour characterized in Fig. 4, a simple explanation arises as to the reason behind the varying effect on size. The higher chosen concentration is closer to the phase boundary relative to the lower concentration, which suggests that less solvent extraction is required to take place in order for phase inversion to occur. Less solvent extraction suggests particles do not have to reduce in size, and therefore increase in non-solvent fraction, as much to

reach the phase boundary required for demixing and eventual phase inversion.

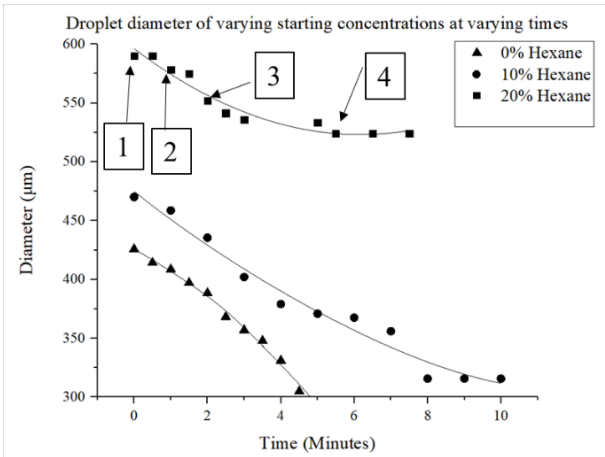

Fig. 7. Variation of droplet diameter with time for varying concentrations of discrete phase of PPPO/DCM/Hexane using 1 wt% PPPO (7 µL min^{-1}) and continuous phase PVA (12 µL min^{-1}). Trend lines are polynomial fits to estimate intermediate particle sizes. Numbers correspond to NIPS process labelled in Fig. 5.

4.3. FNP

NPs were produced via FNP using a CIJ-D geometry where the two inlet streams are PPPO in good solvent, THF, and aqueous bad solvent or non-solvent, H_2O. The two fully miscible solvents are fired at each other in equal volumes and therefore approximate momentums, in a confined volume. Mixing occurs in the turbulent regime, providing the supersaturation conditions required for particle nucleation.

Instantaneous addition of non-solvent to the dilute polymer solution induces single chain collapse into globules before aggregation into clusters or NPs. The particle formation mechanism can be complex but recent studies has evidenced that the controlling nucleation step in particle formation, can change with operating conditions and species concentration. [1]

Hence, operating conditions inside the CIJ-D chamber impact the particle formation mechanism which can be altered by influencing parameters such as inlet polymer concentration. [1] Once formed, diffusion of the residual non-solvent is also important in the process, as they are known to have a plasticising effect on solid polymeric materials, [35] and can be tuned by changing the amount of non-solvent or a posteriori removal of the solvent.

For the FNP system the Reynolds number was calculated using Eq. 7 giving a value of 3600. This value suggests that flow is turbulent which allows for the supersaturation conditions required for particle nucleation.

4.3.1. Effect of polymer concentration

The effect of polymer concentration on particle size was investigated by employing THF as the polymer solvent. We observe an increase in particle size from 114 µm to 244 µm with an increase in polymer concentration from 0.01 wt% to 1.0 wt%. As expected from literature [36] [37] [38], as the concentration of the polymer in the organic phase increases, the particle size increases (Fig. 8).

The increase in particle size can be explained by the increase in polymer-polymer interaction per unit volume. [39] As polymer concentration increases, its corresponding nucleation and growth rates increase faster than its aggregation rate, providing additional time for particle growth before polymer stabilization, and resulting in larger particle size. [27] Additionally, there is an increase in the viscosity of the organic phase which increases diffusional resistance of polymer from the organic phase to the aqueous phase, therefore increasing particle size. [39]

4.3.2. Effect of quench volume

The effect of quench volume on particle size was investigated by employing inlet streams of 0.1 wt% PPPO/THF (0.5 mL) and H_2O (0.5 mL) into varying volumes of H_2O. Fig. 9 indicates an evident decrease in particle diameter with increasing quench volume.

The nanoparticles showed a 46 nm difference in mean particle diameter between 1 mL (218 nm) and 8 mL (170 nm), yet a more significant increase of 144 nm was observed with a 0.5 mL reduction from 1 mL to 0.5 mL (360 nm).

The particle size decrease may result from the increase in volume of the aqueous phase, leading to the increased diffusion of the miscible solvent, THF, into the aqueous phase. [28] [40]

4.3.3. DLS and SEM imaging

Fig. 8 and Fig. 9 compare the size for nanoparticles predicted via DLS analysis compared to SEM images. The solid bars represent the DLS predictions while the striped bars represent the sizes predicted from SEM. The error bars for the DLS measurements were calculated as the standard error between repeat measurements. SEM error bar magnitude is predicted through the standard deviation of the average measurement taken from three particles. Note that no images were obtained for 1.0 wt%, and no conclusive images were obtained from 0.01 wt% as particles produced had aggregated, upon drying, and created bodies of uneven shape and size much higher than predicted, and hence has been excluded as the quality of samples did not allow for definitive conclusions.

Fig. 10 displays images of three samples taken via SEM. Processing of images was performed using ImageJ software. Fig. 10 confirms that the method of calculating sizes through DLS results is a reliable method and accurately predicts the diameter of nanoparticles produced through FNP.

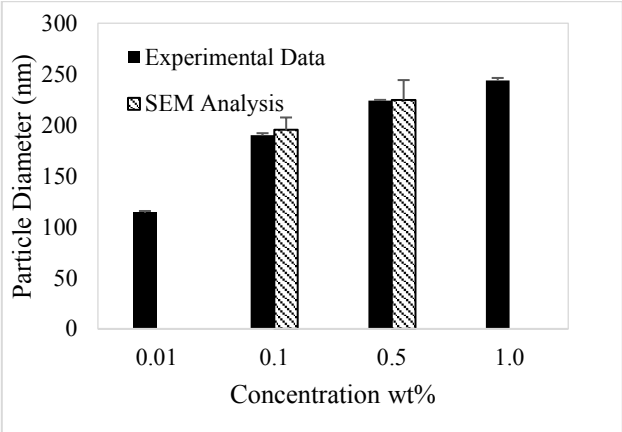

Fig. 8. Comparison of nanoparticle diameter using FNP (mean ± standard error) from DLS experimental values to SEM sizing with varying concentration of PPPO/THF (0.5 m L) using non-solvent H_2O (0.5 mL), into quench volume of H_2O (2 mL).

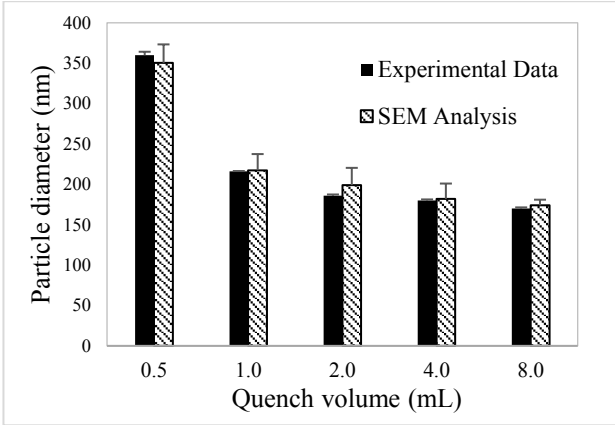

Fig. 9. Comparison of nanoparticle diameter using FNP (mean ± standard error) from DLS experimental values to SEM sizing with varying quench volume of H_2O using 0.1% w/w PPPO/THF (0.5 mL) and H_2O (0.5 mL)

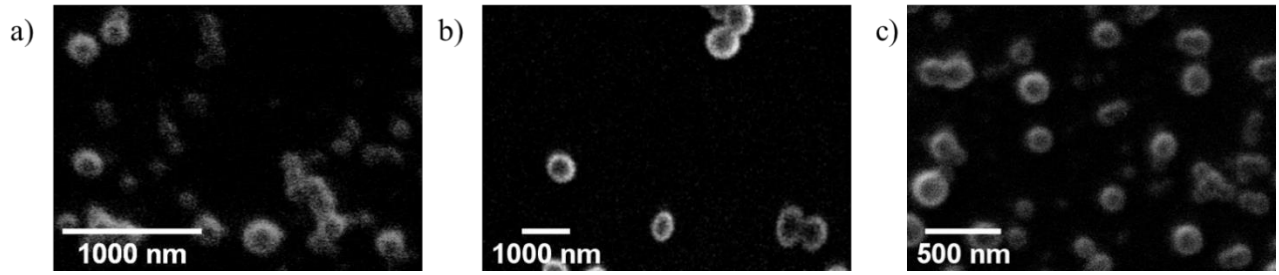

Fig. 10. SEM images of nanoparticles created via NIPS for a system of PPPO/THF/H_2O using FNP for investigating a) the concentration of PPPO at 0.1 wt%. b) a quench volume of 0.5 mL. c) a quench volume of 4 mL.

4.4. Comparison of microfluidic and FNP techniques

Looking at the two techniques, one can draw some direct comparisons with the first being from the flow regimes for both methods. The Reynolds numbers calculated for microfluidics and FNP were 1.03 and 3600 respectively. This suggests laminar and turbulent flow for the respective systems. Reason behind this relates to the relatively high flowrate for FNP compared to microfluidics. This evokes a higher throughput of product per day via FNP method. Production rate for each technique can be calculated using the following equation (Eq. 10)

$$M_F = cQ \qquad (10)$$

Where c is the concentration of PPPO in the solution, and Q is the volumetric flow rate of the solution. Throughput for microfluidics this was found to be 0.01008 g/day/device, whereas for FNP this value is 86.4 g/day/device. Current production of PPPO is found to be around 5 kg/several days, using batch reactors. [41] Therefore, a much greater number of microfluidic devices, run in parallel [42], would be required to meet similar production demands to that using FNP.

Another comparison is the size range of particles produced. From the flow ratio experiments conducted the range that was found was from 200 µm in diameter to 1100 µm. For FNP the values obtained from the DLS analysis ranged from 114 nm to 360nm. The first point of note is that the accessible size range for the FNP system is much smaller than that of the microfluidic approach. A possible reason for this discrepancy is the value for microfluidics does not rely on single chain collapse and aggregation of nanoscale objects but on droplets which can be made from 1-1000 µm, even with 500 um channel dimensions. The minimum occurs due to having a minimum flow rate ratio as discussed in Section 4.2.1, meaning that the droplet formation at the orifice is limited. For FNP the size is governed by nucleation, growth, and aggregation of particles. As mentioned, this system has high flowrates and hence the particle formation timescales are extremely short (milliseconds) suggesting that the size range of particles will also be very small.

The second point of note is the relative sizes produced by each method, from observation microfluidics produces particles in the size range from micro to milli while FNP produces only in the nano-scale. Reasoning for this again, is due to single chain collapse and aggregation leading to stabilisation of NPs whilst µm droplet templates lead to sizes in the micron range. The size of particles produced is very important as it governs the possible uses in industry.

5. Conclusions

The aims of this project were as follows: to investigate two methods for producing particles; microfluidic droplet formation and FNP, and to accurately control various parameters for each, using an understanding of scientific principles and literature. This paper also aimed to investigate the possibility of industrial scale application to produce PPPO particles.

Through experimental work and reference to the scientific literature, the accurate control of particle size was achieved for both microfluidics and FNP. Microfluidic control was achieved through the manipulation of flow ratios and solvent starting concentrations of discrete phase solutions. For FNP this was achieved by controlling quench volume and polymer concentration of PPPO in the organic phase.

Through scientific explanations these results can be explained and predicted in order to control particle size. This leads onto the potential for industrial scale-up, with accurate particle size control using low energy methods, for production of PPPO particles to replace current energy intensive methods that cannot consistently control size. The throughputs for both methods have been calculated in Section 4.4. Although these are extremely low in comparison to current production rates due to their small set-up. Due to the simplicity of the methods, a simple scale up solution should be apparent, including apparatus in parallel and continuous flow.

Each method has benefits and drawbacks that could affect the application of these techniques. Microfluidic droplet formation allows for a large range of micro-sized droplets to be formed in a continuous fashion with easy control over size using flow rate ratios. However, its low throughput would suggest it would be more suited to high value speciality products and research purposes. It also has other potential draw backs such as channel blockage caused by the aggregation of particles, and as mentioned in Section 4.1, PDMS is sensitive to organic solvents which can leading to swelling of the channels. FNP has a much higher throughput which can be easily scaled to enable large production rates of PPPO as discussed in Section 4.4. The particle size associated with this method is in the nano-scale which will apply to different industrial uses compared to particles formed through microfluidics, it also has the drawback of having a small range of size control which may limit its uses.

Overall this study undertaken fulfils the objectives it set out to achieve. Future research, expanding on topics explored in this paper, could be to further investigate upscaling capabilities of the methods outlined and a fundamental examination of the internal porosity generated in particles via the microfluidic-NIPS and FNP approaches.

Acknowledgements

The authors would like to acknowledge William Sharratt, PhD, Imperial College London and Roisin O'Connell, PhD, Imperial College London for their help with SEM imaging, microfluidic fabrication and support throughout this research. They would also like to thank the members of Polymers and Microfluidics group at Imperial College London for their opinions and helpful advice.

References

[1] D. Massella, E. Celasco, F. Salaün, A. Ferri and A. Barresi, "Overcoming the Limits of Flash Nanoprecipitation: Effective Loading of Hydrophilic Drug into Polymeric Nanoparticles with Controlled Structure," *Polymers,* vol. 1092, no. 10, pp. 1-18, 2018.

[2] V. Camel and M. Cause, "Trace enrichment methods for the determination of organic pollutants in ambient air," *Journal of Chromatography A,* vol. 710, pp. 3-19, 1995.

[3] V. Rodríguez-Betancourtt, H. G. Bonilla, M. F. Martínez, A. G. Bonilla, J. P. M. Lazaro, J. T. G. Bonilla, M. A. González and M. O. Amador, "Gas Sensing Properties of NiSb2O6 Micro- and Nanoparticles in Propane and and Carbon Monoxide Atmospheres," *Journal of Nanomaterials,* pp. 1-9, 2017.

[4] D. Zhao and J. J. Pignatello, "Model-aided characterization of Tenax-TA for aromatic compound uptake from water," *Environmental Toxicology and Chemistry,* vol. 23, no. 7, pp. 1592-1599, 2004.

[5] B. Alfeeli, V. Jain, R. K. Johnson, F. L. Beyer, J. R. Heflin and M. Agah, "Characterization of poly(2,6-diphenyl- p-phenylene oxide) films as adsorbent for microfabricated preconcentrators," *Microchemical Journal,* vol. 98, no. 2, pp. 240-245, 2011.

[6] A. Marcillo, V. Jakimovska, A. Widdig and C. Birkemeyer, "Comparison of two common adsorption materials for thermal desorption gas chromatography - mass spectrometry of biogenic volatile organic compounds," *Journal of Chromatography,* vol. 1514, pp. 16-28, 2017.

[7] K. Dettmer and W. Engewald, "Adsorbent materials commonly used in air analysis for adsorptive enrichment and thermal desorption of volatile organic compounds," *Analytical and Bioanalytical Chemistry,* vol. 373, no. 6, pp. 490-500, 2002.

[8] K. Sakodynskii, L. Panina and N. Klinskaya, "A study of some properties of Tenax, a porous polymer sorbent," *Chromatographia,* vol. 7, no. 7, pp. 339-344, 1974.

[9] W. Bertsch, A. Zlatkis, H. M. Liebich and H. J. Schneider, "Concentration and analysis of organic volatiles in Skylab 4," *Journal of Chromatography,* vol. 99, pp. 673-687, 1974.

[10] J. Yeom, "Micro-preconcentrator Technology for Portable Gas Chromatography System," Springer, Dordrecht, 2015.

[11] T. Watanabe, C. G. Lopez, J. F. Douglas, T. Ono and J. T. Cabral, "Microfluidic Approach to the Formation of Internally Porous Polymer Particles by Solvent Extraction," *Langmuir : The ACS Journal of Surfaces and Colloids,* vol. 30, no. 9, pp. 2470-2479, 2014.

[12] A. Bianco, S. L. Burg, A. J. Parnell, C. M. Fernyhough, A. L. Washington, C. J. Hill, P. J. Smith, D. M. Whittaker, O. O. Mykhaylyk and J. P. A. Fairclough, "Control of the Porous Structure of Polystyrene Particles Obtained by Nonsolvent Induced Phase Separation," *Langmuir : The ACS Journal of Surfaces and Colloids,* vol. 33, no. 46, pp. 13303-13314, 2017.

[13] T. Tsuzuki, "Commercial scale production of inorganic nanoparticles," *International Journal of Nanotechnology,* vol. 6, pp. 567-578, 2009.

[14] C. E. Udoh, V. Garbin and J. T. Cabral, "Microporous Polymer Particles via Phase Inversion in Microfluidics: Impact of Nonsolvent Quality," *Langmuir : The ACS Journal of Surfaces and Colloids,* vol. 32, no. 32, pp. 8131-8140, 2016.

[15] D. T. Chiu, A. J. deMello, D. D. Carlo, P. S. Doyle, C. Hansen, R. M. Maceiczyk and R. C. R. Wootton, "Small but Perfectly Formed? Successes, Challenges, and Opportunities for Microfluidics in the Chemical and Biological Sciences.," *Chem,* vol. 2, pp. 201-223, 2017.

[16] J. T. Jung, J. F. Kim, H. H. Wang, E. D. Nicolo, E. Drioli and Y. M. Lee, "Understanding the non-solvent phase separation (NIPS) effect during the fabrication of

microporous PVDF membranes via thermally induced phase separation (TIPS)," *Journal of Membrane Science,* vol. 514, pp. 250-263, 2016.

[17] H. Gu, M. H. G. Duits and F. Mugele, "Droplets formation and merging in two-phase flow microfluidics," *International Journal of Molecular Sciences,* vol. 12, no. 4, pp. 2572-2597, 2011.

[18] A. R. Abate, A. Poitzsch, Y. Hwang, J. Lee, J. Czerwinska and D. A. Weitz, "Impact of inlet channel geometry on microfluidic drop formation," *Physical Review E,* vol. 80, no. 026310, pp. 1-5, 2009.

[19] W. N. Sharrat, A. Brooker, E. S. J. Robles and J. T. Cabral, "Microfluidic solvent extraction of poly(vinyl alcohol) droplets: effect of polymer structure on particle and capsule formation," *Soft Matter,* vol. 14, pp. 4453-4463, 2018.

[20] F. Lapierre, N. Wu and Y. Zhu, "Influence of flow rate on the droplet generation process in a microfluidic chip," *SPIE,* vol. 8204, pp. 1-7, 2011.

[21] M. T. Gokmen and F. E. Du Prez, "Porous polymer particles—A comprehensive guide to synthesis, characterization, functionalization and applications," *Progress in Polymer Science,* vol. 37, no. 3, pp. 365-405, 2012.

[22] J. W. Hickey, J. L. Santos, J. Williford and H. Mao, "Control of polymeric nanoparticle size to improve therapeutic delivery," *Journal of Controlled Release,* vol. 219, pp. 536-547, 2015.

[23] J. Han, Z. Zhu, H. Qian, A. R. Wohl, C. J. Beaman, T. R. Hoye and C. W. Macosko, "A simple confined impingement jets mixer for flash nanoprecipitation," *Journal of Pharmaceutical Sciences,* vol. 101, no. 10, pp. 4018-4023, 2012.

[24] D. Bennet and S. Kim, Polymer Nanoparticles for Smart Drug Delivery, Application of Nanotechnology in Drug Delivery, London: IntechOpen, 2014, pp. 257-310.

[25] S. Ding, N. Anton, T. F. Vandamme and C. A. Serra, "Microfluidic nanoprecipitation systems for preparing pure drug or polymeric drug loaded nanoparticles: an overview," *Expert Opinion on Drug Delivery,* vol. 13, no. 10, pp. 1447-1460, 2016.

[26] B. K. Johnson and R. K. Prud'homme, "Flash NanoPrecipitation of Organic Actives and Block Copolymers using a Confined Impinging Jets Mixer," *Australian Journal of Chemistry,* vol. 56, no. 10, pp. 1021-1024, 2003.

[27] W. S. Saad and R. K. Prud'homme, "Principles of nanoparticle formation by flash nanoprecipitation," *Nano Today,* vol. 11, no. 2, pp. 212-227, 2016.

[28] K. Miladi, S. Sfar, H. Fessi and A. Elaissari, "Nanoprecipitation Process: From Particle Preparation to In Vivo Applications," in *Polymer Nanoparticles for Nanomedicines*, Switzerland, Springer, 2016, pp. 17-53.

[29] K. M. Pustulka, A. R. Wohl, H. S. Lee, A. R. Michel, J. Han, T. R. Hoye, A. V. McCormick, J. Panyam and C. W. Macosko, "Flash Nanoprecipitation: Particle Structure and Stability," *American Chemical Society,* vol. 10, pp. 4367-4377, 2013.

[30] D. C. Duffy, C. McDonald, O. J. A. Schueller and G. M. Whitesides, "Rapid Prototyping of Microfluidic Systems in Poly(dimethylsiloxane)," *Analytical Chemistry,* vol. 70, no. 23, pp. 4974-4984, 1998.

[31] B. J. Frisken, "Revisiting the method of cumulants for the analysis of dynamic light-scattering data," *Applied Optics,* vol. 40, no. 24, pp. 4087-4091, 2001.

[32] A. M. Percebom, J. Janiak, K. Schillen and L. Piculell, "Micellization of water-soluble complex salts of an ionic surfactant with hairy polymeric counterions," *Soft Matter,* vol. 515, no. 9, pp. 515-526, 2013.

[33] H. Zhao, J. Gagnon and U. O. Hafeli, "Process and formulation variables in the preparation of injectable and biodegradable magnetic microspheres," *BioMagnetic Research and Technology,* vol. 5, no. 2, pp. 1-11, 2007.

[34] A. S. Utada, A. Fernandez-Nieves, H. A. Stone and D. A. Weitz, "Dripping to Jetting Transitions in Coflowing Liquid Streams," *The American Physical Society,* vol. 99, no. 094502, pp. 1-4, 2007.

[35] T. G. Fox, "Influence of diluent and of copolymer composition on the glass temperature of a polymer system," *American Physical Society,* vol. 1, pp. 123-132, 1956.

[36] M. Chorny, I. Fishbein, H. D. Danenberg and G. Golomb, "L ipophilic drug loaded nanospheres prepared by nanoprecipitation: effect of formulation variables on size, drug recovery and release kinetics," *Journal of Controlled Release,* vol. 83, pp. 389-400, 2002.

[37] Y. Dong and S. Feng, "In vitro and in vivo evaluation of methoxy polyethylene glycol–polylactide (MPEG–PLA) nanoparticles for small-molecule drug chemotherapy," *Biomaterials,* vol. 28, pp. 4154-4160, 2007.

[38] N. Khayata, W. Abdelwahed, M. F. Chehna, C. Charcosset and H. Fessi, "Preparation of vitamin E loaded nanocapsules by the nanoprecipitation method: From laboratory scale to large scale using a membrane contactor," *International Journal of Pharmaceutics,* vol. 423, pp. 419-427, 2012.

[39] S. Guhagarkar, V. Malshe and P. Devarajan, "Nanoparticles of Polyethylene Sebacate: A New Biodegradable Polymer," *AAPS PharmSciTech,* vol. 10, no. 3, pp. 935-942, 2009.

[40] A. Budhian, S. J. Siegel and K. I. Winey, "Haloperidol-loaded PLGA nanoparticles: Systematic study of particle size and drug content," *International Journal of Pharmaceutics,* vol. 336, no. 2, pp. 367-375, 2007.

[41] R. O'Connell, *Verbal communication,* 2018.

[42] E. Amstad, X. Chen, M. Eggersdorfer, N. Cohen, T. E. Kodger, C. L. Ren and D. A. Weitz, "Parallelization of microfluidic flow-focusing devices," *American Physical Society,* vol. 95, no. 043105, pp. 1-6, 2017.

[43] B. Alfeeli, L. T. Taylor and M. Agah, "Evaluation of Tenax TA thin films as adsorbent material for micro preconcentration applications," *Microchemical Journal,* vol. 95, no. 2, pp. 259-267, 2010.

[44] A. S. Utada, E. Lorenceau, D. R. Link, P. D. Kaplan, H. A. Stone and D. A. Weitz, "Monodisperse Double Emulsions Generated from a Microcapillary Device," *Science,* vol. 308, no. 5721, pp. 537-541, 2005.

[45] A. Prudic, T. Kleetz, M. Korf, Y. Ji and G. Sadowski, "Influence of Copolymer Composition on the Phase Behavior of Solid Dispersions," *American Chemical Society,* vol. 11, no. 11, pp. 4189-4198, 2014.

Development of Sorbents from Sustainable Sources for Biobutanol Recovery

Loui Silawi and Joel Paden
Department of Chemical Engineering, Imperial College London, U.K.

Abstract

Renewable fuels have received wide academic attention in the past few decades due to concerns for the environment and the adverse impact fossil fuel dependence has on it. Biobutanol has desirable characteristics for use as a biofuel though it is produced at low concentrations. This has prompted the investigation in to a sustainable way to separate butanol from water in dilute systems. Cellulose, both in its native composite form as well as in a pure powder form, was used to fabricate cellulose aerogels for use as butanol sorbents. Dissolution by NaOH/Urea, followed by regeneration in dilute HCl and coagulation with an antisolvent was used to produce a hydrogel. The best antisolvent for cellulose agglomeration was investigated and found to be ethanol. Freeze-drying and hydrophobization via a silanization reaction with MTMS were employed in the final step cellulose aerogel fabrication. The aerogels were found to have strong absorptive capabilities in dilute butanol systems with improvements in butanol concentration up to 24.6 g L^{-1} from 2.5 g L^{-1}. Activated carbon from sphagnum peat moss was also synthesised via pyrolysis and chemical activation by acid treatment. Hydrochloric acid and sulfuric acid were trialled and hydrochloric acid was found to be the better acid in the production of activated carbon with improvements in butanol concentration as 17.6 g L^{-1} was attained from a starting concentration of 2.5 g L^{-1}. Cellulose aerogels were characterised using X-ray diffraction, Fourier transform infrared spectroscopy, BET, and X-ray fluorescence. The aerogels were found to have significant improvements in surface area and pore volume, as well as a becoming more amorphous compared to the crystalline cellulose. Activated carbon showed substantial improvements in surface area and pore volume.

1. Introduction

1.1 The Energy Crisis

Transportation fuel demand is projected to grow throughout the next decade as more economies continue to develop with the majority of this fuel being derived from petroleum[1]. Combustion of fuels such as petrol leads to a net increase in CO_2 emissions in the Earth's atmosphere and the transport sector alone accounted for approximately 22% of total energy-related CO_2 emissions in 2015[2]. Due to rising incomes and population growth of 1.8bn people[3], energy consumption is projected to increase by over a quarter in 2040[4]. This has led to a global focus on renewable energy sources as an alternative to diminishing fossil fuels in order to reduce international non-renewable fuel dependency, climate change, and CO_2 emissions.

With growing concerns around the greenhouse gas effect leading to global warming and climate change, the need for a more sustainable fuel is increasing.

1.2 Biobutanol as a Biofuel

Currently the most widely used biofuels are ethanol and biodiesel[5] however biobutanol is attractive as an alternative fuel. Butanol is an aliphatic 4-carbon alcohol[6] that shares the ability with ethanol to blend well with gasoline in any proportion[5]. Butanol can also be used in gasoline engines without modification, unlike ethanol, due to butanol being a longer chained molecule and thus having less polarity and a similar energy density to gasoline[6].

Butanol has more oxygen content than biodiesel so soot can be further reduced. Furthermore, nitrogen oxide emissions can also be reduced as butanol has a higher heat of evaporation than biodiesel and hence a lower combustion temperature[7].

1.3 Current Methods of Biobutanol Production

Biobutanol can be produced by the fermentation of biomass using the bacterium *Clostridium acetobutylicum* in the Acetone-Butanol-Ethanol (ABE) process. The typical substrate for the production of butanol from these bacteria is starch, however, due to this being high in demand in the food industry, use of this would be an inefficient allocation of resources and hence not a long term economic strategy. Algae culture represents a source of biomass for fermentation that is not highly demanded in the food industry and has lower production costs[8].

1.4 Biobutanol Production from Synechocystis PCC 6803

Biobutanol can be produced through bacterial fermentation of cyanobacteria (Synechocystis PCC 6803), commonly known as blue-green algae, which has been genetically modified through protein engineering to alter the metabolic pathway and enhance butanol production. Cyanobacteria are habitable in freshwater as well as marine and terrestrial ecosystems and are also thought to be contribute significantly to the oxygenation of the atmosphere [9]. They are cultivated in a two-stage chemostat which is advantageous as it allows the microbial culture to achieve physiological steady state thus making it possible to maintain the optimum environment for productivity [10].

Butanol usage as a biofuel yields many advantages but the major disadvantage is the low concentration that it is produced at.

2. Background

2.1 Biobutanol Recovery

An n-butanol/water mixture has a heterogeneous azeotrope at 24.8 mol% butanol, meaning that separation must occur in multiple stages as the 2.5 g L^{-1} concentration (0.06 mol%) that is produced during cyanobacteria fermentation is much lower than the azeotropic concentration. An immiscible phase region occurs at butanol concentrations of 1.97 mol% to 48.2 mol% at standard conditions. This signifies the need to increase the butanol concentration up to a value that falls in the immiscible phase region, allowing for a decanter and a distillation column to then further purify the butanol so it can be used as a transportation fuel.

Current separation technologies that can be used to increase the butanol concentration to at least the immiscible phase region include distillation, gas stripping, pervaporation and ionic liquid extraction (ILE), with distillation and ILE being found to be the most viable[11].

The use of a sorbent presents an alternative option that could have the potential to lower butanol separation costs, whilst also ensuring sustainability when produced from renewable sources.

2.2 Cellulose Aerogel

Cellulose is the most abundant organic polymer on earth[12] and is used to manufacture an aerogel for butanol separation from water. It is a polysaccharide consisting of D-glucose[13] and is inherently renewable due to its origin; green plant and bacteria cell walls. Cellulose can be accessed in its pure form from seed hairs of cotton, or in its native composite material with lignin and hemicellulose[12].

Cellulose aerogels have received academic attention for use as an effective sorbent. Cellulose aerogels have been successfully used for the absorption of oil[14] and dyes[15] which can be owed to its high porosity and very low density[16].

Cellulose is inherently highly crystalline[17] and many inter- and intra- molecular hydrogen bonds are present which makes cellulose insoluble in water and most organic solvents[18].

The synthesis of a hydrogel is initiated when cellulose is dissolved and many solvents have been investigated such as N-methylmorphine-N-oxide (NMMO) [19], lithium chloride/N,N-dimethylacetamide (LiCl/DMAC) [20], NH_3/NH_4SCN[21], and NaOH/PEG[16]. NaOH/urea was chosen due to its success as a solvent for cellulose [14][22] [23] as well as its availability and environmental-friendliness compared to the alternatives[16]. Hydrochloric acid is used for the regeneration of cellulose[22]. The gelation step involves the use of an anti-solvent to extract solidified castings from the previous step and initiate cellulose aggregation[24]. Many different antisolvents can be used and are investigated, namely, acetone, methanol, ethanol, propanol, and sulfuric acid[22].

The hydrogel can be converted to an aerogel through various techniques with the most common being supercritical CO_2 exposure [13] [22] [24]. Freeze drying has also been investigated with successful formation of a cellulose aerogel through lyophilization[22][25][26]. Lyophilization is achieved as the vacuum creates an atmosphere that favours sublimation where ice crystals change directly from solid to vapour without passing through a liquid phase[27].

Cellulose is inherently hydrophilic[28] due to the presence of hydroxyl (OH) groups so must be treated to achieve the necessary level of hydrophobicity to be used as an effective sorbent for butanol in water. Methyltrimethoxysilane (MTMS) is used to improve hydrophobicity through a silanization reaction[14], as shown below, via vapour deposition.

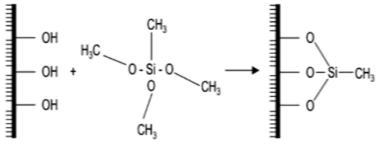

Figure 1: Silanization reaction with cellulose[29]

2.3 Activated Carbon

Activated carbon is another sorbent which can be used to adsorb butanol. Sphagnum peat moss can be used as the starting material for activated carbon production. Peat is partially fossilized plant matter and is formed in wetlands where the rate of plant matter accumulation is greater than that of decomposition; due to the area being poorly oxygenated. Peat is available in large quantities all over the globe and comprises of mainly lignin and cellulose[30].

The peat can be carbonised through pyrolysis at high temperatures as the organic matter decomposes. Activation of the carbon is required and this is achieved either through physical activation, where carbon is exposed to carbon dioxide or steam at temperatures upward of 1200°C, or chemical activation by impregnation with an acid, strong base, or a salt[31]. Chemical activation is more appealing and energy-efficient due to the lower temperatures required. Acid treatment with either hydrochloric or sulfuric acid increases the amount of single-bonded oxygen function groups[32]. Nitric acid treatment improves the adsorptive capacity by increasing surface area, pore volume and pore size distribution. It also removes all contaminants and generates many surface function groups including carbonyl, carboxyl, and nitrate groups[33].

Activated carbon has been used extensively as an adsorbent with great success owing to its high surface area, microporous structure, and high degree of surface reactivity. It has been used in the removal of heavy metals[34] [35], dyes[36], and notably butanol vapour[37] which makes its capability for butanol-in-water adsorption an attractive investigation.

3. Materials and Methods

3.1 Materials

Methanol, ethanol, acetone, nitric acid, hydrochloric acid and sodium hydroxide (pellets) were purchased from VWR Chemicals. Propanol, sulfuric acid, cellulose (fibers, medium) [referred to as high purity cellulose powder], trimethoxymethysilane, urea (pellets), and 1-butanol were purchased from Sigma-Aldrich. Cellulose Oil Only Re-Form Pad [referred to as native cellulose] and Peat Moss Particulate (CANSORB) were purchased from Brady. All chemicals were of analytical grade apart from: nitric acid (68%), hydrochloric acid (37%).

3.2 Fabrication of Cellulose Aerogels

3.2.1 Fabrication of Aerogels from Native Cellulose

Native cellulose (2 wt %) was blended and placed into a solutions of sodium hydroxide and urea (1.9 wt %/ 10 wt %) and dispersed by sonicating for 6 minutes. Five samples were prepared which were then refrigerated for more than 24 hours for gelation.

Solutions were then thawed at room temperature and immersed for 90 minutes in one of five antisolvents for coagulation: methanol, ethanol, propanol, 5% sulfuric acid or acetone.

The coagulated cellulose was then placed in petri dishes to form a cylindrical aerogel with a diameter of 4.8cm and height of 1cm, with immersion in DI water. Samples were then refrigerated for 2 days at -20°C.

Samples were further frozen with liquid nitrogen and then freeze dried at -50°C for 48 hours to remove moisture by lyophilization and form the aerogel.

3.2.2 Fabrication of Aerogels from Pure Cellulose Powder

High purity cellulose powder (2 wt %) was added to a solution of sodium hydroxide and urea (1.9 wt %/ 10 wt %) and stirred for 18 hours for dissolution. Dispersion was achieved successfully by freezing for at least 9 hours, followed by thawing at room temperature with vigorous stirring. This was repeated 4 times. Samples were treated with 1% hydrochloric acid (cellulose solution to HCl volume ratio of 1: 1.7) to regenerate the cellulose.

Ethanol or methanol was then added (HCl/Cellulose solution to antisolvent volume ratio of 1: 1.7) for coagulation. Samples were left in solution for at least 24 hours and this produces the hydrogel. The hydrogel is then vacuum filtered from solution, placed in petri dishes, immersed in DI water and frozen at -20 ºC for 12 hours. Samples were then freeze dried using the same procedure as that done for the native cellulose aerogels.

3.2.3 Hydrophobic Coating of Cellulose Aerogels

Cellulose aerogels from both native cellulose and pure cellulose powder underwent the same hydrophobic coating process. Samples were placed in a desiccator with an open vial containing 1ml of Methyltrimethoxysilane (MTMS) for 24 hours, allowing vapour deposition to occur. Finally, samples were placed in a vacuum oven for 24 hours to remove any excess MTMS.

3.3 Formation of Activated Carbon from Sphagnum Peat Moss Particulate

3.3.1 Formation of Biochar

The sphagnum peat moss particulate was first dried by heating in an oven at 100 °C overnight. The peat moss was then heated from room temperature up to 700 °C in a furnace and held at this temperature for 2 hours. This took place under a nitrogen atmosphere with a flowrate of 150 ml/minute.

3.3.2 Formation of Activated Carbon

The biochar undergoes acid-treatment by immersing in either 2M hydrochloric acid or 1M sulfuric acid (1g biochar/10 ml acid) and heating at 70 °C for 3 hours.

The acid-treated biochar is then washed with DI water and heated from room temperature up to 1000 °C in a furnace and held at this temperature for 3 hours, taking place under a nitrogen atmosphere.

The carbon is then immersed in 68% nitric acid (1g carbon/10ml acid) and heated at 70 °C for 2 hours. Finally, the carbon is further washed with DI water and heated in a furnace at 1000 °C under a nitrogen atmosphere for 3 hours. All heating steps used an N_2 flowrate of 150 ml/minute. Activated carbon samples were individually produced from washing with either 2M HCl or 1M H_2SO_4 to determine the best acid for preparation at a later stage.

3.4 Sorption and Desorption

3.4.1 Native Cellulose Aerogel

A solution of butanol/water with a concentration under 2.5 g L^{-1} was produced. The five cellulose aerogels with different chemical treatment (methanol, ethanol, propanol, 5% sulfuric acid or acetone) were each immersed in 100ml of the butanol solution for 24 hours. The individual cellulose aerogel masses were maintained at 0.55g ± 0.10g.

The aerogels were removed from butanol solutions and placed in individual meshes for 15 minutes to allow any of the insufficiently absorbed solution to drip. Sorbents were then placed in round-bottom flasks and first heated at 100 ºC for 1 hour to ensure that they were not damaged by heat. Heating was then increased to 120 ºC for at least 1 hour to complete desorption. Vapour produced during desorption was condensed and collected in a round-bottom receiver flask.

3.4.2 Activated Carbon

A solution of butanol/water with a concentration under 2.5 g L^{-1} was produced. 4g of HCl-treated carbon was immersed in 100ml of the butanol solution for 24 hours. For H_2SO_4-treated carbon, 6g was immersed in 100ml of the butanol solution for 24 hours.

Activated carbon was vacuum filtered to isolate the sorbent from the remaining butanol solution. The sorbent was then placed in a round-bottom flask and

heated at 140 ºC, with vapour being condensed and collected in a round-bottom receiver flask. HCl-treated carbon was heated for 2 hours and H_2SO_4-treated carbon was heated for 3 hours.

3.5 Aspen Simulation

Aspen Plus V9 was used to model a decanter using the UNIFAC property method, operated at 25 ºC and 1.0133 bar. The concentration of the n-Butanol/Water feed stream was varied, starting at 1.97 mol% (75 g L^{-1}), the minimum value for phase separation to occur. The molar flowrates of butanol in the decanter feed stream and the organic phase stream were recorded as inlet concentration was increased, and the butanol recovery was calculated using the equation:

$$\left(\frac{\text{Molar Flowrate of Butanol in Organic Phase Stream}}{\text{Molar Flowrate of Butanol in Decanter Feed Stream}}\right) \times 100\%$$

3.6 Equipment

The crystalline structures were identified using an X-ray diffraction (XRD) technique using X-ray Diffractometer PANalytical X'Pert Pro (Cu-Kα, 40kV, 20mA) with diffraction angle (2) varied from 5° to 60°. Chemical bonds were recorded by employing use of Fourier transform infrared spectroscopy (FTIR) with the PerkinElmer Spectrum 100 FT-IR Spectrometer. Surface area, pore diameter, and pore volume were determined with Brunauer-Emmett-Tellor method using the Micromeritics TriStar Surface Area and Porosity Analyzer and samples were degassed prior to BET analysis using the Micromeritics FlowPrep 060 Sample Degas system. The elemental composition was investigated using X-ray fluorescence using PANalytical Epsilon 3 XLE X-ray Fluorescence Spectroscopy to confirm the success of the silanization reaction stemming from MTMS treatment. Freeze drying was carried out using Labconco FreeZone 4.5. Concentrations were analysed by gas chromatography, with nitrogen as the carrier gas, using the Hewlett Packard HP 6890 Series GC System.

4. Results and Discussion

4.1 Aspen Simulation

Figure 2 shows how butanol recovery varies with butanol concentration of the decanter feed stream. Whilst phase separation can begin to occur at a concentration of 75 g L^{-1}, recovery is low at 0.3%. However, recovery increases sharply to 50% at a concentration of 135 g L^{-1}, demonstrating the target range of butanol concentrations to be achieved after an initial separation stage before a decanter.

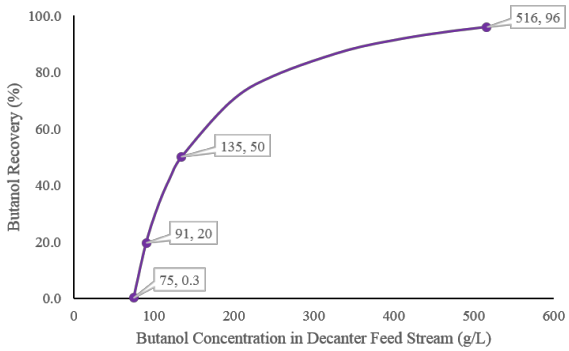

Figure 2: Butanol recovery variation with butanol concentration in decanter feed stream

4.2 Sorbent Preparation

4.2.1 Aerogels from Native Cellulose

The cellulose aerogel derived from native cellulose was yellow-brown in colour which was most likely caused by the lignin in the native material. All five aerogels were similar in colour and had a consistent weight of 0.55g ± 0.10g.

Figure 3: Image of the Native Cellulose Aerogel

4.2.2 Aerogels from Pure Cellulose Powder

Cellulose aerogels from pure cellulose were successfully fabricated with the characteristic steps of formation being most observable. The cellulose powder was converted in to a translucent hydrogel which could be moulded. The Aerogel produced from the hydrogel was blank white and brittle. By observation, the aerogels appeared to be extremely hydrophobic as shown in Figure 7.

Figure 4: Image of Pure Cellulose Powder

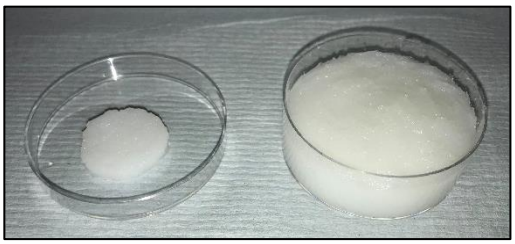

Figure 5: Image of the Pure Cellulose Hydrogel

Figure 6: Image of the Pure Cellulose Aerogel

Figure 7: Image depicting the hydrophobicity of the pure cellulose aerogel

4.2.3 Activated Carbon

The activated carbon was successfully produced from the peat moss starting material. Pyrolysis of the peat moss particulate to form biochar occurred with a 37% yield. A black powder was observed with little to no ash present.

Figure 8: Image of starting material (left) and activated carbon (right)

4.3 Characterisation

4.3.1 Fourier Transform Infrared Spectroscopy

Fourier transform infrared spectroscopy (FTIR) analysis was conducted to aid in the characterisation of the cellulose aerogels. FTIR works on the basic principle of transmittance of infrared through materials to characterise the structure by determining bond types and their bending, stretching, and vibration. This is done by investigating the wavenumber and intensity of the peaks produced.

Figure 9 shows the infrared spectra for native cellulose in its composite material whereas Figure 10 shows the infrared spectra for native cellulose derived aerogels (methanol- or ethanol-treated). The native cellulose exhibits a broad peak at 3286 cm^{-1} (O-H stretching), a sharp peak at 2982 cm^{-1} (C-H symmetrical stretching), a weak peak at 1369 cm^{-1} (in-the-plane C-H bending), and a series of medium-intensity sharp peaks at 1098 cm^{-1} (C-C, C-OH, C-H ring and side group vibrations). There are clear differences between native cellulose and the aerogels though the two aerogels exhibit very similar IR spectra with essentially identical peaks. There is a medium broad peak at 3302 cm^{-1} (O-H stretching), a medium sharp peak at 2848 cm^{-1} (C-H symmetrical stretching), a medium peak at 1627 cm^{-1} (O-H bending), and a strong sharp peak at 995 cm^{-1} (C-C, C-OH, C-H ring and side group vibrations) [38].

Figure 9: IR spectra for Native Cellulose

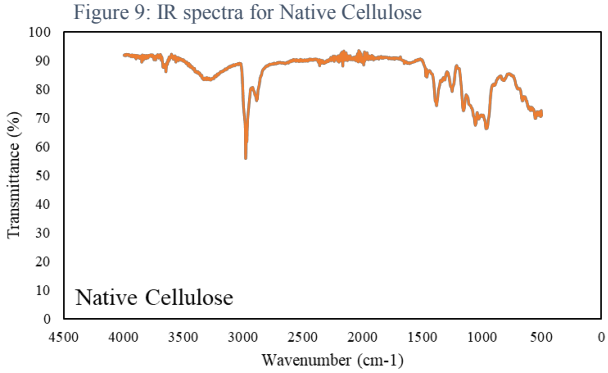

Figure 10: IR spectra for Native Cellulose Aerogels

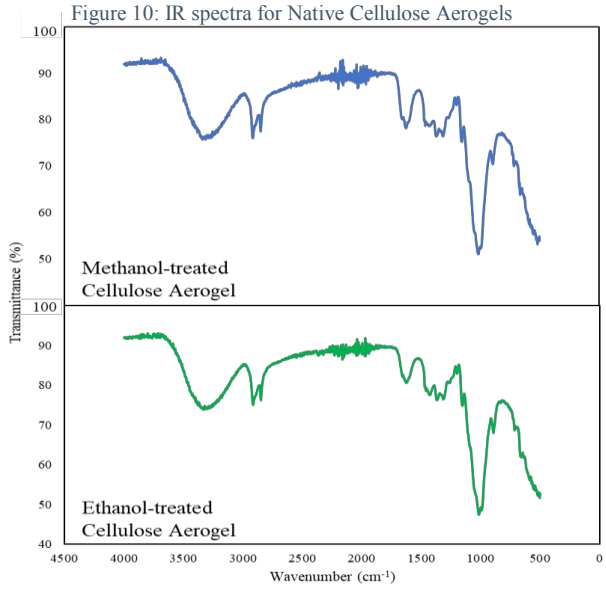

Figure 11: IR spectra for Pure Cellulose Aerogels

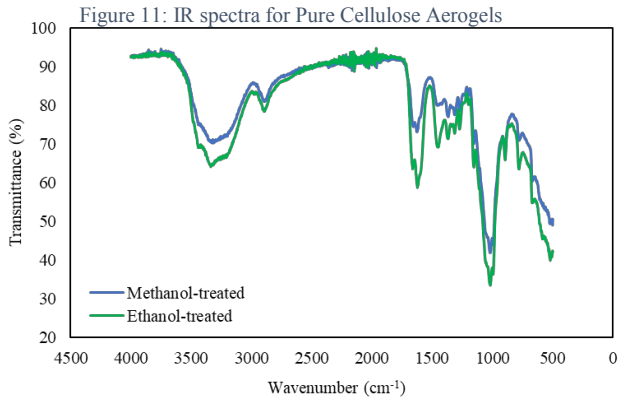

Figure 11 shows the IR spectra of the two pure-cellulose-derived aerogels (methanol- and ethanol-treated). As with the native cellulose batch, these aerogels exhibit very similar peaks though the intensity varies with the ethanol-treated aerogel having a higher intensity at all characteristic peaks. For both, there is a strong broad peak at 3337 cm^{-1} (intermolecular O-H stretching), a weak peak at 2891 cm^{-1} (C-H symmetrical stretching), a sharp peak at 1623 cm^{-1} (O-

H bending), a series of sharp peaks at 1448-1272 cm^{-1} (in-the-phase C-H bending), and a strong sharp peak at 1019 cm^{-1} (C-C, C-OH, C-H ring and side group vibrations) [38].

FTIR with the available equipment was found to be unsuitable for the characterisation of activated carbon.

4.3.2 X-ray Diffraction

X-ray diffraction (XRD) is another technique employed to help characterise the aerogels. XRD uses the ratio of x-rays scattered off a target relative to the incident beam to determine the crystallinity of a material.

Figure 12: XRD graph for native cellulose and the aerogels derived from it

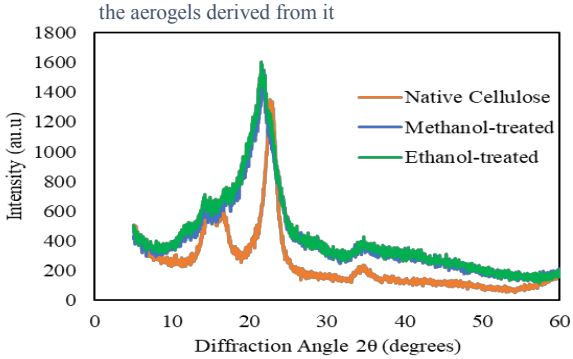

Figure 12 shows the XRD data for native cellulose in its composite material as well as the aerogels derived from it. The native cellulose exhibits multiple peaks owing to its polycrystallinity. The native-cellulose-derived aerogels (methanol- and ethanol-treated) have almost identical spectra whilst having clear differences compared to the native cellulose. The aerogels appear to be crystalline with a sharp peak at 2Θ = 21.5° and interplanar spacing of 4.1313 Å.

The interplanar spacing, or d-value, can be calculated through manipulation of Bragg's law[39]:

$$n \times \lambda = 2 \times d \times sin\theta$$

$$d = \frac{(n \times \lambda)}{(2 \times \sin\theta)}$$

Where n = Order of reflection, λ = Wavelength, and d = Interplanar spacing.

Figure 13: XRD graph for Pure Cellulose and the aerogels derived from it

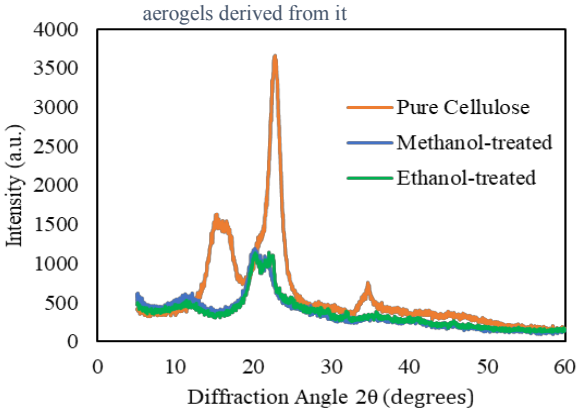

Figure 13 presents the XRD spectra for pure cellulose fibers as well as both pure-cellulose-derived aerogels. The multiple sharp peaks indicate pure cellulose fibers are crystalline and exhibit polycrystallinity. There are clear distinctions between the pure cellulose and aerogels derived from it while both aerogels have almost identical XRD spectra. The crystallinity has significantly decreased as the aerogels have only one split low-intensity peak at 2Θ = 20-22° with a d-value of 4.2286 Å. It is worth noting that both native-cellulose and pure-cellulose derived aerogels have a very similar crystalline structure. XRD was found to be unsuitable for activated carbon characterisation.

4.3.3 X-ray Fluorescence

X-ray fluorescence (XRF) was used to determine the elemental composition of the pure-cellulose-derived aerogels for characterisation purposes as well as to verify the silanization successfully took place in the hydrophobization step. The methanol and ethanol treated aerogels, neglecting any light elements, were confirmed to contain 23.064% and 26.337% silicon by weight, respectively. This confirms the success of the silanization reaction.

4.3.4 BET

Brunauer–Emmett–Teller (BET) analysis was carried out to determine the surface area, pore diameter, and pore volume of both aerogel batches (native-cellulose- and pure-cellulose-derived) as well as activated carbon samples. Surface area presented is the BET surface area, pore volume presented is the single point adsorption total pore volume of pores less than 65.3362 nm at a relative pressure of 0.97, and pore diameter presented is the adsorption average pore width (4V/A by BET).

	Material	Surface Area (m^2 g^{-1})	Pore Diameter (nm)	Pore Volume (cm^3 g^{-1})
	Native Cellulose	0.50	3.90	0.0005
Aerogels	Ethanol-treated	0.28	13.74	0.0009
	Methanol-treated	1.10	11.75	0.0032
	Propanol-treated	1.29	20.86	0.0067
	Acetone-treated	0.90	6.22	0.0014
	Sulfuric Acid-treated	0.94	10.29	0.0024

Figure 14: BET data for Native Cellulose and the Aerogels derived from it

Figure 14 shows the results for native cellulose and the aerogels derived from it. The surface area has doubled after modification for all cellulose aerogels, barring methanol-treated, which is desirable in the search for a good sorbent. Furthermore, the pore volume increases noticeably which again is desirable due to the enhanced holding capacity.

	Material	Surface Area (m^2 g^{-1})	Pore Diameter (nm)	Pore Volume (cm^3 g^{-1})
	Pure Cellulose Powder	1.04	9.07	0.0024
Aerogels	Methanol-treated	17.54	11.66	0.0511
	Ethanol-treated	11.50	6.61	0.0190

Figure 15: BET data for Pure Cellulose and aerogels derived from it

Figure 15 shows the results for the pure cellulose and the aerogels derived from it. There is a clear and

substantial increase in the surface area, with respective increases of 17- and 11-fold for the methanol- and ethanol-treated aerogels which indicates successful modification of the cellulose to produce a suitable sorbent as enhanced surface area is desirable. Equally noteworthy is the increase in pore volume with a 25-fold increase in the methanol-treated aerogel and a 10-fold increase in the ethanol-treated aerogels. The BET results are promising as they present a very high increase in desirable characteristics for an effective sorbent.

	Material	Surface Area (m^2 g^{-1})	Pore Diameter (nm)	Pore Volume (cm^3 g^{-1})
	Peat Moss Particulate	1.08	5.06	0.001
Activated Carbon	HCl-treated	670.43	1.89	0.317
Activated Carbon	H_2SO_4 -treated	1706.76	1.94	0.342

Figure 16: BET data for Peat Moss and the activated carbon derived from it

Figure 16 shows the results for the peat moss particulate and the activated carbon derived from it. Here the largest increases in surface area are observed with the HCl-treated activated carbon surface area of 670 m^2 g^{-1} and H_2SO_4-treated activated carbon displaying a surface area of 707 m^2 g^{-1}. This signifies a massive increase as the starting material, peat moss particulate, had a surface area of 1 m^2 g^{-1}. Since activated carbon uses adsorption for butanol sorption, the surface area increases are significant and desirable as a larger surface area will directly improve adsorption rates. Furthermore, the pore volume showed substantial improvements as the pore volumes increased by 233% and 252% for HCl-treated and H_2SO_4-treated activated carbon, respectively. Compared to literature these results have indicated successful carbonisation and activation of the initial biomass[40].

4.4 Sorption and Desorption

Sorption and desorption experiments were conducted to determine the sorption capacity and ultimately the concentration of butanol that can be attained with the use of the different sorbents.

4.4.1 Aerogels from Native Cellulose

Figure 17 shows the butanol concentration of the liquid collected in the receiver flask after desorption when native cellulose-derived aerogels were used as the sorbent, whilst Figure 18 shows the butanol concentration of the remaining solution after the sorbent was removed.

	Aerogel	Butanol Concentration (g L^{-1})		Increase
		Before Sorption	After Desorption	
Native Cellulose Derived	Ethanol-treated	2.01	24.56	1124%
Native Cellulose Derived	Methanol-treated	2.01	21.33	963%
Native Cellulose Derived	Propanol-treated	2.01	14.25	610%
Native Cellulose Derived	Acetone-treated	2.06	4.22	105%
Native Cellulose Derived	Sulfuric Acid-treated	2.01	2.2	9%

Figure 17: Butanol Concentration changes with Native Cellulose Aerogels

	Aerogel	Butanol Concentration (g L^{-1})		Decrease
		Before Sorption	In Remaining Solution After Sorption	
Native Cellulose Derived	Ethanol-treated	2.01	1.90	5.5%
Native Cellulose Derived	Methanol-treated	2.01	1.83	8.8%
Native Cellulose Derived	Propanol-treated	2.01	1.95	3.1%
Native Cellulose Derived	Acetone-treated	2.06	1.69	17.9%
Native Cellulose Derived	Sulfuric Acid-treated	2.01	1.78	11.1%

Figure 18: Butanol Sorption results with Native Cellulose Aerogels

As shown in Figure 17, the cellulose aerogels have significant increases in butanol concentration from before sorption to after desorption with best increases of 1124%, 963%, 610%, which correspond to final attained butanol concentrations of 24.6, 21.3, and 14.25 g L^{-1}, respectively. Evidently, the ethanol-treated aerogel exhibited the highest increase in butanol concentration after desorption which was expected as ethanol use as a coagulant in cellulose aerogel fabrication has been extensively investigated with good results[14] [41] [42].

Figure 19 shows the sorption capacity of each of the

	Aerogel	Sorption Capacity (g/g)	Absorbed Mass successfully Desorbed
Native Cellulose Derived	Ethanol-treated	16.23	28.8%
Native Cellulose Derived	Methanol-treated	14.97	54.1%
Native Cellulose Derived	Propanol-treated	15.63	52.65%
Native Cellulose Derived	Acetone-treated	7.13	65.31%
Native Cellulose Derived	Sulfuric Acid-treated	3.81	99.65%

Figure 19: Sorption and desorption properties of Native Cellulose Aerogels

cellulose aerogels (defined as mass of solution absorbed per unit mass of sorbent) as well as the percentage of the volume absorbed that was successfully desorbed during the desorption-by-heating. As shown in Figure 19, the three aerogels with the highest sorption capacities are the same three best performers in terms of final butanol concentration after desorption, namely ethanol-, methanol-, and propanol-treated with sorption capacities of 16.23, 14.97, and 15.63 g/g, respectively.

The acetone- and sulfuric acid- treated aerogels had noticeably the lowest increases in butanol concentration with 105%, and 9%, respectively. This, along with the apparent high decrease in butanol concentration in the remaining solution after sorption, the abnormally low sorption capacity, as well as their documented successful use in other fabrication of cellulose aerogels[43][44] indicates that these results may be anomalous.

The two highest performers, ethanol-treated and methanol-treated, were the basis for the fabrication of the pure cellulose powder-derived aerogels.

4.4.2 *Aerogels from Pure Cellulose*

Sorption and desorption experiments were conducted for the pure-cellulose-derived aerogels however negligible amounts of distillate were observed.

4.4.3 *Activated Carbon*

Figure 20 shows the butanol concentration of the liquid collected in the receiver flask after desorption when activated carbon was used as the sorbent, whilst Figure 21 shows the butanol concentration of the remaining solution after sorption.

Activated Carbon	Butanol Concentration (g L^{-1})		Increase
	Before Sorption	After Desorption	
HCl-treated	2.02	17.57	771.15%
H_2SO_4-treated	2.14	12.27	472.64%

Figure 20: Butanol Concentration changes with Activated Carbon

Activated Carbon	Butanol Concentration (g L^{-1})		Decrease
	Before Sorption	In Remaining Solution After Sorption	
HCl-treated	2.02	0.14	93.20%
H_2SO_4-treated	2.14	0.04	98.20%

Figure 21: Butanol Sorption results with Activated Carbon

As shown in Figure 20, the activated carbon had successfully improved the butanol concentration, with the HCl- and H_2SO_4- treated activated carbon demonstrating increases of 771% and 473%, respectively. These increases, coupled with very impressive decreases in butanol concentration of the remaining solution of 93% and 98% in the HCl- and H_2SO_4- treated activated carbon, highlight the fabricated activated carbon's sorption capability.

Activated Carbon	Sorption Capacity (g/g)	Absorbed Mass successfully Desorbed
HCl-treated	2.00	88.13%
H_2SO_4-treated	2.15	100%

Figure 22: Sorption and Desorption properties for Activated Carbon

However, as shown in Figure 22, the mass of solution absorbed per mass of activated carbon, or sorption capacity, is relatively low; 2 and 2.15 g/g. It is worth noting that although sorption capacity per unit mass is quite low, the desorption was very effective in both activated carbon sorbents with the percentage of the volume absorbed that was successfully desorbed being 100% for H_2SO_4–treated activated carbon and 88.13% for the HCl-treated activated carbon.

5. Conclusion and Outlook

Materials with capabilities to significantly improve butanol concentration were successfully fabricated. However, the aim of 75 g L^{-1} butanol was not achieved with the use of neither the cellulose aerogels nor the activated carbon.

Cellulose aerogels made from native cellulose were found to significantly improve butanol concentration and the best coagulating agent was found to be ethanol; attaining a butanol concentration of 24.56 g L^{-1} from 2.5 g L^{-1}. However, there are many ways in which the fabrication process could be improved. For instance, the gelation step could be the first point of improvement, perhaps by using more antisolvent for agglomeration, as a hydrogel was not formed successfully. Furthermore, the native cellulose composite material is riddled with lignin, which has little to no potential for butanol sorption, and delignification to produce a purer starting material could improve results. The hydrophobicity of these cellulose could also be improved as the silanization reaction appeared to not be completely successful as much water was absorbed.

Cellulose aerogels derived from pure cellulose showed super hydrophobicity which was achieved via XRF-confirmed silanization by using MTMS. Unfortunately, the sorption and desorption experiments were unable to be performed due to the super-hydrophobicity of the material and the difficulty submerging the aerogel in the very dilute butanol solution. Therefore, a lower degree of silanization could be attempted or ideally a method for effective contact with most of a dilute solution could be investigated and this may yield very high concentrations of butanol.

Activated carbon was successfully synthesised and tailored to suit butanol adsorption.
Hydrochloric acid was found to be the best acid for chemical activation of the carbon though sulfuric acid was similar in effectiveness. However, the surface area and porosity could have been improved with characterisation showing lower values than literature. This can be achieved with more acid-treatment though the use of a base or salt could also be investigated.

For all investigations, with less time constraints repeats could be conducted which improves the reliability of the results and the conclusions that come from them.

Acknowledgements

We would like to express our deepest gratitude to Zhixuan Wang for her support and help throughout the course of the project.

References

[1] BP. 2018. BP Energy Outlook - 2018 edition. [Online]. Available from: https://www.bp.com/content/dam/bp/business-sites/en/global/corporate/pdfs/energy-economics/energy-outlook/bp-energy-outlook-2018.pdf

[2] GABC. 2017. Global Status Report based on IEA World Energy Balances and Statistics. [Online]. Available from: https://ec.europa.eu/energy/sites/ener/files/documents/020_fatih_birol_seif_paris_11-12-17.pdf?fbclid=IwAR0mexNyNv0XG3bj0Wbg-zSjY0-88NINn3i693mlGk9EDyBmaWXl60QlV0oMax Roser and Esteban Ortiz-Ospina (2018) - "World Population Growth". Published online at OurWorldInData.org. Retrieved from: 'https://ourworldindata.org/world-population-growth' [Online Resource]

[3] Our World in Data. 2017. World Population Growth. [Online]. Available from: https://ourworldindata.org/world-population-growth?fbclid=IwAR3hJ7p7WPpxfxd-g8Kz_W3EZFFBIBN9TMV0opgsYC_EPljjngkEM63_HUc

[4] EIA. 2017. International Energy Outlook 2017. [Online]. Available from: https://www.eia.gov/pressroom/presentations/mead_91417.pdf

[5] (2013) Biofuels Issues and Trends;2013 ASI 3168-234.

[6] Atsumi, S, Hanai, T & Liao, J.C. 2008. Non-fermentative pathways for synthesis of branched-chain higher alcohols as biofuels. Nature. 451, pp. 86-89.

[7] Yilmaz et al. 2014. Effect of biodiesel–butanol fuel blends on emissions and performance characteristics of a diesel engine. Fuel. 135(-), pp. 46-50.

[8] Kaminski, W & Tomczak, Elwira & Górak, Andrzej. (2011). Biobutanol - Production and purification methods. Ecological Chemistry and Engineering S. 18. 31-37.

[9] Antonia Herrero, Alicia M Muro-Pastor & Enrique Flores. (2001) Nitrogen control in cyanobacteria. Journal of Bacteriology. 183 (2), 411-425.

[10] Dechatiwongse, P., Maitland, G. & Hellgardt, K. (2015) Demonstration of a two-stage aerobic/anaerobic chemostat for the enhanced production of hydrogen and biomass from unicellular nitrogen-fixing cyanobacterium. Algal Research. 10 189-201.

[11] Wagner, J. L., Lee-Lane, D., Monaghan, M., Sharifzadeh, M. & Hellgardt, K. (2019) Recovery of excreted n-butanol from genetically engineered cyanobacteria cultures: Process modelling to quantify energy and economic costs of different separation technologies. Algal Research. 37 92-102.

[12] Klemm, D., Heublein, B., Fink, H. & Bohn, A. (2005) Cellulose: fascinating biopolymer and sustainable raw material. Angewandte Chemie (International Ed. in English). 44 (22), 3358-3393.

[13] O'SULLIVAN, A. (1997) Cellulose: the structure slowly unravels. Cellulose. 4 (3), 173-207.

[14] Nguyen, S. T., Feng, J., Le, N. T., Le, A. T. T., Hoang, N., Tan, V. B. C. & Duong, H. M. (2013) Cellulose Aerogel from Paper Waste for Crude Oil Spill Cleaning. Industrial & Engineering Chemistry Research. 52 (51), 18386-18391.

[15] Chin, S., Jimmy, F. B. & Pang, S. (2016) Fabrication of Cellulose Aerogel from Sugarcane Bagasse as Drug Delivery Carriers. Journal of Physical Science. 27 (3), 159-168.

[16] Jian, L., Caichao, W., Yun, L. & Qingfeng, S. (2014) Fabrication of cellulose aerogel from wheat straw with strong absorptive capacity. Frontiers of Agricultural Science and Engineering. 1 (1), 46.

[17] Park, S., Baker, J. O., Himmel, M. E., Parilla, P. A. & Johnson, D. K. (2010) Cellulose crystallinity index: measurement techniques and their impact on interpreting cellulase performance. Biotechnology for Biofuels. 3 (1), 10.

[18] Lindman, B., Karlström, G. & Stigsson, L. (2010) On the mechanism of dissolution of cellulose. Journal of Molecular Liquids. 156 (1), 76-81.

[19] Fink H P, Weigel P, Purz H, Ganster J. Structure formation of regenerated cellulose materials from NMMO-solutions. Progress in Polymer Science, 2001, 26(9): 1473–1524

[20] Tosh B, Saikia C N, Dass N N. Homogeneous esterification of cellulose in the lithium chloride-N,N-dimethylacetamide solventsystem: effect of temperature and catalyst. Carbohydrate Research, 2000, 327(3): 345–352

[21] Cuculo J A, Smith C B, Sangwatanaroj U, Stejskal E O, Sankar SS. A study on the mechanism of dissolution of the cellulose/NH3/NH4SCN system. I. Journal of Polymer Science Part A: Polymer Chemistry, 1994, 32(2): 229–239

[22] Cai, J., Kimura, S., Wada, M., Kuga, S. & Zhang, L. (2008) Cellulose aerogels from aqueous alkali hydroxide-urea solution. ChemSusChem. 1 (1-2), 149-154.

[23] Xiong, B., Zhao, P., Hu, K., Zhang, L. & Cheng, G. (2014) Dissolution of cellulose in aqueous NaOH/urea solution: role of urea. Cellulose. 21 (3), 1183-1192.

[24] Liebner, F., Haimer, E., Wendland, M., Neouze, M., Schlufter, K., Miethe, P., Heinze, T., Potthast, A. & Rosenau, T. (2010) Aerogels from Unaltered Bacterial Cellulose: Application of scCO2Drying for the Preparation of Shaped, Ultra-Lightweight Cellulosic Aerogels. Macromolecular Bioscience. 10 (4), 349-352.

[25] Jin, H., Nishiyama, Y., Wada, M. & Kuga, S. (2004) Nanofibrillar cellulose aerogels. Colloids and Surfaces A: Physicochemical and Engineering Aspects. 240 (1), 63-67.

[26] Ström, V., Nogués, J., Berglund, L. A., Salazar-Alvarez, G., Gedde, U. W., Azizi Samir, M. A. S, Ikkala, O., Olsson, R. T. & Belova, L. (2010) Making flexible magnetic aerogels and stiff magnetic nanopaper using cellulose nanofibrils as templates. Nature Nanotechnology. 5 (8), 584-588.

[27] Wang, W. (2000) Lyophilization and development of solid protein pharmaceuticals. Netherlands, Elsevier B.V.

[28] Song. (2013) Approaching super-hydrophobicity from cellulosic materials: A Review. Nordic Pulp and Paper Research Journal. 28 (2), 216-238.

[29] Thomas, S, Pothan, L.A & Mavelil-sam, R (c2018). Biobased Aerogels: Polysaccharide and Protein-based Materials.

[30] Couillard, D. (1994) The use of peat in wastewater treatment. Elsevier Ltd.

[31] Hayashi, J., Kazehaya, A., Muroyama, K. & Watkinson, A. P. (2000) Preparation of activated carbon from lignin by chemical activation. Carbon. 38 (13), 1873-1878.

[32] Chen, J. P. & Wu, S. (2004) Acid/Base-treated activated carbons: characterization of functional groups and metal adsorptive properties. Langmuir : The ACS Journal of Surfaces and Colloids. 20 (6), 2233-2242.

[33] Allwar, A., Hartati, R. & Fatimah, I. (2017) Effect of nitric acid treatment on activated carbon derived from oil palm shell. AIP Conference Proceedings. 1823 (1).

[34] Kadirvelu, K., Thamaraiselvi, K. & Namasivayam, C. (2001) Removal of heavy metals from industrial wastewaters by adsorption onto activated carbon prepared from an agricultural solid waste. Bioresource Technology. 76 (1), 63-65.

[35] Monser, L. & Adhoum, N. (2002) Modified activated carbon for the removal of copper, zinc, chromium and cyanide from wastewater. Separation and Purification Technology. 26 (2), 137-146.

[36] Namasivayam, C. & Kavitha, D. (2002) Removal of Congo Red from water by adsorption onto activated carbon prepared from coir pith, an agricultural solid waste. Dyes and Pigments. 54 (1), 47-58.

[37] Cao, Yuhe & Wang, Keliang & Wang, Xiaomin & Gu, Zhengrong & Gibbons, William & Vu, Han. (2015). Adsorption of butanol vapor on active carbons with nitric acid hydrothermal modification. Bioresource technology. 196. 525-532. 10.1016/j.biortech.2015.08.027.

[38] Fan, M., Dai, D. & Huang, B. (2012) Fourier Transform Infrared Spectroscopy for Natural Fibres. InTech.

[39] Kacher, J., Landon, C., Adams, B. L. & Fullwood, D. (2009) Bragg's Law diffraction simulations for electron backscatter diffraction analysis. Ultramicroscopy. 109 (9), 1148-1156.

[40] Namane, A., Mekarzia, A., Benrachedi, K., Belhaneche-Bensemra, N. & Hellal, A. (2005) Determination of the adsorption capacity of activated carbon made from coffee grounds by chemical activation with ZnCl2 and H3PO4. Journal of Hazardous Materials. 119 (1-3), 189.

[41] Tkalec, G., Knez, e. & Novak, Z. (2015) Formation of polysaccharide aerogels in ethanol. RSC Advances. 5 (94), 77362-77371.

[42] Karadagli, I., Milow, B., Ratke, L., Schulz, B., Seide, G. & Gries, T. (2012) Synthesis and characterization of highly porous cellulose aerogels for textiles applications.

[43] Geng, H., Yuan, Z., Fan, Q., Dai, X., Zhao, Y., Wang, Z. & Qin, M. (2014) Characterisation of cellulose films regenerated from

acetone/water coagulants. Carbohydrate Polymers. 102 438-444.

[44] Zhou, J., Zhang, L., Shu, H. & Chen, F. (2002) Regenerated cellulose films from NaOH/urea aqueous solution by coagulating with sulfuric acid. Journal of Macromolecular Science, Part B. 41 (1), 1-15.

Development of a Computational Fluid Dynamics Model with Experimental Validation of an Improved Biomass Cookstove

Lionel Ong and Collin Wong
Department of Chemical Engineering, Imperial College London, U.K.

Abstract
This study discusses the development and validation of a Computational Fluid Dynamics (CFD) model of a Prakti biomass cookstove. The improved biomass cookstove aims to reduce particulate matter emissions which afflict 2 billion people with negative health effects every year. ANSYS Fluent was used to build the CFD model with coupled flow and energy considerations. The focus of this research is the improvement on previous work by Hamilton & Lucas (2017), more specifically on combustion modelling. A combustion model adapted from wood dust combustion was implemented and model outputs such as velocity, temperature, emissions mass fraction and air intake were investigated. The model was validated with experiments where temperatures in the model were, on average, 33% lower than experimental measurements at different locations in the cookstove. The CFD model showed that 71% of the air was entering the front air inlet with significant recirculation of that air out of the cookstove, this resulted in reduced air-fuel mixing and incomplete combustion where carbon monoxide (CO) by mass was twice that of carbon dioxide (CO_2). The wood blocks in the model were then lifted by 4 cm to increase air ingress from the bottom of the cookstove, and this resulted in an approximate 50% decrease in CO emissions.

Keywords: *computational fluid dynamics, experimental validation, biomass, improved cookstove, natural convection, radiation, combustion, emissions*

Introduction

Approximately 2.7 billion people rely on solid biomass fuel for their daily energy needs and the use of inefficient cookstoves results in indoor air pollution (IAP) that afflicts 2 billion people with health-related ailments every year (MacCarty & Bryden, 2016). Moreover, an estimated 4.3 million people die prematurely every year from exposure to IAP (Ali & Wei, 2017). Apart from negative health effects, the pollutants released are greenhouse gases which contribute to global warming (Quist et al., 2016). In India, almost 50% of households still rely on solid fuels for their cooking needs; women and children are the most affected with more than 51,000 children dying every year from respiratory infections caused by solid fuel use (India Cookstoves and Fuels Market Assessment, 2018).

Prakti, a social enterprise based in India, is committed to reducing inequality and poverty and contributing to environmental sustainability. As a fully integrated cookstove developer from design to manufacturing to distributing, Prakti seeks to build affordable, clean, and efficient cookstoves that reduce IAP by up to 90 percent. The rural communities in India have traditionally used inefficient three-stone cooking fires or mud stoves, accentuating the need for Prakti to offer affordable and easy-to-use cookstoves to maximise uptake (Prakti, 2018).

Experimentally testing new design features of cookstoves is resource-intensive and time consuming. Moreover, traditional designs of cookstoves use semi-empirical guidelines with limited incorporation of detailed heat transfer mechanisms (Baldwin, 1988). Using Computational Fluid Dynamics (CFD) to model fluid flow and heat transfer in a cookstove can significantly reduce the aforementioned resource and time constraints; however, the caveat is that combustion of non-uniformly distributed biomass fuel results in a complex three-dimensional flame. Additionally, the complex chemistry and kinetics of fuels, and the highly turbulent and unsteady flow in a cookstove present additional challenges in modelling (Wohlgemuth, Mazumder, & Andreatta, 2009).

This report outlines the development of a CFD model of a Prakti biomass cookstove with a focus on combustion modelling. More specifically, this study details incremental steps from building of the mesh to implementing physical models that simulate natural convection, heat transfer and combustion. Additionally, the validity of the CFD model was assessed by comparing with experimental results. The main aim of developing a reliable CFD model is to aid Prakti in further improving their cookstove design by better allocating their resources and time.

Background

Over the last 3 decades, awareness of and the scientific involvement in the social, health and environmental challenges of biomass-fuelled cookstoves has risen; alas, only 30 of 500 journal articles published relating to biomass cookstoves utilised computational tools (MacCarty & Bryden, 2015). This indicates a huge potential for further work in computational modelling of biomass cookstoves.

Computational models of cookstoves have improved over the years. Early models aimed to predict heat transfer and airflow characteristics of the stove (Bussmann and Prasad, 1986, De Lepeleire and Christianes, 1983) and have been optimised by other research groups (Gupta & Mittal, 2010). More recent

models have increased in complexity and included combustion reactions, where analysis on temperature gradients, velocity profiles and combustion products (e.g. soot and carbon dioxide) in basic and improved cookstoves have been carried using ANSYS Fluent (Ali & Wei, 2017). However, less than half of the models were validated against experimental data (MacCarty & Bryden, 2015), indicating a compelling need for validation, especially for complex models involving combustion.

A study on the combustion process in a biomass cookstove has been done on a small-scale wood pellet furnace to develop a simple combustion model (Klason & Bai, 2007). The model only considered combustible volatile fuels produced by pyrolyzed biomass and assumed these volatiles are comprised of light and heavy hydrocarbons, carbon monoxide and hydrogen. The model by Mapelli et al. (2013) makes use of the Eddy Dissipation Method where it is assumed that reaction rates are controlled by turbulence effects and the Discrete Phase Model (DPM) was used for the gaseous combustion of volatiles generated by pyrolysis. The model also assumes the pyrolyzed volatiles have a composition of $CO_{1.075}H_{2.382}$ (Mapelli et al., 2013) and the mass flowrate of the volatiles is set such that the produced power is the average value of the stove.

Another study involved developing a wood combustion model, one of which predicted a fuel burn rate at 16% error and a flame temperature at 29% error compared to experimental data (Burnham-Slipper, 2009). Temperature is an important parameter in assessing the performance of a cookstove. Generally, experimental temperatures are measured using thermocouples and heat transfer is determined by measuring the temperature rise of water in a cookpot over time (Water Boiling Test).

The effects of cookstove configurations (pot support height, secondary air injection and baffle placement) on combustion, flow and heat transfer have also been studied using a 2D axisymmetric CFD model with experimental validation (Pundle et al., 2016). The CFD model included a combustion model of 11 species with a 21-step chemical kinetic mechanism, radiation from the soot-laden gas walls, and heat transfer through the sides of the cookstove and to the cookpot. The parameters used to measure cookstove performance were heat transfer to the cookpot; temperature and species distributions; flow fields inside the stove; inlet and outlet air flow rates.

Specific to Prakti cookstoves, a 3D model using ANSYSCFX was developed to analyse the effects of different geometry baffles on flow path and residence time (Subad, 2016). These baffles are placed inside the cylindrical combustion chamber, closely resembling turbine blades. The performance of each geometry was evaluated using the average flow residence time of a set of definitive streamlines and pressure drop within the stove. A recommendation of the optimal geometry was made without any experimental validation of the CFD model.

Another study on the Prakti cookstove by Hamilton & Lucas (2017) made use of STAR-CCM+ to build a CFD model with coupled flow and energy considerations. Two geometries were considered – the basic cookstove geometry and the addition of a helix blade into the combustion chamber. The initial model was simplified where wood blocks were set at a fixed temperature of 1273K. Experimental temperature measurements were then used to validate the model with an overall error of up to 48%. Radiation and combustion modelling based of Mapelli et al. (2013) were then incorporated.

It is imperative to obtain reliable and representative experimental measurements to assess a cookstove's performance. Initial work determined that the critical parameters contributing to 93% of thermal efficiency uncertainty were Lower Heating Value (LHV) of wood, LHV of char, temperature change of the water in the pot and moisture content of wood (Quist et al., 2016). Thus, experimental procedures, involving a Water Boiling Test, and guidelines, such as reducing moisture content of wood, reducing ratio of char mass to wood mass, using wood with a large LHV, boiling off a significant fraction of water and starting with relatively cold water, have been developed. However, these recommendations have trade-offs like the time to boil water and delta temperature limited by the freezing and boiling temperatures of water. Additionally, it was concluded that the LHV for a single species of wood can vary from tree to tree and by location within the tree, making it difficult to reduce the uncertainty of LHV of unprocessed fuels.

Methods

This study comprises two parts, (1) conducting experiments on the Prakti cookstove to obtain data for the validation of the CFD model and (2) using ANSYS Fluent v17.2 to set up the CFD model of the Prakti cookstove.

Experimental Methodology

Experiments were conducted on the physical cookstove and temperature measurements were taken at different locations of the cookstove. The experimental efficiency of cookstove was calculated using the heat input from the wood fuel and the heat energy received by the pot of water.

Experimental Setup

Three pieces of fresh sawn oak wood samples of approximate dimensions 26 x 26 x 300 mm were used for each experimental run.

Four K-type thermocouples were threaded through hollow metal tubes and the thermocouples were pulled back approximately 0.5 cm from the opening of the metal tubes. This was done so that the metal tubes would

shield the thermocouple from direct radiation. A vacuum pump was used to draw a bit of the hot gases into the tubes to obtain temperature measurements. Another K-type thermocouple was placed in the pot to measure the temperature of the water.

The four threaded K-type thermocouples were affixed to different locations of the cookstove (Figure 1a, 1b)

1. Thermocouple 1 was positioned at the back of the cookstove at the base
2. Thermocouple 2 was positioned at back and middle of the cookstove
3. Thermocouple 3 was positioned near the middle of the cookstove above where the fire was lit
4. Thermocouple 4 was positioned at the top of the cookstove

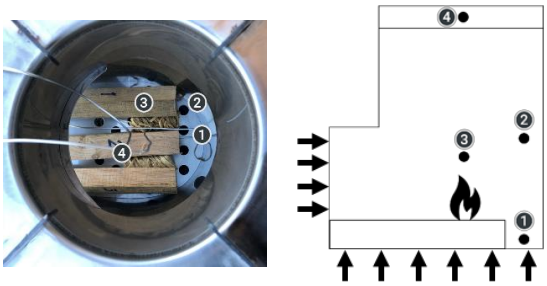

Figure 1a. Top view of cookstove with thermocouple positions (left)
Figure 1b. Side view of cookstove with thermocouple positions where the black arrows signify the airflow into the inlets (right)

The thermocouples were connected to a MAX31855 cold-junction compensated Thermocouple-to-Digital Converter, which outputs temperature data in a 14-bit format. The converters were connected to an Arduino Due which consists of a physical programmable circuit board (microcontroller) and an Integrated Development Environment (IDE). The system was programmed to return temperature values in degrees Celsius at 20 ms intervals.

Drying of Wood Samples

This section outlines the method used to dry the wood samples to match the wood blocks in the CFD model which were specified at 0% moisture content using a wet basis.

The initial mass of three wood samples (26 x 26 x 300 mm) were recorded using an analytical balance (accurate to 0.01g), and placed in the laboratory furnace oven at 130°C. The mass of the three wood samples were measured every hour until the deviation between three consecutive measurements is less than or equal to 0.5g. At this point, it was assumed that the wood samples were completely dry. All other wood samples were then placed into the oven at 130°C and were assumed to require the same duration for reaching complete dryness.

Water Boiling Test

Three wood samples were placed in the cookstove and lit using two firelighters. When the flame was "fully developed", an aluminium pot filled with 2.5 litres of water was placed on the cookstove and a thermocouple was used to measure the initial temperature of the water, $T_{w,i}$. When the temperature of the water reached 100°C, $T_{w,f}$, the experimental run was stopped by putting out the fire and removing the pot of water from the cookstove.

Recalibration of Temperature Measurements

The MAX31855 Converter approximates temperature from voltage via a linear relationship given by

$$V_{out}\,[\mu V] = 41.276\,[\mu V/°C] \times (T_r - T_{amb})\,[°C] \quad (1)$$

where V_{out} is the thermocouple output voltage (μV), T_r is the temperature of the remote thermocouple junction (°C), and T_{amb} is the temperature of the device (°C). V_{out} was calculated using Equation (1) and converted to a corrected temperature via the relevant K-type thermocouple correlations given by NIST (NIST, 2018).

Cookstove Efficiency Calculation

Before each experimental run, the total initial mass of the three wood samples, $m_{wood,i}$, was measured using an analytical balance. The Water Boiling Test was conducted, and the remaining wood residue was weighed to obtain the final mass of the wood samples, $m_{wood,f}$.

The heat input from the wood samples, Q_{wood} can be calculated using Equation (2).

$$Q_{wood}\,[kJ] = (m_{wood,i} - m_{wood,f})\,[kg] \times CV_{wood}\left[\frac{kJ}{kg}\right] \quad (2)$$

where CV_{wood} is calorific value of the wood used.

The heat energy received by the pot of water, Q_w can be calculated using Equation (3).

$$Q_w\,[kJ] = V_w\,[m^3] \times \rho_w\left[\frac{kg}{m^3}\right] \times C_{p,w}\left[\frac{kJ}{kg°C}\right] \times \Delta T\,[°C] \quad (3)$$

where V_w is the volume of water (0.0025 m^3), ρ_w is the density of water (1000 kg/m^3), $c_{p,w}$ is the heat capacity of water (4.186 kJ/kg °C), and $\Delta T = T_{w,f} - T_{w,i}$

The cookstove efficiency, η_{eff}, defined by Equation (4), is the ratio between the energy used to boil the water and the overall energy released by the wood.

$$\eta_{eff}\,[\%] = \frac{Q_w}{Q_{wood}} \times 100 \quad (4)$$

CFD Simulation Methodology

ANSYS Fluent v17.2 was used to set up the CFD model of the Prakti cookstove.

Geometry and Mesh

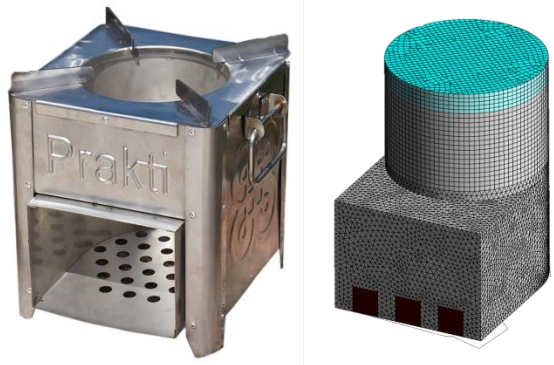

Figure 2a. Prakti cookstove (left),
Figure 2b. Mesh used in CFD model (right) – the top blue section represents the air gap between the pot and the stove due to the skirts and the bottom brown sections represent the wood blocks

Using ANSYS workbench v17.2, the geometry of the newly designed Prakti cookstove was modelled. Air enters from the front and bottom air inlets and exits from the top air outlet as shown in Figure 3. Only the inner compartment that defines the main air flow field (combustion chamber, primary and bottom air inlets, top air outlet and 3 wood blocks) was considered.

The geometry was meshed using the MultiZone Hexa/Prism method. A mixture of hexahedron and tetrahedron elements were used to improve mesh quality and computational efficiency. The walls of the mesh were further adapted in Fluent to increase the number of nodes and improve convergence for turbulent flows. Inlet velocity boundary conditions were imposed and solved to a convergence tolerance of 10^{-6} to ensure that the mesh is of high quality before increasing the complexity of the model.

Boundary Conditions

Atmospheric pressure and temperature conditions were imposed on the air inlets and outlets to simulate real external conditions. All other boundaries were defined as adiabatic walls as summarised in Table 1.

Table 1. Summary of CFD boundary conditions

Boundary	Material	Type	Static Temp. (K)	Gauge Pressure (Pa)
Front & bottom air inlets	-	Pressure inlet	300	0
Top air outlet	-	Pressure outlet	300	0
Wood	Wood	Wall	Adiabatic	-
Pot	Aluminium	Wall	Adiabatic	-
Stove walls	Steel	Wall	Adiabatic	-

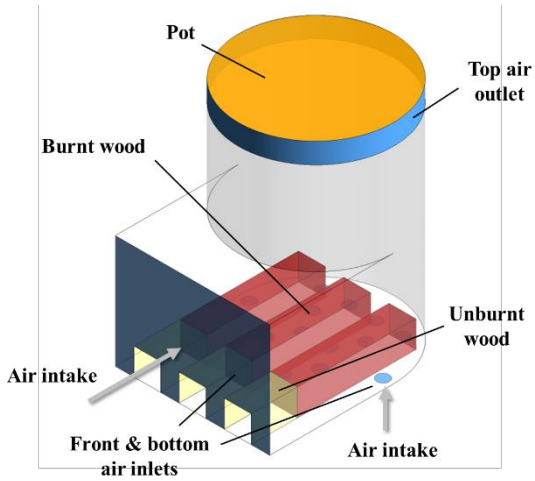

Figure 3: CFD geometry and summary of key features

Solver Settings

The domain to be solved is three-dimensional and the model is steady state. Steady state simulations converge much faster than transient simulations; hence, steady state was used to approximate the transient nature of combustion given project time constraints. The numerical method used was the pressure-velocity coupling method as it is robust and best suited for steady-state simulations (FLUENT). A PRESTO! algorithm was used for pressure and second order algorithms were used for momentum, species and energy discretization.

Physical Modelling: Turbulence

The RANS k-ε realizable method was used as it is an economic approach for modelling turbulent fluctuations and performs well for many industrial applications with complex secondary flow features. The model transport equations for turbulence kinetic energy, k, and rate of dissipation, ε, were used to solve for the Eddy viscosity and close the turbulence problem.

The realizable method was chosen over the standard method as studies have shown that it has superior performance compared to other k-ε model versions. The realizable model also satisfies certain mathematical constraints consistent with the physics of turbulent flow. More information can be looked up in the Fluent help guide (FLUENT).

Physical Modelling: Natural Convection

To simulate natural convection, gravitational acceleration of 9.81 ms^{-2} and atmospheric pressure boundary conditions at the cookstove's inlet and outlet were imposed. The equation of state used was the compressible ideal gas.

Physical Modelling: Radiation

Several radiation models are available in Fluent, namely the P-1 Model, Discrete Transfer Radiation Model (DTRM) and Discrete Ordinates (DO) Model. The DO model was chosen as it is all encompassing – suitable for

solving a range of problems from surface-to-surface radiation to participating radiation in combustion. The P-1 model is less computationally intensive but tends to over-predict radiative fluxes while the DTRM is more accurate but at a much higher computational cost (FLUENT). The DO model requires moderate computational power and was chosen in this model to have an optimal balance between accuracy and computational intensity.

The gray radiation model was adopted and serves as a simplification to the actual radiation in a cookstove. The main assumption of this model is that surface radiative properties are independent of wavelength. The wood surfaces and pot were assumed to be blackbodies and modelled as perfect emitters and absorber respectively. The combustion chamber walls were modelled as perfect reflectors.

Physical Modelling: Combustion

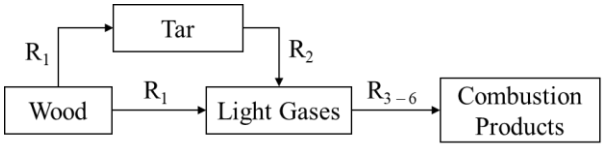

Figure 4. Summary of reactions in combustion model

The combustion model implemented was based on wood dust (Malte, 1996) as summarised in Figure 4. Based on Malte et al. (1996), wood has a composition of $C_{5.155}H_{9.844}O_{3.97}N_{0.0106}$ and tar has a composition of $C_1H_{1.473}O_{0.0529}$. The standard enthalpy, heat capacity and entropy values were based on literature values (Novosselov, 2006). The combustion reaction begins with the pyrolysis of wood (R_1) to form tar and light gases; tar undergoes further pyrolysis (R_2) to form light gases. The light gases then undergo reactions ($R_{3\text{-}6}$) to form combustion products. The wood particles were injected from the surface of the burnt section of the wood at a mass flow rate determined experimentally using Equation (5).

$$\frac{(m_{wood,i} - m_{wood,f})\ [kg]}{experimental\ duration\ [s]} \tag{5}$$

The reactions implemented are summarised below.

R_1 Wood → 4.612 Tar + 0.0969 CH_4 + 0.0375 C_2H_4 + 0.2265 CO + 0.1441 CO_2 + 1.0155 H_2O + 0.0053 N_2

R_2 Tar → 0.2136 CH_4+ 0.1546 C_2H_4 + 0.4254 CO + 0.0518 CO_2

R_3 $CH_4 + 1.5\ O_2 \rightarrow CO + 2\ H_2O$

R_4 $C_2H_4 + 2\ O_2 \rightarrow 2\ CO + 2\ H_2O$

R_5 $CO + 0.5\ O_2 \rightarrow CO_2$

R_6 $CO_2 \rightarrow CO + 0.5\ O_2$

The chemical kinetics are in the form of the Arrhenius rate equation where the pre-exponential factor has units of s^{-1} and the activation energy has units of K^{-1}. The kinetics of the reactions modelled are

$$R_1 = 10^{6.77}\exp\left(-\frac{14313}{T}\right)[\text{Wood}]$$
$$R_2 = 10^{6.63}\exp\left(-\frac{12930}{T}\right)[\text{Tar}]$$
$$R_3 = \text{Eddy Dissipation Model (EDM)}$$
$$R_4 = \text{Eddy Dissipation Model (EDM)}$$
$$R_5 = 10^{10.41}\exp\left(-\frac{156858}{T}\right)[CO]^{1.14}[H_2O]^{0.5}[O_2]^{0.25}$$
$$R_6 = 10^{6.1}\exp\left(-\frac{18135}{T}\right)[CO_2]$$

The main assumptions of the model are

1. Wood is dry-ash free.
2. Wood particles are of a fixed diameter and do not change in size during combustion.
3. No char surface reaction.
4. Light gases comprise CH_4, C_2H_4, CO and CO_2
5. R_3 and R_4 are governed by the transport processes in the flow as the chemical kinetics are relatively faster; thus, EDM was used.

The overall kinetics is expected to be faster in wood dust than wood blocks because combustion of wood blocks would be limited by heat and mass transfer to a larger extent.

Results and Discussion

Experimental Results: Temperature Measurements

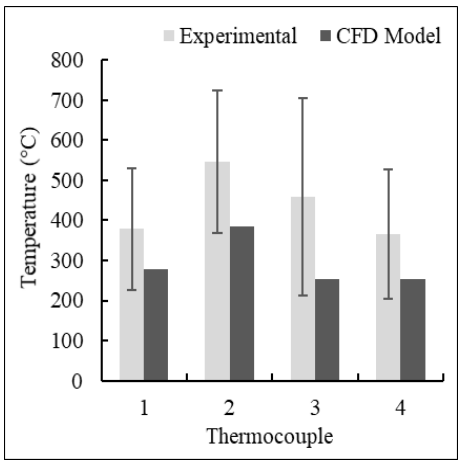

Figure 5. Temperature at different thermocouple positions for experiments and CFD model

In Figure 5, the light grey bars show the average temperatures of two experimental runs, and the dark grey bars represent the corresponding temperatures in the CFD model. The error bars were defined as the sample standard deviation using Equation (6).

$$s = \sqrt{\frac{1}{N-1}\sum_{i=1}^{N}(x_i - \overline{x})^2} \quad (6)$$

where s is the sample standard deviation, N is the number of data points, x_i is the ith data point, and $\bar{x}$ is the sample mean.

Both experimental and CFD model results displayed a similar trend. The highest average temperature was observed at the mid height, towards the back of the stove (Thermocouple 2) at approximately 550°C. The Prakti cookstove experiments done last year by Hamilton & Lucas (2017) also exhibited a similar trend with high temperatures towards the back of the stove. Although the cookstove geometry used by Hamilton & Lucas differed slightly (where the cookstove had a baffle and secondary air inlets), the key flow features like the front air inlet, bottom air inlets and the air flow pathway are similar. This suggests that cookstoves of similar flow features would exhibit this trend.

A comparison between CFD and experimental temperatures would be discussed later in the section *CFD Results vs Experimental Results*.

Table 2. Standard deviation of experimental temperatures

	Thermocouple			
	1	2	3	4
Standard deviation (K)	152.5	177.6	247.3	162.3

Another observation is that Thermocouple 3 displays the largest standard deviation from the mean temperature (Table 2) and this can be attributed to the transient and dynamic behaviour of the flame. This is further exemplified by the raw temperature readings of Thermocouple 3 which was placed close to the flame as shown in Figure 6. This shows that combustion is inherently a transient problem and the steady state simulation results are an approximation of the actual problem.

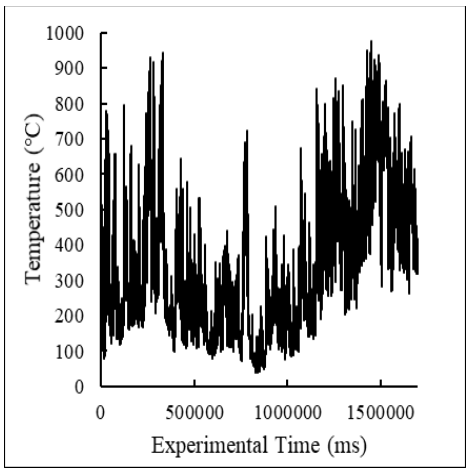

Figure 6. Dynamic temperature readings of Thermocouple 3 for one of the experimental runs

Experimental Results: Cookstove Efficiency

Table 3. Experimental cookstove efficiency

Run	ΔT (°C)	Q_{wood} (kJ)	Q_w (kJ)	η_{eff} (%)
1	86.5	6453.25	908.25	14.1
2	88	6427.53	924.00	14.4

Using the methodology detailed in the section *Cookstove Efficiency Calculation*, the results of the cookstove efficiency are summarised in Table 3.

Quist et al. (2016) reported that thermal efficiency uncertainty depends on measurements, input data (equipment uncertainties, literature values, etc.) and test conditions – The critical parameters contributing to 93% of thermal efficiency uncertainty were

1. Moisture content of wood
2. Temperature change of the water in the pot
3. Lower Heating Value (LHV) of wood and char

Most of the moisture content of the wood samples was removed as detailed in *Drying of Wood Samples* and this reduces the maximum uncertainty in thermal efficiency. Additionally, a higher ΔT reduces the contribution to thermal efficiency uncertainty and for all experimental runs, cold water was used. The LHV for a single species of wood can vary from tree to tree and by location within the tree, making it difficult to reduce the uncertainty of LHV of unprocessed fuels; nonetheless, studies using hard woods generally experience less uncertainty than studies using softwoods and oak used in this study is a hardwood.

Factors contributing to variations in experiments

Table 4 summarises the factors identified by Prakti which contributed to variation in the experiments, and can partially explain the deviation in temperatures observed in Figure 5.

Table 4. Factors causing variations in experiments

Factor	Variation effect	Mitigation
Wood positioning	Large	All runs used 3 wood samples placed parallel to each other without stacking
Wood species	Large	All runs used fresh sawn oak acquired from TimberSource UK
Wood volume	Large	All runs used 3 wood blocks with dimensions 26 x 26 x 200 mm

Wood moisture content	Large	All wood samples were dried as detailed in *Drying of Wood Samples*
Firelighters quantity	Medium	All runs used 2 firelighters
Firelighters positioning	Medium	Firelighters placed at the same position for all runs
Wind speed	Medium	All runs conducted under similar external conditions on the same day
Air temperature	Low	
Air humidity	Low	

CFD Results: Temperature Profiles

The temperature contours shown in Figure 7 shows the heat distribution in the stove. The temperature appears to be higher towards the back of the stove, at about 658K. This trend matched what was observed in the experiments where Thermocouple 2 (at the back of the main combustion chamber) recorded the highest average temperature. The top view of the combustion chamber shown in Figure 8 further exemplifies this trend. This is mainly caused by the air flow from the front inlet which pushes the flame towards the back of the combustion chamber and results in combustion occurring mostly at the back of the combustion chamber. This also results in the back region having the highest CO and CO_2 mass fractions (by-products of the combustion reactions) shown in Figure 11 and 12.

CFD Results vs Experimental Results

Comparing the CFD temperatures to average experimental temperatures in Figure 5, both data plots exhibited a similar overall trend with higher temperatures towards the back of the combustion chamber. The CFD temperatures were lower than the average experimental temperatures by about 100 to 200°C and could be a result of omitting the surface char reaction in the modelling of combustion. Char is the black solid residue formed while burning the wood and char can undergo further oxidation reactions which generates heat. In combustion modelling, char is usually assumed to be carbon and undergoes oxidation to form either CO or CO_2. The process by which the products form depends on the temperature and mass transfer limitations of O_2 in the wood blocks and is a complex reaction to implement in the model (Kops & Malte, 2004). The char reaction is highly exothermic and would likely close the temperature gap between CFD and experiments if implemented.

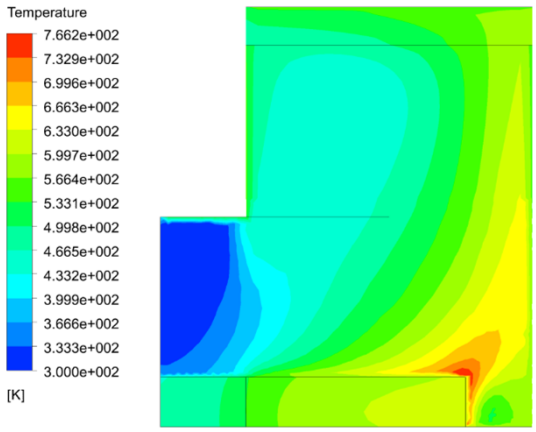

Figure 7. Temperature contours on the vertical mid-section of the combustion chamber

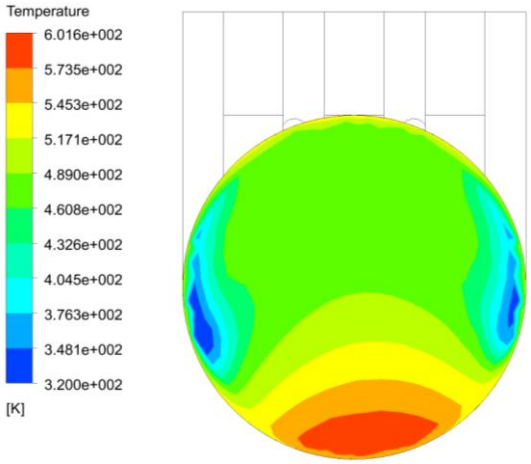

Figure 8. Temperature contours from the top of the combustion chamber

CFD Results: Velocity Profiles

The streamlines in Figure 9 show the natural convection because of the combustion model. Mixing is observed within the main combustion chamber of the stove and is further exemplified by the velocity vector field in Figure 10. Some of the air entering the front inlet recirculates out because the mixing in the main chamber forms a "barrier". The convection in the main combustion chamber is desirable as it would promote mixing of air and fuel to help achieve complete combustion, reduce harmful emissions, and improve heat distribution in the cookstove.

CFD Results: Emission Profiles and Air Intake

The mass fractions of CO and CO_2 are shown in Figure 11 and 12, and there is about twice as much CO as compared to CO_2 in the main chamber of the cookstove. This suggests that there is incomplete combustion in the cookstove. The O_2 concentration in the main combustion chamber is about 16% O_2 by mass as shown in Figure 13, suggesting that there is insufficient mixing of air and fuel which resulted in incomplete combustion.

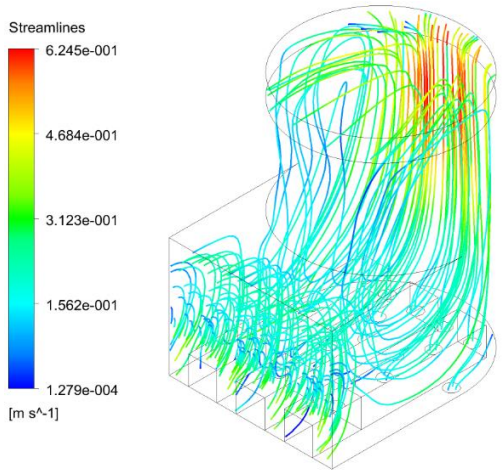

Figure 9. Velocity streamlines in the stove combustion chamber

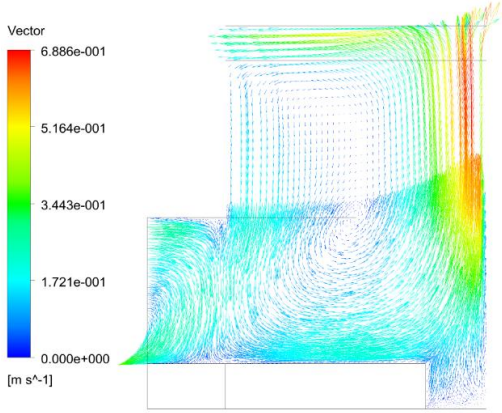

Figure 10. Velocity vector field on the vertical mid-section of the combustion chamber

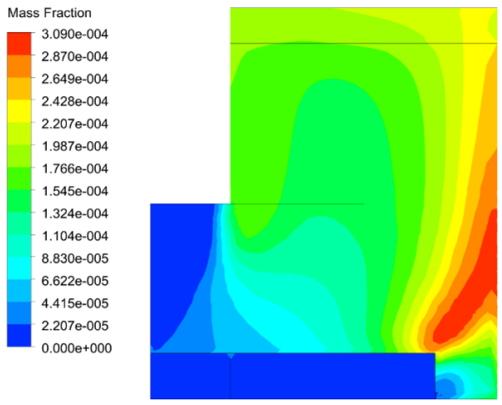

Figure 11. CO mass fractions on the vertical mid-section of the combustion chamber

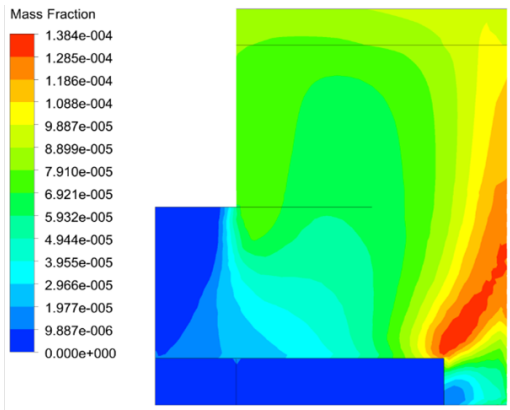

Figure 12. CO_2 mass fractions on the vertical mid-section of the combustion chamber

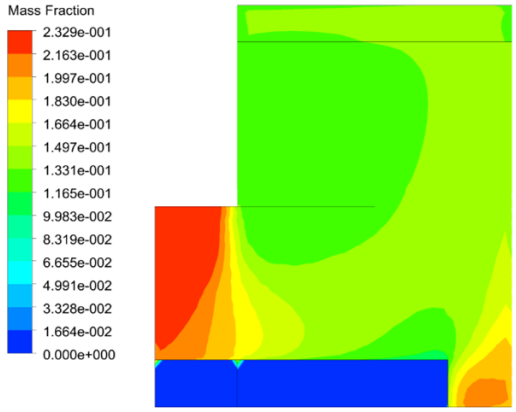

Figure 13. O_2 mass fractions on the vertical mid-section of the combustion chamber

The poor mixing could be attributed to a lack of air entering from the bottom air inlets. From the mass flux calculated in Fluent for the air inlets, the air intake for the front air inlet is about 71% compared to 29% for the bottom air inlets. The higher air intake in the front air inlet could be because of 2 main reasons:

1. The front air inlet is significantly larger than the bottom air inlets.
2. Airflow into the bottom air inlets are partially blocked by the wood blocks placed on top of them.

Increasing the amount of air entering the bottom air inlets by making changes to geometry or including a forced draft fan (which Prakti is currently investigating) could potentially increase mixing in the stove and reduce harmful emissions. Ali & Wei (2017) implemented secondary air inlets in their 2D CFD model which were located close to the cookstove's top air outlet. While the results showed that secondary air inlets helped to improve complete combustion, they were omitted in Prakti's new cookstove design.

Instead of implementing secondary air inlets, the CFD model geometry was slightly altered by lifting the wood blocks 4cm off the bottom surface. This was done to allow for more air to enter via the bottom air inlets and investigate the improvements to mixing. The temperature profile, shown in Figure 14, displays the similar trend of high temperatures towards the back of the stove. Comparing the CO and CO_2 mass fractions shown in Figure 15 and 16 to the current stove geometry (Figure 11 and 12), emissions decreased significantly by approximately 50% when the wood blocks were lifted. This suggests that increasing air flow from the bottom air inlets helped to improve mixing, resulting in more complete combustion and lower emissions. This could be validated experimentally by placing the wood blocks on an elevated metal grill in the combustion chamber.

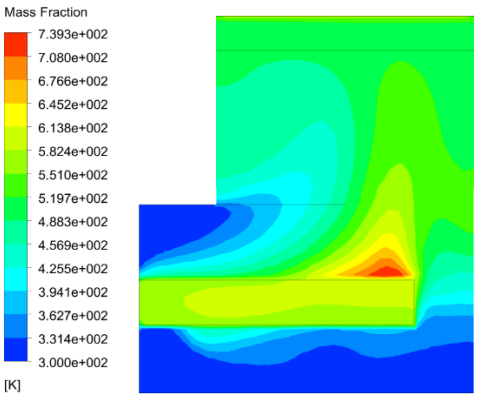

Figure 14. Temperature profile on the vertical mid-section of the combustion chamber with the wood blocks lifted off the bottom surface

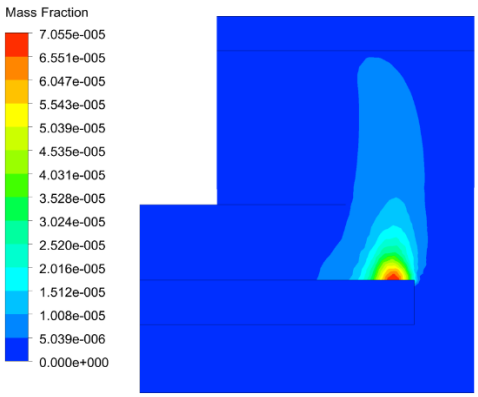

Figure 15. CO mass fractions on the vertical mid-section of the combustion chamber with the wood blocks lifted off the bottom surface

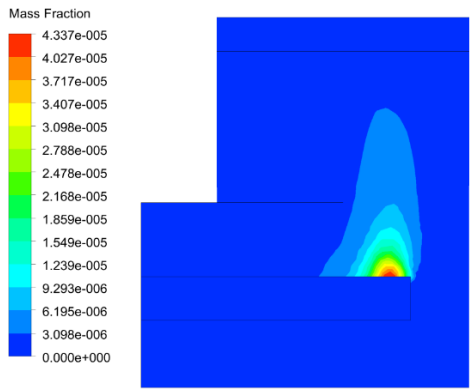

Figure 16. CO_2 mass fractions on the vertical mid-section of the combustion chamber with the wood blocks lifted off the bottom surface

Conclusions & Outlook

The focus of this research is the improvement on Hamilton & Lucas's Prakti cookstove CFD model, more specifically on combustion modelling and validating it with experiments. The main objectives have been met alongside with an experimental investigation into the thermal efficiency of the cookstove.

The CFD velocity profiles and air intake distribution showed that mixing of air and fuel could be improved by increasing the air intake of the bottom air inlets. A CFD model where the wood blocks were lifted 4cm off the bottom surface showed improved mixing and combustion efficiency, halving emissions of CO and CO_2. While the CFD results are promising, experimental validation of this would be desirable.

The CFD temperature profiles shared a similar trend to the experimental data. However, the CFD temperatures were, on average, 33% lower than experimental temperatures. This gap could be closed by including the highly exothermic char reaction, but the complexity of this reaction presents a challenge for future work.

From the experimental data, the Prakti cookstove efficiency was calculated to be approximately 14% via a Water Boiling Test. Additionally, the transient and dynamic behaviour of the flame was exemplified by the large standard deviation from the mean temperature recorded. Sources of variation in the experiments like species of wood used, wood quantity, wood moisture content, and external environmental conditions were identified and mitigated; however, these sources are inherent and can affect the uncertainty of experimental temperature measurements.

The CFD model can be further improved by using a more realistic boundary condition for the aluminium pot to emulate the resistance in series concept where there is convective heat flux on the air side (in the combustion chamber), conduction through the pot wall, and convective heat flux in the water. This can then be compared with the average experimental pot flux which can be determined through the Water Boiling Test – dividing the heat energy of water, Q_w, by the experimental time and area of the pot base.

Furthermore, wood combustion would result in NOx emissions as wood contains approximately 0.1% of nitrogen by mass. NO_X emissions were not modelled in this study as the mechanisms that are applicable to a cookstove have not been understood fully. This remains an area for improvement as analyzing NO_X emissions could be a useful criterion in quantifying improvements made to the cookstove.

Acknowledgements

We would like to thank everyone who helped us with our research – Dr Chris Tighe, Prof Omar Matar, Dr. Mirco Magnini, Dr Aditya Karnik, Mr. Parth Shah, and Elysia Lucas at Imperial College London and Dr Mouhsine Serrar at Prakti.

We would also like to thank Imperial College London Physics Department for allowing us to conduct experiments on their building rooftop.

Supplementary Information

A separate document containing enlarged images of the CFD simulation results is enclosed.

References

Ali, H., & Wei, T. (2017). CFD Study of an Improved Biomass Cookstove with Reduced Emission and Improved Heat Transfer Characteristics. *Journal of Clean Energy Technologies. 5 (6)*, 427-432.

Baldwin, S. F. (1988). *Biomass Stoves: Engineering Design, Development and Dissemination.* Arlington, VA: Vita Publications.

Bryden, K. M., & MacCarty, N. A. (2015, June). Modeling of household biomass cookstoves: A review. *Energy for Sustainable Development, 26*, 1-13.

Burnham-Slipper, H. (2009, January). Breeding a better stove: the use of computational fluid dynamics and genetic algorithms to optimise a wood burning stove for Eritrea.

Bussmann, P., & Prasad, K. (1986, January). PARAMETER ANALYSIS OF A SIMPLE WOODBURNING COOKSTOVE.

De Lepeleire, G., & Christiaens, M. (1983). Heat transfer and cooking woodstove modelling. *Proceedings of the Indian Academy of Sciences Section C: Engineering Sciences. 6 (1)*, 35-46.

FLUENT. (n.d.). *ANSYS FLUENT 17.2 User's Guide.*

Gupta, R., & Mittal, N. D. (2010). Fluid flow and heat transfer in a single-pan wood stove. *International Journal of Engineering Science and Technology. 2 (9)*, 4312-4324.

Hamilton, S., & Lucas, E. (2017). *Development of an Improved Biomass Cookstove Computational Fluid Dynamics Model with Experimental Validation.* Department of Chemical Engineering, Imperial College London.

India Cookstoves and Fuels Market Assessment. (2018). Retrieved from Global Alliance for Clean Cookstoves.

Klason, T., & Bai, X. (2007, July–August). Computational study of the combustion process and NO formation in a small-scale wood pellet furnace. *Fuel, 86*(10-11), 1465-1474.

Kops, S. M., & Malte, P. C. (2004). *Simulation and Modeling of Wood Dust Combustion in Cyclone Burners.* Department of Mechanical Engineering, University of Washington.

Lepeleire, G., & Christiaens, M. (1983, March). Heat transfer and cooking woodstove modelling. *Proceedings of the Indian Academy of Sciences Section C: Engineering Sciences, 6*(1), 35–46.

MacCarty, N. A., & Bryden, K. M. (2015). Modeling of household biomass cookstoves: A review. *Energy for Sustainable Development. 26 (Supplement C)*, 1-13.

MacCarty, N. A., & Bryden, K. M. (2016). A generalized heat-transfer model for shielded-fire household cookstoves. *Energy for Sustainable Development, 33*, 96-107.

Malte, P. C. (1996). *Development of a model for predicting the NOx emissions of burners fired with sawdusts and sanderdusts high in nitrogen.* Department of Mechanical Engineering, University of Washington.

Mapelli, F., Mereu, R., Barbieri, J., & Colombo, E. (2013, June). CFD feasibility analysis of an Improved Cook Stove (ICS) for electricity production.

NIST. (2018). *Temperature correction of type k thermocouple*. Retrieved from https://srdata.nist.gov/its90/download/type_k.tab

Novosselov, I. V. (2006). *Chemical Reactor Networks for Combustion Systems Modeling* . University of Washington .

Prakti. (2018). *Prakti - Smart Stoves for Smart Cooks.* Retrieved from http://prakti.in/

Pundle, A., Sullivan, B., Allawatt, G., Posner, J., & Kramlich, J. (2016). Two dimensional axisymmetric CFD model of a natural draft wood fueled rocket cookstove. *2016 Spring Technical Meeting of the Western States Section of the Combustion Institute, WSSCI 2016*.

Quist, C. M., Jones, R. B., Jones, M. R., & Lewis, R. S. (2016, October). Uncertainty analysis and design guidelines of biomass cookstove thermal efficiency studies. *Energy for Sustainable Development, 34*, 54-61.

Rajesh, G., & Mittal, N. (2010, September). Fluid flow and heat transfer in a single-pan wood stove.

Sowgath, M., Rahman, M., Nomany, S., Sakib, M., & Junayed, M. (2015, October). CFD study of biomass cooking stove using Autodesk Simulation CFD to improve energy efficiency and emission characteristics. *Chemical Engineering Transactions, 45*.

Subad, Y. (2016). Prakti CFD Simulation for Stove. *Vestas Technology R&D Private Ltd.*

Wohlgemuth, A., Mazumder, S., & Andreatta, D. (2009, December). Computational Heat Transfer Analysis of the Effect of Skirts on the Performance of Third-World Cookstoves. *Journal of Thermal Science and Engineering Applications 1(4)*.

Determination of physio-mechanical and thermo-stability of lyophilised model protein lysozyme in trehalose

Hassan Azzan, Wei Ming Goh, Arnold Duralliu and Daryl R. Williams*

Surfaces and Particle Engineering Laboratory, Department of Chemical Engineering, Imperial College London, SW7 2AZ, United Kingdom

Abstract The mechanical and thermo-stability of freeze-dried cakes relate to some of the most important critical quality attributes (CQAs) required for the approval of products for commercial use. Thus, the storage conditions of the freeze-dried cakes should be optimised in terms of storage temperature and moisture content in the vials in order to maintain the overall structural stability of the cakes. In this study, we mapped the critical moisture content at which the 10:1 (protein to sugar) ratio by mass formulation of lysozyme in trehalose would collapse for a range of temperatures. The presence of moisture was found to lower the collapse temperature, T_c of the formulations, where the Young's modulus of the formulations was reduced due to the phase transition from a uniform cake to a collapsed state. It was also shown that the cracking of the cake, an important quality attribute for freeze-dried cakes, was dependent on the position of the vials in the freeze-drier during the freeze-drying process. A correlation between cracking and residual moisture content was identified, and the underlying physics was highlighted. Further potential experimental work will be needed to determine the relationship between physio-mechanical and thermo-stability with protein activity.

* Corresponding author. *E-mail address*: d.r.williams@imperial.ac.uk (D.R. Williams).

Keywords: *Freeze-drying, Trehalose, Thermo-stability, Mechanical stability, Protein, Lysozyme, Cracking*

1. Introduction

Lyophilization, more commonly known as freeze-drying, is the process of drying a frozen solution through sublimation at low temperatures and pressures, resulting in the formation of a solid porous cake. The process consists of three main stages: initial solution freezing, primary drying and secondary drying, as seen on Table 1. Freeze-drying stabilizes otherwise unstable solutions of biologics, improving shelf life and product viability (Manning et al., 2010). These products often contain stabilizers to help increase stability and mechanical properties by maximizing retention of native protein structure through the formation of hydrogen bonds upon drying. Amorphous sucrose and trehalose are two well-known stabilizers used to improve stability and storage performance (Liao et al., 2002).

Freeze-dried cakes are highly hygroscopic (tending to absorb moisture from air), so it is vital to understand the effect of residual and engrossed moisture on the mechanical and thermo-stability. There are several critical quality attributes (CQA) that freeze-dried products need to meet before being used commercially, which include cracking, shrinkage, collapse and discoloration. These are all affected by temperature and moisture, and a decision tree (Figure 1) would help to accept/reject products based on CQAs (Patel et al., 2017).

McCartney (2014) studied the mechanical characterization of freeze-dried cakes and developed a method of quantifying mechanical stability in a variety of manners, including the in-situ flat punch indentation method for fragile cakes that was used in this study.

In terms of thermo-stability with moisture content, two important parameters to note are the glass transition temperature (T_g) and the collapse temperature (T_c). T_g is a critical physical property of all amorphous solid, which is

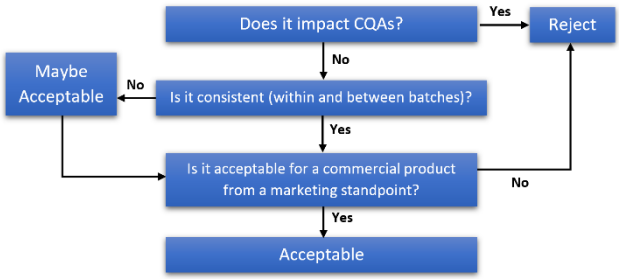

Figure 1: Decision tree used to accept or reject freeze-dried cake based on impact on CQAs (Patel et al., 2017).

characterized by a change of the solid from a solid brittle state to a liquid-like rubbery state (Craig et al., 1999) and T_c in this study is characterized by the temperature at which the freeze-dried cakes start transforming from a uniform cake to a collapsed state (not to be confused with eutectic/collapse temperature (T_c) in the frozen state). T_g is reduced in freeze-dried cakes as moisture content increases due to plasticization (Towns, 1995). This potentially facilitates complete cake collapse back to a liquid solution. Duralliu et. al. (2018) studied the humidity induced collapse in freeze-dried cakes and developed stability maps of relative humidity (RH%) against temperature, using the dynamic vapor sorption (DVS). In this study, an alternative method was developed to produce stability maps for moisture content against temperature.

Cracking is another irregularity that is critical to a lot of applications, especially where cosmetic appearance of the product is important for the end user. (Patel et al., 2017) Ullrich et. al. (2015) found an inverse relationship between cracking and shrinkage of freeze-dried cakes. Cook et. al. (2011) studied the variability of headspace moisture in a freeze-drying batch. The relationship between moisture content and cracking in the shelf-space of the freeze-drier was investigated in this study. A novel in-situ method to quantify cracking on the surface of freeze-dried cakes was developed for this purpose.

Although total or partial collapse and cracking may not be critical with respect to product quality and efficacy, as in the case with pharmaceuticals and food, they remain important factors in determining whether a batch of freeze-dried products is accepted or rejected for commercial use. Currently, most freeze-dried products are quality approved through visual appearance testing, which carries a lot of uncertainty in determining the criticality of certain attributes (Patel et al., 2017). Rejection of such a batch in large scale production would not only yield financial losses, but also would lead to delays in bringing the products to consumers who are in vital need for them (as in the case with newly developed drugs). Thus, it is important to understand the causes for these phenomena and devise methods to study and combat them.

Hence, the main objectives of this study are three-fold: to determine the mechanical stability of different formulations of sugar and protein using lysozyme as a model protein in order to select a formulation best suited for rigorous thermo-stability tests, map the thermo-stability of the selected formulation in order to identify the storage conditions under which the material will be structurally stable, and to develop a method to quantify and map the pattern of cracking in a freeze-drying batch, in order to understand the underlying physics and potential implications on product CQAs. Any potential avenues for future work was discussed, in order to improve experimental method and produce more in-depth results.

2. Method and materials

2.1. Method and materials for preliminary study

Table 1: Freeze-drying cycle run for this study.

	Step	Temp (°C)	Duration (minute)	Hold/ Ramp	Vacuum (mTorr)
1	Precooling	20	20	H	Atm*
2	Ramp to Freeze	-50	90	R	Atm
3	Hold Frozen	-50	300	H	Atm
4	Apply Vacuum	-50	60	H	150
5	Apply Vacuum	-50	60	H	20
6	Ramp to Primary Drying	-50	50	R	20
7	Primary Drying Hold	-50	3765	H	20
8	Ramp to Secondary Drying	20	600	R	20
9	Secondary Drying Hold	15	560	H	20
	Release vacuum to dry nitrogen and remove products	15	n/a	n/a	Atm

* Atmospheric pressure

Table 2: Time exposed to moisture for preliminary study.

Time after exposure to moisture (hours)	0	3	24	44	68

Sucrose (S9378-1KG, Sigma Aldrich, UK) and trehalose (Treha 16400, Cargill Deutschland GmbH, Germany) were used to make 1%, 10%, and 20% (w/w) solutions with purified deionized water. Lyophilized lysozyme (From chicken egg white, L876-5G, Sigma Aldrich, UK) was used as a model biological material. 1 g of lysozyme was weighed and reconstituted, with the aid of magnetic stirring, in a 1.323% (w/w) dibasic sodium phosphate (S7907-500G, Sigma Aldrich, UK) buffer solution to form a 1% (w/w) solution of lysozyme. The pH of this solution was measured to be 8.22 using a pH probe (Mettler Toledo pH meter, UK) and the pH was adjusted to 9.13 by the addition of 0.5 M sodium hydroxide (221465-500G, Sigma Aldrich, UK) solution using a 100 µL pipette (Gilson, UK). Equal volumes of the protein and sugar solutions were mixed to produce the formulations for freeze-drying. 5 mL Type I Vials (5.00 ml Fiolax Clear Screw Neck, Schott, Lukácsháza, Hungary) were filled with these samples to a fill-volume of 1 mL using an automated multi-pipette stream (Eppendorf, UK). All freeze-drying was carried out on the top shelf of a Virtis Advantage plus freeze-drier (SP scientific, Warminster PA, USA). The freeze-drying cycle run for these samples is shown in Table 1. After the cycle was completed, the vials were stoppered down using 14 mm diameter igloo halobutyl stoppers (Adelphi Group, Haywards Heath, UK). Consequently, all samples were simultaneously opened to the atmosphere and stored in nominal laboratory temperature of 20°C and a laboratory humidity of 40 % RH for a range of intervals (seen on table 2) over a period of 68 hours, during which samples were removed periodically and tested for changes in mechanical properties using 3 repeated measurements (as described in 2.2).

2.2. Measuring Young's modulus of lyophilized cake

The Young's modulus of the cakes was analyzed using the flat punch indentation method using the mechanical testing instrument (MTI) developed by McCartney (2014) as shown in Figure 2, along with the purpose written software (written by Gary Bignall from Surface Measurements Systems, London, UK). A 2 mm (d) indenter at a load velocity of 20 µm/sec was used and all experiments were carried out at a nominal laboratory temperature of 20°C and a laboratory humidity of 40 RH%. For calibration, the instrument was inverted, and a 200 g weight was placed on the load cell. Instrument error was calculated by repeated indentation on a sample of elastic foam, yielding an instrument error of 4.77% ($n=20$). The samples were tested in-situ to measure the load exerted by the indenter (m) and displacement of the indenter (Δx) from the initial thickness of the cake (x_o). The stress (σ) and strain (ε) on the samples were calculated before subsequently calculating the Young's modulus (E) for the samples. The initial linear region of the stress-strain plot was used to determine the Young's modulus of the samples (Figure 2).

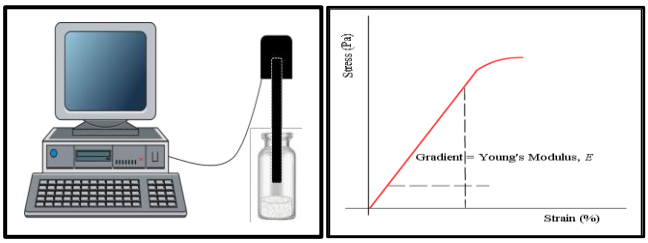

Figure 2: The mechanical testing instrument (MTI) and the stress-strain plot (McCartney, 2014).

$$E = \frac{\sigma}{\varepsilon} = \frac{\frac{mg}{(\pi d^2/4)}}{(\Delta x/x_0)} \quad (1)$$

2.3. Materials and method for mechanical stability test

The model protein solution was made as described in 2.1 for 10:1 trehalose to lysozyme mass ratio. The solution was freeze-dried in 5 ml vials with 1 ml fills, using the same cycle described in Table 1. The vials were then divided into two equal sets, one of which was opened to the atmosphere at 40% RH for 20 hours while the other set was left unopened. After this period, all vials were closed, and each set was divided into 3 equal groups and stored in temperature-controlled ovens (Digital incubators, INCU-Line®, IL 10, UK) at 25, and 65°C, and in a freezer (Lab Freezer with Electronic Controller, Liebherr Premium, Germany) at -20°C. The moisture contents of the two sets of samples (0-hour exposure and 20-hours exposure) initially (storage day 0) were measured using the Karl Fischer titration method (*n=3*). The moisture contents of the samples were reported as 1.94 w/w% moisture (0-hour exposure, low moisture samples) and 9.16 w/w% moisture (20-hours exposure, high moisture samples). Automated Coulometric Karl Fischer (Mitsubishi CA-200, A1-Envirosciences Ltd, Blyth, UK) was used to measure the moisture content of freeze-dried cakes in vials. The samples were prepared and transferred into HPLC vials under low humidity pyramid dry bag (Captair pyramid, 2200A Cole Parmer, London, UK) with less than 5% relative humidity that had been purged with nitrogen gas. The samples were periodically removed from storage and tested for Young's modulus at the intervals in Table 3.

Table 3: Testing intervals for mechanical stability test.

Time stored at thermal control (days)	0	2	7	14	21

2.4. Determining critical moisture content for cake stability

The freeze-dried samples were prepared as described in 2.3. 44 of the resulting vials was divided into 11 groups, each of which opened to atmospheric moisture for a set time. This was done to introduce a varying degree of moisture into each of the groups of vials. After this, 1 vial from each of the groups was used to determine the true moisture content in the samples using Karl-Fischer titration as described in 2.3. Additional repeats were not possible due to constraints in the availability of equipment for Karl-Fischer titration. Consequently, the remaining vials were stoppered to preserve moisture content and then stored in a temperature-controlled environment for a period of 1 week (as described in 2.3). After this, the condition of the cakes was observed, and the moisture intervals at which the cakes showed signs of collapse and discoloration were determined by visual inspection. This process was repeated for different temperatures, in order to obtain Figure 6.

The data points for the mass fraction of water (ω_{water}) were then fitted using the Gordon-Taylor equation for the glass-transition temperature of the mixture $T_{g,mix}$ on OriginPro 2017 (version b9.4.0.220, OriginLab Corporation, USA), using a value for the glass transition temperature of water ($T_{g,water}$) from literature (Handa, Klug & Whalley, 1988), to obtain fitting parameter K and the unknown $T_{g,2}$.

$$T_{g,mix} \approx \frac{K.T_{g,water}.\omega_{water} + T_{g,2}.(1-\omega_{water})}{K.\omega_{water} + (1-\omega_{water})} \quad (2)$$

2.5. Measuring the crack area on freeze-dried cake surface

The model protein solution was made as described in 2.1 for 10:1 trehalose to lysozyme mass ratio. The vials were arranged in grids, (as shown in figure 3) and freeze-dried using the same procedure and cycle described in 2.1. Upon completion of the freeze-drying run, all vials were stoppered down simultaneously with caution to prevent any further cracking due to agitation and moisture ingress.

Opened freeze-dried vials were individually placed on a fixed location on a benchtop with an iPhone 7 plus (Apple, California, USA, Firmware iOS 12) placed 20 cm vertically above the vial with the back camera in-line with the opening of the vial. This position was held fixed using an Amazon Basics 60-Inch Lightweight Tripod (Amazon, USA) (setup shown in Figure 3). Photos of the cake surface were taken at a fixed focal length and aperture using the camera app. As shown in Figure 3, the images were cropped, and the cake surface was processed to convert it to a binary color format where the cracks would be shown in white, and the uncracked areas shown in black, using ImageJ 1.52a (National Institutes of Health, USA). The ratio of white pixels to the total number of pixels on the image of the cake surface was determined using the histogram function of ImageJ and this was used as the fraction of the surface covered by cracks. The fraction of cracked surface area was calculated for all four vials for a specific coordinate and the three most similar values were chosen to calculate the average fraction of cracked area for that coordinate. This fraction was plotted as a function of the location on the freeze-drying tray on Figure 7.

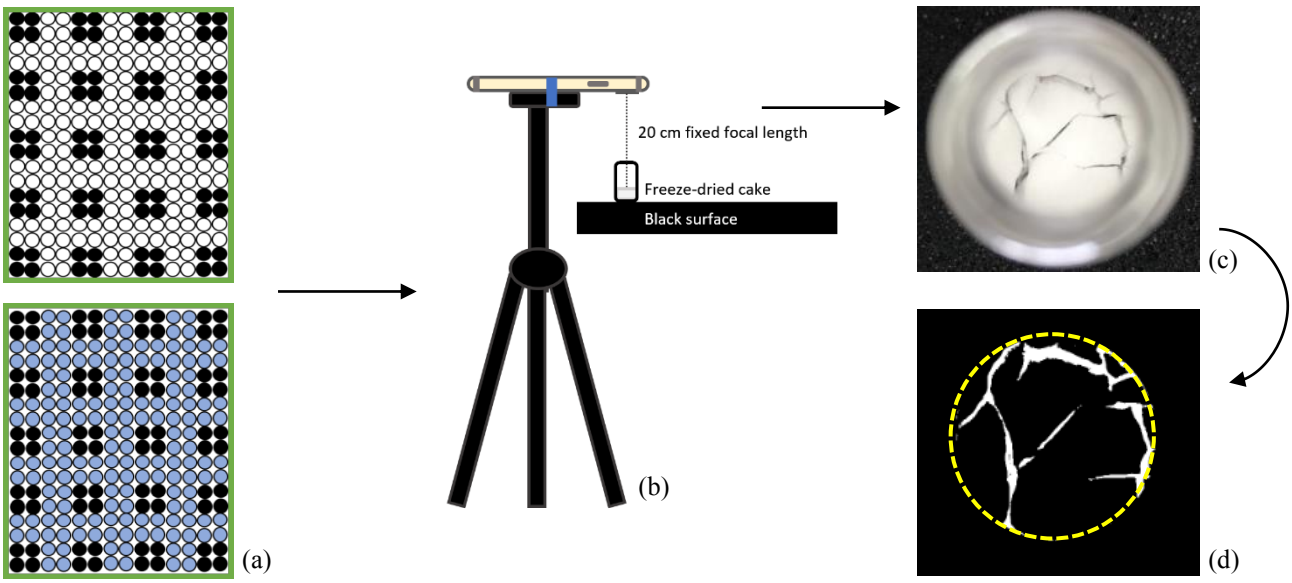

Figure 3: Crack intensity determination in a freeze-dried batch. (a) The configuration of the vials in the tray. Green box represents the outer wall of the tray and black circles represent the vials filled with protein formulations. Top configuration: Run 1, filled vials surrounded by empty vials, represented by white circles. Bottom configuration: Run 2: filled vials surrounded by vials filled with distilled water, represented by blue circles. (b) The photographing setup. (c) Photograph of the top surface of a cake. (d) Processed image of the top surface of cake using ImageJ. White area represents the crack area and black area represents the uncracked top surface of the cake. Yellow dashed circle encircles the total area of the cake.

3. Results and discussion

3.1. Preliminary study

The study started with determining the best formulation in term of mechanical and structural stabilities before subsequent steps were conducted. Disaccharides such as trehalose and sucrose are known to be the most effective stabilizers for protein during lyophilization for several reasons: they stabilize and protect the protein by replacing the hydrogen bonds between water and protein when water is removed during the freeze-drying process, they are non-reducing, and they tend to remain amorphous during freeze-drying (Carpenter et al., 2002).

Mechanical tests were not conducted on the sucrose:lysozyme formulations as the cakes collapsed after they were exposed to moisture uptake for 20 hours. The 10:1 ratio by mass of trehalose:lysozyme suffers a reduction of 28% in the Young's modulus value after a storage time of 70 hours, while the Young's modulus for the 20:1 formulation of trehalose:lysozyme cakes remained relatively unchanged. Cracking was also more prominent in the 20:1 trehalose:lysozyme formulations and this can be attributed to the increase in brittleness of the formulations when the concentration of trehalose increases (Patel et al., 2017). Highly cracked cakes are unsuitable for mechanical testing using MTI, and hence using the 20:1 formulation with trehalose would not yield meaningful results (McCartney, 2014). Therefore, it was decided that the 10:1 ratio by mass of trehalose:lysozyme formulation was to be used in the subsequent steps as it performed better in terms of mechanical tests and retaining cake appearance/structure.

3.2. Mechanical tests

The mechanical test detailed in section 2.3 was carried out to quantify the changes in Young's modulus of the selected formulation at two different moisture levels (9.16 w/w% and 1.94 w/w%) over a range of ageing durations in temperature-controlled environments. Mechanical tests were not conducted on the high moisture samples at 65°C as the samples collapsed almost as soon as they were placed in the temperature-controlled oven. The Young's modulus for each storage condition (temperature and moisture content) was measured using three samples. The average value of the Young's modulus was calculated, and the total error was determined as the sum of the instrument error and the standard deviation for the mean Young's modulus values.

Figure 4 shows the Young's modulus of the samples plotted against storage duration (days). The data shows that the Young's modulus values for the low moisture samples are generally higher than that of the high moisture samples (about 40%) at the start of the experiment (Day 0). This can be explained by the fact that water is a known plasticizer. The stability of freeze-dried formulation is significantly affected by the amount of water present in the protein. The plasticizing effect of water causes an increase in free volume and greater macroscopic mobility of the formulations. This results in the lowering of the glass transition temperature, T_g of the formulations, below the ambient temperature it is stored at (Swallowe, 1999, Towns, 1995). The phase transition occurs from a hard,

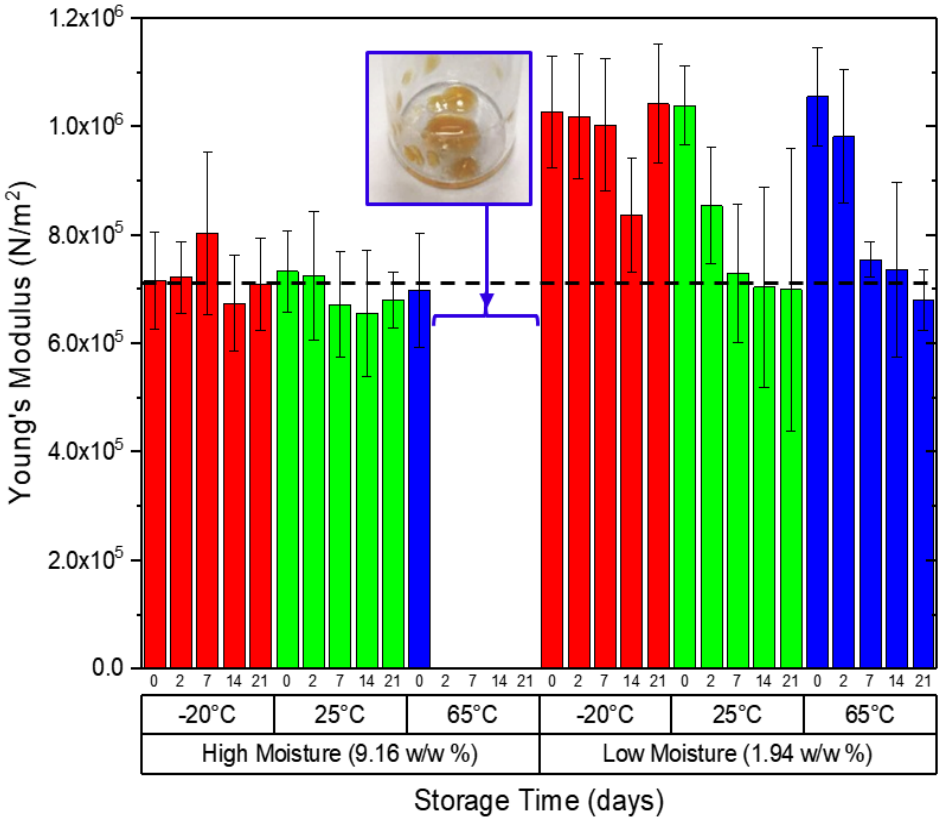

Figure 4: Young modulus against storage time plotted for high (left) and low (right) moisture samples for -20 (Red), 25 (Green) and 65°C (Blue) measured over a period of 21 days. Black dashed line shows the mean value for the initial Young's modulus for the high moisture samples. Photograph in blue box shows the appearance of the high moisture freeze-dried cakes after storage at 65 °C for 1 day.

glassy state to a soft, rubbery type of material. As a result, high moisture samples show a lower Young's modulus.

It can also be shown that the Young's modulus values of the low moisture samples, initially at higher values, reduce by about 40%, to values in the region of those of the high moisture samples after a storage duration of 3 weeks (black dashed line on Figure 4). This reduction in Young's modulus can be explained by moisture ingress throughout the storage duration. Low moisture samples are more hygroscopic than the high moisture samples and will therefore absorb moisture present in the surroundings more easily than the high moisture samples (Swallowe, 1999). The relatively unchanged Young's modulus values of high moisture samples and low moisture samples at -20°C suggest that the effect of moisture ingress is negligible in these samples. However, this will have to be verified using the Karl Fischer titration method to identify the true moisture content of the samples. Due to constraints in time and availability of Karl-Fischer titration equipment, we were unable to verify this during this study.

3.3. Thermo-stability of freeze-dried cakes

From the results in 3.1 for the high moisture cakes at 65°C, it was hypothesized that there must exist a critical moisture content for any temperature, at which the cake will collapse. This temperature would correspond to the collapse temperature (T_c) for the given moisture content shown on Figure 5. The result of carrying out this test at different temperatures was obtaining a thermo-stability map for the formulation at hand seen in Figure 6. The result from this study was fitted with the Gordon-Taylor equation using a T_g for water of -138°C (Handa et al., 1988) on OriginPro 2017, resulting in a value of 4.2 for the fitting parameter K and a y-intercept of 102 °C. This data was compared with literature data *(Chen, Fowler & Toner, 2000)* for the glass transition temperature of binary water-trehalose mixtures and data *(Panagopoulou et al., 2011)* for binary mixtures of water-lysozyme, in order to determine the effect of the addition of trehalose to the thermo-stability of the formulation. Although data from this study is not the T_g but rather the T_c, the difference between the two is not significant to invalidate comparison, especially if the difference between T_c of one material and the T_g of another is large enough. (Meister, 2008)

The first key result from Figure 6 is that trehalose increases the stability of the protein formulation. This is shown by the T_c for the formulation being significantly higher than the T_g for water-lysozyme systems. Protein is stabilized by sugar by forming hydrogen bonds with protein when water is removed, thus preventing dehydration-induced unfolding by replacing water molecules to maintain the protein structure (Schebor et al., 1999). This so called "water replacement mechanism" is supported by several different observations. With infrared

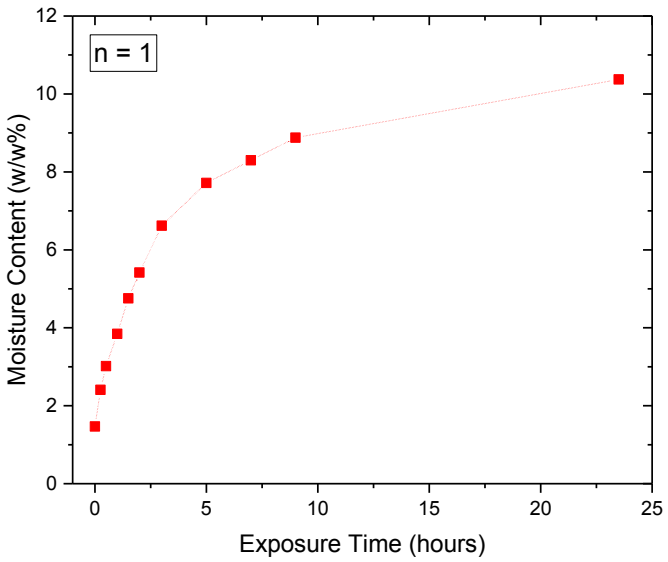

Figure 5: Moisture content (measured by Karl Fischer titration) against the exposure time for the freeze-dried lysozyme cakes used in thermo-stability test.

spectroscopy, it was found that the band at 1583 cm^{-1} in the spectrum for lysozyme, which is due to hydrogen bonding of water to carboxylate groups, is not present in the spectrum for the dried protein (Carpenter & Crowe, 1989). When lysozyme is dried in the presence of trehalose or sucrose, the carboxylate band is retained in the dried sample, indicating that the sugar forms hydrogen bonds in the place of water. Similar results have been obtained with α-lactalbumin and sucrose (Prestrelski et al., 1993).

The second key result is that the collapse temperature for the freeze-dried cakes drops as a function of moisture content. This can be explained by the fact that the adsorbed water may act as a plasticizer, lowering the T_g of the solid, and, hence lowering the T_c (Towns, 1995). This is explained by a resulting increase in free volume and greater macroscopic mobility (Slade & Levine, 1995). This has the implication that the effectiveness of trehalose as a stabilizer drops as a function of moisture content (seen by the reduction in collapse temperature), which is critical in determining storage conditions. Therefore, these results support the findings by Towns (1995) that for most products, levels of residual moisture should range from less than 1.0% to 3.0% so that the chemical and/or conformational stability, and therefore potency of the product, are not compromised over time. This result is also supported by the Gordon-Taylor equation fitted curve for the data points.

Another significant finding is that the fitted curve for the T_c of the freeze-dried cakes and the curve for T_g of water-trehalose systems overlap significantly. This is expected as the freeze-dried cakes are composed mainly of trehalose, and thus the collapse behavior is dominated by trehalose. However, it is important to note that the T_g is generally a few degrees lower than T_c and hence if the T_g for the freeze-dried cake was obtained, it would lie below the line for trehalose (Depaz, Pansare & Patel, 2016). Further experimental analysis is needed to confirm this behavior.

In terms of the physical appearance of the cakes under the different conditions, it was noted that the cakes retained their uniformity with respect to color, texture, and volume under the conditions described in the grey area on the figure. Meanwhile, the cakes obtained after storage in

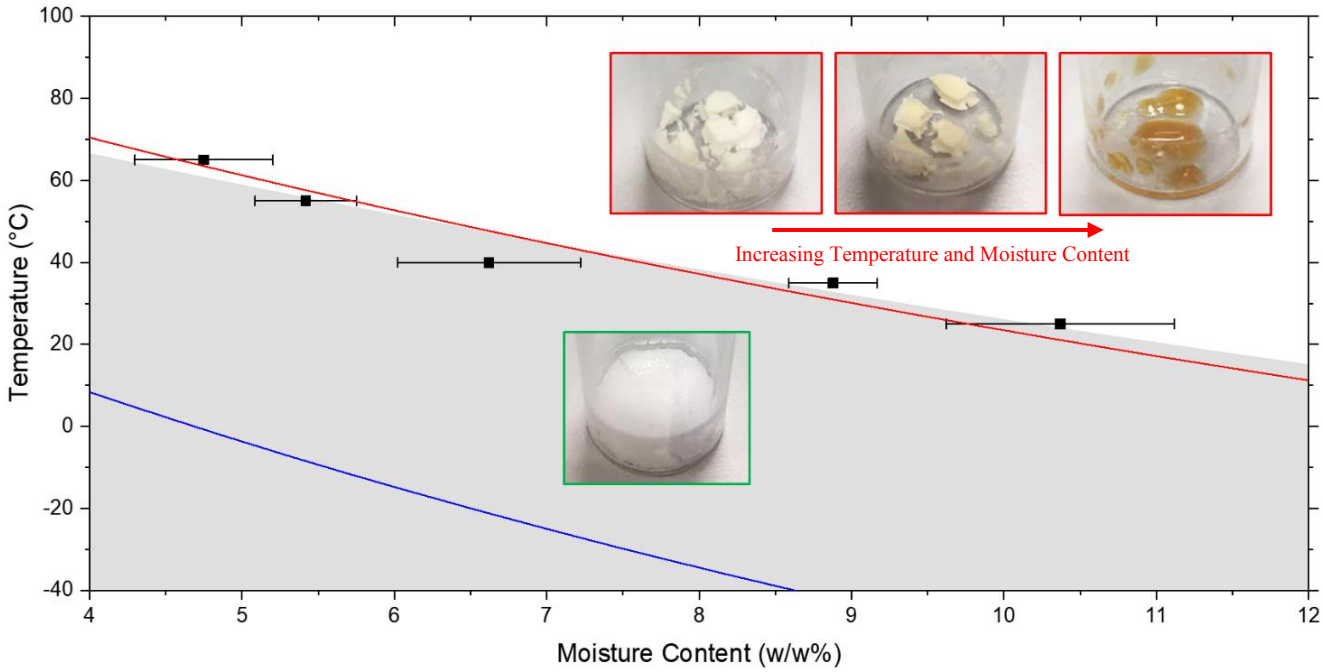

Figure 6: Thermo-stability map of temperature against residual moisture content in the freeze-dried cakes compared against literature data. Black squares represent the data points obtained from this study for the collapse temperature of the freeze-dried cakes (Error bars represent the interval at which the signs of collapse were observed). The grey area represents the Gordon-Taylor equation fitted to these data points, yielding a value for K of 4.2. The red line (upper) represents the Gordon-Taylor fit for the T_g values of water-trehalose (Chen et al., 2000). The blue line (lower) represents the Fox equation fit for the T_g values of water-lysozyme (Panagopoulou et al., 2011). The grey area represents the conditions under which the cakes retained uniformity in terms of appearance, shown in photograph in green box. The white area represents conditions under which the cakes showed signs of collapse and instability, shown in photographs in red boxes.

the conditions represented by the white area showed a spectrum of visible irregularities. As seen on Figure 6, this ranged from a partially collapsed cake with no change in color, partially collapsed with slight browning, to a completely collapsed and caramelized appearance. The change in color and extent of collapse was intensified with increased moisture content and temperature. Trehalose is one of the most stable known disaccharides, with an extremely low disaccharide bond energy (less than 4 kJ/mol) and is not expected to participate in Maillard reactions with proteins or peptides. However, high temperatures and the presence of free moisture could cause it to hydrolyze into glucose, which can participate in Maillard browning. This would explain the complete collapse and subsequent deep browning of the cakes (Schebor et al., 1999). Hence, when selecting sugars to protect dry labile biomaterials, the possibility of hydrolysis followed by browning must be considered.

Another important thing to note is that changes in physical appearance, such as browning, may not affect critical quality attributes (CQA) such as product efficacy, bioavailability or reconstitution (Patel et al., 2017). Moreover, recent data suggests that collapse is a cosmetic issue only and has no impact on CQAs (Schersch et al., 2010). However, some previous studies point to elevated residual moisture content being associated with collapse, leading to decreased stability in some protein formulations, due to the crystallization of stabilizer, which may occur during the freeze-drying process or during storage. This would lead to a loss of stabilizing effect of the sugar (Izutsu, Yoshioka & Kojima, 1994). Thus, it is important to remain well clear of the unstable region on the figure in order to maintain product viability and retain shelf-life, although physical appearance may not strictly be a CQA (Leinen & Labuza, 2006). In a case where the product shows irregularities or non-uniform appearance even under the stable region, further tests will need to be carried out to demonstrate that there is no impact on product quality and reproducibility, including color of reconstituted solution.

3.4. Crack intensity mapping in a freeze-dried batch

Throughout the mechanical and thermo-stability study, it was discovered that the cracking of the freeze-dried formulations may be dependent on the position of the vials in the freeze-drier during the freeze-drying process. A novel method detailed in section 2.5 was carried out to verify this hypothesis.

Figure 7 shows the fraction of cracks on the cake surfaces on fixed coordinates for two different runs. It can be shown that cracking is more prominent in central and rear regions of the tray, compared the shelf front and the sides. A study by Cook et. al. (2011) shows that the headspace moisture in the vials after freeze-drying depends on the position of vials in the freeze-drier when the vials are not in direct contact with the freeze-drier shelf (by means of a tray). It is interesting to note that in Cook's study, the headspace moisture content of the vials in the center and rear of the tray is higher than those surrounding vials. The higher headspace moisture content of the vials can be explained by the heat transfer mechanism in the freeze-drier. Three different pathways of heat transfer occur during the freeze-drying process: conduction form the shelf to the tray and vials, gas convection in the empty spaces between the vials, and radiation from the side walls and the door of the freeze-drier. The central vials have greater shielding form the surrounding vials, resulting

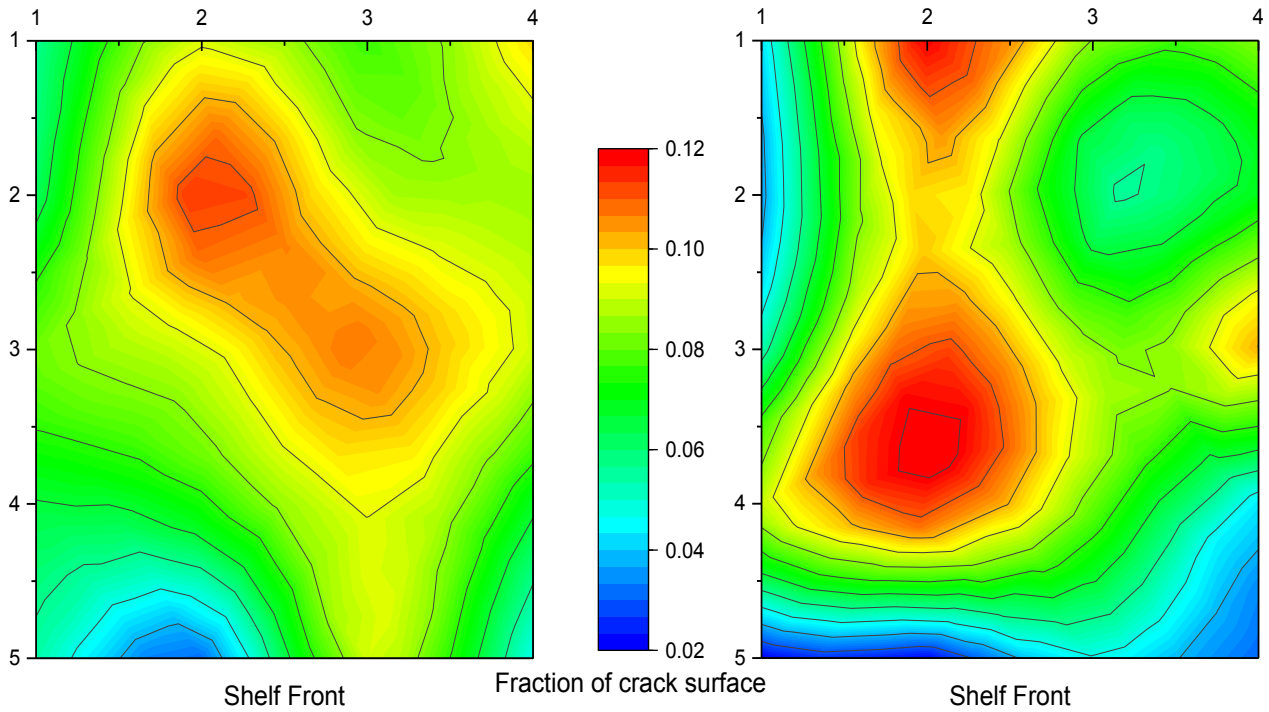

Figure 7: Cracking intensity map for (left) Run 1 where the blank vials were left empty and (right) Run 2 where the blanks were filled with distilled water. The axes represent the horizontal coordinates of the vials placed inside the freeze-drier.

them receiving a smaller radiation heat load from the side of the walls and door. Thus, the headspace moisture content of the central vials appears to be higher. This is more commonly known as the edge effect (Cook & Ward, 2011, Ullrich, Seyferth & Lee, 2015). The cracking of the cakes could potentially be correlated with the moisture content of the cakes due to the similarities in both studies.

According to a study by Rambhatla et. al. (2015), cracking is caused by the same underlying physics as shrinkage, which is another critical irregularity in freeze-dried cakes that is associated with collapse. A correlation was reported between shrinkage and the amount of unfrozen water present in an amorphous system, which when removed during drying, causes a stress buildup in the cake due to volume contraction. This stress can be relieved by either contraction of the cake (shrinkage) or cracking, and the determining factor as to which takes place was hypothesized to be the extent of adhesion of the cake to the inner wall of the vials. An inverse relationship between cracking and shrinkage was determined and cracking was found to dominate at high sugar concentrations (Ullrich, Seyferth & Lee, 2015). Hence, it is possible to explain the extent of cracking by relating it to residual moisture content. Further experiments will be required at different sugar concentrations and by taking shrinkage into account using the method developed in this study in order to confirm this behavior. The true moisture content of all the cakes will also need to be measured to establish a relationship.

It was also noted that the intensity of cracking is generally higher in the second experiment. This may be explained by the fact that more moisture is present in the vials overall initially in the second experiment as the blank vials are filled with distilled water. Therefore, the average thermal load on each vial would be reduced, and hence the temperature distribution on the tray is compromised. This would inevitably lead to a higher residual moisture content in the cakes, and thus may correlate to a greater extent of cracking.

4. Conclusions

Trehalose was found to be an excellent stabilizer for lysozyme. The addition of 5% w/w trehalose to the freeze-drying recipe of 0.5% w/w lysozyme could prolong the shelf life of lysozyme formulations. However, the relationship between the moisture content in the freeze-dried cake and the storage temperature of the cake should be further studied to prevent the collapse of cake. Current and previous studies show that there exists a moisture content for a specific storage temperature, known as the critical moisture content, above which instability of the cake will start to occur. This is particularly important for freeze-dried therapeutics as any changes in the appearance of the cake such as melt back, total collapse, cracked and shrunk cakes could possibly result in the formulations being rejected. As the stabilizing effect of trehalose was found to be moisture content dependent, similar future studies should be conducted at different temperature and moisture content to verify the relationship between temperature and moisture content. Cracking of the cake was found to be dependent on the position of vials in the freeze-drier in this study. This could potentially be correlated with the moisture content in the freeze-dried cakes due to the significant overlap in similarities between the findings of this study and past research. However, the relationship between the moisture content and the extent of cracking will have to be studied thoroughly in order to verify and quantify this phenomenon, particularly by including the effect of shrinkage of the cakes. Coupling the mechanical test and the thermo-stability map of the freeze-dried cakes, one would find it useful to determine the optimum storage temperature and residual moisture content of the freeze-dried cakes to prevent the collapse and rubberization of the cake. For future research, the protein activity of the freeze-dried cakes could be investigated, along with the mechanical and thermo-stability of the freeze-dried cakes, as to determine if there is any correlation between them. Aggregation of protein over the storage time using the Dynamic Light Scattering (DLS) technique could also be used to correlate the activity of the freeze-dried proteins to the mechanical and thermo-stability of the cakes. The culmination of physio-mechanical and thermo-stability of freeze-dried cakes, as studied in this work, was found to have a great impact on key critical quality attributes (CQA) for freeze-dried products, and future study in this area would be imperative in improving the long-term stability and providing consumers with high-quality products.

5. Acknowledgements

We would like to express our gratitude to the members of the Surface and Particle Engineering Lab (SPEL, Imperial College London, UK) for their invaluable support in providing required training and equipment used in this study, and the National Institute of Biological Standards and Control (NIBSC, UK) for allowing us to use the Karl-Fischer titration equipment for the moisture determination steps.

6. Supplementary material

Supplementary data associated with this paper can be found here.

7. References

Carpenter, J. F., Chang, B. S., Garzon-Rodriguez, W. & Randolph, T. W. (2002) Rational Design of Stable Lyophilized Protein Formulations: Theory and Practice. In: Carpenter, J. F. & Manning, M. C. (eds.). *Rational Design of Stable Protein Formulations: Theory and Practice.* [e-book] Boston, MA, Springer US. pp. 109-133. Available from: https://doi.org/10.1007/978-1-4615-0557-0_5.

Carpenter, J. F. & Crowe, J. H. (1989) An infrared spectroscopic study of the interactions of carbohydrates with dried proteins. *Biochemistry.* 28 (9), 3916-22. Available from: doi: 10.1021/bi00435a044.

Chen, T., Fowler, A. & Toner, M. (2000) Literature review: supplemented phase diagram of the trehalose-water binary mixture. *Cryobiology.* 40 (3), 277-282. Available from: doi: 10.1006/cryo.2000.2244 [doi].

Cook, I. A. & Ward, K. R. (2011) Headspace Moisture Mapping and the Information That Can Be Gained about Freeze-Dried Materials and Processes. *PDA Journal of Pharmaceutical Science and Technology.* 65 (5), 457-467. Available from: doi: 10.5731/pdajpst.2011.00760 [doi].

Craig, D. Q. M., Royall, P. G., Kett, V. L. & Hopton, M. L. (1999) The relevance of the amorphous state to pharmaceutical dosage forms: glassy drugs and freeze dried systems. *International Journal of Pharmaceutics.* 179 (2), 179-207. Available from: http://www.sciencedirect.com/science/article/pii/S037851739800338X. Available from: doi: //doi.org/10.1016/S0378-5173(98)00338-X.

Depaz, R. A., Pansare, S. & Patel, S. M. (2016) Freeze-Drying Above the Glass Transition Temperature in Amorphous Protein Formulations While Maintaining Product Quality and Improving Process Efficiency. *Journal of Pharmaceutical Sciences.* 105 (1), 40-49. Available from: doi: 10.1002/jps.24705 [doi].

Handa, Y. P., Klug, D. D. & Whalley, E. (1988) Energies of the phases of ice at low temperature and pressure relative to ice Ih. *Canadian Journal of Chemistry.* 66 (4), 919-924. Available from: https://doi.org/10.1139/v88-156. Available from: doi: 10.1139/v88-156.

Izutsu, K., Yoshioka, S. & Kojima, S. (1994) Physical stability and protein stability of freeze-dried cakes during storage at elevated temperatures. *Pharmaceutical Research.* 11 (7), 995-999.

Leinen, K. M. & Labuza, T. P. (2006) Crystallization inhibition of an amorphous sucrose system using raffinose. *Journal of Zhejiang University.Science.B.* 7 (2), 85-89. Available from: doi: 10.1631/jzus.2006.B0085 [doi].

Liao, Y., Brown, M. B., Quader, A. & Martin, G. P. (2002) Protective Mechanism of Stabilizing Excipients Against Dehydration in the Freeze-Drying of Proteins. *Pharmaceutical Research.* 19 (12), 1854-1861. Available from: https://doi.org/10.1023/A:1021497625645. Available from: doi: 1021497625645.

Manning, M. C., Chou, D. K., Murphy, B. M., Payne, R. W. & Katayama, D. S. (2010) Stability of Protein Pharmaceuticals: An Update. *Pharmaceutical Research.* 27 (4), 544-575. Available from: https://doi.org/10.1007/s11095-009-0045-6. Available from: doi: 10.1007/s11095-009-0045-6.

McCartney, S. (2014) *Mechanical characterisation of freeze-dried biopharmaceuticals.* Imperial College London.

Meister, E. (2008) *A significant comparison between collapse and glass transition temperatures.* Available from: https://www.europeanpharmaceuticalreview.com/article/1479/a-significant-comparison-between-collapse-and-glass-transition-temperatures/ [Accessed 10/12/2018].

Panagopoulou, A., Kyritsis, A., Sabater I Serra, R., Gomez Ribelles, J. L., Shinyashiki, N. & Pissis, P. (2011) Glass transition and dynamics in BSA-water mixtures over wide ranges of composition studied by thermal and dielectric techniques. *Biochimica Et Biophysica Acta.* 1814 (12), 1984-1996. Available from: doi: 10.1016/j.bbapap.2011.07.014 [doi].

Patel, S. M., Nail, S. L., Pikal, M. J., Geidobler, R., Winter, G., Hawe, A., Davagnino, J. & Rambhatla Gupta, S. (2017) Lyophilized Drug Product Cake Appearance: What Is Acceptable? *Journal of Pharmaceutical Sciences.* 106 (7), 1706-1721. Available from: doi: S0022-3549(17)30171-5 [pii].

Prestrelski, S., Tedeschi, N., Arakawa, T. & Carpenter, J. F. (1993) Dehydration-induced conformational transitions in proteins and their inhibition by stabilizers. *Biophysical Journal.* 65 (2), 661-71. Available from: doi: 10.1016/S0006-3495(93)81120-2.

Schebor, C., Burin, L., Buera, M. d. P. & Chirife, J. (1999) *Stability to Hydrolysis and Browning of Trehalose, Sucrose and Raffinose in Low-moisture Systems in Relation to Their Use as Protectants of Dry Biomaterials.* Available from: http://www.sciencedirect.com/science/article/pii/S0023643899905765.

Schersch, K., Betz, O., Garidel, P., Muehlau, S., Bassarab, S. & Winter, G. (2010) Systematic investigation of the effect of lyophilizate collapse on pharmaceutically relevant proteins I: stability after freeze-drying. *Journal of Pharmaceutical Sciences.* 99 (5), 2256-2278. Available from: doi: 10.1002/jps.22000 [doi].

Slade, L. & Levine, H. (1995) Glass transitions and water-food structure interactions. *Advances in Food and Nutrition Research.* 38 103-269.

Swallowe, G. M. (1999) *Mechanical Properties and Testing of Polymers: An A–Z Reference.* Polymer Science and Technology Series. Springer Netherlands.

Towns, J. K. (1995) *Moisture content in proteins: its effects and measurement.* Available from: http://www.sciencedirect.com/science/article/pii/002196739401257F.

Ullrich, S., Seyferth, S. & Lee, G. (2015) Measurement of Shrinkage and Cracking in Lyophilized Amorphous Cakes. Part I: Final-Product Assessment. *Journal of Pharmaceutical Sciences.* 104 (1), 155-164. Available from: http://www.sciencedirect.com/science/article/pii/S0022354915302732. Available from: doi: //doi.org/10.1002/jps.24284.

The effect of porosity on the photocatalytic properties of boron nitride towards CO_2 photoreduction optimisation

Nicholas Oon and Eduardo Rattner
Department of Chemical Engineering, Imperial College London, UK

Abstract

Porous and amorphous boron nitride (BN) has been shown to be capable of CO_2 photoreduction, which has important implications for the production of solar fuels. Its porosity is suspected to be key in enabling photoreduction to occur, as it allows for increased catalytic active sites and reduced bulk charge recombination. The porosity of BN can be tuned by using varying amounts of precursors. However, its effect on photocatalytic properties and performance of BN is currently undetermined. Herein, we synthesise various samples of porous BN and test them for structural and photocatalytic properties. It was found that the band gap decreases as total pore volume and BET surface area increase. Adsorption of CO_2, the first step in photocatalysis, was higher than that of commercially available materials. Samples were multimodally porous, and it was found that currently available pore size distribution models do not accurately describe the pore structure. Nevertheless, the multimodality of all samples using different synthesis methods indicated that a template-free unimodally porous sample is unlikely to be synthesised and subsequently, templated methods have been proposed. A range of unimodally porous samples would give greater understanding into the reason for the change in band gap and allow for photocatalyst optimisation.

Keywords: Boron nitride, porosity, band gap, photocatalysis, unimodal, solar fuels

Introduction

Carbon dioxide emissions have been growing steadily over the last few decades.[1,2] This has led to a move towards renewable energy uptake, with research focussing on producing more sustainable energy. One of the energy sources with the most potential is solar energy, as incident radiation on Earth surpasses current energy needs by 5000 times.[3] This is, however, hindered by the current energy storage capability.[4] Chemical fuels offer an effective way of storing energy, with high specific energy capacity, that can easily be used whenever needed.[5] CO_2 photoreduction is a photocatalytic process that harvests solar energy into chemical fuels or feedstocks, such as CO, CH_4, CH_3OH. One main advantage is that there is potential for reduced net CO_2 production from the consequent fuel combustion, combining carbon capture and energy production. This has been confirmed through a life cycle analysis.[6]

One of the main issues regarding photocatalytic energy production is energy loss, for which charge recombination holds a large share of responsibility.[7] Charge separation is largely influenced by catalyst physical and optical properties, motivating research efforts on developing and optimising photocatalysts.[7,8] The current benchmark is TiO_2 and derivatives and has been for the past 40 years, owing to several key properties.[7,9] Namely, its capability for absorbing solar energy at a suitable band gap (around 3 eV depending on the morphology),[10] its stability under atmospheric conditions[11] and its conductive properties. The latter allows for easy electron mobility from the bulk material to the surface active sites. The photoreduction of CO_2 is a surface reaction, hence, in addition to optical properties, any photocatalyst must be able to efficiently adsorb and desorb the reactants and products, respectively.

Some new semiconductor materials, such as boron nitride (BN), are able to retain photocatalytic abilities whilst also being porous. This means they have a large specific surface area, leading to improved mass transfer capabilities. Porous boron nitride has been shown to be able to reduce CO_2 under UV and visible light illumination.[12] The porous nature of the material allows for increased contact area with CO_2, compared with traditional metallic catalysts. It also reduces the quantity of bulk charge recombination because the average distance between the bulk material, where the electron is excited, and a surface catalytic active site is reduced. Furthermore, the fact that the porosity of boron nitride can be tuned[13] makes it a good candidate to study the relation between porosity and photocatalytic properties.

Herein, we try to establish a link between porosity and band gap of boron nitride, with particular interest in the effect of pore width and size distribution, giving further insights into photocatalytic performance.

Background

A key hurdle for photocatalysis is bulk charge recombination. Photoreduction and oxidation require an exciton to be dissociated into free charge carriers, which then can participate in a reaction. These carriers have very short lifetimes especially when compared to reaction times, and the majority of carriers recombine before being able to react.[7] Extending the carrier lifetimes has been shown to be achievable by modifying the catalyst using cocatalysts. For instance, Ti(IV) has been shown to be effective as a hole trapping centre and so can facilitate oxidation reactions.[14,15] Metallic electron cocatalysts have also been used to allow for multielectron reduction reactions. Fe(III) or Cu(II) acted well as electron cocatalysts with a TiO_2 photocatalyst[14] and

Fe(III) was also suitable when loaded onto a AgBr photocatalytic surface.[15]

Another issue in photocatalysis is obtaining a photocatalyst with a suitable band gap, as this dictates what wavelength of light the molecule is able to absorb. There has been a lot of research into how to reduce or tune the band gap, so that visible light can be absorbed rather than UV light. This is because about 90% of incident solar radiation is within the visible light range.[16] However, the span of the band gap must also encompass the oxidation and reduction potentials of the photocatalysed reaction, i.e. the conduction band must be greater than the reduction potential, but the valence band must be lower than the oxidation potential[17] (Fig. 1). Most previous research in this area has focussed on crystalline metallic materials.

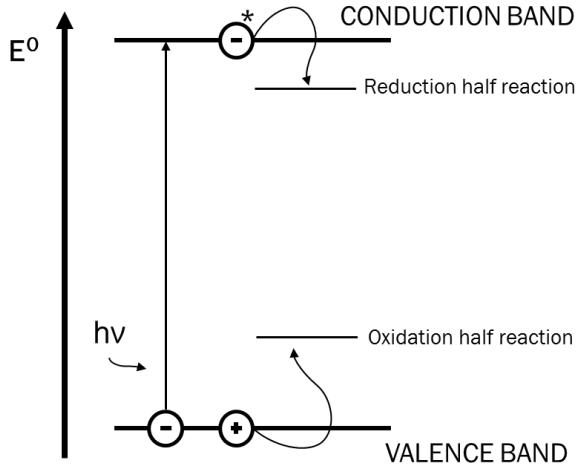

Figure 1. Photocatalytic process on a semiconducting material. A ground state electron is excited through the absorbance of a photon. This creates an electron-hole pair which dissociates into two opposing free charges, as the electron is promoted into the conduction band. The charges may then be used in the reduction and oxidation half reactions.

New materials capable of the photoreduction of CO_2, like carbon-based organic nanomaterials, are advantageous over more conventional inorganic metal oxides and chalcogenides due to them being more cost effective, robust and environmentally sustainable.[7] Graphitic carbon nitride has been of particular interest as it has been shown to be chemically, thermally and mechanically stable.[18] It has also been shown to be capable of CO_2 photoreduction, with the 3D structure playing a key role in the photocatalytic capability.[19] The rate of CO_2 photoreduction has been improved by using a nanosheet nanocomposite made with a combination of TiO_2 and carbon nitride.[20] Graphitic carbon nitride has also been used effectively in a Z-scheme in combination with other catalysts, such as α-Fe_2O_3[21]or with both Ag_2CrO_4 and graphene oxide.[22] Other methods to improve photocatalytic activity include the doping of carbon nitride with different species, such as sulfur,[23,24] phosphorous,[25] fluorine[26] and boron.[27] Boron doped graphitic carbon nitride has been shown to be capable of visible light photoreduction,[28] with its band gap changeable by varying the configuration and proportions of boron to carbon.[29] Carbon doped boron nitride also has CO_2 adsorption qualities comparable with carbon-based materials as well as being able to act as a photocatalyst.[30,31] However, Florent and Bandosz have since demonstrated that porous boron carbon nitride is hydrolysed in the presence of water to nonporous boron carbon nitride oxide.[32]

It has been proven that porous boron nitride is itself capable of capturing and photoreducing CO_2, despite its analogous crystalline form, hexagonal boron nitride (h-BN), behaving as an insulator (5.5 eV).[12] As well as being synthesised from cheap precursors in a facile template-free method,[33] a key advantage of boron nitride is that its porosity can be tuned during the synthesis process.[13] Within a porous material, CO_2 adsorption can increase and bulk charge recombination is less likely. Thus, the rate of CO_2 photoreduction may increase compared with a non-porous equivalent.

Methods

Chemicals

Porous BN was synthesised from a mixture of a B-precursor, boric acid (ACS reagent, 99.0%, Sigma-Aldrich), and N-precursors, urea (molecular biology grade, Sigma-Aldrich) and melamine (ACS reagent 99%, Sigma-Aldrich). The samples are referred to as BN-XYx:y, where X and Y represent different N-precursors and x and y represent the molar ratio of said precursor to boric acid. For example, BN-MU0.5:5 would mean a molar ratio of 0.5 moles of melamine to 5 moles of urea to 1 mole of boric acid was used in the synthesis.

Synthesis of BN samples with multimodal porosity

Five samples were produced using this method. For all samples, boric acid, urea, and melamine when applicable, were mechanically mixed and ground to a fine powder. This resulting mixture was then loaded in an alumina boat crucible, which was placed in a horizontal tubular furnace. The furnace was purged for 2 to 3 hours under a nitrogen flowrate of 250 $cm^3 \cdot min^{-1}$. Following this, the gas flowrate was decreased to 50 $cm^3 \cdot min^{-1}$ the samples were heated to 1050 °C at a heating rate of 10 $°C \cdot min^{-1}$. The temperature was held for 3.5 h and the samples were allowed to cool to room temperature naturally, maintaining the gas flowrate. A white powder was obtained from the synthesis.

Synthesis of BN samples with potential unimodal porosity

For BN-Mm, a method was adapted from the previous work done by Levya et al.[34] Boric acid and melamine were dissolved in boiling distilled water for 10 minutes, after which the solution was placed in an ice bath for 3 hours. The resulting slurry was vacuum filtered for 45 minutes and left to dry overnight in a vacuum oven. The resulting cake was ground for 5 minutes and loaded in an alumina boat, which was then placed in a horizontal tubular furnace. It was then heated to 500 °C at a ramp of 10 $°C \cdot min^{-1}$ under an air atmosphere, with the flowrate held at 20 $cm^3 \cdot min^{-1}$. After three hours of dwelling, the gas supply was switched to nitrogen, at constant flowrate, the temperature was raised to 800 °C, held for one hour

and then raised again to 1200 °C, after which the temperature was held for another hour. All of this was done at a heating rate of 10 °C·min^{-1}. The samples cooled naturally under a flow of nitrogen and a white powder was obtained.

Characterisation

The chemistry of the samples was characterised by Fourier transform infrared (FT-IR) spectroscopy. The samples were first ground to a fine powder and the spectra were measured in the range of 500-4000 cm^{-1} using an Agilent Cary 630 FT-IR spectrometer, equipped with an attenuated total reflectance probe. X-ray photoelectron spectroscopy (XPS) was used to determine the relative elemental composition and the chemical states of the elements in the samples. It was conducted using a Thermo Scientific K-Alpha X-ray Photoelectron Spectrometer equipped with a MXR3 Al-Kα monochromated X-ray source (hν = 1486.6 eV). The ground samples were mounted onto an XPS sample holder using a small rectangular piece of conductive carbon tape. The X-ray gun power was set to 72 W (6 mA and 12 kV). Survey scans were achieved using 200 eV pass energy, 0.5 eV step size and 100 ms dwell times, in two scans of 50 ms. All of the high-resolution spectra (B 1*s*, N 1*s*, C 1*s*, and O 1*s*) were obtained using a 20 eV pass energy and 0.1 eV step size. To analyse the results, the Thermo Avantage data analysis program was used.

The crystallinity and structure of the samples were determined through powder X-ray diffraction (XRD). This was performed in a PANalytical X'Pert Pro X-ray diffractometer in reflection-transmission mode with a spinning stage (2 revolutions/second). The anode voltage and emission current were set to 40 kV and 20 mA, respectively, using monochromatic Cu-Kα radiation (λ = 1.54178 Å). The XRD detector was the X'Celerator silicon strip.

Nitrogen sorption isotherms were measured using a porosity analyser, Micrometrics 3Flex, at -196 °C. All samples were degassed overnight at a pressure of 0.2 mbar and 140 °C. Prior to the actual measurement, they were then degassed again in situ at 120 °C for 4 hours, at a pressure of 0.003 mbar. Specific surface areas were measured using the Brunauer-Emmett-Teller (BET) method.[35] Total pore volumes were determined at a relative pressure of approximately 0.97. Micropore volumes were calculated from the Dubinin-Radushkevich method.[36] The pore size distributions were plotted using in-built software and a density functional theory (DFT) model (N2@77 on Carbon Slit Pores by NLDFT).

Optical behaviour was characterised through ultraviolet-visible diffusive reflectance spectroscopy (UV-Vis). Spectra were measured in a Cary 500 UV-Vis spectrophotometer in the range of 1200 nm to 200 nm. The band gap was found from the absorbance using the transformed Kubelka-Munk function in the Tauc plot, where the first onset of linear behaviour was taken as the start of absorbance and extrapolated (for further information refer to supplementary information). The band gap was obtained from the x-intercept of the extrapolated line. For these experiments, BN was formed into pellets by putting the sample on a base of approximately 1 gram of KBr into a pellet die (Specac, 13 mm evacuable stainless steel). A manual press of 7 tonnes was applied for 5 seconds, and the pellet was carefully removed by applying a gradual counterload at the base.

CO_2 adsorption testing

CO_2 sorption experiments were conducted for the three samples with the highest porosity. CO_2 isotherms were determined at 25 °C, 1 bar, in the same fashion as the N_2 isotherms, with the same instrument and procedure.

Results and Discussion

The chemical bonding of the different samples was analysed using FT-IR spectroscopy. All the samples gave similar spectra (Fig. 2) with the same two main characteristic bands. These are B-N-B out of plane bending at ~800 cm^{-1} and B-N in-plane transverse stretching at ~1360 cm^{-1}.[37] The third highlighted band at ~1200 cm^{-1} corresponds to B-O in plane transverse stretching.[38] This was attributed to a lack of nitrogen precursor in the synthesis, resulting in incomplete boric acid conversion to boron nitride. For the syntheses containing no urea there is another small band at ~3000 cm^{-1}, which was attributed to a C-H stretching mode,[39] likely due to incorporation of carbon. This was confirmed by the analysis of a boron carbon nitride sample (Fig. S1).

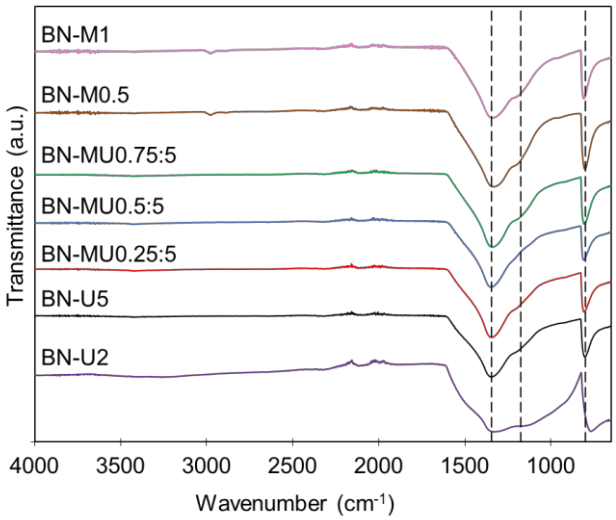

Figure 2. FT-IR spectra of synthesised BN samples. Characteristic bands representing B-N-B bending mode, B-N and B-O stretching have been highlighted.

The XRD patterns (Fig. 3a) indicated the formation of amorphous or turbostratic structures.[40] This is despite the presence of two residual peaks, which are broad and low in intensity, representing the (002) and the (100) crystal facets of h-BN, at around 26° and 43°, respectively.[40] The broadness of the peaks and the absence of further reflections indicate that multilayer h-BN formation is excluded.

To characterise the porosity and surface area, N_2 sorption at -196 °C was conducted. All samples displayed a type IV isotherm, which indicates the presence of both micro- and mesopores (Fig. 3b). Hysteresis loops for

urea-containing samples are of type H3, which point to aggregates of plate-like particles with slit-like pores. The melamine-only samples show type H4 loops, indicating narrower slit-like pores.[41] Table 1 shows the calculated BET surface area, total pore volume and limiting micropore volume. It can be seen that the surface area tends to increase with the ratio of the N-precursor to B-precursor, as expected from literature.[33] This is due to ammonia evolution from the pyrolysis of urea and melamine. However, not all samples exhibited this behaviour, and an inversion was observed for the two samples with the highest ratio. The maximum value for the surface area obtained was 1600 $m^2 \cdot g^{-1}$, with total pore volume of 1.10 $cm^3 \cdot g^{-1}$, for BN-MU0.5:5. For comparison, the theoretical maximum for surface area of single BN sheet is 2630 $m^2 \cdot g^{-1}$.[42] High surface areas indicate potential for photoreduction due to increased contact area and adsorption of CO_2 onto the surface.

Analysis of the pore size distribution (Fig. 3c) reveals both micro- and mesopores, as expected from the BET

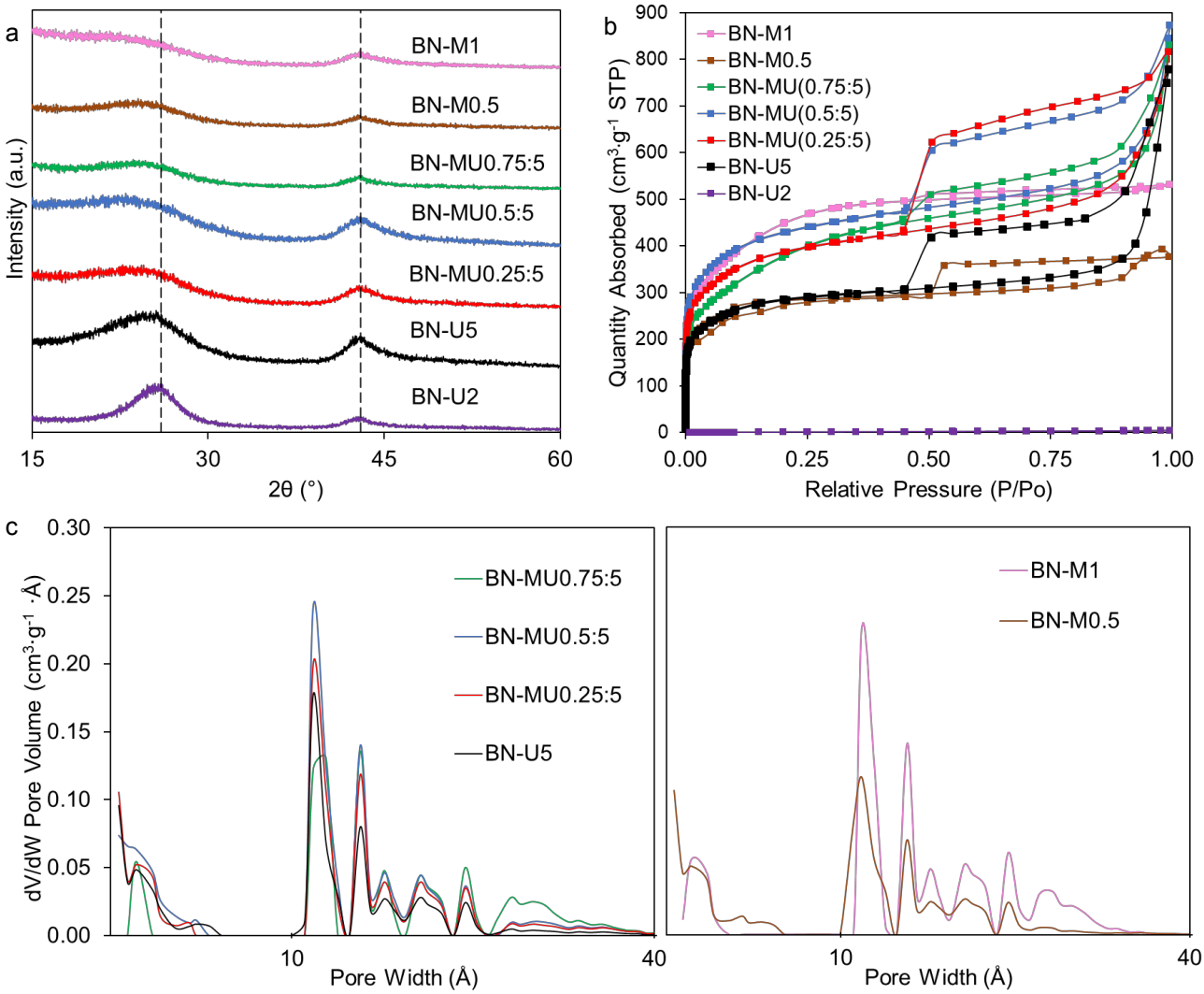

Figure 3. Structural properties of porous BN samples. (a) XRD patterns of synthesised BN samples with residual h-BN characteristic peaks highlighted, (b) N_2 sorption isotherms for synthesised BN samples measured at -196 °C, (c) Pore size distributions for initial samples and for attempted unimodally porous BN samples.

Table 1. Key structural properties measured using N_2 sorption at -196 °C for the synthesised BN samples.

Sample	Total Pore Volume ($cm^3 \cdot g^{-1}$)	BET Surface Area ($m^2 \cdot g^{-1}$)	Limiting Micropore Volume ($cm^3 \cdot g^{-1}$)
BN-M1	0.82	1653	0.64
BN-M0.5	0.59	1054	0.41
BN-MU0.75:5	1.08	1381	0.55
BN-MU0.5:5	1.10	1600	0.65
BN-MU0.25:5	1.03	1345	0.54
BN-U5	0.95	1063	0.42
BN-U2	0.01	5	-

calculations. The pore size distribution appears to be very similar among all samples differing only in total porosity, despite the dissimilar methods used in their syntheses. However, the low amount of hysteresis on BN-M1 compared to other samples indicates a different pore structure. Other built-in DFT models give similarly matching pore size distributions for all samples and classical models have been shown to not describe ångström-scale pores effectively.[43,44] This suggests common existing pore size distribution models are unsuitable for porous BN. Thus, a new pore size distribution model for this material is required. Nevertheless, the type IV isotherms of all samples suggest a multimodal pore structure.[43,44] Therefore, it is possible to conclude that a template-free unimodal porosity sample is very unlikely, and a template will probably be required for this purpose.

The absorbance graph (Fig. 4a) shows that there is a clear red shift between the different samples and the corresponding Tauc plot against photon energy (Fig. 4b) allows the band gap to be found.[45] Overall, it was found to be significantly lower than that of h-BN, which has a band gap of ~5.5 eV.[12] This indicates the porous samples have semiconductive behaviour. Figures 5a and b suggest that a trend does exist between the porosity and band gap, with the band gap decreasing with increasing total pore volume and BET surface area. Optical characterisation was only performed for samples synthesised with urea and melamine as precursors, to keep changing variables to a minimum. XPS was conducted to ensure differences in band gap could not be attributed to changing chemistry, strengthening the trends obtained.

The results show very little difference in composition. Boron composes just over half in each sample at ~53%, followed by nitrogen at ~40% (Fig. 6). This disparity indicated the presence of oxygen defects in the form of in-plane substitution of oxygen (~7%), confirmed by the presence of borooxynitride peaks ($B\text{-}O_x\text{-}N_y$)[13] (Fig. S2).

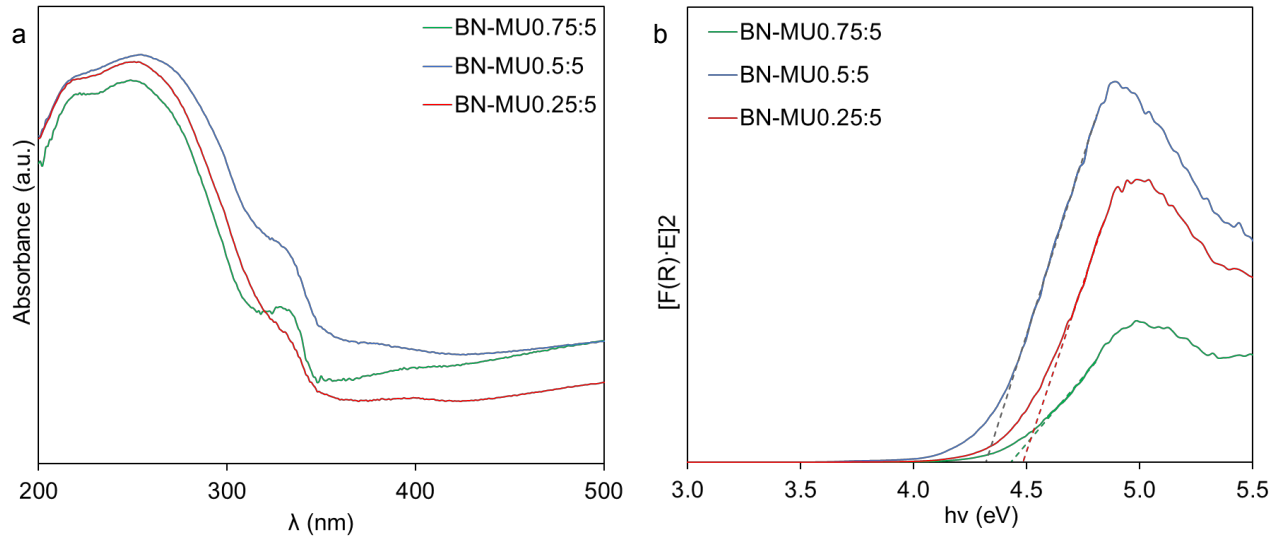

Figure 4. Optoelectronic properties of selected BN samples. (a) Light absorption spectra of selected BN samples obtained through UV-Vis data, (b) Tauc plot of the transformed Kubelka-Munk function against photon energy for selected BN samples showing the optical band gap of the samples.

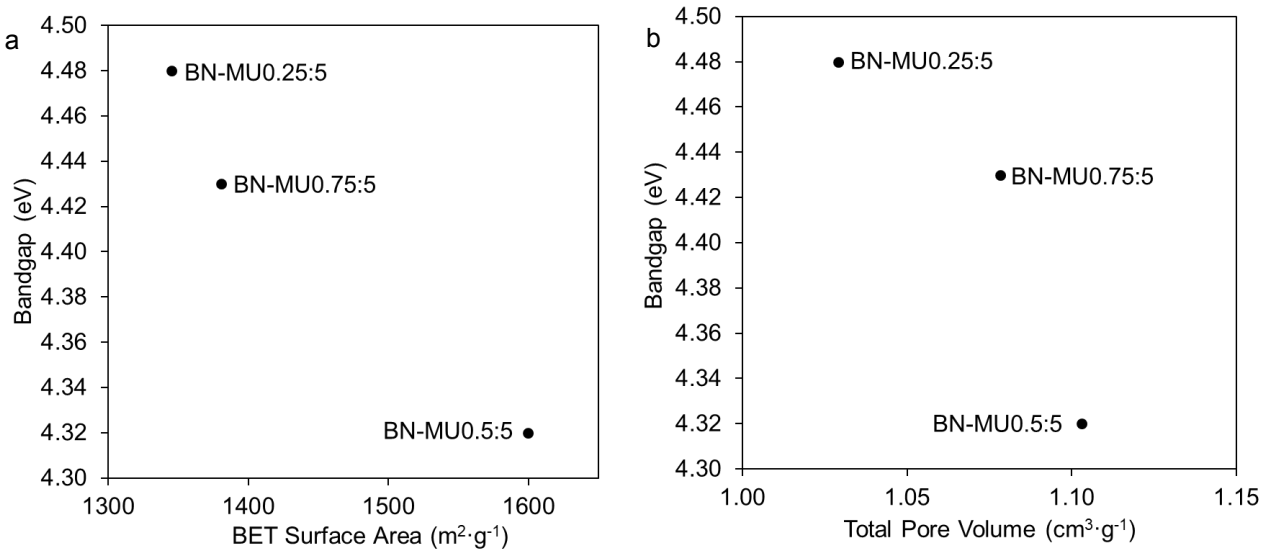

Figure 5. Porosity and band gap trends for selected BN samples. (a) Band gap against BET surface area for BN samples with melamine and urea as nitrogen precursors, (b) Band gap against total pore volume for BN samples with melamine and urea as nitrogen precursors.

These defects enhance CO_2 adsorption and have a band gap lowering effect, as shown in literature.[38,46] A small percentage of carbon was also detected in the sample, but the low intensity of the peak indicates it is likely adventitious in origin (~3% on average).

The above conclusions were obtained from the collection of high-resolution core level spectra. Peaks confirming the formation of boron nitride can be observed through fitted core level spectra for B 1*s* and N 1*s*, which shows B-N bonds (191.2 eV on B 1*s* and 398.8 eV on N 1*s*)[47] and sp^2 hexagonal hybridisation (on the highlighted shake-up satellite peaks)[48] (Fig. S2). The borooxynitride mentioned earlier is also present in these spectra, at 192.8 eV and 400.6 eV, respectively, with it being the sole peak on the O 1*s* at 533.3 eV (Fig. S2).

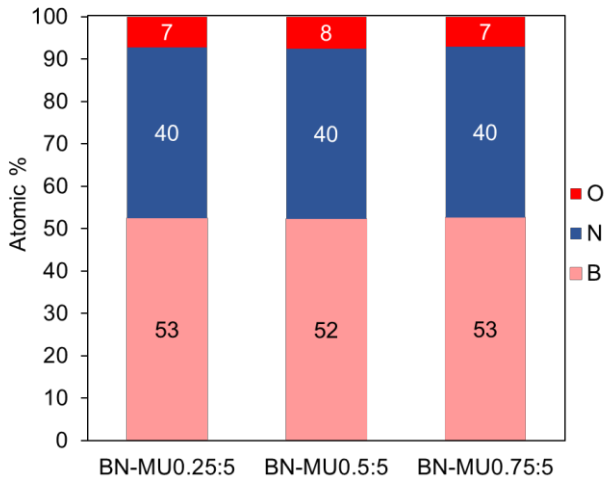

Figure 6. Relative composition of specific BN samples. Obtained through XPS elemental analysis.

To obtain initial data on catalytic performance, the CO_2 adsorption capacity of three selected samples was investigated at reaction conditions (25 °C, 1 bar) (Fig. 7). Results are comparable with those in literature,[12,33,49] with BN-MU 0.5:5 showing the highest adsorption curve, which matches earlier results from the N_2 sorption experiments. The maximum total adsorption reached

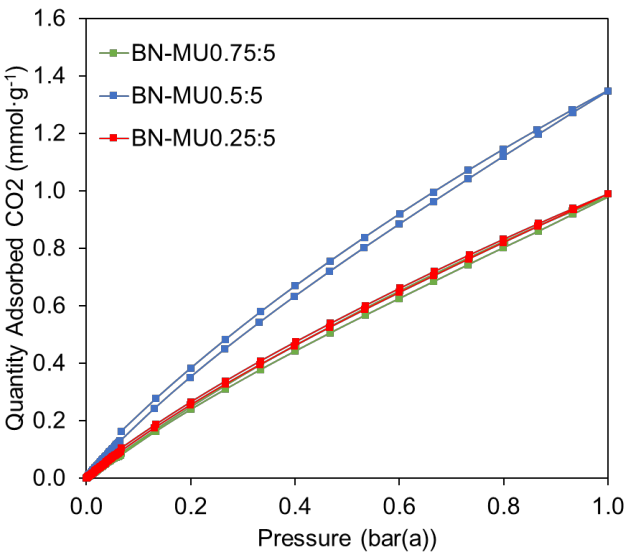

Figure 7. CO_2 sorption isotherms for selected BN samples. These were measured at 25 °C and up to 1 bar(a) pressure.

1.35 mmol·g^{-1}. This result shows promise regarding CO_2 photoreduction, as adsorption is the initial step and high adsorption capacity is essential to keep the process rate-limited rather than mass transfer-limited.

The trends shown in Figure 4 are promising but there are not sufficient data points for a definitive conclusion to be drawn. The exact cause of this trend is uncertain, with micro- or mesoporosity, the presence of certain functional groups and their location within the structure having possible contributions.

A range of unimodally porous boron nitride samples could give further insight into the effect of porosity on the band gap and subsequent consequences on CO_2 photoreduction capabilities. To create a unimodally porous sample, it is likely that a template, such as a metal organic framework, zeolite or silica template, would be required. A general schematic of a templated method is given in Figure 8 and different synthesis ideas are summarised in Table 2. The first method uses a SBA-15 silica template and is based on methods by Xu et al.[50] who manage to synthesise unimodal porous carbon nitride, and Rushton and Mokaya[51] who synthesise boron nitride, both of whom use this template. If this synthesis is successful, the expected pore size would be 74 Å. For this template it has also been shown that the pore size can be tuned for carbon nitride by synthesising the SBA-15 at different temperatures.[52] A higher temperature led to a larger pore size in the template and subsequent carbon nitride sample. If replicated with boron nitride a range of samples with systematically increasing pore size could be synthesised. Other silica templates have been used to make unimodally porous carbon nitride, such as INC-2 by Min et al.[53] and Aldrich Ludox SM-30 by Lee et al.[54] These methods would have to be adapted accordingly for a boron nitride synthesis and would yield pore sizes of 35 and 70 Å, respectively. Carbon nitride syntheses require much lower temperatures than boron nitride so analysis on the effect of temperature would also be required. A major concern with these methods is use of hydrofluoric acid to remove the silica template, as it is unknown if BN is able to withstand it. Another possible synthesis method is using the bacteria *Staphylococcus Aureus*, based on a method by Zhang et al.[55] Bulk graphitic carbon nitride was converted to porous carbon nitride through bacterial etching. Using h-BN rather than graphitic carbon nitride as a precursor could create a porous BN sample in a similar manner. However, it is not known if the bacteria would behave in the same way, especially as the biological usage of boron is much lower than that of carbon. It would create a sample with a pore size of 269 Å.

Conclusion

Amorphous porous BN was successfully synthesised, as indicated by chemical and structural characterisation. High N_2 adsorption quantities were observed as a consequence of micro- and mesopores with multimodal pore size distributions. However, no current model exists to accurately describe the pore size distribution of this material and consequently, the formulation of a new one would be beneficial for further investigation. Promising trends were found regarding the decrease of band gap

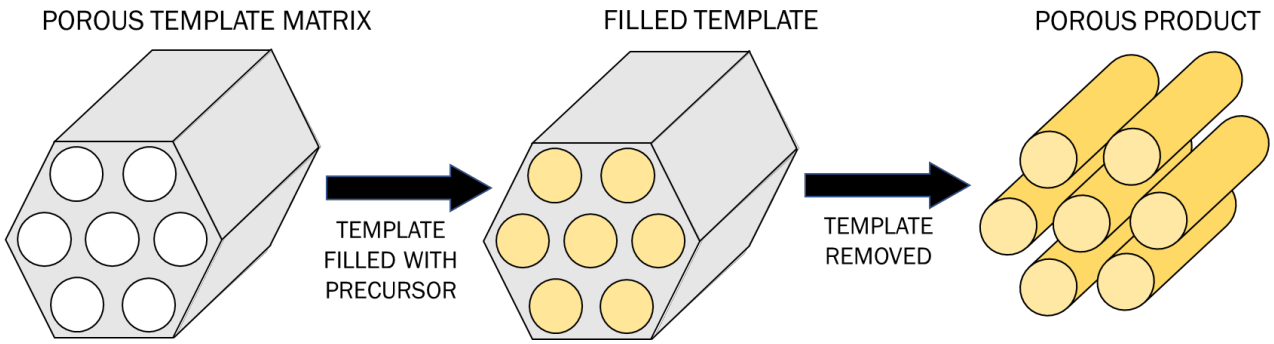

Figure 8. Schematic of a templated synthesis process. The template is filled with precursor in solution, after which it is dried and the template is removed. The final product becomes a negative cast of the template.

Table 2. Summary of key parameters for unimodally porous BN sample synthesis methods.

	Template	Precursors	Pre-treatment	Temperature	Gas	Post-treatment	Reference
Method 1	SBA-15	$BH_3 \cdot NH_3$	Dissolution in ethanol and hexane followed by evaporation	1050 °C, slow heating rate (2.5 °C·min^{-1})	N_2, NH_3	HF	Xu et al.[50] Rushton and Mokaya[51]
Method 2	INC-2	Boric acid, urea, melamine	Nanocasting and polymerising at 90 °C for 9 h	1050 °C, slow heating rate (2.5 °C·min^{-1})	N_2	HF	Min et al.[53]
Method 3	Aldrich Ludox SM-30	Boric acid, urea, melamine	Dissolution in DI water followed by evaporation	1050 °C, slow heating rate (2.5 °C·min^{-1})	N_2	HF	Lee et al.[54]
Method 4	*Staphylo-coccus Aureus*	h-BN	Preparing an *S.Aureus*/LB solution	37 °C	N/A	DI water, ethanol	Zhang et al.[55]

with the increase of porosity. CO_2 adsorption results were shown to be on par with literature results and better than commercial adsorbents. Template-free syntheses are unlikely to yield unimodal pore sizes and concrete suggestions for further work were investigated, with special interest in mesoporous silica templates. A set of unimodally porous samples with varying pore size would give further insight into the effect of porosity on band gap. This will lead to a better understanding of the link between structural and optical properties, with the optimisation of photocatalytic properties in view.

Acknowledgements

The authors would like to thank Ravi Shankar for all his assistance, as well as the rest of the Petit Research Group for their continued collaboration and help.

Supplementary Information

The supporting supplementary information has been attached in the link provided, as required.

References

1. Raupach, M. R. *et al*. Global and regional drivers of accelerating CO2 emissions. *Proceedings of the National Academy of Sciences* **104**, 10288-10293 (2007).
2. Intergovernmental Panel on Climate Change. IPCC Special Report Emission Scenarios. (2000).
3. Søren Dahl & Ib Chorkendorff. Solar-fuel generation: Towards practical implementation. *Nature Materials* **11**, 100 (2012).
4. Dell, R. M. & Rand, D. A. J. Energy storage — a key technology for global energy sustainability. *Journal of Power Sources* **100**, 2-17 (2001).
5. Tarascon, J-M. & Armand, M. Issues and challenges facing rechargeable lithium batteries. *Nature* **414**, 359 (2001).
6. Trudewind, C. A., Schreiber, A. & Haumann, D. Photocatalytic methanol and methane production using captured CO2 from coal-fired power plants. Part I – a Life Cycle Assessment. *J. Clean. Prod.* **70**, 27-37 (2014).
7. Stolarczyk, J. K., Bhattacharyya, S., Polavarapu, L. & Feldmann, J. Challenges and Prospects in Solar Water Splitting and CO2 Reduction with Inorganic and Hybrid Nanostructures. *ACS Catal.* **8**, 3602-3635 (2018).
8. Chen, D. *et al*. Influence of Defects on the Photocatalytic Activity of ZnO. *J. Phys. Chem. C* **118**, 15300-15307 (2014).
9. Inoue, T., Fujishima, A., Konishi, S. & Honda, K. Photoelectrocatalytic reduction of carbon dioxide in aqueous suspensions of semiconductor powders. *Nature* **277**, 637 (1979).
10. Yu, X., Hou, T., Li, Y., Sun, X. & Lee, S. Effective band gap reduction of titanium oxide semiconductors by codoping from first-principles calculations. *Int. J. Quantum Chem.* **113**, 2546-2553 (2013).
11. Hamad, S., Catlow, C. R. A., Woodley, S. M., Lago, S. & Mejías, J. A. Structure and Stability of Small TiO2 Nanoparticles. *J Phys Chem B* **109**, 15741-15748 (2005).
12. Shankar, R., Hankin, A. & Petit, C. (2018) Porous Boron Nitride for Combined CO2 Capture and Photoreduction. Available from: https://chemrxiv.org/articles/Porous_Boron_Nitride_for

_Combined_CO2_Capture_and_Photoreduction/7200881
.13. Marchesini, S., Regoutz, A., Payne, D. & Petit, C. Tunable porous boron nitride: Investigating its formation and its application for gas adsorption. *Microporous and Mesoporous Materials* **243**, 154-163 (2017).
14. Liu, M. *et al*. Enhanced Photoactivity with Nanocluster-Grafted Titanium Dioxide Photocatalysts. *ACS Nano* **8**, 7229-7238 (2014).
15. Yu, H., Chen, W., Wang, X., Xu, Y. & Yu, J. Enhanced photocatalytic activity and photoinduced stability of Ag-based photocatalysts: The synergistic action of amorphous-Ti(IV) and Fe(III) cocatalysts. *Applied Catalysis B: Environmental* **187**, 163-170 (2016).
16. Linsebigler, A. L., Lu, G. & Yates, J. T. Photocatalysis on TiO2 Surfaces: Principles, Mechanisms, and Selected Results. *Chem. Rev.* **95**, 735-758 (1995).
17. Habisreutinger, S. N., Schmidt-Mende, L. & Stolarczyk, J. K. Photocatalytic Reduction of CO2 on TiO2 and Other Semiconductors. *Angew. Chem. Int. Ed.* **52**, 7372-7408 (2013).
18. Thomas, A. *et al*. Graphitic carbon nitride materials: variation of structure and morphology and their use as metal-free catalysts. *J. Mater. Chem.* **18**, 4893-4908 (2008).
19. Zheng, Y., Lin, L., Wang, B. & Wang, X. Graphitic Carbon Nitride Polymers toward Sustainable Photoredox Catalysis. *Angew. Chem. Int. Ed.* **54**, 12868-12884 (2015).
20. Crake, A. *et al*. Titanium dioxide/carbon nitride nanosheet nanocomposites for gas phase CO2 photoreduction under UV-visible irradiation. *Applied Catalysis B: Environmental* **242**, 369-378 (2019).
21. Jiang, Z. *et al*. A Hierarchical Z-Scheme α-Fe2O3/g-C3N4 Hybrid for Enhanced Photocatalytic CO2 Reduction. *Adv Mater* **30**, 1706108 (2018).
22. Xu, D., Cheng, B., Wang, W., Jiang, C. & Yu, J. Ag2CrO4/g-C3N4/graphene oxide ternary nanocomposite Z-scheme photocatalyst with enhanced CO2 reduction activity. *Applied Catalysis B: Environmental* **231**, 368-380 (2018).
23. Liu, G. *et al*. Unique Electronic Structure Induced High Photoreactivity of Sulfur-Doped Graphitic C3N4. *J. Am. Chem. Soc.* **132**, 11642-11648 (2010).
24. Hong, J., Xia, X., Wang, Y. & Xu, R. Mesoporous carbon nitride with in situ sulfur doping for enhanced photocatalytic hydrogen evolution from water under visible light. *J. Mater. Chem.* **22**, 15006-15012 (2012).
25. Ran, J., Ma, T. Y., Gao, G., Du, X. & Qiao, S. Z. Porous P-doped graphitic carbon nitride nanosheets for synergistically enhanced visible-light photocatalytic H2 production. *Energy Environ. Sci.* **8**, 3708-3717 (2015).
26. Xing, F., Liu, Q., Song, M. & Huang, C. Fluorine Modified Boron Carbon Nitride Semiconductors for Improved Photocatalytic CO2 Reduction under Visible Light. *ChemCatChem* **0** (2018).
27. Gu, Q., Liu, J., Gao, Z. & Xue, C. Homogenous Boron-doping in Self-sensitized Carbon Nitride for Enhanced Visible-light Photocatalytic Activity. *Chem. Asian J.* **11**, 3169-3173 (2016).
28. Thaweesak, S. *et al*. Boron-doped graphitic carbon nitride nanosheets for enhanced visible light photocatalytic water splitting. *Dalton Trans.* **46**, 10714-10720 (2017).
29. Cao, X. & Luo, Y. Study of the Electronic and Optical Properties of Hybrid Triangular (BN)xCy Foams. *J. Phys. Chem. C* **118**, 22181-22187 (2014).
30. Chen, S. *et al*. Carbon doping of hexagonal boron nitride porous materials toward CO2 capture. *J. Mater. Chem. A* **6**, 1832-1839 (2018).
31. Huang, C. *et al*. Carbon-doped BN nanosheets for metal-free photoredox catalysis. *Nature Communications* **6**, 7698 (2015).
32. Florent, M. & Bandosz, T. J. Irreversible water mediated transformation of BCN from a 3D highly porous form to its nonporous hydrolyzed counterpart. *J. Mater. Chem. A* **6**, 3510-3521 (2018).
33. Marchesini, S., McGilvery, C. M., Bailey, J. & Petit, C. Template-Free Synthesis of Highly Porous Boron Nitride: Insights into Pore Network Design and Impact on Gas Sorption. *ACS Nano* **11**, 10003-10011 (2017).
34. Ramirez Leyva, J. H. *et al*. Mechanism of Hierarchical Porosity Development in Hexagonal Boron Nitride Nanocrystalline Microstructures for Biomedical and Industrial Applications. *ACS Appl. Nano Mater.* **1**, 4491-4501 (2018).
35. Brunauer, S., Emmett, P. H. & Teller, E. Adsorption of Gases in Multimolecular Layers. *J. Am. Chem. Soc.* **60**, 309-319 (1938).
36. Chen, S. G. & Yang, R. T. Theoretical Basis for the Potential Theory Adsorption Isotherms. The Dubinin-Radushkevich and Dubinin-Astakhov Equations. *Langmuir* **10**, 4244-4249 (1994).
37. Geick, R., Perry, C. H. & Rupprecht, G. Normal Modes in Hexagonal Boron Nitride. *Phys. Rev.* **146**, 543-547 (1966).
38. Weng, Q. *et al*. Tuning of the Optical, Electronic, and Magnetic Properties of Boron Nitride Nanosheets with Oxygen Doping and Functionalization. *Adv Mater* **29**, 1700695 (2017).
39. Mannan, M. *et al*. in Characterization of Boron Carbonitride (BCN) Thin Films Deposited by Radiofrequency and Microwave Plasma Enhanced Chemical Vapor Deposition, (2008).
40. Kurakevych, O. O. & Solozhenko, V. L. Rhombohedral boron subnitride, B$\sb 13$N$\sb 2$, by X-ray powder diffraction. *Acta Crystallographica Section C* **63**, 80-82 (2007).
41. Sing, K. S. W. Reporting physisorption data for gas/solid systems with special reference to the determination of surface area and porosity (Recommendations 1984). *Pure and Applied Chemistry* **57**, 603 (1985).
42. Zhu, Y. *et al*. Graphene and Graphene Oxide: Synthesis, Properties, and Applications. *Adv Mater* **22**, 3906-3924 (2010).
43. Sing, K. S. W., Rouquerol, F., Rouquerol, J. & Llewellyn, P. in *Adsorption by Powders and Porous Solids (Second Edition)* (eds Rouquerol, F., Rouquerol, J., Sing, K. S. W., Llewellyn, P. & Maurin, G.) 269-302 (Academic Press, Oxford, 2014).
44. Sing, K. S. W., Rouquerol, F., Llewellyn, P. & Rouquerol, J. in *Adsorption by Powders and Porous*

Solids (Second Edition) (eds Rouquerol, F., Rouquerol, J., Sing, K. S. W., Llewellyn, P. & Maurin, G.) 303-320 (Academic Press, Oxford, 2014).
45. Tauc, J., Grigorovici, R. & Vancu, A. Optical Properties and Electronic Structure of Amorphous Germanium. *phys. stat. sol. (b)* **15**, 627-637 (1966).
46. Lei, W. *et al*. Oxygen-doped boron nitride nanosheets with excellent performance in hydrogen storage. *Nano Energy* **6**, 219-224 (2014).
47. Cholet, V., Vandenbulcke, L., Rouan, J. P., Baillif, P. & Erre, R. Characterization of boron nitride films deposited from BCl3-NH3-H2 mixtures in chemical vapour infiltration conditions. *J. Mater. Sci.* **29**, 1417-1435 (1994).
48. Park, K. S., Lee, D. Y., Kim, K. J. & Moon, D. W. Observation of a hexagonal BN surface layer on the cubic BN film grown by dual ion beam sputter deposition. *Appl. Phys. Lett.* **70**, 315-317 (1997).
49. Chen, S. *et al*. Carbon doping of hexagonal boron nitride porous materials toward CO2 capture. *J. Mater. Chem. A* **6**, 1832-1839 (2018).
50. Xu, J., Chen, T., Jiang, Q. & Li, Y. Utilization of Environmentally Benign Dicyandiamide as a Precursor for the Synthesis of Ordered Mesoporous Carbon Nitride and its Application in Base-Catalyzed Reactions. *Chem. Asian J.* **9**, 3269-3277 (2014).
51. Rushton, B. & Mokaya, R. Mesoporous boron nitride and boron-nitride-carbon materials from mesoporous silica templates. *J. Mater. Chem.* **18**, 235-241 (2008).
52. Vinu, A. Two-Dimensional Hexagonally-Ordered Mesoporous Carbon Nitrides with Tunable Pore Diameter, Surface Area and Nitrogen Content. *Adv. Funct. Mater.* **18**, 816-827 (2008).
53. Min, B., Ansari, M. B., Mo, Y. & Park, S. Mesoporous carbon nitride synthesized by nanocasting with urea/formaldehyde and metal-free catalytic oxidation of cyclic olefins. *Catalysis Today; Challenges in Nanoporous and Layered Materials for Catalysis* **204**, 156-163 (2013).
54. Lee, S. C., Lintang, H. O. & Yuliati, L. A Urea Precursor to Synthesize Carbon Nitride with Mesoporosity for Enhanced Activity in the Photocatalytic Removal of Phenol. *Chem. Asian J.* **7**, 2139-2144 (2012).
55. Zhang, L. *et al*. Bacteria-motivated pore structure regulation of graphitic carbon nitride for enhanced H2 evaluation under visible light irradiation. *Mater Lett* **234**, 208-211 (2019).

Nature of lignin extracted using dissolution by p- toluenesulfonic acid hydrotrope

Jie Bao and Aireen Choo
Department of Chemical Engineering, Imperial College London, U.K.

Abstract The hydrotropic treatment of biomass is an environmentally friendly process that employs water-soluble chemicals. This study investigates the nature of lignin extracted by a hydrotropic treatment using a 70% p-TsOH acid hydrotrope solution at various temperatures. The chemical and architectural make-up of the extracted lignin was characterised using elemental analysis, gel permeation chromatography (GPC) and 2D HSQC NMR, while the pulp was analysed through carbanilation and saccharification, to determine the degree of delignification and xylan retention. The highest lignin yield obtained was 26.4 % at the treatment temperature of 85 °C and the extracted lignin had low hydrogen and oxygen contents. The hydrotrope treatment resulted in significant changes in the structure of the lignin and the formation of pseudo-lignin. The produced pulps were enriched in cellulose and had high Klason lignin content, indicating the delignification process was inefficient.
Keywords: *hydrotropic lignin, p-TsOH acid hydrotrope, lignin characterisation, GPC, NMR*

Introduction

Lignin is a complex aromatic polymer that is biosynthesised from three basic phenylpropanoid monomers, p-hydroxyphenyl (H), guaiacyl (G), and syringyl (S) units, derived from p-coumaryl, coniferyl, and sinapyl alcoholic precursors, respectively.[1][2] Depending on the biomass source, lignin varies in monomer composition. Softwood lignin is mainly composed of the G unit, whereas hardwood lignin consists of both G and S units, and grass lignin consists of G, S and H units.[3] The monomeric units of phenylpropane in lignin polymers are linked in a complex network through C−C and C−O−C ether bonds in different combinations such as aryl−alkyl, alkyl−alkyl, and aryl−aryl.[4] [5] [6] Up to 80 % of the primary inter-unit linkages of lignin are ether bonds, predominantly β-O-4 ether linkages.[7] Lignin can be hydrolysed *via* cleavage of the ether bonds that are catalysed by [H^+] and [OH^-] or water molecules. [8] The cleavage of β-O-4 linkages in lignin produces phenylpropanoid monomers that can easily be upgraded to value-added fuels and chemicals. [9] However, interunit carbon–carbon (C–C) linkages present in native lignin or formed during lignin condensation in biomass pretreatments remarkably reduce lignin monomer yields.[9]

The variation in technical lignin structure is partly attributed to the botanical origin of the polyphenol but equally important is the delignification process.[10] In this study, technical lignin was obtained from poplar wood using an environmentally friendly hydrotropic process. Hydrotropic treatment has been proven to be effective for lignin removal from hardwood, and no sulfur bond was detected in the isolated lignin.[11] [12] In general, hydrotropic treatment is performed under the acidic conditions.[13] Hydrotropes are amphiphilic substances that are composed mainly of hydrophilic functional groups. Due to their unique properties, they can enhance the solubility of water-insoluble organic substances when used in a concentrated form of the aqueous solutions.[14][15] Above minimal hydrotrope concentration, most hydrotropes aggregate to form non-polar domains to solubilise hydrophobic materials.[16] In the process of delignification, aqueous hydrotrope solutions are used to solubilise the normally insoluble hydrophobic lignin components, leaving the insoluble sugar behind. Sodium Xylene Sulfonate (SXS) is the most commonly used hydrotropic compound for the recovery of lignin from the lignocellulosic material as it is an effective solvent to remove lignin.[17] The major advantage of a hydrotropic treatment is the smooth recovery of the solute from hydrotrope solutions by simple dilution with water.[17]

Hydrotrope solutions are water-based green solvents that are safe to handle.[17] The use of aqueous hydrotrope solution makes the treatment process environmentally friendly as it does not involve the use of organic solvents. [17] Hydrotropic treatment can potentially replace the conventional acid and alkaline pretreatment processes where the recovery of acid/alkali and effluent treatment are major issues. [17] Other advantages include a high-alpha cellulose content of the pulps and low consumption of cooking agents, as spent hydrotrope solutions can be reused until it is saturated with lignin. [18] All in all, these advantages over the commercial processes make this method a promising candidate for biorefinery operations.

Background

Over time, an extensive literature has developed on the properties of hydrotropic pulp. However, the research on the composition and chemical structure of hydrotropic lignin remains limited. Among those few investigations on hydrotropic lignin and its applications, it was claimed that the structure of hydrotropic lignin is unaltered and is very close to the native lignin of wood.[19] On the other hand, some researchers stated the lignin isolated by this method is modified and is different from the corresponding protolignin.[20] [21] Nonetheless, the authors also clarified that the treatment conditions affected the extent of modification and the reactivity of hydrotropic lignin. [21]

Hydrotropic treatment of birch wood for 12 h at 150 °C removed most of the lignin and hemicelluloses present in the wood.[18] [22] Nonetheless, long treatment time made the process impractical. A recent study demonstrated that p-toluenesulfonic acid (p-TsOH) is a good hydrotrope that can solubilise 90 % of wood lignin at temperatures ≤ 80 ℃ in 20 minutes. [23] It was claimed that this hydrotrope left much of the lignin structure intact. However, this study by Liheng Chen cannot be considered as conclusive as it is commonly known that the acidic conditions will induce condensation, consequently leading to the production of chemically changed lignin. Therefore, we are intrigued by the authors' claims that near-complete solubilisation of wood lignin can be achieved and therefore we were motivated to investigate this process further.

The objective of this study is to perform extensive characterisation of the lignin extracted using dissolution by a hydrotropic treatment (i.e. 70 wt% p-TsOH aqueous solutions). Various analytical tools were employed in order to determine whether the structure of the extracted lignin is altered or not. Firstly, elemental analysis (CHNS) was carried out to determine the chemical composition of hydrotropic lignin. Then, multi-detection gel permeation chromatography (GPC) was used to investigate the chemical structure of lignin polymers in an attempt to detect the occurrence of lignin condensation. In addition, 2D HSQC NMR spectroscopy was used to allow in-depth study of the lignin's structural features. Finally, the pulp was analysed *via* saccharification and carbanilation to investigate the effect of the hydrotropic treatment on pulp composition and the degree of polymerisation of cellulose, respectively.

Methodology

Dissolution and extraction of lignin using p-TsOH [23]

A 70 wt% p-TsOH solution was prepared by adding p-TsOH monohydrate (15 g) to DI water (4.29 mL) in a 150 ml conical flask. The acid solution (5 mL) was preheated to the desired temperature before the addition of of oven-dried Poplar wood powders (0.5 g) (2mm pellets, Fa. J. Rettenmaier & Söhne). The fractionation reaction was conducted in a test tube on a shaker at 200 rpm for 20 minutes at various temperatures including 75 ℃, 80 ℃, 85 ℃ and 90 ℃. At the end of the reaction, DI water (31.2 mL) was added to the tube to terminate the reaction and dilute the acid concentration to 11.5 wt%. The water-insoluble solids were separated from the liquid using vacuum filtration. The filtrate was centrifuged and washed with DI water for 2/3 times to produce lignin particles. The pulp retained on the filter paper was also washed with DI water to remove any residual acid on the surface.

Carbanilation of water insoluble particles [24]

The water insoluble particle sample (100 mg) was suspended in dimethyl sulfoxide (DMSO, 2 mL) and phenyl isocyanate (0.25 mL) was added. The reaction forming tricarbanilates (CTCs) was conducted on a heating plate at 80 ℃ for 4 hours

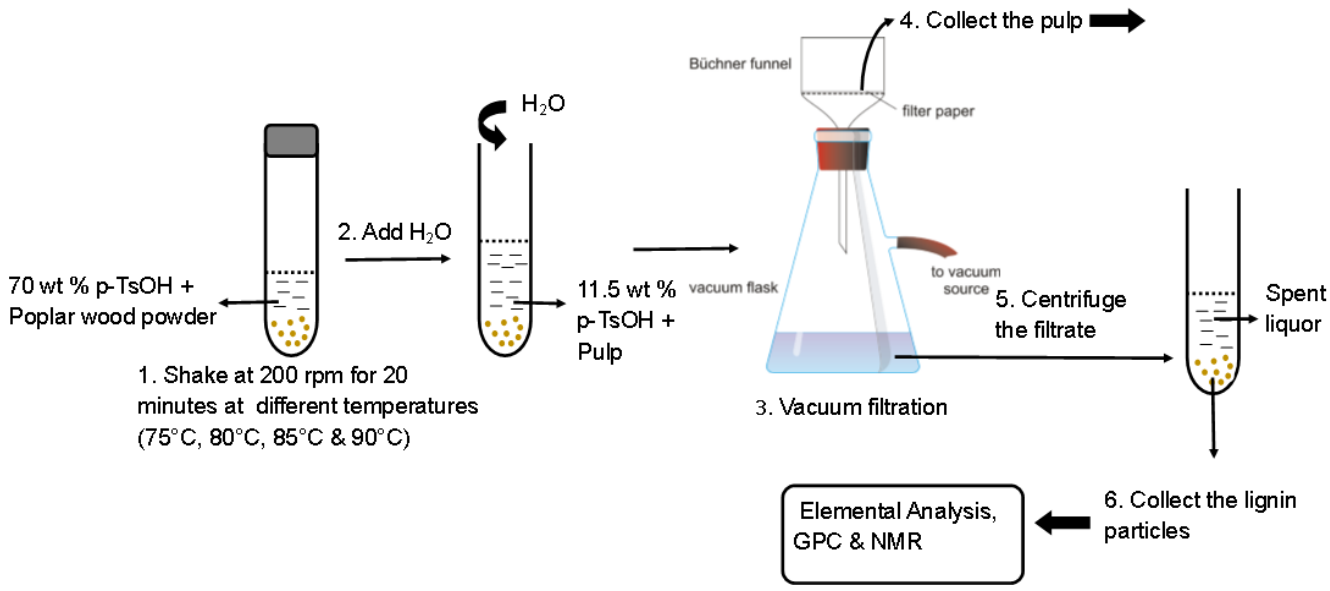

Figure 1. *Schematics diagram showing an overview of experimental methods.*

with a magnetic stirrer at 300 rpm. At the end of reaction, methanol (1 mL) was added to terminate the reaction. DI water (1 mL) was then added to induce the precipitation of CTCs. To fully precipitate and wash the CTCs formed in DMSO a 30:70 v/v methanol/water solution (20 mL) was added. After centrifugation at 9000 rpm for 10 minutes, the liquid was removed, and the washing process was repeated, followed by centrifugation. In the end, a final washing was carried out with DI water (20 mL). After centrifugation, the water was removed, and CTCs were dried overnight in vacuum oven.

Saccharification

Soxhlet extracted and ground sample (50 mg) were mixed with a 72% sulfuric acid solution (0.5 mL) under manual stirring for 25 minutes at 30 ℃. After that, DI water (10 mL) was added to the mixture. The saccharification process was then carried out at 130 ℃ for 2 hours with magnetic stirring. The suspension was left to cool to room temperature before filtration on a glass microfibers filter. A sample of the filtrate (1 mL) was taken to determine the sugar content with liquid chromatography (LC). In the meantime, the filter paper was weighted before filtration. The solid on the filter paper was washed with DI water thoroughly until neutral pH and dried in an oven overnight. The weight of dried solid was calculated by the difference of filter paper and was considered as the residual lignin in the wood. The determination of sugar and lignin contents was performed in three replicates for each sample and the average values were taken.

Gel Permeation Chromatography (GPC) analysis of lignin particles

To analyse the apparent molecular weight distributions, all samples (ca. 10 mg) dissolved in 1 mol of DMF and LiBr (99.9:0.1 vol/vol) solution were filtered prior to injection. The injection volume was 50 µL. GPC analysis were performed at 60 °C on an Aligent apparatus equipped with two columns (a PolarGel L and a PolarGel M column), using DMF and LiBr (99.9:0.1 vol/vol) as the eluent (flow rate 1 mL min^{-1}). For detection, a DAD detector (280 to 420 nm), two viscometers (DP and IP signal) and a RI detector were used. Based on the analysis, Mark-Houwink plots can be generated by using the equation below to compare the lignin structures extracted under different temperatures.

$$IV = K * Mw^{\alpha}$$

From the intrinsic viscosity and molecular weight data obtained, the branching number (Bn, branches per 1000 carbons) can be calculated from the following equations to indicate the degree of branching, assuming average ternary-branching model. [25]

$$g' = \frac{\text{IV branched}}{\text{IV linear}}$$

$$g = g'^{1/\varepsilon}$$

$$g = \left[\left(1 + \frac{Bn}{7}\right)^{0.5} + 4 * \frac{Bn}{9\pi}\right]^{-0.5}$$

The ratio of the IV of the branched sample to the linear standards of the same molecular weight is known as a contraction factor (g') while g indicates ratio of the sizes of branched and linear polymers, which can be measured by light scattering or calculated from g. The parameter ε is the structure factor which is normally between 0.5 and 1.5, and was chosen as 0.75 in this project. Bn values can be then be calculated for corresponding molecular weights.

Elemental analysis (CHNS)

CHNS elemental analyses were performed in triplicate for samples (1-2 mg) on a Vario Micro cube elemental analyser. Upon combustion, the C, H, N and S compositions of the sample are determined. Average values of the triplicate measurements are reported.

Fourier Transform Infrared (FTIR) Spectroscopy

Resolution of 4 cm^{-1} and accumulations of 128 scans was set in an Agilent Cary 630 FTIR Spectrometer to provide an accurate result. A background scan was performed prior to analysis after the crystal surface and tip were confirmed to be clean.

2D HSQC NMR Spectroscopy

Oven-dried lignin samples (ca. 20 mg) were dissolved in DMSO-d6 (1 mL) for NMR measurement. A detailed protocol for heteronuclear single quantum correlation (HSQC) measurements can be found in supplementary information.

Mechanisms of acid catalysed depolymerisation and condensation

Scheme 1 shows the mechanism of depolymerisation of lignin in the presence of p-TsOH acid catalyst. Due to the strong acidity of p-TsOH at room temperature, [26] the acid can easily donate a proton to create an acidic environment in

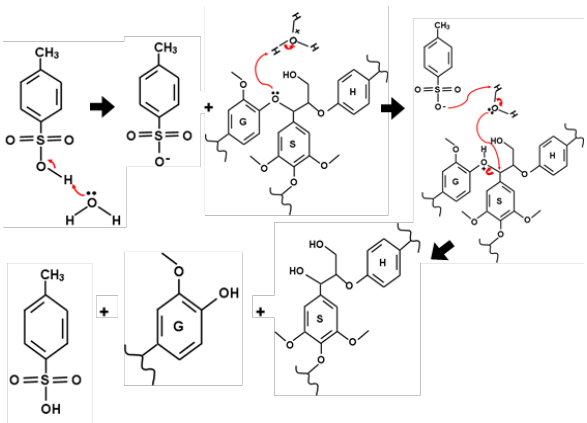

Scheme 1. *The mechanism of depolymerisation by using p-TsOH as acid catalyst.* [23]

aqueous solution and catalyse the reaction. In an acidic environment, the lone pair of electrons on the oxygen of β-O-4 linkage can attract H^+ ion and form a cation. This is followed by subsequent attack of water on the electron-deficient C-O bond in the protonated ether linkage. [27] This reaction cleaves the β-O-4 linkage in lignin, leading to efficient lignin depolymerisation.

However, in the presence of acid catalyst, condensation can also occur. [28] Condensation is considered as a competing reaction to the depolymerisation reaction that cleaves the β-O-4 linkage. The condensation mechanism is as shown in **Scheme 2**. [29] In acidic environment, it is easy to lose the -OH group, forming a carbon cation or an electrophile. The -OH group nearer to the aromatic ring is more likely to be lost because the resulting carbocation charge can be delocalised throughout the aromatic ring via resonance. This stable carbon cation can be problematic because the electrophilic site can easily react with the electron-rich aromatic carbon on the aromatic rings of lignin, which is the nucleophilic site, leading to condensation. [29] This process is thermodynamically favourable and occurs spontaneously. [9]

In a nutshell, condensation reaction is likely to occur in acidic condition and thus altering the structure of lignin. Therefore, the claim that concentrated p-TsOH acid hydrotrope can dissolve 90 % of native lignin is debatable. [23]

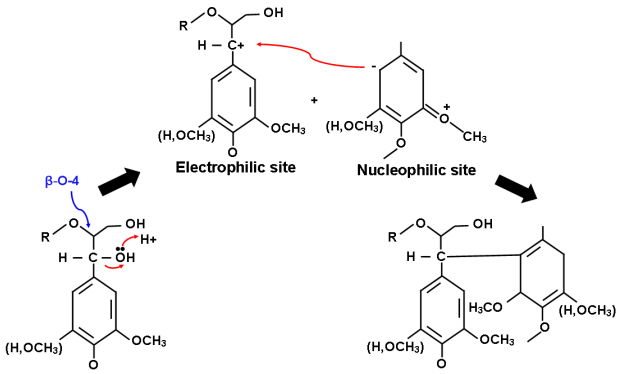

Scheme 2. *The mechanism of acid catalysed condensation.* [29]

Results and discussion

Elemental Analysis

To investigate whether condensation occurred or not, the elemental composition of the lignin extracted from poplar wood was determined *via* elemental analysis. **Table 1** shows the composition of C, H and O in the lignin particles extracted at different temperatures. **[Appendix]** The H/C ratio is a good indicator of the degree of hydrogenation while the O/C ratio indicates the degree of hydrodeoxygenation. [30] As seen from the table, the H and O content of lignin extracted by p-TsOH acid hydrotrope at all temperatures were lower than those of lignin extracted through other methods such as Organosolv and CUB processes. The low H and O contents indicate the elimination of H_2O since dehydration process will result in the loss of two H and one O during the reduction of alcohol to alkene. Therefore, this result strongly supports the hypothesis of condensation occurrence during the lignin extraction process.

Table 1. *H/C and O/C ratios of lignin extracted at different temperatures*

Pretreatment method	Temperature /°C	H/C ratio of lignin	O/C ratio of lignin
p-TsOH	75	1.08	0.33
	80	1.08	0.36
	85	1.06	0.33
	90	1.06	0.33
Organosolv	200	1.245	0.398
CUB	200	1.461	0.396

Analytical GPC

In order to gain in-depth insight into the structural and chemical features imparted by dissolution of lignin by acid hydrotrope, the molecular weights of lignin treated with different temperatures were determined *via* GPC.

Figure 2 displays the GPC chromatograms of lignin extracted at 75 ºC and 80 ºC. The lignin extracted at 85 °C and 90 °C did not dissolve in DMF, therefore could not be analysed by GPC. There are two possible explanations for this. Firstly, the higher temperature may lead to repolymerisation/condensation between lignin monomers, causing them to be insoluble in DMF. Secondly, higher temperature may increase the acid consumption rate, therefore more acid was required at higher temperature to effectively depolymerise the lignin. Due to the insufficient acid in solution, the lignin extracted at high temperature was not depolymerised enough to dissolve in DMF.

Figure 2 depicts that the peak for lignin extracted at 80 ºC is at slightly higher elution times than peak for lignin extracted at 75 ºC. This indicates that the molecular weight of lignin decreased as the treatment temperature increased

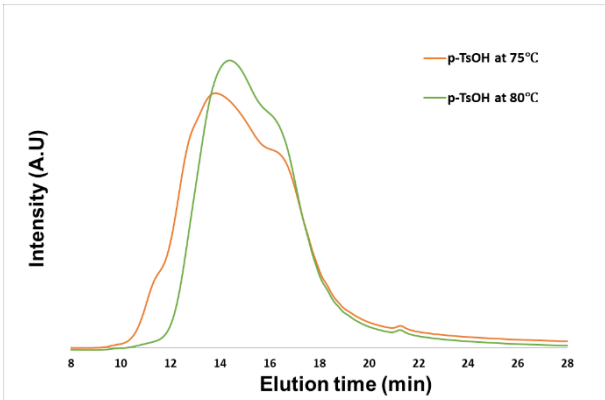

Figure 2. *GPC chromatograms of lignin extracted at 75 °C and 80 °C.*

rom 75 ºC to 80 ºC. However, a further rise in temperature may result in repolymerisation, that is why the lignin extracted at 85 ºC and 90 ºC did not dissolve in DMF. Due to this, the effect of temperature on the hydrotropic treatment could not be investigated.

The GPC traces of both lignin fragments look fairly similar as the temperature difference of 5 ºC is minor. A deeper insight into the molecular weight difference can be seen from the numerical data from GPC. From **Table 2**, it can be concluded that the lignin extracted at 80 ºC has higher molecular weight than lignin extracted at 75 ºC, suggesting the higher temperature promotes depolymerisation through cleavage of β-O-4 linkage, but the pathway for repolymerisation of lignin may be activated at temperature above 80 ºC. [31] In addition, the polydispersity index (PDI) decreases with fractionation severity, indicating that a higher temperature renders lignin streams with a more homogeneous molecular weight. Thus, the peak for 80 ºC is narrower than the peak for 75 ºC in the GPC traces in **Figure 2**.

Table 2. *Molecular weight and polydispersity index of lignin isolated after treatment. M_w=weight-average molecular weight; M_n=number-average molecular weight*

Sample Temperature/ ºC	M_w	M_n	PDI= M_w/M_n
75	46798	2137	21.9
80	10394	2362	4.4

In order to investigate the structural feature of hydrotropic lignin, the UV-Vis spectra of the eluting lignin species were inspected in detail (**Figure 3**). The lignin extracted at 75 ºC and 80 ºC show a non-uniform spectral signature with much stronger absorbance band at wavelengths higher than 300 nm across all elution times. Noticeably, the hydrotropic lignin eluting species are also characterised by a relatively strong UV-Vis absorption in the range between 300 to 400 nm, as shown by the green spot in **Figure 3**. This feature identified in UV-Vis spectra is particularly crucial. Classic studies of lignin structure portrays that p,p'-Stilbene and o,p'-Stilbene phenolic structures show strong absorption bands at wavelength higher than 300 nm. [32] In hydrotropic lignin, these chromophores signify the existence of reactive species towards condensation as well as already condensed species.

Analytic GPC with viscometer

Multidetector GPC was used in order to determine the intrinsic viscosity (IV) of the hydrotropic lignin and to deduce a Mark-Houwink plot of log[IV] against log[M_w], which was used for determining the presence of long-chain

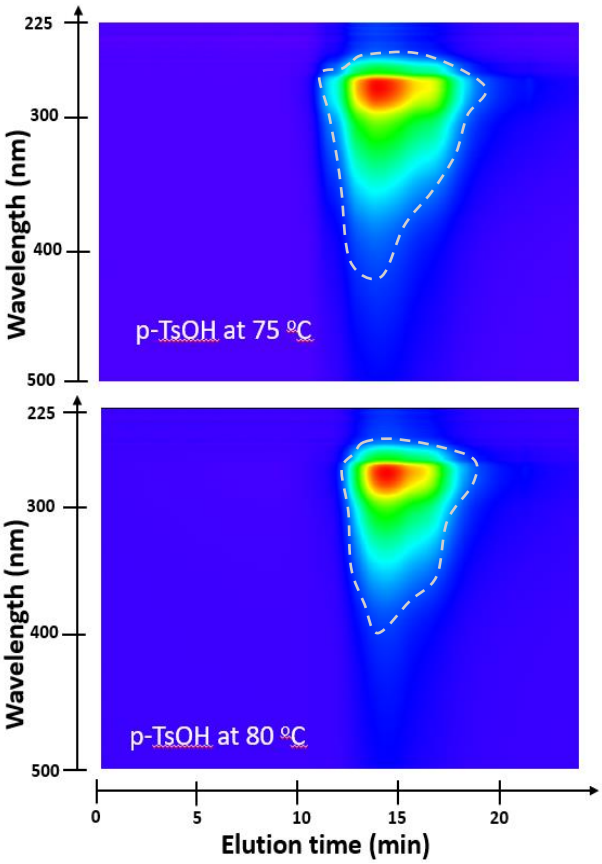

Figure 3. *UV-Vis detector response for lignin species eluting from GPC columns during GPC analysis.*

branching. [33] **Figure 4** compares the Mark-Houwink plots obtained from the hydrotropic lignin extracted at 75 °C and 80 °C as well as the polystyrene standards, providing valuable insights about the polymeric architecture. Evidently, the profile plots for both hydrotropic lignin at 75 °C and 80 °C diverge from the linear polystyrene standards. The hydrotropic lignin demonstrates a less noticeable rise in intrinsic viscosity with increasing molecular weight. This behaviour is characteristic of branched polymers as their

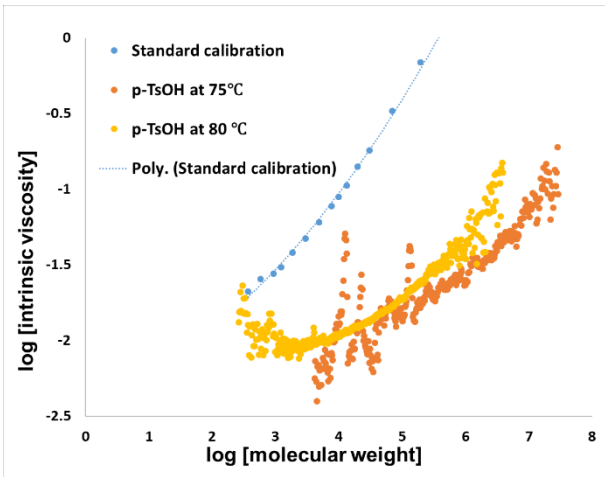

Figure 4. *Mark-Houwink plots of lignin extracted at 75 ºC and 80 ºC in comparison to a universal calibration derived from polystyrene linear standards.*

viscosity is lower in solutions compared to linear polymers of the same molecular weight. This is because branched polymers have denser chain entanglement, leading to reduced hydrodynamic radii and consequently lower viscosity in solutions.

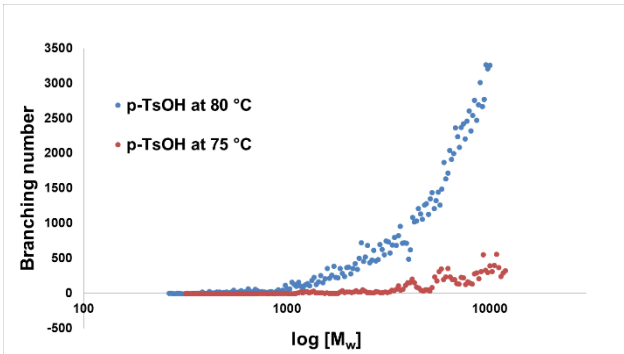

Figure 5. *Evolution of apparent branching number with corresponding molecular weight. (Values expressed as number of branching points per 1000 carbon atoms)*

Since the GPC traces and Mark-Houwink plots demonstrated that there was no marked difference between the lignin samples extracted at 75 °C and 80 °C, the apparent Branching Number (Bn) was determined through correlations between the intrinsic viscosity of the eluting species and its corresponding molecular weight. Bn is expressed as the number of branching points per 1000 carbon atoms. As only the linear standards were used in calibration, the Bn values are not an absolute measure but a relative measure used to rank the lignin based on its apparent branching. **Figure 5** depicts the evolution of apparent Bn for each lignin sample extracted at different temperatures. Considering the species of log [Mw] = 10000, it is evident that the branching degree of hydrotropic lignin extracted at 80 °C is higher than its counterpart extracted at 75 °C by an order of magnitude. This proves that polymers are more prone to condensation at higher temperature in acidic condition, resulting in a more branched polymer. The increased branching of lignin polymers at higher temperature might have caused the hydrotropic lignin extracted at 85 °C and 90 °C to be insoluble as aforementioned. This result is in good agreement with the conclusion drawn from Mark-Houwink plots which demonstrated that the hydrotropic lignin is branched.

NMR spectroscopy

HSQC NMR analysis was carried out to investigate the different structural units of complex lignin polymers. It is important to keep in mind that this method is not completely quantitative since signal relaxation following each pulse may not be complete for some correlations. In addition, this method is restricted by condensation reactions which replace the aromatic C-H bonds with C-C bonds. The C-C bonded aromatic positions do not produce cross correlations in HSQC spectra, leading to misrepresentation when examining condensed lignin. [34] [35]

Prior research on the lignin content versus S:G ratio amongst poplars demonstrated that lignin content decreases with an increase in S:G ratio. [36]

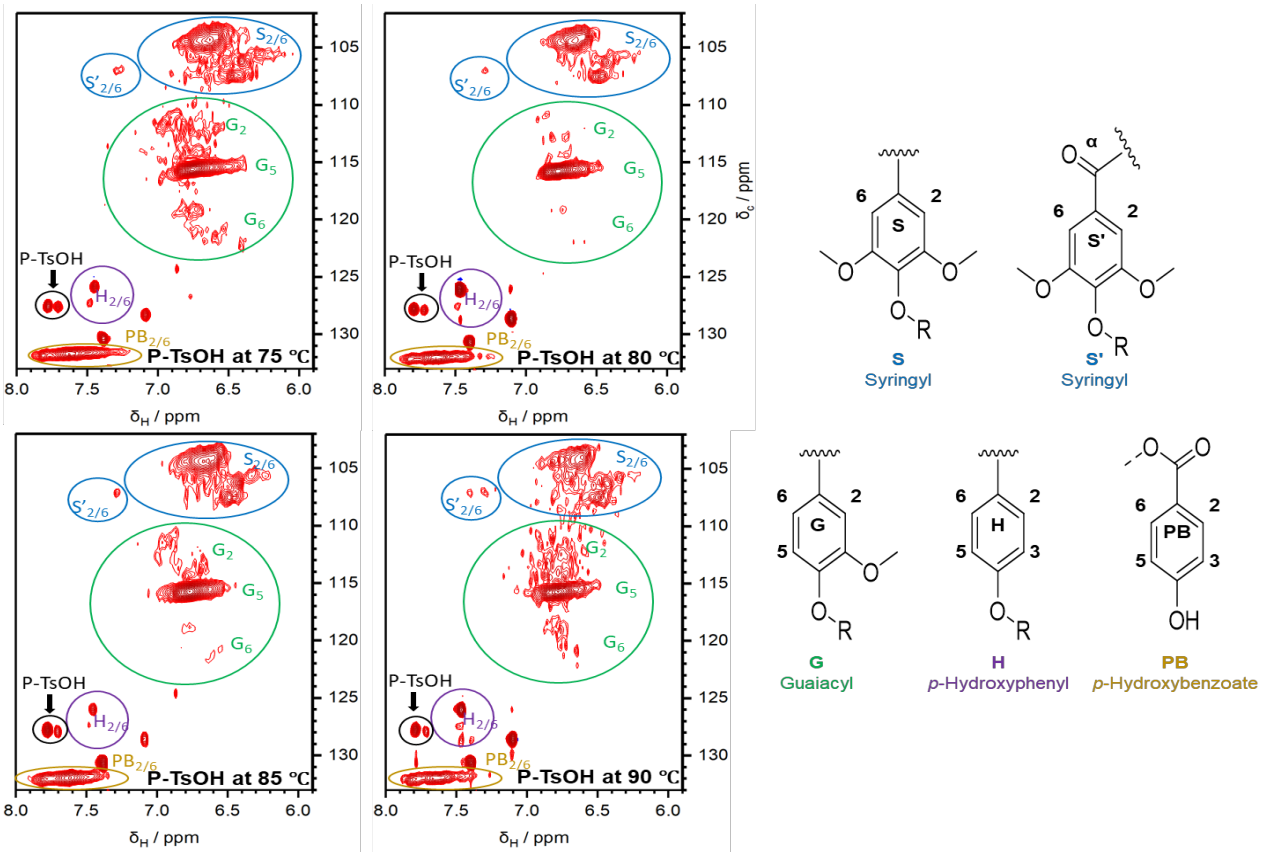

Figure 6. *HSQC NMR spectra in aromatic region of extracted lignin.*

Wood with higher S:G ratio is more easily delignified and renders higher pulp yield. [37] Based on the NMR spectra, the S: G ratio of the hydrotropic lignin extracted continually increased from 75°C (S:G =1.14), 80°C (S:G= 1.20) to 85°C (S:G = 1.28). However, increasing the treatment severity by increasing the temperature to 90 °C led to a decrease in the S:G ratio (S/G = 1.24). **[Appendix]** The trend from 75°C to 85°C suggests that delignification increases with increasing temperature. At 90°C, the S-units in lignin decreased, meaning that the lignin becomes more cross-linked.[38][39]This suggests that lignin undergoes repolymerisation at harsh treatment temperature.

Pulp and lignin recovery after treatment with p-TsOH acid

Figure 7 shows that the physical appearance of the isolated pulp changes significantly with severity of the treatment, indicating that the treatment is successful. It can be observed that higher temperature resulted in a darker pulp, an almost char-like product at 85 °C and 90 °C. This suggests that the carbohydrates in the pulp is degraded by p-TsOH acid hydrotrope. Pseudo-lignin might be formed due to the degradation of the carbohydrates in the pulp. This is because carbohydrates in the pulp can be degraded to carbohydrate monomers such as xylose and glucose, in acidic condition. Carbohydrate monomers are then degraded into compounds such as furfural (FF), 5-hydroxymethylfurfural (5-HMF) and levulinic acid, which are likely to be further degraded into carbon-enriched aromatic structure. [40] Pseudo-lignin can then be formed through the polymerisation or polycondensation of these key intermediates. [40]

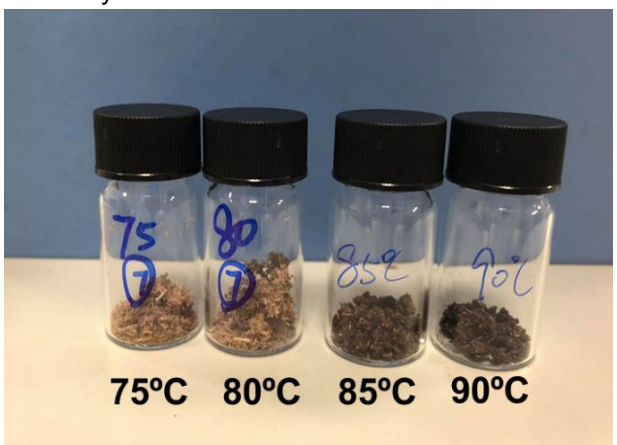

Figure 7. *Example of physical appearance of the pulp after the treatment at different temperatures.*

The pulp and lignin yield after treatment demonstrates the treatment effectiveness.**Figure 8** shows that using p-TsOH acid hydrotrope reduced the amount of poplar wood recovered after treatment compared to the starting material, consistent with the ability of p-TsOH acid hydrotrope to solubilise lignin and some hemicellulose as reported by Liheng Chen et al. [23] In general, the temperature controls the amount of pulp and lignin that were recovered, with higher temperature leading to a lower pulp and a higher lignin yield upon precipitation from the spent acid liquor stream. However, signs of over-treatment of pulp was observed for the treatment at 90 °C such as the increase in pulp recovery and decrease in lignin recovery, signifying that lignin re-deposition on the pulp has occurred. Increasing temperature did not accelerate the lignin extraction but increased the formation of lignin on the pulp. [41]

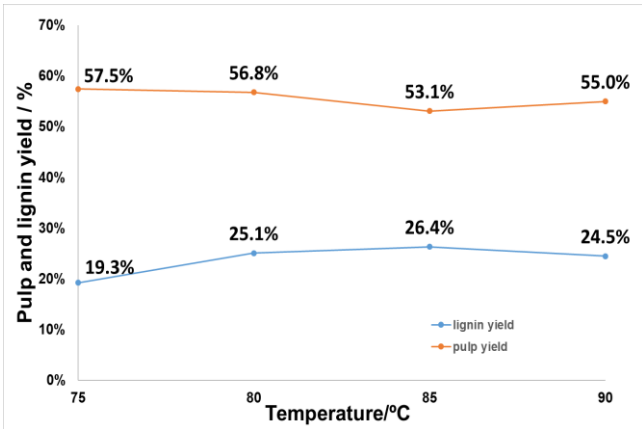

Figure 8. *Pulp and lignin yield at different temperatures.*

Carbanilation of cellulose

Carbanilation of cellulose was carried out to determine the degree of polymerisation of cellulose. Carbanilation is the reaction between cellulose and phenylisocynate to produce cellulose tricarbanilates (CTCs). Cellulose is not soluble in most commonly used solvents, but derivatives of cellulose, i.e. CTCs, can be dissolved in organic solvents, such as Tetrahydrofuran (THF), which is important for GPC measurement. The pulp was derivatized to obtain THF-soluble CTCs for GPC analysis.

During the derivatisation reaction, the pulp could not fully dissolve in DMSO solvent with the addition of phenylisocynate. The CTCs obtained through the derivatisation reaction were also insoluble in THF solvent. The insoluble part in lignocellulosic biomass could not be tested by GPC, of which is the reason is the existence of significant amount of lignin and hemicellulose in the pulp. The presence of lignin renders the cellulose less accessible to the derivatisation agents. Over-estimation of lignin in acidic conditions resulted from the summation of lignocellulosic-derivatives (pseudo-lignin) together with lignin itself.

Acid Saccharification of pulp

Saccharification is the hydrolysis of polysaccharides to soluble sugars. Acid saccharification was performed in order to determine the contents of xylans, glucans and Klason lignin in the pulp. By treatment of pulp with strong acid, all carbohydrates can be solubilized through acid hydrolysis of glucosidic linkages, leaving lignin as the only solid residue. In this

method of determination, lignin (also known as ''Klason lignin'') is defined as a pulp constituent insoluble in 72% sulphuric acid. **Figure 9** shows the contents of xylans, glucans and Klason lignin in the pulp treated with different temperatures and the corresponding literature values at 80 °C.

Compared to the literature data, the xylan content in the pulp at 80 °C is by 3.1% lower while the Klason lignin content is higher by 2.6%. The high lignin content in the pulp shows that the delignification was not efficient. Lignin percentage increase is attributed to the significant removal of hemicellulose due to acid hydrolysis and the partial solubilization of cellulose in acid solution. [42] The significant increase in the Klason lignin content is probably due to lignin re-deposition as well as formation of pseudo-lignin through xylan degradation and re-condensation. [43] In fact, pseudo-lignin can also be generated from pure xylose during acid hydrolysis. [44] Therefore, the low xylan content might be due to the formation of pseudo-lignin.

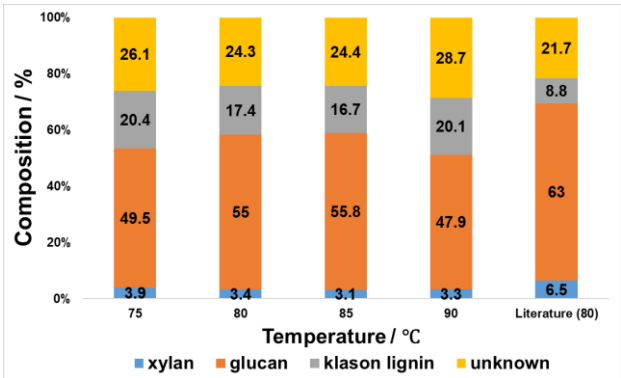

Figure 9. *Comparison of xylans, glucans and Klason lignin contents in pulp treated with different temperatures and the corresponding literature values at 80 °C.*

In theory, delignification increases with the rise in temperature, giving lower Klason lignin content in the pulp. However, a higher Klason lignin content was obtained when the temperature increased to 90 °C, contrary to the general trend. The increase in Klason lignin content at higher temperature shows the formation of pseudo-lignin and thus signs of overtreatment of the pulp, consistent with the conclusion drawn from the pulp yield.

The trend for glucan content is directly opposite to that of Klason lignin content. Generally, the glucan content in pulp increased with increasing temperature and decreasing Klason lignin content, demonstrating that a pulp with higher delignification gives higher glucose yield. The high percentage of glucan content across all temperatures also shows that the produced pulps were enriched in cellulose. Glucose is the sugar that is least affected by the acid hydrolysis conditions, as reported by Carvalho et al. [45]

It can be observed that the unknown components make up over 20% of the pulp composition. Some of the unknown components were verified to be p-TsOH acid hydrotrope and furfural. The presence of the p-TsOH acid hydrotrope residue in the pulp was confirmed by the FTIR analysis (**Figure S1** in supplementary information) in which the peak in the 1230-1120 cm^{-1} region indicates the presence of SO_2 in the pulp. The presence of furfural was confirmed by the diagram from UV detector in liquid chromatography which depicts a strong peak for furfural at around 4.3 minutes. (**Figure S2** in supplementary information) Furfural is hypothesised to be formed from the degradation of carbohydrates in the pulp during saccharification.

Conclusion

This study demonstrated that the structure of hydrotropic lignin extracted using 70wt% of p-TsOH acid hydrotrope is altered. Condensation reaction was confirmed through the low H and O contents in elemental analysis as well as the strong absorbance in the range between 300 nm and 400 nm in UV-Vis detector. The presence of pseudo-lignin was verified from the dark appearance of the pulp and the high Klason lignin content in the saccharification results. The highest lignin yield obtained was 26.4 % at treatment temperature of 85 °C, which is far from the 90 % reported in the study by Liheng Chen. [23] The low lignin yield and the high Klason lignin content in the pulp suggest that the delignification was inefficient. In conclusion, the paper which reported that concentrated p-TsOH acid hydrotrope can effectively dissolve 90% of native lignin from wood at ≤ 80 °C is misleading and irreproducible.

If the project frame were extended, additional factors affecting hydrotropic treatment, such as treatment time and acid hydrotrope concentration, can be investigated. In the future, scale-up experiments could be performed to explore if the findings reported here also apply for larger scales.

Acknowledgements

Authors gratefully acknowledge Dr Ines Biscaya, Claudio Chesi, Dr Robert Woodward and Martin Kessler for their technical help.

References

[1] Li M., Pu Y., Yoo C. G., Ragauskas A. J., " The occurrence of tricin and its derivatives in plants," *Green Chem.,* vol. 18, p. 1439–1454, 2016.

[2] Yoo C. G., Pu Y., Li M., Ragauskas A. J., "Elucidating structural characteristics of biomass using solution-state 2 D Nmr with a mixture of deuterated dimethylsulfoxide and hexamethylphosphoramide," *ChemSusChem,* vol. 9, p. 1090–1095, 2016.

[3] Takao Kishimoto, Wakako Chiba, Kaori Saito, Kazuhiko Fukushuma, Yashmitus Uraki and Makoto Ubukata, "Influence of Syringyl to Guaiacyl Ratio on the Structure of Natural and Synthetic Lignins," *J. Agric. Food Chem.,* vol. 58,

p. 895–901, 2010.

[4] J. E. Holladay, J. F. White, J. J. Bozell, D. Johnson, "Pacific Northwest National Laboratory," 2007. [Online]. Available: http://www.pnl.gov/main/publications/external/technical_reports/PNNL-16983.pdf. [Accessed April 2012].

[5] G. W. Huber, S. Iborra, A. Corma, "Synthesis of Transportation Fuels from Biomass: Chemistry, Catalysts, and Engineering," *Chem. Rev.,* vol. 106, p. 4044–4098, 2006.

[6] C. Lapierre, " Determining lignin structure by chemical degradations," in *Lignin and Lignans − Advances in Chemistry*, FL, USA, CRC Press, 2010, p. 11−48.

[7] R. Rinaldi and F. Schüth, "Design of solid catalysts for the conversion of biomass," *Energy Environ. Sci.,* vol. 2, p. 610–626, 2009.

[8] OrtwinBobleter, "Hydrothermal degradation of polymers derived from plants," *Progress in Polymer Science,* vol. 19, no. 5, pp. 797-841, 1994.

[9] Li Shuai, Masoud Talebi Amiri and Jeremy S.Luterbacher, "The influence of interunit carbon–carbon linkages during lignin upgrading," *Current Opinion in Green and Sustainable Chemistry,* vol. 2, pp. 59-63, 2016.

[10] Jairo H. Lora and Wolfgang G. Glasser, "Recent Industrial Applications of Lignin: A Sustainable Alternative to Nonrenewable Materials," *Journal of Polymers and the Environment,* vol. 10, p. 39–48, 2002.

[11] Korpinen LH, Pääkkönen RJ, "Occupational exposure to electric and magnetic fields during work tasks at 110 kV substations in the Tampere region," *Bio Electro Magnetics,* vol. 31, no. 3, pp. 252-254, 2010.

[12] H. Mou, B. Li, P. Fardim, "Pretreatment of corn stover with the modified hydrotropic method to enhance enzymatic hydrolysis," *Energy Fuels,* vol. 28, no. 7, pp. 4288-4293, 2014.

[13] Travis K.Hodgdon and Eric W.Kaler, "Hydrotropic solutions," *Current Opinion in Colloid & Interface Science,* vol. 12, no. 3, pp. 121-128, 2007.

[14] Procter, A. R, "Review of hydrotropic pulping," *Pulp & Paper megazine in Cananda,* vol. 72, no. 8, p. 247–254, 1971.

[15] Travis K.Hodgdon and Eric W.Kaler, "Hydrotropic solutions," *Current Opinion in Colloid & Interface Science,* vol. 12, no. 3, pp. 121-128, 2007.

[16] Ankit Mangal, Sandeep Singh Bhadoriya, Sorabh Joshi, Gaurav Agrawal, Amit Gupta, Narendra Mandoria , "Extraction Of Herbal Drugs By Using Hydrotropy Solublization Phenomenon," *Int. Res j pharm. App sci.,* vol. 2, no. 1, pp. 63-74, 2012.

[17] Leena P.Devendra, Kiran KumarM. and AshokPandey, "Evaluation of hydrotropic pretreatment on lignocellulosic biomass," *Bioresource Technology,* vol. 213, pp. 350-358, 2016.

[18] Konstantin Gabov, Pedro Fardim and Francides Gomes da Silva Júnior, "Hydrotropic Fractionation of Birch Wood into Cellulose and Lignin: A New Step Towards Green Biorefinery," *BioResources,* vol. 8, no. 3, pp. 3528-3532, 2013.

[19] McKee, R. H., "Use of hydrotropic solutions in industry," *Ind. Eng. Chem.,* vol. 38, p. 382−384, 1946.

[20] Kreicberg, Z. N. and Grabovskij, J. K., "Oxidation of hydrotropic lignin from aspen. Tr. Inst. Lesokhoz. Probl. Khim. Drev.," *Akad. Nauk Latv.,* vol. 21, p. 69−75, 1960.

[21] Zoldners, J. A. and Surna, J. A. , "Comparison of the reactivities of hydrotropic, alkali, and dioxane lignins from aspen," *Khim. Drev.,* vol. 3, p. 123−127, 1969.

[22] Risto I. Korpinen and Pedro Fardim, "Reinforcement potential of bleached sawdust kraft pulp in different mechanical pulp furnishes," *Bioresources,* vol. 4, no. 4, pp. 1572-1585, 2009.

[23] Liheng Chen, Jinze Dou, Qianli Ma, Ning Li, Ruchun Wu,Huiyang Bian, Daniel J. Yelle, "Rapid and near-complete dissolution of wood lignin at ≤80°C by a recyclable acid hydrotrope," *Science advances,* 2017.

[24] Martin Kessler, RobertoT. Woodward, Narumi Wong, Roberto Rinaldi, "Kinematic Modeling of Mechanocatalytic Depolymerization of α-Cellulose and Beechwood," *ChemSusChem,* pp. 552-561, 2017.

[25] A. technology, "A guide to multi- detector gel permeation chromatography.," Aglient technology.

[26] J. P. Guthrie, "Hydrolysis of esters of oxy acids: pKa values for strong acids," *Can. J. Chem,* vol. 56, pp. 2342-2354, 1978.

[27] Chunping Xu, Rick Arneil D. Arancon, Jalel Labidid and Rafael Luque, "Lignin depolymerisation strategies: towards valuable chemicals and fuels," *Chem Soc Rev,* vol. 43, pp. 7485-7500, 2014.

[28] Matthew R. Sturgeon,Seonah Kim, Kelsey Lawrence, Robert S. Paton,Stephen C. Chmely, Mark Nimlos, Thomas D. Foust, and Gregg T. Beckham, "A Mechanistic Investigation of Acid-Catalyzed Cleavage of Aryl-Ether Linkages: Implications for Lignin Depolymerization in Acidic Environments," *ACS Sustainable Chem Eng,* vol. 2, pp. 472-485, 2014.

[29] K. Shimada , S. Hosoya and T. Ikeda, "Condensation Reactions of Softwood and Hardwood Lignin Model Compounds Under Organic Acid Cooking Conditions," *Journal of Wood Chemistry and Technology,* pp. 57-72, 2006.

[30] Xingyu Wang and Roberto Rinaldi, "Exploiting H-transfer reactions with RANEY® Ni for upgrade of phenolic and aromatic biorefinery feeds under unusual, low-severity conditions," *Energy Environ. Sci.,* vol. 5, pp. 8244-8260, 2012.

[31] Lisa Weigand, Shahrokh Mostame, Agnieszka Brandt-Talbot,Tom Welton and Jason P. Hallett, "Effect of pretreatment severity on the cellulose and lignin isolated from Salix using ionoSolv pretreatment," *Faraday Discussions,* vol. 202, pp. 331-349, 2017.

[32] Stephen Y. Lin and Carlton W. Dence, in *Methods in Lignin Chemistry*, Springer Science & Business Media, 2012, pp. 224-226.

[33] Andre M. Striegel, "Multiple Detection in Size-Exclusion Chromatography of Macromolecules," *Anal. Chem.,* vol. 77, no. 5, pp. 104-113, 2005.

[34] S. D. Mandfield, H. Kim, F. Lu and J. Ralph, "Whole plant cell wall characterization using solution-state 2D NMR," *Nat. Protoc.,* vol. 7, no. 9, pp. 1579-1589, 2012.

[35] Agnieszka Brandt, Long Chen, Bart E. van Dongen, Tom Welton and Jason P. Hallett, "Structural changes in lignins isolated using an acidic ionic liquid water mixture," *Green Chemistry,* vol. 17, p. 5019–5034, 2015.

[36] S.K. Bose, R. C. Francis,M. Govender, T. Bush and A. Spark, "Lignin content versus syringyl to guaiacyl ratio amongst poplars," *Bioresour. Technol.,* vol. 100, p. 1628–1633, 2009.

[37] Cláudio F. Lima, Luiz C. A. Barbosa,Cristiana R. Marcelo, Flaviano O. Silvério and Jorge L. Colodette, "Comparison between analytical pyrolysis and nitrobenzene oxidation for determination of syringyl/guaiacyl ratio in Eucalyptus spp. Lignin," *BioResources,* vol. 3, no. 3, pp. 701-712, 2008.

[38] Ana Lourenço,1,*† Jorge Rencoret,2,† Catarina Chemetova, Jorge Gominho, Ana Gutiérrez, José C. del Río, and Helena Pereira, "Lignin Composition and Structure Differs between Xylem, Phloem and Phellem in Quercus suber L.," *Plant Sci.,* vol. 7, p. 1612, 2016.

[39] Ferrer JL, Austin MB, Stewart C Jr and Noel JP, "Structure and function of enzymes involved in the biosynthesis of phenylpropanoids," *Plant Physiol. Biochem.,* vol. 46, no. 3, pp. 356-370, 2008.

[40] Somnath D. Shinde, Xianzhi Meng, Rajeev Kumar and Arthur J. Ragauskas, "Recent advances in understanding the pseudolignin formation in a lignocellulosic biorefinery," *Green chemistry,* vol. 20, p. 2192–2205, 2018.

[41] Poulomi Sannigrahi, Dong Ho Kim, Seokwon Jung and Arthur Ragauskas, "Pseudo-lignin and pretreatment chemistry," *Energy Environ. Sci.,* vol. 4, p. 1306–1310, 2011.

[42] Liu, J., Li, M., Luo, X., Chen, L., and Huang, L, "Effect of hot-water extraction (HWE) severity on bleached pulp based biorefinery performance of eucalyptus during the HWE-Kraft-ECF bleaching process," *Bioresource Technol.,* vol. 181, pp. 183-190, 2015.

[43] Lora, J. H., and Wayman, M, "Delignification of hardwoods by autohydrolysis and extraction," *TAPPI J.,* vol. 61(6), pp. 47-50, 1978.

[44] Kumar, R., Hu, F., Sannigrahi, P., Jung, S., Ragauskas, A. J., and Wyman, C. E., "Carbohydrate derived-pseudo-lignin can retard cellulose biological conversion," *Biotechnol. Bioeng.,* vol. 110(3), pp. 737-753, 2013.

[45] Danila Morais de Carvalho and Jorge Luiz Colodette, "Comparative study of acid hydrolysis of lignin and polysaccharides in biomasses," *BioRes. ,* vol. 12(4), pp. 6907-6923, 2017.

[46] Jia-long Wen, Shao-Long Sun, Bai-Liang Xue and Run-Cang Sun, "Recent Advances in Characterization of Lignin Polymer by Solution-State Nuclear Magnatic Resonance (NMR) Methodology," *Materials,* vol. 6, pp. 359-391, 2013.

Appendix – Sample Calculations

Elemental analysis (H/C and O/C ratios)

Different compositional percentages of C, H, N and S were obtained from elemental analysis. In order to calculate the H/C ratio of lignin obtained at 75 °C, H% and C% were divided by the molar mass, which are 1.008 g/mol and 12.011 g/mol respectively. H/C ratio is calculated as follow:

$$\frac{H}{C} = \frac{\frac{H\%}{molar\ mass\ of\ H}}{\frac{C\%}{molar\ mass\ of\ C}} = \frac{\frac{5.793\%}{1.008\ g/mol}}{\frac{64.18\%}{12.001\ g/mol}} = 1.08$$

Since triplicate measurements were taken, the final value is the average of the three. The O/C ratio can be calculated in the same way.

S/G ratio in NMR

The peaks in NMR spectra were integrated to calculate the S/G ratio. As only two carbons are detected from S units and three carbons are detected from G units, a ratio of 3/2 was multiplied in the calculation. [46] The S/G ratio of lignin extracted at 75 °C is calculated as follow:

$$\frac{S}{G} = \frac{(area\ of\ S' + area\ of\ S) * 3/2}{area\ of\ G} = \frac{(0.02 + 1) * 3/2}{1.34} = 1.14$$

Pulp yield and lignin yield

When 501.4 mg of poplar wood powder was suspended in 70 wt% of p-TsOH acid hydrotrope solution at 75 °C for 20 minutes, 29.0 mg of lignin was dissolved and recovered, while 288.1 mg of insoluble part remaining in pulp. The pulp and lignin yield are calculated as follow:

$$Pulp\ yield = \frac{weight\ of\ pulp}{weight\ of\ wood} = \frac{288.1\ mg}{501.4\ mg} = 57.5\ \%$$

$$Lignin\ yield = \frac{weight\ of\ lignin}{weight\ of\ wood * lignin\ content\ in\ wood} = \frac{29.0\ mg}{501.4\ mg * 30\%} = 19.3\%$$

A Novel Techno-Economic Decision Support Framework for Biogas Exploitation in Waste Water Treatment Plants

D. Wigh, N. Shah
Department of Chemical Engineering, Imperial College London, U.K.

ARTICLE INFO

Keywords:
Biogas
Biomethane
Optimisation
Solid oxide fuel cell
Upgrading
Waste water treatment

ABSTRACT

This work aims to identify the most economic pathway for biogas utilisation by proposing a novel multi-period Mixed Integer Linear Programme (MILP) to minimise the total Equivalent Annual Cost considering the whole plant system. Three pathways were considered: Combined Heat and Power (CHP) production using a Solid Oxide Fuel Cell (SOFC), upgrading biogas to biomethane using water scrubbing technology, and a combination of the two. These three pathways were compared to the Business As Usual (BAU) scenario, where all heat and electricity demands of the plant are met through grid imports. The model was illustrated through a case study of SMAT's Waste Water Treatment Plant (WWTP) in Collegno, Italy. The use of real input data also provides a unique added value to this work. Results show that the upgrade pathway performed best and the SOFC worst in terms of NPV. Sensitivity analysis was conducted to determine the economic drivers for each pathway. Results also show that only when the capital cost of the SOFC was decreased by 50% did it outperform the BAU case. The NPV of all scenarios remained below -€10m in all sensitivity analysis cases, implying that exploiting biogas is not economically feasible without incentives. The upgrade technology showed resilience to change as it maintained the highest NPV in all sensitivity cases considered, therefore upgrading biogas using water scrubbing is the recommended technology as it minimises losses.

1. Introduction

Emissions reduction plays a crucial role in reaching the 2˚C target of the Paris agreement (Gao, Gao & Zhang, 2017) providing significant motivations for optimising biogas exploitation. Renewable energy was estimated to make up 19.3% of global energy consumption in 2015, and its share is expected to continue rising both in the short and long term (Gsr, 2017). A key challenge associated with the use of renewables, particularly wind and solar energy, is reduced flexibility of availability as compared to fossil fuels, and effective utilisation of biomass is one way to mediate this issue (Angelidaki *et al.*, 2018)(Ullah Khan *et al.*, 2017). This is particularly true for upgrading biogas to biomethane, as injecting biomethane into the grid is an effective way to store energy.

The source of biomass considered in this paper is sewage sludge after it has been processed by a Waste Water Treatment Plant (WWTP). Using Life Cycle Analysis (LCA) it has been determined that Anaerobic Digestion (AD) is always the favourable treatment option for municipal solid waste (Lombardi, Carnevale & Corti, 2015). The output of an AD is biogas, which typically consists of 60-70% methane (CH_4), 30-40% carbon dioxide (CO_2), and trace amounts of impurities. The most significant of these impurities is hydrogen sulphide (H_2S), typically present in 0-4000ppm, however other impurities may also be present, such as Carbon monoxide (CO), hydrogen (H_2), nitrogen (N_2), oxygen (O_2), and ammonia (NH_3) (Sun *et al.*, 2015). If biogas is to be exploited in CHP units like SOFC, the hydrogen sulphide (H_2S) must be removed as it is very corrosive and can deactivate the catalytic activity of the nickel anode (Giarola *et al.*, 2018). H_2S must also be removed from biogas before upgrading it to biomethane to meet the grid specifications.

Figure 1 shows a simplified high-level overview of the process of converting sewage sludge to biogas, followed by usage options considered in this paper. The aim of this work is to do a techno-economic appraisal of each of these technologies to determine the appropriate technology to be implemented downstream of SMAT's WWTP in Collegno, Italy.

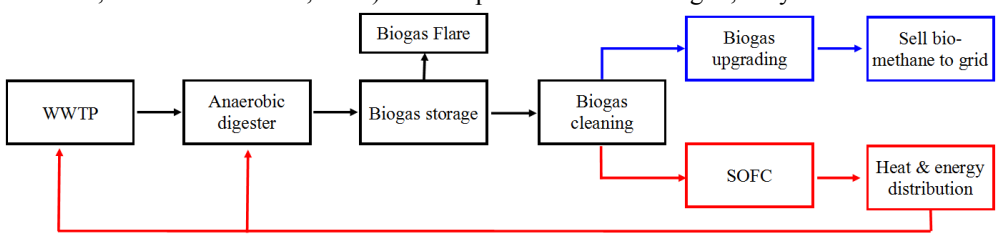

Figure 1. High-level overview of the biomass utilization options.

Nomenclature

Acronyms

BAU	business as usual
BM	biomethane
CHP	combined heat and power
EAC	equivalent annual cost
FC	fuel cell
$MILP$	mixed integer linear programming
NG	natural gas
SG	spark gap
$SOFC$	solid oxide fuel cell
$WWTP$	waste water treatment plant
$OpEx$	operating expenditure
$CapEx$	capital expenditure

Sets

$t, tt \in T$	periods, $T = \{t1, \dots, t365\}$

Subscripts

b	biogas, as in kWh_b
e	electricity, as in kWh_e
f	fuel, as in kWh_f
h	heat, as in kWh_h
t	at time t

Parameters

BM_p	biomethane price, €/kWh
BM_{slip}	biogas lost when converting to BM
BGD_{abs}	biogas absorbed due to shut-down, kW_b
BGS_{abs}	biogas absorbed due to start-up, kW_b
BGf_t	biogas flowrate from AD, kWh_b/day
CFC	capital charge factor
$CapExCF$	capex cost factor for scrubber, €/kW
$CapExCU$	capex of clean-up system, €
ce_{in}	electricity import price, €/kWh_e
ce_{out}	electricity export price, €/kWh_e
cn	natural gas price, €/kWh_f
cp	carbon price, € per $kgCO_2$
DTL_t	heat demand of plant, kWh/day
ee	electricity emission factor, $kgCO_2/kWh_e$
$ei1$	energy intensity blower chiller 1
$ei2$	energy intensity blower chiller 2
η^b	boiler efficiency, kWh_h/kWh_f
η^{th}	fuel cell thermal efficiency, kWh_h/kWh_b
η^{FC}	fuel cell electrical efficiency, kWh_e/kWh_b
MH	maximum number of hours, hours/day
$OpExCF$	opex cost factor for scrubber, €/kWh
$OpExSOFC$	opex of SOFC, €/year
$OpExup$	opex of scrubber, €/year
PSD_{abs}	power absorbed at shut-down, kW_e
PSU_{abs}	power absorbed at start up, kW_e
$PlantEl_t$	plant electricity demand, kWh_e/day
$Pnom$	generator nameplate capacity, kWh
r_{up}	ramp rate of the SOFC
$SizeSOFC$	SOFC capacity, kWh_b/day
$Sizeup$	scrubber capacity, kWh_b/day
$StSuBiogas$	start-up and shut-down waste, kWh_f/day
$UCCc$	capex factor for clean-up system, €/kWh
$UCCf$	capex factor for SOFC, €/kW
$UCCstack$	capex factor for stack replacement, €/kW
UMC	maintenance cost factor, €/kW per year
UOC	clean-up maintenance cost, €/kW per year
yr	number of operating days per year

Decision variables

a_t	electrical output, kWh_e
u_t	binary variable, 1 if SOFC is turned on
BM_{income}	income generated from selling biomethane
BGD_t	biogas wasted due to shut-down, kWh_b
BGS_t	biogas wasted due to start-up, kWh_b
$BGflare_t$	biogas flared, kWh_f
$BGup_t$	biogas flow into upgrade system, kWh_b
$CapEx$	total capital expenditure, €
GEE_t	electricity exported to the grid, kWh_e
GEI_t	electricity imported from the grid, kWh_e
$GasHolder_t$	biogas inside the tank, kWh_b
$NGboiler_t$	flow of natural gas through boiler, kWh/day
OP_t	operating cost, €/day
$OpEx$	total operating expense, €/year
PSD_t	power absorbed at shut down, kWh_e
PSU_t	power absorbed at start-up, kWh_e
$StSuBiogas_t$	start-up and shut-down waste, kWh_f/day
$StSuElec_t$	start-up and shut-down waste, kWh_e/day
$YSOFC$	binary variable, 1 if fuel cell exists
Yup	binary variable, 1 if upgrade system exists

Objective function variable

Z	equivalent annual cost of system, €/year

2. Literature Review

2.1. Background

The techno-economics of biogas-fed systems is a well-studied topic, with some papers utilising real plant data from SMAT's WWTP in Turin, Italy (Giarola *et al.*, 2018). However, a review of the current literature reveals an absence of research comparing the SOFC with biogas upgrade at an industrial scale.

Hydrogen sulphide (H_2S) is highly corrosive and early removal is crucial (Sun *et al.*, 2015). While much literature is available on the appropriate selection of technology for removing hydrogen sulphide, these considerations are beyond the scope of this work, as cleaning technologies are already present on site, and will be used in both the SOFC and upgrade scenario.

2.2. SOFC

Previous research into the techno-economics of SOFCs for CHP show that the capital cost is excessive, resulting in them being economically less feasible than conventional alternatives. Operational considerations are also important when dealing with SOFCs on an industrial scale. One such example is the presence of H_2S in the feed gas which is found naturally in biogas originating from WWTPs; it can deactivate the catalytic activity of the nickel anode and thus increase maintenance costs (Giarola *et al.*, 2018).

One way to improve performance of the SOFC is to couple it with Micro Gas Turbines (MGT). This can increase CHP generation efficiency by 7% compared to using only an SOFC (MosayebNezhad *et al.*, 2018). Alternatives to the SOFC exist, such as the Internal Combustion Engine (ICE); however, it has been shown that the SOFC has a higher efficiency. It has previously been noted that upgrading is likely to be economically cheaper than an SOFC as it requires a lower investment cost. (Gandiglio, Drago & Santarelli, 2016).

2.3. Upgrade

Given the significance of effective biogas upgrading, numerous papers have described various aspects of the value chain and can broadly be split into two categories: assessment of different configurations for upgrade, or a review and selection of appropriate technologies.

A large variety of methods for upgrading biogas are available for selection, however, there are currently only 5 physical/chemical technologies that are commercially viable: water scrubbing, chemical scrubbing, membrane technology, pressure swing adsorption, and organic physical scrubbing. Other technologies, such as cryogenic process or chemical hydrogenation, are still under development, and while biological methods are available, these are still new and not yet commercial. Water scrubbing is the most commonly used upgrade technology, applied at 152 of the 428 upgrade plants in Europe (Angelidaki *et al.*, 2018). There is no one best technology for every case, and the best technology choice will depend on a variety of factors, including, but not limited to: cost, efficiency, methane recovery and loss, whether co-removal of N_2 and O_2 is necessary, and how the biomethane is intended to be used (Sun *et al.*, 2015). It has previously been noted that water scrubbing is the least sensitive to impurities, and ideal for an energy self-sufficient biogas upgrade plant (Magli *et al.*, 2018). In addition, it appears to be the most mature technology (Bauer *et al.*, 2013), therefore water scrubbing has been selected as the biogas upgrade technology considered in this work.

2.4. Modelling methodology

Modelling of sections of the biogas supply chain has been conducted previously. Scheduling is an important part of supply chain analysis, as being able to analyse how the system meets the demands will influence future investment, inventory and other decisions (Dunnett, Adjiman & Shah, 2007). Biogas usage in an SOFC CHP system is a complex process with many constraints and limitations due to the dynamics of the equipment and processes. For instance, SOFCs can degrade due to mechanical stress from rapid changes in electrical output therefore ramp up constraints should be implemented in the model (Giarola *et al.*, 2018).

2.5. Novelty of this study

Current literature covers a variety of topics relating to biogas exploitation and optimisation, and typically focus either on CHP or upgrading. The use of real plant data to do a plant whole system analysis and consideration of the BAU is uncommon. The novelty of this work lies in its consideration of the SOFC and water scrubbing pathway together, on an industrial scale, which has been modelled to allow for multi-period analysis and economic feasibility comparison.

3. Problem Statement

This work sets out to determine the best use of biogas based on minimisation of the total cost from the Collegno WWTP managed by SMAT in Turin (SMAT, n.d.). The three studied configurations, SOFC, upgrading using a water scrubber, and a mixture of the two, are compared to the reference scenario, BAU, where all heat and electricity demand is covered through imports from the grid. Techno-economic appraisal can be conducted on each of these four scenarios, and while the model seeks to minimise the equivalent annual cost, the respective Net Present Values (NPVs) were also calculated.

The problem can be stated in the following way. Given:

- the characterisation of the SOFC in terms of
  - capacity
  - capital, operating, and stack replacement cost
  - electrical and thermal efficiency
  - minimum up- and down-times with associated ramp rates
- the characterisation of the water scrubbing system in terms of
  - capacity
  - capital and operating cost
  - conversion efficiency (biomethane slip)
- the characterisation of the clean-up system consisting of two chillers, a blower, and a compressor (capital and operating cost)
- the supplementary natural gas boiler capacity and efficiency, both of which assumed constant
- the biogas holder minimum and maximum level

- the annual biogas flow from the WWTP on a daily basis
- the annual heat demand of the anaerobic digester on a daily basis
- the capital charge factor and discount rate

the model minimises the equivalent annual cost of each scenario, while fulfilling the thermal and electricity demand of the WWTP and defining the operating schedule on a daily basis. As such the decision variables are:

- whether the SOFC and upgrade units should exist
- the time periods where the SOFC is in operation (defining occurrence of start-up and shut-downs throughout the year)
- the thermal and electrical output of the SOFC on a daily basis
- the amount of biogas and electricity wasted due to start-up and shut-down events
- the natural gas boiler thermal output on a daily basis
- the operating cost for electricity and natural gas bought from the grid, and associated CO_2 emission cost on a daily basis
- the biogas flow used by the SOFC on a daily basis
- the biogas flowing through the water scrubber system on a daily basis
- the biogas holder level on a daily basis
- the amount of unexploited (i.e. flared) biogas on a daily basis

Symbols used for scalars and decision variables are reported in the nomenclature. The biogas flowrate input to the model is the output of the anaerobic digestor, and thus dynamic modelling of the anaerobic digester is not included.

4. Mathematical formulation

The BAU scenario will be presented first, and due to the simplicity of this mode of operation, the EAC and NPV was calculated in excel. MILP models were built in GAMS to describe the three other scenarios considered, SOFC, upgrade, and mix, with the objective of minimising equivalent annual cost.

4.1. Business as Usual

In this scenario there is no associated capital expenditure. The operating expense per day, seen in equation (1), is taken to be the negative cashflow for this scenario, and assumed to stay constant in each year. Using an appropriate discount rate, the EAC and NPV was calculated.

$$OP_t = PlantEl_t \cdot ce_{in} + \left(\frac{DTL_t}{\eta^b}\right) \cdot cn + \left(PlantEl_t \cdot ee + \left(\frac{DTL_t}{\eta^b}\right) \cdot ge\right) \cdot cp \quad (1)$$

4.2. SOFC

4.2.1. Objective function & costs

The objective function's aim is to minimise the equivalent annual cost of the system.

The costs consist of capital expenditure, maintenance, electricity purchased from the grid, back-up boilers utilisation, and start-up/shut-down costs.

$$Z = OpEx + CapEx \cdot CFC \quad (2)$$

$$OpEx = \sum_t OP_t + OpExSOFC + UOC \cdot Pnom \quad (3)$$

$$OP_t = NGboiler_t \cdot cn + GEI_t \cdot ce_{in} - GEE_t \cdot ce_{out} \quad (4)$$

$$OpExSOFC = YSOFC \cdot UMC \cdot SizeSOFC \quad (5)$$

$$CapEx = YSOFC \cdot CapExSOFC + CapExCU \quad (6)$$

$$CapExSOFC = (UCCf + UCCstack \cdot 2) \cdot Pnom \quad (7)$$

$$CapExCU = UCCc \cdot Pnom \quad (8)$$

4.2.2. Energy balance constraints

The energy balance constraints are for flows of biogas, heat and electricity throughout the system. The biogas can be kept in a holder, $GasHolder_t$, flared, $BGflare_t$, wasted due to start-up and shut-down events, $StSuBiogas_t$, or used for CHP.

$$BGf_t = GasHolder_{t+1} - GasHolder_t + BGflare_t + StSuBiogas_t + \frac{a_t}{\eta^{FC}} \quad (9)$$

$$StSuBiogas_t = BGS_t + BGD_t \quad (10)$$

The thermal balance describes how the onsite heat demand can either be met with heat produced by the SOFC or the natural gas boiler.

$$DTL_t = NGboiler_t \cdot \eta^b + \frac{a_t}{\eta^{FC}} \cdot \eta^{th} \quad (11)$$

The demand for electricity arises from the WWTP, start-up and shut-down related consumption, the first blower chiller and any excess which can be exported to the grid (GEI_t). The supply to meet this demand comes from the SOFC and imports from the grid (GEE_t).

$$PlantEl_t + StSuElec_t + ei1 \cdot BGf_t + GEE_t = GEI_t + a_t \cdot \left(1 - \frac{ei2}{\eta^{FC}}\right) \quad (12)$$

$$StSuElec_t = PSD_t + PSU_t \quad (13)$$

4.2.3. Other Constraints on the SOFC

To prevent the degradation the SOFC unit must be shut of periodically, but to optimise the CHP generation, the SOFC is remained shut off for the minimum amount of time required.

$$u_{t-1} - u_t \leq 1 - u_{tt} \quad (14)$$

$$u_{t-1} - u_t \geq - u_{tt} \quad (15)$$

To further increase the longevity of the SOFC a maximum ramp up rate is specified to prevent mechanical stresses building up and damaging the SOFC. This is followed by the capacity constraint of the SOFC.

$$a_t - a_{t-1} \leq r_{up} \cdot MH \quad (16)$$

$$a_t \leq Pnom \cdot u_t \cdot MH \quad (17)$$

The start-up and shut-down events consume power and biogas which is calculated using the following inequalities.

$$PSD_t \geq PSD_{abs} \cdot MH \cdot YSOFC \quad (18)$$

$$PSU_t \geq PSU_{abs} \cdot MH \cdot YSOFC \quad (19)$$

$$BGD_t \geq BGD_{abs} \cdot MH \cdot YSOFC \quad (20)$$

$$BGS_t \geq BGS_{abs} \cdot MH \cdot YSOFC \quad (21)$$

4.3. Biogas upgrade

4.3.1. Objective function & costs

The objective function for the biogas upgrade is similar to that of the SOFC, with the exception of the added variable for cashflow from selling biomethane to the grid. The capital and operating costs for the upgrade system were modelled using cost factors found in literature. The operating cost associated with fulfilling the demands of the WWTP, OP_t, is also notably simpler, as the upgrade system does not produce heat or electricity. The equation for the capital cost of the clean-up system, $CapExCU$, stays the same as per equation (8).

$$Z = OpEx + CapEx \cdot CFC - BM_{income} \quad (22)$$

$$OpEx = \sum_t OP_t + OpExup + UOC \cdot Pnom \quad (23)$$

$$OP_t = PlantEl_t \cdot ce_{in} + \left(\frac{HD_t}{\eta^b}\right) \cdot cn \quad (24)$$

$$OpExup = Yup \cdot OpExCF \cdot Sizeup \cdot yr \quad (25)$$

$$CapEx = Yup \cdot CapExup + CapExCU \quad (26)$$

$$CapExup = Yup \cdot CapExCF \cdot Sizeup/MH \quad (27)$$

$$BM_{income} = (\sum_t BM_t) \cdot BM_p \quad (28)$$

4.3.2. Energy balance constraints

As the electricity and heat costs were included directly into the operating cost equation (24), only conservation of biogas was a necessary energy balance for the upgrade system.

$$BGf_t = GasHolder_{t+1} - GasHolder_t + BGflare_t + BGup_t \quad (29)$$

$$BM_t = BGup_t \cdot (1 - BMslip) \quad (30)$$

4.4. Mix – SOFC & upgrade

Since the mix scenario is built as a combination of the two previous scenarios, with the capacity of each technology halved, the governing equations are very similar.

4.4.1. Objective function & costs

The objective function of the mix pathway, seen in equation (31), is the same as that of the upgrade, seen in equation (22). The constituent parts of the capital and operating costs are also remarkably similar, since the mix model merges the two previous models. The equations for $OpExSOFC$, $OpExup$, $CapExSOFC$, $CapExup$ and $CapExCU$ all stay the same and can been seen in equation (5), (25), (7), (27) and (8), respectively. The daily operating cost, OP_t, stays the same as in the SOFC case, seen in equation (4)

$$Z = OpEx + CapEx \cdot CFC - BM_{income} \quad (31)$$

$$OpEx = \sum_t OP_t + OpExSOFC + OpExup + UOC \cdot Pnom \quad (32)$$

$$CapEx = CapExSOFC \cdot YSOFC + CapExup \cdot Yup + CapExCU \quad (33)$$

4.4.2. Energy balance constraints

The energy balance equations in the mix case are equivalent to the energy balance equations and constraints in the SOFC case, as outlined in equations (10) to (21). The equation governing biogas upgrade, equation (30), will also stay the same. The biogas conservation balance for the mix pathway can be seen below.

$$BGf_t = GasHolder_{t+1} - GasHolder_t + BGflare_t + \frac{a_t}{\eta^{FC}} + StSuBiogas_t + BG_{up} \quad (34)$$

5. Results and discussion

The results and discussion section is split into three sections: the first outlines the economic input data to the model, with the case study values indicating the most likely value for these variables.

Then an evaluation of each of the four scenarios in the case study is presented, followed by discussion of the impact of changing key variables - sensitivity analysis.

5.1. Input data and values for sensitivity analysis

The sensitivity analysis includes considerations of changes in the 6 input variables, as outlines below in Table 1. Each has been assigned a higher (H) and lower (L) value. Where possible, the higher and lower values are based on realistic bounds for the variable that may be reached within a reasonable amount of time.

Table 1 - Variables and corresponding source or assumptions: CapExCF, (Sun et al., 2015); cp, (Baroness Bryony Worthington, n.d.); ce_{in}, ±10%, higher and lower (Eurostat, 2018); cn, Higher and lower vales based on recent historical values (Eurostat, n.d.); Spark Gap (SG), electricity price and natural gas price are changed simultaneously to the values stated previously in this section.

Variable	Unit	Low	Case study	High
SG	€/kWh	N/A	N/A	N/A
cp	€/ton	0	16	32
$UCCf$	€/kWh	4151.5	8303	16,606
$CapExCF$	€/kWh	702	799	896
cn	€/kWh	0.0281	0.032	0.0355
ce_{in}	€/kWh	0.1294	0.1468	0.1642

5.2. Case study evaluation

The three different biogas utilisation pathways (SOFC, upgrade, and mix) and the BAU were evaluated in the case study. The case study values were considered to be the most likely to be valid and the techno-economic output can be seen in Table 2. The case study evaluation shaped how the sensitivity was carried out.

5.2.1. Economic Evaluation

What becomes immediately apparent from the economic evaluation in Table 2 is that the NPV is negative in all the scenarios considered, which does not make an appealing investment. A large part of the reason for this is that the cost of the sewage sludge to biogas pre-treatment (i.e. WWTP and anaerobic digester) must be borne by this project, and with electricity and heat demands in excess of €1m/year, economic feasibility becomes difficult. This is particularly true for the upgrade path, where the operating cost of the plant exceeds the income from selling biomethane to the grid, hence the net cash flow would always be negative, resulting in the non-existence of a payback time when taking the whole plant into account.

A simplification was introduced when choosing to model the water scrubber using cost factors found in literature, but as is apparent, the upgrade operating expense represents less than 3% of the overall operating expense, implying that increased complexity in the upgrade model would not greatly increase the accuracy of the results.

5.2.2. Scheduling

The schedule of the three different pathways in the case study can be viewed on Figure 2.

Table 2. Case study economic evaluation.

	Business as usual		SOFC		Upgrade		Mix	
Operating costs								
El import	€	1,159,139	€	1,020,177	€	1,159,139	€	1,110,283
NG import	€	121,842	€	94,951	€	121,842	€	107,211
CO_2	€	76,5489	€	66,131	€	(11,432)	€	66,802
SOFC	€	-	€	25,886	€	-	€	19,589
Upgrade	€	-	€	-	€	35,5934	€	11,109
Total Operating costs	€	1,357,530	€	1,207,144	€	1,305,143	€	1,314,995
Operating income								
Selling BM	€	-	€	-	€	198,079	€	96,359
Net OpEx	€	1,357,530	€	1,207,144	€	1,071,471	€	1,207,526
CapEx								
SOFC	€	-	€	2,820,000	€	-	€	1,410,000
Upgrade	€	-	€	-	€	432,792	€	215,593
Clean up system	€	-	€	240,575	€	240,575	€	240,575
Total CapEx	€	-	€	3,060,575	€	673,367	€	1,866,168
EAC	€	1,357,530	€	2,217,133	€	1,329,276	€	1,834,471
NPV	€	(15,635,230)	€	(16,955,000)	€	(13,415,800)	€	(15,652,300)

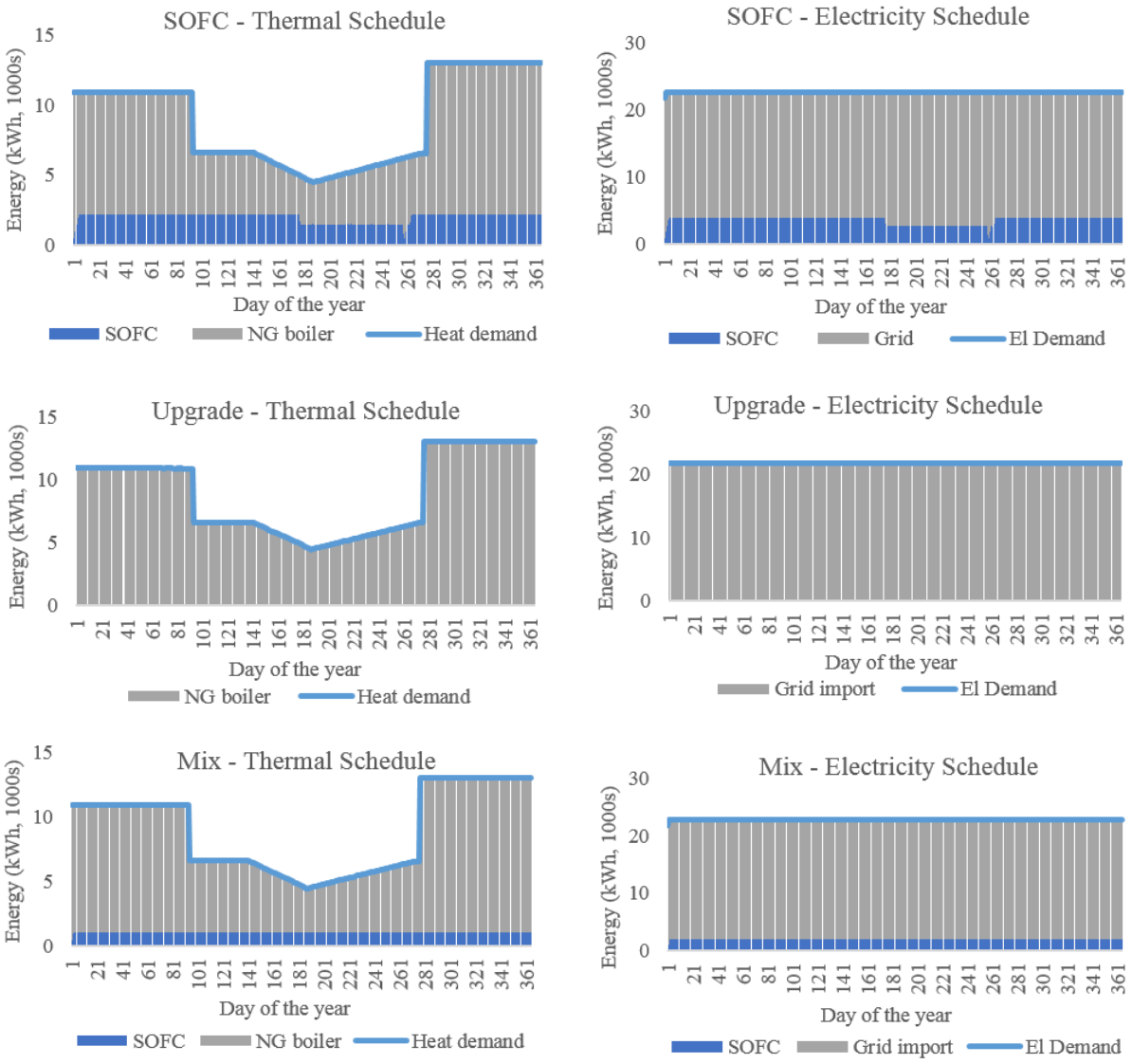

Figure 2. Heat and electricity schedule for each of the biogas utilisation pathways considered in the case study.

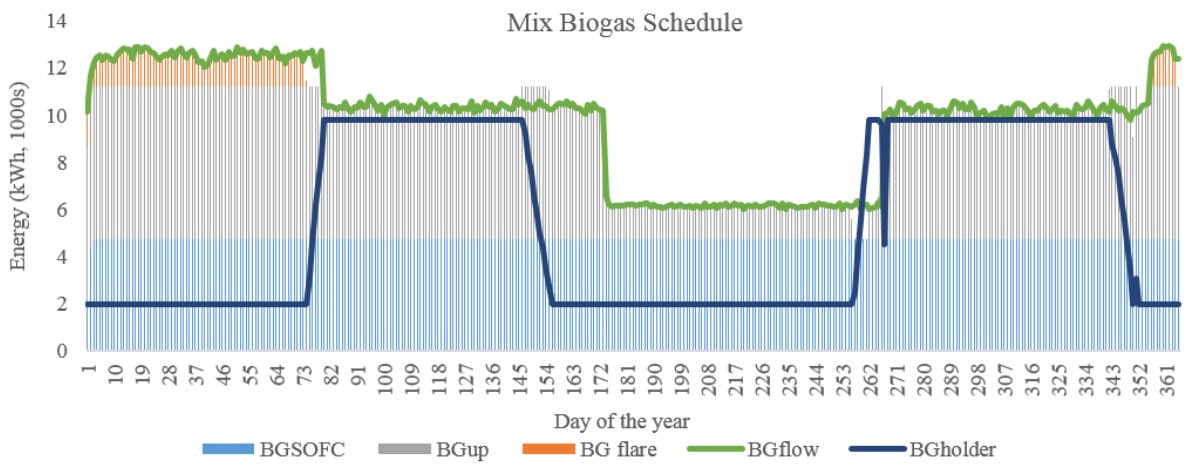

Figure 3. Biogas utilisation schedule for the case study using the mix pathway on a daily basis.

5.2.3. Favoured scenario for case study

The results of the case study show that all three pathways have negative NPVs rendering them economically infeasible. Given that the biogas must be treated regardless of economic feasibility, any NPV more favourable than that of the BAU scenario will reflect a financial improvement, see Table 2. The SOFC and mix scenarios were over €1 million and over €15,000 more expensive, respectively.

Only the upgrade pathway outperformed the BAU on NPV, with an improvement of over €2 million. A breakdown of the costs, as seen in Table 2, shows that the upgrade pathway has much lower capital costs than SOFC and mix pathway, and despite its higher total operating costs, the income generated through sales of biomethane offset the differential in expenses with the other scenarios.

To check if the upgrade is the most suitable pathway, it is important to measure the impact of fluctuations in the input data on the NPV.

5.3. Sensitivity

Sensitivity analysis was conducted to determine the dependence of each scenario on key input variables.

5.3.1. Sensitivity on NPV

The key variables considered, as shown in Table 1, were varied higher (H) and lower (L), and the impact on NPV can be seen on Figure 4. It is immediately obvious that treating biogas is not economically feasible even when considering more favourable conditions than that of the case study, as the NPV consistently stays below -€10m. If a technology outperforms the BAU case then its implementation can be considered beneficial to the project, and as the upgrade technology outperforms the other pathways in terms of NPV in all sensitivity scenarios considered, it shows strong resilience to influence from external factors.

Arguably the biggest drawback of the SOFC is its high capital cost, and only when this parameter is reduced by 50%, do we see the SOFC outperform the BAU case; in all other scenarios, operating with the BAU schedule is cheaper. There is good reason to believe that SOFCs will become cheaper and better performing in the future, (Scataglini, 2015) however at this point in time building an SOFC is not economically feasible.

When calculating costs for the mixed scenario, it was assumed that the cost factors for the equipment would stay the same, however, due to economies of scale, it is likely that making the equipment smaller would result in a higher cost per kWh biogas handled. For this reason, the economic evaluation of the mix case portrays the upper bound for the NPV, and as the mix case is always more expensive than implementing the full-sized upgrade technology, the mix case cannot be recommended.

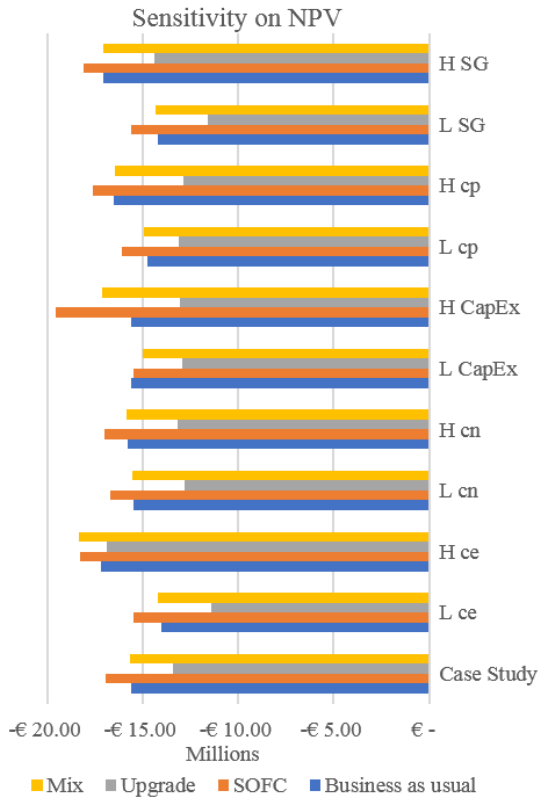

Figure 4. Sensitivity analysis on NPV for each scenario. H: higher. L: Lower. SG: Spark gap. CO2UC: CO2 unit cost. cn: Natural gas price. ce: Electricity price

5.3.2. Carbon price

As is apparent in Table 2 and Figure 4, an increase in the CO_2 price would benefit both the SOFC and upgrade scenario, as it decreases the net CO_2 expense. The SOFC decreases net carbon emissions by using the biogas to produced heat and electricity, thereby effectively displacing carbon emissions associated with importing electricity and natural gas for the boiler. The upgrade system decreases net carbon emissions by displacing natural gas from the buyer of biomethane. Implementing either of these technologies therefore represents an effective hedging against an increase in the carbon emissions tax.

5.3.3. Sensitivity on Scheduling

As is clear from Figure 2, the SOFC's heat and electricity output is significantly lower than the heat and electricity demand of the plant, and thus the optimal operating schedule for the SOFC is to convert all biogas available and import the residual demands from the grid. Therefore, the variable changes considered in the sensitivity analysis would not change the operating schedule.

Similarly, for the upgrade system, the model decides for all the available biogas to be upgraded to biomethane, as there is no benefit to flaring it, and thus the operating schedule for the upgrade system also stays constant throughout the sensitivity analysis. The only exception would be in the case

where natural gas became more expensive than biomethane: in that scenario biomethane would no longer be sold to the grid, instead it would displace the natural gas used on site in the boiler to satisfy the heat demand of the plant.

5.3.4. Investing in the upgrade technology

As biomethane can displace natural gas, the price of natural gas effectively becomes a price floor, and even in the unlikely case that biomethane should decrease in value by such a large amount (€0.054/kg to €0.032/kg), the NPV of the upgrade system is still better than that of the BAU: -€14.4m vs. -€15.6m. This is in part due to the savings achieved from carbon emissions reduction when selling biomethane, as this is independent of the biomethane price.

Considering the implementation of the upgrade pathway in the case study presented, the payback time is 2.69 years, and given the possibility of incentives for biomethane producers that may be implemented in the future, the advantages of the water scrubbing technology only become greater. It is however important to note that the cost of infrastructure that may be associated with selling biomethane to the grid has not been taken into consideration.

6. Conclusions

Through conducting a techno-economic evaluation comparing three biogas use pathways, including upgrade, SOFC and a mix of the two, it has been found that upgrading the biogas is the most favourable pathway for the SMAT WWTP.

The analysis was performed using a multi-period MILP model built in GAMS which minimises the EAC. The result of which shows that NPV is negative in all the scenarios: BAU: - € 15,635,230 SOFC is - €16,955,000; upgrade is - €13,415,800; mix is - €15,652,300.

When compared to the other cases, the upgrade scenario has the best NPV and maintains this advantage throughout sensitivity analysis where a range of important input variables were varied. This is in part due to its low operating costs and steady income generated through selling biomethane onto the grid.

The SOFC has the lowest total operating costs, however, it is less economically feasible than the other pathways due to the savings achieved being too small to justify its relatively high capital cost. The sensitivity analysis shows that its NPV can be improved if the capital expenditure decreases, electricity price decreases, or CO_2 price increases.

The mix case, which is a combination of the upgrade and SOFC, has an NPV mid-way between the other two cases. Additionally, sensitivity analysis shows that mix is always less economically favourable than full-sized upgrade therefore it is not recommended.

To investigate this research further, biomethane demand could be included in the model as there needs to be a market demand for the supply of upgraded biogas. Currently the time scale chosen is 1-day intervals however this could be reduced to smaller periods which would produce more detailed results and scheduling data.

With regards to scope and application, this study can be extended to WWTP across Europe, of which there are over 18,000. Specifically, it can be used to advise plant managers on future investment decisions involving biogas usage (Anon, 2017). The future work will also consider including incentives for biogas exploitation.

7. References

Angelidaki, I., Treu, L., Tsapekos, P., Luo, G., et al. (2018) Biogas upgrading and utilization: Current status and perspectives. *Biotechnology Advances*. [Online] 36 (2), 452–466. Available from: doi:10.1016/j.biotechadv.2018.01.011.

Anon (2017) *Europe's Wastewater in Numbers*. [Online]. 2017. Water World. Available from: https://www.waterworld.com/articles/wwi/print/volume-32/issue-6/technology-case-studies/analysis-europe-s-water-wastewater-in-numbers.html.

Bauer, F., Hulteberg, C., Persson, T. & Tamm, D. (2013) Biogas upgrading-Review of commercial technologies. *Swedish Gas Technology Centre, SGC*. [Online] 82. Available from: doi:SGC Rapport 2013:270.

Dunnett, A., Adjiman, C. & Shah, N. (2007) Biomass to heat supply chains applications of process optimization. *Process Safety and Environmental Protection*. [Online] 85 (5 B), 419–429. Available from: doi:10.1205/psep07022.

Eurostat (2018) *Electricity Prices Non-Household Consumers*. [Online]. 2018. Available from: http://appsso.eurostat.ec.europa.eu/nui/submitViewTableAction.do [Accessed: 7 November 2018].

Eurostat (n.d.) *Gas Prices for Non-household consumer*. [Online] Available from: http://appsso.eurostat.ec.europa.eu/nui/show.do?dataset=nrg_pc_203&lang=en.

Gandiglio, M., Drago, D. & Santarelli, M. (2016) Techno-economic Analysis of a Solid Oxide Fuel Cell Installation in a Biogas Plant Fed by Agricultural Residues and Comparison with Alternative Biogas Exploitation Paths. *Energy Procedia*. [Online] 101 (September), 1002–1009. Available from: doi:10.1016/j.egypro.2016.11.127.

Gao, Y., Gao, X. & Zhang, X. (2017) The 2 °C

Global Temperature Target and the Evolution of the Long-Term Goal of Addressing Climate Change—From the United Nations Framework Convention on Climate Change to the Paris Agreement. *Engineering*. [Online] 3 (2), 272–278. Available from: doi:10.1016/J.ENG.2017.01.022.

Giarola, S., Forte, O., Lanzini, A., Gandiglio, M., et al. (2018) Techno-economic assessment of biogas-fed solid oxide fuel cell combined heat and power system at industrial scale. *Applied Energy*. [Online] 211 (September 2017), 689–704. Available from: doi:10.1016/j.apenergy.2017.11.029.

Gsr, G.F.R. (2017) *Gfr gsr*.

Lombardi, L., Carnevale, E.A. & Corti, A. (2015) Comparison of different biological treatment scenarios for the organic fraction of municipal solid waste. *International Journal of Environmental Science and Technology*. [Online] 12 (1), 1–14. Available from: doi:10.1007/s13762-013-0421-y.

Magli, F., Capra, F., Gatti, M. & Martelli, E. (2018) Process selection, modelling and optimization of a water scrubbing process for energy-self-sufficient biogas upgrading plants. *Sustainable Energy Technologies and Assessments*. [Online] 27 (February), 63–73. Available from: doi:10.1016/j.seta.2018.02.001.

MosayebNezhad, M., Mehr, A.S., Gandiglio, M., Lanzini, A., et al. (2018) Techno-economic assessment of biogas-fed CHP hybrid systems in a real wastewater treatment plant. *Applied Thermal Engineering*. [Online] 129, 1263–1280. Available from: doi:10.1016/j.applthermaleng.2017.10.115.

Scataglini, R. (2015) *A Total Cost of Ownership Model for Solid Oxide Fuel Cells in Combined Heat and Power and Power-Only Applications*. (September), 6–11.

SMAT (n.d.) *Societ metropolitana acque torino S.p.A*. [Online]. Available from: https://www.smatorino.it/ [Accessed: 6 November 2018].

Sun, Q., Li, H., Yan, J., Liu, L., et al. (2015) Selection of appropriate biogas upgrading technology-a review of biogas cleaning, upgrading and utilisation. *Renewable and Sustainable Energy Reviews*. [Online] 51, 521–532. Available from: doi:10.1016/j.rser.2015.06.029.

Ullah Khan, I., Hafiz Dzarfan Othman, M., Hashim, H., Matsuura, T., et al. (2017) Biogas as a renewable energy fuel – A review of biogas upgrading, utilisation and storage. *Energy Conversion and Management*. [Online] 150 (May), 277–294. Available from: doi:10.1016/j.enconman.2017.08.035.

Appendix – A

Supplementary modelling input data (Giarola *et al.*, 2018)

Parameter	Unit	Value
BM_p	€/kWh	0.056
BM_{slip}	%	1
BGD_{abs}	kWh_f/h	17.09
BGS_{abs}	kWh_f/h	17.09
BGf_t	kWh_b/day	varies daily
CFC	%	33
$CapExCF$	€/kWh	799
ce_{in}	€/kWh_e	0.1468
ce_{out}	€/kWh_e	0.1468
cn	€/kWh_f	0.032
cp	€/kg	0.016
DTL_t	kWh	varies daily
ee	$kgCO_2$/kWh_e	0.508502
$ei1$	kWh_e/kWh_f	0.0018
$ei2$	kWh_e/kWh_f	0.0227
η^b	kWh_h/kWh_f	0.85
η^{FC}	kWh_e/kWh_b	0.538
η^{th}	kWh_h/kWh_b	0.2734
MH	hours	24
$OpExCF$	€/kWh	0.0047
PSD_{abs}	kWe/h	5
PSU_{abs}	kWe/h	40
$PlantEl_t$	kWh_e/day	21633
$Pnom$	kWh_e/h	174.9
$discount\ rate$	%	3.5
r_{up}	kWh_e	40
$UCCc$	€/kW	917
$UCCf$	€/kW	8303
$UCCstack$	€/kW	1223
UMC	€/kW	72
UOC	€/kW	76
yr	days per year	365

Simulating Fluid Adsorption on a Heterogeneous Surface

Dora Olah and Weilun Xu

December 2018

Abstract

Adsorption of fluid molecules on solid surfaces is a well-known phenomena which is often studied by using molecular simulation methods such as Grand Canonical Monte Carlo or Molecular Dynamics. The two most common approaches in these computational simulations are the explicit wall approach (whereby interactions between every fluid and solid molecule are calculated separately, thus making the simulation lengthy and computationally intensive) or the continuum wall approach (in which the solid surface is considered as one 'bulk' entity, and only one interaction between solid and fluid is calculated). The simulations using the explicit wall model can become immensely complicated once heterogeneity is introduced to the solid surface. In this research, fluid adsorption on a solid surface with clustered heterogeneity is investigated using both the explicit and the continuum wall approach. It is shown that the results of the explicit wall method can be closely estimated via interpolation from the continuum wall method, which significantly reduces the required computations. The model system to verify the hypothesis was chosen to be methane adsorption on a graphite surface, simulated with Grand Canonical Monte Carlo molecular simulations. Heterogeneity was introduced as a circular region of carbon atoms with altered methane-carbon interaction in the middle of the first layer of the graphite surface. The interaction between fluid and solid particles is governed by the Lennard-Jones (12-6) pair potential.

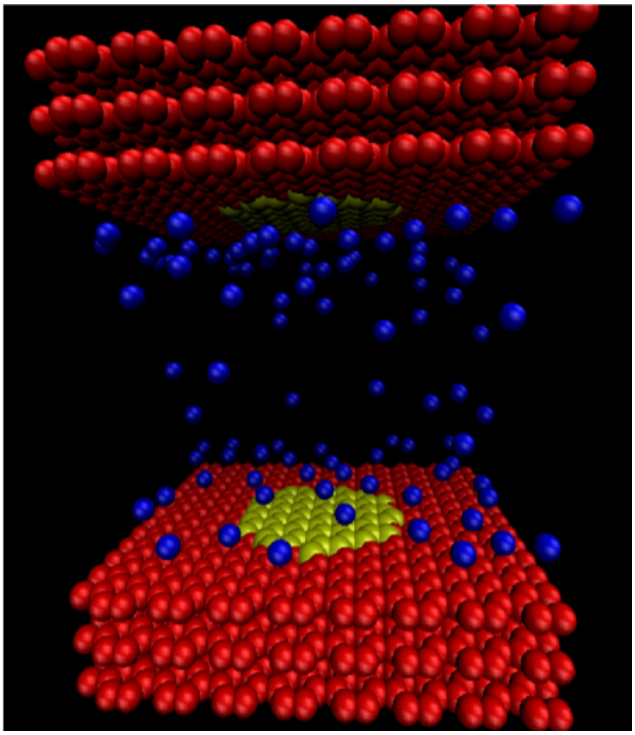

Figure 1: Schematic representation of the model system used to simulate adsorption of methane on a graphite surface: methane (blue spheres), carbon with $\varepsilon_{C-M}k_B^{-1} = 64.374\ K$ (red spheres) and carbon with $\varepsilon_{DC-M}k_B^{-1} = 96.561\ K$ (yellow spheres).

1 Introduction

Fluid adsorption on solid surfaces has gained significant research interest due to its many real-life applications. It appears in a wide range of industries including waste water treatment, gas storage (Zhao & Johnson 2005) and pharmaceutical production (Franz et al. 2000). Due to the large market for utilising fluid adsorption for industrial purposes, developing accurate models is essential.

Two notable adsorption models made significant improvements to the theoretical descriptions in the early 20th century: Polanyi's potential theory (1914, 1963) and Langmuir's adsorption model (1918). Polanyi's theory was based on the assumption that the gas adsorption on solid surface is a result of an attractive force derived from the potential, which depends only on the spatial position of the gas molecule and is independent of any other molecules. On the other hand, Langmuir explained adsorption using experimental results, and claimed - among others - that adsorbed layers have a maximum thickness of one molecule. Both scientists developed a set of equations to support

their respective models.

Their equations, however, are no longer used for real-life situations, as it was shown that they are unable to precisely predict the behaviour of complex surfaces. This is inevitable, given that systems involving complexities, like heterogeneous solid surfaces, are vastly different from the assumptions behind the classic models - these usually assumed smooth surfaces (Tracey et al. 2013). Hence, in order to predict fluid adsorption on complex surfaces at an accurate level, adjustments to the classic adsorption theories needed to be made.

Attempts to reproduce experimental adsorption results or to produce temperature-dependent parameters have largely been unsuccessful (D. Do & D. Do 2005), which is due to the lack of understanding of the effect of temperature in fluid - solid interactions. As a result, using effective potentials is favoured and there has been extensive research on using an average free energy to describe effective potentials (Onsager (1933), Rushbrooke (1940)). This effective potential is often called free-energy-averaged potential, as it is developed by matching the partition function of the explicit wall to that of the continuum wall.

This paper presents an insight into fluid adsorption on solid surface with clustered circular heterogeneity on the first layer from both an explicit and a continuum approach. It also investigates the feasibility to use the interpolation of the free-energy-averaged potential as an estimate for the explicit adsorption model, and thus make the computation of the adsorption isotherms at various heterogeneity sizes significantly easier.

2 Methodology

2.1 Lennard-Jones potential

The interaction between the fluid and solid molecules is described by Lennard-Jones (12,6) potential, which is a widely used potential model to simulate adsorption due to its simplicity (Galindo 2016). As it can be seen from Figure 2, the Lennard-Jones potential is infinite at short distances (due to the Pauli exclusion principle) and converges to zero at large distances (due to the short range of the attractive forces between molecules). It reaches a minimum at precisely r_m where the potential is $V = -\varepsilon$.

The Lennard-Jones (12,6) potential can be described with the following expression:

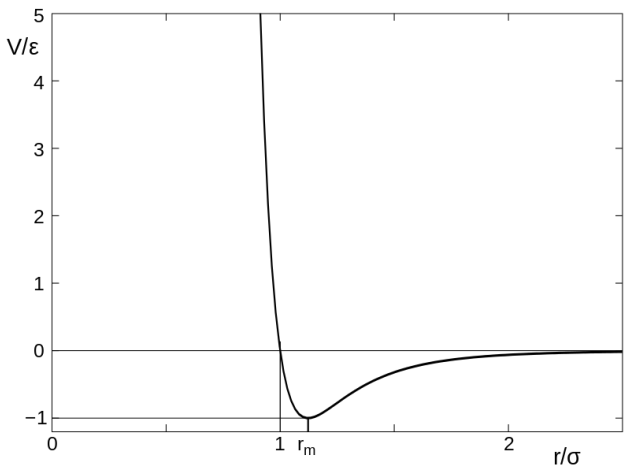

Figure 2: Graph of the potential *versus* separation between two molecules using the Lennard-Jones (12,6) potential as defined by Equation 1. [Image source: Olaf Lenz (2007)]

$$V_{LJ} = 4\varepsilon \left[\left(\frac{\sigma}{r}\right)^{12} - \left(\frac{\sigma}{r}\right)^{6} \right] \tag{1}$$

where r is the separation between the particles, σ is the finite distance where the interaction between particles is zero and ε is the depth of the potential well.

In the simulations presented in this paper, modification of the ε parameter in the Lennard-Jones potential was chosen to introduce the heterogeneity on the solid surface. The parameter $\varepsilon_{S-F} k_B^{-1}$ (the force between solid and fluid normalised with the Boltzmann factor) was increased to 150% of the base case of solid-fluid interactions when modeling the clustered heterogeneity on the surface.

2.2 Explicit description

The atomistic discrete description of the solid surface was studied first (Figure 3). Using this model, every interaction between every fluid and solid molecule is calculated separately. On the one hand, this gives a detailed view of the system and allows for more precise calculation. On the other hand, this approach requires a significant amount of computational power, especially as the pressure (and the number of molecules in the system) increases.

2.3 Free energy mapping

To reduce the complexity of the solid-fluid adsorption system, it is common practice to use free energy mapping instead of the explicit description

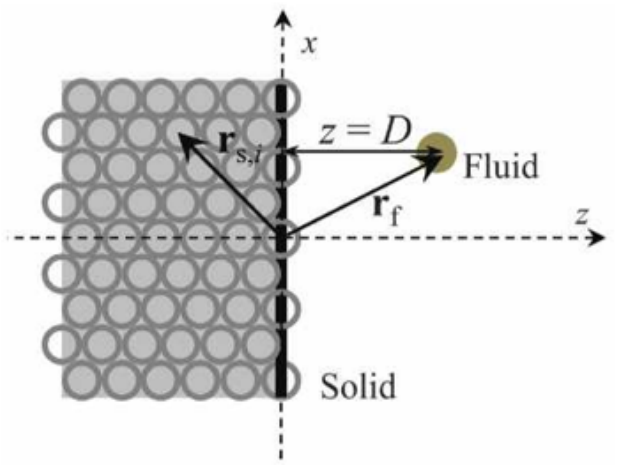

Figure 3: Schematic of the relative positions between an adsorbed fluid molecule and a given particle in the solid. The fluid particle is shown at a distance $z = D$ from the solid surface. [Image source: Forte et al. (2014)]

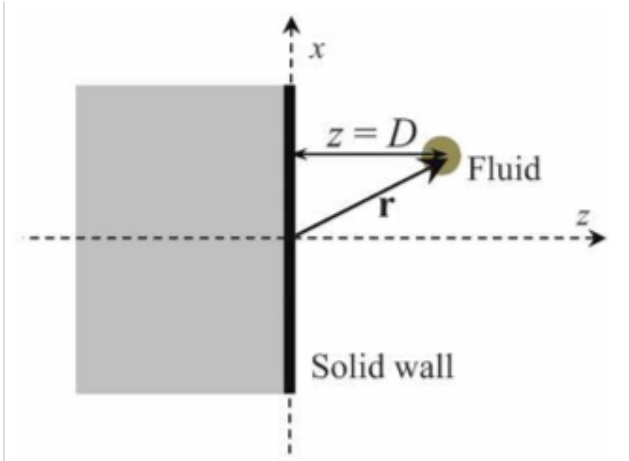

Figure 4: Schematic of the relative positions between an adsorbed fluid molecule and a continuum solid surface or wall. The fluid particle is shown at a distance $z = D$ from the wall. [Image source: Forte et al. (2014)]

of the solid wall (Forte et al. 2014). When using the free energy mapping, the surface can be treated as one unit and can be represented as a coarse-grained continuous wall (Figure 4), thereby greatly reducing the number of calculations required to simulate the adsorption of fluid particles.

The free energy mapping is performed by equating the partition functions of the explicit and continuous models at a certain fluid-solid distance ($z = D$ on Figures 3 and 4). The derivation (described in detail in Forte et al. (2014)) results in an expression for the free-energy-averaged potential as follows:

$$w(D) = (-k_B T)\, ln\langle exp\left[-\frac{1}{k_B T}U(D)\right]\rangle \qquad (2)$$

where $w(D)$ is the effective interaction at distance $z = D$, k_B is the Boltzmann factor, T is the temperature and $U(D)$ is the interaction energy at that distance. The free energy mapping therefore takes the average potential between a single fluid particle and all discrete solid particles to produce a coarse-grained potential.

2.4 Grand Canonical Monte Carlo

To simulate the adsorption for both the explicit and the continuous wall method, Grand Canonical Monte Carlo (GCMC) molecular simulation was used (Frenkel & Smit 2001). This yields the average molecular density under the conditions of fixed chemical potential, volume and temperature; also known as the grand canonical or μVT ensemble.

The basis of every Monte Carlo method is repeated random sampling. In this paper, GCMC molecular simulations were used with the Metropolis Algorithm, in which random sampling occurs in the form of 'moves'. A move is an attempt at translation (displacement to a random location), insertion (generation at a random location) or deletion (elimination at a random location) of a randomly selected molecule. After the attempt, the new system energy is calculated, and compared with the previous system energy to decide whether to accept or reject the move. The simplified description of the Metropolis Algorithm for the case of translational moves can be seen on Figure 5.

2.5 Simulation details

Simulation parameter	Value
Number of moves per cycle	250
Number of equilibration cycles	50,000
Number of production cycles	50,000
Number of averaged cycles	12,500
Temperature	273 K

Table 1: Simulation parameters for the GCMC molecular simulation demonstrated in the present paper.

In the research presented here, GCMC molecu-

1. Select a fluid particle at random and calculate its energy: $\mathbf{U(old)}$
2. Randomly displace this particle and calculate the new energy: $\mathbf{U(new)}$
3. Accept the move with the following probability:

$$\mathbf{acc(o \rightarrow n) = min\left(1, exp\left\{-\frac{1}{k_B T}\left[U(n) - U(o)\right]\right\}\right)}$$

Figure 5: Metropolis Algorithm for GCMC molecular simulations.

lar simulation was carried out to simulate adsorption of fluid molecules on a solid surface containing clustered heterogeneity. A summary of the simulation parameters can be seen in Table 1. Each cycle consisted of 250 moves (equal preference to translation, insertion and deletion). The system was left to converge to a stable state for 50,000 equilibration cycles, then data was collected in 50,000 production cycles. The latter was grouped into four blocks (each with 12,500 cycles) and averages were taken over these groups first, before an overall average was calculated for the four values. This allowed the calculation of errors in the simulation which was used to quantify the uncertainty of the results.

2.6 Model system

A model system was chosen to aid the investigation of adsorption of fluid molecules on a heterogeneous solid surface. The system allowed for realistic parameters to be used in the simulation and thus made the results easier to interpret. The exemplar system of methane adsorption on graphite surface was selected to reduce the complexity of the simulation, as this fluid-solid pair is a commonly used model for such simulations. The solid system in the present research comprises of six graphene layers: three-three layers symmetrically arranged with an enclosed distance of about 30 Å.

Three cases were simulated using the methodology described above (a summary of these cases can be found in Table 3). The first case was the lower baseline model with the carbon atoms in the graphite surface behaving homogeneously. For this case, a $\varepsilon_{C-M}k_B^{-1}$ value of 64.374 K was selected. The second case was the upper baseline in which the carbon atoms were again homogeneous, but the $\varepsilon_{C-M}k_B^{-1}$ parameter was increased to 150% of the lower baseline, to 96.561 K. The surface heterogeneity was introduced in the third case, in the form of two circular clusters located at each end of the enclosure at the centre of the first layer. The modified atoms had $\varepsilon_{C-M}k_B^{-1}$ parameter corresponding to Case 2, while the surrounding carbon atoms followed the lower baseline with $\varepsilon_{C-M}k_B^{-1}$ equal to that of Case 1.

Model parameter	Value
σ_{C-M}	3.565 Å
Number of carbon atoms in Cases 1 and 2	2496
Number of carbon atoms with $\varepsilon_{C-M}k_B^{-1} = 64.374$ K in Case 3	2362
Number of carbon atoms with $\varepsilon_{DC-M}k_B^{-1} = 96.561$ K in Case 3	134
Simulation frame x dimension	31.98 Å
Simulation frame y dimension	34.0806 Å
Simulation frame z dimension	43.2 Å

Table 2: Model parameters for the GCMC molecular simulation demonstrated in the present paper.

In this paper, only the modification of $\varepsilon_{C-M}k_B^{-1}$ was investigated, while other parameters of the model system were constant throughout all three cases. A summary of these parameters can be seen in Table 2. The total number of carbon atoms in the graphite layers were 2496. For the heterogeneous Case 3, 134 carbon atoms were increased to 150% $\varepsilon_{C-M}k_B^{-1}$ value, while the remaining 2362 were at the lower value. This equals to 5.37% of the total carbon atoms being modified, or 16.11% of the top layer (as the heterogeneous cluster was restricted to the first layer). The temperature was chosen to be 273 K to ensure that methane is in supercritical state, therefore eliminating the complexity of a possible phase change.

3 Results and Discussion

3.1 Explicit wall

3.1.1 Fluid density profiles

Firstly, simulation of methane adsorption on a graphite surface was carried out using the explicit

Case 1	Case 2	Case 3
$\varepsilon_{C-M}k_B^{-1} = 64.374\ K$	$\varepsilon_{C-M}k_B^{-1} = 96.561\ K$	$\varepsilon_{C-M}k_B^{-1} = 64.374\ K$ $\varepsilon_{DC-M}k_B^{-1} = 96.561\ K$
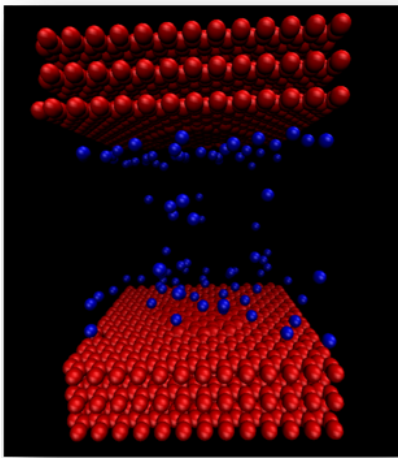	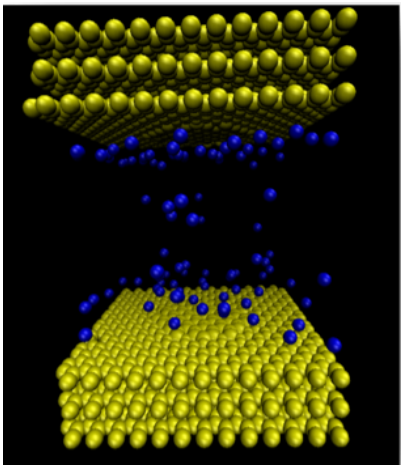	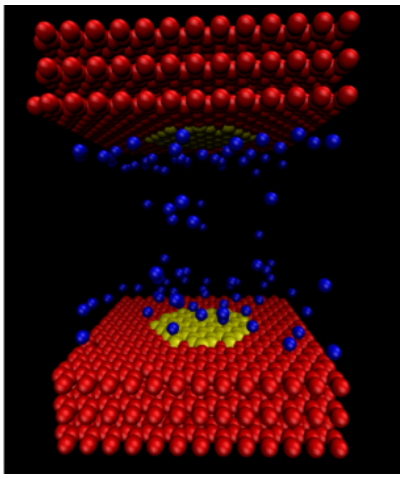

Table 3: The three cases presented in the paper. The index 'C-M' corresponds to carbon - methane, 'DC-M' corresponds to defect carbon - methane. On the graphical representations, red spheres indicate the baseline carbon, yellow spheres indicate the carbon with modified C-M interaction and blue spheres indicate methane. The colour code in the first row corresponds to the colours on Figures 6 – 10.

wall approach described in Section 2.2. In this case, the interaction of every methane molecule with every carbon atom is calculated. This approach allows for a more accurate result, however, it results in a longer simulation time.

Fluid density profiles for the explicit wall approach were obtained at thirty different pressure values ranging from close to 0 Pa to $326,500\ kPa$ (selected ones are shown on Figure 6). As described in Section 2.6, the only modified parameter was the minimum potential in the Lennard-Jones interaction, $\varepsilon_{C-M}k_B^{-1}$. It is immediately visible that all graphs are symmetric. This is due to the arrangement of the graphite layers – symmetrical on the two ends of the simulation frame with an enclosed distance of about 30 Å.

At low pressures, there is nearly negligible adsorption in all three cases due to the small number of methane molecules present in the system. At 0.922 kPa, Case 2 shows relatively high adsorption compared to the other two cases; but in absolute terms, all three cases have low number density values (as shown on Figure 6(a)). It can also be noted that the uncertainty of the data is moderately high at low pressures, which can be improved with more simulation cycles to allow for longer equilibration period.

At medium pressure, there is improved adsorption in all cases. As the pressure increases to 795.4 kPa (Figure 6(b)), the adsorption at the first layer adjacent to the solid surface is the most significant, with the Case 2 adsorption dominating over the other two cases. However, at this pressure, a second layer of adsorption also appears at around ± 8 Å position, which can be explained by the increased number of molecules present in the system. As it can be seen on Figure 6(b), the uncertainty at this pressure decreases significantly compared to Figure 6(a).

As the pressure increases to the 10 MPa order of magnitude, second and third layers of adsorption are clearly observable. Figure 6(c) shows the results of the simulation at $12,790\ kPa$: at this pressure the dominance of Case 2 decreases on the first layer, directly on the solid surface. This can be explained by the fact that at moderate pressures ($100 - 1000\ kPa$), the increased potential of Case 2 has a large relative contribution to the factors affecting adsorption. This is contrasted by higher (and very low) pressures, where the number of molecules have the dominating contribution. On Figure 6(c) it can be seen that the difference between the cases at the peak decreases significantly compared to that of Figure 6(b).

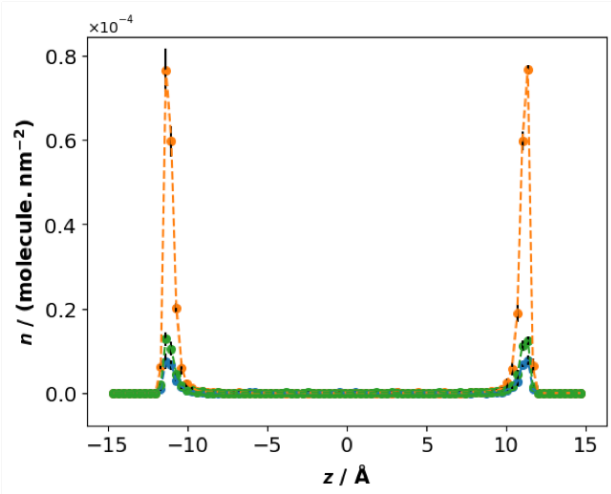

(a) P = 0.922 kPa

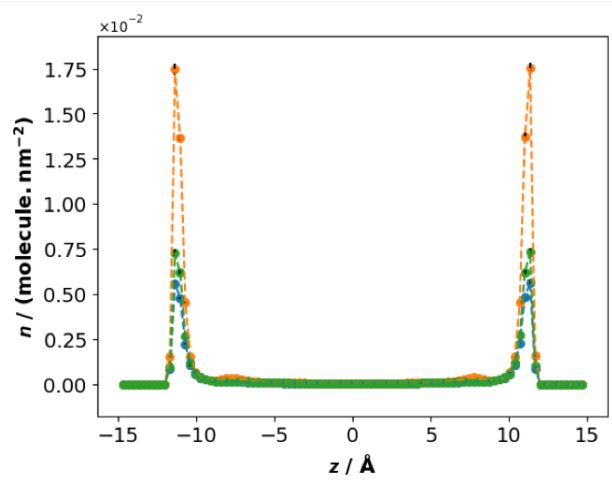

(b) P = 795.4 kPa

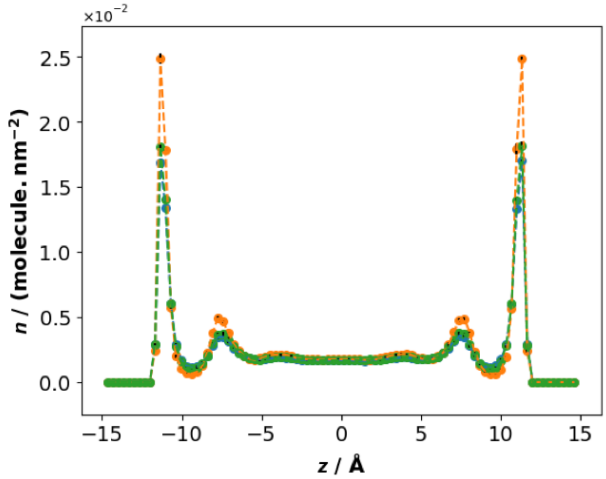

(c) P = 12,790 kPa

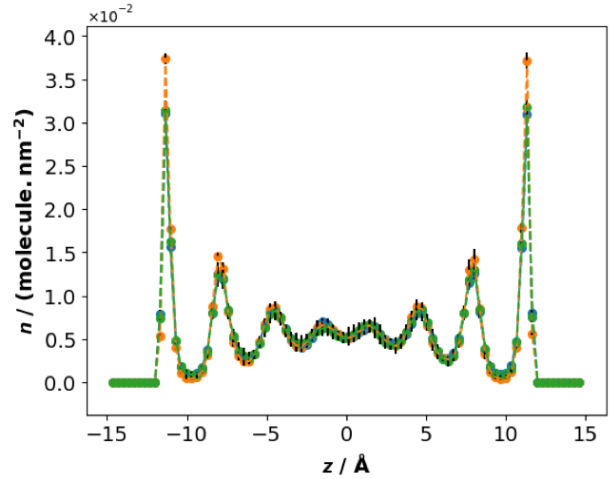

(d) P = 326,500 kPa

Figure 6: Density of adsorbed methane per unit area on graphite *versus* position at different pressures. Temperature $T = 273K$. The symbols correspond to the cases described in Table 3: Case 1 (blue), Case 2 (orange), Case 3 (green).

At very high pressures (in the $100,000\ kPa$ magnitude) the dense fluid state is becoming solid-like, as seen on Figure 6(d), simulated at $326,500\ kPa$. The differences between the three cases become nearly negligible, as the adsorption is less dependent on the respective potentials of the solid wall atoms, and almost solely depend on the large number of methane molecules in the system. This results in orderly peaks, corresponding to the methane molecule diameters. The uncertainty between −5 Å and +5 Å increases significantly.

3.1.2 Adsorption isotherm

The adsorption isotherm shown on Figure 7 was obtained using the explicit wall approach described in Section 2.2. Each set of three points at a given pressure corresponds to a separate fluid density profile mentioned in Section 3.1.1. The adsorption isotherm shows expected behavior: at low and high pressures the three cases are nearly identical, whereas in the middle region (100 kPa to 1 MPa), Case 2 dominates over the other two cases. As explained previously, this is due to the fact that it is only in this pressure region that the solid-fluid potential is a significant contributing factor in the adsorption. At low and high pressures, the contribution related to the number of fluid molecules (low and high, respectively) dominates over the potential difference.

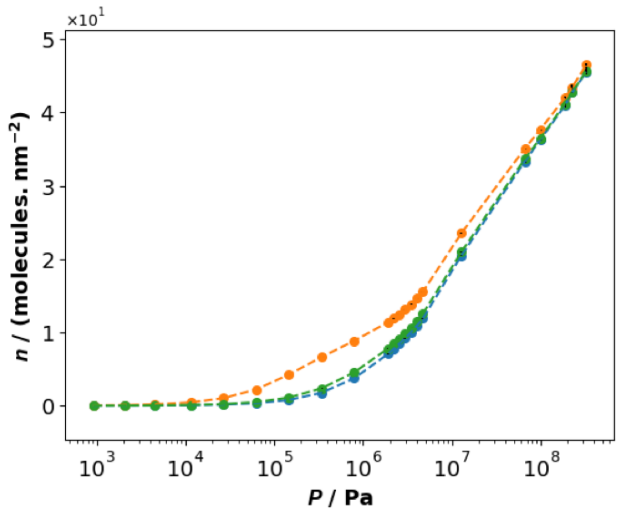

Figure 7: Density of adsorbed methane per unit area on graphite *versus* pressure at a temperature T = 273 K. The symbols correspond to the cases described in Table 3: Case 1 (blue), Case 2 (orange), Case 3 (green).

3.2 Continuum wall

The free-energy-averaged potential was obtained using the continuum wall approach described in Section 2.3. The result is shown on Figure 8. The shape of the graph follows that of the Lennard-Jones potential shown on Figure 2. The main difference between the Lennard-Jones potential and the free-energy-averaged potential shown here is that the latter is symmetric around $z = 0$ Å, whereby the Lennard-Jones potential is not. This comes from the present simulation geometry: two graphite layers surrounding the simulation frame where the methane molecules exist. As a consequence of this, the free-energy-averaged potential graph is not given in terms of distance from the surface (the standard way of describing the Lennard-Jones potential), but rather as the distance between the two surfaces, where one is at −15Å and the other is at +15Å.

3.3 Interpolation

The hypothesis of this study was that by interpolating the free-energy-averaged potential, one can determine the adsorption isotherm of the same system without the need for computational simulation. To verify this hypothesis, an interpolation was performed at the minimum value of the free-energy-averaged potential (shown on Figure 9). Linear combination was assumed to simplify the calculations.

The result obtained from the interpolation means that Case 3 (the heterogeneous case) was decomposed into a linear combination of 76.28% Case 1 (lower baseline with $\varepsilon_{C-M}k_B^{-1} = 64.374\ K$) and 23.72% Case 2 (upper baseline with $\varepsilon_{C-M}k_B^{-1} = 96.561\ K$).

Subsequently, the linear decomposition of Case 3 was used to re-calculate the adsorption isotherm values. The percentages obtained in the previous step were used to calculate Case 3 as a linear combination of Cases 1 and 2 on the adsorption isotherm at $T = 273\ K$ and the result is shown on Figure 10. It is clear to see from the up-scaled graph on Figure 10(b) that the interpolated values are in close agreement with the data obtained from the explicit wall simulation.

It is interesting to note that even though it would be intuitive to think that this interpolated percentage would equal to the fractional heterogeneity on the surface, it is not the case. While purely based on the number of heterogeneous atoms with 150% of the baseline potential the ratio of Case 1 to Case 2 type atoms in the first graphite layer is 83.89 to 16.11 (as shown in Section 2.6), the interpolation gave a result of 76.28 to 23.72. This discrepancy can be explained by the fact that adsorption not only depends on the number of modified atoms, but also on a range of other factors (such as the geometry of the heterogeneity or the factor by which the selected Lennard-Jones parameter was increased.) Therefore, the adsorption isotherm could not have been reproduced using only the number or the surface area of the modified atoms, the extra step involving the interpolation of the free-energy-averaged potential is also necessary.

The verified hypothesis, that interpolation of the free-energy-averaged potential can be used to approximate the explicit model, has important consequences. The previously described method in Section 3.1.2 used to simulate Case 3 directly using GCMC molecular simulations for the adsorption isotherm is a computationally intensive method due to the required calculation of every interaction between each pair of molecules separately. In contrast, simulating free-energy-averaged potential is a quick method, as it uses a largely simplified model of the adsorption system. It is shown that a possible way to speed up calculations and decrease computational efforts is to first simulate the two baselines (upper and lower baseline, corresponding to homogeneous surfaces) using the explicit wall method, then simulate the

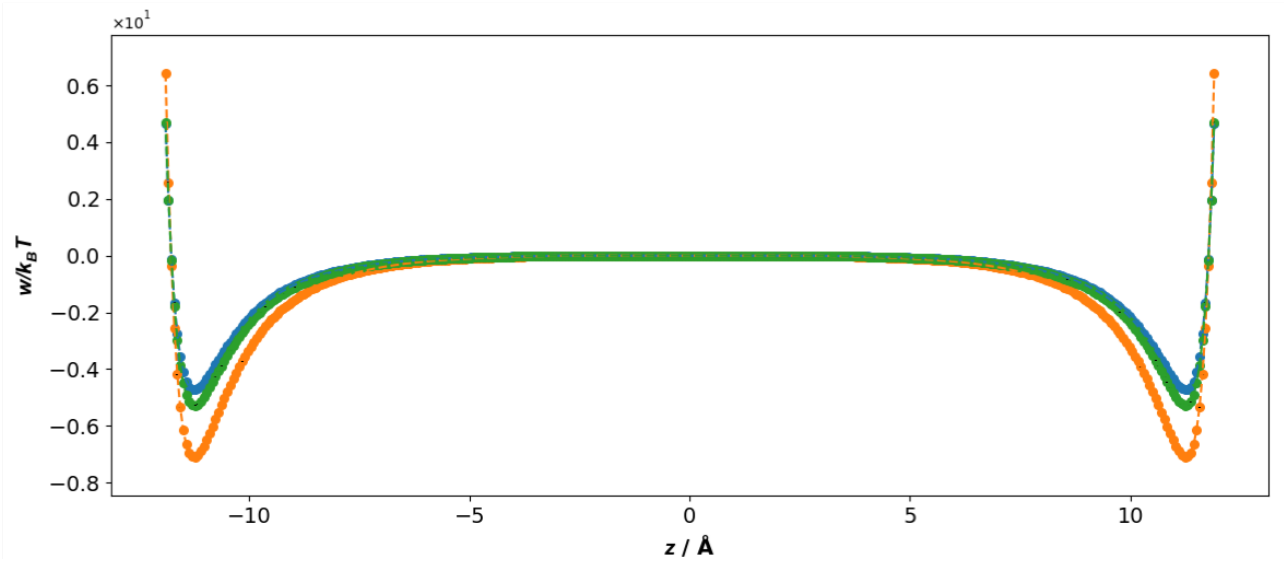

Figure 8: Effective fluid-surface potential as a function of the distance to the surface for the adsorption of methane on graphite surface. The symbols correspond to the cases described in Table 3: Case 1 (blue), Case 2 (orange), Case 3 (green).

free-energy-averaged potential of the same system and any heterogeneous combination required. Using the results of the latter and the interpolation method described here, the adsorption isotherm for all heterogeneous combinations can be then calculated using the existing baselines and the interpolated values from the free-energy-averaged potential.

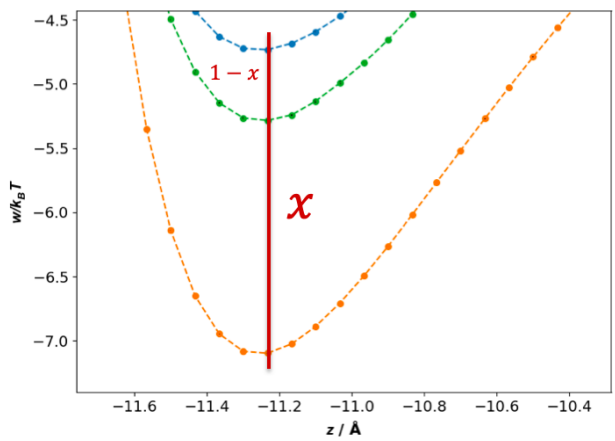

Figure 9: Interpolation from the minimum value of the free-energy-averaged potential. Result of the calculation: $x = 76.28\%$

4 Conclusions

In this paper, explicit wall and continuum wall descriptions of fluid adsorption on solid surface were simulated using Grand Canonical Monte Carlo molecular simulations. A model system comprising of methane and six graphene layers (three-three layers symmetrically arranged) was used to verify the hypothesis and demonstrate the results. Fluid density profiles were obtained at 30 different pressures and subsequently, the adsorption isotherm at $T = 273\ K$ was calculated using the results from the explicit wall approach. The free-energy-averaged potential using the continuum wall description for the adsorption was also simulated, and it was found that it follows the Lennard-Jones potential.

It was found that linear interpolation of the free-energy-averaged potential gives a good estimation for the explicit wall adsorption isotherm while significantly reducing the computational intensity of the task. Using this estimation can speed up simulations: after obtaining the two baseline cases, any other combination of them can simply be calculated with the free-energy mapping. These results can be useful for industrial applications where precision is of secondary importance to speed and computational efforts.

Further areas of research interest regarding the hypothesis described in this paper would be to look at the effect of different types of defects. In this paper only the Lennard-Jones parameter of the depth of the potential well (ε) was modified as a way of simulating clustered heterogeneity on the surface, but another approach would be to modify the finite distance where the interaction between particles is zero (σ). Another arising re-

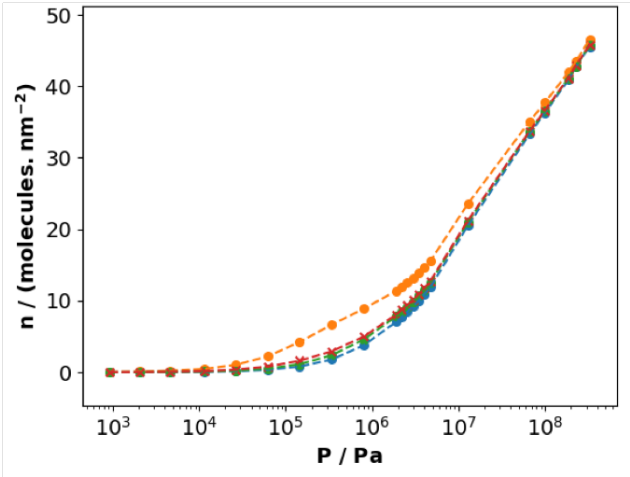

(a) Adsorption isotherm, full-scale

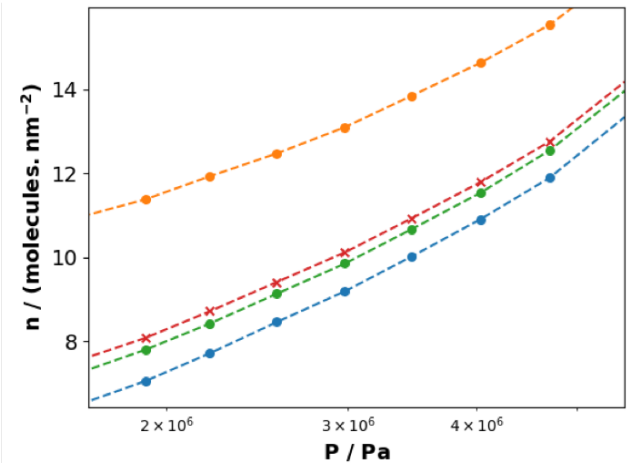

(b) Adsorption isotherm, narrow-scale

Figure 10: Density of adsorbed methane per unit area on graphite *versus* pressure at a temperature $T = 273\ K$. The symbols correspond to the cases described in Table 3: Case 1 (blue), Case 2 (orange), Case 3 (green). Interpolated values using the free-energy-averaged potential are denoted by red crosses.

search question is the validity of these results for the cases of different heterogeneity geometries. In the present research, only circular heterogeneity was considered, but in the future other geometries (such as dome shape affecting several graphene layers or stripes across the top layer) could be investigated. Furthermore, it is assumed that these results are universal, that is, they do not depend on the chosen model system. However, it would be important to verify the interpolation method using other model systems (such as carbon dioxide adsorption in carbonate reservoirs).

5 Acknowledgements

The authors would like to express their gratitude to Dr Srikanth Ravipati for the GCMC code-base and his technical support and the Department of Chemical Engineering at Imperial College London for the computational facilities.

References

D. Do, D. & D. Do, H. (2005), 'Effects of surface heterogeneity on the adsorption of nitrogen on graphitized thermal carbon black', *Molecular Simulation* **31**.

Forte, E., Haslam, A. J., Jackson, G. & Müller, E. A. (2014), 'Effective coarse-grained solid–fluid potentials and their application to model adsorption of fluids on heterogeneous surfaces', *Physical Chemistry Chemical Physics* **16**(36), 19165–19180.

Franz, M., Arafat, H. A. & Pinto, N. G. (2000), 'Effect of chemical surface heterogeneity on the adsorption mechanism of dissolved aromatics on activated carbon', *Carbon* **38**(13), 1807–1819.

Frenkel, D. & Smit, B. (2001), *Understanding molecular simulation: from algorithms to applications*, Vol. 1, Elsevier.

Galindo, A. (2016), 'Thermodynamics 2 lecture notes'.

Langmuir, I. (1918), 'The adsorption of gases on plane surfaces of glass, mica and platinum', *The Research Laboratory of The General Electric Company* **40**, 1361–1402.

Olaf Lenz, R. (2007), '12-6 lennard-jones potential'. [Online; accessed December 12, 2018]. **URL:** *https://commons.wikimedia.org/wiki/File:12-6-Lennard-Jones-Potential.svg*

Onsager, L. (1933), 'Theories of concentrated electrolytes.', *Chemical Reviews* **13**(1), 73–89.

Polanyi, M. (1914), *Verh. Dtsch. Phys. Ges.* **16**(1012).

Polanyi, M. (1963), 'The potential theory of adsorption', *Science* **141**(3585), 1010–1013.

Rushbrooke, G. (1940), 'On the statistical mechanics of assemblies whose energy-levels depend on the temperature', *Transactions of the Faraday Society* **36**, 1055–1062.

Tracey, D., Delley, B., McKenzie, D. & Warschkow, O. (2013), 'Molecular adsorption on silicon (001): A systematic evaluation of size effects in slab and cluster models', *AIP Advances* **3**(4), 042117.

Zhao, X. & Johnson, J. K. (2005), 'An effective potential for adsorption of polar molecules on graphite', *Molecular Simulation* **31**(1), 1–10.

New insights into mechanically-assisted and mechano-catalysed reactions using Kraft lignin

Elise Shui and John Young
Department of Chemical Engineering, Imperial College London, U.K.

Abstract

Kraft lignin is a product of the Kraft paper pulping process. It is extracted as a recalcitrant material, exceptionally resistant to further change because of the harsh alkaline conditions in this process. However, lignin is a highly aromatic material and contains many valuable aromatic monomers, making its depolymerisation an attractive prospect. High energy mill impacts, such as in ball-milling, provide the mechanical forces needed to catalyse solid-state depolymerisation reactions in biomass. This opens a pathway towards a solvent-free process, greatly reducing the mass intensity and energy required. However, the variables and mechanisms driving mechano-catalysis are not well understood. Herein, mechano-catalysis is applied to Kraft lignin. The product of milling Kraft lignin with para-toluenesulfonic acid (p-TSA) and sodium percarbonate is strongly dependent on the energy transferred via ball impacts in the system, whilst the product of milling Kraft lignin with sodium hydroxide is not. Nevertheless, it is shown that the latter system can still be correlated to the process variables studied, suggesting a difference in reaction mechanisms between Kraft lignin and the three catalysts. This difference can be explained by defining mechano-catalysis and mechanically-assisted reactions. Separating these definitions gives a better understanding of the driving force behind the processes, leading to the potential of further optimisation. Studies of mechanically-assisted processes should aim to optimise mixing in the ball-mill, whilst studies of mechano-catalytic processes should aim to optimise the utilisation of impact force for the chemical process.

Introduction

Lignin is a polymer found in plant and some algae cells. It is isolated as a by-product of the Kraft process in the form of Kraft lignin, of which ca. 45 million tons (Hu, 2002) are produced annually. Currently, Kraft lignin is utilised in a waste-to-energy system to make the process more energy efficient (Garoff, 2014). However, effective depolymerisation holds the potential to produce high value chemicals.

In the past, it has been reported that the depolymerisation of lignin is commonly limited by condensation of the products. However, alongside Kraft lignin depolymerisation, the inducing of further condensation reactions to create higher molecular weight polymers may also add value. Demand for high molecular weight lignin polymers is increasing with applications such as adhesives and carbon fibres (Sadeghifar, et al., 2016).

One route to investigate in the search for the depolymerisation or repolymerisation of Kraft lignin is mechanochemistry. This offers a solvent-free avenue. Removing the requirement of a solvent makes this an environmentally appealing pathway as it would lead to significant reductions in mass intensity.

Mechanochemistry is a branch of chemistry studying the use of mechanical forces to drive reactions using kinetic energy. By subjecting Kraft lignin to mechanically-assisted or mechano-catalysed reactions, depolymerisation, repolymerisation or even both processes may occur. A ball mill is often adopted for mechanochemistry, as demonstrated in previous reports studying the depolymerisation of other lignins through grinding with it a catalyst (Kleine, et al., 2013). The first step in assessing the potential effectiveness of ball milling in the treatment of Kraft lignin is to explore the effects of different catalysts. Once this has been established, process variables will be investigated allowing for optimisation of the process.

One eventual goal is to obtain a product consisting of many individual low molar mass aromatic monomers that could be further refined to extract valuable chemicals. These include platform chemicals to agrochemicals, speciality chemicals, and pharmaceuticals. Finally, if non-depolymerised larger molar mass materials remain, they could be burnt in a waste-to-energy system. If successful, this highlights the potential of Kraft lignin to be a more valuable resource than it is currently considered and that it may play a role in a more sustainable future.

Background

In the production of pulps, the Kraft process employs very alkaline conditions and high temperatures to liberate lignin from wood (Tran & Vakkilainen, 2016). In plants, lignin is a reactive, aromatic polymer with no clearly defined structure. It consists of monolignols bonded together with a few different motifs. The most common bond joining monolignols in natural lignin is the β-O-4 linkage. However, in the Kraft process, lignin undergoes several chemical processes in the liquor. As a result, the reactive β-O-4, alkyl aryl ether linkages are mostly cleaved. The formed lignin fragments may condense, leaving carbon-carbon bonds in place of native carbon-oxygen bonds (Li, 2011). Kraft lignin is therefore structurally different from natural lignin as a result of the pulping process. It is resistant to further depolymerisation owing to this condensed structure. As its chemical conversion is difficult, most commercial Kraft pulping mills burn the lignin to recover energy (Gellerstedt, 2015).

Different routes have been explored for tackling the challenge of depolymerising Kraft lignin. One route that has been explored is the use of sodium hydroxide as a catalyst at temperatures of around 300°C and a pressure of 130 bar. This produced a monomer yield of 4.9 %, with pyrocatechol as the major product (Beauchet, et al., 2012). Another

proposed method uses an ethanol-water mixture at 225°C over a Pt/Al_2O_3 catalyst producing a monomer yield of 9 % and 15 %, these monomers were oxygen-free compounds (Jongerius, et al., 2013). Both depolymerisation routes require harsh reaction conditions. A potential process not well exploited is the activation of Kraft lignin by mechanical forces or mechano-catalysis.

Mechanochemistry has been shown to offer alternative reaction routes, different selectivity and improved reaction rates in the field of organic synthesis (Howard, et al., 2018). Grinding under alkaline conditions has been used to depolymerise Organosolv lignin and break down cellulose and hemicellulose into monomeric carbohydrates (Kleine, et al., 2013). Model compounds are chemicals of known structure, designed to mimic specific chemical linkages. Kleine et al. also used model compounds to show, the primary method of lignin depolymerisation is the cleavage of β-O-4 linkages. Cellulose is also depolymerised with mechanical forces using acidic solid catalysts. Clays were identified as potentially effective catalysts for that purpose due to their layered structure which alleviates problems associated with mass transfer. Taking advantage of these types of catalysts can lead to depolymerisation of other biopolymers using mechano-chemistry (Hick, et al., 2010).

There are two main mechanisms proposed to explain mechanochemistry. One is that friction provides local heat, enhancing solid-solid diffusion and allowing the reactions to occur (Hick, et al., 2010). The other proposes that mechanical forces bend and shear molecules into a more reactive state, hence lowering the activation energy and catalysing the reaction (Schüth, et al., 2014).

One study suggested that the product yield of ball-milling is related to the energy of the collisions within the process. Standard reactions of known activation energies are used to calculate these energies which are then correlated to product yield with a degree of success (McKissic, et al., 2014). An advancement on this is to use a kinematic model to calculate the energy dose. Indeed, this has been done and was found to correlate well to the yield of water-soluble products for the depolymerisation of beechwood and α-cellulose (Kessler, et al., 2017). This study used a kinematic model derived for a planetary ball mill used in mechanical alloying processes (Burgio, et al., 1991) and then adapted the model to apply to the Emax ball mill. These two mills are also the mills available for this study, so these kinematic models have been utilised.

It has been shown that adding small amounts of methanol to the reaction mixture of Organosolv lignin and sodium hydroxide improves the monomer yield of ball-milling (Brittain, et al., 2018). The authors suggest that the methanol donates a proton to a reactive carbanion species, or the methanol itself is involved in cleavage of bonds. A route previously suggested for mechano-catalytic Kraft lignin depolymerisation is milling with toluene and potassium hydroxide. Using this route, two main monomers were produced with a 10% yield (Yao, et al., 2018).

Repolymerisation of lignin is often a reported issue as it competes with depolymerisation (Toledano, et al., 2014). However, if encouraged alone, repolymerisation reactions cause an increase in the molecular weight of the lignin. This could be advantageous as high molecular weight lignin can be used to make carbon fibres (Sadeghifar, et al., 2016), although virtually no studies have investigated promoting such reactions.

The scope of the problem ahead is demonstrated well by comparing Kraft lignin to Kevlar. Kevlar, like Kraft lignin, is a highly aromatic polymer. It is used in bullet-proof material, showing how well this structure dissipates mechanical energy. As mechanical energy is utilised in milling, this energy dissipation could also be present when attempting to depolymerise lignin. Therefore, the problem is whether a substantial chemical change in Kraft lignin can be achieved using mechanical forces, understanding why these reactions occur and what is driving them.

Methods

Ball Mills and Energy Models

Two ball mill types were available, a planetary (Fritsch Pulverisette 7) and a high energy (Retsch Emax). These ball mills use different principles to transfer kinetic energy from the grinding medium to a substrate and have varying degrees of temperature control.

Planetary Ball Mill (P7)

The primary working principle of the P7 is to utilise high energy impacts of a grinding medium (stainless steel balls) against the vial walls. Centrifugal force from the vials rotating on their own axis transfers energy to the balls. These vials are within a larger disk rotating in the opposite direction (Fritsch). Importantly, this mill required manual temperature control. Milling breaks of three minutes for every five were adopted to allow the mill to cool to room temperature. The total energy input to the system is then calculated using the kinematic model derived by Kessler et al. elsewhere with the final equation reproduced below.

$$P = -(1-n_v^{\varepsilon})N_b K_a m_b t(\omega_P-\omega_V)\left[\frac{\omega_V^3\left(R_V-\frac{d_b}{2}\right)}{\omega_P}\right]\frac{\left(R_V-\frac{d_b}{2}\right)}{2\pi} \quad (1)$$

where P is the energy transferred to the substrate and catalyst during milling of duration t, N_b is the number of balls, K_a is a parameter depending on the elasticity of the collisions, assumed as 1 (perfectly inelastic), m_b is the mass of one ball, ω_P and ω_V are the absolute angular velocities of the main disc and

vial respectively, R_V is the vial radius and d_b is the ball diameter. Parameters n_v and ε are defined by Kessler (Kessler, et al., 2017).

High Energy Ball Mill (Emax)

The key difference between the planetary and the Emax ball mill is that the Emax utilises both high energy impacts of the grinding medium against the walls and intensive friction of the balls with the vial walls. This combination originates from the vial movement and the vial shape being a rounded rectangle. Instead of being within a singular circular plate like the planetary ball mill, the vials are mounted on two discs, allowing them to move in a circular motion without changing orientation. Coupling that with a straight wall segment leads to strong friction between the balls, lignin, catalyst and vial walls. At the rounded ends of the vial, planetary effects are present with high energy ball impacts. For the Emax, automatic cooling was available and so the temperature range of 35-45°C was not exceeded. The total energy inputted into the system was then calculated using another kinematic model derived by Kessler elsewhere as with for the planetary ball mill. This is reproduced below.

$$P = (1-n_v^{\varepsilon})N_b K_a m_b t \omega_p^{3} \left(R_V - \frac{d_b}{2} + R_p\right) \frac{\left(R_V - \frac{d_b}{2}\right)}{\pi} \qquad (2)$$

where the variables are as defined for Equation 1.

Sample Treatment

Once the milling is complete, the contents of the vials were emptied and processed. This included sieving the contents to create a homogeneous powder. Neutralisation was required for the sodium hydroxide experiments in order to use analytical techniques such as gel permeation chromatography (GPC, a further explanation to follow). Acetic acid was the chemical used for neutralisation. Washing of p-TSA from the samples was achieved by adding water, placing the sample in an ultrasonic bath for approx. 5 mins, centrifuging and then repeating this twice. The sodium hydroxide was unable to be removed through washing since the products became soluble in water under alkaline conditions.

GPC and Multi-detector GPC

GPC was used to measure the molecular weight distributions of the samples. The working principle of GPC utilises the varying size of different molecular weight molecules and so is a form of size exclusion chromatography (SEC). An eluent, in our case dimethylformamide (DMF), is used to dissolve the sample. This then moves through a gel packed column where smaller molecules pass through the most pores and therefore have a longest path length. Hence, smaller molecules take the longest time to elute. Elution time is then correlated to molecular weight upon column calibration. (Study Read, n.d.)

However, the conventional GPC has some limitations. Therefore, the Agilent multi-detector GPC was used for samples milled with p-TSA. One key limitation is that a molecule with the same molecular weight as another, but with different chemistry, could be a different size, as demonstrated in Figure 1. For example, a more branched molecule would have a lower measured molecular weight than its actual molecular weight. Multi-detector GPC uses a viscometer to calculate the intrinsic viscosity of eluting materials. The refractive index increment, or the dn/dc (Held, 2015), was then calculated and manually inputted into the Agilent software. From there, a Mark-Houwink plot, i.e a plot of intrinsic viscosity vs. molecular weight, was produced giving the intrinsic viscosity (IV) branched and IV linear. The IV contraction factor, g', is then the ratio of these. This is then used to calculate the radius of gyration contraction factor (g) using the following relation.

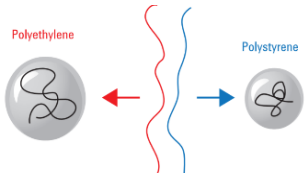

Figure 1: Two polymers dissolved in a common solvent (TCB) of identical molecular weight but with a different size. (Agilent Technologies, 2012)

$$g = g'^{\left(\frac{1}{\varepsilon}\right)} \qquad (3)$$

where ε is the structure factor. From g, the branching number is calculated using Equation 4.

$$g = \left[\left(1+\frac{B_n}{7}\right)^{0.5} + \frac{4B_n}{9\pi}\right]^{-0.5} \qquad (4)$$

The structure factor is assumed to be 0.75 for this case. Perfectly linear molecules have a structure factor of 0.5 and for highly branched molecules it is 1.5. This assumption is the reason the branching number is only relative and not absolute. The absolute branching number is defined as branches per 1000 carbon atoms. (Agilent Technologies, 2012)

Design of Experiments (DoE)

For the depolymerisation experiments, a DoE was decided as the most efficient way to investigate the system. This is due to the multi-variable dependence of the system, with the DoE allowing the investigation of multiple factors and any interactions present. Factors selected were assigned a high level and low level identified from the scoping experiments. These are listed in Table 1.

Table 1: DoE bounds, showing the high and low levels for each factor in both the sodium hydroxide and sodium percarbonate experiments in the planetary ball mill.

Factor	High	Low
Milling time [min]	150	30
Rotational speed [rpm]	600	400
Ball diameter [mm]	8	4
Total ball weight [g]	130	90

A full-factorial design was decided upon which uses every combination of high and low levels. Reproducibility was calculated through running three mid-point replicates, measuring their variance and comparing this to the variance of the whole data

set. Obtaining a reproducibility of more than 0.5 indicates reproducible results (Eriksson, 2018). The responses were measured and fitted with partial least squares regression using MODDE Pro. A selection of responses was measured, with those showing the strongest correlation to the variables investigated being considered further. These responses were weight averaged molecular weight (M_w), number averaged molecular weight (M_n), solubility in tetrahydrofuran (THF) and area ratios when splitting peaks in the M_w distribution. R^2, adjusted R^2, and p-values were all used to deduce which response was the strongest and should be carried forward. R^2 is the proportion of the variance in the response, correlated to the factors. The adjusted R^2, is an extension of R^2 that considers whether the addition of more variables improves the R^2 value only through chance. The p-value is the probability that the regression model shows a correlation just by chance. If the p-value is below 0.05 the model is good.

Experimental

The Kraft lignin used was produced by Suzano Pulp and Paper and more specifically, it was precipitated via acidification with CO_2 from a black liquor (Sundin, 2000). It is a fine brown powder with negligible moisture content, confirmed using a vacuum oven. Since the Emax and planetary vials are different volumes, 50 ml and 80 ml respectively, a different amount of lignin was added to both, 3 g and 5 g respectively. Three catalysts were used, sodium hydroxide (NaOH), a base in pellet form, sodium percarbonate ($3Na_2CO_2.2H_2O_2$), a coarse powdered oxidant, and para-toluene sulfonic acid (p-TSA) of crystalline structure. These catalysts were added at a 1:1 weight ratio in both mills.

Results

Scoping

To screen potential catalysts for lignin depolymerisation, five catalysts (sodium hydroxide, sodium carbonate, p-toluene sulfonic acid, oxalic acid and sodium percarbonate) were explored. Lignin was milled without a catalyst to see whether milling alone could cause any chemical change. Two experiments with solvents added were ran to explore their potential in improving the reaction. Each scoping experiment was performed in both mills under constant conditions respective of each mill, shown in Table 2.

Table 2: Variable conditions used in the scoping experiments for each ball mill.

Variable	P7 mill	Emax mill
Ball size [mm]	9	10
Rotational speed [rpm]	400	800
Mill time [mins]	120	120
Mass of balls [g]	120	60
Mass of substrate [g]	5.0	3.0
Mass of catalyst [g]	5.0	3.0

Firstly, the lignin was milled with these solid catalysts alone. Then, the sodium hydroxide experiment was repeated, once adding 5.6 g of water and once adding 5.6 g of formaldehyde (CH_2O). The product of each milling experiment was analysed using GPC and the M_w and M_n were calculated.

Table 3: Summary of M_w % change of milling products from the original lignin in the scoping experiments.

Milling experiment	P7	Emax [Da]
	Change in M_w	Change in M_w
NaOH	-51 %	-55 %
Na_2CO_3	+1 %	-19 %
p-TSA	+405 %	+668 %
Oxalic acid	+68 %	+76 %
$3Na_2CO_2.2H_2O_2$	-10 %	-46 %
NaOH & water	-33 %	-10 %
NaOH & CH_2O	-25 %	-22 %
No catalyst	-16 %	-16 %

The original lignin has a M_w of 2817. In Table 3 it is shown that sodium hydroxide noticeably reduces the M_w of the lignin. Of the acid catalysts, both show an apparent increase in M_w, however it is important to note that these are unwashed samples. Sodium percarbonate shows a more significant decrease in M_w in the Emax than in the P7. Both solvents seem to inhibit depolymerisation using sodium hydroxide, since the M_w shows a smaller change. By simply milling alone there is a decrease in M_w in both mills to the same magnitude. Of these catalysts, the sodium hydroxide, sodium percarbonate and p-TSA were chosen as they had the most promising results for structural change.

Depolymerisation

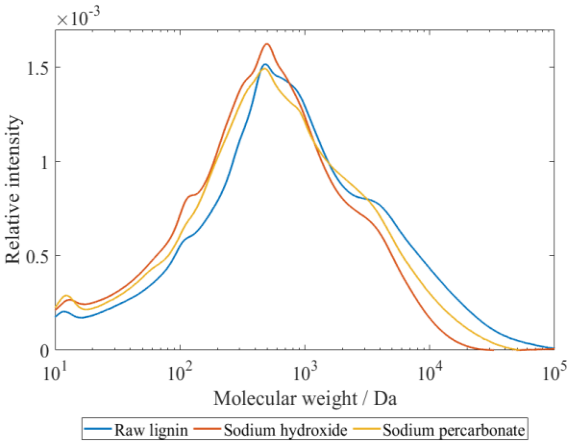

Figure 2: Molecular weight distribution showing the change after milling. Sodium hydroxide milling: 600 rpm, 8 mm balls, 150 mins, 90 g ball weight. $3Na_2CO_2.2H_2O_2$ milling: 600 rpm, 4 mm balls, 150 mins, 90 g ball weight.

Figure 2 shows the molecular weight distributions of samples milled with the depolymerisation catalysts compared to a sample of original lignin prior to any processing. This graph is obtained from transforming the retention time on the x-axis from the GPC chromatogram to molecular weight using linear calibration standards. After this, any baseline drift is eliminated, and the curves are normalised to make them directly comparable.

Table 4: Summary statistics analysing the regression of the DoE for NaOH. Here, area ratio is the ratio of the areas when splitting the peaks in the molecular weight distribution.

Responses	R^2	Adjusted R^2	p-value	Reproducibility
M_w	0.89	0.82	0.00	0.92
M_n	0.70	0.22	0.31	0.93
Solubility in THF	0.78	0.65	0.01	0.23
Area ratio	0.67	0.50	0.02	0.94

Once the design of experiments is fitted to each response, R^2 values, p-values and reproducibility measures can be found for individual responses. The response with the best correlation and reproducibility for the studied factors is analysed further. Table 4 shows for the sodium hydroxide DoE, this was the M_w.

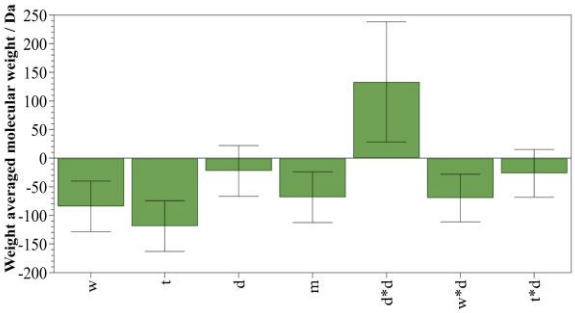

Figure 3: Coefficients, normalized to the factor ranges, of terms in the regression model for sodium hydroxide milling obtained from the DoE where w is speed, t is time, d is ball diameter and m is total ball mass.

Figure 3 shows the coefficients of each factor, squared terms and interactions in relation to M_w. These coefficients are normalised to the range of each factor. Speed and time are the two most influential singular factors with their increase leading to a decrease in M_w. Increasing the mass of the balls in the mill also directly decreases the M_w. Ball diameter only has a small effect falling within the range of error. However, it participates in two interactions and a squared term, so is retained in the model.

An interaction exists between ball diameter and mill speed. At lower ball diameters, the mill speed can be increased with no effect on the M_w of the product, in comparison at high ball diameters increasing the mill speed has a significant effect in reducing the M_w of the product. The interaction between ball diameter and run time means that run time has a greater effect on M_w at larger ball diameters.

The full design area studied is displayed in Figure 4 for this design of experiment. The set of plots in the right-hand column have contours that are close in proximity to each other allowing a lower M_w to be achieved. It also clearly shows the direction of improvement which will aid further studies of optimising depolymerisation.

Table 5: Summary statistics analysing the regression of the DoE for sodium percarbonate. Here, area ratio is the ratio of the areas when splitting the peaks in the molecular weight distribution.

Responses	R^2	Adjusted R^2	p-value	Reproducibility
M_w	0.90	0.87	0.00	0.98
M_n	0.89	0.60	0.11	0.88
Solubility in THF	0.75	0.55	0.03	-0.20
Area ratio	0.86	0.83	0.00	0.93

In the second set of design of experiments studying milling with sodium percarbonate, the M_w was again found to be the best response as shown in Table 5.

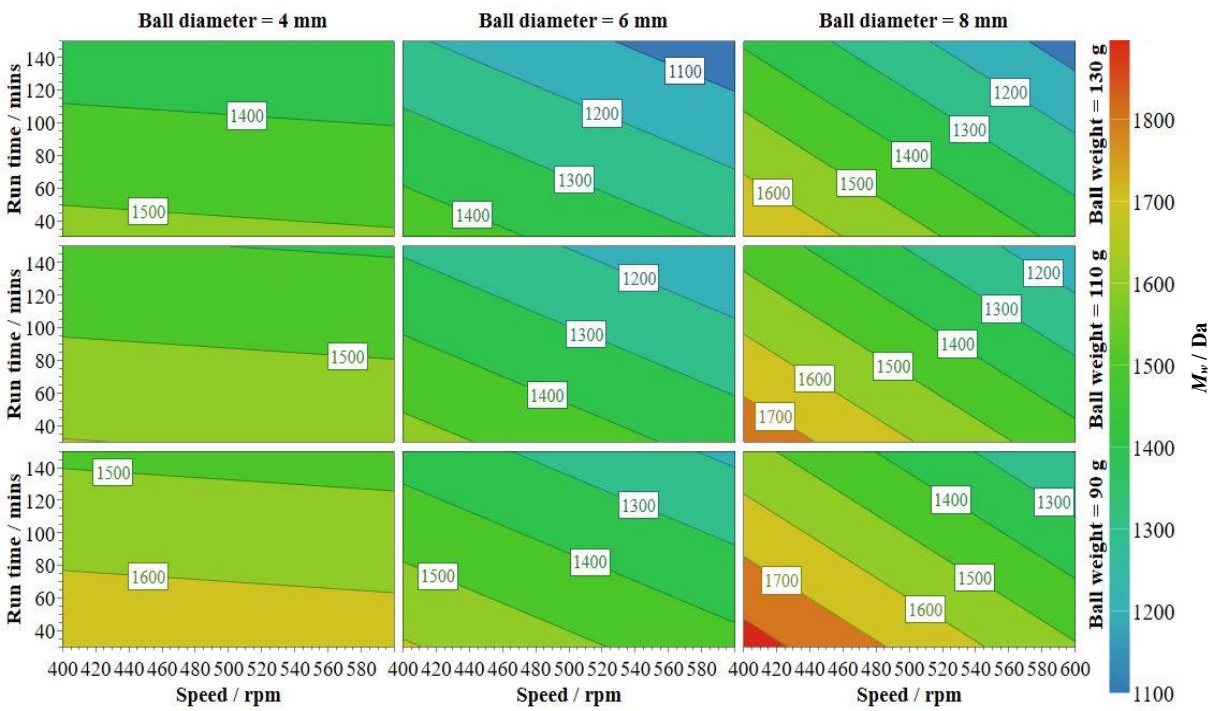

Figure 4: 4D contour plot showing the full design of experiments design space for sodium hydroxide milling.

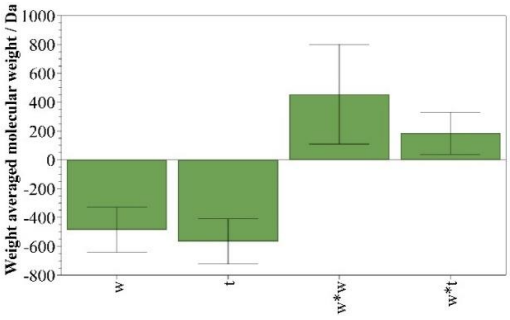

Figure 5: Normalised coefficients of terms in the regression model for sodium percarbonate milling obtained from the design of experiments, where w is mill speed and t is mill time.

Interestingly, Figure 5 demonstrates that the M_w only depends on mill time and speed in the range studied. An increase in mill time and speed both lead to a decrease in M_w. The two variables removed are those associated with the grinding medium, ball diameter and total ball weight. There is also an interaction between speed and mill time, and a squared term for mill speed indicating curvature. Since only two variables are included in the regression model the contour plot, Figure 6, is only a two-dimensional plot.

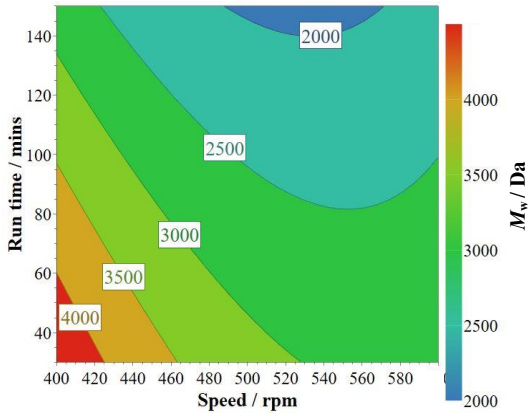

Figure 6: 2D contour plot showing the full design of experiments design space for sodium percarbonate milling.

Figure 7 shows that a larger cake layer is formed when lignin is milled with sodium percarbonate compared with sodium hydroxide and that the resulting product is lighter in colour.

Figure 7: Sample vials after milling in the planetary ball mill for 30 mins at 400rpm, with 90 g of balls with 4 mm diameter. Left is with sodium hydroxide catalyst and right is sodium percarbonate catalyst.

In Figure 8, a logarithmic trend between the M_w of the sodium percarbonate milling product and energy dose is plotted showing a strong correlation. This logarithmic trend has the steepest gradient at low energy doses. The line then flattens out as either the reaction finishes or the cake prevents further reaction occurring. There is an insignificant correlation between energy dose and M_w of the sodium hydroxide milled sample is suggesting other factors are more important than the kinematic energy of the impacts.

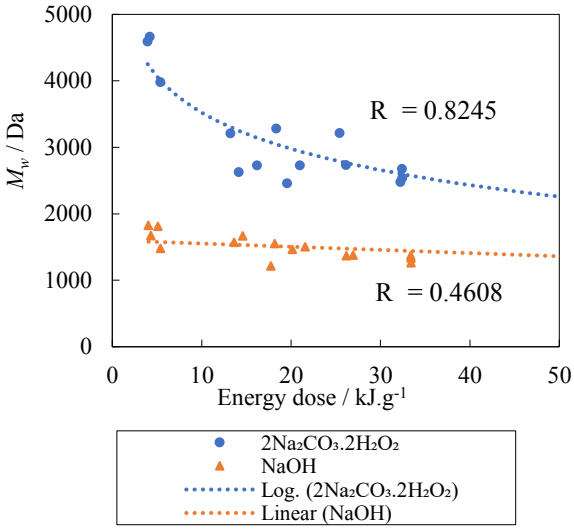

Figure 8: Correlation between M_w and total kinematic energy input per gram of substrate and catalyst.

Repolymerisation

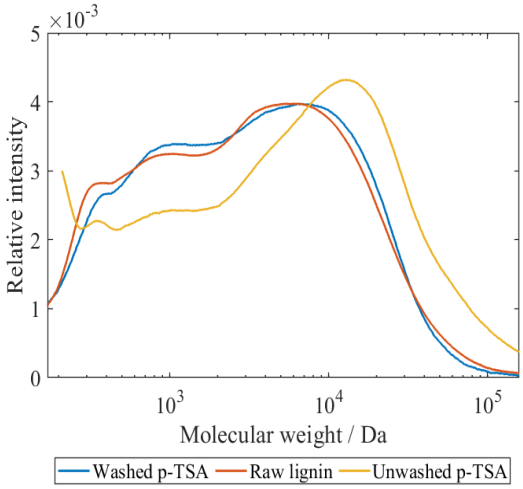

Figure 9: Molecular weight distribution of Kraft lignin milled with p-TSA for 15 mins with balls of 8 mm diameter at 1500 rpm rotational speed.

The chromatogram extracted from the GPC relates the elution time to the molecular weight as demonstrated in Figure 9. Here, it is shown that there is a shift to the right in the molecular weight distribution for the p-TSA milled samples compared to the original lignin. It is noted that the unwashed sample has a peak at very low molecular weights, likely to be p-TSA, and that there is a much larger shift for the unwashed sample compared to the washed sample. However, as p-TSA is acting as a catalyst, not a reaction intermediate, the washed sample is to be investigated further.

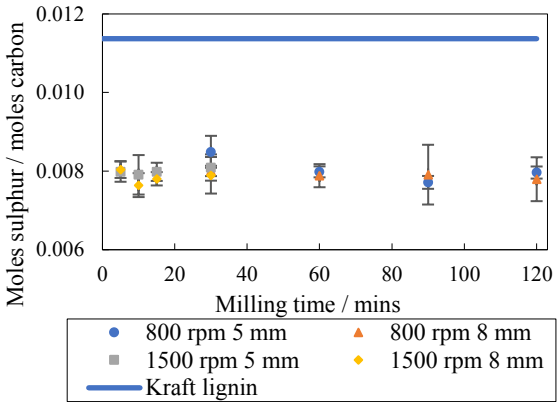

Figure 10: Sulphur content of samples milled with p-TSA at all milling times, ball diameter and rotational speeds tested after washing.

There is no correlation to be drawn from the milling time and the sulphur content of the sample in Figure 10, although identifying a trend was not the purpose of this measurement. The key finding is that the sulphur content has decreased in relation to the original Kraft lignin. Therefore, it can be assumed that the p-TSA has been effectively washed out of the sample since if a small amount were to have remained, the sulphur content would be above that of the original lignin.

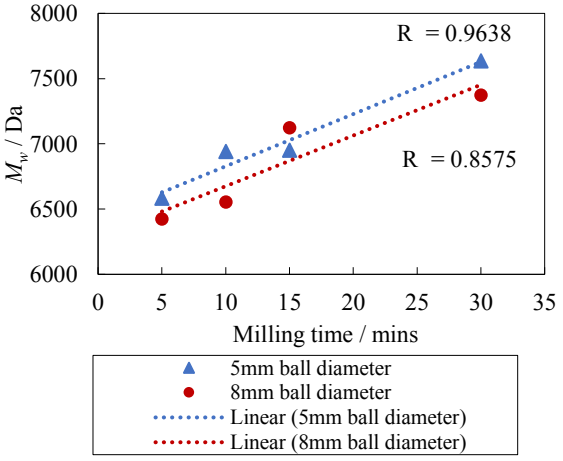

Figure 11: M_w against milling time for p-TSA milling reaction at 1500 rpm rotational speed.

For the two speeds tested, the lower speed of 800 rpm did not show any correlation between M_w and milling time. However, for the higher speed of 1500 rpm, there was a general positive correlation as demonstrated in Figure 11. When the sample was milled for 30 mins, a brittle ball was created where further repolymerisation is unlikely to occur. Therefore, the correlation in Figure 11 indicates that during the milling time selected the reaction had not completed. The M_w for ball diameters of 5 mm and 8 mm both follow a similar trend, but with the 5 mm showing slightly higher M_w values.

Figure 12 clearly demonstrates how the 8 mm ball has a greater polydispersity than the 5 mm, eluding to there not being a direct correlation between the M_w and M_n. In general, there is an upward trend between the polydispersity with milling time. However, since the M_n had a strong dependence upon the manual peak integration, the polydispersity is purely shown here as a trend that seemingly presented itself.

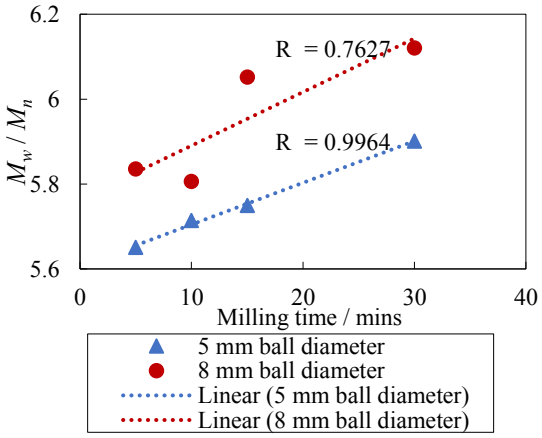

Figure 12: Polydispersity against milling time for the p-TSA milling at 1500 rpm rotational speed.

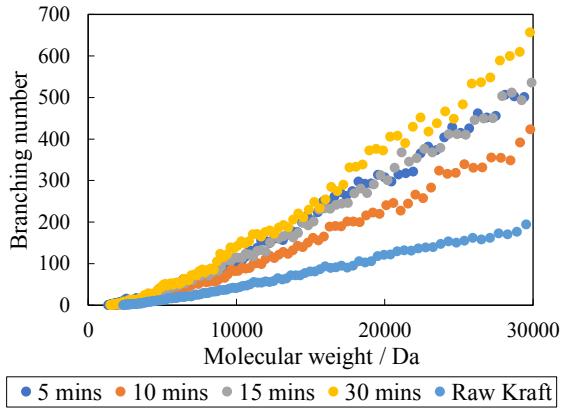

Figure 13: Branching number distribution in the samples milled with p-TSA at 1500 rpm using balls of 8 mm diameter.

There is no definite correlation between the degree of branching and milling time, although if the 5 minute run is excluded, there does seem to be a positive correlation in Figure 13. An important result also demonstrated here is the increase in branching for all molecules compared to the original Kraft lignin.

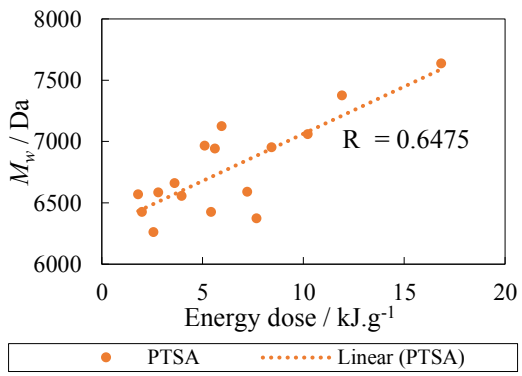

Figure 14 Correlation between M_w and total energy input per gram of substrate and catalyst for the p-TSA milled samples.

In Figure 14 a linear correlation between the mechanical energy input into the system and the M_w has been drawn.

Discussion

Depolymerisation of Kraft lignin

Sodium hydroxide and sodium percarbonate milling affect the molecular weight distribution shown in Figure 2. In both curves the most significant reduction in the intensity from the original lignin is over 4000 Da. This indicates that the highest molecular weight molecules are being depolymerised. Sodium percarbonate causes an additional reduction in intensity at moderate molecular weights between 600 and 1000 Da. Both catalysts exhibit an increase in intensity at molecular weights below 600 Da. This is a result of depolymerisation products being formed. A peak is exhibited in the original raw lignin sample at around 100 Da. This is perhaps due to the sample containing monomers formed in the Kraft process. This peak is amplified in sodium hydroxide milling suggesting that more of these monomers are formed whilst milling. Conversely, in the sodium percarbonate milled sample the peak seems to have disappeared. A possible explanation is that monomers are reforming into oligomers or oxidising into gases.

For sodium hydroxide milling an increase in mill time, mill speed, ball diameter, or total ball weight lead to more depolymerisation. The two interactions present are also of high significance. Both involve the ball diameter and lead to the conclusion that the depolymerisation achieved in the sample is limited by the ball diameter. The energy of individual impacts in the milling process depend on the mass of the balls and hence the ball diameter. It follows that, impacts of higher energy are required to support the reaction. The direction of improvement is clear, and further studies could perhaps shift the experimental design space in this direction.

The level of depolymerisation achieved in sodium percarbonate milling only depends on, mill time and speed. It is unexpected that neither variable relating to the grinding medium is important. A reason could be that the individual impacts have the energy required for the reaction even at the lowest impact energies in the system. There exists a squared term in the model for mill speed, which indicates curvature, clearly represented in Figure 6. Here, an optimum mill speed exists for a given mill time. This can be explained by the tougher cake layer forming at the higher mill speeds for sodium percarbonate milling. The cake absorbs energy and prevents impacts on a large portion of the substrate.

There are a few potential reasons why the sodium percarbonate milling forms a tougher cake. One of them is that sodium hydroxide is more hygroscopic. This small amount of water absorbed by the sodium hydroxide from the atmosphere could help to prevent cake formation by acting as a solvent breaking up intermolecular forces. Another is that there are stronger intermolecular forces between the lignin and the sodium percarbonate due to the peroxide molecules exhibiting significant hydrogen bonding (Giguère & Chen, 1984) with the hydrogen bond-accepting functional groups in lignin. Very small amounts of water could be added to a milling experiment with sodium percarbonate to test whether this could decrease the amount of cake formation. Anti-caking agents are widely used in the food industry and may also help to prevent cake formation in milling, so this could potentially be explored.

Repolymerisation of Kraft lignin

All samples further analysed were the washed samples however the M_w were also measured for the unwashed samples. It was interesting to that despite the low molecular weight p-TSA being washed away, the M_w decreased after washing. One explanation for this is that as Kraft lignin and p-TSA are highly aromatic, so the pi electron rings within them could be causing attractions between the molecules, leading to a shifted M_w distribution. The elemental analysis is useful in confirming that the p-TSA has been washed away.

Curiously, there is no correlation between time and M_w at the rotational speed of 800 rpm, yet there is a correlation at 1500 rpm shown in Figure 11. There is also a correlation between overall energy input and M_w. An explanation is that since the overall energy input is relatively low at the lower speeds, a correlation may present itself if greater time ranges are explored. Overall, the 5 mm balls achieved a greater increase in M_w. Since the overall ball weight was kept constant, a reason for this could be that the overall energy input for smaller diameter balls is larger as calculated through the energy equations.

A larger grinding medium seems to produce a more dispersed product demonstrated through an increase in polydispersity in Figure 12. This is a less desirable trait as separation of valuable products becomes more difficult and less lucrative with greater dispersion. This, coupled with the lower overall M_w, showing a lower conversion, suggests that a smaller ball diameter seems to be the more efficient size. However, it is important to reiterate that the M_n depends heavily on the manual peak integration performed on the GPC machine and, therefore, the polydispersity here was only interesting to see as the M_n values obtained were all relatively close in magnitude.

Figure 13 shows that all milled products are more branched than the original lignin. This is an important result not only as it gives an indication of the chemical properties of the products, but also as it can now be assumed that the M_w measured is lower than the actual M_w in relation to that of the original Kraft lignin. This is due to the limitations of conventional GPC described in the methods. There does not seem to be a trend of branching increasing with time. Although this does not mean a trend does not exist. This is due to an assumption made in the

branching number calculations, potentially causing an error. The assumption is that the structure factor in Equation 3 is 0.75, picked as this its typical value. However, the true value ranges between 0.5 and 1.5 and are likely to be different for each sample, giving a source of error of a large enough magnitude to inhibit a trend from surfacing.

Separating mechano-catalytic and mechanically-assisted reactions using the kinematic energy model

Figure 8 demonstrates that a small correlation exists between total energy dose into the grinding medium via the ball impacts and the M_w of the product after sodium hydroxide milling. Comparing this to the p-TSA and sodium percarbonate milling, a strong relationship exists between the M_w of the product and the energy dose to the system. This is displayed in Figures 8 and 14. Explaining this requires the distinct separation of mechanically-assisted and mechano-catalytic reactions.

Solid-solid reactions are diffusion limited (Tamhankar & Doraiswamy, 1979), so it is possible that during sodium hydroxide milling, the ball mill is enhancing mass transfer by contacting the substrate with the catalyst. Heat energy is also provided in small amounts through these impacts, also helping to overcome the diffusional barrier. This would lead to a small correlation to total energy, but the energy of individual impacts would have a higher importance. Further evidence of this is the interactions with ball diameter. This is a conventional chemical reaction, in which the ball mill acts to enhance mass transfer. The mechanism of basic cleavage of the non-phenolic ethers in lignin involves the removal of a proton from an alcohol group, leaving a negatively charged oxygen which attacks the ether group to form an epoxide (Rinaldi, et al., 2016). Due to this mechanism not requiring the formation of a more reactive state, or a change in geometry, it can be concluded that mechanical forces are not needed for the reaction with sodium hydroxide. Hence this reaction is mechanically assisted. This leads us to an improved explanation as to why adding small amounts of methanol was shown to improve the extent of depolymerisation (Brittain, et al., 2018). Previously it was thought the methanol quenches intermediates likely to repolymerise. A simpler explanation may be that the methanol improves mass transfer by being a medium that enhances diffusion helping to contact reactant and catalyst.

Mechano-catalysed reactions should then be defined as reactions where mechanical forces help lower the activation energy of the reaction. This fits the idea that mechanical forces help to force the lignin into a more reactive state. Under this system, we would expect the response to correlate to the kinematic energy of the ball impacts (Schüth, et al., 2014). Oxidative depolymerisation of lignin is a free radical mechanism (Mottweiler, et al., 2015), leading to the requirement for radical formation to initiate the reaction. Shear forces can induce scissions of lignin forming free-radicals called mechano-radicals (Sakaguchi & Sohma, 1978). If this is occurring, the sodium percarbonate and lignin reaction is mechano-catalytic. This proposition is supported by the correlation between kinematic energy dose and products for oxidative depolymerisation. The correlation is logarithmic, shown in Figure 8, presenting further evidence for a radical mechanism since this rapid reaction nears completion at low energies. Consequently, the line flattens at high energies.

The repolymerisation reaction, induced through milling with p-TSA, is likely to be a Friedel-Crafts aromatic substitution. This entails the protonation of a group containing oxygen, such as an acid, ketone or alcohol (Yang & Kong, 2016). This group is then able to bond to the aromatic electron rings within other molecules in the lignin to form a highly branched product. Products from p-TSA milling products are more branched than the original lignin, supporting this. The lignin molecules are bent through mechanical energy since the electrophilic group created by protonation is being shielded due to the compact nature of Kraft lignin. Since more branched, products have been produced, it is concluded that this reaction is mechano-catalysed. Also, there is a reasonably strong correlation between the M_w of the product and the energy dose, supporting the hypotheses that mechano-catalysed reactions have a correlation to energy dose.

Conclusions

Understanding the difference between mechanically-assisted and mechano-catalysed reactions could lead to better optimisation and more in-depth studies of the different processes. To assess whether a reaction is mechano-catalysed or mechanically-assisted, the kinematic models as suggested (Burgio, et al., 1991) (Kessler, et al., 2017), should be used to correlate the response of the product to the kinematic energy. A strong correlation indicates a mechano-catalysed reaction. The reaction mechanism should be used to reinforce this. To improve mechanically assisted reactions, further studies should focus on the mixing in the system and how solvents and mechanical variables enhance this. For mechano-catalysed reactions, the impacts of the grinding medium should be optimised and the types of mechanical forces most effective in catalysing a specific system should be investigated. For example, such forces would be impact and shear.

A limitation of mechano-chemical processes is the cake formation at the vial walls. Further studies to consider how to reduce this cake formation are subsequently of high importance. Anti-caking agents used in the food industry would potentially reduce this; another idea is the addition of small amounts of solvent to break up intermolecular forces.

Kraft lignin is an incredibly recalcitrant material, and any chemical change undergone by the substrate is minimal. However, a chemical change is still observed and so, with the optimisation of the conditions, a yield of monomers can be produced. Unfortunately, there will always be portions of the Kraft lignin that are so condensed that incredibly harsh conditions, will be required to obtain monomers. However, there is further application for such molecules. For example, Kevlar, as mentioned earlier, is an aromatic polymer which dissipates mechanical energy effectively, making it an exceptional antiballistic material (Lou, et al., 2008). Some polymers in Kraft lignin seemingly behave in a similar manner, so this is an additional avenue to be investigated.

Acknowledgements

We acknowledge the amazing support of Dr I. Biscaya, Mr C. Chesi, Mr M. Kessler, and Dr R. Woodward.

References

Agilent Technologies, 2012. *A guide to multi-detector gel permeation chromatography.* [Online] [Accessed 04 12 2018].

Beauchet, R., Monteil-Rivera, F. & Lavoie, J., 2012. Conversion of lignin to aromatic-based chemicals (L-chems) and biofuels (L-fuels). *Bioresource Technology,* Volume 121, pp. 328-334.

Brittain, A. et al., 2018. Quenching of reactive intermediates during mechanochemical depolymerization of lignin. *Catalysis Today,* Volume 302, pp. 180-189.

Burgio, N., Magini, M., Martelli, S. & Padella, F., 1991. Mechanical alloying of the Fe−Zr system. Correlation between input energy and end products. *Il Nuovo Cimento D,* 13(4), pp. 459-476.

Eriksson, L., 2018. *What tools make DOE data analysis faster and more accurate?.* [Online] Available at: http://blog.umetrics.com/design-and-analysis-of-experiments-tools-for-data-analytics [Accessed 29 11 2018].

Fritsch, n.d. *PULVERISETTE 7.* [Online] Available at: https://www.fritsch-international.com/sample-preparation/milling/planetary-mills/details/product/pulverisette-7-premium-line/ [Accessed 06 12 2018].

Garoff, N., 2014. *Kraft Lignin –Trends regarding industrial production and applications.* Berlin, Fraunhofer Biopolymer-Kolloquium.

Gellerstedt, G., 2015. Softwood kraft lignin: Raw material for the future. *Industrial Crops and Products,* Volume 77, pp. 845-854.

Giguère, P. & Chen, H., 1984. Hydrogen bonding in hydrogen peroxide and water. A Raman study of the liquid state. *Journal of Raman Spectroscopy,* 15(3), pp. 199-204.

Held, D., 2015. Tips & Tricks GPC/SEC: How to Determine dn/dc Values. *The Column,* 10(7).

Hick, S. et al., 2010. Mechanocatalysis for biomass-derived chemicals and fuels. *Green Chemistry,* 12(3), pp. 468-474.

Howard, J., Cao, Q. & Browne, D., 2018. Mechanochemistry as an emerging tool for molecular synthesis: what can it offer?. *Chemical Science,* 9(12), pp. 3080-3094.

Hu, T., 2002. *Chemical Modification, Properties, and Usage of Lignin.* s.l.:Springer.

Jongerius, A., Bruijnincx, P. & Weckhuysen, B., 2013. Liquid-phase reforming and hydrodeoxygenation as a two-step route to aromatics from lignin. *Green Chemistry,* 15(11), pp. 3049-3056.

Kessler, M., Woodward, R., Wong, N. & Rinaldi, R., 2017. Kinematic Modeling of Mechanocatalytic Depolymerization of α-Cellulose and Beechwood. *ChemSusChem,* 11(3), pp. 552-561.

Kleine, T., Buendia, J. & Bolm, C., 2013. Mechanochemical degradation of lignin and wood by solvent-free grinding in a reactive medium. *Green Chemistry,* 15(1), pp. 160-166.

Li, J., 2011. *Isolation of lignin from wood,* Imatra: Saimaa University of Applied Sciences.

Lou, C. et al., 2008. Process and impact properties of ballistic resistant compound material made of polyamide nonwoven fabric and Kevlar woven fabric. *Journal of Advanced Materials,* 40(4), pp. 27-36.

McKissic, K., Caruso, J., Blair, R. & Mack, J., 2014. Comparison of shaking versus baking: further understanding the energetics of a mechanochemical reaction. *Green Chemistry,* 16(3), pp. 1628-1632.

Mottweiler, J. et al., 2015. Iron-catalysed oxidative cleavage of lignin and β-O-4 lignin model compounds with peroxides in DMSO. *Green Chemistry,* 17(11), pp. 5001-5008.

Ragnar, M. et al., 2000. Pulp. In: B. Elvers, ed. *Ullmann's Encyclopedia of Industrial Chemistry.* s.l.:Wiley, pp. 1-92.

Retsch, n.d. *High Energy Ball Mill Emax.* [Online] Available at: https://www.retsch.com/products/milling/ball-mills/emax/function-features/ [Accessed 05 12 2018].

Rinaldi, R. et al., 2016. Paving the Way for Lignin Valorisation: Recent. *Angewandte Chemie,* 55(29), pp. 8164-8215.

Sadeghifar, H., Sen, S., Patil, S. & Argyropoulos, D., 2016. Toward Carbon Fibers from Single Component Kraft Lignin Systems: Optimization of Chain Extension Chemistry. *ACS Sustainable Chemistry & Engineering,* 4(10), pp. 5230-5237.

Sakaguchi, M. & Sohma, J., 1978. Copolymerizations initiated by mechano-radicals on particle surfaces of poly(tetrafluoroethylene). *Journal of Applied Polymer Science,* 22(10), pp. 2915-2924.

Schüth, F. et al., 2014. Mechanocatalytic depolymerization of cellulose and raw biomass and downstream processing of the products. *Catalysis Today,* Volume 234, pp. 24-30.

Study Read, n.d. *Gel Permeation Chromatography| Its Principle Instrument & Applications.* [Online] Available at: https://www.studyread.com/gel-permeation-chromatography/ [Accessed 04 12 2018].

Sundin, J., 2000. *Precipitation of Kraft Lignin under,* Stockholm: Royal Institute of Technology, Department of Pulp and Paper Chemistry and Technology.

Tamhankar, S. & Doraiswamy, L., 1979. Analysis of solid-solid reactions: A review. *AIChE Journal,* 25(4), pp. 561-582.

Toledano, A., Serrano, L. & Labidi, J., 2014. Improving base catalyzed lignin depolymerization by avoiding lignin repolymerization. *Fuel,* Volume 116, pp. 617-624.

Tran, H. & Vakkilainen, E., 2016. The Kraft Chemical Recovery Process.

Yang, D. & Kong, J., 2016. 100% hyperbranched polymers via the acid-catalyzed Friedel–Crafts aromatic substitution reaction. *Polymer Chemistry,* 7(33), pp. 5226-5232.

Yao, S. et al., 2018. Mechanochemical Treatment Facilitates Two-Step Oxidative Depolymerization of Kraft Lignin. *ACS Sustainable Chemistry and Engineering,* 6(5), pp. 5990-5998.

Zakzeski, J., Bruijnincx, P., Jongerius, A. & Bert, W., 2010. The Catalytic Valorization of Lignin for the Production of Renewable Chemicals. *Chemical Reviews,* 110(6), pp. 3552-3599.

Rhodes C and Graham J. Hutchings, *"Studies of the role of the copper promoterin the iron oxide/ chromia high temperature water gas shift catalyst", Phys.Chem. Chem. Phys., 5, 2003, 2719–2723*
J. Klose And M. Baerns(1983) *Kinetics of the Methanation of Carbon Monoxide on anAlumina-Supported Nickel Catalyst Lehrstuhl fir Technische Chemie, Ruhr-Universitiit Bochum, Postfach 102148,*
D-4630 Bochum, West Germany

Application of methane dry reforming, water-gas shift and carbon monoxide methanation to a chemical heat pump

Kerissa Narine and Henry Weir
Department of Chemical Engineering, Imperial College London, U.K.

Abstract Improving the energy efficiency within the process industry is paramount to combating climate change. Integrating heat pumps into process systems is becoming an increasingly popular way of achieving this. This exploratory study aimed to assess the feasibility and performance of a novel chemical heat pump (CHP) system. The system involves 3 reactions: carbon monoxide methanation, dry reforming of methane and water gas shift. Thermodynamic analysis was implemented to determine a desirable temperature range for operation. The aim was to deliver 65 MW of power from the methanation and water gas shift process units and the key performance indicator: coefficient of performance (COP), was measured. A COP of 1.26 was found when upgrading heat from 600 to 700°C. It was found that compressor duty related to the membrane separation system had the most significant impact on the COP. In-depth kinetic analysis found that Langmuir-Hinshelwood kinetic models were best suited to model all three reaction mechanisms at the process conditions prescribed. Compared with systems at similar temperatures, the COP underperforms, however, a number of areas for improvement were identified, including highlighting the importance of an energy-efficient separation system for vapour systems.

Nomenclature

Symbol	Meaning	Units
COP	Coefficient of Performance	-
Q_H	Heat delivered at high temperature	
W	Total work done on system	MW
CHP	Chemical Heat Pump	-
ΔH_R	Heat of reaction	MW
T_H	Temperature of high temperature reservoir/reactor	K/°C
T_L	Temperature of low temperature reservoir/reactor	K/°C
exo	Exothermic	-
endo	Endothermic	-
WGS	Water gas shift reaction	-
DRM	Dry reforming of methane reaction	-
p_i	Permeance of component i	mol/m^2Pas
P_h	Membrane feed-side pressure	Pa
P_l	Membrane permeate-side pressure	Pa
A	Membrane area	m^2
L_f	Total membrane feed flow	mol/s
L_p	Total membrane permeate flow	mol/s
L_u	Total membrane retenate flow	mol/s
X_i	Membrane feed mole fraction of component i	-
y_i	Membrane permeate mole fraction of component i	-
x_i	Membrane retenate molefraction of component i	-
P_i	Partial pressure of component i	kPa, bar
K_i	Adsorption constant of reaction i	specified
k_i	Rate coefficient of component i	specified
r_i	Rate of formation of component I per unit mass catalyst	Mol/unit catalyst mass. Unit time
DEN	Adsorption term	specified

1. Introduction

1.1. Motivation

Energy efficiency is becoming increasingly important, due to several factors, namely climate change. Industry accounts for a large proportion of global energy demand and therefore developing mechanisms to increase industrial energy efficiency should be a key priority (Fleiter et al, 2011).

Several techniques are widely applied in process industries to tackle the problem of energy efficiency, one of which being heat exchanger integration. This can reduce capital and operational related costs by up to 15-45% through a significant reduction in plant-wide energy demand (Morar and Agachi, 2010).

However, to heat up a stream using heat exchangers requires a minimum temperature gradient or driving force to exist, between the streams to be integrated. Hence, this limits the extent of heat integration possible (Douglas, 1988). This is particularly significant where the stream to be heated has a temperature above other streams.

A potential solution to this is using heat pumps. Heat pumps recover waste heat, often at low temperatures, hence adding further energy efficiency. This heat is upgraded to a higher temperature, usually in processes such as drying and cogeneration, which are sufficiently energy-intensive that the energy requirement cannot be fulfilled solely through heat integration (Chua et al, 2010).

1.2. Working Principle

In all heat pumps a flow of waste heat, often at low temperature, enters the system and is upgraded to provide useful heat as an output of the system at a higher temperature. This heat upgrading process is made possible by doing work on the working fluid as it is transferred between the two heat reservoirs within the system, in a closed thermodynamic cycle. Often this work results from a need to compress gas or pump liquid (Industrial Heat Pumps, 2018).

The main performance indicator used to describe the efficiency of all heat pumps is the COP (coefficient of performance). Its definition is the ratio of useful heat supplied at the higher temperature reservoir, Q_H, to the total work required to drive the heat pump, W.

$$COP = \frac{|Q_H|}{|W|} \qquad \text{(Equation 1.2.1)}$$

1.3. Chemical Heat Pumps

Several types of heat pumps have been developed, the most common being the mechanical vapour compression pump, yet absorption types are also used widely. Others such as adsorption heat pumps and chemical heat pumps (CHP) have been developed but are not as widely used (Chua et al, 2010).

CHPs have the advantage over adsorption heat pumps that they can approach a COP equivalent to Carnot efficiency, whereas the former has limited efficiency due to entropy generation (Aydin et al, 2015). Additionally, CHPs deliver a large heat associated with chemical reaction, in comparison to the relatively lower sensible heat released in more common absorption processes. Furthermore, it offers the additional possibility of storage of energy as well as reactants and products (Wongsuwan et al, 2001).

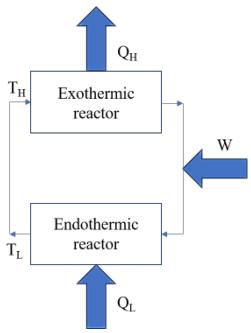

Figure 1.3.1: CHP schematic

In a CHP, waste heat is absorbed in an endothermic reaction and then heat of reaction is released, often by the reverse, exothermic reaction at a higher temperature. Since high temperatures favour endothermic reactions and low temperatures favour exothermic reactions, the system must work against Le Chatelier's principle. This means that variables other than temperature must be varied to shift the equilibrium in the desired direction to obtain sufficiently high endothermic and exothermic conversions to provide the required reaction heat. For example, the reaction pressure may be varied if there is an imbalance of total moles in the reaction stoichiometry. Furthermore, a separation system is often required to separate reactants from products and thus ensure that the concentration of products in reactor inlets is kept sufficiently low so as not to shift the reaction towards the undesired direction. Achieving separation of components and pressure variations will ultimately result in work being done on the system, mainly due to compression of gases and pumping in the case that liquids components are found in the system.

The coefficient of performance can therefore be defined in a similar form to a conventional heat pump where ΔH_{exo}, is equivalent to Q_H.

$$COP_{CHP} = \frac{|\Delta H_{R,exo}|}{|W|} \quad \text{(Equation 1.3.1)}$$

1.4. Project Scope and Objectives

This report focuses on identifying and assessing the feasibility of a novel chemical reaction system to a CHP. In section 2, criteria for selecting reactions are outlined and a reaction system chosen. In section 3, the methodology is discussed for developing a CHP system. Thermodynamic analysis is carried out to determine a suitable temperature range followed by reactor design and separation system design. The reactor and separation systems are then combined to form the overall integrated system. Section 4, evaluates the system performance and compares it to relevant systems using the COP. Finally, section 5 discusses conclusions and suggestions for further work and improvements.

2. Background

2.1. Systems Investigated and Performance

CHPs are often split into two main categories: organic and inorganic. Most organic reactions are classified as liquid-gas systems, where generally, liquid reactants produce vapour products under catalytic conditions in the endothermic reactor, and the reverse takes place in the endothermic reactor. These types of reactions offer the possibility of continuous operation, as liquid-gas separation can be performed continuously, and have high energy density. On the other hand, inorganic reactions are usually solid-gas systems, in which it is difficult to continuously separate solids from the reactors. Hence, basic inorganic solid-gas systems do not operate continuously (Wongsuwan et al, 2001).

The most widely investigated organic CHP system is the Isopropanol/Acetone/Hydrogen system. This is because it has a relatively high reaction heat of 100.4 kJ/mol, so can absorb large amounts of heat at a relatively low temperature of 80 °C, where there is large supply of industrial waste heat. Also, both exothermic and endothermic reactors can operate at 1 bar, minimising work required for pumping and compression between them (Cai et al, 2011). Further developments such as using reactive distillation (Xin et al, 2013) and reactors in series (Xu et al, 2014) have resulted in improvements to COP. A relatively high COP of 3.99 has been predicted (Guo et al, 2015).

Solid-gas systems are often able to operate at higher temperatures than liquid-gas ones. The $CaO/Ca(OH)_2/H_2O$ system has been studied widely and COP values between 1.7 and 2.5 have been achieved, delivering heat over a wide temperature range, up to 600 °C (Ogura et al, 2003). Another system that investigated the CaO/CO_2 and PbO/CO_2 reaction systems. This utilises relatively high temperature heat to upgrade heat up to 880 °C (Kato et al, 1999). Aspects such as reactor heat and mass transfer and limited scale-up studies have been highlighted as key limitations in solid-gas systems (Pardo et al, 2014).

There are several potentially important applications for high temperature processes. For example, steam methane reforming (SMR), which produced 80-85% of the world's hydrogen in 2007, requires a substantial heat supply above 600°C (Simpson and Lutz, 2007). Furthermore, there is merit in investigating whether organic reactions could be used at higher temperatures to overcome the limitations of solid-gas systems.

2.2. Criteria for Choosing Reactions

Reactions are selected using several different criteria. These can include the following (Yan et al, 2015), (Cai et al, 2011):

- High reaction heat
- Good reversibility (without apparent secondary reaction)
- Sufficiently fast forward and reverse reactions

- High conversion and selectivity
- Easily separated and stable components
- Few components involved
- Non-toxic, non-corrosive, non-flammable and non-explosive components
- Small volume variation during reaction
- Available, abundant and cheap components

It is however not made clear what weighting or importance should be ascribed to each of these characteristics. Therefore, assessing the relative importance of several of these factors and their quantitative effects on system performance, specifically on the COP, could be insightful.

2.3. Chosen Reaction System

The reaction system chosen was based on the DRM reaction, which has a very high heat of reaction.

$$CO_2 + CH_4 \leftrightarrow 2H_2 + 2CO, \Delta H_R = 247 \text{ kJ/mol}$$

Initially, the reaction was chosen due to an objective to supply heat at 385 °C to replace a preheater furnace for a crude distillation unit (Fahim, 2010). It was believed that this reaction would provide good conversions for this temperature range. However, after thermodynamic analysis (section 3.2, 4.1), a higher temperature range, from 600-700 °C, was chosen due to significantly better equilibrium conversion.

Kinetic data however was not found for the reverse endothermic reaction. Instead carbon monoxide methanation was chosen as the exothermic reaction since kinetics are more readily available. CO methanation also has a very high heat of reaction and was selected as the exothermic reaction for this reason.

$$CO + 3H_2 \leftrightarrow CH_4 + H_2O, \Delta H_R = -206 \text{ kJ/mol}$$

H_2 is produced in equal stoichiometric amounts to CO, via DRM, thus would be consumed in 3 times the stoichiometry of CO in the methanation reaction. This would lead to a substantial deficit of hydrogen, a precious resource with high production costs (Towler et al, 1996). Therefore, WGS was proposed as a third reaction to balance the system.

$$CO + H_2O \leftrightarrow H_2 + CO_2, \Delta H = -40.6 \text{ kJ/mol}$$

WGS introduces no additional components into the system and produces some of the H_2 deficit. It also consumes some of the excess CO which is produced by the DRM reaction to satisfy the H_2 demand. Furthermore, some H_2O produced in the methanation reaction can be consumed by WGS, and CO_2 would be produced to limit a potential fresh feed flow required into the DRM reactor. All these factors would contribute towards the balancing of the system on a material basis.

If not possible to fully close the system material balance, the system could be used for net consumption of CH_4 and CO_2 via the DRM reaction. The World Bank estimated in that 110 billion cubic metres of natural gas (mainly CH_4) was flared in 2004, to produce CO_2, contributing greatly to global warming (Gerner et al, 2004). Some of this CH_4 and CO_2 could be fed as a system input to reduce its environmental impact. Equally, net hydrogen production would also be useful as it is a valuable resource and could potentially be sold as an additional benefit.

It should be noted that all three reactions take place in the vapour phase. This reaction system is applied to a high temperature range of 600-700 °C. In this range the system could deliver heat to high energy and temperature process demands, such as SMR, as discussed in 2.1.

2.4. Heat Demand Target

To design the system, a target heat to be delivered was selected. Since an initial objective of this study was to supply heat to replace a refinery furnace, it was aimed to deliver at least 65 MW of heat, which is approximately the quantity required to power the furnace on a medium-size (~100,000 bbl/day) refinery (Gadalla et al, 2015).

As the focus shifted away from refineries, this target was retained as it reflects a sizeable industrial heat demand, and the large-scale-nature of the model could be advantageous for potential applications.

3. Methods

3.1. Selection of the Aspen property method

To ensure realistic and accurate interactions are simulated between the components of the designed system, careful consideration needs to be taken when choosing the property package used in Aspen Plus. This package is used in calculation of both the thermodynamic and transport properties of the components, and therefore the effect on chemical and phase equilibria calculations is great. Considering this, the Peng-Robinson equation of state method was implemented to model the CHP system containing only light vapour components with minimal interaction.

3.2. Thermodynamic analysis of proposed mechanisms

A thermodynamic study was undertaken simulating each of the reactions in Gibbs reactors to identify a feasible operating envelope for the reactions considered. Cao et al. (2017) emphasised the importance of reactor temperature, pressure and inlet flow ratio on the conversion and selectivity of the DRM reaction which motivated the selection of these as manipulated variables for this analysis. The effects of temperature and pressure were investigated on the conversions and selectivities of the WGS, motivated by Demirel (2012), and CO methanation reactions using stoichiometric inlet flow ratios. Operating temperatures of 600°C for the endothermic reactor and 700°C for the WGS and exothermic reactors were chosen from this analysis, with further investigation on the effect of these temperatures to be investigated. Stoichiometric inlet flows were chosen for initial design estimates, and pressures of 0.5 atm, 1 atm and 2 atm were selected for the endothermic, WGS and exothermic reactors respectively.

3.3. Selection of Catalyst and Kinetic Model

DRM reaction

The power law model developed by Zhang (2009) over a Ni-Co/Al-Mg-O bimetallic catalyst was considered to describe the kinetics of the dry reforming of methane. Experiments were conducted over a range of 650-750°C and 30-190kPa to develop this model, over which the bimetallic catalyst displayed excellent stability and activity which further appropriated its application to the reaction conditions. The kinetics very closely reflected experimental data with an R^2 value of 0.944 Zhang (2009). The Langmuir-Hinshelwood model developed for this catalyst showed a better fit to the experimental data presented by Zhang (2009), however the kinetic equation did not clearly detail the adsorption and reverse kinetic terms, therefore the simpler power law model was instead chosen. The Langmuir-Hinshelwood model developed by Richardson and Paripatyadar (1990) over Ni/Al_2O_3 catalyst was also considered in modelling the kinetics of the endothermic reaction. The model is one-dimensional thus is suited to a steady-state isothermal fixed-bed reactor Benguerba et al. (2014). Most notably, the temperature dependence of the forward, reverse and adsorption terms were considered in its development, which encouraged its adoption over other models.

Water-gas shift

Commercially available ferrochrome catalyst described only as HTC-2 by Hla et al. (2008) was considered for use in the chosen temperature range for the water-gas shift reaction. Of the commercial catalysts investigated by Hla et al.(2008), the power law model parameters proposed for HTC-2 could be more closely replicated through simulation using a larger scale, high temperature model by Adams and Barton (2009). This power law rate expression was therefore deemed most suitable and allowed use of reported reactor conditions for accurate scale up in this study. A limitation of this model is that its experimental development was done at 450°C, which is significantly lower than that simulated in this study.

Considering this, and the reduced range of validity associated with power law models, the more general Langmuir-Hinshelwood model given by Twigg (1989) was also considered. The empirical model of K_{eq} derived by Moe (1962) was applied to the general rate expression, along with adsorption coefficients given by Criscuoli et al. (2000) and the kinetic constant given by Rhodes (2003) for the Fe_3O_4/Cr_2O_3 catalyst.

CO methanation

The kinetic model developed by Klose and Baerns (1983) for the methanation of CO over 18% Ni catalyst was considered in this study. Confidentiality reasons limit the publishing of detailed kinetic data for commercial Ni catalysts for CO methanation, however Ronsch et al. (2015) validated this model and recommended its use for simulation on a commercial scale over wide temperature and pressure ranges (250-900°C, 5-30 bar). Klose and Baerns (1983) concluded that inhibitive adsorption effects of CO and H_2 diminish at high temperatures, and therefore the model has been adapted to reflect this by excluding the adsorption terms in its denominator. The Langmuir-Hinshelwood model proposed by Xu and Froment (1989) was also considered to investigate the independent effects of the kinetics, driving force and adsorption parameters on the overall rate of the reaction mechanism with temperature.

3.4. Initial Estimation of Flow Rates and Conversions Pre-Convergence

To satisfy the 65 MW demand imposed by the distillation unit, required reaction extents were determined initially using the heat of the exothermic reaction. To minimise required inlets, the extents of both the DRM and WGS reactions were scaled to provide the amount of H_2 needed for this minimum extent in the exothermic reactor. H_2 was found to be the most expensive component (Towler et al, 1996), therefore its inlet was chosen to be minimised. The required flowrates for the extents were estimated using the conversions determined from the thermodynamic study (Section 4.1) corresponding to the temperature, pressure and feed ratio for each reactor. Iterations were completed in Excel assuming 100% separation of components from an undefined separation system at this stage in design, and convergence was achieved within ± 5 mol/s of carbon, ± 1 hydrogen and ± 18 oxygen atoms, as reported in Supplementary Section 1.

3.5. Selection of Separation System

The separation system was for high temperature vapour separations (between 600-700 °C). Hence, condensing components to then re-vaporise them would be extremely energy-inefficient and therefore have a highly adverse effect on the system COP.

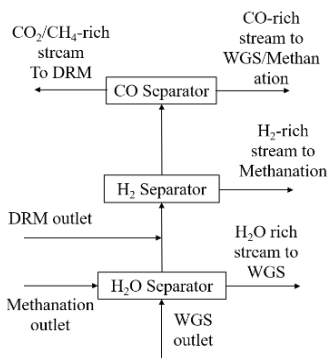

Figure 3.5.1: Simplified separation system diagram

Since all components have normal boiling points of 100 °C or less, very high pressures would be required to condense any one of them. Equally, adsorption, an exothermic process, is favoured by relatively low temperatures, hence very high pressures would be required for selective adsorption. Therefore, cryogenic distillation and pressure swing adsorption were not considered for separations, since the high pressures would lead to high compressor duty and therefore very low COP. Instead, membrane units were chosen, as only a moderate (~10^5 Pa) pressure drop is required, and would not have as significant an adverse effect on COP. The simplified separation system shown in figure 3.5.1, with three stages, for the separation of H_2O, H_2 and CO respectively, was devised.

3.6. Separation System Design

The membranes were simulated in Excel, using the assumption that only two components permeated

through each membrane. Additionally, a negligible pressure drop was assumed from the feed stream to the retenate (non-permeating membrane outlet). However, a significant pressure-drop from the feed to the permeate is necessary to provide a sufficient pressure driving force for separation. P_l, was fixed at 1 atm for all membranes and hence P_h was varied to facilitate the separation. Permeation and material balance equations were used to model membranes and calculate P_h required as well as A. Details of the modelling equations are provided in appendix section 2.

3.6.1 H_2O Separation Membrane

A highly hydrophilic A-type zeolite membrane, on a porous tubular α-Al_2O_3 support, (Aoki et al, 2000) was chosen to separate water from the combined mixed stream of methanation and WGS outlets. The membrane is thermally stable up to 200 °C, but its stability above this temperature unknown, so future testing up to 700 °C is required to verify whether this membrane is suitable for high temperature gas separation.

p_i data for all components except CO was extrapolated from 200 °C, using the same temperature dependences as is shown from ambient to 200 °C. CO permeance was not recorded in the study but was found by multiplying the p_{CO2} by a factor of 0.9, determined from a separate study into a similar zeolite membrane (Diban et al, 2013).

To use the assumption of two-component permeation, CO_2 and CO, whose p_i are very similar, were combined as an effective single component permeating, with H_2O the key permeating component. The combined permeance was weighted due to the relative molar flows in the membrane feed, as in equation 3.6.1.1 below. It should be noted that p_{H2} increases at higher temperatures and non-negligible amounts may permeate.

$$p_{CO,CO2} = \frac{L_f X_{CO} p_{CO} + L_f X_{CO2} p_{CO2}}{L_f X_{CO} + L_f X_{CO2}} \quad \text{(Equation 3.6.1.1)}$$

This relies on the assumption that p_i has a linear dependence on the feed mole fraction. This was verified given that a coefficient $K_2 << p_i$, where the dependence of p_i on X_i can be simplified to the form of equation 3.6.1.2.

$$p_i = \frac{K_1}{X_i + K_2} \quad \text{(Equation 3.6.1.2)}$$

3.7.2 H_2 Separation Membrane

A silica-alumina membrane (on a tubular γ-Al_2O_3 support) prepared by chemical vapour deposition (Gu et al, 2008) was selected for H_2 removal from the combined outlet from the DRM reactor and the retenate from the H_2O membrane. The membrane is hydrothermally stable at 600 °C, with as little as 5% reduction in p_{H2} after 135 h exposure to a 60 mol% steam environment. However, long exposure times to steam can reduce the H_2/CO_2 permselectivity, the ratio of p_{H2}/p_{CO2}.

Permselectivity data at 600 °C was used as the operating temperature is not far above this. p_{H2} however, decreases slightly as a function of temperature. H_2 and CO_2 are the only permeating components, with the others assumed to have negligible y_i. H_2 permselectivites of CO_2, CO and CH_4 are 590, 700 and 940 respectively. In practice, non-negligible amounts of CO and CH_4 would permeate the membrane; a more rigorous model should be tested in future. Some H_2O is fed to this membrane owing to non-perfect separation in the H_2O membrane, yet p_{H2O} data was not found and was assumed to be negligible.

3.7.3 CO Separation

The CO separation design was not fully specified. This is because most suitable membranes operate based on the molecular sieving mechanism, where permeance increases with decreasing molecular kinetic diameter (Gu et al, 2008). The molecular kinetic diameter of CO is between those of CO_2 and CH_4 so separation of CO from the other two using a single membrane would be challenging.

However, it was found that CO could be separated from CO_2 and CH_4 if two membranes were used, the first one like the H_2 membrane to extract CO_2 in the permeate. Secondly, CO could be extracted from CH_4 in the permeate of a separator similar to the H_2O membrane, before re-mixing the CO_2 and CH_4 to feed them into the DRM reactor.

This system was taken to estimate recoveries, using fixed P_h and A for both membranes, and the flows from the material balance on the system with perfect separation. Pressure changes in the CO separation which would require additional compression were not considered in COP calculations.

Overall estimated recoveries in the CO-rich exit stream were calculated for CO, CO_2, H_2O, H_2 and CH_4 as 0.99, 0.02, 1, 0 and 0 respectively. P_h for both membranes is 6 bar and A is 4803 and 1500 m^2 for the CO_2 and CO membranes respectively.

3.8. Reactor and separation system integration

The reactors and membrane separation system were merged across Aspen and Excel to account for the changing molar flowrates on both systems. Iterations were completed across both systems, until convergence was met with the error reported in section 3.4.

Process conditions were manipulated across both the Aspen reactor model and two-component membrane model in order to investigate their effect on system performance and requirements.

4. Results and Discussion

4.1. Thermodynamic study

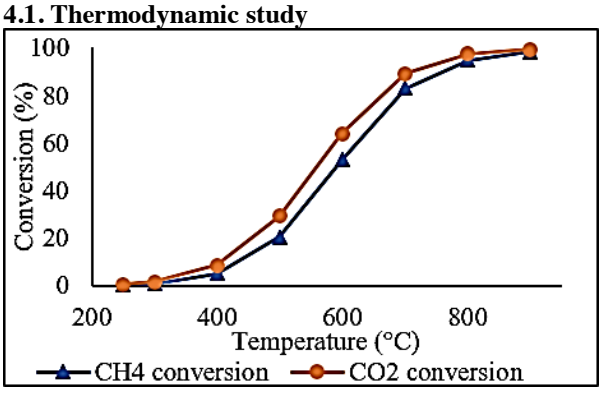

Figure 4.1.1: Plots of CH_4 and CO_2 equilibrium conversion variation with temperature in the DRM reaction under the process conditions: CH_4:CO_2 feed ratio = 1:1, total feed flowrate of 200 kmol/hr, P = 0.5 atm.

The thermodynamic analysis on the endothermic DRM reaction in figure 4.1.1 gives very low CO_2 and CH_4 conversions below 500 °C. However, as the temperature is increased to 600 °C and above the conversions are around 60%, which show promise for application in the CHP system.

From figure 4.1.2, methanation has a high equilibrium conversion over a wide temperature range, but starts to decrease significantly above 500 °C. However, it still has moderate conversions of around 30% at 700 °C. WGS, shown in figure 4.1.3, displays high equilibrium conversion over a wide range, and it remains higher than 55% even at 700°C. From this analysis the DRM operating temperature was chosen to be 600 °C and the methanation and WGS temperature 700 °C.

Table 4.3.1: Summary of kinetic models applied to system of reactors.

Reaction	DRM	WGS	CO methanation
Model type	Langmuir-Hinshelwood		
Equation	$r_{CH4}(\frac{mol}{gs}) = \frac{k_1 K_{CO2} K_{CH4} P_{CO2} P_{CH4}\left(1-\frac{P_{CO}{}^2 P_{H2}{}^2}{K_{P1}}\right)}{DEN^2}$	$r_{CO}(\frac{mol}{gs}) = \frac{k_1 K_{CO} K_{H2O}\left(P_{CO}P_{H2O}-\frac{P_{CO2}P_{H2}}{K_{eq}}\right)}{(1+K_{CO}P_{CO}+K_{H2O}P_{H2O}+K_{CO2}P_{CO}+K_{H2}P_{H2})^2}$	$r_{CO}(\frac{knol}{kghr}) = k_1\left(\frac{P_{CH4}P_{H2O}}{P_{H2}{}^{2.5}} - \frac{P_{H2}{}^{0.5}P_{CO}}{K_1}\right)\times\frac{1}{DEN^2}$
Catalyst	Ni/Al_2O_3	Fe_3O_4/Cr_2O_3	$NiMg/Al_2O_4$
Applicable temperatures(°C)	450-650	380-450	500-575
Pressure	1 bar	1 bar	3-30 bar
Source	Richardson and Paripatyadar (1990)	Twigg (1989), Rhodes (2003)	Xu and Froment (1989)

Component	CO	CO_2	H_2O	H_2	CH_4
Inlet (mol/s)	0	74.62	0	0	26.65
Outlet (mol/s)	98.13	7.74	53.75	0	0

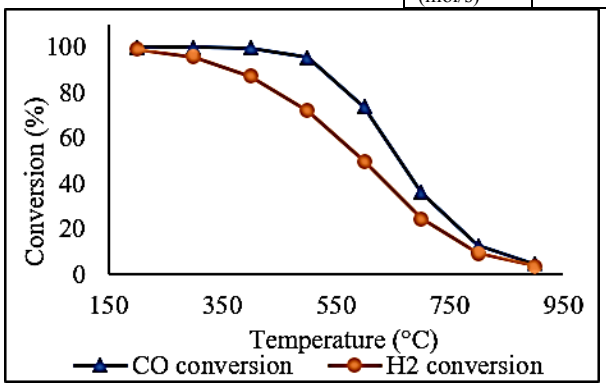

Figure 4.1.2: Plots of CO and H_2 conversion variation with temperature in the methanation reaction under the process conditions: H_2:CO feed ratio = 3:1, total feed flowrate of 400 kmol/hr, P = 1 atm.

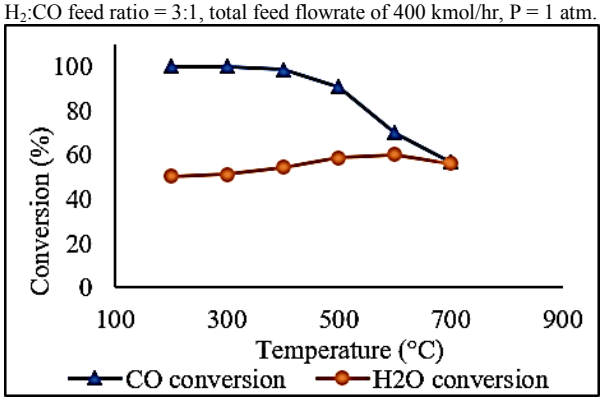

Figure 4.1.3: Plots of CO and H_2O conversion variation with temperature in WGS reaction under the process conditions: CO:H_2O feed ratio = 1:1, total feed flowrate of 200 kmol/hr, P = 1 atm

4.2. Overall flowsheet

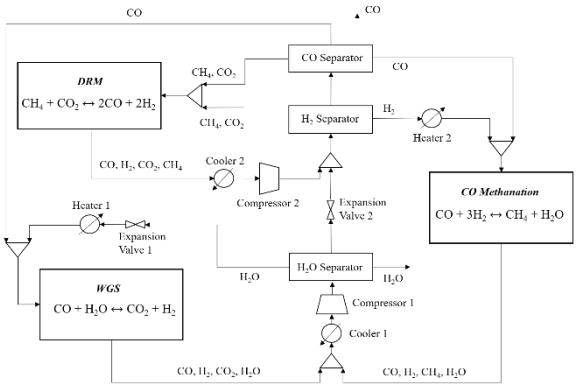

Figure 4.2.1: Overall system flowsheet detailing all process units and component flows

Table 4.2.1: Summarised inlets and outlets for overall CHP system

Table 1.2.2: Area and feed side pressure of both H_2O and H_2 membranes in converged system

Membrane	A (m^2)	P_h (bar)
H_2O	643.20	5.0
H_2	189.77	4.0

4.3. Kinetics and reactor design

Upon implementation of the power law models investigated for each reaction mechanism, it was found that there was significant over-estimation of conversions when compared to the equilibrium conversions

determined under similar reaction conditions. This is owing to the lack of adsorption and reverse reaction parameters within the models, limiting their validity to the experimental conditions over which they were developed and reducing their accuracy when scaled up. As a result, the Langmuir-Hinshelwood model for each reaction was instead applied. A summary of the models implemented can be seen in table 4.3.1. A more detailed breakdown of the equations including temperature dependence of adsorption and kinetic constants is in Supplementary material section 1. The reaction systems outlined from the sources reported in table 4.3.1 were upscaled to suit the inlet flowrates and compositions determined according to the method outlined in section

3.4. The resulting reactor dimensions and performance are summarised in appendix section 1.

4.4. Compression and heating requirements

In order to meet the pressure requirement set out by membrane system design for each separation stage, the simulation of pressure changes was done in Aspen using a system of isentropic compressors and adiabatic expansion valves as shown in figure 4.2.1.
To minimise compressor duty, the inlet streams to the compressors were pre-cooled, while avoiding condensation of water in each stream. The work and thermal requirements for this system are summarised in table 4.4.1.

Table 4.4.1: Summary of the reactor powers, compressor duties, cooler power output and heater power input required.

Unit	Duty (MW)	Heat evolved (MW)
CO methanation power output	-	55.3
WGS methanation power output	-	9.5
DRM power requirement	72.3	-
Compressor 1	38.5	-
Compressor 2	12.2	-
Cooler 1	-	77.2
Cooler 2	-	22.1
Heater 1	6.1	-
Heater 2	30.7	-

The power output from both coolers are significantly larger than the heating requirements of the reactor inlet streams within the same temperature range. Heating requirements were therefore not included in COP calculations under the assumption that integration of a heat exchange system across the heaters and coolers would eliminate the requirement for additional heating. The relative size of heating requirements and compressor duties also supports the assumption that additional heating duty would be negligible in comparison and can therefore be excluded from the COP.

4.5. COP Evaluation and benchmarking against other systems

The COP is evaluated using equation 1.3.1. To find the work term, W, the sum of duties from compressors 1 and 2 is to be combined with the difference in exothermic and endothermic reaction heats. This must be converted into an equivalent form of work and is done by multiplying the difference by the Carnot efficiency for a heat engine operating between 600-700 °C. Carnot efficiency is given in equation 4.5.1, where T_L and T_H are the low and high temperatures respectively.

$\eta_{carnot} = 1 - \frac{T_L}{T_H}$ (Equation 4.5.1)

The total exothermic reaction heat is the sum of the WGS and methanation reaction heats, so the COP expression becomes equation 4.5.2, as shown below.

$$COP_{CHP} = \frac{|\Delta H_{R,exo}|}{|W_{compressors}| + \eta_{carnot}|\Delta H_{R,DRM} - \Delta H_{R,exo}|}$$

(Equation 4.5.2)

The COP found for this system is 1.26. This is relatively low in comparison to other organic CHPs, for instance the isopropanol/acetone/hydrogen system, which achieves COP close to 4. However, these are generally low temperature systems, whereas this system operates at high temperatures.

Table 4.5.1: Comparison of high-temperature CHP systems which operate in a similar temperature range to this study.

System	Temperature range (T_L-T_H) (°C)	COP	Source
$CaO/Ca(OH)_2/H_2O$	250-600	1.7	Ogura et al, 2003
CaO/CO_2, PbO/CO_2	300-870	Not calculated (thermally driven)	Kato et al, 1998
DRM/CO methanation/WGS	600-700	1.26	This study

Table 4.5.1 compares the performance of this system to others which deliver heat to similar temperatures. This reflects a more relevant comparison as the system would aim to compete with CHPs with similar temperature ranges. The two most applicable around the chosen temperature range are $CaO/Ca(OH)_2/H_2O$ and CaO/CO_2, PbO/CO_2, however, a system could not be found for the exact range. The latter has not been developed to the point of investigating COP, possibly due to poor reversibility (Pardo et al, 2014). The former has been investigated more fully and a moderate COP value of 1.7 was found at the highest upgrade temperature of 600 °C. This value is significantly higher than this system's COP, which shows this study is not a competitive system.

4.6. Effect of temperature on reactor performance

The conversions within each reactor were investigated using the reactor design conditions reported in section 4.3. Using the corresponding extents of reaction and heats of reaction, the effect of temperature on power requirements also allowed inferences on the effect of temperature on COP. The equilibrium parameters were

determined using Aspen Gibbs reactors, giving an indication of the range over which, the kinetic model was applicable, and the proximity of reactor performance to thermodynamic equilibrium.

DRM

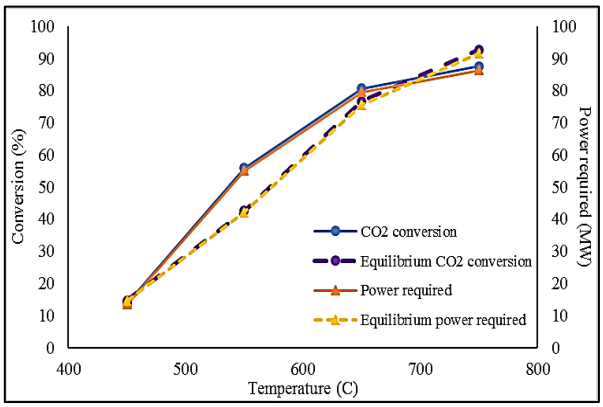

Figure 4.6.1: Plots of DRM CO_2 conversion and reaction power output with temperature in endothermic plug flow reactor. Dotted curves represent equilibrium conversions and power output. Process conditions: P = 0.5 atm, CO_2:CH_4 = 1:0.94, total feed flowrate of 924 mol/s.

From figure 4.6.1, is clear that at temperatures below 650°C, the kinetic model over-estimates the conversion of CO_2 and therefore is not applicable to this temperature range. The converged system in this study provided a CO_2 conversion of 74% using these kinetics, while the corresponding equilibrium conversion for the reactor conditions was 61%.

Inaccuracies in reactant conversion could partially be attributed to the occurrence of endothermic coking reactions. This occurs via CH_4 decomposition, gasification by steam and CO_2 which is likely under the conditions of CO_2 reforming and is the main cause for catalyst deactivation. Implementation of a kinetic model for carbon deposition and gasification alongside the Richardson and Paripatyadar model, such as that proposed by Snoeck et al., would lead to more accurate results, and accounting for the effect of catalyst deactivation would give a more realistic evaluation of the DRM reaction kinetics. This was carried out by Benguerba et al. (2014) and displayed promising results in comparison to experimental data.

This over-estimation of CO_2 conversion limited the realistic study of the endothermic system however, this could be overcome for initial design purposes by fixing the conversion in this reactor to the equilibrium value of 61%. In this study conversion was not fixed in this way.

CO methanation

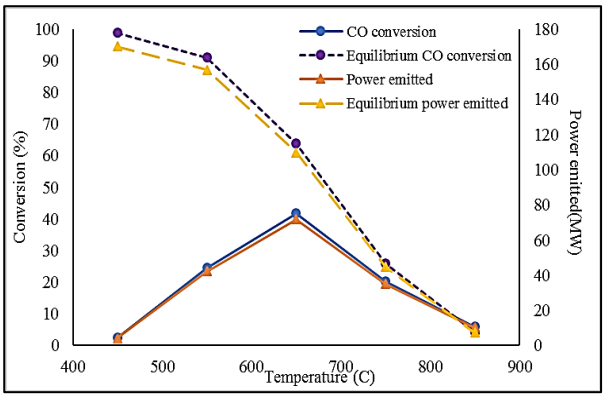

Figure 4.6.2: Plots of CO conversion and reaction power output with temperature in exothermic plug flow reactor. Dotted curves represent equilibrium conversions and power output. Process conditions: P = 2 atm, CO:H_2 feed ratio = 1:3, total feed flowrate of 3493 mol/s.

WGS

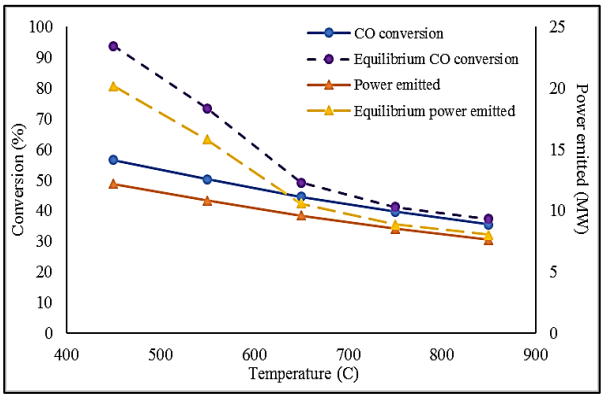

Figure 4.6.3: Plots of WGS CO conversion and reaction power output with temperature in the water-gas shift plug flow reactor. Dotted curves represent equilibrium conversions and power output. Process conditions: P = 1 atm, CO:H_2O = 1:0.7, total feed flowrate of 952 mol/s.

It can be seen in figure 4.6.2 that similar to previous thermodynamic analysis using pure inlet streams, the exothermic conversion decreases with temperature as expected by Le Chatelier's principle. At temperatures below 650°C, the reactor operates far away from equilibrium and therefore power output is not maximised. It can be said however, that at higher temperatures above 650°C the reactor operates close to equilibrium. With a moderate decline in conversion with temperature, as seen in figure 4.6.3, it can be said that the kinetic analysis supports the indication that the WGS can be applied to CHPs across a wide temperature range as seen from the thermodynamic data.

With an increase in temperature, figure 4.6.2 shows that the conversion of CO in its methanation reaction increases steadily, until it peaks at approximately 650°C before decreasing, closely following the line of thermodynamic equilibrium. In looking at the corresponding kinetics describing this reaction mechanism in table 4.3.1, the kinetic constant k_1 will see an increase with temperature as it is decomposed into a simple Arrhenius expression, as seen in Supplementary material section 1. The adsorption term for the reaction, i.e. the DEN^2 expression in the denominator of the equation, sees diminishing effects with increasing temperature, thus enabling an increase in the reaction rate with temperature. The driving force for the reaction

however, as contained in the brackets of the rate expression, is dependent on the respective rate of both the forward and reverse reactions. In applying this to the trend seen in figure x, the increase in conversion with reaction temperature for the exothermic reaction, which contradicts what is expected from Le Chatelier's principle, would be due to the more significant increase in the forward reaction rate due to the effects of the increased kinetic term and decreased adsorption term overcoming the increased prominence of the reverse reaction as we move closer toward thermodynamic equilibrium. This is seen until the optimum conversion where the curve is seen to peak, after-which the rate of the reverse reaction becomes more significant than the positive effect on overall reaction rate caused by the kinetic and adsorptive effects and the net effect on reaction rate with temperature is negative as the reaction approaches equilibrium, where the difference between the rate of forward and reverse reactions are minimised. With the fixed reactor conditions implemented throughout the analysis, the changes in reaction rate can be directly correlated to the conversion in the exothermic reactor.

From this analysis, it can be concluded that operating within a 50°C range of the 650°C mark where an optimum conversion is seen, would best suit the CO methanation reaction under the specified reaction conditions using this model.

It is clear that both the WGS and CO methanation reactors, for which the dependence of kinetics on temperature can be fairly analysed, operate at conditions close to thermodynamic equilibrium in this temperature range. As a result, to optimise the system further at these process conditions, focus should be placed outside of the reactor system and toward the system of separators.

4.7. Effect of Reactor Conversions on Separation System

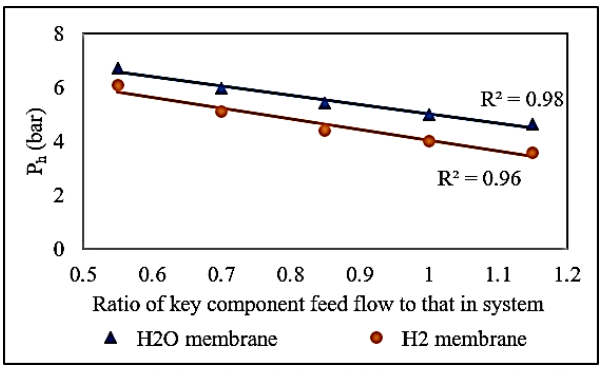

Figure 4.7.1: Variation of required P_h with key component feed flows for constant recovery and feed flow of non-key components at design area, for each membrane

It can be seen from figure 4.7.1 that the required P_h in both membrane shows a strong negative linear relation to the feed flow of key components, H_2O and H_2, in the respective membranes. A 30% reduction in key component feed flow to each membrane would result in P_h increases of 20 and 28% for the H_2O and H_2 membranes respectively.

This result can be used to predict the effect of changes in reactor conversions on the required P_h to achieve the same membrane recoveries. This could be useful in assessing the effect of temperature changes in the reactor on separation system performance and its effect on COP. For example, if the methanation conversion were to increase, more H_2O would be produced, hence more H_2O would be fed to the H_2O membrane and therefore the required P_h would be reduced. The reverse effect would likely be observed in the H_2 membrane, as H_2 is consumed by methanation. The overall effect on the COP may be balanced out as both pressures would deviate in the opposite direction.

If WGS conversion increases, more H_2O would be consumed and more H_2 produced. This would lead to a higher P_h in the H_2O membrane. Yet, the composition of the feed to the H_2 membrane may not change as more CO_2 is also produced, so the pressure across this membrane may not deviate by much. Overall, a decrease in COP is expected.

Increasing DRM conversion would only affect the H_2 membrane on first pass, since the DRM outlet is introduced to the separation system after the H_2O membrane. This would result in more H_2 produced and more CO_2 consumed, hence a lower pressure would be required and would likely increase the COP.

5. Conclusions

5.1 Key findings

An exploratory study was conducted to assess the feasibility and performance of a novel CHP system, incorporating DRM, CO methanation and WGS reactions, aiming to deliver approximately 65 MW of power from both the methanation and WGS reactors.

The key performance indicator for the system, the COP, was found to be 1.26 in upgrading heat from 600 °C to 700 °C. Of the process variables investigated, the COP had the highest dependency on the compressor duty required for the membrane separation system.

In establishing a realistic simulation of the reaction kinetics, it was found that Langmuir-Hinshelwood kinetic models were better suited to model all three reaction mechanisms at the process conditions investigated, over power law models proposed by Zhang (2009), HLA et al (2007), and Klose and Baerns (1983).

Investigation into the effect of reaction conversions on the pressures required in the membrane system suggested that variation in methanation conversion would be unlikely to alter the COP significantly, however improvements in WGS conversion would lower the COP and DRM conversion would increase COP. However, it is difficult to quantify the overall effect of conversions on the COP as the system was not converged in this case.

Compared to alternative high temperature CHP systems identified, the COP is significantly lower,

which reduces its competitiveness. For improvements to be made to the COP of the system the separation process by which the high temperature vapour components are separated should be a key area of focus for efficiency improvements. When assessing the promise of a novel chemical reaction for application to CHPs, in high temperature gaseous systems, the ease of separation of components as well as the equilibrium conversions of reactions considered should be prioritised over the heat of reaction. The former two factors have a more significant effect on COP for light-vapour systems.

5.2 Future Work

For improvements to the separation system in this CHP system a rigorous membrane design model should be simulated to test the validity of the assumptions and simplifications made. Its effect on COP should then be investigated and quantified, although this would only reduce the COP as greater loss of non-key components in the permeate would occur.

A more realistic representation of the DRM reaction kinetics using a different kinetic model would give a fairer evaluation of system performance and dependence of COP on process conditions. To give more conclusive insights into improvements to COP for this system, variations in process conditions such as reactor pressure and temperature and reactor design should be carried out and its effects quantified.

As an unconventional CHP configuration, focus should be given to the effect of overall process inlets and outlets on key performance indicators such as COP and power supply at T_H. The system could be used as a means of converting greenhouse gases into more valuable products such as fuel additives.

CHP systems of different reaction mechanisms should be investigated for lower temperature ranges where separation is less challenging.

Reactions involving cheap and easily disposable components that do not necessarily need to be separated to make the system viable should be incorporated into novel CHP systems.

References

Adams, T.A. and Barton, P.I. (2009). A dynamic two-dimensional heterogeneous model for water gas shift reactors. *Int. Journal of Hydrogen Energy*. **34** (21) 8877-8891. Available from: doi.org/10.1016/j.ijhydene.2009.08.045

Aoki, K., Kusakabe, K. & Morooka, S. (2000) Separation of Gases with an A-Type Zeolite Membrane. *Industrial & Engineering Chemistry Research*. 39 (7), 2245-2251. Available from: doi: 10.1021/ie990902c.

Aydin, D., Casey, S. P. & Riffat, S. (2015) *The latest advancements on thermochemical heat storage systems*. Available from: http://www.sciencedirect.com/science/article/pii/S1364032114007308.

Benguerba, Y.; Dehimi L.; Virginie, M.; Dumas, C. and Ernst,D. (2014) Modelling of methane dry reforming over Ni/Al_2O_3 catalyst in a fixed-bed catalytic reactor. *Reaction Kinetics, Mechanisms and Catalysis* **114**, 109-119

Cai, J., Li, X., Tao, Y., Huai, X. & Guo, Z. (2011) *Advances in Organic Liquid-Gas Chemical Heat Pumps*. Weinheim. Available from: https://onlinelibrary.wiley.com/doi/abs/10.1002/ceat.201100178.

Chua, K. J., Chou, S. K. & Yang, W. M. (2010) *Advances in heat pump systems: A review*. Available from: http://www.sciencedirect.com/science/article/pii/S030626191000228X.

Coto, B.; Martos, C.; Espada, J. J.; Robustillo, M. D. and Peña, J. L. (2010) *Fuel* **89**, 1087–1094.

Criscuoli A.; Basile A. and Drioli, E. (2000*)*. An analysis of the performance of membrane reactors for the water gas shift reaction using gas feed mixtures. *Catalysis Today*. **56**, 53- 64

Debenedetti, P. (1996) *Metastable liquids: concepts and principles*. Princeton University Press.

Diban, N., Urtiaga, A. M., Ortiz, I., Ereña, J., Bilbao, J. & Aguayo, A. T. (2013) Influence of the membrane properties on the catalytic production of dimethyl ether within situwater removal for the successful capture of co2. *Chemical Engineering Journal*. 234 140-148. Available from: doi: 10.1016/j.cej.2013.08.062.

Douglas, J. (1988). Conceptual design of chemical processes. Singapore: McGraw-Hill.

Fahim, M. A. (2010) Fundamentals of petroleum refining. In: Fahim, M. A., Alsahhaf, T. A. & Elkilani, A. S. (eds.). *Fundamentals of Petroleum Refining*. Amsterdam, Elsevier.

Fleiter, T., Worrell, E. & Eichhammer, W. (2011) *Barriers to energy efficiency in industrial bottom-up energy demand models—A review*. Available from: http://www.sciencedirect.com/science/article/pii/S1364032111001286.

Gadalla, M. A., Abdelaziz, O. Y., Kamel, D. A. & Ashour, F. H. (2015) *A rigorous simulation-based procedure for retrofitting an existing Egyptian refinery distillation unit*. Available from: http://www.sciencedirect.com/science/article/pii/S0360544215002418.

Gerner, F., Svensson, B. & Djumena, S. (2004) *Gas flaring and venting: a regulatory framework and incentives for gas utilization*. The World Bank Group.

Gu, Y., Hacarlioglu, P. & Oyama, S. T. (2008) *Hydrothermally stable silica–alumina composite membranes for hydrogen separation*. Available from: http://www.sciencedirect.com/science/article/pii/S037673880700748X.

Guo, J., Huai, X. & Xu, M. (2015) Thermodynamic analysis of an isopropanol–acetone–hydrogen chemical heat pump. *International Journal of Energy Research*. 39 (1), 140-146. Available from: doi: 10.1002/er.3237.

Industrial Heat Pumps. *How It Works*. Available from: http://industrialheatpumps.nl/en/how it works/ [Accessed 10/12/18].

Kato, Y., Saku, D., Harada, N. & Yoshizawa, Y. (1998) *Utilization of high temperature heat from nuclear reactor using inorganic chemical heat pump*. Available from: http://www.sciencedirect.com/science/article/pii/S0149197097000449.

Kato, Y., Harada, N. & Yoshizawa, Y. (1999) *Kinetic feasibility of a chemical heat pump for heat utilization of high-temperature processes*. Available from: http://www.sciencedirect.com/science/article/pii/S1359431198000490.

Moore E. B. and Molinero V. (2010) *J Chem Phys*, **132**, 244504.

Morar, M. & Agachi, P. S. (2010) *Review: Important contributions in development and improvement of the heat integration techniques*. Available from: http://www.sciencedirect.com/science/article/pii/S009813541000089X.

Ogura, H., Yamamoto, T. & Kage, H. (2003) *Efficiencies of CaO/H2O/Ca(OH)2 chemical heat pump for heat storing and heating/cooling*. Available from: http://www.sciencedirect.com/science/article/pii/S0360544203001191.

Pardo, P., Deydier, A., Anxionnaz-Minvielle, Z., Rougé, S., Cabassud, M. & Cognet, P. (2014) *A review on high temperature thermochemical heat energy storage*. Available from: http://www.sciencedirect.com/science/article/pii/S1364032113008289.

Richardson JT, Paripatyadar SA (1990) *Carbon dioxide reforming of methane with supported rhodium*. Appl Catal 61:293–309

Simpson, A. P. & Lutz, A. E. (2007) *Exergy analysis of hydrogen production via steam methane reforming*. Available from: http://www.sciencedirect.com/science/article/pii/S036031990700482X.

Sholl D.S. and Lively R.P. (2016) *Nature* **532**, 435.

Snoeck J-W, Froment GF, Fowles M (1997) *Filamentous carbon formation and gasification: thermodynamics, driving force, nucleation and steady-state growth*. J Catal 169:240–249

Snoeck J-W, Froment GF, Fowles M (1997) *Kinetic study of the carbon filament formation by methane cracking on a nickel catalyst*. J Catal 169:250–262

Snoeck J-W, Froment GF, Fowles M (2002) Steam/CO2 reforming of methane. Carbon filament formation by the Boudouard reaction and gasification by CO2, by H2, and by steam: kinetic study. *Ind Eng Chem Res* 41:4252–4265

Towler, G. P., Mann, R., Serriere, A. J. L. & Gabaude, C. M. D. (1996) Refinery hydrogen management: Cost analysis of chemically-integrated facilities. *Industrial and Engineering Chemistry Research*. 35 (7), 2378-2388. Available from: doi: 10.1021/ie950359+.

Wongsuwan, W., Kumar, S., Neveu, P. & Meunier, F. (2001) *A review of chemical heat pump technology and applications*. Available from: http://www.sciencedirect.com/science/article/pii/S1359431101000229.

Xin, F., Xu, M., Huai, X. & Li, X. (2013) *Study on isopropanol–acetone–hydrogen chemical heat pump: Liquid phase dehydrogenation of isopropanol using a reactive distillation column*. Available from: http://www.sciencedirect.com/science/article/pii/S1359431113003037.

Xu, M., Duan, Y., Xin, F., Huai, X. & Li, X. (2014) *Design of an isopropanol–acetone–hydrogen chemical heat pump with exothermic reactors in series*. Available from: http://www.sciencedirect.com/science/article/pii/S1359431114005213.

Zhang, J., Wang, H. & Dalai, A. (2009) *Kinetic studies of Carbon Dioxide Reforming of Methane over Ni-Co/Al-Mg-O Bimetallic Catalyst*. Available from https://pubs.acs.org/doi/pdf/10.1021/ie801078p

Jianguo Xu, Gilbert F. Froment (1989) *Methane Steam Reforming, Methanationand Water-Gas Shift: 1. Intrinsic Kinetics. Laboratorium voorPetrochemische Techniek Rijksuniversiteit Gent Gent, Belgium*

San Shwe Hlaa,∗, D. Parka, G.J. Duffy b, J.H. Edwards b, D.G. Roberts a, A. Ilyushechkina, L.D. Morpetha, T. Nguyen (2008) *Kinetics of high-temperature water-gas shift reaction over two iron-basedcommercial catalysts using simulated coal-derived syngases Available from: https://www.academia.edu/12324892/Kinetics_of_high-temperature_water-gas_shift_reaction_over_two_iron-based_commercial_catalysts_using_simulated_coal-derived_syngases*

Twigg M V, *"Catalyst Handbook", second edition, Wolfe Publishing Ltd., 1989*

Moe J. M. *"Design of water-gas shift reactors", Chemical Engineering Progress,58, 1962, 33-36*

Rhodes C and Graham J. Hutchings, *"Studies of the role of the copper promoterin the iron oxide/ chromia high temperature water gas shift catalyst", Phys.Chem. Chem. Phys., 5, 2003, 2719–2723*
J. Klose And M. Baerns(1983) *Kinetics of the Methanation of Carbon Monoxide on anAlumina-Supported Nickel Catalyst Lehrstuhl fir Technische Chemie, Ruhr-Universitiit Bochum, Postfach 102148,*
D-4630 Bochum, West Germany

Numerical simulation and classification of multicomponent polymer precipitation

Pavan K. Inguva, Miselle T. Hengardi

Department of Chemical Engineering, Imperial College London, South Kensington, London SW7 2AZ, United Kingdom

Abstract

Multicomponent polymer systems are of immense interest in a wide variety of applications, ranging from organic photovoltaics to drug delivery. These systems have a large number of possible morphologies which can potentially influence their performance. Understanding and classifying these various patterns and developing tools for morphology prediction based on input parameters such as composition will aid in polymer engineering. We use a modified Cahn–Hilliard model coupled with the incompressible Navier–Stokes equations to model polymer precipitation. Three cases are considered: (i) ternary polymer blends (denoted as PPP-static), (ii) two-polymer, one-solvent (PPS-static) systems where mass transport is diffusion-only, and (iii) a PPP system with both convective and diffusive transport (PPP-flow). PPS-static systems have simpler morphologies compared to PPP-static systems. The presence of shear increased the number of patterns possible due to a variety of effects such as shear induced coalescence and stratification. A data-driven method of clustering and classification based on principal component analysis (PCA) was then implemented; clustering was found to be accurate for the static cases, but was less effective in flow cases. Supervised machine learning using Gaussian process classification was subsequently used to predict model clusters according to input parameters. A proof of concept for morphology prediction based on initial concentrations, a_0 and b_0, was implemented with $\sim 100\%$ accuracy.

1. Introduction

Multicomponent polymer systems are of immense interest for their application in a variety of industries. Examples of such applications include high performance plastics,[1] membrane systems,[2,3] nanoparticle and nano-colloidal systems[4–6] and organic photovoltaics.[7] The list of applications is non-exhaustive, and these systems correspondingly are a rich area of on-going research and development. One of the key features is the morphology of the polymeric particles/blends formed, which is of significance in characterising and engineering these systems. Flow and rheology have a large impact on particle/blend morphology[8] and other properties such as miscibility,[9] which influence synthesis, processing and blending operations.

Computational methods provide an excellent tool for modelling various phenomena across various scales in polymeric systems.[10] These modelling techniques are valuable in both the understanding of fundamental properties such as polymer blend miscibility and the development engineering applications which require tuning particle morphology.

On a molecular/atomistic scale, techniques such as Molecular Dynamics (MD) have been widely used in polymer systems to evaluate various properties such as the miscibility and interactions of polymers in a blend or with other species,[11,12] diffusion coefficients and transport characteristics,[13] composite elasticity[14] and nanoparticle morphology.[5] Recent MD simulation studies have also considered the effect of flow on the morphology of anisotropic nanoparticles.[15,16] These anisotropic particles include Janus nanoparticles, which are an interesting case within the possibility space of multicomponent polymer systems.

The limitation with discrete approaches such as MD is that it cannot capture information about the system at larger length and time scales that continuum-scale approaches categorically do. Phase field models such as the Cahn–Hilliard system[17] are immensely useful in capturing the dynamic behaviour of structures and morphologies in heterogenous systems. These models can readily account for various thermodynamic driving forces for morphology evolution, such as homogeneous free energy and interfacial energy, and also account for other relevant transport phenomena such as convection.[18]

Previous work in phase field simulations of multicomponent polymer systems has focused on cases where mass transport occurs by 'uphill' diffusion, as described by the Cahn–Hilliard equation. Examples of this include systems studying two polymers and one solvent (PPS),[19,20] or ternary polymer systems.[1,20] Studies that considered the influence of flow in multicomponent systems have only considered a single polymer in the presence of a solvent and non-solvent (PSS).[21,22] This clearly shows a knowledge gap in the understanding of how systems containing more than one polymer, i.e. PPS and PPP systems, behave in the presence of convective mass transport. We denote systems where mass transport occurs by diffusion only as 'static' and systems with both convective and diffusion as 'flow'.

Machine learning is a powerful tool that can be used in studying polymeric systems under these various conditions. The advent of machine learning has sparked its

December 13, 2018

widespread use in various fields. Within broader material science, machine learning has found widespread use ranging from multiscale prediction of surfactant solutions,[23] to the production of new permanent magnets as part of the green movement[24] and in the optimisation of alloy properties.[25]

In polymer science, machine learning has been gaining traction. Examples of applications in this field include the optimisation of polymer gels screening for injection wells,[26] screening suitable polymers for use in solar cells,[27] and improvements in polymeric interfacial compatibilisation.[28] Machine learning has also been used for classifying and predicting physical features of polymers. For instance, a feed-forward neural network for supervised learning was used to recognise configurations produced from Monte Carlo simulations of polymer models, distinguishing between differently ordered states.[29] The mechanism of self-folding of polymer composite systems comprising active soft hydrogels and passive hard polymers, and the prediction of this process, has been modelled as well.[30] There is however a knowledge gap in the use of machine learning as a tool for classifying and even predicting polymer morphology, despite its suitability.

Machine learning tools such as principal component analysis (PCA) and Gaussian process classification (GPC) can be used in the analysis of polymer systems. PCA simplifies the complexity in high-dimensional data to extract features in a dataset, while GPC is a supervised machine learning algorithm typically used for classification. Some of the current work in the field of materials informatics involve the extraction of datasets from images, and subsequently using various classification techniques to classify the data by shape. This method has been applied to the classification of carbon black aggregates according to their shape,[31] as well as in determining the functional groups which play important roles in the outer structure of nanoparticles.[32] A combination of PCA and GPC will be used for polymer morphology analysis in the following sections.

This study has the following objectives: (i) simulate multicomponent polymer precipitation (static and flow), (ii) develop a data-driven framework for the classification and analysis of polymer morphology, and (iii) predict a morphology from given input parameters.

2. Theory and Methodology

2.1. Cahn–Hilliard system

The multicomponent Cahn–Hilliard system used in this study was based on the work of Petrischeva and Abart.[33] Their approach, which accounted for substitutional interdiffusion with a treatment of the mobility matrix, enabled the modelling of systems where species may have large differences in diffusivities. It is extendable to more components and can be readily coupled to other equations. This is important for systems containing polymers and solvents or polymers of significantly differing chain lengths.[20] Previous approaches for modelling these systems, such as that by Alfarraj and Nauman,[20] not only assumed that j_i only depends on $\nabla\mu_i$ i.e. interdiffusion is neglected, but also formulated N transport equations for an N component system. This can be contrasted to the more conventional approach of treating $N-1$ variables as independent and inferring the last component by a material balance constraint. To ensure that the material balance constraint is met, Alfarraj and Nauman[20] adopted a 'proportional flux model' to ensure the sum of fluxes into a point is zero. This model is firstly not readily implementable in declarative solvers such as FEniCS. Secondly, the impact this model may have on the numerical solution of the system when coupled to the Navier–Stokes equations is unknown.

The flux j_i of species i can be represented as

$$j_i = -\sum_j L_{ij}\nabla\mu_j, \tag{1}$$

where L_{ij} is the mobility coefficient and can be expressed in the square symmetric mobility matrix L.

The following constraints are imposed:

$$L_{ij} = L_{ji}, \quad \sum_i L_{ij} = 0, \quad \sum_i j_i = 0. \tag{2}$$

Correspondingly j_i can be expressed as differences in chemical potentials:

$$j_i = \sum_j L_{ij}\nabla(\mu_i - \mu_j). \tag{3}$$

As the Gibbs energy functional is scaled by RT, L_{ij} can be expressed with the following relationship:

$$L_{ij} = -D_{ij}x_i x_j. \tag{4}$$

L_{ij} is compositionally dependent, but D_{ij} which is the effective diffusion coefficient maybe a constant.

To obtain the relevant transport equation for each species, we apply the continuity equation:

$$\frac{\partial x_i}{\partial t} + \nabla\cdot j_i = 0. \tag{5}$$

An expression for the chemical potentials is required. A generalised Landau–Ginzburg free energy functional for N components which accounts for inhomogeneity in the system is used:[17,34]

$$G_{\text{system}} = \int_v g(x_1, x_2 ... x_N) + \sum_i^{N-1} \frac{\kappa_i}{2}(\nabla x_i)^2 + \sum_{j>i}\sum_i^{N-1} \kappa_{ij}(\nabla x_i)(\nabla x_j)dV, \tag{6}$$

where g is the homogenous free energy contribution, and κ_i and κ_{ij} are the gradient energy parameters. For polymer/solvent systems, the homogeneous free energy is well represented by the Flory–Huggins equation:

$$g(x_1, x_2, \ldots, x_N) = \sum_i^N \frac{x_i}{n_i}\ln x_i + \sum_{\text{j>i}}\sum_i^{N-1} \chi_{ij}x_i x_j, \tag{7}$$

where n_i is the polymer chain length and χ_{ij} is the Flory–Huggins binary interaction parameter. The generalised chemical potential applicable for inhomogenous systems for each species i can be expressed as the variational derivative of the Gibbs energy functional:.[34,35]

$$\mu_i = \frac{\delta G_{\text{system}}}{\delta x_i} = \frac{\partial G}{\partial x_i} - \nabla \cdot \frac{\partial G}{\partial \nabla x_i}. \tag{8}$$

As the focus of this study is on ternary systems i.e. PPP and PPS systems, we replace x_i with a, b, c to represent the mole fractions of species A, B and C respectively. In the PPP system, species A, B and C are all polymers and in PPS, species A and B refer to polymers while species C is the solvent. We can write the following equations for the differences in chemical potential:

$$\mu_{\text{AB}} = \mu_{\text{A}} - \mu_{\text{B}} = \frac{\partial g}{\partial a} - \frac{\partial g}{\partial b} - (\kappa_{\text{A}} - \kappa_{\text{AB}})\nabla^2 a + (\kappa_{\text{B}} - \kappa_{\text{AB}})\nabla^2 b \tag{9}$$

$$\mu_{\text{AC}} = \mu_{\text{A}} - \mu_{\text{C}} = \frac{\partial g}{\partial a} - \frac{\partial g}{\partial c} - \kappa_{\text{A}}\nabla^2 a - \kappa_{\text{AB}}\nabla^2 b \tag{10}$$

$$\mu_{\text{BC}} = \mu_{\text{B}} - \mu_{\text{C}} = \frac{\partial g}{\partial b} - \frac{\partial g}{\partial c} - \kappa_{\text{B}}\nabla^2 b - \kappa_{\text{AB}}\nabla^2 a. \tag{11}$$

The gradient energy parameters for the PPP system[1] and PPS system[36] can be evaluated as follows. We specifically consider the case of all polymer species having the same radius of gyration R_{G} and diffusivity.

PPP:

$$\kappa_{\text{A}} = \frac{2}{3} R_{\text{G}}^2 \chi_{\text{AC}} \tag{12}$$

$$\kappa_{\text{B}} = \frac{2}{3} R_{\text{G}}^2 \chi_{\text{BC}} \tag{13}$$

$$\kappa_{\text{AB}} = \frac{1}{3} R_{\text{G}}^2 \Big(\chi_{\text{AC}} + \chi_{\text{BC}} - \chi_{\text{AB}} \Big) \tag{14}$$

PPS:

$$\kappa_{\text{A}} = \frac{1}{3} R_{\text{G}}^2 \chi_{\text{AC}} \tag{15}$$

$$\kappa_{\text{B}} = \frac{1}{3} R_{\text{G}}^2 \chi_{\text{BC}} \tag{16}$$

$$\kappa_{\text{AB}} = \frac{1}{6} R_{\text{G}}^2 \Big(\chi_{\text{AC}} + \chi_{\text{BC}} - 2\chi_{\text{AB}} \Big) \tag{17}$$

The compositional dependence of κ_i/κ_{ij} is neglected as it significantly simplifies computations. Neglecting this dependence is an approach commonly used by similar simulation studies.[1,20,22]

We correspondingly arrive at the following transport equations tracking species A and B:

$$\frac{\partial a}{\partial t} = \nabla \cdot \Big(D_{\text{AB}} ab \nabla \mu_{\text{AB}} + D_{\text{AC}} ac \nabla \mu_{\text{AC}} \Big) \tag{18}$$

$$\frac{\partial b}{\partial t} = \nabla \cdot \Big(- D_{\text{AB}} ab \nabla \mu_{\text{AB}} + D_{\text{BC}} bc \nabla \mu_{\text{BC}} \Big). \tag{19}$$

Species C is obtained by using a material balance constraint:

$$c = 1 - a - b. \tag{20}$$

In the instance of a symmetric PPP system where the diffusivities of all species can be assumed to be equal, this equation system reduces to that outlined by Nauman and He.[1]

2.2. Coupling to fluid flow

The approach to coupling the effect of fluid flow is to add advection terms to the diffusive transport equations eq. (18) and eq. (19) as follows:

$$\frac{\partial a}{\partial t} + \nabla \cdot (a\boldsymbol{u}) = \nabla \cdot (D_{\text{AB}} ab \nabla \mu_{\text{AB}} + D_{\text{AC}} ac \nabla \mu_{\text{AC}}) \tag{21}$$

$$\frac{\partial b}{\partial t} + \nabla \cdot (b\boldsymbol{u}) = \nabla \cdot (-D_{\text{AB}} ab \nabla \mu_{\text{AB}} + D_{\text{BC}} bc \nabla \mu_{\text{BC}}) \,. \tag{22}$$

The incompressible Navier–Stokes and continuity equations can be formulated as follows:

$$\nabla \cdot \boldsymbol{u} = 0 \tag{23}$$

$$\rho \frac{\partial \boldsymbol{u}}{\partial t} + \rho \boldsymbol{u} \cdot \nabla \boldsymbol{u} = -\nabla p + \nabla \cdot [\mu(\nabla \boldsymbol{u} + \nabla \boldsymbol{u}^{\text{T}})] + \boldsymbol{F}_{\text{b}}, \tag{24}$$

where ρ is the fluid density, μ is the fluid viscosity and $\boldsymbol{F}_{\text{b}}$ is a coupling body force. This coupling body force has been described as a diffuse surface tension force.[22,37,38] Gravity and the random body force due to thermal noise are neglected.[38] $\boldsymbol{F}_{\text{b}}$ can be written as follows based on the derivation by Zhou and Powell[22] and Jacqmin:[39]

$$\boldsymbol{F}_{\text{b}} = -c_{\text{T}} RT (a \nabla \mu_{\text{A}} + b \nabla \mu_{\text{B}}), \tag{25}$$

where c_{T} is the total concentration. It is convenient to express $\boldsymbol{F}_{\text{b}}$ in terms of differences in chemical potential, and this can be done so via a Gibbs–Duhem relationship;

$$\boldsymbol{F}_{\text{b}} = -c_{\text{T}} RT (ac \nabla \mu_{\text{AC}} + bc \nabla \mu_{\text{BC}}). \tag{26}$$

2.3. Non-dimensionalisation

We introduce the following scalings:

$$\boldsymbol{x} = d_{\text{p}} \tilde{\boldsymbol{x}} \tag{27}$$

$$t = \frac{n d_{\text{p}}^2}{D_{\text{AB}}} \tilde{t} \tag{28}$$

$$\boldsymbol{u} = u_{\text{s}} \tilde{\boldsymbol{u}} \tag{29}$$

$$p = \frac{\rho u_{\text{s}} D_{\text{AB}}}{n d_{\text{p}}} \tilde{p}, \tag{30}$$

where d_{p} is the characteristic length scale.The chemical potential and Gibbs energy functional are scaled by RT.

From here onwards, they will be written as $\tilde{\mu}_i$. This results in the following equation system:

$$\frac{\partial a}{\partial \tilde{t}} + n\mathrm{Pe}\tilde{\nabla}\cdot(a\tilde{\boldsymbol{u}}) = \tilde{\nabla}\cdot\left(ab\tilde{\nabla}\tilde{\mu}_{\mathrm{AB}} + \frac{D_{\mathrm{AC}}}{D_{\mathrm{AB}}}ac\tilde{\nabla}\tilde{\mu}_{\mathrm{AC}}\right) \quad (31)$$

$$\frac{\partial b}{\partial \tilde{t}} + n\mathrm{Pe}\tilde{\nabla}\cdot(b\tilde{\boldsymbol{u}}) = \tilde{\nabla}\cdot\left(-ab\tilde{\nabla}\tilde{\mu}_{\mathrm{AB}} + \frac{D_{\mathrm{BC}}}{D_{\mathrm{AB}}}bc\tilde{\nabla}\tilde{\mu}_{\mathrm{BC}}\right) \quad (32)$$

$$\tilde{\nabla}\cdot\tilde{\boldsymbol{u}} = 0 \quad (33)$$

$$\frac{\partial \tilde{\boldsymbol{u}}}{\partial \tilde{t}} + n\mathrm{Pe}\tilde{\boldsymbol{u}}\cdot\tilde{\nabla}\tilde{\boldsymbol{u}} = -\tilde{\nabla}\tilde{p} + n\mathrm{Sc}\tilde{\nabla}\cdot(\tilde{\nabla}\tilde{\boldsymbol{u}} + \tilde{\nabla}\tilde{\boldsymbol{u}}^{\mathrm{T}}) - n\beta(ac\tilde{\nabla}\tilde{\mu}_{\mathrm{AC}} + bc\tilde{\mu}_{\mathrm{BC}}), \quad (34)$$

where Pe is the Péclet number defined as $\mathrm{Pe} = Lu_{\mathrm{s}}/D_{\mathrm{AB}}$, Sc is the Schmidt number defined as $\mathrm{Sc} = \mu/\rho D_{\mathrm{AB}}$ and β is a dimensionless coupling constant $\beta = c_{\mathrm{T}}RTd_{\mathrm{p}}/\rho u_{\mathrm{s}}D_{\mathrm{AB}}$.

2.4. Numerical implementation

Equations (18) to (20) model the static cases while equations eqs. (31) to (34) and eq. (20) model the flow cases. These equations are reformulated in their variational form and solved with the open-source finite-element solver FEniCS. Equations (9) to (11) and eqs. (18) to (19) / eqs. (31) to (32) are treated as a set of coupled second-order equations and declared as such within the FEniCS environment. The Navier–Stokes equations eqs. (33) to (34) are discretised using a three stage incremental pressure correction scheme (IPCS). A full treatment on the discretisation and implementation of the variational problem in FEniCS is available in the supporting information.

An unstructured square mesh of domain length $40d_{\mathrm{p}}$ was generated. Mesh resolution was set such that there were 80 cells on each vertex. All variables were treated implicitly. Time discretisation was performed using the backward Euler method. PPP cases were simulated for $\tilde{t} = 400$ with a time step $\Delta\tilde{t} = 0.05$. PPS cases were simulated for $\tilde{t} = 1.00$ with a time step $\Delta\tilde{t} = 0.0001$. In all cases, this corresponds to a physical time of $t = 16\,\mathrm{s}$. Periodic boundary conditions were applied on the left and right vertices and Neumann boundary conditions were applied to the top and bottom vertices.

Nextflow was used to script batches of simulations.[40] Post-processing to extract the last frame of the simulation was scripted with Paraview 5.4.1.

The following values were used for each of the physical parameters: $R_{\mathrm{G}} = 200 \times 10^{-10}\,\mathrm{m}$, for PPP cases, $d_{\mathrm{p}} = R_{\mathrm{G}}$ and for PPS cases, $d_{\mathrm{p}} = 400 \times 10^{-9}\,\mathrm{m}$,[5] $D_{\mathrm{Polymer}} = 10^{-11}\,\mathrm{m^2s^{-1}}$, $D_{\mathrm{Solvent}} = 10^{-8}\,\mathrm{m^{-2}s^{-1}}$. Values of χ_{ij} simulated ranged from $\mathcal{O}(10^{-3})$ to $\mathcal{O}(10^{-2})$.

2.5. Machine learning

2.5.1. Classification methodology

Numerous analytical methods of distinguishing these different morphologies are possible; in this paper, a form of unsupervised learning known as principal component analysis (PCA) was used. Based on specified parameters comprising the initial component concentrations, χ values and diffusivities, high-resolution images of the predicted multi-polymer systems are generated. From these images, concentration fields corresponding to each of the three components are extracted as grayscale images. These are then resized to 100×100 pixels, and the sets of three images are subsequently flattened and concatenated into a one-dimensional array of length 30,000. These arrays are then subjected to PCA for feature extraction as part of the unsupervised learning component.

Principal component analysis. *scikit-learn*'s principal component analysis tool implements the probabilistic PCA model from Tipping and Bishop.[41] It is a popular technique for dimensionality reduction, for extended use in compressing, analysing and visualising data. Under PCA, for a set of observed d-dimensional data vectors t_n, the q principal axes are the orthonormal axes onto which the retained variance under projection is maximal. A complementary property of PCA is that the projection onto the principal subspace minimises the squared reconstruction error

$$\sum \|t_n - \hat{t}_n\|^2. \quad (35)$$

PCA was used to analyse the arrays obtained from the generated images to determine if any common features exist between the datasets. This analysis found that the use of two principal components (PC1 and PC2) was able to capture approximately 76% of the variance in the images, with only marginal improvements with the inclusion of more principal components (PC). The images are then grouped into clusters using *scikit-learn*'s K-means clustering algorithm.

2.5.2. Morphology prediction methodology

scikit-learn's in-built Gaussian process classifier is subjected to a training set comprising two initial concentrations and the determined cluster. A separate test set is used to check if the classifier returns the correct cluster, given specific parameters. A physical system is chosen, and the initial species concentrations varied within a specific range. The model is then trained on the arrays obtained, and is tested on a separate testing set to determine if the returned cluster predictions are accurate.

Gaussian process classifier. The Laplace approximation is used in the operation of *scikit-learn*'s inbuilt Gaussian process classifier. Gaussian processes are a method of supervised learning, used in problems involving regression and probabilistic classification. The predictions can be interpolated from the observations, and are probabilistic, allowing for empirical confidence intervals to be calculated.

Gaussian process classification is non-parametric, and is based on a Bayesian methodology. It is assumed that the underlying probability densities are based on some prior distribution, thus guaranteeing smoothness. This is done

by taking the smoothness prior into account, while taking into account the observed classification of the training data.

The Bayesian parameter estimation involves firstly the assumption of a prior distribution for a model's parameters, and then factoring in the observed data to obtain a posterior distribution of the parameters. The prediction for a new point can then be estimated by approximating its distribution.

3. Results and discussion

3.1. Model validation

Nauman and He[1] presented multiple simulations for a static PPP case which highlighted a variety of possible morphologies. A sample of the variety of results obtained, comprising twelve images corresponding to twelve different conditions, were presented. These 12 cases were thus selected as a test to benchmark the performance and accuracy of the developed model. A representative comparison between the developed model and the corresponding benchmark is shown in fig. 1. From a visual inspection of the rest of the plates, there is more than 90% agreement between our model and the work of Nauman and He,[1] indicating that the developed model is accurate. The full set of images can be found in the supplementary information. For PPS-static and PPP-flow cases, there is a paucity of literature available to benchmark the model.

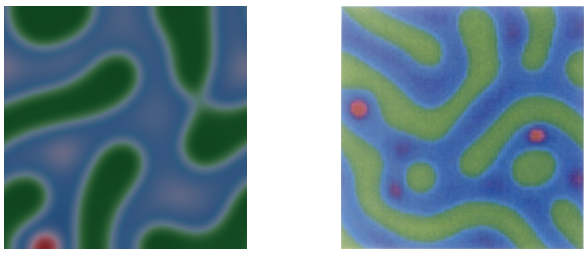

(a) (b)

Figure 1: (a) Simulation Plate 1 and (b) corresponding Plate 1 from Nauman and He[1] benchmark. Reproduced with permission.

To evaluate whether equilibrium states were attained, the Gibbs energy was evaluated across the domain by integrating eq. (6) at each time step. This revealed three possible states that the simulation can take:

1. The Gibbs energy decreased over time and appeared to taper off. In static cases, the run would run for the full $\tilde{t}$, but in flow cases, pattern formation was more rapid. These cases resulted in images where patterns were present.
2. The simulation ran for the full simulation time, but the Gibbs energy appeared to remain constant. These simulations did not generate patterns.
3. The Gibbs energy decreased and a pattern was emerging, but the simulation diverged and terminated early.

Images from the first case were retained and used for subsequent analysis, while data from the other two cases was discarded.

3.2. Morphology clustering and classification

3.2.1. PPP-static

In this dataset, the initial concentration of species A, a_0, is varied between 0.3 and 0.8 while that of species B, b_0, is varied between 0.1 and 0.45. The Flory–Huggins parameters, χ_{AB}, χ_{AC} and χ_{BC}, take values of between 0.003 and 0.006. By using PCA as the basis for clustering and classification, two degrees of freedom are available. These are (i) the number of principal components (PC) used, and (ii) the number of clusters that the dataset is grouped into.

Number of principal components. It was found that the use of two PCs can account for 76% of the variance between the patterns obtained. The use of additional PCs increases this percentage at a diminishingly smaller rate; the use of four and eight PCs explain 82% and 88% of the variance respectively. It was found that there appears to be no significant difference or improvement in the clustering as compared to when only two PCs were used. This suggests that since there is little additional benefit to classification with 3 PCs, it is not worthwhile to include more PCs and therefore increase the computational requirement of the system. As such, two PCs was used as the basis for classifying the patterns obtained.

Number of clusters. The other variable in this process is the number of clusters present, which had to be manually set. This parameter was varied, and the resulting clustered images were visually inspected to determine the optimal number. It was found that six clusters were sufficiently able to capture the variations in morphology across the frames generated from the simulations, and the clusters can be visualised in fig. 2 below. This number also avoids over-segregation that would result in systems exhibiting similar morphological features being classified in different clusters.

The general morphologies observed among the images in each cluster are outlined in table 1.

Accuracy of clustering. The different clusters have been reasonably well segregated. This effective clustering suggests that for the PPP static system, clustering based on PCA is able to distinguish between different polymer blend morphologies. However, there still remains some misclustering when this method is used, with several images in each cluster exhibiting slightly different morphologies compared to the rest.

3.2.2. PPS-static

The method of analysing the static ternary polymer system was extended to the PPS-static system. The results of clustering are shown in fig. 3. Similar ranges for a_0, b_0

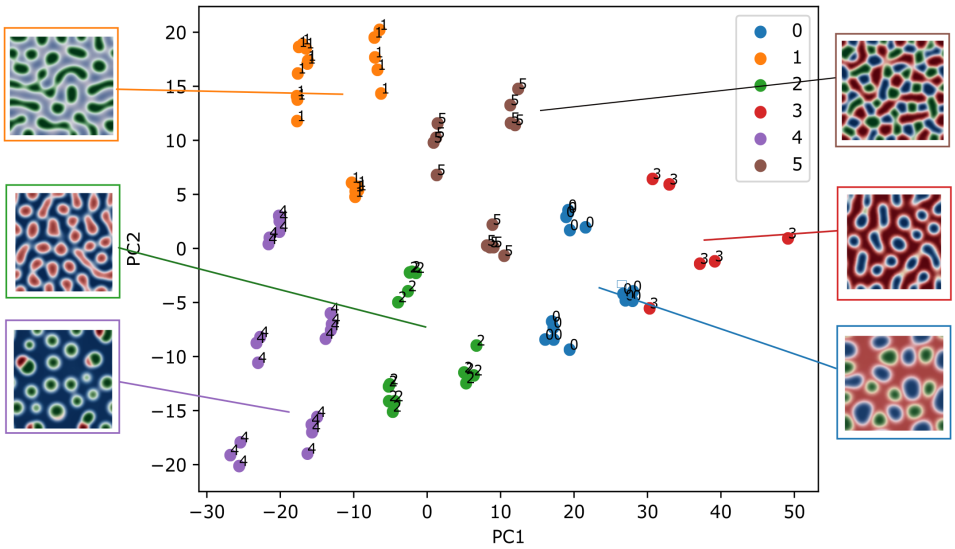

Figure 2: Clustering of PPP-static cases, with 6 clusters. Sample images from each cluster are shown.

and χ_{AB} were tested, however, values of χ_{AC} and χ_{BC} were set at one order of magnitude higher, i.e. between 0.03 and 0.06. It is interesting to note that runs with high polymer concentrations, e.g. $a_0 + b_0 = 0.9$, diverged.

Table 1: Outline of PPP-static morphologies.

Cluster	Observed morphology
0	Two of the phases exist as dispersed, irregular and primarily circular domains.
1	One phase exists as dispersed, compact and mostly elongated (but with several circular) domains, with one of the phases separating the other two at their interface.
2	One phase exists as dispersed, compact and mostly circular (but with several elongated) domains, with one of the phases separating the other two at their interface.
3	One phase exists as dispersed, compact and mostly circular (but with several elongated) domains, with one of the phases separating the other two at their interface.
4	One phase exists as dispersed, compact and circular domains. Several particles comprise two phases attached interfacially.
5	Interconnected webs are observed, with each of the three phases existing as dispersed, compact and irregularly-shaped domains that are connected to each other.

Summary of clustering. In line with the PPP-static base case, the PPS simulations were split into six clusters. It can be seen in fig. 3 that this gives reasonably distinct clusters with identifiable differences between the images that have been grouped into the different clusters. It is, however, worth noting that some of the clusters appear to be segregated according to colour. For example, clusters 1 and 2 appear to both show discrete particles, with the largest identifiable difference between the two clusters being the primary colours that can be observed in their respective images. Similarly, clusters 4 and 5 both show continuous channels, distinguished by the different colour schemes that are observed.

Observed morphologies. The observed morphologies for the PPS system are primarily particles and continuous channels; clusters 1 and 2 most distinctly show separate particles, while the others show continuous channels. It can be seen that the PPS morphologies appear to be simpler than the ones observed for PPP. From analysing the morphology of each species, which is done during the image processing step where each colour channel is extracted, it is found that the solvent species c was largely homogeneously distributed across the domain. This results in the morphological variations arising from the demixing of the two polymer species A and B. As there are only two polymer species, the number of possible morphologies decreases combinatorically, resulting in the simpler morphologies observed. These have been outlined in table 2.

3.2.3. PPP-flow

These simulations were carried out with similar χ_{ij} and a_0 and b_0 values as the PPP-static case. Dimensionless

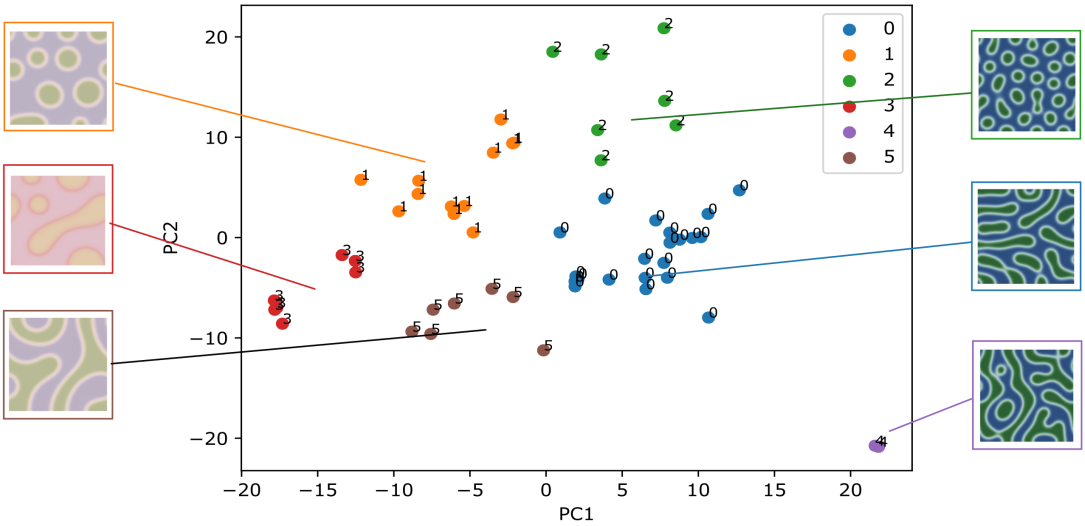

Figure 3: Clustering of PPS-static cases, with 6 clusters. Sample images from each cluster are shown.

values of Sc $= 10^{15}$ and $\beta = 10^4$ were assumed. The large values of Sc and β are a result of the high polymer viscosity and low diffusivity. Pe was tested at 0.001 and 10. When shear was imposed on the ternary polymer system, this resulted in novel morphologies that were not observed in the previous static cases. These include flow-induced coalescence and stratification.

Table 2: Outline of PPS-static morphologies.

Cluster	Observed morphology
0	One phase exists as dispersed, irregular and elongated domains, with one of the phases separating others at their interface.
1	One phase exists as dispersed, compact and mostly circular (but with several elongated) domains, with one of the phases separating the other two at their interface.
2	One phase exists as dispersed and mostly circular domains, with one of the phases separating the others at their interface.
3	One phase exists as dispersed, compact and mostly elongated (but with several circular) domains, with one of the phases separating the other two at their interface.
4	One phase exists as dispersed, irregular and elongated domains. Several domains of this phase are continuous, with the presence of an uninterrupted path from each boundary of the domain to another.
5	One phase exists as dispersed, irregular and elongated domains. Several domains of this phase are continuous, with the presence of an uninterrupted path from each boundary of the domain to another.

Summary of clustering. The number of clusters was once again set at six, i.e. the same number as that of the base case of static ternary polymer system. It can be observed that the implementation of the same analysis results in far less effective clustering once flow has been imposed. Testing various numbers of clusters and principal components did not improve this. Clustering appears to be unable to distinguish between stratified and non-stratified images, as seen in fig. 4, although the presence of stratification is very distinct visually. The primary feature that distinguishes the different clusters once again appears to be the colour schemes observed within each cluster.

Impact of shear. At Pe $= 0.001$, four broad morphological trends can noticed: (i) enlarged domains, (ii) increased connectivity between domains, (iii) deformed domains, and (iv) stratified layers. The first two trends can be understood as a result of shear induced coalescence. Convective mass transport enables domains to come into contact, which correspondingly allows previously separated domains to increase in size or increase in connectivity.[42] Shear can similarly explain trend (iii), as shear can cause deformations of various domains such as droplets of polymer species within a blend in the direction of the shear.[42] The stratification, as can be seen from various sample images in fig. 4, has been experimentally observed in polymer blends subjected to shear. This stratification has been described as a 'droplet–string' transition[43] as can be seen in fig. 5.

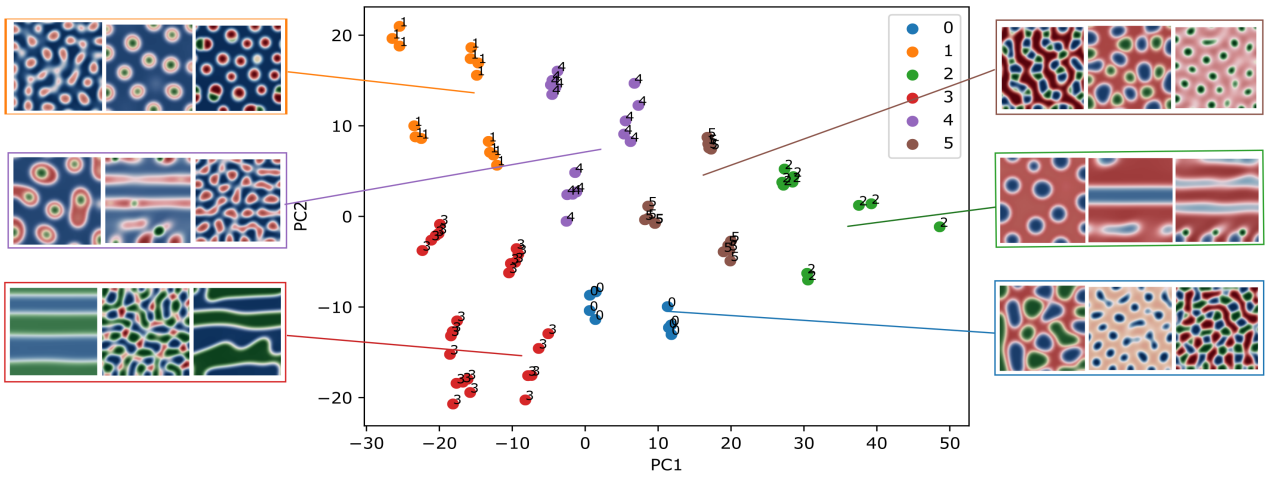

Figure 4: Clustering of PPP-flow cases, with 6 clusters. Sets of three sample images from each cluster are shown.

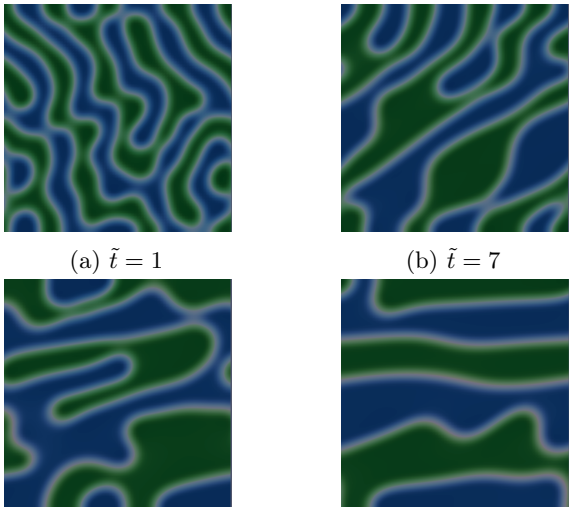

(a) $\tilde{t} = 1$ (b) $\tilde{t} = 7$

(c) $\tilde{t} = 30$ (d) $\tilde{t} = 50.6$

Figure 5: Morphology development of a stratified PPP-flow case.

These trends are a function of multiple variables: shear, composition and the interaction between each species. As such, a more comprehensive study of these phenomena is needed. As Pe was increased to 10, all patterns formed displayed a stratified morphology. It is hypothesised that at even higher Péclet numbers, string break-up may occur.[43] Shear therefore can have a profound impact on the morphology of polymer blends, which increases the number and complexity of possible morphologies. This increased complexity is reflected in the poorer classification power of the current PCA-based technique.

3.2.4. Limitations of PCA

Rotational variance. Rotational invariance refers to the property of a system that behaves the same regardless of how it is spatially oriented. All the images generated from the static ternary polymer simulations were rotated by 90 degrees to check for the rotational invariance of this PCA and clustering method. These rotated images were then subjected to the same post-processing treatment to check if the same clusters are formed, and therefore determine if the clustering process is rotationally invariant.

Upon this treatment, it was found that while the clusters remained largely similar, around 5% of the data points were classified into a different cluster compared to the situation where the images were not rotated. Theoretically, the spatial orientation of the images should not change the cluster it is classified into, as the features are identical. This suggests that there is some level of rotational variance and hence a degree of anisotropy associated with the existing clustering process. Therefore, it appears that the current implementation of PCA based clustering is not accurately capturing the differences arising from morphological variation.

A potential method of addressing this variance is the implementation of image registration upstream of subjecting the datasets to PCA. Image registration is the process of finding the transformation that aligns one image to another; this is necessary for the comparison and integration of data obtained. There is a broad range of techniques of image registration for various types of data,[44] and this process has applications in numerous fields, such as diagnostics.[45] Subjecting the processed images to registration could allow them to be oriented in the same way, minimising the issue of rotational variance.

Linear assumptions. PCA searches for orthogonal projections of the dataset that contain the highest variance to find hidden linear correlations between variables of the dataset. It is therefore an effective tool if the data is linearly correlated; however, when the correlations are non-linear, PCA

will not be adequate for dimensionality reduction. This could potentially have been the reason behind the inaccurate clustering observed with the ternary polymer systems with shear imposed. For this and other such cases, other tools for dimensionality reduction, such as auto-encoders, will have to be explored.

3.3. Cluster prediction

A two-variable study was performed, where the initial concentrations of A and B are varied within a particular range. The classifier on *scikit-learn* was subjected to a training set of data comprising two initial concentrations and the determined clusters, and then tested on a separate testing set which determines if it is effective in cluster prediction. Only a restricted set of species concentrations, imposed on a physical system with fixed χ values, were used to minimise the problem complexity given the relatively limited dataset available for training and testing.

Upon training the classifier on 80% of the available dataset, and testing it on the other 20%, it was found that the predicted clusters returned by the classifier was largely accurate. A confusion matrix, which describes the performance of a classification model, was generated to quantify its efficacy. It returned an accuracy of 100%, suggesting that the classifier is highly effective for the restricted dataset that it was used on. A morphology map displaying the clusters as a function of a_0 and b_0 is shown in fig. 6. From this plot, given specific values of a_0 and b_0, a cluster and hence a morphology can be predicted to a reasonable degree of accuracy. There remains room for improvement, however, as both clusters 0 and 3 were found to show webs, suggesting the existence of some level of misclustering with the current machinery.

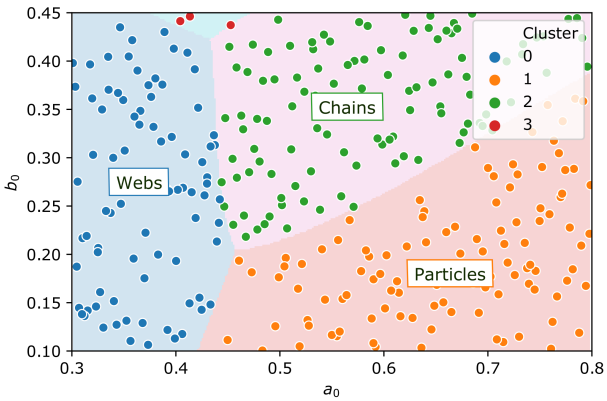

Figure 6: Cluster prediction regions for PPP-static cases, with 4 clusters.

This study serves as a proof-of-concept example of supervised learning that can be performed with the simulation parameters used. Apart from the prediction of the clusters, the study can be extended to other inputs of the system, such as the values of χ_{ij} and the Péclet number.

4. Conclusion

This study has successfully developed and implemented a model for analysing multicomponent polymer precipitation, for cases where mass transport is diffusion-only (static) or where both convective and diffusive transport are present (flow). By varying parameters such as the initial composition and polymer interaction parameters, a rich variety of morphologies can be observed for both the PPP and PPS cases. The morphologies in PPS systems are noticeably simpler as only two polymer species are present. Shear does have an impact on polymer blend morphology, as demonstrated by visible effects such as shear-induced coalescence and stratification. Further work is needed to quantify the effect of various parameters on the morphology of flow systems. The present model can be readily adapted to represent various instances, such as the formation of multicomponent polymer membranes or Janus nanoparticles.

Given the large variety of possible morphologies and input parameters, a data-driven approach for analysing the resultant patterns is advantageous for morphology classification and prediction. A classification framework based on PCA was implemented; this approach was found to be better suited for static cases, with significant misclustering in the PPP-flow case. The PCA-based classification method is unable to entirely capture morphological differences, resulting in clustering having rotational variance. To address this limitation, the use of a more sophisticated approach such as an auto-encoder should be considered. A framework for predicting the morphology of a PPP-static system based on two input variables, a_0 and b_0, was also developed. The predictive framework can be easily expanded to account for more input parameters, but this would require a larger dataset.

5. Acknowledgements

We would like to thank Dr Lachlan Mason and everyone in the Matar Fluids Group for their invaluable support and guidance throughout this project. Thanks also go to Prof. Richard Craster for his insight on model development and numerical implementation.

References

(1) Nauman, E. B.; He, D. Q. *Polymer (Guildf).* **1994**, *35*, 2243–2255.

(2) Yang, H. C.; Xie, Y.; Hou, J.; Cheetham, A. K.; Chen, V.; Darling, S. B. *Adv. Mater.* **2018**, *1801495*, 1–11.

(3) Ulbricht, M. *Polymer (Guildf).* **2006**, *47*, 2217–2262.

(4) Lee, V. E.; Sosa, C.; Liu, R.; Prud'homme, R. K.; Priestley, R. D. *Langmuir* **2017**, *33*, 3444–3449.

(5) Li, N.; Panagiotopoulos, A. Z.; Nikoubashman, A. *Langmuir* **2017**, *33*, 6021–6028.

(6) Rao, J. P.; Geckeler, K. E. *Prog. Polym. Sci.* **2011**, *36*, 887–913.

(7) Li, G.; Shrotriya, V.; Huang, J.; Yao, Y.; Moriarty, T.; Emery, K.; Yang, Y. *Nat. Mater.* **2005**, *4*, 864–868.

(8) Van Puyvelde, P.; Vananroye, A.; Cardinaels, R.; Moldenaers, P. *Polymer (Guildf).* **2008**, *49*, 5363–5372.

(9) Soontaranun, W.; Higgins, J.; Papathanasiou, T. *Fluid Phase Equilib.* **1996**, *121*, 273–292.

(10) Gooneie, A.; Schuschnigg, S.; Holzer, C.; Gooneie, A.; Schuschnigg, S.; Holzer, C. *Polymers (Basel).* **2017**, *9*, 16.

(11) Luo, Z.; Jiang, J. *Polymer (Guildf).* **2010**, *51*, 291–299.

(12) Prathab, B.; Subramanian, V.; Aminabhavi, T. M. *Polymer (Guildf).* **2007**, *48*, 409–416.

(13) Pavel, D.; Shanks, R. *Polymer (Guildf).* **2005**, *46*, 6135–6147.

(14) Han, Y.; Elliott, J. *Comput. Mater. Sci.* **2007**, *39*, 315–323.

(15) Bianchi, E.; Panagiotopoulos, A. Z.; Nikoubashman, A. *Soft Matter* **2015**, *11*, 3767–3771.

(16) Delacruz-Araujo, R. A.; Beltran-Villegas, D. J.; Larson, R. G.; Córdova-Figueroa, U. M. *Soft Matter* **2016**, *12*, 4071–4081.

(17) Cahn, J. W.; Hilliard, J. E. *J. Chem. Phys.* **1958**, *28*, 258–267.

(18) Wodo, O.; Ganapathysubramanian, B. *Comput. Mater. Sci.* **2012**, *55*, 113–126.

(19) Shang, Y.; Kazmer, D.; Wei, M.; Barry, C.; Mead, J. *Polym. Eng. Sci.* **2010**, *50*, 2329–2339.

(20) Alfarraj, A. A.; Nauman, E. B. *Macromol. Theory Simulations* **2007**, *16*, 627–631.

(21) Tree, D. R.; Delaney, K. T.; Ceniceros, H. D.; Iwama, T.; Fredrickson, G. H. *Soft Matter* **2017**, *13*, 3013–3030.

(22) Zhou, B.; Powell, A. C. *J. Memb. Sci.* **2006**, *268*, 150–164.

(23) Inokuchi, T.; Li, N.; Morohoshi, K.; Arai, N. *Nanoscale* **2018**, *10*, 16013–16021.

(24) Möller, J. J.; Körner, W.; Krugel, G.; Urban, D. F.; Elsässer, C. *Acta Mater.* **2018**, *153*, 53–61.

(25) Ward, L.; O'Keeffe, S. C.; Stevick, J.; Jelbert, G. R.; Aykol, M.; Wolverton, C. *Acta Mater.* **2018**, *159*, 102–111.

(26) Aldhaheri, M.; Wei, M.; Bai, B.; Alsaba, M. *J. Pet. Sci. Eng.* **2017**, *151*, 77–93.

(27) Jørgensen, P. B.; Mesta, M.; Shil, S.; García Lastra, J. M.; Jacobsen, K. W.; Thygesen, K. S.; Schmidt, M. N. *J. Chem. Phys.* **2018**, *148*, 241735.

(28) Meenakshisundaram, V.; Hung, J. H.; Patra, T. K.; Simmons, D. S. *Macromolecules* **2017**, *50*, 1155–1166.

(29) Wei, Q.; Melko, R. G.; Chen, J. Z. Y. *Phys. Rev. E* **2017**, *95*, 032504.

(30) Guo, W.; Li, M.; Zhou, J. *Smart Mater. Struct.* **2013**, *22*, 115028.

(31) Martinez, R. F. *J. Mater. Sci.* **2017**, *52*, 569–580.

(32) López-Donaire, M. L.; Sussman, E. M.; Fernández-Gutiérrez, M.; Méndez-Vilas, A.; Ratner, B. D.; Vázquez-Lasa, B.; San Román, J. *Biomacromolecules* **2012**, *13*, 624–635.

(33) Petrishcheva, E.; Abart, R. *Acta Mater.* **2012**, *60*, 5481–5493.

(34) Nauman, E. B.; Balsara, N. P. *Fluid Phase Equilib.* **1989**, *45*, 229–250.

(35) Cogswell, D. A. A phase-field study of ternary multiphase microstructures., Ph.D. Thesis, Massachusetts Institute of Technology, 2010.

(36) Ariyapadi, M. V.; Nauman, E. B. *J. Polym. Sci. Part B Polym. Phys.* **1990**, *28*, 2395–2409.

(37) Badalassi, V. E.; Ceniceros, H. D.; Banerjee, S. *J. Comput. Phys.* **2003**, *190*, 371–397.

(38) Nauman, E. B.; He, D. Q. *Chem. Eng. Sci.* **2001**, *56*, 1999–2018.

(39) Jacqmin, D. *J. Comput. Phys.* **1999**, *155*, 96–127.

(40) Di Tommaso, P.; Chatzou, M.; Floden, E. W.; Barja, P. P.; Palumbo, E.; Notredame, C. *Nat. Biotechnol.* **2017**, *35*, 316–319.

(41) Tipping, M. E.; Bishop, C. M. *J. R. Stat. Soc. Ser. B (Statistical Methodol.* **1999**, *61*, 611–622.

(42) Utracki, L. A.; Shi, H. *Polym. Eng. Sci.* **1992**, *32*, 1824–833.

(43) Migler, K. B. *Phys. Rev. Lett.* **2001**, *86*, 1023–1026.

(44) Brown, L. G. *ACM Comput. Surv.* **1992**, *24*, 325–376.

(45) El-Gamal, F. E.-Z. A.; Elmogy, M.; Atwan, A. *Egypt. Informatics J.* **2016**, *17*, 99–124.

Characterisation of Distributive Three-site Phosphorylation by Parametric Scanning

Thomas Donaldson and Yixin Zhu
Department of Chemical Engineering, Imperial College London, U.K.

Abstract Multisite phosphorylation is ubiquitous in cellular biology, with implications in research on cancer and on degenerative disorders. Both the mathematical modeling and qualitative behaviour of multisite phosphorylation networks have been studied extensively in recent years. In this paper, a model of a three-site phosphorylation cycle following a distributive mechanism is formulated and its behaviour characterised by means of parametric scanning and bifurcation analysis, with a view to identifying novel behaviours and, building on analytical work describing two-site phosphorylation cycles, and identifying the impact of the third phosphorylation site. Key and inconsequential parameters for biphasic and bistable behaviour are identified, and it is found that the addition of a third phosphorylation site allows for bistability in two-site systems in the parameter sub-space for which uniqueness of steady-state is otherwise guaranteed.

1. Introduction

Protein phosphorylation is ubiquitous in cellular biology, being the most common post-translation modification available to cells and a primary means by which enzyme action is regulated. It consists of the addition of a phosphoryl group to a protein by means of a kinase enzyme, and commonly forms half of a covalent modification cycle in which the phosphorylated protein can then be dephosphorylated by a phosphatase enzyme, or in the case of multisite phosphorylation, phosphorylated further by another kinase enzyme (Salazar & Höfer, 2009) .

Much work has been done in recent years to characterise the behaviour of simple covalent-modification cycles. Armed with this knowledge, researchers in molecular systems and synthetic biology can describe and create more complex networks using multi-site phosphorylation networks as building blocks, in full knowledge of their often surprising behaviours.

Furthermore, anomalous protein phosphorylation is implicated in the development of cancer, and also numerous neurodegenerative diseases (Cohen, 2001): in Alzheimer's disease it has been hypothesised that tau protein abnormalities – resulting in hyperphosphorylation - initiate the disease cascade (Rockenstein, et al., 2007), while in the case of Parkinson's disease correlations between the severity of the disease and the concentration of phosphorylated α-Synuclein have been observed.

While covalent modification cycles occur via a number of different mechanisms, this investigation will focus solely on the behaviour of distributive mechanisms: processive mechanisms have comparatively simple behaviour, while a foundation of analytical work exists to describe the varied behaviour of distributive mechanisms and inform the numerical approach taken (Conradi & Shiu, 2018).

Our objective is to identify novel behaviours introduced on the addition of a third site to a two site phosphorylation cycle, and to identify key parameters and mechanisms giving rise to these behaviours and thereby characterising the twenty-one-dimensional parameter space of the system. Of particular interest will be whether the introduction of a third phosphorylation site can allow bistability in two-site networks where analytical work has guaranteed uniqueness of a stable steady-state, and whether parametric scanning is a fruitful approach to identifying combinations of parameters allowing tristability or oscillatory behaviour, should they be possible.

The analysis presented will focus on the existence or non-existence of low co-dimensional bifurcations that may result in generalisable qualitative changes in system behaviour of interest to experimental and synthetic biologists rather than those relying on the confluence of multiple parameters in the parameter space.

2. Background

In the simplest case, a protein might undergo phosphorylation at a single site, and, where both kinase and phosphatase populations are saturated, exhibit 'zero-order ultrasensitivity', that is, a switch-like signal-response curve that serves to filter out noise as stimuli below the threshold concentration fail to trigger the system (Ingalls, 2013).

With the addition of a second phosphorylation site the system becomes far more complex, and such networks have been extensively studied in recent years.

The mechanisms of multisite phosphorylation networks can be classified in a number of different ways. In 'processive' mechanisms, a single substrate-enzyme binding event can facilitate multiple phosphorylation events, while in a 'distributive' mechanism phosphorylation events occur strictly independently and in sequence.

Moreover, successive phosphorylation and dephosphorylation stages can alternate between being distributive and processive, giving rise to 'mixed' networks.

Another dimension differentiates between 'sequential' and 'random' mechanisms, based on the requirement or lack thereof that sites on the protein are phosphorylated in a given order.

These decisions have a profound effect on the qualitative behaviour of a network. Purely processive two-site mechanisms, for example, exhibit global stability (Conradi & Shiu, 2015), while distributive mechanisms exhibit biphasic behaviour and bistability

(Suwanmajo & Krishnan, 2013), and mixed ones can even show oscillations (Suwanmajo & Krishnan, 2015).

Building on analytical and numerical work done on two-site phosphorylation, we'll seek to characterise the behaviour of three-site phosphorylation networks. A review paper published in February describes one knowledge gap your authors hope to address:

> "... but what we really are interested in here, in terms of biology, is bistability... We would also want to go further, to find witnesses for bistability (values of rate constants, conservation-law values, and species concentrations at which the system is bistable) and descriptions of the parameter-space regions for which the system is bistable (or even just multistationary)."

(Conradi & Shiu, 2018)

3. Model

In Figure 1, we introduce three multisite phosphorylation models, illustrating one-site, two-site, and three-site phosphorylation cycles respectively. Our investigation will focus on the behaviour of three-site distributive phosphorylation networks.

To this end, a mathematical model based on mass-action kinetics has been formulated, with a number of assumptions made. Our model follows a generalised version of Michaelis-Menten kinetics; namely, the assumptions of the instantaneous conversion from enzyme-reactant to enzyme-product complex, of irreversible conversion from enzyme-reactant complex to product, of mass-action kinetics for the reversible binding reaction step and irreversible non-binding step, and of the non-complexation of triply-phosphorylated substrate with kinase or unphosphorylated substrate with phosphatase.

It's hoped that the comparatively small number of assumptions implicit—especially with regards to the formation and dynamic concentrations of enzyme-substrate complexes—will aid in generality and novel model behaviour.

Equation 1 details the ordinary differential equations describing a three-site distributive phosphorylation mechanism: $[A]$, $[A_P]$, $[A_{PP}]$ and $[A_{PPP}]$ refer to the concentrations of unphosphorylated substrate, the singly-phosphorylated substrate, doubly-phosphorylated substrate, and triply-phosphorylated substrate respectively. $[K]$, $[AK]$, $[A_PK]$, $[A_{PP}K]$ refer to the concentrations of pure kinase and the corresponding substrate-kinase complexes of $[A]$, $[A_P]$ and $[A_{PP}]$. Concentrations of pure phosphatase and its corresponding substrate-phosphatase complexes are represented by $[P]$, $[A_PP]$, $[A_{PP}P]$ and $[A_{PPP}P]$.

In an N-site phosphorylation model catalysed by a single kinase species and a single phosphatase species, there exists 1 unphosphorylated substrate, 1 pure kinase, 1 pure phosphatase, N phosphorylated substrate species, N substrate-kinase complexes, and N substrate-phosphatase complexes. The model of a multi-site phosphorylation system is characterised by a large number of different parameters: three 'conservation' parameters describing the total mass of phosphatase, kinase, and substrate in the system (denoted Ptotal, Ktotal, and Atotal respectively), six catalytic constants describing the rate of irreversible non-binding reaction

$$
\begin{aligned}
\frac{d[A]}{dt} &= -k_0[A][K] + k_1[AK] + k_{17}[A_PP];\\
\frac{d[K]}{dt} &= -k_0[A][K] + k_1[AK] + k_2[AK] - k_3[A_P][K] + k_4[A_PK] + k_5[A_PK] - k_6[A_{PP}][K] + k_7[A_{PP}K]\\
&\qquad + k_8[A_{PP}K];\\
\frac{d[AK]}{dt} &= k_0[A][K] - k_1[AK] - k_2[AK];\\
\frac{d[A_P]}{dt} &= k_2[AK] - k_{15}[A_P][P] + k_{16}[A_PP] - k_3[A_P][K] + k_4[A_PK] + k_{14}[A_{PP}P];\\
\frac{d[P]}{dt} &= -k_{15}[A_P][P] + k_{16}[A_PP] + k_{17}[A_PP] - k_{12}[A_{PP}][P] + k_{13}[A_{PP}P] + k_{14}[A_{PP}P] - k_9[A_{PPP}][P]\\
&\qquad + k_{10}[A_{PPP}P] + k_{11}[A_{PPP}P];\\
\frac{d[A_PP]}{dt} &= k_{15}[A_P][P] - k_{16}[A_PP] - k_{17}[A_PP];\\
\frac{d[A_PK]}{dt} &= k_3[A_P][K] - k_4[A_PK] - k_5[A_PK];\\
\frac{d[A_{PP}]}{dt} &= k_5[A_PK] - k_{12}[A_{PP}][P] + k_{13}[A_{PP}P] - k_6[A_{PP}][K] + k_7[A_{PP}K] + k_{11}[A_{PPP}P];\\
\frac{d[A_{PP}P]}{dt} &= k_{12}[A_{PP}][P] - k_{13}[A_{PP}P] - k_{14}[A_{PP}P];\\
\frac{d[A_{PP}K]}{dt} &= k_6[A_{PP}][K] - k_7[A_{PP}K] - k_8[A_{PP}K];\\
\frac{d[A_{PPP}]}{dt} &= k_8[A_{PP}K] - k_9[A_{PPP}][P] + k_{10}[A_{PPP}P];\\
\frac{d[A_{PPP}P]}{dt} &= k_9[A_{PPP}][P] - k_{10}[A_{PPP}P] - k_{11}[A_{PPP}P];
\end{aligned}
$$

Equation 1: System of twelve ordinary differential equations describing a distributive three-site phosphorylation mechanism

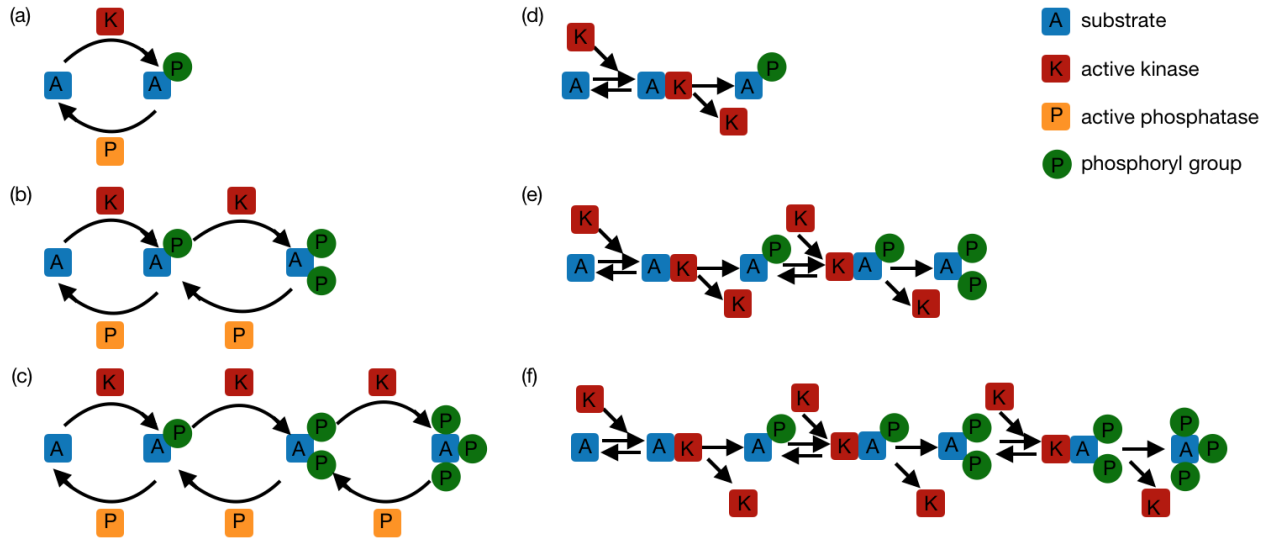

Figure 1. Schematic of distributive phosphorylation models. (a) and (d) shows the distributive one-site phosphorylation mechanism. (b) and (e) shows the distributive two-site phosphorylation mechanism. (c) and (f) shows the distributive three-site phosphorylation

steps, and twelve binding and unbinding reaction constants. Thus, 21 parameters in total exist.

Using the conditions corresponding to conservation of substrate, kinase, and phosphatase, our model was reduced from a set of twelve differential equations to nine following the elimination of the variables $[A]$, $[P]$ and $[K]$, chosen to avoid issues associated with interdependency of the conservation parameters. The reduced set of nine equations is presented in Appendix A.1.

For the purposes of this analysis, the binding and unbinding constants, and the total phosphatase and kinase concentrations are held at unity while the total substrate concentration is set to 5. The binding and unbinding constants were held at one on the basis of previous analytical work (Conradi & Mincheva, 2014). There, inequalities are specified that provide sufficient conditions for a system to exhibit multistationarity for some values of the conservation parameters. These inequalities are functions of the catalytic constants corresponding to the non-binding irreversible conversion steps only, and it is therefore inferred that these parameters are key to characterising the system. Thus, for the purposes of characterising the system behaviour in broad strokes, the scope of this analysis can initially be limited to these six parameters.

During preliminary trials for two-site modification it was found that allowing the substrate conservation parameter to equal the kinase conservation parameter inhibited the network's signature biphasic and bistable behaviours resulting from the sequestration of enzyme in enzyme-substrate complexes; the substrate conservation parameter was therefore set to 5 to allow for this additional complexity.

4. Methods

The primary computational tools employed in our investigation were MATCONT and COPASI

MATCONT is a numerical continuation tool in MATLAB designed for bifurcation analysis of dynamic systems. Of the plethora of numerical solvers available, ODE15s was chosen for its robustness and variable step-size, the latter of which focusses computational resources on accurately mapping the transient and nonlinear aspects of our simulations while conserving resources as the network approaches a stable steady-state.

COPASI was employed for the cross-validation of models and results (see Appendix A.2). Unlike in MATCONT, differential equations needn't be programmed explicitly, rather the reactions that constitute the biochemical network are entered. Therefore, with our results from COPASI being consistent with those from MATCONT, we can be confident of the validity of the results generated from the latter and of the absence of any typographical errors.

Hence, a verified mathematical model for three-site distributive phosphorylation has been formulated, and only a systematic means of exploring the 6-dimentional parameter space remains to be established. Latin hypercube sampling (LHS) was chosen, meeting the criteria of generating a sample set that is both statistically representative and of manageable size.

Latin hypercube sampling is a statistical method for generating a near-random sample of parameter values. Unlike random sampling, new sample points are generated with consideration for previously generated sample points. In Latin hypercube sampling, where N sample parameter sets are to be collected each parameter's domain is divided into N strata. Then for each sample set one random value is selected from a random stratum for each parameter, with no parameter stratum being sampled more than once over the course of the sampling.

The six catalytic constants were each sampled in the range 0.1 to 20, this range of sufficient breadth to allow reactions to almost cease in relative terms at one extreme and approach instantaneity at the other without compromising on resolution at more mundane values.

Table 1. Percentage of continuation diagrams falling under each classification.

	Saturation	Biphasic	Bistability	Linear Climb
Ktotal	98.4	0.8	0.8	0
Atotal	0	35.6	0.8	63.6
k2	94.8	0	5.2	0
k5	98.4	0	1.6	0
k8	99.6	0	0.4	0
k11	92	0	8	0
k14	98.8	0	1.2	0
k17	100	0	0	0

Table 2. Three exemplar parameter sets for which uniqueness of the system steady state would be guaranteed for all conservation parameters on removal of the third site, but for which bistability is apparent on the activation of a third site.

k2	k5	k8	k11	k14	k17	Bifurcation Parameter
8.791198	14.614910	15.553070	0.121021	16.034060	9.135163	k2, k5
19.66570	1.606093	2.670833	0.235203	5.779995	5.827537	k2
2.358372	0.558758	0.633348	0.981272	10.283260	5.533806	k11, Atotal

In our analysis, 500 samples sets have been generated from MATLAB using its LHS Design function, 500 being standard for six-dimensional parameter spaces in the literature. Then, for each of these 500 sample sets, a transient simulation was completed using MATCONT to identify a stable steady-state. Eight continuation diagrams were then created, six of which took catalytic constants as bifurcation parameters and a further two of which took the substrate and kinase conservation parameters as bifurcation parameters.

5. Results

Each continuation diagram obtained was placed into one of four categories based on the behaviour it exhibited (Saturation, Biphasic, Bistability, Linear Climb, the latter three illustrated in Figure 2), and the percentage of continuation diagrams on each parameter corresponding to a particular category calculated and recorded in Table .

The response saturates without exhibiting any particularly exotic behaviours on the majority of continuation diagrams. The subset of continuation diagrams taking the total substrate concentration as the bifurcation parameter is one exception: the concentration of the triply-phosphorylated substrate either increases indefinitely or declines asymptotically.

Phenomena observable in two-site phosphorylation—bistability and biphasic behaviour—were found to be reproducible on a range of bifurcation parameters: biphasic behaviour specifically was observed on both Atotal and Ktotal.

The key parameters enabling multistability were found to be k2 (the catalytic constant corresponding to the first phosphorylation reaction) and k11 (corresponding to the first dephosphorylation reaction), followed by k5 and k14 (denoting catalytic constants for the intermediate phosphorylation and dephosphorylation reactions respectively) with a handful of other parameters also enabling the behaviour. The catalytic constants corresponding to the final phosphorylation and dephosphorylation steps (k8 and k17) were found to have only a small influence on the appearance of a second stable state.

Perhaps surprisingly, precious few noteworthy behaviours were observed when Ktotal was taken as the bifurcation parameter. In previous work (Suwanmajo & Krishnan, 2015) a window of Ktotal values within which oscillations are possible has been shown, and the ratio of substrate to enzyme is one of the defining features of multisite phosphorylation networks.

The sensitivity of limit points to various parameters was analysed using MATCONT, with a broad spread of results. Parameters to which the location of the window of bistability was found to be sensitive are k11, Ptotal, and Ktotal, with the remaining parameters being relatively inconsequential. In particular, the response exhibited relatively extreme sensitivity proximal to a cusp point as shown in Figure 2. Pairs of limit points were found to have similar sensitivities to each parameter, precluding the possibility of creating an arbitrarily large bistable parameter subspace by tuning a single parameter.

Two anomalous continuation diagrams are shown in **Error! Reference source not found.**. The first shows biphasic and bistable features combining to form a distinctive curve characterised by a collapse in A_{PPP} above a threshold value of Atotal. The second illustrates a rare case where bistability is contingent on a narrow window of high k8 values.

Finally, a set of inequalities providing sufficient conditions for the uniqueness of system steady-states for a subset of parameter combinations has previously been presented (Conradi & Mincheva, 2014). It was found, applying these conditions to data collected, that combinations of kinetic parameters for which bistability would not be possible in the case of double-site

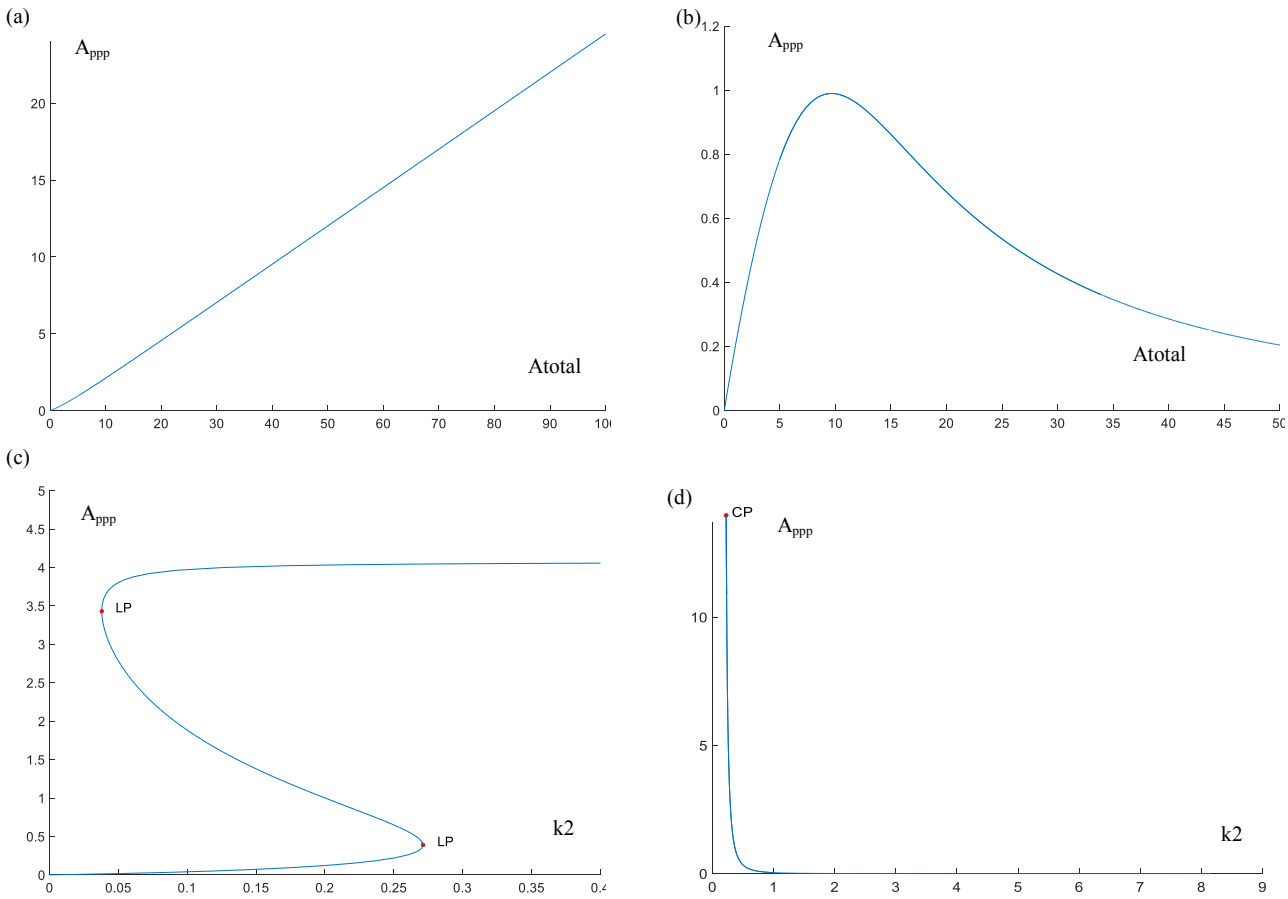

Figure 2. Steady-state dose-response curves in three-site phosphorylation. (a) Showing non-biphasic behaviour. (b) showing biphasic behaviour. (c) showing bistable behaviour. (d) showing the sensitivity of the first limit point in diagram (c) to the total kinase concentration.

phosphorylation can exhibit bistability on the addition of a third site. Some exemplar parameter sets for which this is the case are recorded in Table .

6. Discussion

Systems for which the response (A_{PPP}) is robust to changes in the total substrate concentration are elusive; for a synthetic biologist the best approximation to perfect adaption would be a carefully tuned biphasic response in which the effects of kinase sequestration and the increasing substrate population balance one another

Biphasic behaviour has been described in depth at this time (Suwanmajo & Krishnan, 2013). Such behaviour when the total substrate population is taken as the bifurcation parameter can be attributed to sequestration of kinase by less-phosphorylated substrate species, while this behaviour when the total kinase population is taken as the bifurcation parameter is attributable to the sequestration of substrate by kinase.

A large discrepancy exists between the ease of obtaining biphasic behaviour with these two parameters; a simple explanation is that a much greater total concentration of substrate than kinase was selected, making it more difficult to sequester kinase using substrate than the reverse.

As for the particular importance of k2 and k11 in the formation of bistability, on examining the concentrations in the two stable branches it's quickly apparent why. For the most part, they correspond to cases where both k2 and k11 are low enough to form two bottlenecks and trap substrate as either A or A_{PPP} within the window of bistability. These findings are consistent with Conradi's analytical work which identified the catalytic constants as enabling bistability (Conradi & Mincheva, 2014).

An intuitive explanation exists as to why bistability occurs more easily on k2 and k11 than k5 and k14. Each intermediate phosphorylation step in a multisite phosphorylation network acts analogously to a resistor placed in series in an electrical circuit, limiting the rate (or 'current') by which concentration (or 'charge') bleeds across to the far phosphorylation extreme, stabilising large concentrations at either extrema. As k2 and k11 control the phosphorylation and dephosphorylation reactions at either end of the network, their formation of stable nodes is supported by the largest possible intermediate resistance. Following this logic, the ease of creating higher-order multistability will increase with the number of phosphorylation sites present on the protein.

Your authors note that where find a window of bistability with k5 or k14 as the bifurcation parameter is found, a window is also present with k2 or k11 as the bifurcation parameter. This can be explained by the existence of two preconditions for bistable behaviour. Firstly, that either the initial or the second dephosphorylation step is slow (forming one stable steady-state)—this can be met regardless of the values

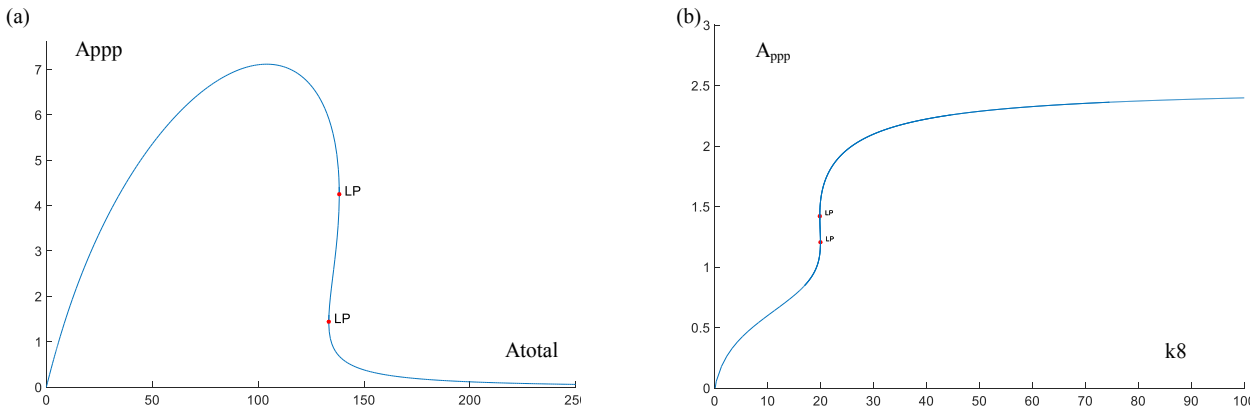

Figure 3. (a) shows a combination of bistability and biphasic behaviours. (b) shows a rare instance of bistability dependent on the catalytic constant corresponding to the final phosphorylation step at a comparatively high value.

of k2 and k5, and secondly that the initial or second phosphorylation step is slow (forming a second stable steady-state). If the first condition is met such that a pair of limit points are apparent on the continuation diagram of k5, then it should be possible and in fact easier for the second condition to be met on k2 (see the resistance in series analogy described above).

The mathematical symmetry of the system is also apparent: the kinetics of phosphorylation and dephosphorylation reactions have been given the same treatment, and accordingly demonstrate broadly similar behaviours with some small deviations attributable to statistical error. We can consequently postulate that behaviours exhibited when the total kinase population is taken as the bifurcation parameter would also be apparent, in reverse, if the total phosphatase was taken as the bifurcation parameter.

Returning to the issue of the addition of a third phosphorylation site enabling bistability in parameter sets for which a unique stable steady-state would otherwise be guaranteed: consider Conradi's first condition to guarantee the uniqueness of steady-states in two-site distributive phosphorylation (Conradi & Mincheva, 2014). The product of the catalytic constants of the first phosphorylation and dephosphorylation steps must exceed the products of the catalytic constants for the second phosphorylation and dephosphorylation steps. This precludes a scenario where substrate can accumulate at either extreme of the network with the rapid reactions towards its centre forming an unstable steady-state.

With the addition of a further phosphorylation site, however, $k_{c,2}$ and $k_{c,3}$ no longer refer to the final phosphorylation and initial dephosphorylation reactions and therefore the inequality has no intuitive basis as a condition in the three-site system. An extension of this inequality to a system with an arbitrary number of sites would likely make reference to the catalytic constants of intermediate reactions that could sequester substrate in an intermediate complex or partially phosphorylated species in addition to giving the same precedence to final phosphorylation and initial dephosphorylation reactions as the initial phosphorylation and final dephosphorylation reactions.

7. Conclusion

Comparing the properties of a three-site system to a two-site, it's apparent the catalytic constants corresponding to the second phosphorylation and dephosphorylation steps take on a different importance. They enable bistable behaviour when low, rather than preventing it when high—a role transferred to the catalytic constants corresponding to the final stages of phosphorylation of dephosphorylation

A number of avenues for further research remain open; the existence or non-existence of oscillations in purely distributive multi-site phosphorylation beyond systems following strictly Michaelan kinetics (Wang & Sontag, 2008) remains to be proven, and heuristics for creating parameter combinations resulting in tristability remain elusive.

Further numerical work would best be informed by analytical work and intuition as to what combinations of parameters should be sampled and within what ranges. Furthermore, the existence and impact of higher codimension bifurcations lay without the scope of this investigation but could provide further insight into system behaviour. Productive to this end would be reduction of the phase-space to a smaller dimension, the promise of which is indicated by the relative simplicity of the plots obtained in this work.

Our findings hint at promising parameter subspaces for tristability. In qualitative terms, bistability is most often attributable to the partition of the substrate between subsets of species in the system by limiting reaction steps—most often the first phosphorylation and dephosphorylation steps. A tristable system would likely have an intermediate stage where substrate stably accumulates in a substrate-enzyme complex or partially-phosphorylated substrate or subset thereof. Therefore, selecting one such species and reducing proximal catalytic and binding constants would be one approach. Consideration should be given to the existence of isolated branches on continuation diagrams that numerical solvers can fail to detect.

The search for oscillations is more challeging to pursue intelligently as the structure of a negative feedback loop that might give rise to such behaviour in a purely distributive network is not immediately apparent.

The addition of a third site enabling bistability for two-site phosphorylation networks guaranteed to have a

unique steady-state provides further distinction between the dynamics of the two and justification for further investigation into the behaviour of larger multisite networks.

The extreme sensitivity of the location of windows of bistability within the parameter space to the total kinase concentration is noteworthy, though results indicate this is not a promising approach to create arbitrarily large subspaces exhibiting this behaviour.

Finally, while declining to vary binding constants for the purposes of reducing the parameter space to a manageable size is convenient, a fully exhaustive analysis should consider their impact—they're likely to be important in the realisation of tristable states, as it's more challenging to constrain the flux of subtrate through intermediate species in the network that can bleed through multiple reaction pathways (e.g. A_P can complex with either free kinase or free phosphatase, unlike A which can only complex with free kinase or A_{PPP} which complexes exclusively with free phosphatase).

8. Acknowledgements

Your authors would like to thank Vaidhiswaran Ramesh for his invaluable guidance and great patience over the course of this project.

9. References

1. Cohen, P., 2001. The role of protein phosphorylation in human health and disease. *FEBS Journal,* 268(19), pp. 5001-5010.
2. Conradi, C. & Mincheva, M., 2014. Catalytic Constants Enable the Emergence of Bistability in Dual Phosphorylation. *Journal of the Royal Society Interface,* 11(95).
3. Conradi, C. & Shiu, A., 2015. A Global Convergence Result for Processive Multisite Phosphorylation Systems. *Bulletin of Mathematical Biology,* 77(1), pp. 126-155.
4. Conradi, C. & Shiu, A., 2018. Dynamics of Posttranslational Modification Systems: Recent Progress and Future Directions. *Biophysical Journal,* 114(3), pp. 507-515.
5. Flockerzi, D., Holstein, K. & Conradi, C., 2014. N-Site Phosphorylation Systems with 2n-1 Steady-states.. *Bulletin of Mathematical Biology,* 76(8), pp. 1892-1916.
6. Ingalls, B. P., 2013. *Mathematical Modeling in Systems Biology: An Introduction.* 1st ed. s.l.:MIT Press.
7. Rockenstein, E. et al., 2007. Neuroprotective Effects of Regulators of the Glycogen Synthase Kinase-3β Signaling Pathway in a Transgenic Model of Alzheimer's Disease Are Associated with Reduced Amyloid Precursor Protein. *Journal of Neuroscience,* 27(8).
8. Salazar, C. & Höfer, T., 2009. Multisite Protein Phosphorylation – from Molecular Mechanisms to Kinetic Models. *FEBS Press,* 276(12), pp. 3177-3198.
9. Strogatz, S. H., 2014. *Nonlinear Dynamics and Chaos.* 2nd ed. s.l.:Avalon Publishing.
10. Suwanmajo, T. & Krishnan, J., 2013. Biphasic responses in multi-site phosphorylation systems. *Journal of the Royal Society Interface,* 10(89).
11. Suwanmajo, T. & Krishnan, J., 2015. Mixed Mechanisms of Multi-site Phosphorylation. *Journal of the Royal Society Interface,* 12(107).
12. Thomson, M. & Gunawardena, J., 2009. Unlimited Multistability in Multisite Phosphorylation Systems. *Nature,* Volume 460, pp. 274-277.
13. Wang, L. & Sontag, E. D., 2008. Singularly Perturbed Monotone Systems and an Application to Double Phosphorylation Cycles. *Journal of Nonlinear Science,* 18(5), pp. 527-550.

Techno-Economic Analysis of the Ionic Liquid Recycle of the ionoSolv Process for Biomass Pretreatment

Jordan Marshall and Stefan Vollmer Firenze
Department of Chemical Engineering, Imperial College London, U.K.

A fully converged flowsheet of the ionoSolv process was developed on Aspen Plus V9. Components and equipment models native to the Aspen databanks were used to improve upon the accuracy of previous models of the process. This iteration of the process model considers the economic effect of different ionic liquid recycle fractions ranging from 95 - 99.5%. The consumption rate of fresh ionic liquid in the process was found to govern the operating costs and subsequently the profitability of the process, becoming less profitable as recycle fraction decreases. However, for the majority of the recycle fractions considered, the process is found to remain profitable over its lifespan and similar predicted profits are found in comparison to previous work.

1. Introduction

Modern day society is highly dependent on fossil fuels, especially in the transport fuels and chemicals production industries.[1] Oil alone contributes to roughly one third of CO_2 emissions, hence being a primary source of global warming, and limiting its emissions will be key in limiting global warming to 1.5°C.[2,3] One promising alternative to oil-based fuels is the use of second-generation biofuels derived from lignocellulosic biomass. Biomass already contributes to 12% of the global energy market and is forecasted to grow further.[4,5]

Lignocellulosic biomass has three main components: cellulose, hemicellulose and lignin.[6] Traditional methods of utilising biomass for energy production have involved fermentation, digestion and crude combustion of biomass, but new research is aiming to fractionate cellulose and lignin from biomass.[7] The cellulose fraction can be converted into bioethanol through enzymatic hydrolysis followed by fermentation.[8] Lignin is incredibly energy dense, and it is estimated that combustion of the extracted lignin fraction could provide more than 1320×10^6 GJ of thermal energy in 2021.[9]

The fractionation process is already widely used in cellulose pulp production for the paper industry. The major manufacturing process for such pulp is the Kraft Process, providing 75-80% of the US pulping capacity.[10] Developed in 1879 it has been the process of choice ever since due to its high lignin removal leading to stronger cellulose fibres, and therefore higher quality paper.[10]

The Kraft Process uses sodium hydroxide (NaOH) and sodium sulphide (Na_2S) as active solvents to chemically dissolve the lignin.[11] The biomass is treated with the solvents, then flashed and the slurry filtered to produce pulp. The balance of the plant then recovers the solvents.[11] The process also requires feeds of lime, water, sulphur and sodium sulphate (Na_2SO_4).[11]

There are many environmental concerns surrounding the Kraft Process, namely its gaseous and aqueous emissions. Due to the intense use of sulphur-containing solvents, Kraft plants are famous for their distinctive smells – these can be attributed to reduced sulphur compounds.[11] The major contributors to these odours are hydrogen sulphide, methyl mercaptan, dimethyl sulphide and dimethyl disulphide.[11] Other gaseous emissions include carbon monoxide contributing to global warming, and sulphur dioxide contributing to acid rain.[12]

The pulp produced in the Kraft Process is ideal for paper manufacture due to its high cellulose content (around 92%) and is sold for up to $1400/tonne.[13,14] Biofuel grade pulp is not required have such a high cellulose content, and hence has a lower market price. It is therefore important for a process to be developed that can provide biofuel grade cellulose pulp at a competitive price.

One promising alternative to traditional biomass pretreatment processes is the ionoSolv process. This takes advantage of ionic liquid (IL) solvents to deconstruct biomass into impure cellulose pulp and dissolved lignin fractions. The purity of cellulose pulp from the ionoSolv process is less than that of traditional pulping processes, making pulp containing up to 85% cellulose. This is still a high enough quality to produce biofuels at a lower selling price of around $875/tonne.[15]

Research into the use of ILs as solvents in biomass pretreatment is still ongoing but suggests that widespread use can further fuel an increase in market shares of biofuels. Ionic liquids are typically organic salts that have melting points below 100°C. They are considered green solvents due to their negligible vapour pressure, and hence are non-volatile, are non-flammable and are excellent in cellulose stabilisation.[16,17,18] In comparison to conventional pretreatment processes, the ionoSolv process is benign to the environment.[19] Current ILs being investigated for use in biomass pretreatment are [C2C1im][OAc], [Emim][OAc] and [TEA][HSO_4], with the latter being the primary IL used in the ionoSolv process due to its low cost and effectiveness in cellulose isolation.[2]

The ionoSolv process model has three main operational areas: pretreatment, IL recovery and IL conditioning.[20] In pretreatment, the IL and biomass feedstock are mixed and reacted, dissolving lignin into the liquid phase and hydrolysing hemicellulose. This product is then separated to produce an IL recycle

stream, a saleable cellulose pulp and an IL-lignin mixture.[20] The latter stream is sent to IL recovery where lignin is precipitated using water as an antisolvent. This produces a lignin cake and an IL stream. The lignin cake is burned to produce energy for the plant, while the IL stream is sent to IL conditioning where it is made up to 80% IL and 20% water to be used in cellulose pulp washing.[20]

Other areas of the ionoSolv process are: wastewater treatment, feed handling, pulp storage, power generation and utilities.[20] The wastewater treatment plant is a series of biological digesters aimed at recovering all spent process water in the plant. Power generation takes the lignin cake as a fuel to produce electricity and steam needed for plant operations. This energy can also be sold to the grid.

2. Background

There have been many studies into the pretreatment of biomass in the ionoSolv process, investigating the effects of: biomass loading, pretreatment temperature and residence time on the glucan recovery, delignification and hemicellulose removal of the biomass.[20] These experiments have concluded the pretreatment conditions which are currently used in process models of the ionoSolv pretreatment process.

This has resulted in two previous iterations of the ionoSolv process model; the first developed by Outon-Gill (2017)[21], and the second an adaptation made by Sukma (2017)[20].

The design proposed by Outon-Gill considers a feedstock of *Miscanthus x giganteus,* fed at 1 Mtonne/yr to produce 2455 tonne/day of cellulose pulp containing 25%wt water using the ionic liquid [TEA][HSO_4].[21] This design is a semi-batch operation; the batch components being the pretreatment reactor and lignin filtration system with the balance of the plant being continuously operated.[21] Outon-Gill (2017) did not consider wastewater treatment or water recycling. The significant water consumption led to high operating costs and was identified as an economic problem in this early model.[21]

The design proposed by Sukma (2017) was an improvement on that by Outon-Gill (2017). While assuming the same feed conditions, Sukma considered the plant as a fully continuous operation, and designed and implemented a wastewater treatment plant in order to reduce the added costs from the feed of fresh water.[20]

One major issue in both designs is the assumption of an infinite recycle of ionic liquid. Research by the Hallett Group suggests that re-use of IL decreases the purity of cellulose pulp produced at low recycle fractions.[2] It is also possible that an accumulation of impurities could occur in the recycle stream, further decreasing IL pretreatment performance.[22]

Therefore, this study will produce the next iteration of the ionoSolv process model, building upon the previous model by Sukma (2017). In particular the research will focus on the fraction of IL recycled and how this effects the overall process economics.

3. Methods

3.1. Component and Property Definition

Of the components considered, water and acetic acid are found in the Aspen databanks, along with good alternatives for glucan and hemicellulose; modelled as cellulose and xylose respectively. Due to the lack of available data an activity coefficient model could not be built to accurately model the components lignin and [TEA][HSO_4]. Lignin was therefore modelled as vanillin due to its similar functional groups and was suggested by Sukma (2017).[23] The ionic liquid was modelled as MEG (monoethylene glycol) due to its similar physical properties and is also used in the design by Sukma (2017).[20] To more accurately simulate the liquid vapour pressure of glucan, lignin and ionic liquid the B coefficient in the Antoine equation was set to -$1x10^{-8}$ for each component, providing a negligible vapour pressure at operating temperatures. A dummy solid of sand (SiO_2) was also added to aid solids modelling. As a hydrolysis product of hemicellulose, furfural was also included as one of the components.

After using the in-built methods assistant in Aspen, the method used was UNIQUAC. Other suggested methods were Wilson, NRTL and UNIFAC. UNIQUAC was chosen over Wilson and NRTL due to its consideration of the additional entropy term in the Excess Gibbs energy equation. UNIFAC was not chosen due to insufficient data being available in the component model for xylose.

3.2. Flowsheet

Each unit was modelled individually, then combined to make the flowsheet of Units-200, 250 and 300. Units-100 and 800 were then added later.

To increase the accuracy of the model, Aspen equipment models were used wherever possible. In particular this included pumps, mixers and flash vessels. More complicated unit models could not be used such as for filtration systems, precipitators and reactors. Filters in Aspen require knowledge of cake properties and operational parameters that are either unknown or have not yet been decided. Precipitators require more accurate component models for lignin and the reactor requires kinetic data which was unavailable. For these cases calculator blocks were used to enforce rudimentary models of these unit operations which were based on the unit models implemented in previous process models.

3.2.1. Unit-100 – Feed Handling

Although not being a necessary component of the plant to model, Unit-100 was added to complete the plant. The biomass feed (139 tonne/hr) enters a series of two hoppers, fed between them by a conveyor modelled as a screw mixer. The composition of the biomass feed is displayed in Table 1. The outlet of the final hopper is fed to the mixer in Unit-200 by a screw pump modelled as a screw mixer to be mixed with recycled IL.

Component	Composition (%wt.)
Glucan	41.4
Hemicellulose	17.1
Lignin	27
Acetic Acid	4.5
Water	10
SiO_2	$1x10^{-7}$

Table 1: *Miscanthus x giganteus* feedstock composition.[20]

3.2.2. Unit-200 – Pretreatment

Pretreatment has six main operations: the mixing of biomass feedstock and IL, hemicellulose decomposition and lignin transfer to the liquid phase, flash removal of water and volatile organics, IL washing, water washing and IL purge and makeup.

Initially, the recycled IL and biomass feed from Unit-100 are mixed in a simple mixer from the Aspen Model Palette. These are then pumped and heated to 8 bar and 180°C before being fed into the pretreatment reactor.

The proposed pretreatment reactor for the process is a horizontal screw reactor. This is not included in the Aspen Model Palette, so was instead modelled as a screw mixer with only one inlet stream. A calculator block was then used to fix the relative amounts of glucan, hemicellulose and lignin that remain in the solid phase. These can be seen in Table 2. The data was taken from a paper by Brand-Talbot et al. (2017), using the cellulose pulp composition at the fourth recycle.[2] Further cycles do not have a marked difference on the pulp composition.[24] The calculator also calculates the production of decomposition products of hemicellulose when treated with IL – of the hemicellulose decomposed, 1/6 becomes furfural and 5/6 becomes lignin which is transferred to the liquid phase.[20]

Component	Fractional recovery in the solid phase
Glucan	89.1%
Hemicellulose	17.6%
Lignin	19.3%

Table 2: Fractional recovery in the solid phase during IL pretreatment.

The slurry outlet of the reactor is fed to a flash blowdown tank operated at 125°C and 0.36 bar. The purpose of this is to remove as much volatile organics (acetic acid and furfural) and water as possible. It is important to note that these should be the only components present in the vapour phase as other components in the system are assumed to be non-volatile at these conditions. The vapour product is condensed and sent to the wastewater treatment plant.

The liquid product of the flash is fed to a vacuum belt filter. Due to a lack of knowledge of cake properties and operating parameters the filter was modelled as a splitter with an attached calculator block. A filter efficiency of 0.9 was assumed (that is, the fraction of inlet liquid in the filtrate outlet), the process was set as non-selective and with constant pressure drop of 2 bar (as is the same for all filters). The lignin-and-IL-rich filtrate from the filter is transferred to Unit-250 for IL recovery and lignin precipitation.

The filter cake containing the glucan pulp then enters IL washing. This is modelled as a mixer and then splitter, with an attached calculator block. The glucan pulp is mixed with IL recycled from Unit-300 – IL conditioning. The mixed stream is then filtered with a similar calculation approach to the previous filter. The IL-rich filtrate is then recycled back to be mixed with the biomass feed from Unit-100.

The glucan pulp cake is then washed with water. This is again modelled as a mixer then a splitter coupled with a calculator block. Water from the wastewater treatment plant is mixed with the glucan pulp and then filtered again. The calculator block assumes that the ratio of moisture to solids in the filter cake is 0.35, and that the only moisture in the cake is water. The filter cake produced consists of a wet glucan pulp with impurities of hemicellulose and lignin in the solid phase. This pulp is then transferred to pulp storage in Unit-500 to be sold as the primary plant product.

Before mixing with the biomass once again, the recycled IL-rich filtrate from the IL washing is first passed through a splitter, where a specified fraction of the stream is purged. The stream is then made up with fresh IL containing 20%wt water with an IL flow equal to that of the IL in the purge stream. The resulting mixture of recycled and fresh IL is then mixed with the fresh biomass feed.

3.2.3. Unit-250 – IL Recovery

IL Recovery firstly precipitates lignin out of the IL solution, produces a lignin filter cake and an IL-water stream.

The lignin-and-IL-rich filtrate from Unit-200 is fed into a mixing tank from the Aspen Model Palette, along with recycled wash water from Unit-200 and water from the wastewater treatment plant. A calculator block is then used to model the precipitation, where it is assumed that all of the dissolved lignin is precipitated.

The resulting slurry is filtered to produce a lignin cake. This is again modelled as a splitter with a calculator block assuming that the filter is 90% efficient, is non-selective and has a 2 bar pressure drop. The filtrate is fed to Unit-300 – IL Conditioning to be recovered and recycled.

The filter cake is then washed with water from the wastewater treatment plant, modelled as a mixer then splitter and calculator block. The ratio of cake moisture to cake solids was once again set at 0.35, all moisture was set to be water and the pressure drop to be 2 bar. The solid lignin cake produced is the secondary product of the plant which is sent to Unit-970 to be burnt. The filtrate is sent to the wastewater plant for cleaning.

3.2.4. Unit-300 – IL Conditioning

IL conditioning produces a recyclable IL stream for IL washing in Unit-200.

The filtrate from the lignin cake filter in Unit-250 is first heated to 120°C before being flashed. The flash vessel is taken from the Aspen Model Palette and operated at 120°C and 0.4 bar. The intention here is to remove as much volatile organics as possible from the

IL-water stream. The vapour fraction is condensed and fed to the wastewater treatment plant.

The liquid stream is mixed with water from the wastewater plant and fresh IL to make up the composition to 80%wt IL and 20%wt water. The resulting stream is recycled and sent to the IL washing in Unit-200.

3.2.5. Unit-800 – Wastewater Treatment

It was not within the scope of the research to fully replicate the model of wastewater treatment. In this iteration of the ionoSolv process wastewater treatment was modelled as a series of mixers and splitters with attached calculator blocks. The first mixer combined all of the wastewater from the plant with fresh water controlled by a calculator block to keep the total recycle of water constant. A splitter and calculator were then used to create impurities and pure water streams; the latter being split and fed back to the plant.

3.2.6. Unit-970 - Burner, Steam and Power Generation

This process includes a power generation system to supply the power and the steam required for the plant and for excess electricity to be sold to the grid. By-products from the process such as lignin cake from Unit-250 and anaerobic gas and biomass sludge from Unit-800 are combusted to produce high pressure steam. This can then be used for heating duty or electricity production. The same model and assumptions reported in Sukma (2017) were followed here to calculate the rate of electricity production.[20]

3.2.7. Recycle

Previous work has suggested that the ionoSolv process will only be economically viable if 96% of the IL is recycled.[2] It has also been found that the maximum recovery possible at lab scale is approximately 99.5%.[24] For these reasons in this study the recycle fraction of IL was varied between 95% and 99.5% to evaluate the process economics from making a loss to making the maximum possible profit. A basis of 99% IL recycle fraction was used for comparative purposes in the costing analysis.

The previous design by Sukma (2017) considers a curve-fitted equation, with the pulp purity being a function of temperature and residence time. However, the previous model does not consider the number of times the IL has been recycled.[20] In the updated model, cellulose pulp composition data for 1-4 recycles of IL from the Hallett Group is used.[2] The number of recycles chosen is 4 – corresponding to a recycle fraction of 75% as data for more recycles of IL is not available. Therefore, the pulp composition for 4 recycles was considered constant for the higher recycle fractions considered in this investigation (95-99.5%).[24]

3.3. Equipment Sizing

The input parameters for sizing such as flowrates, compositions, temperatures and pressures were obtained from the results of the converged Aspen flowsheet. All major equipment was then sized following the modelling and sizing approach demonstrated in Sukma (2017).[20] The remaining input parameters which were not changed by the Aspen model were kept constant as those used in Sukma (2017).[20] The result of these models was a reference attribute for each equipment such as volume or shaft power that could then be used for costing the equipment.

3.4. Costing Estimations

As the level of detail of the process shown here is still within the preliminary step of engineering design, all costs estimations are provided with an accuracy of about ±30%.[25]

3.4.1. Installed Cost

The installed cost covers the cost of the purchase, transport, construction and installation of the equipment in the plant. The plant was subdivided into two sections, Inside Battery Limits (ISBL) which includes Units 100, 200, 250, 300 and 500 and the Outside Battery Limits (OSBL) which includes Units 800, 900 (Utilities) and 970. Each section was costed differently. The purchase cost of both ISBL and OSBL then provided the total Installed Cost (IC).

3.4.1.1. ISBL

A module costing technique was used based on the base attribute of each equipment as shown in Equation 1.[26]

$$log_{10}C_P^0 = K_1 + K_2 log_{10}(B) + K_3[log_{10}(B)]^2 \quad (1)$$

Where B is the reference attribute of the equipment, K_1, K_2 and K_3 are given to specific equipment types and were normalised to a base year of 2001, and C_P^0 is the purchased cost of the equipment for ambient pressure and using carbon steel construction.[26] Equation 2 is then used to adjust the purchased cost to the correct pressure using the pressure factor F_P, and then Equation 3 is used to correct this cost to the correct material using the construction factor F_M.

$$log_{10}F_P = C_1 + C_2 log_{10}(P) + C_3[log_{10}(P)]^2 \quad (2)$$
$$C_{BM} = C_P^0(B_1 + B_2 F_M F_P) \quad (3)$$

Where C_1, C_2, C_3, B_1, B_2, F_M and F_P are coefficients specific to each equipment type and C_{BM} is the bare module cost.[26] As mentioned, this includes all direct and indirect costs involved.[26] It is worth mentioning that Turton (2013) provided a maximum and minimum size to each equipment type.[26] Therefore, for cases where the maximum size was surpassed, a multiple number of the same equipment was required. In these cases, the actual number of equipment will be different from that described in the Aspen flowsheet.

3.4.1.2. OSBL

A historical costing technique was used which compared the reference attribute to a base case equipment which had been previously costed. Equation 4 is then used to scale the price to the required attribute.

$$\frac{c_a}{c_b} = (\frac{A_a}{A_b})^n \quad (4)$$

Where A_a and A_b are the required and base attributes of the equipment, relatively, and c_a and c_b are the required and base purchase costs of the equipment, relatively, and n is the cost exponent.

The base case was a similarly-designed plant reported in Davis et al. (2015), Davis et al. (2013) and Humbird et al. (2011), where costs were obtained from vendor quotations.[27,28,29] As mentioned in Sukma (2017), the exponent n will depend on equipment type and the dependency on economies of scale, however it remains around a value of 0.6.[20,26,27]

3.4.1.3. Effect of Time on Installed Cost

The purchase cost of all equipment must be adjusted to the current year to take the time value of money or inflation into account. This is done by using Equation 5.[25]

$$Cost_{year\ A} = Cost_{year\ B} \times \frac{Cost\ index_{year\ A}}{Cost\ index_{year\ B}} \quad (5)$$

The cost indexes are the Chemical Engineering Plant Cost Index (CEPCI), where year A is 2018 with a CEPCI of 591.3 as of January 2018 and year B is set at 2001 as mentioned previously, with a CEPCI of 394.3.[26,30,31] Costings for all models presented in this paper were adjusted to 2018 values and the economic results were recalculated for comparison purposes.

3.4.2. Total Capital Investment

The total Capital Investment (CI) covers all costs involved in going from an empty field to a fully working process. It can be broken down into the total Fixed Capital Investment (FCI) which includes the total IC, land cost and working capital. The approach described in Sukma (2017) was followed which used set fractions of the total ISBL installed cost to estimate the direct and indirect costs which were then put together to give the FCI.[20] The same was done for the working capital while the fixed land cost reported of $1.8 million was used.[20] The fractions are based on assumptions reported in Sinnott (2005) and Davis et al. (2015).[25,27]

3.4.3. Operational Costs

3.4.3.1. Operating Costs

These are broken down into Direct Manufacturing Costs (DMC) which are primarily raw material costs, Fixed Operating Costs (FOC) such as property insurance and General Expenses (GE) which are general administration costs. The raw material prices reported in were used and are summarised in Table 3.[20] The input flows of materials used in OSBL Units which were not fully modelled in the Aspen flowsheet were considered to be the same as those reported in Sukma (2017) These are also summarised in Table 3.[20]

Most importantly, the price of ionic liquid was set at a value of $1.24/kg (20%wt. water) according to the findings of Chen et al. (2014).[32] The FOC and GE were then estimated relative to the total FCI and the ISBL installed cost following assumptions reported in Davis et al. (2015).[27]

Raw Material	Process Input (kg/h)	Price ($/tonne)
Biomass	138,888	80
Ammonia	120	49.3
Polymer	2	4,961
Boiler Chemicals	0.2	5,558
Cooling Tower Chemicals	3	3,330
Makeup Water	variable	0.29
Ionic Liquid	variable	1240

Table 3: Flowrates and prices of raw materials fed into the process.[20]

3.4.3.2. Operating Revenue

The two sources of revenue considered were pulp sale and electricity sale from excess energy production in Unit 970. The price of pulp was set at $875/tonne as reported and used in Sukma (2017).[15,20] The price of electricity is set at $0.0572/kWh referring to that used by Davis et al. (2015).[27]

3.4.4. Cash Flow

Once the total installed costs, operating costs and operating revenues were obtained, the cash flow over the lifetime of the plant could be modelled. The approach laid out by Sukma (2017) was followed.[20] The same assumptions used by Sukma (2017) and stated in Davis et al. (2015) were used.[20,27] These are summarised in Table 4.

Plant lifetime	20 years
Construction period	3 years
Federal Corporate Tax Rate	35%
After-tax Discount Rate	10%
Depreciation Method	MACRS for 7 years
Working Capital	10% of FCI

Table 4: Assumptions used in modelling plant lifetime cash flow.[20]

The salvage value of the plant i.e. the sale of equipment at the end of the lifetime is not considered. Only the FCI is allowed to depreciate, which includes all physical components in the process excluding the land cost. The depreciation method used is the Modified Accelerated Cost Recovery System (MACRS) which allows for the quickest depreciation, delivering the shortest recovery periods and the largest tax deductions.[27] This is considered for a period of 7 years.

The construction is assumed to take 3 years. The percentage of the total project cost is shared as follows: Year 2 (8%), Year 1 (60%) and Year 0 (32%). At the end of Year 0, the plant would be operational and ready to begin production.

4. Results and Discussion

4.1. Flowsheet

Before the flowsheet was built it was suspected that MEG would not model the IL entirely accurately, and deviations would be found in the temperatures and pressures of some of the process units. Upon modelling

the flash vessels in both Unit-200 and 300 it was found that much lower pressures were required to complete the separations to the given specifications. In the previous model the blowdown tank was operated at 0.87 bar, compared to the Aspen model predicting 0.36 bar. Similarly, the flash tank in Unit-300 is operated at 100°C and 0.47 bar in previous models, whereas Aspen requires conditions of 120°C and 0.4 bar to reach the same outlet compositions.

This is believed to be due to the high polarity of MEG. The hydroxyl groups at each end of the molecule form hydrogen bonds with water in the mixture, reducing its vapour pressure. As the previous model uses data obtained from laboratory experiments, it is expected that in the final plant design will be operating at pressures nearer to 0.87 bar and 0.47 bar and that the Aspen predictions for flash pressure should be overlooked.

It was also found that both of these flash vessels had higher inlet flows of water than expected. The blowdown tank showed 42.8 kg/s compared to an expected 38.5 kg/s, while flash separator showed 132 kg/s compared to an expected 127.3 kg/s. This is suspected to be once again due to the strong MEG-water interactions and the difficulty of separating the two. As more water is fed into the flashes, more water leaves in the top products as vapour. Despite the water flows in the bottom product decreasing, the total volume required for the flash vessels increases due to vapour specific volumes being approximately a factor of 1000 larger than liquid volumes. This leads to increases in equipment volumes of 22% and 11% for the blowdown tank and the flash separator respectively.

The previous model had assumed that 100% of the glucan present in the biomass inlet feed is left untouched by the IL solvent, however Brandt-Talbot et al. (2015) suggest that this is not the case, and that some glucan is dissolved in the IL.[2] There is therefore dissolved glucan in the system, increasing some stream densities and therefore pumping power. This is most apparent in the bottom product discharge pump of the Unit-300 flash separator. The glucan mass fraction of this flow is 0.70, compared to a zero mass fraction in previous design. This leads to an increase in required pumping power of 46%. The increase in mass fraction originates from the glucan recovery used. In the previous model by Sukma (2017) it is assumed that 100% of the glucan is recovered as a solid, and as a consequence has no separation processes aimed at removing any IL-dissolved glucan.[20] The updated process model uses an 89.1% glucan recovery and therefore there is glucan present in the liquid phase which then accumulates. As the model in Aspen is not complete and forces some physical properties, it is not fully understood what consequences such a high glucan mass fraction might have.

Finally, with respect to the ionic liquid recycle, it was found, as expected, that as the recycle fraction was increased, less fresh IL was required in the makeup stream. However, it was also found that fresh water requirements were constant, remaining at around 6.8 kg/s across recycle fractions from 95% to 99.5%. This is due to the recycle stream of IL being approximately 20% water, and the IL makeup stream also being 20% water.

4.2. Pulp Analysis

As the primary saleable product from the ionoSolv process, the pulp's cellulose content (referred to as purity) is key to the economic evaluation of the process model. The pulp composition can be found in Table 5. As it can be seen, the pulp purity from the updated ionoSolv process is higher than that of the previous process.

Due to a higher glucan fraction in the cellulose pulp when compared with that found by Sukma (2017), and a proportion of glucan being lost in the liquid phase, the updated design produces a lower total flow of cellulose pulp.[20] The updated design produces 23.5 kg/s, while the previous design produced 27.7 kg/s.[20] Also, due to the higher linin content in the cellulose pulp, there is less lignin cake produced in Unit-250, and therefore less sent to the burner.

Component	Cellulose Pulp Composition (%wt)	Previous design (%wt)
Glucan	81.8	78.0
Hemicellulose	6.7	8.6
Lignin	11.5	13.4

Table 5: Cellulose pulp composition from the two ionoSolv model.

4.3. Capital Costs

4.3.1. ISBL Installed Cost

No variation was seen at different recycle fractions, therefore the ISBL installed cost can be taken as constant for this model. However, an overall increase of 11% was in comparison to that reported by Sukma (2017) - this is equivalent to an increase of $40.6 million (in 2018) resulting in a final ISBL installed cost of $410.6 million.[20] The increase primarily came from the changes found in Units 200 and 300 as shown in Table 6.

Equipment	Cost Increase ($ million)	Fraction of total increase
(U-200) Blowdown Tank	7.2	18%
(U-300) Flash Tank IL/Water Separator	21.7	53%
(U-300) Flash Tank Vacuum Pump	9.7	24%

Table 6: Main increases in installed costs of ISBL equipment in comparison to values reported by Sukma (2017).[20]

As mentioned in Section 4.1., even after setting the pressure and temperature to the values reported by Sukma (2017), there is still a significant size discrepancy found in both flash tanks due to the increased water inlet flowrate.[20] This therefore results in the installed cost increase shown in Table 6. While the increase in required pumping power in the vacuum pump, resulted in a significant increase in installed cost. These three units cover 95% of the increase, the

remainder is covered by relatively small cost increases and decreases in other equipment.

Additionally, it was found that the share of the total ISBL installed cost for each Unit (100-500) is nearly identical to that found by the previous model as show in Table 7.[20] The only difference being the increase in the share of Unit 300 due to the increase in the cost of its flash tank.

	Fraction of total ISBL installed cost	
Unit	**Aspen Model**	**Previous Model**
100	0%	0%
200	19%	19%
250	8%	9%
300	71%	70%
500	2%	2%

Table 7: Fractions of the total ISBL installed cost for each Unit. Current model and previous model reported by Sukma (2017) shown.[20]

4.3.2. OSBL Installed Cost

Units 800 and 900 (wastewater treatment and utilities) did not see any change in cost relative to the values reported by Sukma (2017).[20] However a decrease in cost was found in Unit 970 (Burner, Steam and Power Generation) from $78 million to $71 million.[20] This is due to the fact that as mentioned in Section 4.2, with the current model there is a decrease in the flowrate of lignin cake being fed into the burner in Unit 970. This will result in a smaller burner required and therefore cheaper equipment.

4.4. Total Installed Cost & Capital Investment

The increase in ISBL installed cost and decrease in OSBL results in an overall increase in total IC of $32.2 million from the value reported in by Sukma (2017), resulting in a total IC of $547.6 million, while the total CI saw an increase of $68.7 million from that reported in the previous model resulting in a total CI of $1.092 billion.[20] As mentioned previously, these values have been adjusted to 2018 values, however, the total CI reported by Sukma (2017) in 2016 values was $555 million. This is a substantial increase resulting in a difference of 2 years. This adjustment follows the method laid out in Sections 3.4.1.2. and 3.4.1.3. Therefore a difference in the total IC is magnified twice, once as the total CI is calculated using the assumptions of Sinnott (2015) and Davis et al. (2015), and once again when updated to 2018 values using the CEPCI indexes.[25,27] The CEPCI is an industry standard, however the scalability of the assumptions used by Davis et al. (2015) may be questioned as the IC reaches significantly higher values.[25,27] At the moment, the fractions used to estimate the total CI based on the total IC are kept constant. This results in a linear relationship between total IC and total CI where total CI is equal to around 1.99 x total IC. However, it may be reasonable in further work to decrease these fractions as IC increases so that once we reach a large enough plant the external costs covered in the total CI do not change much with further increases in total IC.

4.5. Operational Cost

4.5.1. Operating Costs

The total operating cost was found to be dictated by the usage of raw materials, primarily biomass and ionic liquid as shown in Table 8. The remaining costs denoted as 'Other' encompasses all remaining operating costs including the FOC, GE and the remaining DMC.

		Fraction of Total Operating Cost		
IL Recycle Fraction	**IL Feed into the Process (tonne/h)**	**Biomass**	**Ionic Liquid**	**Other**
95%	30	20%	68%	12%
99%	6	44%	30%	27%
100% [20]	3	59%	20%	21%

Table 8: Fraction of total operating cost at different ionic liquid recycle fractions for biomass, ionic liquid and all other remaining operating costs.

As can be seen, the operating cost is found to change at different IL recycle fractions. The biomass feed was taken as a constant and the 'Other' costs remain relatively unchanged, leaving the only significant variable in the operating cost to be the feed of fresh ionic liquid to the plant. This is shown in Figure 1.

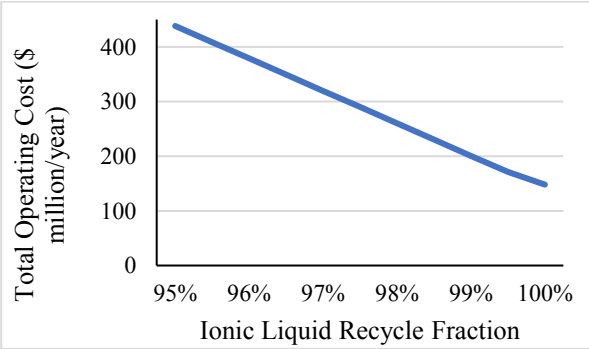

Figure 1: Total Operating Cost of the plant at different ionic liquid recycle fraction from 95% to complete recycle.

As the recycle fraction increases, less fresh makeup ionic liquid needs to be fed into the plant, significantly reducing the operating costs as it has shown to be such a key variable in the operating cost. Once a recycle fraction of 100% is inputted the ionic liquid is at full recycle and the predicted operating cost matches that reported by Sukma (2017).[20] It is worth noting that at this point the IL consumption is not zero as the remaining feed corresponds to the stream of fresh IL used to make up the ionic liquid lost in the product pulp in Unit-200. In summary, the rate at which IL is fed into the plant and therefore the recycle fraction dictates the operating cost of the process.

4.5.2. Operating Revenue

As mentioned previously, the primary revenue is provided by the sale of cellulosic pulp which was found

to be 98% of the total revenue, and sale of electricity to the grid to be 2% to give a total annual revenue of $599 million/year. As the production rate of pulp, the feed of lignin cake and anaerobic gases to the burner is constant for all IL recycle fractions for this model, the total annual revenue is constant. However, it is about 15% smaller than the value predicted in the previous model.[20] This is because, as explained in Section 4.2., the production rate of pulp is lower and the feed of lignin cake to the burner is lower. However, the sale of electricity is still positive (221 GWh/year), this suggests that the plant is still self-sufficient in energy.[20]

4.6. Cash Flow

In summary, the annual revenue remains at $599 million/year while the operating costs range from $140-440 million/year depending on the recycle fraction, meaning that the annual profit will be positive at all recycle fractions considered. An example cash flow over the lifetime (20 years) of the plant is shown in Figure 2 for a 99% recycle fraction.

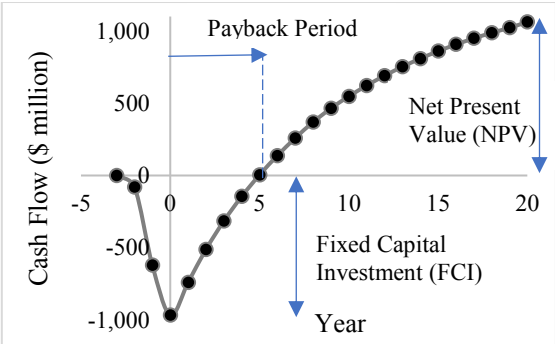

Figure 2: Cash flow of plant at 99% ionic liquid recycle fraction for a 20-year lifespan.

Therefore, after the 3 year construction time the total FCI has been spent and the plant begins to produce a profit. After a payback period of about 5 years (not including construction time) the FCI has been paid off. Finally at the end of the lifetime, the profitability of the plant can be summarised as the Net Present Value (in year 20) which in this case is around $1 billion. Another measure of the feasibility of the plant is the Rate of Return on Investment (ROROI) which is the non-discounted rate at which money is made from the fixed capital investment – 27.87% in this case.

The annual profit, and therefore the profitability of the plant, will be governed by the operating cost which in turn will be governed by the IL recycle fraction as mentioned in Section 4.5.1. This is shown in Figure 3.

Therefore, as the IL recycle fraction increases and the operating costs decreases, the profitability of the plant increases. Analysis shows that a minimum recycle fraction of 95.17% is required for beak-even of the plant (where NPV is zero at the end of the plant lifetime). The case of 99% and maximum case of 99.5% IL recycle fraction were compared to the results reported by Sukma (2017) at infinite recycle in Table 9.[20]

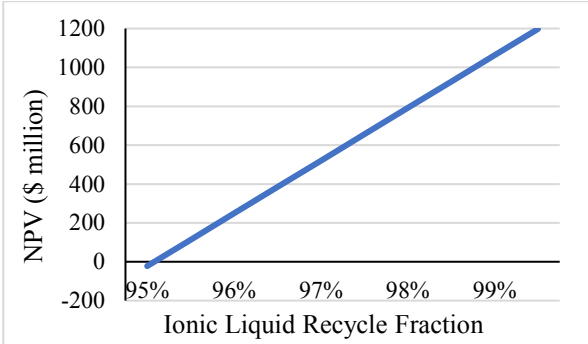

Figure 3: Net Present Value of plant at the end of the 20-year lifespan at different ionic liquid recycle fractions.

Ionic Liquid Recycle Fraction	NPV ($ million)	Payback Time (years)	ROROI
99%	1,062	5.0	27.82%
99.5%	1,198	4.7	29.81%
Sukma (2017) (100%)	1,734	3.5	31.72%

Table 9: Comparison of profitability between different models.

As expected, due to the minimal IL consumption rate, the model reported by Sukma (2017) delivers a higher NPV, ROROI and a shorted payback time – all indicators of a more profitable plant. It is worth noting that although the RORI is at its lowest at 99% recycle, the return is still well above the industry average of around 12% ROROI for 2018.[33] It is also important to note the significant jump in values between 99.5% and 100% in comparison to 99-99.5%. This is because the values at 100% are not the result of setting an infinite recycle in the developed Aspen flowsheet but is the result reported by Sukma (2017).[20] Therefore this not only takes into account the IL consumption but all the previous changes in costs mentioned in this report such as lower total installed cost and higher annual revenue, which increase the profitability of the plant.

4.7. Raw Material Price Sensitivity Analysis

4.7.1. Ionic Liquid

As shown, the IL consumption is one of the main costs that governs the profitability of the plant. Therefore, a sensitivity analysis was done on the price for the case of a 99% recycle fraction. The maximum price for break-even was found to be $6.24/kg, which is significantly higher than the potential production price of $1.24/kg used and reported in Chen et al. (2014).[32]

4.7.2. Pulp

The pulp price of $875/tonne is a commodity price, however the product of this process will most likely be used as an intermediate e.g. for biofuels and therefore its price will be lower. Therefore, a sensitivity analysis was also done on this price for the case of 99% recycle fraction. This found the minimum break-even price to be $500/tonne compared to the price reported by Sukma (2017) of $274/tonne.[20] This will be due to the fact that the previous model reported a higher profitability and therefore can afford to sell the pulp at a lower price.[20] This value can also be compared to the minimum sugar selling price reported in Humbrid (2011) of

$255/tonne.[29] However, in Humbrid (2011), a price of $58.8/tonne for biomass is used rather than $80/tonne used here.[29] When adjusted to $58.5/tonne, the minimum break-even price for pulp is found to be $401/tonne, therefore significantly higher than what is reported in Humbrid (2011).[29]

4.8. Comparison to the Kraft Process

Biermann (1993) reports the total capital investment of a Kraft process plant producing 1000 tonnes/day of paper to cost a total of $1 billion in 1993.[10] This is not directly comparable to the ionoSolv process due to the difference in product, production rate and the 25-year gap. The final product i.e. paper will be sold at a higher price than the intermediate product produced by the ionoSolv process. However, we can focus on the section of the process where the pulp is produced.

Firstly, if we assume that all of the pulp is used in the paper production, we can roughly assume that pulp production rate is somewhat similar to the paper production rate. This would suggest that this plant produces the equivalent of around 1000 tonnes/day of pulp, whereas the ionoSolv process considered is producing 2030 tonnes/day. Secondly, if the Kraft process cost is brought to 2018 values following the method described in Section 3.4.1.2. and a CEPCI of 359.2 for 1993, a total capital investment of $1.65 billion is estimated. This is significantly larger than the total capital investments found for the ionoSolv process. This is however ignoring the paper production section of the Kraft process which is included in the $1.65 billion price. Therefore, this could potentially cause significant discrepancy in the cost of just the pulp production section. Nevertheless, at rough estimation, it would seem that the ionoSolv process has the potential to produce a higher rate of pulp at a smaller total capital investment than the Kraft process.

5. Conclusions

In summary, with this iteration of the ionoSolv process model, the economics indicate that the process remains profitable at ionic liquid recycle fractions above 95.17%. While for recycle fractions such as 99%, an NPV of $1.06 billion is found and a promising ROROI of 27.82% is reported. Additionally, at first estimates would seem to be more economically attractive than alternative processes such as the Kraft process whilst avoiding the environmental impact involved. Therefore, this merits further research and model development of the ionoSolv process.

The Aspen Plus model can be improved firstly, by using user inputted components for non-native components such as lignin and [TEA][HSO4] to more closely resemble the component interactions. This could potentially allow for more sophisticated thermodynamic models to be used such as UNIFAC. Secondly, with the sufficient physical data, more of the equipment blocks can be substituted for equipment models in the Aspen database. This would be especially beneficial for the filters and the reactor.

Further experimental work could also be done to build upon the findings of Brandt-Talbot et al. (2017) and determine the pulp composition at more than 4 IL recycles.[2] This would enable more accurate modelling of higher recycle fractions such as the ones considered in this investigation.

Finally, the process costings could be improved by taking into consideration the cost of treatment and disposal of the waste ionic liquid stream. These processes can be very costly and could potentially result in the process becoming non-profitable at the ionic liquid recycle fractions considered.

6. Acknowledgements

Firstly, we would like to thank Anton J Firth for his support and guidance throughout the entirety of the project. Secondly, we would like to thank Made Santihayu Sukma and Francisco Malaret for their suggestions and aid which were key in our progress. Finally, we would like to thank the entirety of the Hallet Group at Imperial College London who were all willing to help when we were in need of assistance.

7. References

1. AnonymousGlobal Petrol Prices. https://www.globalpetrolprices.com/articles/39/ (accessed 08/12/, 2018).

2. Brandt-Talbot, A.; et al. An economically viable ionic liquid for the fractionation of lignocellulosic biomass. *Green Chemistry* **2017**, *19*, 3078-3102.

3. IPCC Global Warming of 1.5 ºC. **2018**.

4. Muhammad, N.; et al. Effect of Ionic Liquid Treatment on Pyrolysis Products from Bamboo. *Industrial & Engineering Chemistry Research* **2012**, *51*, 2280-2289.

5. Sayigh, A. *Transition Towards 100% Renewable Energy : Selected Papers from the World Renewable Energy Congress WREC 2017;* Innovative Renewable Energy; Springer: Cham, 2018; .

6. Qu, T.; et al. Experimental Study of Biomass Pyrolysis Based on Three Major Components: Hemicellulose, Cellulose, and Lignin. *Industrial & Engineering Chemistry Research* **2011**, *50*, 10424-10433.

7. US Energy Information Administration Biomass - Energy Explained. https://www.eia.gov/energyexplained/?page=biomass_home (accessed 09/12/, 2018).

8. Gao, D.; et al. Lignin triggers irreversible cellulase loss during pretreated lignocellulosic biomass saccharification. *Biotechnology for biofuels* **2014**, *7*, 175.

9. José Horst, D.; et al. Lignin as alternative fuel: an estimate of the thermal energy generation

potential from brazilian crops. *Environmental Progress & Sustainable Energy* **2017**, *36*, 717-722.

10. Biermann, C. J. *Essentials of pulping and papermaking;* Academic Press: San Diego u.a, 1993; , pp 86-91.

11. AnonymousSupplement E to Volume I: Stationary Point and Area Sources (Fifth Edition) : Compilation of Air Pollutant Emission Factors, Fifth Edition. **2001**, 4.

12. Satein, H. Chemical Relationships between Greenhouse Gases and Air Pollutants in Biomass Energy Production. **2009**.

13. Hult, E.; et al. A comparative CP/MAS 13C-NMR study of cellulose structure in spruce wood and kraft pulp. *Cellulose* **2000**, *7*, 35-55.

14. Natural Resources Canada Current lumber, pulp and panel prices. https://www.nrcan.gc.ca/forests/industry/current-prices/13309 (accessed 11/12/, 2018).

15. index mundi Wood Pulp - Monthly Price. https://www.indexmundi.com/commodities/?commodity=wood-pulp&months=120 (accessed 11/12/, 2018).

16. Brandt, A.; et al. Deconstruction of lignocellulosic biomass with ionic liquids. *Green Chemistry* **2013**, *15*, 55-583.

17. Klein-Marcuschamer, D.; et al. Techno-economic analysis of a lignocellulosic ethanol biorefinery with ionic liquid pre-treatment. *Biofuels, Bioproducts and Biorefining* **2011**, *5*, 562-569.

18. Cheenkachorn, K. Enzymatic Saccharification of Rice Straw under Influence of Recycled Ionic Liquid Pretreatments. *Energy Procedia* **2016**, *100*, 160-165.

19. Stark, A. Ionic Liquid-Based Processes in the Biorefinery: A SWOT Analysis. Ionic Liquids in the Biorefinery Concept: Challenges and Perspectives. *The Royal Society of Chemistry* **2016**.

20. Sukma, M. S. Designing an IonoSolv Pretreatment Process in The Biorefinery Plant. **2017**.

21. Outon-Gill, R. Conceptual design, simulation and economic evaluation of the IonoSolv process. *Universitat Ramon Llull* **2017**.

22. Weerachanchai, P.; Lee, J. Recyclability of an ionic liquid for biomass pretreatment. *Bioresource Technology* **2014**, *169*, 336-343.

23. Sukma, M. S. Email Communication. **2018**.

24. Hallett, J. Post-presentation meeting. **2018**.

25. Ray, M. S. Coulson and Richardson's Chemical Engineering Volume 6 (Design), 2nd Edition, by R.K. Sinnott, Pergamon Press, Oxford, UK (1993). 954 pages. ISBN 0-08-041865-1. *Developments in Chemical Engineering and Mineral Processing* **1994**, *2*, 254-255.

26. Turton, R. *Analysis, synthesis, and design of chemical processes;* Prentice Hall: Upper Saddle River, NJ, 2012; .

27. Davis, R.; et al. Process Design and Economics for the Conversion of Lignocellulosic Biomass to Hydrocarbons: Dilute-Acid and Enzymatic Deconstruction of Biomass to Sugars and Catalytic Conversion of Sugars to Hydrocarbons. **2015**.

28. Davis, R.; et al. Process Design and Economics for the Conversion of Lignocellulosic Biomass to Hydrocarbons: Dilute-Acid and Enzymatic Deconstruction of Biomass to Sugars and Biological Conversion of Sugars to Hydrocarbons. **2013**.

29. Humbird, D.; et al. Process Design and Economics for Biochemical Conversion of Lignocellulosic Biomass to Ethanol: DiluteAcid Pretreatment and Enzymatic Hydrolysis of Corn Stover. *National Renewable Energy Laboratory* **2011**.

30. Access Intelligence, L. Chemical Engineering Plant Cost Index. (accessed Aug 8, 2017).

31. Jenkins, S. Chemical Engineering Plant Cost Index. (accessed Aug 10, 2017).

32. Chen, L.; et al. Inexpensive ionic liquids: [HSO4]−-based solvent production at bulk scale. *Green Chem* **2014**, *16*, 3098-3106.

33. CSI Market Industry Management Effectiveness. (accessed Dec 12, 2018).

Modelling of Natural Gas Supply Chain Construction and Investment Pathways in Regions with Minimal Existing Infrastructure

Sachin Gulati and James Toole
Department of Chemical Engineering, Imperial College London, U.K.

Abstract
The aim of this paper was to develop a model which optimises the operation of a natural gas supply chain and the investment pathway for the expansion of the supply chain over a set planning horizon, particularly focussing on a region with minimal existing infrastructure. The focus was on spatial resolution as opposed to temporal to include all the individual elements of the natural gas supply chain. The model was designed as a mixed-integer linear program (MILP); the objective function consisted of the sum of time-discounted costs for each aspect of the supply chain, and detailed constraints described the parts of the supply chain and their interactions with each other. To test the model, it was programmed into GAMS, and applied to the case study of South Brazil, using solver CPLEX. This case study was selected for its lack of existing infrastructure, desire for energy security and large reserves of untapped natural gas. The results obtained from different trade scenarios highlighted the fact that the model constructs logical pathways to meet demand in all grids and time periods, as well as showing flexibility to adjust to different scenarios.

1. Introduction

As coal and oil production are phased out in an effort to reduce carbon emissions and natural gas is implemented in their place, many governments and private investors are looking for the best way to produce natural gas and transport it for consumption.

The American Petroleum Institute provides an illustration of the natural gas supply chain (American Petroleum Institute, 2017). There are three main forms of natural gas throughout its supply chain: unprocessed, processed and liquefied natural gas (LNG). The illustration shows that the supply chain consists of six key components relating to these different forms of natural gas: production, processing, transmission (by pipeline and freight), storage, international trade and consumption.

Production relates to the extraction of unprocessed natural gas from underground reservoirs. Processing deals with conversions between the different forms of natural gas; natural gas processing forms processed natural gas from unprocessed natural gas, liquefaction forms LNG from processed natural gas and regasification is the opposite to liquefaction. Additionally, within the category of processing, there may be biogas production as an alternative way of producing processed natural gas, especially on a local scale. Though biogas is considered equivalent to processed natural gas, it may be permitted within the natural gas supply in limited amounts only (Wetland, 2010).

There are four different types of storage: above ground storage (in vessels), salt caverns, depleted gas reservoirs and aquifers. Different forms of natural gas are stored separately, although unprocessed gas is not stored at all.

Given the complexities of the natural gas supply chain, in particular the many possible pathways natural gas can take through the supply chain (as seen in figure 1), it can be seen that there is a significant opportunity to optimise the operation of the natural gas supply chain and the building of its infrastructure to meet growing demand. Such optimisation can be achieved by a model of the natural gas supply chain and could prove beneficial to policymakers and investors in their decision making.

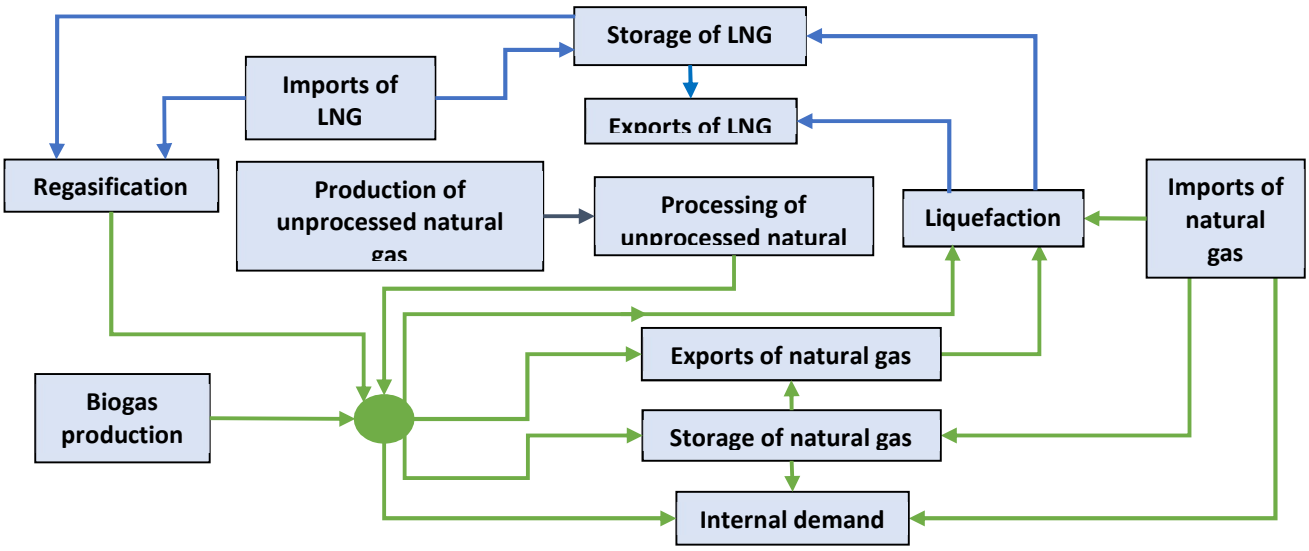

Figure 1 - Superstructure developed for the model, illustrating the structure of the natural gas supply chain

2. Background

Extensive research has previously been conducted in the area of supply chain modelling, particularly with regard to the hydrogen supply chain (Guillén-Gosálbez et al, 2009). The natural gas and hydrogen supply chains are very similar, meaning this formulation is relevant to modelling of the natural gas supply chain. This formulation inputs multi-objective optimisation with environmental impact as a secondary objective; constraints for this are based around Life Cycle Analysis. This formulation expands upon previous work utilising only time-invariant demand and single-objective optimisation (Almansoori and Shah, 2009).

Research has also been focussed on decarbonisation using hydrogen (Strachan et al, 2008). This paper utilised demand disaggregation through demand clusters that centred around UK towns and cities. Supply was also disaggregated through splitting up of other renewable options (such as wind) depending on resource location; carbon storage options; and hydrogen and LNG terminals. Hydrogen infrastructure was disaggregated through three options: small scale production, gaseous pipelines and liquid delivery by tankers. Mixed integer programming is required to detail individual transmission and processing investments.

The trade-off between temporal and spatial resolution has also been discussed by (Samsatli and Samsatli, 2017). This formulation has very high temporal resolution involving hourly, daily, seasonal and yearly variations in demand; it is suggested that this is of particular importance when modelling renewables and energy storage. Additionally, biomass requires very high spatial resolution due to the variation in yield; this must be offset with temporal resolution only on a seasonal scale. Too high a resolution can cause the model to become intractable. The formulation again makes use of mixed-integer linear programming but with multi-objective optimisation, using the weighted-sum method, on the impacts of energy production for different forms of energy.

With regard to modelling of the natural gas supply chain, research has been undertaken to create a mixed-integer non-linear program that models production and transmission (Cafaro and Grossmann, 2014). This program utilises gradual refinement of linear approximations of the objective function to obtain results, as well as the branch-and-bound method. The objective function is based solely on maximising the net present value. This paper follows a similar breakdown of the gas supply chain that is followed in this report, with the exception of only shale gas being considered.

When considering the natural gas supply chain, demand can also be split into three areas: domestic, industry and international (Ghaithan et al, 2017). This paper discusses both shale oil and shale gas supply chains, although both follow similar pathways. The treatment of trade is more rigorous than other efforts, taking OPEC quotas into account (applicable for shale oil only). This paper also has three objectives comprising the total cost, total revenue and revenue from international sale of gas.

It can be seen that there is a clear gap in the literature regarding holistic modelling of natural gas supply chains that deal with operation and expansion of available infrastructure to meet demand. Hence, this paper presents a time-dependent, multi-node, mixed-integer linear program (MIP) to optimise operation of a gas supply chain and investment in its infrastructure.

Given the understanding gained from research, the model focusses on spatial resolution in sacrifice of temporal resolution, enabling the inclusion of detailed constraints for individual elements of the supply chain. Additionally, the objective function could incorporate numerous factors, such as cost, CO_2 and greenhouse gas emissions through multi-objective optimisation. However, it was decided that the objective function should be based solely on total discounted cost (with a fixed interest rate) because this would be the main driving force behind the decisions of policy makers and investors.

To test the model, it was applied in GAMS, using the CPLEX solver, to the case study of South Brazil. This area was selected due to its current lack of gas infrastructure, allowing for a relative blank slate approach. Also, very little research has been conducted with regard to the building of gas infrastructure in the region (Chávez-Rodríguez et al, 2017). South Brazil is a region blessed with large, untapped offshore gas reserves in the pre-salt layer but a current dependence on imports, particularly from Bolivia. The government has a strong desire to achieve energy security and the best way for it to do so is through the building of gas infrastructure. The model constructed in this report was soft-linked with data from MUSE-Brazil (García Kerdan et al, 2018).

3. Methodology

3.1. General Model

The first section shall be further split into smaller sections describing the constraints applied to each aspect of the supply chain, as well as separate sections for the material balances and objective function. Presented here is only a selection of constraints to provide a concise understanding of the formulation; all constraints can be found in Appendix 2 and nomenclature can be found in Appendix 1.

The model has been designed to take input data for the region considered, including the demand for natural gas, and produce the optimal solution for operating and investing in the gas supply chain based on the input data. The model contains multiple indices to tailor the input data and resultant outputs to specific locations, forms of natural gas, time periods and elements of the supply chain.

The region considered is split up into different grid zones, indexed by g, in accordance with spatial dependence of data within the region considered. For example, the grid zones might be drawn out so that demand in each grid zone is similar in magnitude. Further, the chosen planning horizon is divided up into equal time slices of a set length, advisably no shorter than a year given the nature of the constraints within the model, indexed by t.

Similarly, the different forms of natural gas within the supply chain are indexed by i; the production sites in each grid zone are numbered and contained in the set *ipr*; the four types of processing facilities are included in the index *ipg;* the four types of storage facilities considered are indexed by *isf*; and the three forms of freight transport by *itr*.

The following general assumptions were applied to the model:

- Across the formulation, perfect foresight is assumed such that infrastructure is ready as soon as it is required.
- No lifetimes associated with infrastructure, meaning that once infrastructure is built it can continue to operate indefinitely.
- No leakages of any form of natural gas from the supply chain.
- Demand is a parameter, meaning it is unaffected by variables within the model.

3.1.1. Production

Production is focussed on individual gas fields, each with its own fixed volume of reserves. It is assumed that when a field is utilised, infrastructure to exploit its full capacity is installed – although this infrastructure may not always be operational at maximum capacity. It is also assumed the site can produce unprocessed natural gas at up to its maximum capacity. The use of specific sites rather than generic capacity allows the model to be tailored to the individual sites and the resources available to them.

Equation 1a enforces that a production facility can only be built once on a specific site as the binary variable $Z1_{g,ipr,t}$ can only take the value of one in one time-period. Equation 1b forces a change in $Z5_{g,ipr,t}$ to reflect that a site now has developed infrastructure for production. Equation 1c ensures a facility cannot be operational if it has not been built.

Table 1 - Key production constraints for the model.

No.	Constraints (Production)
1a	$\sum_{t=1}^{t=Nt} Z1_{g,ipr,t} \leq 1$
1b	$Z5_{g,ipr,t} = Z5_{g,ipr,t-1} + Z1_{g,ipr,t}$
1c	$Z2_{g,ipr,t} \leq Z5_{g,ipr,t}$
1d	$APr_{g,ipr,t} \leq m * VRes_{g,ipr,t}$
1e	$VRes_{g,ipr,t} = VRes_{g,ipr,t-1} - APr_{g,ipr,t-1} * TP$
1f	$Z2_{g,ipr,t} - Z2_{g,ipr,t-1} = Z3_{g,ipr,t} - Z3_{g,ipr,t}$
1g	$Z3_{g,ipr,t} + Z4_{g,ipr,t} \leq 1$

The production rate ($APr_{g,ipr,t}$) is bounded by a big-M constraint to ensure that there is only production if the site is operational. Equation 1d places a maximum bound on the production rate in terms of the volume of gas reserves available to the production facility ($VRes_{g,ipr,t}$) through an empirical correlation. This correlation is approximated as a linear correlation to fit within the context of a linear program, with the positive parameter *m* as the proportionality constant. It ensures that as gas reserves are depleted, the maximum achievable production rate decreases accordingly. Equation 1e governs the depletion of $VRes_{g,ipr,t}$ from one time period to the next in accordance with the chosen value of $APr_{g,ipr,t}$.

Equation 1f allows a site to change its operational state between time periods and ensures $Z3_{g,ipr,t}$ and $Z4_{g,ipr,t}$ accurately reflect this change. Equation 1g enforces that a site cannot start-up and shutdown in the same time-period.

3.1.2. Transmission

Transmission (and later freight transport) plays a vital role in the model by connecting the various aspects of the supply chain to each other. Constraints are focussed on the building of and flow in pipelines between grid zones. Different forms of natural gas are carried in different pipelines but only one pumping station is required in a single grid zone, effectively treated as the hub for a region. Once a form of gas has entered a grid zone, it is assumed it can freely interact with other aspects of the supply chain existing in that same region without the need for further transmission costs or infrastructure. It is assumed transmission via pipeline between regions is effectively instantaneous.

Equation 2a ensures a pumping station can only be built once across all time periods. Equation 2b similarly enforces a change in $Y2_{g,t}$ to reflect that a pumping station now exists in a grid zone and is ready for use. Equation 2c relates $Y3_{g,g',i,t}$ to $Y2_{g,t}$ (both binary variables) to reflect that a grid zone can only pump fluid to another grid zone if it contains a pumping station.

Equation 2d ensures flow between grid zones is in one direction only in a specific time-period; similarly, it is ensured that a pumping station does not pump to itself.

A big-M parameter is used in combination with $Y3_{g,g',i,t}$ to ensure there is only a flow in a pipeline if a pumping station exists and is in operation in a specific grid zone. The flowrate is then bounded by the number of pipelines ($NP_{g,g',i,t}$) multiplied by their capacities ($CapP_i$) in equation 2e.

Equation 2f allows for construction of new pipelines between grid zones to expand total pipeline capacity, through the variable $NPA_{g,g',i,t}$. Another big-M parameter is used in combination with the binary parameter $Y4_{g,g'}$ to guarantee that new pipelines are built between grid zones that can be linked directly by pipeline only. Equation 2g ensures new pipelines can be used to transport natural gas in both directions.

Table 2 - Key transmission constraints for the model.

No.	Constraints (Transmission)
2a	$\sum_{t=1}^{t=Nt} Y1_{g,t} \leq 1$
2b	$Y2_{g,t} = Y2_{g,t-1} + Y1_{g,t}$
2c	$Y3_{g,g',i,t} \leq Y2_{g,t}$
2d	$Y3_{g,g',i,t} + Y3_{g',g,i,t} \leq 1$
2e	$QP_{g,g',i,t} \leq NP_{g,g',i,t} * CapP_i$
2f	$NP_{g,g',i,t} = NP_{g,g',i,t-1} + NPA_{g,g',i,t}$
2g	$NPA_{g,g',i,t} = NPA_{g',g,i,t}$

Table 3 - Key constraints for freight transport in the model

No.	Constraints (Freight Transport)
3a	$QF_{g,g',i,itr,t} = U1_{g,g'} * \frac{NTr_{g,g',i,itr,t} * CapTr_{itr} * NJ_{g,g',itr}}{TP}$
3b	$NJ_{g,g',itr} = floor\left(\frac{OpTime}{\frac{2 * DistanceF_{g,g'}}{AvSpeed_{itr}} + LUTime_{itr}}\right)$
3c	$\sum_{i}\sum_{g'} NTr_{g,g',i,itr,t} \leq AvNTr_{g,itr,t}$
3d	$AvNTr_{g,itr,t} = AvNTr_{g,itr,t-1} + NTrP_{g,itr,t}$
3e	$0 \leq NTrP_{g,itr,t} \leq MaxNTrP_{itr}$

3.1.3. Freight Transport

Freight transport, as stated above, plays a similar role to transmission in the model. However, freight must be treated differently from pipelines to give an accurate representation of its inner workings whilst fulfilling a similar role.

Travel time between destinations and loading and unloading time are taken into consideration, as opposed to the effectively instantaneous portrayal of pipelines. Freight also comes in discrete units of transport capacity – to better reflect the fixed capacities of individual freight units - rather than continuous variable flow.

Equation 3a calculates the total flowrate of natural gas transported via freight between two grid zones in a specific time-period ($QF_{g,g',i,itr,t}$) in terms of the number of transport units operating between the two grid zones ($NTr_{g,g',i,itr,t}$), assuming that they all operate simultaneously and at full capacity ($CapTr_{itr}$). Also, this equation is dependent on binary parameter $U1_{g,g'}$ to ensure that freight transport connections are made between adjacent grids with sufficient infrastructure only.

The number of journeys that a given mode of freight transport can make in a single time-period ($NJ_{g,g',itr}$) is used in equation 3a and is calculated in equation 3b using the assumption that the transport units operate continuously for the duration of their operational time. Equation 3c places a limit on the number of transport units available to a single grid zone and ensures different transport units can be reassigned to transporting different forms of natural gas to different grid zones between time slices. Equation 3d allows for the purchasing of additional units. However, this expansion is bounded by a maximum in equation 3e.

3.1.4. Processing

Processing facilities are built (or pre-existing) in specific grid zones. The processing rate of each type of processing unit ($PgR_{g,ipg,t}$) is constrained by a maximum value, $CapPg_{g,ipg,t}$ by equation 4a. This maximum can be expanded between time slices, as defined in equation 4b. The level of expansion, $CapEPg_{g,ipg,t}$, is further constrained by the minimum and maximum flow capacities of a single processing unit ($MinCapPg_{ipg}$ and $MaxCapPg_{ipg}$) multiplied by the number of new processing plants constructed ($NPg_{g,ipg,t}$), as illustrated in equation 4c. $CapEPg_{g,ipg,t}$ is further constrained by a big-M constraint, which incorporates the binary parameter $V1_{g,ipg}$, to ensure that processing facilities are built where sufficient infrastructure exists only.

Table 5 - Key constraints for processing in the model

No.	Constraints (Processing)
4a	$PgR_{g,ipg,t} \leq CapPg_{g,ipg,t}$
4b	$CapPg_{g,ipg,t} = CapPg_{g,ipg,t-1} + CapEPg_{g,ipg,t}$
4c	$MinCapPg_{ipg} * NPg_{g,ipg,t} \leq CapEPg_{g,ipg,t}$ $CapEPg_{g,ipg,t} \leq MaxCapPg_{ipg} * NPg_{g,ipg,t}$

3.1.5. Storage

Equation 5a governs changes in the stored volume ($VS_{g,i,isf,t}$) of a specific form of natural gas in a particular grid zone between time-periods in terms of flowrates in and out of storage. Big-M constraints are used to ensure the inflow and outflow from a storage facility are dependent on the binary variables $Win_{g,i,isf,t}$ and $Wout_{g,i,isf,t}$. This is necessary as equation 5b then makes use of these binary variables to ensure a storage facility is not simultaneously adding and removing natural gas from storage. In equation 5c, the volume stored is bounded from above by the maximum storage capacity

Table 4 - Key storage constraints for the model.

No.	Constraints (Storage)
5a	$VS_{g,i,isf,t} = VS_{g,i,isf,t-1} + (QSin_{g,i,isf,t-1} - QSout_{g,i,isf,t-1}) * TP$
5b	$Win_{g,i,isf,t} + Wout_{g,i,isf,t} \leq 1$
5c	$b * CapS_{g,i,isf,t} \leq VS_{g,i,isf,t} \leq CapS_{g,i,isf,t}$
5d	$\sum_{i} \frac{rho_i}{rho('NG')}\left(\sum_{g}\sum_{isf} VS_{g,i,isf,t}\right) \geq c * \sum_{g} D_{g,t} * TP$

($CapS_{g,i,isf,t}$) and from below by the buffer capacity, which is expressed as a fraction (b) of $CapS_{g,i,isf,t}$. The maximum storage capacity can be expanded in much the same fashion as processing facilities and so the constraints are of the same form, including the variable for expansion of storage ($CapES_{g,i,isf,t}$) and the binary parameter $W1_{g,isf}$ to ensure storage is built only where there is sufficient infrastructure.

Equation 5d ensures some fraction c of the volume of natural gas demanded over the subsequent time-period is stored as a safety net in case of demand or supply-side shocks. The constraint allows for this required volume to be stored as any form of natural gas (through the summation over i) and accounts for differences in density between the different forms of natural gas.

3.1.6. Imports and Exports

Due to the inherent complexities of modelling a global market for a good, certain liberties are taken to ensure the modelling of imports and exports retains its focus on the region of interest. Minimum and maximum flowrates are applied to ensure existing trade agreements and geographical or infrastructural limitations can be included in a simple manner. Regarding exports, the maximum is also useful to ensure the region of interest does not flood the global market with gas in the case that inputted global price is greater than the regions costs of producing natural gas.

To ensure a grid zone does not simultaneously import and export the same form of natural gas, equation 6a is required:

$$X1_{g,i,t} + X2_{g,i,t} \leq 1 \qquad (6a)$$

3.1.7. Material Balances

There is a separate material balance for each of the three forms of natural gas within the supply chain, applied to each grid zone and each time-period. The material balances are important to ensure that there are no discrepancies within the model, such as generation of natural gas from nothing, and they take the general form:

$$In - Out + Generation - Consumption = 0 \quad (7a)$$

Within equation 7a inputs include flows into the grid zone by pipeline and freight and flows out of storage, while outputs include flows out of the grid zone by pipeline and freight as well as flows into storage. Generation encompasses production of unprocessed natural gas in addition to any forms of processing that produce the form of natural gas of interest. Analogously, consumption includes forms of processing that convert the form of natural gas of interest into another form of natural gas in addition to demand for natural gas. The resultant material balances can be seen in Table 6.

Equation 7e places a limit on biogas production to ensure that the fraction of biogas within natural gas streams does not exceed the maximum permitted volume fraction fBG. This limit is expressed in terms of the processing rate of natural gas production because this is the only form of generation of natural gas that is guaranteed not to contain any biogas already.

3.1.8. Objective Function

The objective function is based on minimising Total Discounted Cost (TDC), with a fixed interest rate (ir), as exhibited in equation 8a (assuming year-long time-periods):

$$TDC = \sum_{t} \frac{TC_t}{(1+ir)^{t-1}} \quad (8a)$$

The cost functions for every aspect of the supply chain considered feed into a summation to calculate Total Cost (TC_t). Broadly, the cost functions can be split into two categories: capital costs and operating costs. Capital costs consist of any costs associated with the construction of infrastructure; operating costs comprise costs associated with the maintenance of the infrastructure in addition to those associated with achieving the flowrates throughout the supply chain required to meet demand. Import costs and export revenue are also included within the calculation of TC_t, but export revenue is taken away to reflect the fact that it is a revenue rather than a cost.

Table 6 - Material balance constraints for the model

No.	Constraints (Material Balances)
7b	$\sum_{g'}^{N}\left(QP('NG')_{g',g,t} + \sum_{itr} QF('NG')_{g',g,t}\right) + QI('NG')_{g,t}$ $- \sum_{g'}^{N}\left(QP('NG')_{g,g',t} + \sum_{itr} QF('NG')_{g,g',t}\right) - QE('NG')_{g,t}$ $+PgR('NGP')_{g,t} + PgR('BGP')_{g,t} + PgR('RG')_{g,t} - \frac{rho(LNG)}{rho(NG)} * PgR('LF')_{g,t}$ $- \sum_{isf}(QSin('NG')_{g,isf,t} - QSout('NG')_{g,isf,t}) - D_{g,t} = 0$
7c	$\sum_{g'}^{N}\left(QP('LNG')_{g',g,t} + \sum_{itr} QF('LNG')_{g',g,t}\right) + QI('LNG')_{g,t}$ $- \sum_{g'}^{N}\left(QP('LNG')_{g,g',t} + \sum_{itr} QF('LNG')_{g,g',t}\right) - QE('LNG')_{g,t}$ $+PgR('LF')_{g,t} - \frac{rho(NG)}{rho(LNG)} * PgR('RG')_{g,t}$ $- \sum_{isf}(QSin('LNG')_{g,isf,t} - QSout('LNG')_{g,isf,t}) = 0$
7d	$\sum_{g}^{N} QP('UP')_{g',g,t} - \sum_{g'}^{N} QP('UP')_{g,g',t} + \sum_{ipr} APR_{g,ipr,t} - \frac{rho(NG)}{rho(UP)} * PgR('NGP')_{g,t} = 0$
7e	$PgR('BGP')_{g,t} \leq \frac{fBG}{1-fBG} * PgR('NGP')_{g,t}$

3.2. Case Study: South Brazil

The area of South Brazil is split into 12 regions along with a thirteenth offshore region containing the production sites, as illustrated in Figure 2. To apply the general formulation, certain amendments and assumptions are applied.

Firstly, it is assumed that the data obtained, as outlined in Appendix 3, is accurate.

Regarding changes to the formulation, the time slices are five years long, requiring a modification to the objective function:

$$TDC = \sum_{t}\left(\frac{CC_t}{(1+ir)^{5t-5}} + \sum_{n}\frac{OC_t}{5(1+ir)^{5t-n}}\right) \quad (9a)$$

This enables the TDC to continue to be calculated based on a fixed interest rate, despite the increase in length of time periods. The decision was taken to increase the length due to the demand data available from MUSE (García Kerdan et al, 2018).

Further simplifications are introduced into the cost functions. The time dependence from unit costs across the supply chain has been removed to better fit the data available for South Brazil. Additionally, the cost of pumping stations is now contained within the pipeline cost for simplicity. The unit fixed capital cost terms, except for the case of above ground LNG storage, are now set to zero. Unit costs of production are also assumed to be independent of the production facility; the costs of start-up and shutdown are also considered negligible. The operational cost of freight transport has also been reformulated: it is now comprised of two unit costs ascribed to the type of vehicle owned and to the unit distance travelled. This is a simplification combining both wage and fuel expenditure into one term.

Storage is amended such that all forms of underground storage are now considered as one entity. Furthermore, natural gas is stored below ground only and LNG is stored above ground only.

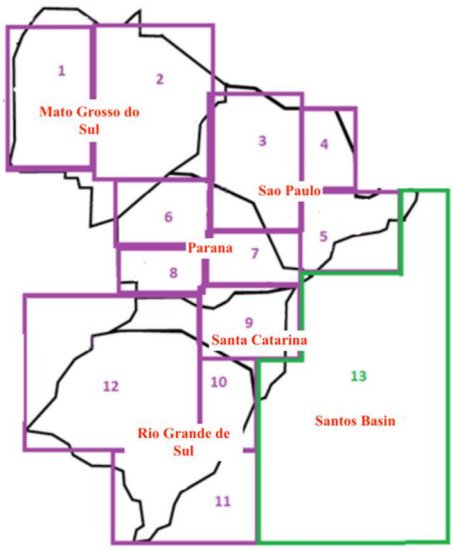

Figure 2 - Map of South Brazil, divided into the 13 grid zones as required for the case study.

Transmission is modified as it is assumed LNG cannot be transmitted via pipeline. This is due to South Brazil currently having no LNG pipelines and the fact that it is unlikely LNG pipelines will become economically viable within the planning horizon (Honoré, 2016). This is achieved simply by setting *CapP('LNG')* to zero.

Freight transport is also reformulated for simplicity to remove the integer variable $NTr_{g,g',i,itr,t}$:

$$CapTrJ_{g,g',i,itr,t} = NTr_{g,g',i,itr,t} * CapTr_{itr} \quad (9b)$$

$CapTrJ_{g,g',i,itr,t}$ is continuous and represents the volume of natural gas of a specific form transported across all freight units per journey. This effectively removes the assumption that all freight units are at full capacity, which may not be an accurate representation of reality. Equations 3a and 3c are therefore altered to:

$$QF_{g,g',i,itr,t} = U1_{g,g'}\frac{CapTrJ_{g,g',i,itr,t} * NJ_{g,g',itr}}{T} \quad (9c)$$

$$0 \leq \sum_{i}\sum_{g'}\frac{CapTrJ_{g,g',i,itr,t}}{CapTr_{itr}} \leq AvNTr_{g,itr,t} \quad (9d)$$

No ship freight is considered due to South Brazil not containing any major waterways. Rail transport is also not considered due to the lack of data available as natural gas transport via rail is still in a fledgling state (Kelly and Horn, 2016).

4. Results and Discussion

This section shall be further split into four sections to reflect the different scenarios presented. First, the formulation containing only the demand across the whole region, production and trade will be discussed as a proof of concept. Following that will be the scenario with an export upper bound equal to the import upper bound and then a third scenario with no exports whatsoever.

The focus was placed on trade scenarios as this is the area South Brazil will have the least control over in terms of managing existing and novel agreements. Additionally, trade is the simplest aspect of the model and so is very much subject to other inputted data and has limited scope for variation during the time horizon.

4.1. Proof of Concept Program

The purpose of this program was to determine whether demand in the region could be satisfied given the available natural gas resources from both within the region and from imports. It was successful because demand was satisfied in South Brazil in all time-periods. Although, reserves were depleted from a starting level of 500 billion m^3 to 200 billion m^3.

4.2. Full Formulation with Export Limit Equal to Import Limit

Despite the previous findings in 4.1, further analysis showed that demand in grid zones 6 and 8 could not be satisfied in the first time-period due to the lack of existing infrastructure (Figure 3). To circumvent this problem a tolerance was implemented which ensured demand in these grid zones did not have to be met in this time-period. It could be assumed that this demand could be met through alternatives to natural gas.

The Total Discounted Cost is $800 billion in this scenario. The reserves at the end of the time horizon are equal to 140 billion m^3. The offshore sites are utilised to varying degrees, with site 2 beginning production immediately. Figure 4 illustrates the final infrastructure across all grid zones at the end of the time horizon.

Biogas was not utilised at all within the model despite existing infrastructure, while freight was used minimally, so these were omitted from the diagram (Figure 4). The preferred mode of transmission was natural gas pipelines, with unprocessed gas pipelines used between grid zones 13 and 5 only due to grid zone 5 being the coastal region closest to the production sites. The presence of existing natural gas processing there will have further incentivised this result for the model. Logically, grid zone 5 contained all the natural gas processing.

Natural gas is exported through grid zone 5 as well, which makes sense given this context because it would have no further transmission costs associated with exporting it. However, the fact that natural gas is exported through grid zone 12 as well shows that the cost of production of South Brazilian natural gas is lower than the cost of gas on the world market regardless of the distance it is transmitted for exportation.

South Brazil is able to offset a large proportion of its costs by producing a surplus and exporting this up to the bounds placed on exports. This does leave it with minimal reserves at the end of the planning horizon, suggesting it is not in fact a viable solution. However, it should be considered that this is because the model places no weight on any consequences realised after the planning horizon, so a different solution may be obtained for the same scenario with a longer planning horizon.

In the case that initial resources are almost completely depleted, new infrastructure to exploit another energy resource at the end of 2050 may have to be implemented. If some proportion of profits were to be reinvested across new infrastructure – perhaps in renewables – growing in tandem with the natural gas infrastructure, South Brazil may be able to make a smoother transition to this energy resource.

Natural gas is imported from Bolivia in every time-period, and much smaller volumes into grid zone 12 in the first and last time periods. LNG is also imported in the first and last time periods at significantly smaller volumes than natural gas, even accounting for density differences. The preference for Bolivian imports is a direct consequence of the existing trade agreement placing a lower bound on the flowrate of imports from Bolivia.

The sudden need for imports of natural gas in the last time-period is explained by the slowdown in production associated with depletion of reserves. This suggests that the depletion of reserves is affecting Brazil's ability to meet demand towards the end of the model. This highlights the trade-off between producing less, to require less imports in the final time-period but selling less exports, and producing more, to sell more exports but necessitating the use of imports in the final time-period. The model evaluates the latter as the better option due to the decreasing price of most imports in the last time-period and the discount rate making costs in the last time-period less significant.

The new pipelines built throughout the duration of the model stem from a combination of grid zones 5 and 1 due to these being the main sources of inputs of natural gas to the region. The motivation of this is to minimise transmission costs associated with transporting significant portions of the natural gas supply. For example, the pipeline connecting grid zones 8 and 12 is clearly implemented to minimise the distance of transmission of Bolivian imports to grid zone 12.

Regasification plants exist initially in grids 5, 7, 9, 10 and 11 and no further plants are constructed. The existing regasification capacity is often left unused, particularly between the second and penultimate time periods, due to the absence of LNG imports in these periods. These unused regasification facilities could be a genuine consequence of Brazil's transition towards self-sufficiency in terms of gas supply.

Liquefaction sites are built in the same grid zones as the existing regasification plants; this is due to their usage together to manage LNG storage and the involvement of these grid zones in trade of LNG (they all either import or export LNG throughout the duration of the model).

Some storage is built to meet the minimum storage requirements in terms of demand. Above ground LNG storage is preferred over constructing new natural gas storage, although the existing natural gas storage is utilised extensively.

4.3. Full Formulation with Export Limit Set to Zero

The Total Discounted Cost is $170 billion in this scenario. The reserves are 270 billion m^3 at the end of the time horizon. The largest reserve of 160 billion m^3 is left untouched until the final time-period and the reserve of 54 billion m^3 remains untapped until the penultimate time-period. Like scenario 2, there is no biogas production at any stage and minimal use of freight transport, meaning these are omitted from Figure 5 as well.

Imports are drastically reduced with the minimum bound of natural gas imports from Bolivia enforced throughout, except in the first time-period. During this period, significantly more imports are required to compensate for the limitation on domestic production resulting from the relatively small offshore pipeline (between grid zones 5 and 13). There are no imports in any other grid zone outside of the first time-period.

The added pipeline infrastructure changes significantly from 4.2. The capacities of added pipelines are reduced significantly due to less natural gas being transported throughout the region because of fewer imports and no exports. The pipeline connecting grid zones 8 and 12 is removed altogether because of a lower demand for natural gas in grid zone 12 resulting from the fact that it does not export in this scenario. Further, a new pipeline is added between grid zones 11 and 12; this is initially added instead of the pipeline from 10 to

11, which is added later to satisfy demand for LNG storage in grid zone 11.

Storage capacities remain broadly similar, with LNG storage the preferred choice for expanding storage capacity. However, one key change and exception was expansion of storage of natural gas in grid zone 1 in the final two time-periods. This shows that the model is evaluating that the Bolivian imports are best to satisfy demand in the immediate vicinity of grid zone 1 only, so is storing the surplus. Demand further afield, such as in key demand centres like grid zones 5 and 10, is satisfied more cost-effectively by increasing production rates in grid zone 13, especially if existing production facilities have surplus capacity.

In terms of processing, regasification remains unchanged, while liquefaction capacities fall considerably due to their purpose being to manage storage only.

The capacities of the offshore pipeline and unprocessed natural gas processing facilities fall considerably due to the lower production rate required, which results from the region not exporting. South Brazil is now only producing for itself and is not maximising production to maximise export revenue, perhaps leading to the aforementioned lower capacities.

There is a clear trade-off with enforcing zero exports: the TDC is almost doubled but so are the remaining reserves at the end of the time horizon. This provides a much more sustainable solution beyond the time horizon, ensuring South Brazil will not have to completely restructure its methods of meeting natural gas demand. The infrastructure in both Scenarios 2 and 3 remains broadly the same ensuring demand continues to be met in all grid zones for all time periods.

Figure 3 - Initial infrastructure in South Brazil, including maximum available import quantities.

Key for figures 3, 4 and 5:

- LNG Trade Flows Scale (million m3 per annum)
  - <0.1
  - 0.1-0.5
  - 0.51-1
  - >1
- Natural Gas Trade Flows Scale (million m3 per annum)
  - <2000
  - 2000-40000
  - >40000
- Pipeline Scale (Number of Pipelines):
  - 1-4
  - 5-9
  - 10-14
  - 15+
- LNG Storage Capacity Scale: (million m3)
  - <0.001
  - 0.001-0.099
  - 0.1-1
  - >1
- Natural Gas Storage Capacity Scale: (million m3)
  - <10
  - 11-100
  - >100
- Regasification and Unprocessed Natural Gas Processing Facility Capacity Scale (million m3):
  - <1000
  - 1001-10000
  - >10000
- Liquefaction Processing Facility Capacity Scale (million m3):
  - <0.005
  - 0.0051-0.0099
  - >0.01

- Black circles: grid zone nodes
- Inward arrows: import quantities
  Outward arrows: export quantities
  - Natural gas
  - LNG
- Lines: pipeline capacities
  - Natural gas
  - Unprocessed natural gas
- Squares: processing facility capacities
  - Regasification
  - Liquefaction
  - Natural gas processing
- Triangles: storage capacities
  - Natural Gas
  - LNG

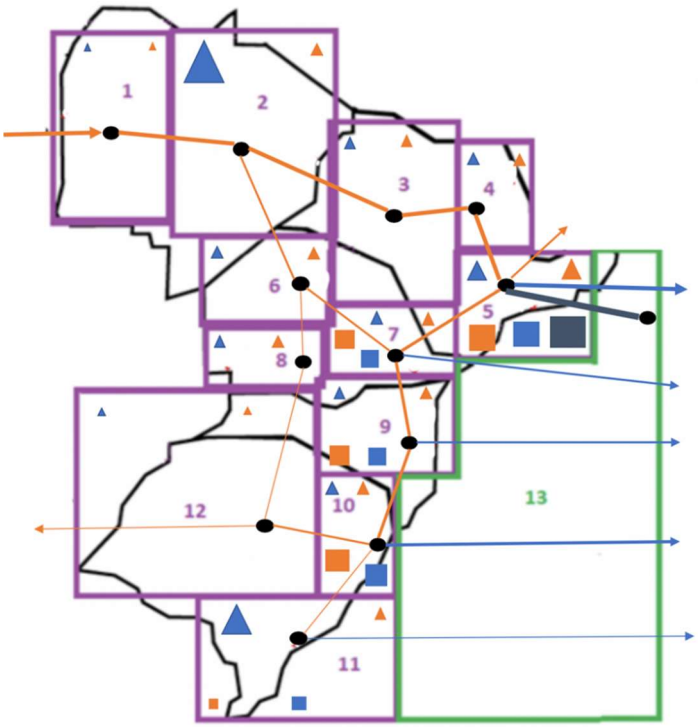

Figure 4 - Final infrastructure and net trade across the planning horizon in the situation that export upper bounds are equal to import upper bounds.

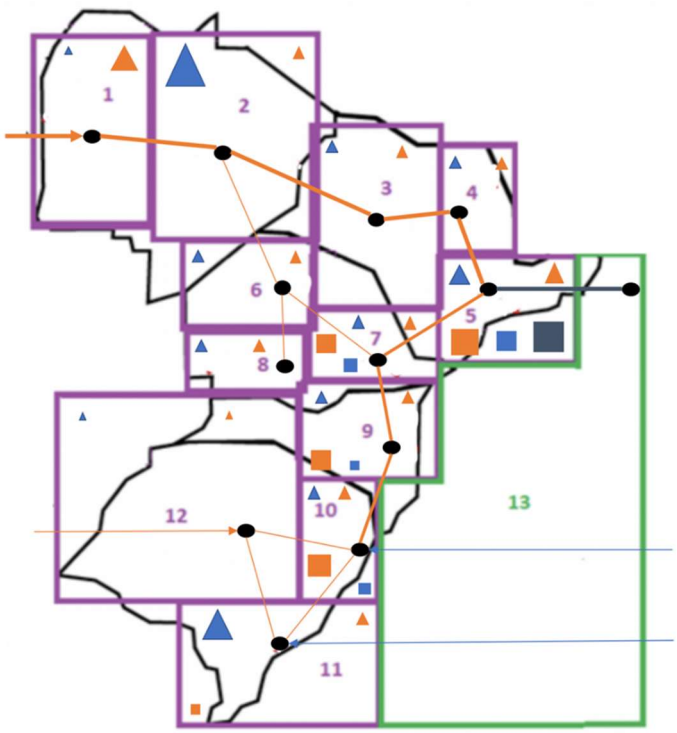

Figure 5 - Final infrastructure and net trade across the planning horizon in the situation that export flowrates are restricted to zero.

5. Conclusion

Ultimately, a mixed-integer linear program was constructed such that it could successfully model construction and investment pathways for the natural gas supply chain. The model was effectively implemented using the CPLEX solver and applied to the specific case study of South Brazil.

This application demonstrated the flexibility of the model with regard to varying input data, such as existing trade agreements and infrastructure.

Additionally, the results from the South Brazil case study highlighted an important trade-off between long-term energy security and short-term revenue from exports. Due to the implementation of a time horizon and no incentive to maintain reserves, the model produces as much as possible in order to maximise export revenue. Extending the time horizon to mitigate against depletion of reserves may not be sufficient to offset this due to the discount of cost by the fixed interest rate incentivising the maximisation of exports in the earlier time periods.

The model does produce logical results in terms of the location of infrastructure. Regasification and liquefaction take place in the same region, reflecting their related usage in the management of trade and storage. The construction of the pipeline network is also designed such that all grid zones are connected to either a source of production or import site. Additionally, Brazil is currently considering construction of a pipeline between what has been denoted as grids 10 and 12, and this is confirmed in the model as a logical endeavour.

However, the model does have significant limitations with regard to input data. The model is highly sensitive to a lot of time-dependent data, such as costs and demand. For example, small changes in global natural gas pricing impact the decision to export or import large volumes of natural gas, having a knock-on effect upon production rates and chosen pipeline routes and capacities. Given such data is difficult to accurately forecast, this underlines the importance of carrying out sensitivity analysis on this input data.

6. Further Work

The general formulation constructed in this report could be expanded upon in several ways. Firstly, multi-objective optimisation could be implemented, with the additional objective functions evaluating greenhouse gas emissions or Life-Cycle Analysis. This would be particularly effective if the model is expanded to include leakages from the supply chain, which are a significant contributor to global green-house gas emissions, and alternatives to natural gas, such as renewable energy sources. An additional objective could incentivise maintaining gas reserves at the end of the time planning horizon to offset the issue of resource depletion making the projected solution unsustainable beyond the planning horizon.

The temporal resolution could be increased to enable the inclusion of seasonal and perhaps daily variations in demand. Greater temporal resolution could also allow for implementation of construction times, as construction times are insignificant in comparison to the length of the current time periods.

This thread could be further developed by not simply inputting demand as a fixed parameter in the model. It may be possible to allow the model to adjust demand depending on prices and supply through a demand function. This would move the model towards real-time

optimisation and would remove the assumption of perfect foresight for demand.

A more comprehensive modelling of the global trade environment could also be beneficial, in particular to respond to the actions of the region of interest. For example, to reflect the consequences of flooding the global market.

7. References

1. American Petroleum Institute (2017) Energy Infrastructure – Natural Gas Supply Chain. [ONLINE] Available at: http://www.energyinfrastructure.org/energy-101/natural-gas-supply-chain. [Accessed 12 December 2018]
2. Almansoori, A. & Shah, N. (2009) Design and operation of a future hydrogen supply chain: Multi-period model. *International Journal of Hydrogen Energy.* 34 (19), 7883-7897.
3. Chávez-Rodríguez, M. F., Dias, L., Simoes, S., Seixas, J., Hawkes, A., Szklo, A. & Lucena, A. F. P. (2017) Modelling the natural gas dynamics in the Southern Cone of Latin America. *Applied Energy.* 201 219-239.
4. Diego C Cafaro & Ignacio E Grossmann. (2014) Strategic planning, design, and development of the shale gas supply chain network. *American Institute of Chemical Engineers. AIChE Journal.* 60 (6), 2122.
5. Ghaithan, A. M., Attia, A. & Duffuaa, S. O. (2017) Multi-objective optimization model for a downstream oil and gas supply chain. *Applied Mathematical Modelling.* 52 689-708.
6. Gonzalo Guillén-Gosálbez, Fernando D Mele & Ignacio E Grossmann. (2010) A bi-criterion optimization approach for the design and planning of hydrogen supply chains for vehicle use. *American Institute of Chemical Engineers. AIChE Journal.* 56 (3), NA.
7. Jalil-Vega, F. & Hawkes, A. D. (2018) Spatially resolved model for studying decarbonisation pathways for heat supply and infrastructure trade-offs. *Applied Energy.* 210 1051-1072.
8. Honoré, A (2016) South American Gas Markets and Role of LNG. *The Oxford Institute for Energy Studies.*
9. Samsatli, S. & Samsatli, N. J. (2018) A multi-objective MILP model for the design and operation of future integrated multi-vector energy networks capturing detailed spatio-temporal dependencies. *Applied Energy.* 220 893-920.
10. Strachan, N., Balta-Ozkan, N., Joffe, D., McGeevor, K. & Hughes, N. (2009) Soft-linking energy systems and GIS models to investigate spatial hydrogen infrastructure development in a low-carbon UK energy system. *International Journal of Hydrogen Energy.* 34 (2), 642-657.
11. Weiland, P. (2010) Biogas production: current state and perspectives. *Applied Microbiology and Biotechnology.* 85 (4), 849-860.
12. Kelly, S and Horn, S (2016). LNG-By-Rail Hits Tracks in Alaska: What are the Risk and Why the Secrecy? [ONLINE] Available at: https://www.desmogblog.com/2016/10/13/lng-rail-alaska-risks-secrecy. [Accessed 12 December 2018]
13. García Kerdan I., Giarola S., Hawkes A. Implications of Future Natural Gas Infrastructure on Bioenergy Production, Land Use Change and Related Emissions: A Brazil Case Study In: *1st Latin American Conference on Sustainable Development of Energy, Water, and Environment Systems,* Rio de Janeiro, Brazil; January 28-31

8. Acknowledgements

We would like to express our gratitude to Dr Ivan Garcia Kerdan and Dr Francisca Jalil Vega for their efforts in supporting our research project.

Development and Investigation of Hydrophobic Silica Nanoparticles

Carlos Sheppard and Leonardo Giustiniani
Department of Chemical Engineering, Imperial College London, U.K.

Abstract The following investigation explores the hydrophobicity of silica nanoparticles through manipulation of the ammonia catalysed hydrolysis of tetraethoxysilane (TEOS) following the Stöber method, and further silanization using trichloro(dodecyl)silane (TC). It was found that reducing the ammonium hydroxide concentration resulted in a decrease in the mean particle diameter, leading to an increase in measured contact angle (CA). Increasing batch volumes resulted in larger mean particle diameters due to greater retained heat and extended handling time, both promoting particle agglomeration. TC reduction had little CA influence compared to reduction amount. Short-term ambient sample decay also had little influence on surface hydrophobicity, while binary films proved ineffective in creating superhydrophobic surface conditions due to extensive stratification.

Keywords: Silica nanoparticles, TEOS, Silanization, Hydrophobic, Contact Angle

Introduction

Silica nanoparticles have a broad range of applications not just limited to physical chemistry. They have found use as fillers in plastics, improving material properties such as tensile strength and as biomedical drug delivery systems (Bitar *et al.*, 2012). The creation of hydrophobic silica nanoparticles has relevance for several industrial applications- especially for creation of maritime paint coatings. The development of a hydrophobic coating has potential to prolong paint lifetime and reduce maintenance costs due to higher intermittent recoating periods. While certain waterproof or corrosion resistant paints exist, the use of hydrophobic silica nanoparticles dispersed within a paint resin is an avenue currently being explored as proprietary technology by Saudi Aramco and serves as the basis of this report (Saudi Aramco Oil Company 2018, Personal Communication, 20 June).

The following investigation was made to explore the different factors influencing particle creation and the resulting impact these factors have on hydrophobic effectiveness. Objectives included characterising the impact different reagent ratios had on particle size synthesis and exploring silanization agent and binary colloidal particle suspension influence on particle hydrophobicity.

Although it was not possible to explore the nanoparticle-resin interactions during the course of this research, several conclusions were drawn regarding preliminary preparation of hydrophobic silica. Notably, into the hydrophobic effectiveness of silanization using TC under different reaction scenarios, the influence of different Stöber process reagent ratios on sample size and the development of binary colloidal suspensions in creating water resistant films.

Background

Multiple studies exist exploring the synthesis of silica nanoparticles for various applications. The primary framework for controlled growth of monodisperse silica was introduced by Kolbe (1956). Stöber *et al.* (1966), then built upon this work through repeating Kolbe's experiment with a systematic investigation into the influencing factors of what is now labelled the Stöber process. Stöber developed a system of chemical reactions for creating particles in the 0.05 to 2 micron size range using an alcoholic solvent, tetra-alkyl silicate as the silica precursor and anhydrous ammonia as a morphological catalyst (Stöber *et al.*, 1966).

More recently, work has been done to investigate semi-batch gas-phase nanoparticle synthesis (Kim and Kim, 2001) and even silanization agent hydrophobicity analysis using contact angle (CA) (Sehlleier *et al.*, 2012). Postulation into the underlying mechanisms behind TEOS hydrolysation and condensation polymerisation has also been considered (Li *et al.*, 2013). It is noted that while vapour phase silica nanoparticle synthesis has merits in glass vessel coating applications, for the context of this research, the greater dispersion potential with a wet state solvent was more conducive for silica powder creation.

Barthlott and Neinhuis (1997) provide an informative background paper into the Lotus-effect; the relationship between surface roughness and cleaning properties desired by the binary colloidal film as an outcome of Saudi Aramco's research. Although Sehlleier *et al.* investigate hydrophobic silanization with CA analysis, the silica particles are orders of magnitude smaller and do not consider binary colloidal suspensions or evaluate the influence of silating agent reduction- this is where our contribution can be found.

Methods

Reagents Used

Table 1: *Reagent sourcing information.*

Chemical	Specifications
Tetraethoxysilane	Sigma Aldrich, 98%
Ethanol, Absolute	VWR chemicals, assay VW 99.97%
Ammonium hydroxide	Sigma Aldrich, 25%
Trichloro(dodecyl) Silane	Sigma Aldrich, >95.0% GC
Dodecane	Sigma Aldrich, >90% GC
Deionised Water	Analytical Lab, Imperial College London

Silica Synthesis Process

Silica nanoparticles were synthesized using the well documented Stöber process then isolated through repeated centrifugation in ethanol. In close but not exact emulation of the Stöber process, the silica precursor, TEOS, $Si(OC_2H_5)_4$, was hydrolyzed in ethanol in the presence of the morphological catalyst, ammonium hydroxide. In the Stöber process hydrolysis and polycondensation of the alkoxides groups and their subsequent condensation leads to crosslinking, resulting in silica nanoparticle creation (Stöber *et al.*, 1966).

For a typical batch, 33mL of TEOS was added to a mixture of 400mL of ethanol absolute and 150mL of ammonium hydroxide solution. This mixture was placed on a stirrer plate and left to react using a magnetic stirrer for 24 hours at room temperature. The silica nanoparticles were collected in disposable centrifuge tubes and then repeatedly centrifuged in absolute ethanol. The concentrated mixture of silica nanoparticles and absolute ethanol was then left to dry under a fume cupboard. This procedure was scaled up by a factor of eight to produce a total batch volume of roughly five liters. The overall chemical reaction is as following:

$$Si(OC_2H_5)_4 + 12\ O_2 \rightarrow SiO_2 + 8\ CO_2 + 10\ H_2O \quad (1)$$

The growth of the silica particles in the Stöber process has been explained by two widely accepted mechanisms: namely, the monomer-addition model and the aggregation-only model (Han *et al.*, 2017). The monomer-addition model is suited for high ammonia concentrations and justifies the formation of silica nuclei through TEOS hydrolysis/condensation and ensuing growth by preferential deposition of silanol monomers (Matsoukas and Gulari, 1989). The aggregation-only model is suited for low ammonia concentrations, and postulates growth stemming from small primary silica particle seeding and following growth by surface attachment of silanol monomers or oligomers (Bogush and Zukoski, 1991, Lee *et al.*, 1997). Both models however, fail to explain how altering the ammonia concentration impacts the size and size distribution of the silica particles.

The fundamental kinetic role of the morphological catalyst is still not fully understood. However, it is known that ammonium hydroxide raises the pH of the solution and increases the rate of the polycondensation reaction (Nudelman *et al.*, 2010). An increase in the basicity of the solution also serves to bring the solution to a pH above the isoelectric point, inducing repulsion between silica particles- a force vital for monodispersity (Green *et al.*, 2003).

Recently, an effort has been made to shed light on the role of ammonia in the kinetic balance and resulting growth of the silica particles. To elucidate the importance of the ammonia, studies have replaced the morphological catalyst for other substances, namely for electrolytes (Nakabayashi *et al.*, 2010), amino acids (Wang *et al.*, 2011) and acids (De, Karmakar and Ganguli, 2000). Despite these efforts, an elementary understanding of how the kinetic relationship between hydrolysis and condensation impacts silica particle size is still not understood. This dictates difficulty in obtaining a high degree of control in silica particle size, size distribution, interior structure and chemical characteristics- especially at smaller particle sizes.

Particle Size Measurement

Particle size measurements were conducted using a Malvern Panalytical Zetasizer µV. The instrument uses dynamic light scattering as a means of measuring particle size. Dilute samples of silica particles in absolute ethanol were sonicated for three minutes to minimize particle agglomeration before particle diameter readings were taken.

Silica Silanization

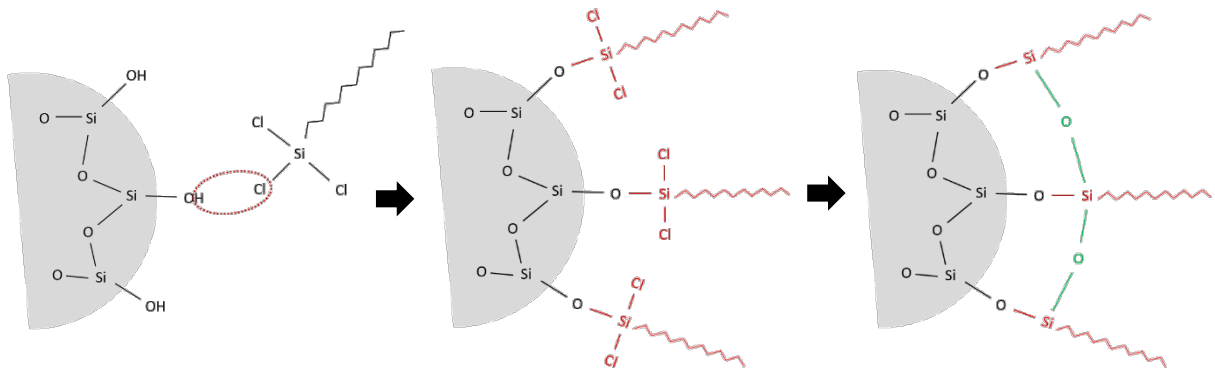

Figure 1: *Schematic of the Silica Silanization process using Trichloro(dodecyl)silane.*

Figure 1 above describes the silica silanization process. In the first picture you can see the silica particle with the hydroxyl surface group. This bond is very polar and covalent with electron density focused on the oxygen atom. The Cl-Si bond is also polar with the electron density residing on the chlorine atom. This gives way to interactions between the surface reactive groups forming the Si-O-Si bonds observable in the middle image. A similar process occurs with hydroxyl groups in solution to form the additional Si-O-Si bonds. Note that it is possible to use a wide range of silanization ligands; trimethoxyoctysilane is an example of the ligand used by Saudi Aramco in their research, however, TC was favoured in our experiment due to the higher reactivity possible with the Si-Cl reactive groups. This can be evidenced as Saudi Aramco's research required use of heating and longer reaction times to facilitate their silanization reaction.

The ligand surface provides hydrophobicity because the long surface chain functional groups of the alkanes lack availability of places for water to interact and form hydrogen bonds. The C-H bond is relatively non-polar thus water minimizes surface energy as attraction between water molecules is stronger than the attraction available between the liquid-solid interface. Surface morphology is also a factor relating to the contact area of the surface which is available- a rougher surface can improve this CA.

Sehlleier *et al.*'s analysis explored silanization agents including alternate functional groups containing C-H, C-F and N-H bonds and the resulting impact this had on hydrophobicity. Their results demonstrated a weak CA with N-H functional groups due to the polar nature of the bond providing favourable interactions with water molecules. The opposite was true for the C-F bonds which displayed strong superhydrophobicity from the lack of hydrogen bonding availability (Sehlleier *et al.*, 2012).

For a typical batch, 5 grams of silica nanoparticles were dispersed in 37.5mL of dodecane and mixed for one hour. The silica particles were then sonicated (Fisher Scientific FB1504B) to minimize particle agglomeration. 11.5mL of TC, the silanization agent, was added to the mixture and mixed overnight at room temperature to allow for complete reaction. The hydrophobic silica particles were isolated using the same centrifugation process as stated above and subsequently left to dry in the fume cupboard.

Contact Angle (CA) Measurement

CA measurements were carried out on circular glass cover slips coated with hydrophobic silica particles. The glass slips were prepared by mixing the dried hydrophobic silica with pure ethanol to create a highly concentrated liquid. This liquid was then poured on the microscope slides and left to dry in a fume cupboard to ensure an even surface was created. CA measurements were carried out using a Krüss Drop Shape Analyzer supplied with their ADVANCE software for interpreting CA. 10 µL distilled water droplets were systematically placed on the silica covered slips, where 20 – 30 images were taken and analysed to produce CA measurements.

Scanning Electron Microscope (SEM)

To inspect the surface of the hydrophobic silica coating, samples were prepared using double sided carbon tape (Electron Microscopy Sciences) and analyzed using a SEM (Leo 1525 Gemini) under a near vacuum (1.5×10^{-5} Torr).

Results

Silica Particle Size

Table 2: *Particle diameter measurements for varying reagent quantities.*

Batch	Particle Diameter (nm)	Ammonia : TEOS (ml:ml)	Ethanol (ml)	Ammonia (ml)	TEOS (ml)
1	751	4.54	400	150	33
2	885	4.54	3200	1200	264
3	49	0.5	500	20	40
4	120	0.8	500	32	40
5	141	0.8	4000	256	320

Decreasing the ammonia to TEOS ratio in the reagent mixture decreased the mean particle diameter. Batches 1, 3 and 4 totalled roughly 570ml upon initial mixing, while batches 2 and 5 were approximately 4.6L. Comparing the smaller volume batches, the ammonia to TEOS ratio was decreased from 4.54 to 0.8 to 0.5. The resulting particle diameter decreases accordingly from 751 to 49nm. A similar trend is observed for batches 2 and 5.

Keeping the reagent ratios constant and increasing the batch size (by a factor of eight) resulted in larger particle sizes. This is evident when comparing batches 1 and 2, where the ammonium hydroxide to TEOS ratios were kept constant at 4.54. The first batch resulted in a particle size of 715nm while the second batch, which was eight times larger in volume, resulted in a particle size of 885nm. This result is repeated when observing batches 4 and 5. Again, with the reagent ratios constant, the smaller batch volume produced silica particles of 120nm in diameter while the larger batch produced silica particles of 141nm.

Contact Angle- Particle Size

Table 3: *Contact angle results of varying particle sizes and for uncoated glass.*

Particle Size (nm)	Average (deg)	St. Dev. (deg)	Sample 1 (deg)	Sample 2 (deg)	Sample 3 (deg)
751	137.3	0.9	136.5	138.6	136.9
885	138.3	2.1	136.1	137.7	141.1
120	141.3	0.4	141.2	141.8	140.9
Plain Glass	14.9	0.4	14.8	15.2	14.7

Table 3 above characterises the resulting CA observed after silica particles of varying size underwent silanization. A sample standard deviation calculation is provided in the supplementary information section. It is visible that all the coated discs exhibited strong hydrophobicity when compared to the plain glass reference measurement. The general degree of precision was also very consistent with only the 885nm sample showing a noticeable standard deviation. An observable general trend appears that smaller particles have a more favourable CA. Particles within a similar size range such as the 751nm and 885nm sample exhibited minute differences in CA and thus it can be said that particle size has some degree of influence on CA within the size range observed, albeit minor.

Contact Angle- Silanization Agent Reduction

An important consideration relating to the development of hydrophobic silica particles was to consider what influence reduction in the silanization agent had on the CA observed. This would provide insight into the effective use of the silanization ligand and quantify any possible production efficiencies achievable. A brief cost analysis of this reduction was conducted and is provided in the supplementary information section. To investigate the reduction, the amount of TC was reduced incrementally from the 100% base case down to 25%.

Table 4: *Contact angle results for varying silanization agent quantities using 120nm particles.*

Amount of TC	Average (deg)	St. Dev. (deg)	Sample 1 (deg)	Sample 2 (deg)	Sample 3 (deg)
100%	141.3	0.4	141.2	141.8	140.9
75%	148.8	0.6	148.8	149.6	148.0
50%	141.9	1.2	143.5	141.5	140.6
25%	138.0	0.8	137.3	137.6	139.2

As visible from Table 4 above, the general trend was a reduction in the associated CA, however, it is important to note that an initial decrease yielded a CA trade-off which was little to none- if not better. Another worthwhile point is that although the CA did decrease, the numerical value of reduction in hydrophobicity was small when compared to the relatively large decrease in silanization agent.

Contact Angle- Sample Decay

Table 5: *Contact angle results of hydrophobic sample decay after ambient exposure for 5 days.*

Sample Size (nm)	Initial Average (deg)	Second Average (deg)	Change (deg)	Percent Change
751	137.3	137.9	+0.6	0.4%
885	138.3	139.5	+1.2	0.9%
120	141.3	142.2	+0.9	0.6%

Investigation into the influence time had on sample hydrophobicity manifested that there was little influence over the short-term. All of the samples observed were within <1% of their original value when remeasured after a 5-day period. The samples were left at ambient conditions to more closely simulate the type of environment expected should implementation occur.

Contact Angle- Binary Colloidal Film

Table 6: *Contact angle results for binary films with varying particle size combinations plus 885nm and 120nm contact angles for reference.*

Size combination	Average (deg)	St. Dev. (deg)	Sample 1 (deg)	Sample 2 (deg)	Sample 3 (deg)
90wt% (885nm) 10wt% (120nm)	125.1	0.4	125.2	125.6	124.5
70wt% (885nm) 30wt% (120nm)	139.7	2.4	142.0	140.8	136.4
50wt% (885nm) 50wt% (120nm)	127.5	3.2	128.1	123.2	131.1
885nm	138.3	2.1	136.1	137.7	141.1
120nm	141.3	0.4	141.2	141.8	140.9

The experiments presented in Table 6 above were conducted in an attempt to further increase the CA. Binary mixtures of small (120nm) and large (885nm) silica particles were silanized together with the intention of creating an interspersed binary film. Small particle weight fractions of 0.1, 0.3 and 0.5 were analysed using SEM. Table 6 describes the outcome was in stark contrast with what was desired as the CA for small particle weight fractions of 0.1 and 0.9 were actually well below the uniformly sized cases (125.1° and 127.5°, respectively, compared to 138.3° for pure 885nm particles and 141.3° for pure 120nm particles). The small particle weight fraction of 0.3 did yield above average results however.

Scanning Electron Microscope Imaging

Investigation into the surface structure of the binary colloidal films was critical toward understanding the particle interactions present and CA results achieved. The two images in Figure 2 below are both taken from the same 50/50wt% sample used in CA calculations. The images clearly display the strong agglomeration of the small 120nm particles together, forming large ridge-like structures while the larger 885nm particles are dispersed on the surface. These images give insight into the lack of interparticle dispersion desired as an outcome of these experiments.

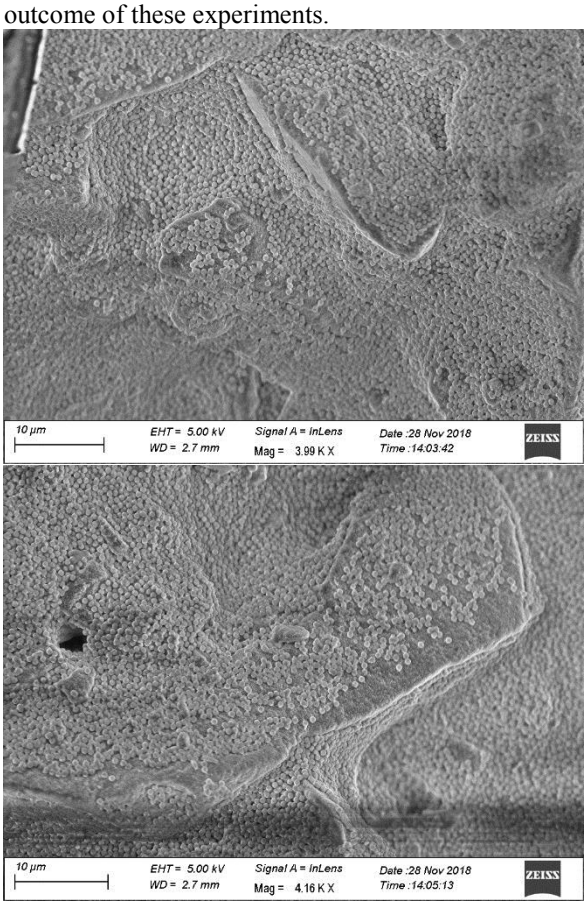

Figure 2: *SEM imaging results for the 50/50wt% binary film sample. Both images are of the same sample and illustrate the agglomeration of the smaller 120nm particles into mounds.*

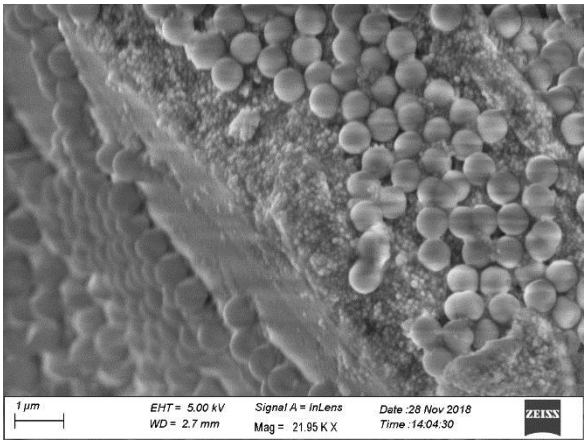

Figure 3: *An SEM imaging magnification of one of the ridges observed in Figure 2. Displays the strong agglomeration of the smaller 120nm particles with larger 885nm particles on surface.*

Figure 3 is taken from the same sample observed in Figure 2 but under a higher magnification. This image provides greater observation of the agglomeration present within the binary mixture. It can be seen that the small particles are very accumulated with an external layer of larger 885nm particles existing superficially. Similar phenomenon was observed for both the 70/30wt% and 90/10wt% samples however the presence of fewer smaller particles resulted in less pronounced groupings. Example images of those samples are provided in the supplementary information section.

Discussion

Silica Particle Size

Reducing the amount of ammonium hydroxide decreased the mean particle diameter. This is in alignment with the literature and occurs in part because ammonia acts as a morphological catalyst (Greasley, 2016). Greasley showed that in the range of 1 – 1000 nm, the increase in particle size due to increased ammonium hydroxide concentration is almost linear, with a doubling (0.5 to 1.0M) of the ammonium hydroxide concentration resulting in a 375nm of particle size increase.

From Table 2, batches 3 and 4 keep all conditions constant except for the amount of ammonium hydroxide solution. An increase of 62.5% (from 20ml to 32ml) resulted in an increase of mean particle diameter of 71nm. When this result was extrapolated for a doubling in ammonium hydroxide concentration, the mean particle diameter increase was calculated at 114nm. Given the crude nature of the calculation and the subtle condition changes of the Greasley report, a similar magnitude change is in alignment.

The increase in silica nanoparticle size due to larger batch volumes could be due to larger vessels having a lower surface area to volume ratio. This would result

in lower heat loss and increased temperature, elevating the reaction rate. The increase in particle size could also be due to a larger batch size inherently taking more time to handle (longer to centrifuge and dry) allowing particles more time to agglomerate. These two potential explanations were explored by analysing the enthalpy of reaction, specific heats of the reagents, and agglomeration over time.

The thermodynamics of the formation of silica nanoparticles was studied in great detail to obtain the enthalpy of the TEOS polycondensation reaction (Rimer *et al.*, 2008). In the Rimer study, the silica nanoparticles were synthesis by adding TEOS to an alkali-metal hydroxide solution in deionized water. A dependency of the enthalpy of reaction on the TEOS to alkali metal ratio was found, varying from -70 to -50kJ/mol of SiO_2 as the TEOS to alkali-metal ratio was increased. It is noted that in the study mentioned, ammonium hydroxide was replaced by an alkali-metal hydroxide solution, however, enthalpy values were taken to represent the ammonium hydroxide catalysed reaction for future calculations.

Assuming an upper limit for the exothermic enthalpy of reaction of -70kJ/mol for SiO_2, complete reaction, constant specific heat values over the temperature range for ethanol and water, using assay values from Table 1, and under idealised adiabatic conditions, the temperature change of the system is roughly 7 °C. Rahman *et al.* (2007) found that particle size generally decreases with an increase in reaction temperature (increasing the temperature from 45 to 55°C, decreased particle size from 92.3 to 35.2nm). It was postulated that the particle size reduction is due to a higher nucleation rate at elevated temperatures.

This goes against the proposal that elevated temperatures lead to increased reaction rate and therefore larger silica nanoparticles. The 7 °C increase is a maximum value and doesn't take into account heat loss to the environment. Even if scale up reduces heat loss, the overall temperature increase is relatively small, implying no significant temperature difference.

The much larger contribution to increasing particle size is most likely due to post reaction agglomeration. Rahman *et al.* found that silica nanoparticles that formed at higher temperatures tended to aggregate more than at lower temperatures. It was postulated that higher levels of aggregation at higher temperatures was due to increased solubility and a larger frequency of collisions between particles. The larger batches would have retained heat for longer, allowing more time for agglomeration. This, in combination with an inherently longer handling time, allowing for even further agglomeration, explaining the larger particle size in the bigger batches.

Contact Angle Discussion- Particle Size

The observation that smaller particle sizes correspond with an improved CA is a conclusion which corresponds with research found in the literature (Vafaei *et al*., 2006, Saulick, Lourenço and Baudet, 2016). Although the quoted papers utilise different nanoparticles in their experiments, the prevailing rationale behind the observed trend is still applicable. The presence of smaller nanoparticles supports a larger surface to volume area for the hydrophobic surface. This provides a greater liquid-solid interface with the water droplet wherein the water molecules find the cohesive attraction greater than the attraction between the solid and liquid. This results in a higher CA as the water molecules try to minimize surface energy. From a surface morphology perspective, smaller particles also provide possible higher degrees of surface roughness, also an influencing factor for surface wettability.

Contact Angle Discussion- TC Reduction

The results of the reduction in silanization agent yield some interesting conclusions towards the extent of TC required to provide effective hydrophobicity. While there was an extent of CA reduction, the amount was small in contrast to the large reduction in silanization agent; a 75% reduction only resulted in a 3-degree change. It can be logically deduced that the initial amount used in the 100% case of 6.91mL per 4 grams of SiO_2 is far greater than required. Saudi Aramco correspondence described reaction of 20 grams of 500nm SiO_2 with 40mL of trimethoxy(octyl)silane (Saudi Aramco Oil Company 2018, Personal Communication, 20 June). While a similar silica mass to silanization agent ratio was used, the experimental results suggest the amount used by Saudi Aramco is more than required; even when taking into consideration the resulting surface area to volume ratio increase through use of 120nm spherical particles. This revelation has big implications on the actual amount of silanization agent reacted and is very probable evidence towards over addition. Further research into greater TC reduction is highly recommended as a point of interest moving forward in light of these considerations.

Contact Angle Analysis- Sample Decay

While it was observed that there was little decay in sample hydrophobicity over the span of 5 days this does not necessarily correlate to longer term retention. The laboratory environment is also very inert and pollutant free and would not create much opportunity for sample decay. There is little literature information regarding long term exposure degradation of samples specific to our experiment, however, a peripheral experiment examined coating CA decay of

Si-based potassium methyl siliconate resins (Cappelletti *et al*., 2015). The paper found that after exposure to ambient conditions for 110 days the coating did display a degree of hydrophobic decay, although no particle size information was given (Cappelletti *et al*., 2015). The coating was also applied to a brick mortar material which would impact results. Additional accelerated UV exposure testing for 40 hours also yielded detrimental results. As such, additional investigation into longer term deterioration effects should warrant investigation- especially with exposure to additional environmental pollutants a prospective coating could be subject to.

Binary Film Colloidal Film and Scanning Electron Microscope Imaging

In the past years, studies have analysed the stratification in binary colloid films (Makepeace *et al.*, 2017). Makepeace *et al.* found that for a particle size ratio of 7, stratification occurred when initial small particle volume fractions where larger than 0.12. In our study, the silica nanoparticle sizes used were 885 and 120nm, resulting in a particle size ratio of 7.38. If constant density of small and large silica particles is assumed, volume fractions of 0.1, 0.3 and 0.5 were calculated. Most (0.1 falls just short) of these binary mixtures fall under the stratification zone outlined by Makepeace *et al.* This is confirmed by the SEM results. In Figures 1 and 2, compact clustering of the small molecules can be observed, while the large particles are dispersed on top in a distinct layer. Dispersed larger particles on the surface are elevated, creating ridges for water to seep into the silica hydrophobic layer. This seepage reduces the hydrophobicity of the surface, lowering the CA. The small particle volume fraction should be lowered well below 0.1 to achieve a more homogenous and potentially more hydrophobic layer.

Conclusions

The hydrophobicity and resilience of silica nanoparticles was investigated by altering factors in both the particle fabrication and salinization processes. It was found that a reduction in ammonium hydroxide concentration resulted in a decrease in the mean particle diameter. Increasing batch volumes resulted in larger mean particle diameters due to a combination of retained heat and extended handling time promoting particle agglomeration.

Upon CA analysis it was found that smaller particle sizes gave rise to better hydrophobic features. This was due to the higher surface area to volume ratio present providing greater impetus for water particles to minimize surface energy at the solid-liquid interface. Additional surface morphology advantages could also be attributed. A large reduction in amount of silanization agent also provided helpful insight into operational efficiencies achievable through silanization optimization. It was found that even with large reductions of TC, the CA reduction was minimal. This was likely due to the initial quantities presented being in excess of what was required. It was also found that ambient sample decay in the short-term had little influence on surface hydrophobicity, although literature findings constitute additional investigation into further exposure analysis, especially in more harmful conditions.

Binary films proved unsuccessful in creating superhydrophobic surface conditions due to extensive stratification. To reduce stratification and increase binary mixing the small particle volume fraction should be reduced below 0.1. Makepeace *et al*. found that for a low small particle volume fraction (0.08 and lower) the surface is nearly fully covered with small particles, indicating better particle mixing. In fact, further research is needed in the hydrophobic surface creation stage, for binary and single size cases alike.

The procedure in creating the hydrophobic silica nanoparticle covered glass slips proved just as pivotal as the silanization process itself. Indeed, ensuring proper surface creation greatly affected CA measurements, potentially more than how successful the silanization process itself was. Multiple methods were trialled with the most successful involving creating a highly concentrated and viscous liquid of the superhydrophobic silica particles in absolute ethanol. This solution was then poured on the glass slips and left to evaporate, creating a relatively smooth and homogenous surface. Liquid viscosity and pouring were hard to control resulting in some inconsistency in layering. Potential improvements could involve gas phase coating (Sehlleier *et al.*, 2012) or atomization in direct spraying.

During CA analysis it was observed that the measurements were transient. When left for an extended period of time the water droplet would slowly seep through microfractures in the superhydrophobic silica layer and attract to the hydrophilic glass cover slips, reducing the CA reading. This could be avoided by using a hydrophobic base layer, increasing the hydrophobic time resilience of the combined layers.

The next stage in commercialization of the superhydrophobic silica particles in the paint creation process. This would involve incorporating the hydrophobic silica nanoparticles into a paint resin. This must be done in such a way to attain hydrophobic resilience over time, structural integrity and compatibility with the paint application process.

If the silica particles could somehow be fluidized while ensuring minimal particle agglomeration, the silanization agent could be pumped in allowing the silanization reaction to take place in a continuous process. This would be difficult to achieve for numerous reasons, namely, avoiding blowout of the nanoparticles and creating a suitable reaction environment in the gas phase.

References

Barthlott, W. and Neinhuis, C. (1997). Purity of the sacred lotus, or escape from contamination in biological surfaces. *Planta*, 202(1), pp.1-8.

Bitar, A., Ahmad, N., Fessi, H. and Elaissari, A. (2012). Silica-based nanoparticles for biomedical applications. *Drug Discovery Today*, 17(19-20), pp.1147-1154.

Bogush, G. and Zukoski, C. (1991). Studies of the kinetics of the precipitation of uniform silica particles through the hydrolysis and condensation of silicon alkoxides. *Journal of Colloid and Interface Science*, 142(1), pp.1-18.

Cappelletti, G., Fermo, P., Pino, F., Pargoletti, E., Pecchioni, E., Fratini, F., Ruffolo, S. and La Russa, M. (2015). On the role of hydrophobic Si-based protective coatings in limiting mortar deterioration. *Environmental Science and Pollution Research*, 22(22), pp.17733-17743.

De, G., Karmakar, B. and Ganguli, D. (2000). Hydrolysis–condensation reactions of TEOS in the presence of acetic acid leading to the generation of glass-like silica microspheres in solution at room temperature. *Journal of Materials Chemistry*, 10(10), pp.2289-2293.

Green, D., Lin, J., Lam, Y., Hu, M., Schaefer, D. and Harris, M. (2003). Size, volume fraction, and nucleation of Stober silica nanoparticles. *Journal of Colloid and Interface Science*, 266(2), pp.346-358.

D., Han, M. and Yang, W. (2017). Unraveling the Growth Mechanism of Silica Particles in the Stöber Method: In Situ Seeded Growth Model. *Langmuir*, 33(23), pp.5879-5890.

J., Bakar, M., Adnan, R. and Chee, C. (2007). An optimized sol–gel synthesis of stable primary equivalent silica particles. *Colloids and Surfaces A: Physicochemical and Engineering Aspects*, 294(1-3), pp.102-110.

Kim, K. and Kim, H. (2002). Formation of Silica Nanoparticles by Hydrolysis of TEOS Using a Mixed Semi-Batch/Batch Method. *Journal of Sol-Gel Science and Technology*, 25(3), pp.183-189.

Kolbe, G. (1956). *Das komplexchemische Verhalten der Kieselsäure*. Jena, Math.- naturwiss. F., Diss. v. 5. Mai 1956 (Nicht f. d.Aust.).

Lee, K., Look, J., Harris, M. and McCormick, A. (1997). Assessing Extreme Models of the Stöber Synthesis Using Transients under a Range of Initial Composition. *Journal of Colloid and Interface Science*, 194(1), pp.78-88.

Li, J., Zhang, H. and Xue, W. (2013). Synthesis of TEOS-Based Silica Spherical Particles by Sol-Gel Process. *Advanced Materials Research*, 773, pp.606-610.

Makepeace, D., Fortini, A., Markov, A., Locatelli, P., Lindsay, C., Moorhouse, S., Lind, R., Sear, R. and Keddie, J. (2017). Stratification in binary colloidal polymer films: experiment and simulations. *Soft Matter*, 13(39), pp.6969-6980.

Matsoukas, T. and Gulari, E. (1989). Monomer-addition growth with a slow initiation step: A growth model for silica particles from alkoxides. *Journal of Colloid and Interface Science*, 132(1), pp.13-21.

Nakabayashi, H., Yamada, A., Noba, M., Kobayashi, Y., Konno, M. and Nagao, D. (2010). Electrolyte-Added One-Pot Synthesis for Producing Monodisperse, Micrometer-Sized Silica Particles up to 7 µm. *Langmuir*, 26(10), pp.7512-7515.

Nudelman, F., Sonmezler, E., Bomans, P., de With, G. and Sommerdijk, N. (2010). Stabilization of amorphous calcium carbonate by controlling its particle size. *Nanoscale*, 2(11), p.24-36.

Rahman, I., Vejayakumaran, P., Sipaut, C., Ismail, J., Bakar, M., Adnan, R. and Chee, C. (2007). An optimized sol–gel synthesis of stable primary equivalent silica particles. *Colloids and Surfaces A: Physicochemical and Engineering Aspects*, 294(1-3), pp.102-110.

Rimer, J., Trofymluk, O., Lobo, R., Navrotsky, A. and Vlachos, D. (2008). Thermodynamics of Silica Nanoparticle Self-Assembly in Basic Solutions of Monovalent Cations. *The Journal of Physical Chemistry C*, 112(38), pp.14754-14761.

Sarah L. Greasley, Samuel J. Page, Slobodan Sirovica (2016). Controlling particle size in the Stöber process and incorporation of calcium. *Journal of Colloid and Interface Science,* 469, pp.213-223.

Saulick, Y., Lourenço, S. and Baudet, B. (2016). Effect of particle size on the measurement of the apparent contact angle in sand of varying wettability under air-dried conditions. *E3S Web of Conferences*, 9, p.09003.

Sehlleier, Y., Abdali, A., Schnurre, S., Wiggers, H. and Schulz, C. (2012). Functionalization of SiO2 nanoparticles and their superhydrophobic surface coating. *NanoFormulation*, 1(1), pp.113-120.

Stöber, W., Fink, A. and Bohn, E. (1968). Controlled growth of monodisperse silica spheres in the micron size range. *Journal of Colloid and Interface Science*, 26(1), pp.62-69.

Vafaei, S., Borca-Tasciuc, T., Podowski, M., Purkayastha, A., Ramanath, G. and Ajayan, P. (2006). Effect of nanoparticles on sessile droplet

contact angle. *Nanotechnology*, 17(10), pp.2523-2527.

Wang, J., Sugawara-Narutaki, A., Fukao, M., Yokoi, T., Shimojima, A. and Okubo, T. (2011). Two-Phase Synthesis of Monodisperse Silica Nanospheres with Amines or Ammonia Catalyst and Their Controlled Self-Assembly. *ACS Applied Materials & Interfaces*, 3(5), pp.1538-1544.

Viability of Hybrid Solar PV-thermal Systems for Residential Applications in Europe: Techno-Economic Considerations

Ashtak M. Maharaj, Jake L. Goodway
Department of Chemical Engineering, Imperial College London, South Kensington Campus, London, SW7 2AZ, United Kingdom.

ABSTRACT

A viability study for the implementation of a 105m^2 solar hybrid photovoltaic-thermal (PVT) collector array, combined with an Organic Rankine cycle (ORC) engine was performed for a residential application in different cities across mainland Europe. Emphasis was placed on satisfying the electricity, direct heating water and space heating demands. A human centred approach to determining viability was also considered and the results were compared to that of a PVT-only system subject to the same conditions. The primary reason for the ORC engine coupling was to generate supplementary electricity from excess thermal energy stored in a thermal storage tank. Secondarily, the ORC inclusion served as a means of relieving the PVT collectors of constant high temperatures, thereby preventing overheating and damage. The findings of this research suggest that the ORC does not in fact, provide a large enough electricity demand coverage to be considered viable. An average electrical demand coverage of 34% was found for the PVT-ORC system; whilst the PVT-only model covered an average of 31% of electrical demand. An average additional 8.5% of electricity is generated by the ORC engine. The electrical and thermal demand coverage, scales as expected during the summer months. Consequently, the cities with the most solar radiation performed the best. The economic and human centred design analysis performed insinuates that the addition of the ORC is infeasible as a payback time range of 14.6yrs – 32.3yrs was found for the PVT-only model whereas the PVT-ORC model had significantly higher payback times ranging from 30.7yrs - 78yrs. These considerably and consistently higher payback times associated with the PVT-ORC S-CHP system relative to the PVT-only system indicate that the addition of an ORC to a PVT system is not a viable means with which to provide household residential combined heating and power (CHP).

Keywords: PV-thermal (PVT), Organic Rankine Cycle (ORC), solar energy, residential application, Europe, electrical demand, direct heating water, space heating, payback time (PBT), solar-Combined Heating and Power (s-CHP).

1. Introduction

The global growth of energy demand[1] coupled with the phenomenon of global warming has led both developed and developing countries to begin considering renewables in order to reform their energy infrastructure.

According to the IEA's World Energy Outlook Report 2017[1], the global average net capacity of Solar PV technologies is projected to double by 2040.

In the EU, where this present research is based, the strategy of energy diversification to achieve a target reduction in greenhouse gas emissions by 20% [2] is prominent. This is to be achieved through increasing the final energy consumption of the EU to 27% renewables-based by 2030. These goals are in alignment with the global push to move away from the reliance on the diminishing supply of fossil fuels and towards a cleaner and more sustainable energy portfolio.

This project is aimed at evaluating the viability of implementing a hybrid solar PVT-ORC s-CHP system into residential apartment buildings in nine (9) representative settlements (London, Vienna, Magdeburg, Bucharest, Chambery,

Cyprus, Athens, Madrid and Bari) across mainland Europe.

Additionally, a comparison between a PVT-ORC system and a PVT-only system was carried out in order to provide a bench mark for the results obtained, as well as to continue to build upon the current research regarding the ORC addition to the system[3-6].

The addition of an ORC engine not only increases the total electrical output of the system, but also assists in maintaining the integrity of the solar PV cells (through cooling), which are prone to damage from the high temperatures during the summer season.

It should be noted that research was limited to a ten (10) week time scale and consequently, the results and conclusions considered, reflect intrinsically.

2. Background

Hybrid PV-thermal (PVT) systems have been highly researched and consequently commercialized in recent times, due to their ability to provide both electrical and thermal energy outputs therefore meeting electricity, hot water and space-heating demands.

Work has been done to build on the flexible design of the PVT systems. Attractive integration of thermal storage and suitable thermodynamic (heat) engines have sparked great academic interest in hybrid solar technologies.

The recently proposed addition of an ORC system, due to its low-grade heat conversion to useful power, to a PVT array, has been extensively tested and optimised[3,6].

As noted by Freeman, et al[3], the practicality of these hybrid solar-CHP (Combined Heating and Power) technology, is however limited by economic and spatial feasibility.

Previous studies on combined heating and power systems have focused on specific applications, optimisation and evaluation of the integrated technologies. The work done by Herrando and Markides[4] provides an in-depth techno-economic analysis into a similar model without the ORC addition; however, within a target population. Perhaps the most relevant previous research undertaken in relation to this study is the work done by Gurracino, et al[5] in which the performance and economics involved with a PVT-ORC system were evaluated and compared to a PVT-only system for a single residence in both the UK and Cyprus.

This study intends to build-up upon the previous research in the field of renewables, solar power and specifically the newly introduced solar ORC, by scaling the application of the solar PVT-ORC system across mainland Europe, thus giving perhaps the most comprehensive test of the technology yet.

3. Methodology

Modelling

The proposed model (shown in the schematic below, **Figure 1**), is comprised of PV-thermal collectors, a hot water storage tank and an ORC thermodynamic (heat) system designed to meet thermal (space-heating and direct heating water) and electrical demands of residents within a three-storey apartment building. 75% of the building's rooftop space (105m^2) was used as an appropriate approximation for the solar PVT collector's area.

The hourly weather and demand data over one year for each city used for these simulations, were obtained from Meteonorm weather database and EnergyPlus energy simulations, respectively and were based on average energy usage of six 70m^2 flats within the three-storey building (i.e. two flats per floor).

Although considering a more horizontal orientation of the six flats (i.e. one or two storeys rather than three) may have yielded better results due to a larger collector area, the increasing number of high-rise residential buildings in Europe must be considered when

analysing solar technology potential. The model specification chosen therefore represented a typical type of multi-family building within Europe[18].

The ORC engine was designed using MatLab and integrated with the PVT collectors, heat exchangers, thermal storage tank and other ancillary components into the TRNSYS simulation software (see **Figure 2**).

The specifications for the ORC sizing as well as the most appropriate working fluid (0.3R245fa/0.7R227ea) were taken from the work done by Wang, et al[6] for a swimming pool application in Bari, Italy.

Commercial flat-plate PVT collectors[7] with a nominal power of 240W and PV module efficiency of 14.1% were selected for the system design.

Following the optimisation of thermal storage tanks performed by Wang, et al[6], a ratio of 50litres/m^3 of collector area was used to determine a suitable tank volume of 5000 litres.

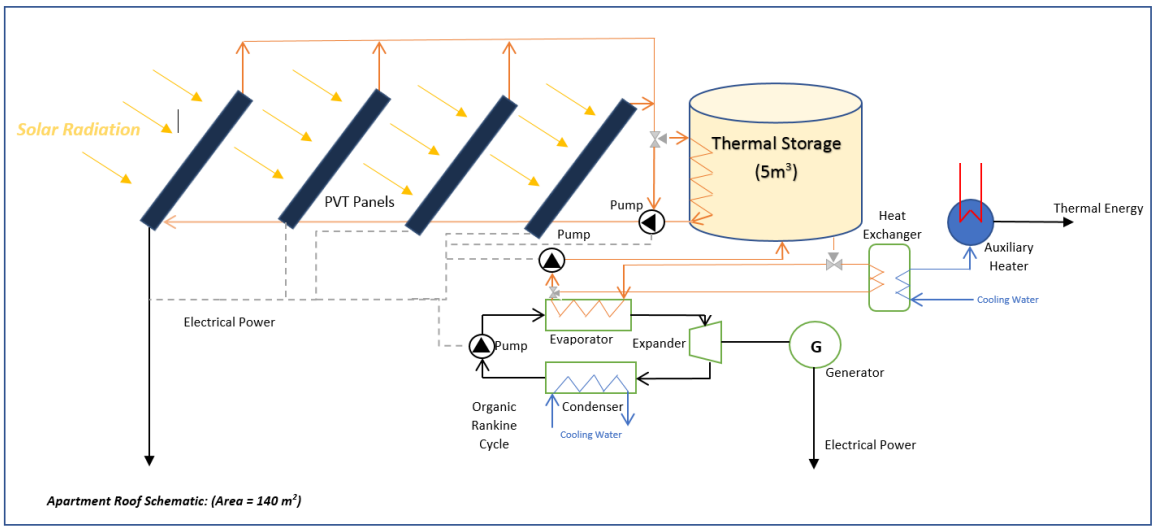

Figure 1: *Simplified schematic of PVT-ORC system on the apartment building roof.*

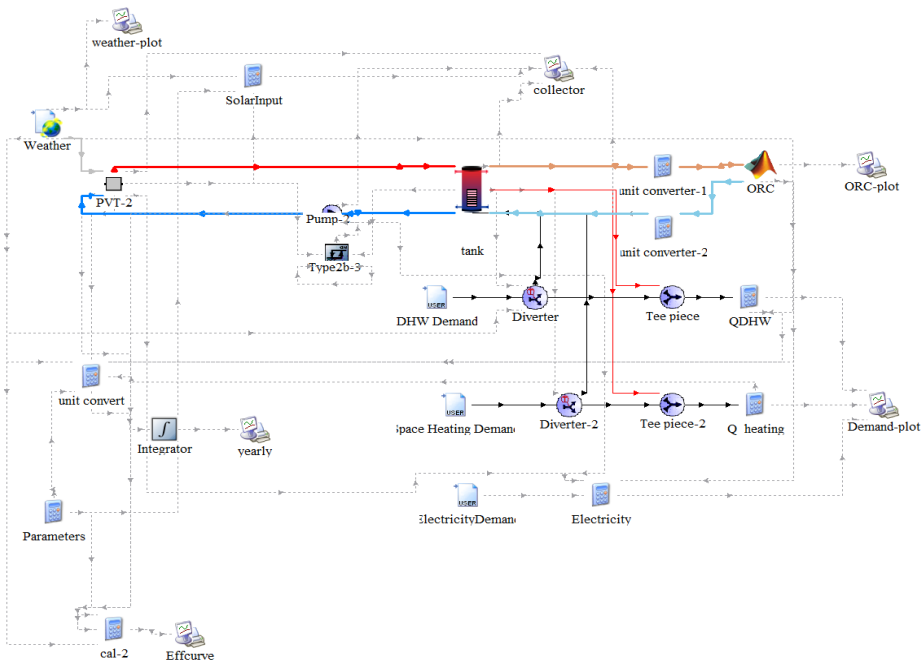

Figure 2: *TRNSYS model schematic for residential application.*

The full-bodied design of this system was analysed in this research; therefore, a PVT-only control, subject to the same parameters and simulations as the aforementioned PVT-ORC model, was studied and used as a benchmark for results comparison.

Transient hourly simulations over a period of one year were conducted and the relevant demand coverages and efficiencies analysed for both the PVT-only and PVT-ORC systems.

Economic Analysis

The components of the PVT-ORC systems, such as the PVT collector, thermal storage tank, condenser, evaporator, and other auxiliary facilities were costed separately[6] and summed in order to find the investment costs associated with the technologies. The total upfront cost (C_0) of the PVT-ORC S-CHP system was calculated through the sum of the upfront/investment costs for each of the PVT and ORC contributions. The ORC was costed according to the method laid out by Ramos et al[9] and the contribution to cost from the PVT collector array, was costed in line with the method employed by Wang et al.

A techno-economic analysis was undertaken through the utilisation of two key metrics regarding the economic performance of the PVT-ORC system. The first of which is the annual fuel savings which gives the electricity and natural gas cost not incurred as a result of the electricity and thermal demands covered by the PVT-ORC s-CHP system. Fuel savings were calculated for the PVT-ORC system configuration and for a PVT-only control, for each of the European residential areas.

The annual fuel savings were calculated using the subsequent formula:

$$FS = E_{cov} * c_e + \frac{Q_{cov}}{\eta_b} c_{ng} - C_{O\&M} \quad (1)$$

Where E_{cov} and Q_{cov} represent the amount of energy supplied by the system from electricity and heat.

The thermal coverage (Q_{cov}) is calculated as the sum of the direct heating water coverage and the space heating coverage. The electricity and natural gas prices are represented within the formula as c_e[10] and c_{ng}[11] respectively, η_b is the boiler efficiency and $C_{O\&M}$ is the operating and maintenance cost of the system.

Payback time was then calculated for each of the residential areas for both the PVT-ORC and PVT-only systems. The payback time represents the time in years it would take to recover the monetary investment associated with the relevant s-CHP systems.

The payback time was calculated according to the following formula:

$$PBT = \frac{\ln(\frac{C_0(i_F - d)}{FS} + 1)}{\ln(\frac{1+i_F}{1+d})} \quad (2)$$

Here C_0 represents the total upfront cost associated with the s-CHP systems and FS is the annual fuel savings. i_F is the inflation rate[12,13] and d is the discount rate[14], both of which are specific to each residential geographical location. In order to account for the volatile nature of inflation rates over time, a representative 10-year averaged inflation rate was used for each residential area.

European Weighted Averages

Population data[15-17] from each country considered in this research was used to calculate a European weighted average for payback time, fuel savings and CO_2 emission reduction.

Bari, Chambery and Magdeburg were deemed as inappropriate representations of their respective countries, due to their relative size to the capital city. This led to the decision to base the average on the country's total population rather than that of the respective individual residential area.

These values were used to quantify the impact of implementing s-CHP systems within Europe.

Human Centred Approach

To provide a holistic approach to the viability of the model used, considerations of a human

perspective[8] of the s-CHP systems was explored.

An economic consumer viability index was developed based on the highest and lowest values of payback time obtained from the PVT-only economic analysis. These values were used along with an average thermal coverage per hour to establish the financial and practical feasibility of using these s-CHP systems for residential applications based on the relevant E_{cov}/E_{demand} ratio.

4. Results and Discussion

The spread of yearly temperatures across the chosen cities, as seen in **Figure 3** below, allowed for a broad analysis of the proposed model.

Even though solar technology by intuition, is more feasible in tropical climates due to sunlight intensity, the results from this study can be considered representative of countries with seasonal climates.

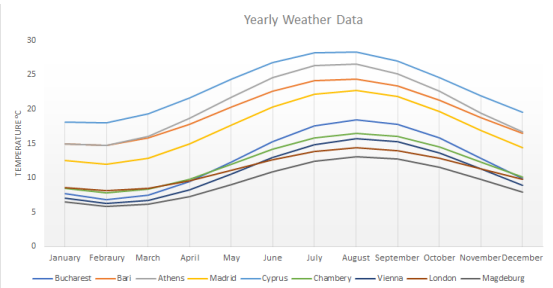

Figure 3: *Yearly average temperatures for each city.*

Demand Coverage (PVT vs PVT-ORC)

An average of 14.35 MWh was generated from the PVT collectors which operated at an efficiency of 14.1%

The total electricity demand coverage results obtained were in line with those reported by Wang, et al.[6] Average electricity coverage of 31% for the PVT-only model and 34% for the PVT-ORC model was found (see **Figure 4**). The two notable increases in demand coverage were that of Cyprus and Madrid. This was in accordance with the weather conditions in both countries as noted in **Figure 3**. Both areas have relatively high levels of solar radiation during the summer season which correlates to a decreased thermal demand thereby allowing for increase in electrical energy output.

The average ORC contribution to electricity generated by the system was found to be approximately 8.5%. Once more, the cities with higher yearly temperatures yielded above average ORC contributions, with the highest coming from Cyprus (12.2%).

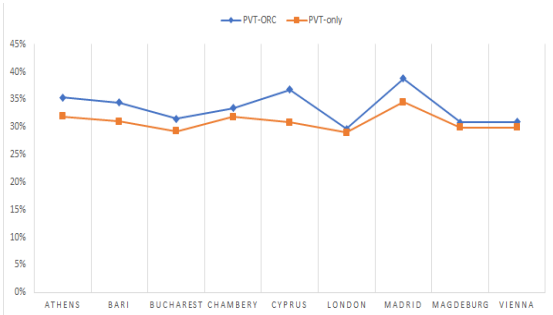

Figure 4: *Showing total Electricity coverage.*

The thermal demand coverage by the PVT-only system was on average 95% for direct heating water and 58% for space heating, whilst the thermal demand coverage for the PVT-ORC system was on average 94% for direct heating water and 55% for space heating.

As is also evident from **Figure 5** and **Figure 6**, the integration of an ORC engine to provide extra electricity, did little to the direct heating water and space heating coverages throughout the year. This result is in line with the 4% efficiency[6] of the ORC system used.

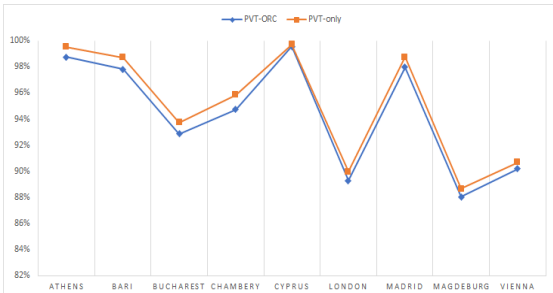

Figure 5: *Showing total Direct Heating Water coverage.*

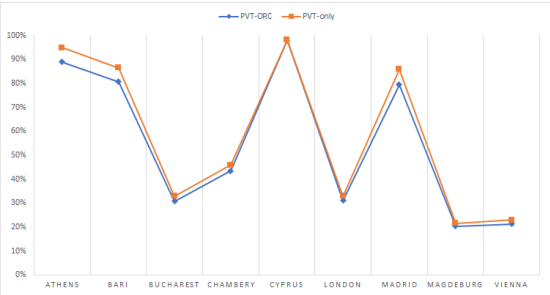

Figure 6: *Showing total Space Heating coverage.*

Economic Analysis

Figure 7: *PVT-ORC and PVT Fuel Savings for European residential areas.*

As can be seen from **Figure 7**, the residential areas which experienced the largest fuel savings was Madrid and Bari. This can be explained by their relatively hot and sunny climate allowing for comparatively good coverages and their relatively high utility prices (electricity and natural gas). Bucharest and London showed the lowest fuel savings. This can be attributed to a combination of their cool and relatively less sunny climates and their low utility prices compared to the other residential areas. **Figure 7** also illustrates the difference in fuel savings for each residential area between the PVT-ORC and PVT-only systems. Generally, the fuel savings from the two systems are very similar in value. There is minimal difference between the calculated European weighted average for the systems. The weighted-averaged fuel savings were found to be €2,640 for the PVT-ORC system and €2,550 for the PVT-only system.

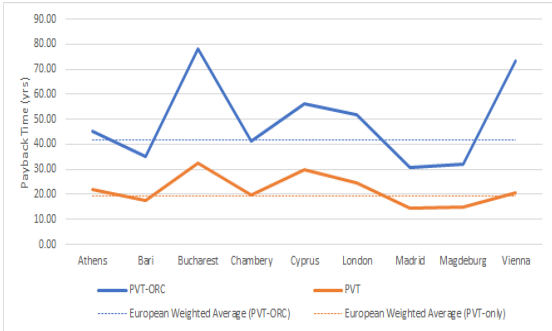

Figure 8: *PVT-ORC and PVT Payback Time for European residential areas.*

From **Figure 8**, it is clear that the payback time for the PVT-ORC system is consistently higher than that for the PVT-only system. The European population-based weighted average for the PVT-ORC system and the PVT system was found to be 41.6 years and 19.4 years respectively. This is because the electrical and thermal coverage achieved by both systems is very similar, however the total upfront cost associated with the PVT-ORC system is considerably larger due to the extra costs incurred due to the investment required for the ORC system.

The difference in payback time between the systems is particularly evident in this study because of the relatively small area of the PVT collector array in comparison to the size of the ORC. For this six-apartment residential application, the ORC makes up approximately 42% of the total upfront cost. As a result, for this specific application, the total upfront cost increases by approximately 73% when moving from a PVT-only system to a PVT-ORC system. This large increase in upfront cost dominates the increases in electricity coverage and any potential increases in fuel savings from the addition of the ORC engine, and thus increases payback time significantly.

The significantly and consistently higher payback times for the PVT-ORC system compared to the PVT-only system means that at present the implementation of PVT-ORC s-CHP systems are not viable for household residential applications.

While it is true that payback times are higher for the PVT-ORC system, the payback times for both systems follow the same pattern. The

lower the payback time for a residential area, the more viable the implementation of a PVT-ORC system, for household combined heating and power in that area. For both systems, Madrid had the lowest payback time with 30.7 years for the PVT-ORC system.

CO_2 Reduction

CO_2 savings were calculated for each residential area using the relevant CO_2 emission factors[18]. The population-based CO_2 savings weighted average was calculated for Europe was found to be 3.61-t per apartment building per year or 0.60-t per flat per year.

Human Centred Approach

In many instances, it was found that the electrical energy produced exceeded the demand. In order to consider a human perspective on the average demand coverage throughout the year, the electrical coverage was standardised with the demand. **Figure 9** and **Figure 10** both show the average electrical and thermal coverages to be expected by a resident/landlord at any point in time.

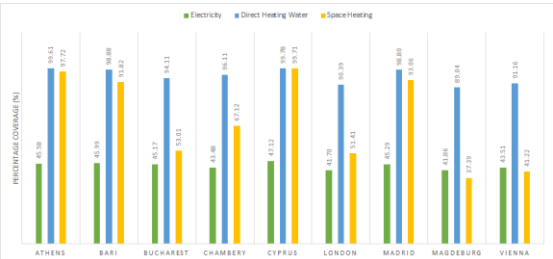

Figure 9: *Showing average coverage for the PVT-only model at any given time throughout a year.*

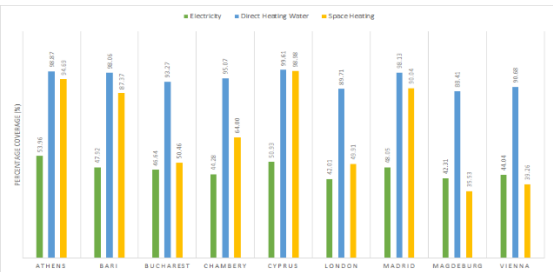

Figure 10*: Showing average coverage for the PVT-ORC model at any given time throughout the year.*

The trends observed in this analysis, complement those observed in the previous calculations and further emphasize the insignificant change in electrical energy coverage at the expense of a small amount of thermal coverage across all cities.

After the fuel savings and relevant payback times were calculated for both PVT-only and PVT-ORC systems, a consumer viability index was designed.

In line with the current increasing adoption of PV-thermal systems, and the aim of this research to determine the viability of the new PVT-ORC system, the highest and lowest values of payback time from the PVT-only results (32.3yrs and 14.6yrs respectively) were used in calculating the boundaries for the viability metric.

Since it has been noted that the total thermal demand coverage by both s-CHP systems (PVT-only and PVT-ORC) was >50% in all cases, Q_{cov} was averaged and used along with the aforementioned PBT values in equations (1) and (2) to calculate the distinct $E_{cov}/E_{demand,av}$ ratio boundaries for the metric.

The 'More Viable than PVT-only' region of the plot as shown in **Figure 11** below represented those cities where the system had E_{cov}/E_{demand} ratio greater than 3.04. The only city to lie in this region was Cyprus.

The 'Comparable with PVT-only' region represented those with a ratio between 3.04 and 1.77. The majority of cities considered in this study were within this region thereby lending validity to the comparison performed in this research.

The 'Less Viable than PVT-only' region, in which London, Vienna and Magdeburg fell, represented a E_{cov}/E_{demand} ratio lower than 1.77.

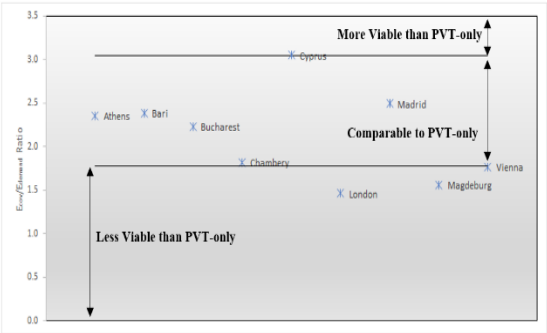

Figure 11: *Viability metric scatter plot*

Sensitivity Analysis

In order to ensure the model was robust, a sensitivity analysis regarding the ORC sizing was conducted. The size of the ORC is directly related to three key parameters (mass flowrates of: working fluid and the cold and hot water flowrates). Interestingly, it was found that decreasing the ORC size by 50% led to an average increase in electricity coverage by 1%. Subsequently, increasing the ORC size by 50% saw a 0.5% decrease in electricity coverage. There were however, no notable changes observed in thermal coverages.

Another parametric analysis was conducted on the orientation of the apartment building model used. Since the rooftop area is limited to the area of two flats (140m^2), expanding the orientation to a two-storey building (roof area now: 210m^2) leads to an average increase in electrical coverage of approximately 8% for the PVT-ORC system. The average thermal coverage, although already substantial, also increases by approximately 2%. A sample calculation of payback time, carried out for Athens showed a new PBT of 16yrs (1/3 of the initial value calculated). This can be attributed to the greater number of PVT collectors used.

5. Further Discussions

Renewable energy infrastructure must be robust and capable of meeting electrical and thermal demands whilst ensuring economical and spatial feasibility. This study highlights the fact that, at present, PVT-ORC s-CHP technology is not yet fully viable within the residential domain. There is, however, potential that further developments could enable PVT-ORC s-CHP systems to transition to a viable means of residential energy provision.

The PVT-ORC system produces a relatively large amount of excess electricity in comparison to the amount of useful electricity generated. As a result, the development of new energy storage technologies for solar and by extension all renewable energy sources, has the potential to significantly increase electricity demand coverage and fuel savings as well as reduce the associated payback times.

Due to the wide-reaching nature of this study across Europe and time constraints, government incentives for the adoption of hybrid solar-PVT technology by households for specific countries, have not been accounted for, such as the sale of electricity back to the grid at a reduced electricity price. Inclusion of these incentives would help further refine the techno-economic analysis undertaken and reduce payback time. Future schemes and incentives specific to PVT-ORC s-CHP technology by governments can also help to further reduce the payback time and increase the viability of the system in a residential setting.

The development of s-CHP systems including the ORC engine have also become a talking point for industrial applications where there is excess, or waste heat generated. The further optimisation of the ORC efficiency can also lead to renewed confidence in this hybrid technology and as such research surrounding this area will continue to challenge current barriers.

6. Conclusion

A study centred around the viability of hybrid solar PVT-ORC for residential integration in cities has been done.

The results of the consumer metric developed in this research, lend the belief that less persons would be inclined to implement the PVT-ORC system over the traditional PVT-only system.

The results of this research show that further developments are needed before PVT-ORC s-CHP systems can be considered feasible in residential applications across Europe. Whilst the integration of an ORC engine into a PVT s-CHP system works to increase electricity coverage, currently PVT-ORC systems do not generate enough additional electrical coverage to offset their considerably higher upfront cost for residential application as compared to PVT-only systems. As such, payback times associated with the PVT-ORC system are significantly greater (30.7yrs - 78yrs vs 14.6yrs – 32.3yrs for the PVT-only model) and thus hybrid PVT-ORC s-CHP systems are currently not a viable method for conventional household energy provision.

7. Acknowledgements

This work was supported by the Clean Energy Process (CEP) Laboratory within the Department of Chemical Engineering at Imperial College London.

Data supporting this paper can be obtained on request from cep-lab@imperial.ac.uk.

8. References

[1] Iea.org. (2018). *WEO 2017: Key Findings*. [online] Available at: https://www.iea.org/weo2017/

[2] Eur-lex.europa.eu. (2018). [online] Available at: https://eur-lex.europa.eu/legal-content/EN/TXT/HTML/?uri=CELEX:52016PC0767R(01)&from=EN

[3] Freeman, J., Hellgardt, K., Markides, C. N., "Working fluid selection and electrical performance optimisation of a domestic solar-ORC combined heat and power system for year-round operation in the UK", Applied Energy, 2017;186(3):291-303. https://doi.org/10.1016/j.apenergy.2016.04.041

[4] Herrando, María & Markides, Christos. (2016). Hybrid PV and solar-thermal systems for domestic heat and power provision in the UK: Techno-economic considerations. Applied Energy. 161. 512-532. https://doi.org/10.1016/j.apenergy.2015.09.025

[5] Guarracino, I., Mellor, A., Ekins-Daukes, N. J., Markides, C. N., "Dynamic coupled thermal-and-electrical modelling of sheet-and-tube hybrid photovoltaic / thermal (PVT) collectors", Applied Thermal Engineering, 2016;101:778-795. https://doi.org/10.1016/j.applthermaleng.2016.02.056

[6] Wang, Kai & Herrando, María & Pantaleo, Antonio & Markides, Christos. (2018). Thermodynamic and Economic Assessments of a Hybrid PVT-ORC Combined Heating and Power System for Swimming Pools.

[7] Ecomesh.es. (2018). [online] Available at: http://ecomesh.es/pdf/FT-ecomesh-EN.pdf

[8] UserTesting Blog. (2018). *IDEO's Human Centered Design Process*. [online] Available at: https://www.usertesting.com/blog/how-ideo-uses-customer-insights-to-design-innovative-products-users-love/

[9] Freeman, J., Chatzopoulou M. A., Markides, C. N., "Optimisation of a High-Efficiency Solar-Driven Organic Rankine Cycle for Applications in the Built Environment" (2017). Proceedings of ECOS 2017-The 30th International Conference on Efficiency, Cost, Optimisation, Simulation and Environmental Impact of Energy Systems. Paper: 184

[10] Ec.europa.eu. (2018). *Electricity price statistics - Statistics Explained*. [online] Available at: https://ec.europa.eu/eurostat/statistics-explained/index.php/Electricity_price_statistics

[11] Ec.europa.eu. (2018). *Natural gas price statistics - Statistics Explained*. [online] Available at: https://ec.europa.eu/eurostat/statistics-explained/index.php/Natural_gas_price_statistics#Natural_gas_prices_for_household_consumers

[12] Tradingeconomics.com. (2018). *United Kingdom Inflation Rate | 2018 | Data | Chart | Calendar | Forecast*. [online] Available at: https://tradingeconomics.com/united-kingdom/inflation-cpi

[13] Media, T. (2018). *Historic inflation Greece – historic CPI inflation Greece*. [online] Inflation.eu. Available at: https://www.inflation.eu/inflation-rates/greece/historic-inflation/cpi-inflation-greece.aspx

[14] Cleanenergypipeline.com. (2018). [online] Available at: http://www.cleanenergypipeline.com/Resources/CE/ResearchReports/renewable-energy-discount-rate-survey-2017.pdf

[15] Worldometers.info. (2018). *Cyprus Population (2018) - Worldometers*. [online] Available at: http://www.worldometers.info/world-population/cyprus-population/

[16] Worldpopulationreview.com. (2018). [online] Available at: http://worldpopulationreview.com/world-cities/madrid-population/

[17] Population.city. (2018). *Magdeburg · Population*. [online] Available at: http://population.city/germany/magdeburg/

[18] Energy. (2018). *EU Buildings Database - Energy - European Commission*. [online] Available at: https://ec.europa.eu/energy/en/eu-buildings-database [Accessed 13 Dec. 2018].

Assessing and Understanding Prakti Cookstove Corrosion

Martina Ivanova & Stanley Ho
Department of Chemical Engineering, Imperial College London, U.K.

Abstract

A major challenge for Prakti, a cookstove developer in India, is to reduce the degree of corrosion in their product. This paper assesses the corrosion resistance of type 304, 409 and 316L stainless steel (SS) under relevant conditions for Prakti's cookstoves. The analysis and evaluation of samples generated at the Prakti testing facility, as well as new SS samples prepared both with and without coatings in parallel accelerated corrosion furnace tests, intend to help Prakti make improved material selection in their future cookstoves. Surface examination, using optical microscopy, profilometry, and Raman spectroscopy, showed that SS 304 was the best choice of material in terms of cost and corrosion resistance. The findings of this paper support the continued use of SS 304 as Prakti's cookstove material. Furthermore, the effectiveness of coatings was also confirmed, particularly the use of Rust-Oleum ® paint.

Keywords: *Cookstove, Accelerated Corrosion, Furnace, Stainless Steel, Coating*

Introduction

Background and Motivation

Traditional biomass cookstoves are ubiquitous in the developing world, where nearly 3 billion people use them as a source of cooking and heating both indoors and outdoors. (Brady et al., 2017) Indoor cooking lacks the natural ventilation required to lower particulate matter concentration levels. (Langbein, Peters, & Colin, 2017) The hazards of cookstoves are immediate to the users and their families, with toxic emissions including fine particles, carbon monoxide and products of incomplete combustion that cause an approximate 4.3 million premature deaths, including 783,000 in India, every year. (Brady et al., 2017) The emissions are also consequential to global climate change, producing greenhouse gases and roughly 20% of the global black carbon.

A wide variety of fuels are utilised for cookstoves, where geographical availability of the fuels strongly dictates what is used rather than its efficiency or safety. 43% of India's population uses solid fuels for cooking purposes. (Clean Cooking Alliance , 2018) Reliance on biomass results in environmental degradation and necessitates troublesome and inefficient biomass collection time as well as physical risk for women and children.

Prakti is an Indian enterprise developing cookstoves which address problems in the traditional models and work towards combating the causes of respiratory diseases and environmental sustainability. The company is dedicated to the design, manufacture and distribution of these improved, fuel-efficient and affordable cookstoves which they hope will also aid in promoting gender equality and poverty reduction. Critically, Prakti has focused on addressing extensive social science research on how the stove is used and important factors which would encourage the purchase of their low-cost existing cookstove. The current design reduces: toxic emissions by 80% compared to traditional cookstoves, firewood consumption by 50%, and the cooking time by 50%. (Prakti, 2018)

The material of construction is crucial for the longevity and cost efficiency of the improved cookstove where significant constraints limit the choices. Firstly, the combustion of biomass fuels at high temperatures (> 600 °C) releases highly corrosive anions, like Cl, which attack the metal surface. This is known to induce extensive pitting corrosion. (Brady et al., 2017) Secondly, Prakti must provide their product at an increasingly affordable price to remain accessible for the vast income constrained Indian population. Lastly, the selling point of their product is that it is made from 100% stainless steel (SS), which limits the implementation of other materials. Prakti is looking to address these constraints and make improved material selection in their future cookstoves.

Stainless Steels and Corrosion Resistance

In general, SS are often chosen because they are strong, formable, easy to clean/sterilise, have a long-life cycle and are 100% recyclable. But above all, the property that makes them so widely adopted and why Prakti chose them is for their corrosion resistance. (Metal Supermarkets , 2016) SS possess a Cr content > 10.5 % which is the principal alloying element that is attributed with corrosion resistance of the material. On contact with oxygen, a thin chromium oxide layer (passive layer) is formed on the SS surface which protects the surface from corrosion. The general rule of thumb is that SS corrosion resistance increases with increasing Cr content. Other elements such as Molybdenum (Mo) can be added to SS to enhance corrosion resistance. The chromium oxide layer protects itself because it can re-passivate. (Arcelor Mittal, 2010)

Although SS provide very good corrosion resistance, they are still susceptible to corrosion if the passive layer is damaged or if conditions are particularly harsh such as the high temperature in the combustion chamber of a cookstove.

Types of Corrosion

Corrosion is the deterioration of metals due to interactions with their environment by chemical or electrochemical means. (Shaw & Kelly, 2006) There are two broad classification for corrosion: general and local (which has several variants), and some specialised types (e.g. galvanic and stress corrosion cracking). Prakti is

predominantly focused on reducing the first two. General corrosion is a uniform attack on the entire surface of the metal. A common example is the exposure of a surface to water, where oxidation is apparent as a thin layer of rust.

Localised corrosion occurs in a small local area rather than uniformly across the entire metal surface. Out of the three most common types of localised corrosion: pitting, crevice, and filiform; it is pitting corrosion which is most prevalent in SS. (Bell, 2017) Pitting corrosion arises from a local break in the protective oxide layer or coating. This exposed local area will corrode at a rate much faster than its neighbouring area, thus creating a pit. Pitting is known to occur under certain corrosive conditions, for example high concentration of Cl^- ions (anions) which interfere with the passive layer's stability and regeneration capabilities (Fig. 1). In aggressive aqueous environments, pitting and crevice corrosion caused by Cl^- are common phenomena for SS. (Gibson Stainless & Specialty Inc., 2017)

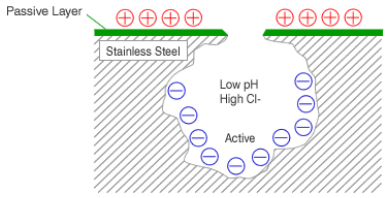

Figure 1: Pit formation. The positive symbols represent the cathodic region, whilst the negative symbols represent the anodic region under corrosive attack. (Misumi Technical Tutorial, 2010)

Project Objective

Herein, the objective is to investigate the corrosion resistance of SS under relevant conditions for Prakti's cookstoves used in South-eastern India. This will be accomplished by firstly analysing and evaluating samples generated at the Prakti testing facility. Secondly, new SS samples prepared both with and without possible coatings in parallel tests were executed in a furnace. Thirdly, artificially accelerated tests were conducted to mimic Cl ions found in biomass and determine longer-term behaviour of SS.

Materials and Methods

Test Samples Supplied by Prakti

Coupons of mild steel, SS 304, SS 409 and SS 409 coated with Rust-Oleum ® paint (RP) (110 x 25 x 1 mm) were burned in the Prakti test facility (Table 1). The surface was examined using optical microscopy, profilometry, and Raman spectroscopy.

Table 1: Burning Times of Prakti Samples

Test Type	Burning Time	Samples Tested
Screening Test	2 x 1 h	mild steel, SS 304, SS 409 with RP
Simulated Cycle Test	5 x 2 h	SS 304, SS 409 with RP
Extended Duration Test	30 h	SS 304, SS 409, SS 409 with RP

Lab Furnace Experiments

Tests were conducted with 72 × 22 × 2 mm 304 and 316L SS coupons in three variants: unpainted, and with two different paints: RP and No Nonsense (NNP). Samples were coated twice, one hour apart, and hung vertically to air-dry overnight.

Accelerated corrosion testing procedures used the following protocol. The coupons were submerged in 3.5 wt% NaCl (Acros, purity ≥ 99.0 %) solution using DI water for one hour at 20 °C.

Three furnace experiments (Carbolite CWF 1200), were executed to be consistent with those at Prakti (Table 1). A schematic of the temperature profile during the three experiments illustrates the heating and cooling cycles (Fig. 2). A borehole at the top of the coupon was used to suspend the coupons in the furnace (Fig. 3).

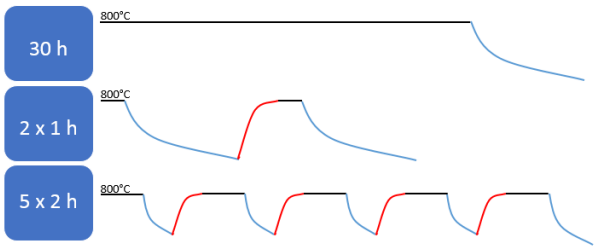

Figure 2: A schematic of the temperature profiles of the 30 h, 2 x 1 h and 5 x 2 h experiments where the black is the pre-set temperature equal to 800 °C, the blue is during shutdown and the red during reheating to the pre-set temperature.

Figure 3: Coupon Set-up for the Furnace Experiments

Table 2: Chemical Compositions of Candidate Metals (% Weight) (Atlas Steels, 2000)

Metal	Cr	Ni	Fe	Si	Mn	Mo	C
Mild Steel	-	-	~98	0.40	0.7	-	0.16
SS 304	18.0	8.0	~70	0.75	2.0	-	0.08
SS 409	10.5	0.5	~85	1.00	1.0	-	0.08
SS 316L	16.0	10.0	~69	0.75	2.0	2.0	0.03

Mass measurements of the coupons were taken both before and after the experiment, always at room temperature.

Cookstove Experiments

This experiment was conducted on a dry day outside using a Prakti 100% SS 304 cookstove.

Three coupons each of SS 304 and SS 316L were used in this experiment. The coupons had boreholes at the top which enabled them to be hung vertically inside the cookstove using hooks. The other end of the hooks rested on a metal rod which lay horizontally across the top of the cookstove as shown in Fig. 4.

The fuel placed in the fuel shelf was chopped fresh sawn oak (approx. 26 × 26 × 200 mm). 12 pieces of the oak were used throughout the experiment to maintain the flame and the experiment was run with a metal pot of water placed on the combustion chamber to simulate real cooking conditions.

Only the 2 x 1 hour experiment was conducted due to the restrictive nature of the experiment. The fuel was lit using a gas lighter and a strong, steady flame was sustained for 1 hour by the addition of wood when required. After the first 1 hour, the fire was extinguished, allowing the stove and the coupons inside to cool down to ambient temperature. Fig. 5 shows the coupons after the first hour of burning. The cooling lasted approx. 10-15 minutes after which the same procedure was repeated for another hour. The temperature in the middle of the combustion chamber where the flame was burning was approx. 450 °C.

Mass measurements of the coupons were taken both before and after the experiment, always at room temperature.

Figure 4: Set-up of Cookstove Experiment

Figure 5: Coupons After the First Hour of Burning

Results

Prakti

Samples tested at Prakti resulted in an incomplete matrix of variables. However, these reflect issues of interest and thus will be presented herein. Firstly, the susceptibility of an alternative steels to SS 304, where mild steel was only studied at 2 x 1 h and SS 409 at 30 h. Secondly, the enhancement of SS 409 with a corrosion protection paint. Thirdly, the comparative impact of direct flame contact to heat only.

Alternatives to SS 304

The optical microscope images show SS 304 (Fig. 6a) remained smooth and uniform after 2 x 1 h of burning, by contrast the mild steel (Fig. 6b) had a rough surface (average roughness (Ra) of 0.50 (Fig. 7a) *vs.* 14.42 μm (Fig. 7b)). Using Raman spectroscopy, the hematite (Fe_2O_3) signature peak (290 cm^{-1}) was observed in mild steel nearly three times greater than that on SS 304 (Fig. 8a & 8b). Identical Raman light setting were used.

Figure 6a: Optical microscope of Prakti 2 x 1 h – SS 304

Figure 6b: Optical microscope Prakti 2 x 1 h – Mild Steel

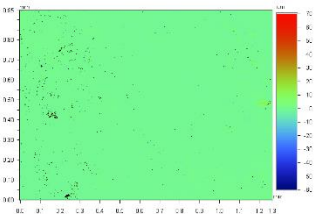

Figure 7a: Profilometry of Prakti 2 x 1 h – SS 304

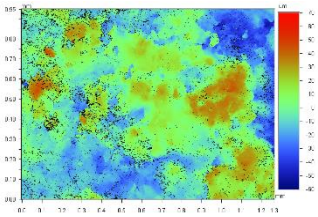

Figure 7b: Profilometry of Prakti 2 x 1 h – mild steel

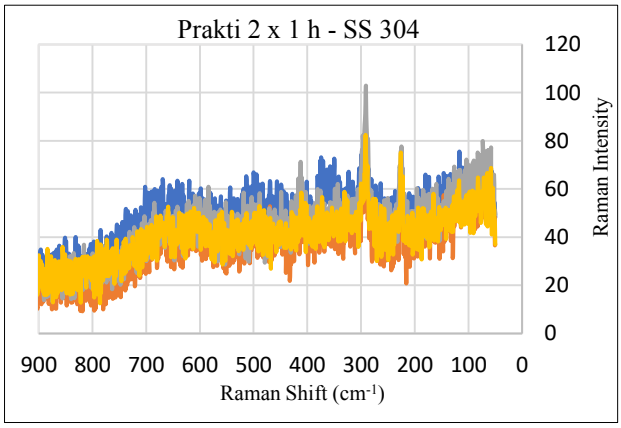

Figure 8a: Raman spectrum of Prakti SS 304 from 2 x 1 h test

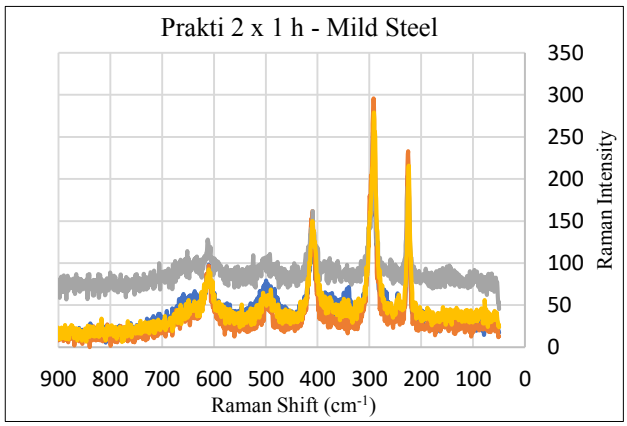

Figure 8b: Raman spectrum of Prakti mild steel from 2 x 1 h test

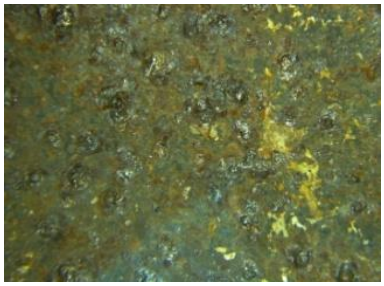

Figure 9a: Optical microscope of Prakti 30 h – SS 304

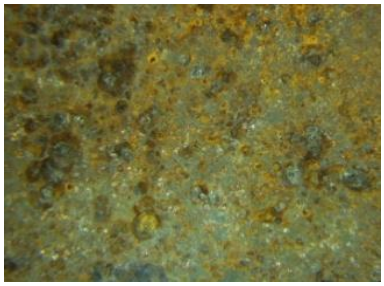

Figure 9b: Optical microscope of Prakti 30 h - SS 409

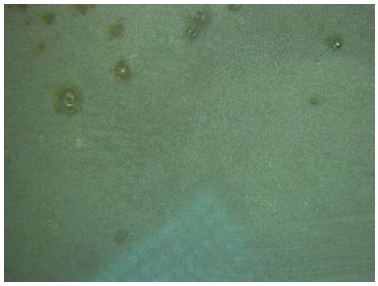

Figure 9c: Optical microscope of Prakti 30 h - SS 409 with RP

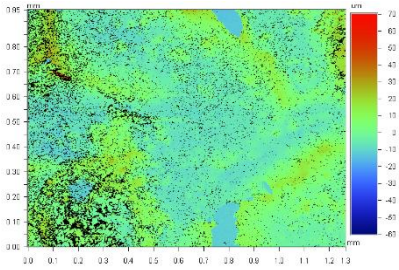

Figure 10a: Profilometer of Prakti 30 h – SS 304

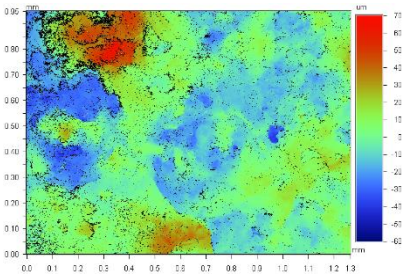

Figure 10b: Profilometer of Prakti 30 h – SS 409

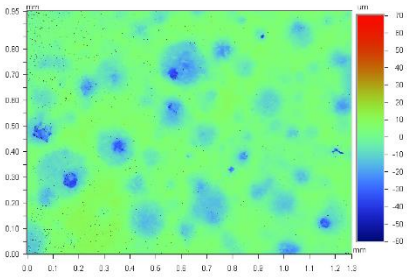

Figure 10c: Profilometry of Prakti 30 h – SS 409 with RP

After 30 h burn time, SS 304 and SS 409 exhibited similar pitting and discolouration as shown in Fig. 9a and Fig. 9b. Whilst both samples appear heavily corroded, profilometry revealed that SS 409 had a Ra more than double that of SS 304 (12.00 *vs*. 5.97 µm). Notably, both show hematite, according to the Raman spectra in both metal types, suggesting both were corrosion susceptible (Fig. 11a & 11b). SS 409 had a higher maximum peak intensity than SS 304 (173 *vs*. 135 Raman intensity).

Application of RP to SS 409

The optical microscope images of Fig. 9b & 9c clearly show the painted SS 409 sample to exhibit significantly less discolouration, roughness, pits and non-uniformity. From profilometry, the surface of the painted SS 409 sample had an average roughness less than half that of the non-painted sample (4.88 vs 12.00 µm). Additionally, a Raman spectrum corresponding to hematite was clearly observed in the non-painted sample, whereas no spectra corresponding to any common corrosion product was observed for the painted sample (Fig. 11b & 11c). However, a peak at ~604 cm^{-1} was detected in the painted sample but this was later established to be characteristic of the paint itself.

Furnace

The 5 x 2 h experiment was used as a model case as this burning cycle duration is the most representative of a real-life cookstove usage and is suitable in verifying the validity of cookstove environment using a furnace.

Burning Time

The role of exposure type (screening, cycling, or extending) was considered to address appropriate testing methodologies. Raman spectroscopy was used to compare the coupons of SS 304 painted with RP for the three different burning durations. The intermittent 5 x 2

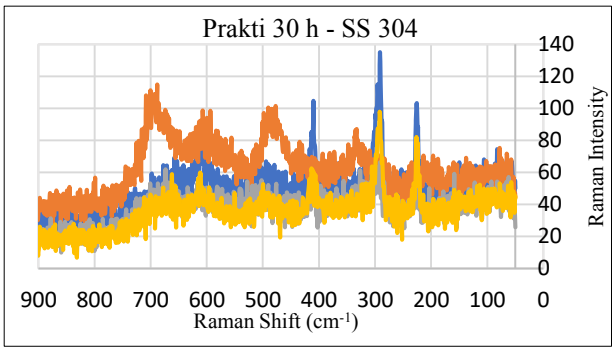

Figure 11a: Raman spectrum of Prakti 30 h – SS 304

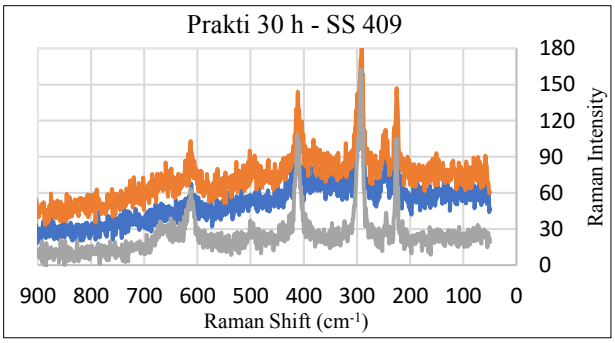

Figure 11b: Raman spectrum of Prakti 30 h – SS 409

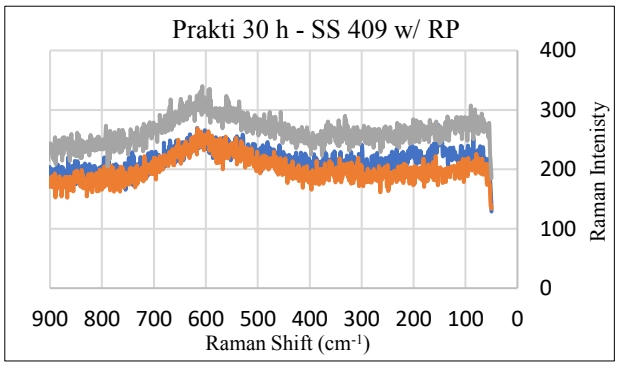

Figure 11c: Raman spectrum of Prakti 30 h – SS 409 with RP

h burning cycle revealed the presence of both hematite and magnetite (Fig. 12b). Contrastingly, no corrosion products were identified in the 2 x 1 h experiment, nor the continuous 30 h experiment (Fig. 12a & 12c).

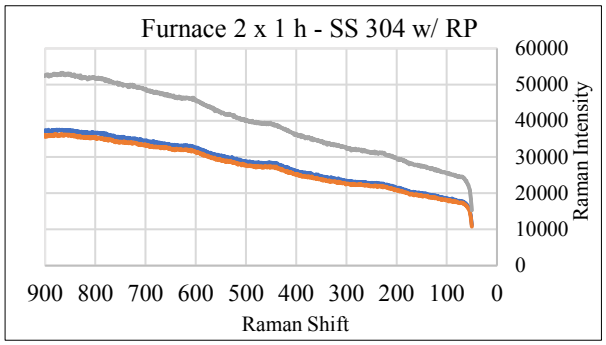

Figure 12a: Raman spectrum of Furnace 2 x 1 h – SS 304 with RP

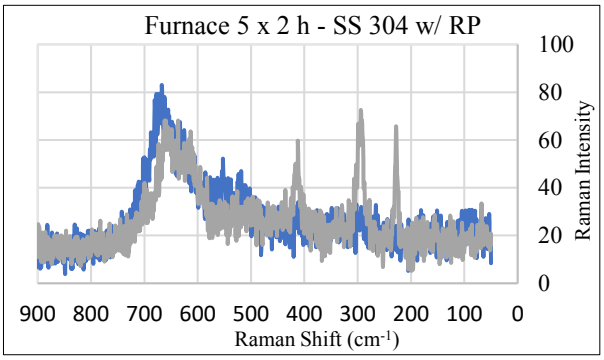

Figure 12b: Raman spectrum of Furnace 5 x 2 h – SS 304 with RP

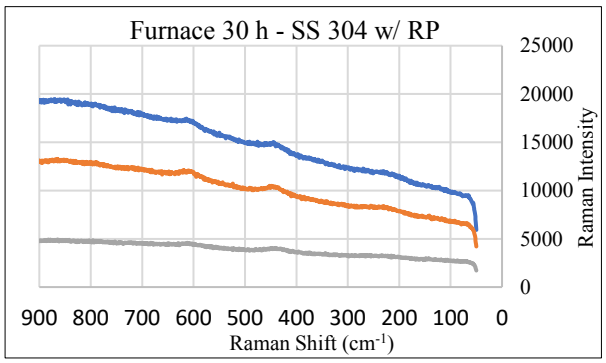

Figure 12c: Raman spectrum of Furnace 30 h – SS 304 with RP

Furnace Treatment

Visually from the profilometer images, both SS 304 and SS 316L underwent surface changes after being burned for 5 x 2 h (Fig. 13a-d). This was clearly seen from the substantial increase for the Ra values pre-furnace vs. post-furnace. Comparing the before and after Raman spectra (Fig. 15a-d), it could be concluded that the heat treatment resulted in emergence of magnetite for both metals. This corrosion product was absent in the pre-furnace coupons as expected.

SS 304 vs SS 316L After Furnace

Profilometer images and roughness indicate little difference between SS 304 and SS 316 for the 5 x 2 h experiment (Fig. 13b & 13d). The composition of corrosion products detected by Raman for 2 x 1 h and 5

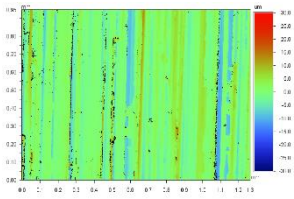

Figure 13a: Profilometry of new SS 304

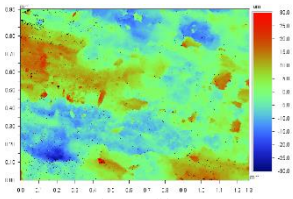

Figure 13b: Profilometry of Furnace 5 x 2 h – SS 304

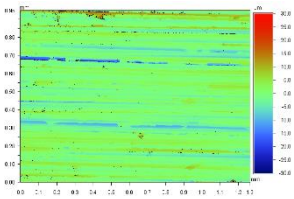

Figure 13c: Profilometry of new SS 316L

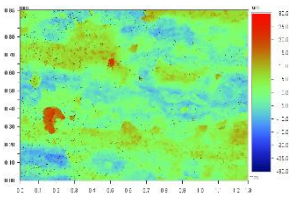

Figure 13d: Profilometry of Furnace 5 x 2 h – SS 316L

x 2 h were similar for the two alloys tested. However, whilst hematite was found at 2 x 1 h as the predominant species, it was superseded by magnetite after 5 x 2 h. There is some indication based on the strength of the magnetite signature peaks at 5 x 2 h that its presence is more significant for SS 316L than SS 304 (164 *vs*. 69 Raman intensity).

Paint

There was poor adhesion of RP on both SS 304 and SS 316L after the 5 x 2 h experiment (Fig. 14). In regions where the RP was removed corrosion product was observed to be consistent with uncoated samples, *i.e.* hematite/magnetite. In contrast, areas where RP was visually present, appeared to be consistent with the Raman spectra with only the 'RP band'. There was no remaining NNP on either the SS 304 or SS 316L after any exposure time in the furnace.

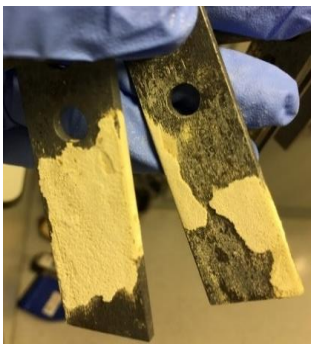

Figure 14: Rust-Oleum painted SS 304 (left) and SS 316L (right).

Cookstove

After 2 x 1 hours in the cookstove, no corrosion was detected from Raman spectroscopy for any of the SS coupons. RP remained intact, however, NNP flaked off like it did in the furnace experiments.

Discussion

Prakti

Alternatives to SS 304

The use of alternative steels, either cheaper to reduce cost or more expensive to increase corrosion resistance,

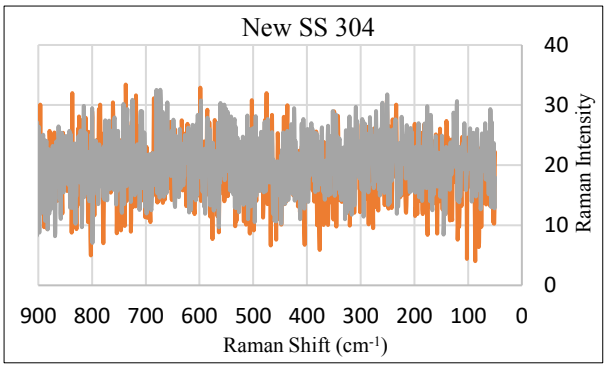

Figure 15a: Raman spectrum of new SS 304

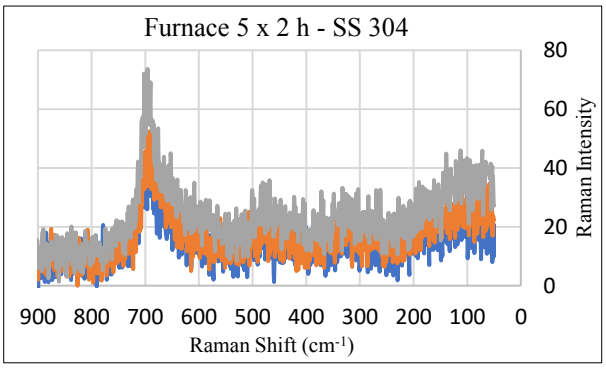

Figure 15b: Raman spectrum of Furnace 5 x 2 h – SS 304

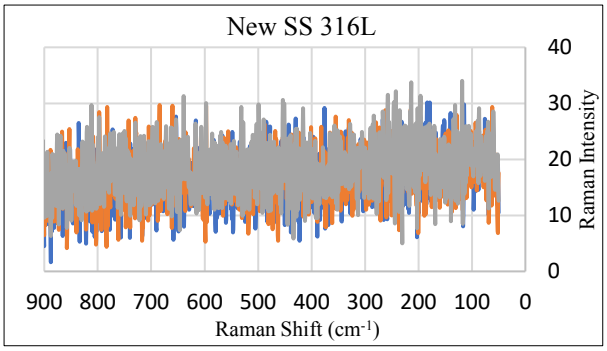

Figure 15c: Raman spectrum of new SS 316L

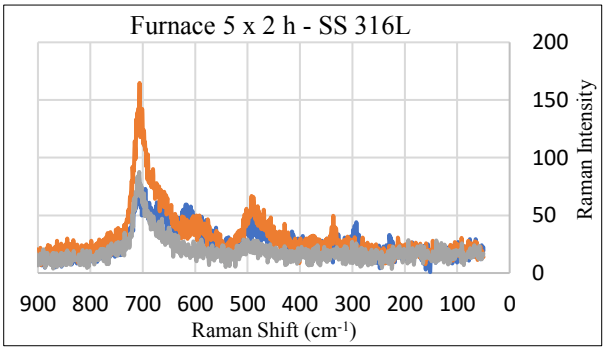

Figure 15d: Raman spectrum of Furnace 5 x 2 h – SS 316L

are important considerations in the manufacturing of low-cost cookstoves for rural India. An assessment of cheaper materials, comparing mild steel to the standard SS 304, for a screening test (*i.e.* 2 x 1 h) indicated that mild steel is less corrosion resistant, this is indicated by the greater hematite (Fe_2O_3) signature peak observed in mild steel. This reduced corrosion resistance, of mild steel, is due to its predominant Fe composition. By contrast, SS 304 is alloyed with Cr. The absence of Cr in mild steel allows the oxidation of Fe, and consequently the formation of the corrosion product: Fe_2O_3. These processes deteriorate the integrity of the material. In particular, this corrosion product leads to metal expansion, which produces great stress that weakens the metal and makes it flaky and brittle. (Metal Supermarkets , 2015) Moreover, this process generally continues due to the corrosion product's permeability to both air and water. Increasing the C content of metals, often increases their corrosion susceptibility. As seen in Table 2 there is twice the composition of C in mild steel than in SS 304. For continued operation in high temperature environment, the C content of SS 304 is often reduced to 0.02% to avoid corrosion susceptibility. (The International Nickel Company , 2018)

Whilst the comparable SS 304 samples appeared less damaged, Raman also indicated the presence of hematite. Whilst this might be counter-intuitive, in fact when SS is subjected to temperatures between 430 and 900 °C it undergoes intergranular corrosion. This process results in the formation of chromium carbides that precipitate in the grain boundaries of SS and, therefore, result in areas with depleted Cr. These regions where the Cr has been leached out have low corrosion resistance. (The International Nickel Company , 2018). As the cookstove typically operates in the range of 450 – 650 °C, this process could have occurred and therefore the hematite could have formed in these Cr-depleted regions. (Bossuet & Serrar, 2018)

Another alternative is the use of a cheaper SS, *e.g.* 409, which has alloying elements attributed with corrosion resistance (*e.g.* Cr, Ni), although in lower concentrations than SS 304. (Table 2) Notably, the increased Cr content is known to specifically address the susceptibility to pitting corrosion, which can occur in the presence of oxidising agents or Cl^- ions. The increased Ni content, in SS 304 by contrast to SS 409, is specifically beneficial because it encourages Austenite, which contributes to enhanced high heat resistance. (Aalco, 2018) This suggests why less hematite was observed in SS 304 in the extended duration test (*i.e.* 30 h) when the maximum Raman intensities of the two metals, strongly dependent on porosity and surface roughness, were compared. The profilometer findings showed that SS 409 exhibited higher roughness than SS 304 (higher values for Ra 12.00 *vs* 5.97 µm). The higher roughness values suggest a larger surface contact area between the metal and the corrosive environment as well as the presence of deep grooves which trap corrosion products and corrosive ions, forming pits. (Stoilov & Northwood, 2017) These pitting processes increase the corrosion on the surface.

The relationship between surface roughness and corrosion requires further investigation as limited number of samples were screened in this study. Nevertheless, it is reasonable to assume that the corrosion observed is induced not only by the break in

protective passive layer but also by the increase in surface roughness.

Analysis and evaluation of the Prakti samples determined that SS 304 is the most suitable metal to withstand corrosion environments. The usage of SS 304 also ensures longevity, low maintenance and aesthetic exterior of the low-cost cookstove.

Application of RP to SS 409

The abundance of hematite on SS 409 and the absence of any corrosion product on SS 409 with RP confirms the effectiveness of paint in preventing corrosion. The paint effectively creates a barrier between the metal surface and the moisture in the environment, thus preventing the metal from reacting into a more stable form, namely, its oxide or hydroxide.

Direct flame contact

The two sides of the coupons tested by Prakti show a demonstrable difference, where the conditions must have been different. Despite not knowing the positional set-up of the samples suspended in the cookstove, the conjecture can be made that the more corroded side was the side facing towards the flame (front of sample). For example, for SS 304 the front had an average roughness > 4 times that of the back (5.97 *vs* 1.41 µm). This suggests the cookstove would benefit more from a coating inside than outside the cookstove. Potentially, it might be more economical to only coat the inside and leave the outside uncoated as it is less affected by corrosion.

Furnace

Burning Time

Thermal cycling has been known to increase corrosion rates in SS compared to isothermal conditions. (Bradshaw & Goods, 2001) The cycles of heating and cooling compromise the passive layer in two ways. One being thermal expansion, as the metal and oxide have different thermal expansion coefficients; the other being tensile stress gradients, arising from rapid cooling of the passive layer. (Bradshaw & Goods, 2001)

This could explain why corrosion product was observed on the SS coupons painted with RP for the 5 x 2 h simulated cycle test, whereas no corrosion product was observed on the SS coupons painted with RP in the 2 x 1 h and 30 h experiments. This suggests that despite overall burning time being 3 times less for the simulated cycle test (*i.e.* 10 h vs 30 h), the cycle of heating and cooling has a profound impact on corrosion for SS 304.

Furnace Treatment

As neither the mild steel nor the SS 409 appear suitable from the tests conducted at Prakti in either the screening or extended duration tests, it was vital to identify if a more expensive material, such as SS 316L, would offer enhanced corrosion resistance.

The use of enhanced corrosion testing was essential to establish the long-term stability of materials without requiring indefinite testing. In the use of biomass for cookstoves, the presence of Cl^- as a source of pitting corrosion is significant. As such, the accelerated testing reflected this aggressive corrosive agent.

The tests conducted herein indicated that accelerated corrosion testing at 800 °C enhanced the roughness on the metals' surface, resulting in pitting corrosion and emergence of magnetite (Fe_3O_4). 3.5 wt% NaCl solution was used as literature sources disclosed that corrosion increases with increasing NaCl concentration up to 4%, beyond which the additional increase in concentration has negligible impact. (The International Nickel Company , 2018) The solution likely caused pitting as halogen ions induce the penetration of passive films. The profilometer images for the 5 x 2 h furnace experiment showed a loss of surface uniformity and the appearance of deeper grooves with increased roughness values in both metals. Rougher surfaces with deeper grooves are on average less open (higher ratio of depth to width at grooves' opening) (Fig. 1), restricting the diffusion of corrosive ions such as Cl^- out of the grooves and inducing the propagation of metastable pits. (Toloei & Northwood, 2013)

SS 304 vs SS 316L After Furnace

The inclusion of 2-3% Mo in SS 316L enhances its pitting resistance, particularly in saline or Cl environments. Published experimental results signify that the critical temperature, associated with the abrupt increase in pitting, in a NaCl solution is higher for SS 316L than SS 304: ~ 71 °C and ~54 °C for SS 316L and SS 304 respectively. (The International Nickel Company , 2018) Furthermore, the oxidation resistance of SS 316L is maintained up to 860 °C indicating that the 800 °C used in the furnace did not thermally damage the metal.

For the simulated cycle test, magnetite was found on not only SS 304 but also SS 316L suggesting the occurrence of Cr leaching as a result of intergranular corrosion. Raman spectra was consistent across multiple areas sampled on the coupons, showing the presence of magnetite only. It is possible that the extended cycling permitted the conversion between hematite and magnetite. Since only hematite was observed in the 2 x 1 h experiment, upon further burning it is likely that an accumulation of hematite occurred, thereby increasing the corrosion product layer thickness. (Qui, Chen, & Yang, 2016) This may have hindered oxygen diffusion into the inner layer, resulting in magnetite formation from incomplete oxidation of iron. (Qui, Chen, & Yang, 2016)

Considering the fact that SS 304 is cheaper and both metals exhibited corrosion, a material change to SS 316L cannot be justified from these results.

Paint

The poor adhesion of RP and the subsequent corrosion occurrence on both SS 304 and SS 316L in the simulated cycle test potentially resulted from the method of painting. The method of painting could therefore be crucial in minimising the extend of corrosion. The two paints employed in this study were spray paints, leading to inconsistencies in paint thickness, therefore, different

results may have been obtained if other application methods were employed, such as water-based paints or the use of a primer before applying the paint. The presence of corrosion-free areas where RP remained intact after the 5 x 2 h test, strongly suggests that RP effectively prevents corrosion product formation.

In contrast, no NNP remained adhered after the burning, indicating the paint's unsuitability for high-temperature environments. All NNP painted samples exhibited the presence of hematite which was consistent with the Raman spectra of the uncoated samples.

Mass Loss

Whilst the ASTM standard weight loss method provides a basal gravimetric analysis of the change to the coupon, it fails to provide adequate insights into the corrosion occurring. In particular, it fails to highlight if localised corrosion phenomena are present.

A net mass loss was obtained for all coupons after experimentation, this was most likely caused by initial mass gain from oxide scale formation, followed by a greater mass loss from oxide scale spallation. Spallation is generally due to differences in thermal expansion coefficients between the metal and the oxide scale upon cooling (U.S Department of Energy, 2015).

Screening materials or paints using this mass loss method does not provide a reliable metric in determining corrosion resistance of the tested coupons. As such, profilometry and Raman spectroscopy proved effective in distinguishing the relative degrees of corrosion resistance of the coupons.

Cookstove

The absence of corrosion products observed in the cookstove experiment is likely due to differences in experimental conditions compared to those used in the furnace testing and the experiments conducted by Prakti. Firstly, the temperature measured in the cookstove experiment did not exceed 450 °C which is in contrast to the furnace temperature of 800 °C used to accelerate the corrosion process. Secondly, the wood used in the cookstove experiment was idealised wood, rather than either the wood/biomass that would have been employed at Prakti or a pre-soaked with NaCl model system. Hence, the lack of corrosion products might be due to the lack of Cl^- ions that could have been otherwise artificially added. Thirdly, the type of wood burned might have had an impact on the degree of burning and consequently on the corrosion of the samples because the Indian wood used by Prakti was different to the wood burned in our own experiment, affecting the composition of the flame and hence the corrosion products determined from the Raman spectroscopy. Lastly, the cookstove experiment was conducted for 2 hours only due to limitations in time and available location for cookstove usage. Hence, the oversimplification and screening experiment are clearly unsuitable as a metric for determining material corrosion resistance for implementation in Prakti's cookstove.

Conclusion

Candidate metals for a cookstove can successfully be screened inside a laboratory furnace under accelerated corrosion conditions.

Despite being the cheapest alternative analysed, mild steel proved to be the most susceptible to corrosion and therefore the worse material choice, followed by SS 409. Both SS 316L and SS 304 exhibited good corrosion resistance but the results did not justify the additional cost of SS 316L compared to SS 304. Therefore, it is strongly recommended that Prakti continue using SS 304 as their cookstove material.

Coatings proved to effectively prevent corrosion product formation. However, not all coatings were suitable: NNP offered no benefits, where as RP provided excellent protection against corrosion product formation on the regions where RP remained adhered. Therefore, Prakti should explore further into suitable coatings as this could significantly prolong the life of their cookstoves. Furthermore, the inside of the cookstove suffers greater corrosion than the outside. Therefore, from an economical point of view, Prakti may wish to consider coating only the inside of their cookstoves.

Acknowledgments

The authors gratefully acknowledge. Dr. K.L. Sedransk Campbell for the immense guidance and support provided throughout the project. Special thanks to E. Hadjittofis for assistance with the experimental work and for providing expertise.

References

Clean Cooking Alliance . (2018). *India*. Retrieved from Clean Cookstoves: http://cleancookstoves.org/country-profiles/focus-countries/5-india.html

Aalco. (2018, November 14). *Alloying Elements in Stainless Stee*. Retrieved from The UK's largest independent multi-metals stockholder: http://www.aalco.co.uk/datasheets/Stainless-Steel-Alloying-Elements-in-Stainless-Steel_98.ashx

Arcelor Mittal. (2010). *Stainless Steel and Corroison*. Retrieved from ArcelorMittal: http://www.aperam.com/uploads/stainlesseurope/Brochures/Leaflet%20corrosion_Eng_374Ko.pdf

Asma, N., Yuli, P., & C.I., M. (2011). Study on the Effect of Surface Finish on Corrosion of Carbon Steel in CO2 Environment. *Journal of Aplied Sciences* . Retrieved from https://scialert.net/fulltextmobile/?doi=jas.2011.2053.2057#64944_b

Atlas Steels. (2000). *Stainless steel grade chart*. Retrieved from ATLAS STEELS – SPECIALTY STEELS PRODUCT REFERENCE MANUAL: http://www.atlassteels.com.au/documents/Stainless+Steel+Grade+Composition+Chart.pdf

Begum, B. (2015). Comparison of a TraditionalCook Stove with ImprovedCookStoves Based on Their Emission Characteristics. *Nuclear Science and Application*.

Bell, T. (2017, March 17). *What is Corrosion?* Retrieved from TheBalance : https://www.thebalance.com/what-is-corrosion-2339700

Bhojvaid, V., Jeuland, M., Kar, A., & Lewis, J. J. (2014). How do People in Rural India Perceive Improved Stoves and. *International Journal of Envronmental Research and Public Health* .

Bossuet, J., & Serrar, M. (2018). Prakti Design: the challenge of clean combustion for the poor. *The Journal of Field Actions*.

Bradshaw, R., & Goods, S. (2001). *Corrosion Resistance of Stainless Steels.*

Brady et al., M. P. (2017). Alloy Corrosion Considerations in Low-Cost, Clean Biomass Cookstoves for the Developing World. *Energy for Sustainable Development*, 20-32.

Clean Cooking Alliance. (2018). *India*. Retrieved from Clean Cooking Alliance: http://cleancookstoves.org/country-profiles/focus-countries/5-india.html

Ekouevi, K., Freeman, K., & Soni, R. (2014). Understanding the Differences between Cookstoves. *LiveWire A Knowledge Note Series for the Energy Practice* .

Gibson Stainless & Specialty Inc. (2017, June). *CORROSION TYPES AND PREVENTION*. Retrieved from Gibson Stainless & Specialty Inc.: https://www.gibsonstainless.com/types-of-corrosion.html

Gulland, J. (2005 , January). *The Art of the Wood-Burning Cookstove*. Retrieved from Mother Earth News : https://www.motherearthnews.com/homesteading-and-livestock/the-art-of-the-wood-cookstove-zmaz04djzsel

Gulland, J. (2005 , Janiary). *The Art of the Wood-Burning Cookstove*. Retrieved from Earth News: https://www.motherearthnews.com/homesteading-and-livestock/the-art-of-the-wood-cookstove-zmaz04djzsel

Jeuland, M. (2016). Analyzing the costs and benefits of clean and improved cooking solutions. *Sanford School of Public Policy and Duke Global Health Institute*.

Joseph, W. (n.d.). *Cleaner cookstoves help save lives, put more money in people's pockets and protect precious forests*. Retrieved from Ashden: Sustainable solutions, better lives : https://www.ashden.org/sustainable-energy/ashden-guides/clean-cookstoves#continue

Langbein, J., Peters, J., & Colin, V. (2017). Outdoor cooking prevalence in developing countries and its implication for clean cooking policies. *Environmental Research Letters* .

Mal, R., Prasad, R., Vijay, V. K., & Verma, A. R. (n.d.). The design, development and performance evaluation of thermoelectric generator (TEG) integrated forced draft biomass. *Science Direct* .

Metal Supermarkets . (2015, July 31). *HOW TO PREVENT RUST*. Retrieved from Metal Supermarkets : https://www.metalsupermarkets.co.uk/how-to-prevent-rust/

Metal Supermarkets . (2016, February 23). *MOST COMMON USES OF STAINLESS STEEL*. Retrieved from Metal Supermarkets: https://www.metalsupermarkets.co.uk/most-common-uses-of-stainless-steel/

Misumi Technical Tutorial. (2010). *Pitting Corrosion*. Retrieved from http://www.misumi-techcentral.com/tt/en/surface/2010/09/056-pitting-corrosion.html

Ochieng, C. A., Tonne, C., & Vardoulakis, S. (2013). A comparison of fuel use between a low cost,improved wood stove and traditional three-stonestove in rural Kenya. *Biomass & Bioenergy*.

Prakti. (2018). *About*. Retrieved from Prakti: http://prakti.in/about-prakti/

Prakti. (2018). *Prakti Smokeless Wood Stove*. Retrieved from Prakti: http://prakti.in/smokeless-wood-stoves/

Qui, P., Chen, Z., & Yang, H. (2016). The Transformation of Corrosion Products on Weathering Steel by Visible-Light Illumination under Simulated Marine Atmospheric Condition . *International Journal of Electrochemical Science* .

Sedighia, M., & Salarian, H. (2017). A comprehensive review of technical aspects of biomass cookstoves. *Renewable and Sustainable Energy Reviews*.

Shaw, B. A., & Kelly, R. G. (2006). *What is Corrosion?* Retrieved from The Electrochemical Society Interface: https://www.electrochem.org/dl/interface/spr/spr06/spr06_p24-26.pdf

Stoilov, V., & Northwood, D. (2017). Simultaneous effect of surface roughness and passivity on corrosion resistance of metals. *Corrosion: Material Performance and Cathodic Protection* .

The International Nickel Company . (2018). *Corrosion Resistance of the Austenitic Chromium-Nickel Stainless Steels in Chemical Environments* . Retrieved from Parrinst : http://www.parrinst.com/wp-content/uploads/downloads/2011/07/Parr_Stainless-Steels-Corrosion-Info.pdf

Toloei, A., & Northwood, D. (2013). The Relationship Between Suraface Roughness and Corrosion .

Proceedings of the ASME 2013 International Mechanical Engineering Congress & Exposition.

U.S Department of Energy. (2015). *Mitigation and Prediction of Spallation of Oxide Scales on Ferritic Stainless Steel.*

An Investigation into HFC Transition Strategies for a Major Food Retailer

William Austin and Matthew Hart
Department of Chemical Engineering, Imperial College London, U.K.

Abstract: High GWP refrigerant leakage is the second-highest source of carbon emissions for a supermarket company. Recent stringent UN and EU legislation targeting HFC refrigerants have therefore been introduced, and this study uses optimisation modelling to devise suitable investment strategies, in compliance with these regulations. The economic, environmental and business-risk implications of various investment levels was analysed, and scenarios were then applied to stress-test the models. The major food retailer's current £6m/yr investment was found to leave the business at significant risk of lost revenue. Increased down-time of poorly performing systems results in stock-loss and reduction in sales. Retrofitting existing systems, though not improving performance, does enable 68% reduction in carbon emissions for this budget by 2030. However, complete mitigation of business-risk, to a level deemed sufficient by the retailer, requires £50m/yr investment across the first six years, enabling installation of the new R-744 systems required. The balance between minimising expenditure on refrigeration system upkeep and sufficient spending to minimise downtime is crucial. Additionally, installation of new R-449A systems gives poorer investment returns than R-744 and so is never advised. Finally, thorough legislation and its effective implementation means sound business decisions have the secondary effect of significantly reducing carbon emissions.

1 Introduction

Science-based targets (SBT) are designed to provide ambitious goalposts helping drive significant, tangible change towards decarbonisation within organisations. Defining clearly the extent of current emissions, highlighting the speed of transition required and establishing a framework for recording carbon footprint evolution is shown to catalyse effective action[1]. These targets should mean a relatively swift policy shift is required across all business sectors. The commitments include both scope 1 (direct) and scope 2 (indirect) emissions, the latter comprising electricity generation's inherent carbon factor, currently heavily dependent on government motivation for national grid decarbonisation.

Analysing a supermarket company's emissions, refrigerant leakage accounts for 26% of the total carbon dioxide equivalent (CO_2e) released, as shown in Figure 1, and is a direct (scope 1) emission source. This means reduction should be possible dependent only on appropriate decision making by senior management and not relying on external agents to also change their practices. The second largest greenhouse gas (GHG) emissions source after electricity, refrigerants are increasingly regulated by the international community.

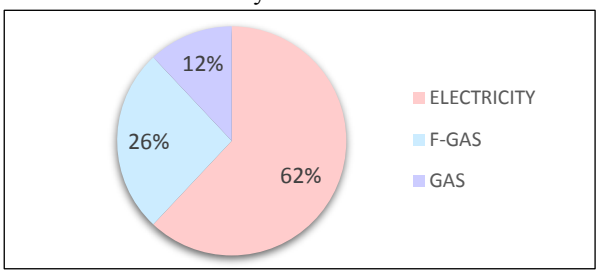

Figure 1: A pie chart showing the emissions breakdown of a major food retailer.

Refrigerant leakage, more specifically hydrofluorocarbons (HFCs), does not specifically require the accountability introduced by science-based targets, as the Kigali Amendment to the UN Montreal Protocol officially ratifies a phase-out plan[2]. The Montreal Protocol, initially introduced to target chlorofluorocarbons (CFCs) in 1989, was overwhelmingly successful at transitioning through hydrochlorofluorocarbons (HCFCs) to HFCs. However, the realisation that HFCs are up to 4000x more powerful than CO_2 as GHGs led to the subsequent Kigali Amendment. Agreed in October 2016, signatory countries are bound to restrict both production and consumption of HFCs, ultimately aiming to achieve 15% of 2011-13 CO_2e emissions by 2036. However, preceding EU regulation from 2014 applies even tighter restrictions dictating a phase-out to 20% by 2030, including a ban on both new installations ***and*** adaptations to existing plants with refrigerants >2500 GWP after 2020[3]. This is in fact the greatest motivator towards switching to a <2500 GWP refrigerant, with R-448A and R-449A the most commonly used. Up to 2030, reclaimed R-404A refrigerant may be used for servicing old systems, though this will then be banned.

The introduction of these regulations has provided financial incentive for supermarkets to transition away from the most prevalent R-404A refrigerant with a GWP of 3922x CO_2. There are a couple of main options available for this, namely replacing existing systems with CO_2 (R-744) or retrofitting existing equipment with a <2500 GWP refrigerant. Installing new systems with R-449A refrigerant is an option, though given the previous success in eliminating categories of refrigerants, it will likely be the next target for legislation. However, in the short-term, given approximately 10x lower costs of retrofitting an existing refrigeration system, R-449A may be used to enable rapid removal of R-404A before the 2030 cut-off. The high-expense of new systems inhibits the number of stores possible to update, meaning a mixture of the two solutions will be necessary to transition without excessive expenditure.

Given the medium-term potential for online grocery shopping to begin dominating the market, the necessity for sales floor-space may be diminished[4]. This uncertainty could delay installation of new systems and lead to pushing current systems beyond their target lifetime.

With the focus on reducing carbon emissions, using R-744 in new systems may seem counter-intuitive. The higher operational pressure required leads to greater absolute leakage rates and the thermodynamic properties of R-744 require more involved process-control mechanisms. However, the 3922x reduction in GWP compared to R-404 renders the emissions largely insignificant. Though R-744 refrigeration is relatively new technology, performance and operation costs are now comparable with new HFC systems. Near parity has been reached due to comprehensive research on best-practice operation[5] coupled with operators developing intuition in using the equipment. Zero GWP alternatives such as ammonia are used in certain applications but the inert, non-toxic, non-flammable nature of R-744 makes it ideal for applications in a food-retail setting. However, high-pressure R-744 pipework is not suitable in some convenience stores, particularly in residential blocks, where shared service infrastructure means accidental interference with pipes could cause serious injury. In this instance ethylene glycol or propane may be used with ammonia's toxicity ruling it out. This is rarely necessary in supermarket settings which have private services supply networks. Previous research, from which Figure 2 is replicated, has indicated that a major food retailer's supermarket emissions were both higher and consisting of a far greater proportion of outlier sites than convenience stores[6], meaning this study will focus on the supermarket estate.

2 Background (Literature Review)

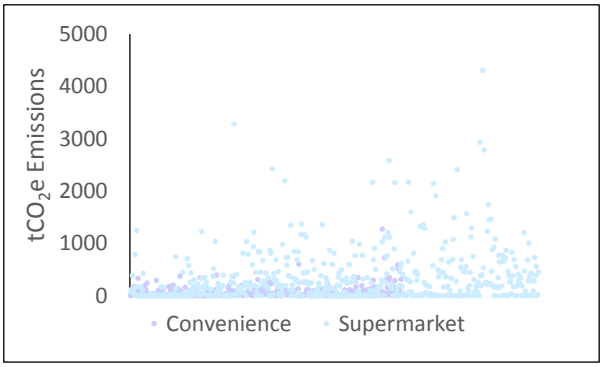

Figure 2: The distribution of CO_2e emissions separated into store type.

The House of Commons report on the 'UK Progress on Reducing F-gas Emissions'[7] earlier this year identified the 'modest progress' being made by the phased EU market-based quota system. The quota aims to reduce availability of high GWP HFCs (F-gas) and promote transition towards alternatives. This should provide additional incentives to help the UK meet its legally-binding Carbon Budgets. The report also highlights the benefits successful implementation of global regulations would have, highlighting that all countries meeting HFC reduction targets would 'reduce global temperature rises across this century by half a degree, significantly reducing the impact of global warming'. The UK government has also indicated that Brexit will have no impact on these regulations, even in the event of a 'no deal' scenario; the reporting requirements of UK companies will not change, and a new UK IT system would be established and administered by the Environment Agency[8]. Additionally, the UK is independent to the EU as a signatory to the relevant UN regulation.

The EU's commitment to reducing GHG emissions by 95% of the 1990 levels by 2050 has led to the creation of a variety of low carbon road-maps[9]. Equally, around the world strategies and road-maps are developed to analyse the transition to low carbon economies on the macro-scale of entire countries and industries[10]. For UK food retailers specifically, studies into environmental performance reporting and low-carbon roadmaps have focused on reducing supermarket's heat/energy carbon footprint. It has been shown that ambitious environmental targets are achievable if robust corporate action plans are followed, demonstrating the value of this report[11]. Using the strategies outlined, it serves to aid management with fact-based strategies to aid compliance with legislation and improve CSR performance.

An investment strategy road-map, specifically designed for a company to optimise FM decision-making, has not previously been reported. This research is unique in using real up-to-date data from a major food retailer's estate, and particularly useful because it incorporates all supermarkets, meaning no further scale-up is required.

Aims & Objectives

2.1 Stakeholders

The challenge facing decarbonisation initiatives is the diverse objectives of various stakeholders within both industries and companies. Clearly, SBTs are championing concerns of the environment, often in itself considered a stakeholder. Senior management however have responsibilities to maximise returns on investments made into the business, whilst minimising exposure to risk. Regarding management of refrigeration systems this means maximising equipment lifespan, increasing returns on the initial investment, and minimising upkeep expenditure. The latter includes reducing lost revenue resulting from refrigeration system down-time. This is a crucial because refrigeration system failures cause both revenue and stock losses, meaning not maintaining and updating systems when necessary can be costly. The supermarket company have expressed a desire to introduce a more *fact-based* process for managing their estate and informing investment decisions. On top of this, store managers themselves have sales targets to meet and so benefit from uninterrupted cooling supply. Therefore, when reporting on plant condition there is motive to be over cautious regarding expected lifetime, which has been suggested during our research. Contractors, though not influential stakeholders, benefit from a steady stream of projects.

2.2 Project Objectives

Objectives for this research are to advise on the trajectory required for transitioning away from HFCs using real data from a supermarket company. This includes optimising investment decision making for a business-as-usual (BAU) case, before applying various

scenarios. The economic, environmental and business-risk implications of the suggested strategies will be analysed and both internal and external factors varied to stress-test for future policy and market disturbances.

Successful carbon mitigation strategies often, by necessity, impinge on purely profit-maximising decision making. At the very least they require significant initial capital investment, with operational savings alone providing the cash flow, giving distant payback times. Understanding the extent to which carbon mitigation strategies coincide with sound facility-management decisions is crucial in critiquing the supermarket company's current strategy.

3 Methods

3.1 Case-Study

Individual store case-studies were used to crystallise the decision-making process undertaken by management on the 'micro-scale' and so understand the data required to inform these decisions. This ensures the best possible individual store strategies are developed. Case-studies enable consideration of the various factors when choosing HFC mitigation and refrigeration-plant upgrade strategy. This process is then translated, as accurately and realistically as possible, to a large-scale model incorporating the company's entire supermarket estate.

To assist in better understanding these decisions, a case-study analysis of the A0226 supermarket is shown (Table 1)

Store Number	A0226
Model Size	30K
Refrigerant Type	R-404A
System Age/yrs	18
Risk Category	Amber
Leakage/tCO2e	806

Table 1: A0226 Store Data

A0226 uses R-404A refrigerant meaning by 2030 either retrofitting with R-449A or installing a new system must be completed. Since the store has been assigned an 'amber' risk category by Facilities Management (FM) (see section 3.2), the target is to update the system within 3 years. This information is used in conjunction with the current system age; since the system will be over 20 years old in two years, installation of a new R-744 system is recommended by the end of FY 20/21. System upgrades do not take place on refrigeration plants under 20 years old. This 20/21 investment decision will of course be subject to budget availability. The investment cost for an R-744 system in this year, for a 30K store, is over £1.1m. This is a significant capital investment, especially considering a system update does not generate income. However, overrunning risk categories will ultimately lead to potential lost revenue through system down-time and stock losses. Therefore, annual budget restrictions mean, if higher-priority stores (regarding risk and age) require updates, this investment may be postponed.

Additionally, the potential to retrofit should also be considered. Retrofitting not only provides a route to remove R-404A from the estate but can also offer overall operating savings, hence potentially returning the investment (see section 3.8). Figure 3 shows the Marginal Abatement Cost (MAC) curve, relating to CO_2e abatement, for a 30K store, and demonstrates the benefit of R-404A. Allowing 31% of the R-744 CO_2e savings at just 9% of the MAC, R-449A is a useful stepping-stone towards the superior, but costly, R-744 CO_2e savings available. The 60K store model (see SI section 8.5) shows an almost identical MAC to 30K, for both retrofit and R-744, along with a 34% increase in CO_2e yearly savings for both. Higher leakage-rate of larger stores means greater CO_2e abatement potential. In this example however, using the leakage rate and forecasted prices (see section 3.8), the operational savings are not sufficient to quickly repay the over £78k initial investment amount (30K store in FY 18/19). The payback time for this investment would be 8.5 years. Therefore, investment in retrofit would not be advised since impending new R-744 system installation means

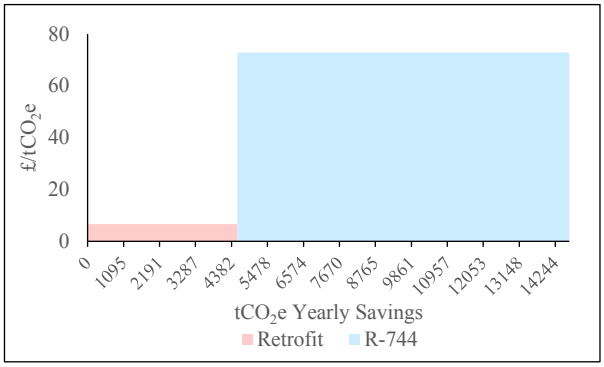

Figure 3: Marginal Abatement Cost (MAC) curves comparing retrofit and R-744 investment, shown for the 30K store model.

financial gains would not be realised.

Highlighting the nuanced nature of this decision-making process, it is important to recognise that tight budgets will limit investment in updating 'at-risk' and 'old' supermarkets, meaning 'red' stores may take priority over 'amber' A0226. Therefore, retrofit may become financially advisable for A0226 and even essential if investment was delayed to near 2030. The impact on business-risk associated with these systems, given conservative investment, is demonstrated in this study.

3.2 Store Data

The data given above for A0226 needed accessing for all supermarkets to replicate the described process across the entire estate and develop an overall investment strategy. The supermarket company's FM have developed a risk-categorisation database with 'red' and 'amber' risk-stores indicating system upgrades are required within 18 months and 3 years respectively. Green risk stores are well-performing and have no designated replacement timeline. However, 69% of the supermarket company's supermarkets are 'amber' and 'red' and installing so many new systems within 3 years is unfeasible. As such, these timelines were relaxed to 3 years and 6 years respectively, deemed a more reasonable approach. The risk database consists of all the company's assets, including refrigeration related

equipment, with data on installation date and assigned risk level. However, separating these refrigeration assets from the rest was both challenging and crucial to quality of data extracted. Three parallel splices were carried out on the database, assigning only refrigeration-related assets to a separate database of the company's supermarkets. Following this, 145 supermarkets remained unassigned and so were given green risk-categories as no assets had been flagged. System age for these unassigned supermarkets was then assumed from available data on supermarket initial build-date and last investment date; last investment >20 years after store build implies the refrigeration system, new with the store, was updated with the latest investment. The company informed us systems would likely have been updated at 20 years old if a significant investment was made.

All data used was up-to-date 2017/18 data, other than refrigerant leakage rates which were averaged over 2015-18. This leakage is approximated by amount refilled into systems, carried out only when system performance is weak. This may not be every year so significant fluctuations are possible, and a 3-year average was used. Finally, the 30K and 60K model store assumptions used were allocated based on available store square footage data.

3.3 MILP Optimisation

To transfer these learnings from the case study into a macro-level investment strategy, an optimisation model has been developed. This uses mixed-integer linear programming (MILP) to minimise the combined cost of capital investment (retrofit or new-system) and operating cost (refilling high-leakage systems). This includes all supermarkets and years up to 2030. Leakage rate is assumed to be constant every year, using average historical leakage rates (see section 3.2), and where a new R-744 system is installed, the leakage is assumed equal to the average R-744 30K or 60K supermarket leakage. The optimisation objective function is shown below in Equation 1:

$$\min T = \sum_j \left(\sum_i \{x(i,j) \times O_1(i,j) + y(i,j) \times O_2(i,j) + z(i,j) \times O_3(i,j)\} + \sum_k \{v(k,j) \times C_2(k,j) + w(k,j) \times C_3(k,j)\} \right) \quad (1)$$

Where possible, decisions will be made ensuring overall saving from switching to a cheaper refrigerant is maximised in a trade-off with the investment cost of implementing the switch. In the simplest comparison of two similar stores with the same age and risk category, the highest-leakage supermarket with the greatest operating cost (and so potential savings) will be a higher priority for transition to a cheaper alternative.

3.4 Decisions

The optimisation uses binary variables to replicate the decisions available each year for each store. These are:

i. $x(i,j)$: no action taken in year i at store j.
ii. $y(i,j), v(k,j)$: retrofit to R-449A refrigerant in year i/k at store j.
iii. $z(i,j), v(k,j)$: new R-744 system installed in year i/k at store j.

In the baseline BAU model, an annual budget of £6m/yr is imposed in line with the supermarket company's current investment level in their refrigeration systems. A priority is therefore required, made up of risk category and the store age, to dictate stores for installation of new systems. In consultation with the company, a normalised priority is obtained from a combination of age and twice risk. This is because risk categorisation is more significant since an 'old' system which is performing well is unlikely to be prioritised for update. Equally, a relatively young system will not be as high a priority since maximising system lifetime is important.

Within the model, the current refrigerant used in the system determines the possible set of decisions for that store. For stores currently operating R-407A systems, retrofitting with R-449A is not considered an option since R-407A already complies with the 2500 GWP legislative limit. For R-449A systems, retrofit is obviously not an option. To replicate these limitations in the model, binary matrices are used to dictate the options available for each decision.

3.5 Baseline Models

The baseline optimisation models operate with four different levels of investment. Firstly, the BAU case of £6m/yr. In this model, the risk category and age restrictions cannot be entirely satisfied and instead the priority ratings described in section 3.4 are used. As many upgrades as possible are invested in whilst still meeting the legislative requirements of removing all R-404A by 2030.

From these models, the implications on business risk can be analysed, which is one of the crucial outputs of this investigation. Due to the transition away from R-404A being legislatively enforced, profitability in fact carrys less importance. The other extreme model tackles the problem in reverse, utilising the minimum budget possible to fully satisfy risk categories, calculated as £50m/yr. It is important to note here that this refers to the relaxed targets discussed in section 3.2.

These two models demonstrate the balance between what is achievable under current spending, and the spending required to satisfy risk-category targets. Between these are two intermediate £10m/yr and £20m/yr budgets. Both models allow greater reduction in business-risk associated with refrigeration systems. These four investment levels are chosen as significant for analysis and subsequent potential implementation by the supermarket company. Increasing from £20m/yr to £30m/yr means *total* spend is greater than the £50m/yr *total* spend, as £50M/yr transitions all 'at risk' stores within six years, before annual investment then falls. The other models however look to spread investment evenly up to 2030, meaning the £30m/yr *total* spend exceeds the £50m/yr and so it has been rejected.

3.6 Scenarios

Having developed the baseline models, the following scenarios were applied and analysed for insights into the

behaviour of the models, subject to internal and external factors:

- Minimisation of CO_2e emissions: to analyse the relationship between financial benefit and environmental policy.
- HFC tax: considering the implementation of a GWP-weighted tax on HFCs, similar to that proposed in multiple European countries. This aims to understand the potential influence of additional legislation, promoting low GWP refrigerants, on both strategic decisions and financial outlook. Three levels of taxation have been imposed with a conservative and aggressive level based around the original proposed French taxation[12].
- R-449A price fluctuation: a significant portion of the industry will be transitioning from R-404A to R-449A. R-449A price could increase above the baseline forecasted, potentially impacting optimal strategy.
- Installing new R-449A systems: a competing investment option for new R-449A systems is included in the model. Only R-744 was available for the baseline models. This will indicate whether the company's current strategy of only investing in natural refrigerants for new systems is sound and if not, to what extent should returning to HFCs be considered.

3.7 Constraints

In the MILP optimisation, constraints are used to control the feasible region. Most constraints effectively reproduce the 'real' site-by-site decisions ordinarily made by management. The key constraints which are used to model the investment strategies are shown below. Remaining equations which calculate outputs such as CO_2e emissions or R-404A bank properties are available in SI section 8.2. Nomenclatures for the following equations can be found in SI section 8.1.

- Investment in retrofit or CO2 can only happen once:

$$\sum_k v(k,j) \leq 1 \qquad \forall j \qquad (2)$$
$$\sum_k w(k,j) \leq 1 \qquad \forall j \qquad (3)$$

- A decision must be made in every year for every store:

$$x(i,j) + y(i,j) + z(i,j) = e = 1 \qquad \forall i,j \quad (4)$$
$$G(i,j) \times x(i,j) + B(i,j) \times y(i,j) + A(i,j) \times z(i,j) = 1 \quad \forall i,j \quad (5)$$

- After action is taken, this decision must be carried forward to the following year:

$$y(i,j) + z(i,j) \geq y(i-1,j) + z(i-1,j) \qquad \forall i,j \qquad (6)$$

$$B(i,j) \times y(i,j) + A(i,j) \times z(i,j) \geq B(i-1,j) \times y(i-1,j) + A(i-1,j) \times z(i-1,j) \qquad \forall i,j \qquad (7)$$

- Constraints to ensure operation **after** investment:

$$\sum_{k=18/19}^{k=i} w(k,j) \geq z(i,j) \qquad \forall i,j \qquad (8)$$
$$\sum_{k=18/19}^{k=i} v(k,j) \geq y(i,j) \qquad \forall i,j \qquad (9)$$
$$\sum_{k=18/19}^{k=i} D(k,j) \times w(k,j) \geq z(i,j) \qquad \forall i,j \qquad (10)$$
$$\sum_{k=18/19}^{k=i} E(k,j) \times v(k,j) \geq y(i,j) \qquad \forall i,j \qquad (11)$$

- Retrofit and R-744 investment criteria met using matrices to allow/disallow the option:

$$w(k,j) \leq D(k,j) \qquad \forall k,j \qquad (12)$$
$$v(k,j) \leq E(k,j) \qquad \forall k,j \qquad (13)$$

- All stores off R-404A by 2030:

$$\sum_k v(k,j) + w(k,j) \geq R404Matrix(j) \qquad \forall j \qquad (14)$$

- Budget:

$$Budget \times (1-\alpha) \leq YrInvT(k) \leq Budget \times (1+\alpha) \quad \forall k \quad (15)$$

3.8 Price forecasts

Due to the HFC phase-down across the EU, subject to the 2015 regulation, HFC market price is expected to fluctuate significantly. Forecasting these prices is a challenge both for the industry and this research. The decision-making process is dependent on these prices as they dictate the potential operating costs for each decision, and so the savings available. This is incorporated into the cost minimisation and therefore also the final investment strategy. The leading research into the future of HFC prices has been led by *Öko-Recherche*, an organisation dedicated to environmental research and monitoring, on behalf of the European Commission. This research, conducted in 2015, concluded an increase in European HFC prices up to 2030, based on CO_2e, and so GWP weighted[13]. As can be seen in figure 4, the market is expected to anticipate stepped phase-downs with a steep price increase, as historically shown, followed by an over-correction as the market settles.

Figure 4: R-404A price forecast according to Öko-Recherche.

The two proposed price scenarios present likely extremes for the price predictions and have been proved accurate using 2015-18 historical data. 2018 data was found to be between the given scenarios for all HFCs investigated and has been used to adjust the forecasts. The subsequent position between the two scenarios is then projected up to 2030 with current EUR/GBP exchange rates applied. R-744 price has been assumed to rise in line with inflation at 2.5%/yr but is still low compared to HFCs.

3.9 Cost parameters

As discussed previously, the operating and investment costs are crucial parameters used in the model to influence the decisions made. Data for the current investment costs, for 30K or 60K model stores, has been provided by the supermarket company. The detailed breakdown of the data provided has allowed the incorporation of refrigerant price forecasts. For R-449A retrofits, the project cost varies with year of investment due to R-449A price fluctuations. For new R-744 systems, refrigerant filling cost also varies with price, with the equipment and wider project costs assumed to grow at 2.5% p/a.

The 'operating cost' parameters are calculated from the product of current-year refrigerant price and store leakage rate. Prior to updating a system, the leakage is assumed constant at the 2015-18 average as described in section 3.2. Following a retrofit, the leakage rate from a given system is assumed unchanged, since no substantial equipment alterations are made. Finally, following installation of a new R-744 system, the leakage is assumed equal to the average historical leakage from current 30K and 60K R-744 systems.

3.10 Banking

A significant element of the supermarket company's current HFC transition strategy is to 'bank' the R-404A refrigerant when it is removed either during a retrofit or new-system implementation. The bank is operated by a contractor who clean and bank the refrigerant and is essential as, beyond 2020, only reclaimed R-404A can be used. The bank will be needed to meet the estate's residual demand[14].

It must be considered however that, as the supermarkets transition away from R-404A, demand on the bank will decrease while volume of banked refrigerant will grow. This is likely to occur towards 2030, regardless of the investment strategy implemented. Current options for using the excess level in the bank include; trading R-404A for alternative refrigerants with the contractor, incinerating excess refrigerant (either before 2030 regulation or gradually, to reduce storage costs), or finally to separate the blend into constituent parts and recover useful components, incinerating the rest. The latter though is likely more expensive than valuable.

Since the financial outlook of the banking system is still unclear, dependent on a variety of industry and regulatory factors, the bank has not been included in the objective function. It has however been analysed post-optimisation to understand the bank behaviour.

The key outputs are:

- Yearly bank refrigerant level: modelled as sum of previous-year level and reclaimed volume from updated systems, less yearly demand.
- Demand on bank: assumed equal to the lesser of leakage from the estate and bank level.
- Refrigerant cleaning cost: assumes 65% of system entrained volume is reclaimed.
- Bank storage cost: based on yearly bank level.
- Asset value: the product of demand and market price. This is not a cash-flow and so should be handled cautiously, but is nevertheless essential in estimating reclaimed R-404A value.

4 Results & Discussion

4.1 Baseline Models

The baseline models highlight clearly the supermarket company's challenge in having ageing refrigeration systems in need of investment, coupled with needing to transition their entire estate away from R-404A refrigerants by 2030. On their own, ageing systems can be carefully managed, but having to update 63% of all supermarkets puts additional strain on budgets. Pushing systems beyond industry-standard lifetimes has implications both for the environment and the company; increased leakage of older systems will increase CO_2e emissions and increase maintenance costs in replacing lost refrigerant. Additionally, older systems' reduced reliability increases business risk in potential for lost revenue in sales and stock-loss. It should be noted that analysis was carried out on a financial year basis meaning R-404A removals planned for 2029/2030 must be completed within the first nine months of 2029, to meet the December 31st EU regulation cut-off.

For a £50m/yr budget, the minimum necessary to satisfy the relaxed risk category targets discussed in section 3.2, minimal retrofit is recommended as the number of 'red' and 'amber' risk category stores mean investment in R-744 systems is forced. Figure 5 illustrates that, following the first six years in which 319 of 352 (91%) stores using R-404A refrigerant are converted to R-744, yearly investment drops significantly to an average £11.34m/yr across the next four years, followed by no investment in the final two. The heavy frontloading of investment is a symptom of the estate's ageing/risk-prone refrigeration systems, however interestingly £50m/yr also provides the best CO_2e reduction of any investment level. Unfortunately, the 833% increase on the company's current £6m/yr spending level means a compromise on business risk will likely need to be made.

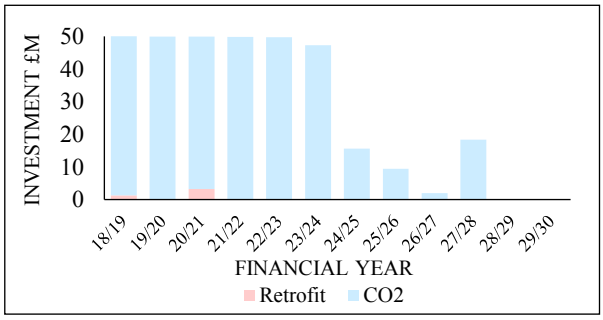

Figure 5: A bar chart showing the £50m/yr budget investment breakdown, separated by update type.

The £6m/yr budget on the other hand favours solely retrofit investment in the first three years, illustrated in Figure 6, to quickly access the savings available using the cheaper, lower GWP, R449-A. The 10x lower cost of retrofitting a system over installing new means 10x more stores can be updated within the budget, enabling a rapid shift away from R-404A, maximising operational savings. Retrofit investment is also promoted by a tight budget meaning the lower

installation cost of retrofitting is favourable to transition all R-404A systems. Though it is possible to transition all stores in line with relevant EU regulation under the £6m/yr budget, the implications for business risk are significant. Figure 7a and 7b show a 69% increase in the number of stores overrunning their risk categories and an increase in the average risk overrun from 1.5 years to 8.7 years. Quantitative data was unfortunately unavailable to illustrate numerically the financial or reliability losses incurred due to extending the risk-category assigned deadlines. However, given the data used to assign the categories, overrunning can implicitly be assumed to equate to more refrigeration downtime and greater revenue losses. Additionally, the significant reliance on R-449A introduced by the strategy, clearly illustrated in comparing the 2030 maps (Figures 9a and 9b), leaves the business vulnerable to further legislation now targeting <2500 GWP refrigerants. The UK's Kigali Amendment phase-down commitments, ultimately requiring HFC CO_2e emissions reduction to 15% of 2011-13 levels, apply for all HFCs across all business sectors. R-449A is likely to be a further legislative focus. Additional restrictive legislation on these refrigerants could therefore come into force as early as 2025 with a potential 2035 ban ten years later, mirroring the timescale of current EU regulation. However, by this time R-449A retrofitted systems will be approaching end of life, with even the youngest stores exceeding 20 years old. Replacing these systems will be a necessity and returns in operational savings from previous retrofit investments will be maximised. The

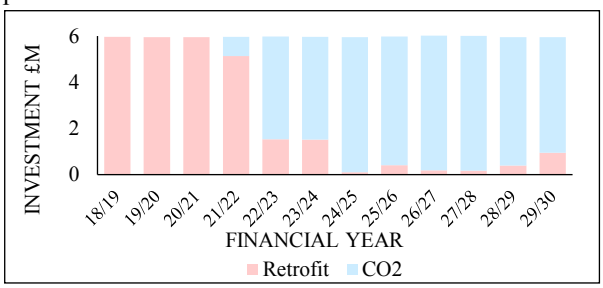

Figure 6: A bar chart showing the £6m/yr budget investment breakdown, separated by update type.

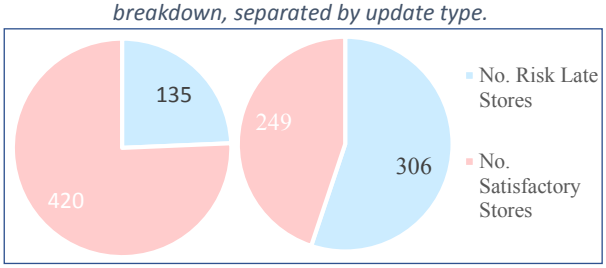

Figure 7a and 7b: Proportion of stores overrunning risk-category targets for £6m/yr (right) and £50m/yr (left).

company is therefore relatively well placed to adjust to future policy under current investment levels. However, the level of business risk incurred under the £6M budget, as described, remains of considerable concern.

As the budget increased to £10m/yr and £20m/yr (see SI section 8.7.1), proportional investment in retrofit reduced as the extra investment available is used to update high-priority stores with new R-744 systems. New R-744 investments account for almost all increased budget spend, enabling significant business-risk mitigation as risk-associated old stores are taken offline. The clear trend observed is an increased business risk as annual budget decreases. Retrofit investment is also pushed into earlier years as the budget increases, maximising operational savings and allowing quicker transition away from expensive R-404A.

The CO_2e emissions are significantly reduced across all budgets, shown in Figure 8, with even current spending levels allowing 68% reduction by 2030. However, 96% reduction is possible with the £50m/yr budget, which interestingly was designed to reduce business risk but is also the overwhelming leader environmentally. The higher investment clearly leads to a speedier and more complete mitigation of CO_2e emissions as show in Figures 9a and 9b. The differing ultimate aims of the two budget models are also made clear in the number and size (indicating tCO2e emissions) of R-449A data-points still on the £6m/yr 2030 map (Figure 9b). The focus here is clearly on replacing only the riskiest stores whilst accepting the modest improvement provided by R-449A as a stepping-stone to R-744. £50m/yr however opts to 'future-proof' in minimising both business-risk and exposure to externalities affecting refrigerant prices. The limited ability of R-449A retrofitting to reduce refrigeration-system leakage emissions relative to R-744 leads to the large number of medium-sized R-449A data-points observed in 2030 of the £6m/yr budget model (figure

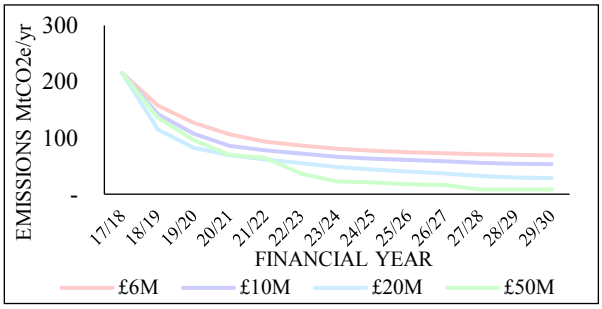

Figure 8: Graph showing CO_2e emissions reduction up to 2030.

9b). In the £50m/yr model, the reduction in refrigerant GWP dominates the CO_2e reduction but real-terms leakage reduction of new systems will contribute to an extent.

Our research shows R-744 must ultimately be the refrigerant of choice as, when given the option of installing new R-449A systems, no stores invested. Additionally, the discussed likelihood of new restrictive regulations on R-449A within the near future would now, for new installations, significantly shorten equipment lifetime and so reduce returns on the initial investment. Additionally, R-744 prices are expected to, at most, rise in-line with inflation but this is considered conservative given the recent IPCC report[15]. The report highlights carbon capture's importance in combating climate change, meaning liquid CO_2 may become abundantly available and even cheaper than currently.

4.2 CO_2e Minimisation

The constraints of the £6m/yr and £50m/yr models, in aligning with regulation and conforming to risk categories respectively, causes a level of rigidity. However, significant changes in strategy when

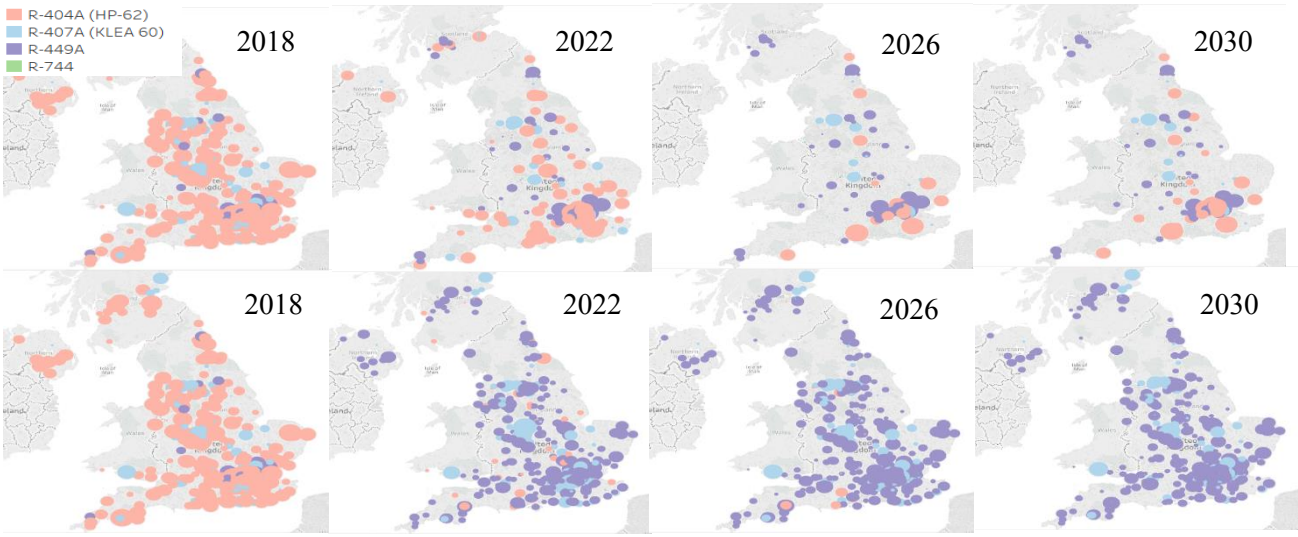

Figure 9a and 9b: Timeline maps for the £50m/yr (top) and £6m/yr (bottom) budget respectively. All supermarkets with sufficient data are included on the maps, with bubble size indicating relative extent of CO_2e emissions.

minimising CO_2e emissions was observed. The £6m/yr model shifted 77% of the retrofit investment from FY 23/24 to 22/23, accessing the extra year of CO_2e reductions, despite the resulting £1.20 /kg higher R-449A price at the time of update. Though the prices are tough to predict, the increase prior to step phase-downs has been repeatedly observed and so investment in these periods is not advised. With all stakeholders considered, accessing the extra year of lower emissions does not justify the higher expenditure, given investment is certain the following year. Overall, minimising CO_2e emissions for the £6m/yr model does result in 3% greater reductions at 2030.

A noticeably different strategy is also observed for the £50m/yr budget, particularly significant set against the constrained nature of the model, highlighted by its rigidity when tested under other scenarios. The 600% increase in retrofit investment level leads to substantially the highest £50m/yr retrofit investment under any tested scenario. As cost is no longer a constraint, it is always preferable to retrofit, even if investment in a new system is planned for the following year. Therefore, half the first-year budget is used to retrofit, from previously minimal levels under cost-minimisation. This £25m/yr retrofit investment is the maximum proportion of budget not required to fulfil risk-categorisation constraints necessitating new R-744 systems. However, again considering all stakeholders, retrofitting a store to then replace within a few years will likely be considered a poor investment. Like the £6m/yr budget, a 2% larger reduction in CO_2e emissions compared to cost-minimisation is achievable. The minimal gains demonstrate the strong relationship between sound investment strategies through the course of the transition and significant reduction of the company's environmental impact. This is a positive outcome regarding sustainability and environmental performance; the legislation in place means a strong focus on purely financial business decisions will have the secondary effect of significantly shrinking the carbon footprint.

4.3 HFC Tax

Implementation of a French-style GWP-weighted HFC tax on CO_2e emissions had the expected effect on the £6m/yr investment strategy, as retrofit investment was maximised in the early years. 91% of retrofit investment from 23/24 was hastened to 22/23, where retrofit investment swelled 181%, minimising the overall tax expenditure. An extra £1m in retrofit budget was allocated to 22/23, meaning 100% retrofit expenditure in that year. In many ways, the tax has the desired effect by encouraging swifter transition away from R-404A to <2500 GWP refrigerants, the clear goal of current legislation. Interestingly though, the CO_2e emissions reduction observed, under the tax levels tested, were only 1% lower than the baseline model. This indicates that, though the shifts in investment observed may be minimising cost, the influence of operational savings using lower GWP refrigerants is not sufficient to impact emissions. The lower emissions-reduction achieved by minimising CO_2e than with the carbon tax also suggests further legislation, within the existing frameworks, is unlikely to significantly hasten emissions reduction. Instead, informed strategic decision making and only a modest £900,000 (1%) increase in capital investment can achieve 2% greater reduction. However, though these extra gains can be important, the existing regulation is broadly effective in promoting the necessary change.

Considering the intermediate 'French level' of taxation, the total tax liability up to 2030 is over £30m for the BAU £6m/yr budget and over £6.3m for the £50m/yr budget. This is due to a significant shift away from HFCs with the higher investment. When instead tailoring the investment strategy to the introduced tax, the reduction in tax liability from BAU £6m/yr is £2.2m and under £1m for £50m/yr. This is relatively small because of the restriction placed on both investment strategies by the legislation and risk targets, as discussed previously. This demonstrates that the best way to mitigate a similar tax is to focus on transition to R-744 systems, potentially using the further tax mitigation achievable as a motivation for increasing the budget towards the upper £50m/yr.

Analysing the total investment and overall savings over the time horizon provides supporting evidence for these transition strategies. A tax level equal to or above the 'France' scenario would result in a significant growth in overall savings when compared with no action. For example, the proposed investment strategy under a 'France' tax would result in a net return on investment, when considering the operational savings and capital cost of almost £10m. This is a signifcant finding considering the vast majority of the strategies employed do not see returns on investment. Positive return on investments is not expected given that the transition away from R-404A is driven by legislation and system performance, not profitability. Similarly the investment strategy using a £50m/yr budget sees overall cost (investment less savings) decrease by over £70m.

To conclude, these findings demonstrate that in the event of taxation policy the investment strategies suggested are robust enough to reduce the tax liability associated with the refrigerants and in fact place the supermarket company in a strong position, relative to BAU.

4.4 R-449A Price

Having understood the implications of taxation based on GWP, the impact of refrigerant pricing on optimal investment is interesting to contrast. The already strong uptake of retrofitting with R-449A systems means the industry may end up over-reliant on this single refrigerant and, as regulatory phase-outs commence, and prices rise, companies could be left exposed. The £50m/yr model therefore behaves in-line with expectation as minimal baseline investment in retrofitting means significant changes were not observed. However for the £6m/yr model, as the R-449A price increases, retrofit investment in years 26/27 and 29/30 rises to 3136% and 438% respectively, for the highest price scenario. The 47% and 97% retrofit investment reduction in years 20/21 and 21/22 respectively is expected with the model maximising operational savings available from R-744. High R-449A prices slash operational savings of retrofitting. The model though still must ensure complete transition of all R-404A systems by 2030 and, as such, late retrofit investment is forced. Therefore, R-744 is preferred in early years to maximise the available savings, and retrofitting is pushed back. The £6m/yr budget, under high R-449A prices, is therefore a potentially risky investment strategy, as high R-449A price may not realsitically encourage late retrofit investment. A higher budget may be more appropriate to allow R-744 system installation and reduce business exposure to further R-449A price volatility. The placing of late retrofit investment in years following implementation of phase-down regulation is an interesting result as, although in this instance the retrofit investment may not be advised, the under-lying logic in delaying investments from years prior to phase-down is sound. Prices have repeatedly been observed to inflate in anticipation of phase-down dates and subseqeuntly over-correct.

To understand the financial impact of an R-449A price rise, the operating costs of the baseline model under high-prices can be compared to those of the tailored high-price strategy; the high-price investment strategy is the optimum under the scenario and costs will be slightly inflated if the BAU strategy is implemented. With a £6m/yr budget the operating costs over the period will increase by almost £17m whereas with the implementation of the £50m/yr model the increase would be just over £3m. This is a result of the signficant reduction in reliance on R-449A, with greater investment in R-744.

4.5 New HFC systems

The baseline models have been used to analyse whether the company's current strategy of installing only R-744 new systems (both for upgrades and new supermarkets) is optimal, or whether new HFC systems should be considered. These models showed no investment in new R-449 systems over R-744. This occurs because the difference in the capital cost is marginal compared to the difference in future operating savings, due to the price discrepancy between these refrigerants.

This result confirms the supermarket company's currently employed strategy and may be used in the future to justify investment in natural refrigerants.

4.6 Other Considerations

4.6.1 Refrigeration Banking

As discussed in section 3.10, banking R-404A removed from refrigeration systems is a significant resource, particularly in the period 2020-30. The bank has been analysed post-optimisation to ensure it is providing a feasible solution to the estate's demand for reclaimed refrigerant.

Analysing the £6m/yr and £50m/yr baseline models confirms the hypothesis that bank level will significantly exceed demand, especially with the low number of R-404A systems approaching 2030.

Contrasting the two investment levels, £6m/yr sees an accelerated growth in the bank level compared with £50m/yr, due to the rapid early-years removal of R-404A via retrofit. This is matched by a faster decline in the estate's demand. In both cases there is a significant gap between the level and the yearly demand, arriving at 29/30 with a bank level of 190 tonnes for £6m/yr and 140 tonnes for £50m/yr. The remaining level will therefore need incinerating, having already incurred storage costs up to 2030. However, the financial opportunity of this reclaimed refrigerant is heavily dependent on market conditions and agreements with the contractors. Even if R-404A cannot be traded for fresh refrigerant, with the market value of R-404A as forecast in section 3.8, the bank has the potential to add value of ~£10m, including 2030 incineration costs. A trading agreement with the relevant contractor, pursuing options described in section 3.10, could further increase the value of this strategy.

The recommendation therefore is to continue the company's current banking strategy since it provides the necessary source of reclaimed R-404A for estate maintenance, without significant costs. This holds even if a large bank of refrigerant is stored unnecessarily and incinerated. However, it is highly advisable to monitor

bank level, estate demand, market conditions and potential trading agreements to investigate early incineration and minimise costs.

4.6.2 Store Layout

The company's estate-wide template for supermarket layout was recently changed and, as of 2008, they have been updating legacy stores when convenient. Implementing the layout change comes at a significant cost in lost sales with disruption resulting in diminished display capacity. Combining with a refrigeration system update can therefore effectively halve the combined interruption. When system updates are recommended in stores, if layout has not been updated, these changes should also be implemented.

4.6.3 Future of Retail

There is an uncertain outlook for the food-retail industry, with the increasing penetration of e-commerce in most consumer-goods sectors generating concern. There is the possibility of an industry shift whereby supermarket floor-space is no longer of such importance. Convenience stores and large outer-city distribution centres for online-sales could dominate, however a detailed analysis of the food-retail industry would be required to reliably predict such changes. This is well beyond the project scope but is certainly a factor for companies considering refrigeration system investments. This is shown in the study by refrigeration systems being run past recommended lifetimes, postponing investment to first observe market behaviour.

5 Conclusions

The various stakeholders with an interest in this project have some crucial learnings. Environmentally, the best returns in emission reduction are achieved through the high £50m/yr budget, albeit averaging only 7.56m/yr across the second half of the 12-year investment horizon. Almost entire investment is in new R-744 systems. This strategy also best mitigates business-risk, important to senior management, whilst maintaining course for long-term CO_2e emission reduction targets. The commitment to immediately investing heavily in latest technology, a result of the estate's poorly-performing supermarkets, is the reason for the model's success.

However, the supermarket company's current spending levels leave the overall state of their supermarket refrigeration systems at significant risk of downtime and lost revenue. Increasing spending will mitigate this risk and the extent to which this is done is dependent on senior management. The current spending level does however still leave the company well placed to adapt to any future, more aggressive regulation. There is a crucial balance to be struck between minimising expenditure on refrigeration system upkeep and mitigating business-risk, inherent in low-performing refrigeration systems, which itself can prove costly. Further research quantifying revenue losses would therefore be illuminating, and with appropriate data, this could be subsequently optimised upon.

Additionally, the potential for e-commerce to penetrate the food-retail market adds further uncertainty when investing in expensive new systems. Favouring retrofit until further indicators are available may therefore be an attractive strategy. Again, this would expose the company to business risk. To contrast, if R-449A price becomes prohibitively high, the increased operating cost means new R-744 systems may be favoured. This would instead reduce business risk, however the £6m/yr budget may not be sufficient to support such an investment, whilst still transitioning all systems away from R-404A by 2030.

This research also aimed to consider the potential to invest in new R-449A systems, in place of R-744, given the slightly lower system cost. However, in all baseline models, no investment in this technology was allocated due to the higher operating costs.

In general, necessary business decisions will lead, in varying degrees, to significant reductions in a major food retailer's carbon footprint. This is a direct consequence of thorough legislation and its effective implementation. R-404A can be successfully phased-out, and a refrigerant bank should be used to protect against subsequent shortages during the transition. Maximising value from the bank would be a valuable focus for further study. Additionally, the falling price of the relatively new R-744 refrigeration technology means it is economically preferable to installing new R-449A systems, despite the latter's slightly cheaper capital cost.

6 Acknowledgments

We would like to thank Dr. Salvador Acha for his amazing support and guidance throughout this project and Romain Lambert for his technical help when developing the optimisation model.

7 References

[1] Why Set a Science Based Target? (2018). Retrieved from Science Based Targets: https://sciencebasedtargets.org
[2] UN (2016). The Kigali Amendment to the Montreal Protocol.
[3] Parliament, European. (2014). Regulation on Fluorinated Greenhouse Gases. EU.
[4] Chua, C. S. (2018). Future of grocery retail shopping: challenges and opportunities in e-commerce grocery shopping. Massachusetts Institute of Technology.
[5] I.P. Koronaki *et al.* (2-1 Refrigerant emissions and leakage prevention across Europe – Results from RealSkillsEurope project
[6] Waabis, M. (2018) Supermarket Store Outlier Analysis, Dpt.of Chemical Engineering, Imperial College London.
[7] Committee, H. o. (2018). UK Progress on Reducing F-gas Emissions. House of Commons.
[8] Department for Environment, F. a. (2018, September 13). Using and trading in fluorinated gases and ozone depleting substances if there's no Brexit deal. Retrieved from Gov.uk.
[9] Commission, E. (2012). Energy Roadmap 2050. EU.
[10] Zhao, Z. e. (2018). Low-carbon roadmap of chemical production: A case study of ethylene in China. .
[11] Caritte, V., Acha, S., & Shah, N. (2013). Enhancing Corporate Environmental Performance Through Reporting and Roadmaps. Wiley Online Library.
[12] R744.com. (2018, October 9). French Parliament Pushes for HFC Tax Adoption. Retrieved from R744: http://www.r744.com
[13] Öko-Recherche. (2015). The new F-gas regulation.
[14] EPEE Global. (2018). Stay in business: Stop Installing R-404A/R-507A!
[15] UN, I. P. (2018). Special Report: Global Warming of 1.5C.

Corrosion-Resistant Sol-Gel Coatings for 304 Stainless Steel Cookstoves

George Booth & Richard Metcalfe
Department of Chemical Engineering
Imperial College London, United Kingdom

ABSTRACT: TiO_2 coatings were applied to 304 stainless steel using the Pechini process of sol-gel production for the purpose of increasing the corrosion resistance of the metal used to make Prakti clean cookstoves. Different pre-treatment, coating, drying, and calcining methods were investigated and the results tested with SEM imaging, EDX analysis and Raman spectroscopy. The most effective pre-treatment method for the surfaces was silicon carbide scrubbing hand pads followed by washing with deionised water. Applying a thin coating with a spatula, imitating industry-scale roll coating, gave the most even and uniform surface coating with minimal surface shrinkage of the gel, and when the gel was layered with inter-stage drying the best overall coating was observed. Once applied, the gel was dried in an oven at 100°C for one hour before calcining at 500°C for one hour with a 6°C/min ramp. EDX analysis confirmed the presence of titanium on the surface. Whilst SEM showed signs of surface cracking, there was visibly less cracking on multi-layered samples compared to single-layer applications, and on the layered samples there was titanium identified by EDX in the crevices. Initial combustion tests proved successful, with coatings remaining after burning over a Prakti cookstove for one hour.

1 INTRODUCTION

In the pursuit of alleviating the poverty gap across the world and empowering women in impoverished countries, Prakti is pushing towards efficient, corrosion resistant, and cheap cookstoves. These long-lasting cookstoves will allow families access to cheap, efficient cooking, increasing life expectancies, as well as liberating more disposable income to spend on food and education. Currently it is estimated nearly three billion cookstoves or open fires are used to cook with in areas with poor ventilation in developing countries. [1] Open fires often lead to uncontrolled and incomplete combustion, which increases the evolution of incomplete combustion products such as carbon monoxide and soot, which can have serious negative consequences to health. In addition to physical damage to the alveoli within the lungs, the NHS advise that ”long-term exposure to low levels of carbon monoxide can also lead to neurological symptoms”. [2]

Although Prakti cookstoves are twice as efficient as traditional open fires in fuel combustion, [3] there is a serious threat to high-temperature corrosion which can compromise the integrity and the lifespan of their cookstoves. [4] Within the same Prakti research group, specific research in to corrosion of cookstoves as well as the computational modelling of cookstove systems is being conducted. Complementing this, this paper explores the development of a corrosion-resistant ceramic coating for Prakti cookstoves that increases the longevity of the cookstoves at a relatively low cost, and provides the basis for impregnation of catalytically-active compounds to promote oxidation of harmful incomplete combustion products to promote the lifespan and quality of Prakti products.

Figure 1: Example of a standard Prakti cookstove [3]

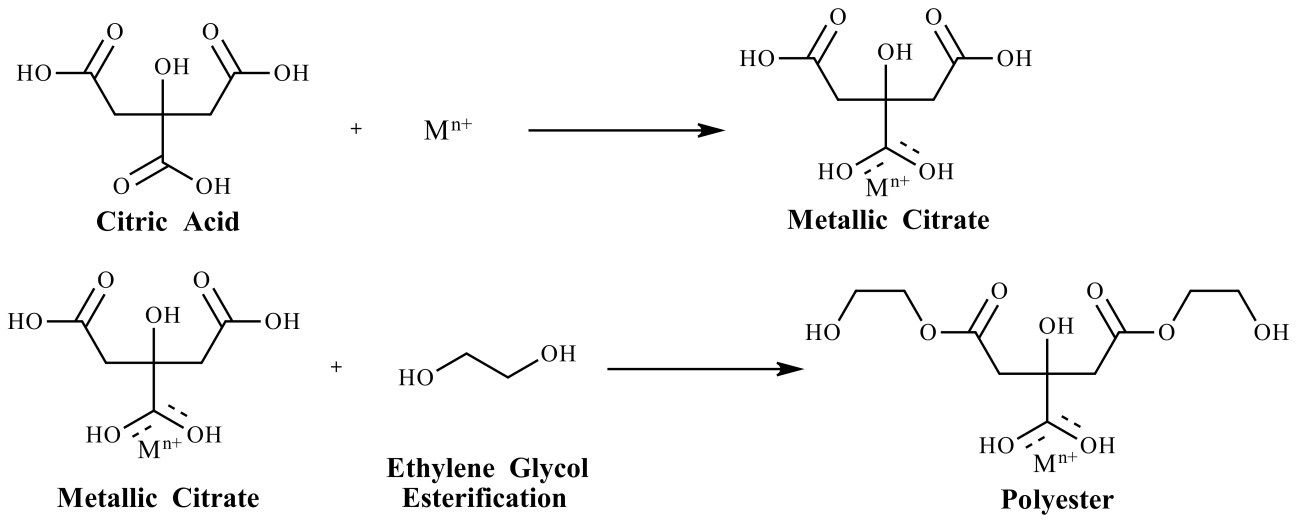

Figure 2: Pechini method reactions for sol-gel synthesis, re-created from L. Dimesso, *Pechini Process: An Alternate Approach of the Sol-Gel Method, Preparation, Properties, and Applications* [5]

2 BACKGROUND

2.1 *Sol-Gels*

The origin of sol-gel chemistry dates back as far as 1845, [6] however it remains a novel and increasingly popular method of ceramic production due to the low cost and versatility of its liquid precursors. [5–8] The general principle involves the chelation of metal ions to cross-linking polymers which can subsequently be dried to a solid surface. Calcination at high temperatures burns off the organic matter and oxidises the remaining metal atoms to form a protective, corrosion-resistant metal-oxide layer.

The Pechini method, as shown in figure 2, is a well-reported sol-gel method for the production of TiO_2 coatings through esterification of citric acid in ethylene glycol with titanium isopropoxide (TIP), and has been used to successfully coat solid titanium. [9] The titanium ions chelate to one of the acid groups on the citric acid, and following polymeric esterification and calcination, a well-structured lattice is formed. [5]

Ćurković et al. also investigated a further TIP-based sol-gel process via synthesis with an i-propanol solvent, nitric acid catalyst and acetylacetone as a chelating agent, which has shown improved corrosion-resistance of 304 stainless steel. [8]

2.2 *Viscoelasticity*

One downside of the Pechini method is that the polymeric gel displays rheological properties of a viscoelastic fluid. Viscoelastic fluids exhibit time-dependent strain, by demonstrating properties of both viscous liquids that strain with respect to time when stress is applied, and elastic fluids that will deform back to its original state once stress ceases. This can cause difficulties when coating a solid surface with a viscoelastic fluid as the fluid will exhibit surface shrinkage as the total volume decreases due to water evaporation, and additionally as the liquid deforms to its least energetic conformation. [10]

2.3 *Gel Coating*

The most prevalent method seen in literature is dip-coating; the slow removal, in the order of 1 mm/s, of samples after being dipped into the gel solution. [7, 11–15] This allows for solvent evaporation as a thin film is deposited on the surface. [10]

Alternatively, where the solvent is trapped in the system due to mass transfer limitations, the lab scale equivalent of roll coating has successfully been used to apply thin layers of gel to the surface. [9]

As micrometre-thin coatings can often develop micro-cracks in the coating which can compromise the integrity of the corrosion-resistant layer, the effect of increased layering has been explored by Yu et al. as a method to increase the durability of the corrosion-resistant coating and reduce the number of cracks on the surface. [12]

2.4 *Gel Drying and Calcining*

It is commonly reported that the gel is either dried in air or in an oven at a variety of high temperatures before calcination. [8, 11–14, 16, 17] As the gel dries into a solid its volume decreases, and once

the gel has adhered to the surface this leads to internal stresses in the system. If the gel is too thick or is not dried evenly, these stresses can cause deformation of the coating during calcination. [10]

Once the sample has been dried, a variety of different calcining temperatures and ramp speeds can be used to achieve different properties of the ceramic coating. Ramp speeds in the order of 5°C/min are most commonly used to avoid cracking or flaking of the surface. [7]

TiO_2 has multiple crystalline phases that form at different temperatures. When calcined at temperatures of 300-500°C an amorphous coating is formed, at higher temperatures around 500-600°C the anatase phase is formed, and at temperatures of around 700°C and higher the phase transitions to rutile. [14] The most desirable phase for corrosion resistance is the anatase phase as this displays enhanced corrosion resistance for the same amount of titanium deposited. [14]

2.5 *Metal Surface Pre-Treatment*

A commonly reported method and slight variations of such for stainless steel pre-treatment is to use abrasive silicon carbide disks of varying grit size, followed by polishing with diamond paste and finally washing in a heated sonicated acetone bath. [7, 8, 13–15] Alternative pre-treatment methods have been investigated, including an alkali bath to dissolve surface grease and residual lipids, [18] and heating the surface prior to treatment to improve surface wetting. [19]

2.6 *Corrosion*

Corrosion in fired cookstoves occurs when impurities such as chlorine and sulphur-containing organic compounds in the wood are vapourised and adhere to the surface of the stove. [20] When liquid water comes in to contact with the steel, these harmful chemicals dissolve, lowering the pH of the system to accelerate corrosion. If there is significant cracking or pitting in the coating, then it is easier for these chemicals to reach the iron in the steel and accelerate the local corrosion rate.

Corrosion in pits and crevices is accelerated compared to general corrosion, and can compromise the structural integrity of the material. Deep pits can lead to stress corrosion and cracking, reducing the lifetime of the steel. [21] It is therefore necessary to ensure that the coating layer is as even as possible, and that any crevices that do appear do not expose the steel.

3 METHODS

3.1 *Metal Preparation*

All samples were made from 1.2 mm thick 304 stainless steel. All experiments were conducted using 20 mm by 10 mm coupons, however, some edge effect tests were carried out using 50 mm by 50 mm coupons.

3.2 *Gel Preparation*

The Pechini method was followed to achieve a titanium-based gel using a titanium isopropoxide (TIP) precursor. Ethylene glycol was heated to 65°C before the citric acid was added. Once fully dissolved, the TIP was slowly added whilst vigorous mixing was carried out with a magnetic stirrer at a total molar ratio of ethylene glycol : citric acid : TIP of 1:0.26:0.028. The temperature was subsequently raised to 90°C for two hours with vigorous mixing to allow for a true homogeneous dispersion of titanium ions across the gel polymer network. Following this, the temperature was lowered to 60°C for another half an hour of mixing and then left to cool to room temperature.

Additionally, an alternative methodology achieved by Ćurković et al. first dissolved TIP in i-propanol, before adding acetylacetone to the mixture and finally adding the HNO_3 catalyst before vigorously stirring for two hours. The molar ratio of TIP : i-propanol : acetyl acetone : HNO_3 used was 1:38.3:0.7:0.02. [8] Instead of sonicating for half an hour as suggested by Ćurković et al., [8] as it was deemed unsuitable for potential scale up, the mixture was left exposed to air for varying lengths of time to investigate gelling times.

3.3 *Surface Pre-Treatment Method*

In addition to a control sample, three pre-treatment methods were investigated to assess the effect of pre-treatment on surface coverage of the gel; Scotch Brite silicon carbide hand pads, steel wool, and ammonium hydroxide. For the hand pads and steel wool pre-treatment, samples were scrubbed with their respective materials for two minutes, followed by a deionised water wash to remove surface contaminants. For the alkali pre-treatment method, samples were bathed in a 60°C solution of ammonium hydroxide for thirty minutes, followed by a deionised water wash to remove residual contaminants.

3.4 *Coating Method*

In total, four coating methods were investigated. Firstly, dip-coating was achieved by dipping one side of the metal coupon in to the gel and removing the excess using gravity by leaving to drain for approximately 30 seconds. Spatula application, or equivalent roll coating was achieved using silicon spatulas to evenly wipe the gel across the metal surface. Thin application methodology used a solid glass surface to remove more excess gel, whereas lastly, the ultra-thin method used laboratory paper to apply and wipe off excess gel.

3.5 *Multi-Layer Method*

In assessing the impact of multiple gel layers on coating durability, repeated coatings via either the spatula or ultra-thin coating method were conducted with intermediate oven-drying for one hour at 100°C.

3.6 *Drying Method*

Natural air-drying was investigated by leaving coated samples exposed to air at 20°C. Oven-drying through a laboratory-scale oven was investigated at temperatures between 70-150°C for up to two hours.

3.7 *Calcination Methods*

Two different calcining techniques were trialled. Initially, samples were calcined at 700°C with a ramp speed of 20°C/min. Later experiments used a lower temperature of 500°C with a ramp speed of 6°C/min. Both methods raised the samples to peak temperature for one hour before being left to naturally cool to room temperature.

3.8 *Analysis Methods*

Scanning electron microscopy (SEM) was used to analyse the morphology of the surfaces prepared, and energy dispersive x-ray (EDX) spectroscopy was used to analyse the elemental composition. Raman spectroscopy and imaging was used to analyse the surface composition and to detect if any crystalline structures had been formed. Contact angle measurements were taken to assess the surface wetting of the gel on the metal surface.

3.9 *Combustion Testing*

Samples that had been coated and calcined using different methods were tested over a Prakti cookstove burning at 450°C for one hour. The samples were then analysed using SEM imaging and EDX spectroscopy.

4 RESULTS & DISCUSSION

4.1 *Surface Pre-Treatment Method*

To quantify surface shrinkage of the polymer on the surface to find the optimal pre-treatment method, successful surface pre-treatment was determined by contact angle measurements between gel synthesised through the Pechini method and pre-treated 304 stainless steel coupons. A contact angle below 90° indicates sufficient surface wetting of the liquid phase on the solid surface, however a contact angle above this indicates poor surface wetting and provides evidence for potential repulsion between the two phases.

Contact angle measurements can be found in figure 3, where the largest angle is found for ammonium hydroxide pre-treated metals, both at the centre and the edge of the coupon, with contact angles greater than 90° at 0 minutes.

The control sample appears to have the smallest initial contact angle at the centre of the coupon at 67.87°, however a 6° increase is observed over a one hour period, showing an apparent increased repulsion over time. Conversely, both hand pads and steel wool resulted in an increased surface wetting over time, with hand pads resulting in an almost 50% decrease in contact angle at the centre over an hour period.

Across all pre-treatment methods, we see a noticeably higher contact angle at the edge of the coupon than at the centre of the coupon, suggesting edge effects are significant when coating solid surfaces. This provides an explanation for surface shrinkage away from the edge of our samples in combination with the viscoelastic properties of the fluid, as coatings on the edge are less favourable than at the centre of a sample because of a higher contact angle and therefore reduced surface wetting in this region. In reality, the surface area of the cookstoves in question are considerably greater than a 10 mm by 20 mm metal coupon, therefore edge effects can be considered negligible.

Findings show that hand pads were the best pre-treatment method and indicate that the abrasive qualities of silicon carbide effectively remove the top layer of the oxidised steel and any grease, revealing a clean stainless steel surface for effective coating that would allow good wetting of the gel. Steel wool offers competition to the silicon carbide scrubbing as it shows comparable starting contact angles both at the centre and the edge at zero minutes. However, silicon carbide

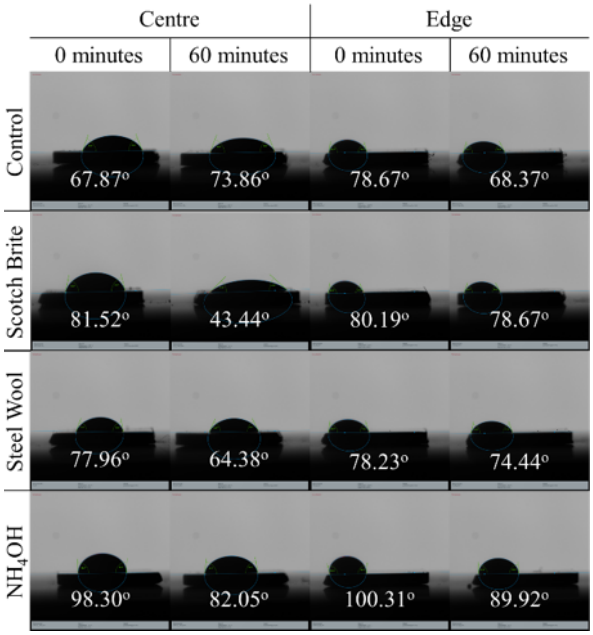

Figure 3: Contact angle measurements of gel on 304 stainless steel, comparing varying pre-treatment methods at different drop positions at 0 minutes and 60 minutes

provides a larger decrease in contact angle at the centre over the period of one hour as seen in figure 3, suggesting improved surface wetting can be obtained with this over steel wool pre-treatment. In addition to this, the lifetime of steel wool compared to the Scotch Brite product is considerably less as the steel wood shreds and breaks away more readily, which would require regular replacing despite how common it is in a laboratory environment. The extremely high contact angle shown by NH_4OH treatment, suggesting the surface is hydrophobic, could be caused by the base removing the surface grease but not removing any of the passive layer on the steel. This layer could have unfavourable interactions with the gel, leading to poor wetting. Alternatively, the NH_4OH may not have been strong enough to dissolve the grease present on the surface.

To further reduce the contact angle, samples pre-treated with silicon carbide hand pads were followed by a pre-treatment of a very thin layer of gel applied using the ultra-thin method. This resulted in the lowest observed contact angle both at the start (43.6°) and after one hour (28.0°). As there is a base layer of gel already applied to the surface, the subsequent drop applied has more favourable interactions due to the intermolecular attractions between the gel surfaces, causing increased wetting and a decreased contact angle. Therefore, this was sufficient evidence to further explore the effect of layering.

4.2 *Coating Method*

Coating methods were compared through their surface coverage before drying, as well as the amount of gel required to achieve the same coating, whilst observing surface shrinkage effects prior to drying and calcination. Dip-coating was found to yield a significantly thicker coating than alternative coating methods at around 0.3 mm thick, however there was some surface shrinkage once applied and dried. Additionally, once the samples had been calcined, a large amount of TiO_2 powder was found on the surface formed during the calcination process. This means that there is a considerable amount of material wastage and therefore immediate additional and avoidable costs incurred through this which can be mitigated by using a thinner coating.

Thin application methods yielded better initial surface coverage, with a considerably thinner surface coating at around 0.1 mm thick. However, this too underwent significant surface shrinkage upon drying to expose the metal surface underneath because this method caused inefficient and non-uniform application. Building on this, it was found that ultra-thin applications led to considerably less gel required for the same surface coverage, however surface shrinkage upon oven-drying led to poor distribution of the polymer across the metal surface, and as there was less gel on the surface, this led to a considerable uncovered surface area.

Spatula application was found to be the least objectionable across all methods explored, whereby a thin application of around 0.1 mm thick was achieved with reduced surface shrinkage compared to alternative methods explored.

When investigating the multiple layer methodology, samples with 1-5 layers were prepared to compare the thickness and appearance side by side of the differing number of layers. It was seen that the 4 and 5 layered samples that were coated with the spatula method saw the best surface coating that observed minimal wrinkling and surface shrinkage. The ultra-thin layers saw a good surface coverage, but after calcining the steel was observed to be coated only in minimal patches consistent with ultra-thin single-layer applications. Therefore, it was concluded that spatula application was the most effective coating method.

4.3 *Drying Method*

Drying methods were compared based qualitatively on the energy requirement for each method, as well as the overall time taken

to dry, in order to find an optimum suitable for industrial scale-up.

It was found that there was no observed drying after two weeks of natural air-drying, confirming this as an inefficient and unsuitable method. The gel appeared unaltered both in colour and viscosity, suggesting that the gel was stable at room temperature and therefore suitable for repeated usage from a single batch.

When investigating oven drying, similar results were obtained at 70°C, however at 150°C oven-drying there was visible burning or discolouration of the gel with trapped air bubbles in the polymer matrix, alongside significant surface wrinkling. However, a suitable medium was found at 100°C, whereby the gel dried effectively, without burning, within two hours. With a view to optimise this time and reduce energy consumption, continuous observation of the samples in the oven found that one hour at 100°C was sufficient drying time. However, it is worth noting that surface wrinkling was observed in all samples that dried successfully, regardless of temperature or length of time, although it was found that the wrinkling does not impact on the quality of the coating following calcination.

It is hypothesised that the gel did not air-dry because water is trapped in the system by the polymer network, and mass transfer limitations within this at room temperature prevent it from evaporating. This can also be observed at lower oven-drying temperatures, where there is insufficient thermal energy present to liberate the water molecules from the polymer matrix and facilitate drying. The discolouration of the gel at 150°C can be attributed to the aggressive heating of the sample, causing the top layer of the gel to burn. The evidence of bubbles trapped in the dried gel suggests the nucleation of bubbles from boiling within the gel due to the high temperatures, indicating a lower temperature is required. Therefore, it was found that 100°C for one hour was the most optimal solution that led to sufficient drying.

Surface wrinkling across all samples can be attributed to uneven heat distribution across the gel surface. As localised sections dry earlier than others, the gel is subsequently pulled towards these, leading to an uneven and irregular surface profile. This is also further proof of viscoelastic properties of the gel whereby the highly viscous polymer will conform to achieve the lowest energy state on the metal surface.

4.4 *Sol-Gel Method*

With the Pechini method showing some surface shrinkage even with the optimised preparation techniques, alternative sol-gel processes that produce TiO_2 coatings were investigated. The method presented by Ćurković et al. required the same TIP precursor for gel production but did not require any heating during the manufacturing process. [8] This has clear cost and energy benefits, and if this method could be used, a cheaper manufacturing route could be taken.

Despite multiple attempts at producing the gel, inconsistencies between batches in viscosity and colour indicated that this method is impractical in industrial scale-up. Furthermore, the i-propanol solvent is highly volatile and without careful handling can evaporate to leave behind orange powder deposits, which again would be unsuitable for somewhere with such a hot climate such as India.

On the other hand, we see the Pechini method results in a much more viscous gel, which is ideal when working with intricate geometries to reduce liquid run-off. Although challenges are met when dealing with the gel's viscoelastic properties, optimsing surface pre-treatment can overcome this. Furthermore, the gel formed by the Pechini method is much more stable at room temperature compared to the solution presented by Ćurković et al., with no visible change in rheological properties after two weeks. This is much more desirable for application beyond laboratory-scale production, and again is suitable for large batch productions of gel that can be used repeatedly.

4.5 *Calcination Method*

SEM analysis contrasting the calcination process at ramp speeds of 20°C/min versus 6°C/min reinforces results found by Liu et al., [7] suggesting better coatings with less cracking are observed when calcined at lower ramp speeds. It is clear to see in figure 5 a mixture of pitting and cracks on the surface of the sample calcined with a higher ramp speed. When comparing figure 5 with figure 7, the samples calcined at a lower temperature with a lower ramp speed have far fewer micro-defects on the surface. Whilst figure 7 shows multi-layered samples, this should not effect the formation of micro-defects, only the potential to reduce larger cracks and crevices. Therefore, it can be concluded that a lower calcination temperature and ramp speed results in a more uniform, protective coating.

When comparing the effect of calcination at 500°C and 700°C, we see an obvious

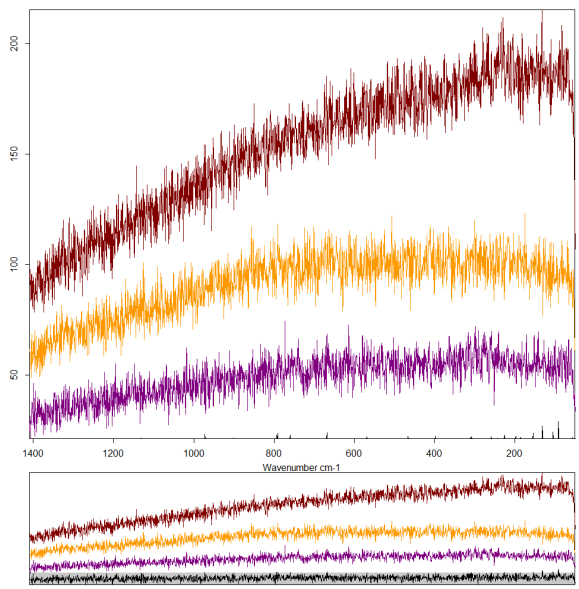

Figure 4: Raman spectrum of 5-layered TiO_2 coating applied using the ultra-thin application method

reduction in energy requirement at the lower temperature due to the reduced energy input required to achieve the coating. Furthermore, lower calcination temperatures also aim to achieve the more corrosion-resistant anatase TiO_2 phase over the rutile phase achieved at temperatures over 700°C, [14] therefore in terms of reducing production cost and achieving a higher quality coating, 500°C is the more desirable option.

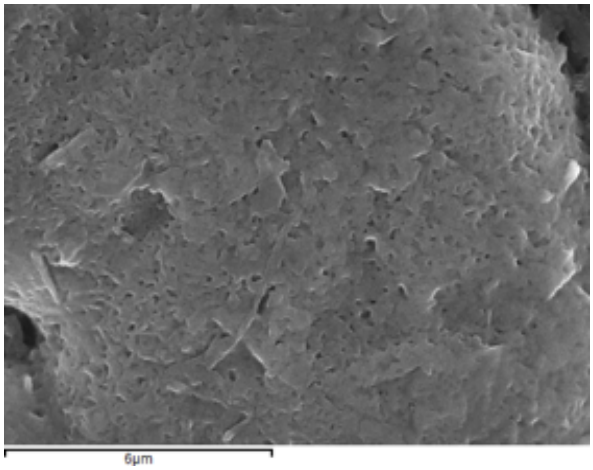

Figure 5: Micro-cracks and pits observed through SEM of a sample pre-treated with silicon carbide scrubbing, coated thinly, with 100°C oven-drying for one hour and calcination at 700°C

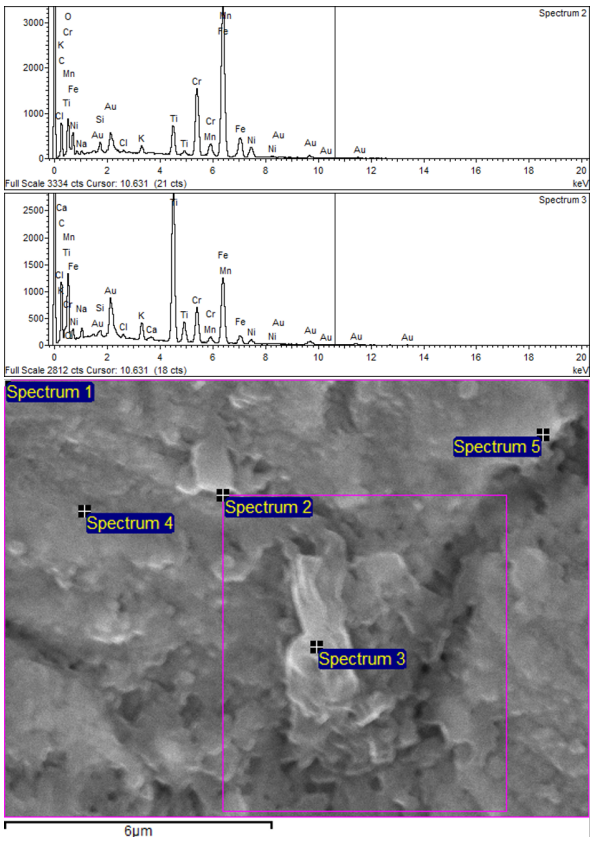

Figure 6: EDX spectra across coating crack (spectrum 2, top); EDX spectra of singular point (spectrum 3, middle); SEM image of a sample, post-combustion testing, that was pre-treated with silicon carbide scrubbing, with five layers of gel (bottom)

4.6 *SEM, EDX & Raman Validation*

Whilst the SEM images suggested a level and even coating as seen in figure 7, there were bumps and crevices. These crevices could limit the coatings ability to resist corrosion as they could be the start of cracks forming that could lead to to pitting and localised corrosion. The cause of these micro-cracks could either be drying or heating stress. Alternatively, the samples had to be cut down to 8 mm by 8 mm squares so they could be analysed through SEM. Cutting metal coupons to this size is achieved using a band saw or milling machine, during which large stresses are placed upon the surface, potentially causing these fractures in the coating. Coating pre-cut 8 mm by 8mm samples and imaging using SEM could verify the source of this cracking, however when comparing to literature we see cracking is common in thin sol-gel coatings and therefore cannot be initially ruled out as a potential root cause. [7, 13, 14]

When SEM images of single-layer coatings are compared to those of multi-layered samples,

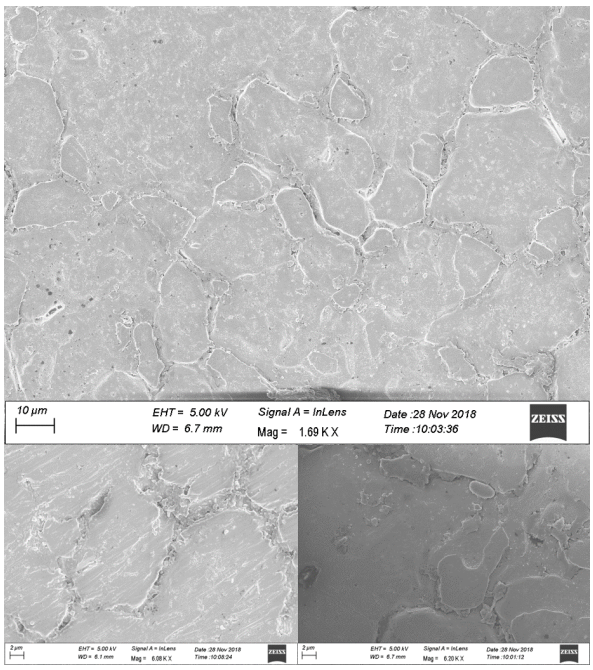

Figure 7: 4 layers applied with spatula, oven dried and calcined at 500°C (top); Ultra-thin application of 5 layers (bottom right) versus spatula application of 4 layers (bottom left), with both samples oven dried and then calcined at 500°C

as exemplified in figure 6 and figure 7, we see dramatically reduced cracking on the sample surface, suggesting a validation of previous research confirming that increased gel layering leads to increased durability and reduced cracking. [12] Although there are recognisable cracks, spectrum 2 taken across an example crack in a multi-layered coating shows there are strong titanium peaks, indicating there is still a protective coating here that does not expose the steel surface underneath to corrosion. Therefore, for a more applicable industrial application, repeated gel layers with intermediate drying would be most suitable.

Conversely, Raman spectra as seen in figure 4 reveal an inconclusive surface composition for a 5-layered ultra-thin application calcined at 500°C. Figure 4 predominantly presents noise, which is usually indicative of a non-crystalline structure or a lack of coating. However, EDX spectroscopy confirmed the presence of titanium, affirming that a coating was achieved. This is therefore indicative of an amorphous coating layer with no crystalline structure, which is an unexpected result as a 500°C calcination temperature should yield some anatase phase structure for the TiO_2, which would appear on the Raman spectrum. [14] Therefore, further optimisation of the calcination temperature and ramp-up speed is required to achieve the more corrosion-resistant anatase phase.

4.7 *Combustion Testing*

Visual observation of all samples heated in the cookstove showed an obvious resistance to the high temperatures of over 450°C, with no physical signs of corrosion. Comparable to the back of the metal samples that were not coated, there is a visible colour difference between the two surfaces, indicating very different physical interactions with the high temperatures. When observed using EDX, there was still a substantial peak for titanium for all samples post-combustion as exemplified in figure 6, indicating that the coating had remained during the hour-long exposure to combustion.

The presence of titanium peaks in EDX following combustion indicates a TiO_2 coating has successfully been made. Confirmed by the visual evidence of differing colouration between the treated and un-treated areas, we can see that the coating has been successful in protecting the metal underneath from corrosion. It is worth noting that after one hour of burning of untreated 304 stainless steel there is no visible corrosion product formation as there was no clear pitting or flaking from iron oxide production. Therefore, longer combustion tests would be required to validate this.

4.8 *Financial Analysis*

The main purpose of this investigation is to find an affordable coating that can increase the lifespan of the cookstoves, so that any additional cost to the consumer is returned to the consumer through the additional usage the cookstove would have. Initial lab scale costings were carried out to see if this coating would add significant costs to the consumer. Assuming a gel thickness of 0.1 mm the surface area coverage was calculated from a standard volume of gel produced. Costs were found from Sigma Aldrich for small scale quantities. [22]

The analysis led to a price of £9.50/m^2. If taken up in industry, costs will obviously be lower as reagents would be bought in bulk, but this initial costing gives a good idea into how applicable the coating would be. The total cost to the consumer currently is approximately £22 (INR to GPB exchange rate taken on 11/12/2018), and the surface area of the combustion chamber that would be coated is 0.11m^2. If the full additional cost is passed onto the consumer there would be a 4.7% increase in price.

As this small initial capital cost of around £1 would constitute a dramatic increase in the lifespan

of the Prakti cookstove, it would be pertinent to conduct future studies to quantify the extent of the increased lifespan compared to untreated cookstoves.

5 CONCLUSIONS

By investigating key synthesis, application and drying parameters in sol-gel coating methodology, an optimal solution was formed for the increased corrosion-resistance of 304 stainless steel Prakti cookstoves through a cost-effective and quick methodology reproducable in India. It was discovered that the Pechini method was the most efficient sol-gel methodology, and that silicon-carbide-based scrubbing provided the biggest decrease in contact angle between the gel and the surface, leading to the most optimal surface wetting for coating of the surface. For coating of the stainless steel, roll coating through application with a spatula provided the thinnest, most even coverage with minimum surface shrinkage and surface wrinkling upon drying, and to increase the durability of the coating, it was found that multiple spatula layers with inter-stage drying proved the most crack-free. Drying at 100°C for one hour provided the least energy-intensive route for the quickest drying time, which in industry will provide greater scope for efficient industrial scale-up. Although this optimal process works well, there is potential for further research in to alternative sol-gel methods and surface pre-treatment methods to further increase surface coverage and overcome surface shrinkage and surface wrinkling. However, strong steps have been made to ensure that Prakti cookstoves not only remain cheap, but will last for longer, and continue to provide consumers with the tools they need to lift themselves out of poverty.

6 ACKNOWLEDGEMENTS

We would like to express our gratitude to: **Mrs. Janet Skitt** for her assistance throughout the project and her insights into potential avenues for the research; **Mr. Parth Shah** for his assistance with use of the SEM and EDX analysis of the samples; **Ms. Martina Ivanova** and **Mr. Stanley Ho** for their use of the Raman spectrometer for our analysis of the surface coating; **Mr. Richard Wallington** for his assistance throughout the project with the cutting and sizing of the small samples used; **Ms. Lotte Weerts** for assistance learning LaTex.

REFERENCES

[1] Ewan Bloomfield. Gender and livelihoods impacts of clean cookstoves in south asia. Technical report, Nov 27 2014. URL https://cleancookstoves.org/binary-data/RESOURCE/file/000/000/363-1.pdf.

[2] NHS. Carbon monoxide poisoning¡br¿, May 23 2016. URL https://www.nhs.uk/conditions/carbon-monoxide-poisoning/.

[3] Prakti - smart stoves for smart cooks. URL http://prakti.in/.

[4] Michael P. Brady, Kelly Banta, John Mizia, et al. Alloy corrosion considerations in low-cost, clean biomass cookstoves for the developing world. *Energy for Sustainable Development*, 37:20–32, Apr 2017. doi: 10.1016/j.esd.2016.12.002. URL https://www.sciencedirect.com/science/article/pii/S0973082616303672.

[5] Lucangelo Dimesso. Pechini processes: An alternate approach of the solgel method, preparation, properties, and applications. *Handbook of Sol-Gel Science and Technology*, 2016.

[6] Y. Dimitriev, Y. Ivanova, and R. Iordanova. History of sol-gel science and technology. *Journal of the University of Chemical Technology and Metallurgy*, 43(12), May 27 2008. doi: 10.1002/chin.200912249. URL http://dl.uctm.edu/journal/node/j2008-2/1_Ivanova_Dimitriev_181.pdf.

[7] Jing-Xiao Liu, Da-Zhi Yang, Fei Shi, et al. Solgel deposited TiO_2 film on niti surgical alloy for biocompatibility improvement. *Thin Solid Films*, 429(1-2):225–230, Apr 2003. doi: 10.1016/S0040-6090(03)00146-9. URL https://www.sciencedirect.com/science/article/pii/S0040609003001469.

[8] Lidija Ćurković, Helena Otmai Ćurković, Sara Salopek, et al. Enhancement of corrosion protection of aisi 304 stainless steel by nanostructured solgel TiO_2 films, 2013. URL http://www.sciencedirect.com/science/article/pii/S0010938X13003557. ID: 271639.

[9] Jussara F. Carneiro, Jssica R. Silva, Robson S. Rocha, et al. Morphological and electrochemical characterization of ti/mxtiysnzo2 (m = ir or ru) electrodes prepared by the polymeric precursor

method. *Advances in Chemical Engineering and Science*, 6(4):364–378, 2016. doi: 10.4236/aces.2016.64037.

[10] C. J. Brinker, A. J. Hurd, P. R. Schunk, et al. Review of sol-gel thin film formation. *Journal of Non-Crystalline Solids*, 147:424–436, 1992. doi: 10.1016/S0022-3093(05)80653-2. URL https://www.sciencedirect.com/science/article/pii/S0022309305806532.

[11] C. Garzella, E. Comini, E. Tempesti, et al. TiO_2 thin films by a novel solgel processing for gas sensor applications. *Sensors and Actuators B: Chemical*, 68(1-3):189–196, , August 2000. doi: 10.1016/S0925-4005(00)00428-7. URL https://www.sciencedirect.com/science/article/pii/S0925400500004287#BIB7.

[12] Jiaguo Yu, Xiujian Zhao, Jincheng Du, et al. Preparation, microstructure and photocatalytic activity of the porous TiO_2 anatase coating by sol-gel processing. *Journal of Sol-Gel Science and Technology*, 17(2):163–171, Feb 2000. doi: 1008703719929. URL https://link.springer.com/content/pdf/10.1023%2FA%3A1008703719929.pdf.

[13] G. X. Shen, Y. C. Chen, and C. J. Lin. Corrosion protection of 316 l stainless steel by a TiO_2 nanoparticle coating prepared by solgel method. *Thin Solid Films*, 489(1-2):130–136, Oct 2005. doi: 10.1016/j.tsf.2005.05.016. URL https://www.sciencedirect.com/science/article/pii/S0040609005005134.

[14] Ainun Rahmahwati Ainuddin and Norhaslina Abdu Aziz. Thermal post-treatment of TiO_2 films via sol-gel for enhanced corrosion resistance. *ARPN Journal of Engineering and Applied Sciences*, July, 2014. URL http://www.arpnjournals.org/jeas/research_papers/rp_2016/jeas_0716_4663.pdf.

[15] A. Balamurugan, S. Kannan, and S. Rajeswari. Evaluation of TiO_2 coatings obtained using the solgel technique on surgical grade type 316l stainless steel in simulated body fluid. *Materials Letters*, 59(24-25):3138–3143, Oct 2005. doi: 10.1016/j.matlet.2005.05.036. URL https://www.sciencedirect.com/science/article/pii/S0167577X05004945.

[16] Dreidy Vsquez, Oscar Jerez, Rodrigo Schrebler, et al. Induction heating consolidation of TiO_2 sol-gel coating on stainless steel support for photocatalysis applications. *Periodica Polytechnica. Chemical Engineering*, 60(3):141, Jan 1, 2016. doi: 10.3311/PPch.8879. URL https://search.proquest.com/docview/1875395280.

[17] M. L. Zheludkevich, I. Miranda Salvado, and M. G. S. Ferreira. Sol-gel coatings for corrosion protection of metals. *Journal of Materials Chemistry*, 15(48):599–5111, Dec 2, 2005. doi: 10.1039/b419153f.

[18] Zuwei Feng. *Formation of Sol-gel Coatings on Aluminium Alloys*. PhD thesis, 2011. Increased organic content reduced shrinkage.

[19] Product Knowledge Network. Solgel ceramic coating. Technical report. URL http://www.productknowledge.com/pdf/PKN%20PDF_Sol-Gel%20Ceramic%20Coating.pdf.

[20] Mitsubishi Chemical Analytech. Determination of chlorine and sulfur in wood chips. URL https://www.mccat.co.jp/archives/003/201602/AQF_PP_030E.pdf.

[21] Don W. Green and Robert Howard Perry. *Perry's Chemical Engineers' handbook*. McGraw-Hill, New York [u.a.], 8. ed. edition, 2008. ISBN 9780071422949.

[22] Sigma Aldrich. Sigma aldrich. URL https://www.sigmaaldrich.com/united-kingdom.html.

Assessing the Environmental Impact of Building the Northwest Runway at Heathrow Airport

Mi Xia Yeo and Tu Yuan Neoh
Department of Chemical Engineering, Imperial College London, U.K.

Abstract This paper examines the environmental impact of the Northwest Runway (NWR) at Heathrow Airport (LHR) by comparing the expected CO_2 emissions near LHR with those outside of LHR. Previous work done by the Department for Transport (DfT) and Airports Commission (AC) studied the resulting change in airport passenger demand, along with associated changes in air travel, surface access and airport operations emissions for LHR and the rest of the UK. However, it was not known where specifically the CO_2 emissions attributable to LHR are generated, how individual regional airports contribute to the aggregated CO_2 levels, and the mechanism by which the change in passenger demand affects surface access emissions. Besides classifying airport demand by type to elucidate trends in demand migration, this paper quantifies the amount of CO_2 emitted near LHR by defining a Principal Study Area (PSA), and then compares it to the total CO_2 attributable to LHR. A case study is also done on the two largest non-London regional airports, Birmingham (BHX) and Manchester (MAN) airports, modelling how reduced demand from those airports would increase surface access emissions for LHR. It could be concluded that by 2050, (a) the CO_2 generated within the PSA would increase by 0.43MtCO_2 to account for 3% of the total UK emissions, while outside the PSA CO_2 increases by 2.41MtCO_2. (b) CO_2 attributable to LHR would increase by 4.57MtCO_2, accounting for 50% of total UK aviation emissions. (c) the total CO_2 emitted in the NWR scheme would have exceeded the Committee on Climate Change's (CCC) aviation emissions limit by at least 2.8MtCO_2.

Introduction

In 2012, an independent body known as the Airports Commissions (AC) was set up by the Department for Transport (DfT) to solve London's airport capacity problem, in line with growing demands of an expanding aviation market (Department for Transport, 2012). After narrowing the various expansion options to three short-listed schemes[1] and examining the economic and environmental impacts of each scheme, the AC concluded that the proposal for a new Northwest Runway (NWR) at Heathrow Airport (LHR) was the best solution. Consequently in 2016, the British government gave its approval to proceed with AC's recommendation, with construction works at LHR expected to begin by 2021 (Spero & Pickard, 2018).

This decision is highly controversial, with one major issue being the environmental impacts of the NWR scheme on the UK. Compared to the impact assessments done for other mega aviation hubs, e.g. Hong Kong International Airport's (HKIA) third-runway expansion which did not consider any resulting increase in greenhouse gas (GHG) emissions (Airport Authority Hong Kong, 2014), the AC appears to be thorough in covering this issue using state-of-the-art analyses. However, multiple organisations such as (AirportWatch, 2018) and (Friends of The Earth, 2008) have published their disagreement with AC's projections. Such peer reviews only challenge high-level assumptions of AC's methodology on environmental assessment, as they also cover a broad range of issues outside of environmental impact – they thus lack the depth of a rigorous, focused look into a specific environmental issue. Additionally, the DfT did not release all forecasts pertaining to its environmental assessments, creating an information gap which impedes granular analysis of available but aggregated forecasts.

This paper will focus on quantifying the environmental impacts after LHR's NWR expansion – specifically the increase in CO_2 emissions, which is in line with the DfT's assumption that CO_2 account for ~99% of GHG from UK aviation (Department for Transport, 2017). The change in carbon emissions will be evaluated from three main sources covered by the AC: Air travel (including cruise and ground movement components), airport operations, and passenger surface access journeys (Jacobs, 2014). While the AC is optimistic about the UK aviation sector meeting the 2050 carbon cap of 37.5MtCO_2 set by the Committee on Climate Change (CCC) (Airports Commission, 2015), many parties remain sceptical, believing that CO_2 emissions are currently set to overshoot the 37.5MtCO_2 target even without any new runways (AirportWatch, 2018). Moreover, it is unclear how much more CO_2 generated due to an expanded LHR would be emitted in other UK regions, hence the resulting carbon impact of the NWR scheme on the rest of the UK seems inadequately discussed.

In lieu of this, this paper intends to address the following problem statement: *How do the CO_2 emissions outside LHR compare with those at LHR upon expansion?*

Background

To determine how CO_2 emissions would change in the NWR scheme, it is essential to first understand the demand shift that will be experienced by each UK airport. The DfT has developed its own methodology to estimate future demand for each airport, involving the National Air Passenger Demand Model (NAPDM) and

[1] Shortlisted schemes include building a new runway at Gatwick (GAL), building a Northwest Runway at LHR (LHR-NWR), or extending the Northern Runway at LHR (LHR-ENR).

the National Air Passenger Allocation Model (NAPAM) (Department for Transport, 2009). The NAPDM first predicts a national-level unconstrained passenger demand based on several demographic and econometric drivers, which is fed into the NAPAM, where the demand is allocated across 31 of the largest UK airports plus four competing overseas hubs (Department for Transport, 2017), taking into account the airports' capacity constraints. While there have been slight changes to the model's assumptions since its inception in 2009, the methodology remains broadly similar and has been adopted within AC's assessments. Building upon DfT's estimates of future demand, this paper goes a step further to define and identify types of demand for the airports, so that the full effect of the NWR scheme could be understood in a more granular context, rather than just an absolute change in aggregate demand.

The AC has identified the following three major sources of CO_2 emissions in its carbon impact analyses, which this paper will adopt:

Table 1 Main sources of CO_2 emissions considered by the AC in its carbon assessment.

Sources	Scope covered
Air Travel	Ground movement • Fuel used in aircraft whilst taxing and holding on the ground during the Landing and Take Off cycle (LTO) • Estimated from Air Transport Movements (ATMs), i.e. departing and arriving flights Cruise • Fuel used during flight journey outside of the LTO • Emissions are attributed only to the departing airport's inventory, to avoid double-counting
Airport operations	Electricity use, gas use, fuel used in airport operational vehicles
Passenger surface access journeys	Car, bus and train travel by passengers to/from airport

When assessing the carbon impact of the LHR NWR expansion, previous analyses carried out by the AC and DfT forecasted the amount of CO_2 attributable to LHR and compared it against the emissions due to other UK airports. Using this approach, no physical boundary is defined for inventory accounting, rather any CO_2 that is generated as a direct result of an airport's existence will be attributed to that airport. For example, if a flight departs from LHR and lands in Paris, then the resulting CO_2 emissions for the whole flight journey is accounted as those of LHR. Similarly, the CO_2 emitted during a passenger's surface journey from their origin to LHR will count towards LHR's emissions.

While this approach is a good way of measuring LHR's contribution to the CO_2 levels within the UK aviation sector, it is unclear where exactly the CO_2 would be generated. Thus, to say that LHR as a physical point source would be fully responsible for increased CO_2 levels because of the NWR expansion would be misleading, since a lot more CO_2 that is attributable to LHR would actually be emitted outside of its locality. Being able to identify how much CO_2 is physically generated at LHR (vs everywhere else) would therefore help visualise the CO_2 reductions that ought to be achieved within that locality, so as to offset the additional CO_2 emitted within after the expansion. As such, this paper will define a Principal Study Area (PSA) encompassing a 2km boundary around LHR, and quantify the CO_2 generated within the PSA. While the DfT and AC have never undertaken such approach to modelling carbon impact, the AC has defined the PSA to be an area of sensitive properties likely to be substantially affected by the scheme, in line with the scope of AC's assessment for air pollutants like NO_x and particulate matter (Jacobs, 2015).

With regards to emissions due to passenger surface access, the NWR scheme will bring about two offsetting effects – increasing emissions for LHR and decreasing those for regional airports. In (Jacobs, 2015), there is published information on the surface access emission for all UK airports as an aggregate, as well as that specific to LHR. However, there is no information on the individual emissions of regional airports, hence a Freedom of Information request was submitted to the DfT to bridge this gap. While this request was ultimately fulfilled, the DfT did not disclose how each airport's demand shift contributes to the increase in LHR's surface access emissions. Therefore, as a representative case study of this relationship, this paper will address that gap via a self-developed model for two of the biggest regional airports by passenger numbers, Birmingham (BHX) and Manchester (MAN).

Methods

Demand type for each airport

Capacity expansion affects airport demand and in turn, emissions. Hence, understanding airport demand and how it changes with capacity is crucial to provide physical context to the change in carbon emissions.

The DfT's aviation demand model, NAPDM forecasts the number of passengers travelling from, to or through the UK, at a national-level. NAPAM then allocates this demand across each UK airport on both an unconstrained and constrained basis. Unconstrained demand is calculated from demographic factors such as the travel distance to airports and availability of flights, but not the actual capacity of airports to accommodate this demand – therefore is considered unrealistic (Department for Transport, 2009). Constrained demand on the other hand, accounts for the capacity constraints of airports by applying "shadow costs" which inflate air

fares, so that demand from over-capacity airports spills into under-capacity ones. This is therefore a more realistic estimate of airport demand.

Building upon DfT's predictions, it is possible to define two types of constrained demand received by each airport:

(a) Real Demand: Demand that could fly from a preferred airport.
(b) Spilled Demand: Demand that is forced to fly from a less preferred but under-capacity airport, because the originally preferred airport is full.

The relationship between real and spilled, constrained and constrained demand for an airport is as follows:

If $D_{unc} < D_c$, then $D_{real} = D_{unc}$, $D_{sp} = D_c - D_{unc}$
If $D_{unc} > D_c$, then $D_{real} = D_c$, $D_{sp} = 0$

Where D_c = constrained demand, D_{unc} = unconstrained demand, D_{real} = real demand, D_{sp} = spilled demand.

Air travel emissions by airport

While an aggregated estimate for air travel emissions is made publicly available by the DfT (Department for Transport, 2017), the individual emissions attributable to non-London airports are not known, as can be seen in Table 2:

Table 2 Existing gap within DfT's 2017 report, i.e. lack of disaggregated carbon emissions data for individual UK airports in the NWR scheme.

Information required	Scenarios	Included in DfT's report?
ATMs by airport	Baseline	✓·
	LHR NWR	✓·
Carbon emissions by airport	Baseline	✓·
	LHR NWR	×·

It is possible to extrapolate the carbon emissions for 8 of the largest regional airports outside of London[2] using the following equation:

$$E^{NWR}{}_{airport} = \frac{E^{Baseline}_{airport}}{ATM^{Baseline}_{airport}} \times ATM^{NWR}_{airport} \quad (1)$$

Where $E^{NWR}{}_{airport}$ and $E^{Baseline}{}_{airport}$ are the emissions for individual airports in the NWR and baseline cases respectively, while $ATM^{NWR}{}_{airport}$ and $ATM^{Baseline}{}_{airport}$ are the number of ATMs (flights) for individual airports in the NWR and baseline cases respectively.

[2] Airports include Birmingham, Bristol, East Midlands, Edinburgh, Glasgow, Liverpool, Manchester, and Newcastle.

Though this equation is capable of first-level approximation, it assumes that carbon emissions per ATM would remain constant for each airport in the NWR scheme, i.e. ratio of short to long-haul flights, fleet mix, type of fuels used, etc. would not change. The estimates obtained for each regional airport are then compared against DfT's predictions, which are later obtained after submitting a Freedom of Information (FOI) request.

Air travel emissions within PSA

Since the PSA is confined to just a small 2km radius around LHR, the CO_2 emitted within the PSA is assumed to only be associated with the take-off/landing cycle (LTO), covering Taxi-in/out, Take-Off, Climb-out and Approach, as depicted in Figure 1. The AC only considers components of LTO which are ground-based as its Ground Movement emissions (Jacobs, 2014). As such, additional emissions from the "elevation" that happens within the boundary also need to be included to estimate the total CO_2 emitted in the PSA. The following variables are used:

1) On the ground emissions: Quoted directly from (Jacobs, 2015).
2) Ground to elevation emissions ratio: Computed using CO_2 emitted on the ground, as well as during elevated components of the LTO cycle (Walker, 2017). The ratio is calculated for 2015, and is assumed to apply to all years in this analysis. This would likely be a slight overestimation as future technological advancements are ignored.

The total air travel emissions within the PSA can then be calculated:

$$E_{Total\ air\ travel,\ PSA} = E_{ground,\ LTO} \times \left(\frac{E^{2015}_{air,LTO}}{E^{2015}_{ground,LTO}}\right) + E_{ground,\ PSA} \quad (2)$$

Where E_{air} is air travel emissions, $E_{ground,}$ is the aircraft ground movement emissions and $E_{total\ air\ travel}$ is total air travel emissions.

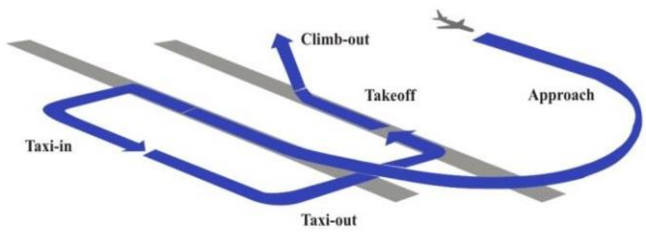

Figure 1 LTO-cycle assumed to happen within the PSA. Only the emissions from the Taxi-in, Taxi-out, and Take-off components are included in Jacobs' assessment. Figure taken from (T.G. Fregnani & Mattos, 2016)

Surface access emissions by airport

The data for surface access emissions by airport was not publicly available, but was obtained after submitting a Freedom of Information (FOI) request to the DfT.

Since BHX and MAN airports are the two largest regional airports by demand (see Table 6 in Supplementary Information), BHX and MAN are modelled as representative case studies to elucidate how the migration of demand towards LHR post-expansion would affect surface access emissions for BHX, MAN and LHR. In other words, the demand lost from BHX and MAN to LHR would have two effects, as shown in Figure 2: (i) Reduction in surface access emissions for BHX or MAN and (ii) Increase in surface access emissions for LHR.

(i) is calculated from DfT's data obtained via the FOI request:

$$\Delta E_{SA,airport} = E^{NWR}_{SA,airport} - E^{Baseline}_{SA,airport} \qquad (3)$$

Where $E_{SA,airport}$ is the surface access emissions for BHX or MAN.

(ii) is calculated from a set of variables shown in Equation 4. DfT's data from the FOI request contains a breakdown of where demand for BHX and MAN originates from. The amount of demand lost from each UK region post-expansion is then determined for those airports. Next, the most populous city within each region is chosen as a representative point source to calculate the average travel distance by rail and road to LHR. The other inputs to the model are regional transport modal shares for LHR (also from the FOI request), and DfT's estimates of emissions per transport mode. Assuming 1.58 passengers per vehicle (European Environment Agency, 2016), increases in surface access emissions attributable to LHR due to loss in demand from BHX and MAN can be calculated.

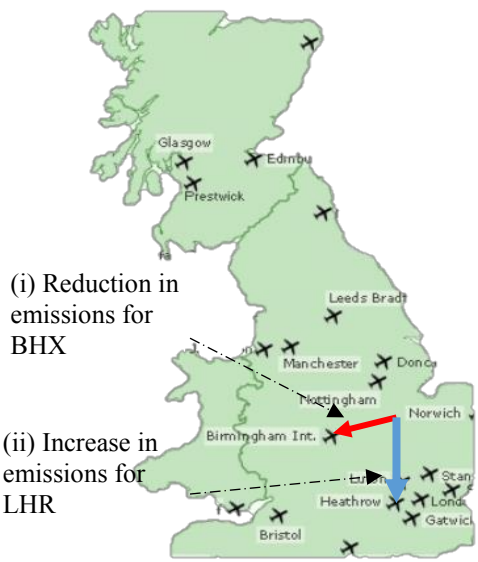

Figure 2 Two offsetting effects for surface access journey emissions in the NWR scheme, if demand shifts from BHX to LHR. Figure adapted from (Airports Commission, 2015)

$$\Delta E_{SA,LHR}\,[MtCO_2] = \sum_{i}^{region}\sum_{j}^{mode}\sum_{k}^{airport} \Delta D_{i,k}[mppa] \times M_i\left[\frac{mode\ trip}{mppa}\right] \times L_{i,LHR}\left[\frac{km}{mode\ trip}\right] \times I_j\left[\frac{MtCO2}{km}\right] \qquad (4)$$

Where $\Delta E_{SA,LHR}$ is the increase in surface access emissions due to lost demand from BHX and MAN, ΔD_i is the loss in demand for BHX and MAN by region, M_i is the modal share to LHR by region, L_i is the travel distance to LHR by regional point source and by mode

Surface access emissions within PSA

The methodology and working assumptions here are exactly the same as employed in Equation 4, with a few differences. L_i is 2km, i.e. the radius of the PSA, ΔD_i is the increase in demand for LHR, and M_i is that of LHR.

Airport operations

The AC has forecasted the carbon emissions due to airport operational energy use (i.e. electricity, fuel and gas) for LHR in both the baseline and NWR scenarios (Jacobs, 2014). However, since this analysis was not done for non-LHR airports, the operational emissions for all UK airports were linearly extrapolated using the same assumptions applied to LHR:

(i) Electricity use depends on passenger numbers (kWh/PAX)
(ii) Heating (gas) use depends on terminal floor space (kWh/m^2)
(iii) Fuel use in airport operational vehicles depends on number of flights (kWh/ATM)

For example in the NWR scheme, the emissions from electricity use for the entire UK airport system including LHR is:

$$E^{NWR}_{elec,all\ UK\ airports} = \frac{E^{NWR}_{elec,LHR}}{passengers^{NWR}_{LHR}} \times passengers^{NWR}_{all\ UK\ airports} \qquad (5)$$

Where $E_{elec,LHR}$ and $E_{elec,all\ UK\ airports}$ are the emissions due to electricity use for LHR and all UK airports respectively. Similar calculations are carried out for gas and fuel use to get the total operational emissions, both for the baseline and NWR scenarios.

Results and discussions

Demand shift and type for each airport

Table 3 compares the demand breakdown between four largest regional airports and LHR. Around one-third of BHX is made up of spilled demand, indicating that it absorbs excess demand from nearby overcapacity airports, most likely LHR. Hence, it is not surprising that when LHR expands, demand for BHX drops drastically (see Table 4) as passengers who originally wanted to fly from LHR but could not because of the over-capacity, could now do so after expansion. This provides an interesting contrast to airports having only real demand like MAN, where the loss in demand is considerably less.

Furthermore, Figure 3 indicates that after expansion, all regions will see an aggregated decrease in demand for their regional airports, except for London due to the drastic increase in LHR's demand. This would inevitably lower the availability of flights in those regional airports, as the reduction in passenger numbers would entail cancellation of flight routes due to low occupancies. These route cancellations would also mean further demand migration to LHR from regional airports, given LHR would now have much higher flight availability.

Table 3 Composition of baseline demand by airport. About one-third of BHX's demand is "spilled in" from an at-capacity LHR.

Airport	Baseline demand composition			Total baseline demand (mppa)		
	2030	2040	2050	2030	2040	2050
Heathrow	●	●	●	86.2	89.6	93.4
Edinburgh	◔	●	●	12.5	15.4	17.6
Birmingham	◕	◕	◕	18.2	27.4	32.9
Manchester	●	●	●	30.8	38.6	50.3
Glasgow	●	●	●	12.2	13.1	15.3

Key:
● Real demand
○ Spilled demand

Table 4 Change in demand by airport in the NWR scheme.

Airport	ΔDemand in NWR (mppa)		
	2030	2040	2050
Heathrow	45.8	45.4	42.6
Edinburgh	0.5	0.6	1.4
Birmingham	-3.2	-6.4	-1.9
Manchester	-1.8	-1.6	-5.3
Glasgow	-0.2	-1.1	-1.3

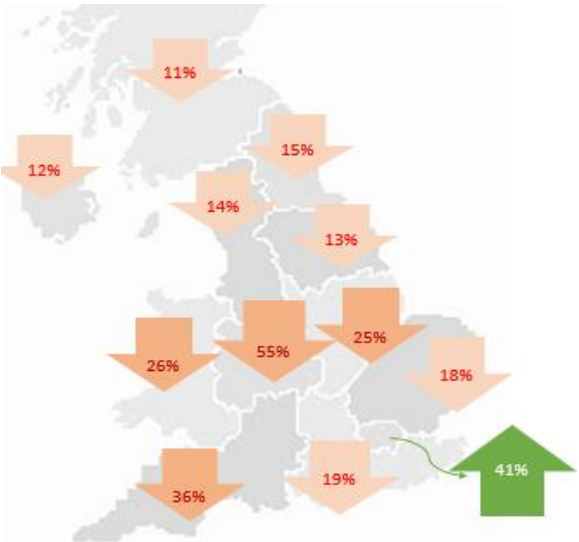

Figure 3 Change in demand by 2050 in the NWR scheme compared to the baseline case, obtained by grouping airports of similar regions. Grouping analysis done by (Aviation Environment Federation, 2015), using AC's forecasts.

Air travel emissions

An approximation of emissions attributable to individual airports obtained using Equation 1 was found to be in close agreement to DfT's data. Further details can be found in Table 5 of the Supplementary Information. Knowing the emissions due to individual airports, a graph comparing several airports with the greatest change in carbon emissions can be plotted, as shown in Figure 4.

Based on Figure 4, it is evident that CO_2 emissions attributable to LHR increase in the NWR scheme. However, over time the increase in emissions drops from 37% above the baseline case in 2030, to 27% in 2050. This trend could potentially be explained by better matching of aircraft to route flown, reduction in cruising speeds, improvement in fuel efficiency, and higher biofuel penetration (Airports Commission, 2015). Given the rather substantial decline in emissions from 2030 to 2050, further work needs to be done to determine if the assumptions made on technological advancements or efficiencies are realistic.

The opposite trends can be observed for the BHX and MAN airports, where CO_2 is predicted to go down upon expansion. This is not surprising since demand from these two airports will be "pulled" to LHR once it expands. It is also interesting to note that CO_2 is predicted to increase over time for BHX and MAN. If the same efficiency improvements for LHR apply to

every airport, then the increasing trend would imply that the increase in passenger demand received by BHX and MAN over the years (for the baseline and NWR case individually) far outweighs the reduction in CO_2 emissions from any technological assumptions. Comparing DfT's predictions for passenger numbers at LHR, MAN and BHX in the NWR case (Department for Transport, 2017), it can be seen that while demand increases steadily for BHX and MAN, LHR's demand almost plateaus by 2040, indicating that even with a third runway LHR would eventually be at capacity.

Overall, CO_2 emissions is expected to increase in the NWR scheme, as the increased CO_2 from LHR far outweighs the reductions that will be experienced in other UK airports.

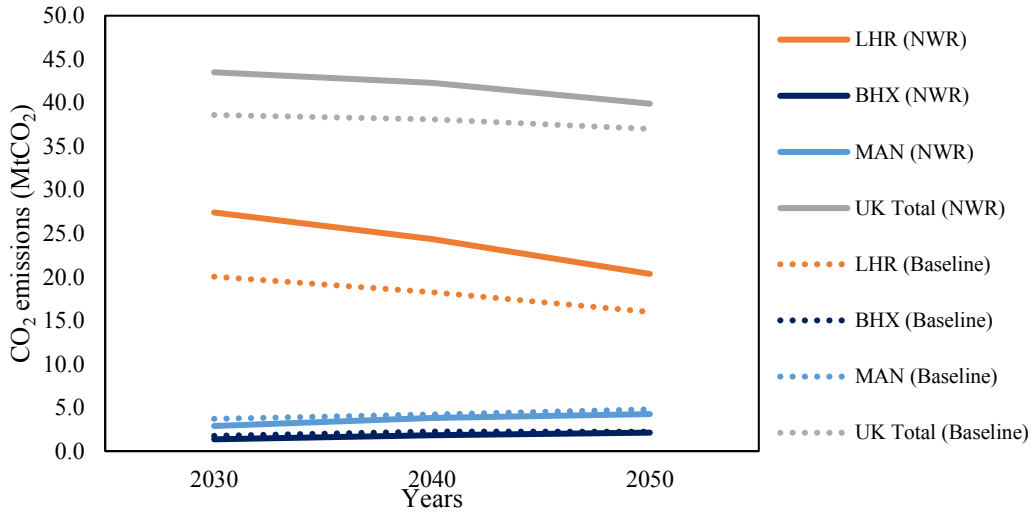

Figure 4 CO_2 emissions due to air travel in the baseline case and NWR scheme, for LHR, BHX, MAN and the whole of UK.

Figure 5 on the other hand shows a comparison of the CO_2 attributable to LHR, the proportion which is emitted within the PSA, as well as the CO_2 generated by other UK airports. After expansion, 60% of the total emissions in the UK aviation would be due to LHR as of 2030. Even in 2050 after taking into account efficiency improvements, LHR would still represent half of UK's total CO_2 emissions. Another interesting insight is that 4% of CO_2 attributable to LHR is emitted within the PSA. Considering the PSA only covers ~0.1% of the total flight distance for a long-haul journey (i.e. 2km compared to an average long-haul flight distance of ~5000km), it can be deduced that the LTO cycle is very carbon intensive process. Finally, merely based on air travel alone, CO_2 emissions would have exceeded the 2050 carbon limit of 37.5MtCO_2 by 2.8MtCO_2 in the NWR scheme. It is worth remembering that the actual emissions level will be even greater after including a multiplier for non-CO_2 greenhouse gases.

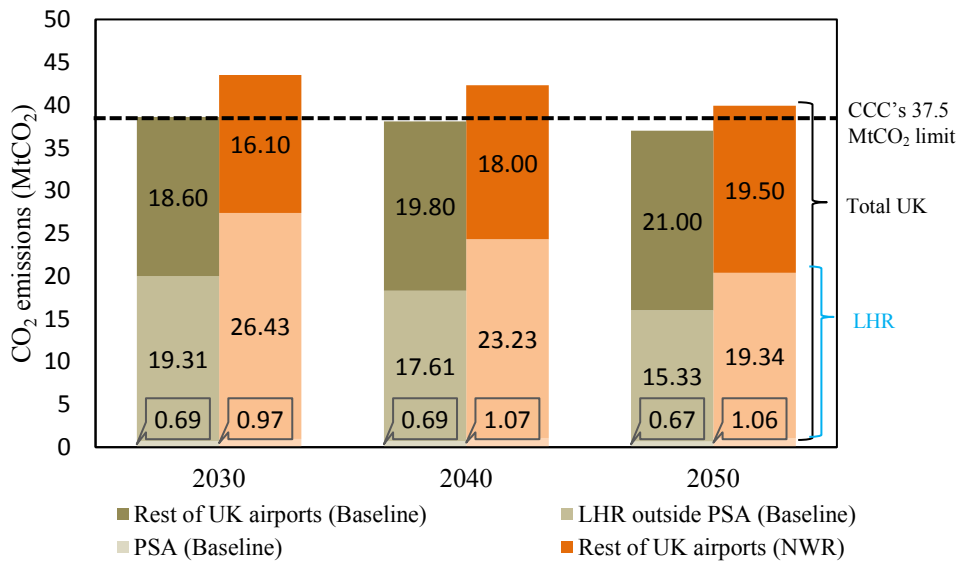

Figure 5 Breakdown of CO_2 emitted within the PSA, amount attributable to LHR and those generated by other UK airports due to air travel, both for the baseline case and NWR scheme.

Surface access emissions

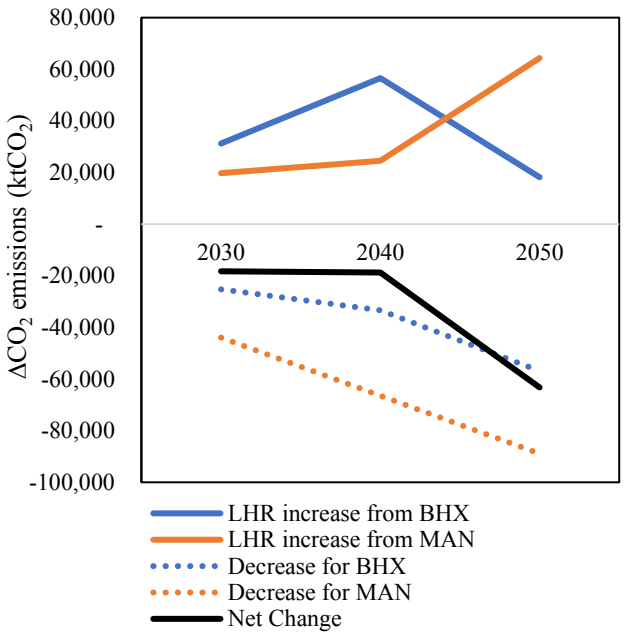

Figure 6 Reduction in surface access emissions for BHX and MAN, and the resulting increase for LHR.

As mentioned in the Methods section, the demand shift away from BHX and MAN to LHR engenders two opposing effects seen in Figure 6, which are decreases in surface access emissions for BHX and MAN, and increases in those for LHR. The resulting effect is a decrease in the cumulative surface access emissions for these three major airports. The case study model offers a few potential reasons for this phenomenon: (1) LHR has the highest public transport connectivity, having 70% of passengers taking public transport compared to around 50% for BHX and MAN, as per DfT's model assumptions. This means overall, more people are taking public transport after changing their choice of airport from regional ones to LHR. (2) DfT's data from the FOI request indicates that around 30%-40% of the loss in demand for BHX comes from London and South-East England. Since the travel distances between these regions and BHX are significantly greater than to LHR, these passengers are making shorter journeys post-expansion and hence generating less surface access emissions.

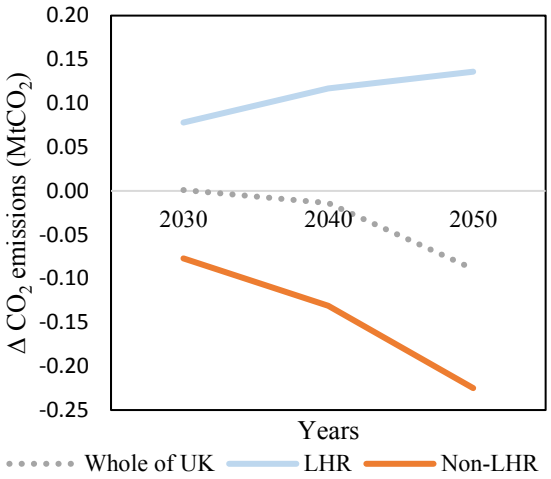

Figure 7 Change in surface access emissions for LHR, Non-LHR airports and Whole of UK airports upon expansion.

Trends in Figure 7 exhibit a good agreement with those shown in Figure 6. The drastic decrease in emissions between 2040 and 2050 for non-LHR airports appears to be driven by the trend seen in the BHX and MAN case studies, which is not surprising as BHX and MAN make up almost 80% of the change in non-LHR demand in 2050, further underlining the significant impact of the expansion scheme on these regional airports. The net effect of the expansion is a decrease in overall surface access emissions, which might be driven by the two factors as explained for Figure 6.

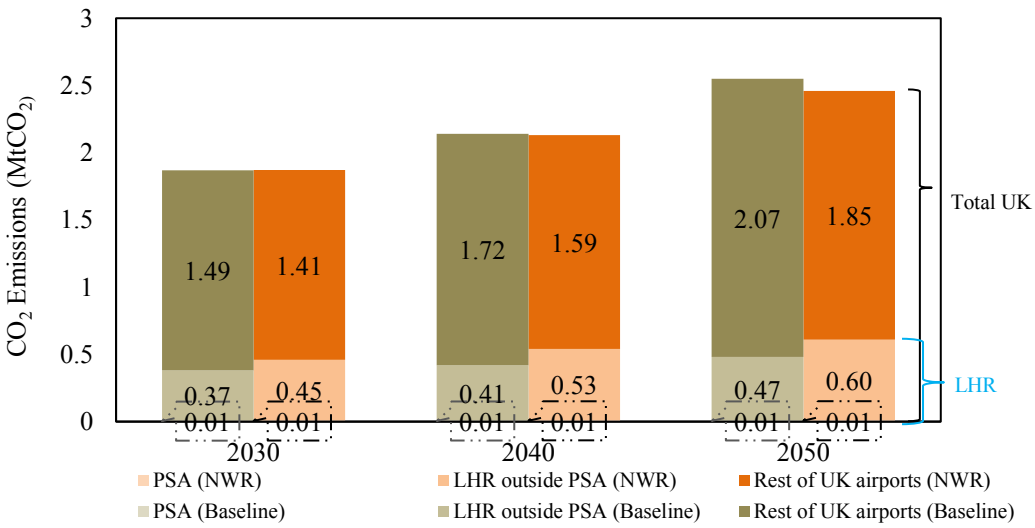

Figure 8 Breakdown of CO_2 emitted within the PSA, amount attributable to LHR and those generated by other UK airports due to surface access journeys, both for the baseline case and NWR scheme.

Interestingly, the trends in surface access emissions run contrary to those in air travel. As seen in Figure 8, the proportion of LHR's surface access emissions for the entire UK's is comparatively stagnant across time: 20% in the baseline case and increasing slightly to 25% post-expansion. A plausible reason for this stagnation is that while DfT has assumed certain future improvements in air travel carbon efficiency, i.e. biofuel penetration rate and fleet engine efficiency, surface access is assumed to be comparatively static with regards to technological progress. Additionally, the surface access emissions within the PSA (1%) is also in line with the proportion of the PSA radius (2km) to the average surface access journey length (200km to 400km). This particular discrepancy with air travel is sensible, since the carbon intensity of surface travel is intuitively uniform throughout the entire journey.

Airport operations emissions

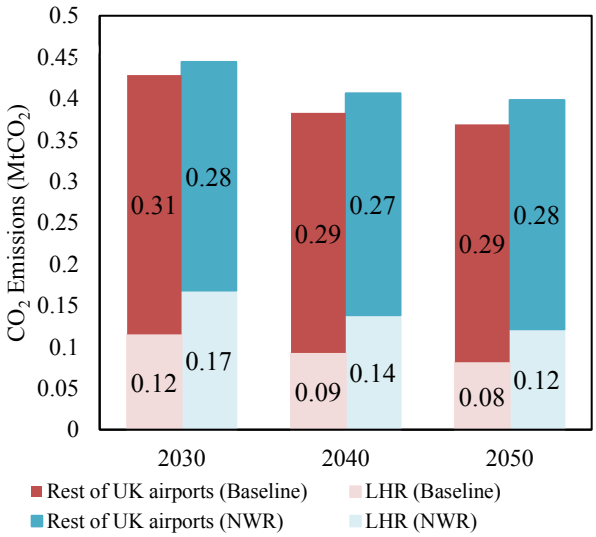

Figure 9 Carbon emissions due to airport operations for LHR and airports in the rest of the UK.

From Figure 9, it is not surprising that LHR's airport operations emissions would increase by around 50% after expansion, as all drivers of airport activity – passenger numbers, ATMs and physical floor space increase significantly.

Summary of change in emissions

Based on Figure 10, it is obvious that air travel accounts for the largest change in emissions out of the three sources, and evidently the magnitude of the increase in LHR's emissions is larger than the decrease for the rest of UK airports. This reiterates the point that expanding the new runway at LHR is going to increase the carbon emissions for the entire UK aviation industry.

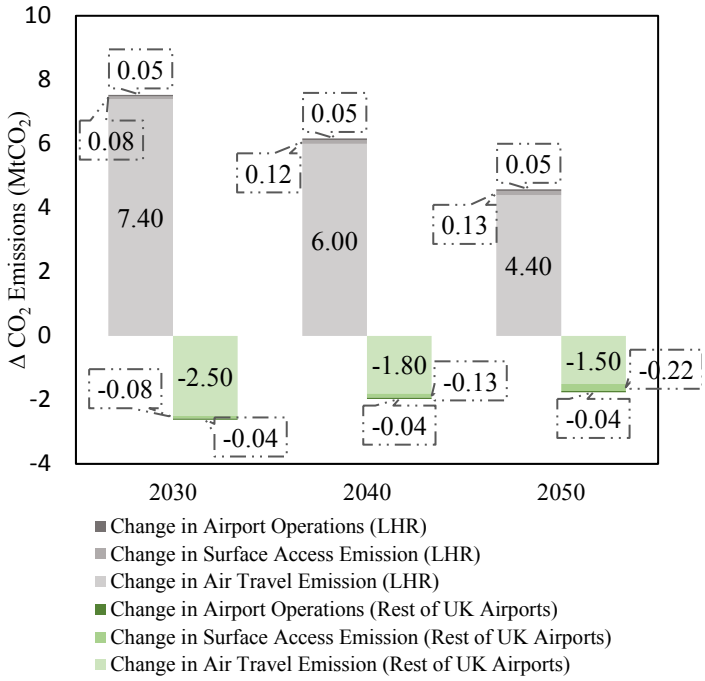

Figure 10 Changes in air travel, surface access and airport operations emissions for LHR and airports in the rest of the UK

Conclusion

By breaking down airport demand into real and spilled demand, a possible explanation was found for the apparent differences in the extent of demand migration from regional airports to LHR, whereby airports with real demand lose less demand to LHR than those with spilled demand. This migration of passenger demand brings about a drastic change in emissions for LHR and also regional airports, which was the focus of the framed problem statement – "How *do the CO_2 emissions outside LHR compare with those at LHR upon expansion?"* Subsequent analyses showed that in 2050, LHR would originally account for 40% of all UK aviation carbon emissions at 16.45$MtCO_2$, which then increases by 28% to account for 50% of the UK total after expansion. Using the other approach of defining a physical space of emission, the CO_2 emitted within the PSA in 2050 would increase by 0.43$MtCO_2$ upon expansion (accounting for 3% of total UK aviation emissions), while outside of the PSA the emissions increase by 2.41$MtCO_2$. Both methods however, confirm that the UK aviation industry will exceed its carbon emissions limit of 37.5 $MtCO_2$ in 2050 with the planned expansion.

A few interesting directions have been identified for future works. DfT's NAPAM model adopts carbon prices which inflate air fares to suppress passenger

demand, in order to limit the increased aviation emissions post-expansion due to the resulting surge in air travel demand. This methodology is principally inconsistent with the original motivation to expand LHR, which is to accommodate growing demand, thereby rendering this motivation quite self-defeating. A possible research angle would be to investigate alternative demand forecasting methods which do not curtail demand in order to meet a carbon emissions target. Additionally, DfT's assumptions on future advancements in carbon efficiency, e.g. biofuel penetration rates and aircraft fleet efficiency are quite optimistic, even unrealistic as deemed by other peer review literatures (Barasi & Murray, 2016). It would be interesting to then see how the emissions forecasts would compare if more realistic assumptions were used instead. Lastly, a new physical boundary for emissions could be defined in future work, looking at densely populated areas in LHR's proximity, i.e. South London and considering the effect of all aviation emissions – predominantly CO_2, NO_x and particulate matter in this area.

Acknowledgements

This research would not be possible without the guidance of Professor Hans Michel of Imperial College London, whose ideas helped shape our analyses and research direction.
We would also like to thank Caroline Ganzer who provided insight and technical expertise that greatly assisted the research, and for her comments on an earlier version of the manuscript.
Finally, we thank the DfT for their prompt response to our FOI request, without which it would have been significantly harder to analyse the surface access emissions of the UK airport system.

Supplementary Information

Table 5 Comparing CO_2 emissions by airport estimated via Equation 1 vs DfT's forecasts in the NWR scheme.

	Estimations via eqn. 1 ($MtCO_2$)			DfT's forecasts ($MtCO_2$)			% difference		
Airports	**2030**	**2040**	**2050**	**2030**	**2040**	**2050**	**2030**	**2040**	**2050**
Gatwick	3.5	3.3	3.0	2.9	2.8	2.7	-21%	-19%	-11%
Heathrow	31.1	28.0	24.5	27.3	24.3	20.3	-14%	-15%	-21%
London City	0.1	0.2	0.2	0.1	0.2	0.3	-49%	-6%	27%
Luton	1.0	0.9	0.8	1.0	0.9	0.8	3%	2%	3%
Stansted	1.2	1.3	1.4	1.4	1.6	1.7	15%	19%	13%
London	36.9	33.7	29.9	32.9	30.0	25.9	-12%	-12%	-16%
Birmingham	1.5	1.7	2.2	1.4	1.8	2.1	-9%	7%	-3%
Bristol	0.4	0.4	0.5	0.4	0.4	0.4	-12%	10%	-8%
East Midlands	0.4	0.6	0.7	0.9	1.0	1.1	54%	42%	40%
Edinburgh	0.6	0.8	0.8	0.7	0.8	0.8	6%	-2%	6%
Glasgow	0.9	0.8	0.8	0.9	0.9	0.8	-1%	5%	-1%
Liverpool	0.1	0.1	0.3	0.2	0.1	0.3	30%	25%	1%
Manchester	3.5	4.1	4.4	2.9	3.8	4.3	-21%	-8%	-3%
Newcastle	0.2	0.2	0.3	0.2	0.2	0.3	9%	10%	-15%
Larger regional airport total	7.7	8.7	9.9	7.4	9.1	10.1	-3%	4%	2%
Other regional	0.8	1.1	1.8	0.6	0.7	1.5	-53%	-54%	-22%
Non London Total	8.5	9.8	11.7	8.0	9.8	11.6	-6%	0%	-1%
Total	45.4	43.6	41.6	43.5	42.3	39.9	-4%	-3%	-4%

Table 6 Passenger demand by airport in 2016. Data taken from (Department for Transport, 2017).

Airports	Passenger demand (mppa)
Gatwick	43.4
Heathrow	76.0
London City	4.0
Luton	14.5
Stansted	24.5
London total	162.5
Birmingham	12.3
Bristol	7.6
East Midlands	4.8
Edinburgh	11.8
Glasgow	8.2
Liverpool	4.8
Manchester	26.8
Other regional airports	28.0
Total outside London	104.2

The organisation you are asking to provide this information:

Department for Transport

Subject of request

Aviation

Your request

I am currently working on a project with Imperial College London's Centre for Environmental Policy, analysing the projected changes in carbon emission caused by air travel and surface access in the London area vs. the rest of the UK following the expansion of Heathrow's North-West Runway (NWR).

With reference to the Carbon: Assessment report published by Jacobs in Nov 2014, we are presented with the following data on surface access emissions, at an aggregated level (pg 40-41):
1. Emissions due to surface access for 2026 – 2050 for baseline and Heathrow NWR forecast scenarios, tonnes CO2
2. Emissions due to surface access across the UK airport system, 2026 – 2050 for baseline and Heathrow NWR forecast scenarios, tonnes CO2

As for carbon emissions from air travel, the UK Aviation Forecasts report by DfT in Oct 2017 presents us with the following data (pg 145-146):
1. Carbon emissions by individual airports, baseline capacity, MtCO2
2. Carbon emissions on an aggregated UK level (Total UK) in the NWR scheme, MtCO2

However, I would like to understand how the disaggregated data for the surface access and air travel emissions attributed to individual UK airports would look like. This would essentially be an output of the National Air Passenger Allocation Model (NAPAM), which predicts where demand from each airports would come from, and hence, estimating the surface access emissions attributed to the journeys to those airports. In particular, it would be very helpful if I could obtain the following data:
1. Carbon emissions from surface access journeys attributed to individual airports in the UK, both in the baseline and NWR scenarios.
2. Origin of demand estimated for each airport (i.e. where – in the 455 zones within the UK as split by the Passenger Airport Choice Model – are the passengers travelling from), both in the baseline and NWR scenarios.
3. Carbon emissions from air travel by individual UK airports for the NWR scenario, having the same granularity as the baseline case.

Thank you for your help. I look forward to hearing from you soon.

Figure 11 Freedom of Information (FOI) request sent to the DfT.

References

Airport Authority Hong Kong, 2014. *Expansion of a Hong Kong International Airport into a Three-Runway System,* Kowloon, Hong Kong: Airport Authority Hong Kong.

Airports Commission, 2015. *Airports Commission: Final Report,* London: Airports Commission.

Airports Commission, 2015. *Economy: Carbon Policy Sensitivity Test,* London: Airports Commission.

AirportWatch, 2018. [Online]
Available at: http://www.airportwatch.org.uk/2018/01/beis-minister-admits-uk-aviation-co2-emissions-will-not-be-kept-below-necessary-37-5mtco2-level/

Aviation Environment Federation, 2015. All set for take off? Aviation emissions to soar under Airports Commission proposals. p. 10.

Barasi, L. & Murray, L., 2016. *Air traffic controls: the hidden costs of a new London runway,* London: Campaign for Better Transport.

Department for Transport, 2009. *UK Air Passenger Demand and CO2 Forecasts,* London: Department for Transport.

Department for Transport, 2012. *Airports Commissions membership.* [Online]
Available at: https://www.gov.uk/government/news/airports-commission-membership

Department for Transport, 2017. *UK aviation forecasts 2017,* London: Department for Transport.

European Environment Agency, 2016. *Occupancy rate of passenger vehicles.* [Online]
Available at: https://www.eea.europa.eu/data-and-maps/indicators/occupancy-rates-of-passenger-vehicles/occupancy-rates-of-passenger-vehicles

Friends of The Earth, 2008. *DfT Heathrow Consultation - Our Response,* London: Friends of the Earth UK.

Jacobs, 2014. *Carbon: Assessment,* London: Airports Commission.

Jacobs, 2015. *Air Quality: Local Assessment,* London: Airports Commission.

Jacobs, 2015. *Carbon: Further Assesssment,* London: Airports Commission.

Pickard, S., 2018. *Financial Times.* [Online]
Available at: https://www.ft.com/content/f848985a-7945-11e8-8e67-1e1a0846c475

Spero, J. & Pickard, J., 2018. *Financial Times.* [Online]
Available at: https://www.ft.com/content/f848985a-7945-11e8-8e67-1e1a0846c475

T.G. Fregnani, J. A. & Mattos, B., 2016. *Aviation and Electrical Road Vehicles.* Brazil, s.n.

Walker, C., 2017. *Haethrow Airport 2015 Emission Inventory,* Didcot: Ricardo Energy & Environment.

A Nash Equilibrium Approach to Understanding the Methionine Salvage Pathway

Shashi Hazra, Johnny Tsang
Department of Chemical Engineering, Imperial College London, U.K.

Abstract
The understanding of metabolite interactions in the methionine salvage pathway (MSP) serves as a basis for studies on cancer metabolism. The reliance of key metabolites on co-factor concentrations within the MSP was studied using a Nash Equilibrium (NE) model. The NE model is advantageous in that it considers competition between enzymes as well as participation of co-factors (rather than just key metabolites) in a metabolic network. The methodology used to study these concentration interdependencies involved considering a cell deficient of regular metabolite concentrations. Large sample trials of varied co-factor perturbations were then conducted to determine the optimum combination of co-factor perturbations required to drive key metabolite concentrations from deficient to regular levels. An optimum solution was found showing that perturbations to concentrations of methionine, ATP, glycine, spermidine, adenine, putrescine, adenosine and methylglycine were required in regulating concentrations of key metabolites in the MSP. This solution showed that almost all the key metabolites within the MSP could recover to regular concentration levels.

Background

Methionine is an essential amino acid that plays an important role in many cellular functions such as initiation of protein synthesis and methylation of DNA (Danchin, n.d.). It cannot be synthesised in mammals and thus needs to be consumed externally through food or supplements. Foods containing high amounts of methionine include eggs, chicken breast, fish and dairy (Schnekenburger & Diederich, 2015).

Methionine plays a key role in the Methionine Salvage Pathway (MSP) – a metabolic pathway that takes place entirely in the cytosol (Prikov, et al., 2008), (Albers, 2009). In the MSP, methionine is consumed through the utilisation of S-adenosylmethionine (SAM), which releases 5'-methylthioadenosine (MTA) that continues to regenerate methionine. As *de novo* synthesis of methionine is energetically intensive, the continuous regeneration of methionine from MTA is important in regulating intracellular conditions (Danchin, n.d.). Figure 1 shows a detailed representation of the MSP. Since methionine and SAM both feed into the methylation cycle, a coupled metabolic system of both the MSP and methylation cycle was depicted.

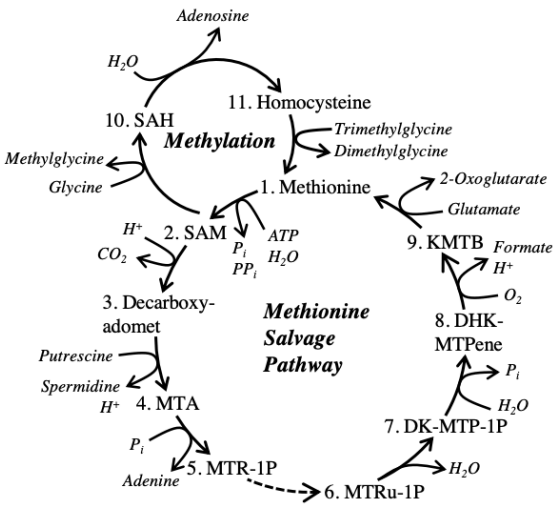

Figure 1. Schematic of the MSP (full set of reactions can be found in the Supplementary Information sheet)

Understanding the MSP and the relationship between its metabolites is important in understanding cancer metabolism. Many studies have shown that in many cancers, the human gene that encodes the enzyme S-methyl-5'-thioadenosine phosphorylase (MTAP), is often homozygously co-deleted due to its proximity to the CDKN2A tumour suppressor (Marjon, et al., 2016). MTAP is also the enzyme that catalyses the conversion of MTA to MTR-1P in the MSP. With MTAP absent in cancer cells, this effectively terminates the MSP and expectedly results in a build-up of MTA which has a toxic effect on both the cancer and healthy cells (Lucia & DiMaggio, 2018).

Restricting methionine to low concentrations has been proposed as a solution to prevent this accumulation in MTA. As such, MTAP-positive healthy cells can continue to regulate MSP without MTA accumulation, while MTAP-deficient cancer cells will suffer as the MSP cannot be regulated. It also should be noted that methionine cannot be restricted to extreme low concentrations. Studies have shown that methionine concentrations of at least 25 μM is required for cell proliferation and to meet regular physiological conditions (Mentch, et al., 2015).

However, there is currently limited understanding on the MSP and how the metabolites interact with each other. A firm understanding of the MSP serves as a basis to further study the potential benefits of restricting methionine even to extreme low levels. This paper focuses on developing a deeper understanding into the MSP by studying the inter-dependency between metabolites within the cycle.

Computational Approaches to Understand MSP

One of the reasons why there is limited information on the MSP is because of the limited amount of experimental data on regular physiological

intracellular metabolite concentrations. While experimental values often serve as a benchmark for accuracy, measurements of intracellular concentrations can be extremely time consuming – especially for pathways with large number of metabolites. On the other hand, a computational approach provides scalability to study all metabolites in a predictive manner. This would allow one to study metabolite concentrations over a variety of conditions to draw conclusions about the dependence of certain metabolites on others. The following sections discuss two computational approaches – Flux Balance Analysis (FBA) and Nash Equilibrium (NE). This paper uses an NE approach to study the MSP and the following sections justify why the NE approach was selected.

Flux Balance Analysis

Flux-Balance Analysis (FBA) is one of the most commonly used mathematical approaches to analyse the flow of metabolites through a metabolic network. It is a network flow problem that can be solved using two assumptions – steady state and optimality. The steady state assumption reduces the problem to a linear system of mass balance equations which act as constraints. The second assumption provides an objective function for this linear programming problem. The objective function selected can be some biological goal relevant to the context. Examples of objective functions include maximum output flux, minimum nutrient intake, and minimum ATP production (Lucia & DiMaggio, 2018). Finally, an upper and lower bound needs to be defined representing the minimum and maximum rates of flux for every reaction in the network. A mathematical representation of an FBA linear programming problem is presented below (Orth, et al., 2010).

$$\text{objective} \quad c^T v \tag{1}$$

$$\text{subject to} \quad Sv = 0 \tag{2}$$

$$v^L \le v \le v^U \tag{3}$$

This FBA problem seeks to maximise/minimise the objective function, $c^T v$, where c is a vector of weight coefficients, corresponding to how much each reaction contributes to the objective function. S is a stoichiometric matrix, while v is a vector representing the flux for each reaction in the network. v^L and v^U are the lower and upper bounds respectively.

One benefit of FBA in contrast to traditional kinetic models, is that it does not require knowledge about the enzyme kinetics or the metabolite concentrations in the system. However, because it operates in the flux plane without using kinetic parameters, it cannot predict metabolic concentrations (Orth, et al., 2010). In some studies, FBA was only able to predict the direction of change in concentrations (whether up/down) and even then, was only 70% accurate (Plata, et al., 2010). The need to present an upper and lower bound flux constraint is another drawback as it assumes some prior knowledge to the solution. Studies have also shown that FBA solutions are sensitive to the selection of these bounds (Lucia & DiMaggio, 2018). In addition, regulatory constraints cannot be modelled in the FBA approach. Finally, in crowded intracellular environments where metabolites are continuously produced, an element of competition between enzymes exists. These enzymes are competing for nutrients available to catalyse their own reactions and FBA does not account for that (Lucia & DiMaggio, 2018).

Introduction to Nash Equilibrium

Recently, Lucia and DiMaggio have proposed modelling metabolic pathways using a predictive NE approach from first principles. The NE model has already been applied to well-studied metabolic pathways such as glycolysis and the citric acid cycle. When compared to experimental data, the numerical predictions generated by the NE model showed good agreement with experimental measurements of metabolite concentrations. In addition, a study by Lucia and DiMaggio comparing FBA with the NE model for the citric acid cycle (Lucia & DiMaggio, 2018) demonstrated that the NE model was much more accurate in its numerical predictions of metabolic concentrations (Lucia & DiMaggio, 2018). The primary benefits of the NE Model over FBA is its ability to model concentrations, charge balances, and regulatory effects. It also considers the consumption/production of co-factors rather than just key metabolites as in FBA. In this paper, key metabolites are defined as a metabolite that is produced by a metabolic reaction and has a reaction that subsequently consumes it. On the other hand, co-factors are species that participate and assist these metabolic reactions. The key metabolites in MSP are numbered in Figure 1, while the co-factors are shown in italics.

Only one other study has applied an NE approach to the MSP. In that study, the focus was on validating the NE Model for the MSP and understanding of effects of MTAP deletion. Furthermore, the MSP was studied as an isolated pathway.

This paper however will use the validated NE Model to investigate the dependence of key metabolites on co-factors. In addition, this study is investigating MSP as a coupled system with the methylation cycle as depicted in Figure 1.

Nash Equilibrium Model

Nash equilibrium is a stable state of a system involving the interaction of different participants, in which no participant can gain by a unilateral change

of strategy if the strategies of the others remain unchanged. In this system, enzymes are participants with an objective function of minimising the Gibbs free energy of the reaction it catalyses (Fudenberg, et al., 1991).

The NE model considers two phenomena – competition amongst the enzymes for nutrients within the cell, and cooperation between them to find an optimum solution for the metabolic network. The overall objective function in this non-linear programming (NLP) problem is the summation of the minimum dimensionless Gibbs energy for each enzyme in the system. The constraints are element mass balances per reaction. The NLP problem is shown in Equation 4 below.

$$\sum_{j=1}^{N} \min \frac{G_j(v_j)}{RT} \quad (4)$$

subject to $$A_{ik,j} v_{k,j} = E_{i,j} \quad (5)$$

Subscripts *i, j and k* represent a species index, reaction number, and trial number respectively. *A* is a matrix of element coefficients and *E* is a vector of the amount of the corresponding elements in the metabolic pool (Lucia & DiMaggio, 2018).

Element Mass Balances

An example of using Equation 5 for a given reaction is shown in Equation 6 and 7. It uses key metabolites SAM and Decarboxy-adomet in the MSP.

$$C_{15}H_{23}N_6O_5S^+ + H^+ \rightleftharpoons C_{14}H_{24}N_6O_3S^{2+} + CO_2 \quad (6)$$

$$\begin{bmatrix} 15 & 0 & 14 & 1 \\ 23 & 1 & 24 & 0 \\ 6 & 0 & 6 & 0 \\ 5 & 0 & 3 & 2 \\ 1 & 0 & 1 & 0 \end{bmatrix} \begin{pmatrix} v_{SAM} \\ v_{H^+} \\ v_{Decarboxy-adomet} \\ v_{CO_2} \end{pmatrix} = \begin{pmatrix} C \\ H \\ N \\ O \\ S \end{pmatrix} \quad (7)$$

Using the Model

Figure 2 demonstrates a simplification of the NE model. The initialisation of the NE model required the feeding of data related to all 13 known metabolic reactions in the coupled MSP and methylation cycle. The required data consists of the Gibbs free energy of formation, reaction stoichiometry, and element composition.

For a given set of fluxes, the NLP problem can be solved as the model works towards to the objective function iteratively. For example, consider the simplified system in Figure 2. This system consists of 3 nodes/reactions. The model calculates a value of G_j / RT for each reaction, and then sums up the values calculated for all reactions to give $\sum_{j=1}^{3} G_j$. This iterative process continues until $\sum_{j=1}^{3} G_j$ converges to a minimum value as seen in the graph in Figure 2. For a given input of fluxes, the NE model returns a concentration for each species as the output at each iteration.

Application of NE Model to the MSP

The NE model was used to understand the dependence of key metabolites on certain co-factors.

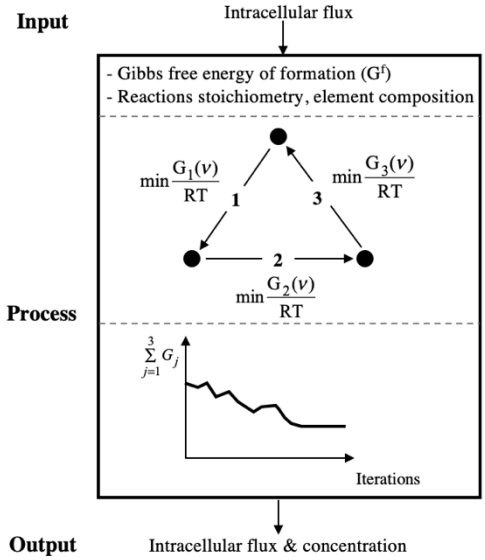

Figure 2. Schematic of application of NE model to the MSP

To simulate this, consider a parent cell split into two daughter cells. Assuming two identical daughter cells, the resultant concentration of all metabolites in each daughter cell is now halved. This is effectively a transfer of metabolic burden from the parent to daughter cell. With only half the key metabolite concentrations, each daughter cell cannot regulate the metabolic cycle and keep the key metabolites at the same concentrations as the parent cell. However, with the help of the right combination of additional co-factors supplied, the daughter cell may be able to continue to regulate the cycle as these additional co-factors can help to bring up the concentrations of the key metabolites to levels like that of the parent cell. With the NE model, one can identify this right combination of additional co-factors and then draw conclusions on the reliance of certain key metabolites on certain co-factors.

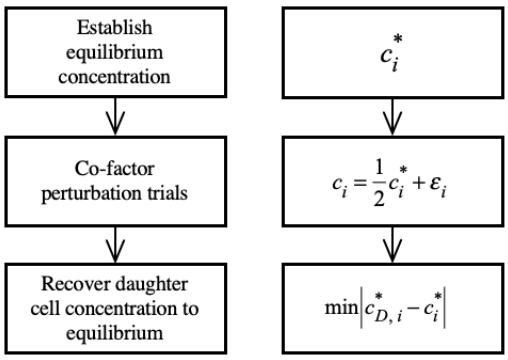

Figure 3. Simplified illustration of the structure and flow of the Nash equilibrium model

Figure 3 shows the approach this study used to identify the dependencies between key metabolites and co-factors. Initially, an equilibrium concentration for each key species, c_i^*, is established where the superscript indicates equilibrium This concentration is representative of the metabolites in the parent cell. Metabolite concentrations for each daughter cell will subsequently be $\frac{1}{2}c_i^*$. By supplying

the daughter cell with additional co-factors via some form of perturbation, the concentration of a given species i can be raised by a value, ε_i. In doing so, the concentration of i at a given iteration can be expressed as c_i shown in Equation 8.

$$c_i = \frac{1}{2} c_i^* + \varepsilon_i \quad (8)$$

The daughter cell then establishes a new concentration equilibrium, $c_{D,i}^*$, for all metabolites. The subscript D represents daughter cell concentrations. Finally, by minimising $|c_{D,i}^* - c_i^*|$, one can narrow the scope to identify the specific co-factors required to drive key metabolite concentrates back up. In the ideal case when $|c_{D,i}^* - c_i^*| = 0$, this shows that the co-factors supplied were sufficient in driving the key metabolite concentrations from $\frac{1}{2} c_i^*$ back to c_i^* exactly. This study used a sampling approach to identify the right combination of co-factor perturbations to minimise $|c_{D,i}^* - c_i^*|$. The sampling method is detailed further in the paper.

Establishing Equilibrium Concentrations

Empirical data was used as an initial input to the NE model to obtain equilibrium concentrations, c_i^*, for all species, i, in the MSP. These equilibrium concentrations were then used as 'target' concentrations that the daughter cell should drive towards. The values of c_i^* can be found in Table 1 in the *Supplementary Information* section.

Single Perturbation Trials

Before being able to determine the right combination of co-factors required to drive concentrations back up, the effect of each individual co-factor was studied through a series of co-factor perturbation trials. While one could look at the metabolic chemical reactions to get an understanding of which co-factors would directly interact with specific key metabolites, that does not account for indirect interactions with other metabolites within the MSP.

In the single perturbation analysis, a key metabolite of interest was first selected. Concentrations of all 20 co-factors were then doubled individually, to understand the dependency of a specific co-factor on the key metabolite of interest. The doubling of each co-factor serves as an arbitrary perturbation to the system. Each perturbation represents one trial and the value of $c_{D,i}^*$ generated from each trial was then recorded.

This process was repeated 11 times for all key metabolites and provided a good first approximation to understand how perturbations such as changes to co-factor concentrations can affect the concentrations of key metabolites in the MSP.

When a co-factor perturbation resulted in $c_{D,i}^*$ differing from c_i^* by greater than 15%, it was deemed that the co-factor had some effect on altering the key metabolite concentration on a first approximation basis. It should be noted that running all trials was not computationally intensive and only took 144 seconds to determine all results. The trials were run on Apple macOS Mojave using Python scripts, Terminal and Automator. Table 1 shows the results from running the trials. Each tick indicates a relationship established between a key metabolite and co-factor. For example, SAM responds to changes in glycine, methylglycine and HPO_4.

Table 1. Dependency of key metabolites when varying individual co-factors

	Met	SAM	Decarboxy-adomet	MTA	MTR-1P	MTRu-1P	DK-MTP-1P	DHK-MTPene	KMTB
ATP									✓
Water								✓	✓
HPO_4		✓	✓	✓					✓
Diphosphate									✓
H^+			✓	✓	✓	✓	✓	✓	✓
Carbon dioxide			✓	✓					✓
Putrescine				✓					✓
Spermidine				✓					✓
MTAP									✓
MTAP-MTA									✓
Adenine				✓					✓
Oxygen			✓	✓	✓	✓	✓	✓	✓
Formate							✓	✓	✓
Glutamate									✓
2-oxoglutarate									✓
Glycine		✓	✓						✓
Methylglycine		✓	✓						✓
Adenosine									✓
Trimethylglycine									✓
Dimethylglycine									✓

Multiple Perturbations

With a first approximation relationship established between individual co-factors and key metabolites, the next step was to determine the optimum magnitude of each co-factor perturbation and what combination of co-factors would minimise $|c^*_{D,i} - c^*_i|$. To determine the right magnitude of a co-factor perturbation, initial concentrations of a given co-factor was varied in multiples ranging from 0.1x to 4.0x in a series of trials. Each trial consists of a set of co-factor perturbations and the aim of each trial is to investigate whether such a set of co-factor perturbations can drive concentrations of key metabolites back to equilibrium concentrations, c^*_i.

To determine the right combination of co-factors, each key metabolite was studied cumulatively. To explain the 'cumulative' nature of this sampling method, consider a metabolic pathway of 3 reactions, 3 key metabolites and 5 co-factors. When studying key metabolite 1, changes to co-factors 1 and 2 were found to minimise $|c^*_{D,1} - c^*_1|$. These changes would be recorded and continue to be used as an input when studying key metabolite 2. The recorded changes to co-factor 1 and 2 would then be used as a base case for studying key metabolite 2 and any changes made to the other 3 co-factors would be in addition to the changes recorded from studying key metabolite 1. This is repeated for the rest of the key metabolites.

Establishing Dependencies

For each trial, the NE model produces a concentration output, c_i, for each species at each iteration to form a concentration profile. Concentration against concentration pair plots were then used to investigate the dependency of metabolite concentrations against one another. When the objective of minimising $|c^*_{D,i} - c^*_i|$ was achieved, results of $c^*_{D,i}$ were compared with literature values where available. Such values include intracellular concentrations under regular physiological conditions.

Interpreting Pair Plots

Figure 4 shows a sample pair plot. Initial concentrations are denoted by oversized markers. All other markers represent a concentration at a given iteration. The direction of the concentration-concentration profile over the iterations can be determined by the starting point and the dotted line tracing the pathway of iterations. The black cross on each pair plot represents the equilibrium concentration of the species, c^*_i, while the final iteration marker represents $c^*_{D,i}$. The objective of minimising $|c^*_{D,i} - c^*_i|$ visually corresponds to getting the final iteration marker as close to the black cross as possible. Every pair plot has a legend with a one trial representing a base case. The base case for each individual figure is described in the relevant figure caption. All other trials in the legend represent marginal adjustments in addition to the base case.

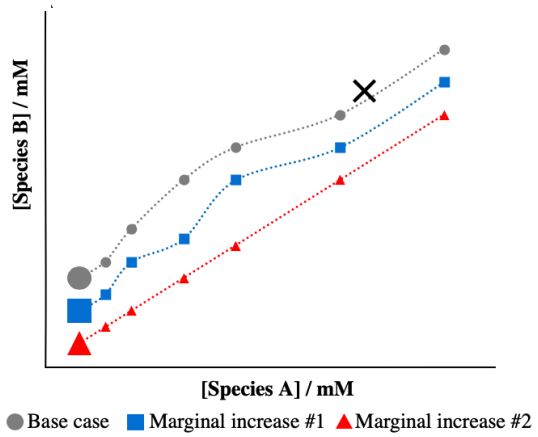

Figure 4. Sample pair plot with arbitrary Species A, Species B and base case

Results and Discussion

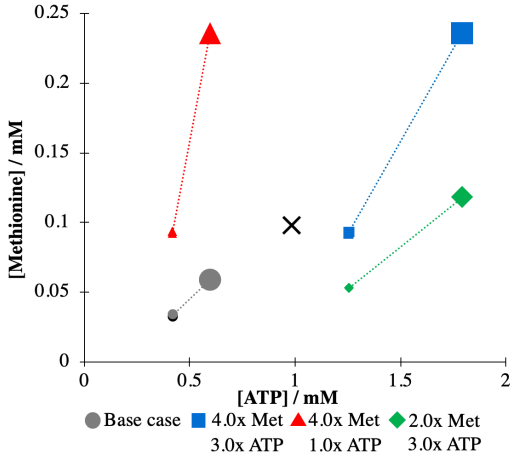

Figure 5. Effect of methionine (met) and ATP perturbations with base case of all species at initial concentrations of $0.5c^*_i$

*Methionine (1) **

The first key metabolite studied was methionine. It should be noted that methionine is the only key metabolite that does not require co-factor perturbations to drive its concentration back to equilibrium. Instead, methionine concentrations itself can be varied because methionine can be supplied externally via food and supplements.

Figure 5 shows that at a base case of $\frac{1}{2}c^*_i$ with no perturbations, methionine could not recover to equilibrium concentrations. In addition, it was found that changes to initial methionine concentrations had minimal impact on other metabolites in the pathway (data not shown). As such, initial methionine concentrations were varied until it converged near equilibrium. Interestingly, while not a key metabolite, changes in ATP were also found to have minimal impact on other metabolites. Optimum values were found when methionine and ATP concentrations increased by a factor of 4.0x and 3.0x respectively.

**Number denotes key metabolite shown in Figure 1*

DK-MTP-1P (7) and DHK-MTPene (8)

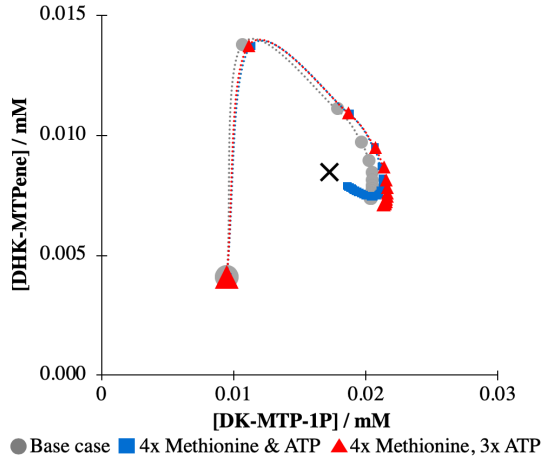

Figure 6. Interdependence between DHK-MTPene and DK-MTP-1P with base case of 4.0x methionine, 3.0x ATP

Upon initialisation without any co-factor perturbations, it was found that DHK-MTPene and DK-MTP-1P both could drive back towards equilibrium as expected. Figure 6 also demonstrates the limited effect of changes in methionine and ATP on other metabolites as all three plots move in a very similar pathway to one another.

MTR-1P (5) and MTRu-1P (6)

As shown in Table 1, both MTRu-1P and MTR-1P are sensitive to changes in H^+. The MSP contains both HPO_4 and H^+ as co-factors and since HPO_4 dissociates to form H^+, it is expected that MTRu-1P and MTR-1P will be sensitive to changes to both species. Furthermore, trials ran showed that HPO_4 increased with H^+ (data not shown).

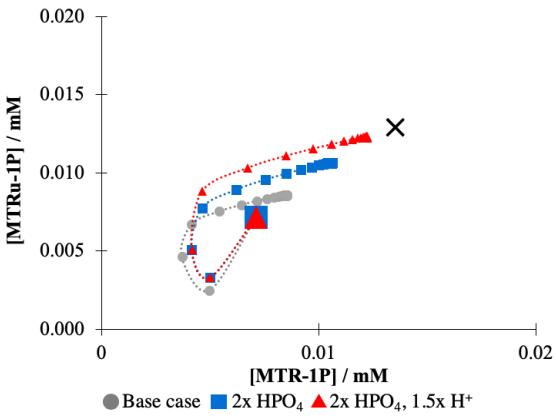

Figure 7. Effect of acidity on MTRu-1P and MTR-1P with base case as 4.0x methionine, 3.0x ATP

Figure 7 shows that when the pH of the system is lowered, both MTRu-1P and MTR-1P move closer towards equilibrium.

$$MTA + HPO_4 \rightleftharpoons MTR-1P + Adenine$$

$$MTR-1P \rightleftharpoons MTRu-1P$$

$$MTRu-1P \rightleftharpoons DHK-MTPene + H_2O$$

A closer look at the relevant metabolic equations as seen above explains this. According to Le Chatelier's Principle (LCP), as H^+ and HPO_4 increases, the production of MTR-1P is favored. Subsequently, the production of MTRu-1P is favored as well. Thus, both MTRu-1P and MTR-1P's concentration increases and moves closer to equilibrium.

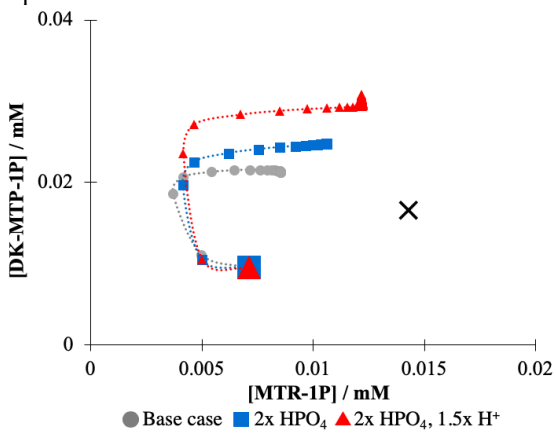

Figure 8. Effect of acidity on DK-MTP-1P with base case as 4.0x methionine, 3.0x ATP

While increasing the acidity of the system drives MTRu-1P and MTR-1P towards equilibrium, there is a trade-off. Figure 8 shows that as acidity increases, DK-MTP-1P's concentration increases and moves away from equilibrium. Nonetheless, changes of 2.0x HPO_4 and 1.5x H^+ was still considered to be a reasonable solution. However, this result does suggest that 1.5x H^+ should be considered as an upper limit threshold when controlling DK-MTP-1P. It should be noted that changes to acidity had minimal impact on DHK-MTPene concentrations (data not shown).

MTA (4)

The key reactions* involving MTA are below:

$$DCA + Putrescine \rightleftharpoons MTA + Spermidine + H^+$$

$$MTA + MTAP \rightleftharpoons MTAP - MTA$$

$$MTA + HPO_4 \rightleftharpoons MTR-1P + Adenine$$

Upon running trials, it was found that co-factors adenine, putrescine, and spermidine were exhibiting linear dependencies between each other. Figure 9, shows the dependence between adenine and putrescine for varied initial concentrations of adenine. The following linear relationships were established:

1. Putrescine concentrations increased as adenine concentrations decreased
2. Putrescine concentrations increased as spermidine concentrations decreased (data not shown)
3. Spermidine concentrations decreased as adenine concentrations decreased (data not shown).

**Note that DCA stands for decarboxy-adomet*

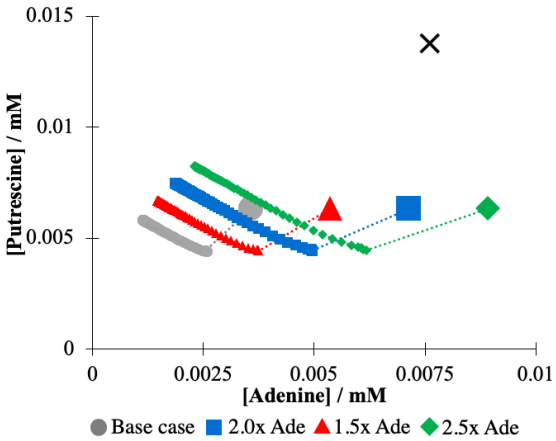

Figure 9. Relationship between adenine (Ade) and putrescine with base case as 4.0x methionine, 3.0x ATP, 2.0x HPO_4, 1.5x H^+

Adenine, putrescine and spermidine perturbations were then trialled to understand the relationship between MTA and these co-factors. Figures 10 and 11 show the effect of varying adenine and putrescine concentrations on MTA respectively.

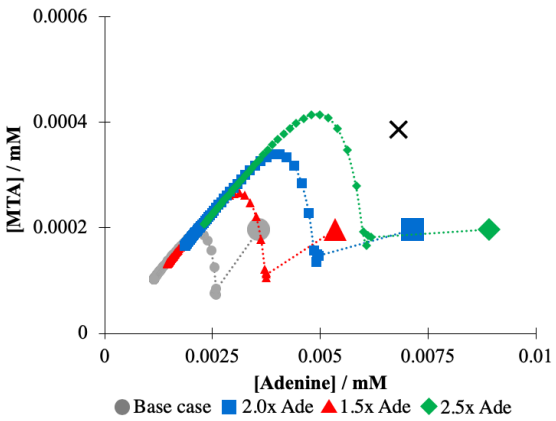

Figure 10. Effect of adenine (Ade) on MTA with base case as 4.0x methionine, 3.0x ATP, 2.0x HPO_4, 1.5x H^+

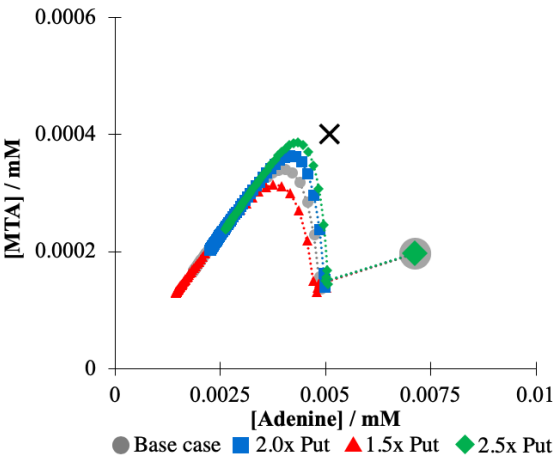

Figure 11. Effect of putrescine (Put) on MTA with base case as 4.0x methionine, 3.0x ATP, 2.0x HPO_4, 1.5x H^+

In both cases, peak MTA concentrations increase as the co-factor concentrations increase. However, MTA is more sensitive to changes in adenine than changes in putrescine as the increase in peak MTA concentrations are much more significant with changes to adenine than putrescine. It should be noted that trials had showed that moderate concentration increases of 2.0x for both adenine and putrescine was more effective in raising MTA peak concentrations than increases to adenine or putrescine individually (data not shown). In all cases, MTA concentrations would peak but then subsequently crash and settle at a lower concentration.

$$DCA + Putrescine \rightleftharpoons MTA + Spermidine + H^+$$

One reason why this was occurring is that despite an increased amount of putrescine in the system, the backward reaction of the equation above was being favoured – resulting in the depletion of MTA. To address the MTA crash, the effect of restricting spermidine to drive the forward reaction was investigated. Figure 12 shows the effect of reducing spermidine on MTA concentrations and its ability to stabilise MTA concentrations to prevent this crash.

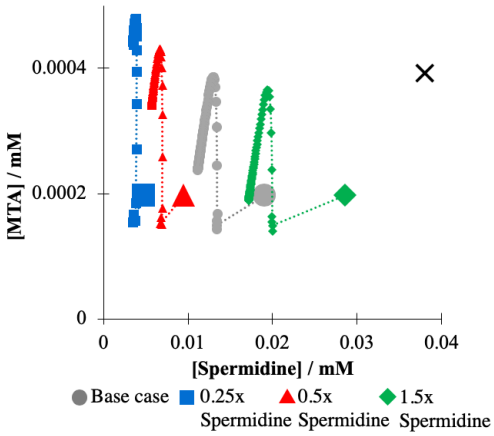

Figure 12. Effect of restricting spermidine on MTA with base case as 4.0x methionine, 3.0x ATP, 2.0x HPO_4, adenine & putrescine, 1.5x H^+

However, spermidine concentrations cannot be restricted heavily. Figure 13 shows that it will exceed literature values of regular physiological putrescine/spermidine ratios (Kenyon, et al., 1996). As such it was determined that the best combination of co-factor perturbations to regulate MTA and minimise $|c^*_{D,MTA}-c^*_{MTA}|$ was to conduct perturbations of 0.5x spermidine, 2.0x putrescine and 2.0x adenine.

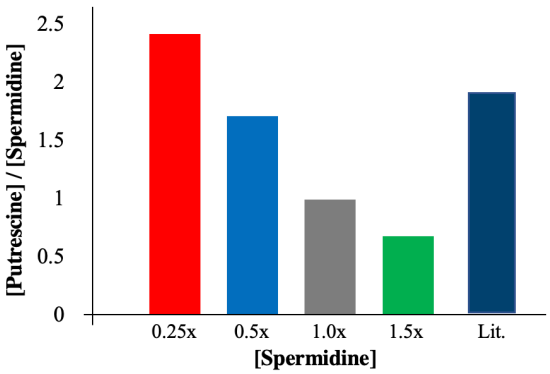

Figure 13. Comparison of putrescine/spermidine ratio with literature values

Decarboxy-adomet (3)

The base case trial showed that decarboxy-adomet was moving away from its equilibrium concentration. Changes to the co-factors identified in the decarboxy-adoment column in Table 1 had limited effect in changing its concentration pathway (data not shown). Only extreme changes to H^+, by using initial concentrations of 4.0x H^+ helped to drive it closer equilibrium as shown in Figure 14.

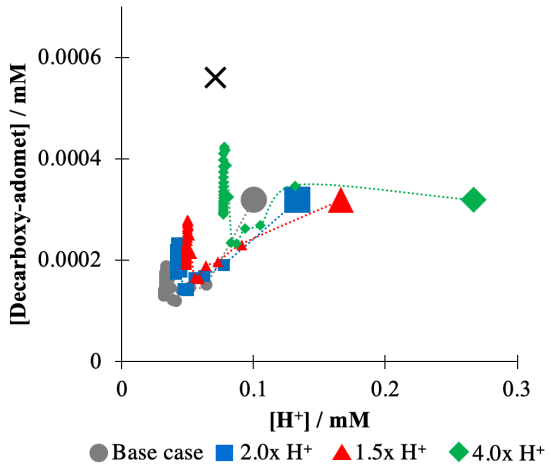

Figure 14. Effect of H+ on decarboxy-adomet with base case as 4.0x methionine, 3.0x ATP, 2.0x HPO_4, adenine & putrescine, 1.5x H+, 0.5x spermidine

Even then, results were not promising as decarboxy-adomet concentrations would rise to a peak and continue to crash right after. Unlike MTA, it was not possible to reduce this crash through a co-factor perturbation. In addition, it should be noted that such extreme H^+ changes would affect the concentration profiles of key metabolites that are sensitive to pH changes such as DK-MTP-1P and MTA.

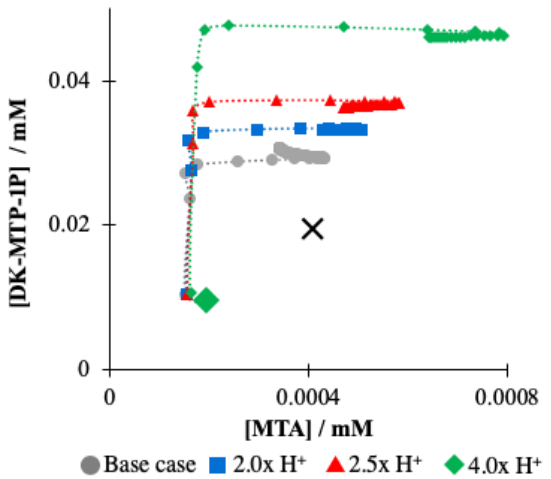

Figure 15. Effect of H+ on DK-MTP-1P and MTA with base case as 4.0x methionine, 3.0x ATP, 2.0x adenine, HPO_4 & putrescine, 1.5x H+, 0.5x spermidine

Figure 15 shows that the additional H^+ perturbations would drive both DK-MTP-1P and MTA away from equilibrium. Based on this, it was determined that extreme H^+ perturbations should not be used to regulate decarboxy-adomet and at this stage, no co-factor perturbations could drive decarboxy-adomet back to equilibrium concentrations.

SAM (2)

As a key metabolite in both the methylation cycle and the MSP, using co-factors from the methylation cycle to regulate SAM would potentially have less interference on key metabolite concentrations in the MSP. From Table 1, it was established that it would be possible to control SAM concentrations through glycine and methylglycine perturbations. In addition, the chemical reactions involving SAM in the methylation cycle suggest that SAM can be controlled by the co-factor, adenosine. The reactions are presented below.

$$SAM + Glycine \rightleftharpoons SAH + Methylglycine$$

$$SAH + H_2O \rightleftharpoons Homocysteine + Adenosine$$

According to LCP, as adenosine concentrations increase, the reverse reaction producing SAH will be favored, which will drive the production of SAM. Figure 16 shows the effect of adenosine perturbations in pushing up SAM concentrations.

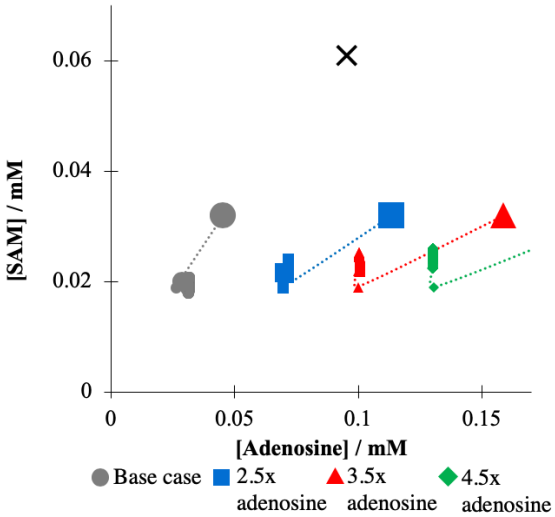

Figure 16. Effect of adenosine on SAM with base case as 4.0x methionine, 3.0x ATP, 2.0x HPO_4, adenine & putrescine, 1.5x H+, 0.5x spermidine (Note that starting point of 4.5x adenosine is out of the frame)

Similarly, restricting glycine concentrations to levels as low 0.25x had a slight positive effect on SAM concentrations as well (data not shown). The combined effect of restricting glycine at 0.25x and increasing adenosine to 2.5x was then studied with varied methylglycine perturbations as shown in Figure 17.

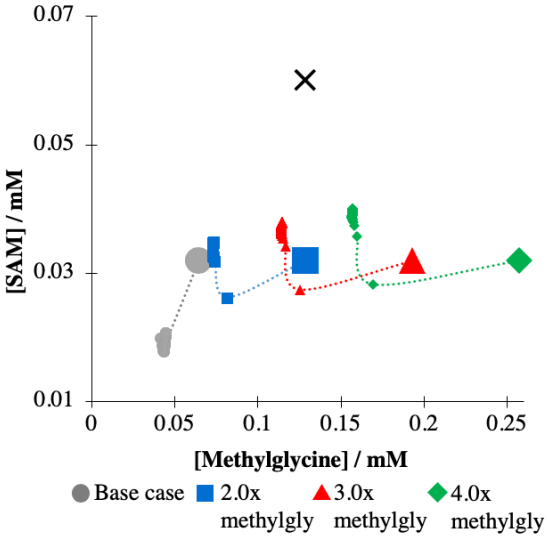

Figure 17. Effect of methylglycine on SAM with base case as 4.0x methionine, 3.0x ATP, 3.5x adenosine, 2x HPO_4, adenine & putrescine, 1.5x H+, 0.5x spermidine, 0.25x glycine

The combined effect of conducting all three co-factor perturbations was a significant improvement in regulating SAM concentrations. It is worth noting that individual methylglycine perturbations, (data not shown) did not yield such positive results and thus this combined effect of co-factors should be emphasised. In addition, these perturbations had limited impacts on affecting other key metabolites in the MSP (data not shown).

While SAM concentrations never reached close to equilibrium values, this was still considered a reasonable result with all cases seeing SAM driving in the right direction. Furthermore, literature values measuring SAM concentrations on a relative basis are also available in the form of [Methionine]/[SAM]. Figure 18 shows that SAM concentrations were in relatively good agreement with literature data as well.

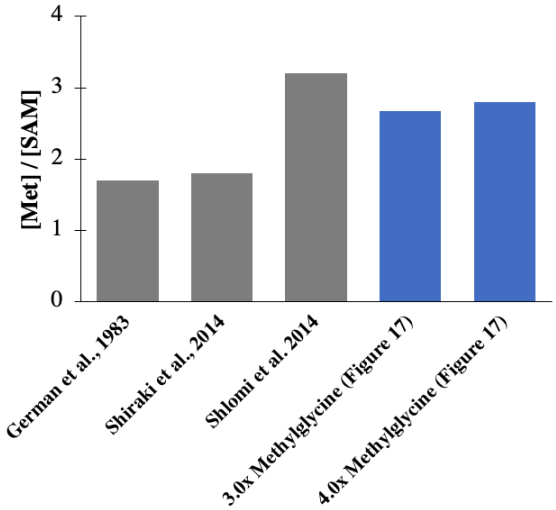

Figure 18. Comparison of methionine (met) /SAM ratio with literature values

Regulation of Adenine

[SAM]/[MTA] literature ratios were also available and used for comparison as shown in Figure 19. The trial results had moderately weak agreement with literature which presented lower ratios.

As established earlier, MTA was noted to be particularly sensitive to changes in adenine concentrations. In a recent study, Lucia and DiMaggio (2018) showed that regulation of adenine concentrations helped to stabilise MTA levels and lower [SAM]/[MTA] ratios.

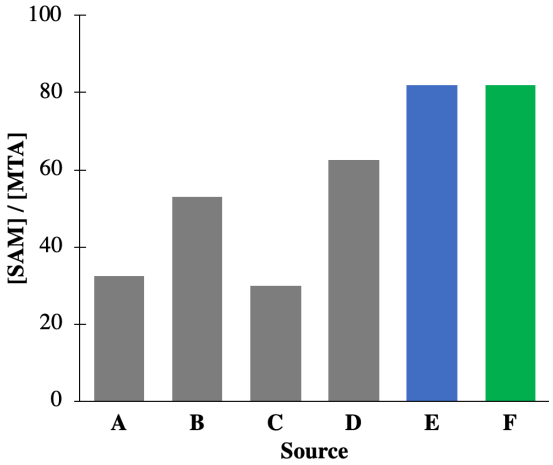

Figure 19. Comparison of SAM/MTA ratio with literature values

Table 2. Legend of Figure 19

Source #	Origin
A	(Bigaud & Corrales, 2016)
B	(Marjon, et al., 2016)
C	(Kirovski, et al., 2011)
D	(Stevens, et al., 2010)
E	2.0x adenine – unregulated (Figure 20)
F	2.0x adenine – regulated (Figure 20)

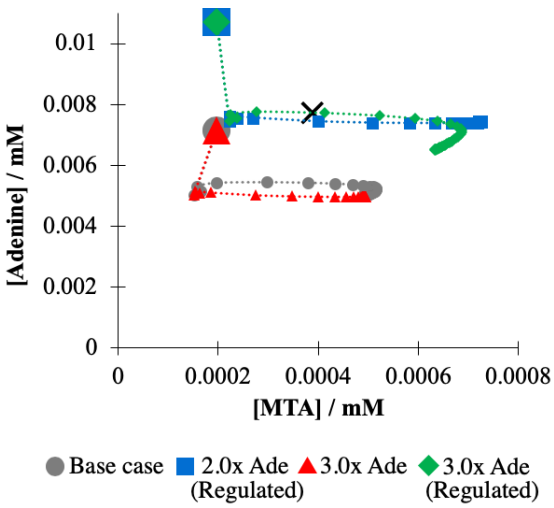

Figure 20. Effect of adenine regulation on MTA and adenine with base case as 4.0x methionine, 4.0x methylglycine, 3.0x ATP, 3.5x adenosine, 2x HPO_4, adenine & putrescine, 1.5x H+, 0.5x spermidine, 0.25x glycine

However, this study found that regulation of the current system (4.0x methylglycine in Figure 17) did not have a significant impact on [SAM]/[MTA] values. Figure 20 shows that the unregulated adenine in the current system/base case was already relatively stable and thus it is not surprising that regulation had a limited effect on [SAM]/[MTA].

Investigating Additional Dependencies

Due to the cumulative nature of the methodology applied, it is worth discussing whether stabilisations of the key metabolites established later could have reduced the need for co-factor perturbations found earlier on in the section. For example, H^+ concentrations were increased to help bring MTR-1P and MTRu-1P closer to equilibrium. It was worth considering whether the stabilisation of MTA and SAM (key metabolites upstream of MTR-1P and MTRu-1P) could reduce this need to increase H^+. This would be particularly useful as it would also prevent DK-MTP-1P from deviating away from equilibrium. However, it was found that when H^+ was lowered, MTR-1P and MTRu-1P do not converge to equilibrium. Despite the stabilisation of key metabolites upstream of MTR-1P and MTRu-1P, they were still found to be reliant on H^+.

Summary of Results

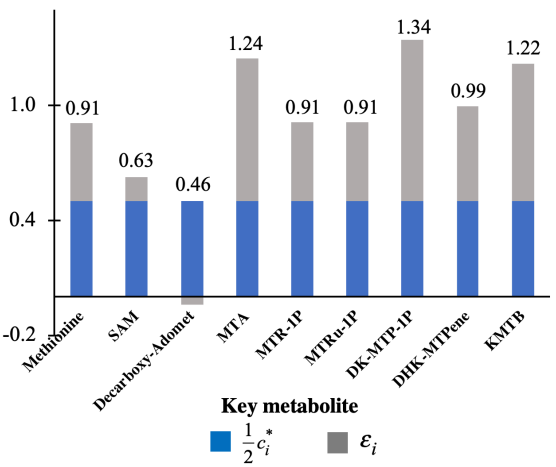

Figure 21. Summary of key metabolite results normalised to equilibrium concentration, c_i^*. Grey bars represent the marginal increase of key metabolite concentrations due to perturbation. Data labels represent values of $c_{D,i}^*$

Figure 21 shows the final solution to min $|c_{D,i}^* - c_i^*|$ for all key metabolites in the MSP. Almost all key metabolites could at least drive back close to equilibrium or further, except for SAM and decarboxy-adomet. While SAM failed to drive back to equilibrium, it was moving in the right direction. Decarboxy-adomet however stood out as it was moving away from equilibrium – so much so that ε_{DCA} was negative and $c_{D,DCA}^* < \frac{1}{2}c_{DCA}^*$.

Conclusion

The NE Model was successfully applied to the MSP to understand the relationships between key metabolites and co-factors. An optimal solution using 0.25x glycine, 0.5x spermidine, 1.5x H^+, 2.0x HPO_4, adenine & putrescine, 3.0x ATP, 3.5x adenosine, 4.0x methylglycine & methionine was found to minimise $|c_{D,i}^* - c_i^*|$. Below are the key steps identified that led to this optimum solution:

1. Increasing ATP and methionine had minimal impact on other metabolites in the MSP
2. Additional increases to HPO_4 and H^+ drove MTR-1P and MTRu-1P to equilibrium
3. Additional increases to adenine and putrescine drove peak MTA concentrations higher
4. Restriction of spermidine helped to prevent MTA concentrations from crashing below equilibrium concentration values.
5. Additional increases to methylglycine and adenosine while restricting glycine drove SAM towards equilibrium concentration values

References

Albers, E., 2009. Metabolic characteristics and importance of the universal methionine salvage pathway recycling methionine from 5'-methylthioadenosin. *IUBMB Life,* 61(12), pp. 1132-1142.

Bigaud, E. & Corrales, F. J., 2016. Methylthioadenosine (MTA) Regulates Liver Cells Proteome and Methylproteome: Implications in Liver Biology and Disease. *Mol Cell Proteomics,* 15(5), pp. 1498-1510.

Danchin, A., n.d. *The methionine salvage pathway.* [Online] Available at: https://www.normalesup.org/~adanchin/science/methionine-salvage-pathway
[Accessed 3 December 2018].

Fudenberg, Drew & Tirole, J., 1991. *Game Theory.* Cambridge, MA: MIT Press.

Kenyon, S. H., Nicolaou, A., Ast, T. & Gibbons, W. A., 1996. Stimulation in vitro of vitamin B12-dependent methionine synthase by polyamines. *Biochem J.,* Volume 316, pp. 661-665.

Kirovski, G. et al., 2011. Down-regulation of methioadenosine phosphorylase (MTAP) induces progression of hepatocellular carcinoma via accumulation of 5-deoxy-5'-methylthioadeosine (MTA). *Am. J. Pathol.,* 178(3), pp. 1145-1152.

Lucia, A. & DiMaggio, P. A., 2018. *A Multi-Scale Computational Approach to Understanding Cancer Metabolism,* s.l.: s.n.

Lucia, A. & DiMaggio, P. A., 2018. Metabolic pathway analysis using a nash equilibrium approach. *J Glob Optim,* 71(3), pp. 537-550.

Marjon, K., Cameron, M. J., Quang, P. & Clasquin, M. F., 2016. MTAP Deletions in Cancer Create Vulnerability to Targeting of the MAT2A/PRMT5/RIOK1 Axis. *Cell Reports,* 15(3), pp. 574-587.

Mentch, S., Mehrmohamadi, M., Huang, L. & Liu, X., 2015. Histone Methylation Dynamics and Gene Regulation Occur through the Sensing of One-Carbon Metabolism. *Cell Metab,* 22(5), pp. 861-73.

Orth, J. D., Thiele, I. & Palsson, B., 2010. What is flux balance analysis?. *Nat Biotechnol,* 28(3), pp. 245-248.

Plata, G., Hisao, T.-L. & Olszewski, K. L., 2010. Reconstruction and flux-balance analysis of the Plasmodium falciparum metabolic network. *Molecular Systems Biology,* Volume 6, p. 408.

Prikov, I., Norbeck, J., Gustafsson, L. & Albers, E., 2008. A complete inventory of all enzymes in the eukaryotic methionine salvage pathway.. *FEBS J,* 275(16), pp. 4111-4120.

Schnekenburger, M. & Diederich, M., 2015. Nutritional Epigenetic Regulatoers in the Field of Caner. In: S. Gray, ed. *Epigenetic Therapy.* s.l.:Academic Press, pp. 393-425.

Stevens, A., Dettmer, K., Kirovski, G. & Samejima, K., 2010. Quantification of intermediates of the methionine and polyamine metabolism by liquid chromatography-tandem mass spectrometry in cultured tumor cells and liver biopsies. *J Chromatogr A,* 1217(19), pp. 3282-3288.

Enzymatic saccharification of pretreated lignocellulosic biomass for downstream catalytic conversion of sugars to hydrocarbons

Myriam Belmekki
Department of Chemical Engineering, Imperial College London, U.K.

Abstract This article provides insights on the comparison of two different lignocellulosic biomass feedstocks each pretreated with a different method and both aiming at downstream conversion to hydrocarbon fuels after enzymatic saccharification. Simulation processes of the latter process step are deployed for both scenario using Aspen Plus simulation software. It was reported that the highest yields of carbon sources was attributed to Miscanthus pretreated with ionic liquid 170°C for 30 minutes. By contrast, a blend of corn stover and switchgrass pretreated with dilute acid entailed poor yields.

Introduction

To date, our transportation system and the production of chemicals still mainly rely on fossil resources. Nonetheless, the forecasted depletion of the latter, the increasing demand for energy and environmental concerns are all reasons why a substantial fossil fuel displacement is required. Instead, a recent strategy consists in expanding biorefinery and biotransformation technologies by developing the use of biomass feedstock and ways to convert it into clean energy fuels and other commodities.

In this regard, lignocellulosic biomass is considered as an interesting alternative to petroleum because of its abundance and renewability. Along with unused agricultural wastes, lignocellulosic crops are classified as second-generation biomass feedstock [1] which, unlike first-generation biomass feedstock (e.g. edible agricultural crops), does not directly compete with the food industry but stands in need of burdensome and expensive pretreatment technologies.

Indeed, lignocellulosic biomass is a natural composite material difficult to break down, which is defined as recalcitrance, resulting in no direct route to convert the sugars it contains into fuels or chemicals. This material is made of lignin and carbohydrate polymers, namely cellulose and hemicellulose (Figure 1).

Cellulose is a large and linear polymer composed of glucose molecules joined together with hydrogen bonds between parallel chains, forming a highly crystalline structure. It is not soluble in water and it is resistant to depolymerisation. Hemicellulose is an amorphous and branched polymer of hexoses and pentoses, respectively mainly represented by glucose and xylose. Lignin is a complex polymer of phenylpropanoid units. Unlike carbohydrates, it cannot be converted into sugars but it has a high energy value as a boiler fuel in integrative biorefineries.

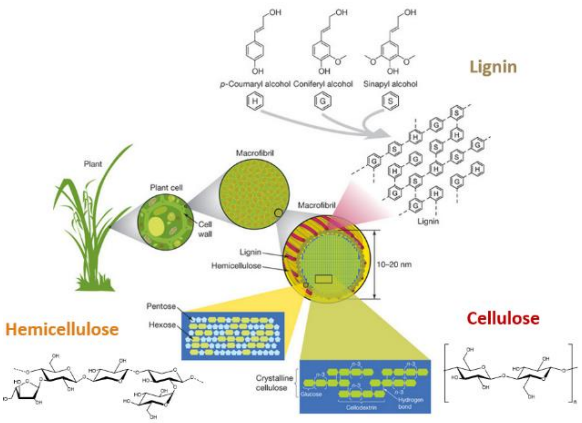

Figure 1. Structural composition of lignocellulosic biomass [2].

Pretreatment is one of the most costly step in processes converting lignocellulosic biomass to fuels via saccharification. Regardless of the pretreatment methods, the role pretreatment plays is identical. The goal is to remove lignin and hemicellulose in order to increase the accessibility of the enzyme to cellulose for easy saccharification of cellulose and xylose downstream [3].

This paper aims at comparing two specific lignocellulosic feedstocks each pretreated with a different method and both destined for enzymatic saccharification and downstream conversion to hydrocarbons: a mixture of corn stover and switchgrass pretreated with dilute sulfuric acid on the one hand; and Miscanthus pretreated with ionic liquid on the second hand.

Background

The production of ethanol from lignocellulosic feedstock is a mature technology . This process has been described in detail by the National Renewable Energy Laboratory (NREL) in the "2011 design report" [4]. However, ethanol cannot be used as a fuel for aircrafts since they require naphtha (linear alkanes of 8 to 12 carbons). In 2013, NREL decided to widen the scope of its research regarding lignocellulose transformation by investigating possible pathways to convert it to hydrocarbon fuels, mainly diesel and naphta. At that point, sugar conversion to hydrocarbon fuels was processed through a biological route involving microbial fermentation [5]. This pathway had the asset of producing specific and easily identifiable hydrocarbon products but showed a shortcoming on the carbon efficiency and poor yields due to metabolic conversion, and difficulties for large-scale implementation.

That is why, in 2015, NREL explored a new pathway: the catalytic conversion route, which consists in transforming all convertible carbon sources (including sugars) via a series of complex reactions allowing deoxygenation and carbon-carbon bonding in catalytic reactors [6]. Throughout all three reports the feedstock used is milled cornstover blended with switchgrass as illustrated in Figure 4. This feedstock is pretreated with dilute sulfuric acid to liberate the hemicellulose sugars and disrupt the biomass for enzymatic hydrolysis followed by catalytic conversion as described in Figure 2.

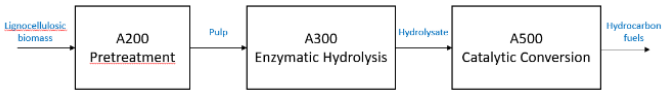

Figure 2. Overview of the main steps to catalytic conversion

A recent pretreatment method consists in using ionic liquid. This paper leverages the findings of Brandt-Talbot et al. [7] on the fractionation of Miscanthus with the low-cost ionic liquid is triethylammonium hydrogen sulfate as illustrated in Figure 3.

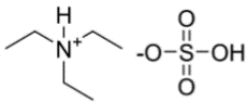

Figure 3. Triethylammonium hydrogen sulfate ([TEA][HSO4]).

This process, which is known as ionoSolv preatreatment, disrupts lignocellulose and dissolves most lignin and hemicellulose while maintaining cellulose as a filterable solid. Miscanthus has been investigated in-depth with different pretreatment methods and is acknowledged as a fast growing and high yield energy crop [8]. This feedstock is a key candidate for conversion processes of biomass to biofuel because of its high concentration of carbohydrates and low concentration of moisture and ash [9], as shown in Figure 4.

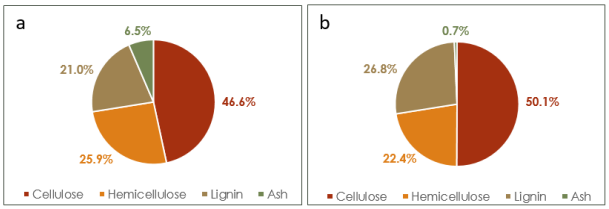

Figure 4. Percent dry weight composition of milled corn stover blended with switchgrass (a) and Miscanthus (b).

Methods

This section describes how the two different pretreatment strategies were compared for efficient downstream catalytic conversion to hydrocarbons. For both strategies, only the enzymatic hydrolysis step (A300 on Figure 3), also known as enzymatic saccharification, was modelled based on the process simulation developed by NREL in 2017 [10], using Aspen Plus software. As a basis, a pretreated feedstock stream of 100,000 kg/h was considered for both strategies and the flow rate of carbon sources contained in the concentrated hydrolysate was extracted.

The input composition of the pretreated blend of corn stover and switchgrass was calculated by running the dilute sulfuric acid pretreatment step of NREL 2015 model [6]. The composition of the untreated feedstock was the same as described in Figure 4.a with a moisture content of 20% by weight. The output of the process was exploited to determine the percent composition of the pulp in order to use it as an input in the simplified NREL 2017 simulation process presented in Figure 5.

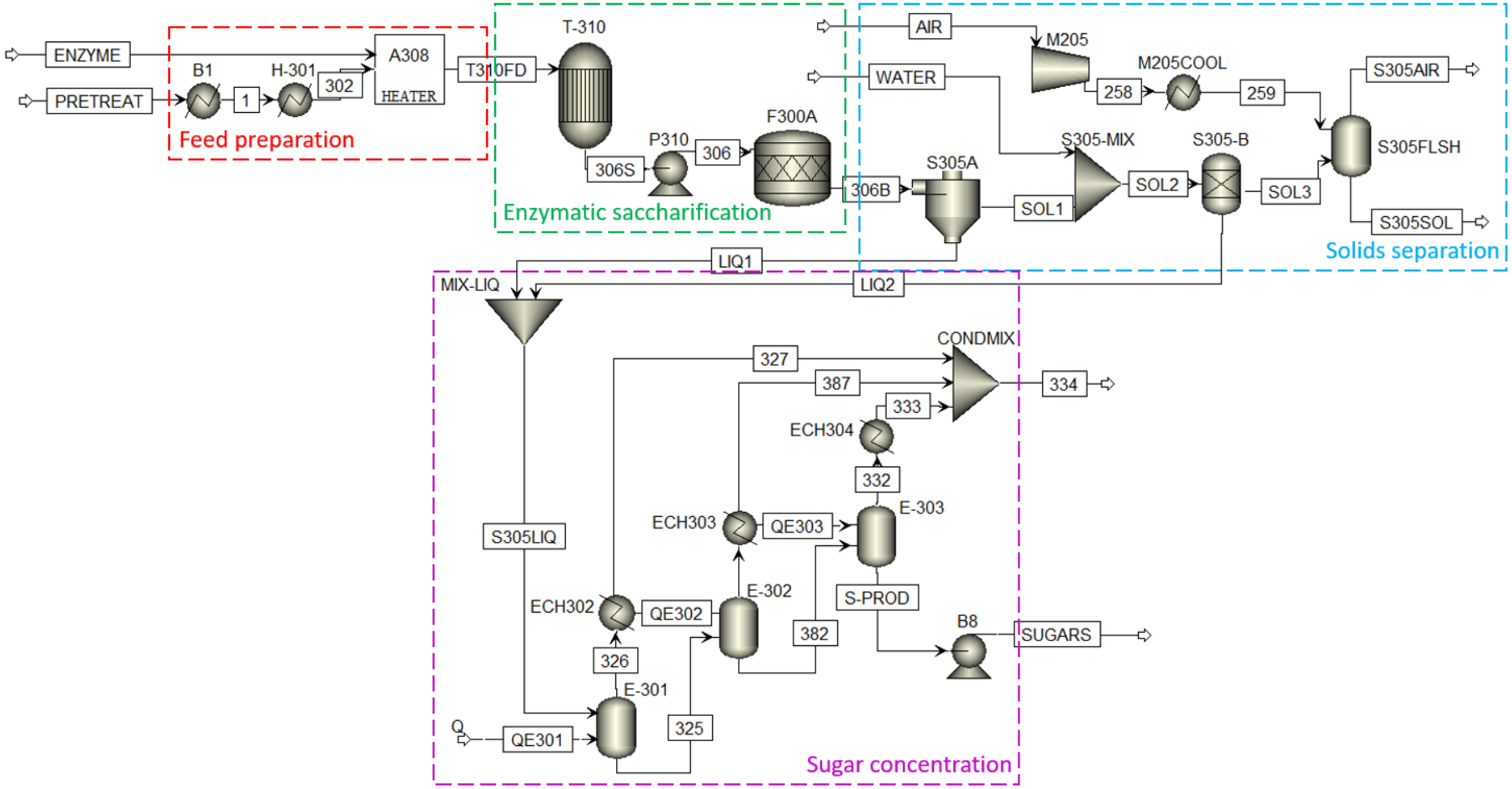

Figure 5. Process flowsheet area A300 converting pretreated lignocellulosic feedstock into concentrated sugars.

As for the pretreated Miscanthus feedstock with ionic liquid, the composition was calculated based on experimental results provided by Gschwend et al. in the electronic supplementary information and giving numerous temperature and time conditions [9]. The moisture content is assumed to be 26% by weight as per Outon-Gil process design [11].

In both cases, the enzyme is supposed to be produced on site, available at 29°C and 1.7 atm and connected as an input to the enzymatic hydrolysis step. As recommended by NREL 2015 [6], the necessary mass flow rate of the enzyme is assumed to be hundred time less than the one of cellulose contained in the pretreated pulp to achieve a 90% conversion to glucose and the water flow rate accounts for 96.2% of the total input. In the "Results" section, Table 2 summarizes all input information used in the simulation process.

The process starts with reducing both temperature and pressure conditions of the input streams in order to carry out the enzymatic hydrolysis at 48°C and 1 atm. Thus, in the case of corn stover blended with switchgrass available at 66°C and 7.7 atm after dilute acid preatreatment, two consecutive coolers (B1 and H-301) are required to achieve the reaction conditions. On the opposite, Miscanthus pretreated with ionic liquid is available at 38°C and 1 atm, thus the two coolers were removed from the general flowsheet in that case. Finally, the mixer A308 allows to mix the enzyme into the slurry and set both temperature and pressure to the targeted conditions.

The slurry is above 20% total solids and is therefore not pumpable. As a consequence, it is first fed by gravity to a continuous high-solids hydrolysis reactor, which is conceived as an empty tower where no reaction is happening in the process simulation. Then, the slurry is transferred with a pump to a batch hydrolysis reactor where different reactions take place. These reactions and their associated conversions are listed in Table 1. As mentioned in NREL 2015 report, hydrolysis is already initiated on xylose during the dilute acid pretreatment step and part of the lignin is solubilized. That is why reactions 5 to 7 occurring in the pretreatment step were not implemented in reactor F300A and only cellulose saccharification was considered (reactions 1 to 4). By contrast, hydrolysis reactions are not initiated during ionic liquid pretreatment according to Brandt-Talbot et al. Thus, it was assumed that hydrolysis reactions were not only applied to cellulose but also to hemicellulose and that lignin solubilisation occurred. The conversion rates were taken from the preatreatment and enzymatic hydrolysis steps of NREL 2015 report. Cellulose is not only hydrolysed into glucose but also into glucose oligomers named Glucolig in the simulation and cellobiose, a disaccharide of glucose which is itself further hydrolysed into glucose. Hemicellulose is hydrolysed into xylose and xylose oligomers named Xylolig in the simulation. The degradation products of cellulose to hydromethylfurfural and hemicellulose to furfural were neglected due to the low conversion of the associated reactions and because these products are negligible in the final output stream from A300.

Once the hydrolysis saccharification is completed, the hydrolysate is purified by using a solids separation. This step is essential for downsteam catalytic conversion since catalytic reactors would otherwise be subjected to fouling and heavy pressure drop. Moreover, ash concentration also needs to be minimized since it is known to either deactivate or clog catalysts. First, a rough separation is processed through the filter S305A with split fractions of 15% for the liquid substream and 99.5% for the solid substream in the stream SOL1. This output stream, which is mainly composed of lignin and other unreacted structural components of the biomass, is then washed with water in order to recover more convertible carbon sources. A second filtration occurs in S305-B with split fractions of 75% for water, 90% for all soluble constituents in LIQ2 while all insoluble components are assumed to exit in the stream SOL3. The latter is sent to the evaporator S305SOL, which is fuelled with air and allows the recovering of lignin with a lower moisture content in order to further use it in a boiler.

Table 1. Hydrolysis reactions and assumed conversions.

Number	Reaction	Reactant	Percentage of reactant converted to product
1	Cellulose → Glugolig	Cellulose	4.0%
2	2 Cellulose + H_2O → Cellobiose	Cellulose	1.2%
3	Cellulose + H_2O → Glucose	Cellulose	90%
4	Cellulobiose + H_2O → 2 Glucose	Cellobiose	100%
5	Hemicellulose → Xylolig	Hemicellulose	2.4%
6	Hemicellulose + H_2O → Xylose	Hemicellulose	90%
7	Lignin → Soluble Lignin	Lignin	5.0%

The last step of the process consists in concentrating the sugars (i.e., reducing the water content) for easier and more efficient downstream catalytic conversion. The filtrates coming from LIQ1 and LIQ2 are mixed and routed to a triple-effect evaporation system subsequently evaporating water through three flash tanks set at different pressures: 0.6 atm, 0.3 atm and 0.2 atm. The advantage of such system is the reduced use of energy because the vapour from the first evaporator can be used to heat the second one and so on. The evaporator condensate are mixed together and can be used as a heating source for other unit operations. Finally, the stream S-PROD, which contains concentrated sugars, is processed through the pump B8 to increase the pressure to 3 atm.

Once the flowsheets for both strategies were simplified and adapted from the NREL 2017 simulation process, the ionic liquid was modelled using the Aspen component "POLY(ETHYLENE-GLYCOL)" due to its similar physical properties, notably for its high viscosity. The vapour pressure was modified and set to an arbitrary low value: -1E10 atm in order to represent the non-volatile behaviour of the ionic liquid. Unfortunately, the Aspen Plus software showed errors due to adding a new component with insufficient properties. Owing to the lack of data and unnecessary complexification of the process since the ionic liquid represents a minor fraction of the pretreated Miscanthus, ionic liquid was chosen to be removed from the input in the stream named PRETREAT. In order to treat both strategies in the same way, sulfuric acid was also decided to be removed from the pretreated blend of corn stover and switchgrass.

Results

After completing the above mentioned modifications, both simulation strategies ran successfully. The output concentrated sugar stream, which is named SUGARS as described in Figure 5, contains variable amounts of water, xylose, glucose, cellobiose, xylose oligomers, glucose oligomers and soluble lignin. All of these carbon-containing components, except water, are assumed to be convertible to different hydrocarbon fuels such as diesel and naphta, as mentioned in NREL 2015 report [6].

All results are reported in Table 2. For the sake of clarity, the first column is described by the letter "C" which stands for corn stover and switchgrass pretreated with dilute acid. All other columns represent the case of Miscanthus pretreated with ionic liquid under a variety of temperature and

Table 2. Mass balance information and percent composition of the main input and output streams for A300 enzymatic hydrolysis process.

Pretreatment conditions	T (°C)	160	150 *(A)*							160 *(B)*						170 *(C)*				180 *(D)*			
	t (min)	5	30 *(1)*	45 *(2)*	60 *(3)*	90 *(4)*	120 *(5)*	180 *(6)*	240 *(7)*	20 *(1)*	40 *(2)*	60 *(3)*	80 *(4)*	100 *(5)*	120 *(6)*	15 *(1)*	30 *(2)*	45 *(3)*	60 *(4)*	15 *(1)*	30 *(2)*	45 *(3)*	60 *(4)*
PRETREATED FEEDSTOCK	TOTAL (kg/h)	100000	100000	100000	100000	100000	100000	100000	100000	100000	100000	100000	100000	100000	100000	100000	100000	100000	100000	100000	100000	100000	100000
	Mixed (kg/h)	87200	26000	26000	26000	26000	26000	26000	26000	26000	26000	26000	26000	26000	26000	26000	26000	26000	26000	26000	26000	26000	26000
	water (%)	92.01	100	100	100	100	100	100	100	100	100	100	100	100	100	100	100	100	100	100	100	100	100
	xylose (%)	6.37	-	-	-	-	-	-	-	-	-	-	-	-	-	-	-	-	-	-	-	-	-
	glucose (%)	1.26	-	-	-	-	-	-	-	-	-	-	-	-	-	-	-	-	-	-	-	-	-
	xylolig (%)	0.15	-	-	-	-	-	-	-	-	-	-	-	-	-	-	-	-	-	-	-	-	-
	soluble lignin (%)	0.21	-	-	-	-	-	-	-	-	-	-	-	-	-	-	-	-	-	-	-	-	-
	Cisolid (kg/h)	12800	74000	74000	74000	74000	74000	74000	74000	74000	74000	74000	74000	74000	74000	74000	74000	74000	74000	74000	74000	74000	74000
	cellulose (%)	69.57	67.72	74.20	75.76	81.09	81.30	78.98	74.27	74.54	85.37	85.98	81.61	79.31	73.56	66.31	86.62	87.01	81.85	76.50	88.49	78.89	49.28
	hemicellulose (%)	1.10	13.32	11.22	9.24	6.72	5.68	4.60	3.70	10.52	3.47	1.89	0.96	0.38	0.37	14.50	3.98	1.38	0.20	9.31	1.39	0.23	0.24
	lignin (%)	26.62	17.86	14.29	14.39	12.03	12.85	16.26	20.80	14.63	10.79	11.55	16.48	19.73	25.51	18.66	8.68	10.83	17.14	13.56	9.33	19.95	49.52
	ash (%)	2.71	1.10	0.29	0.61	0.16	0.17	0.16	1.23	0.30	0.37	0.57	0.96	0.57	0.56	0.54	0.72	0.79	0.81	0.63	0.79	0.93	0.96
ENZYME ON SITE	TOTAL (kg/h)	2431	13188	14449	14753	15792	15833	15381	14463	14516	16626	16744	15892	15445	14324	12913	16868	16944	15940	14897	17233	15362	9596
	Mixed (kg/h)	2342	12686	13900	14192	15192	15231	14796	13913	13965	15994	16108	15288	14858	13780	12422	16227	16300	15334	14331	16578	14778	9232
	water (%)	100	100	100	100	100	100	100	100	100	100	100	100	100	100	100	100	100	100	100	100	100	100
	Cisolid (kg/h)	89	501	549	561	600	602	584	550	552	632	636	604	587	544	491	641	644	606	566	655	584	365
	enzyme (%)	100	100	100	100	100	100	100	100	100	100	100	100	100	100	100	100	100	100	100	100	100	100
CONCENTRATED OUTPUT	TOTAL (kg/h)	30917	82916	88810	88630	92641	91804	87752	80647	88510	94495	93596	87059	83510	75952	82426	96575	94348	86540	89658	96170	82753	41031
	water (%)	49.79	26.98	28.31	28.50	29.43	29.42	28.89	27.57	28.35	30.04	30.10	29.15	28.55	26.79	26.73	30.28	30.27	29.14	28.69	30.50	28.40	6.45
	xylose (%)	17.07	11.55	9.08	7.50	5.22	4.45	3.77	3.30	8.55	2.64	1.45	0.79	0.34	0.35	12.65	2.96	1.05	0.17	7.47	1.04	0.20	0.42
	glucose (%)	30.74	57.42	58.74	60.09	61.53	62.26	63.27	64.74	59.20	63.51	64.58	65.90	66.76	68.09	56.55	63.05	64.83	66.49	59.98	64.69	67.02	84.43
	cellobiose (%)	0.35	0.73	0.74	0.76	0.78	0.79	0.80	0.82	0.75	0.80	0.82	0.83	0.85	0.86	0.72	0.80	0.82	0.84	0.76	0.82	0.85	1.07
	xylolig (%)	0.40	0.27	0.21	0.18	0.12	0.10	0.09	0.08	0.20	0.06	0.03	0.02	0.01	0.01	0.30	0.07	0.02	0.00	0.18	0.02	0.00	0.01
	glucolig (%)	1.09	2.30	2.35	2.40	2.46	2.49	2.53	2.59	2.37	2.54	2.58	2.64	2.67	2.72	2.26	2.52	2.59	2.66	2.40	2.59	2.68	3.38
	soluble lignin (%)	0.56	0.76	0.57	0.57	0.46	0.49	0.65	0.91	0.58	0.40	0.43	0.67	0.83	1.18	0.80	0.32	0.40	0.70	0.53	0.34	0.85	4.24
	Total convertible components (kg/h)	15524	60544	63668	63369	65376	64795	62403	58415	63417	66108	65424	61679	59672	55605	60397	67335	65786	61321	63939	66835	59251	38386

duration of pretreatment. Each group of temperature was labelled with a letter and each time subgroup was labelled with a figure for easier identification in the naming of the Aspen Plus simulation files, one of which is available in the Supplementary Information section, along with the simulation for the first strategy.

Discussion

According to a recent patent providing ways to make distillate fuels from sugars [12], the hydrocarbon yields is based on the percent weight of carbon sources fed to the catalytic conversion process. Thus, the best strategy is assessed by comparing which of them generates the highest amount of carbon-containing components. To this end, the total mass flow rate of convertible components was calculated for each scenario.

Table 2 clearly shows that the first strategy consisting in hydrolysing a blend of corn stover and switchgrass pretreated upstream with dilute sulfuric acid provides low yields of carbon sources for downstream catalytic upgrading. Among all different cases related to Miscanthus pretreated upstream with ionic liquid, the pretreatment at 170°C for 30 minutes entails the highest amount of convertible components after enzymatic saccharification.

Moreover, Miscanthus is an interesting feedstock candidate by itself since it has a very low ash content (inferior to 1% as shown in Figure 4.b) and thus can reduce the pretreatment and filtration equipment in terms of ash removal for the protection of catalytic systems.

Furthermore, ionic liquid is recycled in the pretreatment process while sulphuric acid, which is hazardous, toxic and corrosive, is not recycled in the pretreatment process but neutralized. Thus, ionic liquid is a more economic and environmental friendly alternative compared to acid processing which needs to be continuously renewed.

Conclusions

In this study, a comparative insight of two scenario was presented using Aspen Plus simulation process based on NREL 2017 work.

It was demonstrated that the blend of corn stover and switchgrass pretreated with dilute sulfuric acid entailed poor carbon sources yields after enzymatic hydrolysis and concentration steps. On the opposite, Miscanthus pretreated upstream with ionic liquid achieved high carbon sources yields. The best pretreatment conditions were reported to be 170°C for 30 minutes.

For more accuracy and reliability, this comparison requires further analysis including techno-economic viability and environmental impacts.

Supplementary Information

For additional information regarding the simulations operated on Aspen Plus software for A300, readers are invited to consult the following files: “PROJECT-ACID” and “PROJECT-IL-A.1” joined to this paper. They respectively simulate the case of the blend of corn stover with switchgrass pretreated with dilute acid and Miscanthus pretreated with ionic liquid at 150°C for 30 minutes.

References

[1] Srirangan, K., Akawi, L., et al., 2012, *Towards sustainable production of clean energy carriers from biomass resources*, Applied Energy, Elsevier, 172-86.

[2] Hao, Z., Loqué, D., 2017, *Plant Cell Walls: Improved Resources for Biofuels and Value-Added Products through Genetic Engineering*, Wiley Online Library

[3] Mosier, N., Wyman, C., et al., 2014, *Features of promising technologies for pretreatment of lignocellulosic biomass,* Bioresource Technology, Elsevier, 96:673-86.

[4] Humbird, D., Davis R., et al., 2011, *Process Design and Economics for Biochemical Conversion of Lignocellulosic Biomass to Ethanol Dilute-Acid Pretreatment and Enzymatic Hydrolysis of Corn Stover*, National Renewable Energy Laboratory. Available from:

https://www.nrel.gov/docs/fy11osti/47764.pdf.
[5] Davis, R., Tao, L., et al., 2013, Process *Design and Economics for the Conversion of Lignocellulosic Biomass to Hydrocarbons: Dilute-Acid and Enzymatic Deconstruction of Biomass to Sugars and Biological Conversion of Sugars to Hydrocarbons*, National Renewable Energy Laboratory. Available from: https://www.nrel.gov/docs/fy14osti/60223.pdf.
[6] Davis, R., Tao, L., et al., 2015, *Process Design and Economics for the Conversion of Lignocellulosic Biomass to Hydrocarbons: Dilute-Acid and Enzymatic Deconstruction of Biomass to Sugars and Catalytic Conversion of Sugars to Hydrocarbons*, National Renewable Energy Laboratory. Available from: https://www.nrel.gov/docs/fy15osti/62498.pdf.
[7] Brandt-Talbot, A., Gschwend, F. J. V., et al., 2017, *An economically viable ionic liquid for the fractionation of lignocellulosic biomass*, Green Chemistry, The Royal Society of Chemistry, 19: 3078-102.
[8] Brosse, N., Dufour, A., et al., 2012, *Miscanthus: a fast- growing crop for biofuels and chemicals production*, Wiley Online Library.
[9] Gschwend, F. J. V., Malaret, F., et al., 2018, *Rapid pretreatment of Miscanthus using the low-cost ionic liquid triethylammonium hydrogen sulfate at elevated temperatures Green Chemistry, The Royal Society of Chemistry, Electronic Supplementary Information*. Available from: file://icnas1.cc.ic.ac.uk/mb2718/downloads/c8gc00837j1.pdf.
[10] Tao, L., Davis, R., 2017, *NREL 2017 Biochemical Sugar Model*. Available at: https://www.nrel.gov/extranet/biorefinery/aspen-models/.
[11] Outon-Gil, R., 2017, *Conceptual design, simulation and economic evaluation of the IonoSolv process*. Master Thesis. Universitat Ramon Llull.
[12] Blommel, P., et al., 2012, *Method and systems for making distillate fuels from biomass*, U.S. Patent No. 2012/0198760 A1.

Analysis and modelling of immobilized β-1,4-galactosyltransferase for an artificial Golgi reactor

Louis Boyer and Cleveland Douglas
Department of Chemical Engineering, Imperial College London, U.K.

Abstract Monoclonal antibodies (mAbs) are the largest group of approved biopharmaceuticals and are widely used in immunotherapy to treat cancer and autoimmune diseases. As the therapeutic efficacy of mAbs is dependent on their glycosylation pattern, the heterogeneity of products formed through current methods of glycosylation is a challenge to the biopharmaceutical industry. An artificial Golgi reactor (AGR) has been designed to enhance control over the glycosylation pathway. However, a glycosylation enzyme used in the reactor, β-1,4-galactosyltranferase (β-1,4-GalT), has not been well studied in its immobilised form. Favourable experimental conditions for galactosylation catalysed by the immobilised form of β-1,4-GalT were investigated using analytical methods of MALDI-TOF MS and HPLC. Empirical results were used to study process feasibility using a mathematical model of the packed bed AGR. An excess of UDP-Gal favoured higher conversions, but UDP formed from hydrolysis of UDP-Gal appeared to inhibit enzyme activity. The required reactor length for an AGR achieving 55% conversion is 72 meters. The experimental results may be used to inform the design of an AGR but the feasibility of such a process is unlikely.

Introduction

Glycosylation is a crucial process for the biopharmaceutical industry due to the need for therapeutically effective glycoproteins.[1] Monoclonal antibodies (mAbs) dominate this group, making up 27% of approved biopharmaceuticals in the industry between 2010 and 2014.[2] Glycosylation is one of the most common and complex post-translational modifications of proteins.[3] It involves the addition of a monosaccharide or glycan to a protein via a glycosidic bond, catalysed by glycosyltransferases.[4] The glycans are provided by nucleotide sugar donors (NSDs). The addition of glycans to the protein structure is known to affect properties such as serum half-life, stability, folding of the protein (polypeptide chain) and can prevent immunogenicity[5,6] which in turn impacts the safety of the product.[7] Therefore, glycosylation of mAbs requires a particular focus.

Although most currently available mAbs are glycosylated with the aim of improving the biological activity of the pharmaceutical product[5], it is common that they exhibit suboptimal therapeutic efficacies nonetheless. This is due to the challenge in controlling the glycosylation pathway as enzyme promiscuity can occur.[8] This is where many enzymes compete for the same substrate, creating a variety of glycosylation pathways leading to the production of many glycoprotein structures. Some of these structures, such as high-mannose types, are immunogenic or have a low serum half-life.[9] Therefore, we require a way to control the glycosylation process to follow the correct pathway, producing glycoproteins with the desired glycan profile.

Until now, many *in vitro* methods of glycosylation have been established to combat enzyme promiscuity and produce homogenous glycoprotein therapeutics. Methods of *in vitro* glycosylation include chemo-enzymatic, chemo-selective and site-specific methods. In chemo-enzymatic glycosylation, a core glycan is expressed *in vivo*, removed, trimmed down and remodelled via *in vitro* transglycosylation with the necessary glycosyltransferases.[10] However, a homogenous product is not guaranteed since not all enzymatic reactions will go to completion, allowing other enzymes which are present to act upon any incomplete substrates.[11] In chemo-selective glycosylation, expressed proteins are tagged using site-directed mutagenesis.[12] This tag is usually introduced at a cysteine residue, chosen as the established site for glycosylation.[11,13] This process is limited due to the complex chemistry and again a lack of product homogeneity.[11] This has led to a search for a new method to more effectively combat enzyme promiscuity.

The need to control glycosylation is also particularly significant now as there is an emphasis of the Quality-by-Design (QbD) approach in the pharmaceutical industry.[14] QbD aims to build quality into a product by applying knowledge of the product into each step of the manufacturing process.[15] To satisfy all these criteria, an artificial Golgi reactor (AGR) has been proposed which would lead to considerable enhancements in the

quality and efficacy of mAbs.[7] Uniquely, the spatial separation of immobilised enzymes into reactor compartments (mimicking the Golgi apparatus) will allow us to gain control over the glycosylation pathway as enzymes will be unable to act freely upon any substrate. The immobilisation of the glycosylation enzymes allows for increased enzyme stability and ease of separation from the product.[16] And the modular design of the reactor allows modifications so that many glycosylation pathways can be followed, therefore a range of mAbs with different glycan profiles can be constructed if necessary.

The AGR is formed of four compartments, each housing a specific enzyme. The four enzymes to be used are *N*-acetylglucosaminyltransferase I (GnTI), *N*-acetylglucosaminyltransferase II (GnTII), α-mannosidase II (ManII), and β-1,4-galactosyltransferase (GalT). Since GalT competes for the same substrate as both ManII and GnTII, implementing the pathway of GnTI-ManII-GalT-GnTII will allow us to form a homogenous product. In three of the compartments the reactions involve additions of either galactose (Gal) or *N*-acetyl-D-glucosamine (GlcNAc) to the mAb using the NSDs, UDP-Gal and UDP-GlcNAc respectively. This leaves behind UDP (uridine diphosphate) as a by-product, a potential enzyme inhibitor.[7] UDP is also formed via the hydrolysis of the NSDs, furthering the problem of its presence as UDP remains in equilibrium with the UDP-enzyme complex formed, preventing further NSDs from binding to the enzyme. UDP's inhibitory behaviour on GnTI, has been documented in the past[17,18] and it is also a "well-known" inhibitor of Gal-T.[19] Interestingly, it has been indicated in literature that the immobilisation of GalT can reduce the inhibitory effect of UDP.[20]

We have chosen to study β-1,4-GalT due to its ability to compete for multiple substrates, deeming it to be an obstacle towards achieving limited enzyme promiscuity in this reactor. β-1,4-GalT catalyses the transfer of galactose from UDP-Gal to a GlcNAc residue forming a β-1,4-glycosidic bond.[21] This research aims to focus on this galactosylation reaction in the reactor to understand the conditions which are favoured by GalT and reactor system in terms of the ratio of the NSD, UDP-Gal, to the acceptor $GlcNAcMan_3GlcNAc_2$ and consequently the ratio of UDP-Gal to β-1,4-GalT.

The experimental data obtained from this research will be used in the reactor model to inform modifications to reaction parameters. This is especially relevant for UDP-Gal as it must be present in excess of the acceptor and is one of the most expensive reactants. Adjusting the UDP-Gal concentration will also work toward minimising costs for the AGR. Alongside this, we aim to discover the extent to which UDP could inhibit the reaction, which will determine the need for measures that reduce the concentration of UDP present in the reactor to potentially increase conversion.

Background

Work done on an artificial Golgi apparatus - The benefits of an artificial Golgi apparatus include control over enzyme concentration, kinetics and reaction conditions. Previous efforts to mimic the Golgi apparatus notably include the creation of a functional artificial Golgi prototype on a digital microfluid chip[22] and a microfluidic chip with separate chambers for sequential enzymatic reactions.[23] Martin, J. G. et al.[22] looked at glycosylation of proteoglycans rather than glycoproteins however, their motivations were similar in that the *in vivo* modification lacked control, producing a heterogenous product. They successfully achieved glycosylation but with low conversions.[22] Ono, Y. et al.[23] looked at synthesis of a tetrasaccharide, using immobilised enzymes, and succeeded in producing it.

Available information on β-1,4-GalT - β-1,4-GalT is among the most well studied glycosyltransferases and is commercially available. β-1,4-GalT can recognise a variety of sugar donors and glycosylation reaction schemes indicate it is a large contributor to enzyme promiscuity.[24]

Palacpac, N. Q. et al.[25] performed galactosylation using β-1,4-GalT expressed in plant cells. This gave us an idea of the ratios of UDP-Gal that were required to carry out the reaction successfully. Also, we used this to understand the conditions needed in terms of pH and concentration of $MnCl_2$. Previous work in our laboratory was also valuable to our knowledge of ratios and conditions to utilise. To our knowledge, optimal conditions for immobilised β-1,4-GalT are not very well documented, besides the work done by Ito, T. et al.[26]. This is a knowledge gap that our research will help continue to fill.

Work performed on UDP-inhibition - The inhibitive effects of UDP on glycotransferases have been

demonstrated in literature. Nishikawa et. al.[18] and Bendiak et.al.[17] established a competitive relationship between UDP and UDP-GalNAc for mammalian GnTI. The reaction mechanism follows a sequential-order bi-bi with competitive and product inhibition of UDP.[24] UDP has not yet been confirmed as an inhibitor for β-1,4-GalT.

Materials and methods

Chemicals, enzymes and reagents - The galactosylation enzyme, β-1,4-galactosyltransferase was immobilized on streptavidin beads on each day of use and provided by the Polizzi lab, Imperial College London. Uridine 5′-diphosphogalactose disodium salt (UDP-Gal) and uridine 5′-diphosphate disodium salt (UDP) were purchased from Sigma Aldrich at 97% and 96% purity respectively and stock solutions were made using ddH_2O. The acceptor, $GlcNAcMan_3GlcNac_2$ was produced on each day it was used and came from a previous glycosylation reaction utilising GnTI as the enzyme, therefore UDP was present in this mixture. 1M $MnCl_2$ solution was purchased from Sigma Aldrich, as well as 99.8% Tris was used to create a 1M stock solution.

β-1,4-GalT functionality confirmation assay - The assay was conducted in a final volume of 400 µL containing 0.5 µM of acceptor. 20 mM Tris-HCl buffer (pH 7.4), 1 mM $MnCl_2$ with 0.375 µM of β-1,4-GalT. UDP-Gal was present at 5 mM, 10000 times the acceptor concentration. The mixture was incubated at 37°C on a shaking plate for 4 hours, after which the enzyme was separated via centrifugation at 3000 G for 5 minutes. MALDI-TOF was used to analyse the samples.

β-1,4-GalT with variation of UDP-Gal assays - The five assays were conducted in a final volume of 200 µL containing 0.4 µM of acceptor, 20 mM Tris-HCl buffer (pH 7.4), 1 mM $MnCl_2$ with 0.75 µM of β-1,4-GalT. With amounts of UDP-Gal varying at 500, 1000, 5000, 10000 and 43750 times the concentration of the acceptor. The mixtures were incubated at 37°C on a shaking plate for 20 hours. After 20 hours the mixture containing tubes were removed from the incubator and centrifuged at 5000 G for 5 minutes to separate the immobilised enzyme from the remaining reagent and product mix. The analytes were transferred to new Eppendorf tubes prior to analysis. MALDI-TOF mass spectrometry was used here to determine the conversion of acceptor to product ($GalGlcNAcMan_3GlcNac_2$) using the intensities of each.

The intensity of peaks was used to calculate conversion using **Equation 1**.

$$conversion = \frac{I_P}{I_A + I_P} \times 100 \qquad (1)$$

Where I is the intensity of a peak, and subscripts A and P denote the acceptor and the product respectively.

HPLC analysis of potential UDP-Gal hydrolysis - Two assays, one containing 7.5 mM UDP-Gal and 0.75 µM Gal-T, and the other containing 7.5 mM UDP-Gal as a negative control were conducted. This was carried out in a final volume of 200 µL. Both assays also contained 20 mM Tris-HCl buffer (pH 7.4) and 1 mM $MnCl_2$. The mixtures were incubated at 37°C for 4 hours after which the assay containing GalT was centrifuged to remove the enzyme. The samples were diluted 75-fold in ddH_2O to give a maximum UDP-Gal reading of 0.1 mM and analysed by HPLC. The HPLC analysis was performed on an Alliance HPLC system (Waters, UK), consisting of the e2695 separations module and 2998 photodiode array detector. The mobile phases used as eluents were 3 mM NaOH (E1) and 1.5M sodium acetate in 3 mM NaOH (E2). E1 was prepared on the day of analysis whilst E2 was pre-prepared for prior use. For both preparations the eluents were filtered. The experimental procedure from Jimenez del Val et. al.[27] was followed and the analysis of the chromatographic data was carried out using the Empower 2 software (Waters, UK).

Calibration of the HPLC method was performed by creating five separation stock solutions of UDP, UDP-Gal and a combination of both at various concentrations (0.025, 0.05, 0.075, 0.1, 0.125 and 0.15 mM). HPLC analysis allowed for the construction of a standard curve for each component.

Galactosylation reaction inhibition assay - Two 200 µL assays were conducted. One assay with no addition of extra UDP and one with UDP added up to 16 mM. Aside from the difference in UDP concentration, both assays contained 0.75 µM GalT,

0.4 μM acceptor, 4 mM UDP-Gal, 20 mM Tris-HCl (pH 7.4) and 1 mM $MnCl_2$. After incubation at 37°C for 4 hours the enzyme was removed via centrifugation and analysis was carried out with MALDI-TOF MS.

Modelling – The mathematical model of an AGR designed by Klymenko et al.[7] was used to learn information about the physical implications of the experiments. The model configuration considered was a packed bed reactor with non-porous pellets because this best matches the previous experimental set up. The pellets mimic the non-porous beads used for immobilisation and the bed packing provides a comparable contact of phases provided by the shaking in experiments. The same model parameters were used. GnTII was removed from the model's reactor sequence for the model to produce $GalGlcNAcMan_3GlcNAc_2$ at its outlet. This was achieved by setting the turnover rate to zero and the module length was set to be negligibly small at 0.1cm. The module length for GalT was extended for the residence time of the model to match the incubation time in experiments. The turnover rate of GalT was modified by trial and error as a controlled variable to reach the same conversion of acceptor as that observed experimentally. The inlet concentration was modified as a controlled variable to determine the module length required to achieve a known experimental conversion using the new value for the catalyst turnover.

Costing calculations were performed by calculating the cost of UDP-Gal required per mg of product formed using the data from the experiments. It was assumed that the price of UDP-Gal in a theoretical process would equal 10% of commercially available UDP-Gal, because reactants are bought in bulk in industrial processes. Prices were taken from the Sigma Aldrich sales website. The molecular weight of the mAb was assumed to be 150kDa. The cost of donor per mg of product formed was plotted against desired conversion and was fitted using MATLAB's *fit* function.

The rate of reaction used in the mathematical model is taken from Jimenez del Val et al.[24] and can be found in **Equation 2,** where $[E]_0$ is the total concentration of GalT, UDP is uridine diphosphate and OS is an oligosaccharide complex. Other terms include the concentration of NSD, k_{cat}^{E} the catalytic rate constant, and dissociation constants of enzyme-NSD complex K_{NSD}^{E}, the enzyme-reactant oligosaccharide K_{i}^{E}, the enzyme-competing oligosaccharide K_{j}^{E}, the enzyme-product K_{j+1}^{E}, and the enzyme-UDP complex K_{UDP}^{E}.

$$r_E = \frac{k_{cat}^{E}[E]_0[NSD][OS_i]}{K_{NSD}^{E}K_i^{E}\left(1+\frac{[NSD]}{K_{NSD}^{E}}+\frac{[NSD]}{K_{NSD}^{E}}\Sigma\frac{[OS_j]}{K_j^{E}}+\frac{[UDP]}{K_{UDP}^{E}}\Sigma\frac{[OS_{j+1}]}{K_{j+1}^{E}}+\frac{[UDP]}{K_{UDP}^{E}}\right)} \quad (2)$$

Results

β-1,4-GalT functionality confirmation assay – MALDI-TOF MS analysis identified the presence of the galactosylated product $GalGlcNAcMan_3GlcNAc_2$, which confirmed activity of the immobilised enzyme. The relative peak intensity of the product to the acceptor was 5.2%, which was equivalent to a conversion of 5.5%. To achieve higher conversions, the incubation time in further experiments was extended to 20 hours. This was preferred to increasing enzyme, NSD or acceptor concentrations, because these components were only available in limited supply. It is hypothesised that this would have also increased conversion.

β-1,4-GalT with variation of UDP-Gal assays – MALDI-TOF MS analysis showed that the peak associated with the galactosylated product increased in height as the ratio of UDP-Gal to acceptor increased. The measured conversion for each ratio is plotted in **Figure 1**.

The experimental data seems to suggest that the maximum achievable conversion after 20 hours reaches a limit at around 54%. Conversion was found to best fit a logarithmic relationship with the donor/acceptor ratio with an R^2 value of 0.89. A logarithmic relationship would suggest that there is no limit for the conversion since the natural logarithm tends to infinity. This raises two problems; firstly, conversion has an upper boundary of 100%. Secondly, the donor/acceptor ratio required to reach conversions higher than 55% exceed ratios that are within operational reason, and that are found in literature.[25] Because of these reasons, the logarithmic relationship was neglected in further analysis. An inverse exponential fit was attempted, but this did not match with experimental data.

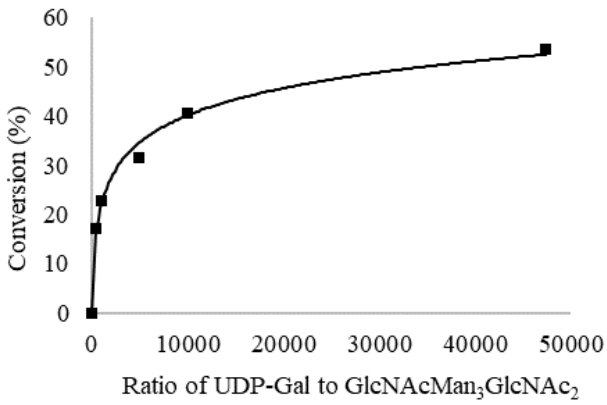

Figure 1 - Dependence of conversion on the variation of UDP-Gal to $GlcNAcMan_3GlcNAc_2$

HPLC analysis of UDP-Gal hydrolysis - Absorbance peaks associated with UDP were detected within the UDP-Gal assays, both for the negative control as well as in presence of the enzyme. **Figure 2** shows an example of these absorbance peaks. The presence of UDP indicates that the hydrolysis of UDP-Gal occurs under the given experimental conditions.

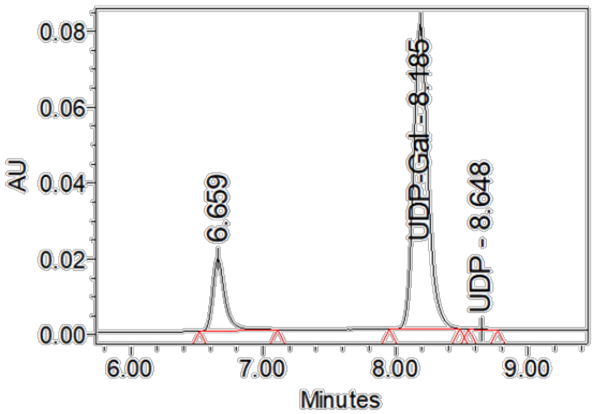

Figure 2 - An HPLC chromatogram showing peaks at 6.659, 8.185, and 8.648 minutes for an unknown compound, UDP-Gal, and UDP

The standard curves used for quantitative analysis can be found in **Figure 3**. Data for the linearity of the standard curves can be found in **Table 1**. The standard curve for UDP-Gal has a high R^2 value, but not for UDP. Neither values for the gradient of these curves concurred with literature values.

Peaks associated with unknown compounds were also detected, suggesting that UDP-Gal and UDP further hydrolyse into their constituent nucleotide, nucleoside and phosphate groups. One of the unknown peaks is believed to be UMP due to its similar relative retention time found in literature (Jimenez del Val et. al.[27]). The unknown quantities of unidentified compounds prevented the calculation of the total amount of substance present in assays. High standard deviations also prevented accurate calculations of the amount of UDP produced from hydrolysis.

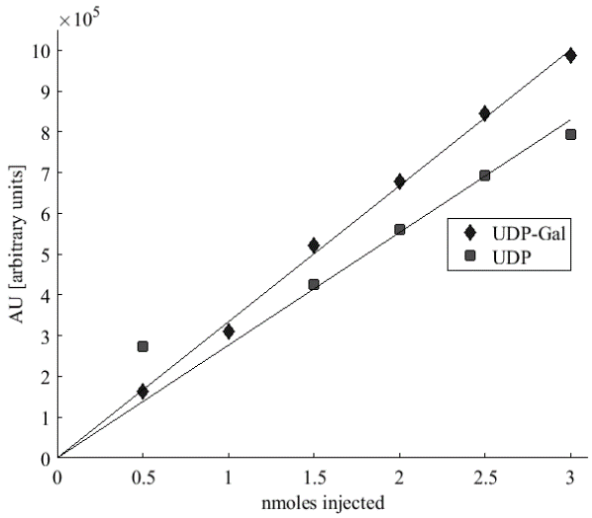

Figure 3 - Standard curves constructed for UDP and UDP-Gal

Table 1 - A comparison of gradients of standard curves obtained in literature and our experimental work

	Gradient (mVs/pmol)	Gradient (Jimenez del Val et al.[27])	R^2
UDP	277	919	0.88
UDP-Gal	334	258	0.99

Galactosylation reaction inhibition assay – The inhibitory effect of UDP was studied by comparing the measured conversion of the acceptor to the product at low and high concentrations of UDP. The rate of reaction is expected to be highest at the start of the incubation due to the high concentration of substrate and co-substrate. **Figure 4** and **Figure 5** show the mass spectra attained from analysis of each assay. The conversion of the assay with 16mM UDP was 84% lower than that of the assay with no added UDP. This is evidence that the rate of reaction decreased due to a higher concentration of UDP. The unknown peaks observable on the MALDI-TOF spectra were also observed in the negative control assay. This is evidence that the unknown compounds associated with these peaks can be attributed to contamination.

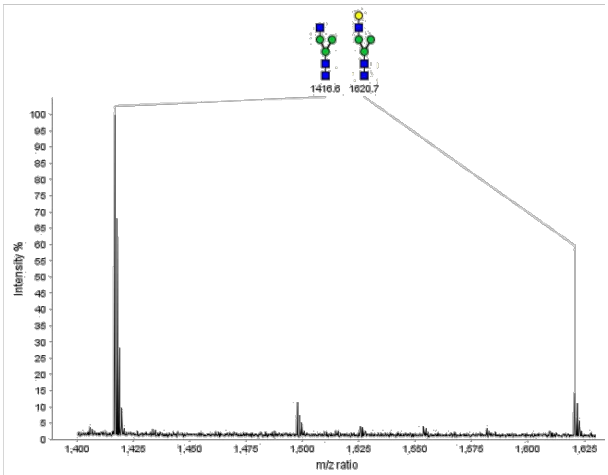

Figure 4 - Mass spectrum showing relative intensities of acceptor and product after 4-hour incubation with no additional UDP added

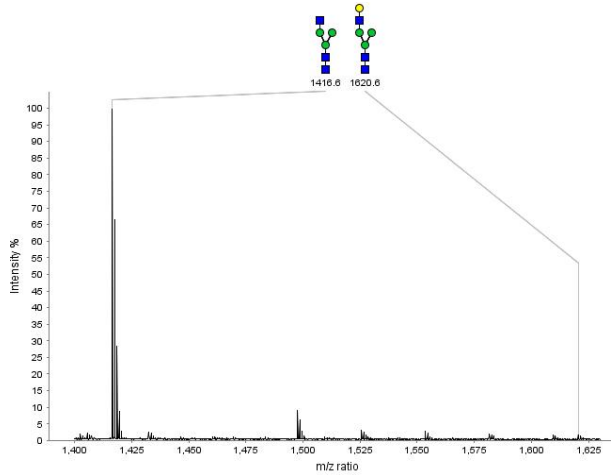

Figure 5 - Mass spectrum showing relative intensities of acceptor and product after 4-hour incubation with 16 mM of UDP added

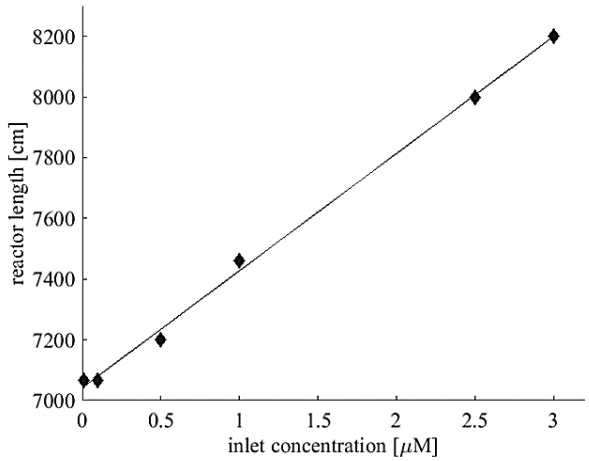

Figure 6 – Required reactor length to achieve 55% conversion against AGR inlet concentration

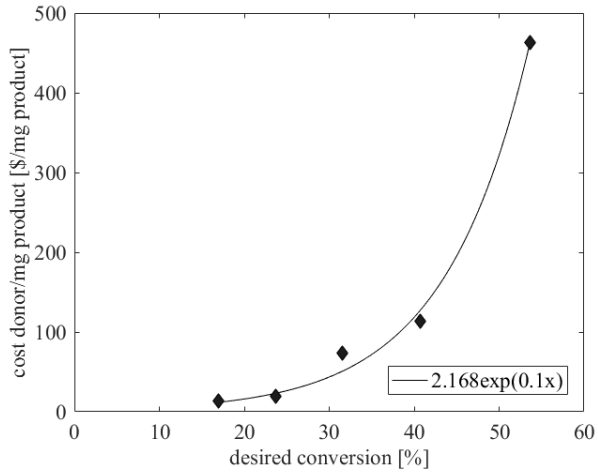

Figure 7 – Cost of UDP-Gal required per mg of mAb product formed against conversions for a 20-hour residence time.

Simulation analysis – The experimental data for the role of the enzyme indicated that the length of the PBR would have to be extended from 6.4m to 72m to achieve a residence time of 20 hours. The rate of reaction of the catalyst K_{cat} was adjusted by a factor of 2.10^{-4} for the model to achieve a 55% conversion after 20 hours. This demonstrated that the K_{cat} was overestimated in the design of the mathematical model. Increasing the inlet concentration of the reactor was found to increase the length required to achieve 55% conversion, shown in **Figure 6.** A linear increase of reactor length with respect to inlet concentration was found to have a R^2 of 0.99. The results of the costing analysis showed a strong fit to the exponential function with a R^2 value of 0.98. The results of the costing analysis are shown in **Figure 7**. Experimental data showed a strong fit to the exponential function with a R^2 value of 0.98. The need for an excess of UDP-Gal to reach high conversions exponentially increases process costs. The totality of the simulation analysis shows that the experimental data challenges the feasibility of the PBR as a viable reactor configuration for the artificial Golgi reactor.

Discussion

β-1,4-GalT functionality confirmation assay – The presence of the peak associated with the galactosylated product is strong evidence that the immobilised form of the enzyme is a viable form of the enzyme. To compare the activity of the commercially available enzyme, a control assay with the commercial enzyme would be performed. MALDI-TOF analysis provides qualitative analysis of the reaction, and therefore the exact value of the conversion cannot be used for a kinetic analysis, which would require more accurate quantitative methods. Additionally, triplicates would have to be performed to obtain more precise information. The additional experiments mentioned above were not permissible within the time frame of the project and due to material limitations.

β-1,4-GalT with variation of UDP-Gal assays – The rate equation for the galactosylation (del Val et.al.[24]) accounts for an increase in the rate of reaction as the NSD concentration increases. For a given residence time, the conversion will be greater for an assay of the highest donor concentration. The variation of UDP-Gal assays agrees with the kinetic model proposed by Jimenez del Val et al.[24].

Despite its high R^2 value, the logarithimic fit does not concur with a physical interpretation of reaction kinetics. Conversion has an upper bound of 1 whereas the natural logarithm tends to infinity. The log fit does not replicate the conversion tending towards a limit of 55%. A solution to this would have been an inverse exponential function of the form $\chi(\mu) = \chi_{max} - ae^{b\mu}$ where χ is conversion, χ_{max} is the maximum achievable conversion after 20 hours, a and b are exponential factors. The *fit* function in MATLAB & methods of trial and error were unable to provide a suitable fits for the experimental data.

Due to the reaction kinetics, it is reasonable that conversion after 20 hours reaches a limit when the cosubstrate concentration is increased. The rate equation in **Equation 2** can be expressed as a Michaelis-Menten type rate equation with respect to the concentration of UDP-Gal. This is an appropriate transformation because all other terms were held constant throughout our experiments. The transformation gives $r_e = \frac{A\,[NSD\}}{B+[NSD]}$, where A and B are grouped terms for the oligosaccharide complex concentrations, UDP concentration, and the dissociation constansts. At high substrate concentrations, the rate reaches its maximum value A. Since the conversion is dependent on the rate of reaction, this explains why the conversion observed tends to a limit for a given residence time. This emperical evidence greatly strengthens the validity of the kinetic model used to describe enzyme kinetics for GalT in our AGR model.

HPLC analysis of UDP-Gal hydrolysis – The presence of UDP in UDP-Gal assays provides strong evidence for the hydrolysis of UDP-Gal. The presence of UMP in all assays with UDP and UDP-Gal and negative controls strengthens the hypothesis that UDP-Gal breaks down into its constituent nucleotides. No conclusive evidence is available to determine whether the enzyme accelerates the hydrolysis.

Pipetting was the largest source of error in this experiment and prevented an accurate measurement of UDP & UDP-Gal. An injection error of the HPLC system is improbable. The experiments were performed in triplicates from the same diluted aliquot from the same stock solution. A more accurate experimental design would include a higher number of replicates, as well multiple stock solutions to account for errors during the experimental preparation.

It is unexpected that the gradients or the standard curves are different to literature values because the experimental procedure and set up for both was identical. This reinforces the argument that the errors in the preparation of the stocks and aliquots were a cause for the differences observed. The R^2 value of UDP is higher than that of UDP-Gal because of a statistical outlier observed for UDP for an injection of 0.5 nmoles. This is further evidence of errors made during the stock solution and aliquot preparation.

Galactosylation reaction inhibition assay - The decrease in conversion does not confirm that UDP is an inhibitor of GalT, however it agrees with the hypotheses found in literature.[7] Further experiments at different concentrations of UDP should be conducted to confirm with certainty the inhibitive role UDP plays in this reaction. MALDI-TOF data cannot be used for precise quantitative analysis, but it does show a large decrease in the concentration of the product. The consistency of both the experimental conditions and the stocks used supports the validity of the results. Possible sources of error in the experimental preparation include pipetting accuracy and a loss of enzyme, acceptor or product during the preparation of the analytes for spectrometry.

Simulation analysis – It was expected to observe a much larger length of reactor when increasing the residence time to match the experimental incubation time. This was because the previous residence time was 1.67 hours and the new value is 20 hours. The previous module length was 583cm and the new value is 7200. The proportionality coefficient is 12.34 for both parameters.

Although K_{cat} was modified was modified by a high order of magnitude, it was expected that the K_{cat} value in the model would have to be significantly adjusted. This is because the parameters used in the reactor model were all based on different experimental conditions. Most notably for the case

of reaction kinetics, the pH and reactor temperature of the model are different to the experiments. The turnover number of the catalyst is assumed to remain at its maximal theoretical value, which does not account for the loss of enzyme activity observed in previous experimental work.[26] Most of the parameters used in the model are from different sources and different cell lines, which limits the confidence in the calculation. The turnover number was calculated using kinetic information of GalT from purified rat liver, whereas the experimental GalT was expressed in an engineered E-coli host cell line. Additionally, the model also makes assumes ideal flow and enzyme concentration uniformity on pellet surfaces.

Figure 6 shows that the reactor length increases with inlet concentration. This is due to the rate of reaction for glycosylation in Equation 2 having a term for UDP in the denominator. The model is designed such that there is a stoichiometric amount of NSD for full conversion of the substrate in each enzyme module. Because the GalT module is placed last in the reactor, UDP is present at twice the concentration of the substrate at the GalT module inlet. Increasing the reactor inlet concentration therefore also increases concentration of inhibitor of GalT.

The reactor length does not change significantly because of the large excess of co-substrate, which is the biggest term in the rate equation. Additionally, enzyme turnover rates tend to a limit at high substrate concentrations.

The assumption of 10% of commercially available prices of UDP-Gal is reasonable because bulk buying reduces process costs substantially. The prices are deemed to be accurate as they are taken from Sigma Aldrich's website. The assumption that the molecular weight of the mAb 150kDa is deemed accurate as it taken from chemical data pertaining to IgG, a widely documented mAb common in mammals. The high R^2 value for an exponential function is coherent with previous analysis when considering the relationship previous shown between conversion and UDP-Gal excess, since the cost is proportional to the concentration of UDP-Gal used.

Conclusions

Immobilised β-1,4-galactosyltransferase and its reactions were studied. The data attained was used to model the reaction in the AGR model. This is incredibly important to the biopharmaceutical industry as we will be able to create an AGR and produce glycoprotein-based drugs which are more therapeutically effective.

β-1,4-GalT activity was assessed and found to be viable in its immobilised form which is significant since the immobilisation of the enzyme is crucial to the design of the AGR as it helps achieve optimum conversions. If activity were not to be detected, an alternative enzyme support could have been trialled to assess if activity improves.

The influence that UDP-Gal's concentration had upon conversion was then determined. It was demonstrated that the conversion will reach a limit with respect to increasing UDP-Gal concentration, which tells us that we need to alter other conditions in our AGR in order to reach higher conversions, rather than increasing the concentration of UDP-Gal, an expensive material.

Lastly, evidence was found supporting the argument that UDP inhibits the galactosylation catalysed by GalT. Because UDP-Gal is present in large excess in galactosylation, a large quantity of UDP will be present due to the hydrolysis of UDP-Gal. If the inhibitory effect of UDP is significant, this will be a large limitation to the process. UDP is also formed as a by-product of previous enzyme modules, notably GnTI. This leads us to consider methods that could regulate the amount of UDP present in the reactor such as recycling and UDP to NSD regeneration, thus decreasing UDP's inhibitory impact.

Simulation analysis showed that current kinetic models are insufficient for an accurate description of experimental data. It also showed that the GalT reactor module would have to be extended to a physically unfeasible length, and that the residence time of 20 hours for a low conversion brought the economic feasibility of the process into question. Changing the inlet concentrations was inconsequential in changing the length of the reactor, suggesting that the modifications to the reactor conditions and process design need to be made to increase conversion. The costing analysis showed costs rise exponentially when to trying increase conversion. More precise costing analysis should be performed to investigate detailed process costs if this reactor configuration is to be industrialised.

To further understand how the galactosylation reaction will perform in the physical AGR, the

reaction should be carried out using actual proteins rather than glycans. As proteins are much more complicated and bulkier than sugars we would be able to see how steric hindrance could influence conversion, increasing our understanding of the requirements to reach high conversions. This must be taken into consideration for design of the real reactor.

Acknowledgements
We thank Dr. Ignacio Moya-Ramirez (Imperial College London) for assistance with performance of the HPLC analysis and Elli Makrydaki (Imperial College London) for technical and academic assistance, carrying out immobilisation of the enzyme and production of the acceptor.

References

1. Solá RJ, Griebenow K. Glycosylation of therapeutic proteins: An effective strategy to optimize efficacy. BioDrugs. 2010.
2. Walsh G. Biopharmaceutical benchmarks 2014. Nat Biotechnol. 2014;32(10):992–1000.
3. Zhong X, Somers W. Recent Advances in Glycosylation Modifications in the Context of Therapeutic Glycoproteins. Integr Proteomics. 2012;183–96.
4. Lisowska, E, Jaskiewicz E. Protein Glycosylation, an Overview. 2012;(May):50.
5. Costa AR, Rodrigues ME, Henriques M, Oliveira R, Azeredo J. Glycosylation: Impact, control and improvement during therapeutic protein production. Crit Rev Biotechnol. 2014;34(4):281–99.
6. McDonald AG, Hayes JM, Bezak T, G uchowska SA, Cosgrave EFJ, Struwe WB, et al. Galactosyltransferase 4 is a major control point for glycan branching in N-linked glycosylation. J Cell Sci. 2014;127(23):5014–26.
7. Klymenko O V., Shah N, Kontoravdi C, Royle KE, Polizzi KM. Designing an Artificial Golgi reactor to achieve targeted glycosylation of monoclonal antibodies. AIChE J. 2016;
8. Dicker M, Strasser R. Using glyco-engineering to produce therapeutic proteins. Expert Opin Biol Ther. 2015;15(10):1501–16.
9. Choi BK, Actor JK, Rios S, D'Anjou M, Stadheim TA, Warburton S, et al. Recombinant human lactoferrin expressed in glycoengineered Pichia pastoris: Effect of terminal N-acetylneuraminic acid on in vitro secondary humoral immune response. Glycoconj J. 2008;
10. Schwarz F, Huang W, Li C, Schulz BL, Lizak C, Palumbo A, et al. A combined method for producing homogeneous glycoproteins with eukaryotic N-glycosylation. Nat Chem Biol. 2010;
11. Wang, L., and Lomino J V. Emerging Technologies for Making Glycan-Defined Glycoproteins. ACS Chem Biol. 2012;7(1):110–22.
12. Gamblin DP, Scanlan EM, Davis BG. Glycoprotein synthesis: An update. Chem Rev. 2009;109(1):131–63.
13. Chalker JM, Bernardes GJL, Davis BG. A "tag-and-modify" approach to site-selective protein modification. Acc Chem Res. 2011;
14. Rathore AS, Winkle H. Quality by design for biopharmaceuticals. Nat Biotechnol. 2009;27(1):26–34.
15. Jimenez del Val I, Kontoravdi C, Nagy JM. Towards the implementation of quality by design to the production of therapeutic monoclonal antibodies with desired glycosylation patterns. Biotechnol Prog. 2010;26(6):1505–27.
16. Polizzi KM, Bommarius AS, Broering JM, Chaparro-Riggers JF. Stability of biocatalysts. Current Opinion in Chemical Biology. 2007.
17. Bendiak B, Schachter H. Control of glycoprotein synthesis. Kinetic mechanism, substrate specificity, and inhibition characteristics of UDP-N-acetylglucosamine:alpha-D-mannoside beta 1-2 N-acetylglucosaminyltransferase II from rat liver. J Biol Chem. 1987;262(12):5784–90.
18. Nishikawa Y, Pegg W, Paulsen H SH. Control of Glycoprotein Synthesis. Purification and Characterization of Rabbit Liver UDP-N-acetylglucosamine:Alpha-3-D- mannoside beta-1,2-N-acetylglucosaminyltransferase I. J Biol Chem. 1988;263(17):8270–81.
19. Warnock, D., Bai, X., Autote, K., Gonzales, J., Kinealy, K., Yan, B., Qian, J., Stevenson, T., Zopf, D., Bayer R. In Vitro Galactosylation of Human IgG at 1 kg Scale Using Recombinant Galactosyltransferase. Biotechnol Bioeng. 2005;92(7):831–42.
20. Nishiguchi S, Yamada K, Fuji Y, Shibatani S, Toda A, Nishimura SI. Highly efficient

oligosaccharide synthesis on water-soluble polymeric primers by recombinant glycosyltransferases immobilised on solid supports. Chem Commun. 2001;
21. Bajazawa K, Furukawa K, Narimatsu H, Kobata A. Kinetic study of human β- 1,4-galactosyltransferase expressed in E.coli. J Biochem. 1993;
22. Martin JG, Gupta M, Xu Y, Akella S, Liu J, Dordick JS, et al. Toward an artificial Golgi: Redesigning the biological activities of heparan sulfate on a digital microfluidic chip. J Am Chem Soc. 2009;
23. Ono Y, Kitajima M, Daikoku S, Shiroya T, Nishihara S, Kanie Y, et al. Sequential enzymatic glycosyltransfer reactions on a microfluidic device: Synthesis of a glycosaminoglycan linkage region tetrasaccharide. Lab Chip. 2008;
24. Jimenez del Val I, Nagy JM, Kontoravdi C. A dynamic mathematical model for monoclonal antibody N-linked glycosylation and nucleotide sugar donor transport within a maturing Golgi apparatus. Biotechnol Prog. 2011;27(6):1730–43.
25. Palacpac NQ, Yoshida S, Sakai H, Kimura Y, Fujiyama K, Yoshida T, et al. Stable expression of human beta1,4-galactosyltransferase in plant cells modifies N-linked glycosylation patterns. Proc Natl Acad Sci U S A. 1999;96(8):4692–7.
26. Ito T, Sadamoto R, Naruchi K, Togame H, Takemoto H, Kondo H, et al. Highly oriented recombinant glycosyltransferases: Site-specific immobilization of unstable membrane proteins by using staphylococcus aureus sortase a. Biochemistry. 2010;49(11):2604–14.
27. Jimenez del Val I, Kyriakopoulos S, Polizzi KM, Kontoravdi C. An optimized method for extraction and quantification of nucleotides and nucleotide sugars from mammalian cells. Anal Biochem. 2013;

Author Index

Linked to paper number

Abdulla, Omar 3
Adeogba, Eniola 27
Al-Hijji, Mohammed 26
Ankers, Laurence 2
Ang, Del-Wyn 1
Austin, William 53
Azzan, Hassan 35
Baek, Seong Ho 28
Bao, Jie 38
Barty, Peter 27
Begley, Sorcha 29
Belmekki, Myriam 60
Bongirwar, Anshul 3
Booth, George 55
Boyer, Louis 61
Buckley, James 4
Cheung, Siu Kwong 54
Choo, Aireen 38
Chua, Zhi Yuan 23
Clark, Robert 48
Daborn, Emily 13
Dhorajiwala, Manoj 59
Dickman, Karlson 23
Doherty, Caitlin 31
Donaldson, Thomas 45
Douglas, Cleveland 61
Duckworth, Andrew S. 21
Favero, Silvia 19
Fesard, Axelle 5
Flood, Jack 9
Fraser, Dugald 14
Giustiniani, Leonardo 49
Goh, Wei Ming 35
Goodway, Jake L. 50
Gosiamemang, Tsaone 29
Gulati, Sachin 47
Haque, Yasmin 58
Harris, Anisha 10
Hart, Matthew 53
Hassan, Beth 10
Hau, Jonathan 40
Hazra, Shashi 57
He, Serena 16
Hengardi, Miselle T. 44
Ho, Stanley 52
Inguva, Pavan K. 44
Ivanova, Martina 52
Joshi, Revati 58
Kesavadasa, Hariprasad Nair 51
Kong, Fanlu 7
Lee, Sang Ju 15
Lee , Marvin 15
Liang, Haoming 36
Lim, Chia Yin 6
Lim, Tse Puay 11
Liman, Sandy 54
Lister, Roger Percy 9
Loh, Yew Shang 11
Loo, Ping 25
Maharaj, Ashtak M. 50
Marshall, Jordan 46
McAuliffe, Thomas 32
Metcalfe, Richard 55
Moore, Sophia 32
Morrison, Ailsa 4
Narine, Kerissa 43
Neoh, Tu Yuan 56
Ong, Lionel 34
Olah, Dora 41
Ooi, Wei Xiang 59
Oon, Nicholas 37
Paden, Joel 33
Papadimitriou, Aris 40
Papaeracleous, Eleni 17
Park, Sung Joon 7
Patching , Alexandra 8
Pooranawattankul, Darunrat 24
Rattner, Eduardo 37
Qiu, Zhiyan 28
Quigley, Jessica 30
Ramyananda, Saranchana 24
Rinken, Raul 12
Savage, George 14
Shah, Nimil 39
Sheppard, Carlos 49
Shi, Wenbo 20
Shivdas, Prashant 13
Shui, Elise 42
Silawi, Loui 33
Siddique, Humza 26
Sun, Zhuotong 16
Tan, Jin An 51

Tan, Shyang Shin 51
Tarafdar, Aaheli 48
Tee, Zu Yan 2
Teng, Melissa 6
Teo, Jaime 25
Thain, Jack 8
Thomas, Conor 17
Toole, James 47
Tsang, Johnny 57
Vollmer Firenze, Stefan 46
Wang, Si 19
Wang, Xiyu 20
Weir, Henry 43
Wigh, Daniel 39
Wong, Collin 34
Wong, Narumi 30
Wong, Shi Jinn 22
Wong, So-On 21
Wright, George 31
Xu, Jiaming 36
Xu, Weilun 41
Xu, Xiyue 18
Yeo, Mi Xia 56
Young, John 42
Zhang, Huimin 22
Zheng, Bowen 18
Zhu, Yixin 45

Supervisor Index

Linked to paper number

Adjiman, Claire S.	11
Cabral, Joao	51, 32
Campbell, Kyra	52
Chachuat, Benoit	14, 59
Chadwick, David	20
Chen, Rongjun	6, 16
DiMaggio, Pete	57
Duralliu, Arnold	35
Garbin, Valeria	4, 13
Guillén Gosálbez, Gonzalo	40
Guo, Miao	27, 60
Hallett, Jason	46
Hawkes, Adam	39, 3, 47
Heng, Jerry	58, 7, 22
Hellgardt, Klaus	28, 2, 33, 41
Huang, Yu	6
Jackson, George	41
Kelsall, Geoff	12
Kontoravdi, Cleo	61
Ladewig, Bradley	21, 30
Luckham, Paul	49, 17, 15
Magnini, Mirco	23
Markides, Christos	25, 50
Martin, Jeffrey	41
Matar, Omar K.	19, 44, 23, 55
Michels, Hans	56
Millan-Agorio, Marcos	43
Negro, Emanuela	41
Oram, Paul	59
Petit, Camille	37,29, 31
Rinaldi, Roberto	38, 48, 42
Saha, Saikat	4
Shah, Nilay	41, 18, 9, 53
Song, Qilei	36, 26,54
Tighe, Chris	34, 55
Trusler, J.P. Martin	5
Williams, Daryl	35, 24, 8
Xiao, Fu	41
Xu, Yun	10